



PHYSICAL CHEMISTRY 2012

¹¹th International Conference
on Fundamental and Applied Aspects of
Physical Chemistry

Under the auspices of the
University of Belgrade

Proceedings

The Conference is dedicated to
Professor Ivan Draganić

September 24-28, 2012
Belgrade, Serbia

ISBN 978-86-82475-27-9 <i>Volume 1</i> ISBN 978-86-82475-28-6 <i>Volume II</i>

Title: PHYSICAL CHEMISTRY 2012 (Proceedings)

Editors: S. Anić and Ž. Čupić

Published by: Society of Physical Chemists of Serbia, Studenski trg 12-16,
11158, Belgrade, Serbia

Publisher: Society of Physical Chemists of Serbia

For Publisher: S. Anić, President of Society of Physical Chemists of Serbia

Printed by: “Jovan” Printing and Publishing Company; 200 Copies;

Number of pages: 6+ 497; **Format:** B5; Printing finished in September
2012.

Text and Layout: “Jovan”

200- Copy printing

CONTENTS

Volume 1

Organizers	V
Committees	VI
Sponsors	VIII
Professor Ivan Draganić	IX
Plenary lectures	1
Chemical Thermodynamics	35
Spectroscopy, Molecular Structure, Physical Chemistry of Plasma	65
Kinetics, Catalysis	137
Nonlinear Dynamics	225
Electrochemistry	301
Biophysical Chemistry, Photochemistry, Radiation Chemistry	337
Radiochemistry, Nuclear Chemistry	
Material Science	415

Volume II

Solid State Physical Chemistry	505
Macromolecular Physical Chemistry	515
Environmental Protection	
Forensic Sciences Pharmaceutical Physical Chemistry	557
Phase Boundaries	667
Complex Compounds	681
General Physical Chemistry	707
Geophysical Chemistry	719
Education, History	731
Food Physical Chemistry	743
Free Topic	783
Index	791

ORGANIZERS

PHYSICAL CHEMISTRY 2012

*11th International Conference on
Fundamental and Applied Aspects of
Physical Chemistry*

*Under the auspices of the
University of Belgrade*

*Organized by
The Society of Physical Chemists of
Serbia*

*in co-operation
with*

Institute of Catalysis Bulgarian Academy of Sciences

*Boriskov Institute of Catalysis of Siberian Branch of the Russian Academy
of Sciences*

Faculty of Physical Chemistry, University of Belgrade, Serbia

*Institute of Chemistry Technology and Metallurgy,
University of Belgrade, Serbia*

Vinča Institute, University of Belgrade, Serbia

Institute of General and Physical Chemistry, Serbia

Faculty of Pharmacy, University of Belgrade, Serbia

COMMITTEES

International Organizing Committee

Chairman: S. Anić (Serbia)

Vice-chairmans: M. Gabrovska (Bulgaria)

V. A. Sadykov (Russia)

B. Adnadjević (Serbia)

Members: Z. Cherkezova-Zheleva (Bulgaria), N. Cvjetičanin (Serbia), S. N. Blagojević (Serbia), M. Daković (Serbia), T. Grozdić (Serbia), Lj. Ignjatović (Serbia), D. Jovanović (Serbia), N. Jović-Jovičić (Serbia), M. Kuzmanović (Serbia), D. Marković (Serbia), N. Kovačević (Serbia), J. Marković-Dimitrić (Serbia), B. Milosavljević (USA), Š. Miljanić (Serbia), N. Miljević (Serbia), A. Milutinović-Nikolić (Serbia), M. Mojović (Serbia), Z. Mojović, (Serbia), N. Ostrovski (Serbia), I. Pašti (Serbia), C. Pona (Italy), B. Simonović (Serbia), D. Stanisavljev (Serbia), B. Šljukić (Serbia), N. Vukelić (Serbia), V. Vukojević (Sweden)

International Scientific Committee

Chairman: Ž. Čupić (Serbia)

Vice-chairmans: V. N. Parmon (Russia)

S. Rakovsky (Bulgaria)

Members: A. Antić-Jovanović (Serbia), G. Bačić (Serbia), R. Cervellati (Italy), R. Compton (UK), V. Dondur (Serbia), Biljana Gaković (Serbia), V. Gaspar (Hungary), S. Gorodsky (Russia), V. Goussev (France), K. Hedrih (Serbia), Florou Heleny (Greece), M. Jeremić (Serbia), A. L. Kawczyński (Poland), Lj. Kolar-Anić (Serbia), V. Kuntić (Serbia), S. Mentus (Serbia), S. Milonjić (Serbia), Š. Miljanić (Serbia), Lj. Morozova-Roche (Sweden), P. Misaelides (Greece) M. Perić (Serbia), M. Plavšić (Serbia), V. Sadykov (Russia), G. Schmitz (Belgium), I. Schreiber (Czech), P. Sevcik (Slovakia), Natalia Skorodumova (Sweden), Dalimil Snita (Czech), N. Stepanov (Russia), D. Todorović (Serbia), M. Trtica (Serbia), V. Vasić (Serbia), D. Veselinović (Serbia), M. Zdujić (Serbia)

Local Executive Committee

Chairman: B. Adnadjević

Vice-chairman: S. Blagojević

Members: A. Abu Rabi-Stanković, P. Banković, N. Begović, J. Dostanić, A. Đerić, A. Ignjatović, A. Ivanović, A. Jović, D. Lončarević, J. Krstić, J. Maksimović, M. Milenković, S. Maćešić, V. Marković, B. Nedić, M. Petković, A. Popović-Bjelić, N. Potkonjak, D. Ranković, M. Stević, I. Stojković, M. Žunić

Honorary Committee

Nikola Hajdin,	President of Serbian Academy of Sciences and Arts
Branko Kovačević,	Rector of University of Belgrade
Radivoje Mitrović	Secretary of State for Education and Science
Vera Dondur	President of the Council for Scientific and Technological Development
Vladimir Bumbaširević	Dean of the Faculty of Medicine of University of Belgrade
Paula Putanov,	Member of Serbian Academy of Sciences and Arts
Momčilo Ristić,	Member of Serbian Academy of Sciences and Arts
Ankica Antić Jovanović,	Honorary President of Society of Physical Chemists of Serbia

SPONSORS

Ministry of Science and Technological Development

University of Belgrade, Belgrade

The Faculty of Physical Chemistry, University of Belgrade

Institute of Chemistry Technology and Metallurgy, University of Belgrade

Vinča Institute, University of Belgrade

Institute of General and Physical Chemistry, Belgrade

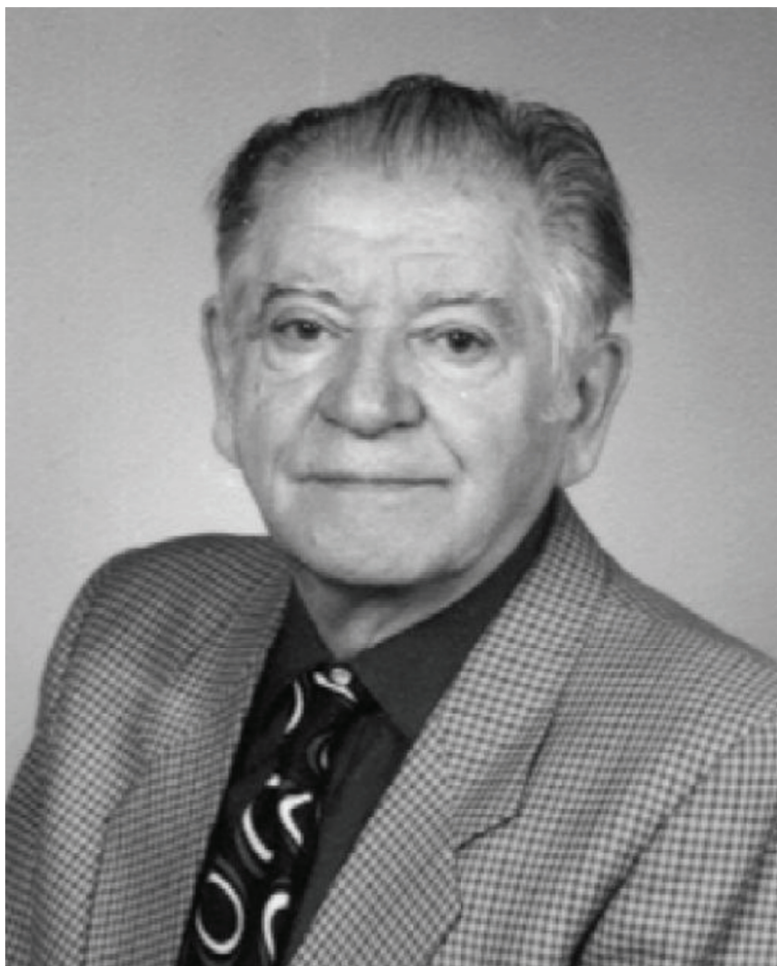
NovoLab, Belgrade

MOL, Belgrade

Gradski zavod za zaštitu zdravlja, Belgrade

Analysis DOO, Belgrade

Ivan G. Draganić¹ (1924-2012)



Ivan G. Draganić - Honorary member by the decision on the 7th annual Convention of the Society of Physical Chemists of Serbia, held on April 29, 1998.

Ivan G. Draganić was born in 1924 in Belgrade. He graduated in physical chemistry at the Faculty of Sciences in 1950, and received his doctorate at the Sorbonne in Paris in 1958. Since September 1949 until his retirement in 1981, he worked at the Institute of Nuclear Sciences - Vinča in all scientific positions. In the Institute, he founded a Group for Nuclear Contamination in 1950, and also the Department of Radiation Dosimetry in 1955, that was in 1960 transformed in the Laboratory of Radiation Chemistry. At the Department of Physical Chemistry, Faculty of Sciences, he organized the Radiochemical Practicum in 1956. For the Federal

¹ 15 years of Society of Physical Chemists of Serbia, Ankica Antić-Jovanović (ed.) Society of physical chemists of Serbia, Belgrade, 2005.

Commission for Nuclear Energy, he founded in Belgrade in 1958 the Center for Specialist Courses designed for users of radionuclides and radiation, popularly known as the "School of Isotopes". He was an author or a co-author of 18 books, of which we would like to mention: 1. "Introduction to radiochemistry" (Naučna knjiga, Belgrade, 1957); 2. "Radiochemical practicum: work with radioactive isotopes" in cooperation with O. Gal and M. Radotić (Naučna knjiga, Belgrade, 1959), intended for the participants of the courses in the Center, which the U.S. Atomic Energy Commission published in English in 1962; 3. "Radioactive isotopes and radiation" Vol. I-III, in three Editions (Naučna knjiga, Belgrade, 1962/3, 1968, 1981/3) used for the needs of the Center, and as an extra textbook in nuclear sciences in universities in Yugoslavia; 4. „The Radiation Chemistry of Water” with Z. Draganić (Academic Press, New York 1971), embodying the results of the study of chemical changes resulting from the effect of radiation on water and aqueous solutions; 5. „Radiation and Radioactivity on Earth and beyond” (CRC Press, USA), which gives a general view of radiation and radioactivity - the book has two U.S. editions (1990 and 1993), one Serbian (1991) and one in Japanese (1996).

As one of the pioneers in the field of radiation and radioactivity, he participated, by invitation, in writing the history of radiation chemistry, published by the Royal Chemical Society of Great Britain (Cambridge, 1989). He was one of thirty internationally recognized scientists, who were invited to celebrate the centenary from the discovery of radioactivity in their special issue of the journal *Radiochimica Acta* and a Monograph „One Hundred Years after the Discovery of Radioactivity” (Oldenburg Verlag, Munich, 1996).

By his research at the Institute Vinča (1970-1980's) and cooperation with colleagues in research centers in the United States, Denmark and Mexico, he drew attention to the role of ionizing radiation as a source of energy for the chemical evolution of the early Earth and the comet nuclei, which was also the subject of his introductory lecture „Radiation chemical Approaches to Chemical Evolution Processes on Earth and Beyond” at the International Conference on the Role of Radiation in the Origin and Evolution of Life, held in Osaka in 1998.

From 1952 until 2001, he actively participated in 29 domestic and 52 international scientific meetings. As a visiting scientist, he held seminars and specialized courses at research centres and universities in Denmark, Finland, France, Greece, Iran, India, Mexico, Poland, the USA, the USSR, and Thailand. He published 150 papers, including 107 in scientific journals, and 25 chapters in scientific publications. He was cited in the professional literature about 1500 times. He received The Seventh of July award for science from the Serbian Assembly (with Z. Draganić) and two Work Medals with the Golden Wreath.

He was a plenary lecturer at the 3rd Conference of the Society of Physical Chemists of Serbia with international participation „Physical Chemistry '96”, and a member of the Honorary Committee of the 5th and 6th International Conferences „Physical Chemistry 2000” and „Physical chemistry 2002”.

Editors

PLENARY LECTURES

PROBING ACOUSTICAL, OPTICAL AND ACOUSTO-OPTICAL PROPERTIES OF NANOSTRUCTURED MATERIALS BY PICOSECOND LASER ULTRASONICS

Vitalyi Gusev

LPEC, UMR-CNRS 6087, Université du Maine, av. O. Messiaen, 72085 Le Mans, France

Abstract

Research results on the characterisation of the thin (submicrometers thick) films of the nanostructured materials by the experimental methods of picosecond laser ultrasonics are reviewed. These methods make use of femtosecond lasers to generate and to detect GHz-THz acoustic waves. In this communication, theoretical backgrounds of the fs-laser-based opto-acousto-optic techniques that are used for the evaluation of the material properties are first introduced. Then the results of the experiments on nanoporous low- k films (for the microelectronics), on nanogranular sol-gel colloidal optical coatings (for laser optics), on anodized alumina (for the nanomaterial/nanostructure templates), on synthetic opals, on metallic nanoparticles super-crystals, and other nanostructured materials are discussed. The emerging opto-acousto-optic technology for the depth-profiling of acoustical, optical and acousto-optical properties of inhomogeneous transparent films and materials with the nanometers scale spatial resolution is also presented.

PL-2

CATALYTIC TRANSFORMATION OF FUELS INTO SYNGAS AND HYDROGEN AT SHORT CONTACT TIMES: KINETICS, MECHANISM AND FUNDAMENTALS OF CATALYSTS DESIGN

V. Sadykov, N. Mezentseva, E. Sadovskaya, A. Bobin
*Boreskov Institute of Catalysis, Novosibirsk State University, Novosibirsk,
630090, Russia*

Abstract

Main factors controlling performance of metal-supported doped ceria-zirconia catalysts of natural gas and biofuels transformation into syngas and hydrogen at short contact times are elucidated by using combination of structural, spectroscopic and unsteady-state kinetic methods. Realization of bifunctional mechanism with fuel molecules activation on metal sites, oxidants activation on oxide sites followed by the diffusion of oxygen-containing species to metal/support interface where they transform CH_xO_y species into syngas was reliably demonstrated, and kinetic parameters of basic stages were estimated. Strong metal-support interaction, specific defect structure and developed interfaces are crucial for high activity and coking stability of these catalysts. Monolithic catalysts comprised of optimized nanocomposites on heat-conducting substrates provide high and stable performance in transformation of a variety of fuel into syngas at short contact times.

Introduction

Design of catalysts able to efficiently transform natural gas/bio-gas/biofuels into syngas and hydrogen at short contact times in the intermediate temperature range at a small excess of oxidants (O_2 , CO_2 , H_2O) without coking is a vital task for hydrogen/renewable energy field and synfuels production [1]. A promising approach consists in synthesis of nanocomposites comprised of metal/alloy clusters supported on complex oxides with a high mobility/reactivity of the surface/lattice oxygen. Their tailor-made design requires elucidation of physico-chemical properties of such systems controlling their catalytic performance-real/defect structure, surface features and details of reaction mechanism as considered here for the case of Me-supported doped ceria-zirconia systems.

Results and discussion

As basic systems, nanocrystalline $\text{Ln-Ce-Zr-O}_{2.8}$ (Ln=La, Sm, Gd, Pr) oxides prepared via Pechini route and promoted with Pt, Ru, Ni, La(Pt,Ru)NiO_3 etc were used. The real structure of these systems was studied by TEM with EDX, neutron and X-ray diffraction, EXAFS, Raman, FTIRS of lattice modes; the surface properties were studied by XPS and FTIRS of adsorbed CO [2-4]. Oxygen bonding strength, mobility and reactivity were characterized by O_2 TPD, oxygen isotope exchange, microcalorimetry, isothermal and temperature-programmed

reduction by H₂ and CH₄ [4- 5]. Catalytic activity was studied in reactions of CH₄, ethanol and acetone partial oxidation, steam and dry reforming for both fractions and thin layers supported on ceramic single channels or metal substrates [6-8]. Rates and constants of separate steps were estimated by transient methods (pulse studies including TAP [8, 9], kinetic transients including SSITKA [5, 10]) with respective modeling.

Applied synthesis procedure produced single-phase oxides comprised of stacked nano-sized domains. The oxygen mobility was found to be controlled by rearrangement of coordination spheres of Ce (Zr) cations caused by association of dopants with oxygen vacancies; lattice expansion; segregation/clustering of dopants at interfaces, incorporation of supported metals as cationic species (Pt²⁺, etc) into the surface layers of oxides generating oxygen vacancies. Coefficients of oxygen diffusion along domain boundaries in Pr/ (Pr+Sm)-doped nanocrystalline Ce-Zr-O ($\sim 10^{-11}$ cm²/s at 600 °C) exceed by up to 3 order of magnitude those for diffusion within domains, the highest mobility provided by red-ox Pr^{3+/4+} dopant [8, 10]. Rate constants of the surface oxygen diffusion (>50 s⁻¹) are comparable with those of oxygen diffusion along interfaces (>10 cm⁻¹).

In partial oxidation of CH₄ (POM) on oxidized Pt/LnCeZrO catalysts, direct route of syngas generation was reliably established by transient studies [8-10]. This is explained by a high rate constant of step of selective oxidation of CH₄ into syngas by PtO ($k\sim 10^4$ s⁻¹ at 650 °C) equal to the rate of step of oxygen adsorption and exceeding much those for CH₄ combustion ($\sim 10^2$ s⁻¹) and CO and H₂ oxidation ($<3 \cdot 10^2$ s⁻¹). Hence, strong Pt-support interaction, which results in domination of Pt cationic forms, enhances the chemical reactivity of Pt towards CH₄ selective transformation into syngas and hampers its combustion activity. The same Pt species can be responsible for fast water-gas shift reaction ($>10^4$ s⁻¹) occurring via associative mechanism [10]. For CH₄ dry reforming, enhanced catalytic activity of oxidized Pt/PrCeZrO catalyst and slow kinetic transients were observed and modelled within the reaction scheme including participation of surface carbonates stabilized in coordination sphere of Pt cations in transformation of CH₄ molecules into syngas [11]. High oxygen mobility provides stabilization of partially oxidized Pt species in reaction conditions. The rate constants of CH₄ consumption estimated by SSITKA and TAP correlate with catalytic activity (Pt~LaNiO₃ <Ru < Ru+Ni), while constants of CO₂ transformation exceed those by an order of magnitude. The strength of oxygen bonding with the steady-state (ss) surface corresponds to bridging M₂O forms (heat of O₂ adsorption ~ 600 kJ/mol). CH₄ transformation in pulses fed to ss surface proceeds with the rate and products selectivities close to those in CO₂+CH₄ pulses without coke deposition until up to 30% of oxygen monolayer is removed. For Ni, Ni+Ru- supported catalysts, steady-state reaction of CH₄ dry reforming is described by a simple redox scheme with independent stages of CH₄ and CO₂ activation. This is provided by easy CO₂ dissociation on reduced oxide sites followed by a fast oxygen transfer along the surface/domain boundaries to metal particles where activated CH_x molecules are transformed to CO and H₂.

For the reactions of biofuels transformation into syngas, the oxygen mobility and reactivity in nanocrystalline complex oxides play decisive role due to much easier activation of oxygenates as compared with methane [7, 12].

Monolithic catalysts comprised of optimized nanocomposites supported on heat-conducting substrates (Fe-chraloy foil/gauze, Ni-Al foam substrate) were tested in partial oxidation/autothermal reforming of natural gas and liquid fuels (gasoline, diesel, ethanol, sunflower oil etc) in specially designed pilot reactors including those equipped with internal heat exchangers and unique evaporation/mixing units heated by electric current [6, 7, 11]. A high and stable performance was demonstrated with syngas yield close to equilibrium at space velocity of up to 25 m³/h of syngas per ~ 1 liter of reactor volume.

Conclusion

For metal-supported doped ceria-zirconia catalysts, their uniquely high and stable performance in transformation of a variety of fuels into syngas is ensured by high oxygen mobility and reactivity in nanocrystalline oxides and strong metal-support interaction stabilizing small reactive metal nanoparticles, affecting their reactivity and providing developed metal-support interface. Proper optimization of active component composition and preparation procedures as well as application of heat-conducting substrates provide highly efficient and stable structured catalysts successfully tested in pilot reactors at short contact times.

Acknowledgment

This work was supported by FP7 OCMOL Project and Russian Federal Innovation Agency.

References

- [1] D. A. Bulushev, J. R. H. Ross, *Catal. Today*, 2011, 171, 1-13.
- [2] V.A. Sadykov et al, *Solid State Phenomena*, 2007, 128, 81-88.
- [3] V. A. Sadykov et al, *Solid State Phenomena*, 2007, 128, 239-248.
- [4] I. V. A. Sadykov et al, in: *New Topics in Catalysis Research*, Nova Science Publishers, NY, USA, 2007, 97-19
- [5] C. Mirodatos, Y. Schuurman, A. C. van Veen, V. A. Sadykov, L. G. Pinaeva and E. M. Sadovskaya, *Stud. Surf. Sci. Catal.*, 2007, 167, 287-292
- [6] V. Sadykov, V. Parmon, J. R. H. Ross, C. Mirodatos et al, in: *Syngas: Production Methods, Post Treatment and Economics*, Nova Science Publishers, Inc., Hauppauge, NY, 2009, 53-140
- [7] V. Sadykov, N. Mezentseva, G. Alikina et al, in: *Nanocomposite Materials, Theory and Applications*, INTECH, Austria, Vienna, 2011, 909-946
- [8] V. Sadykov, V. Muzykantov, C. Mirodatos et al, *Catal. Today*, 2010, 157, 55–60
- [9] E. L. Gubanova, V. A. Sadykov et al, *React. Kinet. Catal. Lett.*, 2009, 97, 349–354
- [10] V. A. Sadykov et al, *Catal. Today*, 2011, 169, 125–137
- [11] V. A. Sadykov, C. Mirodatos et al, *Catal. Today*, 2011, 171, 140– 149
- [12] V. Sadykov et al, *Fuel*, 2010, 89, 1230–124

THE RADIOLOGICAL EVALUATION IN GREECE AFTER THE FUKUSHIMA ACCIDENT IN COMPARISON TO THE RESPECTIVE CHERNOBYL IMPACT ASSESSMENT

Florou H., Kritidis P., Evangeliou N.

*NCSR "D"/INRASTES/ERL
Aghia Paraskevi 15310, Athens, Greece
<http://www.ipta.demokritos.gr/erl/erl2005/erl.html>*

Abstract

The affected air masses by the radioactive plume emitted after the Fukushima accident, started on March 11, 2011, were transferred to various regions of the Northern hemisphere including Europe. Twenty five years ago this accident, the Chernobyl radiological impact on Greece changed the artificial background radioactivity and formed a new radiological status, with ^{137}Cs to remain as a main radionuclide to be concerned in terms of public and ecosystem health.

Based on the measured activity concentrations of ^{137}Cs , ^{134}Cs , ^{131}I in environmental components and consuming goods, we conclude that the radiological impact of the Fukushima nuclear accident in Greece was very low, especially as compared to that of the Chernobyl accident and also to that of natural radioactivity. These levels are usually 1-2 orders of magnitude lower than the lowest, which can be still considered as "radiologically significant". Therefore, a question of optimization arises, at least for scientific units, for which the radiation protection of the population is of highest priority. The optimization, besides the sampling parameters and supporting data, concerns mainly advances in measuring systems, which assure precision of results compatible with the very low radiological significance of the event.

Keywords: Radioactive pollution, Fukushima nuclear accident, Chernobyl nuclear accident, Radioactivity impact, Greece

ALTERNATING CURRENT ELECTRO-OSMOSIS

D. Snita, J. Hrdlicka

*Prague Institute of Chemical Technology, Department of Chemical Engineering,
CZ 16628 Prague 6, Czech Republic*

Abstract

Alternating current (AC) electro-osmosis represents the flow of a liquid electrolyte resulting from the Coulombic force in the electric double layer near electrolyte-metallic electrode surfaces. A single phase AC applied to a pair of symmetrical co-planar electrodes causes a flow pattern consisting of two counter rotating eddies with no net velocity. Non-zero net velocity can be observed in the case of non-symmetrical arrangement of co-planar electrodes or by the application of a traveling wave potential to an array of symmetrical electrodes. Results of mathematical modeling based on i) the Laplace-Stokes-Helmholtz-Smoluchowski-resistor-capacitor model and ii) the Poisson-Nernst-Planck-Navier-Stokes equations are presented. The effects of geometry, electrolyte composition, frequency and amplitude of AC driving on the performance (volumetric flow, applied back-pressure gradient and efficiency) are discussed.

Introduction

In electro-osmotic pumps, a part of the phase interfaces is charged, due to the presence of charged molecules at the interface or by the application of an external electric field. The charged surface (micro-channel wall or electrode surface) generates an electric field, which causes the migration of charged particles (ions) in the electrolyte. Oppositely charged ions (counter-ions) are attracted to the charged surface and generate secondary electric field, which weakens the external one. The ions with the same sign of charge as the charged surface (co-ions) are repelled, which further weakens the external electric field. The reorganization of the ions tends to eliminate the influence of the external electric field on the electrolyte bulk. The accumulation (or depletion) of ions near the interface triggers diffusion, which tends to eliminate deviations in fields of ionic concentrations. Also, in the case of a flowing electrolyte, the convection can influence the ionic concentrations and also the distribution of the electrical potential. In the resulting region near the interphase, the electro-neutrality is disturbed and the values of electric potential and ionic concentrations differ from those in the bulk electrolyte. These regions are called the electric double layers.

In a unit volume of the bulk electrolyte, the numbers of cations and anions are the same and the electric fields generated by the ions cancel each other. In other words, the mean electric charge density is zero. In the double layers, the number of counter-ions surpasses the number of co-ions and the unbalanced counter-ions, representing a non-zero charge density, generate an electric field, which acts against the external field.

The external field may have also a (tangential) component which acts along the surface, either generated by a set of electrodes placed in the inlet and outlet chambers or by a set of coplanar electrodes, which generate non-uniform electric fields. Charged particles in a non-uniform electric field experience the Coulomb force, which is a product of the electric charge (density) and the electric field intensity. The tangential component of the external field exerts the Coulomb force on the electric double layers, in which there is non-zero charge density, and drags them along the micro-channel walls. The moving electric double layers share the gained momentum with the bulk of electrolyte via viscous forces. This kind of fluid motion is called the electro-osmotic flow.

The electro-osmotic micro-pumps are powered by either direct or alternating electric current. In the direct current electro-osmotic pumps, the electric double layers form due to the difference in properties of the electrolyte and the micro-channel wall. The walls often involve charged molecules, which cause the polarization of an electrolyte. The potential difference, which results from the interaction of a particular material forming the micro-channel wall and an electrolyte, is called the zeta potential. The tangential component of electric field is provided by a pair of electrodes, one in the channel inlet, and the other in the outlet. In alternating current electro-osmotic pumps, a part of micro-channel wall is occupied by electrodes (which may or may not extend into the electrolyte). The electrodes are connected to a source of alternating current and form a coplanar array with a periodical structure. The coplanar arrangement of electrodes ensures both the formation of the electric double layer by the field component perpendicular to the channel wall and the actuation of the electro-osmotic flow by the tangential component.

The lecture is focused on the alternating current electro-osmotic pumps. To induce the electro-osmotic flow, the required Coulomb force necessitates the electric intensities to be of the order of 10^5 V/m and above. In case of the direct current alternative, the driving electrodes are often separated by several centimeters and the required voltage is in the order of kV. Power supplies able to provide such a voltage difference are not likely to be a part of autonomous devices integrated on a chip. The alternating current electro-osmotic pumps employ arrays of coplanar electrodes placed on (or embedded in) micro-channel walls. The required field strength may be achieved by small applied voltages, if the electrodes are close enough. For example, for an array of electrodes separated by one micrometer gaps, the voltage could be lower than one Volt. Such a voltage could be provided by a standard battery cell, which could be integrated on a chip. Of course, the fabrication of alternating current electro-osmotic pumps is a demanding process, compared to the direct current alternative.

Alternating current electro-osmotic pump

The simplest alternating current electro-osmotic pump is a pair of symmetric coplanar electrodes separated by a narrow gap [1]. Each electrode is subjected to an

alternating current; the phase shift between the driving fields is 180° . It has been theoretically predicted and experimentally proved, that such a system produces no net flow. The flow pattern consists of four counter-rotating rolls. The inherent symmetry causes that the forces acting on the electrolyte cancel each other and the average (net) velocity of the fluid flow is zero, the flow is non-directional. In order to transport the electrolyte, the symmetry of the system has to be broken.

The flow direction can be forced by introducing asymmetry into the electrode array or by using a directional driving. These two options are the base for two basic kinds of alternating current electro-osmotic pumps, the asymmetric [2] and traveling wave pumps [3]. The electrode arrays forming the alternating current electro-osmotic have a periodical structure and can be represented by a chain of repeating periodical segments. Under the assumption that the properties describing the alternating current electro-osmotic pump are periodical along the microchannel, the behavior and structure of such pumps can be shown and studied on just one periodical segment. The asymmetric pumps employ arrays consisting of pairs of narrow and wide electrodes separated by narrow inner gap (between the electrodes in one pair) and wide outer gap (between the pairs of electrodes). The electrolyte flows from the narrow electrodes to the wide electrodes. The traveling wave pumps consist of groups of n uniform electrodes separated by narrow gaps connected to an n -phase power supply. The phases powering the electrodes in the group are shifted by $360^\circ/n$. The electrodes in the periodic segment are charged consecutively, which generates a traveling wave potential. The traveling wave determines the direction of the fluid flow.

There are two approaches to the mathematical modeling of electro-osmotic flow [4], [5]. The creeping flow of monovalent, symmetric electrolyte is described by the local balances of ionic species, the Gauss law of electrostatics, the Navier-Stokes equation and the equation of continuity. The equations are coupled and have to be solved as one system, which we call the full model. The solution of the full model is quite demanding, which is the reason for the extensive use of simplified models. In the simplified models, the domain of electrolyte is formally divided into the bulk electrolyte and electric double layers. The behavior of the electric double layer is described using a substitute circuit and incorporated (collapsed) into a boundary condition. In the balances of ionic species, convection term is dropped, which allows the decomposition of the model into electrochemical and hydro-mechanical parts. In the bulk regions, the Gauss law of electrostatics in form of the Poisson equation is replaced by the Laplace equation. In the Navier-Stokes equation, the non-linear advection and the accumulation terms are neglected due to the extremely low values of the Reynolds number.

According to dimensional analysis of the governing equations, the performance of alternating current electro-osmotic micro-pumps inversely proportional to the micro-pump scale [6]. In the simplified mathematical models, the electrical double layer is assumed to be infinitely thin compared to the micro-channel height. To pump against reasonable back-pressures with decent flow rates, both electrode widths and micro-channel height have to be smaller than one micrometer. In sub-micrometer

scales, the channel height becomes comparable to the thickness of the double layer, which results in discrepancies between the simplified and full models [4]. Therefore, the simplified models, in their essence, are not suitable for the analysis of viable designs of alternating current electro-osmotic pump. The assumption of infinitely thin double layers simplifies the structure of the objects, which play a key role in the origin of the electro-osmotic flow. Although the full model provides more precise predictions, it also has several fundamental limitations.

Results and Discussion

We studied theoretically the performance of the electro-osmotic pump in the form of a prismatic channel consisting of n spatially periodical segments of coplanar electrodes on the bottom of the channel. Length of the periodical segments is L . Electrodes are driven by AC voltage

$$U(x,t) = A \sin\left(\frac{2\pi}{L}(x + v_0 t)\right).$$

Here $f = \frac{v_0}{L} = \frac{D}{\lambda_D L}$ is the frequency, $v_0 = \frac{D}{\lambda_D}$ is the phase shift velocity, A is the amplitude, x is the spatial coordinate, t is time, D is the ions diffusivity, $\lambda_D = \sqrt{\frac{\epsilon RT}{2c_0 F^2}}$ is the Debye length, c_0 is the molar concentration of ions in a uni-valent symmetrical electrolyte.

Length, width and height of the channel are $L_{ch} = nL$, W_{ch} , $H_{ch} = 0.5L$.

We studied effects of parameters $\frac{L}{\lambda_D} \in (10, 1000)$ and $A \frac{F}{RT} \in (0, 5)$ (

See the table 1). The examples of quantitative results are given at

$$L_{ch} = nL = 10 \text{ mm}, \quad W_{ch} = 1 \text{ mm}, \quad H_{ch} = 0.5L, \quad A = 5RT/F \doteq 125 \text{ mV}, \\ \lambda_D = 10 \text{ nm} \Leftrightarrow c_0 = 0.018 \text{ mol dm}^{-3}.$$

Table 1.

Segment length	L	100 nm	1 μm	10 μm	100 μm
Frequency	$f \approx L^{-1}$	1 MHz	100 kHz	10 kHz	1 kHz
Input power	$P_{in} \approx A^2 L^{-1}$	43 mW	4.3 mW	0.43 mW	43 μW
Output power	$P_{out} \approx A^4 L^{-3}$	2.6 mW	2.6 μW	2.6 nW	2.6 pW

PL-4

Efficiency	$\eta \approx A^2 L^{-2}$	6 %	0.06 %	6 ppm	60 ppb
Net flow velocity	$v \approx A^2 L^{-1}$	66 mm s ⁻¹	6.6 mm s ⁻¹	66 mm s ⁻¹	66 μm s ⁻¹
Volumetric flow	$\dot{V} \approx A^2$	330 μl/day 3.3 nl s ⁻¹			
Pressure gradient	$\frac{\Delta p}{L} \approx A^2 L^{-3}$	78 GPa m ⁻¹	78 MPa m ⁻¹	78 kPa m ⁻¹	78 Pa m ⁻¹
Pressure difference	$\Delta p \approx A^2 n L^{-2}$	780 MPa	780 kPa	780 Pa	0.78 Pa
Number of elements	$n = \frac{L_{ch}}{L}$	100,000	10,000	1000	100

Conclusions

Up to now published experimental observations were obtained at condition near to the last column of the Table 1. Such small pressure gradient makes experiments very difficult and inconclusive and disqualifies any practical use. Our analysis predicts that AC-electro-osmosis pumping is practically usable only in sub-micrometer scale.

References

- [1] A. Ajdari, Pumping liquids using asymmetric electrode arrays, *Physical Review E*, 2000, R45-R48.
- [2] A. Ramos, A. Gonzalez, A. Castellanos, N. G. Green and H. Morgan, Pumping of liquids with ac voltages applied to asymmetric pairs of microelectrodes, *Physical Review E*, 2003, 67, 056302.
- [3] B. P. Cahill, L. J. Heyderman, J. Gobrecht and A. Stemmer, Electro-osmotic streaming on application of traveling-wave electric fields, *Physical Review E*, 2004, 036305.
- [4] J. Hrdlicka, P. Cervenka, M. Pribyl and D. Snita, Mathematical modeling of AC electroosmosis in microfluidic and nanofluidic chips using equilibrium and non-equilibrium approaches,” *Journal of Applied Electrochemistry*, 2010, 40, 967-980.
- [5] A. Gonzalez, A. Ramos, N. G. Green, A. Castellanos and H. Morgan, Fluid flow induced by nonuniform ac electric fields in electrolytes on microelectrodes. II. A linear double-layer analysis, *Physical Review E*, 2000, 61(4), 4019-4028.
- [6] J. Hrdlička, P. Červenka, T. Jindra, M. Příbyl, D. Šnita, Mathematical modeling of traveling wave micropumps: Analysis of energy transformation, *IEEE Transactions on Industry Applications* 2011-EPC-248.R2 (accepted 2012).

DICTIONARY OF THE BASIC TERMS, METHODS AND PHENOMENA OF NONLINEAR DYNAMICS

Katica R. (Stevanović) Hedrih

*Mathematical Institute SANU, Department of Mechanics,
11 000-Belgrade, Kneza Mihaila 36/III,
and Faculty of Mechanical Engineering University of Niš, Serbia,
Priv. address: 18000- Niš, Serbia, ul. Vojvode Tankosića 3/22
e-mail: khedrih@eunet.rs*

Abstract

Nonlinear Dynamics reaches across the whole range of scientific research and study, and is applied in fields as diverse as mechanics, complete interdisciplinary area of physics, chemistry, physical chemistry, mechanical, electrical and civil engineering, technology, biology, biogenetics, economics and medicine. Phenomenological mapping and mathematical analogy is very important for transfer knowledge and new scientific research results from one area of science through other disparate area of sciences. For that reason is very important that scientists understand each other in use different key words and terms as well as notations in presenting new knowledge about nonlinear phenomena and new methods for investigation and research in different area of sciences. For understanding between researchers working in area of nonlinear dynamics and disparate area of nonlinear sciences is very important to have a dictionary of basic terms with properties descriptions as well as mathematical descriptions. In this lecture short list of main basic terms and nonlinear phenomena is presented. Basic terms of nonlinear dynamics are presented in the form of a general dictionary, containing main keywords with corresponding definitions and mathematical descriptions through presentation a number of dynamical system models as abstraction of real nonlinear dynamics.. Also, a number of the methods applied in nonlinear dynamics research are presented.

I. Introduction

Nonlinear Dynamics [1-29, 32, 34, 44, 55,-56, 58] reaches across the whole range of scientific research and study, and is applied in fields as diverse as mechanics, multidisciplinary area of physics, physical chemistry, chemistry, different area of mechanical, electrical and civil engineering, technology, biology, economics and medicine. It is possible to make a general conclusion that the study of nonlinear dynamics is one of the most active fields in modern science.

However, the mathematical language used to describe nonlinear dynamics and nonlinear phenomena, and the proliferation of new terminology, can make the use of nonlinear dynamics a daunting task to the researchers in different area of sciences as well as to the non-specialist.

Also, the simultaneous growth in the use new discoveries and knowledge of nonlinear dynamics across different scientific fields, and the cross-fertilization of ideas from different disciplines, mean that models of abstractions of different real systems, differential equations, names and methods used and developed in one field may be altered when “re-discovered” in a different context, making understanding the literature a difficult and time-consuming problem (see Refs. [45-46], [54] and [31]).

Our Dictionary of Nonlinear Dynamics addresses to the basic definitions, phenomena and methods on nonlinear dynamics. It presents, in non alphabetical list, but the key terms, nonlinear models abstractions of real nonlinear system dynamics, nonlinear differential equations, theorems and nonlinear phenomena which arise in the research and study of nonlinear dynamic states and processes.

Choused new nonlinear dynamic phenomena are mathematically described and explained with examples and, where appropriate, illustrations are included to aid clarification and understanding. The descriptions are self-contained, but should more detail be required, references are included for further reading.

This lecture titled Dictionary of the basic terms on Nonlinear Dynamics is focused to be an valuable reference source for all those participants who use nonlinear dynamics in their research and different area of sciences, whether they need help to understand the literature, or more experienced researchers who need a concise and handy references.

On the basic of current research results, we can conclude that the study of nonlinear dynamical systems is a quickly developing field of research in modern science. Starting from pioneering works in pure and applied mathematics and mechanics, it is now of great impact on many disciplines in natural sciences like physics, physical chemistry, chemistry, biology and engineering but also in medicine and social sciences like economy. For this lecture and to make a short Dictionary of Nonlinear Dynamics we follows basic idea to provides an explanation for many terms from the vocabulary used in textbooks on nonlinear dynamics as well as in original papers (see Refs. [1-29]). This dictionary contains not only the mathematical concepts and descriptions, but also terms from various, frequently investigated models as abstractions of real nonlinear dynamical systems. This makes the dictionary to a helpful source of information for everybody interested in nonlinear science.

The majority of the most studied models of nonlinear differential equations and different maps like the Lorenz system, the George Duffing oscillator, the logistic and circle maps are presented. Also, the majority of the most used methods for solving or to obtain approximation of the solutions as they are asymptotic Krilov-Bogolyubov-Mitropolyski method (see Refs. [35-43]), phase plane method, and theorems for investigation stability of the nonlinear dynamics are presented.

On the other hand, if the reader is interested in more details, he can look into the references in the large bibliography. This is especially recommended for newcomers in the field, who might need a textbook for further reading,

At the internet is possible to identify information of a publication [33] written by Tomasz Kapitaniak and Steven R. Bishop titled by: „The Illustrated Dictionary of Nonlinear Dynamics and Chaos“. I can recommend this publication for more information in considered area, then content of this lecture.

II. List of the basic keywords of nonlinear dynamics

Basic terms or *keywords* of nonlinear dynamics are: *dynamical system, phase space state, orbit or trajectory, phase portrait, flow, non-wandering set, Poincaré section and Poincaré map, Lyapunov exponents, Lyapunov spectrum and Lyapunov function.*

Dynamical system is possible to define as a part of the world which can be seen as a self-contained entity with some temporal behavior. Mathematically, a dynamical system is defined by its *state* and by its *dynamics*. Also, mathematically, a dynamical system is the system in a *state* with well defined *dynamics*. Hence, the main characteristic of a dynamical system is *dynamical state*.

In Figure 1.**a***, a models of a dynamical system with nonlinear dynamics in the form of a heavy mass particle moving along ideal circle line which rotate with constant angular velocity about skew positioned axis with respect to horizon (**a*1**) or about a vertical centric axis (**a*2**) or about a vertical eccentric axis (**a*3**) is presented. In Figure 1.**b*** the phase portrait of nonlinear dynamics of the model of dynamical system (**a*3**) of a heavy mass particle moving along ideal circle line which rotate with constant angular velocity about vertical eccentric axis is presented.

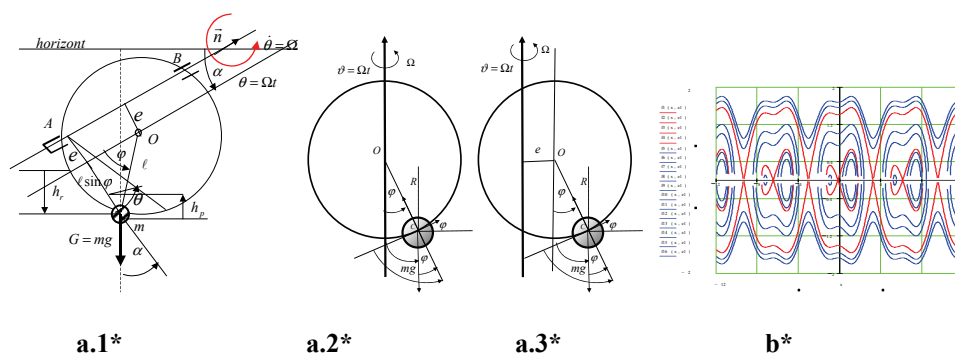


Figure 1. **a*** Models of a heavy mass particle moving along ideal circle line which rotate with constant angular velocity about skew positioned eccentrically axis with respect to horizon (**a*1**), or about a vertical centric axis (**a*2**) or about a vertical eccentric axis (**a*3**).

b* Phase portrait of nonlinear dynamics of the model (**a*3**) of a heavy mass particle moving along ideal circle line which rotate with constant angular velocity about vertical eccentric axis.

By introducing the following denotations

$$\dot{\theta} = \Omega, \quad \lambda = \frac{g \sin \alpha}{\ell \Omega^2} \quad \text{and} \quad \Omega_{rez}^2 = \frac{g \sin \alpha}{2\ell}, \quad (1)$$

for the model of a heavy mass particle moving along ideal circle line which rotate with constant angular velocity $\dot{\theta} = \Omega = const$ about skew positioned centrally ($e = 0$) axis with respect to horizon (Figure 1.a*1), we can write the following nonlinear differential equation expressed by generalized coordinate φ see Refs. [1] and [48-51]):

$$\ddot{\varphi} + \Omega^2(\lambda - \cos \varphi) \sin \varphi = \Omega^2 \lambda \operatorname{ctg} \alpha \cos \varphi \cos \Omega t \quad \text{for } e = 0 \quad (2)$$

Also for obtaining expression of a couple M_θ necessary to obtain constant angular velocity $\dot{\theta} = \Omega = const$ of circle rotation, we can obtain in the following form:

$$M_\theta = m\ell^2 \left\{ \frac{d}{dt} (\Omega \sin^2 \varphi) + \frac{g}{\ell} \sin \theta \cos \alpha \sin \varphi \right\} \quad (3)$$

For the model of a heavy mass particle moving along ideal circle line which rotate with constant angular velocity $\dot{\theta} = \Omega = const$ about vertical centrally ($e = 0$) axis (Figure 1.a*2), we can write the following nonlinear differential equation expressed by generalized coordinate φ :

$$\ddot{\varphi} + \Omega^2(\lambda - \cos \varphi) \sin \varphi = 0 \quad (4)$$

It is easy to obtain first integral of the nonlinear differential equation (4) in the following form:

$$\dot{\varphi}^2 = \dot{\varphi}_0^2 - 2\Omega^2 \left\langle -\lambda(\cos \varphi - \cos \varphi_0) + \frac{1}{4}(\cos 2\varphi - \cos 2\varphi_0) \right\rangle \quad (5)$$

where $\varphi_0 = \varphi(0)$ and $\dot{\varphi}_0 = \dot{\varphi}(0)$ are generalized angular coordinate and relative angular velocity at initial moment of the system dynamics.

For the model of a heavy mass particle moving along ideal circle line which rotate with constant angular velocity $\dot{\theta} = \Omega = const$ about vertical eccentrically ($e \neq 0$) axis (Figure 1.a*3), we can write the following nonlinear differential equation expressed by generalized coordinate φ :

$$\ddot{\varphi} + \Omega^2 \langle \lambda - \cos \varphi \rangle \sin \varphi - \Omega^2 \varepsilon \cos \varphi = 0 \quad (6)$$

It is easy to obtain first integral of the nonlinear differential equation (6) in the following form:

$$\dot{\varphi}^2 = \dot{\varphi}_0^2 - 2\Omega^2 \left\langle -\lambda(\cos \varphi_2 - \cos \varphi_{20}) + \frac{1}{4}(\cos 2\varphi_2 - \cos 2\varphi_{20}) \right\rangle - \Omega^2 \varepsilon (\sin \varphi_2 - \sin \varphi_{20}) \quad (7)$$

where $\varphi_0 = \varphi(0)$ and $\dot{\varphi}_0 = \dot{\varphi}(0)$ are generalized angular coordinate and relative angular velocity at initial moment of the system dynamics.

By use equation (7) for the series of the initial values of the $\varphi_0 = \varphi(0)$ and $\dot{\varphi}_0 = \dot{\varphi}(0)$ in Figure 1.b* series of the phase trajectories are presented building a phase portrait of nonlinear dynamics of the model (Figure 1. a*3) of a heavy mass

particle moving along ideal circle line which rotate with constant angular velocity $\dot{\theta} = \Omega = \text{const}$ about vertical eccentric ($e \neq 0$) axis.

Equations (5) and (7) represent corresponding equations of *phase trajectory* in the plane of generalized coordinate and its first derivative, $(\varphi, \dot{\varphi})$ for corresponding initial Nonlinear differential equations (4) and (6) no contain explicate time t and formally represent mathematical description of corresponding *autonomous dynamical system*, and differential equation (2) contain explicit time t and formally represent mathematical description of corresponding *no autonomous dynamical system*. In really all three nonlinear differential equations represent mathematical descriptions of the corresponding *rheonomic nonlinear system dynamics*, which is constrained by a *rheonomic constraint*. condition described by $\varphi_0 = \varphi(0)$ and $\dot{\varphi}_0 = \dot{\varphi}(0)$.

State of a dynamical system is defined by a number of generalized coordinates and their derivatives with respect to time including their initial values at the initial time. Stationary states of dynamical system, it is possible to define a* as a state of absolute equilibrium when system is in the equilibrium position or configuration and with zero all velocities or b* as a state of relative equilibrium positions and with zero relative velocities or general c* as a stationary state with constant some of kinetic parameters. Also, kinetic state of the system is possible to be no stationary or stationary. Mathematical description of the dynamical system state is possible to define by a vector which elements are generalized coordinates and their derivatives.

For previous considered examples state is defined by generalized angular coordinate φ correspond to relative position of the heavy mass particle on the rotate circle, and relative angular velocity $\dot{\varphi}$ on the circle. State of the model of a heavy mass particle moving along ideal circle line which rotate with constant angular velocity about skew positioned eccentrically axis with respect to horizon is defined by $(\varphi, \dot{\varphi})$.

In general, in spatially extended dynamical systems, the *state* is often a *field* (a scalar field or a vector field). Mathematically spoken, fields are functions with space coordinates as independent variables. The velocity field of a fluid is a well-known example.

Phase space is build by all possible states of the dynamical system. Each point in the phase space corresponds to a unique state.

In the case of the heavy mass particle motion along rotate circle line about vertical axis (Figure 1.b* and c*), the phase space has two dimensions whereas for the case that circle rotate around skew positioned axis according vertical, it has three dimensional phase space. The dimension of the phase space is infinite in cases where the system state is defined by a field.

Dynamics of a dynamical system is the causal relation between the present state of dynamical system and the next its state in the future. It is a *deterministic rule* which tells us what happens in the next time step of the state of dynamical

system. In the case of a **continuous time**, the time step of dynamical system state is infinitesimally small. Thus, the equation of motion is a **differential equation** or a system of differential equations.

Nonlinear dynamics of a dynamical system is the causal nonlinear relation between the present state of dynamical system and the next its state in the future. It is a *deterministic nonlinear rule* which tells us what happens in the next time step of the state of dynamical system. In the case of a **continuous time**, the time step of dynamical system state is infinitesimally small. Thus, the equation of motion is a **nonlinear differential equation** or a *system of nonlinear differential equations*.

The sets of points, in the phase space of a dynamical system, have the following properties:

- * All orbits starting from a point of this set come arbitrarily close and arbitrarily often to any point of the set.

- * Non-wandering sets contain singular attractors and come in *four variations*: fixed points, limit cycles, quasi periodic orbits and chaotic orbits.

The first three types (fixed points, limit cycles, quasi periodic orbits) can also occur in linear dynamics. *The fourth type appears only in nonlinear systems*, whose possibilities were first anticipated by the genius of *Henri Poincaré (1854-1912)*.

In the seventies, this irregular behaviour was termed deterministic chaos.

In the Poincaré map, limit cycles become fixed points.

A *non-wandering* set can be either stable or unstable. Changing a parameter of the system can *change the stability* of a non-wandering set. This is accompanied by a change of the number of non-wandering sets due to the *bifurcation*.

When three points are coupled in a trigger of coupled singularities, a homoclinic orbit in the form of number eight exists, as it is presented in Figure 1.b*.

Lyapunov exponents, *Lyapunov spectrum* and *Lyapunov function* are very important objects in theory of nonlinear dynamics.

While playing with the driven pendulum, for e.g., irregular sequences of left and right turns may be noticed. This behavior, called deterministic chaos, is the most prominent effect of nonlinear dynamics. The term "*deterministic chaos*" seems to be a contradiction in itself. How can something be *deterministic and chaotic* at the same time?

The key element of deterministic chaos is the *sensitive dependence* of the trajectory on the initial conditions. As an example, the plot on the first 15 seconds of a demonstration of this effect for a horizontally driven pendulum with two different initial conditions is characteristic. In the beginning, the distance of the trajectories increases on average exponentially (it is visible by the distance in phase space). The rate of divergence is measured by the largest Lyapunov exponent.

A quantitative measure of the sensitive dependence on the initial conditions is the Lyapunov exponent. It is the averaged rate of divergence (or convergence) of two neighboring trajectories. Actually, there is a whole spectrum

of *Lyapunov exponents*. Their number is equal to the dimension of the phase space. When speaking about the Lyapunov exponent, the largest one is meant. It is important because it determines the prediction horizon. Even qualitative predictions are impossible for a time interval beyond this horizon.

In mathematics, especially in stability theory, Lyapunov functions, named after Aleksandr Mikhailovich Lyapunov, are functions which can be used to prove the stability or Instability of the fixed points in dynamical systems and autonomous differential equations.

There is no general method to construct a Lyapunov function and the inability to find a Lyapunov function is inconclusive with respect to stability or instability. For physical systems, conservation laws can often be used to construct a *Lyapunov function*.



The memorial board devoted to memory of Academician A.M. Lyapunov.



Kharkov Polytechnic University 2007.

III. General functional (nonlinear, generalized) transformation of coordinates and functional nonlinear mappings.

Let consider two systems of variables q^i and \bar{q}^i , with *nonlinear relation* between them in the following forms: $\bar{q}^i = \bar{q}^i(q)$ or $q^i = q^i(\bar{q})$. These two relations are inverse first according second and opposite (see Refs. [48-53]). These relation satisfy condition that *functional determinants (Jacobians)* are different them zero:

$\bar{\mathbf{J}} = \left| \frac{\partial \bar{q}^i(q)}{\partial q^k} \right| \neq 0$, and also $\mathbf{J} = \left| \frac{\partial q^i(\bar{q})}{\partial \bar{q}^k} \right| \neq 0$. In the case that transformation is linear (*afine*)

these functional determinates are in the form: $\left| \frac{\partial x^j}{\partial y^i} \right| = |\mathbf{A}| = |a_i^j| = \text{const}$ and with constant

values, but in the case of functional, *nonlinear transformation* functional determinants (Jacobians) are nonlinear or linear functions of coordinates or variables q^i or \bar{q}^i . For the case of general, functional, nonlinear transformation we can write

$$d\bar{q}^i = \frac{\partial \bar{q}^i(q)}{\partial q^k} dq^k \quad \text{or} \quad dq^i = \frac{\partial q^i(\bar{q})}{\partial \bar{q}^k} d\bar{q}^k \quad (7)$$

It is necessary to point out that, in the case of *nonlinear mapping* straight lines are mapped in the corresponding curvilinear lines, and those only differential elements of curvilinear lines mapped by affine mapping.

It is known that a vector position of the mass particle (and also of geometrical, or kinetic point) is invariant, but in the case of nonlinear mapping,, affine mapping is right to applied only to the elementary parts of the vector position, $d\bar{r}(q)$, and that we can write:

$$d\bar{r}(q) = \frac{\partial \bar{r}(y(q))}{\partial q^k} dq^k = \frac{\partial y^i(q) \bar{e}_i}{\partial q^k} dq^k = \bar{g}_k dq^k, \quad i, j = 1, 2, 3, \dots, N \quad (8)$$

where

$$\bar{g}_k = \frac{\partial \bar{r}(y(q))}{\partial q^k} = \frac{\partial y^i(q)}{\partial q^k} \bar{e}_i, \quad i, j = 1, 2, 3, \dots, N \quad (9)$$

are basic vectors of the tangent space of a vector position $\bar{r}(q)$ of the mass particle (or of geometrical, or kinetic point) at the point $N(q)$, expressed by basic vectors \bar{e}_i of a affine fixed coordinate system.

IV. Linearization of nonlinear differential equation around singular points

Now, let consider special cases of the heavy material particle dynamics described by nonlinear differential equation (2) as a no autonomous system (see Refs. [4]). For beginning, we consider small oscillations around stable relative equilibrium positions of autonomous system described by nonlinear differential equation (4) and taking these singular point for no autonomous system described by nonlinear differential equation (2) for the cases: 1* $\lambda > 1$, $\varphi = 0$ and 2* $\lambda < 1$, $\varphi = \pm \arccos \lambda$.

1* For the case that $\lambda > 1$ we study small oscillations around stable relative equilibrium position $\varphi = 0$ by using corresponding linearization of the nonlinear differential equation (2) in the form of:

$$\ddot{\varphi} + \Omega^2(\lambda - 1)\varphi \approx \Omega^2 \lambda \text{ctg} \alpha \cos \Omega t \quad (10)$$

when, we take that approximations are: $\sin \varphi \approx \varphi + \dots$ and $\cos \varphi \approx 1 + \dots$. We can conclude that these small oscillations around $\varphi = 0$ for $\lambda > 1$ are simple forced two frequency oscillations with following frequencies: "own" frequency $\omega \approx \Omega \sqrt{\lambda - 1}$ and forced frequency Ω equal to constant angular velocity of the circle line rotation, and with amplitudes depending of initial conditions and of the forced excitation amplitude $\Omega^2 \lambda \text{ctg} \alpha$ in the function of the axis angle α to the horizon and square of angular velocity of the circle line rotation. We can conclude that in this case the resonance regime is possible when $\Omega = \Omega_{rez}$ and for $\lambda = 2$, than $\lambda > 1$,

and that angular velocity of the circle are critical. But, this conclusion is opposite with preposition that oscillations are with small amplitude. In that case linearization is not correct.

For nonresonant case, for approximate low of the heavy material particle small relative oscillations around relative stable equilibrium position $\varphi=0$ when $\lambda > 1$ we can write the following expression:

$$\varphi(t) \approx A \cos \Omega t \sqrt{\lambda-1} + B \sin \Omega t \sqrt{\lambda-1} + \frac{\lambda \operatorname{ctg} \alpha}{(\lambda-2)} \cos \Omega t \quad (11)$$

For resonant case, for approximate low of the heavy material particle small relative oscillations around relative stable equilibrium position $\varphi=0$ when Ω_{rez}^2 and $\lambda=2$, $\lambda > 1$, and for short period of the time, we can write the following expression:

$$\varphi(t) \approx \varphi_0 \cos \frac{\omega_0 t \sqrt{2}}{2} + \frac{\sqrt{2} \dot{\varphi}_0}{\omega_0} \sin \frac{\omega_0 t \sqrt{2}}{2} + \left[\frac{\omega_0 t \sqrt{2}}{2} \sin \frac{\omega_0 t \sqrt{2}}{2} \right] \operatorname{ctg} \alpha \quad (12)$$

where $\Omega_{rez}^2 = \frac{g \sin \alpha}{2\ell} = \frac{\omega_0^2}{2}$, $\omega_0^2 = \frac{g \sin \alpha}{\ell}$, $\lambda = \frac{\omega_0^2}{\Omega^2}$, $\lambda_{rez} = 2$.

2* For the case when $\lambda < 1$, we study small oscillations around stable relative equilibrium position $\varphi_s = \pm \arccos \lambda$ for applying corresponding linearization of the differential equation, we write the following form of equation:

$$\ddot{\varphi} + \Omega^2 [\lambda - \cos(\varphi_s + \varphi)] \sin(\varphi_s + \varphi) = \Omega^2 \lambda \operatorname{ctg} \alpha \cos(\varphi_s + \varphi) \cos \Omega t \quad (13)$$

where we make change of the generalized coordinate φ by following $\varphi_s + \varphi$. After linearization, we obtain the following linearized equation:

$$\ddot{\varphi} + \Omega^2 (1 - \lambda^2) \left[1 + \frac{\lambda \operatorname{ctg} \alpha}{\sqrt{1 - \lambda^2}} \cos \Omega t \right] \varphi \approx \Omega^2 \lambda \operatorname{ctg} \alpha \cos \Omega t \quad (14)$$

This linearized equation is *Mathieu-Hill type*. From this linearized differential equation, we can conclude that these small oscillations around $\varphi_s = \pm \arccos \lambda$ for $\lambda < 1$ are not simple forced two frequency oscillations, but are type of the *Mathieu parametric and forced oscillations*. In this case we can pointed out possibilities of the appearance of the parametric resonance. In the first linearized approximation, around relative equilibrium position $\varphi_s = \pm \arccos \lambda$ for $\lambda < 1$ small oscillations are described by Mathieu's oscillator in the form of the following equation:

$$\frac{d^2 \varphi}{d\tau^2} + (\tilde{\lambda} + \tilde{\gamma} \cos \tau) \varphi = h \cos \tau \quad (15)$$

with circular frequency and parameters:

$\omega = \Omega \sqrt{1 - \lambda^2}$, $\tilde{\lambda} = 1 - \lambda^2$ i $\tilde{\gamma} = \lambda \sqrt{1 - \lambda^2} \operatorname{ctg} \alpha = h \sqrt{\tilde{\lambda}}$, $\tau = \Omega t$, and external forced excitation amplitude $h = \lambda \operatorname{ctg} \alpha$ and frequency equal to the angular velocity of the rotation of the circle.

For general solution *Mathieu's differential equation* see Ref. [34] or *Floquet, Annales de l'Ecole Normale*, 1883. On the basis of these references we can write $\varphi(t) = A e^{\mu t} p_1(t) + B e^{-\mu t} p_2(t)$, where A and B are integral constants; μ is

characteristic exponent and $p_i(t), i=1,2$ are periodic functions with period 2π depending of parameters: $\tilde{\lambda}$ i $\tilde{\gamma}$. Main and principal problem is investigation of the stability of solutions (see Refs. [52-53]). By Ince and Strutt (see Refs. [30] and [55]), the domains of the stability and unstability graphically are presented in the form of *Ince-Strutt's stability cart* for different values of the parameters $\tilde{\lambda}$ and $\tilde{\gamma}$.

V. Linear and nonlinear approximation of nonlinear differential equation around singular points

Let's consider properties of the nonlinear dynamics a heavy mass particle motion by coupled rotations around two no intersecting axes of which one is fixed vertically or skew positioned un relation to vertical as it is presented for two cases in Figure 2.a* and b*.

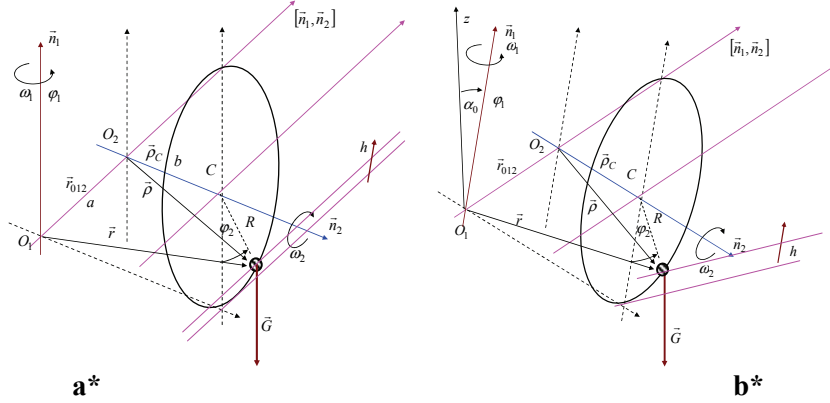


Figure 2. Motion of a heavy mass particle by coupled rotations around two no intersecting axes of which one is fixed vertically (a*) or skew (b*) positioned in relation to vertical.

This model of dynamical system (Figure 2.a* and b*) is rheonomic and with two degrees of mobility and one degree of freedom, when one component angular velocity $\vec{\omega}_1 = \Omega \vec{n}_1 = \text{const}$ and second is unknown $\vec{\omega}_2 = \dot{\varphi}_2 \vec{n}_2$. Nonlinear differential equation for describing dynamical equilibrium for the model in Figure 2.a* is in the form (6) and with equation of phase trajectory in the form (7).

For obtaining *stationary points* we compose the following conditions:

$$\frac{d\varphi_2}{dt} = v = 0 \tag{16}$$

$$\frac{dv}{dt} = -\Omega^2 \langle \lambda - \cos \varphi_2 \rangle \sin \varphi_2 + \Omega^2 \varepsilon \cos \varphi_2 = 0$$

and also from which follows:

$$f(\lambda_s) = \lambda_s^4 - 2\lambda\lambda_s^3 + \langle \lambda^2 + \varepsilon - 1 \rangle \lambda_s^2 + 2\lambda\lambda_s - \lambda^2 = 0 \tag{17}$$

From previous nonlinear characteristic equation is possible to find four roots λ_s , $s=1,2,3,4$, $\lambda_s = \cos \varphi_s$ and corresponding sets of characteristic numbers: $\varphi_s = \arccos \lambda_s$, $s=1,2,3,4$, for $\lambda_s < 1$, and $v_s = 0$, numerically.

After obtaining singular (stationary) points $(\varphi_s, v_s = \dot{\varphi}_s)$ by numerical solving nonlinear equation (17), we can build linear or nonlinear approximation of the nonlinear differential equation around singular points $(\varphi_s, v_s = \dot{\varphi}_s)$, depending of necessary precisions.

Let's consider approximation of the system of nonlinear ordinary differential equation (16) taking its corresponding general form:

$$\frac{d\varphi}{dt} = f(\varphi, v) ; \quad \frac{dv}{dt} = f_1(\varphi, v) \quad (18)$$

around its stationary – singular points $N_s(\varphi_s, v_s)$ $s=1,2,3,4\dots$ or for $\varphi = \varphi_s$, $v = v_s$ obtained numerically by roots of nonlinear equation (16) or (17).

First, we write *linear approximation* of the dynamical system of nonlinear differential equation (18) around singular points $N_s(\varphi_s, v_s)$, $s=1,2,3,4\dots$ or for $\varphi = \varphi_s$, $v = v_s$ in the following form:

$$\begin{aligned} \frac{d\varphi}{dt} &= \left(\frac{\partial f(\varphi, v)}{\partial \varphi} \right) \Big|_{\substack{\varphi=\varphi_s \\ v=v_s}} \varphi + \left(\frac{\partial f(\varphi, v)}{\partial v} \right) \Big|_{\substack{\varphi=\varphi_s \\ v=v_s}} v \\ \frac{dv}{dt} &= \left(\frac{\partial f_1(\varphi, v)}{\partial \varphi} \right) \Big|_{\substack{\varphi=\varphi_s \\ v=v_s}} \varphi + \left(\frac{\partial f_1(\varphi, v)}{\partial v} \right) \Big|_{\substack{\varphi=\varphi_s \\ v=v_s}} v \end{aligned} \quad (19)$$

in which now coordinate φ and $v = \dot{\varphi}$ are with start in the digular point $N_s(\varphi_s, v_s)$.

Second, if our intention is to make a *nonlinear approximation* of the system of nonlinear differential equation (18) around singular points $N_s(\varphi_s, v_s)$, $s=1,2,3,4\dots$ or for $\varphi = \varphi_s$, $v = v_s$, then nonlinear approximation is in the following form:

$$\begin{aligned} \frac{d\varphi}{dt} &= \left(\frac{\partial f(\varphi, v)}{\partial \varphi} \right) \Big|_{\substack{\varphi=\varphi_s \\ v=v_s}} \varphi + \left(\frac{\partial f(\varphi, v)}{\partial v} \right) \Big|_{\substack{\varphi=\varphi_s \\ v=v_s}} v + \frac{1}{2!} \left(\frac{\partial^2 f(\varphi, v)}{\partial \varphi^2} \right) \Big|_{\substack{\varphi=\varphi_s \\ v=v_s}} \varphi^2 + \frac{1}{2!} \left(\frac{\partial^2 f(\varphi, v)}{\partial v^2} \right) \Big|_{\substack{\varphi=\varphi_s \\ v=v_s}} v^2 + 2 \frac{1}{2!} \left(\frac{\partial^2 f(\varphi, v)}{\partial v \partial \varphi} \right) \Big|_{\substack{\varphi=\varphi_s \\ v=v_s}} \varphi v + \\ &+ \frac{1}{3!} \left[\left(\frac{\partial^3 f(\varphi, v)}{\partial \varphi^3} \right) \Big|_{\substack{\varphi=\varphi_s \\ v=v_s}} \varphi^3 + 3 \left(\frac{\partial^3 f(\varphi, v)}{\partial \varphi^2 \partial v} \right) \Big|_{\substack{\varphi=\varphi_s \\ v=v_s}} \varphi^2 v + 3 \left(\frac{\partial^3 f(\varphi, v)}{\partial \varphi \partial v^2} \right) \Big|_{\substack{\varphi=\varphi_s \\ v=v_s}} \varphi v^2 + \left(\frac{\partial^3 f(\varphi, v)}{\partial v^3} \right) \Big|_{\substack{\varphi=\varphi_s \\ v=v_s}} v^3 \right] + \dots \\ \frac{dv}{dt} &= \left(\frac{\partial f_1(\varphi, v)}{\partial \varphi} \right) \Big|_{\substack{\varphi=\varphi_s \\ v=v_s}} \varphi + \left(\frac{\partial f_1(\varphi, v)}{\partial v} \right) \Big|_{\substack{\varphi=\varphi_s \\ v=v_s}} v + \left(\frac{\partial^2 f_1(\varphi, v)}{\partial \varphi^2} \right) \Big|_{\substack{\varphi=\varphi_s \\ v=v_s}} \varphi^2 + \left(\frac{\partial^2 f_1(\varphi, v)}{\partial v^2} \right) \Big|_{\substack{\varphi=\varphi_s \\ v=v_s}} v^2 + 2 \frac{1}{2!} \left(\frac{\partial^2 f_1(\varphi, v)}{\partial v \partial \varphi} \right) \Big|_{\substack{\varphi=\varphi_s \\ v=v_s}} \varphi v + \\ &+ \frac{1}{3!} \left[\left(\frac{\partial^3 f_1(\varphi, v)}{\partial \varphi^3} \right) \Big|_{\substack{\varphi=\varphi_s \\ v=v_s}} \varphi^3 + 3 \left(\frac{\partial^3 f_1(\varphi, v)}{\partial \varphi^2 \partial v} \right) \Big|_{\substack{\varphi=\varphi_s \\ v=v_s}} \varphi^2 v + 3 \left(\frac{\partial^3 f_1(\varphi, v)}{\partial \varphi \partial v^2} \right) \Big|_{\substack{\varphi=\varphi_s \\ v=v_s}} \varphi v^2 + \left(\frac{\partial^3 f_1(\varphi, v)}{\partial v^3} \right) \Big|_{\substack{\varphi=\varphi_s \\ v=v_s}} v^3 \right] + \dots \end{aligned} \quad (20)$$

in which now coordinate φ and $v = \dot{\varphi}$ are with start in the digular point $N_s(\varphi_s, v_s)$. Previous nonlinear approximation is obtained by use development of the nonlinear functions of two variable into *Taylor's series* around point $N_s(\varphi_s, v_s)$.

Open is a question: What is reason for linear or for nonlinear approximation around singular points?

Reason and answer is that these approximations around singular poit are power and simples tools for investigation stability or no stabilityas well as properties of dynamical system dynamics around singular poitsa, and followed present nonlinear dynamics properties around singular points.

By use linear approximation (19), applied to the nonlinear differential equation (6) around singular point $N_s(\varphi_s, v_s)$, it is possible to obtain its linear approximation in the following form:

$$\begin{aligned} \frac{d\varphi_2}{dt} &= v \\ \frac{dv}{dt} &= -\Omega^2 \left\langle \left\langle \lambda\lambda_s - 2\lambda_s^2 + 1 \right\rangle + \varepsilon\sqrt{1-\lambda_s^2} \right\rangle \varphi \end{aligned} \quad (21)$$

or in the form of one ordinary linear differential equation second order:

$$\frac{d^2\varphi}{dt^2} + \Omega^2 \left\langle \left\langle \lambda\lambda_s - 2\lambda_s^2 + 1 \right\rangle + \varepsilon\sqrt{1-\lambda_s^2} \right\rangle \varphi = 0 \quad (23)$$

in which now coordinate φ and $v = \dot{\varphi}$ are with start in the digular point $N_s(\varphi_s, v_s)$.

Circular frequency of the free small linearized vibrations around singular point is in the following form:

$$\omega_{0,lin} = \Omega \sqrt{\left\langle \left\langle \lambda\lambda_s - 2\lambda_s^2 + 1 \right\rangle + \varepsilon\sqrt{1-\lambda_s^2} \right\rangle} \quad (24)$$

for $\lambda = \frac{g}{R\Omega^2}$ $\varepsilon = \frac{r_{012}}{R}$, and for $\lambda_s = \cos\varphi_s$, $\lambda_s < 1$.

By use nonlinear approximation (20), applied to the nonlinear differential equation (6) around singular point $N_s(\varphi_s, v_s)$, it is possible to obtain its nonlinear approximation in the following form:

$$\begin{aligned} \frac{d\varphi_2}{dt} &= v \\ \frac{dv}{dt} &= -\Omega^2 \left\langle \left\langle \frac{g}{R\Omega^2}\lambda_s - 2\lambda_s^2 + 1 \right\rangle + \frac{r_{012}}{R}\sqrt{1-\lambda_s^2} \right\rangle \varphi + \Omega^2 \left\langle \left\langle \frac{g}{R\Omega^2}\sqrt{1-\lambda_s^2} - 4\lambda_s\sqrt{1-\lambda_s^2} \right\rangle - \frac{r_{012}}{R}\lambda_s \right\rangle \varphi^2 \\ &+ \frac{\Omega^2}{3!} \left\langle \left\langle \frac{g}{R\Omega^2}\lambda_s - 8\lambda_s^2 + 4 \right\rangle + \frac{r_{012}}{R}\sqrt{1-\lambda_s^2} \right\rangle \varphi^3 + \dots \end{aligned} \quad (25)$$

or in the form of nonlinear approximation of one ordinary nonlinear differential equation second order:

$$\begin{aligned} \frac{d^2\varphi}{dt^2} + \Omega^2 \left\langle \left\langle \frac{g}{R\Omega^2}\lambda_s - 2\lambda_s^2 + 1 \right\rangle + \frac{r_{012}}{R}\sqrt{1-\lambda_s^2} \right\rangle \varphi - \Omega^2 \left\langle \left\langle \frac{g}{R\Omega^2}\sqrt{1-\lambda_s^2} - 4\lambda_s\sqrt{1-\lambda_s^2} \right\rangle - \frac{r_{012}}{R}\lambda_s \right\rangle \varphi^2 - \\ - \frac{\Omega^2}{3!} \left\langle \left\langle \frac{g}{R\Omega^2}\lambda_s - 8\lambda_s^2 + 4 \right\rangle + \frac{r_{012}}{R}\sqrt{1-\lambda_s^2} \right\rangle \varphi^3 + \dots = 0 \end{aligned} \quad (26)$$

in which now coordinate φ and $v = \dot{\varphi}$ are with start in the singular point $N_s(\varphi_s, v_s)$

By use the denotations of the coefficients in nonlinear approximation of the differential equation (26) in the following forms:

$$\begin{aligned}\omega_{0,lin}^2 &= \Omega^2 \left\langle \left\langle \frac{g}{R\Omega^2} \lambda_s - 2\lambda_s^2 + 1 \right\rangle + \frac{r_{012}}{R} \sqrt{1 - \lambda_s^2} \right\rangle \\ \kappa_2 &= \Omega^2 \left\langle \left\langle \frac{g}{R\Omega^2} \sqrt{1 - \lambda_s^2} - 4\lambda_s \sqrt{1 - \lambda_s^2} \right\rangle - \frac{r_{012}}{R} \lambda_s \right\rangle \\ \kappa_3 &= \frac{\Omega^2}{3!} \left\langle \left\langle \frac{g}{R\Omega^2} \lambda_s - 8\lambda_s^2 + 4 \right\rangle + \frac{r_{012}}{R} \sqrt{1 - \lambda_s^2} \right\rangle\end{aligned}\quad (27)$$

this previous nonlinear differential equation (26) is possible to rewrite in the following form:

$$\ddot{\varphi} + \omega_{0,lin}^2 \varphi = \kappa_2 \varphi^2 + \kappa_3 \varphi^3 \quad (28)$$

VI. Asymptotic approximation of the solution of a nonlinear approximation of the nonlinear differential equation around singular point

In this part we pay our attention to the application of the *Krilov-Bogolyubov-Mitropolyski asymptotic method* (see References. [35-43]) for obtaining first asymptotic approximation of the solution of nonlinear approximation of nonlinear differential equation in the form (28) around stable singular point $N_s(\varphi_s, v_s)$, $s = 1, 2, 3, 4, \dots$ for $\varphi = \varphi_s$, $v = v_s$.

First asymptotic approximation of the solution of nonlinear differential equation in the form (28) we take in the following form:

$$\varphi(t) = a(t) \cos \Phi(t) \quad (29)$$

in which amplitude $a(t)$ and full phase $\Phi(t) = \omega_{0,lin} t + \phi(t)$, or difference of phase $\phi(t)$ is function of the time defined by system of *the nonlinear differential equations along amplitude $a(t)$ and phase $\phi(t)$ in first approximation* in the following form:

$$\dot{a}(t) = 0, \quad \dot{\phi}(t) = \frac{3\kappa_3}{8\omega_0} [a(t)]^2 \quad (30)$$

or in the form:

$$\dot{a}(t) = 0, \quad \dot{\phi}(t) = \frac{\Omega \left\langle \left\langle \frac{g}{R\Omega^2} \lambda_s - 8\lambda_s^2 + 4 \right\rangle + \frac{r_{012}}{R} \sqrt{1 - \lambda_s^2} \right\rangle}{16 \sqrt{\left\langle \left\langle \frac{g}{R\Omega^2} \lambda_s - 2\lambda_s^2 + 1 \right\rangle + \frac{r_{012}}{R} \sqrt{1 - \lambda_s^2} \right\rangle}} a_0^2 \quad (31)$$

After integrating of the previous system (31) for amplitude $a(t)$ and difference of phase $\phi(t)$, we obtain the following expressions:

$$a(t) = a_0 = const,$$

$$\phi(t) = \frac{\Omega \left\langle \left\langle \frac{g}{R\Omega^2} \lambda_s - 8\lambda_s^2 + 4 \right\rangle + \frac{r_{012}}{R} \sqrt{1-\lambda_s^2} \right\rangle}{16 \sqrt{\left\langle \left\langle \frac{g}{R\Omega^2} \lambda_s - 2\lambda_s^2 + 1 \right\rangle + \frac{r_{012}}{R} \sqrt{1-\lambda_s^2} \right\rangle}} [a(t)]^2 t + \phi(0) \quad (32)$$

We can see that amplitude $a(t)$ in first asymptotic approximation is constant and equal to initial value a_0 , and that difference of phase $\phi(t)$ is linear function of time and square function of initial value of amplitude a_0 .

Full phase $\Phi(t) = \omega_{0,lin} t + \phi(t)$ in first asymptotic approximation is defined by following expression:

$$\Phi(t) = \left\langle \Omega \sqrt{\left\langle \left\langle \frac{g}{R\Omega^2} \lambda_s - 2\lambda_s^2 + 1 \right\rangle + \frac{r_{012}}{R} \sqrt{1-\lambda_s^2} \right\rangle} + \frac{\Omega \left\langle \left\langle \frac{g}{R\Omega^2} \lambda_s - 8\lambda_s^2 + 4 \right\rangle + \frac{r_{012}}{R} \sqrt{1-\lambda_s^2} \right\rangle}{16 \sqrt{\left\langle \left\langle \frac{g}{R\Omega^2} \lambda_s - 2\lambda_s^2 + 1 \right\rangle + \frac{r_{012}}{R} \sqrt{1-\lambda_s^2} \right\rangle}} [a(t)]^2 \right\rangle t + \phi(0) \quad (33)$$

Circular frequency of the free nonlinear free vibrations in first asymptotic approximation is defined by following expression:

$$\omega_{nel} = \Omega \sqrt{\left\langle \left\langle \frac{g}{R\Omega^2} \lambda_s - 2\lambda_s^2 + 1 \right\rangle + \frac{r_{012}}{R} \sqrt{1-\lambda_s^2} \right\rangle} \left\{ 1 + \frac{\left\langle \left\langle \frac{g}{R\Omega^2} \lambda_s - 8\lambda_s^2 + 4 \right\rangle + \frac{r_{012}}{R} \sqrt{1-\lambda_s^2} \right\rangle}{16 \sqrt{\left\langle \left\langle \frac{g}{R\Omega^2} \lambda_s - 2\lambda_s^2 + 1 \right\rangle + \frac{r_{012}}{R} \sqrt{1-\lambda_s^2} \right\rangle}} a_0^2 \right\} \quad (34)$$

and is quadratic function of initial value a_0 of amplitude in first asymptotic approximation. We can see that nonlinear vibration around stable singular point is no isochrous and depend of initial value of amplitude.

VII. Concluding remarks

In previous parts, we present numerous terms and keywords of nonlinear dynamics theory through examples of nonlinear dynamical systems- abstractions of real system dynamics to the models. Also, numerous keywords from theory of nonlinear dynamics are not included in this lecture for the reason that, paper and lecture is bounded by time and by pages.

In Figure 3, 4, 5, 6 and 7 numerous graphical presentation of the different properties of nonlinear dynamics of different dynamical systems, and also some ideas concerning phenomenological mappings of phenomena through disparate nature of nonlinear dynamics.

In concluding remarks we can make a short list of these as it is:

***Poincaré section** and **Poincaré map** is possible to obtain as sections between a carefully chosen (curved) plane in the phase space that is crossed by almost all orbits. Poincaré section is a tool developed by Henri Poincaré (1854-1912) [47] for a visualization of the flow of phase trajectories in a phase space of more than two dimensions. The Poincaré section has one dimension less than the phase space. The Poincaré map maps the points of the Poincaré section onto itself (see Figure 4). A Poincaré map turns a continuous dynamical system into a discrete one.

***An attractor** of a dynamical system is a subset of the state space to which orbits originating from typical initial conditions tend as time increases. Nonlinear dynamical system usually has more than one attractor.

* **Basin of attraction** of one attractor in a dynamical system is the set of initial conditions leading to long-time behavior that approaches that attractor. Thus the qualitative behavior of the long-time motion of a given nonlinear dynamical system can be fundamentally different depending on which basin of attraction the initial condition lies in. Depending of initial conditions taken from a basin of attraction of an attractor between other of nonlinear dynamical system is possible to initiate different regimes of nonlinear dynamics as it is: e.g., attractors can correspond to periodic oscillatory dynamics, quasiperiodic motion or chaotic behaviors of different types. (see Refs. [35-43]).

At end, we can point out the following questions: What is linear dynamics? What is nonlinear dynamics? This is two principal questions.

If we have dynamical system with one degree of freedom, we can conclude, that system is linear in the case when system posses one equilibrium position, stable on no stable and when its dynamics is described by one linear differential equation along generalized independent coordinate. In mathematical description, the system possesses only one singular point.

If we have dynamical system with one degree of freedom, we can conclude, that system is nonlinear in the case when system posses more them one equilibrium position, stable on no stable and when its dynamics is described by one nonlinear linear differential equation along generalized independent coordinate. In mathematical description, the system possess more them one singular point. In nonlinear system, more them one atractor exists, and also stable and no stable, with corresponding basin of attractions or basin of rejections.

If we have dynamical system with many degrees of freedom, we can conclude that this system is linear when it posses one equilibrium position or one equilibrium configuration, and its dynamic state is described by system of linear differential equations along corresponding number of independent generalized coordinates.

If we have dynamical system with many degrees of freedom, we can conclude that this system is nonlinear when it posses more then one equilibrium position or more then one equilibrium configuration, and its dynamic states are described by system of nonlinear differential equations along corresponding number of independent generalized coordinates. In mathematical description, the system possess more them one singular point.

Dynamics of nonlinear dynamical systems is very sensitive and dependent of initial conditions and external excitations. Then, depending of initial conditions system can change character of nonlinear dynamics and passing through transient kinetic state to remove from area of attraction of the one equilibrium state to the area of other equilibrium state. With this we can conclude that self-organization is one of main nonlinear phenomena in nonlinear system dynamics.

Self-organizational structures are known in as a results in nonlinear dynamics of physical - chemical nonlinear dynamical processes (see Ref. [34]).

In nonlinear dynamical systems, nonlinear phenomena is bifurcation of the equilibrium position and appearance one or more them one trigger of coupled singularities.

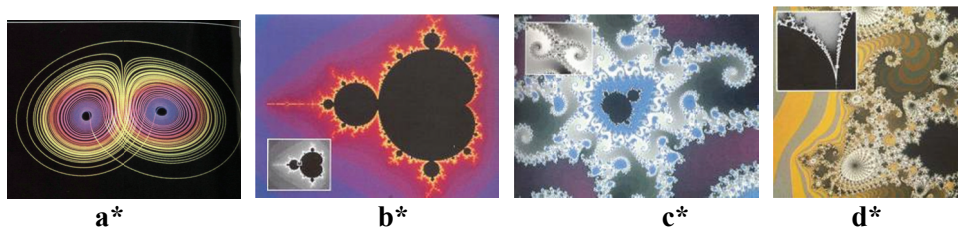


Figure 3. a* Lorenz's strange attractor; b*, c* and d* butifull fractal Malderbroyy and Julia sets.[31]

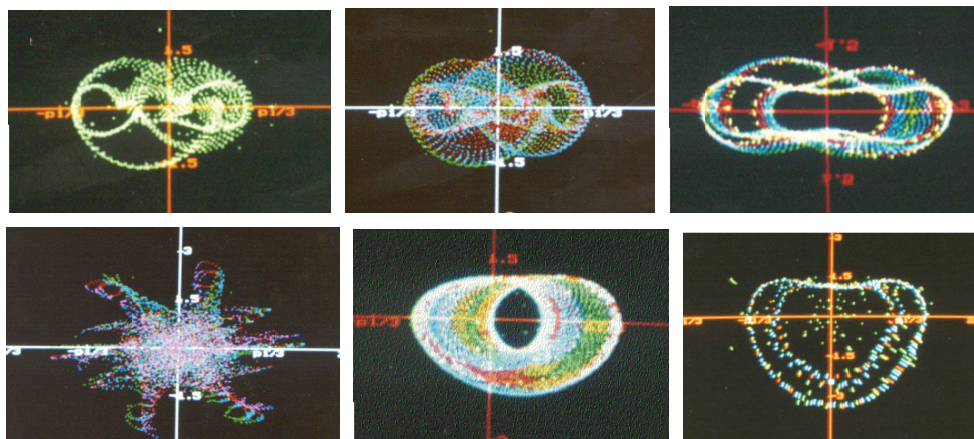


Figure 4. Poincaré sections (maps) for Mthieu-Hill's rheo-nonlinear noautomats differential equation describing nonlinear dynamics of heavy mass particle along ideal circle line with one frequency forced oscillations of the center and mass particle excited by two-frequency external excitation (see Reference by Hedrih and Pavlov [27]).

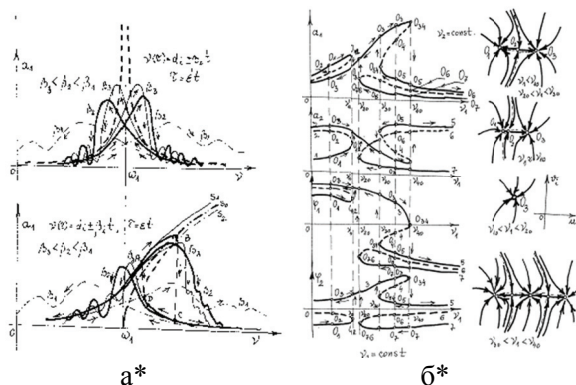


Figure 5. a* Sketch of a single frequency stationary amplitude frequency curves and no stationary amplitude frequency curves of forced vibration regimes for linear and nonlinear dynamical system with one degree of freedom passing through the resonant frequency ranges with different velocity of the external excitation frequency.
 b* Sketch of a single frequency stationary amplitude frequency curves for nonlinear dynamical system with two degrees of freedom excited by two-frequency external excitation (see Monographs by Mitropolyski [35-43]).

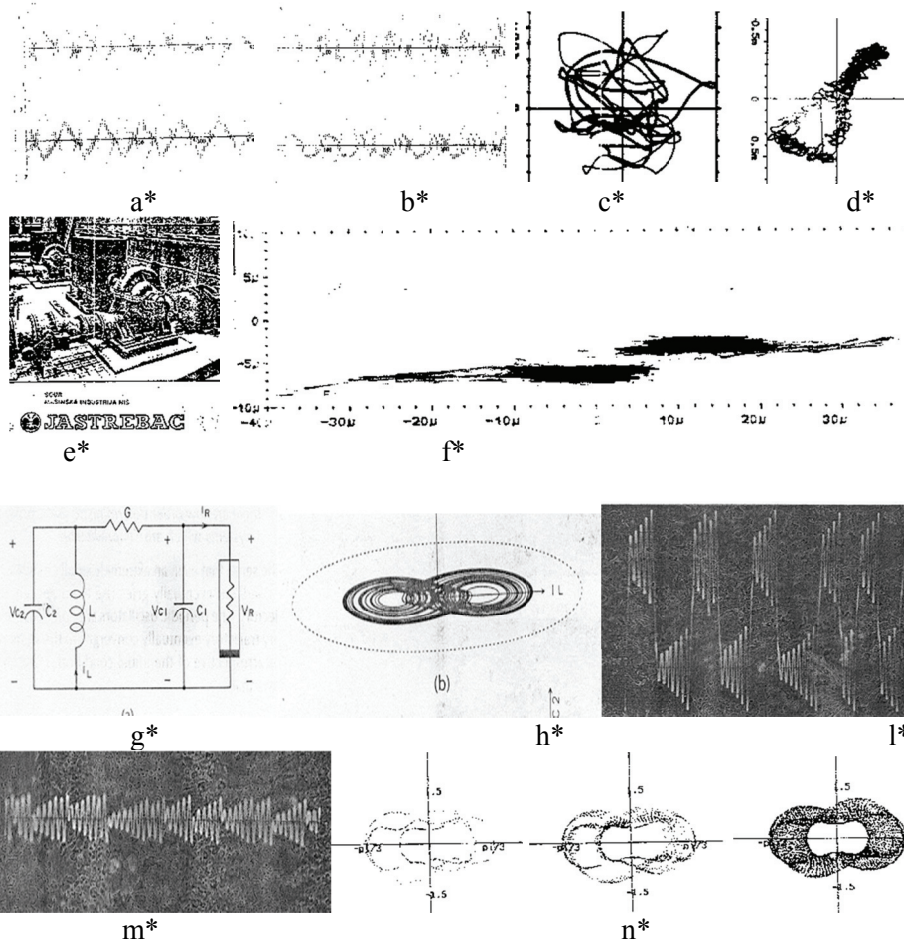


Figure 6. Graphical presentation of the trigger of coupled singularities in disparate nonlinear dynamical systems. a*, b*, c*, d* e* and f* graphical presentation of the kinetical parameters data obtained experimentally for nonlinear oscillations of centrifugal pump in working regimes. In f* and d* is visible a trigger of coupled singularities of trajectory of center of a pump bearing [28]. In c* chaotic motion is visible by trajectory of center of pump bearing. g*, h*, i* and m* graphical presentation of a strange attractor and corresponding time history diagrams for nonlinear dynamics of electrical dynamical system with trigger of coupled singularities [24]. n* a presentation of a trigger of coupled singularities and strange attractor in a nonlinear dynamical system [27].

Then it is possible to talk about *sensitive dependence* of nonlinear dynamics of initial conditions in area around some saddle unstable homoclinic points and orbits. Then, by use different initial conditions from different basin of attraction is possible to excited corresponding types of the nonlinear dynamics regimes.

The Logistic Map is one of the most simple forms of a chaotic process. Basically, this map, like any one-dimensional map, is a rule for getting a number from a number.

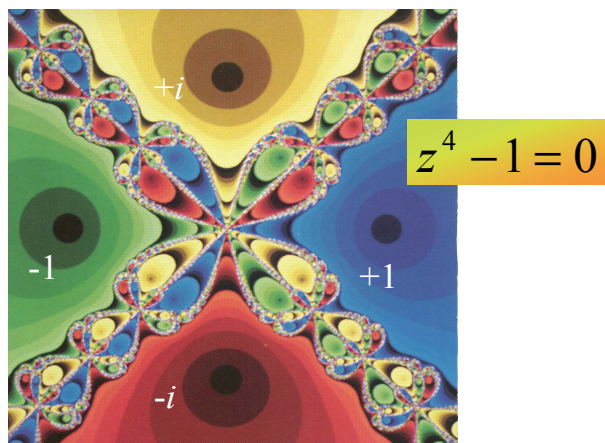


Figure 7. Graphical presentation of a dynamical system pure mathematical iterations as dynamical process on a example of numerical approximation of the roots of a biquadratic equations $z^4 - 1 = 0$ with known roots ∓ 1 and $\mp \sqrt{-1} = \mp i$ in the form of a fractal set constructed by different initial value of numerical iterations for obtaining numerical approximations of the four roots and number of iterations for convergence or divergence to the precise known roots [31].

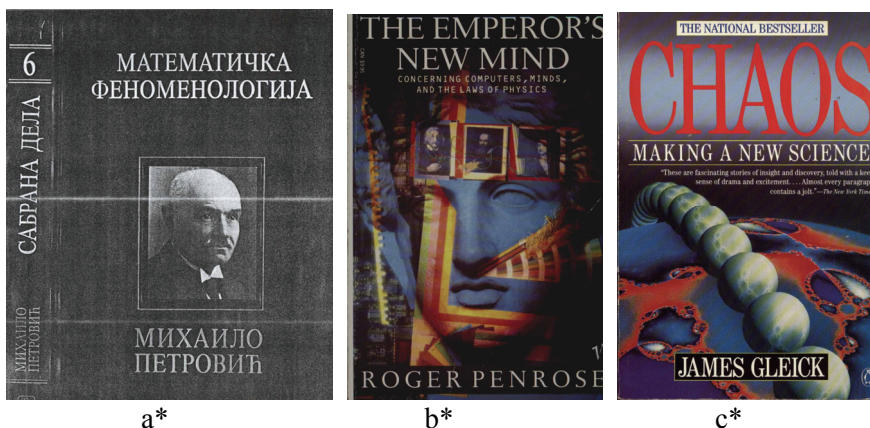


Figure 8. Cover of the three publications with basic idea of phenomenological mapping from different periods: by Petrović Mihailo published in 1911 and 1933, by Roger Penrose published in 1985 and by James Gleick published in 1988 [31].

(Petrović, M., Fenomenološko preslikavanje Phenomenological mapp), Srpska kraljevska akademija, Beograd, 1933. str. 33.

Petrović, M., Elementi matematičke fenomenologije (Elements of mathematical phenomenology), Srpska kraljevska akademija, Beograd, 1911. str. 89.

James Gleick, *Chaos, Making a new Sciences*, Penguin BOOKS, ISBN 014 00 92501, 1987/1988. u Roger Penrose, *The Emperor's New Mind, concerning Computers, Minds and the Laws of Physics*, ISBN 009 977170 S, Oxford University Press 1985/ 1990., koje sadrže i ideje Mihaila Petroviћа o fenomenološkom preslikavanju, koje se prepoznaju u "komjuterizovanom izdaњу".)

Acknowledgment

Parts of this research were supported by the Ministry of Education and Sciences of Republic of Serbia through Mathematical Institute SANU Belgrade Grant ON174001 Dynamics of hybrid systems with complex structures, and through Faculty of Mechanical Engineering University of Niš.

References

- [1] Andronov, A. A. Vitt, S. E. Haykin, *Teoriya kolebaniy*, Nauka, Moskva, 1981, 568.
- [2] Gerard, J. Daniel, *Elementary Stability and Bifurcation Theory*, Springer Verlag, 1980.
- [3] J. Guckenheimer, Ph. Holmes, *Nonlinear Oscillations, Dynamical Systems, and Bifurcations of Fields*, Springer-Verlag, 1983pp. 461.
- [4] K. Hedrih (Stevanović), *Nonlinear Dynamics of a Heavy Material Particle Along Circle which Rotates and Optimal Control*, in G. Rega, F. Vestroni (Eds.), *Chaotic Dynamics and Control of Systems and Processes in Mechanics 2005*, 37-45; IUTAM Book, in Series Solid Mechanics and Its Applications, Edited by G. M. L. Gladwell, Springer. 2005, XXVI, 504.
- [5] K. Hedrih (Stevanović), *Trigger of Coupled Singularities (Invited plenary lecture)*, *Dynamical Systems-Theory and Applications*, J. Awrejcewicz and all (Eds.), Lodz 2001, 51-78.
- [6] K. Hedrih (Stevanović), *A Trigger of Coupled Singularities*, *MECCANICA*, 2004, 39 (3), 295-314.
- [7] K. Hedrih (Stevanović), *Nonlinear Dynamics of a Gyro-rotor, and Sensitive Dependence on initial Conditions of a Heav Gyro-rotor Forced Vibration/Rotation Motion*, in F. L. Chernousko, A. I. Fradkov (Eds.), *IEEE, CSS, IUTAM, SPICS*, St. Petersburg, Inst. for Problems of Mech. Eng. of RAS, 2000, (2), 259-266.
- [8] K. Hedrih (Stevanović), (2008), *The optimal control in nonlinear mechanical systems with trigger of the coupled singularities*, in F. L. Chernousko, G. V. Kostin, V. V. Saurin (Eds.), *Advances in Mechanics: Dynamics and Control (Proceedings of the 14th International Workshop on Dynamics and Control)* A. Yu. Ishlinsky Institute for Problems in Mechanics RAS, Moscow, Nauka, 2008, 174-182.
- [9] K. Hedrih (Stevanović), *Dynamics of coupled systems*, *Nonlinear Analysis: Hybrid Systems*, 2008, 2 (2), 310-334.
- [10] K. Hedrih (Stevanović), *Vibrations of a Heavy Mass Particle Moving along a Rough Line with Friction of Coulomb Type*, ©Freund Publishing House Ltd., *International Journal of Nonlinear Sciences & Numerical Simulation*, 200910(11), 1705-1712.
- [11] K. Hedrih (Stevanović), *Discontinuity of kinetic parameter properties in nonlinear dynamics of mechanical systems*, *Proceedings of the 9th Brazilian Conference on Dynamics Control and their Applications*, Brazil, Serra Negra, 2010, 8-40.
- [12] K. Hedrih (Stevanović), *Existence of trigger of coupled singularities in nonlinear dynamics of mechanical system with coupled rotations*, *Scientific Technical Review*, 2012, 62 (1), *in press*.
- [13] K. Hedrih (Stevanović), *Nonlinear Dynamics and Aleksandr Mikhailovich Lyapunov (1857 – 1918)*, Dedicated to 150th anniversary of academician A. M. Lyapunov, *Scientific Technical Review*, 2007, LVII (1), 1-10.
- [14] K. Hedrih (Stevanović), *On Rheonomic Systems with Equivalent Holonomic Conservative System* (Int. Conf. ICNM-IV, Shanghai), in W. Chien and all. (Eds.), *Nonlinear dynamics*, 2002, 1046-1054.

- [15] K. Hedrih (Stevanović), The Vector Method of the Heavy Rotor Kinetic Parameter Analysis and Nonlinear Dynamics (Monograph.), University of Niš, 2001, 252.
- [16] K. Hedrih (Stevanović), On Rheonomic Systems with Equivalent Holonomic Conservative Systems Applied to the Nonlinear Dynamics of the Watt's Regulator, Proceedings of the eleventh world congress in Mechanism and machine Sciences, IFToMM, China Machine Press, Tianjin, China, 2004, 2, 1475-1479.
- [17] K. Hedrih (Stevanović), Vibrations of a Heavy Mass Particle Moving along a Rough Line with Friction of Coulomb Type, International Journal of Nonlinear Sciences & Numerical Simulation 200910(11),1705-1712.
- [18] K. Hedrih (Stevanović), Discontinuity of kinetic parameter properties in nonlinear dynamics of mechanical systems, Proceedings of the 9th Brazilian Conference on Dynamics Control and their Applications, Serra Negra, 2010, 8-40.
- [19] K. Hedrih (Stevanović), Energy and Nonlinear Dynamics of Hybrid Systems, in A. Luo (Ed.), *Dynamical Systems and Methods*, 2012, 29-83.
- [20] K. Hedrih (Stevanović), Vibrations of a Heavy Mass Particle Moving along a Rough Line with Friction of Coulomb Type, International Journal of Nonlinear Sciences & Numerical Simulation 2009, 10(11), 1705-1712.
- [21] K. Hedrih (Stevanović), Existence of trigger of coupled singularities in nonlinear dynamics of mechanical system with coupled rotations, Scientific Technical Review, 2012, 62 (1), 48-56.
- [22] K. Hedrih (Stevanović), *On mathematical methods in mechanics with applications – (MMA) or Mechanics between two fires: Mathematics and Engineering*, Zbornik radova simpozijuma Matematika I primene, Matematički fakultet Univerziteta u Beogradu I Zavod za udzbenike - Beograd, 2012, 35-116.
- [23] K. Hedrih (Stevanović), Energy and Nonlinear Dynamics of Hybrid Systems, in Albert Luo, Tenreiro Machado and D Baleanu (Eds.), *Dynamical Systems and Methods*, Springer New York, 2012, 29-83.
- [24] K. Hedrih (Stevanović), Beseda o Mihajlu Petroviću, Legende Beogradskog Univerziteta, Univerzitet u Beogradu, Univerzitetska biblioteka Svetozar Markovic, Beogradu, 2005, 37-48.
- [25] K. Hedrih (Stevanović), V. Raičević, S. Jović, Phase Trajectory Portrait of the Vibro-impact Forced Dynamics of Two Heavy Mass Particles Motions along Rough Circle, Communications in Nonlinear Science and Numerical Simulations, 2011, 16 (12), 4745-4755.
- [26] K. Hedrih (Stevanović), V. Raičević, S. Jović, Vibro-impact of a Heavy Mass Particle Moving along a Rough Circle with Two Impact Limiters, International Journal of Nonlinear Sciences & Numerical Simulation 2009, 10(11), 1713-1726.
- [27] K. Hedrih (Stevanović), B. Pavlov Strange attractors of the phase portrait of motion of a heavy material point along the circle with an oscillating center and under the influence of two frequency couple, Proceedings of the 2nd International Conference on nonlinear Mechanics, Beijing 1993, Peking University Press, 1993, 938-944.
- [28] K. Hedrih (Stevanović), M. Prašćević, Oscilatorni fenomeni u radu hidroagregata, X naučni skup čovek i radna sredina, Preventivni inženjering i informacione tehnologije, Zbornik radova, Fakulteta zaštite na radu, 1994.
- [29] K. Hedrih (Stevanović), Izabrana poglavlja teorije nelinearnih oscilacija, Izdanje Univerziteta u Nišu, 1977, 180.
- [30] E. L. Ince, *Proce. Roy. Society Edinburg*, 1931, 52, 32.
- [31] J. Gleick, *Chaos, Making a new Sciences*, Penguin BOOKS 1987/1988.
- [32] S. Jović, Energijaska analiza dinamike vibroudarnih sistema sa krivolinijskim putanjama i neidealnim vezama (Doktorska teza), Fakultet tehnickih nauka, K. Mitrovica, Univerzitetu Pristini, 2011.
- [33] K. Tomasz, S. R. Bishop, *The Illustrated Dictionary of Nonlinear Dynamics and Chaos - Book Description*, John Wiley & Sons; 1 edition, 1999).
- [34] 34. E., Mathieu, *Cours de Physique Mathématique*, Paris, 1873.; M. J.. O. Strutt: *Lamésche, Mathieusche und verwandte Funktionen in Physik und Technik*, Berlin, 1932.
- [35] Yu. A. Mitropolyskiy, *Problemi asimptoti-cheskoy teorii nestashionarnih kolebaniy*, Nauka Moskva, 1964.

- [36] Yu. A. Mitropolyskiy, Nestashionarnie proshesi v nelineynih sistemah, AN USSR, Kiev, 1955.
- [37] Yu. A. Mitropolyskiy, B. I. Mosseenkov, Lekciyi po primeniyu metodov k recheniyu uravneniy v chastnih proizvodnih, Int. Math. AN USSR, Kiev, 1968.
- [38] Yu. A. Mitropolyskiy, Problemi asimptoti-cheskoy teorii nestashionarnih kolebaniy, Nauka Moskva, 1964.
- [39] Yu. A. Mitropolyskiy, B. I. Mosseenkov, Assimptoticheskie recheniya uravneniya v chastnih proizvodnih, Vic haya chkola Kiev, 1976.
- [40] Yu. A. Mitropolyskiy, Nguyen Van Dao, Lectures on Asymptotic Methods of Nonlinear Dynamics, Vietnam National University Publishing House, Hanoi, 2003, 494.
- [41] Yu. A. Mitropolyskiy, Some problems in the development in nonlinear mechanics theory and applications, Facta Universitatis, Series Mechanics, Automatic Control and Robotics, 1995, 1, 539-560.
- [42] Yu. A. Mitropolyskiy, On Application of asymptotic methods of nonlinear mechanics for solving some problems of oscillation theory, Facta Universitatis, Series Mechanics, Automatic Control and Robotics, 1996, 2, 1-9.
- [43] Yu. A. Mitropolyskiy, Adiabaticheskie processi v nelineynih kolebatelnyh sistemah, Simpozijum '83 – Nelinearni problemi dinamike, Arandjelovac, 23-25., Novembar 1983, IT-Društvo za mehaniku Srbije, Beograd, 1983, I-1-I-12.
- [44] V. I. Neimark, P. S. Landa, (), Stohasticheskie i haoticheskie kolebaniya, Nauka, Moskva, 1987, 423.
- [45] M. Petrović, Fenomenološko preslikavanje, Srpska kraljevska akademija, Beograd, 1933, 33.
- [46] M. Petrović, Elementi matematičke fenomenologije, Srpska kraljevska akademija, Beograd, 1911, 89.
- [47] H. Poincaré, É. Picard, Darbox, Ch. Hermite, P. Painlevé, Apell, Tannery, Boussinesq, Koenigs, Lippmann.
- [48] P. D. Rašković Osnovi tenzorskog računa, Mašinski fakultet Kragujevac, 1974.
- [49] P. D. Rašković, Mehanika II- Kinematika, Zavod za izdavanje udžbenika, 1953, 1966, 347.
- [50] P. D. Rašković, *Mehanika III - Dinamika*, X i dalja izdanja, Naučna knjiga, 1962, 424.
- [51] P. D. Rašković, Mehanika – Dinamika, Naučna knjiga, 1972.
- [52] P. D. Rašković, Teorija oscilacija, Naučna knjiga, 1952.
- [53] P. D. Rašković, Analitička mehanika, Mašinski fakultet Kragujevac, 1974.
- [54] R. Penrose, The Emperor's New Mind, concerning Computers, Minds and the Laws of Physics, S, Oxford University Press, 1985/ 1990.
- [55] M. J. O Strutt, Lamésche, Mathieusche und verwandle Funktionen in Physik und Technik, Berlin, 1932.
- [56] J. Simonović, Dinamika i stabilnost hibridnih dinamičkih sistema, Doktorska teza, Faculty of Mechanical Engineering, Niš, 2011.
- [57] J. J. Stoker, *Nonlinear Vibrations*, Interscience Publishers, New Yor, 1950, 273.
- [58] Lj. Veljović, Nelinearne oscilacije giro-rotora, Doktorska teza, Faculty of Mechanical Engineering in Niš, 2011.

CHEMICAL THERMODYNAMICS

THE ESTIMATION OF Fe – Si SYSTEM OXIDATION AT 298 K IN AIR AND WATER ENVIRONMENTS

P. A. Nikolaychuk, A. G. Tyurin

*Department of Analytical and Physical Chemistry, Chelyabinsk State University,
Chelyabinsk, Russian Federation, npa@csu.ru, tag@csu.ru*

Abstract

Thermodynamic description of systems Fe – Si, Fe – Si – O and Fe – Si – H₂O at standard conditions is performed. The Fe – Si – O system state diagram and potential – pH diagram of Fe – Si – H₂O system are plotted. Thermodynamic features of chemical and electrochemical stability of iron silicides are analyzed.

Introduction

Fe – Si is important binary system, and the thermodynamic features of its oxidation and corrosion processes were modeled many times [1-3]. However, these studies do not cover all possible chemical and electrochemical equilibria in system. The purpose of this study is to make revision of previous researches and take into account all uncounted thermodynamic properties.

Results and Discussion

The Fe – Si phase diagram [4] assumes, that two stable iron silicides, FeSi and FeSi₂, exist in system at standard temperature. FeSi has a small homogeneity range, from FeSi_{0,961} to FeSi_{1,033}. Maximum solid solubility of Si in α -Fe is equal to about 25 atomic percent. It corresponds to fully ordered α_2 -phase, and this solution composition is often considered as subsilicide “Fe₃Si” [5]. Thermodynamic properties of α -phase are described in terms of substitution solution model. The comparison between different approaches [6-8] is performed with and without considering “Fe₃Si” phase existence. The activities of iron and silicon in “saturated” solid solution are equal to 0,473 and $5,5 \cdot 10^{-20}$ respectively, meaning strong negative deviations from ideal behaviour. There are a lot of different thermodynamic data on various iron silicides, which often do not agree with each other. The revision and estimation of these data is performed and the correct values are chosen. The standard Gibbs energy of formation of nonstoichiometric FeSi_x compound is estimated by a following equation:

$$\Delta_f G_{298}^{\circ}(\text{FeSi}_x) = 34100 \cdot x^2 - 107800 \cdot x, \text{ J/mol} \quad (1).$$

In order to describe chemical resistance of Fe-Si system alloys to corrosion in oxygen environments the consecutive scheme of oxidation reactions is considered, the Fe-Si-O state diagram is plotted (see fig. 1) and the characteristics of system conditions are calculated. There is an experimental approval that there is a solid solubility of SiO₂ in Fe₂O₃ and Fe₃O₄ in Fe₂SiO₄ at elevated temperatures [9]. Using these data and according to strictly regular solution model the energy of

A-1-O

mixing (Q_{12}) and the Gibbs energies of phase transitions of SiO_2 from diamond lattice to the lattice of Fe_2O_3 and of Fe_3O_4 from magnetite lattice to the lattice of Fe_2SiO_4 are estimated to be the following:

$$Q_{\text{SiO}_2-\text{Fe}_2\text{O}_3} = 8740 \text{ J/mol}, Q_{\text{Fe}_3\text{O}_4-\text{Fe}_2\text{SiO}_4} = 25200 \text{ J/mol} \quad (2),$$

$$\Delta_{\text{tr}}G_T^0(\text{SiO}_2, \text{diamond} \rightarrow (\text{SiO}_2)_{\text{Fe}_2\text{O}_3}) = 2,621 \cdot T + 6557, \text{ J/mol} \quad (3),$$

$$\Delta_{\text{tr}}G_T^0(\text{Fe}_3\text{O}_4, \text{magnetite} \rightarrow (\text{Fe}_3\text{O}_4)_{\text{Fe}_2\text{SiO}_4}) = 0,235 \cdot T - 1523, \text{ J/mol} \quad (4),$$

The solubility of SiO_2 in Fe_2O_3 is estimated equal to $1,54 \cdot 10^{-3}$ mole percent at 298 K. The activities of the components are $a_{\text{SiO}_2} = 0,0541$ and $a_{\text{Fe}_2\text{O}_3} = 0,998$. The solubility of Fe_3O_4 in Fe_2SiO_4 is equal to $6,85 \cdot 10^{-5}$ mole percent and $a_{\text{Fe}_3\text{O}_4} = 0,00233$, $a_{\text{Fe}_2\text{SiO}_4} \approx 1$. The small positive deviations from ideal behaviour for both these solutions are revealed.

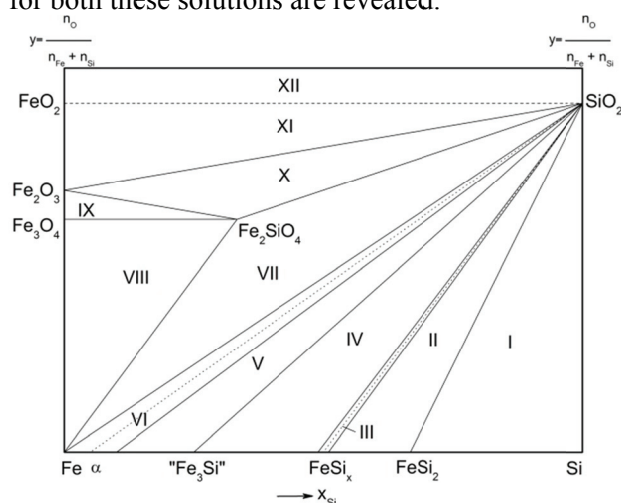


Figure 1. Fe-Si-O system state diagram at 298 K

Domains at the diagram (fig. 1) correspond to the following system states: I – $\text{FeSi}_2 - \text{Si} - \text{SiO}_2$, II – $\text{FeSi}_{1,033} - \text{FeSi}_2 - \text{SiO}_2$, III – $\text{FeSi}_x - \text{SiO}_2$, IV – “ Fe_3Si ” – $\text{FeSi}_{0,961} - \text{SiO}_2$, V – $\alpha_1 - \text{SiO}_2$, VI – $\alpha - \text{SiO}_2$, VII – $\alpha - \text{Fe}_2\text{SiO}_4 - \text{SiO}_2$, VIII – $\alpha - (\text{Fe}_3\text{O}_4, \text{Fe}_2\text{SiO}_4)$, IX – $(\text{Fe}_3\text{O}_4, \text{Fe}_2\text{SiO}_4) - \text{Fe}_2\text{O}_3$, X – $(\text{Fe}_2\text{O}_3, \text{SiO}_2) - \text{Fe}_2\text{SiO}_4$, XI – $\text{Fe}_2\text{O}_3 - \text{FeO}_2 - \text{SiO}_2$, XII – $\text{FeO}_2 - \text{SiO}_2 - \{\text{O}_2\}$.

The standard Gibbs energy of formation

of metastable iron dioxide is estimated to be equal to about -360000 J/mol . The calculations show, that equilibrium oxygen pressure, needed for FeO_2 formation, exceeds $6 \cdot 10^5$ bar. Thus it can not be formed in air environments at standard conditions.

The best way to describe thermodynamic features of electrochemical stability of Fe-Si system in liquid environments is to plot the diagram of electrochemical equilibrium (potential-pH) [10]. It was plotted at 298 K, air pressure of 1 bar and activities of ions in solution, equal to 1 mol/l (see fig. 2). Thermodynamic properties of basic chemical and electrochemical equilibria in Fe-Si- H_2O system are calculated.

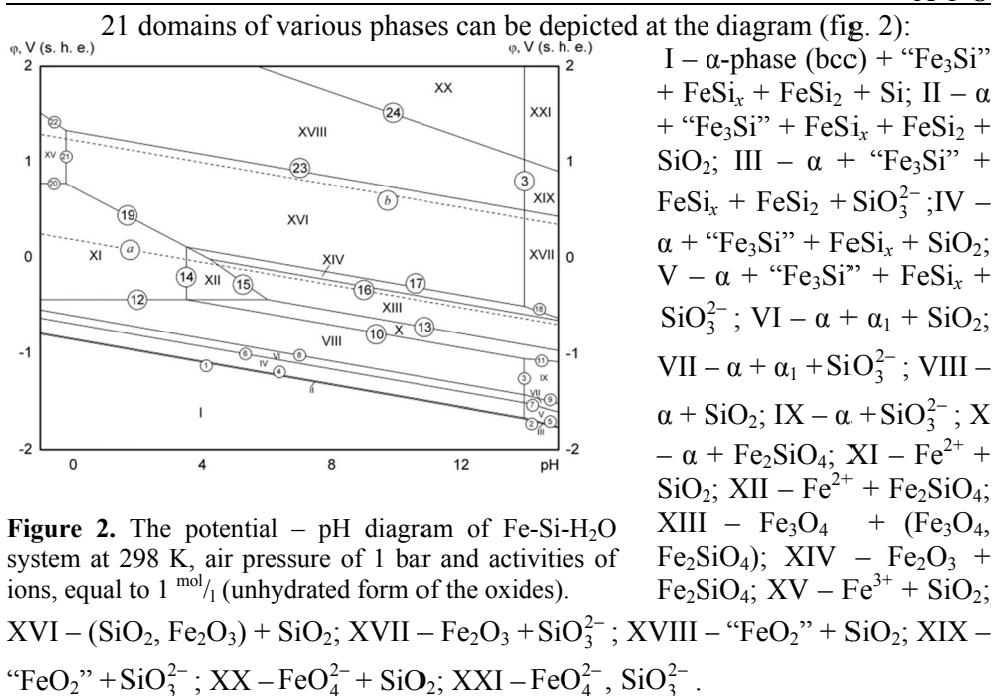


Figure 2. The potential – pH diagram of Fe-Si-H₂O system at 298 K, air pressure of 1 bar and activities of ions, equal to 1 mol¹/_l (unhydrated form of the oxides).

The primary passivation film on the Fe-Si system alloys in the area of water electrochemical stability (between the lines *a* and *b* on fig. 2, corresponding to hydrogen and oxygen electrodes, respectively) consists of Fe₂O₃ and SiO₂. Its specific composition depends on silicon content in the system.

Conclusions

The Fe – Si – O system state diagram and the potential – pH diagram of Fe – Si – H₂O system at 298 K and 1 bar are revised to take into account all uncounted thermodynamic properties of these systems. Thermodynamic description of chemical and electrochemical stability of iron silicides is performed.

References

- [1] A. Atkinson, Corrosion Science, 1982, 22(2), 87-102.
- [2] G. Kelsall et al, Journal of the Electrochemical Society, 1991, 138(4), 931-940.
- [3] A. Tyurin, Protection of Metals, 2004, 40(1), 14-22.
- [4] Phase diagram – Web, <http://www.crct.polymtl.ca/fact/documentation>.
- [5] A. Gude, Philosophical Magazine A, 2006, 76(1), 1-29.
- [6] L. Kaufman, CALPHAD, 1979, 3(1), 45-76.
- [7] B. Lee et al, CALPHAD, 1987, 11(2), 253-270.
- [8] J. Lacaze, Metallurgical Transactions A, 1991, 22, 2211-2223.
- [9] A. Lykasov et al, Butlerov Communications, 2010, 21(7), 42-49.
- [10] Pourbaix diagrams / Substances & Technologies, http://www.substech.com/dokuwiki/doku.php?id=pourbaix_diagrams.

AUXILIARY COMPONENT METHOD: HOW TO BYPASS THE PROHIBITIONS OF NATURE?

A. Zavrazhnov, A. Naumov, A. Kosyakov, S. Berezin, V. Pervov
Chemistry Dep., Voronezh State University, Russia, E-mail: AlZavr08@rambler.ru

Abstract

The present work reveals the opportunities of auxiliary component use for the study of thermodynamical properties of inorganic compounds and homogeneity regions of solid phases as well as for the phase diagram study. The possibility of getting the information that cannot be obtained by routine vapor pressure methods is shown. It is also discussed that the auxiliary component method can be used both for the delicate composition (non-stoichiometry) control of solids and for the synthesis of non-equilibrium materials.

Introduction

The synthesis of solids with precise composition control is one of the important problems of inorganic chemistry and material science. It's well known that even insignificant composition variations can change functional properties of materials in a principal way. It's crucial to have the information about the phase diagram of a system for the synthesis of compounds with necessary properties. And it's indispensable to have measurable values of pressure p for p - T - x -diagrams study by means of well-known and fully developed methods.

Unfortunately, it is possible not for any system. Too low values of saturated vapor pressure over the phases to be studied (for manometric method <100 Pa) or kinetic difficulties in obtaining an equilibrium can be the reason of the above-mentioned problem. Just for such kind of systems the method of auxiliary component can be used. The essence of this method is in avoiding the equilibrium of the component X from a condensed phase X_nY_m , and its own vapor



and in making an appropriate equilibrium with auxiliary component additionally introduced in the system. For example,



where Z is an auxiliary component, and even one of Z or XZ_q is volatile and can form vapor phase.

In equations (1), (2) and so on the symbol «''» corresponds to the component which is in a condensed phase, and the symbol «'» corresponds to the component which is in a vapor phase.

Unfortunately, potentialities of this method are developed insufficiently. The analysis of different opportunities of the auxiliary component method both for research problems and directed synthesis of new materials is the objective of the present work.

Research aspect

Firstly, let's consider the research advantages of the method, namely, phase diagrams scanning for both the whole systems and distinct phases of variable

composition. Let's restrict our consideration to the case when an auxiliary component is presented only in a vapor phase, and condensed phases belong to a binary system.

When introducing Z, the component number of the system increases by one. Considering Z to be fully insoluble in the phases explored, one can get a subsystem which contains only the initial phases with the initial component number. Then the rest part of the system, containing the auxiliary component, plays the role of an external environment with regard to this subsystem.

In addition, this fact is an indicator gage of state for investigated systems. In particular, this indicator vapor phase let one "read" information (from the studied phases) about chemical potentials of the components of these phases.

For example, when studying inorganic low-volatile sulfides with the use of hydrogen, we can obtain the equilibrium



Then from the necessary equilibrium condition

$$\mu_S'' + \mu_{H_2}' - \mu_{H_2S}' = 0 . \quad (4)$$

we can get

$$\mu_S'' = RT \ln K_p^\# + F , \quad (5)$$

where in (4) and (5) μ_S'' is the chemical potential of sulfur in solid sulfide; μ_{H_2}' and μ_{H_2S}' are the chemical potentials of hydrogen and hydrogen sulfide in the vapor; $K_p^\#$ is the quantity often named as heterogeneous equilibrium constant which relates pressures of hydrogen and hydrogen sulfide as

$$K_p^\# = \frac{p_{H_2S}}{p_{H_2}} , \quad (6)$$

and F , which depends only on temperature, is the difference between standard chemical potentials of the gas species:

$$F = \mu_{H_2S}'^\circ - \mu_{H_2}'^\circ . \quad (7)$$

The equation (5) is also correct for the more general case (2) – of course, after changing corresponding components in this equation. It's significant to notice that, unlike the equilibrium "condensed phase – intrinsic saturated vapor", the equilibria with auxiliary component reflect the states of condensed phases in which these phases exist over their "intrinsic" vapor. Here we name the vapor, which is realized in heterogeneous equilibria without auxiliary component, as "intrinsic" vapor.

As far as we know, the auxiliary component method has not been used for such kind of problems. It's also important to notice that almost all instrumental methods of solid state investigation are directly (routine vapor pressure methods) or by implication (electrophysical methods) connected with the study of the coexistence between the phases and the saturated ("intrinsic") vapor. On the contrary, there is a limited number of methods for research in the areas of the existence of a *single* phase. Moreover, these methods are not very precise. So the approach considered here can be useful, for example, in high pressure material science or in that part of astrochemistry which deals

with the analysis of the planet's crust composition using the known composition of the atmosphere contacting with this crust. This problem can be very relevant for the research of exoplanets, which are often discovered in present time.

If the pressure dependency of μ_X is significant then the correct $T-x$ – sections study, including homogeneity regions, becomes possible **only** with the use of the auxiliary component method (μ_X is the chemical potential of a condensed phase).

Applied aspect (method of selective vapor chemical transport – SCVT)

The same method and the same equilibria can be used for composition (non-stoichiometry) control of inorganic compounds. In such a form the method of composition control with the use of auxiliary component is similar to classical chemical vapor transport reactions (CVT). Unlike classical CVT, in the case of composition control with the use of auxiliary component the initial sample is not exposed to re-sublimation: only the changes in the proportion of its constituents take place due to the strong selectivity of the reaction (2).

The SCVT method is based on the idea that selective chemical vapor transport reaction – depending on conditions – can be realized in forward direction (**extraction** of the component **from** the sample) or in reverse direction (**saturation** of the sample by the component to be transported). Composition control is performed in a closed system (ampoule), in which the sample and the charge are placed. The latter serves as a source or getter of the transported component. The vapor in the ampoule consists of vapors of different forms of the transporting component. These vapors provide selective transfer. According to our conclusions, the direction of selective chemical vapor transport can be regulated only by the temperature of the sample (T_2) and the charge (T_1), and by the charge composition (x_1). (Charge is the condensed phase, the source or absorbent material of the component, which reacts with the transporting agent and undergoes the selective chemical transfer in the SCVT-process.) The evolution of the sample and charge compositions ceases when the system achieves steady state with no mass transfer. One can say that the composition of the sample (x_2) “tunes” to variables T_2 , T_1 и x_1 . The condition (Eq. 8) is a criterion of the steady state attainment.

$$K_p^\#(1) = K_p^\#(2). \quad (8)$$

The method SCVT can be especially useful in the situations when the material with required structure can be synthesized relatively easy but precise control of its composition is rather difficult (for example, because of low volatility). Thus, we demonstrated the possibility of delicate composition and properties control of selenides and sulfides of gallium, indium and copper. In our opinion, it's promising to use auxiliary component for the synthesis of catalytic materials.

Acknowledgements

This work was supported by Russian Foundation for Basic Research, pr. 11-03-90430.

SOLUBILITY OF THE QUATERNARY SYSTEM K₂SO₄+Na₂SO₄+MgSO₄+H₂O AT T = 298.15 K

B. V. Djulinčević, D. Ž. Popović, J. M. Miladinović, M. D. Todorović
Faculty of Technology and Metallurgy, University of Belgrade,
Karnegijeva 4, 11 000 Belgrade, Serbia

Abstract

For the salt solubility predictions of the K₂SO₄+Na₂SO₄+MgSO₄+H₂O system the treatment of thermodynamic data of three-component subsystems at T = 298.15 K involved the application of the extended ion–interaction model for the mixed electrolyte solutions and criteria of phase equilibria. Osmotic coefficients data of three-component systems were revised according to recently published parameters of the solutions NaCl(aq) and KCl(aq) that served as reference standards in isopiestic measurements. Parameters of the extended ion–interaction model of K₂SO₄(aq) are determined by treatment of experimental and predicted values of osmotic coefficient in supersaturated region obtained by the Zdanovskii–Stokes–Robinson rule. Results of salt solubility prediction were compared to experimental solubility data from literature.

Introduction

The estimation of phase equilibria in aqueous solutions of complex salt systems, such as K₂SO₄+Na₂SO₄+MgSO₄+H₂O, is the basis for understanding, conducting and controlling the processes of dissolving, evaporation and crystallization of salts. Various solid phases appear in saturated solutions of the investigated system at T = 298.15 K: *arcanite* – K₂SO₄(s); *schoenite* – K₂SO₄·MgSO₄·6H₂O(s); *epsomite* – MgSO₄·7H₂O(s); *glaserite* – Na₂SO₄·3K₂SO₄(s); *mirabilite*– Na₂SO₄·10H₂O(s) and *bloedite* – Na₂SO₄·MgSO₄·4H₂O(s). The investigated system is of particular interest due to low solubility of K₂SO₄ in water (molality $m \leq 0.7 \text{ mol}\cdot\text{kg}^{-1}$) at T = 298.15 K.

Extended ion–interaction model for binary and mixed electrolyte solutions [1] that was used in treatment of data give following relations for the osmotic coefficient function (1) and activity coefficients of ions (2) and (3) that appear in criteria of phase equilibria.

$$\phi - 1 = \left(2 / \sum_i m_i \right) \left[-A_\phi I^{3/2} / (1 + 1.2I^{1/2}) + \sum_c \sum_a m_c m_a (B_{ca}^\phi + ZC_{ca}^{\pi\phi}) + \sum_{c < c'} \sum_{c'} m_c m_{c'} (\varphi_{cc'}^\phi + \sum_a m_a \psi_{cca}) \right] \quad (1)$$

$$\ln(\gamma_M) = z_M^2 F + \sum_a m_a (2B_{Ma} + ZC_{Ma}^T) + \sum_c m_c (2\varphi_{Mc} + \sum_a m_a \psi_{Mca}) + z_M \sum_c \sum_a m_c m_a C_{ca}^T \quad (2)$$

$$\ln(\gamma_X) = z_X^2 F + \sum_c m_c (2B_{cX} + ZC_{cX}^T) + \sum_{c < c'} \sum_{c'} m_c m_{c'} \psi_{Xcc'} + |z_X| \sum_c \sum_a m_c m_a C_{ca}^T \quad (3)$$

where parameters B and C^T are for the binary systems as mixed solution constituents and φ and ψ are mixing parameters for the three-component systems.

Results and Discussion

In Table 1 are given the parameters of binary aqueous solutions K₂SO₄(aq), MgSO₄(aq), Na₂SO₄(aq), as mixture constituents, and reference standards,

A-3-P

NaCl(aq)[2] and KCl(aq) [3] according to which the osmotic coefficient data of three-component systems have been revised. For the K₂SO₄(aq) parameters are determined by treatment of experimental and predicted values of osmotic coefficient in supersaturated region obtained by Zdanovskii–Stokes–Robinson rule, with standard deviation of the fit being $s = 0.0019$ [4]. In Table 2 are given the mixed solution parameters, $\varphi(M, c)$ and $\psi(M, c, X)$ for three-component subsystems obtained by treatment of experimental osmotic coefficient data, together with maximum ionic strength and standard deviation of the fit, s .

Table 1. Parameters of the extended ion–interaction model for binary aqueous systems at $T = 298.15$ K and $p = 101.325$ kPa

	K ₂ SO ₄ (aq)	MgSO ₄ (aq)	Na ₂ SO ₄ (aq)	KCl(aq)	NaCl(aq)
$\beta_{MX}^{(0)}$	0.038666	-0.03089	0.011976	0.0511414	0.080634
$\beta_{MX}^{(1)}$	0.75339	3.7687	0.951276	0.201879	0.263098
$\beta_{MX}^{(2)}$		- 37,3659			
$\alpha_{1,MX}$	2.0	1.4	2.0	2.0	2.0
$\alpha_{2,MX}$		12			
$C_{MX}^{(0)}$	0.000393	0.016406	0.0024359	-0.68023·10 ⁻³	2.624·10 ⁻⁴
$C_{MX}^{(1)}$	0.093221	0.34549	0.236044		-1.0052·10 ⁻²
ω_{MX}	2.5	1.0	2.5		2.5
max. m (mol/kg)	5.2	3.6176	3.8140	~ 4	~ 6

Table 2. Mixing parameters of the extended ion–interaction model for three-component systems at $T = 298.15$ K and $p = 101.325$ kPa

System	$\varphi(M, c)$	$\psi(M, c, X)$	max. I (mol·kg ⁻¹)	s
Na ₂ SO ₄ + K ₂ SO ₄ +H ₂ O	-0.093728	0.019478	6.5	0.0085
Na ₂ SO ₄ + MgSO ₄ +H ₂ O	-0.0068432	-0.014316	14	0.0030
K ₂ SO ₄ + MgSO ₄ +H ₂ O*	-0.0537	-0.0375	12	0.0015

* mixing parameters determined by inclusion of higher order electrostatic terms

In salt solubility predictions, calculated values by extended ion–interaction model deviate from experimental solubility data of Linke [5] in average by 0.4 % for the system K₂SO₄ + MgSO₄ +H₂O and by 0.8 % for systems Na₂SO₄ + K₂SO₄ +H₂O and Na₂SO₄ + MgSO₄ +H₂O at $T = 298.15$ K. Excellent agreement between calculated values of salt solubilities in the investigated system can be ascribed to successful estimation of predicted thermodynamic data of K₂SO₄(aq) in supersaturated region as mixed solution constituent. In Figure 1. are presented the results of salt solubility predictions of Na₂SO₄·10H₂O(s), Na₂SO₄·MgSO₄·4H₂O(s) and MgSO₄·7H₂O(s) by extended ion–interaction model and data of Linke [5].

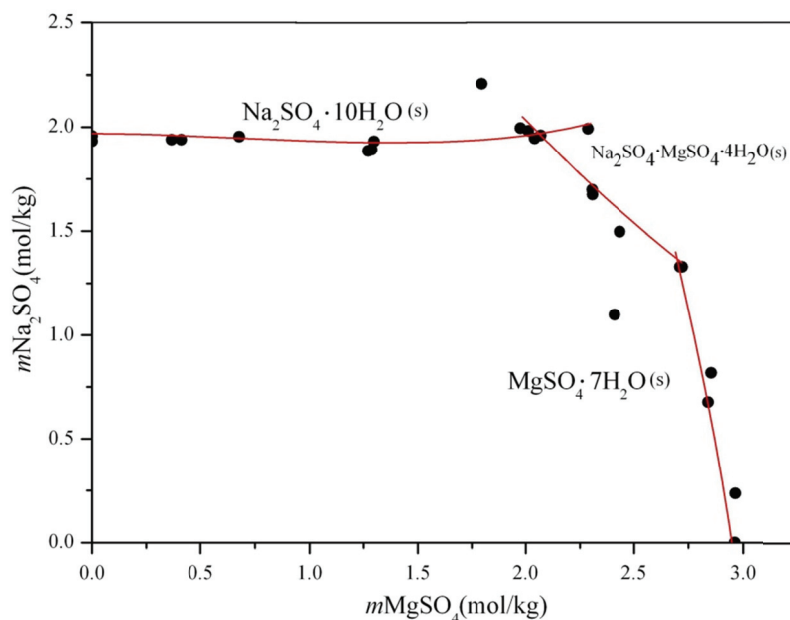


Figure 1. Solubilities of salts in the system $\text{Na}_2\text{SO}_4+\text{MgSO}_4+\text{H}_2\text{O}$ at $T = 298.15$ K: curves—calculated values by ion–interaction model and data from Tables 1 and 2; ●—data of Linke [5].

Conclusion

Extended ion–interaction model for pure and mixed electrolyte solutions gave excellent agreement between predicted and experimental solubilities of salts in the system $\text{K}_2\text{SO}_4+\text{Na}_2\text{SO}_4+\text{MgSO}_4+\text{H}_2\text{O}$ at $T = 298.15$ K.

Acknowledgment

This work was supported by the Ministry of Education Science and Technology of the Republic of Serbia under Project No. 172063.

References

- [1] S. L. Clegg, J. A. Rard, K. S. Pitzer, *J. Chem. Soc. Faraday Trans.*, 1994, 90, 1875-1894.
- [2] D. G. Archer, *J. Phys. Chem. Ref. Data*, 1992, 21, 793-829.
- [3] D. G. Archer, *J. Phys. Chem. Ref. Data*, 1999, 28, 1-17.
- [4] R. R. Ninković, J. M. Miladinović, M. D. Todorović, A. V. Rumyantsev, B. R. Božović, *J.Chem.Eng.Data*, 2005, 50, 735-741.
- [5] W. F. Linke, *Solubilities of Inorganic and Metal-Organic Compounds*, Volume II, Fourth Edition, American Chemical Society, Washington D. C., 1965.

PARTITIONING OF ACETIC ACID BETWEEN THE PHASES IN A SOYBEAN OIL-ACETIC ACID-HYDROGEN PEROXIDE-WATER SYSTEM

O. Borota¹, M. Janković¹, S. Sinadinović-Fišer¹, V. Rafajlovska²

¹*Faculty of Technology, University of Novi Sad, R. Serbia*

²*Faculty of Technology and Metallurgy, Ss Cyril and Methodius University in Skopje, R. Macedonia*

Abstract

Dependency of the liquid-liquid equilibrium constant for acetic acid (K_A) in a system soybean oil (SO)-acetic acid (A)-hydrogen peroxide (HP)-water (W) from temperature and composition was examined. The results were compared with those found in a literature for the liquid-liquid equilibrium constant for acetic acid in a system soybean oil-acetic acid-water.

Introduction

Epoxidized soybean oil is commercially produced by epoxidation of soybean oil (SO) with peracetic acid formed *in situ* usually from aqueous hydrogen peroxide (HP) and acetic acid (A) in the presence of an acidic catalyst. The reaction mixture is either two-phase (water-oil), if the catalyst is a mineral acid, or three-phase (water-oil-resin), if the catalyst is an ion exchange resin.

Epoxidation involves two successive reactions: the first is the reaction of acetic acid and hydrogen peroxide in the water phase that gives peracetic acid; the second reaction requires partial migration of peracetic acid to the oil phase where it reacts with double bonds of triglycerides, the main constituents of the oil, forming an epoxy ring and releasing an acetic acid which returns to the water phase. Partition equilibrium of acetic and peracetic acids ensures the occurrence of both reactions if interphase area is sufficient to enable a mass transfer. Therefore, for a mathematical model of a reaction system which takes into consideration existence of two liquid phases, the knowledge of partition coefficient of acetic acid is necessary [1-3].

Partition coefficient of acetic acid ($K_{C,A}$) is defined as the ratio of the concentrations of acetic acid in oil (C_A^o) and in water (C_A^w) phase. It can be calculated from the liquid-liquid phase equilibrium condition and known molar phase volumes *via* Eq. 1:

$$K_{C,A} = \frac{C_A^o}{C_A^w} = K_A \cdot \frac{v^w}{v^o} \quad (1)$$

where K_A is the liquid-liquid equilibrium constant for acetic acid and v^w and v^o are the molar volumes of oil and water phases, respectively.

The aim of the present work was to experimentally determine the liquid-liquid equilibrium constant for acetic acid in the system soybean oil-hydrogen peroxide-

acetic acid-water within ranges of temperature and composition significant for industry.

Determination of the Liquid-Liquid Equilibrium Constant for Acetic Acid

The liquid-liquid equilibrium constant for acetic acid is defined as:

$$K_A = \frac{x_A^o}{x_A^w} \quad (2)$$

where x_A is the molar fraction of acetic acid in oil (o) and in water (w) phase.

The molar fraction of A in the phase i (x_A^i) can be expressed as:

$$x_A^i = \frac{m_A^i \cdot M_A^{-1}}{\sum_{j=1}^4 m_j^i \cdot M_j^{-1}} \quad (3)$$

where m_A^i and m_j^i (g) are the masses of A and component j , respectively, in phase i and M_A and M_j (g/mol) are molecular masses of A and component j , respectively.

The experimental value of the liquid-liquid equilibrium constant for acetic acid was determined on the basis of weighted masses of the oil and water phase samples and the masses of the acetic acid in the oil and water phase, determined by alkali titration. The immiscibility of hydrogen peroxide and water with soybean oil was assumed.

Experimental Work

A mixture of soybean oil, acetic acid, 30% aqueous solution of hydrogen peroxide and water was poured in a three-neck round bottom flask placed in a water bath on top of a magnetic stirrer and equipped with thermometer and reflux condenser. The equilibration was done at desired temperature ($\pm 1^\circ\text{C}$) for an hour under the constant stirring (1000 rpm). Samples were taken without stopping the stirring. After centrifugation, the content of acetic acid in separated phases was determined by NaOH titration in a presence of phenolphthalein. Titrations were done in triplicate. To check the accuracy of the analytical method a comparison of the measured and determined total mass of acetic acid in the system was done.

Results and Discussion

The liquid-liquid equilibrium constant was determined for nine mixtures at four temperatures. The compositions of the investigated mixtures (S1-3/a-c), temperatures of equilibration and determined liquid-liquid equilibrium constants are given in Table 1. The compositions were varied to simulate changes of components concentrations with reaction time in the system during the epoxidation i.e. the amount of hydrogen peroxide was reduced in the mixtures due to its consumption during the process, while the amount of water was increased as its amount in the reaction system increases with time.

The relative error of the determination of the acetic acid total mass in the mixtures was -2.36-4.41%. K_A values ranged from 1.40 to 1.65 and defined trends neither for temperature nor for composition were observed.

A-4-P

Table 1. Composition and liquid-liquid equilibrium constants for acetic acid at 20, 35, 50 and 65°C for soybean oil (SO)-acetic acid (A)- aqueous hydrogen peroxide (aqHP)-water (W) mixtures (S1-3/a-c) and mixtures free of HP (M1-M3)

Mixture	Mass (g)				K_A			
	SO	A	aqHP	W	Temperature (°C)			
					20	35	50	65
S1/a	100.03	12.02	22.80	38.94	1.458	1.540	1.643	1.599
S1/b	100.03	21.00	22.77	38.94	1.560	1.456	1.491	1.395
S1/c	100.13	30.03	22.81	38.89	1.380	1.412	1.416	1.423
S2/a	100.07	12.05	45.38	19.60	1.482	1.455	1.644	1.508
S2/b	100.10	21.16	45.38	19.51	1.565	1.590	1.578	1.588
S2/c	100.05	30.02	45.32	19.54	1.556	1.549	1.561	1.554
S3/a	100.02	12.05	68.01	0	1.488	1.491	1.604	1.624
S3/b	100.10	21.01	68.10	0	1.459	1.468	1.515	1.511
S3/c	100.81	30.26	68.17	0	1.401	1.402	1.388	1.401
M1	100.00	12.70	0	53.96	1.652	1.755	1.733	1.866
M2	100.26	22.22	0	53.5	1.611	1.806	1.705	1.755
M3	100.00	29.33	0	53.33	1.426	1.491	1.514	1.424

The results were compared with K_A determined in our previous work for the mixtures free of hydrogen peroxide (M1-M3) [2]. It was concluded that K_A values were higher for the system free of hydrogen peroxide when the amount of acetic acid was around 12 and 21 g per 100 g oil. However, comparison of the values for mixtures with around 30 g A per 100 g oil, showed that K_A values for system without HP were in a range of values determined for the system with HP. It was also observed that range of K_A values for mixtures with HP (1.380-1644) is smaller than for the mixtures free of HP (1.424-1.866).

Conclusion

Liquid-liquid equilibrium constant for acetic acid in the system soybean oil-acetic acid-hydrogen peroxide-water was determined at four temperatures by employing nine different compositions. There was no defined trend of K_A values dependent of temperature and composition of the investigated reaction system, similar as for system free of hydrogen peroxide. The presence of hydrogen peroxide, however, reduced the range of K_A values for applied conditions.

Acknowledgment

This work is part of the Project #III 45022 supported by the Ministry of Education and Science of the R. Serbia.

References

- [1] A. Campanella, B. Mandagarán, E. Campanella, J. Am. Oil Chem. Soc., 2009, 86, 513-519.
- [2] S. Sinadinović-Fišer, M. Janković, J. Am. Oil Chem. Soc., 2007, 84, 669-674.
- [3] M. Janković, S. Sinadinović-Fišer, J Am. Oil Chem. Soc., 2010, 87, 591-600.

THERMODYNAMIC STUDY OF THE ADSORPTION OF THE ACID DYE ONTO ORGANOBEENTONITE

N. Jović-Jovičić, A. Milutinović-Nikolić, M. Žunić, P. Banković,
A. Ivanović-Šašić, D. Lončarević, D. Jovanović

University of Belgrade- Institute of Chemistry, Technology and Metallurgy, Center for Catalysis and Chemical Engineering, Njegoševa 12, 11000 Belgrade, Serbia

Abstract

Removal of Acid Orange 10 (AO10) dye from aqueous solutions using organobentonite was investigated. In this study experiments were carried out at different temperatures (298–333 K) in order to obtain thermodynamic parameters for adsorbate/adsorbent system i.e. activation energy (E_a), Gibbs free energy (ΔG°), enthalpy (ΔH°) and entropy (ΔS°). The results of thermodynamic studies indicate that adsorption of AO10 onto organobentonite is an endothermic process ($\Delta H^\circ=31$ kJ/mol), while the value for E_a of 76 kJ/mol suggests chemisorption as adsorption mechanism.”

Introduction

The world-wide high level of production and use of dyes generates colored wastewaters that are threat to environment [1]. Adsorption is widely used for the removal of contaminants from wastewaters. The data based on adsorption isotherms plays an important role in predictive modeling for analysis and design of adsorption systems [2]. In this paper local bentonite clay (Bogovina) rich in smectite was modified with HDTMA ion. The obtained organoclay was used for adsorption of textile dye – Acid Orange 10 (AO10) from water solution at different temperatures. The thermodynamic parameters were deduced from the adsorption measurements. This data could be very useful in elucidating the nature of adsorption.

Experimental

Bentonite was obtained from Coal and Bentonite Mine “Bogovina”, Serbia. It was crushed, ground and sieved through a 74 μm sieve. Hexadecyl trimethylammonium (HDTMA) bromide and Acid Orange 10 (AO10) dye were supplied from Alfa-Aesar Chemical Company, with a chemical purity of 98% and 80% respectively. The organobentonite was obtained followed common procedure [3], with surfactant/bentonite ratio corresponding to double value of cation exchange capacity (2.0 HDTMA-B).

All experiments were carried out at differed temperatures (298, 313, 323 and 333 K) with solution volume ($v= 0.050$ dm^3); concentration of AO10, $C_0=50$ mg dm^{-3} ; mass of adsorbent ($m_{\text{adsorb}} = 0.01$ g). A period of 24 h was taken as equilibrium although in some experiments equilibrium was reached much earlier.

The AO10 concentration was estimated by spectrophotometer Nicolet Evolution 500 UV-VIS, Thermo Electron using $\lambda_{\max}=478$ nm.

Results and Discussion

Arrhenius relationship was used to evaluate the activation energy of adsorption:

$$\ln k_2 = \ln A - \frac{E_a}{RT} \quad (1)$$

Where k_2 is pseudo-second-order rate constant, E_a is the Arrhenius activation energy (kJ/mol), A the Arrhenius factor, R the gas constant (8.314 J/mol K) and T(K) is the temperature of solution.

The thermodynamic parameters such as change in standard free energy (ΔG°), enthalpy (ΔH°) and entropy (ΔS°) were determined by using the following equations [4]:

$$K_C = \frac{q_e}{C_e} \quad (2)$$

$$\ln K_C = \frac{\Delta S^\circ}{R} - \frac{\Delta H^\circ}{R} \quad (3)$$

$$\Delta G^\circ = -RT \ln K_C \quad (4)$$

Where K_C is the standard thermodynamic equilibrium constant defined by ratio between the amount of adsorbed dye per 1 g of adsorbent (q_e) and equilibrium concentration of dye after adsorption process (C_e) – Eq. 1. When $\ln k_2$ is plotted versus $1/T$ a straight line with slope $-E_a/R$ is obtained (Fig. 1a). By plotting a graph of $\ln K_C$ vs. $1/T$ (Eq. 2, Fig. 1b) the values ΔH° and ΔS° were estimated.

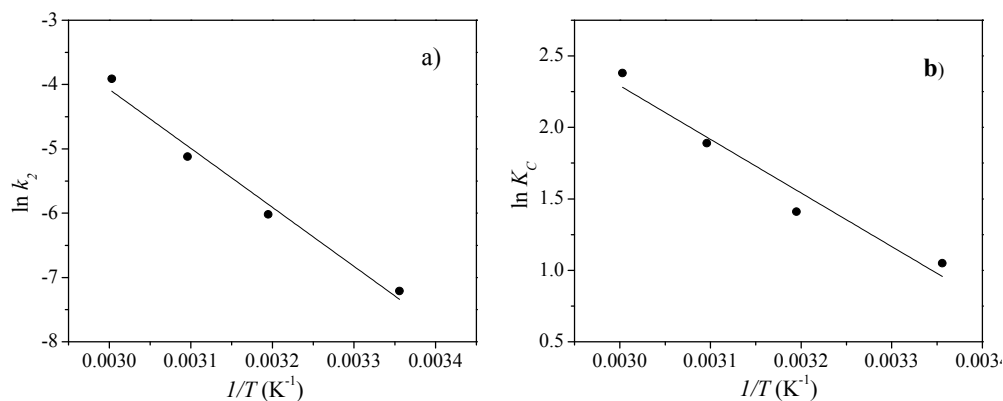


Figure 1. a) Arrhenius plot and b) plot of $\ln K_C$ vs $1/T$.

Calculated thermodynamic parameters are presented in Table 1.

Table 1. Thermodynamic parameters for the adsorption of AO10 onto organobentonite 2.0 HDTMA-B

T[K]	E_a (kJ mol ⁻¹)	ΔG° (kJ mol ⁻¹)	ΔH° (kJ mol ⁻¹)	ΔS° (J K ⁻¹ mol ⁻¹)
298	76	-2.8	31	113
313		-3.4		
323		-5.2		
333		-6.6		

The obtained positive ΔH° value indicates that adsorption process of the AO10 dye is endothermic. Higher temperatures promote the adsorption of AO10 on the organomodified bentonite since ΔG° value is negative and ΔS° positive.

The common values of E_a for chemisorption are within range 40-800 kJ/mol, while lower E_a values (5–40 kJ/mol) suggest physisorption mechanism [5]. The obtained E_a of 76 kJ/mol confirmed that chemisorption is mechanism of the adsorption of acid dye AO10 onto organobentonite 2.0 HDTMA-B.

Conclusions

Organobentonite was obtained by modification of local clay (Bogovina) with hexadecyl trimethylammonium ion. The adsorption of AO10 on the obtained organobentonite in temperature range 298 – 323 K was investigated. Thermodynamic parameters were calculated. The E_a of adsorption was evaluated using the pseudo-second-order rate constant. The estimated $E_a = 76$ kJ mol⁻¹ indicates that chemisorption occurred. The obtained positive ΔH° and negative values of ΔG° indicate that adsorption process of the AO10 dye is endothermic and show that equilibrium is shifted to the side of product (adsorbed AO10), which is more pronounced at higher temperatures.

Acknowledgment

This work was supported by the Ministry of Education and Science of the Republic of Serbia (Project III 45001).

References

- [1] A. Özcan, E. M. Öncü, A. S. Özcan. J. Hazad. Mater., 2006, B129, 244-252.
- [2] S.J. Allen, G. Mckay, J.F. Porter, J. Colloid Interf. Sci., 2004, 280, 322–333.
- [3] N. Jović–Jovičić, A. Milutinović–Nikolić, P. Banković, Z. Mojović, M. Žunić, I. Gržetić, D. Jovanović. Appl. Clay Sci., 2010, 47, 452–456.
- [4] B. S.Chu, B. S. Baharin, Y. B. Che Man, S. Y. Quek, J. Food Eng., 2004, 62, 97-103.
- [5] B. H. Hameed, A. A. Ahmad, N. Aziz, Chem. Eng. J., 2007, 133, 195–203.

A-6-P

STUDIES OF MOLECULAR INTERACTIONS IN SOLUTIONS OF SOME SYNTHESIZED AZOMETHINES

Shipra Baluja*, Rahul Bhalodia

*Physical Chemistry Laboratory, Department of Chemistry
Saurashtra University, Rajkot-360005 (Gujarat) INDIA*

**E mail: shipra_baluja@rediffmail.com*

Abstract

Density, ultrasonic velocity and viscosity of some azomethines containing Sulfamethoxazole nucleus have been measured in dimethyl sulfoxide and tetrahydrofuran solutions over a wide range of concentration at 308.15 K. From these experimental data, various acoustical parameters have been evaluated, which helps in understanding the molecular interactions occurring in these solutions.

Introduction

Azomethines are an important class of compounds which have extensive applications in different fields^[1-4]. Further, many workers reported a wide range of biological activity^[5-10].

Thus, significant biological properties associated with azomethines derivatives have aroused considerable interest to study the acoustical properties of some azomethines in different solvents.

In this work, some new azomethines have been synthesized and density, viscosity and ultrasonic velocity of their solutions in N, N-dimethylformamide and tetrahydrofuran solutions were measured at 308.15K over a wide range of concentrations. From these experimental data, various acoustical properties have been evaluated to understand the molecular interactions in these solutions.

Results and Discussion

The ultrasonic velocity is found to increase with concentration for all the compounds in both the solvents whereas intermolecular free path length is found to decrease. The decrease of intermolecular free path length is due to strong interaction between solvent and compound molecules, which causes velocity to increase. The isentropic compressibility and relaxation strength of solutions for the studied compounds in both the solvents are also found to decrease with increase of concentration. Due to solute-solvent interactions in the system, compressibility of the solution decreases with the increase in solute concentration. The increase in viscosity in both solvents also confirms the same. The association between solute and solvent molecules is further confirmed by relative association values, which are found to increase continuously with concentration for all the compounds in both the solvents.

As indicated in Fig. 1, different compounds have different group at different positions. The compounds R-1 and R-3 contains chloro group at meta and

ortho positions whereas R-2 and R-4 contains nitro group at meta and ortho positions respectively.

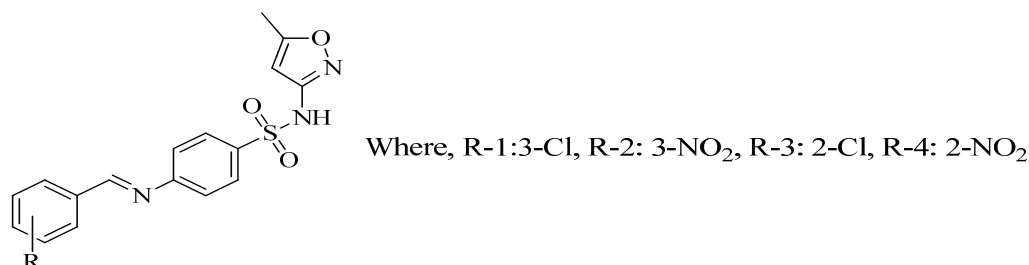


Figure 1. General structure of R series.

The interactions in a solution can also be confirmed by the solvation number, which is a measure of structure forming or structure breaking tendency of a solute in a solution. For all the compounds, solvation number increases with concentration and are positive. The positive solvation number suggests structure forming tendency of compounds in solution, Fig. 2. This also confirms that there exist strong solute-solvent interactions in studied solutions.

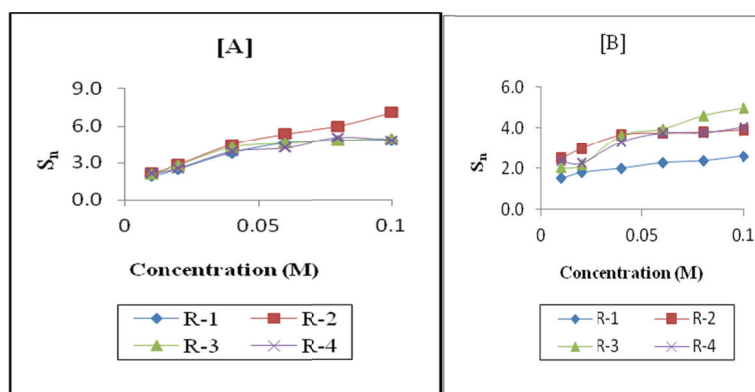


Figure 2. Variation of Solvation Number (S_n) with concentration in [A] DMF and [B] THF.

Further, apparent molar compressibility and apparent molar volumes of the solutions were calculated. From the plots of these apparent properties against square root of concentration, some coefficients, which are the measure of solute-solvent and solute-solute interactions, are evaluated from the intercept and slope. The values of these coefficients further indicate solute-solvent interactions in studied systems.

References

- [1] M. Pilecki, Z. Marczewski and J. Gora, Kosmetyki, 1984, 28, 223-227.
- [2] M. N. Ibrahim and S. E. A. Sharif, E J. Chem., 2007, 4, 531-535.

A-6-P

-
- [3] S. M. A. Hosseini and A. Azimi, *Material and Corrosion*, 2008, 59, 41-45.
- [4] Q. Luo, H. Zheng, Y. Peng, H. Gao, L. Lu and Y. Cai, *J. Poly. Sci.*, 2009, 47, 6668-6681.
- [5] P. Mishra, P. N. Gupta, A. K. Shakya, R. Shukla and R. C. , Srimal, *Ind. J. Phys. Pharma.*, 1995, 39, 169-171.
- [6] S. K. Sridhar, S. N. Pandeya, and E. De Clercq; *Bull. Chim. Farma.*, 140, 302-305 (2001).
- [7] A. Kundu, N. A. Shakil, D. B. Saxena, P. Kumar and J. S. Walia, *J. Environ. Sci. Health*, 44, 428-434 (2009).
- [8]. V. E. Kuz'min, A. G. Artemenko, R. N. Lozytska, A. S. Fedtchouk, V. P. Lozitsky, E. N. Muratov and A. K. Mescheriakov, *SAR and QSAR in Environ. Res.*, 2005, 16, 219-230.
- [9] A. Cinarli, D. Gürbüz , A. Tavman and A. S. Birteksöz, *Bull. Chem. Soc. Ethiop.* ,2011, 25, 407-417.
- [10] J. M. Xavier, M. A. Raj, J. M. Marie, *J. Chem. Pharma. Res.*, 2012, 4, 669-672.

THERMODYNAMICS OF THE SOLUBILITY OF ESOMEPRAZOLE MAGNESIUM TRIHYDRATE IN SOME ALCOHOLS FROM 298.15 TO 318.15 K

Sumitra Chanda^{1*}, Shipra Baluja², Kapil Bhesaniya²

¹ *Phytochemical, Pharmacological and Microbiological Laboratory
Department of Biosciences,*

² *Physical Chemical Laboratory, Department of Chemistry,
Saurashtra University, Rajkot (360005), Gujarat, India*

**E. mail:svchada@gmail.com*

Abstract

The solubility of esomeprazole magnesium trihydrate in methanol, ethanol, 1-propanol and 1-butanol was measured at temperatures ranging from (298.15 to 318.15) K at atmospheric pressure using gravimetric method. The solubility is found to be maximum in 1-butanol and minimum in ethanol. The experimental solubility data is correlated with the modified Apelblat equation. Some thermodynamic parameters such as dissolution enthalpy, Gibb's energy, and entropy of mixing have also been calculated.

Introduction

Esomeprazole Magnesium trihydrate (ESO) is member of prazole series with the name bis(5-methoxy-2-[(S)-[(4-methoxy-3,5-dimethyl - 2 -pyridinyl)methyl]sulfinyl] - 1-H -enzimidazole - 1 -yl) magnesium trihydrate^[1] (CAS number [217087-09-7]). It inhibits gastric acid secretion and relieves heartburn. Further, it is cost effective in the treatment of gastric oesophageal reflux diseases. It is S-isomer of omeprazole and is the first single optical isomer proton pump inhibitor. It provides better acid control than current racemic proton pump inhibitors and has a favorable pharmacokinetic profile relative to omeprazole^[2]. The benefits of esomeprazole have been extensively studied^[3-6]. It is necessary to know the solubility of ESO in different solvents for the design of an optimized crystallization process.

In the present study, solubility of esomeprazole magnesium trihydrate in pure methanol, ethanol, 1-propanol and 1-butanol was measured in the temperature range from (298.15 to 318.15) K at atmospheric pressure by gravimetric method. Further, some thermodynamic parameters such as enthalpy, Gibb's energy, and entropy have also been calculated.

Result and Discussion

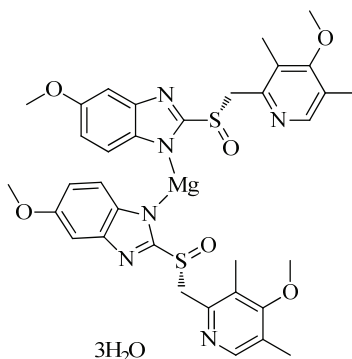
It is observed that solubility of esomeprazole magnesium trihydrate is maximum in 1-butanol and minimum in ethanol. It is of the order: 1-butanol > methanol > 1-propanol > ethanol.

With increase in temperature, solubility is found to increase in all the four alcohols.

A-7-P

The solubility of esomeprazole magnesium trihydrate as a function of temperature is correlated by the modified Apelbat equation^[7-9].

Esomeprazole magnesium trihydrate



For all the four alcohols, thermodynamic parameters i.e., dissolution enthalpy, Gibb's energy and entropy are found to be positive, Table 1. The positive enthalpy indicates the endothermic dissolution of drug^[10]. This may be due to interaction between drug and alcohol molecules. The newly formed bond energy with drug molecules and alcohol molecules is not enough powerful to compensate for the energy needed for breaking the original association bond with alcohol.

Table 2. Thermodynamic parameters: Gibbs's energy (ΔG_{sol}), dissolution enthalpy (ΔH_{sol}), and entropy (ΔS_{sol}), of ESO in different alcohols.

Solvent	ΔG_{sol} kJ·mol ⁻¹	ΔH_{sol} kJ·mol ⁻¹	ΔS_{sol} J·mol ⁻¹ ·K ⁻¹
Methanol	12.450	38.552	84.7380
Ethanol	18.463	37.238	60.9521
n-propanol	17.498	40.356	74.2084
n-Butanol	9.634	52.236	138.3119

The entropy changes in the following order: 1-butanol > methanol > 1-propanol > ethanol, which is same as that of solubility of drug in these alcohols, Table 1. The increase in entropy can be explained by the fact that due to addition of drug, alignment of alcohol molecules are disrupted thereby decreasing the degree of order in the system. The positive enthalpy and entropy suggest that solubility of studied drug is entropy driving process^[11]. The positive values of Gibb's energy indicate that the dissolution process is not spontaneous^[11].

References

- [1] T. Andersson, M. A. Hassan, G. Hasselgren, K. Rohss and L. Weidolf, *Clinical Pharmacology*, 2001, 40, 411-426.

-
- [2] L. J. Scott, C. J. Dunn, G. Mallarkey and M. Sharpe, *Drugs*, 2002, 62, 1503-1538.
- [3] L. Olbe, E. Carlsson and P. Lindberg, *Nat. Rev. Drug Disc.*, 2003, 2(2), 132-139.
- [4] P. B. Kale-Pradhan, H. K. Landry and W. T. Sypula, *Ann. Pharmacother.*, 2002, 36(4), 655-663.
- [5] P. Lindberg, D. Keeling, J. Fryklund, T. Andersson, P. Lundborg and E. Carlsson, *Aliment. Pharmacol. Ther.*, 2003, 17(4), 481-488.
- [6] E. Chong and M. H. Ensom, *Pharmacotherapy*, 2003, 23(4), 460-471.
- [7] A. Apelbat and E. Manzurola, *J. Chem. Thermodyn.*, 1999, 31, 85-91.
- [8] A. Apelbat, E. Manzurola and N. A. Balal, *J. Chem. Thermodyn.*, 2006, 38, 565-571.
- [9] L. S. Gan, Z. Z. Wang and C. X. Zhou, *J. Chem. Eng. Data* 2009, 54, 160-161.
- [10] A. Z. El-Sonbati, A. A. A. El-Bindary, A. G. F. Shoair and R. M. Younes, *Chem. Pharm. Bull.* 2001, 49, 1308-1313.
- [11] C. L. Zhang and Y. Wang, *J. Chem. Eng. Data*, 2008, 53, 1295-1297

PHASE DIAGRAMS OF In-S and Ga-Se SYSTEMS

A. Zavrazhnov¹, A. Naumov¹, A. Kosyakov¹, S. Berezin¹,
V. Sidey², V. Zlomanov³

¹- Chemistry Dep., Voronezh State University, Russia, E-mail: AlZavr08@rambler.ru

²- Chemistry Department, Uzhgorod State University, Uzhgorod, Ukraine

³- Chemistry Department, Moscow State University, Moscow, Russia

Abstract

The present work is concerned with the investigation of the phase diagrams for the systems In-S and Ga-Se (it is known that gallium and indium chalcogenides are promising materials for new technologies). It is underlined that the general appearance of T - x diagrams for these systems is reproduced in a number of different works of 1970s to the 2010s. However, there are considerable discrepancies concerning the types and temperatures of the solid phase transformations and homogeneity regions of these phases. These discrepancies can be caused by the very low volatility of solid gallium and indium chalcogenides as well as ambiguous interpretation of the results of electrical measurements.

Results and Discussion

So, to refine T - x -diagrams of mentioned above systems we worked out and applied a new way of the *thermal analysis*. This way is based on the analysis of a series of the computer color images of the substance surface, shined with reflected light. In course of the experimental procedure the powder of investigated sample is placed into the optical cuvette; the temperature of the sample can be varied. It is noticed, that this way of thermal analysis is static. It enables to obtain trustworthy information concerning the phase diagrams for the systems, which are distinguished by very hard kinetics also. Some criteria allow one to precise the temperatures of the phase transformations are under consideration.

The refined T - x -diagrams of Ga-Se and In-S systems are given and discussed. In particular, the retrograde solidus for the GaSe phase is reaffirmed. Concerning the In-S system

- the existence of high-temperature modification of indium monoselenide (InS''), which is the stable at narrow temperature range (663-690 °C) and
- the presence of the congruent InS'' \leftrightarrow InS' transformation point (distectoid point) at such T - x -diagram are confirmed (fig. 1).

For the scanning of P - T - x -diagram of the In-S system the spectrophotometric technique is elaborated. We suggested studying the equilibria of indium sulfides with hydrogen as an auxiliary component. It is proved that the equilibrium in this system after introducing hydrogen must be described by the following equation



So, there is no noticeable vaporization of chemically bounded indium to the vapor. When the equilibrium shift (1) takes place, this element should be accumulated (consumed) in the condensed part of the system and cause transformations of some sulfides into other sulfides or changes of their non-stoichiometry.

Vast thermodynamic information about phases of In-S system can be received if it is possible to determine $K_p^\#$, which relates pressures of hydrogen and hydrogen sulfide as

$$K_p^\# = \frac{p_{\text{H}_2\text{S}}}{p_{\text{H}_2}} \quad (2)$$

To find the value of $K_p^\#$, one needs to know partial pressure of, at least, one of two molecular forms - H_2 or H_2S . Then the equilibrium pressure of another form (for example, hydrogen - p_{H_2}) can be determined if the pressure of initially introduced hydrogen (P°) is known:

$$p_{\text{H}_2} = P^\circ - p_{\text{H}_2\text{S}} \quad (3)$$

where in (3) all the terms - p_{H_2} , P° , $p_{\text{H}_2\text{S}}$ - relate to room temperature (at which the ampoule is being filled with hydrogen at the beginning of the experiment and the optical research is carried out). According to Charles's Law and (3), the equation (2) can be written as

$$K_p^\# = \frac{p_{\text{H}_2\text{S}}}{P^\circ - p_{\text{H}_2\text{S}}} \quad (4)$$

Hydrogen sulfide is known to have an electronic absorption spectrum in the "air" ultraviolet spectral region ($\lambda_{\text{max}} = 196 \mu\text{m}$). This enables quantitative determination of H_2S in the vapor phase by spectrophotometry. The fulfilled experiments give the opportunity of getting data about the In-S phase diagram.

The objective of this work is refinement of the phase diagram of the In-S system within the composition field of 50-60 mol. % and analysis of homogeneity region of the phase $\text{In}_{3-x}\text{S}_4$.

To achieve this goal, we solved the following problems:

A. Worked out the method allowing us to get the equilibrium state between indium sulfides and hydrogen at different temperatures within the closed system, to harden this equilibrium and to study it by spectrophotometry.

B. Carried out calibrating experiments which let us establish the dependency between hydrogen sulfide pressure and its absorption characteristics in UV-absorbing region of H_2S .

C. For different series of composition of In-S system and different temperatures, we attained the equilibrium state between indium sulfides and hydrogen, and performed hardening. Then analyzed the absorption spectrum of hydrogen sulfide for every experiment with frozen equilibrium, that let us obtain the temperature dependencies of $K_p^\#$ and p_{S_2} for different compositions of In-S system.

The experiments on In-S system were carried out using hydrogen as follows.

A-8-P

1. In-S alloys containing 48 to 60 mol % S were prepared by direct elemental synthesis (alloying at $T=1100\text{ }^{\circ}\text{C}$ for 5 hours, annealing at $T=630\text{ }^{\circ}\text{C}$ for 12 hours). The alloys were ground in a mortar to a particle size of 0.1 mm.

2. A weighed amount of the powder (about 1 g) was placed on the bottom of an ampule made from a one piece optical cuvette of KU-1 silica glass.

3. The ampule was filled with hydrogen to a controlled pressure from $3\cdot 10^4$ to $8\cdot 10^4$ Pa. Measurement was accomplished using digital sensor XP_{i2} with an error less than 27 Pa. After that the cuvette was sealed off, and placed in the isothermal zone of a resistive furnace.

4. Next, the powder was isothermally annealed at temperatures from 350 to 750°C for 1–30 h. Annealing was finished by hardening in water or air.

5. The study of absorption spectrum was realized in the interval of wavelength from 190 to 290 μm at room temperature ($20\text{--}22^{\circ}\text{C}$).

6. Annealing experiments were also hold for the same ampule but under other temperature or time conditions. After hardening the study of absorption spectrum was repeated, and the process took place again from the beginning.

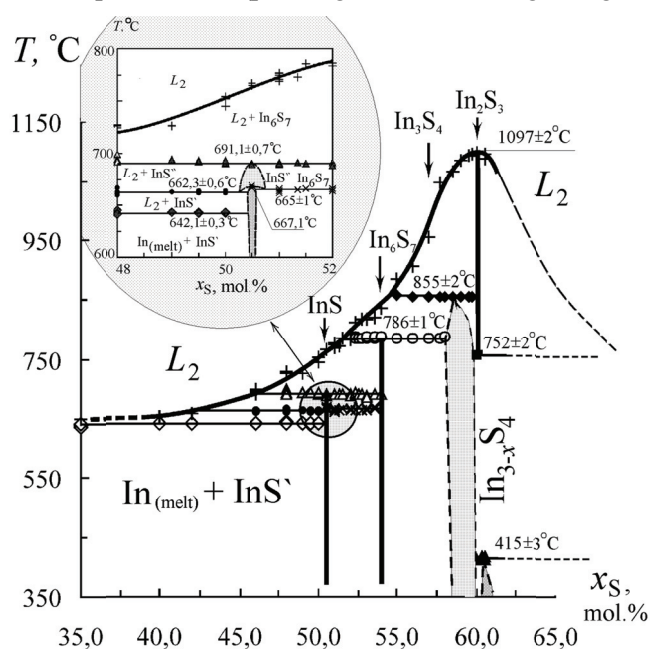


Figure 1. T - x -phase diagram of the In-S system.

Analyzing the $K_p^{\#}$ - T – dependences we assume that the $\text{In}_{3-x}\text{S}_4$, a phase with a broad homogeneity range (fig. 1), has a tendency to decompose into two separate phases in a wide temperature range. Moreover, our results confirm the existence of a narrow two phase field between $\text{In}_{3-x}\text{S}_4$ and In_2S_3 at low temperature region.

Acknowledgements

This work was supported by Russian Foundation for Basic Research, pr. 11-03-90430.

CORRELATION OF pK_a VALUES FOR SERIES OF BENZOIC ACIDS WITH THE THEORETICALLY CALCULATED ATOMIC CHARGES

Ž. J. Vitnik,¹ V. D. Vitnik,² S. V. Pokorni¹, I. O. Juranić²

¹ Faculty of Chemistry, University of Belgrade, Belgrade, Serbia

² Department of Chemistry, IChTM, University of Belgrade, Belgrade, Serbia

Abstract

The four-parameter linear-regression involving partial atomic charges was defined of all atoms of carboxylic group, as the quantum-chemical descriptor for predicting physico-chemical properties (pK_a). Based on these four-parameter equations, the new QSPR equations for prediction of pK_a values of series of benzoic acids have been derived.

Introduction

The acid dissociation constant, K_a , which describes the extent to which the compound dissociates in the gas phase or in the solution, is a fundamental property of many chemical compounds. It is a key feature which governs the chemical reactivity of the substances in any solvent, and the interaction with the solvent itself. In aqueous solution, the pK_a is responsible for several pharmacokinetic properties. Jointly with integrity, lipophilicity, solubility, and permeability, pK_a has been considered as one of the five key physico-chemical profiling screens to predict the key properties that affect ADME(T) characteristics [1].

Computational details

Two semiempirical models MNDO-AM1 and MNDO-PM3 from MOPAC program package version 7.01 have been used in this work, and the solvent has been simulated by COSMO model implemented in it. Program Gaussian 03 has been used for *ab initio* calculations at the HF/6-311++G** and B3LYP/6-311++G** levels, in vacuum and with the simulation of solvent (water) by CPCM model.

The geometries of all conformers are fully optimized; energies of conformers were calculated, as well as the atomic partial charges on all atoms of COOH group. The Boltzmann analysis was used for calculation of statistical contribution of conformers in equilibrium, N_i . By summing contribution of conformers N_i and charges for an atom $q_{i,A}$ by equation:

$$Q_A = \sum_i N_i q_{i,A}$$

we defined a new, so-called, 'equilibrium' charge Q_A [2].

Results and Discussions

The partial atomic charges of all atoms for carboxylic group, are exploited as quantum-chemical descriptors for estimating physico-chemical properties [3,4], such as pK_a , through a four-parameter linear regression equation, defined as:

$$pK_a = Aq(H) + Bq(-O-) + Cq(=O) + Dq(C) + E$$

where $q(H)$, $q(-O-)$, $q(=O)$, $q(C)$ are the partial atomic charge on hydrogen atom, hydroxylic oxygen, carbonyl oxygen, and carbon atom of the carboxylic group, A, B, C and D are parameters for corresponding descriptors, and E is interception on the y-axis.

In order to determine the applicability of the equation, as well as to find the most useful types of partial atomic charges (Coulson, Mulliken, NBO, ...), and the best calculation method for estimation of partial charge descriptors (AM1, AM1-COSMO, PM3, PM3-COSMO, HF/6-311++G**, HF/6-311++G**/CPCM, B3LYP/6-311++G**, B3LYP/6-311++G**/CPCM) for predicting pK_a values, the correlations have been made with series of benzoic acids that can exist in solution in different conformations and in differently charged states (cationic, anionic and zwitter-ion).

Correlation results of the four-parameter equation have been compared with the results acquired by other equations.

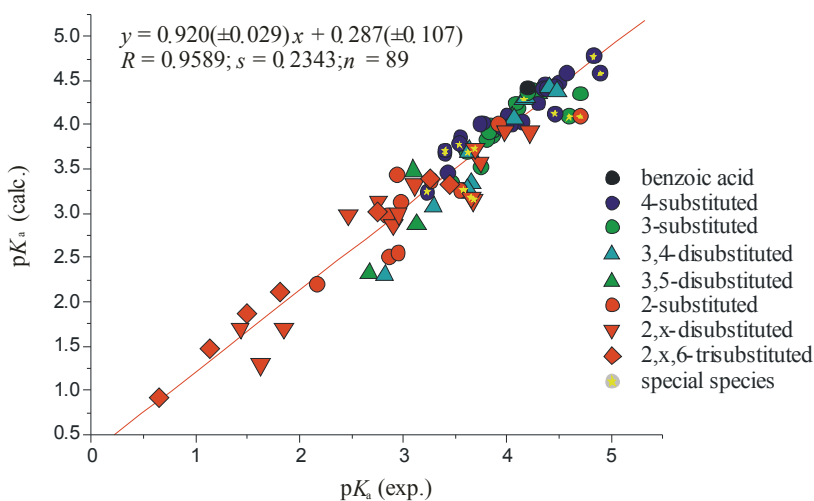


Figure 1. Relation between experimentally determined and calculated pK_a values for series of 89 substituted benzoic acids.

For a series of 89 benzoic acids the best result was obtained from correlation of 'equilibrium' Mulliken charges obtained with semiempirical PM3 model with the simulation of solvent (water) by COSMO model. New QSPR equations for prediction of pK_a values for benzoic acids have been suggested based on this four-parameter equation:

$$pK_a(\text{calc.}) = -100.43Q_M(\text{H}) - 39.70Q_M(\text{-O-}) - 54.77Q_M(\text{=O}) - 68.81Q_M(\text{C}) + 29.02$$

and result of correlation is shown on Fig. 1.

Conclusion

This four-parameter equation has produced better correlation results in almost all series of benzoic acids we have examined, thus proving that partial charges of all atoms of carboxylic group must be used to obtain good QSPR equations for prediction of pK_a values. Unlike LFER equations, it can be successfully used to predict pK_a values of compounds with *ortho*-substituents and/or other substituents that have no evaluated substituent constants.

It has been established that Coulson, Mulliken, and "natural" partial atomic charges obtained through semiempirical and *ab initio* calculations combined with our four-parameter equation produce good QSPR descriptors for prediction of pK_a values of benzoic acids. Analysis of the correlation results obtained, has shown that in order to provide good correlations, use of solvation models (COSMO and CPCM) is mandatory in geometry optimization and calculation of atomic charges, as well as use of statistically averaged charges, calculated by Boltzmann analysis, in case when molecules can exist in multiple conformations or in states of different charge (cations, anions and zwitter-ions).

Comparing correlation results obtained by semiempirical models and those from *ab initio* models, it can be concluded that semiempirical models produce correlations that - in most situations - have similar or even higher quality than those acquired from *ab initio* models. It can be inferred that use of sophisticated, and computationally demanding methods, is not obligatory for producing good correlations. A good correlation result, as well as good predictivity of equations thus obtained, can be achieved through use of semiempirical methods.

Acknowledgments

This work has been financially supported by Ministry of Education and Science, Republic of Serbia, under Grant No. 172035 and by EU FP7 project HP-SEE, <http://www.hp-see.eu/>, contract number 261499.

References

- [1] H. Wang, J. Ulander, *Expert Opin. Drug Metab. Toxicol.* 2006, 2, 139-155.
- [2] Ž. Vitnik, Correlations between physical and chemical properties of carboxylic acids with a calculated atomic charges, PhD thesis, Belgrade, 2011.
- [3] B. Jovanović, I. Juranić, M. Mišić-Vuković, D. Brkić, Ž. Vitnik, *J. Chem. Research (S)*, 2000, 506-507; *J. Chem. Research (M)*, 2000, 1257-1264.
- [4] L. Pfenndt, B. Dražić, G. Popović, B. Drakulić, Ž. Vitnik, I. Juranić, *J. Chem. Research (S)*, 2003, 247-248; *J. Chem. Research (M)*, 2003, 501-514.

**SPECTROSCOPY,
MOLECULAR STRUCTURE,
PHYSICAL CHEMISTRY OF
PLASMA**

STUDY OF ANTIOXIDATIVE MECHANISMS OF QUERCETIN

Zoran Marković

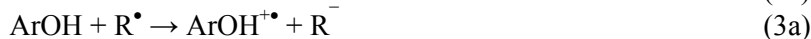
*Department of Chemical-Technological Sciences, State University of Novi Pazar
36300 Novi Pazar, Republic of Serbia*

Abstract

The extensive theoretical study of the interactions of one of the most abundant and reactive flavonols, quercetin (Q), with hydroperoxy radical and hydroxide anion was performed. The results indicating that quercetin is not a planar molecule are in accord with the X-ray analysis. Our investigation reveals that the reaction of Q with the hydroperoxy radical is governed by the HAT mechanism. It was found that Q cannot undergo the SET-PT mechanism in the presence of hydroxide anion in the gaseous phase, whereas it is a plausible mechanism in the aqueous solution.

Introduction

Flavonoids are natural phenolic compounds recognized as potent external defense factors against oxidative damage. Their protective role correlates well with their antioxidant activity which is manifested through different actions, like direct radical scavenging, transition metal chelation, inhibition of certain enzymes, or removing oxidatively changed and damaged biomolecules. [1-3] In the radical scavenging mechanisms reactive radical species are inactivated by accepting a hydrogen atom from a hydroxyl group of the flavonoid. This transfer can be visualized through at least three mechanisms: hydrogen atom transfer (HAT, Eq. 1), sequential proton loss electron transfer (SPLET, Eq. 2), and single electron transfer followed by proton transfer (SET-PT, Eq. 3) [4-6].



This paper addresses the potential antioxidant activity of each of the quercetin reactive sites in simulated reactions with hydroperoxy radical. The structure–activity relationships are examined in the light of the obtained results. In addition, possible reaction pathways of once formed $\text{Q}^{\bullet+}$ in the presence of the hydroxide anion are considered. The reactions of Q are investigated at the M052X/6-311+G(d,p) level of theory.

Results and Discussion

Energetics related to radical scavenging mechanisms, which all have the same net result, are governed by different molecular properties: bond dissociation enthalpy (BDE) of ArOH in the HAT mechanism, proton affinity (PA) of ArOH together with electron transfer energy (ETE) of ArO⁻ in the SPLET mechanism, and ionization potential (IP) of ArOH in the SET-PT mechanism. Reaction enthalpies related to the three mechanisms (HAT, SPLET, and SET-PT) of Q were calculated for both gaseous and aqueous phases (Table 1).

Table 1. Calculated parameters for radical scavenging activity of quercetin (kJ/mol)

position	gaseous phase					aqueous solution				
	HAT BDE	SPLET PA ETE		SET-PT IP PDE		HAT BDE	SPLET PA ETE		SET-PT IP PDE	
				737					334	
5	419	1422	318		1004	383	112	270		48
7	386	1363	345		971	383	94	289		49
3'	368	1429	261		953	349	116	232		14
3	355	1403	273		940	334	108	226		0
4'	319	1338	303		904	333	93	240		-1

It can be concluded, on the basis of the BDE values, that among five OH groups of Q, the 4'-OH has the greatest ability to donate H atom. The 4'-OH group has the lowest BDE value in both phases, so it represents the first site that can donate its H atom, followed by 3-OH and 3'-OH. Table 1 reveals that the HAT mechanism is dominant in the gaseous phase, because the BDE values are significantly lower than the corresponding IP and PA values. In the aqueous solution the PAs are significantly lower than the corresponding BDE values. This indicates that the SPLET mechanism represents thermodynamically most probable reaction pathway in polar solvents. On the other hand, if we compare BDE to the sums PA + ETE (SPLET), and IP + PDE (SET-PT), it is clear that these values are mutually very similar. One can conclude, on the basis of these facts, that all three mechanisms are competitive in the aqueous solution. The BDE, PA and PDE values show that the 4'-OH group is the most reactive OH group of Q.

Reactions of quercetin with the hydroperoxy radical. Bearing in mind the reactivity of OH groups of Q, we take a step further, and investigate the reactions of all OH groups with hydroperoxy radical. Hydroperoxy radical is chosen because numerous natural peroxides are of the similar structure (ROO[•]), so that the obtained results can demonstrate their general behavior. The calculations reveal that detachment of H atom by hydroperoxy radical can be performed with all five hydroxyl groups.

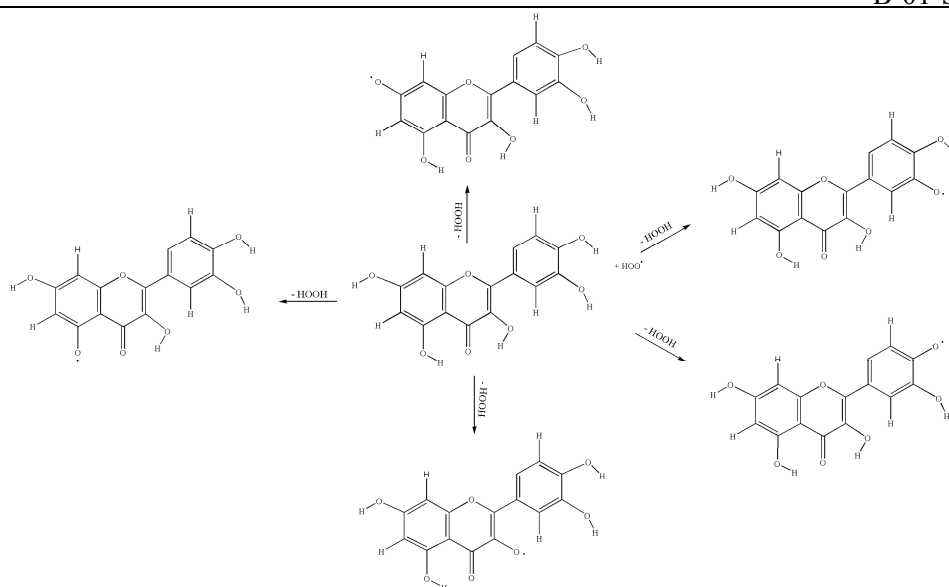


Figure 1. Five reaction pathways for the reaction of quercetin with hydroperoxy radical

Table 2. Total energy (E), enthalpy (H^{298}), and free energy (G^{298}) for the species under investigation. All energies are given in Hartrees

	E	H^{298}	G^{298}	Ratio
Q	-1103.9226	-1103.9080	-1103.9702	
HOO	-150.8684	-150.8650	-150.8896	
HOOH	-151.4981	-151.4948	-151.5195	
4'OH	-1103.3016	-1103.2888	-1254.8385	0.45
3'OH	-1103.2982	-1103.2846	-1254.8392	1
3OH	-1103.2894	-1103.2751	-1254.8317	3×10^{-4}
5OH	-1103.2650	-1103.2504	-1254.8179	2×10^{-10}
7OH	-1103.2765	-1103.2618	-1103.3244	3×10^{-7}
TS4'	-1254.7861	-1254.8385	-1103.3474	
TS3'	-1254.7862	-1254.7690	-1103.3440	
TS3	-1254.7802	-1254.7632	-1103.3360	
TS5	-1,254.7648	-1,254.7473	-1103.3474	
TS7	-1,254.7717	-1,254.7543	-1103.3120	

Each reaction proceeds via one transition state and one intermediate (corresponding radical form). The mechanism is presented in Fig. 1, and the values of total energies, enthalpies and free energies of all relevant species are given in Table 2. Fig. 2 presents the optimized geometries of all transition states and corresponding SOMOs.

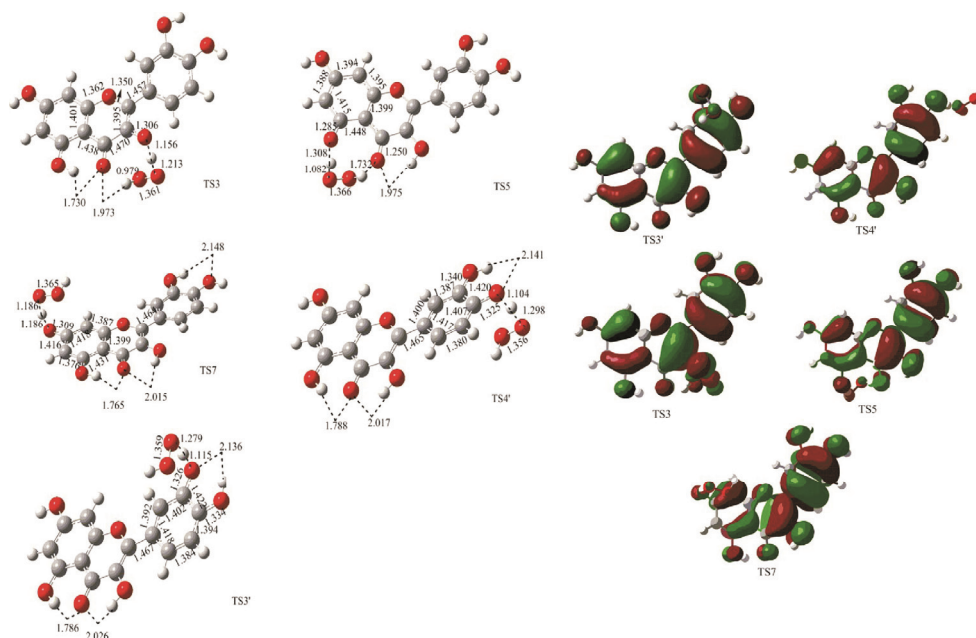


Figure 2. The geometries of transition states (left), and the shapes of the corresponding SOMOs (right).

A detailed analysis of the transition states charges shows that the QO and HOO fragments carry negative charge, while transferred H has a positive charge in all cases. In addition, spin density is also located on HOO and QO fragments. Actually, spin density associated with QO moiety is increased, while that associated with OOH fragment is decreased, in comparison to the reactants. However, there is no spin density associated with a transferred hydrogen atom. These facts indicate that reactions of quercetin OH groups with \bullet OOH radical proceed via the HAT mechanism. Although the spin density on the transferred hydrogen can not be generally used to distinguish the HAT from PCET mechanism [7] some other results also point to the HAT mechanism: the analysis of the SOMOs shapes in transition states and the results of the optimized transition states with orientation of \bullet OOH moiety corresponding to the PCET mechanism. The latter one shows that PCET is energetically unfavorable (for example for Q3' and Q4' the activation energies are higher by 15.1 and 10.9 kJ/mol) in comparison to HAT.

The singly occupied orbital (SOMO) of TS3' TS4', and TS3 (Fig. 2) shows that the unpaired electron is mainly delocalized among ring B, C3 atom of the ring C, and corresponding oxygen atoms (where reaction takes place). Fig. 2 also reveals that delocalization of SOMO is significantly weaker in other two transition states (TS5 and TS7). These differences in delocalization of the SOMOs can explain the higher activation energies for the reactions in the TS5 and TS7 positions.

The following energy activation sequence for the OH groups is found: 3'OH < 4'OH < 3OH < 7OH < 5OH (Table 2). According to the Curtin-Hammond principle the distribution of the products is determined by the difference in free energies of the transition states. The resulting ratios between the concentrations of the products are given in Table 2. On the basis of activation energies and distribution of the products it is obvious that the reactivity of the B-ring is higher than that of the C-ring and particularly A-ring. This is consistent with what is known from literature concerning structure-activity relationships of antioxidant flavonoids [8].

Reactions with the hydroxide anion in the gaseous and aqueous phases. The reactions of the hydroxide anion with all OH groups of Q^{+•} in the gaseous phase were examined. The transition states (TSs) for the reactions in the positions 3, 3', 4', and 7 were revealed. A reaction pathway in the position 5 was not found out, probably due to the strong O4 – H5 hydrogen bond, which is reflected in very high BDE, PA, and PDE values (Table 1).

An inspection of the partial charges (Table 3) shows that O11 (see Fig. 3) bears unexpectedly low partial negative charge in all reactant complexes (RCs). Actually, among all oxygens in each RC, O11 bears the lowest partial negative charge. Taking into account that O11 should belong to the hydroxide anion moiety, this finding is quite unusual. During the reaction course, the partial negative charge on O11 increases. The phenolic oxygens exhibit entirely opposite behavior, i.e. their partial negative charges decrease throughout the conversion of the RCs to the corresponding product complexes (PCs). The partial positive charges on phenolic hydrogens amount to around 0.5, with small variations during the reactions. On the other hand, the spin density value on O11 is very close to unity in all RCs (Table 3), whereas the spin density values on all other atoms are practically equal to zero. These findings show that RCs consist of Q and hydroxyl radical in different positions. Since hydroxyl radical is electron deficient, the partial negative charge on O11 in RCs is significantly low. The hydroxide anion has two very high lying p orbitals where the lone pairs reside, whose energy (-0.02274 au) is higher than that of the SOMO of Q^{+•} (-0.41278 au). Thus, one of the HO⁻ electrons is spontaneously transferred to Q^{+•}, yielding Q and hydroxyl radical. In TSs the spin density is shared between O11 and the proximate phenolic oxygen (Table 3). Finally, the spin density is distributed over the Q moiety, and its value on O11 is equal to zero in PCs (i.e. water molecule and the corresponding Q^{*}). During the course of all reactions, the spin density on the phenolic hydrogens remains equal to zero. All these facts clearly reveal that phenolic hydrogen is not transferred as a proton, but as an atom. Namely, the reaction (3a), at least in the case where R⁻ = HO⁻, is completely shifted to the left, implying that the reaction (3b) does not occur at all. As expected, Q and hydroxyl radical conform to the HAT mechanism.

B-01-SL

Table 3. Partial charge and spin density values on the oxygens of interest. RC, TS and PC stand for reactant complex, transition state, and product complex, respectively

Reaction in the position	Atom	Partial charge			Spin density		
		RC	TS	PC	RC	TS	PC
7	O7	-0.689	-0.599	-0.546	0.00	0.25	0.36
	O11	-0.473	-0.642	-0.966	0.96	0.66	0.00
3'	O3'	-0.692	-0.669	-0.549	0.02	0.18	0.73
	O11	-0.415	-0.655	-0.958	1.01	0.73	0.00
3	O3	-0.697	-0.685	-0.563	0.00	0.18	0.33
	O11	-0.416	-0.641	-0.961	1.02	0.74	0.00
4'	O4'	-0.733	-0.723	-0.628	0.00	0.12	0.28
	O11	-0.474	-0.618	-0.970	0.96	0.78	0.00

The thermodynamical data for the investigated reactions showed that the O4'-H4' homolytic bond cleavage requires the lowest activation energy, which can be attributed to the weakness of the O4'-H4' bond, due to the involvement of O4' in the strong hydrogen bond with H3'. In addition, this reaction path yields the most stable PC. These findings are in accord with the results presented in Table 1, and with those obtained in the investigation of the reaction of Q with $\cdot\text{OOH}$ and $\text{CH}_3\text{O}\cdot$ radicals [9, 10]. The optimized geometries of RC, TS, and PC for the most favorable hydrogen atom transfer reaction are depicted in Fig. 3.

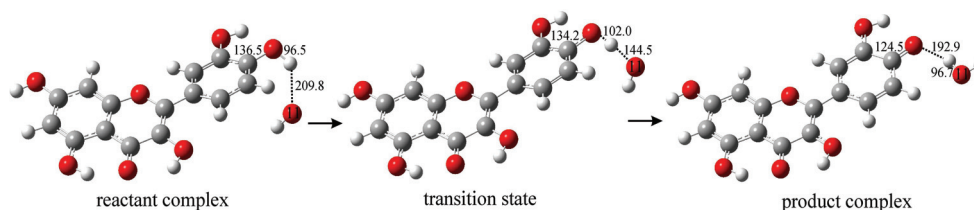


Figure 3. Reaction path for the H atom transfer from the 4' position of quercetin to the hydroxyl radical. Selected bond distances are given in pm

Transition states for the reactions of the hydroxide anion with phenolic groups in different positions of $\text{Q}^{\cdot+}$ in the aqueous solution were not revealed. On the other hand, our numerous attempts to optimize RCs led to the corresponding PCs, with the stabilization of the systems of -63.2, -67.8, -98.4, -114.7, and -121.1 kJ/mol, for the reactions in the positions 5, 7, 3', 3, and 4', respectively. These facts indicate that, in the aqueous solution, phenolic hydrogen is spontaneously transferred to O11. To determine which mechanism is operative in the aqueous solution, it was assumed that the first structure which results from the optimization of a RC is most similar to the structure of the hypothetical RC in the aqueous solution. The NBO analysis for this structure, as well as for the corresponding PC, was performed. The results are summarized in Table 4.

Table 4. The results of the NBO analysis for the reactions of hydroxide anion with $Q^{+\bullet}$ in the aqueous solution

Structure	Charge			Spin density		
	O5	H5	O11	O5	H5	O11
First	-0.755	0.536	-1.388	0.01	0.00	0.00
Product complex	-0.642	0.511	-1.023	0.25	0.00	0.00
	O7	H7	O11	O7	H7	O11
	First	-0.730	0.541	-1.392	0.01	0.00
Product complex	-0.655	0.507	-1.025	0.26	0.00	0.00
	O3'	H3'	O11	O3'	H3'	O11
	First	-0.694	0.547	-1.386	0.08	0.00
Product complex	-0.655	0.509	-1.025	0.31	0.00	0.00
	O3	H3	O11	O3	H3	O11
	First	-0.629	0.526	-1.327	0.18	0.00
Product complex	-0.641	0.508	-1.024	0.30	0.00	0.00
	O4'	H4'	O11	O4'	H4'	O11
	First	-0.692	0.559	-1.337	0.10	0.00
Product complex	-0.676	0.508	-1.025	0.26	0.00	0.00

In each first structure O11 and corresponding phenolic hydrogen bear the largest negative and positive charges, and their spin density values are practically equal to zero. An inspection of the spin density values reveals that spin density is distributed over the Q moiety. These facts indicate that each RC consists of $Q^{+\bullet}$ and hydroxide anion. In the aqueous solution the energy of the degenerate HOMOs of the hydroxide anion (-0.31160 au) is lowered, whereas the energy of the SOMO of $Q^{+\bullet}$ is elevated (-0.29050 au), in comparison to the gaseous phase. Due to this fact, an electron is not spontaneously transferred from the hydroxide anion to $Q^{+\bullet}$. In the PCs the partial negative and positive charges on O11 and phenolic hydrogens are reduced in comparison to the first structure, whereas spin density is distributed in the manner exhibited by the corresponding Q^{\bullet} [9]. All these facts clearly show that phenolic hydrogens are transferred as protons, i.e., that SET-PT is a plausible mechanism of Q in the aqueous solution.

Conclusions

The analysis of the natural bond orbital charges and orbital occupancies, as well as the SOMOs of the reactants, transition states and products shows that the reaction of Q with the hydroperoxy radical is governed by HAT mechanism. In the gaseous phase $Q^{+\bullet}$ and hydroxide anion spontaneously transform into Q and hydroxyl radical, which further conform to the HAT mechanism. Due to the stabilization of the charged species in polar solvents (implying that the HOMO energy of the anion is decreased, whereas the SOMO energy of the radical cation is increased), Q can undergo the SET-PT mechanism in the presence of hydroxide anion in the aqueous solution.

Acknowledgement

The work is supported by the Ministry of Science and Technological Development of the Republic of Serbia (Grant No. 142025).

References

- [1] B. Halliwell, R. Aeshbach, J. Loliger, O.I. Aruoma, *Food Chem.Toxicol.* 1995, 33, 601–617.
- [2]. R.H. Stadler, J. Markovic, R. J. Turesky, *Biol. Trace Elem. Res.* 1995, 47, 299–305.
- [3] W. F. Hodnick, D. L. Duval, R. S. Pardini, *Biochem. Pharmacol.* 1994, 47, 573–580.
- [4] G. Litwinienko, K.U. Ingold, *Acc. Chem. Res.* 2007, 40, 222-230.
- [5] J.S. Wright, E.R. Johnson, G.A. DiLabio, *P J. Am. Chem. Soc.* 2001, 123, 1173–1183.
- [6] E. Klein, V. Lukeš J. *Phys. Chem. A* 2006, 110, 12312-12320.
- [7] J. M. Mayer, *Annu. Rev. Phys. Chem.* 2004, 55, 363–390.
- [8] C. A. Rice-Evans, N. J. Miller, G. Paganga, *Free Radic. Biol. Med.* 1996, 20, 933–938.
- [9] Z. S. Marković, J. M. Dimitric Marković, Ć. B. Dolićanin, *Theor. Chem. Acc.* 2010, 127, 69–80.
- [10] S. G. Chiodo, M. Leopoldini, N. Russo, M. Toscano, *Phys. Chem. Chem. Phys.* 2010, 12, 7662–7670.

SPECTROSCOPIC PROPERTIES OF THE MOLECULAR STRUCTURE OF 2-(P-BROMOBENZYL)-5- ETHYLSULPHONYL-BENZOXAZOLE

Hüseyin Ünver^{1*}, Özlem Temiz Arpacı², Kamran Polat³, N.O. İskeleli⁴

¹Ankara University, Department of Physics, Faculty of Science, TR-06100
Tandoğan, Ankara-Turkey

²Ankara University, Faculty of Pharmacy, Department of Pharmaceutical
Chemistry, TR-06100 Tandoğan Ankara-Turkey

³Ankara University, Department of Chemistry, Faculty of Science, TR-06100
Tandoğan, Ankara-Turkey

⁴Department of Physics, Faculty of Science and Arts,
Ondokuz Mayıs University, TR-55139 Kurupelit, Samsun, Turkey

Abstract

2-(p-bromobenzyl)-5-ethylsulphonyl-benzoxazole has been synthesized from the reaction of 4-ethylsulphonyl-2-aminophenol with p-bromophenylacetic acid in PPA. The title compound has been characterized by using elemental analysis, MS, FT-IR, ¹H-NMR and ¹³C-NMR spectroscopic, and crystallographic techniques. The title compound crystallizes in the monoclinic space group P21/n with a = 13.1930(6), b = 7.8921(2) (2), c = 16.3574(8) Å, β = 112.515(3)°, V = 1573.33(11) Å³ and D_x = 1.605 g.cm⁻³ respectively. The crystal structure has been solved by direct methods and refined by full-matrix least squares and found R₁ = 0.0357 and wR₂ = 0.0732 for 2909 observed reflections [I > 2σ(I)].

Introduction

Benzoxazoles are the structural isomers of natural nucleotides and interact easily with the biopolymers. So that benzoxazole ring is one of the most common heterocyclics in medicinal chemistry [1-3]. A number of benzoxazole derivatives possess diverse biological activities including antibiotic [1, 2], antimicrobial [3], antiviral, topoisomerase I and II inhibitors [4-5] and antitumor activities [6]. During the last years, the studies of the synthesis and biological activities of benzoxazole derivatives have been investigated extensively. To examine their chemical properties and antimicrobial activity, a series of 2,5-disubstituted-benzoxazole derivatives were synthesized, one of them which is the title compound. The title compound was obtained by heating 4-ethylsulphonyl-2-aminophenol with p-bromophenylacetic acid in PPA (polyphosphoric acid) as the cyclodehydration reagent in a one step procedure. The synthesis of the compound is shown in Fig. 1. In present study, we reported the synthesis, characterization and crystal structure of the 2-(p-bromobenzyl)-5-ethylsulphonyl-benzoxazole.

Synthesis of 2-(p-bromobenzyl)-5-ethylsulphonyl-benzoxazole

5-Ethylsulphonyl-2-(p-bromobenzyl)benzoxazole derivative was synthesized by heating 0.01 mol 4-ethylsulphonyl-2-aminophenol. HCl with 0.01 mol p-bromophenylacetic acid in 24 g polyphosphoric acid with stirring for 2.5 hours. At the end of the reaction period, the residue was poured into ice-water mixture and neutralized with excess of % 10 NaOH solution extracted with benzene; the benzene solution was dried over anhydrous sodium sulphate and evaporated under diminished pressure. The residue was boiled with 200 mg charcoal in ethanol and filtered. After the evaporation of solvent *in vacuo*, the crude product was obtained and recrystallized from ethanol-water mixture and needles are dried *in vacuo* [10]. Formula; C₁₆H₁₄SO₃NBr, M.p.; 141 °C, Yield; 22 %. Carbon, nitrogen and hydrogen analyses were within ±0.4% of theoretical values. IR (KBr, cm⁻¹); νAr-H (3098), νAlifatic C-H (2965-2928), νC=C Aromatic (1609-1612), νC=N Aromatic; 1648, νSO₂; 1254, νAr-Br; 1122, νC-O-C; 1304-1280. ¹H-NMR(CDCl₃); δ ppm, 8.26(1H, s), 7.90-7.89(1H, m), 7.66-7.63(1H,m), 7.50-7.49(2H,d, j=5.6), 7.28-7.26(2H, d, j=5.6), 4.28(2H, s, benzylic CH₂ protons), 3.16(2H, q, CH₂ protons), 1.28(3H, t, CH₃ protons) ¹³C-NMR(CDCl₃); δ ppm, 167.35, 154.21, 142.05, 135.29, 133.07, 132.32, 131.03, 125.48, 121.97, 121.21, 111.58, 51.21, 34.86, 7.80. MASS m/e; 380(%54)(M+), 382(%56)(M+2),

X-Ray structure determination

The crystal of title molecule was mounted on goniometer of a STOE IPDS 2 diffractometer with a graphite monochromatized Mo-K_α radiation ($\lambda = 0.71073\text{\AA}$). Data collection, reduction and corrections for absorption and decomposition were achieved using X-AREA, X-RED software [7]. The crystal structure was solved by a direct method based on difference Fourier and refined by least squares on F² with anisotropic displacement parameters for non-H atoms. All the calculations to solve the structure, to refine the proposed model, and to obtain the derived results were carried out with the computer programs of SHELXS-97 [8], SHELX-L97 [9]. The positions of the H atoms bonded to C atoms were calculated and refined using a riding model. The H atom displacement parameters were restricted to be 1.2U_{eq} of the parent atom. The details of the X-ray data collection, structure solution and structure refinements are given in Table 1. Selected bond distances and angles are listed in Table 2. The molecular structure with the atom-numbering scheme is shown in Fig.1 [10].

Result and Discussion**FT-IR, ¹H-NMR, ¹³C-NMR and Mass spectroscopic studies**

The IR spectra of the compounds are given in synthetic procedures by using experimental techniques. Vibration bands with the wave numbers of 3098 cm⁻¹ (νAr-H stretching band), 2965-2928 cm⁻¹ (νAlifatic C-H stretching band), 1609-1612 cm⁻¹ (νAromatic C=C stretching band), 1648 cm⁻¹ (νAromatic C=N stretching band), 1254 (νSO₂ stretching band), 1122 cm⁻¹ (νAr-Br), 1304-1280cm⁻¹ (νC-O-C) were observed for compound, respectively.

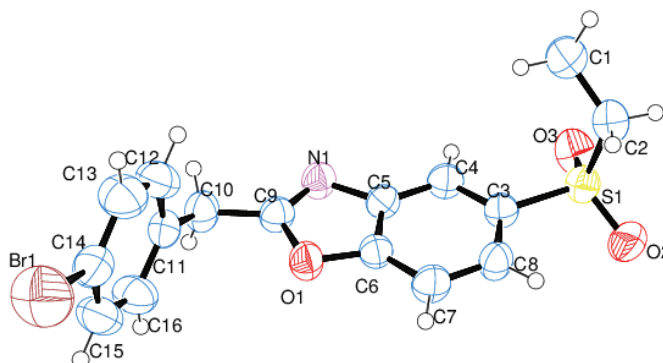


Figure 1 The molecular structure of the title compound.

According to the ^1H NMR spectra (Table 4), proton of position on 4 of benzoxazole ring is observed as singlet $\delta=8.26$ ppm for compound 1. Protons of position on 6 and 7 of benzoxazole ring appear as multiplets $\delta=7.90-7.89$ and $\delta=7.66-7.63$ ppm respectively. The phenyl protons on meta positions of benzoxazole ring are observed as doublet (2H) $\delta=7.50-7.49$ ppm, $j=5.6$ Hz. Other phenyl protons on ortho positions of benzoxazole ring are detected as doublet (2H) $\delta=7.28-7.26$ ppm $j=5.6$ Hz. Benzylic protons are observed $\delta=4.28$ ppm as a singlet. CH_2 protons on the ethylsulphonyl group are observed $\delta=3.16$ ppm as quartet and CH_3 protons on the ethylsulphonyl group are detected $\delta=1.28$ ppm as triplet. According to the proton de-coupled ^{13}C NMR spectra, the title compound has 14 signals. The aliphatic CH_3 and CH_2 carbons are observed $\delta=7.80$ and 34.86 ppm respectively. Also benzylic carbon is detected $\delta=51.21$ ppm. Also the chemical shifts of aromatic carbons are observed δ ppm; 167.35, 154.21, 142.05, 135.29, 133.07, 132.32, 131.03, 125.48, 121.97, 121.21, 111.58 for compound. The mass spectra of the compound is observed molecular ion peak m/e ; 380(%54)(M+H) and 382(%56)(M+H+2) because of brom isotopes. In conclusion; FT-IR, ^1H NMR, ^{13}C NMR and mass results confirm that the compound.

Crystallographic study

The title compound consists of two parts. The phenyl part A [C10-C16 and Br1; planar with a maximum deviation of $0.3422(8)$ Å for the S1 atom] and another part benzoxazole B [C3-C9, O1 and N1; planar with a maximum deviation of $0.1289(12)$ Å for the N2 atom] are inclined at an angle of $10.07(3)^\circ$. The N1-C9 and N1-C5 bond distances were found to be 1.283 and 1.409 respectively. The corresponding values in 2,5-dichloro-1-(p-chlorobenzyl)-1H-benzimidazole[11] 1.296(2), 1.391(2) and 1-(p-fluorophenylmethyl)-2-(4-methyl-1-piperazinyl)-1H-benzimidazole[12] hydrogen fumarate 1.395(5) and 1.319(5). The bond C2-S1=1.758(1) and C3-S1 1.768(1) Å is significantly longer than a C=S double bond. This (C-S) distance is smaller than single C-S bond distance of 1.82 Å but bigger

B-02-O

than double C–S bond of 1.56 Å [12]. Consequently, the C–S bond like in these compounds possesses only partial double-bond character. S1–O2 and S1–O3 bond lengths respectively. The O1–C9 bond distance was found to be 1.380 Å. This value in [11] was 1.372 Å. The bond lengths and angles for the benzimidazole moiety of the molecule are in good agreement, within experimental errors with those observed in other benzimidazole derivatives [11-12].

Conclusions

2-(p-bromobenzyl)-5-ethylsulphonyl-benzoxazole ($C_{16}H_{14}SO_3NBr$) has been studied by using an elemental analysis, FT-IR, 1H NMR, ^{13}C NMR, MS and X-Ray analysis. As a result; the data obtained for the title compound from the elemental analysis, MS, FT-IR, 1H -NMR, ^{13}C -NMR spectra are in agreement with the proposed structure.

References

- [1] M. Prudhomme, J. Guyot, G. Jeminet, J. Antibiot., 1986, 39, 934.
- [2] D. D. Martin, N. R. Kotecha, S.V. Ley, S. Maqteгани, J. C. Menendes, H. M. Organ, A. D. White, Tetrahedron, 1992, 7899.
- [3] H. K. Sarma, B. K. Sharma, S. C. Tiwari, Curr. Sci., 2003, 85, 1401.
- [4] Pınar, P. Yurdakul, I. Yıldız, O. Temiz-Arpacı, N. L. Acan, E. Aki-Sener, I. Yalcin, Biochemical and Biophysical Research Communications, 2004, 317, 670.
- [5] E. Oksuzoglu, B. Tekiner-Gulbaş, S. Alper, O. Temiz-Arpacı, T. Ertan, I. Yıldız, N. Diril, E. Aki-Sener, I. Yalcin, J. Of Enzyme Inhibition and Med. Chem. , 2008, 23, 37.
- [6] D. Kumar, M. R. Jacob, M. B. Reynolds, S. M. Kerwin, Bioorg. And Med. Chem., 2002, 3997.
- [7] Stoe & Cie (2002), X-Area (Version 1.18) and X-RED32 (Version 1.04) Stoe&Cie Darmstadt, Germany
- [8] Sheldrick GM, SHELXS-97, Program for the solution of Crystal Structures. Univ. of Goettingen, Germany, 1997.
- [9] Sheldrick GM, SHELXL-97, Program for the refinement of Crystal Structures. Univ. of Goettingen, Germany, 1997.
- [10] Farrugia LJ, J. Appl. Crystallogr., 1997, 30, 565.
- [11] E. Kendi, S. Özbey, H. Göker, Acta Crystallogr C, 1999. 55, 243.
- [12] S. Özbey, E. Kendi, H. Göker, M. Tunçbilek, J. Chem. Cryst., 1998, 28,461.

THE ELECTRON NUMBER DENSITY OF ARGON-NITROGEN ATMOSPHERIC PRESSURE PLASMA

D. P. Rankovic¹, M. M. Kuzmanovic¹, B. M. Gakovic², M. S. Pavlovic²,
M. M. Stoiljkovic², J. J. Savovic²

1 Faculty of Physical Chemistry, University of Belgrade, Studentski trg 12, 11000 Belgrade, Serbia

2 Institute Vinca, University of Belgrade, Mike Alasa 12-14, 11000 Belgrade, Serbia

mail:ranko@ffh.bg.ac.rs

Abstract

In this study, the influence of nitrogen gas addition on argon plasma electron number density was investigated. The plasma source is a wall stabilized direct current arc burning in argon at atmospheric pressure with continual water aerosol supply. To the argon gas carrying water aerosol a variable amounts (4, 8 and 11%) of nitrogen was added. The addition of the molecular gas was carried out by increasing the flow rate of the N₂ and decreasing that of Ar, so that the total flow rate of the mixed gas was constant 2.7 Lmin⁻¹. The arc was operating in the current intensity range 4 to 11 A. The electron number density was calculated from the measured *Stark* profiles of H_β 486.13 nm spectral line at the arc axis, for different arc currents. The radial distribution of electron number density was obtained from the measured radial profiles of H_β □ line. The addition of the molecular gas to the argon plasma resulted in considerable changes in electron number density.

Results and discussion

The electron number density have been obtained from measured radial profile of *Balmer*- H_β spectral line (486.13 nm) using a program proposed by Zikic *et al* [1]. The method was chosen because it does not require local thermodynamic equilibrium (LTE) condition to be satisfied. Plasmas consisting of mixtures of species including molecules are more complex than pure noble gas plasma. In our case, the situation is additionally complicated by the presence of large density and temperature gradients in radial direction. In order to describe the state of plasma we need to know the spatial distribution of temperature, pressure and composition. Although the assumption of LTE is often used in the modeling and diagnostics of atmospheric-pressure plasmas, the assumption of LTE is valid only for relatively high electron densities, at temperatures above approximately 10,000 K. Under such conditions the rapid collisions between charged and neutral particles, the large Coulomb cross section for collisions between charged particles, and rapid three-body recombination all tend to promote equilibration.

Figure 1a illustrates the influence of the arc current on the electron number density in argon plasma with three different nitrogen contents. In Fig 1b the influence of gas composition on a radial distribution of electron number density for the arc current of 7A is presented.

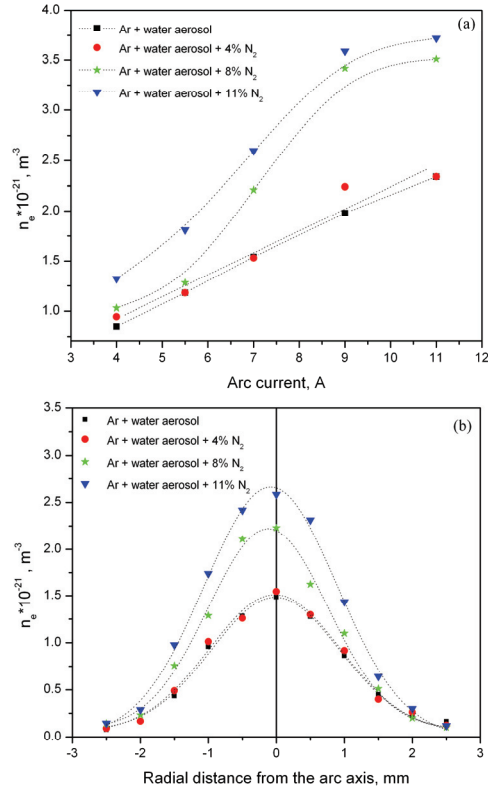


Figure 1. Variation of electron number density in argon-nitrogen plasma with: a) arc current and b) radial position for 7A arc current.

For all three gas compositions the increase of the arc current results in an increase of electron number density, but to a variable extent, Fig. 1. The increase of n_e with the increase in arc current is linear for small N_2 content and almost the same as for pure argon plasma. Increased content of molecular gas resulted in large n_e increase especially for the arc currents above 7 A. For a fixed arc current, measured at the arc axis, the small addition of nitrogen has almost negligible influence on n_e and the increase in n_e is considerable for larger N_2 additions. From the Fig. 1b it is seen that the largest influence of the variable gas composition on n_e is in the arc core region while when moving from the arc axis toward the plasma periphery the effect is lessening.

Direct current argon arc plasma is characterized by a large n_e and temperature gradients in radial direction. The addition of molecular gas is expected to influence the energy transport through the discharge which will influence the fundamental plasma properties (electron temperature, electron number density and gas temperature), the bulk plasma characteristics (thermodynamic functions and transport coefficients including diffusion coefficient, viscosity, thermal conductivity, and electrical conductivity) and radiation properties (net emission

coefficient) of the plasma. For instance, the thermal conductivity of the argon-nitrogen plasma will differ from the thermal conductivity of pure argon plasma. The thermal conductivity of argon increases monotonically with temperature while that of N_2 rises to a peak at about 6500 K, falls to a minimum at approximately 9000 K and then increases again with higher temperature. In the case of Ar- N_2 mixture, each plasma constituent will influence the transport properties according to its amount present in plasma. The changes of thermal conductivity will certainly result in changed temperature and electron number density distributions. On the other hand, the effect of demixing [2] does not seem to be important for Ar- N_2 mixtures as ionization potential of nitrogen is similar to that of argon (14.53 and 15.76 eV, respectively) and at higher temperatures both argon and nitrogen are ionized to the same extent. The increase in n_e may thus be explained by changes in plasma temperature as the number of charge carriers is closely correlated to temperature. The result is interesting since it implies increase in plasma temperature in spite of energy utilization for dissociation of nitrogen molecules and increased energy losses due to changed plasma composition.

Conclusions

The addition of easily ionisable elements or molecular gases [3] to argon plasma is a common spectrochemical practice in order to improve excitation conditions of the source or to minimize matrix effects. Because argon-nitrogen arc plasma may provide unique spectrochemical results, investigation of its operation and properties have been conducted. The obtained results may be important in analytical applications of this plasma source. For three different nitrogen contents we have measured the influence of the arc current on the electron number density variation and the radial distribution of the electron number density for a fixed current. The results have shown that the changes in N_2 content considerably influence the changes in electron number density through changes in plasma temperature and thermal conductivity.

Acknowledgments

The authors acknowledge the financial support from the Republic of Serbia Ministry of Education and Science, Project No. 172019.

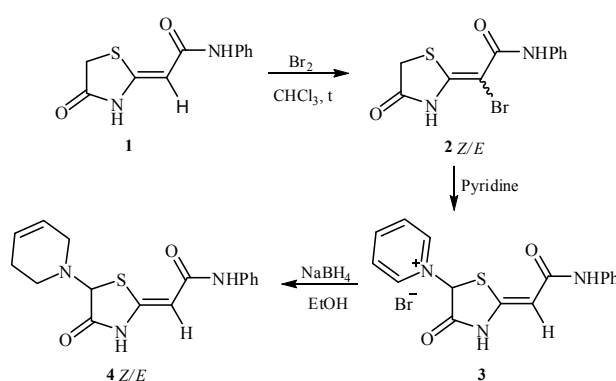
References

- [1] R. Zikić, M. A. Gigosos, M. Ivković, M. A. Gonzalez and N. A. Konjević, *Spectrochim. Acta B*, 2002, 57, 987–998.
- [2] A. B. Murphy, *J. Phys. D: Appl. Phys.*, 2001, 34, R151–R173.
- [3] Y. Fujishiro, M. Kubota and R. Ishida, *Anal. Chim. Acta*, 1982, 142, 173-182.

This work will show how the strength of the push-pull effect of the C=C double bond changes following the structural variations throughout the reaction sequence leading from the 4-oxothiazolidine **1** to its 5-substituted derivative **4** (Scheme 1).

Results and Discussion

Substrate **1** is regioselectively brominated to vinyl bromide **2**, which undergoes pyridine-induced bromine transfer to the C-5 ring position with subsequent substitution to give the pyridinium salt **3** [6]. Reduction with NaBH₄ yields the tetrahydropyridine derivative **4** (Scheme 1). Both tetrahydropyridine and 4-oxothiazolidine fragments are significant structural parts of compounds with interesting biological and pharmacological properties.



Scheme 1. Synthesis of 5-substituted 4-oxothiazolidine.

We employed two parameters to assess the push-pull activity of **1-4**: ¹³C NMR chemical shift difference ($\Delta\delta_{C=C}$), available both experimentally and theoretically, and the occupation quotient (π^*/π) calculated theoretically (Table 1).

Table 1. Experimental and calculated ¹³C NMR chemical shift differences ($\Delta\delta_{C=C}$), calculated bond lengths, occupation numbers of π bonding and π^* antibonding orbitals and their quotient (π^*/π) for compounds **1-4**.^a

comp.	$\Delta\delta_{C=C}$ (exp.)	$\Delta\delta_{C=C}$ (calc.)	$d_{C=C}/\text{\AA}$	π	π^*	π^*/π
1	61.92	64.28	1.355	1.8729	0.3030	0.16
2	70.75	57.36	1.361	1.8819	0.3577	0.19
3	52.18	43.74	1.345	1.8885	0.2488	0.13
4	59.17	61.87	1.355	1.8716	0.2977	0.16

^a All calculations were done at the B3LYP/6-31G(d) level.

The occupation quotient showed a good linear correlation with the computed bond lengths (Fig. 2). The calculated $\Delta\delta_{C=C}$ are also in good agreement with the experimentally obtained data (Fig. 3). The only value which is out of line is for the vinyl bromide **2**, and this is due to the relativistic effects. Introduction of bromine

B-04-P

into the C=C double bond seems to have the strongest impact on the push-pull effect ($\pi^*/\pi = 0.19$). However, as bromine is a donor, this result should be taken with care. An analysis of π bonding and π^* antibonding occupation numbers (Table 1) shows that bromine actually increases the donating ability of S and N but decreases the accepting power of EWG [5]. The strong electron-withdrawing pyridinium ring attached to the C-5 in **3** decreases the push-pull effect ($\pi^*/\pi = 0.13$ in **3** compared to 0.16 in **1**), which returns to its original strength upon reduction to tetrahydropyridine **4**.

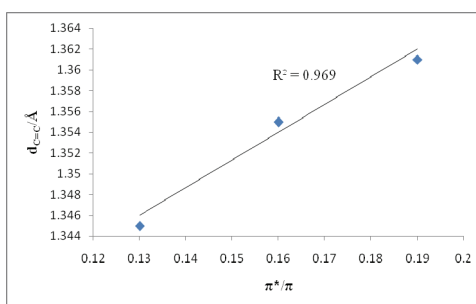


Figure 2. Correlation of the occupation quotient (π^*/π) and $d_{C=C}/\text{\AA}$.

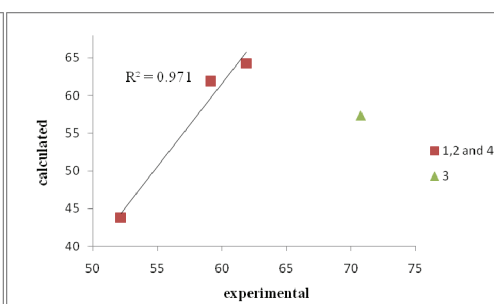


Figure 3. Correlation of the experimental and calculated $\Delta\delta_{C=C}$.

Conclusion

Occupation quotient (π^*/π) method and ^{13}C NMR chemical shift difference ($\Delta\delta_{C=C}$) proved as sensitive parameters to trace the changes in push-pull activity of the C=C double bond, even when structural changes take place at a distant position (C-5 ring atom, in this case).

Acknowledgement

This work was supported by the Ministry of Education and Science of the Republic of Serbia, project N^o 172020.

References

- [1] J. Sandström, *Top. Stereochem.* 1983, 14, 83.
- [2] G. Fischer, W. D. Rudolf, E. Kleinpeter, *Magn. Reson. Chem.*, 1991, 29, 212.
- [3] E. Kleinpeter, *J. Serb. Chem. Soc.*, 2006, 71, 1.
- [4] G. Ye, S. Chatterjee, M. Li, A. Zhou, Y. Song, B. L. Barker, C. Chen, D. J. Beard, W. P. Henry, C. U. Pittman, *Tetrahedron*, 2010, 66, 2919.
- [5] M. Baranac-Stojanović, U. Klaumünzer, R. Marković, E. Kleinpeter, *Tetrahedron*, 2010, 66, 8958.
- [6] M. Baranac-Stojanović, J. Tatar, M. Stojanović, R. Marković, *Tetrahedron*, 2010, 66, 6873.

BISTHIAZOLIDINE-FUSED 1,5-DITHIACYCLOOCTANE: SYNTHESIS AND STRUCTURE ANALYSIS

M. Stojanović¹, Z. Džambaski¹, J. Aleksić¹, R. Marković^{1,2} and M. Baranac-Stojanović^{1,2}

¹Center for Chemistry, Institute of Chemistry, Technology and Metallurgy, University of Belgrade, Njegoševa 12, P.O. Box 473, 11000 Belgrade, Serbia;

²Faculty of Chemistry, University of Belgrade, Studentski Trg 12-16, P.O. Box 153, 11000 Belgrade, Serbia

Abstract

Synthesis and structure analysis of the tricyclic system **4**, with two thiazolidine rings condensed to the central 1,5-dithiacyclooctane, is reported. The reaction outcome and stereochemistry are rationalized using quantum chemical calculations at B3LYP/6-31G(d) level. Six energy-minimum structures were located for the molecule, of which the *cis-transoid-cis* ring fusion was calculated to be the most stable. The central eight-membered ring adopts *crown* conformation.

Introduction

Iminium ion (Figure 1a) based cyclizations are widely employed for the formation of a variety of nitrogen-containing heterocycles.¹ A large range of nucleophiles, such as π -nucleophiles (aromatic rings, carbon-carbon double and triple bonds), σ -nucleophiles and heteroatom based nucleophiles, have been used to react with various acyclic and cyclic iminium ions, usually generated prior to use. For less reactive nucleophiles, iminium ions activated by *N*-acyl groups (Figure 1b) are employed. These *N*-acyl iminium ions² are much more reactive because of the electron-attracting properties of the carbonyl group on nitrogen, which makes the iminium carbon more electron-deficient. A subtype of *N*-acyliminium ions with a carbon-carbon double bond conjugated to an acyl group on nitrogen are referred to as *vinylogous N-acyliminium ions* (Figure 1c). Despite the rich chemistry of iminium ions, just a few reports on the reactivity of this type of iminium ions

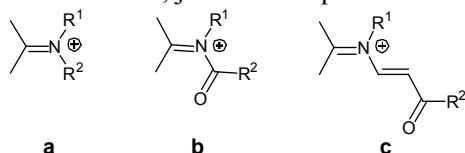


Figure 1. (a) *N*-Alkyliminium ions, (b) *N*-acyl iminium ions, (c) vinylogous *N*-acyl iminium ions.

are published thus far.³ Herein, we present the explanation of the reaction outcome of ring closure of vinylogous *N*-acyliminium ion **3** and structure analysis of the product **4**, based on Density Functional Theory (DFT) calculations at the B3LYP/6-31G(d) level.⁴

3) is small (so that they are present in comparable amounts in the reaction mixture). This exactly proved to be the case ($\Delta\Delta G_{cis/trans} = -0.15$ kcal/mol). *cis*-Isomer is obviously stabilized by the formation of hydrogen bond where the SH group acts as a hydrogen donor.

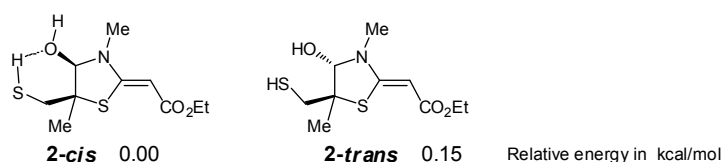


Figure 3. *Cis* and *trans* isomers of 4-hydroxy intermediate **2**.

Quantum chemical calculations predict the eight-membered 1,5-dithiacyclooctane ring to exist in crown conformation (Figure 4).



Figure 4. The most stable conformation of **4a**.

Conclusion

With the aid of quantum chemical calculations we explained that vinylogous *N*-acyliminium ion **3**, possessing sulfhydryle group as an internal nucleophile, dimerizes to the energetically more stable tricyclic system **4**. Kinetic control of the reaction led to the formation of diastereomeric mixture.

Acknowledgements

This work was supported by the Ministry of Education and Science of the Republic of Serbia, No. 172020 (to R. M.) and Deutscher Akademischer Austauschdienst (DAAD) – project ID: 504 252 70.

References

- [1] J. Royer, M. Boni, L. Micouin, *Chem. Rev.*, 2004, 104, 2311.
- [2] (a) B. E. Maryanoff, H.-C. Zhang, J. H. Cohen, I. J. Turchi, C. A. Maryanoff, *Chem. Rev.*, 2004, 104, 1431; (b) W.N. Speckamp, M. J. Moolenaar, *Tetrahedron*, 2000, 56, 3817.
- [3] (a) D. Fasseur, B. Rigo, P. Cauliez, M. Debacker and D. Couturier, *Tetrahedron Lett.*, 1990, 31, 1713 (b) D. J. Hart, *J. Org. Chem.*, 1981, 46, 367.
- [4] (a) A. D. Becke, *J. Chem. Phys.*, 1993, 98, 5648; (b) C. Lee, W. Yang R. G. Parr, *Phys. Rev. B*, 1988, 37, 785.
- [5] M. Stojanović, R. Marković, E. Kleinpeter, M. Baranac-Stojanović, *Org. Biomol. Chem.*, 2012, 10, 575.

B-06-P

ROTATIONAL ISOMERS, NMR AND REACTIVITY ANALYSES OF TERT-PENTYL-1-BENZYL-4-METHYL-2,6-GLUTARIMIDE-3-CARBOXYLATE (PBMG)

V D. Vitnik,¹ J B. Popović-Đorđević,² Ž J. Vitnik,³
M D. Ivanović³, I. O. Juranić¹

¹ *Department of Chemistry, IChTM, University of Belgrade, Belgrade, Serbia*

² *Faculty of Agriculture, University of Belgrade, Belgrade, Serbia*

³ *Faculty of Chemistry, University of Belgrade, Belgrade, Serbia*

Abstract

The stable isomers of *tert*-pentyl-1-benzyl-4-methyl-glutarimide-3-carboxylate (PBMG) are determined. Optimized geometrical parameters of the stable isomers of PBMG are predicted by DFT/B3LYP/6-311++G(d,p). The ¹H and ¹³C nuclear magnetic resonance (NMR) chemical shifts of the molecules were calculated using the GIAO method and conform to the experimental values. To assess chemical reactivity of the molecule, the molecular electrostatic potential (MEP) surface map is plotted over the optimized geometry of the molecule.

Introduction

Glutarimide derivatives are recognized as anticonvulsants [1], sedatives [2] and antitumor agents [3]. Substituted imide rings are also found in some of the pharmacologically active natural products, such as cycloheximide [4], sesbanimide [5], izomigrastatine and migrastatine [6]. Numerous compounds containing six-membered imide ring are synthesized and express different pharmacological activities such as anxiolytic (buspirone, tandospirone) [2], immunosuppressive (thalidomide and analogues) [2], and others.

In our previously reported research PBMG has been synthesized by a novel tandem process [7].

The understanding of molecular geometry and reactive electrophilic and nucleophilic sites of the compound are of particular importance in the synthesis of a drug. Hence, in the present study, the energies and stability of different possible rotational isomers of PBMG are determined, as well as ¹H and ¹³C nuclear magnetic resonance (NMR) spectra for the title molecule are analyzed. Moreover, molecular electrostatic potential (MEP) surface is plotted over the optimized geometry to elucidate the reactivity of PBMG molecule.

Experimental

The chemical structure and purity of the synthesized compound was confirmed by its melting point, ¹H and ¹³C NMR and FT-IR spectra. ¹H and ¹³C NMR spectra were recorded in CDCl₃ using TMS as an internal standard on a Varian Gemini 200 spectrometer at 200 MHz and 50 MHz, respectively.

Computational details

All the calculations were performed using Gaussian 03 program package. Geometry of PBMG was fully optimized with DFT/B3LYP/6-311++G(d,p) method. ^1H and ^{13}C NMR chemical shifts are calculated with GIAO approach by applying B3LYP/6-311++G(d,p) method. To investigate the reactive sites of the title compound, the molecular electrostatic potentials for the 0.002 a.u. isosurfaces of electron density was evaluated using the B3LYP/6-311++G(d,p) method.

Results and Discussions

Molecular geometry

The molecule of PBMG could exist as *trans* and *cis* diastereomers. To find most stable isomer geometry, the DFT energy calculation is performed on the eight possible isomers of PBMG. The possible isomer geometry is found by locating $-\text{CH}_2\text{Ph}$ group of the title molecule in two different orientations, above and below the plane of the glutarimide ring. The positioning of *tert*-pentyl group in two different orientations gives rise to eight isomers. The DFT energy calculation and the statistical Boltzmann distribution (shown in Table 1) reveal that, the isomers **1d** and **1h** acquire dominant stability among others *trans* (**1a-1d**) and *cis* (**1e-1h**) isomers, respectively. The optimized molecular structure of the most stable isomer **1d** of the title molecule is shown in Fig. 1.

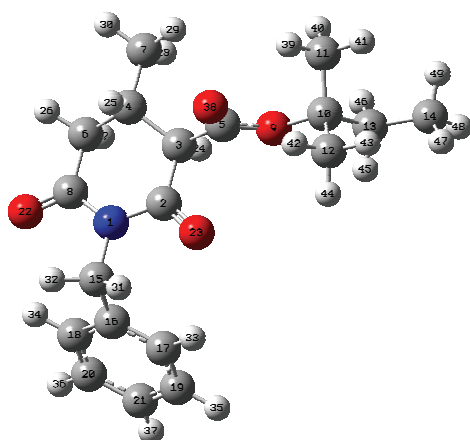


Figure 1. Geometry optimized structure of **1d** isomer of PBMG.

Table 1. The energies and the statistical Boltzmann distribution weighted values of the most stable PBMG isomers.

Isomer	Energy / a.u.	%
1a	-1095.0792247	11.22
1b	-1095.0801943	31.15
1c	-1095.0793179	12.38
1d	-1095.0804938	42.69
1e	-1095.0750486	0.14
1f	-1095.0769821	1.06
1g	-1095.0750302	0.14
1h	-1095.0771161	1.22

NMR spectra

From experimental data the ratio between *trans/cis* diastereomers (5:1) is determined by ratio of the two signals at 3.08 and 3.45 ppm (two doublets from atom H(24) on C(3)). The same signal ratios are found at 1.26 (1.34) ppm from two singlets of methyl groups at C(11) and C(12) in *trans/cis* isomers, as well as for signals at 0.94 (0.98) ppm from methyl groups on C(7) and at 0.68 (0.77) ppm from methyl groups on C(14). Doublets at 2.62 (2.70) ppm mark methylene of

B-06-P

glutarimide ring, while quartets at 2.20 (2.45) and 1.66 (1.68) ppm mark atom H(25) on C(4) and methylene hydrogens on C(13), respectively. Singlet at 4.82 (4.84) ppm mark methylene hydrogens on C(15). Peaks at 7.05-7.26 ppm indicate the presence of aromatic hydrogen atoms. In ^{13}C NMR spectra signals for carbonyl groups are at 170.54 (171.29), 168.54 (168.79) and 167.03 (165.83) ppm in *trans/cis* isomers. The peaks appearing in the range 138.62–127.09 ppm are assigned to the carbon atoms of phenyl group. The signals at 84.76 (85.43) is assigned to C(10) carbon. The aliphatic CH_2 (C(6), C(13), and C(15)) carbons are observed at 42.55, 38.24 (36.62) and 57.55 (55.04) ppm, respectively. The carbon atoms of the CH groups belonging to the glutarimide ring are observed at 33.09 and 26.27 (27.4) ppm, for C(3), and C(4), respectively. Methyl groups are at 24.87 (24.95), 18.69 (17.03) and 7.74 ppm, for C(11, 12), C(7), and C(14), respectively. The theoretical ^1H and ^{13}C chemical shift results for PBMG are generally close to the experimental ^1H and ^{13}C shift data.

MEP

The MEP map shows that the negative potential sites are on electronegative O atoms of the carbonyl groups and the positive potential sites are around the carbon C(4) of the glutarimide ring. These sites give information about the region from where the compound can make intermolecular interactions. Thus, it would be predicted that the carbonyl groups fragment of PBMG will be the most reactive site for electrophilic, and C(4) atom for nucleophilic attack.

Acknowledgments

This work has been financially supported by Ministry of Education and Science, Republic of Serbia, under Grant No. 172035, 172032 and by High-Performance Computing Infrastructure for South East Europe's Research Communities European project.

References

- [1] S. A. Dandekar, S. N. Greenwood, T. D. Greenwood, S. Mabic, J. S. Merola, J. M. Tanko, J. F. Wolfe, *J. Org. Chem.*, 1999, 64, 1543-1553.
- [2] The Merck Index, 13th Ed; Merck & Co., Inc., NJ, 2001.
- [3] D. K. K. Ha, W. H. Lau, *Cancer Lett.*, 1988, 41, 217-224.
- [4] C. Christner, R. Wyrwa, S. Marsch, G. Küllertz, R. Thiericke, S. Grabley, D. Schumann, G. Fischer, *J. Med. Chem.*, 1999, 42, 3615-3622.
- [5] F. Matsuda, S. Terashima, *Tetrahedron*, 1988, 44, 4721-4736.
- [6] J. Ju, S. R. Rajska, S.-K. Lim, J.-W. Seo, N. R. Peters, F. M. Hoffmann, B. Shen, *Bioorg. Med. Chem. Lett.*, 2008, 18, 5951-5954.
- [7] J. B. Popović-Đorđević, M. D. Ivanović, V. D. Kiricojević, *Tetrahedron Lett.*, 2005, 46, 2611–2614.

QUANTUM MECHANICAL AND SPECTROSCOPIC INVESTIGATIONS OF POTENT ANTIEPILEPTIC DRUG 1-(4-CHLORO-PHENYL)-3-PHENYL-SUCCINIMIDE

V. D. Vitnik,¹ Ž. J. Vitnik,² N. R. Banjac,³ N. V. Valentić³, I. O. Juranić¹

¹ *Department of Chemistry, IChTM, University of Belgrade, Belgrade, Serbia*

² *Faculty of Chemistry, University of Belgrade, Belgrade, Serbia*

³ *Department of Organic Chemistry, Faculty of Technology and Metallurgy, University of Belgrade, Belgrade, Serbia*

Abstract

This study represents an integrated approach towards understanding the vibrational, electronic, NMR, reactivity and structural aspects of 1-(4-Chloro-phenyl)-3-phenyl-succinimide (CPPS). Theoretical calculations were performed by density functional theory (DFT)/B3LYP method using 6-311++G(d,p) basis set. The scaled theoretical wavenumber showed very good agreement with the experimental values. HOMO-LUMO energy gap for the title molecule has been analyzed. Furthermore, molecular electrostatic potential map (MEP) of the compound has been calculated.

Introduction

Succinimides and their derivatives have been considered as an important class of nitrogen-containing heterocycles. There has been increasing interest in the study of succinimides due to their anticonvulsant activity. Ethosuximide [1] is a succinimide anticonvulsant, used mainly in absence seizures. Methsuximide is an anticonvulsant with the therapeutic efficacy due to its pharmacologically active metabolite, *N*-desmethylnmethsuximid [2]. Phensuximide used to treat epilepsy and other seizure disorders [3].

Moreover, we are performing the synthesis and the properties relevant to pharmacokinetics of two series of newly synthesized succinimide derivatives [4]. Compound 1-(4-Chloro-phenyl)-3-phenyl-succinimide (CPPS) is one of the four agents picked as the best candidate for compromising the human intestinal absorption and plasma protein binding properties. To the best of our knowledge the spectroscopic properties of CPPS have not yet been studied in detail.

Experimental details

The chemical structure and purity of the synthesized compound was confirmed by its melting point, ¹H and ¹³C NMR, FT-IR and UV spectra. FT-IR spectra were recorded with a Bomem MB 100 spectrophotometer. The ultraviolet absorption spectrum of CPPS was examined in the range 200-500 nm using Shimadzu 1700 UV/Vis spectrophotometer. The UV pattern was taken from a 10⁻⁵ molar solution of CPPS, solved in ethanol. ¹H and ¹³C NMR spectra were recorded in CDCl₃ using

B-07-P

TMS as an internal standard on a Varian Gemini 200 spectrometer at 200 MHz and 50 MHz, respectively.

Computational details

All the calculations were performed using Gaussian 03 program package. Geometry of CPPS was fully optimized with DFT/B3LYP/6-311++G(d,p) method. The harmonic frequencies were calculated by B3LYP method using 6-311++G(d,p) basis set and then scaled by 0.9686. The assignments of the calculated wavenumbers were aided by the animation option of Gauss View 3.0 graphical interface from Gaussian programs. Furthermore, the theoretical vibrational spectra of the title compound are interpreted by means of Potential Energy Distribution (PED) using VEDA 4 program. ^1H and ^{13}C NMR chemical shifts are calculated with GIAO approach by applying B3LYP/6-311++G(d,p) method. The frontier molecular orbital energies and HOMO-LUMO energy gap are also calculated in the same method. UV absorption energies of this compound were calculated by TD-DFT method in ethanol solvent. To investigate the reactive sites of CPPS, the molecular electrostatic potentials for the 0.002 a.u. isosurfaces of electron density was evaluated using the B3LYP/6-311++G(d,p) method.

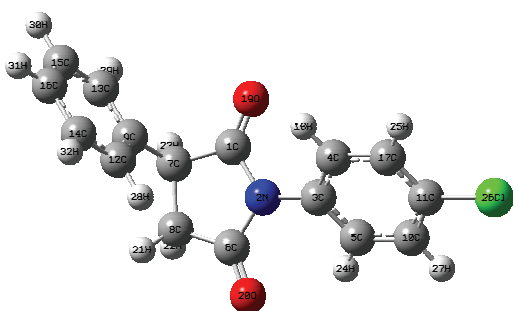


Figure 1. Optimized geometry of CPPS.

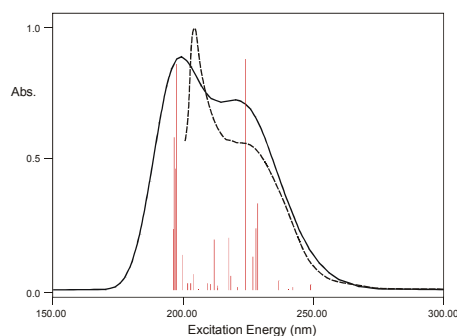


Figure 2. Experimental and predicted UV spectra of CPPS.

Results and Discussions

The molecular structure of the CPPS belongs to C_1 point group symmetry. The optimized molecular structure of the title molecule was obtained from Gaussian 03 program as shown in Fig. 1. The minimum energy of the title compound was calculated by structure optimization at B3LYP/6-311++G(d,p) is -1282.59117675 a.u. To the best of our knowledge, exact experimental data on the geometrical parameters of CPPS are not available in the literature.

For CPPS the very weak absorption band at 3098 and 3062 cm^{-1} in FT IR are assigned to C-H stretching modes of the phenyl ring systems. The bands at 3031 and 2975 cm^{-1} are assigned to asymmetric and symmetric C-H stretching modes of the CH_2 -group, respectively. The pattern of band observed at 1781 and 1707 cm^{-1} in FT IR are assigned C=O stretch vibrations. The pattern of band

observed at 1625, 1283 and 1167 cm^{-1} are assigned as C-C stretching vibrations of the aromatic systems (skeletal vibrations). The aromatic C-H in- and out-of-plane bending vibrations are at 1196 and 950, 929, 842 cm^{-1} , respectively. In our present study the C-N stretching band is found to be present at 1234 cm^{-1} . All the calculated wavenumbers show excellent agreement with the experimental data.

In ^1H NMR spectra two doublets of doublets at 2.95 and 3.32 ppm mark the methylene hydrogens in the succinimide ring. The hydrogen atom of C-H group appears at higher chemical shift of 4.14 ppm due to influence of phenyl ring. Peaks at 7.22-7.46 ppm indicate the presence of aromatic hydrogen atoms, i.e. in the benzene rings. C3 and C4 in succinimide ring appear at lower chemical shift of 36.99 and 45.79 ppm due to neighbouring electronegative carbonyl groups. C2 and C5 of carbonyl groups are at 174.51 and 176.35 ppm. Peaks at 127.3-136.8 ppm were due phenyl groups. The predicted chemical shift values of DFT were in close agreement with the experimental.

As can be seen from the Figure 2, electronic absorption spectrum of CPPS shows three bands at 202, 204, and 224 nm, respectively. From TD-DFT calculation, the theoretical absorption bands are predicted at 193, 197 and 223 nm and can easily be seen that they correspond well with the experimental. The frontier orbitals, HOMO and LUMO determine the way a molecule interacts with other species. The frontier orbital energy gap for CPPS is -5.61 eV.

Molecular electrostatic potential surface map indicates that the most suitable atomic sites for electrophilic attack are O(19) and O(20) atoms, while the most probable sites which could be involved in nucleophilic process are at C(7) and C(8) atoms of succinimide ring.

Conclusion

Based on the density functional theory (DFT)/B3LYP/6-311++G(d,p) method, vibrational, electronic, NMR, reactivity and structural aspects of 1-(4-Chlorophenyl)-3-phenyl-succinimide (CPPS) were studied in detail and the results were also compared with the experimental.

Acknowledgments

This work has been financially supported by Ministry of Education and Science, Republic of Serbia, under Grant No. 172035, 172013 and HP-SEE European project.

References

- [1] P. N. Patsalos, *Epilepsia* 2005, 46 (9), 140–144.
- [2] R. J. Porter, J. K. Penry, J. R. Lacy, M. E. Newmark, H. J. Kupferberg, *Neurology* 1979, 29, 1509-1513.
- [3] G. Cheng, J. K. Weston, A. C. Jr. Bratton, *Epilepsia*, 1963, 4, 66-76.
- [4] N. Perišić-Janjić, R. Kaliszan, P. Wiczling, N. Milošević, G. Ušćumlić, N. Banjac, *Mol. pharmaceutics*, 2011, 8, 555-563.

B-08-P

DETERMINATION OF SULFOXIDE CONFIGURATION IN THIAZOLIDINONE RING USING NMR SPECTROSCOPY AND DFT CALCULATION

Z. Džambaski¹, J. Aleksić¹, M. Stojanović¹, M. Baranac-Stojanović^{1,2}, R. Marković^{1,2}

¹ ICTM, Center for Chemistry, University of Belgrade, Njegoševa 12, 11000 Belgrade, Serbia (zdzambas@chem.bg.ac.rs)

² Faculty of Chemistry, University of Belgrade, Studentski trg 16, 11000 Belgrade, Serbia

Abstract

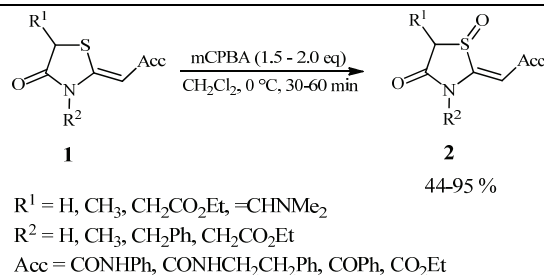
Cyclic five-membered ring sulfoxides were prepared by oxidation of the corresponding sulfides with *meta*-chloroperbenzoic acid in appropriate solvent. The oxidation was followed by NMR and both ¹H and ¹³C NMR data were collected. The geometries of all of the compounds were optimized using the DFT B3LYP/6-31G(d) method and the ¹³C and ¹H chemical shifts were calculated for geometry-optimized structures at the same level of theory. The calculated ¹³C NMR chemical shifts were in very good agreement with the experimental data. The characteristic differences in chemical shifts of the carbon atoms in the α - and β -position to sulfur, were successfully used to distinguish between the diastereoisomeric sulfoxides and allowed configuration determination.

Introduction

Although 4-thiazolidinone *S*-oxides have been frequently investigated, usually no information concerning their diastereomeric purity or stereochemical structure has been given or it is unclear. In many cases, the reported data have been used only to verify compound identities, and there have been only several discussions of relationships between NMR data and structure [1-2]. The availability of stereochemical data on this transformation is useful from both, the mechanistic and synthetic standpoints.

Results and Discussion

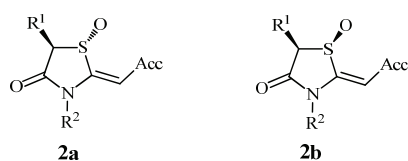
As a part of our ongoing investigation of reactivity and synthetic application of thiazolidinone core containing heterocycles, N-substituted 2-alkylidene-4-thiazolidinones **1** were oxidized in satisfactory yields to give sulfoxides **2**, which appeared to be relatively stable compounds (Scheme 1). In the course of oxidation of precursors **1**, during which the second stereogenic center was created, mixtures of two diastereomeric sulfoxides **2a** and **2b** were produced. A diastereomeric ratio, depending on the substituent at the C-5 position, after chromatographic purification was 87:13 (R¹ = CH₃) to 77:23 (R¹ = CH₂CO₂Et).



Scheme 1.

The diastereomeric distribution is negligibly affected by an electron-accepting group and substituent at the N-3 position. Diastereomeric sulfoxides were not isolated as pure isomers because of the isomerization occurring in solution, during the work-up procedure and chromatographic purification. The final diastereomeric distribution of the reaction products, i.e., the isomers, was determined by the ^1H NMR. To determine the relative configuration of the diastereomeric sulfoxides ^{13}C NMR data were analyzed. The assignments were made by (i) analogy to those reported for thiazolidinone derivatives [3] and (ii) by the known fact that the oxidation of sulfur in this heterocyclic system causes a deshielding effect of the carbon atoms at the α position to sulfinyl function, and shielding of the C atoms at the β position [4]. Indeed, a downfield shift of the absorption going from sulfides **1** to sulfoxide **2** can be observed for the C-2 and C-5 carbon atoms, while the C-4 and C-5' atoms undergo shielding effect. It is also evident that the deshielding effect seen by the C-5 is stronger in minor isomers, while the shielding of the C-5' atom is more pronounced in major isomers (Table 1).

To gain insight into the results obtained during our experiments, we were interested to evaluate thermodynamic stability of both diastereomers. It turned out, according to theoretical calculation performed at the B3LYP/6-31G(d) level, that the energy of *syn*-**2b** isomers was lower by 1.60-1.65 kcal/mol than that of the corresponding *anti*-**2a** diastereomer. Therefore, the position of equilibrium, favoring the *syn* isomers can be anticipated.



Subsequently, employing GIAO method, ^{13}C NMR chemical shifts were calculated at the same level of theory in the gas phase and with inclusion of a solvent, and compared with experimental data. The structures optimized at the same level of theory in the gas phase served as a basis for these calculations. Close agreement was found between experimental and calculated data for the carbon atoms C-5 and C-5' (Fig. 1 and Table 1).

B-08-P

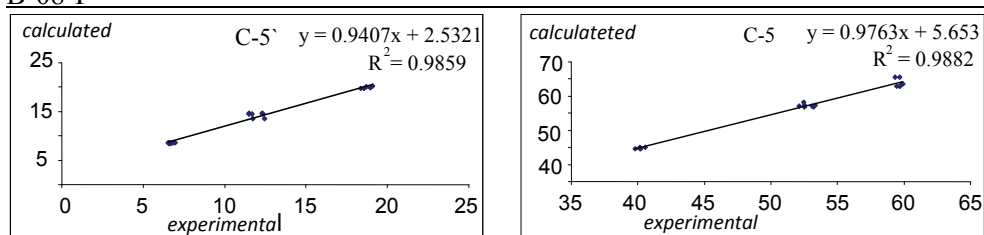


Figure 1. Correlation of experimental and theoretically calculated ^{13}C NMR chemical shifts of thiazolidines **1** and **2** ($R^1 = R^2 = \text{CH}_3$), at B3LYP/6-31G(d) level of theory, in the gas phase.

Table 1. Effect of the S=O group on chemical shifts of C-5 and C-5' carbons of **2a** and **2b** ($R^1 = R^2 = \text{CH}_3$), in comparison with the values of unoxidized compounds.

		diamagnetic displacement of the C5' signals ($\Delta\delta$, ppm)	paramagnetic displacement of the C5 signals ($\Delta\delta$, ppm)
major	experimental	- 11.6-12.6	+ 12.3-12.9
diastereomer	calculated	- 11.1-11.6	+ 12.3-13.5
minor	experimental	- 5.2-7.2	+ 19.1-19.9
diastereomer	calculated	- 5.1-6.6	+ 18.3-20.9

Conclusion

The comparison of the calculated data with the experimental values suggests *syn*-orientation of the oxygen atom of the sulfinyl group relative to the methyl group in the major isomer **2b**, and *anti*-orientation of the oxygen atom of the sulfinyl group relative to the methyl group in the minor isomer **2a**.

Acknowledgement

This work was supported by the Ministry of Science of the Republic of Serbia and the Deutscher Akademischer Austauschdienst (DAAD)-project ID: 504 252 70.

References

- [1] C. R. Harrison, P. Hodge, J. Chem. Soc., Perkin Trans. 1, 1976, 1772-1775.
- [2] M. D. Rozwadowska, A. Sulima, Tetrahedron, 2003, 59, 1173-1179.
- [3] M. Baranac-Stojanović, U. Klauwünzer, R. Marković, E. Kleinpeter, Tetrahedron, 2010, 66, 8958-8967.
- [4] U. Zoller, in The Chemistry of Sulphones and Sulfoxides, edited by S. Patai, Z. Rappoport and C. Stirling, 1988, p 396. Wiley Chichester.

MODELING ENDOHEDRAL FULLERENES IN THE CASE OF THE PHOTOIONIZATION PROCESS

Aleksandar R. Tančić

Vinča Institute for Nuclear Sciences, 11001 Beograd, POB 522, Serbia

Abstract

Endohedral fullerenes (EF) $A@C_{60}$ (atom A is confined inside of the carbon fullerene C_{60}) have attracted much attention of investigators in recent years not merely as new, fascinating subjects for studies, but because of an industrial interest in these objects as well. The spectroscopy of the EA is turning into a promising area of new exciting investigations. Because of that, detailed knowledge of the modifications in the structure and photo-spectra of the EA is extremely important. In this paper are presented some simple models for the theoretical investigations of the photoionization (PI) of the EA and some corresponding results of calculations.

Introduction

The description of the interaction of electromagnetic radiation with an endohedral fullerene is a complicated theoretical problem. Because of that the simplifications of the problem are useful. Here we present two semiempirical models [1,2,3]. They assume that the encaged atom is simulated by a spherical attractive short range potential well V_n (radius R_n , thickness Δ and depth U_n). One of the models [1,2], the Δ -potential model, accounts for the finite thickness Δ of the C_n cage. The other model [3,4,5] is the δ -potential model: C cage is simulate by $\approx \delta(r - R_n)$ ($\Delta = 0$; no interaction between the ground state of the atom and the C cage). The atom A , located well inside $A@C_n$ (denoted by AC) can be easily treated in the Random Phase Approximation (RPA) using the initial step the one-electron Hartree-Fock (HF) method, while the “fullerene-atom A ” interaction can be considered as a sort of perturbation [3,4]. In the case of the PI processes the results produced by the both potential models are compared using the frozen cage approximation FCA and dynamical (polarization) cage approximation DCA. In the framework of presented models results in this paper are obtained by the improved version of the RPA method- IPRPA [4].

Atomic units (au) are used throughout the paper.

Models

The following relations gives the differential PI cross section (c.s.) of a spherically-symmetric endohedral shell by non-polarized light [3,5]

$$d\sigma_{nl}^{AC}(\omega)/d\Omega = \left[\sigma_{nl}^{AC}(\omega)/(4\pi) \right] \left[1 - \beta_{nl}^{AC}(\omega)P_2(\cos\theta)/2 + \kappa\gamma_{nl}^{AC}(\omega)P_1(\cos\theta) + \right. \\ \left. + \kappa\eta_{nl}^{AC}(\omega)P_3(\cos\theta) \right]$$

where $\kappa = \omega/c$, P_i are Legendre polynomials, θ is the angle between photon and photoelectron linear momentums, $\beta_{n\ell}$ is the dipole and $\gamma_{n\ell}$, $\eta_{n\ell}$ are non-dipole angular anisotropy parameters (which are defined in [3]) and they are formed by the combination of the dipole D and quadrupole Q matrix elements of photoelectron transitions and photoelectron scattering phases. The cross section $\sigma_{n\ell}^{AC}(\omega)$ is determined by the dipole $D_{n\ell \rightarrow \ell\ell \pm 1}^{AC} (\equiv D_{\ell \pm 1}^{AC})$ amplitude and is given by the expression [3,4]

$$\sigma_{n\ell}^{AC}(\omega) = (16\pi^2 \omega / 3c) [(\ell + 1) |D_{\ell+1}^{AC}|^2 + \ell |D_{\ell-1}^{AC}|^2]$$

where D, Q matrix elements are obtained by solving the RPA (or IPRPA) equations [4] in the framework of the Δ and δ potentials models (defined above).

Results and Conclusions

In Fig.1. are presented the Xe 5p PI cross sections of $Xe@C_{60}$. This work and other authors calculations [1,4,5] demonstrated that the dynamical screening [1,3,4,5] of the incident radiation by the C_n cage can drastically change the PI cross section compared to the FCA calculations. Present calculations demonstrated that the FCA results of calculated PI c.s. with both potential (δ, Δ) predict a noticeable confinement resonance in the Xe 5p PI c.s. near threshold. The DCA results show the impressive enhancement of the Xe 5p PI cross section compared to the FCA results.

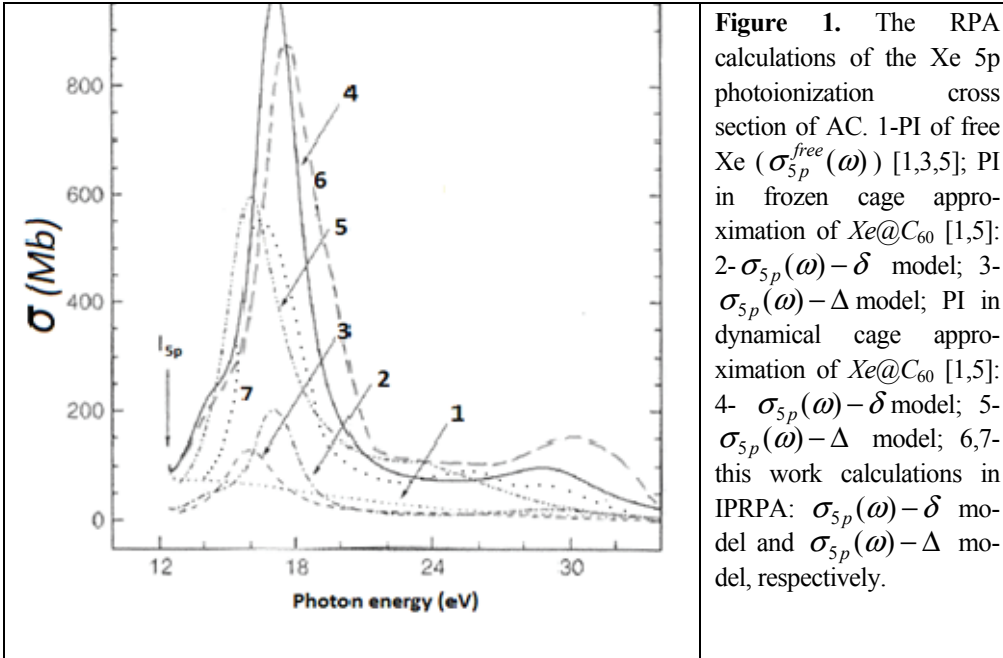


Figure 1. The RPA calculations of the Xe 5p photoionization cross section of AC. 1-PI of free Xe ($\sigma_{5p}^{free}(\omega)$) [1,3,5]; PI in frozen cage approximation of $Xe@C_{60}$ [1,5]: 2- $\sigma_{5p}(\omega) - \delta$ model; 3- $\sigma_{5p}(\omega) - \Delta$ model; PI in dynamical cage approximation of $Xe@C_{60}$ [1,5]: 4- $\sigma_{5p}(\omega) - \delta$ model; 5- $\sigma_{5p}(\omega) - \Delta$ model; 6,7- this work calculations in IPRPA: $\sigma_{5p}(\omega) - \delta$ model and $\sigma_{5p}(\omega) - \Delta$ model, respectively.

Acknowledgments

I am much indebted to Professor M.Ya. Amusia and Professor V. K. Dolmatov for many helps in preparation of this work.

References

- [1] V. K. Dolmatov, *Adv. in Quant. Chemistry*, 2009, 58, 13.
- [2] H. Shinohara, *Rep. Prog. Phys.*, 2000, 63, 843.
- [3] M. Ya. Amusia, A. S. Baltenkov, *Phys. Rev A*, 2006, 73, 062723.
- [4] A. Tančić, M. Kutin, M. Davidović, *Acta Phys. Polonica A*, 2009, 115, 838.
- [5] M.Ya. Amusia, A. S. Baltenkov, L. Chernisheva, *JETP Let.*, 2008, 87, 230.

B-10-P

BARRIER HEIGHTS FOR METHYL GROUP TORSION AND CONFORMATIONAL DEFORMABILITY IN 1,4,6- TRIMETHYLNAPHTHALENE

B. D. Ostojić^a, D. S. Đorđević^a

*^aInstitute of Chemistry, Technology, and Metallurgy, University of Belgrade,
Studentski trg 12-16, 11001 Belgrade, Serbia*

Abstract

Toxic, mutagenic, and carcinogenic effects among trimethylnaphthalenes (TMNs) may differ considerably. Different approaches have been employed to determine the barrier heights for methyl group torsion in the ground electronic state of 1,4,6-TMN. In the HOMO and LUMO of 1,4,6-TMN a type of orbital interaction named $\pi^* - \sigma^*$ hyperconjugation is observed. The results of calculations show that there is an increase in the conformational flexibility of the aromatic system in 1,4,6-TMN compared to naphthalene while its nucleus-independent chemical shift (NICS) values are lower.

Introduction

Naphthalene derivatives have many applications in industrial processes. On the other hand, alkylated naphthalene derivatives are widespread environmental pollutants. Trimethylnaphthalenes as well as other alkylated naphthalenes such as methyl- and dimethyl-naphthalenes are components of diesel fuel and residues of oil product refining. Various TMNs are among alkylated naphthalenes which are main volatile polycyclic aromatic hydrocarbons (PAHs) of bitumen emissions. The results of Lindberg et al. [1] suggest that fumes from asphalt mixed with recycled additives contain direct-acting genotoxic components.

The methylation of the aromatic system of PAHs can induce, enhance, reduce or abolish their toxic, carcinogenic or mutagenic properties [2]. The number and the position of substitutions can be important in the evaluation of the carcinogenic activity of alkylated PAHs. Small changes in structure can have a large effect on carcinogenic activity.

Taking into account little information on TMNs [3,4], we present the first theoretical report on geometry, vibrational frequencies, barrier heights for internal rotation of methyl groups in the ground electronic state (S_0), the influence of $\pi^* - \sigma^*$ hyperconjugation effects on the torsional barriers as well as the conformational deformability of the aromatic system and aromaticity of 1,4,6-TMN [5].

Results and discussion

The equilibrium geometry of the 1,4,6-TMN isomer in the ground electronic state and the transition state (TS) structures of its rotamers were fully optimized using the B3LYP method and the cc-pVTZ basis set. The frequency calculations were

carried out at the same level of theory. The introduction of three methyl substituents into the naphthalene rings results in an increase in the ring area compared to the corresponding value for the naphthalene molecule. The major structural change compared to naphthalene is found for the bond length between C₁₀ and the carbon atom bound to the methyl group in the α position, C₄. For the C-C bond length between C₁ and the carbon atom bound to another methyl group in the α position, the lengthening of the bond length is also found. The most remarkable changes of the bond angles from those in the naphthalene molecule can be noticed for the angles C₈-C₉-C₁ and C₄-C₁₀-C₅. The geometries of the ground electronic state of 1,4,6-TMN and the TS structures of the corresponding rotamers are reasonably close to each other. The only exception is the increasing of the corresponding C-CH₃ bond length.

The investigated molecule is a triple rotor case. In this two-ring system characterized by the asymmetry about the rotor axes, each barrier height is different. The rotamers 1 and 2 have higher values of the barrier heights, 821 and 843 cm⁻¹, than the rotamer 3, 194 cm⁻¹, in correlation with higher values of the barrier heights of 1-methylnaphthalene (1-MN), 809 cm⁻¹ [6] compared to the barrier height of 2-methylnaphthalene (2-MN), 234 cm⁻¹ [6].

In the highest occupied molecular orbital (HOMO) of the 1,4,6-TMN minimum energy structure, the frontier electron density is highest at the positions 1, and 4. The π^* - σ^* hyperconjugation (HC) [7] appears and causes a bonding interaction between carbon atom at the α position and out-of-plane hydrogen atom of the methyl group. On the other hand, in the 1,4,6-TMN transition state structure of the rotamer 1 and the rotamer 2, the HC does not appear at the position 1 and the position 4, respectively. This contributes to the stability of the energy of HOMO for the 1,4,6-TMN minimum energy structure. Nakai and Kawamura [8] noticed HC in the HOMO of 2-MN but hyperconjugative contribution is smaller than in 1-MN. In the HOMO of the 1,4,6-TMN the HC appears also at the position 6 and is smaller compared to the positions 1 and 4 in consistency with the lower stability of the HOMO of the rotamer 3.

The torsional angle ϕ with the smallest difference in energy between planar geometry and the non-planar geometry (torsional angle of 20°) was selected. Two parameters for the characterization of the ring flexibility were calculated: the deformational energy, E_{def} , and the rigidity constant, k . The results of calculation reveal that naphthalene possesses higher deformational energy [9] than 1,4,6-TMN. In both rings of 1,4,6-TMN the degree of aromaticity is lower compared to naphthalene rings [9] but 1,4,6-TMN possesses still high degree of π -electron delocalization.

Conclusion

The results of *ab initio* and DFT calculations of the equilibrium molecular geometry, vibrational spectrum, and assignments in the ground electronic state of 1,4,6-TMN are presented. The stability of HOMO and LUMO is determined by π^* - σ^* hyperconjugation. The variations of the rotational barriers in the S₀ state are

B-10-P

shown to be directly connected with the stability of HOMO. The results reveal that 1,4,6-TMN possesses higher conformational flexibility of the aromatic system than the naphthalene molecule. The NICS values of 1,4,6-TMN indicate aromaticity.

Acknowledgments

We wish to thank the Ministry of Education and Science of Serbia (Contract No. 172 001) for financial support.

References

- [1] H. K. Lindberg, V. Väänänen, H. Järventaus, H. Suhonen, J. Nygren, M. Hämeilä, J. Valtonen, P. Heikkilä, and H. Norppa, *Mutat. Research* 2008, 653, 82-90.
- [2] D. W. Jones, R. S. Matthews, in: G. Ellis, G. B. West (Eds.), *Progress in Medicinal Chemistry*, North-Holland, Amsterdam, 1974, 159.
- [3] W. L. Mosby, *J. Am. Chem. Soc.*, 1952, 74, 2564-2569.
- [4] T. J. Mayer, J. M. Duswalt, *J. Chem. Eng. Data*, 1973, 18, 337-344.
- [5] B. D. Ostojić and D. S. Đorđević, *Chem. Phys. Lett.*, 2012, 536, 19-25.
- [6] X.-Q. Tan, W. A. Majewski, D. F. Plusquellic, D. W. Pratt, *J. Chem. Phys.*, 1991, 94, 7721-7733.
- [7] H. Nakai, M. Kawai, *Chem. Phys. Lett.*, 1999, 307, 272-276.
- [8] H. Nakai, Y. Kawamura, *Chem. Phys. Lett.* 2000, 318, 298-304.
- [9] M. V. Zhigalko, O. V. Shishkin, L. Gorb, J. Leszczynski, *J. Mol. Struct.*, 2004, 693, 153-159.

CONICAL INTERSECTIONS BETWEEN X^2A_1 AND 1^2B_2 STATES OF THE B_2H MOLECULE

Ljiljana Stojanović

Faculty of Physical Chemistry, University of Belgrade

Abstract

Ab initio investigation of nonadiabatic interactions between X^2A_1 (X^2A') and 1^2B_2 ($2^2A'$) electronic states in the B_2H molecule was performed. The seam of conical intersections between studied states was located, and radial nonadiabatic coupling matrix elements were computed. Quasi-diabatization in two-dimensional subspace was performed. The first derivatives of obtained transformation angle were compared to nonadiabatic coupling matrix elements.

Introduction

Possible nonadiabatic interactions between electronic states could be analyzed using nonadiabatic coupling matrix elements (NACMEs) τ_{12} , defined as $\tau_{12} = \langle \Psi_1 | \nabla \Psi_2 \rangle$, where Ψ_1 and Ψ_2 are the wave functions of the electronic states, and ∇ is the gradient operator of the position vector. In the case of two-dimensional surfaces, radial ($\tau_{12,R} = \langle \Psi_1 | \partial \Psi_2 / \partial R \rangle$) and angular ($\tau_{12,\theta} = \langle \Psi_1 | \partial \Psi_2 / \partial \theta \rangle$) components can be defined. Nonadiabatic couplings are the largest where the two adiabatic states are very close in energies. The transformation from adiabatic to diabatic states can be expressed using a single parameter denoted as transformation angle γ ,

$$H_1 = E_2 \sin^2 \gamma + E_1 \cos^2 \gamma, \quad H_2 = E_1 \sin^2 \gamma + E_2 \cos^2 \gamma, \quad H_{12} = (E_2 - E_1) \sin \gamma \cos \gamma,$$

where E_1 and E_2 are adiabatic potentials, H_1 and H_2 are diabatic potentials, and H_{12} is the diabatic coupling potential. In an ideal model of nonadiabatic interactions between two states which neglects coupling with other electronic states, NACMEs can be related to the first derivative of the transformation angle with respect to radial (or angular) coordinate.

Results and Discussion

In numerous cases of molecules of X_3 type, conical intersections are observed at D_{3h} geometry. According to this, in the case of B_2H molecule it is expected that it occurs when the highest, C_{2v} , symmetry is reached, i.e. when the geometry becomes that of an isosceles triangle B-H-B. Therefore, the computations of potential energy surfaces of X^2A' and $2^2A'$ states are restricted to C_{2v} geometries, where these species correlate with the X^2A_1 and 1^2B_2 states, respectively, i.e. the bond lengths are varied in the same manner in all computations (Figure 1). Multireference configuration interaction method (MRCI) limited to single and double excitations [1], with Dunning's cc-pVTZ

B-11-P

basis set [2] is employed. Calculations are performed in the framework of C_s group using internal coordinates as variables.

The seam of conical intersections is located at B-H bond lengths larger than 1.1 Å (at C_{2v} symmetry) and bond angles in the range of 45 to 60 degrees.

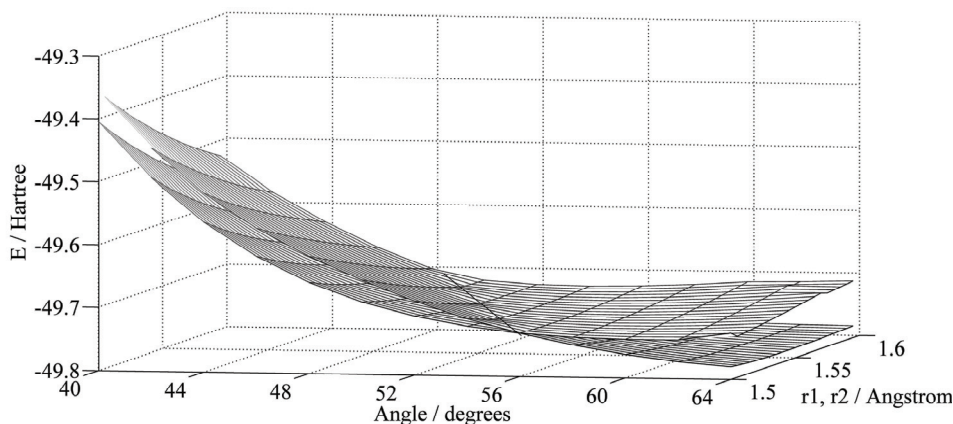


Figure 1. Potential energy surfaces of X^2A' and $2^2A'$ states of the B_2H obtained with CASSCF/cc-pVTZ method.

The quasi-diabatization of the states by means of the method implemented in MOLPRO code is performed [3,4]. The geometry near dissociation limit (equilibrium bond lengths and bond angle of 150°), where the states are sufficiently separated, is used as reference, assuming their negligible mixing in this case. The results of quasi-diabatization at fixed values of two coordinates ($r_1 = 1.538$ Å, $\theta = 50^\circ$) and variable third one (r_2) are presented in Figure 2. It can be seen that adiabatic states avoid crossing, as the diabatic states intersect each other. The minimal energy difference between adiabatic states in this case is 88 cm^{-1} . It can be concluded according to very large values of nonadiabatic coupling matrix elements in the vicinity of the avoided crossings that the states are strongly coupled.

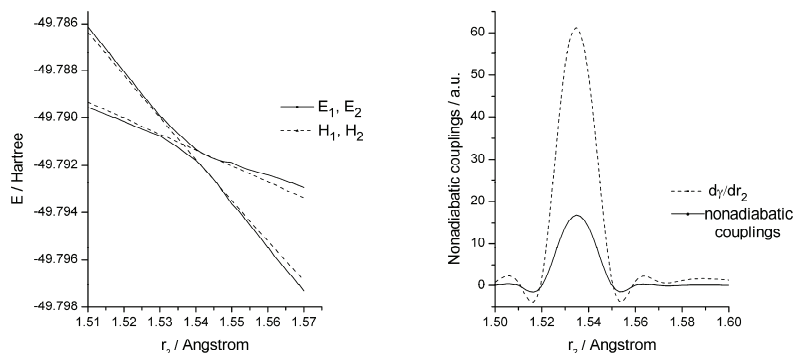


Figure 2. Diabatic and adiabatic potential energy curves (left) and NACMEs (right).

The X^2A' state is optimized, and its global minimum is at bond lengths of 1.4444 Å and bond angle of 72.9°. Since the geometries of the conical intersections are not far from the equilibrium one, they could be reached during the bending and symmetric stretching vibrations. This occurrence is of large importance for the dynamics of the nuclei in the ground and first excited state.

Conclusion

The series of avoided crossings between X^2A_1 and $2^2A'$ states of B_2H is located at C_{2v} symmetries of molecule. Large nonadiabatic couplings between the states occur in the vicinity of intersections. Since the geometries of intersections are reachable from the equilibrium one, large influence of nonadiabatic couplings on nuclei dynamics in the ground state is expected.

References

- [1] H. J. Werner, P. J. Knowles, J. Chem. Phys. 89 (1988) 5803; H. J. Werner, P. J. Knowles, Theor. Chim. Acta 84 (1992) 95.
- [2] T.H. Dunning, Jr. J. Chem. Phys. 90, 1007 (1989).
- [3] D. Simah, B. Hartke, H. -J. Werner, J. Chem. Phys. 111 (1999) 4523.
- [4] MOLPRO, version 2010.1, ab initio program package, H. J. Werner, P. J. Knowles, R. Lindh, F. R. Manby, M. Schütz, et al.

B-12-P

THE STRUCTURE OF HYPERLITHIATED Li_5I MOLECULE

M. Milovanović

*Faculty of Physical Chemistry, University of Belgrade, Studentski trg 12-16,
P.P.Box 47, 11158 Belgrade, Serbia*

Abstract

We report the geometry, distribution of electrons, ionization energies and thermodynamical stability of Li_5I species, calculated at the B3LYP3/aug-cc-pVTZ(Li), aug-cc-pVTZ-PP level of theory. The analysis show that this molecule has ionization energy (IE) lower than lithium and dissociation energies that varies dependent on whether dissociated species have an odd or even number of electrons. Adiabatic IE = 4.49 eV.

Introduction

The structure, nature of bonding, thermodynamical stability, and ionization energy of 'hyperlithiated' molecules with unusual stoichiometry have been studied theoretically and experimentally since the discovery of Li_3O in 1978.[1]. This work is a continuation of investigation of hyperlithiated iodine species [2].

The structures have been predicted by *ab initio* calculations, precisely B3LYP3 functional in the aug-cc-pVTZ basis set for lithium and aug-cc-pVTZ-PP set for iodine. The later set has ECP28MDF functions for 28 inner core electrons. All calculations were performed by MOLPRO 2010.1 software package [3].

Results and Discussion

The predicted equilibrium geometries of the ground states of the neutral Li_5I and single charged Li_5I^+ species are presented in Figure 1. Li_5I with an even number of electrons (68) has a planar structure (C_s symmetry), and single charged species Li_5I^+ , with an odd number of electrons, has C_1 symmetry. We can see displacement of molecular structure in the ionization of Li_5I . Electrons in the highest occupied molecular orbital (HOMO) and the lowest unoccupied MO (LUMO) in Li_5I and Li_5I^+ species are delocalized over the five lithiums. Mulliken charges, arisen from the Mulliken population analysis, are presented in Figure 2. Population analysis allocates the negative charge on the two lithium atoms that are most distant from the iodine atom. Dipole moments in the global minima are predicted to be 4.75 Debye for neutral and 13.62 Debye for charged species.

Ionization energies (IEs) of hyperlithiated Li_5I molecule are shown in Table 1: vertical (vIE) is obtained as the difference between the energies of the neutral Li_5I (with zero point vibrational energy, ZPVE) and charged Li_5I^+ at the equilibrium geometry of the neutral; and adiabatic (aIE) is obtained as the difference between the energies (including ZPVEs) of the neutral species and charged one at their equilibrium geometries. As well as other hyperlithiated

molecules, the ionization energy is remarkably lower than that of lithium atom (5.39 eV). In this respect, the molecule is superalkali.

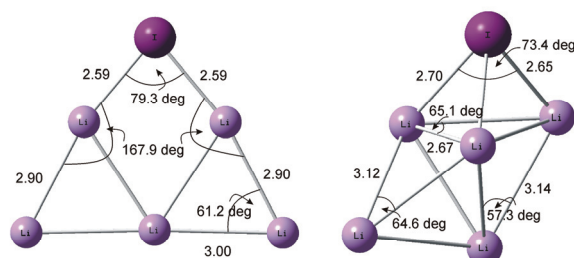


Figure 1. The equilibrium geometries of the ground states of Li_5I and Li_5I^+ .

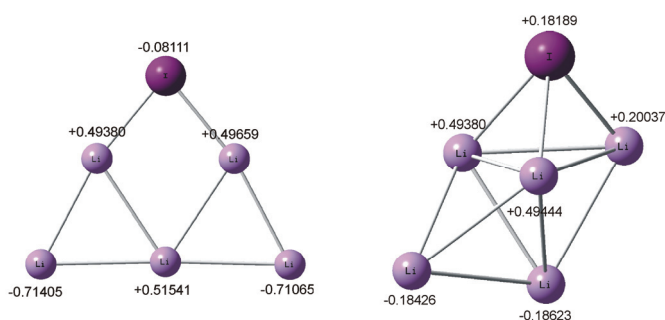


Figure 2. The charge distribution in Li_5I and Li_5I^+ .

Table 1. The ionization energy of Li_5I molecule in its ground electronic state calculated at the B3LYP3/Li=aug-cc-pVTZ, I=aug-cc-pVTZ-PP level.

	Electronic energy / Hartree	ZPVE / Hartree	EE + ZPVE / Hartree	vIE/eV	aIE/eV
Li_5I (equilibrium geometry)	-333.525799	0.005504	-333.520295		
Li_5I^+ (eq.geometry of the neutral)	-333.338174			4.956	
Li_5I^+ (equilibrium geometry)	-333.360906	0.005713	-333.355193		4.493

We have also calculated the thermodynamical stability of Li_5I . The dissociation energy (D_e) of the reactions $\text{Li}_5\text{I} \rightarrow \text{Li}_4\text{I} + \text{Li}$, $\text{Li}_5\text{I} \rightarrow \text{Li}_3\text{I} + \text{Li}_2$, $\text{Li}_5\text{I} \rightarrow \text{Li}_2\text{I} + \text{Li}_3$, $\text{Li}_5\text{I} \rightarrow \text{LiI} + \text{Li}_4$, $\text{Li}_5\text{I} \rightarrow \text{I} + \text{Li}_5$ have been calculated to be 103, 81,

B-12-P

156, 137 and 417 kJmol⁻¹. In general, dissociation energy is lower when dissociated species have an even number of electrons. The highest value corresponds to dissociation on iodine atom and Li₅ cluster.

Table 2. The dissociation energies (in kJmol⁻¹) of Li₅I. Final values (De corr) are obtained from uncorrected values (De) by taking into account zero point vibrational energies (ZPVE) and basis set superposition error (BSSE).

Reaction	De	De with BSSE	ZPVE (Li ₅ I=14.45)	De corr
Li ₅ I → Li ₄ I + Li	107.92	106.83	Li ₄ I=10.83	103.21
Li ₅ I → Li ₃ I + Li ₂	85.13	83.79	Li ₂ =2.06 Li ₃ I= 9.15	80.55
Li ₅ I → Li ₂ I + Li ₃	161.39	160.56	Li ₂ I=5.53 Li ₃ =4.02	155.66
Li ₅ I → LiI + Li ₄	142.51	140.19	LiI= 2.93 Li ₄ =8.07	136.74
Li ₅ I → I + Li ₅	421.61	420.47	Li ₅ =10.53	416.55

Conclusion

The present paper reports IEs of Li₅I cluster and discusses electronic and geometric structures, as well as its thermodynamical stability. We can conclude that this small heterogeneous lithium cluster is a superalkali. This investigation together with investigation on similar species, could provide useful information in studying changes that occurs in energy and bonding from small clusters to bulk metal.

Acknowledgement

The author acknowledges the Ministry of Education and Science, Republic of Serbia, for financial support (Contract No. 172040).

References

- [1] H. Kudo, C. H. Wu, H. R. Ihle, J. Nucl. Mater., 1978, 78, 380.
- [2] J. Djustebek, S. Veličković, S. Jerosimić, M. Veljković, J. Anal. At. Spectrom., 2011, 26, 1641-1647.
- [3] MOLPRO, version 2010.1, a package of ab initio programs, H.-J. Werner, P. J. Knowles, G. Knizia, F. R. Manby, M. Schütz, and others, see <http://www.molpro.net>.

THEORETICAL ANALYSIS OF THE THYMINE-CYTOSINE CYCLOPYRIMIDINE DIMER

M. Petković, M. M. Ristić, M. Etinski

*Faculty of Physical Chemistry, University of Belgrade
Studentski Trg 12-16, P. O. Box 47, 11158 Belgrade, Serbia
ristic@ffh.bg.ac.rs*

Abstract

In this study we employed a quantum-chemical method to characterize the structure of thymine-cytosine cyclobutane pyrimidine dimer. Its ground state geometry was optimized, and vibrational frequencies were obtained in harmonic approximation. Two conformers were found and their structures and stability compared. The N-H, C-H and C=O stretching vibrations were analyzed and the change of corresponding peak positions upon conformational change was briefly discussed.

Introduction

The ozone layer above the Earth absorbs the UV radiation below 290 nm. The UVB (290-320 nm) radiation is partially absorbed while UVA (320-380 nm) radiation is not absorbed. The main cellular target for UV radiation are nucleic acids. Sequences containing two or several pyrimidine basis are hotspots prone to formation of photolesions. These photolesions can change the genotype of cells and remove the normal capacity to inhibit cell growth. The most frequent photochemical reaction of nucleic acids is intrastrand pyrimidine dimerization. It covalently links two neighboring pyrimidine basis, creating a cyclobutyl pyrimidine dimer (CPD) and a small amount of pyrimidine-(6,4)-pyrimidone ((6-4)PP) adduct and related Dewar valence isomer.

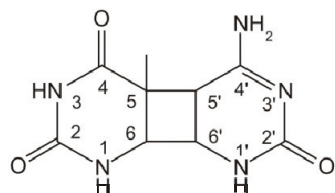


Figure 1. Chemical structure and atom labels of TC CPD.

In our previous papers we examined the structures and vibrational spectra of methylthymine-methylthymine (mTmT) CPD [1] and (6-4)PP [2]. In this work we examine the thymine-cytosine (TC) CPD (Fig 1) structure and infrared spectrum.

Theoretical Methods

We employed density functional theory (DFT) with B3-LYP functional [3] for electronic structure calculations. All optimizations were performed without symmetry constraints. We used Dunning's [4] correlation-consistent basis set cc-pVTZ (C, N, O, 10s5p2d1f /4s3p2d1f; H, 5s2p1d /3s2p1d). All calculations have been performed with the Gaussian 09 programme package [5].

Results and Discussion

The ground electronic state of CPD was optimized. Two conformers were found (Fig 2) and labeled CPD1 and CPD2 according to their stability.

The CPD1 conformer is more stable by 935 cm^{-1} (zero point energy included). Its optimized geometry with the most significant bond lengths is presented in Fig. 2. Both of its pyrimidine rings are non-planar. The dihedral angles $\text{C}_4\text{C}_5\text{C}_6\text{N}_1$ and $\text{C}_4'\text{C}_5'\text{C}_6'\text{N}_1'$ in the pyrimidine rings are 27.6 and 16.3 degrees, respectively. The corresponding dihedral angles in the less stable conformer CPD2 are 24.0 and 22.8 degrees, respectively.

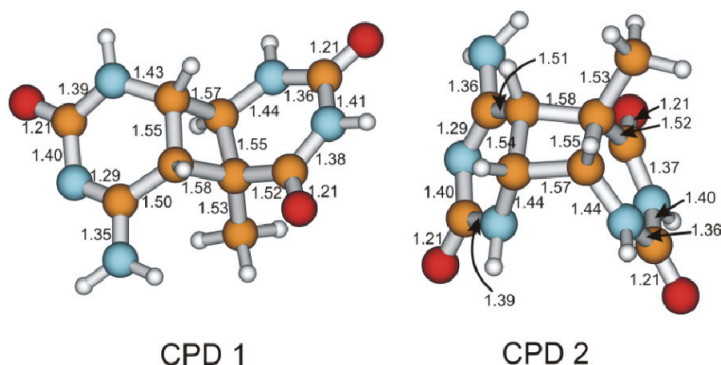


Figure 2. The optimized geometries of CPD1 and CPD2 isomers. All bond lengths are in Å.

The pyrimidine rings within either of the conformers are not in plane. The dihedral angles between the pyrimidine rings $\text{C}_5\text{C}_6\text{C}_6'\text{C}_5'$, $\text{C}_5\text{C}_6\text{C}_6'\text{N}_1'$ and $\text{N}_1\text{C}_6\text{C}_6'\text{N}_1'$ in the CPD1 conformer are 13.0, 130.0 and 110.0 degrees, while the corresponding values in

the CPD2 conformer are 13.9, 97.9 and 22.5 degrees.

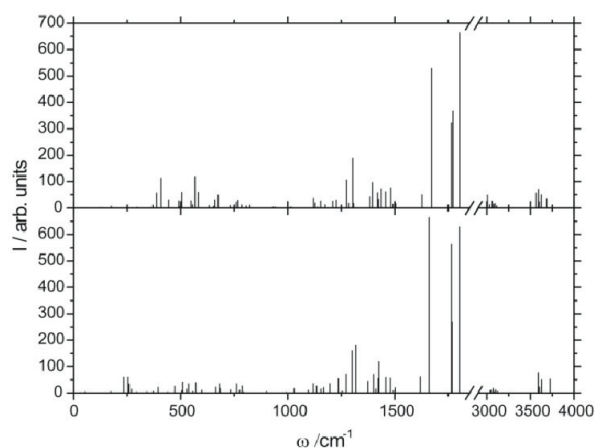


Figure 3. Vibrational spectrum of CPD1 (down) and CPD2 (up) isomers. There is a break in frequency axis from 1850 to 2900 cm^{-1} .

The differences in bond lengths of CPD1 and CPD2 conformers are not larger than 0.01 Å. When bond lengths of both conformers are compared to CPD product of photoreaction between two methylthymine molecules [2] most of them differ by less than 0.02 Å, with the exception of $\text{N}_3=\text{C}_4$, where a double bond is formed.

The conformers have 78 normal modes, which results in relatively large zero-point energy above 47 000 cm^{-1} .

Fig. 3 represents vibrational spectra of the conformers.

We will discuss the N-H, C-H and C=O stretching vibrations and check whether

there is a difference in peak position upon conformational change. First, we will analyze the high frequency region above 3000 cm^{-1} . This is the region of the C-H and N-H stretching modes. Since the difference in electronegativity of hydrogen and carbon atoms is small, the dipole moments do not drastically change upon C-H stretching motion, which results in small intensity of the corresponding peaks. Peak intensities of N-H stretching vibrations are generally larger than intensities that correspond to C-H stretching modes. The frequency intervals of N-H and C-H vibrations are $3588\text{-}3725\text{ cm}^{-1}$ and $3037\text{-}3121\text{ cm}^{-1}$ for CPD1 and $3565\text{-}3688\text{ cm}^{-1}$ and $3007\text{-}3111\text{ cm}^{-1}$ for CPD2. Thus, a small red shift in the C-H and N-H stretching region is noticed upon conformational change.

From three C=O stretching mode, $\text{C}_4=\text{O}$ and $\text{C}_2=\text{O}$, have coupled vibrations with frequencies equal to 1765 (for asymmetric stretching) and 1768 cm^{-1} (for symmetric stretching), while $\text{C}_2=\text{O}$ vibrates at 1802 cm^{-1} , in CPD1 conformer. Concerning the CPD2 conformer, frequency values are just slightly changed: 1765 , 1772 and 1803 cm^{-1} , respectively. Intensities of symmetric and asymmetric C=O vibrations in CPD1 and CPD2 are noticeably different.

Conclusions

We investigated geometries and vibrational properties of thymine-cytosine cyclobutane pyrimidine dimer, a photolesion created by a photochemical reaction between neighboring thymine and cytosine in a DNA strand. The two conformers were optimized. Their bond lengths do not differ significantly. On the other side, the dihedral angles between the pyrimidine rings are quite different. The energy difference is 935 cm^{-1} .

The vibrational spectra in the harmonic approximation were calculated. Due to the large number of normal modes, the analysis of spectra was limited to N-H, C-H and C=O stretching vibrations. The change of corresponding peak position and intensity upon conformational change showed that there is only slight difference in vibrational properties between two conformers.

Acknowledgement

The authors acknowledge the Ministry of Education and Science of Serbia for the financial support (Contract No. 172040).

References

- [1] M. M. Ristić, M. Petković, M. Etinski, J. Serb. Chem Soc., submitted.
- [2] M. Petković, M. Etinski, M. M. Ristić, Hem. Ind., submitted.
- [3] A. D. Becke, J. Chem. Phys., 1993, 98, 5648.
- [4] T.H. Dunning, J. Chem. Phys., 1989, 90 1007.
- [5] Gaussian 09, Revision A.02, M. J. Frisch et al.

B-14-P

THE THEORY OF MOLECULAR VIBRATIONAL STATE POLYADS AND THE VAN VLECK PERTURBATION THEORY

N. F. Stepanov, S. V. Krasnoshchekov

Faculty of Chemistry, Lomonosov Moscow State University
e-mail: nifest@classic.chem.msu.su

Abstract

An anharmonic vibration analysis for polyatomic molecules is usually performed on the ground of the second order Rayleigh – Schroedinger perturbation theory. To some extent a more convenient approach is a canonical van Vleck perturbation theory based on the creation-annihilation operator technique. This technique is closely related to the selection of special sets of vibrational states called polyads which correspond to definite values of a polyadic quantum number as an additional constant of motion, or (secondary) quantum number. Here we discuss some advantages of applying the canonical van Vleck perturbation theory in particularly together with the polyadic approach to the consideration of some problems concerning the molecular vibration analysis and present new results obtained in our lab.

Introduction

Modern vibrational analysis for polyatomic molecules enters two main problems, related to the numerous resonances among the manifold of vibrational states and to the development of such computational procedures which provide the possibility to reduce the problem (in a matrix representation) to comparatively small blocks. Today the vibrational analysis is usually performed in a frame of the second order Rayleigh – Schroedinger perturbation theory. Shortcomings of the ordinary perturbation theory are mainly connected with the description of resonant states, in particular the cases of Fermi and Darling-Dennison resonances. To some extent a more convenient approach summarized in 1988 by E.L.Sibert [1] relies on a canonical van Vleck perturbation theory (CVPT) based on the creation-annihilation operator technique. This technique is closely related to the selection of special sets of highly excited vibrational states called polyads which are determined by the definite values of the so called polyadic quantum number as an additional constant of motion, or as a secondary quantum number.

Here we discuss the main ideas and some advantages of applying the canonical van Vleck perturbation theory in particularly together with the polyadic approach to the consideration of some problems concerning the molecular vibration analysis. Some new results obtained in our lab are discussed as well..

Results and discussion

An ordinary approach to the introduction of CVPT is based on applying harmonic oscillator zero order Hamiltonian and creation-annihilation operator technique. In a case one-dimensional oscillator these operators are defined as

$$\tilde{a}_+ = \tilde{p} + i\tilde{q}, \tilde{a}_- = \tilde{p} - i\tilde{q}, H_0 = \frac{1}{2m}\tilde{p}^2 + \frac{k}{2}\tilde{q}^2$$

or if the variables $q = \sqrt[4]{mk}\tilde{q}$ and $p = \sqrt[4]{mk}\tilde{p}$, as well as the oscillator frequency $\omega = \sqrt{k/m}$ are introduced:

$$a_+ = p + iq \text{ и } a_- = p - iq, H_0 = \frac{\omega}{2}(p^2 + q^2).$$

The equations $\frac{\omega}{2}a_+a_- = H_0 - \frac{\omega}{2}$ and $\frac{\omega}{2}a_-a_+ = H_0 + \frac{\omega}{2}$ distinctly show that left-hand operators can serve as the operators of vibrational quantum number or, as it often said, the operators of vibrational quanta number.

The generalization of this approach can be carried out without difficulty. Moreover, the zero order Hamiltonian need not to represent only the harmonic oscillator. The main condition in constructing the creation-annihilation technique is the proper choice of the a_+ and a_- operators the product of which should provide the equations analogous to given above. In particular, we did it for the perturbed Morse oscillator.

Representing the vibrational potential as a series in q and going over to creation and annihilation operators one can obtain the operator expressions appropriate for CVPT employing. An essential feature of CVPT lies in the application of canonical transformations to the sequential elimination of non-diagonal terms in the corresponding orders of perturbation theory. It makes the CVPT procedure somewhat cumbersome but on the other hand it allows choosing the perturbation theory orders in a more systematic way.

The CVPT approach allows reliable evaluating the intensities in vibrational spectra as well as the corresponding frequencies in the presence of resonances. We also used it successfully to calculate Darling–Dennison and higher order resonance coupling coefficients for such classic examples of molecules as water and formaldehyde. The technique how to avoid the resonant denominators was offered. Besides, we showed that the coefficients of the Dunham’s Hamiltonians satisfy some equality rules for the orders of perturbation theory higher than the second one as it was established earlier for diatomic molecules

The technique of CVPT turns out to be very effective in solving the excited level problem for polyatomic molecules when the manifold of basis functions gets very large and the matrices of physical quantities in such bases need at first to be reduced to matrices of essentially lower dimension. The basic idea of the reduction rests nowadays on the selection of subspaces of resonant levels and so called vibrational polyads. The resonance of zero order states is determined by the (exact or approximate) energy equality some vibrational levels which seems to be a rather ordinary situation for excited levels of polyatomic molecules. Each resonance can be determined by the vector, positive elements of which are quantum numbers of one level and negative are of the other so that the remaining elements are equal zero and the total number of the elements is equal to the number of vibrational

B-14-P

degrees of freedom. All the elements of such vectors are integer numbers, the vectors give rise to the resonance subspace, and a scalar product of each of these vectors and the vector composed of fundamental frequencies of a molecule under consideration is exactly or approximately equal to zero.

The dimension of the resonance subspace for the selected set of n vibrational modes is equal to $n-1$ if the subspace is a non-degenerate one. For the total set of N vibrational modes of a molecule this number is $N-1$. The rest vector orthogonal to every vector of resonance subspace and composed of integer numbers as well is called polyad vector [2, 3]. All its elements are positive numbers (otherwise its definite linear combination with resonance vectors gives a resonance vector once again), the sum of the elements is a polyad number which in classical mechanics corresponds to the conserving action. The polyad of vibrational states and the quantum number vector of each of them correspond to one and the same polyad quantum number.

For molecules of comparatively large size, the construction of the initial polyad vector as a vector which is orthogonal to the resonant vectors can be performed in an approximate way. (Remember, that its elements should be integer!) Nevertheless, this approach allows simplifying the spectrum assignment and classification of the manifold of vibrational transitions. Its main computational advantage is connected with the block-diagonal matrix representation of physical quantities. Indeed, the matrix element $\langle \varphi_\alpha(q) | f(q) | \varphi_\beta(q) \rangle$ is equal to zero if the functions φ_α and $f\varphi_\beta$ belongs to different subspaces, e.g. one of them belongs to a resonance subspace and the other to the polyad subspace or they belong to manifolds of different polyad numbers. That means the matrix reduces to the single blocks related each to definite polyad quantum number, i.e. to a manifold of resonance states.

Conclusion

Canonical van Vleck perturbation theory is perfectly suited for anharmonic vibrational analysis of polyatomic semirigid molecules. Together with the corresponding classification of resonant operators and resonance wave functions it brings forward the technique of calculating the excited states as well.

Note, that some of our results were published this year in the Journal of Physical Chemistry A [4].

References

- [1] E. L. Sibert, J. Chem. Phys. 1988, 88, 4378.
- [2] M. E. Kellman, J. Chem. Phys. 1990, 93, 6630.
- [3] Polik, W. F.; van Ommen, J. R. In *Highly Excited Molecules: Relaxation, Reaction, and Structure*; Mullin, A., Schatz, G. C., Eds.; ASC Symposium Series 678; American Chemical Society; Washington, DC, 1997.
- [4] Krasnoshchekov, S. V.; Isayeva, E. V.; Stepanov N. F. J. Phys. Chem. A, 2012, 116

B-15-P

alkylation of the ethyl acetoacetate anion. Even though there are no experimental data for the O4-ethylation, we examined all possible alkylation reactions with four ethyl halides (fluoride, chloride, bromide, and iodide), implying that twelve different reaction pathways were considered (Fig. 2). The intrinsic reaction coordinates, from the transition states down to the two lower energy structures, were traced in order to verify that each saddle point is linked with the corresponding reactant and product complexes. The obtained geometries were verified, by vibrational analysis, to be minima (no imaginary frequencies), or maxima on the potential energy surface (one imaginary frequency). The calculated activation free energies and reaction free energies are presented in Table 1.

Table 1. Activation free energies (ΔG_a^\ddagger) and reaction free energies (ΔG_r) in kJ/mol for the reactions of the ethyl acetoacetate anion with ethyl halides

Position → Halide ↓	O4		C3		O2	
	ΔG_a^\ddagger	ΔG_r	ΔG_a^\ddagger	ΔG_r	ΔG_a^\ddagger	ΔG_r
fluoride	185.1	136.9	161.6	16.0	155.4	87.0
chloride	106.3	42.4	92.6	-80.3	79.9	-7.6
bromide	89.3	19.7	81.2	-96.8	63.2	-31.0
iodide	77.3	3.5	66.5	-116.8	53.0	-47.8

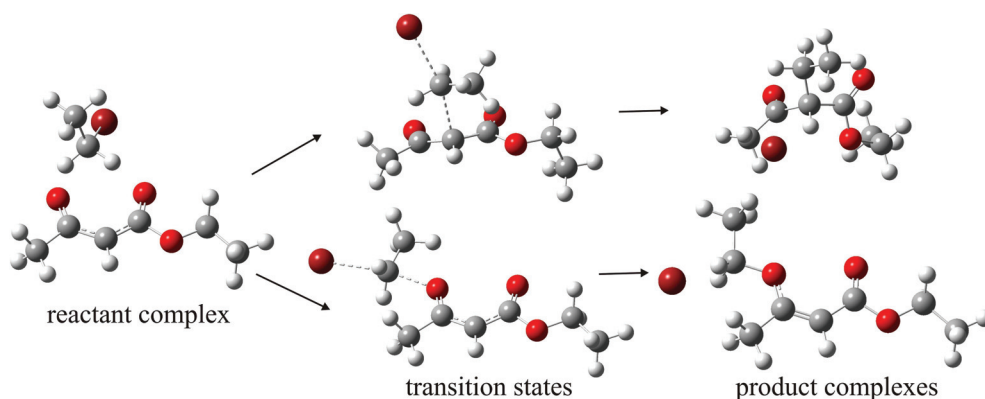


Figure 2. Calculated pathways for the alkylation of the ethyl acetoacetate anion with ethyl bromide in the position C3 (top) and O2 (bottom).

The reactions in the O4 position are endothermic, and characterized with high activation barriers, implying that the reverse reactions are faster. The same holds for the reactions with ethyl fluoride in all positions of the anion. These findings are in agreement with the experiments which show that these reactions do not occur at all, and can be attributed to the smaller negative charge on O4 in comparison to O2, and very strong C-F bond in ethyl fluoride. As expected, the activation barriers decrease with the increasing atomic number of the halogen.

The activation energies for the reactions in the position O2 are lower in comparison to the position C3, but the products of the reactions in the C3 position are more stable than those in the position O4. In the case of the reactions with ethyl chloride, where the activation barriers are high, the reaction preferably occurs via the transition state of lower energy, leading to the O2-product, implying that the reaction of the ethyl acetoacetate anion with ethyl chloride is under kinetic control. In the case of the reactions with ethyl bromide, where both activation energies are moderately high, both competitive reactions take place, leading to the mixture of the O2- and C3-products. Finally, in the case of the reactions with ethyl iodide, where the activation energies for the two competitive reactions are noticeably low, the reaction preferentially occurs towards the formation of the more stable C3-product, i.e. the alkylation reaction with ethyl iodide is thermodynamically controlled.

Conclusion

It is well-known that ethyl iodide, with the soft leaving group, iodide, primarily reacts with the softer carbon site, whereas the hard leaving group, chloride, reacts preferentially at the hard oxygen site of the enolate. This reasoning is complemented by our investigation as follows: Ethylation reaction with the hard leaving group is under kinetic control and leads to the formation of the O2-product, whereas the reaction with the soft leaving group is under thermodynamic control and leads to the formation of the C3-product. The experimental fact that the ethylation reaction of the ethyl acetoacetate anion does not occur in the position O4 with any halide, and with ethyl fluoride in any position is explained with very high activation energies and thermodynamic instability of the hypothetical products.

Acknowledgement

This work is supported by the Ministry of science of Serbia, grant nos 172016 and 174033.

References

- [1] A. L. Kurts, N. K. Genkina, A. Macias, I. P. Beletskaya, O. A. Reutov, *Tetrahedron*, 1971, 27, 4777-4785.
- [2] F. A. Carey, R. J. Sundberg, in *Advanced Organic Chemistry*, 2007, 253-388.
- [3] *Gaussian 09*, Revision A.01, Gaussian Inc., Wallingford, CT, 2009.

B-16-P

SIMULATIONS OF BORON MONOXIDE EMISSION BANDS

A. Antić-Jovanović¹, M. Kuzmanović¹, M. A. Khakoo², R. R. Laher³

¹*Faculty of Physical Chemistry, University of Belgrade, P.O. Box 47, 11158 Belgrad 118, Serbia*

²*Department of Physics, California State University Fullerton, Fullerton, CA 92834 USA*

³*Spitzer Science Center, California Institute of Technology, M/S 314-6, Pasadena, CA 91125 USA*

Abstract

Franck-Condon simulations of emission energy intensities for the $B-X$ and $B-A$ band systems of the boron monoxide (BO) molecule are given. The agreement between the experimental and simulated $B-X$ spectra supports the reliability of our simulated $B-A$ bands. Our results were computed under the assumption that the electronic transition moment function (ETMF) for each band system is constant.

Introduction

Electronic spectrum of BO chiefly consists of three band systems involving ground-state transitions: $A \ ^2\Pi_i - X \ ^2\Sigma^+$, $B \ ^2\Sigma^+ - X \ ^2\Sigma^+$ and $C \ ^2\Pi_r - X \ ^2\Sigma^+$. The $A-X$ and $B-X$ systems, lying in the regions of 350-650 nm and 220-330 nm respectively, were first identified by Mulliken, as early as 1925 [1]. The $C-X$ system, lying below 230 nm, was discovered by Chretien in 1950 [2]. All three systems were the subject of many studies, which yielded accurate spectroscopic constants for the electronic states of these transitions, i. e. for the X , A , B and C states [3, 4].

In addition to the red-degraded $A-X$ and $B-X$ bands, Mulliken recognized in all photographs of the $A-X$ system, between 455 and 600 nm, weak bands of a peculiar structure, which looked like a group of lines or band heads, some of which were shaded to violet. Mulliken identified these bands as belonging to an intercombination system involving transitions from the B to the A states. The lack of other experimental data thus far concerning these bands is surprising in view of the astrophysical interest in the BO spectrum and its significance in combustion processes, and the suggestion that the BO radical could be the basis of a chemical laser. The data dearth is probably related to the serious difficulties of their experimental observation, as the $B-A$ bands lie within the region of the much stronger $A-X$ bands, some of which overlap them.

In this report, we perform Franck-Condon (FC) simulation of the $B-X$ and $B-A$ systems, the latter of which will be useful to experimentalists in future studies.

Methodology

The emission band spectra were simulated via the so-called intensity at infinite temperature, $I_{v \rightarrow v'}^\infty$ [5], which is proportional to $p_{v \rightarrow v'} v_{v \rightarrow v'}^4$, where $p_{v \rightarrow v'} = R_e(r_{v \rightarrow v'})^2 q_{v \rightarrow v'}$ is the relative vibrational transition probability of the $v \rightarrow v'$ band, $v_{v \rightarrow v'}$ is the

band-origin wavenumber, and $q_{v'v''}$ is the FC factor. (The available intensity data were measured in terms of energy, hence the additional power of $v_0 v''$; cf. Eq. 9 of Ref. [6].) In cases where the ETMF is unknown, it is considered to be constant, as in the case of the B - A band system, which leads to the useful, but sometimes crude approximation of relative intensity $\cong q_{v'v''} V_{v'v''}^A$.

Our FC factors and band origins, were computed from Rydberg-Klein Rees (RKR) potential energy curves for the A , B , and X states, using the latest available molecular constants [3], as input data to Espy's computer program [6]. Only the more abundant $^{11}\text{B}^{16}\text{O}$ isotopic species was considered.

Results and discussion

FC factors and band-origin wavenumbers of the BO B - A band system were computed for the first time for transitions involving v' and v'' levels up to 20. The full data set is too large to be presented here; it will be reported elsewhere. The results show that the most prominent FC factors form a narrow Franck-Condon envelope with the highest values on the diagonal axis of the Deslandres scheme, predicting the most intense bands for the $\Delta v = 0$ sequence, and weaker, but significant bands for the $\Delta v = \pm 1$ and $\Delta v = \pm 2$ sequences.

$v'-v''$	$q_{v'v''}$	ν_0 (cm^{-1})		Relative intensity (const x $q_{v'v''} V_{v'v''}^A$)
		a	b	
2-0	1.3531E-01	21787.6	21783.7	0.3
3-1	3.5432E-02	21767.9	21763.3	0.8
4-2	6.2192E-02	21750.5		1.3
5-3	9.1437E-02	21736.1	21732.1	2.0
1-0	2.2752E-01	20548.1	20545.5*	3.9
2-1	3.6778E-01	20549.0	20545.5*	6.3
3-2	4.4940E-01	20551.1	20546.4*	7.6
0-0	7.5891E-01	19287.1	19284.4	10.0
1-1	4.0393E-01	19309.5	19306.0*	5.4
2-2	2.0433E-01	19332.2	19328.3	2.9
3-3	8.9884E-02	19335.9	19343.2*	1.2
4-4	3.1183E-02	19381.3	19377.7*	0.4
5-5	5.9149E-03	19409.1	19405.4	0.1
0-1	1.8723E-01	18048.5	18044.5*	1.9
1-2	2.4198E-01	18092.7	18090.0	2.5
2-3	2.3187E-01	18137.0	18134.0	2.4
3-4	1.9479E-01	18181.9	18177.2*	2.0
0-2	4.1786E-02	16831.7	18826.6	0.3
1-3	8.5076E-02	16897.5	16894.5	0.7
2-4	1.1508E-01	16963.0	16959.7	1.0

Table 1. FC factors ($q_{v'v''}$), band origins (ν_0), and simulated relative emission energy intensities (const x $q_{v'v''} V_{v'v''}^A$) for the BO B - A band system. Band origins: a) our calculations; b) derived from A_1 and B_1 band-head positions; *superposed or masked.

Table 1 contains our FC factors (second column) and band-origin positions (third column) only for the bands observed by Mulliken [1]. We note that the measured band positions are very close to those predicted from the spectroscopic constants. Differences of about $3\text{-}5\text{ cm}^{-1}$ are reasonable, bearing in mind that Mulliken's measurements were not of high accuracy, and some band overlape each

B-16-P

other or are masked by $A-X$ band structure. The FC-simulated intensities are normalized to 10.0 for the 0-0 band, and are listed in fifth column of Table 1.

The left panel of Figure 1 graphs our FC-simulated BO $B-A$ band intensities. The lack of corresponding band intensity measurements prevents a direct comparison of simulated and experimentally observed relative band intensities. For this reason, the quality of our FC simulation of the BO $B-A$ bands was tested by simulation of the well-known BO $B-X$ bands. The right panel of Figure 1 compares our intensity values for the $B-X$ bands, normalized to 10.0 for the 0-2 band, with the experimentally measured intensities reported in Ref. [5].

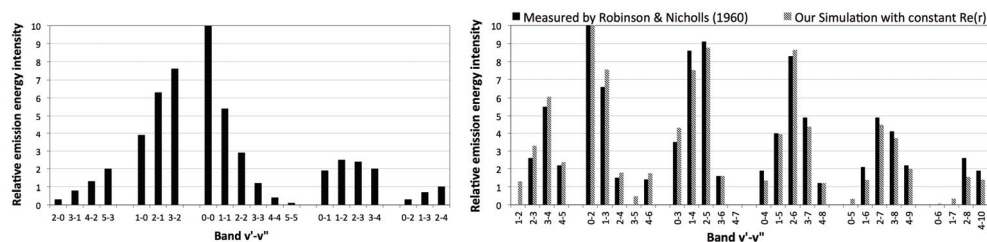


Figure 1. Simulated BO $B-A$ bands (left) and comparison of BO $B-X$ bands (right).

The differences between the simulated and measured relative intensities of the BO $B-X$ bands are reasonable, and not unexpected due to the measurement error. Our simulated $B-X$ band intensities herein do not include the ETMF derived in Ref. [5] for this band system; this will be studied in a subsequent paper. Nevertheless, the simulated intensity pattern matches well with the experimental intensity distribution, and thus offers good support for the viability of our calculated FC factors and simulated band intensities of the lesser-studied BO $B-A$ band system.

Conclusion

Using improved molecular constants and RKR potentials, FC factors are computed for the BO $B-A$ intercombination system, and then used to simulate their band intensities. The reliability of the applied method was tested by comparison of the observed and simulated BO $B-X$ spectrum. The observed FC-simulated $B-A$ spectrum of the BO molecule will be very useful in its future experimental studies.

Acknowledgments

This work was supported by the Ministry of Education and Science of the Republic of Serbia, Project No 172019.

References

- [1] R. S. Mulliken, Phys. Rev., 1925, 25, 259-294.
- [2] M. Chretien, Helv. Phys. Acta, 1950, 23, 269-286
- [3] F. Melen, L. Dubois, and H. Bredohl, J. Phys.B: At. Mol. Phys., 1985, 18, 2423-2432.
- [4] F. Melen, L. Dubois, and H. Bredohl, J. Mol. Spectrosc., 2001, 208, 14-17.
- [5] D. Robinson, and R. W. Nicholls, Proc. Phys. Soc, 1960, 75, 817-825.
- [6] F. R. Gilmore, R. R. Laher, and P. J. Espy, J. Phys. Chem. Ref. Data, 1992, 21, 1005- 1107.

SPECTROFOTOMETRIC AND FLUORESCENCE STUDY OF J-AGGREGATION OF THIACYANINE DYE IN THE PRESENCE OF AG NANOPARTICLES

B. B. Laban, V. Vodnik*, A. Vujačić*, S. P. Sovilj**, M. Dramićanin*,
A. B. Jokić, V. Vasić*

Department of chemistry, Science University of Pristina, Kosovska Mitrovica

**Vinča Institute of Nuclear Sciences, P.O. Box 522, Belgrade*

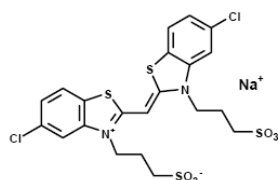
***Faculty of Chemistry, University of Belgrade, P.O. Box 118, 11158 Belgrade*

Abstract

The aim of the work was to investigate the formation of J-aggregates of thiacyanine dye (TC, 5,5'-disulfopropyl 3,3'-dichlorothiacyanine sodium salt) in the presence of 6 nm spherical silver nanoparticles (Ag NPs) using spectrophotometric and fluorescence methods. The formation of J-aggregates was concentration dependent and characterised by the appearance of the new absorption band with the maximum at 481 nm. The measurements of fluorescence of the nanoparticle – dye assembly clearly indicated that the fluorescence of TC was quenched by Ag NPs on the concentration dependent manner. This process was found to be quantitatively related to the surface coverage of the dye on the Ag NPs.

Introduction

During the last few years the attention has been paid to important class of organic cyanine dyes because of their strong absorption in visible region and fluorescence properties. Certain types of cyanine dyes shows a unique ability to form associates such as dimers, as well as H- and J-aggregates [1]. J-aggregation, was found to occur in aqueous solution in presence of metal ions, surfactants, nanoparticles, as well as in the presence of macromolecules [2]. It is believed that the dyes' ability to aggregate on the surface of metal nanoparticles rely primarily on electrostatic attractions between the ionic molecular building blocks of the aggregates and charged nanoparticles. Modification of the surface of noble metal particles leads to changes in their electronic properties. The possibility of controlled modification of electronic properties of colloidal metal particles provides greater opportunity for their application in nonlinear optics. In the present work we represent the results of the study of J-aggregate formation of 5, 5'-disulfopropyl 3, 3'-dichlorothiacyanine sodium salt on surface of Ag NPs.



Thiacyanine dye, (3, 3'-disulfopropyl-5,5'-dichloro-thiacyanine sodium salt)

Experimental

Chemicals: Silver nitrate (AgNO_3), sodium borohydride (NaBH_4 , 99%), potassium chloride (KCl), all from Aldrich, were used as received. Thiocyanine dye (TC), (3,3'-disulfopropyl-5,5'-dichloro-thiocyanine sodium salt) was purchased from Hayshibara Biochemical Laboratories, Okayama, Japan and 50 μM aqueous TC stock solution, containing 1mM KCl was prepared. Water purified with a Millipore Milli-Q water system was used in all cases. Ag colloids were prepared by the reduction of silver ions using sodium borohydride, according the standard procedure [3]. The concentration of stock dispersion of Ag NPs (3.78×10^{-8} M) was determined from the absorbance at 390 nm and molar absorptivity for the Ag NPs with the average size $\sim 6\text{nm}$.

Apparatus: Absorption spectra of colloidal solutions were measured by using Perkin Elmer Lambda 35 UV – Vis spectrophotometer with quartz cuvette with a path length of 1cm. Fluorescence measurements were carried out on a spectrofluorimeter Fluorolog-3-Model FL3-221 (HORIBA – Jobin – Yvon). The size distribution of Ag NPs was estimated using a JEOL 100CX transmission electron microscope (TEM)-at 100kV.

Results and Discussion

The TEM measurement of prepared Ag NPs confirmed that the shape of NPs is nearly spherical and the average particle diameter was 6 nm. A colloidal Ag NPs possesses an intense surface plasmon resonance band centered on 390 nm, characteristic for a yellow color of dispersion (Fig.1a). Such intensive absorption of Ag NPs arising from the collective oscillations of the free conduction band electrons are induced by the incident electromagnetic radiation. As a result, the position of this maximum depends on the size and shape of the particles as well as on the dielectric constant of the medium [3]. The absorption spectrum of TC dye (Fig.1a) contains two absorption bands with the maximum at 428 nm assigned to monomer (TC^{\cdot}) of TC dye, and the other one at 409 nm assigned to dimer (TC_2^{\cdot}). In aqueous solution, TC dye is present as equilibrated mixture of monomers and dimers. After the mixing of Ag colloid and TC dye, the J-aggregates were formed on the surface of nanoparticles, with appearing new absorption band characterised by the sharp maximum at 481nm.

The formation of J-aggregates in the presence of Ag NPs was further investigated as the function of dye concentration in the range from 0.16 to $1.66 \times 10^{-5}\text{M}$, keeping the concentration of Ag NPs $3.78 \times 10^{-8}\text{M}$. Fig. 1 (a), inset represents the absorbance at 481 nm vs. concentration curve. The plateau was reached above 5×10^{-6} M TC dye, indicating that above this TC concentration no further J-aggregates formation was observed. Similarly as demonstrated in our previous paper[3], J-aggregate formation on the surface of Ag NPs occurred via a two-step process. The first step includes adsorption of the initial dye layer, followed by slower growth of consecutive layers. Taking into account [2] that the cyanine dye can be approximated as a rectangular box with dimensions $2.5 \times 1.5 \times 0.5$ nm, the flat orientation can be considered as possible orientation of TC dye on the nanoparticle surface. The calculated number of TC molecules needed to cover the nanoparticle

surface corresponds to 1.13×10^{-6} M TC. Considering electrostatic arguments, namely repulsive interactions between the negatively charged surface of nanoparticles and the terminal sulfonate groups on the dye, it is unlikely that the TC molecules lie flat on the surface. This allows more than 1.13×10^{-6} M TC to pack on the surface in the first layer, and most likely the optimal exciton signal is reached with at least 3 layers of TC J-aggregates covering the surface. This is in agreement with the more than three times higher experimentally obtained value, indicating that more than one layer of TC was needed to reach the optimal exciton signal of TC J-aggregates covering the surface.

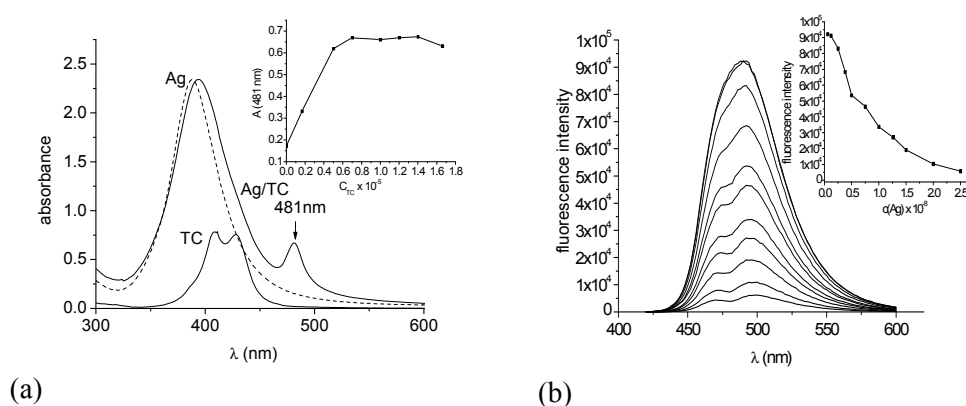


Figure 1. a) Absorption spectra of Ag dispersion (3.78×10^{-8} M), TC dye (5×10^{-6} M) and their mixture; inset: dependence of absorbance on TC concentration. b) Fluorescence spectra of Ag dispersion, TC dye and their mixture; inset: dependence of fluorescence on the Ag NPs concentration.

Fig. 1 (b) shows that TC dye exhibits a strong fluorescence with maximum at ~ 485 nm in aqueous solution and also the fluorescence spectral changes of 1×10^{-5} M TC before and upon the addition of Ag colloid. The intensity of fluorescence dye became weaker in the presence of Au NPs, indicating that TC dye-Au colloid assembly displayed fluorescence quenching properties. For 1×10^{-5} M TC the titration end point was reached in the presence of 2.5×10^{-8} M Ag NPs. Assuming that the quenching occurs only for those TC molecules that have direct interaction with the Ag NPs surface, the maximum of the quenched TC dye is then restricted to full monolayer coverage of TC on the nanoparticle surface, which depends on the orientation of the adsorbed TC. As described above, the concentration of Ag NPs needed to quench 1×10^{-5} M TC was calculated as 5.5×10^{-8} M. This value is about two folds higher than the experimentally obtained result. In general, the experimentally obtained results indicate that more TC molecules are quenched than needed to cover the nanoparticle surface completely in the flat orientation of TC. These results are in agreement with the spectrophotometrically obtained data.

Conclusion

In this paper we investigated the formation of J-aggregates of TC dye on the surface of nanoparticles and characterized them by absorption and fluorescence spectra. It was shown that formation of J-aggregates leads to appearance of the new absorption band at 481 nm and the quenching of TC fluorescence.

Acknowledgement

Authors would like to thank to the Ministry of Education and Science of the Republic of Serbia (Project No. 172023) for their financial support.

References

- [1] V. V. Vodnik, J.M. Nedeljković, J. Serb. Chem. Soc., 1998, 63, 995-1000.
- [2] I. I. S. Lim, F. Goroleski, D. Mott, N. Kariuki, W. Ip, J. Luo, C. J. Zhong, J. Phys. Chem., B 2006, 110, 6673-6682.
- [3] A. Vujačić, V. Vasić, M. Dramićanin, S. P. Sovilj, N. Bibić, J. Hranisavljević, G. P. Wiederrecht, J. Phys. Chem., C 2012, 116, 4655-4661.

MALDI TOF AND AFM STUDIES OF DNA/SWNT HYBRIDS

Đ. Trpkov*, Z. Rogić Miladinović, D. Aćimović, J. Cvetičanin, Z. Rakočević, O. Nešković,

Vinča Institute of nuclear sciences, 11000 Belgrade

**djordjet@vinca.rs*

Abstract

A primer is a strand of nucleic acid that serves as a starting point for DNA synthesis. DNA, as a large molecule, is very difficult for analysis by means of mass spectrometry. However, primer, as a short sequence of nucleic acid, is much more convenient for e.g. MALDI TOF MS analysis. Mass spectrometric experiment resulted in quality MALDI TOF spectra of 3 primers. Compound 3-HPA (3-hydroxypicolinic acid) showed the best results as matrix. AFM studies were also conducted, for both pure primer samples and hybrids of primer molecule with single wall carbon nanotubes (SWNT). Thus, obtained functionalisation of SWNT with DNA primers was confirmed by AFM imaging. AFM images clearly showed wrapping of DNA structures around nanotube „template“. Functionalisation of SWNT is very important for potential applications of nanotubes in biomedical field. MALDI TOF mass spectrometry, in combination with AFM imaging, proved its great potential in analysis of short DNA sequences, and indicated the possibility of investigating more complex DNA structures.

Introduction

One of the most commonly used strategies to render carbon nanotubes (CNT) soluble in aqueous media, and therefore, potentially useful to biomedical applications, is through their surface functionalization (f-CNT). Functionalization of carbon nanotubes can be achieved either by covalent or noncovalent methodologies [1]. Noncovalent association of DNA with CNTs is an effective way to disperse individual CNTs in aqueous solution and has already been used to investigate nanotube optoelectronic and spectroscopic properties and classification of nanotubes according to their length and chirality. Aim of this work is functionalisation of CNTs with DNA primers and AFM characterisation of obtained hybrids. These DNA/SWNT hybrids may have better solubility, compared to „raw“ CNTs and this property will facilitate applications of carbon nanotubes. Another aim is to develop a protocol for MALDI TOF and AFM studies of oligonucleotides and hopefully, longer DNA sequences.

Results and discussion

Samples of DNA primers and primer/SWNT hybride were studied by Atomic Force Microscopy (AFM) and matrix assisted laser desorption/ionisation mass

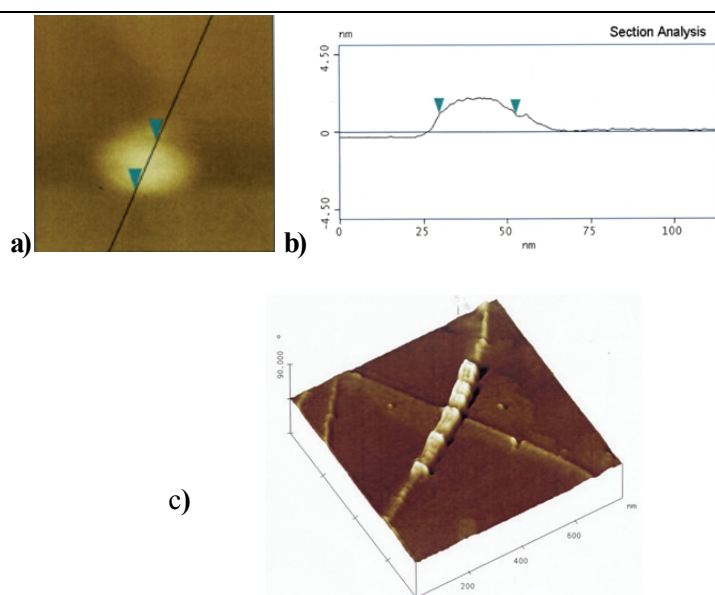


Figure 3. Image of part of GSTT1R primer (a), its dimensions (b) and decoration of SWNT with primer (c).

Figure 2. is AFM image of GSTT1R primer with „caps“, which can be attributed to small fragments within primer strand. Dimension of single fragment is shown in figures 3a and 3b, so observed length was 23.062 nm. Figure 3c shows image which indicate that primer (DNA oligomer) wrap in several layers around the nanotube, forming a strand-like spindle. DNA sequences form compact structures near the tube surface due to the formation of self-assembled structures consisting of a few DNA fragments.

Conclusion

In this work, we developed method for MALDI TOF MS analysis of short DNA sequences, known as DNA primers. AFM studies enabled us to observe dimensions of small fragments within primer samples. Single wall carbon nanotubes (SWNT) were functionalised by primers, and this was confirmed by AFM technique. AFM images confirmed assumption that layers of DNA will wrap around nanotube backbone and this is very important for future investigations of enhancing the solubility of carbon nanotubes.

Acknowledgment

This work was financially supported by the Ministry of Education and Science of the Republic of Serbia under Project No. III45005.

Reference

- [1] R. Singh, D. Pantarotto, D. McCarthy, O. Chaloin, J. Hoebeke, C. D. Partidos, J. P. Briand, M. Prato, A. Bianco, K. Kostarelos, *J. Am. Chem. Soc.*, 2005, 127 (12), 4388–4396.

B-19-P

APPLICATION OF COMPERATIVE VIBRATIONAL SPECTROSCOPIC AND MECHANISTIC STUDIES IN QUALITATIVE ANALYSIY OF MORIN STRUCTURE

J. M. Dimitrić Marković¹, Z. S. Marković², T. P. Brdarić³,
D. Milenković⁴, J. Đorović⁴, B. Lučić⁵, D. Amić⁶

¹ Faculty of Physical Chemistry University of Belgrade Studentski trg 12-16, 11000 Belgrade, Republic of Serbia,

² Department of Bio-chemical and Medical Sciences, State University of Novi Pazar, Vuka Karadžića bb, Novi Pazar 36300, Republic of Serbia

³ Kirilo Savić Institute, Vojvode Stepe 51, 11000 Belgrade, Republic of Serbia

⁴ Bioengineering Research and Development Center, 34000 Kragujevac, Republic of Serbia

⁵ NMR Center, Rudjer Bošković Institute, P.O. Box 180, HR-10002 Zagreb, Croatia,

⁶ Faculty of Agriculture, The Josip Juraj Strossmayer University, P.O. Box 719, HR-31107 Osijek, Croatia

Abstract

Detailed vibrational spectral analysis and the assignments of the bands, done on the best-fit basis comparison of the experimentally obtained and theoretically calculated Raman spectra, match quite well indicating DFT calculations as very accurate source of normal mode assignments.

Introduction

Morin is pentahydroxy flavone isolated as yellow pigment from almond hulls, old fustic (*Chlorophora tinctoria*) and members of the Moraceae family, such as mulberry, figs and other Chinese herbs. Although its biological effects are not fully understood there is some circumstantial evidence that morin has the ability to: suppress the proliferation of a wide variety of tumor cells, inhibit lipooxygenase-1, induces differentiation of keratinocytes, inhibit P-glycoprotein or reduce the incidence of lipopolysaccharide (LPS)-induced septic shock [1, 2]. All these effects rank morin as highly biologically potent and active flavonoid. The present study comprises *in vitro* experimental (Raman) and theoretical approaches in analysis of morin structure.

Results and discussion

Conformational analysis of morin

It is found that morin has a non planar geometry with the part of the molecule, containing cycles A and C, which has complete planarity. In order to examine potential energy surface, the torsion angle τ was scanned in steps of 15° without constraints on all other geometrical parameters. Removing constrain for the

torsional angle τ the conformational absolute minimum is found at $\tau = -38.52^\circ$, followed by a relative minimum at $\tau = -149.35^\circ$. The energy difference between these two minima is $2.3 \text{ kcal mol}^{-1}$. The maximum of the potential energy lies at $\tau = -92^\circ$ and the introversion barrier between the two minima is about $6.2 \text{ kcal mol}^{-1}$. There is also another maximum at 0° , with energy of $3.5 \text{ kcal mol}^{-1}$ which indicates the planar conformation of morin as easily obtainable.

The most stable structure of morin indicates strongly localized double bonds at the C2-C3 and C4-O positions of the ring C. The bond order values suggest a highly independent electronic delocalization in the rings B and A, which is also one of the main structural features implicated in antioxidant activity of flavon-3-ols. The C2-C1' bond lies in the chromone plane, because the torsional angle τ is 168.8° and its length is 1.464 \AA . The bond order of the C2-C1' bond obtained by the NBO analysis is close to 1 while its length is 1.464 \AA . Both these values indicate that there is very small conjugation across all the rings of the π system.

IR and Raman spectra analysis

The experimentally obtained, theoretically calculated and scaled band positions, wavenumbers, along with the corresponding assignments for the first 69 vibrational modes (of total 90) appearing in the $3700\text{-}500 \text{ cm}^{-1}$ region, are calculated. Relative descriptions of IR and Raman intensities, potential energy distribution (PED) values and the description of the largest vibrational contributions to the normal modes are also calculated. The comparative analysis of morin spectrum and the spectra of structurally related quercetin (2-(3,4-dihydroxyphenyl)-3,5,7-trihydroxy-4H-chromen-4-one) is performed in order to validate the assignment of the bands.

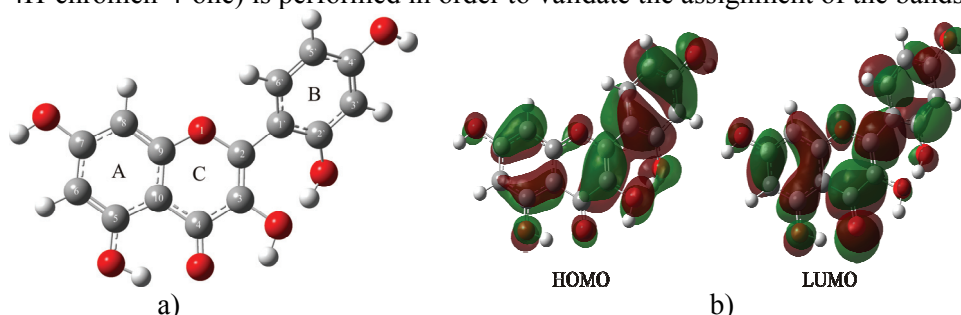


Figure 1. Structure and atomic numbering of morin (a) HOMO and LUMO orbitals of morin (b).

In the $3500\text{-}2500 \text{ cm}^{-1}$ Raman region there are no bands easily assignable to the various O-H and C-H stretching modes which are the most distinct and recognizable bands in the spectra of all polyphenols generally. The most intense bands in morin Raman spectrum are to be found in the $1800\text{-}1500 \text{ cm}^{-1}$ wavenumber region. As in the other flavone derivatives this region involves a combination of the C=O stretching (1626 and 1579 cm^{-1}) (modes ν_{79} and ν_{76}), C2=C3 stretching (1667 and 1626 cm^{-1}) (ν_{80} and ν_{79}) and C-C stretching (1667 , 1626 , 1579 , 1501 cm^{-1}) modes ($\nu_{80}\text{-}\nu_{74}$). As the result of increased conjugation of

B-19-P

the carbonyl group with the pyrone ring through the C2=C3 bond the frequencies of the most intense bands, assigned to both the C=O and C2=C3 stretching modes (ν_{79} and ν_{80}), are little bit decreased and positioned at lower values compared to flavanone (1695 cm^{-1}), flavone (1649 cm^{-1}), and 5-OH flavone (1657).

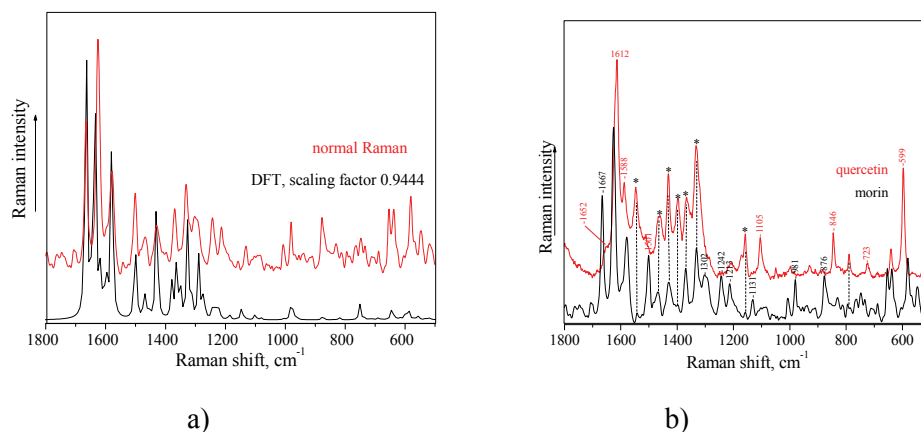


Figure 2. 1800-500 cm^{-1} Raman region of the experimentally obtained and theoretically calculated spectra of morin (a) Comparison of the 1800-500 cm^{-1} Raman region of morin and quercetin spectra.

In quercetin spectrum discriminant bands are positioned at: 1105 cm^{-1} (ν_{54}) ($\text{C}3'-\text{OH}$ bending), 846 cm^{-1} (ν_{47}) ($\text{H}2'-\text{C}3'-\text{C}4'$ bending), 723 cm^{-1} (ν_{42}) ($\text{C}3'-\text{C}4'-\text{O}4'$ $\text{C}3'-\text{C}4'-\text{C}5'$ bending) and 599 cm^{-1} (ν_{34}) ($\text{C}3'-\text{C}4'-\text{O}4'$ and $\text{C}2'-\text{C}3'-\text{O}3'$ bending). It is evident that all listed bands solely assign different bending modes of the ring B.

Conclusion

The obtained results demonstrate the applicability and performance of DFT calculations to give a conformational analysis of morin at the state of isolated molecule. The DFT calculations are proven as an accurate source of normal mode assignments since they quite acceptably reproduce the main characteristics of the experimental morin spectrum.

Acknowledgements

The authors acknowledge financial support by the Ministry of Science of Republic of Serbia (Grant No. 172015 and Serbia–Croatia Bilateral agreement 2011–2012).

References

- [1] J. Brown, J. O'Prey, P. R. Harrison, *Carcinogenesis* 2003, 24, 171–7.
- [2] P. Thuillier, A.R. Brash, J.P. Kehrer, J. B. Stimmel, L. M. Leesnitzer, P. Yang, R. A. Newman, S. M. Fischer, *Biochem J.* 2002, 366, 901–910.

A JOINT APPLICATION OF SPECTROSCOPIC AND THEORETICAL APPROACHES IN EVALUATION OF ANTIOXIDANT ACTIVITY OF KAEMPFEROL AND ITS IRON COMPLEX

J. M. Dimitrić Marković¹, Z. S. Marković², T. P. Brdarić³, D. Milenković⁴, S. Jeremić², V. Stepanić⁵, B. Lučić⁶, Dragan Amić⁷

¹ Faculty of Physical Chemistry University of Belgrade Studentski trg 12-16, 11000 Belgrade, Republic of Serbia,

² Department of Bio-chemical and Medical Sciences, State University of Novi Pazar, Vuka Karadžića bb, Novi Pazar 36300, Republic of Serbia

³ Kirilo Savić Institute, Vojvode Stepe 51, 11000 Belgrade, Republic of Serbia

⁴ Bioengineering Research and Development Center, 34000 Kragujevac, Republic of Serbia

⁵ Laboratory for Epigenomics, Division of Molecular Medicine, Rudjer Bošković Institute, P.O. Box 180, HR-10002 Zagreb, Croatia

⁶ NMR Center, Rudjer Bošković Institute, P.O. Box 180, HR-10002, Zagreb, Croatia,

⁷ Faculty of Agriculture, The Josip Juraj Strossmayer University, P.O. Box 719, HR-31107 Osijek, Croatia

Abstract

Combined spectroscopic and theoretical approaches were used to evaluate relevant interaction of kaempferol and its iron(III) complexes with DPPH and hydroxyl radicals. The results on iron complexation specify the stoichiometry and the relevant structural form entering the chelation. The spectroscopic DPPH assay specifies the antioxidant activity and its iron complex both in terms of EC₅₀ values and stoichiometry. The results of 2-deoxyribose degradation suggest that antioxidant activity of kaempferol may be originating from its combined effect of iron chelation and radical scavenging.

Introduction

Flavonoids are the group of low molecular weight phenolics found in higher vascular plants [1]. Among very diverse activities the most interest has been focused to their antioxidant activity which operates at different levels in the oxidative process [2]. Kaempferol is a strong antioxidant and helps to prevent oxidative damage of our cells, lipids and DNA. Kaempferol seems to prevent arteriosclerosis by inhibiting the oxidation of low density lipoprotein and the formation of platelets in the blood. Current evidences indicate that kaempferol not only protect LDL from oxidation but also prevent atherogenesis through suppressing macrophage uptake of oxLDL. The present study comprises in vitro experimental and theoretical approaches proposing a possible explanation for

different antioxidant efficiencies of kaempferol and its iron complex towards a stable nitrogen-centred DPPH and oxygen-centred hydroxyl radicals.

Results and discussion

Complex formation

Kaempferol enters complexation only at pH 8. By considering kaempferol polyhydroxylated nature (Fig. 1a) and the arguments obtained from experimental and theoretical results it is possible to implicate the 3-hydroxyl-carbonyl and 5-hydroxyl-carbonyl groups in the formation of the iron-kaempferol complex at pH 8.

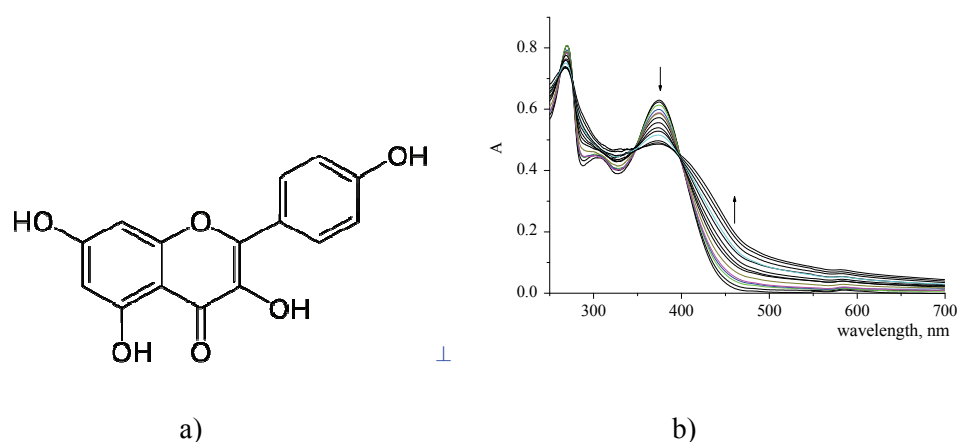


Figure 1. Structure of kaempferol (a) Titration curves of kaempferol with Fe(III) at pH 8.

Conformational analysis

The structure of most stable conformation of kaempferol is defined using B3LYP local density functional method in combination with 6-311G (d, p) basis as implemented in the Gaussian 09 package. It is found that molecule of kaempferol has planar structure, with two hydrogen bonds: O(3)-H(3)---O(4) (1.995 Å) and O(5)-H(5)---O(4) (1.760 Å). Planar structure of molecule provided possibility for good reactivity as bioactive compound, such as anticancer, anti-inflammatory and the antioxidant activities of molecule.

DPPH test

The percentage of the remaining DPPH molecules, calculated at the steady state approximation, against the kaempferol/DPPH mole ratio, is presented in Fig 2a. Exponential decay indicates increased kaempferol activity for the bigger mole ratios. Iron-kaempferol complex shows the same trend.

2-deoxyribose degradation test, inhibition of the Fenton reaction

Almost complete inhibition of 2-deoxyribose degradation is observed at a concentration of 0.15 mM of kaempferol (Fig. 2b, trace). Anti-Fenton activity of kaempferol originates predominantly from its iron chelation ability. When only

kaempferol is present in the system (Fig. 2b, trace \square), it acts as an iron chelator inhibiting hydroxyl radical production well. In the presence of EDTA (Fig. 2b, trace \diamond) kaempferol inhibits the reaction less effectively than when only EDTA is present. This trend of activity most probably originates from the less capability of kaempferol to compete with stronger chelators like EDTA.

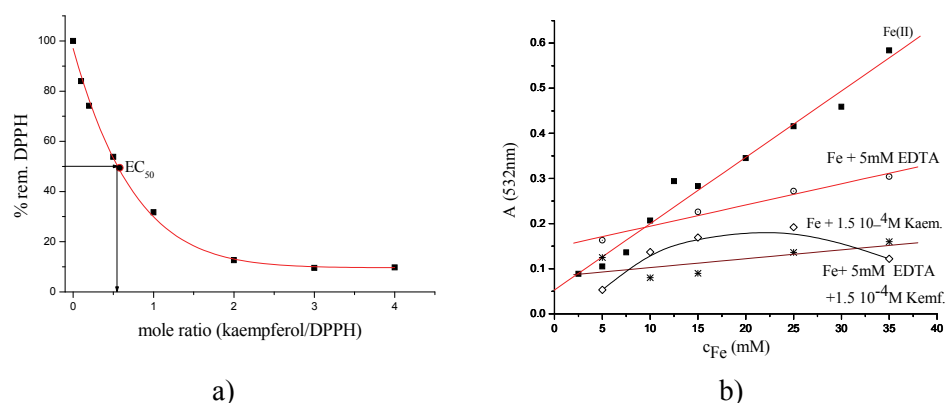


Figure 2. Percentage of the remained DPPH as a function of different kaempferol/DPPH mole ratios (a) Absorbance of malonaldehyde–TBA complex at 532nm: at various Fe(II) concentrations in the presence or absence of EDTA and kaempferol (concentrations are indicated on the spectra) (b).

Conclusion

In terms of EC₅₀ values, reaction stoichiometry and the number of deactivated DPPH molecules per mole of the antioxidant, kaempferol is less potent antioxidant than quercetin. The results of 2-deoxyribose degradation suggest that anti-Fenton activity of kaempferol may originate predominantly from its effect of iron chelation rather than radical scavenging itself.

Acknowledgements

The authors acknowledge financial support by the Ministry of Science of Republic of Serbia (Grant No. 172015 and Serbia–Croatia Bilateral agreement 2011–2012).

References

- [1] J. B. Harborne, in *Plant flavonoids in biology and medicine 11: Biochemical, cellular and medicinal properties*, ed. A. R. Liss, New York, USA, 1988, 17-40.
- [2] V. Cody, E. Middleton and J. B. Harborne, in *Plant flavonoids in biology and medicine–Biochemical, pharmacological and structure–activity relationships*, in Alan R. Liss (Ed.), New York, 1986, 429–440.

B-21-P

THE EMISSION ENHANCEMENT IN SINGLE PULSE LASER INDUCED BREAKDOWN SPECTROSCOPY

M. Vinić^{1,2}, M. Ivković¹

¹*Institute of Physics, University of Belgrade, P.O.Box 68, 11080 Belgrade, Serbia*

²*Faculty of Physical Chemistry, University of Belgrade, 11001 Belgrade, Serbia*

Abstract

The results of an experimental study of the optical emission enhancement possibilities during single pulse laser induced breakdown spectroscopy of aluminum alloy are presented. Investigations were performed in air, argon and helium at different pressures with and without additional fast electric discharge.

Introduction

Application of lasers for analytical purposes started only three years after their invention. The laser radiation having energies around 100 mJ and duration of several nanoseconds was focused to a submillimeter spot on a solid, liquid, or gaseous sample the breakdown occurred. Namely, the free electrons created through multiphoton ionization and inverse bremsstrahlung processes absorb energy from the laser pulse, colliding with and freeing yet more electrons in an ionization cascade until thermally hot, charge-neutral laser-induced plasma is produced. Spectral recordings of this plasma showing lines of all elements present in sample, opened possibility for a new analytical technique – laser induced breakdown spectroscopy – LIBS. Main advantages of LIBS are 1) simplicity, 2) lack of sample preparation for the analysis of gases, liquids, and solids, 3) simultaneous multi-element detection, 4) ability to detect high and low z elements, 5) only optical access to the target is required and 6) standoff analysis capabilities [1, 2]. On the contrary, detection limits of laboratory analytical techniques like ICP-MS are favorable. This disadvantage was mainly overcome by enhancing optical emission by use of additional laser pulse in different double pulse technique configurations. In this work for same goal alternative but cheaper technique like use of different surrounding atmospheres and additional fast discharge (initiated with a same laser pulse) were studied.

Experiment

A typical single pulse stand-off LIBS equipment consists of Nd-YAG laser with focusing optics, light collection system (mostly fiber optics), detection system (like echelle spectrometer equipped with ICCD camera) and computer and electronics system for synchronization, detector gating and spectrum storage. In this experiment, see Figure 1a, we have used Nd-YAG laser with energy of 50 mJ, pulse duration of 20 ns focused by the use of 5 cm diameter lens L_1 having focal length of 10 cm. Aluminum alloy target was positioned 2 mm in front of the focal point, so the 0.2 mm spot i.e. fluence of $\approx 1.5 \text{ J/mm}^2$ was obtained. In order to perform study in controllable

atmosphere, the target was settled inside a specially designed glass tube. The discharge part of the tube (having internal diameter 10 mm and tungsten electrodes 12 cm apart) was positioned perpendicular to the laser beam. In order to increase optical signal reproducibility the target was rotated with a speed of the 2 °/s. A 1:1 plasma image was projected on the 10 μm wide entrance slit of the 0.3 m imaging spectrometer Andor Shamrock 303, equipped with ICCD camera. The camera gating was performed by processing the Q switch signal from laser with digital delay generator -DDG. The spectra were recorded at different delays between laser and current pulse measured with Rogowski coil and digital storage oscilloscope -DSO. The fast pulse discharge is driven by a different capacitors – C, charged with high voltage power supply - HV PS up to 3 kV and fired by the laser pulse.

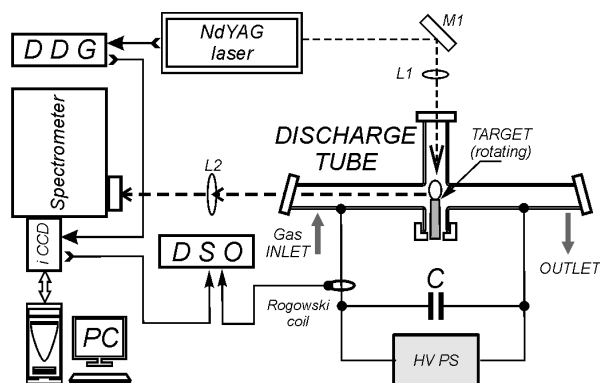


Figure 1. a) Experimental setup.

Results

The experiments were conducted in air, He and Ar atmosphere, without the use of additional fast discharge.

The effect of surrounding atmosphere on optical signal intensity

The observed optical signals were higher for Ar and lower for He gas, compared to the signal obtained in an air atmosphere, Figure 2a. The enhancement was attributed to lower ionization potential of Ar leading to higher electron density [3]. The signal enhancement changes with the gas pressure, see Figure 2b. The optimum argon pressure in our case is 150 mbar.

The effect of additional fast discharge on signal intensity

The investigations of optical signal enhancement, earlier performed only in air at atmospheric pressure [4] were broadened to studies in air, Ar and He at different pressures. First influence of the applied voltage on the selfbreakdown at different pressures (Pashen curve) and on time delay between laser and current pulse was determined. The optimum capacitance and gas type and pressure was determined from following conditions: a) prevention of glow discharge development after laser

B-21-P

initiation and b) lowering energy losses, due to the multiple ionizations of elements present in plasma.

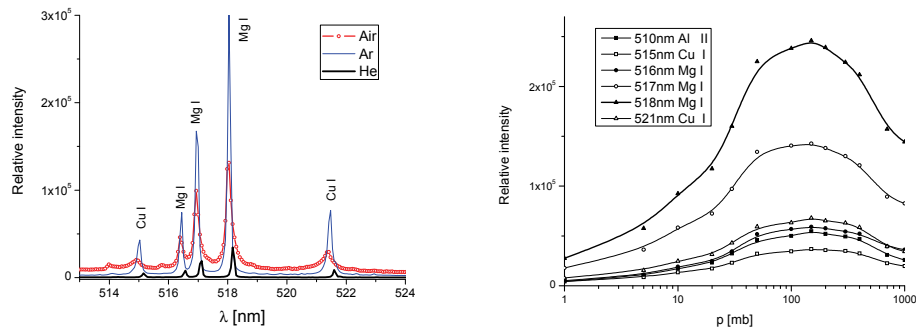


Figure 2 a) Part of the spectrum emitted from Al alloy target at pressure of 50 mb of: air, Ar and He; b) Relative line intensities for different argon pressures.

Enhancement of signals, shown in Figure 3 for He at 30 mb and $C = 0.33 \mu\text{F}$, may be attributed to increase of plasma volume as well as its prolonged duration.

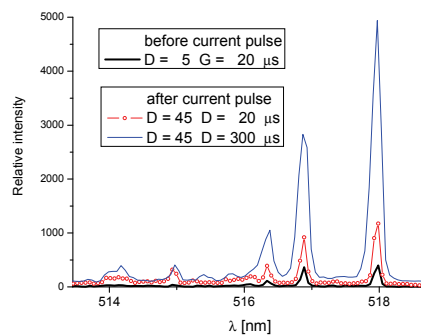


Figure 3. Comparison of optical signals at different delays – D and gate widths – G.

Acknowledgements

This work has been partially financed by the Ministry of Education and Science of the Republic of Serbia under Project 171014.

References

- [1] Handbook of Laser-Induced Breakdown Spectroscopy – D.A.Cremers & L.J. Radziemski, 2006, John Wiley & Sons Ltd.
- [2] D.A.Cremers & R.C.Chinni, Applied Spectroscopy Reviews, 2009, 44, 457-506.
- [3] J.A. Aguilera & C. Aragon, Appl. Phys. A, 1999, 69, S475–S478.
- [4] W. Zhou et al., Optics Letters, 2011, 36, 296-2963.

KINETICS CATALYSIS

PHYSICO-CHEMICAL AND CATALYTIC CHARACTERIZATION OF M-MODIFIED ZIRCONIUM OXIDE IN *N*-HYDROCARBON CONVERSION

A. Zarubica¹, M. Randjelovic¹, M. Momcilovic¹, P. Putanov²

¹*Faculty of Science and Mathematics, University of Nis, 18000 Nis, Serbia*

²*Serbian Academy of Sciences and Arts, 11000 Beograd, Serbia*

Abstract

The modification of sulfated zirconia by incorporation of metals (platinum and rhenium) significantly affects catalytic performances in *n*-hydrocarbon conversion reaction. Favorable activity/selectivity data comparing to unpromoted sulfated zirconia depend on the crystal phase composition, critical crystallites sizes, platinum dispersion, moderate total acidity and type of acidity, as well.

Introduction

The recent world-wide environmental requirements on so called “clean fuels” maintaining their high research octane number (RON) have pressed on petroleum industry to produce reformulated fuels with suitable constituents. Namely, most of traditionally used RON boosters present environmental hazards. Therefore, their usage is banned/restricted in the last few decades of the XX century (*i.e.* unleaded gasoline is introduced in USA in early 1970s, MTBE is firstly banned in California, the maximal allowed content of benzene is 1 vol.%, and of derived aromatic compounds up to 25 vol.%) [1].

The selective isomerization of light naphtha (middle chain *n*-hydrocarbons, C₅-C₇) as cost effective and relatively simple petroleum process presents a superior alternative in providing satisfying/increasing RON of the gasoline pool. Specifically, branched paraffins possess higher RON than their linear counterparts (that is, *n*-C₆ and *n*-C₇ are characterized with RON 25 and 0, respectively, while the (hydro)isomerization process would increase the RON to 74 and 45, correspondingly) [2]. Firstly, traditional (hydro)isomerization processes were carried out by using liquid catalysts (HF and/or H₂SO₄); however, these catalysts have shown serious plants corrosion problems and health risks (very low concentrations are lethal doses). Further conventional technologies have introduced new generations of heterogeneous catalysts in the process conveying it alternatively over Pt/chlorinated alumina or Pt/zeolite based catalysts [1,3]. The both catalytic systems failed to satisfy environmental or process/economic parameters. Explicitly, the former being catalytically active, unfortunately, faces environmental problems due to use of unfriendly promoter and expense drawbacks being sensitive to catalytic poisons, while the latter although proved resistance to feed impurities exhibits lower activity requiring higher reaction temperatures [3].

Relevantly, a design of environmentally friendly and effective catalytic material with both appropriate structure and bi-functional properties (metal and acidic) has been recognized as a challenging task for the near future. Sulfated zirconium oxide (SZ) has attracted a considerable attention due to its acidity and activity in isomerization of middle chain alkanes at relatively mild process conditions [4]. On the other side, a short operating cycle and fast deactivation make it impractical one. Possible solution is offered in transition metals (Pt, Fe, Mn and/or Ni) use as modifiers/promoters of zirconia resulting in catalysts with higher activity than unmodified SZ counterparts for *n*-C₄ isomerization [5-7]. Despite the fact that SZ promoted by both iron and manganese exhibited higher activity in conversion of *n*-butane, still, there is no consensus on the impact of incorporated metals and nature of SZ activity promotion [6]. Platinum loaded SZ significantly inhibited a coke formation as well as fast deactivation by secondary reactions thus improving catalyst stability [7]. Chlorinated alumina promoted by both platinum and rhenium is widely used in petroleum industry for the catalytic reforming of naphtha, and alkylation processes [8]. Although the role of platinum in Pt-Re/Al₂O₃ is very well established, the impact of rhenium still remains a subject of investigations [9]. To the best of our knowledge, *n*-C₆ conversion/isomerization has not been studied earlier over SZ-based catalyst modified by rhenium, and by two metals containing Pt-Re and Re-Pt as catalysts modifiers. Additionally, the exact role of Re, and its combination with Pt is still unlighted. Moreover, the effect of the order of the particular metal grafting in bimetallic catalysts has not been considered. Several techniques (HRTEM, EPR and FTIR) were applied in order to characterize particular metal role, their potential interactions, and to investigate the final influence on the catalytic behavior and catalyst life-time in process conditions.

Experimental part

Preparation of Catalysts

Zirconium based catalysts were prepared by the modified sol-gel method [10,11] using the 2-propanol 70% solution of zirconium(IV) iso-propoxide (Aldrich Co.). The catalysts synthesis procedure and mixing of two solutions (alkoxide based, and dissolved alcohol as solvent) were performed by keeping pH of medium at 9.0 proved to result in the beneficial physico-chemical properties of the nano-structured material [12]. The sulfating was done by incipient wetness impregnation of the zirconium hydroxide with 0.5 M sulfuric acid for the nominal sulfates content of 4 wt.% following calcinations at 600°C in synthetic air for 3h. Aqueous solutions of hexachloroplatinic acid and ammonium perrhenate were used as metal-promoter precursors. The content of Pt in the mono- and bimetallic catalysts was 0.5 wt.%, and Re loading in each sample also was 0.5 wt.%. Additional catalyst calcinations at 450°C in synthetic air flow of 25 ml/min for 3h followed the incorporation of every particular metal. Besides, the order of particular metal incorporation in bimetallic catalysts samples was varied in order to investigate the potential effect on the final catalytic performances.

Characterization

The textural properties (surface areas, the pore size distribution, the mean pore diameter) of the catalysts were measured by the BET method using a Micromeritics ASAP 2010 device. The pore size distributions (PSD) were calculated by the Barret-Joyner-Halenda (BJH) method [13]. Desorption branches of nitrogen (pre)adsorbed were used for comparisons. The mean pore diameter was determined as the BJH desorption average pore diameter [10,13]. The pore size distribution curves were additionally plotted by using the computer program [14], and implementing the Kelvin equation [15].

X-ray diffraction analysis, performed at X-ray diffractometer APD-1700, was used for the determination of the crystal structure of the zirconium oxide-based catalysts. Crystallites sizes and volume fractions of particular crystal phases were calculated by using Scherer's equation.

Hydrogen and oxygen chemisorption/titration over mono- and bimetallic catalysts was studied in the corresponding volumetric apparatus. The amount of the chemisorbed hydrogen/oxygen was determined at room temperature, based on the adsorption/desorption isotherms. The subtraction of the isotherms has shown the number of hydrogen/oxygen molecules chemisorbed on the metal particles. In such a way, also, data on metal dispersions were obtained.

Surface properties of the catalysts samples were investigated by FTIR analysis of the catalyst surface pre-adsorbed with pyridine. The adsorption of pyridine on pre-evacuated catalysts following additional final evacuation in order to remove physisorbed pyridine preceded the FTIR measurements.

TEM characterization was carried out using a TEM/EDX microscope CM20, Philips, Lab 6 operated at 200 KeV. Electron micrographs were recorded at magnification of 600.000x. Catalysts samples were supported on holey carbon-coated copper grids by simply grinding the specimen between two glass plates and bringing the powder into contact with the grid.

EPR spectra in X-band ($\nu \approx 9.5$ GHz) were recorded with the cw-spectrometer ELEXSYS 500-10/12 (Bruker) using a microwave power of 6.3 mW, a modulation frequency of 100 kHz and a modulation amplitude of 0.5 mT. The magnetic field was measured with respect to the standard 2, 2-diphenyl-1-picrylhydrazyl hydrate (DPPH). Samples were measured at 77 K in as-received form as well as after 1h treatment in a flow of 5 ml/min H₂ at 230°C without subsequent contact to the lab atmosphere.

Catalytic Tests

Primary catalytic features (activity, selectivity, stability) in the catalytic run – in the reaction of n-hexane isomerization were evaluated using a fixed bed quartz micro-reactor under atmospheric pressure and partial n-hexane pressure of 60.5 mbar. The operating conditions were: reaction temperature 250°C at atmospheric pressure

C-01-SL

using hydrogen as reaction/carrier gas premixed with $n\text{-C}_6$, and space velocity of $6 \cdot 10^{-2}$ mmol $n\text{-C}_6/\text{g}_{\text{CAT}} \cdot \text{min}$. The fresh catalyst loading (0.5 g) was activated by reducing procedure in hydrogen flow of 20 ml/min at 300-350°C during 2.5h preceding the reaction. The reaction runs were studied for as long as activity was recorded.

The analysis of the reaction products was done by gas chromatograph (GC) using the HP Series 5890 II equipped with a flame ionization detector (FID). Injected volume of each sample was 0.5 ml. Products of the isomerization were separated on PONA GC-capillary column (30 m), where 10 ml/min flow of nitrogen was used as carrier gas. Products mixture consisted of hydrocarbons beginning with methane to benzene. Activities of different catalysts samples were ranked by means of n -hexane conversion normalized by the number of C-atoms in the concrete product. Selectivity was calculated as a sum of monobranched and dibranched C_6 – isomers. Yield is determined by multiplication of conversion and selectivity data.

Results and Discussion

The textural features (BET surface area, BJH cumulative desorption pore volume, average pore diameter and pore size distribution) of all catalysts (monometallic and bimetallic SZ - based samples) are presented in Table 1. These properties are in line with the synthesis history/method of the catalysts, type of the metal modification, metal doping content, and an order of metal incorporation in bimetallic catalysts samples.

Table 1. BET specific surface areas, average pore diameters, BJH pore volumes for sulfated zirconia (as a reference) and M-modified SZ.

Catalyst	BET surface area, m^2/g	Average pore diameter, nm	BJH pore volume, cm^3/g
SZ	73	7.2	0.15
Pt-SZ	116	4.6	0.14
Re-SZ	65	8.3	0.15
Pt-Re-SZ	101	5.4	0.14
Re-Pt-SZ	82	7.5	0.17

The general textural feature of all catalysts is bimodal pore distribution with a dominant fraction of meso-pores (Fig. 1) that is expectable taking in mind the origin of the SZ-based catalyst or support in the case of M-modified catalysts. The origin of the zirconia-based catalysts from an alkoxide precursor using the sol-gel procedure determined textural features of the final catalysts over memory effects [12,16,17]. It is noticeable that grafting of bare SZ with Pt, and both Pt and Re, highly affects the BET surface areas by

increasing them (Table 1). The incorporation of platinum attributes to texture stabilization over BET surface area increase and decrease of average pore diameter. Nitrogen isotherms and pore size distributions for unmodified SZ and M-modified SZ catalysts are shown in Fig. 1. The N_2 isotherms for all catalysts exhibited typical *s*-shape behavior of type-IV with a type-H1 desorption hysteresis (not shown all). Pores are characterized with predominant cracks-shape. The pore size distribution, preferably in the meso-pores range, is changed slightly and shifted towards bigger meso-pore average diameter with involving of platinum in bare SZ. Bimodal pore size distribution and relevant meso-pores fraction are known as responsible for the significant positive effect on the primary features of SZ-based catalytic performances – activity, stability and catalyst-life [11]. Platinum has shown a role of textural promoter by improving fundamental textural features of M-modified SZ-catalyst.

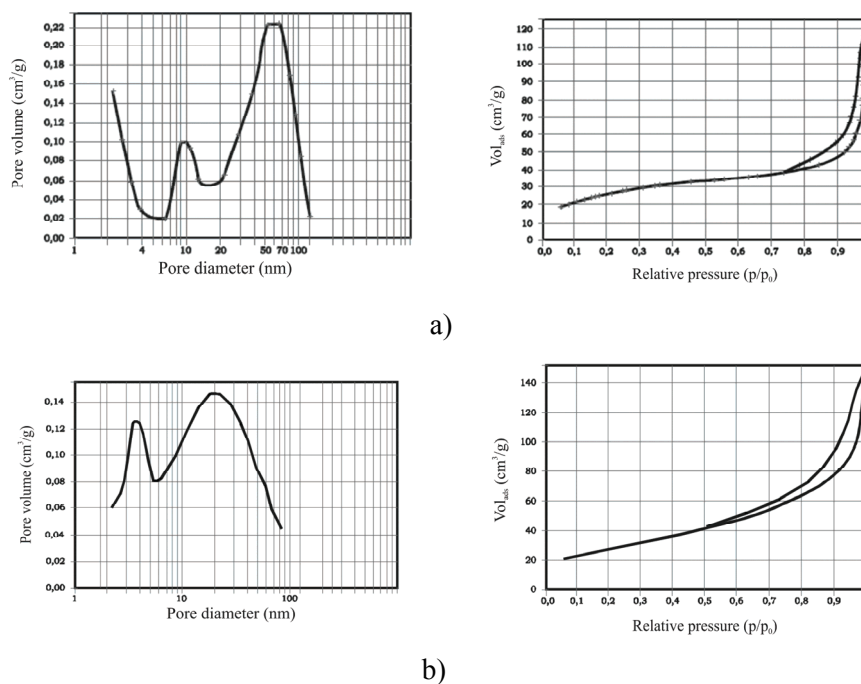


Figure 1. N_2 adsorption-desorption isotherms and pore size distributions for catalysts: a) SZ; b) Re-Pt-SZ.

Dominant meso-pore size (Table 1, Fig. 1) was not crucial for the catalytic activity, but rather for a specific kind of slower catalyst deactivation mechanism reported earlier. Namely, coverage of individual active sites with coke was found previously when pores of larger size were involved, which resulted in longer catalyst life [11]. In the case of two metals incorporation (Pt and Re), here, it is imposed that an order of particular metal loading significantly affects final textural properties of the catalysts. In case when firstly Re was incorporated in SZ followed with a step of

C-01-SL

calcination, and then Pt as a second promoter, which preceded the final thermal treatment, textural properties of such catalyst (Re-Pt-SZ) are reduced by diminishing the specific surface area, and width pore broadening (Table 1). The authors force that Re in such a case is encapsulated in pores, filling the most pore volume, and simultaneously blocking closer contact and interaction of Pt with SZ support. A quite opposite situation is when firstly platinum is incorporated, and afterwards rhenium as a second-order modifier in SZ support. It seems that both metals (Pt and Re) form “egg-white” model structure with platinum being covered/protected in deeper layer as it was recently reported for other and/or similar catalytic systems [18,19]. In this model, the authors suppose that rhenium exhibits so called “skin effect” partially covering active metal, platinum, and at the same time stopping unfavorable metal migration over SZ support [20]. In the same time, rhenium protects platinum from potential catalytic poisons from a feed that may be observed during the catalytic run.

Bimetallic platinum-rhenium modified SZ-based catalyst (Pt-Re-SZ) represented improved textural properties characterized by favorable features comparing to the unmodified SZ catalyst (Table 1). This catalyst exhibits almost equal pore volume and similar specific surface area as monometallic one, and increasing as a rule in the following way: $SZ < Pt-Re-SZ \sim Pt-SZ$. Comparable discussion on textural properties for bimetallic reforming catalysts (platinum and platinum-rhenium alumina based catalysts) after the introduction of the second metal was given elsewhere [21].

Comparing the results on XRD analysis of M-modified SZ support and bare SZ catalyst, which is taken as referent material, obviously indicate that platinum affected the stabilization of the crystal structure of primary SZ catalyst (Table 2, Fig. 2.). Namely, the incorporation of platinum has caused a great increase of the fraction of catalytically active tetragonal crystal phase as well as a decrease of its crystallite size comparing to unmodified SZ catalyst [22-24]. Therefore, the authors claim an inhibiting impact of platinum on the undesirable SZ sintering process occurring.

Table 2. Crystal phase composition, zirconia crystallite size.

Catalyst	Typical crystal phase composition	Volume fraction of T/M crystal phases, %	Crystallite size T/M (nm)
SZ	T/M	86.7 / 13.3	11.7 / 12.1
Pt-SZ	T/M	93.9 / 6.1	8.2 / 16.4
Re-SZ	T/M	60.8 / 39.2	9.2 / 11.7
Pt-Re-SZ	T/M	94.8 / 5.2	8.2 / 10.9
Re-Pt-SZ	T/M	78.2 / 21.8	12.7 / 23.4

In Pt-SZ catalyst an oxide form, PtO is registered ($2\theta = 34.65^\circ$) (Fig. 2.), therefore, the authors impose Pt in the oxidation state +2 as active state during the reaction course. In addition, it is possible the presence of Pt-Zr interaction ($2\theta = 41.00^\circ$), which is probably responsible for the optimal active metal-support interaction, moreover, affecting higher dispersion of metal promoter together with improved resistance to sintering process. It seems that Pt plays a crucial role as both textural and structural promoter of SZ by stabilizing the catalytic active tetragonal crystal phase, keeping its size below the established critical value of 10 nm [25], and consequently delaying the process of sintering.

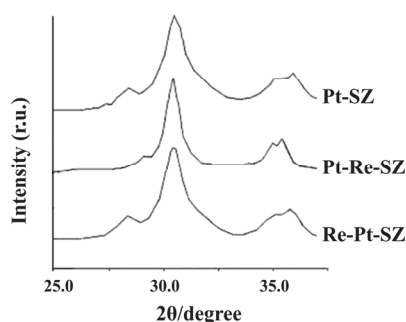


Figure 2. XRD patterns for mono-metallic and bi-metallic SZ-based catalysts.

In bimetallic catalysts, the metal impact on the crystallite size is not essential one, but rather the one concerning the fraction of tetragonal active crystal phase. In case of Pt-Re-SZ catalyst generated in previously mentioned “egg-white/egg-yolk” model, highly enhanced amount of ZrO₂ (111) tetragonal crystal phase is registered. This effect regarding crystal phase composition and crystallite size (below critical value) is completely comparable in Pt-Re-SZ as in monometallic catalyst, Pt-SZ (Table 2). An explanation lies in previously cited “skin effect”, and protecting role of rhenium by which undesirable migration/transport of platinum crystallites is delaying. That is why detrimental agglomeration, and resulted sintering of catalytically active tetragonal crystal phase is postponed [20].

Moreover, the introduction of rhenium next to platinum has increased the dispersion of platinum from 7% up to 21% that is proved by H₂/O₂ titration. The impact of rhenium on platinum dispersion may be additional reason that Pt-Re-SZ catalyst possesses the highest amount of tetragonal crystal phase and smallest crystallite size among all catalysts samples (M-modified and unmodified SZ) (Table 2). Roughly similar situation was established earlier [21] where the platinum dispersion was increased by introducing Re in reforming catalyst supported on γ -alumina.

2D-3D micrographs of the selected locations on Pt-SZ catalyst and crystallographic zirconium oxide orientations are registered by using the HRTEM (Fig. 3.). The dominant crystallographic orientation of zirconia is $\langle 010 \rangle$ characterized with a presence of so called “short atomic steps” [26]. These are probably named taking

C-01-SL

in mind the concurrent existence of two or three particular orientations at an atomic level. Such orientations include following ones: $\{101\}$ – an orientation as a crystal lattice continuation in a regular direction; $\{100\}$ – roughly shaped/smooth plane, and finally $\{001\}$ – a plane the most tailored by deformations that may include the most Schottky vacancies [26] and/or so called “stairs structure” at the edges.

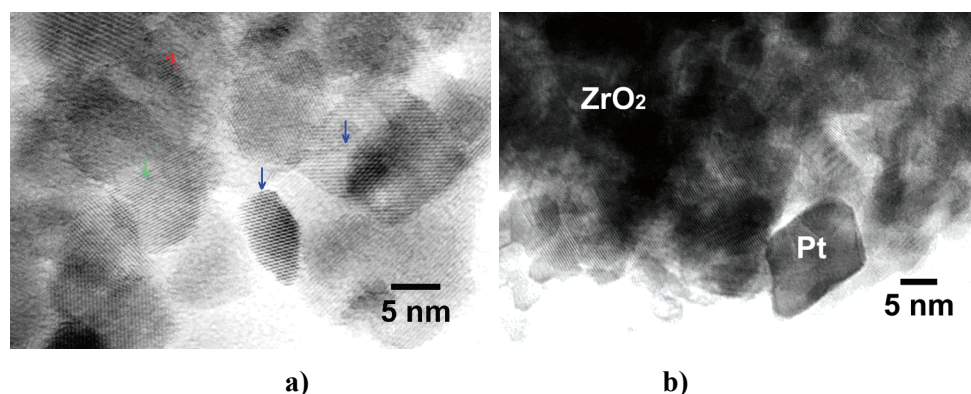


Figure 3. a) HRTEM micrographs of Pt-SZ; b) HRTEM micrographs of Pt-Re-SZ.

Crystallites of high Miller indices are characterized by two the last mentioned crystal planes potentially presenting very active adsorption sites [27]. The presence of these sites in Pt-SZ catalyst is also proved by XRD analysis followed with a dominant content of tetragonal crystal phase additionally stabilized with sulfates, and acidic features determination that showed an enhanced presence of Brønsted acid sites (BAS), and Lewis acid sites (LAS), as well.

In catalyst Pt-SZ, Schottky vacancies are presented at the crystallographic plane $\langle 010 \rangle$ where sulfates are incorporated between Zr atoms, also, periodically repeated acting roles of potentially active catalytic sites. On the other side, it can be furthermore supposed that a genesis of highly active acidic sites and their reproduction during crystal growing is relatively slow, *i.e.* there are only few crystallites of ZrO_2 that exhibit high Miller index.

HRTEM micrograph of Pt-Re-SZ catalyst (Fig. 3) shows that modification of pure SZ by Pt and Re maintains ZrO_2 primary grain in size as in the Pt-SZ catalyst, and also pre-dominant orientation of crystallographic planes. Pt grains in size remain almost unchanged comparing to the monometallic catalyst Pt-SZ. The authors impose that all these features would result in synergistic effect on the final catalytic performances in the test reaction.

Surface properties of the catalysts, proved by FTIR analysis (not shown), demonstrated the dominant presence of BAS (at 1540 cm^{-1}), and two types of LAS (at 1490 and 1610 cm^{-1}) in monometallic Pt-SZ catalyst being the most active one. These facts may speak in favor of its high acidity as a promising feature related to relevant activity in isomerization of *n*-hexane [24,28]. The group of authors have earlier claimed that Lewis acid sites played a key role in exhibited high activity and

selectivity of metallic promoted sulfated zirconia-based catalysts in *n*-hexane isomerization [29].

The EPR spectrum of the as-synthesized Pt-SZ catalyst does virtually not differ from that of the pure SZ support (not shown). However, as soon as rhenium is present, an additional multi-line spectrum occurs in the middle field range, which is weak for sample Re-SZ and most intense for sample Pt-Re-SZ (not shown). This might arise from paramagnetic Re species. EPR-active valence states of rhenium are Re^{6+} ($S = 1/2$) and Re^{4+} ($S = 3/2$). Moreover, Re has two isotopes with a nuclear spin of 5/2 and a natural abundance of 37% (^{185}Re) and 63% (^{187}Re). By coupling of the nuclear with the electron spin, the EPR signal should split into six hyperfine lines. This is obviously observed for the Re-containing as-synthesized catalysts (not shown) and visualized in more details in EPR spectrum. There are only very few literature data on spin Hamiltonian parameters of paramagnetic Re species, which differ tremendously depending on the matrix in which they are embedded [30,31] (Table 3).

Table 3. g and A tensor values of Re^{6+} and Re^{4+} .

	Matrix	G	A / G
Re^{6+}	KCl	$\parallel 1.85, \perp 1.79$	$\parallel 143, \perp 166$
Re^{6+}	CaWO_4	$\parallel 1.85, \perp 1.716$	$\parallel 42, \perp 324$
Re^{4+}	MoO_3	1.617, 1.606, 1.667	330, 687, 370
Re^{4+}	SnO_2	1.626, 1.593, 1.81	682, 461, 399
Re^{4+}	$(\text{NH}_4)\text{PtCl}_6$	1.817, 1.815	399, 395
Re^{4+}	K_2PtCl_6	2.05	109
Re^{4+}	Al_2O_3	2.25	780

In general, hyperfine coupling constants are much smaller for Re^{6+} than for Re^{4+} . The hfs constants hint to a Re^{6+} rather than to a Re^{4+} species, although the g values are larger than in Table 3, but this can be due to the different matrix. Thus, we assign the signals to three Re^{6+} species which differ slightly in their local geometry. Interestingly, in the Pt-free Re-SZ catalyst, only the hfs signal with $g = 2.015$ and $A = 96.0$ G appears. This might be related to Re^{6+} in the vicinity of Zr^{4+} in $\text{Zr}(\text{OH})_4$. Consequently, the two additional signals in the Pt-Re-SZ catalyst should arise from Re^{6+} the coordination of which is slightly modified, probably in the vicinity of Pt. This suggests that already in the as-synthesized state, Re and Pt are in close contact.

All discussed properties have an impact on catalyst activities in *n*-hexane isomerization reaction. Pt-promoted SZ catalyst performs an initial activity at as low as 175°C and reaches a significant yield at 200°C. In the case of bimetallic catalysts (Pt-Re-SZ and Re-Pt-SZ), better catalytic performances were achieved after reduction at higher temperature of 350°C. Catalyst Re-Pt-SZ with totally opposite order of two metals loading exhibits somewhat lower activity/selectivity probably due to poorer physico-chemical properties being determined with the

C-01-SL

order of particular metal incorporation, and calcinations steps. It is important to stress that the increased reduction temperature applied over Pt-Re-SZ catalyst contributes to catalytic characteristics almost a half of those achieved for Pt-SZ catalyst under the same operating conditions.

Table 4. Catalytic performances of monometallic and bimetallic SZ-based catalysts.

Catalyst	Reaction temperature	Conversion, X (%)	Selectivity to <i>i</i> -C ₆ (%)	Yield, Y (%)
SZ	200/300	9.8 / 14.0	33.9 / 40.9	/
Pt-SZ	175/200/250	7.2/69.6/74.1	95.1/55.0/34.8	6.8/38.3/25.8
Re-SZ	200/250	4.4/6.6	92.0/96.0	4.1/6.4
Pt-Re-SZ	200/250	4.5/34.3	95.0/94.4	4.3/32.3
Re-Pt-SZ	200/250	3.1/29.4	94.9/95.5	3.0/28.0

It is widely known that Pt-Re-oxide support catalyst is bifunctional one wherein noble metal acts as a center for chemisorption and activation of reactants transformation, and the oxide support additionally helps spill-over mechanism, and especially platinum may improve this mechanism in hydrogenation/dehydrogenation of alkenes/alkanes in the *n*-alkane isomerisation reaction course [32,33]. In our case, bimetallic catalyst (Pt-Re-SZ) showed lower activity than monometallic (Pt-SZ), promoted with platinum, probably due to several reasons: *a*) rhenium is partially present in the oxidized form ReO_x, *b*) rhenium oxide may take a part in the redox route of the reaction mechanism diminishing the isomers yield, *c*) the increase of platinum dispersion has positive effect on the catalytic performance, but, unfortunately, it is not sufficient condition for the process run.

Conclusions

The modification of bare sulfated zirconia with platinum significantly increases its primary catalytic performances. Bimetallic promotion of pure sulfated zirconia by both platinum and rhenium enables an achievement of almost a half of the results obtained over platinum promoted zirconia under the same process conditions. Mono- and bimetallic promoted sulfated zirconia undergo to bifunctional reaction route, while unmodified zirconia takes part in the oxidative dehydrogenation reaction exhibiting only the initial activity.

Acknowledgment

The authors wish to thank to the Ministry of Education and Science – Republic of Serbia (Project ON 172061), and Serbian Academy of Sciences and Arts for financial supports.

References

- [1] H. Weyda, E. Köhler, *Catal. Today*, 2003, 81, 51-55.
- [2] C. Jiménez, F. J. Romero, R. Roldán, J. Marinas, R. Gómez, *Appl. Catal. A: General*, 2003, 249, 175-185.
- [3] A. Corma, *Chem. Rev.*, 1995, 95, 559-614.
- [4] G. D. Yadav, J.J. Nair, *Micropor. Mesopor. Mater.*, 1991, 1, 1-99.
- [5] G. X. Yu, X. L. Zhou, C. Tang, C. L. Li, O. Navaro, *Catal. Commun.*, 2008, 9, 1770-1774.
- [6] E. A. Garcia, E. H. Rueda, A. J. Rouco, *Appl. Catal. A: General*, 2001, 210, 363-370.
- [7] T. Kimura, *Catal. Today*, 2003, 81, 57-63.
- [8] Yu. V. Gurvey, I. I. Ivanova, V. V. Lunin, W. Grünert, M. W. E. van den Berg, *Appl. Catal. A: General*, 2007, 329, 16-21.
- [9] C. L. Pieck, M. B. Gonzales, J. M. Parera, *Appl. Catal. A: Gen.*, 2001, 205, 305-312.
- [10] C. Breitkopf, A. Garsuch, H. Papp, *Appl. Catal. A: Gen.* 2005, 296, 148-156.
- [11] A. R. Zarubica, M. N. Miljkovic, E. E. Kiss, G. C. Boskovic, *React. Kinet. Catal. Lett.*, 2007, 90, 145-150.
- [12] G. Boskovic, A. Zarubica, P. Putanov, *J. Optoelect. Adv. Mater.*, 2007, 9, 2251-2257.
- [13] E. P. Barrett, L. G. Joyner, P. P. Halenda, *J. Am. Chem. Soc.*, 1951, 73, 373-380.
- [14] M. I. Zaki, Y. L. Sidrak, R. B. Fahim, *Proc. Int. Symp. Chem. Control*, Vienna, 1981, 155.
- [15] J. Kelvin, *Phil. Mag.*, 1871, 42, 488-493.
- [16] G. Boskovic, A. Zarubica, M. Kovacevic, P. Putanov, *J. Therm. Anal. Cal.*, 91, 2008, 849-854.
- [17] A. Zarubica, P. Putanov, G. Boskovic, *J. Serb. Chem. Soc.*, 72, 2007, 679-686.
- [18] A. Zarubica, Ph.D thesis, University of Novi Sad, 2008 (in Serbian).
- [19] A. Zarubica, P. Putanov, D. Kostic, G. Boskovic, *J. Optoelect. Adv. Mater.*, 12, 7, 2010, 1573-1576.
- [20] G. Bošković, G. Vljanić, E. Kiš, P. Putanov, L. Gucci, K. Lazar, *Ind. & Eng. Chem. Res.*, 33, 1994, 2090-2095.
- [21] I. Coletto, R. Roldan, C. Jimenez-Sanchidrian, J. P. Gomez, F. J. Romero-Salguero, *Fuel*, 86, 2007, 1000-1007.
- [22] K. Föttinger, G. Kinger, H. Vinek, *Appl. Catal. A: General*, 266, 2004, 195-202.
- [23] E. A. Blekkan, K. A. Johnsen, T. Loftén, *React. Kinet. Catal. Lett.*, 86, 2005, 149.
- [24] A. Zarubica, G. Boskovic, P. Putanov, D. Kostic, M. Pohl, *J. Optoelect. Adv. Mater.*, 12, 2010, 1183-1188.
- [25] R. C. Garvie, M. F. Goss, *J. Mater. Sci.*, 21, 1986, 1253-1257.

C-01-SL

- [26] M. Benaissa, J.G. Santiesteban, G. Diaz, C. D. Chang, M. Jose-Yacaman, J. Catal., 161, 1996, 694-703.
- [27] G. A. Somorjai, "Chemistry in Two Dimensions: Surfaces", Cornell Univ. Press, Cornell, NY, 1981, 157 .
- [28] E. A. Blekkan, K. A. Johnsen, T. Loften, React. Kinet. Catal. Lett., 86, 2005, 149-155.
- [29] G. Volkova, S. Reshetnikov, L. Shkuratova, A. Budneva, E. Paukshtis, Chem. Eng. J., 134, 2007, 106-110.
- [30] J. R. Pilbrow, Transition Ion Electron Paramagnetic Resonance, Clarendon Press, Oxford, 1990, 302.
- [31] H. C. Yao, M. Shelef, J. Catal., 44, 1976, 392-403.
- [32] K. G. Azzam, I. V. Babich, K. Sechan, L. Lefferts, Appl. Catal. B: Environ., 80, 2008, 129-140.
- [33] G. Olympiou, C. Kalamaras, C. Zeinnalipour-Yazdi, A. Efstathiou, Catal. Today, 127, 2007, 304-318.

THE ROLE OF ACTIVE COMPONENT LOCALIZATION IN SUPPORTED CATALYST

Nickolay M. Ostrovskii

HIPOL a.d., Odžaci, Serbia

Fax: +381-25-464-702, E-mail: nikolaj.ostrovski@hipol.rs

Abstract

The role of active component (AC) distribution among the pores of different size (micro-distribution) in supported catalyst is considered. Its influence on a catalyst pellet activity and stability is analyzed. It is demonstrated that micro-distribution of AC does not affect the pellet effectiveness factor in the case of gas-phase reaction. Such localization of AC becomes affecting in the case when micropores are filled with liquid, or constituted of zeolite channels.

Introduction

Active component distribution along the pellet radius (macro-distribution) has been studied from the early 60-th, and was summarized in excellent reviews [1, 2]. On the contrary, a role of micro-distribution practically was not studied. An experimental method for measurement of micro-distribution was worked out only in 1986 [3]. It consists in controlling the blockage of pores of different size by water (due to capillary condensation) and following chemisorption measurement of active component in empty pores. A possible domain of influence of AC micro-distribution on pellet effectivity has been estimated in [4].

The problem of AC micro-distribution is related, first of all, with the porous structure of the catalyst. Therefore, it makes a sense only for nonuniform structure, like a simplest bidisperse particle (Fig. 1).

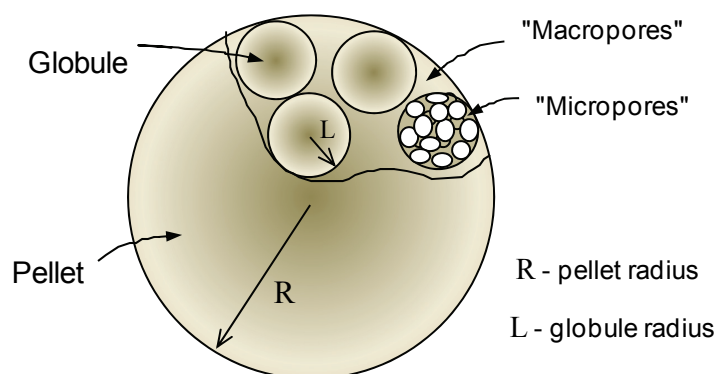


Figure 1. Bidisperse globular structure of a catalyst particle.

Bidisperse structure has advantages under internal diffusion limitation, because the effectiveness factor of a single globule is close to unity ($\eta_L \rightarrow 1$) due to its small size ($L/R \ll 1$). Actually, for commercial catalysts $R = 1-5$ mm, and the radius of globule L is comparable with the radii of large pores formed by globules. So its size consist approximately 100-500 nm and therefore $L/R \approx 10^{-4}$.

In precipitated catalyst the reaction rate is proportional to the specific surface. Then the bidisperse structure allows increasing the specific surface (due to small pores inside globules) without decreasing in total rate of diffusion, determined by large pores. It leads to increasing the observed reaction rate referred to unit pellet volume.

In supported catalysts the influence of bidisperse structure is more intricate. It depends on micropores accessibility for impregnation with the active component; on its surface concentration in micro- and macropores, *etc.* The latter is important for bifunctional catalysts, where supports are not inert, moreover, when phenomena such as “spillover effect” and AC deactivation can occur. Thus the problem of active component micro-distribution becomes rather complicated, and is not reduced to diffusion aspects only.

Process in bidisperse pellet

Let us consider the catalytic process in a bidisperse pellet presented in Fig.1. For the more detailed analysis one can write the following simplest equations describing concentration profiles in micro- (C_L) and macropores (C_R) [4]:

$$\frac{d^2 C_L}{d\xi^2} + \frac{s}{\xi} \frac{dC_L}{d\xi} = \frac{\alpha}{\varepsilon} \psi_L^2 f(C_L) \quad (1)$$

$$\frac{d^2 C_R}{d\rho^2} + \frac{s}{\rho} \frac{dC_R}{d\rho} = \frac{1-\alpha}{1-\varepsilon} \psi_R^2 f(C_R) + \frac{\varepsilon(s+1)}{1-\varepsilon} \frac{\psi_R^2}{\psi_L^2} \frac{dC_L}{d\xi} \Big|_{\xi=1} \quad (2)$$

Boundary conditions:

$$\begin{aligned} \xi = 0: \quad dC_L/d\xi = 0, \quad \xi = 1: \quad C_L = C_R(\rho), \\ \rho = 0: \quad dC_R/d\rho = 0, \quad \rho = 1: \quad C_R = C_R^0. \end{aligned}$$

For the only first-order reaction the equation system has an analytical solution. Then effectiveness factor for a plate shape pellet ($s=0$) can be derived as:

$$\eta = (1-\varepsilon) \frac{\Phi th\Phi}{\psi_R^2}, \quad \Phi = \psi_R \left[\frac{1-\alpha(1-\eta_L)}{1-\varepsilon} \right]^{1/2}, \quad \eta_L = \frac{th(\psi_L \sqrt{\alpha/\varepsilon})}{\psi_L \sqrt{\alpha/\varepsilon}} \quad (3)$$

In the region of deep intraparticle diffusion ($\psi_R > 0.5$):

$$\eta \approx (1-\varepsilon) \Phi / \psi_R^2 \quad (4)$$

The equation (4) enables to examine the influence of AC micro-distribution on a pellet effectiveness factor (η).

Estimates for gas-phase reaction

Let us estimate the role of micro-distribution as “a matter of principle”. For this purpose, it is useful to compare the limiting cases [4]:

- the active component is located only in large pores ($\alpha = 0$, $\eta = \eta_0$);
- the active component is located only in small pores ($\alpha = 1$, $\eta = \eta_1$):

$$\eta_0 = \frac{\sqrt{1-\varepsilon}}{\psi_R}, \quad \eta_1 = \frac{\sqrt{1-\varepsilon}}{\psi_R} \sqrt{\eta_L}. \quad \text{Therefore } \eta_1 / \eta_0 = \sqrt{\eta_L} \quad (5)$$

It is seen from the relation (η_1 / η_0) that the influence of micro-distribution depends completely on effectiveness factor for globules (η_L), which is in fact an accessibility of small pores. As was noted above, for real catalysts $\eta_L \rightarrow 1$. This follows from a low globule radius in comparison with pellet radius $L/R \approx 10^{-4}$.

Thus, the ratio of Thiele modulus for globule and for pellet is also low:

$$\psi_L / \psi_R = (L/R) \sqrt{D_R / D_L};$$

as $L/R \approx 10^{-4}$, and $D_R/D_L \leq 10^2$, therefore $\psi_L/\psi_R \leq 10^{-3}$.

This estimate allows concluding that in gas-phase reactions the AC micro-distribution does not affect the observed reaction rate as well as selectivity.

These peculiarities determine the dependence of η on the catalyst porous structure, because of diffusivities D_L and D_R are proportional to pores size within the Knudsen range. Practically, the effectiveness factor η is insensitive to D_L but changes sharply with variation of D_R (Fig. 2).

Therefore, in supported bidisperse catalyst the diffusion limitation of the reaction can be regulated only by variation of “macropores” size (globule radius), but not “micropores” size (globule internal structure).

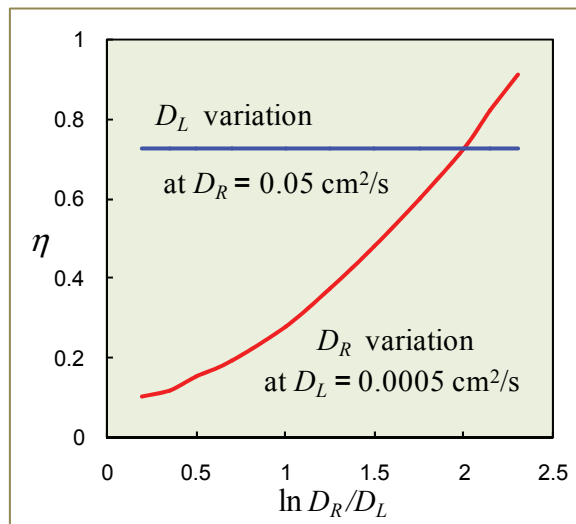


Figure 2. The influence of pores size on pellet effectivity [4]. $L/R = 10^{-4}$, $\varepsilon = 0.2$, $\alpha = 0.5$. The ratio of macro- and micropores radius $r_{\text{mac}}/r_{\text{mic}}$ is proportional to D_R/D_L .

When AC localization takes effect

Let us try now to estimate the range of parameters in which the influence of micro-distribution is possible. In such a case, the accessibility of AC inside globule should be lower than on its surface.

It means, in accordance with formulas (5), that the ratio (η_1/η_0) should be at least ≤ 0.8 , or $\eta_L \leq 0.7$. The corresponding dependences are presented in Fig. 3.

Assuming that $\varepsilon_{min} = 0.1$ and $\alpha_{max} = 0.9$, one can obtain that $\sqrt{\alpha/\varepsilon} = 3$ and consequently $\psi_L > 0.4$. Then at $k = 1 \div 10 \text{ s}^{-1}$ and $L = 10^{-5} \div 10^{-4} \text{ cm}$ the diffusivity in “micropores” must be $D_L < 10^{-8} \text{ cm}^2/\text{s}$. Similar values ($10^{-12} \div 10^{-8} \text{ cm}^2/\text{s}$) are observed only at configuration or surface diffusion, for example in zeolites [5, 6].

An appreciable diffusion resistance in small pores is expected also in the case of capillary condensation of some reagents, when small pores can be filled with liquid while large pores - with gas [7]. Then the equation system (1, 2) has to be completed with equations of phase equilibrium, mass transfer, and reaction kinetics in the liquid phase. However, this problem has been considered separately in papers on catalytic reactions accompanied by capillary condensation [7–9].

It has been shown that diffusion in capillary condensed liquid (in typical range of $D_L = 10^{-7} \div 10^{-4} \text{ cm}^2/\text{s}$) does not limit the overall rate of the process. Meanwhile, the rate of catalytic reaction in the liquid (in small pores) can entirely serve as a rate limiting step [9]. In this case, the increasing of AC fraction in small pores, increase the catalyst activity without decreasing in effectiveness factor.

Such a feature is observed in hydrodesulfurization process (HDS), where the reaction rate in “wetted” small pores (filled with heavy fraction of hydrocarbons) is much lower than in large pores (filled with gas), because of low hydrogen solubility in liquids [9]. In this case of liquid formation only in small pores (capillary condensation), the rate and mechanism of active component deactivation in large and small pores become also different [10].

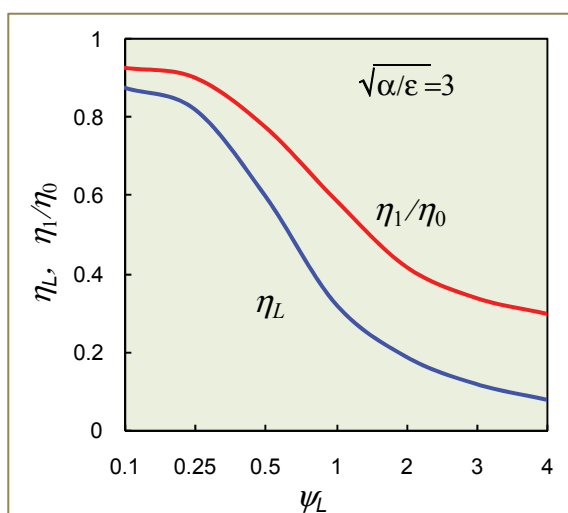


Figure 3. The influence of diffusion in globule on its effectivity [4].

Influence on catalyst deactivation

A marked difference in deactivation rates in small and large pores [10] leads to an idea to regulate the catalyst deactivation by means of AC micro-distribution. From estimates presented above, it is clear that the mechanism of such an influence can not be diffusional, at least for gas-phase reactions.

Therefore, only the difference in deactivation rates in large and small pores may cause the influence of AC localization on catalyst stability. The examples are:

- blockage of small pore mouth by coke unlike surface coking in large pores;
- difference in coke formation in zeolite channels and on external surface;
- “pollution” of small pores by metals in demetallization process.

Since diffusional limitation is absent in “micropores” ($\eta_L \rightarrow 1$), no concentration gradient in these pores can be assumed, $C_L(\rho, \xi) = C_R(\rho)$. Therefore, the simplest model for qualitative analysis of the influence of micro-distribution parameter on catalyst deactivation can be written as [4, 11]:

$$\frac{d^2 C_R}{d\rho^2} + \frac{s}{\rho} \frac{dC_R}{d\rho} = \psi_R^2 [\alpha \theta_L + (1 - \alpha) \theta_R] C_R = \psi_R^2 F(\theta) C_R \quad (6)$$

$$\frac{d\theta_L}{dt} = -k_{PL} C_R \theta_L, \quad \frac{d\theta_R}{dt} = -k_{PR} C_R \theta_R \quad (7)$$

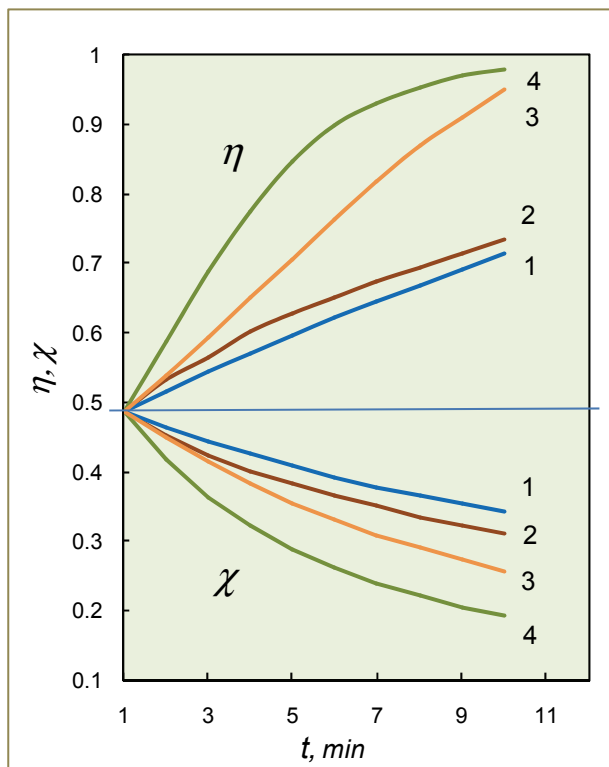


Figure 4. The influence of micro-distribution on catalyst deactivation. η and χ are defined in text.

$$\beta = k_{PL}/k_{PR}$$

$$1 - \alpha = 0.3, \beta = 5;$$

$$2 - \alpha = 0.3, \beta = 10;$$

$$3 - \alpha = 0.7, \beta = 5;$$

$$4 - \alpha = 0.7, \beta = 10.$$

Then effectiveness factor (η) and pellet effectivity (χ) are expressed as:

$$\eta = \frac{3}{C_R^0} \int_0^1 C_R(\rho) F(\theta, \rho) \rho^2 d\rho, \quad \chi = \eta F(\theta, 1) \quad (8)$$

It was supposed in calculations, that the catalyst active component in small pores is deactivated (poisoned) more rapidly than in large pores ($\beta = k_{PL}/k_{PR} > 1$). The fraction of small pores was fixed at 20 % ($\varepsilon = 0.2$). The results of model analysis are presented in Fig. 4.

It is seen that with catalyst deactivation, the effectiveness factor (η) is increased (Fig. 4), because it represents the accessibility of active centers that remain active. In opposite, the total pellet effectivity (χ) is decreased, because of decreasing in number of active centers.

The influence of micro-distribution parameter (α) is marked only at $\alpha > 0.4$, when more than 40 % of AC is located in small pores (Fig. 4). This influence becomes stronger with increasing of $\beta = k_{PL}/k_{PR}$, which is the ratio of deactivation rate constants in small and large pores.

These estimates show that a high catalyst stability can be provided not only at full lack of active component in “micropores” ($\alpha = 0$), but also when its fraction does not exceed 30-40 %, else deactivation rate constants k_{PL} and k_{PR} differ less than five times.

This regularity has been proved in experiments on catalyst deactivation, using supported catalyst Pt/Al₂O₃ with different fraction of Pt in small pores (Fig. 5).

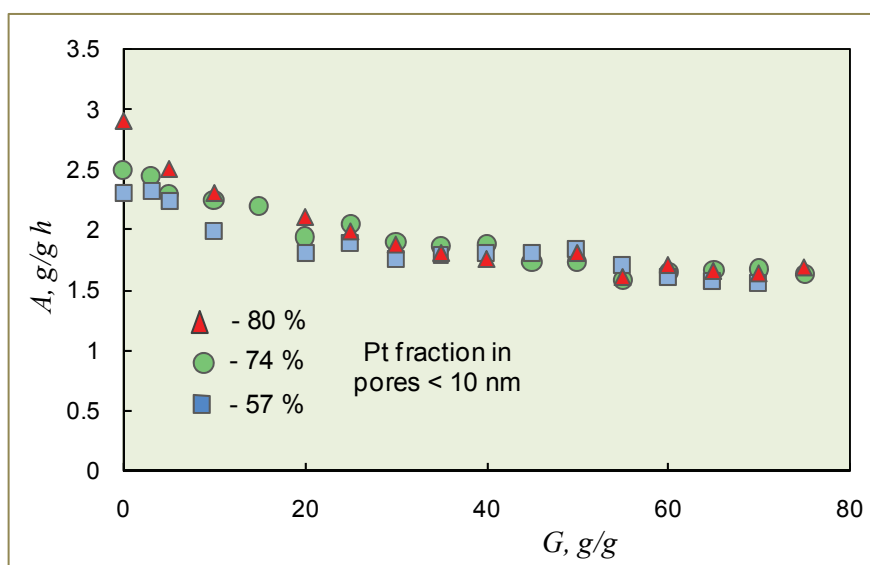


Figure 5. Rate formation of toluene (A) in heptane reforming over Pt/Al₂O₃ vs. the total heptane is fed per gram of catalyst (G) [11].

Localization of active component in zeolites

In zeolite catalyst, the role of AC localization is of fundamental importance. For example, Pt clusters can be located inside the zeolite cavities and on the edges of the zeolite crystals [12]. The catalytic properties of these two types of active centers are usually different.

Simplest estimations can be made for the first order reaction with different rate constants in small k_L , and large pores k_R . Equations (1, 2) one can reduce to a single equation at ($s = 0$, $\alpha = 0.5$):

$$\frac{d^2 C_R}{d\rho^2} = \frac{\psi_R^2}{1-\varepsilon} \left(1 + \frac{\varepsilon}{\psi_L} \frac{k_L}{k_R} \right) C_R \quad (9)$$

The effect of diffusion in zeolite crystals depends strongly on the activity of AC located inside zeolite cavities. When this activity is lower than in large pores ($k_L/k_R < 1$), the influence of diffusivity (D_L) is mild (Fig. 6).

In an opposite case ($k_L/k_R > 1$), the increasing of diffusivity (D_L) leads to the lower effectiveness factor (Fig. 6). Such a strange effect is explained by increasing of total pellet activity with respect to diffusivity in the large (transport) pores.

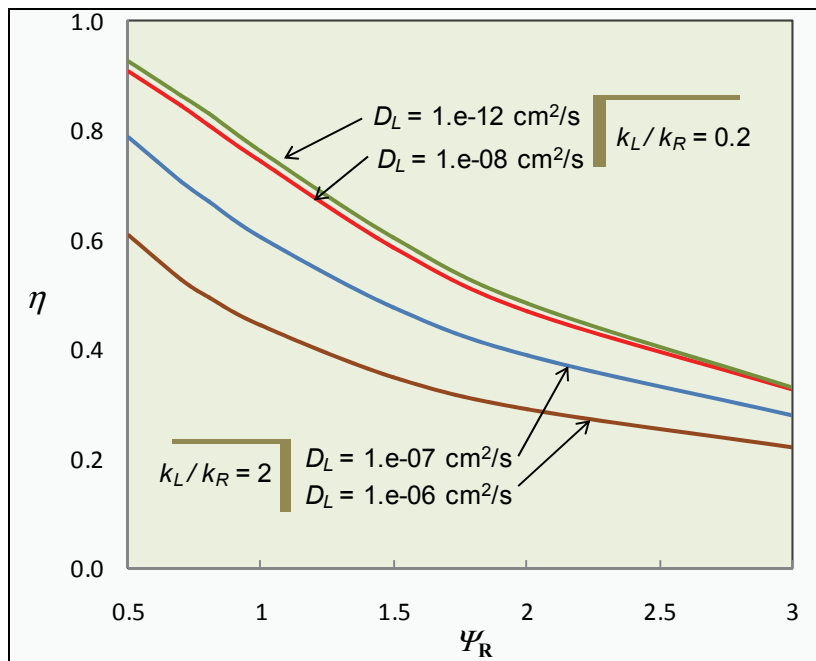


Figure 6. The influence of diffusivity in zeolite crystals on the effectiveness factor of pellet.

Nomenclature

b_A, b_B – adsorption equilibrium constants;
 C_L, C_R – concentrations in “micro-” and “macropores”;
 D_L, D_R – diffusivities in “micro-” and “macropores”;
 k – reaction rate constant at uniform micro-distribution;
 k_L, k_R – reaction rate constants in “micro-” and “macropores”;
 k_{PL}, k_{PR} – corresponding deactivation (poisoning) rate constants;
 s – pellet shape parameter;

α – fraction of active component in “micropores”;
 β – ratio of deactivation rate constants;
 ε – volume fraction of “micropores”;
 η, χ – effectiveness factor and total pellet effectivity;
 θ_L, θ_R – are relative activities in “micro-” and “macropores”;
 ξ, ρ – dimensionless coordinate in globule and in pellet;
 $\psi^2_L = L^2 k/D_L, \psi^2_R = R^2 k/D_R$ – Thiele moduli for globule and for pellet.

References

- [1] S.-Y. Lee, R. Aris – Catal. Rev. - Sci. Eng., 1985, 27, 207-340.
- [2] R. C. Dougherty, X. E. Verykios – Catal. Rev. - Sci. Eng., 1987, 29, 101-130.
- [3] A. S. Belyi, M. D. Smolikov, V. B. Fenelonov, V. Yu. Gavrilov, V.K. Duplyakin – Kinet. Katal., 1986, 27, 703-708; 1414-1418.
- [4] N. M. Ostrovskii, T. P. Mitsulya – React. Kinet. Catal. Lett., 1996, 58, 161-168.
- [5] R. Krishna, T. J. H. Vlugt, B. Smit – Chem. Eng. Sci., 1999, 54, 1751-1757.
- [6] F. J. Keil, R. Krishna, M-O. Coppens – Rev. in Chem. Eng., 2000, Vol. 16, No. 2: Modeling of diffusion in zeolites, 71-197.
- [7] N. M. Ostrovskii, N.M. Bukhvtsova – React. Kinet. Catal. Lett., 1995, 56, 391-399.
- [8] N. M. Bukhvtsova, N. M. Ostrovskii – React. Kinet. Catal. Lett., 1998, 65, 322-329.
- [9] N. M. Ostrovskii, J. Wood, in A. M. Spasic, J.-P. Hsu (Eds), Finely Dispersed Particles: Micro-, Nano-, and Atto-Engineering, Taylor & Francis Group, London, New-York, 2006, Chapter 23, 601-640.
- [10] N. M. Bukhvtsova, N. M. Ostrovskii – Kinet. Catal., 2002, 43, 81-88.
- [11] N. M. Ostrovskii – Catalyst Deactivation Kinetics, Nauka, Moscow, 2001, (in Russian).
- [12] A. Yu. Stakheev, L. M. Kustov – Appl. Catal. A: General, 1999, 138, 3-35.

KINETICS AND MECHANISMS OF OZONE REACTIONS WITH SOME OXYGEN-CONTAINING ORGANIC COMPOUNDS

S. Rakovsky, M. Anachkov, M. Deneva, A. Eliyas and D. Jovanović*

*Institute of Catalysis, Bulgarian Academy of Sciences, Sofia 1113, Bulgaria
(rakovsky@ic.bas.bg)*

**University of Belgrade, Institute of Chemistry, Technology and Metallurgy
(I.Ch.T.M.), Department of Catalysis and Chemical Engineering, Njegoseva 12,
11000 Belgrade, Republic of Serbia*

Abstract

This paper is focused on degradation of organics by ozonation and it comprises various classes of oxygen-containing organic compounds – alcohols, ketones and ethers. The mechanisms of a multitude of ozone reactions with these compounds in organic solvents are discussed in details, presenting the respective reaction schemes and the corresponding kinetic parameters are given as well as some thermodynamic parameters. The dependences of the kinetics and the mechanisms of the ozonation reactions on the structure of the reacting compounds, on the reaction environment and on the experimental conditions are revealed. The various possible applications of ozonolysis are specified and discussed. All these reactions have practical importance for the protection of the environment.

Keywords: ozonation, alcohols, ketones, ethers, kinetics, mechanisms

Introduction

The ozonolysis of oxygen-containing compounds is a promising process that takes place under mild conditions and yields compounds of a higher oxidation level than that of the starting compounds. It may find various applications in chemical and pharmaceuticals industries, in fine organic synthesis, etc. Moreover, this process is extremely important from an ecological point of view for the utilization and purification of waste industrial waters through their partial or complete oxidation. The importance of this process for theory and practice gave us an impetus for making systematic investigations

Experimental

UV-, IR-, ESR-, HPLC-, and GC-spectra were registered on standard equipments.

Kinetic Measurements:

Static method

Pure reagent or reagent solution was injected into thermally regulated 1 cm quartz cell, containing a solution of ozone in CCl₄, the time of mixing being less than 0.2

C-03-SL

second. The decrease in the ozone concentration was monitored spectrophotometrically at 270-290 nm. At concentration ratio $[RH]_0/[O_3]_{i0} > 100$, the ozone pseudomonomolecular constant $k' = k[RH]_0$ was determined based on the equation $\lg([O_3]_{i0}/[O_3]_{it}) = k't$, where $[O_3]_{i0}$ and $[O_3]_{it}$ are the initial and the current concentrations of ozone in the solution, respectively [1,2].

Dynamic method

Ozone was bubbled into a cylindrical glass reactor having an inner diameter $\phi = 1.7-3.7$ cm and height 7-15 cm, equipped with sintered glass frit G2 at its lower end. Conventionally, gas stream flow rate was $v = 0.1$ l/min; solutions volume $V = 10$ ml; ozone concentrations at the reactor inlet ($[O_3]_0$) – $10^{-6} - 10^{-3}$ M; the solvent- CCl_4 ; $[RH]_0 = 10^{-4} - 10^1$ M. The inlet and outlet ozone concentrations were measured in gas phase in the spectral range of 254-300 nm. The determination of rate constants is based on the approach [3,4], which connects the amount of consumed ozone with the rate of the chemical reaction:

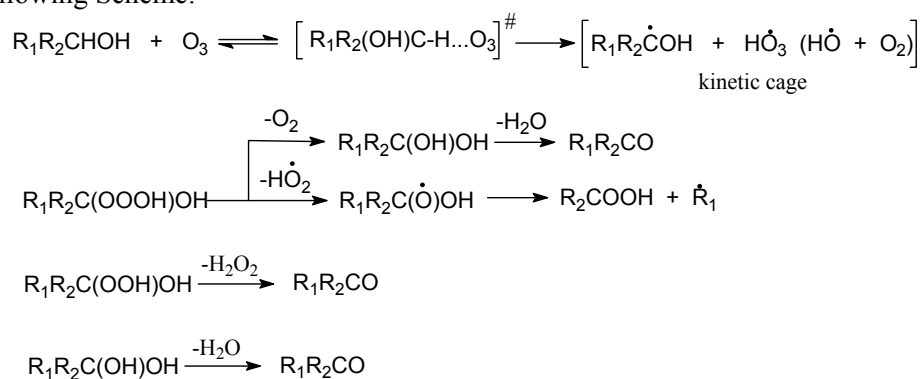
$$\omega([O_3]_0 - [O_3]_g) = k[O_3]_l[RH]$$

where ω is the relative flow rate of ozone–oxygen gas mixture (in litres of gas mixture per L of solution per sec); $[O_3]_0$ and $[O_3]_g$ are ozone concentrations at the reactor inlet and outlet, respectively, $[O_3]_l$ is the ozone concentration in the solution; $[RH]$ is the concentration of the reagent.

Results and Discussion

Alcohols

The experimental and theoretical results on alcohol ozonation conform well to the following Scheme:

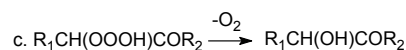
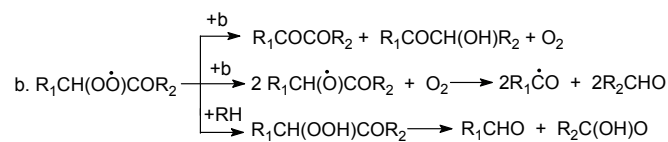
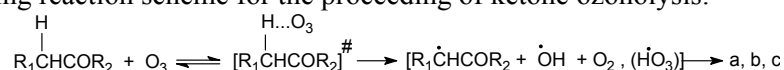


Ozone attacks the α -H atom, forming a linear activated complex, which undergoes further decomposition into a radical (or ion) pair in one kinetic cage. The α -hydroxy alcohol, α -hydroxyperoxy alcohol and α -hydroxytrioxy alcohol being unstable leave the cage decomposing rapidly to the corresponding aldehyde or ketone liberating water, hydroperoxide and oxygen or alternatively forming hydroperoxy and alkoxy radicals [2,5]. The latter species can further undergo monomolecular decomposition.

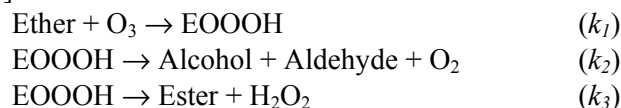
Ketones

The values of k vary within a wide range, depending on the ketone structure, particularly on the content of primary, secondary or tertiary α -C-H-bonds. The ratio between their reactivities is 1 : 3.4÷24.8 : 33.4÷47.4. In contrast to the case of paraffins, these values for the ketones are quite similar, which can be attributed to the activation of α -C-H-bonds by the keto group. Ozone is sensitive not only to the activation of the α -C-H bonds but also to the keto-enol equilibrium [3,5].

On the basis of the kinetic results obtained and the product analyses we propose the following reaction scheme for the proceeding of ketone ozonolysis:

*Ethers*

Based on our results the principle scheme of the ozone reaction with aliphatic ethers in general is [4,5]:

**Conclusions**

On the basis of the correlations between experimental results and calculated values the particular mechanisms of the ozone reaction with alcohols, ketones and ethers are elucidated.

References

- [1] S. D. Razumovskii, S. K. Rakovsky, D. M. Shopov, G. E. Zaikov, *Ozone and Its Reactions with Organic Compounds*, [in Russian], Publishing House of the Bulgarian Academy of Sciences, Sofia, Bulgaria, 1983.
- [2] S. K. Rakovsky, D. R. Cherneva, *International Journal of Chemical Kinetics*, 1990, 22, 4, 321.
- [3] S. K. Rakovsky, D. R. Cherneva, *Oxidation Communications*, 1989, 12, 3, 108.
- [4] S. K. Rakovsky, D. R. Cherneva, Deneva, M., *International Journal of Chemical Kinetics*, 1995, 27, 2, 153.
- [5] G. E. Zaikov, S. K. Rakovsky. *Ozonation of Organic & Polymer Compounds*, Smithers Rapra, Shawbury, UK, 2009.

C-04-O

NI-AL LAYERED DOUBLE HYDROXIDES AS CATALYSTS FOR CO PURIFICATION PROCESSES

M. Gabrovska^{1*}, V. Idakiev¹, K. Tenchev¹, D. Nikolova¹,
R. Edreva-Kardjieva¹, D. Crisan²

¹*Institute of Catalysis, Bulgarian Academy of Sciences, Sofia 1113, Bulgaria
(margo@ic.bas.bg; margarita.gabrovska@abv.bg)

²*Institute of Physical Chemistry "Ilie Murgulescu", Romanian Academy, 202
Splaiul Independentei Str., 060021 Bucharest-12, Romania*

Abstract

The co-precipitated Ni-Al layered double hydroxides were studied as catalyst precursors for CO purification processes, namely CO oxidation and water-gas shift reaction. It was established that the CO oxidation activity strongly depends on the nickel amount and reaction temperature, while the activity in the water-gas shift reaction is affected by the presence of alkali additives.

Introduction

Ni-Al layered double hydroxides (LDHs), also known as takovite-like (TKl) compounds, represent a class of natural or synthetic inorganic lamellar materials with chemical composition expressed by the general formula $[\text{Ni}^{2+}_{1-x} \text{Al}^{3+}_x (\text{OH})_2]^{x+} [\text{A}^{n-}_{x/n}]_m \cdot m\text{H}_2\text{O}$. Here, Ni^{2+} and Al^{3+} ions are located in the brucite-like hydroxide layers, while the charge compensating exchangeable anions and water molecules are situated in the interlayer space $[\text{A}^{n-}_{x/n}]_m \cdot m\text{H}_2\text{O}$ of the layered structure, ($\text{A}=\text{NO}_3^-, \text{SO}_4^{2-}, \text{CO}_3^{2-}, \text{Cl}^- \dots$), x represents the fraction of the Al^{3+} ion and m is the number of the water molecules [1]. The aim of this study is to investigate the activity of the Ni-Al LDHs in the catalytic processes, related principally to the environmental protection. It is well known that the conversion of CO by water vapor (water-gas shift reaction, WGS) and CO oxidation are commonly applied reactions for purification of the CO-containing gaseous mixtures used for different purposes. The effects of the nickel content as well as the reaction temperature on the catalytic activity of the Ni-Al layered systems in both model reactions were studied. The influence of the alkali additives (K^+ ions) on activity of the Ni-Al systems in the water-gas shift reaction was also investigated.

Experimental

The TKl precursors with $\text{Ni}^{2+}/\text{Al}^{3+}$ molar ratio of 1.5 and 3.0 were synthesized by co-precipitation of a Ni-Al mixed aqueous nitrate solution with an aqueous solution of Na_2CO_3 at 80°C and constant $\text{pH}=8$. For preparation of the K-containing samples, a drop-wise addition of 0.1N solution of K_2CO_3 to the washed wet precipitates was performed. The obtained samples were dried at 80°C for 20 h and designated as $x\text{NiAl-}y\text{K}$, where x represents the $\text{Ni}^{2+}/\text{Al}^{3+}$ molar ratio and y denotes the amount of deposited K_2O .

The catalytic activity measurements of the as-synthesized samples in both reactions are studied in the temperature range $150\text{--}300^\circ\text{C}$. The WGS was carried

out in a flow reactor at atmospheric pressure using gaseous mixture of 5.0 vol. % CO in Ar at GHSV = 3000 h⁻¹, partial pressure of water vapor = 31.1 kPa and steam/gas ratio = 0.7. The degree of CO conversion was determined by measuring the CO and CO₂ contents at the outlet of the IR-gas analyzer ‘Infralyt 2100’. More detailed description was presented in ref. 2. CO oxidation reaction was performed in a fixed-bed flow reactor setup by heating and cooling procedures, using gaseous mixture with a composition of CO/O₂/Ar = 1.0/6.0/93.0 at GHSV = 8000 h⁻¹. The degree of CO conversion was evaluated by measuring the CO concentration at the outlet of the IR-gas analyzer ‘Hartmann-Braun’ in the range 0–6 vol. % CO. More detailed description was presented in ref. 3.

Results and Discussion

The temperature dependence of the catalytic activity of the non-promoted and K-promoted Ni-Al samples in the WGS is represented in Fig. 1.

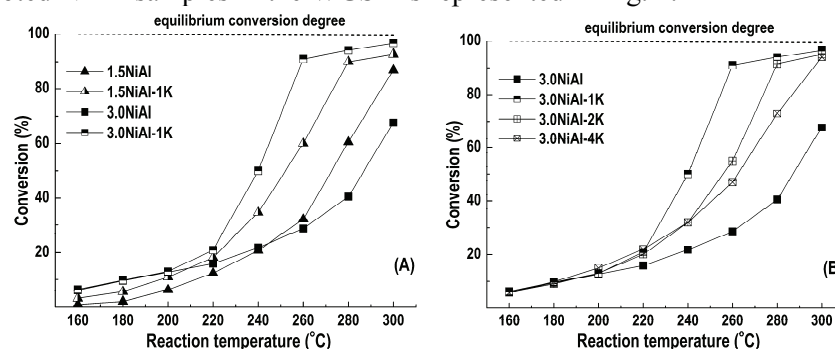


Figure 1. Catalytic activity of the $x\text{NiAl-}y\text{K}$ samples in WGS.

It is clearly shown that 1.5NiAl catalyst demonstrates higher activity than 3.0NiAl one only in the temperature range of 280–300°C (Fig. 1A). Obviously, the increase of Ni amount does not enhance the catalytic activity. Contrariwise, the deposition of 1 wt % K₂O on the surface of both catalysts (1.5NiAl-1K and 3.0NiAl-1K) causes increase of the activity in the temperature range 240–300°C. The promoting role of the potassium is more clearly demonstrated in the case of the catalyst with higher Ni amount (3.0NiAl-1K) reaching equilibrium conversion value of 97 % at 300°C (Fig. 1A). However, the further increase of the K₂O loading 2 and 4 wt% diminishes the activity comparison to 3.0NiAl-1K (Fig. 1B). Nevertheless, all they are more active than the non-promoted 3.0NiAl catalyst, namely: 3.0NiAl < 3.0NiAl-4K < 3.0NiAl-2K < 3.0NiAl-1K.

It was suggested in our former study [2] that under the influence of the reaction medium, the catalyst surface undergoes reduction hydrolysis with formation of active species such as NiOOH and Ni(OH)₂-like structures, bearers of the Ni³⁺ and Ni²⁺ ions. It was supposed that the WGS proceeds over Ni(OH)₂-like structures *via* an associative reaction mechanism which considers the formation of an intermediate surface formate species with participation of active OH groups from the catalyst surface and a topotactical redox transformation Ni²⁺ ↔ Ni³⁺. The

potassium promoting effect on the activity of 3.0NiAl catalyst can be explained by stabilizing of the Ni^{3+} state, the presence of active OH groups at the catalyst surface as well as the electron transfer between the oxidation states $\text{Ni}^{2+} \leftrightarrow \text{Ni}^{3+}$.

The CO oxidation reaction is realized by step-wise increase and decrease of the reaction temperature. A gradual enhance in the catalytic activity is observed during heating of both catalysts to 300°C revealing the higher activity of 3.0NiAl catalyst (Fig. 2). Apparently, the formation of active surface species starts after 200°C during the heating step and completes at 300°C.

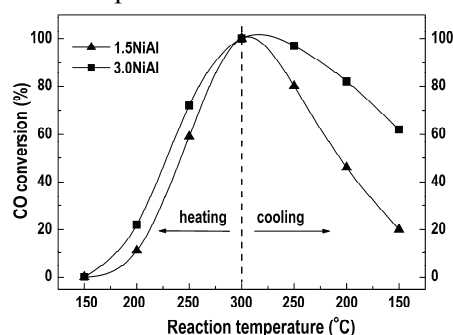


Figure 2. Catalytic activity of Ni-Al samples in CO oxidation reaction

Evidently, some reduction and reconstruction of the surface occur during the activity test in the catalytic oxidation of CO to CO_2 , leading to the generation of the active sites in the heating step. They involve the redox couple $\text{Ni}^{2+}/\text{Ni}^{3+}$ and the mobile surface lattice oxygen. An assembly is formed by the redox couple $\text{Ni}^{2+}/\text{Ni}^{3+}$ adjacent/associated to Al^{3+} anion vacancy, thus generating O_2^{x-} radicals stabilized on Al^{3+} ion. The assembly remains active on cooling exhibiting stronger dependence on the nickel amount in the catalysts. A similar scheme was proposed in the case of Co-Al LDH systems [3]. The scheme explains the relatively lower activity of the 1.5NiAl sample: the increased Al^{3+} content increases the number of stabilized adsorbed O_2^{x-} radicals. However, the latter are no longer close to $\text{Ni}^{2+}/\text{Ni}^{3+}$ pair because of the lesser nickel amount thus reducing the number of active assemblies.

Conclusions

It may be concluded that the Ni-Al LDHs are promising precursors of effective catalysts for CO purification processes. The CO oxidation activity strongly depends on the nickel amount and reaction temperature, while the activity in WGS is affected by the presence of alkali additives.

References

- [1] A. Vaccari, *Catalysis Today*, 1998, 41, 53–71.
- [2] A. Andreev, V. Idakiev, K. Kostov, M. Gabrovska, *Catalysis Letters* 1995, 31, 245–252.
- [3] M. Gabrovskaa, R. Edreva-Kardjieva, K. Tenchev, P. Tzvetkov, Al. Spojakina, L. Petrov, *Applied Catalysis A: General*, 2011, 399, 242–251.

INFLUENCE OF DIFFERENT PARAMETERS ON BIODIESEL YIELD USING CAO HETEROGENEOUS CATALYST

A. Zarubica, N. Stojkovic, M. Randjelovic,
M. Marinkovic, N. Radulovic, M. Vasic

Faculty of Science and Mathematics, University of Nis, 18000 Nis, Serbia

Abstract

CaO was evaluated as a base solid catalyst in the reaction of biodiesel synthesis by transesterification of sunflower oil. An influence of catalyst activation conditions and process parameters (*i.e.* catalyst calcination temperature; reaction temperature and process pressure) on the biodiesel yield was investigated. The catalyst calcined at 750°C demonstrated the highest activity, while the catalyst thermally treated at 900°C showed somewhat lower activity. Transesterification reaction temperature of 100°C was the optimal one, since the conversion of more than 90% was obtained after only 2h of the reaction run. The reaction pressure increase up to 10 bars had an affirmative effect on the biodiesel yield, while further increase in pressure to 20 bars lowered the yield of fatty acids methyl esters.

Introduction

High CO₂ emission rates as well as the limited nature of fossil fuel reserves have led to a search for alternative fuels, which would be renewable, environmentally friendly, and their price and availability independent on the geopolitical and economical factors. In the last decade, the biodiesel has been established as a viable fossil fuel substitute. Biodiesel is still most often produced by the transesterification using homogeneous NaOH as a catalyst [1]. In such a catalyzed process, a high biodiesel yield is obtained, but both products (biodiesel and glycerol) are contaminated by the catalyst and need to be refined with a large volume of water in order to achieve a satisfying purity. This waste water from the refining procedure becomes an environmental hazard due to its relatively high NaOH content and have to be removed in an appropriate manner [2], while the catalyst cannot be reused. In addition, due to the catalyst is an aggressive compound (very strong base), the reactor plants may be difficult to maintain. The usage of heterogeneous catalysts eliminates these problems. The economical viability of solid catalysts depends on the expenditure of resources on heating and/or pressure increase. This work is aimed at researching the potential of CaO for the catalyst usage in the transesterification reaction of sunflower oil with methanol. A wide range of different parameters (catalyst activation and process conditions), such as reaction temperatures and pressures were applied in order to determine the optimized conditions for a maximal fatty acids methyl esters (FAME) yield.

Experimental

Catalyst based on CaO (Aldrich, Co.) was activated/prepared at a wide range of temperatures (500-1000°C). The detailed physico-chemical characterization of catalysts samples were conducted over textural (BET), structural (XRD), thermal (TGA/DTA), morphological (SEM) and surface analyses (acid-base properties by FTIR). Reagents, a sunflower oil obtained from a domestic producer (“Vital”), and HPLC grade methanol (Aldrich, Co.) were used in the process. The catalyst pellets fractions were selected to avoid possible internal extrudate diffusion restrictions, the catalyst loading was 1 mas.%. The sunflower oil to methanol molar ratio was 1:6, also kept constant during reaction runs. Particular reactions were carried out in a commercial bench stirred tank reactor of 2dm³ in volume under stirring of 200 rpm. Two separate experiment sets of reaction runs were performed in order to evaluate FAME yield dependance on a reaction temperature and/or pressure. In the first reaction set, constant pressure of 1 bar was kept, and the reaction temperature was varied from 60 to 120°C, while in the second reaction set, reaction temperature of 80°C was maintained, and the pressure was changed from 1 to 20 bars.

Results and Discussion

Unexpectedly low FAME yields were obtained over the catalyst calcined at the lowest activation temperature used (*i.e.* 500°C), as shown in Fig. 1.

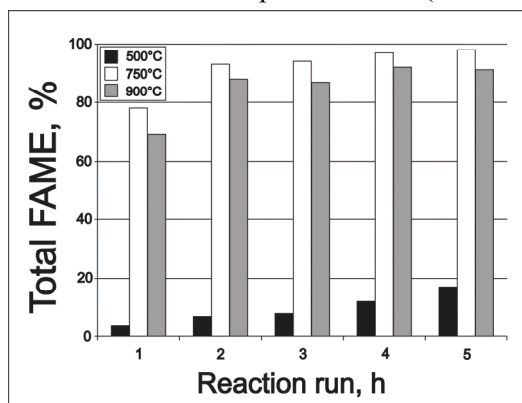


Figure 1. Total FAME amount obtained at 80°C, and atmospheric pressure, in dependence on selected catalyst samples activated at 500, 750 and 900°C, and reaction run (h).

BET results did not show a significant difference between the catalysts textural properties, that is, the biggest differences were reflected in pore volumes and mean pore diameters (Fig. 2a). However, XRD and TGA/DTA analyses (not shown) reveal that the calcination/activation temperature is higher the lower amounts of corresponding hydroxide and carbonate are registered (Fig. 2b). The catalyst sample calcined at 500°C did not undergo to the thermal treatment at 740°C that is attributed to a decomposition of remaining CaCO₃ [3], which showed no activity in the transesterification reaction.

FTIR results indicated a presence of weak base sites on the surface of the catalyst calcined at 500°C, that is an additional explanation for a low activity of catalyst.

BET results did not show a significant difference between the catalysts textural properties, that is, the biggest differences were reflected in pore volumes and mean pore diameters (Fig. 2a). However, XRD and TGA/DTA analyses (not

shown) reveal that the calcination/activation temperature is higher the lower amounts of corresponding hydroxide and carbonate are registered (Fig. 2b). The catalyst sample calcined at 500°C did not undergo to the thermal treatment at 740°C that is attributed to a decomposition of remaining CaCO_3 [3], which showed no activity in the transesterification reaction. FTIR results indicated a presence of weak base sites on the surface of the catalyst calcined at 500°C, that is an additional explanation for a low activity of catalyst.

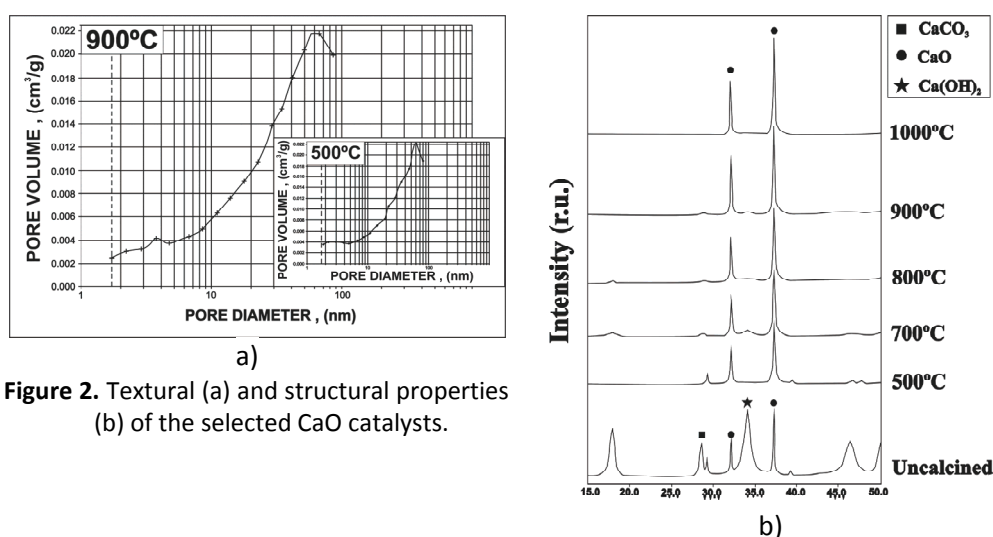


Figure 2. Textural (a) and structural properties (b) of the selected CaO catalysts.

The temperature of 60°C was proven insufficient for the heterogeneous base catalyzed reaction (lower catalyst activity observed). The highest FAME yield was obtained over CaO activated at 750°C at the reaction temperature of 80°C after 4h of time-on-stream. Conversion of reagents toward FAME was somewhat lower at process temperature 120°C than at 80-100°C, and at the same time enough high, starting even at the beginning of the reaction. A lower yield at higher operating temperature can be attributed to internal and/or external diffusion restrictions or a potential competitive reaction occurrence. The curve of total FAME fraction as function of time-on-stream in dependence of the process pressure demonstrated a maximum at 10 bars following with a further drop, while reaction temperature was kept constant at 80°C.

Conclusions

When activated at 500°C, CaO is an inefficient catalyst in the examined transesterification reaction conditions. Catalyst activated at 750°C showed an optimal pore volume (no internal diffusion restrictions on reagents pathway to catalyst active sites), the absence of hydroxide phase and no calcium carbonate known as inactive in the reaction. These structural CaO-750°C catalyst features together with a favorable surface features resulted in an optimal conversion to desirable products under the selected transesterification reaction conditions.

Acknowledgment

The authors wish to thank to the Ministry of Education and Science – Republic of Serbia for a financial support (Project ON 172061).

References

- [1] Y.C. Sharma, B. Singh, S.N. Upadhyay, Fuel, 2008, 87, 2355-2373.
- [2] A. Demirbas, Energy Conv. Manage., 2002, 43, 2349–2356.
- [3] Dj. Vujcic, D. Comic, A. Zarubica, R. Micic, G. Boskovic, Fuel, 2010, 89, 2054-2061.

INVESTIGATION OF PHYSICOCHEMICAL AND PHOTOCATALYTIC PROPERTIES OF MAGNETITE-TYPE NANOSIZE MATERIALS

Z. Cherkezova-Zheleva¹, K. Zaharieva¹, J. Krstić², M. Tsvetkov³,
I. Mitov¹, M. Milanova³

¹*Institute of Catalysis, Bulgarian Academy of Sciences,*

Acad. G. Bonchev St., Block 11, 1113 Sofia, Bulgaria, zzhel@ic.bas.bg

²*University of Belgrade, Institute of Chemistry, Technology and Metallurgy*

Center of Catalysis and Chemical Engineering, Belgrade 11000, Serbia

³*Faculty of Chemistry and Pharmacy, St. Kliment Ohridski University of Sofia,*

1 J. Bouchier Blvd., 1164 Sofia, Bulgaria

Abstract

The study presents investigation of physicochemical properties of series of materials - members of solid solutions of magnetite and partially substituted magnetite materials. Samples are prepared by different procedures such as co-precipitation or combination of co-precipitation and low temperature treatment or mechanochemical activation. Textural characteristics, dispersity, crystallite size and microstrains, magnetic behavior, as well as initial photocatalytic activity tests are registered. The results show the influence of chemical composition and preparation methods on the dispersity, physicochemical and catalytic properties of studied ferrite samples.

Introduction

The usage of ecofriendly ferrites for efficient solar energy has been an important topic in the visible light photocatalysis research. Ferrites are well known for their tremendous applications in the field of magnetic and electronic materials, but there are only a few reports on their photocatalyst applications. Unlike TiO₂, the ferrites offer an advantage of displaying the desirable optical absorption for the low energy photons ($h\nu \sim 2$ eV), and of exhibiting the well suited electronic structure desirable for photocatalytic applications. Additionally, the perovskite or spinel related oxide photocatalysts exhibit enhanced efficiency due to the available extra catalytic sites by virtue of their crystal lattices [1]. Semiconductor photocatalysts have been widely studied for environmental remediation applications, e.g. air and water purification [2].

The main purpose of our research was to study the influence of partially substituted iron (II) cations with other M (II) ion (M=Mg, Co, Ni and Cu) and the impact of synthesis procedures on the physicochemical and photocatalytic properties of nanodimensional powder materials with magnetite-type spinel structure

(M_xFe_{3-x}O₄, x = 0.5).

Experimental

The nanometer ferrite materials Fe_3O_4 , $\text{Mg}_{0.5}\text{Fe}_{2.5}\text{O}_4$, $\text{Co}_{0.5}\text{Fe}_{2.5}\text{O}_4$, $\text{Ni}_{0.5}\text{Fe}_{2.5}\text{O}_4$, $\text{Cu}_{0.5}\text{Fe}_{2.5}\text{O}_4$ were synthesized by co-precipitation chemical and mechanochemical activation methods. The preparation conditions as well as different investigation techniques - X-ray diffraction, TG, DTG, DTA analysis, IR and Moessbauer spectroscopy allow establishing the structure and dispersity of ferrite samples (Fe_3O_4 , $\text{Mg}_{0.5}\text{Fe}_{2.5}\text{O}_4$, $\text{Co}_{0.5}\text{Fe}_{2.5}\text{O}_4$, $\text{Ni}_{0.5}\text{Fe}_{2.5}\text{O}_4$, $\text{Cu}_{0.5}\text{Fe}_{2.5}\text{O}_4$) [3-5]. The specific surface area was determined at -192°C using nitrogen as adsorbate. The photocatalytic measurements are made under UV irradiation (Sylvania 18 W BLB T8, light intensity $5 \times 10^{-5} \text{ W/cm}^2$). Aqueous solution of malachite green (10^{-5} M) as model pollutant and 1 g/l prepared nanosized ferrite catalysts are used for the tests.

Results and Discussion

Results of physisorption measurements reveal a variety of values of all determined textural parameters for synthesized ferrite materials (Table 1). Textural differences originated from the substitution of cations used in synthesis as well as from applied synthesis procedure. For example, the ferrite specific surface area of $\text{Cu}_{0.5}\text{Fe}_{2.5}\text{O}_4$ sample is $264 \text{ m}^2/\text{g}$ compared to $175 \text{ m}^2/\text{g}$ of unmodified Fe_3O_4 . The samples of the same chemical composition $\text{Ni}_{0.5}\text{Fe}_{2.5}\text{O}_4$ - **sample A** (thermally treated at 300°C) and **sample B** (synthesized by mechanochemical activation) have different values of S_{BET} , $124 \text{ m}^2/\text{g}$ compared to $168 \text{ m}^2/\text{g}$ respectively. The mesopore size varying from 3.5 nm to 8.6 nm is calculated for nanosized ferrite materials.

Table 1. Textural characteristics of nanosized ferrite catalysts.

Sample	$S_{\text{BET}}, \text{m}^2/\text{g}$	Pore volume, cm^3/g	Maximum pore diameter, nm
Fe_3O_4	175	0,216	5,3
$\text{Mg}_{0.5}\text{Fe}_{2.5}\text{O}_4$	198	0,280	5,8
$\text{Co}_{0.5}\text{Fe}_{2.5}\text{O}_4$	233	0,300	4,4
$\text{Ni}_{0.5}\text{Fe}_{2.5}\text{O}_4$ - sample A	124	0,339	8,6
$\text{Ni}_{0.5}\text{Fe}_{2.5}\text{O}_4$ - sample B	168	0,129	3,5
$\text{Cu}_{0.5}\text{Fe}_{2.5}\text{O}_4$	264	0,288	4,7

The registered Moessbauer spectra of the prepared ferrite catalysts show the presence of superposition of doublet lines. The doublet and sextet components are observed in the case of magnetite [3]. The obtained X-ray diffraction patterns have low-intensity peaks and X-ray amorphous halo. The reflections of non-stoichiometric phases $\text{Me}_{0.5}\text{Fe}_{2.5}\text{O}_4$, $\text{Me} = \text{Fe}, \text{Mg}, \text{Co}, \text{Ni}$ and Cu (PDF 19-0629; PDF 88-2182; PDF 88-2152; PDF 87-2338; PDF 73-2317) are registered. The average crystallite size of prepared ferrite catalysts calculated by Scherrer equation is below 15 nm [3-5,6].

The photocatalytic activity studies show decreasing of rate constant in order $\text{Co}_{0.5}\text{Fe}_{2.5}\text{O}_4$ ($k=7.9 \times 10^{-3} \text{ min}^{-1}$) > $\text{Cu}_{0.5}\text{Fe}_{2.5}\text{O}_4$ ($k= 6.5 \times 10^{-3} \text{ min}^{-1}$) > $\text{Mg}_{0.5}\text{Fe}_{2.5}\text{O}_4$ ($k= 0.7 \times 10^{-3} \text{ min}^{-1}$) for the malachite green degradation under UV irradiation. The

highest rate constant was observed in the presence of cobalt ferrite catalyst $\text{Co}_{0.5}\text{Fe}_{2.5}\text{O}_4$ for the photocatalytic process.

Conclusions

The non-supported ferrite samples (Fe_3O_4 , $\text{Mg}_{0.5}\text{Fe}_{2.5}\text{O}_4$, $\text{Co}_{0.5}\text{Fe}_{2.5}\text{O}_4$, $\text{Ni}_{0.5}\text{Fe}_{2.5}\text{O}_4$, $\text{Cu}_{0.5}\text{Fe}_{2.5}\text{O}_4$) exhibit nanodimensional particle size and predominantly mesoporous character. The obtained crystallite size, specific surface area and pore size distribution of samples prepared by direct co-precipitation synthesis are higher than those of mechanochemically prepared samples, which are higher than those of thermally treated samples. Therefore not only variations in synthesis procedure, but changes in chemical composition of materials having the same spinel structure give a result in different dispersity of materials. Partial substitution of iron (II) ions in magnetite structure by different metal (II) cations leads to changes in physicochemical properties and electronic structure of materials. This allows to investigate an optimal catalyst composition for photocatalytic degradation of water pollutants.

Acknowledgments

The authors are grateful to the financially support of National Science Fund of Bulgaria (projects DO 02-295/2008 and DDVU 02-07/2010) and Serbian Ministry of Education and Science (Project 45001).

References

- [1] Rekha Dom, R. Subasri, K. Radha, Pramod H. Borse, *Solid State Communications*, 2011, 151, 470–473.
- [2] Seung-woo Lee, Jack Drwiega, David Mazyck, Chang-Yu Wu, Wolfgang M. Sigmund, *Materials Chemistry and Physics*, 2006, 96, 483–488.
- [3] Z. Cherkezova-Zheleva, M. Shopska, G. Kadinov, I. Mitov, *Nanoscience & Nanotechnology*, 11, edited by E. Balabanova and I. Dragieva (Prof. Marin Drinov Academic Publishing House, Sofia, 2011), 134-137.
- [4] Z. Cherkezova-Zheleva, K. Zaharieva, B. Kunev, M. Shopska, I. Mitov, *Nanoscience & Nanotechnology*, 12, edited by E. Balabanova and I. Dragieva (Prof. Marin Drinov Academic Publishing House, Sofia, 2012) in press.
- [5] Z. Cherkezova-Zheleva, K. Zaharieva, V. Petkova, B. Kunev, I. Mitov, *Preparation and investigation of nanodimensional nickel ferrite*, *Bulgarian Chemical Communications*, 2012, in press.
- [6] U. Schwertmann and R. Cornell, *Iron Oxides in the Laboratory*, Weinheim, New York-Basel-Cambridge, 1991.

C-07-P

INFLUENCE OF THE REDUCTION TEMPERATURE ON THE NICKEL SURFACE STATE IN THE NI/SILICA GEL VEGETABLE OIL HYDROGENATION CATALYSTS

D. Nikolova^{1*}, Pl. Stefanov², J. Krstić³, M. Gabrovska¹, L. Spasov¹,
D. Lončarević³, D. Jovanović³

¹*Institute of Catalysis, Bulgarian Academy of Sciences, Acad. G. Bonchev str.,
bl. 11, Sofia 1113, Bulgaria,*

**E-mail: dimi@ic.bas.bg; dimi_nik@abv.bg*

²*Institute of General and Inorganic Chemistry, Bulgarian Academy of Sciences,
Acad. G. Bonchev str., bl. 11, 1113 Sofia, Bulgaria*

³*Institute of Chemistry, Technology and Metallurgy, Department of Catalysis and
Chemical Engineering, University of Belgrade, Njegoseva 12,
11 000 Belgrade, Serbia*

Abstract

The influence of the reduction temperature on the nickel surface state in the Ni/silica gel vegetable oil hydrogenation catalysts has been examined by XPS study. The nickel catalyst precursors with identical composition ($\text{SiO}_2/\text{Ni}=1.0$) has been synthesized on the three types of silica gel with different pore structures. The XPS data shown that the metallic nickel presence and dispersion are higher at 430°C reduction temperature in comparison with 530°C one. It was established that two opposite processes controlled the amount of Ni^0 present on surface. First process is reduction of Ni^{2+} entities $(\text{Ni}(\text{OH})_x(\text{CO}_3)_y$ and/or $\text{Ni}^{2+}-\text{O}(\text{OH})-\text{Si}$) presented in precursor or partially reduced precursors, which increased Ni^0 present on surface. Second process is agglomeration of metallic nickel particles, which decreases amount of Ni^0 on surface.

Introduction

The supported nickel- SiO_2 system is still the most commonly used vegetable oil hydrogenation catalysts. The usage of synthetic SiO_2 supports as silica gels contributes to the overcome of the disadvantages of the natural silica sources as composition variation and remarkable content of different metals as aluminum, iron and heavy metals.

In our previous work [1], it was established that the usage of the silica gel supports with different texture as source of SiO_2 causes different location of Ni-species into the support pores and on the external surface area. The formed surface species, $\text{Ni}(\text{OH})_x(\text{CO}_3)_y$ and/or $\text{Ni}^{2+}-\text{O}(\text{OH})-\text{Si}$, have different strength of interaction, different dispersion and different texture properties. These surface characteristics of the precursors will pre-determine the formation of the active nickel metallic phase as well as the mass transfer of the reactants and products to and from the catalytic sites.

The aim of this work is to study the influence of the reduction temperature on the nickel surface state in the Ni/silica gel vegetable oil hydrogenation catalysts by XPS technique.

Experimental

Three types of silica gel (SIG), with different well-defined pore structure have been prepared at different pH values, namely: acidic (SIG-A), neutral (SIG-B) and alkaline (SIG-C). The nickel catalyst precursors with identical composition ($\text{SiO}_2/\text{Ni}=1.0$) were synthesized by precipitation using aqueous solutions of $\text{Ni}(\text{NO}_3)_2 \cdot 6\text{H}_2\text{O}$ with Na_2CO_3 on every type of SIG. The samples were dried at $110^\circ\text{C}/20\text{h}$. Details of the preparation procedures have been reported elsewhere [1, 2].

The activation of the vegetable oil hydrogenation catalysts is commonly accomplished by reduction of the precursors in the interval $430\text{--}550^\circ\text{C}$, the precursors under study were reduced at 430 and 530°C for 5 h with a gas mixture of H_2/N_2 (1/1 v/v at a flow rate of $10\text{ dm}^3/\text{h}$ and a heating rate of $2^\circ\text{C}/\text{min}$) followed by a passivation with a gas mixture of O_2/N_2 after cooling down to room temperature for purpose of XPS study.

The *X-ray photoelectron spectroscopy* (XPS) spectra were recorded on a VG ESCALAB II electron spectrometer, using Al K_α radiation ($h\nu=1486.6\text{ eV}$). The binding energies (BE) were determined with an accuracy of $\pm 0.1\text{ eV}$, utilizing the C1s line at 285.0 eV as a reference. The peak-fitting of the $\text{Ni}2\text{p}_{3/2}$ spectra was made according "Phimat" programme.

Results and Discussion

The peak-fitting of the composite $\text{Ni}2\text{p}_{3/2}$ level evidences the presence of the two types of the nickel oxidation states, Ni^0 and Ni^{2+} . The values of the BE in the range of $852.8\text{--}852.4\text{ eV}$ at 430°C and $853.8\text{--}851.7\text{ eV}$ at 530°C , respectively, characterize the Ni^0 state. The presence of metallic nickel after passivation is also confirmed by X-ray diffraction data [2]. The BE values in the range of $856.6\text{--}855.5\text{ eV}$ at 430°C and $856.9\text{--}854.9\text{ eV}$ at 530°C , respectively, characterize Ni^{2+} state in Ni-O species originated both from the unreduced nickel phyllosilicate phase and dispersed two-dimensional "NiO"-like phase on the metallic nickel particles.

The Ni^0 oxidation state contribution on the samples, established from peak-fitting of the $\text{Ni}2\text{p}_{3/2}$ spectra, after 430°C reduction (Table 1) is the highest at Ni/SIG-A and Ni/SIG-C and it is arranged in the order: Ni/SIG-C>Ni/SIG-A>Ni/SIG-B. After 530°C reduction, it is observed the diminution of the Ni^0 contribution at Ni/SIG-A and Ni/SIG-C in contrast to Ni/SIG-B where the Ni^0 contribution slightly increased. The order is changed as follows: Ni/SIG-B>Ni/SIG-A>Ni/SIG-C. These XPS data are in accordance with TPR profiles of the precursors, which evidence different strength of Ni-O and Ni-O-Si bonds [2]. The reduction process in both Ni/SIG-A and Ni/SIG-C samples predominates at lower temperatures, namely 320°C and 430°C . The stronger interaction is observed

at Ni/SIG-B, where the main maximum of the reduction is located at higher temperature equal to 520°C.

Table 1. Ni⁰ oxidation state contribution, Si surface concentration and surface Ni⁰/Si ratios in the reduced Ni/SIG samples.

Sample	*Ni (wt %)	*Si (wt %)	Ni ⁰ contribution (at %)		Si surface concentration (at %)		Surface Ni ⁰ /Si ratio	
			430°C	530°C	430°C	530°C	430°C	530°C
Ni/SIG-A	43.7	20.7	17.1	10.7	29.2	34.7	0.59	0.31
Ni/SIG-B	45.5	19.7	11.6	13.3	23.7	26.6	0.49	0.50
Ni/SIG-C	43.7	20.8	21.7	8.1	28.6	30.8	0.76	0.26

*Ni and Si content in the as-synthesized precursors.

The calculation of the surface Ni⁰/Si ratios at both reduction temperatures (Table 1) reveals that the Ni⁰ dispersion at 430°C is highest on the Ni/SIG-C precursor and it decreases in the order: Ni/SIG-C>Ni/SIG-A>Ni/SIG-B. After reduction at 530°C the surface Ni⁰/Si ratio diminishes at Ni/SIG-A and Ni/SIG-C, whereas it preserves at Ni/SIG-B. The reason can be found in the agglomeration of the metallic nickel particles at higher reduction temperature as have been documented by PXRD and H₂-chemisorption studies [2].

Conclusion

In conclusion, the analysis of the nickel surface state on the reduced Ni/silica gel precursors discloses higher metallic nickel presence and dispersion at 430°C reduction temperature in comparison with 530°C one. Reason for this can be related with two opposite process that controlled amount of Ni⁰ present on surface. First processes is reduction of Ni²⁺ entities (Ni(OH)_x(CO₃)_y and/or Ni²⁺-O(OH)-Si) present in precursor or partially reduced precursors, which increased Ni⁰ presented on surface. Second process is agglomeration of metallic nickel particles, which decreases amount of Ni⁰ on surface.

Acknowledgements

The authors are grateful to Prof. R. Kardjieva (Institute of Catalysis, Bulgarian Academy of Sciences) for the useful discussion. J. Krstić, D. Lončarević and D. Jovanović are grateful to the Serbian Ministry of Science (Project 45001).

REFERENCES:

- [1] D. Nikolova, J. Krstić, L. Spasov, D. Simeonov, D. Lončarević, Pl. Stefanov, D. Jovanović, Russ. J. Phys. Chem-A, 2011, 85, 2380-2385.
- [2] M. Gabrovska, J. Krstić, P. Tzvetkov, K. Tenchev, M. Shopska, N. Vukelić, D. Jovanović, Russ. J. Phys. Chem-A, 2011, 85, 2392-2398.

HYDROGENATION OF SUNFLOWER OIL OVER NI/SILICA GEL CATALYSTS

J. Krstić¹, M. Gabrovska^{2*}, D. Lončarević¹, D. Nikolova²,
D. Simeonov³, M. Stanković¹, N. Vukelić⁴

¹University of Belgrade, Institute of Chemistry, Technology and Metallurgy,
Department of Catalysis and Chemical Engineering, Belgrade 11000, Serbia

²Institute of Catalysis, Bulgarian Academy of Sciences, Sofia 1113, Bulgaria
*(margo@ic.bas.bg; margarita.gabrovska@abv.bg)

³Institute of General and Inorganic Chemistry, Bulgarian Academy of Sciences,
Sofia 1113, Bulgaria

⁴University of Belgrade, Faculty of Physical Chemistry, Belgrade 11000, Serbia

Abstract

Three types of commercial silica gel, denoted SIG-A, SIG-B and SIG-C, distinguish one from another in their texture characteristics, were applied as supports for the synthesis of Ni/SiO₂ sunflower oil hydrogenation catalysts. It was established that the usage of different types of silica gel leads to obtaining of catalysts with different activities following the order: Ni/SIG-A>Ni/SIG-C>>Ni/SIG-B. The highest activity of Ni/SIG-A catalyst is due to the facilitated reduction of the Ni²⁺ species at 430°C and to the creation of adequate number of accessible Ni⁰ active sites. The number and the accessibility of Ni⁰ active sites are critical parameters for the activity of the catalysts under study.

Introduction

The partial hydrogenation of the vegetable oils is an important practice in the oil industry due to its wide applications, such as modification of the oils physical characteristics for the specific uses. Conventional batch hydrogenation uses slurry reactors, hydrogen gas, high temperatures (140–230°C), low pressures, long reaction times, and metal nickel supported catalysts on different sources of silica [1]. In this study, an attempt were made to elucidate the support role of the sunflower oil hydrogenation activity of Ni/silica gel catalysts, synthesized on three types of silica gel, having different texture parameters.

Experimental

Three types of commercial silica gel (SIG), after grinding, were applied as supports for the synthesis of the Ni/SIG catalyst precursors. The silica gels distinguish one from another in their texture characteristics, such a specific surface area (S_{BET}) and average pore diameter (d_{aver}), namely SIG-A ($S_{\text{BET}}=777$ m²/g and $d_{\text{aver}}=2.7$ nm), SIG-B ($S_{\text{BET}}=581$ m²/g and $d_{\text{aver}}=5.7$ nm) and SIG-C ($S_{\text{BET}}=387$ m²/g and $d_{\text{aver}}=9.5$ nm) [2]. The Ni/SIG samples with identical composition (SiO₂/Ni=1.0) were synthesized by precipitation using aqueous solutions of Ni(NO₃)₂·6H₂O and Na₂CO₃ on every type of silica gel [3].

The preliminary reduction of the as-synthesized precursors after drying at 105°C was performed in a laboratory set-up using a quartz reactor by means of a

“dry reduction” method at 430°C for 5 h with H₂ at a flow rate of 10 l/h and a heating rate of 1.5°C/min. After cooling down to room temperature, the precursors were impregnated with pure paraffin oil in order to prevent the exceptional pyrophority of the metallic nickel.

The partial hydrogenation of a sunflower oil was performed in a 1500 cm³ glass reactor Series 5100 (Parr, USA), computer coupled with Mass Flow Controller F-201C and Pressure Meter F-502C (Bronkhorst, Nederland) under the following conditions: oil mass - 900 g; catalyst concentration - 0.06 wt. % of Ni with respect to the amount of oil; stirring rate - 1200 rpm; hydrogenation temperature - 160°C and H₂ pressure - 0.2 MPa. The hydrogenation activity of the catalysts was evaluated by measuring the changes in the Refraction Index at 50°C (RX-5000α, Atago) of the starting oil and periodically collected partially hydrogenated oil in conformity with ISO 6320 [4]. The quantity of the consumed hydrogen during the hydrogenation process was determined by post processing integration of the differential data from the Mass Flow Controller F-201C.

Results and Discussion

A diminution of the Refraction Index (RI) value of the crude oil (1.46368) and the quantity of the consumed hydrogen as a function of hydrogenation time for the studied catalysts are represented in Figure 1. The value of RI at the end of the hydrogenation reaction downs to the level of 1.45674 (Ni/SIG-A), 1.45783 (Ni/SIG-C) and 1.46101 (Ni/SIG-B). These results are in accordance with the quantity of the consumed hydrogen (cm³) at the end of the reaction, namely: Ni/SIG-A (48013) > Ni/SIG-C (40632) >> Ni/SIG-B (20034).

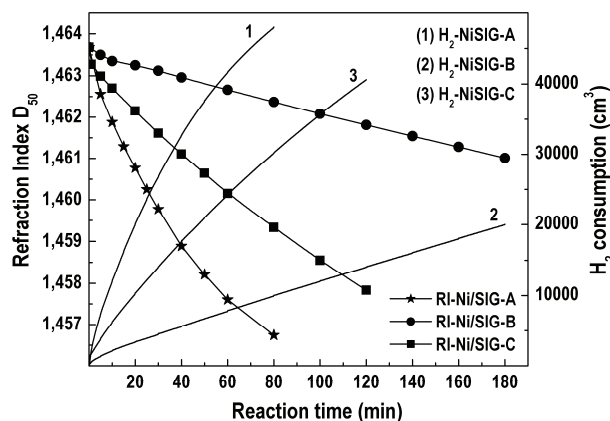


Figure 1. The changes in the RI and the quantity of the consumed hydrogen vs the reaction time.

The comparison of the hydrogen consumption at one and the same hydrogenation time (80 min), normalized for the amount of the consumed hydrogen by Ni/SIG-B (most inactive catalyst) reveals, 3.1 and 4.9 times greater values for Ni/SIG-C and Ni/SIG-A catalysts, respectively. The results confirm the dominant hydrogenation activity of the Ni/SIG-A catalyst.

A possible interpretation of the demonstrated catalytic activity may be found in

our former studies [2, 3]. It was documented that the usage of the silica gel supports with different texture properties provokes formation of two types of Ni^{2+} species in different amount: Ni-phyllsilicate situated in the pores of the supports and basic nickel carbonate, located over the Ni-phyllsilicate surface. It was established the existence of readily reducible Ni^{2+} entities (more pronounced in Ni/SIG-A precursor) and hardly reducible Ni^{2+} entities (predominated in Ni/SIG-B and Ni/SIG-C precursors), which during the reduction process create metal nickel in different amount, too. Although the existence of the reduced species is a necessary condition for the catalyst activity, high reducibility does not provide always high activity. It is well known that the sufficient metal dispersion on the catalyst surface is necessary conditions for the catalytic activity. However, the Ni^0 dispersion, determined from the H_2 -chemisorption measurements shows the order: Ni/SIG-C>Ni/SIG-B>>Ni/SIG-A, which is quite opposite to the catalytic activity order (Ni/SIG-A>Ni/SIG-C>>Ni/SIG-B). It may be supposed that the lower catalytic activity of Ni/SIG-C and Ni-SIG-B catalysts is attributed to its pore system which does not provide the accessibility of the reactant molecules involved in the hydrogenation reaction (triacylglycerols and/or hydrogen) to the active Ni^0 sites. Obviously, the number and the accessibility of Ni^0 active sites are decisive parameters for the activity of the catalysts under study.

Conclusions

The role of the silica gel support type on the sunflower oil hydrogenation activity of the synthesized catalysts is clearly demonstrated. The texture parameters of the carriers determine the type, location and reducibility of Ni^{2+} species presented in precursors. The use of SIG-A support contributes to the formation of easy reducible Ni^{2+} species at 430°C which generate sufficient number of accessible Ni^0 active sites on the surface of Ni/SIG-A catalyst. Therefore, Ni/SIG-A is the most active catalyst for the sunflower oil hydrogenation among the three presented in this study.

Acknowledgements

The authors are grateful to Prof. R. Kardjieva (Institute of Catalysis, BAS) for the useful discussion. The Serbian authors are grateful to the Serbian Ministry of Science (Project 45001).

References

- [1] E. Jang, M. Jung, D. Min, *Comprehensive reviews in food science and food safety*, 2005, 1, 22–30.
- [2] D. Nikolova, J. Krstić, L. Spasov, D. Simeonov, D. Lončarević, Pl. Stefanov, D. Jovanović, *Russ. J. Phys. Chem. A*, 2011, 85, 2380–2385.
- [3] M. Gabrovska, J. Krstić, P. Tzvetkov, K. Tenchev, M. Shopska, N. Vukelić, D. Jovanović, *Russ. J. Phys. Chem. A*, 2011, 85, 2392–2398.
- [4] *Animal and vegetable fats and oils: Determination of refractive index. Standard method: ISO 6320 (2000).*

C-09-P

AG AND CU MODIFIED NI/DIATOMITE CATALYSTS: CORRELATION BETWEEN CATALYST SURFACES STRUCTURE AND HYDROGENATION ACTIVITY

M. Stanković¹, M. Shopska², D. Jovanović¹, D. Skala^{1,3}

¹*University of Belgrade, Institute of Chemistry, Technology and Metallurgy, - Department of Catalysis and Chemical Engineering, Njegoševa 12, 11000 Belgrade, Serbia*

²*Institute of Catalysis, Bulgarian Academy of Sciences, Acad. G. Bonchev str., bl. 11, 1133 Sofia, Bulgaria*

³*University of Belgrade, Faculty of Technology and Metallurgy, Karnegijeva 4, 11000 Belgrade, Serbia*

Abstract

Two series of M-Ni/D catalyst samples (M = Ag or Cu; D = diatomite) were synthesized by the precipitation-deposition (PD) method. Ag- and Cu-Ni/D catalyst samples were characterized using the methods of chemisorption (H₂ adsorbate) and physisorption (N₂ adsorbate). The activity of Ag- and Cu-Ni/D catalysts was tested in the reaction of soybean oil hydrogenation.

A good correlation between the catalyst surfaces structure and the activity of catalyst was determined. An observed trend of increasing activity with the increase of both the specific surface of catalysts and the active surface of Ni indicates the existence of relationships between structural and catalytic properties of the M-Ni/D catalysts.

Introduction

Initially, studies of the surface sciences in catalysis were directed mostly at understanding catalytic activity, in order to make more product molecules per catalyst site for some chemical reaction. The key experimental observations showed that metal surfaces were covered with strongly adsorbed monolayer of reactant species, either ordered or disordered, and that low coordination surface sites at defects or in clusters of metal atoms readily broke chemical bonds and strongly bound adsorbates. The catalyst surface structure and the mobility of adsorbed species are the key ingredients that control activity.

Development of molecular concept of active sites in heterogeneous catalysis suggested that the concentration of sites where rate-determining catalytic reaction steps occur was much smaller than the total concentration of available surface sites.

Correlation of catalyst surface structure with the rates of different reactions indicated that the nature of the active site was different for different chemical bonds. H₂ may dissociate at a single metal atom, or at step and kink sites on metal surfaces, while it may not dissociate on a smooth, coordinate crystal face of metal.

Dispersion measurements have recently acquired a remarkably great practical significance in the field of supported metal catalysts. Dispersion of active metal is commonly measured by selective chemisorption of a suitable gas on the surface of active metal. Hydrogen chemisorption is used as a suitable and reliable tool for determination of the number of active sites on the nickel surface. The metallic dispersion data is dependent on the kinetics, energy and stoichiometry of hydrogen adsorption, which in turn depends on the synthesis methods, added metals, degree of reduction and metal-support interaction.

Various nickel-supported catalysts were previously synthesized and employed in the reaction of hydrogenation of edible oils by our group [1-3]. In our previous papers we studied the synthesis conditions to obtain active Ni/D catalyst [1], the support effect on the properties of nickel catalysts [2], and modification of catalyst surface to improve isomerization (*cis/trans*) selectivity [3].

This research aims to determine the effect of the nature and load of ad-metal (Ag, Cu) on the chemisorptive and textural characteristics of M-Ni/D catalyst. In the second part of this study we compared the activities of Ag- and Cu-Ni/D catalysts in the hydrogenation reaction of soybean oil.

Experimental

Ag- and Cu-Ni/D catalyst samples were synthesized by the PD method using nitrate metal salts, sodium carbonate (precipitant) and chemically and thermally activated diatomite - tuff Barosevac, Kolubara Coal Basin (supporting material).

Details concerning the H₂-chemisorption measurements and characterization of textural characteristics using N₂-physisorption method are compiled in our previous studies [2, 3]. The reaction of hydrogenation of soybean oil was performed in a three-phase slurry reactor, under conditions described in our previous paper [3].

Results and Discussion

The chemical composition, chemisorptive, textural and catalytic characteristics of synthesized M-Ni/D catalyst samples are presented in Table 1.

Table 1. Characteristics of surfaces structure and hydrogenation activity of M-Ni/D catalysts

^a S _{code}	Ni _{load}	Ag _{load}	Cu _{load}	S _{BET}	^b H ₂ _{ads-S}	^c H ₂ _{ads-Ni}	^d S _{spNi}	^e D _{Ni}	^f Δt _{R(IV_{t=t_e})}	^g r _{R_Hydr}	^h A _{SNi}
	wt%	wt%	wt%	m ² g ⁻¹	μmolg ⁻¹	μmolg ⁻¹	m ² _{Ni} g ⁻¹ _{Ni}	%	min	mmolH ₂ min ⁻¹	mmolH ₂ min ⁻¹ g ⁻¹ _{Ni}
Ag _{1-Ni/D}	35.94	0.16	-	164	254.8	708.9	55.4	8.3	81	95.8	106.6
Ag _{2-Ni/D}	35.16	1.55	-	157	189.1	537.8	42.1	6.3	155	50.8	57.8
Ag _{3-Ni/D}	33.51	5.88	-	136	172.1	513.5	40.2	6.0	255	30.9	36.9
Cu _{1-Ni/D}	33.15	-	1.50	151	158.5	478.1	37.4	5.6	115	66.3	80.0
Cu _{2-Ni/D}	31.40	-	3.38	121	133.7	425.7	33.3	5.0	235	33.0	42.1
Cu _{3-Ni/D}	29.63	-	6.73	94	86.3	291.1	22.8	3.4	400	19.6	26.5

^aAbbreviated designation for sample; ^bAmount of chemisorbed H₂ per gram of sample; ^cAmount of chemisorbed H₂ per gram of nickel; ^dSpecific surface of metallic nickel; ^eDispersion of Ni: $D_{Ni} = N_{i, surface} / N_{i, load}$; ^fTime of reaction;

^gRate of reaction; ^hSpecific activity of catalyst sample per gram of nickel.

The hydrogenation activity (A_{SNi}) of the M-Ni/D catalysts is represented as a ratio of the iodine value change (measure for the decrease of unsaturated $-C=C-$ bonds in the hydrogenated oil) $\Delta IV_{t_0-t_e} = IV_{t_0} - IV_{t_e}$ (from starting $IV_{t=t_0} = 130$ to ending $IV_{t=t_e} = 90.4 \pm 0.8$ corresponding to a total decrease of iodine value of 39.6 ± 0.6) and elapsed time of reaction ($\Delta t_{R(IV_{t=t_e})}$) required for reaching $IV_{t=t_e}$.

Figure 1a shows the H₂-chemisorption isotherms of the studied catalyst samples. Functional relationship between the dispersive characteristics of M-Ni/D catalysts represented by average crystallite size of Ni (\bar{d}_{Ni}) and their hydrogenation activities, is shown in Figure 1b.

In the first estimate we used total hydrogen uptake (Figure 1a) to determine the number of accessible nickel atoms (Table 1). However, we have already discussed that this estimate may not seem realistic, concerning the true number of sites for hydrogenation of unsaturated oil molecules [3]. Hydrogenation rates, as well as specific activity (Table 1), have been claimed as a source of actually available surface sites better than hydrogen chemisorption data (Table 1, Figure 1a and b).

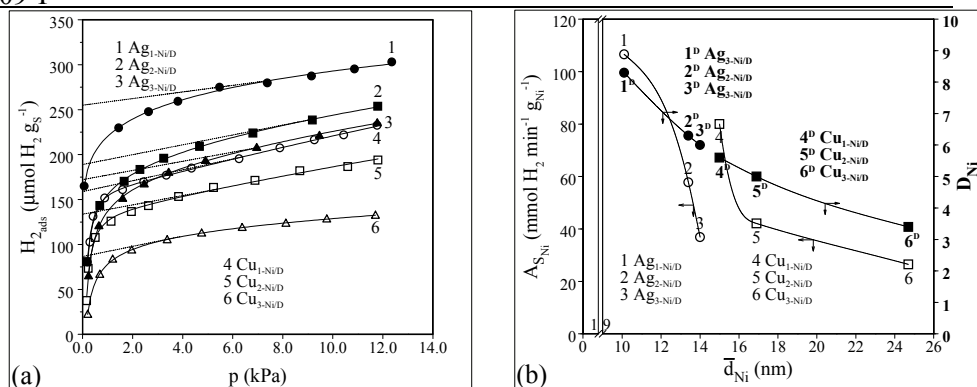


Figure 1. (a) H₂ chemisorption isotherms; (b) specific activity vs. average Ni particle.

In order to explain these results, two hypotheses could be used. Although there is still a great controversy about the mechanism of edible oil hydrogenation on nickel catalysts, it was postulated that the hydrogenation of edible oil on nickel is structure-insensitive [4]. Hence, the sharp drop obtained for the hydrogenation activity (Figure 1b) can be explained as a result of a dramatic inhibition of adsorption of unsaturated oil molecules. It can be assumed that there is a physical blocking of the nickel surface sites or changes in the morphology of the metallic particles by ad-metal took place here. It is difficult to discriminate between these different possibilities.

Apart from the effect of ad-metal blocking the surface nickel atoms for oil molecules adsorption, it should also be noted that an electronic effect has been taken into account. The role of ad-metal (Ag, Cu) can be generally explained by modification of the electronic state of nickel due to the electron donor character of the ad-metal - Ag: [Kr].4d¹⁰.5s¹; Cu: [Ar].3d¹⁰.4s¹.

Conclusion

Strong effect of the ad-metal (Ag, Cu) on chemisorptive and textural characteristics of M-Ni/D catalysts was observed. The Ag-Ni/D catalysts had larger H₂-chemisorption capacity and higher specific surface compared with the Cu-Ni/D catalysts. The H₂-chemisorption ability and specific surface of M-Ni/D catalyst samples decreased significantly with the increasing of ad-metal (Ag, Cu) load. The hydrogenation activity of the M-Ni/D catalysts depended on the load of ad-metal (Ag, Cu); the activities in the series increased in the following order:

Ag: Ag_{1-Ni/D} > Ag_{2-Ni/D} > Ag_{3-Ni/D};

Cu: Cu_{1-Ni/D} > Cu_{2-Ni/D} > Cu_{3-Ni/D}.

Acknowledgment

This work is supported by the Ministry of Education and Science of the Republic of Serbia (Project III45001).

References

- [1] D. Jovanović, R. Radović, Lj. Mareš, M. Stanković, B. Marković, Catal. Today, 1998, 43, 21-28.
- [2] M. Gabrovska, J. Krstić, R. Edreva-Kardjieva, M. Stanković, D. Jovanović, Appl. Catal. A: Gen., 2006, 299, 73-83.

-
- [3] M. Stanković, M. Gabrovska, J. Krstić, P. Tzvetkov, M. Shopska, T. Tsacheva, P. Banković, R. Edreva-Kardjieva, D. Jovanović, *J. Mol. Catal. A: Chem.*, 2009, 297, 54-62.
- [4] J. Coenen, B. Linsen, Structure and activity of silica supported nickel catalysts, in: B. Linsen (Ed.), in: J. Fortuin, C. Okkerse, J. Steggerda (Co-eds). *Physical and Chemical Aspects of Adsorbents and Catalysts*, AP, New York, 1970.

PREPARATION AND CHARACTERIZATION OF HYDROGENATION Ni/D-DPU CATALYST PRECURSORS

M. Stanković¹, M. Shopska², Z. Vuković¹, V. Radonjić¹, D. Skala^{1,3}

¹*University of Belgrade, Institute of Chemistry, Technology and Metallurgy, Department of Catalysis and Chemical Engineering, Njegoševa 12, 11000 Belgrade, Serbia*

²*Institute of Catalysis, Bulgarian Academy of Sciences, Acad. G. Bonchev str., bl. 11, 1133 Sofia, Bulgaria*

³*University of Belgrade, Faculty of Technology and Metallurgy, Karnegijeva 4, 11000 Belgrade, Serbia*

Abstract

Hydrogenation nickel catalyst precursors, supported on diatomite (Ni/D), were prepared by the homogenous basification of nickel(II)-nitrate solution/diatomite suspension *via* the decomposition of urea. The precipitation of Ni(II) phase onto diatomite surface using deposition-precipitation urea (DPU) method was performed under different deposition-precipitation times (DPT). It was found that DPT was affecting the distribution of precipitated Ni(II) phases, resulting in an overall change in the precursor characteristics, especially textural, structural and reducible.

The evolution of the Ni/D-DPU precursors with increasing DPT was studied using N₂-physisorption, Hg-porosimetry, X-ray diffraction (XRD), infrared (IR), and temperature-programmed reduction (TPR) methods.

Introduction

The design of edible oils hydrogenation supported nickel metal catalysts goes through several preparation steps (formation of precursors by precipitation of Ni(II) phase onto the support surface, drying and reduction), all of them potentially contributing to the catalytic properties of the final material [1]. Research on nickel catalysts for edible oils hydrogenation was largely confined to nickel on an oxide supports, generally prepared using deposition-precipitation method. A drawback of these support materials is their reactivity toward nickel, which during preparation results in the formation precipitated Ni(II) phases that are reducible only at high reduction temperatures. For example, the procedure with urea, in which the degree of supersaturation is gradually increased, leads to the precipitation not only Ni(II)-hydroxide but also various Ni(II) phases produced in metal-support interaction [2].

In this paper we investigate the preparation of Ni/D-DPU catalyst precursors using urea-containing solutions for the homogenous deposition-precipitation of Ni(II) phases onto the diatomite surface under different DPT. Textural, structural and reducible properties of the precursor samples were determined using the following measurement techniques: N₂-physisorption, Hg-porosimetry, XRD, IR, and TPR.

Experimental

Materials. Diatomite (D) - chemically and thermally activated: origin-Kolubara Coal Basin; Nickel(II)-nitrat *zur Analyse: reagenzien* Merck; Urea, 99.3+% Solid Crystalline CO(NH₂)₂: Alfa Aesar; Nitric acid, 69% *reagent grade* HNO₃: Merck.

Preparation procedures. The Ni/D-DPU precursor samples were prepared by DPU method. Reaction mixture was prepared by mixing suspension containing Ni(II)-nitrate (0.28 mol dm⁻³), urea (0.84 mol dm⁻³), nitric acid (0.02 mol dm⁻³) and

diatomite support (2 g) at pre-fixed temperature (90°C) for different DPT (4, 12, and 20 h). Starting solutions were prepared by mixing the necessary amounts of solid reactants (nickel salt and urea) and liquids (nitric acid and water). Diatomite was put into a reaction vessel containing starting solutions, magnetically stirred. Reaction vessel was placed in a thermostatic water bath, preheated at the working temperature. After pre-fixed DPT, the reaction vessel was removed from the water bath and immersed in an ice-water mixture to quench the reaction. The precipitated solids were collected by filtration, washed, and dried at 120°C for 24 h.

Characterization. The nickel contents in the precursors were determined using standard method of quantitative analysis. Textural parameters of diatomite and precursors were obtained by N₂-physisorption (Sorptomatic 1990) and porosimetric (Porosimeter 2000; Macropore Unit 120) measurements. XRD patterns of the samples were recorded on a PW1710 Philips diffractometer using Cu-K α radiation ($\lambda = 0.154178$ nm). The IR measurements of the studied samples were carried out on a Perkin Elmer 983 G spectrometer. TPR studies were performed in a laboratory apparatus, in which the H₂ consumption was measured with a TC cell. Heating was carried out at a rate of 10°C min⁻¹ up to 900°C. TPR measurements of the prepared catalyst precursors were studied according to the criteria given by Monti et al. [3].

Results and Discussion

Ni contents and textural characteristics of the prepared samples are collected in Table 1. Results show that longer DPT caused a change in chemical composition and textural characteristics of the prepared precursor samples, manifested through the increase of nickel content and decrease in pore volume. In comparison to the diatomite support, containing mostly macropores, all precursor samples had a pore structure with pore sizes that characterize both macro- and mesopores. Despite the large amount of active metal entered, the prepared precursors had a very favorable distribution of pores and total porosity. It is known that reduction conditions in the final stage of preparing hydrogenation Ni/D-DPU catalyst may exhibit pronounced effect on the porous structure of the finished catalyst. A careful choice of reduction conditions can preserve the distribution of pores and total porosity, which would allow the use of Ni/D-DPU catalyst in the hydrogenation reactions of edible oils.

Table 1. Nickel content and textural characteristics of Ni/D_U catalysts and D support

Sample code/DPT	Ni content (wt%)	Hg-porosimetry			N ₂ -physisorption	
		Pore volume _{total} (cm ³ g ⁻¹)	Pore volume _{macro} (cm ³ g ⁻¹)	Porosity (P) (vol%)	Pore volume _{meso} (cm ³ g ⁻¹)	Pore volume _{micro} (cm ³ g ⁻¹)
Ni/D _{U-1} /DPT = 4 h	32.01	0.747	0.527	59.8	0.210	0.010
Ni/D _{U-2} /DPT = 12 h	35.37	0.661	0.478	51.6	0.174	0.009
Ni/D _{U-3} /DPT = 20 h	39.35	0.575	0.462	48.9	0.106	0.007
^a D _{support}	-	1.447	1.408	77.9	0.039	-

^aNote: Surface area of D_{support} determined according to the BET method was 20.4 m²g⁻¹.

Figure 1a presents X-ray diffraction patterns for the precursor samples dried at 120°C. The diffractograms are similar to those previously reported [2] for Ni/SiO₂-dried samples and are characteristic for Ni(II) phase in a layered silicate structure. However, the results obtained here suggest that we cannot rule out the presence of the Ni(II)-hydroxide, whose X-ray diffraction patterns may be masked by those of the layered silicate. Comparisons of the X-ray diffractograms in Fig. 1a show the effect of increased DPT on the amount of unreacted silica remaining in the precipitated solids. For longer DPT (12 and 20 h) the broad band of amorphous silica at about 4.2 Å disappears, and the XRD pattern is better resolved.

C-10-P

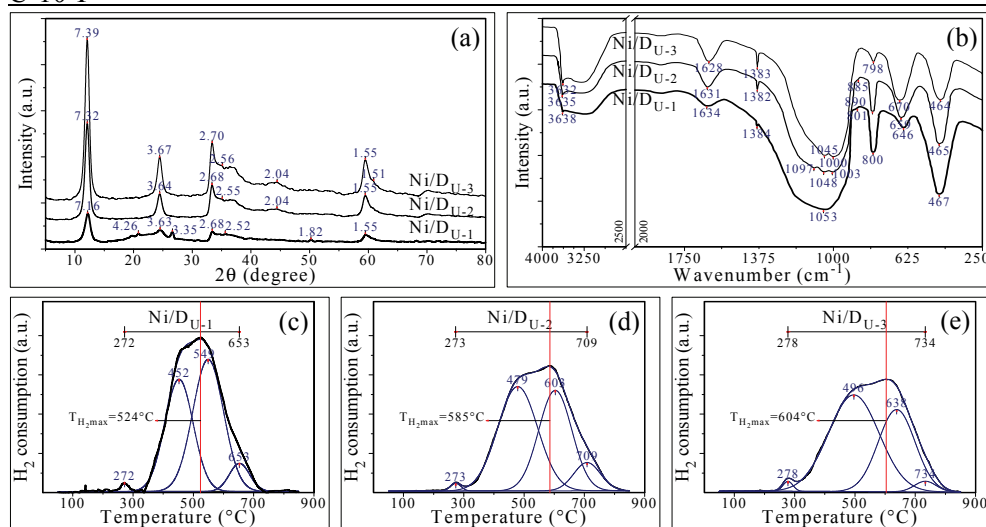


Figure 1. Characterization of Ni/D_U catalyst precursors: (a) XRD diffractograms, (b) IR spectra, (c-e) TPR profiles.

The IR spectra of Ni/D-DPU precursors (Fig. 1b) exhibit bands characteristic of SiO₄ tetrahedra in silica around 1100 cm⁻¹ (asymmetrical stretch), and at 800 cm⁻¹ (symmetrical stretch), and at 470 cm⁻¹ (bending), which have already been assigned [2]. When a single band in the 650-670 cm⁻¹ range is observed, it always concerns a poorly-crystallized phase (Fig. 1b). The nature of this ill-crystallized silicate phase (1:1 or 2:1 structure), or brucite-like phase (α -Ni-hydroxide) is questionable.

The reducibility of Ni(II) phases formed by thermal decomposition of samples was studied by TPR (Fig. 1c-e). Although the complexity of H₂ consumption profiles in TPR experiments made it difficult to identify the nature of Ni(II) phases and reduction steps, it is obvious that increasing DPT affects the difficulty of precursor reduction. These differences are most probably due to suppression in reducibility by formation of the less reducible nickel silicate layered structure.

Conclusion

Hydrogenation nickel catalyst precursors supported on diatomite were prepared by deposition-precipitation urea method under different deposition-precipitation times. Different times of deposition-precipitation affect considerable variation in textural, structural and reducible characteristics of prepared precursor samples.

The results obtained show that longer deposition-precipitation time increases nickel content and reduces the pore volume. Structural changes are believed to be due to an increase of Ni(II) layered silicates produced in metal-support interaction, which are difficult to convert to metallic nickel during reduction treatments.

Acknowledgment

This work is supported by the Ministry of Education and Science of the Republic of Serbia (Project III45001).

References

- [1] D. Jovanović, R. Radović, Lj. Mareš, M. Stanković, B. Marković, *Catal. Today*, 1998, 43, 21-28.
- [2] P. Burattin, C. Louis, M. Che, *J. Phys. Chem. B*, 1997, 101, 7060-7074.
- [3] D.A.M. Monti, A. Baiker, *J. Catal.*, 1983, 83(2), 323-335.

INHIBITION OF TRANSGLYCOSYLATION SYNTHESIS OF BENZYL ALCOHOL GLUCOSIDE BY GLUCOSYL ACCEPTOR

M. Pavlović¹, A. Dimitrijević¹, J. Trbojević¹, N. Milosavić¹,
M. Gavrović-Jankulović¹, D. Bezbradica², D. Veličković¹

¹ Faculty of Chemistry, University of Belgrade, Studentski trg 12, 11000 Belgrade, Serbia

² Faculty of Technology and Metallurgy, University of Belgrade, Karnegijeva 4, 11000 Belgrade, Serbia

Abstract

In this paper we examined kinetically mechanism for transglucosylation reaction of benzyl alcohol. Glucoside synthesis is performed by Ping-Pong mechanism with inhibition by both substrates (benzyl alcohol and maltose). We determined all kinetically constants for both substrates of this reaction and found out that this reaction is very strong inhibited by glucose acceptor.

Introduction

Transglycosylation is a mechanism of glycosidic bond formation in which a glycosyl moiety from a donor compound is transferred to the hydroxyl group of an acceptor molecule other than water. If molecule of water is acceptor of glycosyl moiety, reaction is termed as primary hydrolysis [1]. Although, glycosyl transferases *in vivo* mediate highly regioselective formation of glycosidic bonds, glycosidases are less expensive and more stable in experimental conditions. *In vivo* glycosidases catalyse the hydrolytic reaction and *in vitro*, by different medium manipulation [2], they can be used for glycoside synthesis [3]. Because a lot of different molecules are involved in transglucosylation reaction [4], it is very hard to determined type of these enzymatic reactions. It is well known that a lot of transglucosylation reactions are inhibited by excess of glycosyl donor [5], but very rare with glycosyl acceptor [6]. In this paper we have investigated kinetic of transglucosylation synthesis of benzyl alcohol glucoside by maltase from *S. cerevisiae*, and determined all relevant kinetic constants for this system.

Experimental

8 different concentration of maltose (0.2%, 1%, 5%, 10%, 30%, 40%, 50 % and 60%, (w/v)) was varied with 7 different benzyl alcohol concentration (2.2 mM, 10 mM, 30 mM, 50 mM, 100 mM, 150 mM i 220mM). Reactions were incubated at 36°C and pH of reactions were 6.5. Maltase concentration was 0.191 U/mL. Aliquots are withdrawn in different period of time and quenched by acidification at pH 3. After centrifugation samples were applied at HPLC column. Column used was Waters Spherisorb ODS2 4.6 x 250 mm, analytical Column. Mobile phase was 45% methanol with 1mM phosphoric acid in isocratic mode, at flow rate of

C-11-P

1.0 mL/min. Peaks were monitored using UV detector at 257 nm. From concentration/time curve for each experimental point it was calculated initial velocities (v_0). Using MATLAB software it was calculated K_m , V_{max} and inhibition constants of this reaction when experimental results (dependence of rate of reaction from substrates concentrations) were fitted with most adequate model.

Results and discussion

Influence of different concentration of substrates at transglucosylation rate was presented at Fig. 1 as 3D plot.

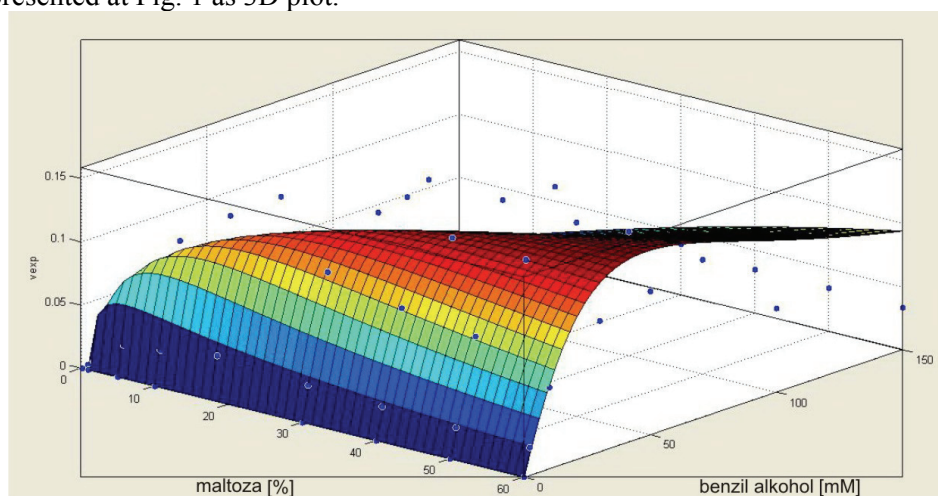


Figure 1. Influence of maltose and benzyl alcohol concentration at rate of transglucosylation reaction. Blue spots present experimental values which are fitted for ping-pong mechanism with inhibition by both substrates (curve).

As it can be seen from experimental values there are strong inhibition of benzyl alcohol glucoside synthesis by benzyl alcohol and mild inhibition by excess of maltose. For that reason experimental values were fitted by models that describes inhibition by both substrates. The most adequate model was ping-pong, which could be described by following equation:

$$v = \frac{V_{max}[A][M]}{K_m^M[A] \left(1 + \frac{[A]}{K_{i,A}} \right) + K_m^A[M] \left(1 + \frac{[M]}{K_{i,M}} \right) + [A][M]}$$

where A is benzyl alcohol; M is maltose; V_{max} is maximal rate of transglucosylation reaction; K_m^A is Michaelis constant toward benzyl alcohol in saturated concentration of maltose; K_m^M is Michaelis constant toward maltose in saturated concentration of benzyl alcohol; $K_{i,M}$ inhibition constant of maltose to maltase; $K_{i,A}$ inhibition constant of benzyl alcohol to maltase.

Kinetic constants for this transglucosylation reaction are determined to be:

Table 1. Kinetic constants for transglucosylation synthesis of benzyl alcohol glucoside by maltase from *S.cerevisiae*. $K_{s,A}$ specific constant of maltase for benzyl alcohol; $K_{s,M}$ specific constant of maltase for maltose.

Constant	Value of constant
V_{max}	0.7 mM/min
K_m^A	24.31mM
K_m^M	1.953% (57mM)
$K_{i,A}$	0.834 mM
$K_{i,M}$	21.72% (634mM)
$K_{s,A}$	0.029 min ⁻¹
$K_{s,M}$	0.012 min ⁻¹

From the specific constants of this transglucosylation reaction, it is obvious that maltase has almost three times higher affinity toward glucosyl acceptor than glucosyl donor. However, it is very interesting very low inhibition constant for benzyl alcohol, indicated that although maltase has very high affinity toward this substrate, benzyl alcohol inhibits its own glucosylation very strong.

Conclusion

It was shown that maltase catalyse transglucosylation of benzyl alcohol by ping pong mechanism with mild inhibition by maltose and strong inhibition by glucose acceptor. These results of maltase enzyme kinetic can be very usefull for synthesis of maltase inhibitors which are known to be very potent in HIV prevention.

Acknowledgments

The authors are grateful for the financial support of the Ministry of Science of the Republic of Serbia (Project No. 172049, Project No.046010 and 451-03-00605/2012-16/51).

References

- [1] F.van Rantwijk, M. W. V. Oosterom, R. A. Sheldon, Journal of Molecular Catalysis B-Enzymatic, 1999, 6(6),511-532.
- [2] D.Velickovic, A. Dimitrijevic, F. Bihelovic, D. Bezbradica, R. Jankov, N. Milosavic, Process Biochemistry, 2011, 46(8),1698-1702.
- [3] D. H. G. Crout, G. Vic, Current Opinion in Chemical Biology, 1998, 2(1), 98-111.
- [4] D. Velickovic, A. Dimitrijevic, F. Bihelovic, R. Jankov, N. Milosavic, Russian Journal of Physical Chemistry A, 2011, 85(13),2317-2321.
- [5] R. Kawai, K. Igarashi, M. Kitaoka, T. Ishii, M. Samejima, Carbohydrate Research, 2004, 339,2851-2857.
- [6] D.E. Stevenson, R.A. Stanley, R.H. Furneaux, Enzyme and microbial technology, 1996, 18, 544-549.

C-12-P

APPLICATION OF MULTIVARIATE CURVE RESOLUTION-ALTERNATING LEAST SQUARES (MCR- ALS) METHOD FOR THE STUDY OF CU(II) ION INFLUENCE ON THE PYROGALLOL AUTOXIDATION IN AQUEOUS SOLUTION

G. M. Nikolić, A. M. Veselinović, Ž. J. Mitić, F. S. Miljković

*University of Niš, Faculty of Medicine, Department of Chemistry, 18000 Niš,
Serbia*

e-mail: goranhem@yahoo.com

Abstract

Multivariate curve resolution-alternating least squares (MCR-ALS) method has been applied for the analysis of UV/Vis spectra recorded during the autoxidation of pyrogallol in aqueous solutions. Autoxidation of pyrogallol was performed at pH 7.4 in pure aqueous solution and in the presence of Cu(II) ions. By using MCR-ALS we were able to obtain spectra of individual components formed during the reaction as well as their concentration profiles. In both autoxidation processes reaction followed the first order reaction kinetics. For the system without Cu(II) ions purpurogallin was found to be the main autoxidation product. Presence of Cu(II) ions greatly influenced the autoxidation of pyrogallol in terms of increased reaction rate and formation of different autoxidation product(s).

Introduction

Pyrogallol (1,2,3-benzenetriol) is commonly used in many industries and consumer products and is also very important because pyrogallol-type structure is often present in many physiologically active compounds of various plants [1]. Pyrogallol autoxidation in biological systems may generate free radicals and presents a significant source of reactive oxygen species [2]. It is well documented that the presence of Cu(II) ions can influence the antioxidant properties of various phenolic compounds including those containing pyrogallol-type structures [3, 4]. In this study the influence of Cu(II) ions on the pyrogallol autoxidation in aqueous solutions at physiological pH was studied by UV/Vis spectrophotometry. A soft MCR-ALS technique [5] was employed to obtain information about spectral profiles of compounds formed during the autoxidation process.

Experimental

Materials and methods

All the chemicals used in this study were of analytical (p.a.) grade. Deionized, air saturated, water was used and pyrogallol solutions with concentration of 0.5 mmol dm^{-3} were prepared just prior the use by dissolving exactly weighted amount of

pyrogallol. Autoxidation process was initiated by mixing pyrogallol solution with equal volume of phosphate buffer (pH 7.4, $C(\text{Cu}) = 0$) - solution A or phosphate buffer (pH 7.4, $C(\text{Cu}) = 0.25 \text{ mmol dm}^{-3}$) - solution B. Evolution 60 UV/Vis spectrophotometer (Thermo Scientific, USA) with 1.0 cm quartz cells was used for recording spectra in the 220-700 nm range at regular time intervals of 5 min for solution A, and 2 min for solution B. In order to prevent possible complexation of Cu(II) ions with pyrogallol or some autoxidation products, all spectra were recorded after mixing 1 cm^3 of working solution with 1 cm^3 EDTA solution (0.5 mmol dm^{-3}). Spectra were recorded against blank solutions which contained all compounds except pyrogallol in adequate concentrations.

Chemometrics

The aim of MCR-ALS is to find the theoretical solution by factor analysis of the experimental data matrix D , and obtain the matrices C and S^T which have real chemical significance [5]. With this curve resolution method the data matrices are modeled according to the following equation:

$$D = C \times S^T + E$$

where D is data matrix of the spectra, matrix $C(m \times p)$ has column vectors corresponding to the concentration profiles of the p pure components that are present in matrix D . The row vectors of matrix $S^T (p \times n)$ correspond to the spectra of pure p components, and E is the matrix of the residuals. Both matrices D and E have dimensions $m \times n$. Computations were performed with the MATLAB software (Mathwork Inc., version 7.12) and MCR-ALS user-friendly interface tool [6].

Results and Discussion

The spectra recorded during the autoxidation of pyrogallol in solutions A and B are shown in Figure 1, together with the MCR-ALS resolved pure spectral components and their concentration profiles. For solution A two species were indicated with their concentration profiles following the first order kinetics. One component (a) was pyrogallol while other component (b) was probably purpurogallin since its spectrum obtained by MCR-ALS was very similar to the spectrum already reported in the literature [7]. After approximately 2 hours only purpogallin was detected in solution A. The presence of Cu(II) ions in solution B increased the autoxidation rate of pyrogallol although reaction again followed the first order kinetics. Also, different reaction product was formed (spectrum b). Changes in the autoxidation process of pyrogallol induced by the presence of Cu(II) ions may be explained by the fact that Cu(II) ions have ability to generate hydroxyl radicals in the interaction with polyphenolic compounds. MCR-ALS resolved UV/Vis spectra can not give the conclusive answer about the structure of pyrogallol autoxidation product in the presence of Cu(II) ions but the appearance of intensive absorption maximum at higher wavelengths might indicate that some kind of condensation product was formed.

C-12-P

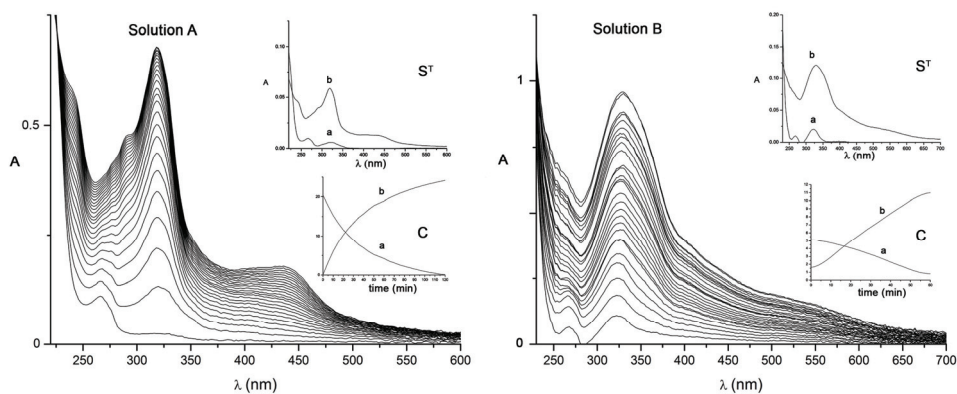


Figure 1. UV/Vis spectra recorded during the pyrogallol autoxidation in solution A and solution B. MCR-ALS resolved concentration profiles and spectra of pure compounds obtained by the analysis of UV/Vis spectra for the individual autoxidation processes are shown as insets.

Conclusion

We performed a spectrophotometric study of pyrogallol autoxidation at pH 7.4 in pure aqueous solution and in the presence of Cu(II) ions. MCR-ALS resolved concentration profiles and spectra of pure compounds indicated that presence of Cu(II) ions had profound effect on the autoxidation of pyrogallol. Based on the UV/Vis spectra of pure compounds we concluded that main autoxidation product of pyrogallol in pure aqueous solution was purpurogallin while in the presence of Cu(II) ions probably some kind of condensation product was formed.

Acknowledgments

This work was supported by the Ministry of Education and Science of the Republic of Serbia under the project no. 172044.

References

- [1] K. Saeki, S. Hayakawa, M. Isemura, T. Miyase, *Phytochemistry*, 2000, 53, 391-394.
- [2] W. H. Park, Y.H. Han, S. H. Kim, S. Z Kim, *Toxicology*, 2007, 235, 130-139.
- [3] J. E. Brown, H. Khodr, R. C. Hider, C. A. Rice-Evans, *Biochem. J.*, 1998, 330, 1173-1178.
- [4] J. F. Severino, B. A. Goodman, T. G. Reichenauer, K .F. Pirker, *Free. Radical. Res.*, 2011, 45, 123-132.
- [5] R. Tauler, *Chemom. Intell. Lab. Syst.*, 1995, 30, 133-146.
- [6] A. D. Juan, R. Tauler, J. Jaumont, <http://www.mcrals.info> (accessed 21.01.2012).
- [7] S. M. Siegel, B. Z. Siegel, *Nature*, 1958, 181, 1153-1154.

MECHANISM AND KINETICS OF DEGRADATION OF *D* METAL COMPLEXES WITH *N*-BENZYLOXICARBONYLGLYCINATO LIGAND

D. M. Minić¹, M. Šumar Ristović², A. Grković¹, V. Blagojević¹, D. Poletić³,
K. Anđelković²

¹*Faculty of Physical Chemistry, University of Belgrade, Serbia*

²*Faculty of Chemistry, University of Belgrade, Serbia*

³*Department of General and Inorganic Chemistry, Faculty of Technology and Metallurgy, University of Belgrade, Serbia*

Abstract

Thermal behavior of Co(II), Cd(II) and Zn(II) complexes with *N*-benzyloxycarbonylglycinato ligand was investigated using the results of TG, DTA and DTG analysis obtained at different heating rates (5 to 25°C min⁻¹), from room temperature to about 900 °C. Mechanisms of complex degradation, as well as kinetics of the degradation processes for each compound, were determined. Complex degradation processes were deconvoluted to obtain kinetic triplets of individual steps. The results indicate that each of the compounds exhibits distinct mechanism of thermal degradation.

Introduction

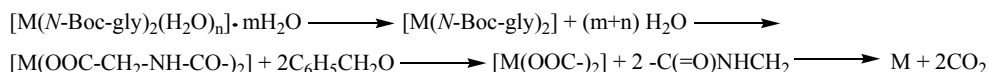
The synthesis, characterization, antimicrobial and antifungal activity of Co(II), Cd(II) and Zn(II) complexes with the *N*-benzyloxycarbonylglycinato (*N*-Boc-gly) ligand have been previously investigated [1]. Although all three studied compounds are *d* metal complexes incorporating the same ligand, their chemical compositions and crystal structures are different. Difference in chemical composition comes from the presence of water molecules in inner or outer sphere of individual complexes. Co(II) complex, with water molecules in inner and outer sphere, exhibits octahedral geometry, Cd(II) complex, with water molecules in inner sphere, exhibits pentagonal-bipyramidal polymeric structure and Zn(II) complex, containing no water molecules, exhibits tetrahedral geometry. Because of these differences, different mechanisms and kinetics of degradation of the investigated substances are expected.

Results and discussion

Thermal degradation of Co(II) and Cd(II) complexes occurs in four, whereas that of Zn(II) complex occurs in three main steps. In complexes containing water molecules in inner and/or outer sphere (Co(II) and Cd(II)), multi step degradation starts with loss of crystalline and coordinated water molecules, respectively. First step of degradation of dehydrated complexes involves the loss of two C₆H₅CH₂O- fragments, and ligand chain degradation continues in the second step with loss of two -C(=O)NHCH₂- fragments. The last stage of degradation involves the loss of two molecules of CO₂ and part of Cd or Zn (in Cd(II) and Zn(II) complex,

C-13-P

respectively). Therefore, it is likely that defragmentation of ligand chains occurs with similar mechanism for all three complexes. In light of this, we suggested the mechanism of degradation for all three complexes as follows:



M= Co, Cd, Zn

n= 4, 2, 0; respectively

m= 2, 0, 0; respectively

The kinetics of multi-step thermal degradation of Co(II), Cd(II) and Zn(II) complexes with *N*-benzyloxycarbonylglycinato ligand in non-isothermal conditions was studied using isoconversional (Kissinger-Akahira-Sunose's (KAS)) method [2, 3]. The calculated values of the apparent activation energies, E_a as a function of the conversion degree for different degradation steps of all three complexes, calculated using KAS method, are shown in Fig. 1. Changes of the apparent activation energies with conversion degree indicate complex processes involving more than one step. Different shapes for all complex processes indicates different mechanisms, which is expected taking into account the structure of the complex and the nature of the degradation fragments.

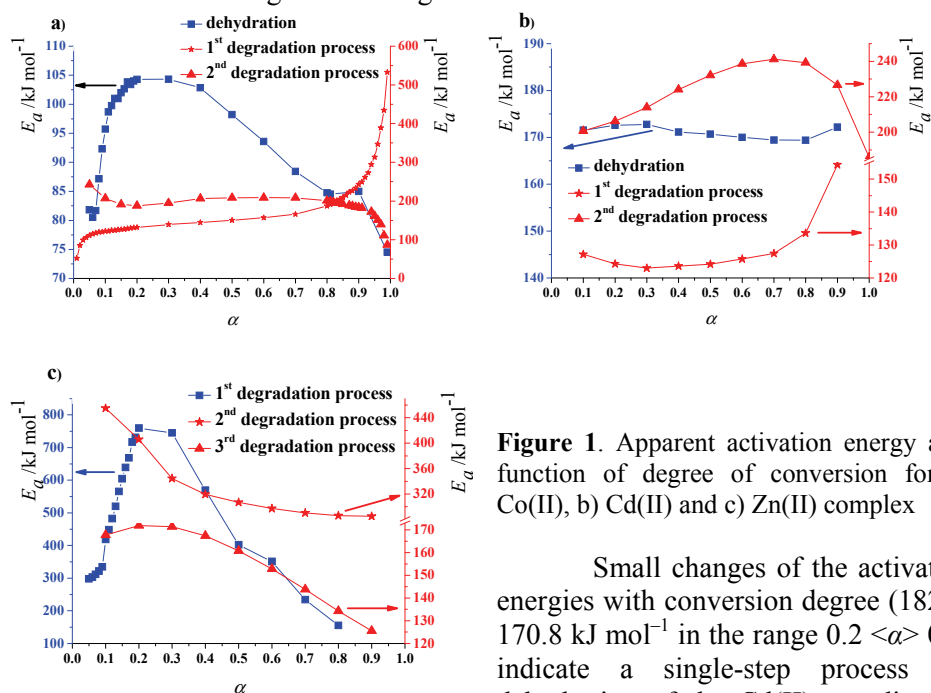


Figure 1. Apparent activation energy as a function of degree of conversion for a) Co(II), b) Cd(II) and c) Zn(II) complex

Small changes of the activation energies with conversion degree (182.8-170.8 kJ mol^{-1} in the range $0.2 < \alpha < 0.8$) indicate a single-step process for dehydration of the Cd(II) coordination polymer (Fig. 1b), with the average value of $E_a = 171.1 \pm 1.2 \text{ kJ mol}^{-1}$. Application of Vyazovkin's algorithm suggests that the degradation consists of parallel and consecutive reactions [4]. Complexity of the degradation processes have led us to deconvolute the complex curves in order to obtain data for individual steps that can

be modeled. Kinetic triplets for these individual steps are given in Table 1. In all complexes, thermal degradation process is always preceded by an additional step, which probably entails structural changes necessary for subsequent degradation, but whose exact nature could not be determined. The difference in values of apparent activation energies of equivalent steps in different complexes can be attributed to their different structure, where dehydrated Co(II) and Cd(II) complexes have planar coordination, while Zn(II) is close to tetragonal, making it more stable.

Table 1. Kinetic triplets for all individual steps of degradation (apparent activation energy, E_a , pre-exponential factor, Z and reaction model, $f(\alpha)$).

		E_a /kJ mol ⁻¹	Z /min ⁻¹	$f(\alpha)$
Co(II) complex degradation I	Step 1	137.4	$1.1 \cdot 10^{15}$	$\alpha^{0.44}(1-\alpha)^{1.18}$
	Step 2	168.4	$1.0 \cdot 10^{18}$	$\alpha^{0.36}(1-\alpha)^{1.46}$
Cd(II) complex degradation I	Step 1	125.0	$3.2 \cdot 10^{13}$	$\alpha^{0.59}(1-\alpha)^{1.36}$
	Step 2	130.4	$3.5 \cdot 10^{13}$	$\alpha^{0.56}(1-\alpha)^{1.30}$
Zn(II) complex degradation I	Step 1	535.3	$8.5 \cdot 10^{57}$	$\alpha^{0.19}(1-\alpha)^{1.68}$
	Step 2	254.0	$1.5 \cdot 10^{27}$	$\alpha^{0.52}(1-\alpha)^{1.21}$

Conclusion

Multi-step thermal degradation of Co(II), Cd(II) and Zn(II) complexes with *N*-benzyloxycarbonylglycinato ligand was investigated and all degradation processes, except dehydration of Cd(II) complex, were found to be complex, involving more than one elementary step. Kinetic triplets for each individual step were determined, suggesting that different compounds exhibit different mechanisms of thermal degradation.

References

- [1] Đ. U. Miodragović, D. M. Mitić, Z. M. Miodragović, G. A. Bogdanović, Ž. J. Vitnik, M. D. Vitorović, M. Đ. Radulović, B. J. Nastasijević, I. O. Juranić, K. K. Anđelković, *Inorg. Chim. Acta*, 2008, 361, 86-94.
- [2] H. E. Kissinger, *Anal. Chem.*, 1957, 29, 1702-1706.
- [3] T. Akahira, T. Sunose, *Trans. Joint Convention of Four Electrical Institutes*, Paper No. 246, 1969. *Res. Rep. Chiba Inst. TechnolSci Technol.*, 1971, 16, 22-31.
- [4] S. Vyazovkin, A.I. Lesnikovich, *Thermochim. Acta*, 1990, 273-280.

C-14-P

THE EFFECT CO-SOLVENT ON KINETICS OF TRANSESTERIFICATION OF SUNFLOWER OIL

B. Adnadjević, B. Beljić Durković, T. Djajić, J. Jovanović

*Faculty of Physical Chemistry, Belgrade University, Studentski Trg 12-16,
Belgrade, 11050, R. Serbia*

Abstract

The effect of introducing co-solvent in reaction system on the kinetics of transesterification of sunflower oil (TESO) was investigated. It was found that co-solvent introduce leads to the considerable increase in the transesterification rate, change in kinetics model of transesterification and decrease in the activation energy of the process. The established changes in the kinetics of transesterification of sunflower oil are explained with the increasing rate of the mass transfer between oil and methanol, which is caused with the one-phase reaction system formation.

Introduction

The transesterification rate for fatty acid methyl ester (FAME) production is limited by agitation efficiency, temperature, alcohol amount and/or catalyst [1]. Boocock et al. [2] developed a new procedure of a single-phase process for FAME preparation based on the introduce of an inert co-solvent in the reaction system. With that in mind, in this work, the effect of co-solvent introduced in the reaction system for FAME preparation was investigated in detail (kinetics model, parameters, complexity).

Materials and Methods

Materials for FAME preparation: refined commercial sunflower oil, purchased from "Dijamant"(Serbia); Methanol 100%, supplied from VWA International S.A.S, France; Sodium methoxide, 30% solution in methanol, purchased from Acros Organics, USA; and Tetrahydrofuran 99%, purchased from J.T.Baker, Holland.

Preparation of FAME: Transesterification reactions of sunflower oil were performed in a 250-L three-necked flask equipped with a reflux condenser, a thermometer, and a sampling port. The reactor was immersed in a constant-temperature water bath equipped with a temperature controlled, that was capable of maintaining the temperature within $\pm 0,2^{\circ}\text{C}$. Agitation was provided with a magnetic stirrer, which was set at a constant speed throughout the experiment. Initially, the reactor was filled with 50g sunflower oil and heated to the desired temperature. A known amount of sodium methoxide (the catalyst) was dissolved in the required amount of methanol and heated separately to desired temperature. Subsequently, this methanolic CH_3ONa was added to the preheated oil. At predetermined time intervals, aliquots were withdrawn and the content of FAME was determined. Content of methyl esters of fatty acids in ester-phase was

determined by gas chromatography (GC). Analyses were performed on Hewlett-Packard, 5880A series gas chromatograph equipped with an on-column injector, a flame-ionization detector (FID) and a DB-1 fused silica capillary column.

Results and discussion

Figures 1 and 2 presents kinetics curves of TESO without and with introduced co-solvent, respectively.

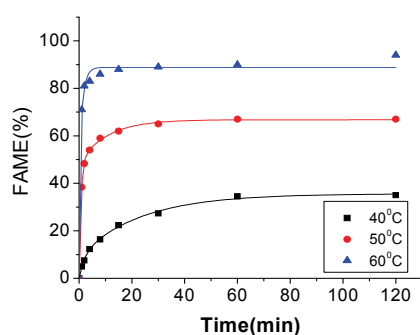


Figure 1. Kinetics curves of TESO without co-solvent.

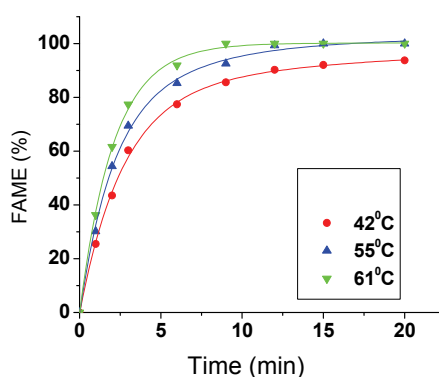


Figure 2. Kinetics curves of TESO with co-solvent.

As can be seen, the introduce of co-solvent leads to considerably increase in rate of transesterification and to changes in the kinetics curves shapes.

By the analyses of kinetics curves it was found that the kinetics of TESO in a two-phase system can be modeled with the kinetics model of chemical reaction of second order:

$$\alpha = \frac{kt}{1 + kt} \quad (1),$$

whereas in an one-phase system it can be modeled with first order kinetics:

$$\alpha = 1 - \exp(-kt) \quad (2)$$

where: α is normalized degree of conversion of FAME and k is model's rate constant.

By linearization of (1) and (2), the values of model's rate constant of transesterification of sunflower oil in a two- and one-phase system, were determined.

Table 1, presents the effect of temperature on the determined values of model's rate constant of transesterification of sunflower oil.

Table 1. The effect of temperature on the values of model's rate constant of transesterification of sunflower oil.

Without co-solvent			With co-solvent		
T (°C)	k(min ⁻¹)	kinetics parameters	T (°C)	k(min ⁻¹)	kinetics parameters
40	0.35±0.02	Ea=73kJ/mol ln (A/min ⁻¹)=27	42	0.311±0.004	Ea=11 kJ/mol ln (A/min ⁻¹)=3
50	0.71±0.02		55	0.353±0.005	
60	1.59±0.09		61	0.44±0.02	

Significant increase in the rate of transesterification of sunflower oil which was caused with the introduce of a co-solvent in a reaction system can be explained as a consequence of increased rate of mass transfer of a triglyceride in a methanol phase which – happens due to the disappearance of boundary phase between oil and methanol.

Due to that, kinetics of transesterification is determined with the concentration of triglyceride in methanol phase and apparent energy of activation, first of all for triglyceride conversion to diglyceride, is almost 7 lower than in the case of two-phase system.

Conclusion

The introduce of co-solvent in reaction system in which occurs transesterification of sunflower oil leads to the one-phase reaction system formation, which in turn leads to the changes in the kinetics model of transesterification, decrease in the values of Ea and to significant increase in the rate of transesterification.

Acknowledgements

This investigation was supported by the Ministry of Science and Technical Development of the Republic of Serbia through project 172015OI.

Literature

- [1] J. Park, D.Kim, Zh. Wang, J.Lee, Fast biodiesel production with one-phase reaction, *Appl. Biochem. Biotechnol*, 2009, 154, 246-252.
- [2] D. Boocock, Single-phase process for production of fatty acid methyl esters from mixture of triglyceride and fatty acids, 2003, USA patent 6642399.

KINETICS OF OSMOTIC DRYING OF ALGINATE BEADS

D. Dimić, J. Jovanović, B. Adnađević

Faculty of Physical Chemistry, Univeristy of Belgrade, Studentski trg 12, Belgrade, Serbia

Abstract

The kinetics of osmotic drying of alginate beads in 50% sucrose solution was investigated. The isothermal kinetic curves were determined in the temperature range from 298 to 318 K. The kinetic model was found to be Jander's 3D diffusion, with the values of the kinetic parameters: $E_a=10.6$ kJ/mol, $\ln(A/s^{-1}) = -4.0$. The mechanism of the osmotic drying of alginate beads was established.

Introduction

Bioaerogels present novel class of materials with very attractive and specific physicochemical properties [1]. Their synthesis is usually based on the natural resources – hydrocolloid forming polysaccharides: alginate, carrageenan, and chitosan, by the method of supercritical drying or lyophilisation [2]. In order to develop new pathways of bioaerogels production, the kinetics of osmotic drying of alginate beads was examined.

Experimental

Materials for the alginate beads synthesis: Alginic acid sodium salt was purchased from Fluka Biochemica, Buchs, Switzerland. Sucrose (99.8 %) was supplied from Analytika, Ltd, Prague, Czech Republic. Calcium-chloride hexahydrate ($CaCl_2 \cdot 6H_2O$, p.a.) was purchased from Centrohem, Stara Pazova, Republic of Serbia.

Preparation of alginate beads: Sodium alginate was dissolved in distilled water at a concentration of 2% (w/w). The alginate solution was added dropwise at the room temperature to a stirred $CaCl_2$ (0.24 M) solution using a syringe with a 0.8 mm diameter needle. The spheres were left to completely cure solution for 24h.

Osmotic drying of alginate beads: 10 g of alginate beads was suspended in 50 ml of 50 wt % sucrose solution in the range of temperatures from 298 to 318 K. The reaction mixture was homogenized by stirring with the magnetic stirrer at the rate of 400 rpm. The sample of reaction mixture ($v=0.5$ ml) was taken and the sucrose concentration was determined using the refractometry method.

Results and Discussion

Figure 1. shows the kinetic curves of water loss from alginate beads in osmotic solution.

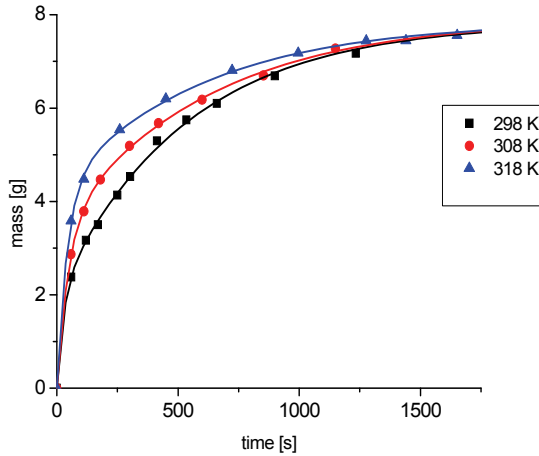


Figure 1. Kinetic curves of the water loss from alginate beads at different temperatures.

The kinetic curves are of the same shape, and have the characteristic saturation plateau.

Using the model fitting method [3], it was determined that the kinetics of the osmotic drying of alginate beads can be described by the Jander's equation, 3-D diffusion model:

$$\alpha = 1 - [1 - (k_m t)^{1/2}]^3 \tag{1}$$

where α presents the degree of dehydration of the alginate beads and k is the rate constant obtained from the model.

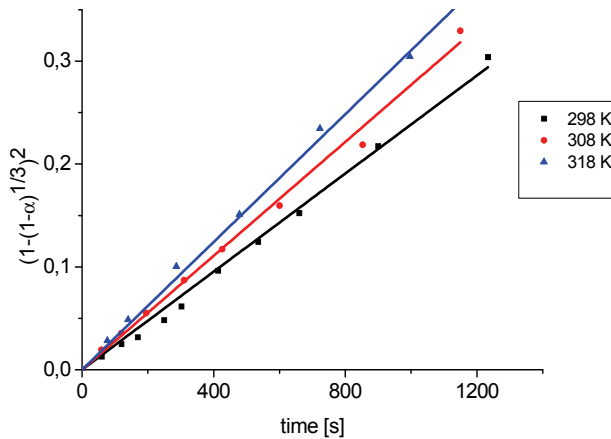


Figure 2. The plot of $[1 - (1 - \alpha)^{1/3}]^2$ versus time for osmotic drying of alginate beads.

If model was right the dependence of $[1 - (1 - \alpha)^{1/3}]^2$ on time should be linear, with the slope equal to k_m .

The dependence of $[1 - (1 - \alpha)^{1/3}]^2$ on time for the osmotic drying of alginate beads at different temperatures is presented in Figure 2.

Since all of the plots are the straight lines, it can

be said that the kinetic model described by eq. (1) determines the behavior of the system.

The values for the rate constants were obtained for different temperatures from the slope of the straight lines. The change of k with temperatures is shown in the Table 1.

Table 1. The effect of osmotic drying temperature on the k_m values and the kinetic parameters of the osmotic drying of alginate beads.

T / K	$k_m \cdot 10^4 / s^{-1}$	Range of applicability / %	Kinetic parameters
298	2.38	99.7	$E_a = (10.6 \pm 0.7) \text{ kJ/mol}$ $\ln(A/s^{-1}) = -4.0 \pm 0.3$
308	2.77	99.6	
318	3.11	99.1	

Because the k_m values exponentially increase with temperature, it was possible to determine the kinetic parameters (the activation energy, E_a , and preexponential factor, A) by using the Arrhenius equation. These values are presented in Table 1, column 4.

The osmotic drying is a novel and effective procedure for the bioaerogels preparation, which is kinetically controlled by the diffusion of water molecules from alginate beads to osmotic solution.

Conclusion

Osmotic drying is a very effective method for water removing from alginate beads. The drying kinetics is predetermined by the water diffusion from alginate beads to osmotic solution. The energy of activation of the investigated process was found to be 10.6 kJ/mol.

Acknowledgment

This paper was supported by Ministry of Education and Science, Republic of Serbia, under a project number 172015OI.

References

- [1] F. Quignard, R. Valentin, F. D. Renzo, *New Journal of Chemistry*, 32, 1300-1310
- [2] T. Mehling, I. Smirnova, U. Guenthen, R. Neuberl, *Journal of noncrystalline solids*, 2009, 355, 2472-2479
- [3] A. Khawam, D. R. Flanagan, *Physical Chemistry B*, 2006, 110, 17315-1732

C-16-P

A NOVEL APPROACH TO THE EXPLANATION THE EFFECTS OF MICROWAVE HEATING ON ISOTHERMAL KINETIC OF CROSSLINKING POLYMERIZATION OF ACRYLIC ACID

J. Jovanovic, B. Adnadjevic

Faculty of Physical Chemistry, University of Belgrade, Studentski Trg 12-16, 11001 Belgrade, R. Serbia

Abstract

The effect of microwave heating (MWH) on the isothermal kinetic of crosslinking-polymerization of acrylic acid (CPAA) was investigated. The reaction rate constants of CPAA were ~40 times higher for the MWH than for the conventionally heated (CH) process. The kinetics parameters (activation energy (E_a) and pre-exponential factor ($\ln A$)) of the CPAA are significantly lower than the corresponding values for CH process. Based on model of selective energy transfer a novel explanation of the effects of MWH on the kinetics of CPAA is suggested. A quantized nature and value of activation energy was confirmed. The decrease in the activation energy of CPAA under MWH is explained with the increased energy of ground vibration level of resonant oscillator ($\nu = 1417 \text{ cm}^{-1}$) in the acrylic acid (AA) molecule.

Introduction

The effect of microwave irradiation in chemical reactions and physico-chemical processes is ordinary explained as combination of thermal effects (overheating, hot-spots and selected heating as well as specific microwave effects. The issue of specific microwave effects is still a controversial matter. Several theories have been postulated and also some predicted models have been published [1]. A detailed comparative analysis of isothermal kinetics of investigated isothermal CPAA under the CH and MWH was performed in this work, including determination of kinetics model, values of kinetics parameters and complexity of kinetic with the aim of to find new explanation of the effects of MWH on the kinetics of chemical reactions.

Experimental

Materials: Acrylic acid was used as monomer, N,N-methylene bisacrylamide was crosslinker and the initiator was 2,2-Azobis-[2-(2-imidazoline-2-il)-propane dihydrochloride (VA044). **Synthesis:** CP of AA: was based on the general procedure of PAA hydrogel preparation described in our previous papers [2]. **The microwave-assisted** reactions were conducted in a commercially available monomode microwave unit. (Discover, CEM Corporation, Matthews, North

Carolina, USA). **Determination of the yield and the degree of CPAA:** The yield (Y , %) of the obtained product was determined gravimetrically and calculated as the ratio of the weight of the product W_t in time (t) and the weight of the monomers (monomer and crosslinker) in the reaction mixture (W_o): $Y = W_t / W_o$; whereas the degree of CP of AA (α) was calculated as: $\alpha = Y / Y_{\max}$; where Y is the yield of the obtained hydrogel at time t , and Y_{\max} is the maximum value of the hydrogel yield obtained at a certain temperature. Model-Fitting and Differential Isoconversion methods have been applied for evaluation the kinetic parameters of CP of AA.

Results and Discussion

Figure 1 shows the isothermal conversion curves of CPAA under conventional and microwave heating at different temperatures.

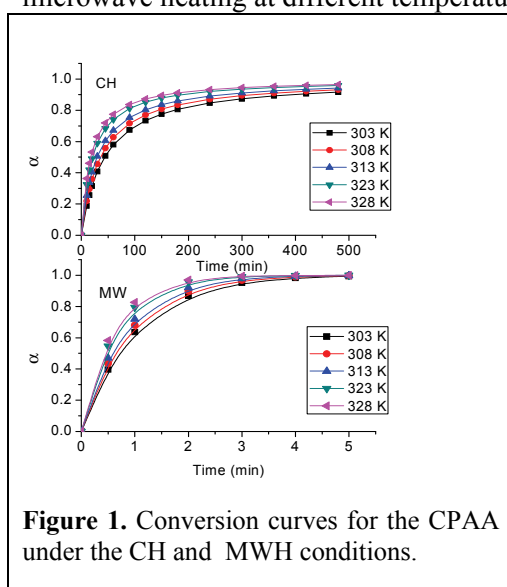


Figure 1. Conversion curves for the CPAA under the CH and MWH conditions.

It is clear from Figure 1 that microwave heating has a pronounced effect on the CP of AA, i.e. the degree of AA conversion is significantly increased for same temperature when microwave heating is applied. By using the “model fitting method”, it was found that the isothermal kinetics curves of CPAA during the CH can be described by the so-called kinetic model of a second-order chemical reaction and a first-order chemical reaction for MWH.

The postulated kinetic models was confirmed and enabled to calculate values of model rate constant of CPAA and calculate kinetic parameters (E_a and $\ln A$) by application the Arrhenius

Equation.

The values of the model’s rate constant for MWH were 34 to 44 times higher than the constants for the CH process depending on temperature. The energy of activation of CPAA under MWH was $E_a=18.6$ kJ/mol, which is 1.6 times lower than the energy of activation under CH ($E_a=29.6$ kJ/mol, while the $\ln A$ value is 10 % lower for the MW process.

Figure 2 presents the dependence of $E_{a,\alpha}$ on the degree of conversion for CPAA, obtained by application the Friedman’s differential isoconversional method.

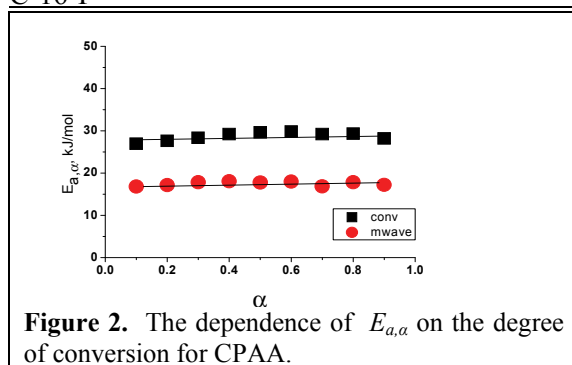


Figure 2. The dependence of $E_{a,\alpha}$ on the degree of conversion for CPAA.

As it was found that the E_a of CPAA is independent on α for both CH and MWH process, it means in both case occurs kinetically elementary process.

A new theoretical approach to the activation mechanism based on selective energy transfer is given [3]. In accordance with that model, the established changes in the kinetics model

and the values

of kinetics parameters under MWH compared to the CH, are consequences of a specific formation of “active complex” by selective energy transfer of vibration energy; quantized nature of activation energy and the increasing in the values of the ground vibration level of resonant vibrator in the AA molecule [$\text{C}=\text{O}$ symmetric stretching vibration of carboxyl group ($\omega = 1417 \text{ cm}^{-1}$)], due to the absorption of non-thermal effects of energy of microwave field. This leads in the decreasing value of E_a because the number of quantum of vibration energy transferred from the heat bath to the resonant oscillator decrease, whereas the anharmonicity constant of the oscillator for MWH increases.

Conclusions

Kinetics of isothermal CPAA under the CH can be described with the model of reaction of second order while under the MWH it can be described with the first order chemical reaction. The values of kinetics parameters of isothermal CPAA under the MWH are significantly lower than the ones under the CH. The decreased value of activation energy under the isothermal MWH in comparison to the CH is a consequence of the increased energy of ground vibrational level of resonant oscillator in acrylic acid molecule ($\text{C}=\text{O}$ symmetric stretching vibration of carboxyl group in AA molecules) which is caused with non-thermal effects of microwave field. The decreased value of $\ln A$ under the MWH in comparison to the CH is a consequence of increased value of anharmonicity factor of the resonant oscillator.

Acknowledgements

This investigation was supported by the Ministry of Science and Technical Development of the Republic of Serbia through project 172015OI.

References

- [1] B. Adnadjevic, J. Jovanovic, in *Advances in Induction and Microwave Heating of Mineral and Organic Materials*, 2011, 391- 422.
- [2] B. Adnadjevic, J. Jovanovic, *J. Appl. Polym. Sci.*, 2008, 107, 3579-3587.
- [3] R. Larsson, *J. Molecular Catalysis*, 1989, 55, 70-83.

DETERMINATION OF REACTION PARAMETERS FOR POLYMERIZATION OF CASTOR OIL WITH AROMATIC AND CYCLOALIPHATIC DIISOCYANATE

Z. Bjelović, I. S. Ristić, M. Jovičić, R. Radičević, B. Pilić, N. Vukić,
J. Budinski-Simendić

University of Novi Sad, Faculty of Technology, Bulevar cara Lazara 1, Serbia

Abstract

In this paper were studied curing kinetics of catalysed and noncatalysed polyurethane synthesis, based on castor oil and different types of diisocyanates (aromatic-toluene diisocyanate and cycloaliphatic-isophorone diisocyanate). Due to the presences of hydroxyl group on ricinoleic acid in castor oil, this oil is suitable for polyurethane preparation, as polyol component. The differential scanning calorimetry (DSC) has been employed to study the polyurethane formation reaction. Addition of the catalyst decreases the activation energy and that system with isophrone diisocyanate shows lower activation energy compared to toluene diisocyanate based polyurethane.

Introduction

The kinetic parameters of polyurethane reaction formation can be determined through the degree of conversion of the functional groups over a certain time period. Quantification of the kinetic parameters of the reaction, as well as the structural modifications in the analyzed system can be observed by the physical and chemical methods. The physical methods of the analysis are usually more suitable than the chemical ones. The relationship between the reaction rate and conversion α is different for each process and must be determined experimentally. Dynamic mode of differential scanning calorimetry (DSC) measurement is often used for monitoring the curing process of thermosets. The following methods for determination of the kinetic parameters of the simple chemical reactions could be applied: Ozawa, Freeman-Carroll, Crane-Ellerstein and Kissinger [1]. In this study, the dynamic DSC measurements were used to monitor the curing process of a polyurethane (PU) system. We also applied the Ozawa isoconversional model [2] to predict the activation energies (E_a) at different curing conversions.

Experimental

Materials

All components were supplied from Sigma Company. Castor oil (CO) having the hydroxy number ($\text{OH}_\#$) 170 mg KOH/g and acid value 1.27 mg KOH/g. Toluene diisocyanate (TDI) and isophorone diisocyanate (IPDI), which are used as received.

Methods

Curing of polyurethanes were carried out on differential scanning calorimeter (DSC) using a model Q20 TA Instruments. The activation energy and the reaction order were determined using non-isothermal direct differential method, presented by equation 1:

$$\ln \frac{\frac{d\alpha}{dT}}{(1-\alpha)^n} = \ln \frac{A}{\beta} - \frac{Ea}{RT} \quad (1)$$

Its slope gives the activation energy (E_a) while the intercept is equal to the frequency factor (A). In the first step the reaction order was determined. The following approach was applied: the correlation coefficient between the left-hand side of eq. 1 and $1/T$ was expressed as a function of the reaction order. The value of the reaction order was chosen on the basis of the maximum correlation coefficient.

The Ozawa isoconversional method was applied with three heating rates (5, 10 and 20 °C min⁻¹) in a scanning temperature range from 25 to 200 °C:

$$\log \beta = \left[\log \left(\frac{k_0 Ea}{Rg(\alpha)} \right) - 2.315 \right] - 0.4567 \frac{Ea}{RT} \quad (2)$$

where β is the heating rate ($\beta = dT/dt$ (K/s)), α is curing degree, k_0 is the pre-exponential factor of Arrhenius law, Ea is the activation energy (J mol⁻¹), R is the gas constant (8.314 J mol⁻¹ K⁻¹), T is the reaction temperature given in °K and $g(\alpha)$ is integral form of the kinetic model $f(\alpha)$. Therefore, for different heating rates at a constant degree of conversion ($\alpha(T)$), a linear relationship is observed by plotting $\log \beta$ vs. $1/T$, and the activation energy (Ea) is obtained as slope of the straight line.

Results and discussion

On the basis of the DSC measurements and according to the applied equation 1 the activation energy values and the reaction order for the polyurethane samples with and without catalyst have been calculated and summarised in Table 1.

Table 1. Reaction order (n) and activation energy (Ea) of polyurethane formation reactions, determined by DSC technique at three different heating rates

Sample	n			Ea [kJ mol ⁻¹]		
	5 °Cmin ⁻¹	10 °Cmin ⁻¹	20 °Cmin ⁻¹	5 °Cmin ⁻¹	10 °Cmin ⁻¹	20 °Cmin ⁻¹
PU-IPDI not catalysed	1.10	1.13	0.87	39.8	52.6	55.1
PU-IPDI catalysed	0.94	0.96	1.15	30.1	38.9	44.7
PU-TDI not catalysed	0.98	1.08	0.90	40.3	41.3	51.3
PU-TDI catalysed	1.08	0.92	1.27	31.1	34.9	44.6

The isoconversional Ozawa principle is based on the assumption that the reaction rate at a given degree of conversion is only a function of the temperature. Results from the application of the isoconversional method in the conversion range

between 5 and 95 % are shown in Figure 1 for all investigated samples. The change of activation energy with the curing degree is observed. The catalyst addition decreases the activation energy and that system with isophrone diisocyanate shows lower activation energy compared to toluene diisocyanate based polyurethane.

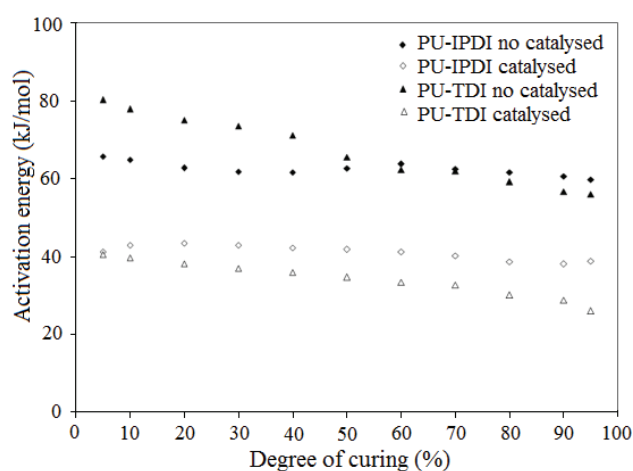


Figure 1. The activation energy dependence on curing degree, obtained by utilization of Ozawa isoconversional model.

Conclusions

Based on the DSC analysis, applying non-isothermal direct differential method, the kinetic parameters of the polyurethane system reaction, with different types of isocyanate, have been determined. The results obtained from the DSC measurements shown kinetic parameters dependence on polyol content, types of isocyanate and presence of catalyst. E_a significantly decreased in the presence of catalyst in the reaction mixture, while reaction order was independent of the presence of catalyst. Kinetic analysis of dynamic DSC data was also performed applying Ozawa isoconversional method. The change of activation energy with the curing degree is observed. Catalyst addition decreases the activation energy and that system with isophrone diisocyanate shows lower activation energy compared to toluene diisocyanate based polyurethane.

Acknowledgment

This paper was supported by Ministry of Education and Science-Republic of Serbia, project number III 45022.

References

- [1] Z. Petrović, Z. Zavargo, J. Appl. Polym. Sci., 1986, 32, 4353.
- [2] T. Ozawa, Thermochim. Acta, 2000, 356, 173.

THERMODYNAMICS OF MOLYBDENUM ADSORPTION ONTO POROUS COPOLYMER

B. Ekmešćić¹, D. Maksin², Lj. Suručić³, J. Marković², D. Marković²,
Z. Vuković¹, A. Onjia²

¹*University of Belgrade, Institute of Chemistry, Technology and Metallurgy,
Njegoševa 12, Belgrade, Republic of Serbia*

²*University of Belgrade, Vinča Institute of Nuclear Sciences, P.O.Box 522,
Belgrade, Republic of Serbia*

³*University of Belgrade, Faculty of Forestry, Kneza Višeslava 1, Belgrade,
Republic of Serbia*

Abstract

Macroporous glycidyl methacrylate and ethylene glycol dimethacrylate copolymer functionalized with diethylene triamine, PGME-deta, was tested as molybdate ion adsorbent from aqueous solutions. Kinetics of Mo(VI) sorption was investigated in batch static experiments, in the temperature range 298-343 K. The temperature rise promotes Mo(VI) removal, with the maximum experimental adsorption capacity of 585 mg g⁻¹ at 343 K. Thermodynamic parameters revealed spontaneous and endothermic nature of Mo(VI) adsorption onto PGME-deta.

Introduction

Molybdenum is the most concentrated trace element in the seawater due to its stability and weak adsorption behavior [1]. It is essential for some biological functions in plants and animals. Its compounds exhibit all oxidation states from +2 to +6 with the predominant Mo(IV) and Mo(VI) [2]. Since high concentrations of molybdate (>5 ppm) cause an environmental problem, the removal of mainly anionic molybdenum species from wastewater and groundwater becomes greatly significant. Macroporous PGME-deta seems to be a very promising adsorbent for the removal of toxic pollutants which, depending on pH, proved to be adaptable for adsorption of cations, like Cu(II) and Co(II) at pH 5.5 [3] and anions of Pt(IV), Au(III) and Rh(III) [4], Cr(VI) [5]. In this paper, macroporous PGME-deta was used as adsorbent for molybdenum anion species. Kinetic data for Mo(VI) removal on PGME-deta was collected at different temperatures and the thermodynamic parameters were evaluated.

Experimental

PGME-deta (surface area 29 m²g⁻¹, specific pore volume 0.89 cm³g⁻¹, pore diameter 212 nm, particle size 150-300 μm, amino groups concentration 6.51 mmolg⁻¹), obtained as described elsewhere [5] was used in molybdenum adsorption experiments. The sorption kinetics of Mo anions from acidic aqueous solutions (C_i= 0.1M; pH=2) was investigated in batch experiments at different temperatures. Copolymer (0.50 g) was contacted with 50 mL of Mo salt solution. Aliquots (0.5 mL) were removed at appropriate times, diluted and analyzed by ICP-AES (Perkin Elmer, Model ICP 400).

Results And Discussion

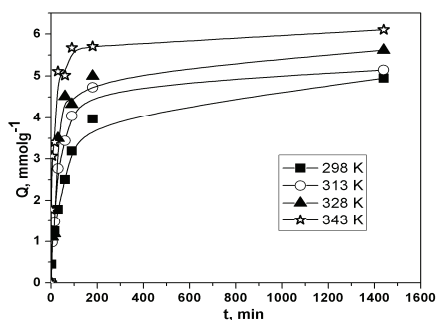


Fig. 1. Effect of temperature on Mo(VI) adsorption rate on PGME-deta.

superior Mo(VI) uptake. The temperature rise promotes Mo(VI) sorption by PGME-deta (Fig. 1), with the maximum experimental sorption capacity of 585 mg g⁻¹ at 343 K. Thermodynamic considerations of an adsorption process are necessary to establish whether the process is spontaneous or not. The used equations are listed in Table 1.

Table 1. Thermodynamics equations.

Apparent equilibrium constant equation	$\log K_c = \frac{F_e}{1 - F_e}$	[6]
Van't Hoff equation	$\log K_c = \frac{\Delta S}{2.303R} - \frac{\Delta H}{2.303RT}$	[6]
Arrhenius equation (linearized)	$\ln k_2 = \ln A - \frac{E_a}{RT}$	[7]

Where: K_c - equilibrium constant, F_e - fraction adsorbed at equilibrium, ΔS - entropy change (kJ mol⁻¹ K⁻¹), R - universal gas constant (8.314 J mol⁻¹ K⁻¹), ΔH - enthalpy change (kJ mol⁻¹), T - temperature (K), k_2 - pseudo-second order rate constant (g⁻¹ mmol⁻¹ min⁻¹), A - Arrhenius factor and E_a - activation energy (kJ mol⁻¹). The data obtained for Mo(VI) adsorption at various temperatures were used for calculating the thermodynamic parameters (Table 2). Results show positive ΔH value and increase of Mo(VI) adsorption with temperature, both characteristics of chemical adsorption (endothermic process). Mo(VI) anion is likely at first adsorbed by electrostatic (physisorption) interactions. Thus, both processes occur with chemisorption being predominant, possibly due to the transition metal nature of Mo; during adsorption process d orbitals become filled with electrons from nitrogen or oxygen from PGME-deta. The negative Gibbs free energy change (ΔG) indicates spontaneous Mo(VI) adsorption onto PGME-deta. Value of ΔG is negative only because of ΔS positive contribution again indicative of chemisorption ($\Delta G = \Delta H - T\Delta S$). This contribution increases with temperature elevation, suggesting improved adsorption at higher temperatures.

C-18-P

Table 2. Thermodynamic parameters for Mo(VI) sorption onto PGME-deta.

<i>T</i> , K	ΔG , kJ mol ⁻¹	E_a , kJ mol ⁻¹	$T\Delta S$, kJ mol ⁻¹	ΔH , kJ mol ⁻¹
298	-3.78	22.3	25.7	19.6
313	-5.08		27.0	
328	-6.37		28.3	
343	-7.67		29.6	

The positive ΔS value reflects an increase in randomness at the solid/solution interface expected to occur during chemisorption of Mo(VI) onto PGME-deta [1].

When sorption rate is governed by intraparticle diffusion mechanism, activation energy is low and within the range of values of 8–22 kJ mol⁻¹ [8]. In

this case, calculated E_a value is only marginally higher than 22 kJ mol⁻¹. Considering that the sorption capacity increased with temperature, this may indicate that chemisorption process is rate-controlling as well as pore diffusion.

Conclusion

Kinetics of Mo(VI) adsorption onto macroporous PGME-deta was investigated in the temperature range 298–343 K. Thermodynamic parameters revealed spontaneous and endothermic nature of Mo(VI) adsorption, with increased randomness in the system. The temperature rise promotes Mo(VI) removal.

Acknowledgements: This work was supported by the Ministry of Education and Science of the Republic of Serbia (Projects III 43009 and III 45001).

References

- [1] A. A. Atia, A. M. Donia, H. A. Awed, *J. Haz. Mat.*, 2008, **155**, 100-108.
- [2] D. Malinovsky, I. Rodushkin, D.C. Baxter, J. Ingri, B. Ohlander, *J. Mass Spectrom.*, 2005, **245**, 94–107.
- [3] A. Nastasović, S. Jovanović, D. Đorđević, A. Onjia, D. Jakovljević, T. Novaković, *React. Funct. Polym.*, 2004, **58**, 139-147.
- [4] A. Nastasović, D. Jakovljević, Z. Sandić, D. Đorđević, Lj. Malović, S. Kljajević, J. Marković, A. Onjia, in: M. I. Barroso ed. "Reactive and Functional Polymers Research Advances", Nova Science Publishers, Inc. Chapter 2, 79-112 (2007).
- [5] D. D. Maksin, A. B. Nastasović, A. D. Milutinović-Nikolić, Lj. T. Suručić, Z. P. Sandić, R. V. Hercigonja, A. E. Onjia, *J. Hazard. Mater.*, 2012, **209-210**, 99-110.
- [6] E. Oguz, B. Keskinler, *Colloids Surf. A*, 2005, **268**, 124–130.
- [7] R. S. Juang, F. C. Wu, R. L. Tseng, *Environ. Technol.*, 1997, **18**, 525-531.
- [8] S. Glasston, K. J. Laidler, H. Eyring, *The Theory of Rate Processes*, McGraw-Hill, New York, 1941.

DIFFUSION-BASED KINETIC MODELING OF TEXTILE DYE ADSORPTION BY POROUS COPOLYMER

Z. Sandić¹, D. Maksin², N. Jović-Jovičić³, B. Ekmešćić³, A. Nastasović³,
A. Onjia², A. Popović⁴

¹*University of Banja Luka, Faculty of Science, 78000 Banja Luka, Mladena Stojanovića 2, Bosnia and Herzegovina*

²*University of Belgrade, Vinča Institute of Nuclear Sciences, P.O. Box 522, 11001 Belgrade, Republic of Serbia*

³*University of Belgrade, ICTM, Njegoševa 12, 11000 Belgrade, Republic of Serbia*

⁴*Faculty of Chemistry, University of Belgrade, Studentski trg 12-16, 11000 Belgrade, Republic of Serbia*

Abstract

Macroporous glycidyl dimethacrylate and ethylene glycol dimethacrylate copolymer functionalized with diethylene triamine, PGME-deta, was tested as adsorbent for removal of Acid Orange 10 (AO10) and Reactive Black 5 (RB5) from aqueous solutions. Diffusion-based kinetic models (intraparticle diffusion, Bangham and Boyd model) were used for interpretation of experimental data.

Introduction

The removal of synthetic dyes from the industrial effluents becomes a critical issue. Over 7×10^5 t of nearly 100,000 commercially available dyes are produced annually worldwide while 2% of dyes are discharged directly into the environment [1]. Among the most attractive polymeric adsorbents for textile dyes removal from aqueous media are amino-functionalized glycidyl methacrylate (GMA) copolymers [2]. In this paper, kinetic data of textile dyes adsorption onto PGME-deta were interpreted with intraparticle diffusion, Bangham and Boyd model.

Experimental

PGME-deta (surface area $53 \text{ m}^2\text{g}^{-1}$, pore diameter 50 nm, particle size 150-500 μm , amino groups concentration 5.01 mmolg^{-1}) was obtained as described elsewhere [2]. AO10 [CAS: 1936-15-8], and RB5 [CAS: 17095-24-8] were purchased from Alfa-Aesar and used as received. The experiments were carried out at 25 °C, with the initial dye concentration of 30; 50 and 70 mg L^{-1} , m_{adsorb} of 25.0 mg and $V=50.0 \text{ mL}$, at unadjusted pH values of 5.1 for RB5 and 7.4 for AO10. The solution aliquots were withdrawn and the absorbance of supernatant solution was measured using Thermo Electron Nicolet Evolution 500 UV-VIS spectrophotometer (absorption peaks of AO10 and RB5 were at 478 and 597 nm, respectively).

Results And Discussion

The prediction of the rate-limiting step in the adsorption process is essential for understanding the adsorption mechanism. Our previous studies showed that the adsorption of AO10 and RB5 by PGME-deta obeyed the pseudo-second-order kinetic model, suggesting that the adsorption rate is controlled by both adsorbent

C-19-P

capacity and adsorbate concentration. For further analysis and the assessment of the influence of diffusion on adsorption, kinetic data were analyzed using diffusion-based models given in Table 1.

Table 1. Kinetic models.

Kinetic model	Equation	Reference
Intraparticle diffusion	$Q_t = C_{id} + k_{id} \cdot t^{0.5}$	[3]
Bangham	$\log \log \left[\frac{C_i}{C_i - C_s Q_t} \right] = \log \left[\frac{k_b C_s}{2.303V} \right] + \alpha \log t$	[4]
Boyd	$Bt = -0.4977 - \ln(1 - F)$	[5]

Where: Q_t is the amount of adsorbate at time t (mg g^{-1}), C_{id} - intercept proportional to the boundary layer thickness (mg g^{-1}), k_{id} -intraparticle diffusion rate constant ($\text{mg g}^{-1} \text{min}^{-0.5}$), t -time (min), C_i -initial adsorbate concentration in solution (mg L^{-1}), C_s -weight of adsorbent per L of solution (g L^{-1}), V -solution volume (mL), α (< 1) and k_b are constants of the systems, Bt - time constant (min^{-1}), F - fractional attainment of equilibrium at t (min).

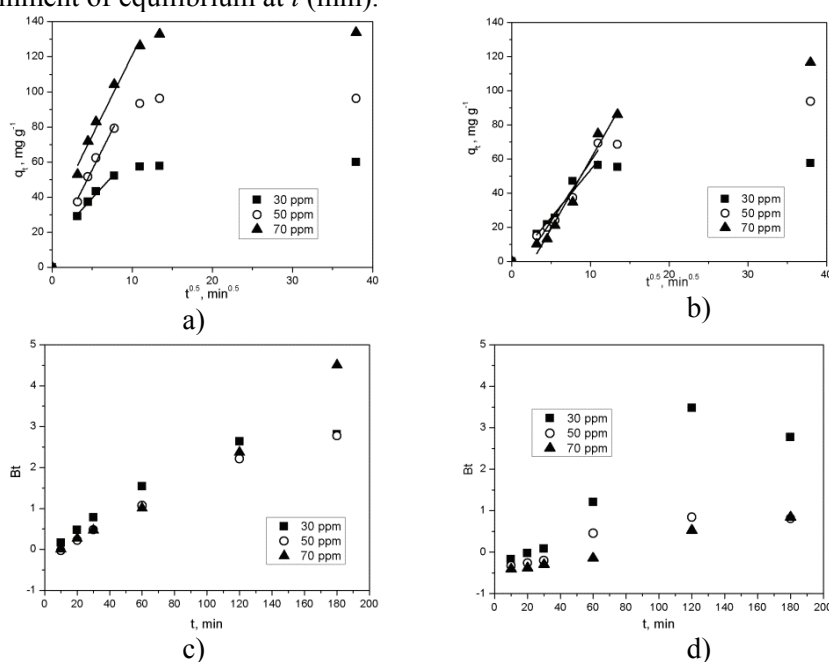


Figure 1. Intraparticle diffusion plots for RB5 (a) and AO10 (b); Boyd plots for RB5 (c) and AO10 (d) using PGME-deta as sorbent.

The intraparticle diffusion model plots did not pass through the origin suggesting that even though the adsorption process involved intraparticle diffusion, it was not the only rate-controlling step. Also, the positive (RB5) and negative (AO10) value of intercept C_{id} is indicative of some degree of boundary layer control. Bangham's

parameters also confirmed that these sorption processes were at least partly pore diffusion controlled. In a Boyd plot, if a straight line passes through the origin, it indicates that particle-diffusion mechanisms govern sorption processes. If not, they are controlled by film-diffusion. It is evident from the presented data, that under the same conditions, the contribution of intraparticle diffusion in sorption of RB5 in comparison with AO10 on PGME-deta is more notable. Eventhough the Boyd plots for RB5 do not pass through origin, they are approaching straight-line dependance, while for AO10 these plots were neither linear nor passed through the origin, indicating the film diffusion-controlled mechanism is dominant in overall adsorption regardless of initial concentration.

Table 2. Kinetic parameters for A10 and RB5 using PGME-deta as adsorbent (pH=unadjusted, $t=25$ °C).

	RB5			AO10		
	30	50	70	30	50	70
C_i , mg L ⁻¹	30	50	70	30	50	70
Q_e , mg g ⁻¹	60.00	96.2	133.7	57.5	93.74	116.5
Intraparticle						
k_{id} , mg g ⁻¹ min ^{-0.5}	4.99	9.08	9.18	5.57	6.99	8.11
C_{id} , mg g ⁻¹	14.4	10.3	29.2	-2.14	-11.4	-21.2
R^2	0.982	0.988	0.978	0.957	0.962	0.974
Bangham						
$k_b \cdot 10^3$, g ⁻¹	16.3	8.63	10.2	3.99	2.4	0.68
α	0.61	0.72	0.65	0.84	0.79	0.95
R^2	0.991	0.998	0.997	0.952	0.932	0.977

Conclusion

Kinetic data of textile dyes adsorption onto PGME-deta were interpreted with three diffusion-based models: intraparticle diffusion, Bangham and Boyd model. The results suggest that involved intraparticle and film diffusion both play important part in the adsorption process, besides the previously established influence of adsorbent capacity and adsorbate concentration.

Acknowledgements

This work was supported by the Ministry of Education and Science of the Republic of Serbia (Projects III 43009 and III 45001).

References

- [1] K. Z. Elwakeel, M. Rekaby, J. Hazard. Mater., 2011, 188, 10-18.
- [2] Z. P. Sandić, A. B. Nastasović, N. P. Jović-Jovičić, A. D. Milutinović-Nikolić, D. M. Jovanović, *J. Appl. Polym. Sci.*, 2011, 121, 234-242.
- [3] G. E. Boyd, A. M. Adamson, L. S. Myers, *J. Am. Chem. Soc.*, 1947, 69, 2836-2848.
- [4] N.Y. Mezenner, A. Bensmaili, *Chem. Eng. J.* 2009, 147, 87-96.
- [5] Y. Qu, C. Zhang, F. Li, X. Bo, G. Liu, Q. Zhou, *J. Hazard. Mater.*, 2009, 169, 146-152.

C-20-P

NON-ISOTHERMAL KINETICS OF DEHYDRATION OF AG/PVA HYDROGEL NANOCOMPOSITE SYNTHESIZED BY Γ -IRRADIATION

J. Krstić, J. Spasojević, A. Radosavljević, Z. Kačarević-Popović

Vinča Institute of Nuclear Sciences, University of Belgrade, P.O. Box 522,

11001 Belgrade, Serbia (jelenak@vinca.rs)

Abstract

In this study, the non-isothermal kinetics of dehydration of γ -radiolytically synthesized PVA and Ag/PVA nanocomposite hydrogels was investigated by thermogravimetric analysis (TGA). Kinetic analysis was performed by applying different model fitting and model-free kinetic analysis to estimate kinetic parameters, the activation energy (E_a) and pre-exponential factor (A). The analysis showed that incorporation of silver nanoparticles (Ag NPs) into PVA hydrogel matrix has influence on kinetic parameters of dehydration process.

Introduction

Metal NPs embedded in crosslinked polymer matrices, i.e. hydrogels, are the novel class of materials, which have attracted great attention due to applications in catalysis, photonics, optics, pharmaceuticals and biomedicine. Incorporation of small amount of metal NPs as nanofiller into polymer matrix leads to improvement of their thermal conductivity, mechanical toughness, optical and catalytic activities [1]. The properties of nanocomposites are strongly dependent on the method of preparation and experimental conditions. Radiolytic method has proved as excellent tool for *in situ* synthesis of Ag/PVA hydrogel nanocomposite. The growth and aggregation processes of Ag NPs are well controlled by polymer molecules, and the interactions between polymer molecules and NPs is responsible for the stability of nanocomposite systems [2].

TGA is a common experimental method used to study variety of chemical and physical processes (thermal degradation, crosslinking, crystallization, dehydration, glass transition, etc.) in polymer systems, induced by temperature changes. Kinetics of degradation can be determined by applying the computational analysis which allows estimating the parameters of the thermal degradation process with specific information about thermal stability of nanocomposites [1].

The aim of this study was to investigate non-isothermal kinetics of dehydration process of PVA and Ag/PVA nanocomposite hydrogels. Kinetic analysis was performed by applying model fitting (Coats-Redfern (CR), Van-Krevelen (VK) and Horowitz-Metzger (HM)) and isoconversional "model-free" methods (Flynn-Wall-Ozawa (FWO), Kissinger-Akahira-Sunose (KAS) and Tang (T)) to estimate kinetic parameters.

Experimental

The investigated hydrogels, PVA and Ag/PVA nanocomposite, were synthesized following procedure published elsewhere [3]. Non-isothermal thermogravimetric measurements were carried out using a SETSYS Evolution 1750 Thermogravimetric Analyzer. The measurements were conducted on equilibrium swollen PVA and Ag/PVA nanocomposite hydrogels, at heating rates (β) of 2.5; 5; 10 and 15 °C/min in a dynamic argon atmosphere (flow rate 25 cm³/min), in the temperature range from 20 to 280 °C.

Results and Discussion

The TG and DTG curves (not presented) of the dehydration of equilibrated swollen PVA and Ag/PVA nanocomposite hydrogels, obtained at different heating rates, show a one step process. Characteristic temperatures of dehydration process (initial (T_i), at the maximum rate (T_m), final (T_f)) increase with increasing of heating rate, and their values are presented in Table 1.

Table 1. Characteristic temperatures of dehydration process of hydrogels.

β (°C/min)	PVA			Ag/PVA		
	T_i (°C)	T_m (°C)	T_f (°C)	T_i (°C)	T_m (°C)	T_f (°C)
2.5	34	98	129	33	90	124
5	42	105	133	41	110	162
10	50	120	162	46	134	206
15	53	99	173	44	147	230

Kinetic parameters (E_a and A) were estimated using different model fitting and model-free methods, assuming the first-order reaction model for investigated dehydration of equilibrated swollen hydrogels (Table 2) [4, 5].

Table 2. Kinetic parameters determined by different model fitting method.

Method	β (°C/min)	PVA			Ag/PVA		
		lnA	A (1/min)	E_a (kJ/mol)	lnA	A (1/min)	E_a (kJ/mol)
CR	2.5	11.98	$1.60 \cdot 10^5$	43.8	12.04	$1.69 \cdot 10^5$	43.3
	5	12.55	$2.82 \cdot 10^5$	44.2	9.81	$1.82 \cdot 10^4$	37.5
	10	11.39	$8.84 \cdot 10^4$	41.4	7.02	$0.11 \cdot 10^4$	29.6
	15	11.50	$9.87 \cdot 10^4$	38.9	6.82	$0.09 \cdot 10^4$	28.8
VK	2.5	13.80	$9.85 \cdot 10^5$	48.9	13.71	$9.00 \cdot 10^5$	47.9
	5	14.50	$1.98 \cdot 10^6$	49.7	11.55	$1.04 \cdot 10^5$	42.6
	10	12.95	$4.21 \cdot 10^5$	46.0	8.55	$0.52 \cdot 10^4$	34.1
	15	12.82	$3.70 \cdot 10^5$	42.6	8.38	$0.43 \cdot 10^4$	33.4
HM	2.5	15.34	$4.59 \cdot 10^6$	53.6	15.33	$4.55 \cdot 10^6$	52.8
	5	16.02	$9.07 \cdot 10^6$	54.4	13.09	$4.84 \cdot 10^5$	47.5
	10	14.69	$2.40 \cdot 10^6$	51.7	10.30	$2.97 \cdot 10^4$	40.0
	15	14.61	$2.21 \cdot 10^6$	48.2	10.14	$2.53 \cdot 10^4$	39.6

As can be seen from table 2, the highest values for E_a and A was obtained by using HM method, while CR and VK methods give lower values. Independently of the applied method, increase of the β leads to decrease of kinetic parameters.

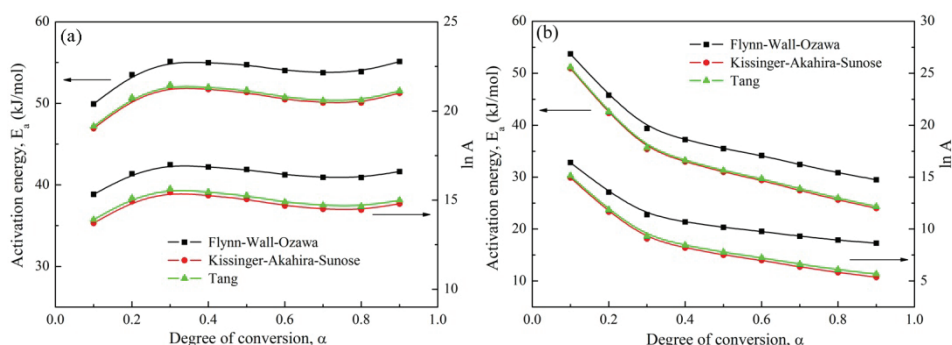


Figure 1. Kinetic parameters E_a and $\ln A$ as a function of degree of conversion for PVA (a) and 16 mM Ag/PVA nanocomposite (b) hydrogels.

Fig. 1 shows the variation of E_a and $\ln A$ with the degree of conversion (α) obtained using isoconversion model-free kinetic methods. Values of kinetic parameters for PVA increase with increasing α in the range of 0.1-0.3, and after this range the values are almost the same. On the other hand, for Ag/PVA the values of E_a and $\ln A$ decrease on the whole range of α , indicating that incorporation of Ag NPs into PVA hydrogel has influence on dehydration process. The stabilization of Ag NPs occurs by interaction with OH groups [3], which probably affect the formation of hydrogen bond between molecules of water and hydrogel and thus changing the mechanism of dehydration.

Conclusion

Kinetic parameters of dehydration of PVA and Ag/PVA nanocomposite hydrogels were determined by model-fitting and model free kinetic analysis. The obtained values of E_a and A are lower for Ag/PVA nanocomposite. The interactions of Ag NPs with OH groups probably affect the structural rearrangements, and thus induce changing of relaxation mechanism of hydrogel and dehydration process.

Acknowledgements

This work is financed by the Ministry of Education and Science of Republic of Serbia (III 45005) and International Atomic Energy Agency (IAEA), CRP: F22501/contract 16733.

References

- [1] J. Kuljanin-Jakovljević, et al., Polym. Degrad. Stabil., 2009, 94, 891-897.
- [2] A. Krklješ, et al., Thermochim. Acta, 2007, 460, 28-34.
- [3] J. Krstić, et al., 10th International Conference on Fundamental and Applied Aspects of Physical Chemistry, Proceedings, 2010, Vol. I, 110-112.
- [4] B. Janković, et al., J. Therm. Anal. Calorim., 2005, 82, 7-13.
- [5] B. Janković, et al., Thermochim. Acta, 2007, 452, 106-115.

KINETICS OF CRYSTALLIZATION OF $\text{LiGe}_2(\text{PO}_4)_3$ PHASE IN GLASS

S. D. Matijašević¹, M. B. Tošić¹, S. R. Grujić², V. D. Živanović¹,
J. N. Stojanović¹, J. D. Nikolić¹, S. N. Zildžović¹

¹*Institute for Technology of Nuclear and other Mineral Raw Materials, 86
Franchet d'Esperey St, 1100 Belgrade, Serbia*

²*Faculty of Technology and Metallurgy, University of Belgrade 4 Karnegijeva
St., 11000 Belgrade, Serbia*

Abstract

This paper presents the crystallization of $\text{LiGe}_2(\text{PO}_4)_3$ phase in the glass under non-isothermal condition. In the powdered glass with particle sizes less than 0.048 mm, surface crystallization was dominant. It was shown that the exothermal peak temperature, T_p , shifted toward the higher temperatures with increasing heating rate. The activation energy of crystal growth of $E_a=462\pm 11 \text{ kJ mol}^{-1}$ was calculated.

Introduction

$\text{LiGe}_2(\text{PO}_4)_3$ crystalline phase possess NASICON-type structure, which consists of GeO_6 octahedra and PO_4 tetrahedra [1]. Both units linked by their corners form a three-dimensional network. NASICONs possess 'open' structures in which the alkali ion can move with significantly reduced activation barriers and hence they can be utilized as fast ion conductors. The NASICONs constitute a very versatile class of materials [2-4]. $\text{LiGe}_2(\text{PO}_4)_3$ can be synthesized by conventional ceramic method, glass-ceramics method, solution-sol-gel method or hydrothermal method. In comparison with the sintered materials, glass-ceramics have much advantage because they can be easily manufactured into desired size or shape and have dense microstructure. Therefore, it is significant to understand the processes in the crystallization of these glass-ceramics materials. In this study, the attention was focused on the kinetics of crystallization of $\text{LiGe}_2(\text{PO}_4)_3$ phase in the germanophosphate glass.

Experimental

The glass was prepared by melting a homogeneous mixture of reagent-grade Li_2CO_3 , A_2O_3 , GeO_2 and $(\text{NH})_2\text{HPO}_4$ in a covered platinum crucible. The melting was performed in an electric furnace BLF 17/3 at $T=1400 \text{ }^\circ\text{C}$ during $t=0.5 \text{ h}$. The melt was cast and cooled between two steel plates. Powder X-ray diffraction (XRD) analysis confirmed the quenched melts to be vitreous. The samples were transparent, without visible residual gas bubbles

The experiments under non-isothermal conditions were performed on the samples grain size $<0.048 \text{ mm}$ using a Netzsch STA 409 EP device and Al_2O_3 powder as the reference material. The glass powder was prepared by crushing of bulk glass in an agate mortar and sieving it to appropriate grain size. In the

C-21-P

experiments, a constant weight (100 mg) of the samples were heated at different rates of 5, 10, 12, 15 and 20 °C/min from 20 °C to $T = 800$ °C.

The XRD method was used to determine the phase composition and the XRD patterns were obtained by using a Philips PW-1710 automated diffractometer with a Cu tube operated at 40 kV and 30 mA. The XRD measurements were performed at room temperature in a stationary sample holder.

Results and Discussion

The results of the chemical analysis show that a glasses composition of $22\text{Li}_2\text{O} \cdot 10\text{Al}_2\text{O}_3 \cdot 30\text{GeO}_2 \cdot 38\text{P}_2\text{O}_5$ (mol%) was obtained. In Figure 1 the DTA curves of the powder samples recorded at different heating rates in the temperature range of 20-800°C are shown. On the curves recorded the exothermal temperature peaks which correspond to the crystallization of glass were registered.

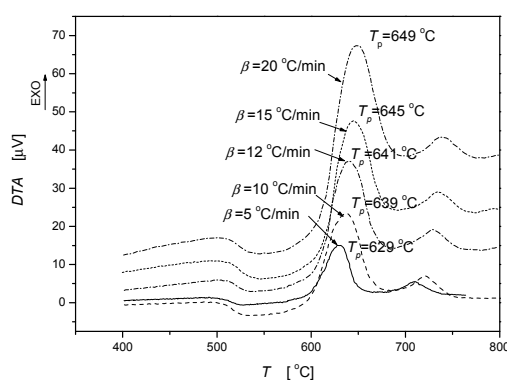


Figure 1. DTA curves recorded for powder samples particle size <0.048 mm at the heating rates 5, 10,12, 15 and 20 °C.

As can be seen in Figure 1, the exothermal peak temperature, T_p , shifted toward the higher temperatures with increasing the heating rate.

The analysis of the effect of particle size of the glass on the crystallization mechanism showed that for powder samples with granulation of < 0.048 mm the surface mechanism of crystallization is dominant. For particle size in the range 0.048-0.4 mm both surface and volume crystallization are significant, while for particle size >0.4 mm the volume crystallization is dominant

In the case of interface controlled crystal growth, non-isothermal methods can be used for evaluation of the kinetics parameters of glass crystallization. These methods, requiring small sample masses, are relatively easy to perform. However, the majority of these methods assume the Arrhenian temperature dependence of the transformation kinetics, and so do not have general validity [5]. This makes the calculated kinetic parameters reliable and unambiguous only in certain controlled cases.

In the range of the smallest granulation, in the total number of present nuclei, the number of surface with respect to internal nuclei is dominant. Therefore,

the number of nuclei does not significantly change with heating, while the crystal growth rates become considerable.

On the basis of the recorded T_p 's at various heating rates and value of Avrami parameter $n=1$, the values of the activation energy of crystal growth were calculated according to Kissinger equation[6]. Fig. 2 shows the plot of $\ln(\beta/T_p^2)$ versus $1/T_p$. The $E_c = 462 \pm 11 \text{ kJ}\cdot\text{mol}^{-1}$ was calculated.

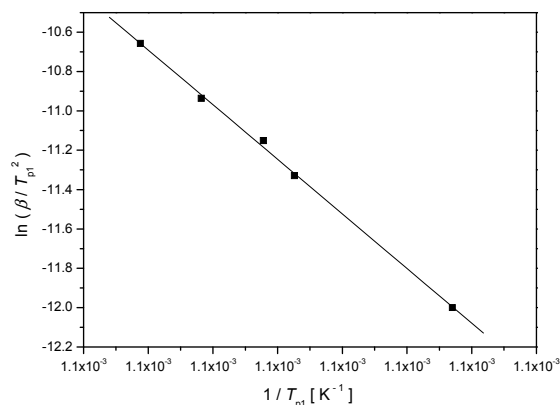


Figure 2. $\ln(\beta/T_p^2)$ vs. $1/T_p$ for powder sample of particle size $<0.048 \text{ mm}$.

Conclusion

The kinetics of crystallization of $\text{LiGe}_2(\text{PO}_4)_3$ phase from glass was studied. Investigations under non-isothermal conditions with powder samples of particle sizes $<0.048 \text{ mm}$ was performed. On the basis of the recorded T_p 's at various heating rates the values of the activation energy of crystal growth of $E_c = 462 \pm 11 \text{ kJ}\cdot\text{mol}^{-1}$ was calculated.

Acknowledgment

The authors are grateful to the Ministry of Education and Science, Republic of the Serbia for financial support (Projects 34001 and 172004).

References

- [1] P. P.Kumar, S. Yashonati, J. Chem. Sci., 2006, 118, 135-154.
- [2] A. S. Wills, VALIST (2009) Program available from www.CCP14.ac.uk.
- [3] M.Cretin, P. Fabry, J. Eur. Ceram. Soc., 1999, 19, 2931-2940.
- [4] P. Maldonado-Manso, E. R. Losilla, M. Martinez-Lara, M. A. G. Aranda, S. Bruque, F. Mouahid, M. Zahir, Cem. Mater., 2003, 15, 1879-1885.
- [5] H. Yinnon, D. R. Uhlmann, J. Non-Cryst. Solids, 1983, 54, 253-275.
- [6] H. E. Kissinger, Anal. Chem., 1959, 29, 1702-1706.

NUMERICAL CALCULATION OF THE KINETICS OF $HOI \rightleftharpoons H(^2S) + OI(X^2\Pi_i)$ THERMAL REACTION IN THE GAS PHASE

N. Begovic¹, S. Anic²

¹*Institute of General and Physical Chemistry, Belgrade, Serbia*

²*Institute of Chemistry, Technology and Metallurgy, University of Belgrade, Serbia*

Abstract

Using the MP4 method in the temperature range of 100 – 373 K we analyzed the kinetics of $HOI \rightleftharpoons H(^2S) + OI(X^2\Pi_i)$ gas reaction. The temperature dependence of the rate constants ($k_f = 9.88E^{-219} \text{ s}^{-1}$ at T=100 K to $k_f = 3.85 \times 10^{-50} \text{ s}^{-1}$ at T=373 K; and $k_r = 6.15 \times 10^{-16} \text{ s}^{-1}$ at T=100 K to $k_r = 2.24 \times 10^{-13} \text{ s}^{-1}$ at T=373 K) and equilibrium constants ($K = 1.61 \times 10^{-203}$ at T=100 K to $K = 1.72 \times 10^{-37}$ at 373 K) were determined. In the above temperature range, the activation energies of the forward (E_f) and reverse (E_r) reactions of 105.40 and 1.60 kcal/mol were found.

Introduction

It is well known that the reaction of HOI decomposition is very important for atmospheric chemistry and can proceed via four possible channels.

Table 1.

$HOI \rightleftharpoons O(^3P) + HI(X^1\Sigma^+)$	(R1)
$HOI \rightleftharpoons I(^2P) + OH(X^2\Pi)$	(R2)
$HOI \rightleftharpoons H(^2S) + OI(X^2\Pi_i)$	(R3)
$HOI \rightleftharpoons O(^1D) + HI(X^1\Sigma^+)$	(R4)

The photolysis of HOI has been studied by Vogt and Schindler [1], Bell [2] but the studies of kinetics of decomposition by reaction R3 (Tabl.1) don't exist in literature, which is the object of our investigation in this paper. Studying this type of reaction can be generally

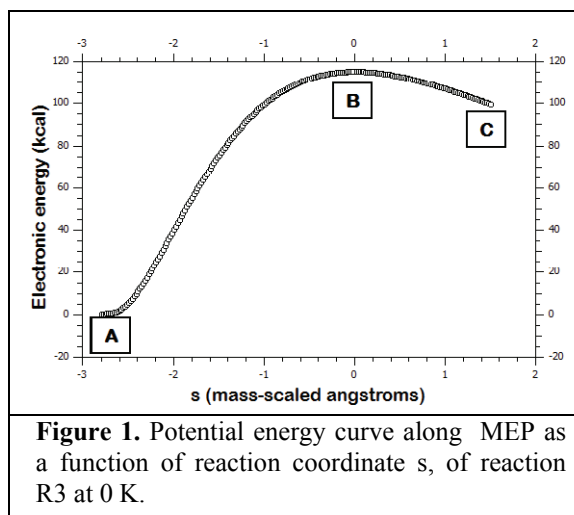
useful for the understanding of mechanism of oxy-iodine oscillating reactions.

Methodology

To elucidate all necessary data for kinetic calculation the Gaussian 09 [3] quantum-mechanical program package was used. All calculation was done at the MP4 [4], a Møller-Plesset correlation energy correction truncated at fourth-order level of theory. The 6-311++G(df,3pd) basis set was used for oxygen and hydrogen. The Lanl2DZdp basis sets combined with the relativistic effective core potential of Wadt and Hay [17] and augmented with uncontracted diffuse s and p functions (exponents 0.0569 and 0.0330, respectively), [18] and d and f polarization functions (exponents 0.292 and 0.441, respectively), [18] are used for iodine. The rate constants were calculated using canonical variational theory (CVT) with multidimensional approximation for tunneling, specially small-curvature (SCT) and large-curvature (LCT) tunneling methods. For interfacing the Polyrate 2010 [5] (program for the calculation of chemical reaction rates of polyatomic species) and Gaussian 09 program and for the purpose of carrying out direct dynamical calculations of chemical reaction rates of interest we used Gaussrate 2009 [5] scripts.

Results And Discussion

Potential energy curve along minimum energy path (MEP) in kcal as a function of the reaction coordinate s (mass-scaled angstroms) for decomposition of HOI is shown in Fig. 1. The mark A, B and C correspond to structure of reactant, transition state and products, respectively.



The mechanism of the reaction R3 can be presented by the following scheme, Fig. 2. The most left picture, A, correspond to HOI in his equilibrium ground state conformation, which is in this case reactant. On the opposite side, on the right most picture, C, is the system of H and OI, which correspond to products. The all distance on schema are in angstroms.

There has been found rate constant for forward and reverse reaction in temperature range from 100-373 K. In this condition k_f is from $9.88 \times 10^{-219} \text{ s}^{-1}$ to $3.85 \times 10^{-50} \text{ s}^{-1}$ and k_r from $6.15 \times 10^{-16} \text{ s}^{-1}$ to $2.24 \times 10^{-13} \text{ s}^{-1}$ while in the same time the equilibrium constant has value from 1.61×10^{-203} to 1.72×10^{-37} . The determined activation energies for forward and reverse reaction are 105.4 and 1.60 kcal/mol, and are calculated for temperature interval 100 – 373 K, while enthalpy ΔH_r is 103.12 kcal/mol.

From kinetically calculation we get the transmission coefficient for forward and reverse reaction which is 3.84×10^{-06} and 2.132 at 100 K and 373 K, respectively. The tunneling probabilities for reverse reaction are significant at low energies but for forward reaction they take values only at higher energies. This is one of the reasons why diagram for forward reaction rate on Fig. 3 show deviation from linearity at high temperature. On opposite, tunneling is active mechanism for reverse reaction even at low temperature when the system is in low energetic condition. For reverse reaction, Fig. 3, two different temperature ranges exists. In one, on low temperature, we can say that reaction rate is weakly dependent of temperature. In that range reaction rate curve is almost parallel with $1/T$ axis. In second temperature range, at higher temperature, reaction is faster and show lower influence of tunneling

Conclusion

Kinetic values for $\text{HOI} \rightleftharpoons \text{H}(\text{S}) + \text{OI}(\text{X}^2\Pi_i)$ thermal decomposition were calculated for the first time. The high value for reverse rate constant suggest us that the reverse reaction can be understand as concurrent to photolysis reactions which produce IO, I and other reactive species responsible for ozone layer depletion.

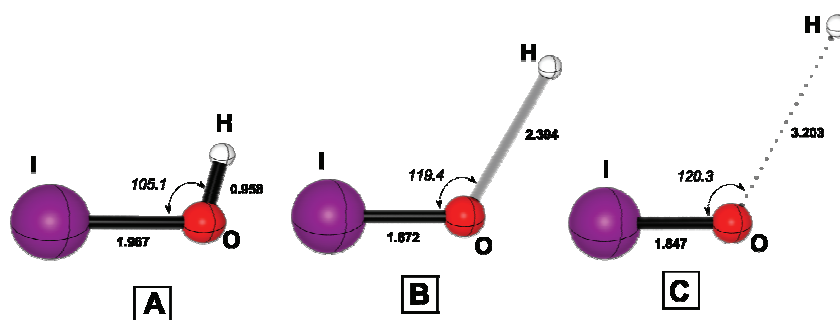


Figure 2. Structure which corresponds to reactant, A, transition state, B and product at almost infinite distance C. Units for distances are angstroms (in bold) and for angles are degrees (in italic).

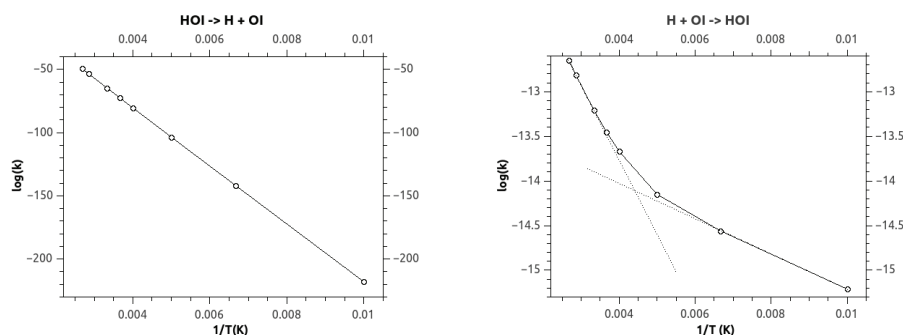


Figure 3. Influence of temperature on rate constant. On the left side is diagram for forward and on the right for reverse R3 reaction.

Acknowledgements

This work is supported by Ministry of Science and Environmental of Serbia, project no. 172015 and 45001.

References

- [1] R.Vogt, R.N. Schindler, Ber. Bunsenges. Phys. Chem., 1993, 97, 819-829.
- [2] A. Bell, P. Pardon, C. Hickman, J. Frey, J. Chem. Soc. Faraday. Trans., 1990, 86, 3831-3836.
- [3] Gaussian 09, Revision A.1, Gaussian, Inc., Wallingford CT, 2009.
- [4] K. Raghavachari, J. A. Pople, Int. J. Quantum Chem., 14 (1978) 91-100.
- [5] POLYRATE 2008, GAUSSRATE 2008, Donald G. Truhlar, Department of Chemistry and Supercomputing Institute University of Minnesota, Minneapolis
- [6] H. Dunning Jr. and P. J. Hay, in Methods of Electronic Structure Theory, Vol. 2, H. F. Schaefer III, ed., PLENUM PRESS (1977).
- [7] P. J. Hay, W. R. Wadt, J. Chem. Phys., 82, 284 (1985).

NUMERICAL CALCULATION OF THE KINETICS OF $H\text{OBr} \rightleftharpoons H(^2S) + \text{OBr}(X^2\Pi_1)$ THERMAL REACTION IN THE GAS PHASE

N. Begovic¹ and Z. Marković²

¹*Institute of General and Physical Chemistry, Belgrade, Serbia*

²*Department of Chemical-Technological Sciences,
State University of Novi Pazar, 36300 Novi Pazar, Republic of Serbia*

Abstract

Using the MP4 method in the temperature range of 100 – 373 K we analyzed the kinetics of $H\text{OBr} \rightleftharpoons H(^2S) + \text{OBr}(X^2\Pi_1)$ gas reaction. The temperature dependence of the rate constants ($k_f = 2.31 \times 10^{-223} \text{ s}^{-1}$ at $T=100 \text{ K}$ to $k_f = 5.25 \times 10^{-50} \text{ s}^{-1}$ at $T=373 \text{ K}$; and $k_r = 6.88 \times 10^{-17} \text{ s}^{-1}$ at $T=100 \text{ K}$ to $k_r = 5.84 \times 10^{-14} \text{ s}^{-1}$ at $T=373 \text{ K}$) and equilibrium constants ($K = 3.35 \times 10^{-207}$ at $T=100 \text{ K}$ to $K = 8.99 \times 10^{-37}$ at 373 K) were determined. In the above temperature range, the activation energies of the forward (E_f) and reverse (E_r) reactions of 103.6 and 1.83 kcal/mol were found.

Introduction

It is well known that the reaction of HOBr decomposition is very important for atmospheric chemistry and can proceed via four possible channels.

The photolysis of HOBr has been studied by Vogt and Schindler [1], Bell [2]

but the studies of kinetics of decomposition by reaction R3 (Table 1) don't exist in literature, which is the object of our investigation in this paper. Studying this type of reaction can be generally useful for the understanding of mechanism of oxy-bromine oscillating reactions.

Table 1.

$H\text{OBr} \rightleftharpoons O(^3P) + H\text{Br}(X^1\Sigma^+)$	(R1)
$H\text{OBr} \rightleftharpoons Br(^2P) + OH(X^2\Pi)$	(R2)
$H\text{OBr} \rightleftharpoons H(^2S) + \text{OBr}(X^2\Pi_1)$	(R3)
$H\text{OBr} \rightleftharpoons O(^1D) + H\text{Br}(X^1\Sigma^+)$	(R4)

Methodology

To elucidate all necessary data for kinetic calculation the Gaussian 09 [3] quantum-mechanical program package was used. All calculation was done at the MP4 [4], a Møller-Plesset correlation energy correction truncated at fourth-order level of theory. The 6-311++G(df,3pd) basis set was used for oxygen and hydrogen. The Lanl2DZdp basis sets combined with the relativistic effective core potential of Wadt and Hay [17] and augmented with uncontracted diffuse s and p functions (exponents 0.064 and 0.0402, respectively), [18] and d and f polarization functions (exponents 0.427 and 0.574, respectively), [18] are used for iodine. The rate constants were calculated using canonical variational theory (CVT) with

multidimensional approximation for tunneling, specially small-curvature (SCT) and large-curvature (LCT) tunneling methods. For interfacing the Polyrate 2010 [5] (program for the calculation of chemical reaction rates of polyatomic species) and Gaussian 09 program and for the purpose of carrying out direct dynamical calculations of chemical reaction rates of interest we used Gaussrate 2009 [5] scripts.

Results and Discussion

Potential energy curve along minimum energy path (MEP) in kcal as a function of the reaction coordinate s (mass-scaled angstroms) for decomposition of HOBr is shown in Fig. 1. The mark A, B and C correspond to structure of reactant, transition state and products, respectively. The mechanism of the reaction R3 can be presented by the following schema, Fig. 2. The most left picture, A, correspond to HOBr in his equilibrium ground state conformation, which is in this case reactant. On the opposite side, on the right most picture, C, is the system of H and OBr, which correspond to products. The all distance on schema are in angstroms. The mechanism of the reaction R3 can be presented by the following schema. The most left picture correspond to HOBr in his equilibrium ground state conformation, which is in this case reactant. On the opposite side, on the right most picture is the system of H and OBr, which is near his local minimum (distance 4.55 angstroms), which correspond to products. The all distance on schema are in angstroms.

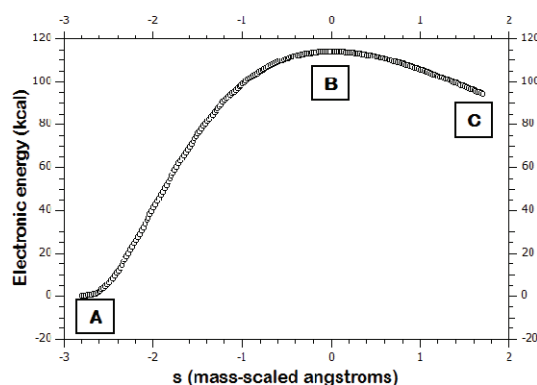


Figure 1. Potential energy curve along MEP as a function of reaction coordinate s , of reaction R3 at 0 K.

1.20×10^{-21} . The determined activation energies for forward and reverse reaction are 78.22 and 7.39 kcal/mol, and are calculated for temperature interval 100 – 373 K, while enthalpy ΔH_r is 101.10 kcal/mol.

From kinetical calculation we get the transmission coefficient for forward and reverse reaction which is $7.53E^{+07}$ and 2.16 at 100 K and 373 K, respectively.

The tunneling probabilities for reverse reaction are significant at low energies but for forward reaction they take values only at higher energies. This is one of the reasons why diagram for forward reaction rate on Fig.3 show small deviation from linearity only at high temperature. On opposite, tunneling is active mechanism for

reverse reaction even at low temperature when the system is in low energetic condition. For reverse reaction, Fig. 3 right, exists two different temperature ranges. In one, on low temperature, we can say that reaction rate is weakly dependent of temperature. In that range reaction rate curve is almost parallel with $1/T$ axis. In second temperature range, at higher temperature, reaction is faster and show lower influence of tunneling

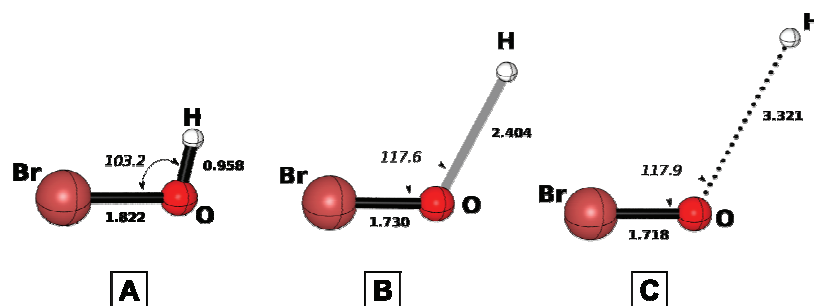


Figure 1. Structure which corresponds to reactant, A, transition state, B and product at almost infinite distance C. Units for distances are angstroms (in bold) and for angles are degrees (in italic).

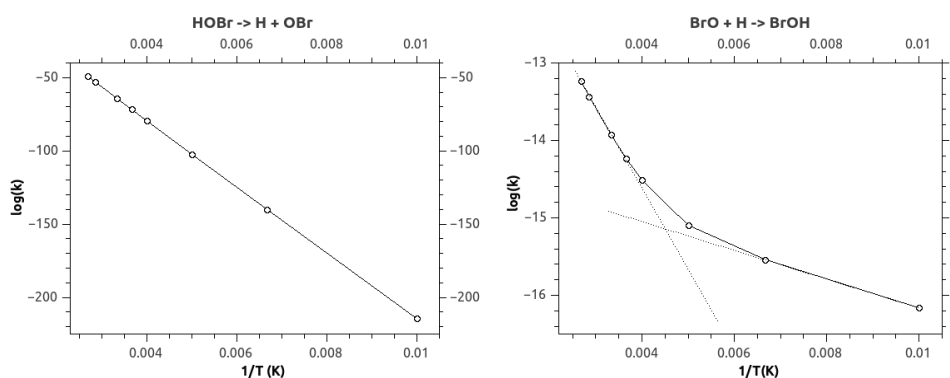


Figure 3. Influence of temperature on rate constant. On the left side is diagram for forward and on the right for reverse R3 reaction.

Conclusion

Kinetic values for $HOBr \rightleftharpoons H(^2S) + OBr(X^2\Pi_i)$ thermal decomposition were calculated for the first time. The high value for reverse rate constant suggest us that the reverse reaction can be understand as concurrent to photolysis reactions which produce BrO, Br and other reactive species responsible for ozone layer depletion.

Acknowledgements

This work is supported by Ministry of Science and Environmental of Serbia, project no. 172015.

References

[1] R.Vogt, R.N. Schindler, Ber. Bunsenges. Phys. Chem., 1993, 97, 819-829.

C-23-P

- [2] A. Bell, P. Pardon, C. Hickman, J. Frey, *J. Chem. Soc. Faraday. Trans.*, 1990, 86, 3831-3836.
- [3] Gaussian 09, Revision A.1, Gaussian, Inc., Wallingford CT, 2009.
- [4] K. Raghavachari, J. A. Pople, *Int. J. Quantum Chem.*, 14 (1978) 91-100.
- [5] POLYRATE 2008, GAUSSRATE 2008, Donald G. Truhlar, Department of Chemistry and Supercomputing Institute University of Minnesota, Minneapolis
- [6] H. Dunning Jr. and P. J. Hay, in *Methods of Electronic Structure Theory*, Vol. 2, H. F. Schaefer III, ed., PLENUM PRESS (1977)
- [7] P. J. Hay, W. R. Wadt, *J. Chem. Phys.*, 82, 284 (1985).

NONLINEAR DYNAMICS

THE BRAY-LIEBHAFSKY AND BRIGGS-RAUSCHER OSCILLATING REACTIONS

Guy Schmitz^a, Stanley Furrow^b

^a Faculty of Applied Sciences, Université Libre de Bruxelles, CP165/63, Av. F.
Roosevelt 50, 1050 Brussels, Belgium. E-mail: gschmitz@ulb.ac.be

^b Penn State Berks College, The Pennsylvania State University, Reading,
Pennsylvania 19610. E-mail: f13@psu.edu

Abstract

The common points and differences between the Bray-Liebhafsky and Briggs-Rauscher reactions are discussed. The reactants of the non-catalyzed version of the Briggs-Rauscher reaction being the same as those of the Bray-Liebhafsky reaction plus a reducing organic compound, the mechanisms of these two systems must have several common points. The marked difference between the oscillating behaviours comes from radical reactions that could be initiated by the new pathway of the iodate reduction by hydrogen peroxide at high concentrations.

Foreword

... to conduct my thoughts in such order that, by commencing with objects the simplest and easiest to know, I might ascend by little and little to the knowledge of the more complex...

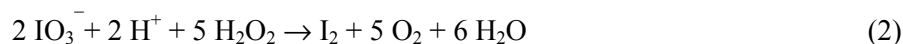
René Descartes (1596–1650). Discourse on Method.

Comparison of the Bl and Br Reactions

The Bray-Liebhafsky (BL) [1] reaction is the decomposition (1) of hydrogen peroxide catalyzed by iodate in acidic solutions.



Reaction (1) is the result of two reactions where hydrogen peroxide acts as a reducing (2) or as an oxidizing (3) agent. The sum of reactions (2) and (3) gives reaction (1).



Within a narrow range of concentrations, reactions (2) and (3) dominate alternately and oscillations are observed in the concentrations of iodine and iodide ions and in the rate of oxygen production. The mechanism of these reactions is complicated involving, beside IO_3^- and I_2 , numerous iodine intermediates. The main part of the mechanism proposed recently [2] is given in Table 1. It explains the main features of the oscillations, but for simulating quantitatively the complex observed behaviours, it must be supplemented by reactions describing the perturbing effect of oxygen.

Table 1. Main part of the mechanism of the BL reaction.

$\text{IO}_3^- + \text{I}^- + 2 \text{H}^+ \rightleftharpoons \text{IOH} + \text{IO}_2\text{H}$	R1
$\text{IO}_2\text{H} + \text{I}^- + \text{H}^+ \rightleftharpoons \text{I}_2\text{O} + \text{H}_2\text{O}$	R2
$\text{I}_2\text{O} + \text{H}_2\text{O} \rightleftharpoons 2 \text{IOH}$	R3
$\text{IOH} + \text{I}^- + \text{H}^+ \rightleftharpoons \text{I}_2 + \text{H}_2\text{O}$	R4
$\text{IOH} + \text{H}_2\text{O}_2 \rightarrow \text{I}^- + \text{H}^+ + \text{O}_2 + \text{H}_2\text{O}$	R5
$\text{I}_2\text{O} + \text{H}_2\text{O}_2 \rightarrow \text{IOH} + \text{IO}_2\text{H}$	R6
$\text{IO}_3^- + \text{H}^+ + \text{H}_2\text{O}_2 \rightarrow \text{IO}_2\text{H} + \text{O}_2 + \text{H}_2\text{O}$	R7
$2 \text{IO}_2\text{H} \rightleftharpoons \text{I}_2\text{O}_3 + \text{H}_2\text{O}$	R8a
$\text{I}_2\text{O}_3 + \text{H}_2\text{O}_2 \rightarrow \text{IO}_3^- + \text{H}^+ + \text{IO}_2\text{H}$	R8b
$\text{I}_2\text{O}_3 + \text{H}_2\text{O} \rightarrow \text{IO}_3^- + \text{H}^+ + \text{IOH}$	R8c

The BL oscillations can be observed conveniently only above 40°. The oscillations at room temperature are irregular and the periods are very long (several hours). However, a modification of this system, discovered by Briggs and Rauscher [3], oscillates nicely at room temperature with a period usually shorter than one minute. The mixture contains the same compounds as the BL reaction, acid, iodate and hydrogen peroxide, and also an organic reducing compound like malonic acid (MA) and a metal-ion catalyst (Mn^{++} in the original recipe). The classical mechanism [4] includes reactions (R1)-(R5), reactions of iodination and oxidation of the organic compound and radical reactions with the metal-ion catalyst initiated by reaction (4).



However, estimations of Gibbs energies of formation (ΔG_f) [5] indicate that the equilibrium constant of reaction (4) is so small that the recombination of OIO^\cdot radicals (-4) is nearly irreversible. Thus the classical mechanism must be revised. Moreover, BR like oscillations can be observed without metal-ion catalyst.

The Non-Catalysed Br Reaction

An acidic mixture of iodate, hydrogen peroxide and malonic acid can show oscillations similar to the BR oscillations. This was already recognized by Briggs and Rauscher in their original paper and one of us [6] has found that the range of these oscillations is wider than originally thought. An example is given in Fig.1. These non-catalyzed oscillations are observed only at high hydrogen peroxide concentrations.

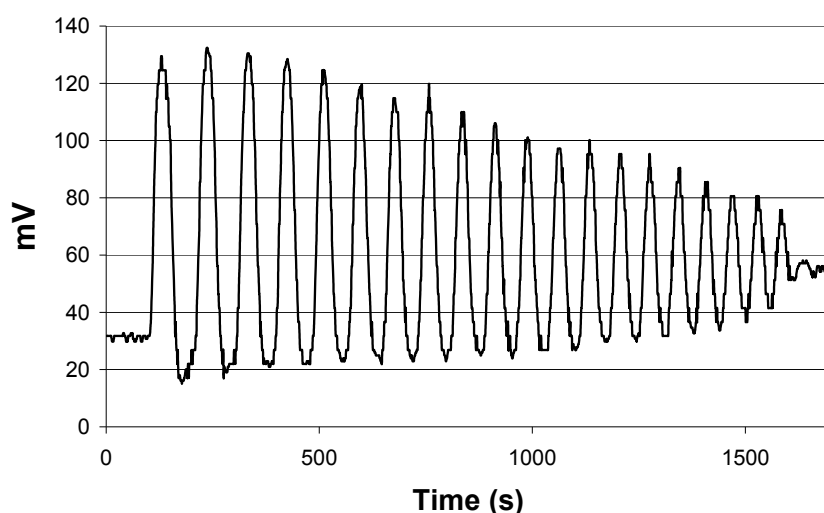


Figure 1. BR oscillations at 25° without catalyst. $[\text{HClO}_4]_0 = 0.10\text{M}$, $[\text{KIO}_3]_0 = 0.0033\text{M}$, $[\text{H}_2\text{O}_2]_0 = 1.0\text{M}$, $[\text{MA}]_0 = 0.002\text{M}$. H_2O_2 was added at 104 s. The ordinate gives the potential of an iodide selective electrode. Higher potential means lower $[\text{I}^-]$.

The oscillations in Fig.1 are important because they make a link between the BR and BL systems: the BR reaction without catalyst is also the BL system plus malonic acid. Thus, we have tried to simulate these oscillations adding malonic acid reactions to the model in Table I, but without success. The system is more complicated, is inhibited by radical scavengers and, consequently, involves radical reactions. In the example of Fig.1, addition of 2×10^{-6} mol/l of catechol stopped the oscillations for 208 s. Then oscillations resumed at about half the

D-01-SL

previous amplitude and continued for about 1480 seconds. This restart is explained by the iodination/oxidation of catechol. With 5×10^{-6} mol/l of catechol, no restart is observed. The oscillations are also inhibited by resorcinol and ferroin. Knowing that the initiation of the radical reactions is not reaction (4), the elucidation of the radical part of the non-catalyzed BR reaction mechanism remains a major challenge.

Reactions Common to the Bl and Br Systems

In order to understand complicated systems, it is always useful to study simpler subsystems. Independent information about reaction (R1) - (R7) was obtained previously (see references in [2]) but, apart from a mention in a pioneering document [7], nothing was known about reaction (R8). It was introduced into the model to allow good simulations of the kinetics of the component (2) of the BL reactions [2]. According to reaction (R8), the oxidation of IO_2H by hydrogen peroxide should follow a second order rate law. This rate law is obtained assuming that the concentration of the intermediate I_2O_3 is so small that we can make the steady state approximation $r_{8a} = r_{8b} + r_{8c}$.

$$k_{8a} [\text{IO}_2\text{H}]^2 = (k_{8a} + k_{8b} [\text{H}_2\text{O}_2] + k_{8c}) [\text{I}_2\text{O}_3]$$

The sum (R8a) + (R8c) gives the IO_2H disproportionation $2 \text{IO}_2\text{H} \rightarrow \text{IO}_3^- + \text{H}^+ + \text{IOH}$ with the rate law

$$r_{8c} = \frac{k_{8a} k_{8c}}{k_{8a} + k_{8b} [\text{H}_2\text{O}_2] + k_{8c}} [\text{IO}_2\text{H}]^2$$

The sum (R8a) + (R8b) gives the IO_2H oxidation $\text{IO}_2\text{H} + \text{H}_2\text{O}_2 \rightarrow \text{IO}_3^- + \text{H}^+ + \text{H}_2\text{O}$ with the rate law

$$r_{8b} = \frac{k_{8a} k_{8b} [\text{H}_2\text{O}_2]}{k_{8a} + k_{8b} [\text{H}_2\text{O}_2] + k_{8c}} [\text{IO}_2\text{H}]^2$$

A kinetic study of these reactions is under progress and confirms that the rate of IO_2H oxidation by low concentrations of hydrogen peroxide is proportional to $[\text{H}_2\text{O}_2][\text{IO}_2\text{H}]^2$. Fig.2 shows an example of our results. This second order with respect to $[\text{IO}_2\text{H}]$, instead of the first order assumed previously, is important for modelling the BL and BR reactions [2].

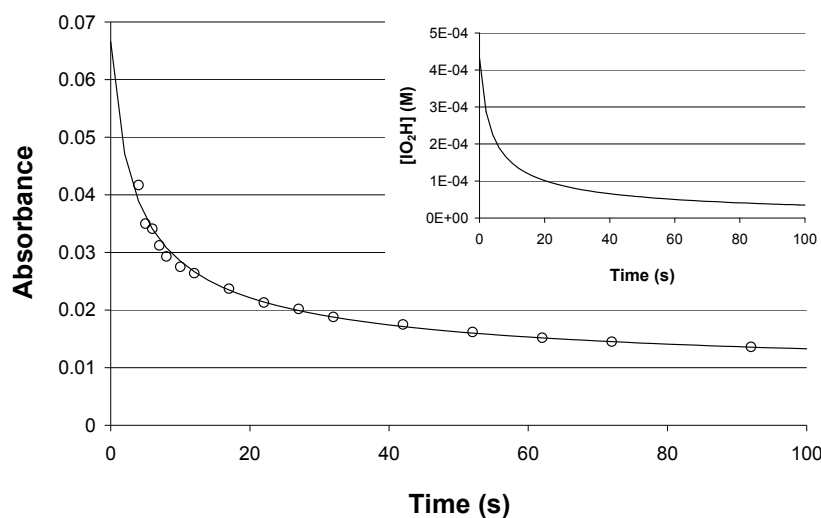


Figure 2. Time evolution of the experimental absorbance (o) and of the absorbance calculated (—) using the rate law $-d[\text{IO}_2\text{H}]/dt = 1.2 \times 10^6 [\text{H}_2\text{O}_2][\text{IO}_2\text{H}]^2$. $[\text{H}_2\text{SO}_4] = 0.26 \text{ M}$, $[\text{H}_2\text{O}_2]_0 = 5.7 \times 10^{-4} \text{ M}$, $[\text{IO}_2\text{H}]_0 = 4.32 \times 10^{-4} \text{ M}$. The insert shows the calculated evolution of $[\text{IO}_2\text{H}]$.

Another important subsystem is the iodate reduction by hydrogen peroxide. Reaction (R7) with its associated rate law was widely accepted but a new study [5] revealed another reaction pathway. It appears at high hydrogen peroxide concentrations, has a rate more than proportional to $[\text{H}_2\text{O}_2]^2$ and is inhibited by scavengers of free radicals. The discovery of this new pathway gives a partial answer to an essential question about the BR reaction: what is the source of radicals in the absence of catalyst? Knowing that the kinetics of the iodate reduction by hydrogen peroxide changes suddenly at high peroxide concentrations and that the non-catalysed BR oscillations are observed only at high hydrogen peroxide concentrations, we suggest that the two mechanisms are closely related. They are not completely elucidated but the radical part of the mechanism is probably initiated by $\text{IOH} + \text{H}_2\text{O}_2 \rightleftharpoons \text{IOOH} + \text{H}_2\text{O}$ and $\text{IOOH} + \text{H}_2\text{O}_2 \rightarrow \text{IO}^\cdot + \text{H}_2\text{O} + \text{HOO}^\cdot$ [5]. These reactions are also important for explaining the effect of oxygen on the BL reaction [2].

Conclusion

The oscillating behaviour of the BL and BR reactions are different but their essential components, acidic iodate and hydrogen peroxide, are the same and the BL reaction is a subsystem of the BR reaction. The mechanisms of these two reactions are strongly related and we propose that the mechanism of the BR oscillations should be build starting with the mechanism of the BL reaction and adding radical reactions. Progress in this direction is supported by the kinetic study of constituent reactions and of the effect of radical scavengers.

References

- [1] (a) W. C. Bray, *J. Am. Chem. Soc.*, 1921, 43, 1262; (b) W. C. Bray and H. A. Liebhafsky, *J. Am. Chem. Soc.*, 1931, 53, 38.
- [2] (a) G. Schmitz, *Phys. Chem. Chem. Phys.*, 2010, 12, 6605; (b) G. Schmitz, *Phys. Chem. Chem. Phys.*, 2011, 13, 7102.
- [3] T. S. Briggs and W. C. Rauscher, *J. Chem. Educ.*, 1973, 50, 496.
- [4] (a) S. D. Furrow and R. M. Noyes, *J. Am. Chem. Soc.*, 1982, 104, 38; (b) *idem* p.42; (c) *idem* p.45; (d) S. D. Furrow, *J. Phys. Chem.*, 1995, 99, 11131.
- [5] G. Schmitz and S. D. Furrow, *Phys. Chem. Chem. Phys.*, 2012, 14, 5711.
- [6] S. D. Furrow, unpublished results.
- [7] S. D. Furrow, *J. Phys. Chem.*, 1987, 91, 2129.

**A NOVEL CLASS OF THE OSCILLATING REACTIONS:
HOMOGENEOUS CARBONYLATION OF
UNSATURATED COMPOUNDS IN Pd COMPLEXES
SOLUTIONS**

Sergey N. Gorodsky

M.V. Lomonosov State University of Fine Chemical Technologies (MITHT)

86 Vernadsky Avenue, 119571 Moscow, Russia

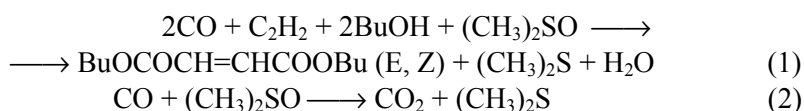
E-mail: Gorodsky@yandex.ru

Introduction

The oscillating reactions were discovered in many chemical and biological systems. The most part of oscillatory homogeneous reactions investigated in chemistry are processes of organic substrate oxidation by strong oxidants [1]. The investigations of oscillating modes of the oxidative carbonylation reactions in homogeneous catalysis by metal complex in alcohol solutions of palladium complexes with various organic substrates were conducted in MITHT for several years. We have demonstrated that the phenomenon of oscillations can be observed for reactions with participation of different alkynes, and also in different catalytic systems.

Results and discussion

Our team has discovered the critical phenomenon in typical reactions of the organometallic catalysis in which synthesis of complex molecules occurs. So, the reactions 1, 2 proceed in the system PdBr₂ – KBr – HBr – BuOH–dimethylsulphoxide:



with periodic change of carbon monoxide and acetylene consumption rate, values of platinum electrode potential (E_{Pt}), pH and color of the reaction solution [2]. Oscillations of E_{Pt} and pH were found out [3, 4] during the study of various alkynes oxidative carbonylation reactions in the system PdI₂ - KI - MeOH (reaction 3)



where R: Ph, Me. Oxidation CO to CO₂ in this system occurs at the same time. It was the first examples of oscillating processes in homogeneous catalysis with

metal complexes, as we know (Fig. 1). We have proposed the preliminary mechanism of oscillations appeared in this process.

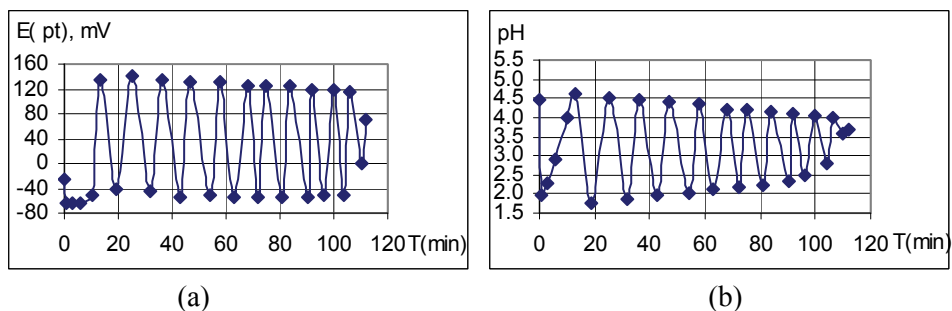
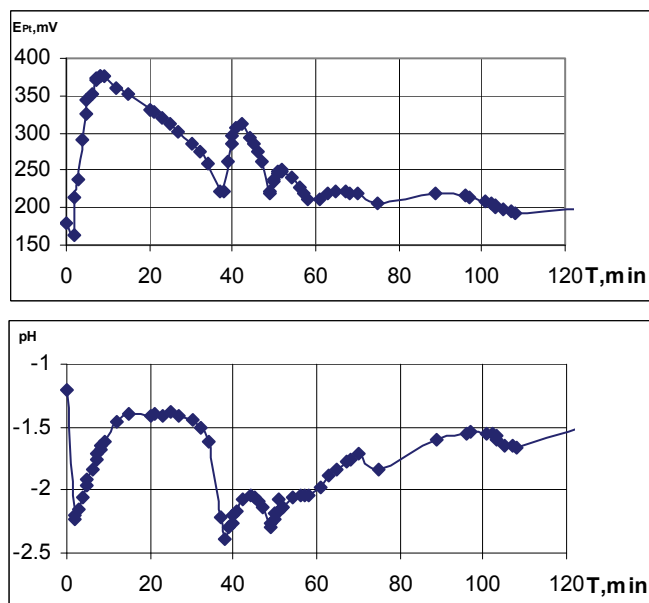


Figure 1. The change of E_{Pt} (a) and pH (b) in the contact solution during of phenylacetylene oxidative carbonylation reaction; KI(0,4 M) – PdI₂(0,01 M) – PhC≡CH(0,1 M) – CO(60% v.) – O₂(40% v.).

We have showed that the phenomenon of oscillations can be observed for reactions with participation of different alkynes, and also in different catalytic systems, for example, in system PdBr₂ - LiBr, in which the occurrence of chaotic oscillations was demonstrated. The modes of developed oscillations in reactions involving phenyl- and methyl acetylene, 2-methyl-3-buten-2-ol, 2-propin-1-ol in the systems PdI₂-KI-CO-O₂-CH₃OH; PdBr₂-LiBr-CO-O₂-CH₃OH; PdBr₂-LiBr-CO-O₂-(CH₃)₂CO-H₂O have been found [5, 6] (Fig.2).



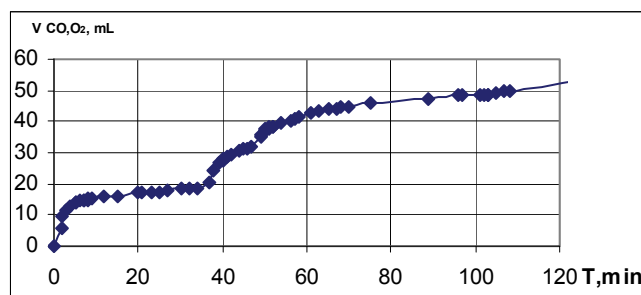


Figure 2. Oxidative carbonylation of phenylacetylene in system. LiBr-PdBr₂-H₂O- acetone LiBr(0,2M); PdBr₂(0,01M); PhA(0,1M); H₂O (0,75M); V_{(CH₃)₂CO}=10мл; [CO]₀: [O₂]₀ = 1:1.

Recently interesting modes of oscillations in carbonylation reactions of 1-nonin, 1-decin and 1-dodecin in the system PdI₂-KI-CO-O₂-CH₃OH were found.

Conclusion

The study of mechanisms of some other processes in organometallic catalysis allows to expect the occurrence of self-oscillations and other critical phenomena. The searching for such phenomena is important for development of the catalytic reaction mechanisms theory. The presence of oscillations is the powerful tool of the mechanistic hypotheses discrimination.

Acknowledgements

This work was supported by the Russian Foundation for Basic Research (project № 09-03-01072).

References

- [1] R. J. Field, M. Burger, Oscillations and Travelling Waves in Chemical Systems, Wiley, New York, 1985.
- [2] G. M. Shul'akovskiy, O. N. Temkin, N. V. Bykanova, A. N. Nyrkova, Chemical kinetics in catalysis: in Kinetic models of liquid-phase reactions, Chernogolovka: IPC, 1985, 112.
- [3] S. N. Gorodsky; A. N. Zaharov; A. V. Kulik; L. G. Bruk; O. N. Temkin, Kinetic and Catalysis, 2001, 42(2), 285-293.
- [4] S. N. Gorodsky, E. S. Kalenova, L. G. Bruk, O. N. Temkin, Russ. Chem. Bull., 2003, 52 (7), 1534 - 1543.
- [5] S. N. Gorodsky, A. V. Kurdiukov, O. N. Temkin, ICC 14 Pre-Symposium, 50th Anniversary of the Catalysis Society of Japan, Kyoto, 2008, 39.
- [6] S. N. Gorodsky, L.G. Bruk, A.E. Istomina, A.V. Kurdiukov, O.N.Temkin, Topics in Catalysis, 2009, 52(6-7), 557-562.

D-03-SL

STOICHIOMETRIC NETWORK ANALYSIS OF MAPK CASCADE

O. Hadač, I. Schreiber, M. Kohout

*Institute of Chemical Technology, Prague, Department of Chemical Engineering,
and Center for Nonlinear Dynamics of Chemical and Biological Systems,*

Technická 5, 166 28 Prague 6, Czech Republic, tel.: +420 220443107, e-mail:

Otto.Hadac@vscht.cz, Igor.Schreiber@vscht.cz

Abstract

The Mitogen Activated Protein Kinase (MAPK) cascade, one of most studied signalling systems, is a highly conserved series of three protein kinases. The cascade topology has unexpected consequences for dynamics of the MAPK signalling. Using reaction network theory, we analysed the Huang-Ferrell model of MAPK, especially a system involving activation of MAPKKK and first of the two double-phosphorylation cascades.

1. Introduction

Mitogen activated protein kinases belong to serine/threonine-specific protein kinases that respond to extracellular stimuli and modulate cellular activities. The MAPK cascade is one of the most studied signalling biochemical pathways in the eucaryotic cell where proteins transmit a signal from a receptor on the surface of the cell to the DNA in the nucleus of the cell. This biochemical network involves many proteins, including MAPK, which communicate by adding phosphate groups to a neighbouring protein, which in turn acts as an "on" or "off" switch. Although the biological responses associated with MAPK signalling are highly varied, the basic structure of the MAPK cascade is well conserved [1]. The MAPK cascade always consists of a MAPK kinase kinase (MAPKKK), a MAPK kinase (MAPKK), and a MAPK. MAPKKKs activate MAPKKs by phosphorylation at two conserved serine residues and MAPKKs activate MAPKs by phosphorylation at conserved threonine and tyrosine residues, see Fig. 1.

Physicochemical models of signalling pathways are characterized by high levels of structural and parametric uncertainty, reflecting both incomplete knowledge about signal transduction and the intrinsic variability of cellular processes [2]. As a result, these models try to predict dynamics of the systems with ten or even hundreds of free parameters [3-4]. Stoichiometric network analysis and monotone systems methods can characterize dynamics of biochemical networks based only on their structure, independently of a particular choice of parameters [5]. These approaches can admit whole classes of dynamical behaviour, such as bistability or oscillations. The combination of continuation methods with random parameter sampling enables the statistical exploration of systems-level properties, such as stability and robustness [2].

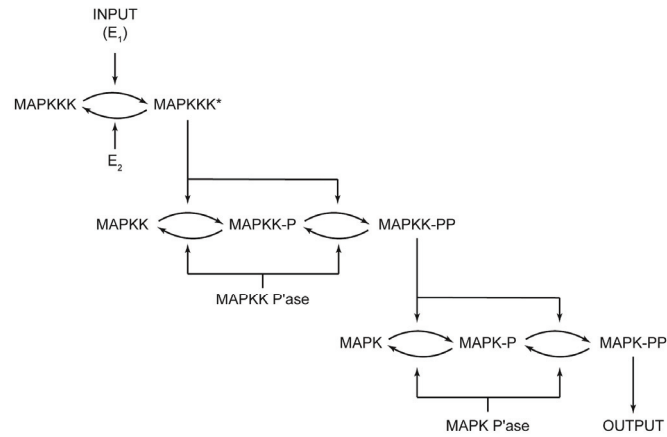


Figure 1. Schematic view of the MAPK cascade [1].

Results and Discussion

Based on the Huang-Ferrell model, we analysed dynamical behaviour of the single-phosphorylation cascade model, which is a system involving activation of MAPKKK and first of the two double-phosphorylation cascades (the first two steps in Fig. 1). The Huang-Ferrell model assumes that each enzymatic reaction obeys Michaelis-Menten kinetics, the reaction network of the system involves 18 elementary reaction steps, see Fig. 2. For simplicity of the network diagram, A , A^* , B , B_1 , and B_2 stand for MAPKKK, MAPKKK*, MAPKK, MAPKK-P, MAPKK-PP, respectively.

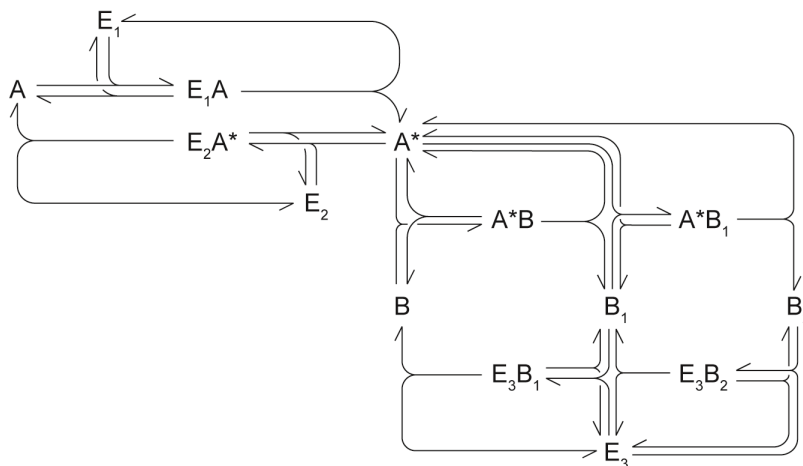


Figure 2. Network diagram of the single-phosphorylation cascade model.

We used the stoichiometric networks analysis (SNA) [6-7] to decompose the whole network of the system into irreducible or elementary subnetworks. Then we identified those elementary subnetworks that are potentially sources of nontrivial dynamical instabilities leading to bistability or oscillations. By using the classification system for chemical oscillators [8-10] we further simplified the topology of the MAPK reaction network into the smallest network which still preserves bistability but does not allow for oscillations. This network can be examined analytically using both convex parameterization employed by the SNA and classical kinetic parameters (i.e., rate coefficients) to determine multiple steady states and their stability.

3. Conclusions

We analyzed the single-phosphorylation cascade model by using numerical continuation and determine what is the role of various subnetworks in forming the bistability. The SNA was used to find the smallest network which still preserves bistability but does not allow for oscillations.

4. Acknowledgements

The authors thank for the support of the research by the grant of the MŠMT ČR KONTAKT ME10036.

5. References

- [1] C.-Y. F. Huang, J. E. Ferrell, Ultrasensitivity in the Mitogen-Activated Protein Kinase cascade, *Proc. Natl. Acad. Sci. USA*, 1996, 93, 10078.
- [2] L. Qiao, R. B. Nachbar, I. G. Kevrekidis, Bistability and oscillations in the Huang-Ferrell model of MAPK signaling, S.Y. Shvartsman, *PLoS Comput. Biol.*, 2007, 3, 1819.
- [3] J. J. Tyson, K. Chen, B. Novák, Network dynamics and cell physiology, *Nat. Rev. Mol. Cell. Biol.*, 2001, 2, 908.
- [4] N. B. Kholodenko, Cell-signalling dynamics in time and space, *Nat. Rev. Mol. Cell. Biol.*, 2006, 7, 165.
- [5] G. Craciun, Y. Z. Tang, M. Feinberg, Understanding bistability in complex enzyme-driven reaction networks, *Proc. Natl. Acad. Sci. USA*, 2006, 103, 8697.
- [6] B. L. Clarke, Stability of complex reaction networks, *Advances in Chemical Physics*, 1980, 43, 1.
- [7] J. Ross, I. Schreiber and M.O. Vlad, *Determination of Complex Reaction Mechanisms*, Oxford University Press, New York, 2006.
- [8] Eiswirth, M., A. Freund and J. Ross, Mechanistic classification of chemical oscillators and the role of species, *Adv. Chem. Phys.*, 1991, 80, 127.
- [9] T. Chevalier, I. Schreiber, J. Ross, Toward a systematic determination of complex-reaction mechanism, *J. Phys. Chem.*, 1993, 97, 6776.
- [10] J. D. Stemwedel, I. Schreiber, J. Ross, Formulation of oscillatory reaction-mechanisms by deduction from experiments, *Adv. Chem. Phys.*, 1995, 89, 327.

ADDITIVES THAT PERTURB OSCILLATIONS IN THE BRIGGS-RAUSCHER REACTION. A REVIEW

Rinaldo Cervellati

Dipartimento di Chimica "G. Ciamician", Università di Bologna, Via Selmi 2, Bologna, Italy

Abstract

The Briggs-Rauscher oscillating reaction is perturbed by several chemical species with different physico-chemical properties, from bromide ions to polyphenols to iron complexes. Perturbations by some of these species as far as their mechanistic interpretations are described in this review.

Introduction

The Briggs-Rauscher (BR) oscillating reaction consists of the oxidation and iodination of malonic acid (or its C2 substituted derivatives) by acidic iodate in the presence of hydrogen peroxide and with Mn(II) as catalyst[1]. Using a starch solution as indicator, the mixture gives rise to spectacular periodic colour changes: from colourless to yellow to blue and repeat; accordingly, the BR reaction is widely used as a demonstration of oscillating chemical systems[2] or to present the 'magic aspects' of chemistry[3]. In batch conditions the duration of the oscillatory regime depends on the initial reagent concentrations and temperature. The main inorganic intermediates of the BR are: Γ^- , I_2 , I_3^- , (responsible for colour changes since oscillations of iodide and iodine concentrations don't have the same phase), HOI, HOIO, IO^\bullet , HOO^\bullet , and the catalyst that periodically varies between Mn(II) and Mn(III) [4]. The oscillating regime is very sensitive to addition of several additives, also at very low concentrations. The goal of this review is to report the main additives that perturb the BR oscillatory regime and the mechanisms proposed to interpret these perturbations.

The early studies

A number of adducts were added to the important subsystem, iodate-peroxide-Mn(II), of the BR reaction (IP subsystem) by Furrow and Noyes[5] to seek evidence in order to propose a reasonable mechanism for the complete oscillator. They tried **crotonic acid**, **phenol**, **acrylamide**, **silver ion**, **chloride ion** and **ferric ion**. They found that crotonic acid is an efficient scavenger of HOI; its presence slows and alters the stoichiometry of reaction in the IP subsystem. Phenol is an even more efficient scavenger and acts as an inhibitor of reaction in the subsystem. Acrylamide does not seem to be a particularly effective radical scavenger in this subsystem. Silver ion, which is a scavenger of Γ^- , has rather little effect on the behavior of the subsystem. Chloride ion at 2×10^{-4} M noticeably slows the reaction; but fluoride ion at the same concentration has little effect. Ferric ion at the same concentration also has little effect even though this species is a

D-04-SL

catalyst for hydrogen peroxide disproportionation. On the basis of these results and a previous detailed investigation of subsystems of the BR reaction[6] the first realistic mechanism (called NF model) for the oscillator was proposed[7].

Inhibitory effects by bromide ion [8]

This effect was studied in detail starting from a “blank” oscillating BR mixture in which the order of reagents’ addition was as suggested in [2]: H_2O_2 , $\text{IO}_3^- + \text{HClO}_4$, Malonic acid(MA)+ MnSO_4 . The addition of bromide ions (1.0×10^{-4} M in mixture) to the component solutions produces a variety of phenomena, depending on the sequence of the addition and on the initial bromide concentration. If the addition is made some minutes after mixing H_2O_2 and acidic IO_3^- and before adding malonic acid and Mn^{2+} ions, the oscillations last for five or six cycles, then suddenly cease. If the addition is made immediately after the mixing of H_2O_2 and acidic and IO_3^- before adding malonic acid and Mn^{2+} ions, the oscillations do not start at all. The addition of bromide ions to an actively oscillating BR reaction causes a rapid suppression of the oscillations.

Spectroscopic and potentiometric measurements on subsystems and kinetic and thermodynamic considerations lead to the choice of formation of IBr species to account for these observations. The model interpretation was that Br^- can compete with step I1 of the NF mechanism ($\text{HOI} + \text{I}^- + \text{H}^+ \leftrightarrow \text{I}_2 + \text{H}_2\text{O}$) giving IBr, i.e.:



IBr is an iodinating agent for malonic acid via its enol form:



Therefore, at suitable Br^- ion concentrations, reactions I1' and C4' can compete with reactions I1 and C4 of the NF model ($\text{MA}(\text{enol}) + \text{I}_2 \rightarrow \text{IMA} + \text{I}^- + \text{H}^+$), thus preventing the growth of I^- ions and consequently the oscillatory regime.

A convincing rationale to interpret the different inhibition modes is also given in ref. [8].

Effect of soy antioxidants

The inhibitory effect of polyphenols contained in aqueous extracts of soy antioxidants was discovered almost fortuitously. In fact as part of an Italian student thesis work done at the Berks-Lehigh Valley College, Penn State Univ., it was decided to check the effect of superoxide dismutase on oscillation of the BR reported in the column ‘Tested Demonstrations’ of the Journal of Chemical Education[9]. In brief, the author reported that the addition of a crumbled superoxide dismutase pellet (2000 SOD units) to an actively reacting BR mixture caused an immediate cessation of oscillations, checked visually using starch as indicator, but he also claimed that the same amount of pure SOD had the same effect, and concluded that, since SOD is a scavenger of HOO^\bullet radicals, this inhibitory effect strongly suggests involvement of HOO^\bullet in the BR system. The student performed a number of experiments on the same mixture and found that the addition of pure SOD at up to 11600 units causes only a slight lowering of the oscillation amplitude (monitored potentiometrically with a iodide-ion-selective

electrode)[10]. Then, we decided to perform a study to investigate the real SOD effect and to identify some other possible inhibitory agents contained in the SOD pellets. For this purpose, we used SOD pellets from GNC (2000 units/pellet), preparing an aqueous extract of two finely crumbled pellets. Adding 1.0 ml of a 10-fold diluted filtered extract to 30 ml of an active BR mixture, dramatic effects were observed with respect to a reference mixture. At first, oscillations were damped, then ceased, but, after some time, the oscillatory behavior was regenerated with amplitude, frequency, number and duration of oscillations different from the reference mixture [10]. Among the ingredients of the SOD pellets declared in the label of the bottle there were soy fiber as fillers. Since it is well known that soybeans contain a number of glycosides that show strong free-radical scavenging activity, it was decided to perform a detailed investigation of inhibitory effects of aqueous extracts of soy wholeflour on the oscillations of the BR reaction in order to obtain reasonable indirect evidence of the involvement of hydroperoxyl radicals as intermediates of the BR reaction. The aqueous extract was accurately prepared and filtered. An aliquot was used to determine the weight of the dry residue (mg/mL). 1.0 mL of suitably diluted extract was then added to 30 mL of an active BR mixture. Typical recordings of the potential of a couple iodide selective electrode –reference electrodes are reported in Fig. 1 a-d.[11]. As can be seen the addition of the extract causes an immediate cessation of the oscillations that resume after a period of time called *inhibition time*, t_{inhib} . [11]. Inhibition times at different concentration of the extract added are satisfactorily fitted by a straight line as shown in Fig.2[11].

Other extracts were prepared also in mixed EtOH/H₂O and their relative “activity” was evaluated using the straight line of Fig. 2.

Two preponderant products contained in the soy wholeflour extract were identified and characterized as malonyldaidzin (MD) and malonylgenistin, (MG), two isoflavones contained in the soy with antioxidant free radical scavenging activity. The inhibitory effects of authentic samples of MD and MG were observed to be similar to those of the soy extract at very lower concentration (mg/mL) with respect to the extract. This means that the pure substances have a greater antioxidant activity. It is then reasonable to interpret the perturbation as due to the transfer of the H atom from the phenolic OH to the HOO• radical, i.e.:

$\text{Ar}(\text{OH}) + \text{HOO}\bullet \rightarrow \text{ArO}\bullet + \text{H}_2\text{O}_2$, where Ar(OH) indicates the antioxidant and ArO• the corresponding radical.

From Fig. 2 it can be seen that below 3.6 mg/mL of material added, the behavior deviates from linearity. In fact, at low concentrations of material added, the inhibition times become too low to be measured. At concentration higher than 25.6 mg/mL oscillations do not restart; this means that the reaction reaches its end, unable to produce more radicals. These findings are decisive indirect evidence of the involvement and important role played by HOO• radicals in establishing oscillations in the Briggs-Rauscher (BR) system.

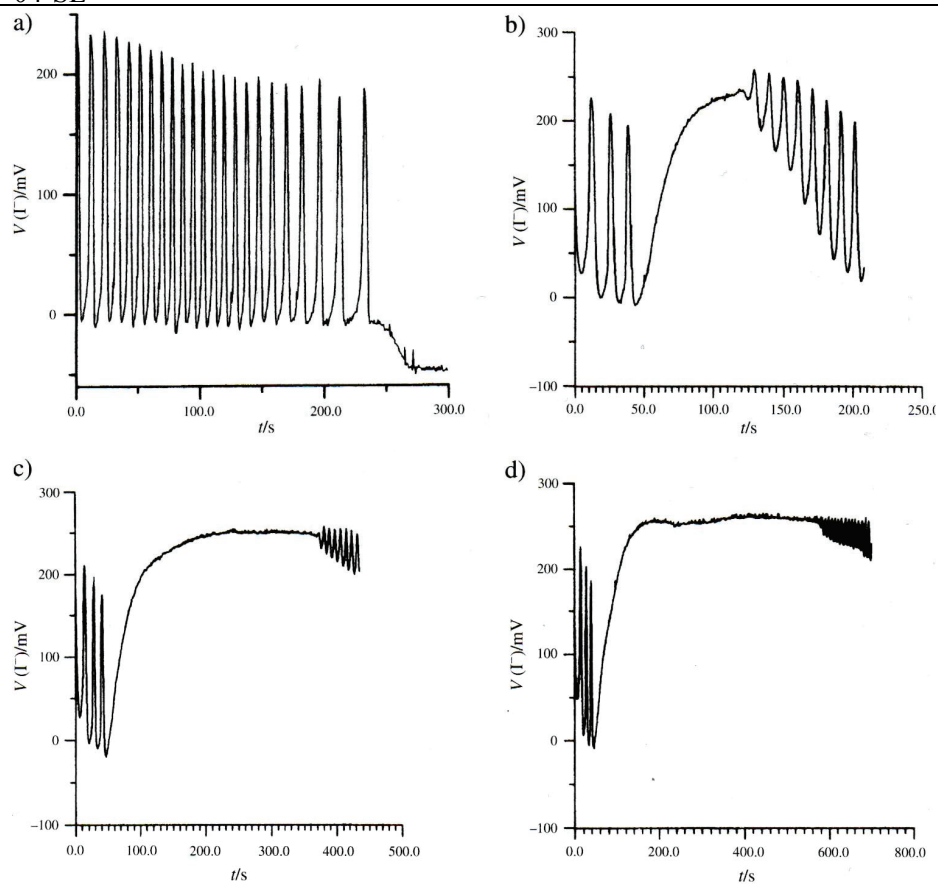


Figure 1. Recordings of potential of the iodide-selective electrode ws. Time. a) Reference mixture, initial conditions: $[H_2O_2]_0 = 1.20M$, $[IO_3]_0 = 6.67 \times 10^{-2}M$, $[HClO_4]_0 = 1.00 \times 10^{-2}M$, $[MA]_0 = 5.00 \times 10^{-2}M$, $[Mn^{2+}]_0 = 6.67 \times 10^{-3}M$; b), c), and d): effect of addition of 3.9 mg, 8.5 mg, and 12.8 mg of substances.

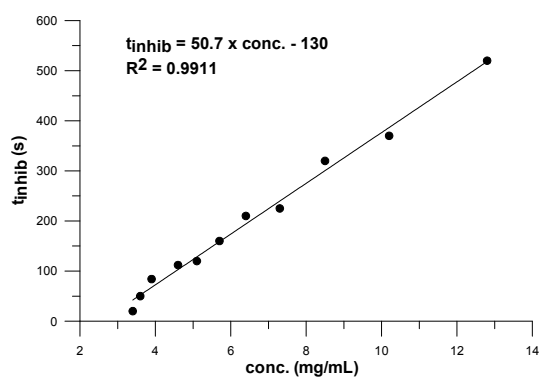
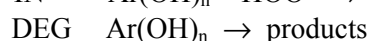


Figure 2 Graph of t_{inhib} vs concentration of material added to 30 mL of the BR mixture.

Perturbations by polyphenols

Inhibitory effects by soy active molecules lead to the implementation of a test to measure the relative activity of antioxidants based on the BR reaction[12]. The effects of ten antioxidants (pyrocatechol (PC), ferulic acid (FA), caffeic acid (CA), 2,6-,3,4-,2,4-, 3,5-, and 2,5-dihydroxybenzoic acids (DHBAs), homovanillic acid (HA), and resorcinol (benzene-1,3-diol, Re)) were studied in detail. Relative antioxidant activities of these substances with respect to resorcinol were determined in different ways on the basis of inhibition times. The limits of the calculated values of relative activity based on the Briggs-Rauscher reaction (BR method) are similar or better than those obtained with other analytical procedures. The order of activity of the ten diphenols is similar to that obtained with the TEAC (Trolox Equivalents Antioxidant capacity) method[12]. A mechanistic interpretation of the inhibitory phenomenon was given adding the following two steps to the FCA model[13] (a modification of the NF model that takes into account the role of HOO^\bullet radicals in the onset of oscillations):



The step IN represents the typical way of subtraction of a radical by an antioxidant, in the simulations $\text{Ar}(\text{OH})_{n-1}\text{O}^\bullet$ was considered an end product. The 1st order step DEG represents the possible parallel degradation of the inhibitor to unspecified products. The degradation may be due to oxidation or iodination of $\text{Ar}(\text{OH})_n$.

The kinetic constants of the model steps were kept fixed to those reported in [13], while k_{IN} and k_{DEG} were allowed to vary for the best fit to experimental behaviors.

Experimental and simulated behavior of $\text{Log}[\text{I}^-]$ vs. time for a typical BR mixture perturbed by caffeic acid are reported in Fig. 3.

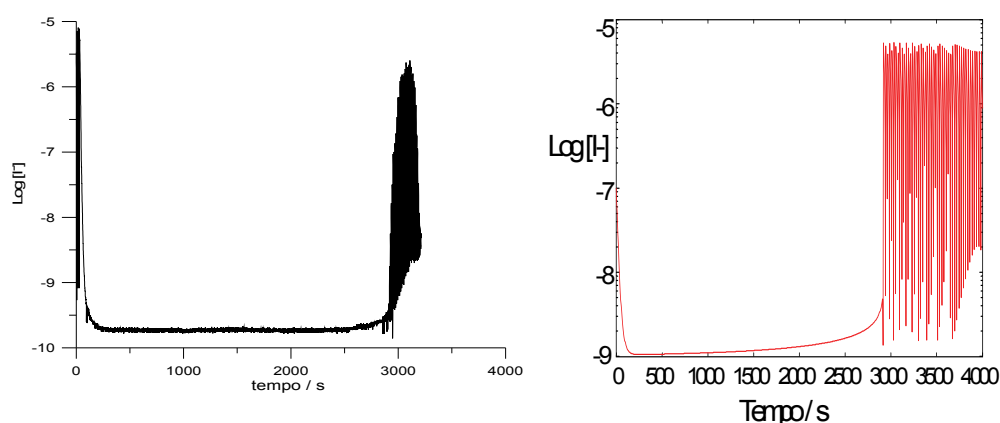


Figure 3. left) Experimental behavior of $\text{Log} [\text{I}^-]$ vs. time for an inhibited BR mixture (initial conditions: $[\text{H}_2\text{O}_2]=1.20\text{M}$, $[\text{HClO}_4]=0.0266\text{M}$, $[\text{IO}_3^-]=0.0667\text{M}$, $[\text{MA}]=0.050\text{M}$, $[\text{Mn}^{2+}]=0.0067\text{M}$, 1.0 ml of caffeic acid (0.03 mg/ml) added after the 3rd oscillation. **right)** Simulated behavior of $\text{Log} [\text{I}^-]$ vs. time for a mixture of the same composition.

D-04-SL

From Fig. 3 it can be seen the very good agreement between experimental (2794 s) and simulated (2778 s) inhibition times.

The same agreement was found for all explored concentration of caffeic acid, finding the following unique values for the rate constants: $k_{\text{IN}} = 1.0 \times 10^8 \text{ M}^{-1}\text{s}^{-1}$, $k_{\text{DEG}} = 8.0 \times 10^{-4} \text{ s}^{-1}$. [12]

The kinetics of the possible parallel reactions of oxidation of diphenols to quinones by acidic iodate or benzene ring iodination by I_2 were studied in detail [14]. The conclusion was that the values for k_{IN} are composite values for processes that consume HOO^\bullet radicals by both phenols and quinones, and likewise, k_{DEG} is a composite depending on degradation of both phenols and quinones to nonactive oxidation or iodinated products. Values for k_{IN} and k_{DEG} were calculated for all the diphenols, ranging from 10^5 to $10^8 \text{ M}^{-1}\text{s}^{-1}$ and from 0 to 10^{-4} s^{-1} respectively. The order of antioxidant activity based on values of k_{IN} is similar to that obtained with the experimental values (same standard: Re) [14]. This means that the ratio $[\text{std}]/[\text{smp}]$ where $[\text{std}]/[\text{smp}]$ are the concentrations of the sample and the standard that give the same inhibition time is a measure of the relative antioxidant capacity of phenolic compounds.

Effect of ascorbic acid (and of iodide ion)

Ascorbic acid (vitamin C) is a recognized antioxidant in living systems. In order to have an inhibitory effect on the BR oscillations system, substantially higher concentrations ($>10^{-3} \text{ M}$) are required compared to phenolic additives. The major interaction of ASC has been experimentally shown to be interaction with iodine in oxidation states V, III, I, and 0 and reduction to iodide. A 5-step model including the oxidation of ascorbic (ASC) to dehydroascorbic (DHA) acid by IO_3^- , HOIO and HOI, and the equilibrium $\text{I}_2 + \text{I}^- \leftrightarrow \text{I}_3^-$, reproduced well the experimental values of $[\text{I}_3^-]_{\text{max}}$ and t_{max} (inhibition time at $[\text{I}_3^-]_{\text{max}}$). Reaction of ascorbic acid with HOO^\bullet was not included in this model, because ASC contains no H atom transferable to this radical. The mechanism by which ASC acts as antioxidant is different from radical scavenging antioxidants as phenolic substances as far as the very different mechanisms of interaction with the BR oscillator [15].

Effect of α -tocopherol

α -Tocopherol (vitamin E) a typical highly lipophilic antioxidant in living systems containing an OH phenolic group is soluble in acetone that also is a suitable substrate for the BR reaction. Perturbations of a highly concentrated acetone-based BR oscillator by acetic solutions of vitamin E were studied [16]. The inhibitory effects were found similar to those provoked by hydrophilic polyphenols in the malonic acid (MA)-based oscillator, but to obtain reasonable inhibition times, the concentration of vitamin E must be at the mM level instead μM . However, there is a region of concentrations where there is a nearly linear relation between concentration and inhibition time. Inhibitory effects by vitamin E were modelled assuming its reaction with HOO^\bullet radicals by using the FCA mechanism reported with some minor modifications [16], obtaining the following unique values for k_{IN}

and k_{DEG} : $k_{\text{IN}} = 750 \text{ M}^{-1}\text{s}^{-1}$, $k_{\text{DEG}} = 4.2 \times 10^{-2} \text{ s}^{-1}$. A comparison with a hydrophilic diphenol (2,6-dihydroxybenzoic acid) in the acetone-based oscillator showed that the inhibitory reaction is much slower in this system than in the MA one [16, 12].

Effect of phenantroline-iron complexes

Perturbations of the oscillatory regime of the Briggs–Rauscher (BR) reaction by the iron(II)–phenanthroline (ferroin) complex were observed in batch conditions [16]. The path of the perturbation (immediate quenching of oscillations – inhibition time – resumption of oscillations) is similar to that provoked by antioxidant free-radical scavengers; however, perturbations occur in a ferroin concentration range much lower than that in which antioxidants act. To investigate this effect, reactions between the iron(II)–or iron(III)–phenanthroline (ferriin) and reagents or intermediates of the BR system were studied in detail. Results of these studies showed that the interaction of the ferroin/ferriin couple with iodine production (IP Subsystem) is responsible for the observed perturbation. In fact a spectrophotometric study of a reference IPS (acidic iodate, H_2O_2 and MnSO_4) without and with ferroin added, following both the ferroin and I_2 peaks (510 and 460 nm respectively), showed that ferroin in the 0.25– 0.50 μM range causes a decrease in iodine production by five or six fold. The study of the system ferriin + H_2O_2 (H^+) was followed spectrophotometrically at 510 nm. It was found that the mixture turned fairly rapidly back to red, from which a rough rate constant of $\approx 0.02 \text{ M}^{-1} \text{ s}^{-1}$ was calculated. A mechanistic interpretation involving HOO^\bullet radical was proposed [17].

Addition of products and intermediates

In the classic MA-based BR oscillators the first organic product is mono iodo malonic acid (IMA). Iodomalonic acid (IMA) can serve as a substrate also; thus, the first product in that case is diiodomalonic acid (I_2MA) [18]. With IMA-based oscillators having some initial I_2MA (generated in situ by slow addition of KI solution, added before H_2O_2), the number of oscillations is either reduced or none are seen, and there is immediate transition to state (II), high $[\text{I}^-]$ and $[\text{I}_2]$, as defined by Vanag [19]. (State (II) is the ending state for the reference mixture shown in Figure 1a). The higher the $[\text{I}_2\text{MA}]$ or the higher the ratio of $[\text{I}_2\text{MA}]$ to $[\text{IMA}]$, the fewer number of oscillations and shorter time before transition to state (II). Iodination of IMA by HOI , I_2 or other intermediates to I_2MA was spectrophotometrically investigated as far as their degradation. Some of the reactions of IMA and I_2MA and other possible degradation/oxidation products of those compounds were studied in detail using NMR spectrometry [20]. It was found that oxalic acid (OA) is one of the main products in the BR reaction. In non-oscillating solutions, oxidation of IMA and/or I_2MA by Fenton-type reactions also produced OA as well as I_2 . Tartronic acid (TTA) was nearly inert to Fenton-type reactions; however, TTA was oxidized by iodate and iodine to MOA (mesoxalic), which in turn could form OA in the presence of H_2O_2 plus catalyst. In conclusion,

D-04-SL

degradation pathways for both IMA and I₂MA to oxalic acid, CO₂ and CO must be included in the mechanism for BR oscillators [18, 20].

Effect of addition of phenol

Fig. 4 shows the dramatic effect of the addition of phenol at 3.0×10^{-5} M

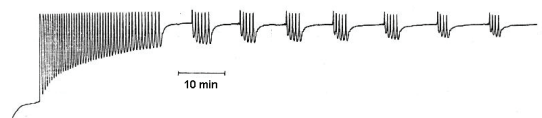


Figure 4. Initial concentrations: $[\text{HClO}_4] = 0.10$ M; $[\text{KIO}_3] = 0.020$ M; $[\text{MnSO}_4] = 0.0020$ M; $[\text{MA}] = 0.016$ M; $[\text{H}_2\text{O}_2] = 1.20$ M; $[\text{phenol}] = 3.0 \times 10^{-5}$ M.

This intermittent phenomenon was discovered by S.D. Furrow in 1980 [21] and it is now under deep investigation by the physical chemistry group of the Belgrade University in cooperation with S.D. Furrow and myself.

References

- [1] T. S. Briggs, W.C. Rauscher, *J. Chem. Educ.*, 1973, 50, 496.
- [2] B. Z. Shakhshiri, Briggs–Rauscher Reaction. In *Chemical Demonstrations*; The University of Wisconsin Press: Madison, WI, 1985, 2, 248–256.
- [3] H. V. Roesky, K. Möckel, K. *Chemical Curiosities*, VCH: Weinheim, Germany, 1996; 131–132.
- [4] P. V. Lalhita, P. Sambasiva Rao, R. Ramaswamy, *Current Science*, 1991, 61, 352–353.
- [5] S. D. Furrow, R. M. Noyes, *J. Am. Chem. Soc.*, 1982, 104, 38–40.
- [6] S. D. Furrow, R. M. Noyes, *J. Am. Chem. Soc.*, 1982, 104, 40–45.
- [7] R. M. Noyes, S. D. Furrow, *J. Am. Chem. Soc.*, 1982, 104, 45–48.
- [8] R. Cervellati, B. Mongiorgi, *Int. J. Chem. Kinet.*, 1998, 30, 641–646.
- [9] D. A. Franz, *J. Chem. Educ.*, 1991, 68, 57.
- [10] R. Cervellati S. D. Furrow, G. Amadori, presented at the XXIX Congresso Nazionale di Chimica Fisica, Italy, Book of Abstract, 1998, 94–95. (in English)
- [11] R. Cervellati, N. Crespi-Perellino, S. D. Furrow, A. Minghetti, *Helv. Chim. Acta*, 2000, 83, 3179–3189.
- [12] R. Cervellati, K. Höner, S.D. Furrow, C. Neddens, S. Costa, *Helv. Chim. Acta*, 2001, 84, 3533–3547
- [13] S. D. Furrow, R. Cervellati, G. Amadori, *J. Phys. Chem. A*, 2002, 106, 5841–5850.
- [14] R. Cervellati, K. Höner, S.D. Furrow, F. Mazzanti, S. Costa, *Helv. Chim. Acta*, 2004, 87, 133–155.
- [15] S. D. Furrow, K. Höner, R. Cervellati, *Helv. Chim. Acta*, 2004, 87, 735–741.
- [16] R. Cervellatui, S. D. Furrow, E. Greco, K. Höner, M.L. Venturi, *Helv. Chim. Acta*, 2004, 93, 837–846.
- [17] R. Cervellati, S. D. Furrow, *Inorg. Chim. Acta*, 2007, 360, 842–848.
- [18] R. Cervellati, E. Greco, S. D. Furrow, *J. Phys. Chem. A*, 2010, 114, 12888–12892.
- [19] V. K. Vanag, *J. Chem. Biochem. Kinet.*, 1992, 2, 75–83.
- [20] S. D. Furrow, D. J. Aurentz, *J. Phys. Chem. A*, 2010, 114, 2526–2533.
- [21] S. D. Furrow, Intermittent Oscillations in a Modified Briggs-Rauscher Oscillator, poster presented at a Gordon Conference in the 1980s.

MIXED-MODE OSCILLATIONS IN MULTIPLE-TIME-SCALE DYNAMICS OF THE BRAY-LIEBHAFSKY OSCILLATORY REACTION

Željko Čupić

*University of Belgrade, Institute of Chemistry, Technology and Metallurgy,
Department of Catalysis and Chemical Engineering,
Njegoševa 12, 1100 Belgrade, Serbia (zcupic@nanosys.ihm.bg.ac.rs)*

Abstract

The mixed-mode dynamical states in the concentration phase space of the Bray-Liebhafsky oscillatory reaction are discussed theoretically in a related multiple-time-scale model. With aim to explain the mixed-mode oscillations obtained by numerical simulations of the various dynamical states of a model for the Bray-Liebhafsky reaction under CSTR conditions, the folded singularity points on the critical manifold of the full system and Andronov-Hopf bifurcation of the fast subsystem are calculated. The interaction between those singularities causes occurrence of tourbillion structure and canard solutions.

Introduction

Any reaction system starting from some arbitrary initial conditions tends to final steady or equilibrium state that plays the role of an attractor, passing through distinct regions of the phase space while its different chemical species simultaneously transform through the reaction network. Since, almost all complex many variable dynamical systems are characterized by multiple-time-scales, various forms of attractors and transitions between different dynamical states were studied in such systems. Typical example is an oscillatory reaction, known as the Bray-Liebhafsky (BL) one, that consists of a complex homogeneous catalytic oscillatory process involving numerous iodine intermediates such as I_2 , I^- , HIO , HIO_2 and I_2O , that all oscillates [1]-[4]. The concentrations of mentioned species in the considered process differ for several orders of magnitudes among themselves. Thus, typical concentration of hydrogen peroxide during oscillatory state of the system is between 10^{-2} and 10^{-1} mol dm $^{-3}$, the concentration of iodine is between 10^{-5} and 10^{-4} mol dm $^{-3}$, whereas the concentrations of other species are much lower, between 10^{-9} and 10^{-6} mol dm $^{-3}$. Consequently, their simultaneous time variations are different, resulting in dissimilar behaviors characteristic for multiple-time-scale systems with, at least, slow (large-concentration) and fast (low-concentration) species. In systems, where concentrations of crucial species differ significantly, the relaxation oscillations are common. Furthermore, in multiple-time-scale systems with more than one slow variable, mixed-mode oscillations (MMO-s) may appear in the region with simple sustained oscillations. [5] They generally consist of two types of oscillations with distinct amplitudes: large-

D-05-SL

amplitude oscillations (LAO-s) and small-amplitude oscillations (SAO-s). Depending on numbers of small (S) and large (L) oscillations in a period, different periodic dynamical states can be identified and assigned by state enumeration L^S . Between every two successive periodic states with different dynamical assignment, the chaotic states appear. [6] Here we analyze emerging of chaotic attractor in the model [7] of BL reaction (Table 1) with multiple-time-scale dynamics.

Numerical simulations and analysis

We have analyzed time series obtained by numerically simulating the model of the Bray-Liebhafsky oscillatory reaction under isothermal CSTR conditions ($T = 60$ °C). Reaction rate constants at 60°C are: $k_1 = 1.383 \times 10^2 \text{ min}^{-1}$; $k_{-1} = 7.91 \times 10^7 \text{ mol}^{-1} \times \text{dm}^3 \times \text{min}^{-1}$; $k_2 = 4.79 \times 10^{10} \text{ mol}^{-1} \times \text{dm}^3 \times \text{min}^{-1}$; $k_3 = 5.00 \times 10^3 \text{ min}^{-1}$; $k_{-3} = 3.15 \times 10^8 \text{ mol}^{-1} \times \text{dm}^3 \times \text{min}^{-1}$; $k_4 = 3.00 \times 10^{11} \text{ mol}^{-1} \times \text{dm}^3 \times \text{min}^{-1}$; $k_{-4} = 46.97 \text{ min}^{-1}$; $k_5 = 1.487 \times 10^4 \text{ mol}^{-1} \times \text{dm}^3 \times \text{min}^{-1}$; $k_6 = 5.00 \times 10^5 \text{ mol}^{-1} \times \text{dm}^3 \times \text{min}^{-1}$; $k_7 = 2.00 \times 10^3 \text{ mol}^{-1} \times \text{dm}^3 \times \text{min}^{-1}$; $k_8 = 2.2303 \times 10^{-4} \text{ min}^{-1}$.

All calculations were performed using MATLAB program package. System of the ordinary differential equations was solved by means of ode15s solver. Relative and absolute error tolerance values 3×10^{-14} and 1×10^{-20} , respectively, were used in all simulations. Initial values of concentrations were $[\text{IO}_3^-]_0 = 0.0474 \text{ mol} \times \text{dm}^{-3}$, $[\text{H}^+]_0 = 0.0958 \text{ mol} \times \text{dm}^{-3}$ and $[\text{H}_2\text{O}_2]_0 = 0.155 \text{ mol} \times \text{dm}^{-3}$. Flow rate j_0 and inflow hydrogen peroxide concentration $[\text{H}_2\text{O}_2]_{\text{in}}$, as control parameters, were varied in wide region of values.

With aim to explain the MMO-s obtained by numerical simulations of the various dynamical states of a model for the Bray-Liebhafsky reaction under CSTR conditions, the folded singularity points on the critical manifold of the full system and Andronov-Hopf bifurcation of the fast subsystem are calculated.

The critical manifold of the BL reaction model under consideration is a two-dimensional surface placed in a six-dimensional phase space. It is completely determined by steady-state equations of four fast species. Hence, we have to solve the system of four equations with six variables. The concentrations of H_2O_2 and HIO are selected to be the parametric variables in our calculations. The points on the manifold are obtained by symbolic calculations.

Points at the fold line were determined according to ref. [5], from the condition:

$$\text{Det}(J(X_i)) = 0, \quad (1)$$

where X_i denotes the fast species HIO, HIO_2 , I_2O and Γ^- and J is the Jacobian of corresponding fast subsystem. This request must be fulfilled on the border between stable and unstable branch of the critical manifold.

Table 1. Model of the BL reaction used in numerical simulations [7].

Reaction	No.
$\text{IO}_3^- + \text{I}^- + 2\text{H}^+ \rightleftharpoons \text{HIO} + \text{HIO}_2$	(R1) (R-1)
$\text{HIO}_2 + \text{I}^- + \text{H}^+ \longrightarrow \text{I}_2\text{O} + \text{H}_2\text{O}$	(R2)
$\text{I}_2\text{O} + \text{H}_2\text{O} \rightleftharpoons 2\text{HIO}$	(R3) (R-3)
$\text{HIO} + \text{I}^- + \text{H}^+ \rightleftharpoons \text{I}_2 + \text{H}_2\text{O}$	(R4) (R-4)
$\text{HIO} + \text{H}_2\text{O}_2 \longrightarrow \text{I}^- + \text{H}^+ + \text{O}_2 + \text{H}_2\text{O}$	(R5)
$\text{I}_2\text{O} + \text{H}_2\text{O}_2 \longrightarrow \text{HIO} + \text{HIO}_2$	(R6)
$\text{HIO}_2 + \text{H}_2\text{O}_2 \longrightarrow \text{IO}_3^- + \text{H}^+ + \text{H}_2\text{O}$	(R7)
$\text{IO}_3^- + \text{H}^+ + \text{H}_2\text{O}_2 \longrightarrow \text{HIO}_2 + \text{O}_2 + \text{H}_2\text{O}$	(R8)
$(\text{H}_2\text{O}_2)_{\text{in}} \longrightarrow \text{H}_2\text{O}_2$	(R9)
$\text{H}_2\text{O}_2 \longrightarrow (\text{H}_2\text{O}_2)_{\text{out}}$	(R10)
$\text{I}^- \longrightarrow (\text{I}^-)_{\text{out}}$	(R11)
$\text{HIO} \longrightarrow (\text{HIO})_{\text{out}}$	(R12)
$\text{HIO}_2 \longrightarrow (\text{HIO}_2)_{\text{out}}$	(R13)
$\text{I}_2\text{O} \longrightarrow (\text{I}_2\text{O})_{\text{out}}$	(R14)
$\text{I}_2 \longrightarrow (\text{I}_2)_{\text{out}}$	(R15)

The singularity point on the fold line was calculated according to ref. [5], from the condition:

$$\frac{df_1}{dt} \cdot \frac{\partial g}{\partial x_1} + \frac{df_2}{dt} \cdot \frac{\partial g}{\partial x_2} = 0, \quad (2)$$

where x_1 and x_2 are concentrations of slow species, f_1 and f_2 are their corresponding rates and g is a rate of the fast variable. In our case this gives for e.g. [HIO]:

$$\frac{d}{dt} \left(\frac{d[\text{H}_2\text{O}_2]}{dt} \right) \cdot \frac{\partial}{\partial [\text{H}_2\text{O}_2]} \left(\frac{d[\text{HIO}]}{dt} \right) + \frac{d}{dt} \left(\frac{d[\text{I}_2]}{dt} \right) \cdot \frac{\partial}{\partial [\text{I}_2]} \left(\frac{d[\text{HIO}]}{dt} \right) = 0. \quad (3)$$

Furthermore, two nullclines were evaluated from corresponding rate equations for sets of all four fast species combined with each of two slow ones. Hence, we have one nullcline that describe the steady state condition of species I_2 , HIO, HIO₂, I₂O and Γ (the iodine nullcline) and the other one for the combination H₂O₂, HIO, HIO₂, I₂O and Γ (the hydrogen peroxide nullcline). Each one of two subsystems gives as a solution a line, located in the critical manifold of the fast species. Disproportionation steady-state of the full system is placed in the point where two nullclines intersect.

Finally, Andronov-Hopf point was identified numerically on the iodine nullcline using simple test ensuring that the real part of two complex eigenvalues (corresponding to five-dimensional Jacobian) is passing through zero.

Results and Discussion

The reaction dynamics characteristic for a BL system with multiple time scales in CSTR is strongly related to the dynamics of the corresponding system in batch reactor, which is already explained in the light of multiple time scale systems. [8], [9] Both dynamical systems are organized by principally identical hypersurface in phase space (Fig. 1). The main difference between them is caused by inflow of hydrogen peroxide that exists only in CSTR. Hence, when the system is in the oscillatory state under batch conditions, the hydrogen peroxide decomposes monotonously while in CSTR the concentration of hydrogen peroxide, although constant in average, periodically decreases and increases. Under batch conditions there are regular oscillations, but variable in time (the limit "cycle" is not closed) since the concentration of hydrogen peroxide, as main slow variable, always decreases. The system approaches to the stable steady state by spiraling around the unstable one, which is shifted through phase space by changing value of the hydrogen peroxide concentration. More or less smooth moving along the two stable branches corresponds to R and O pathways stoichiometries, involving the I_2 as the only slow species in the batch reactor. At the ends of the two stable branches system jumps between them, revert direction and alternate the stoichiometry between R and O. [8] Under the CSTR conditions, system can also start from arbitrary initial conditions, but eventually it comes to limit cycle of the sustained oscillations.

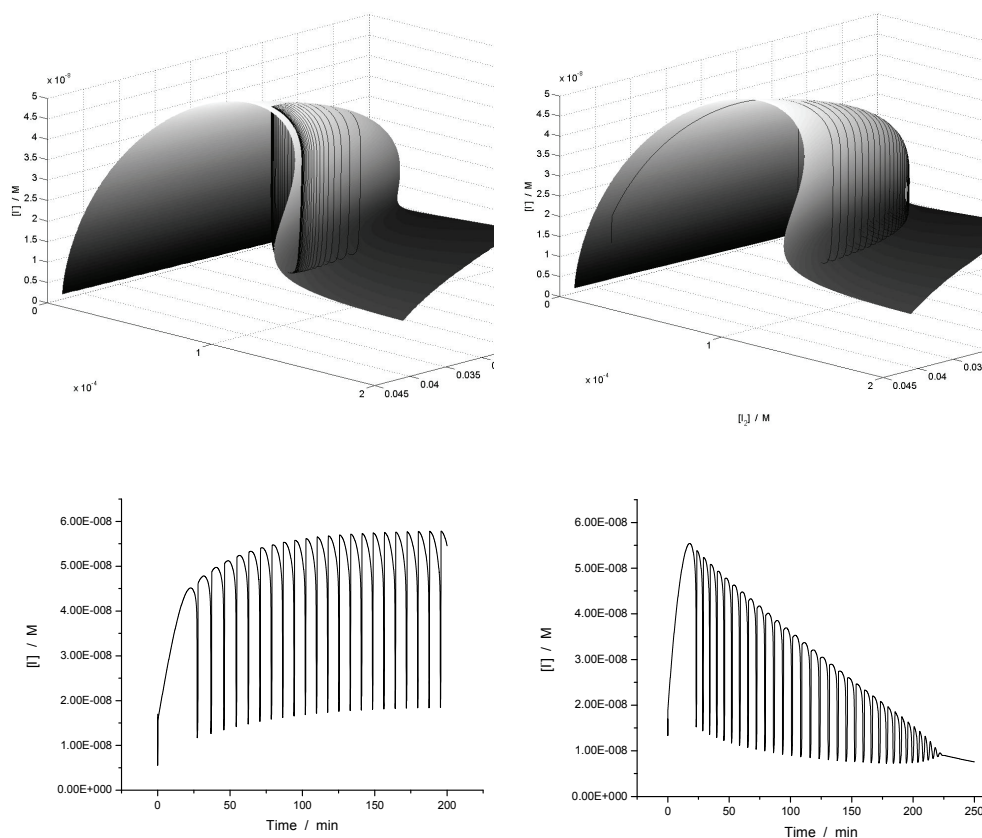


Figure 1. (up and left) Critical manifold of the slow-fast BL reaction system in the CSTR, $[H_2O_2]_0 = 2 \times 10^{-4}$ M; (up and right) Surface of nullclines for the batch reactor, $[H_2O_2]_0 = 4 \times 10^{-4}$ M. Corresponding time series are given below.

Unlike global dynamics of LAO-s, the occurrence of SAO-s in MMO-s is caused by local singularities on the critical manifold. More precisely, the SAO-s are spiraling around the fold line (Fig. 2). There are different mechanisms that can cause MMO-s. The main role in those mechanisms belongs to one of singularities, either if it is Folded Node, or Dynamical Andronov-Hopf point. However, different mechanisms of MMO-s lead to different properties of SAO-s.

D-05-SL

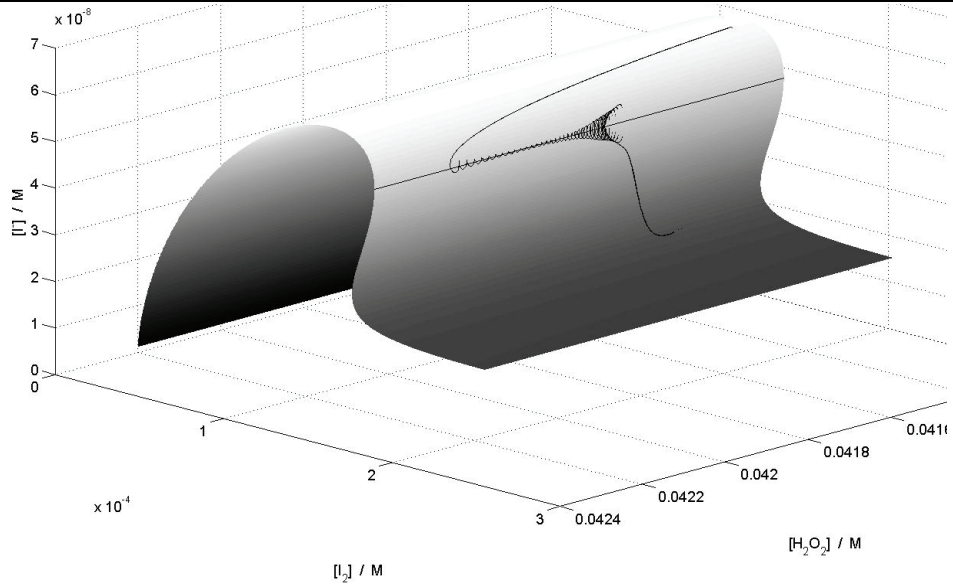


Figure 2. Part of the critical manifold for the BL model in CSTR, with MMO-s.

Folded Node, and Dynamical Andronov-Hopf point of the BL system are plotted in Fig. 3.

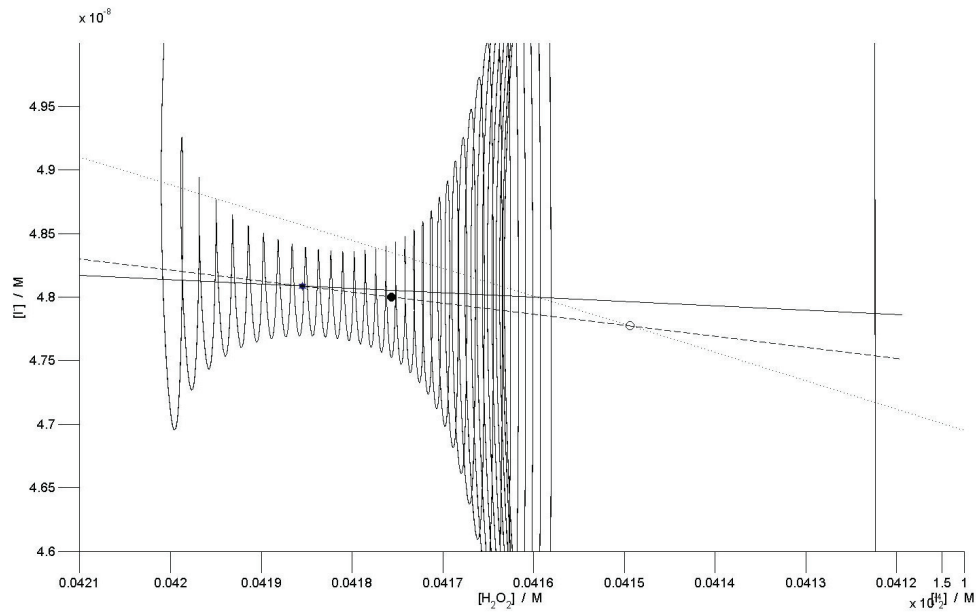


Figure 3. Folded singularity and Dynamical Andronov-Hopf bifurcation point of the fast subsystem with iodine, found on the iodine nullcline (dashed line).

The interaction between those singularities causes occurrence of tourbillion structure and canard solutions, leading to development of SAO-s, and combined with global return mechanism subsequently also to MMO-s.

Iodine plays the most important role in this system being in a part fast, and otherwise slow variable. In the model discussed here, dynamical Andronov-Hopf bifurcation is present only in the five dimensional fast subsystem where iodine is included also. Therefore, the SAO-s emerging from dynamical Andronov-Hopf bifurcation, are developed only if the limit cycle of LAO-s, governed by folded singularity is close enough to iodine nullcline, so that iodine can behave like fast species.

Conclusion

Analyzing a model for the BL reaction in open reactor, with six independent intermediate species, with concentrations that differ for several orders of magnitudes, resulting therefore in multiple-time-scale evolution, we have found mixed-mode oscillations in some range of flow rate values.

The key detail in mixed mode oscillations mechanism is that iodine change its slow species property transforming to fast species at the moment when system would jump from one to the other stable branch of the manifold. Thus, the BL reaction system having two slow and four fast variables, in the mixed-mode oscillatory region, transforms for instant to the system with one slow and five fast variables. There, the Andronow-Hopf bifurcation occurs in the five dimensional fast subsystem, with appearance of two complex conjugate eigenvalues changing the sign of their real part. Lower dimensional fast subsystem posses no complex eigenvalues.

Acknowledgement

This work was partially supported by the Ministry for Science of the Republic of Serbia (Grants no. III 45001 and ON 172015).

References

- [1] W. C. Bray, *J. Am. Chem. Soc.*, 43 (1921) 1262-1267.
- [2] W. C. Bray, H. A. Liebhafsky, *J. Am. Chem. Soc.*, 53 (1931) 38.
- [3] Lj. Kolar-Anić, Ž. Čupić, S. Anić, G. Schmitz, *J. Chem. Faraday Trans.*, 93 (1997) 2147-2152.
- [4] G. Schmitz, Models for the oscillating reactions nullclines and steady states, in S. Ribnikar, S. Anić (Eds.), *Physical Chemistry '98*, Soc. Phys. Chemists of Serbia, Belgrade, 1998, 173-179.
- [5] M. Desroches, J. Guckenheimer, B. Krauskopf, C. Kuehn, H. Osinga, M. Wechselberger, *SIAM Review*, 54 (2012) 211-288.
- [6] A. Z. Ivanović-Šašić, V. M. Marković, S. R. Anić, Lj. Z. Kolar-Anić, Ž. D. Čupić, *Phys. Chem. Chem. Phys.*, 13 (2011) 20162-20171.
- [7] Lj. Kolar-Anić, Ž. Čupić, G. Schmitz, S. Anić, *Chem. Eng. Sci.*, 65 (2010) 3718-3728.
- [8] Lj. Kolar-Anić, Ž. Čupić, S. Anić, G. Schmitz, *J. Chem. Faraday Trans.*, 1997, 93, 2147-2152.

D-05-SL

- [9] G. Schmitz, Models for the oscillating reactions nullclines and steady states, in S. Ribnikar, S. Anić (Eds.), Physical Chemistry '98, Soc. Phys. Chemists of Serbia, Belgrade, 1998, 173-179.

MEMORY STORAGE PROCESSES IN SELECTED EMULSIONS AND DOUBLE EMULSIONS

Aleksandar M. Spasic

*Institute for Technology of Nuclear and Other Mineral Raw Materials
86 F. d'Esperey St. 11000 Belgrade, Serbia*

Abstract

Since the events at developed liquid-liquid interfaces have to be considered at the molecular, atomic, and/or entities level for their studies it is inevitable to introduce the electron transfer phenomenon beside the classical heat, mass, and momentum transfer phenomena commonly used in chemical engineering. This research presents a new theory of electroviscoelasticity using a developed constitutive model of liquids. Three possible mathematical formalisms have been derived and discussed related to this physical formalism. In order to justify and corroborate more general approach the obtained calculated results were compared to those experimentally measured. Finally, a new idea to consider the selected emulsions and double emulsions as memristive systems is proposed.

Previous Work: Electrohydrodynamics - Theory and Modeling

The first model is the stretching tensor model, where the normal and tangential forces are considered, only in mathematical formalism, regardless to their origin, mechanical and/or electrical. The second model is classical integer order van der Pol derivative model:

$$C \frac{dv}{dt} + \left(\frac{1}{R} - \alpha \right) v + \gamma v^3 + \frac{1}{L} \int v dt = -2A_n \cos \omega t \quad (1)$$

where v is the overall potential difference at the junction point of the spherical capacitor C and the plate, L is the inductance caused by potential difference, and R is the ohm resistance (resistance of the energy transformation, electromagnetic into the mechanical or damping resistance), t is the time; α and γ are constants determining the linear and nonlinear parts of the characteristic current and potential curves. A nonhomogeneous solution may be obtained only when Eq. (1) is linearized, where A is the amplitude, and ω is the frequency of the incident oscillation. Finally, the third model comprise an effort to generalize the previous van der Pol differential equations, both, linearized and nonlinear; where the ordinary time derivatives and integrals are replaced by the corresponding fractional-order time derivatives and integrals of order $p < 2$ ($p = n - \delta$, $n = 1, 2$, $\delta \ll 1$). In order to justify and corroborate more general approach the obtained calculated results were compared to those experimentally measured using the representative liquid-liquid system [1-11].

Selected Emulsions and Double Emulsions as Memristive Systems

Based on the definition of a “missing” basic element *memristor* for electrical circuit analysis, and taking into account four fundamental circuit variables, electric current i , electromotive force v , charge q , and magnetic flux ϕ the set of fundamental functional relations is given by [12]:

$$dv = Rdi; dq = Cdv; d\phi = Ldi; d\phi = Mdq; d\phi = vdt; dq = idt; \quad (2)$$

Hence, the memristor as a current-controlled device is defined with the Eqs. (3) and (4), where w is the state variable of the device and R is a generalized resistance that depends upon the internal state of the device. In 1976 Chua and Kang generalized the memristor concept to a much broader class of nonlinear dynamical systems, named memristive systems, described by the Eqs. (5) and (6), where w is a set of state variables and R and f can, in general, be explicit functions of time [12].

$$v = R(w)i \quad (3) \quad \text{and} \quad \frac{dw}{dt} = i \quad (4); \quad v = R(w,i)i \quad (5) \quad \text{and} \quad \frac{dw}{dt} = f(w,i) \quad (6)$$

Further on, when an incidental uniform physical field, for example electromagnetic, is applied on the system emulsion/droplet or double emulsion/droplet-film-structure, causing the motions of both electrons and ions, than the memristance may be obtained as:

$$M(q) = R_{bul} \left[1 - \frac{\mu_i R_{int}}{D^2} q(t) \right] \quad (7)$$

where R_{int} is the low resistance at the interface and close to the interface layers, R_{bul} is the much higher resistance in the bulk layers, μ_i is the average ion mobility, D is the thickness of the considered fragment/”device”. Now, according to the presented electrohydrodynamic approach, emulsions and double emulsions will be considered as the composite system “droplet + film” or “droplet-film structure + droplet homophase (S + E)”. The history of this system consists of the initial/formation, intermediate/transition, and final/rigid states. 1. Every stationary state (initial, intermediate, and final) is characterized by interaction in the composite system that is of the same kind – being able to give rise to the occurrence of decoherence with the cluster arrangements as the “pointer basis states”. 2. The nonstationary state is characterized by the change in the character of interaction in the composite system. The net effect takes the following “phases” each having its own characteristic time: a) under the action of an external or incidental physical field a formation of the droplet-film structure occurs, producing the nonstationary state; b) the transition or relaxation of the electroviscoelastic droplet-film structure into the rigid one, establishing the new final stationary state, this transition or relaxation process may be considered as a kind of a memory storage process, therefore, the system either electroviscoelastic droplet or droplet-film structure submerged into the other immiscible liquid phase, could be

considered as the particular example of memristive systems; c) decoherence process, the final stationary state. Based on these statements following important propositions may be withdrawn: * the resistor R_D for every nonstationary state has to be exchanged with the memristor M_D ; * for every stationary state (initial, intermediate, and final) the nonlinear memristance M (the generalized resistance) degenerate into the linear resistance R .

Implications

Entrainment problems in solvent extraction, breaking of emulsions, deeper elucidation of adhesive processes, rupture processes, and coalescence; colloid and interface science, chemical and biological sensors, electro-analytical methods, biology or biomedicine (hematology, genetics, electroneurophysiology), classical limit of quantum mechanics, ionics, spintronics, fractional-quantum Hall effect-fluids, decoherence sensitivity, quantum computation, entities-quantum particles entanglement, [13-16].

Acknowledgments

Financial support by Ministry of Education and Science - Republic Serbia, grants: former 142034 and present 34009 and 46010.

References

- [1] A. M. Spasic CHISA 2012.
- [2] A. M. Spasic, J. M. Jovanovic, M. Jovanovic, Adv. Colloid Interface Sci., 2012, 174c, 31-49.
- [3] A. M. Spasic, CHISA 2010 & ECCE 7, D2.1.
- [4] J-P Hsu, A. M. Spasic, Interfacial Electroviscoelasticity and Electrophoresis, CRC Press-Taylor & Francis, Boca Raton London New York, 2010.
- [5] A. M. Spasic, M. P. Lazarevic, M. V. Mitrovic, D. N. Krstic, in A.M. Spasic and J.P. Hsu(Eds.), Finely Dispersed Particles: Micro-, Nano-, and Atto-Engineering, CRC Press/Taylor and Francis, Boca Raton London New York, 2006, 3-23 & 371-394. [6] A. M. Spasic, M. P. Lazarevic, J. Colloid Interface Sci., 2005, 282, 223-230.
- [7] A. M. Spasic, M. P. Lazarevic, J. Colloid Interface Sci., 2007, 316, 984-995.
- [8] A. M. Spasic, V. Jokanovic, D. N. Krstic, J. Colloid Interface Sci., 1997, 186, 434-446.
- [9] A. M. Spasic, N. N. Djokovic, M. D. Babic, M. M. Marinko, G. N. Jovanovic, Chem. Eng. Sci., 1997, 52, 657-675.
- [10] A. M. Spasic, Chem. Eng. Sci., 1992, 47, 3949-3957.
- [11] A. M. Spasic, in A. V. Delgado(Ed.), Interfacial Electrokinetics & Electrophoresis, Marcel Dekker, New York, 2002, 837-868.
- [12] D. B. Strukov, G. S. Snider, D. R. Stewart, R. S. Williams, Nature, 2008, 453/1, 80.
- [13] M. Dugic, Decoherence in a classical limit of quantum mechanics, Notebooks of Physical Sciences, SFIN XVII (2), Institute of Physics, Belgrade, 2004.
- [14] H. T. Elze, (Ed.) Decoherence and Entropy in Complex Systems, Selected lectures from DICE 2002, Springer, Lecture Notes in Physics, Berlin Heidelberg New York, 2003.
- [15] M. Dugic, D. Rakovic, M. Plavsic, in A. M. Spasic, J-P. Hsu(Eds.), Finely Dispersed Particles: Micro-, Nano-, and Atto-Engineering, CRC Press-Taylor & Francis, Boca Raton London New York, 2006, 317-331.
- [16] A. M. Spasic, Russian J. Phys. Chem. A, 83 (2009) 1563.

D-07-P

DYNAMIC INSTABILITY OF METHANOL OXIDATION FROM ALKALINE SOLUTION ON STATIONARY PT ELECTRODE

T. Mudrinić^{1*}, Z. Mojović¹, A. Abu Rabi-Stanković¹, N. Jović-Jovičić¹,
S. Marinović¹, M. Milenković², D. Stanisavljev²

¹*IHTM-Center of Catalysis and Chemical Engineering, Njegoševa 12, Belgrade*
²*Faculty of Physical Chemistry, Belgrade University, Studentski Trg 12, Belgrade,*
**tihana@nanosys.ihtm.bg.ac.rs*

Abstract

Cyclic voltammetry (CV) was used to study the dynamic instability of electrochemical oxidation of methanol in alkaline solution at stationary platinum electrode. Methanol oxidation was carried out in bicarbonate, carbonate and different pH values of sodium hydroxide solution. Experiments were conducted with and without previous stabilization of the working electrode in alkaline solution.

Introduction

The occurrence of dynamic instabilities in electrochemical systems are a widespread phenomena such as periodic oscillations, quasiperiodic oscillations, chaos and mixed-mode oscillations [1]. Many investigations on complex electrochemical instabilities were conducted under conditions where either the current or the potential of the working electrode was held constant. Schell et al. [2-3] have investigated the occurrence of instability using cyclic voltammetry. The CVs revealed high-order periodic as well as aperiodic behavior that appeared during electro-oxidation of methanol in alkaline solution using rotating platinum electrode. The various types of CV behavior were found by systematically varying different control parameters: upper potential limit (UPL), lower potential limit (LPL), concentration of methanol, rotation rate and sweep rate.

In this paper, cyclic voltammetry was used to study the dynamic instability during methanol oxidation in alkaline solution on stationary Pt electrode at different UPL values. Electro-oxidation of methanol was carried out in bicarbonate, carbonate and different pH values of sodium hydroxide solution.

Experimental

Electro-oxidation of methanol was investigated in 0.01 M, 0.1 M, 0.5 M, 1 M NaOH, 0.01 M NaHCO₃ and 0.01 M Na₂CO₃ solutions that contained 1M CH₃OH. Platinum electrode was pretreated in alkaline solution by cycling in the potential range from -600 mV to +600 mV until stable CV was obtained. The electrode was then transferred to the alkaline solution containing methanol. The cycling was performed from same LPL while UPL was varied in the range from 300 to 580 mV. For each UPL value 50 cycles were performed. Methanol electro-oxidation

was also investigated on fresh Pt electrode without previous pretreatment in the alkaline solution. All measurements were recorded at polarization rate of 100 mV/s. The device used for electrochemical measurements was Gamry PCI4G750-51093. The reference electrode was Ag/AgCl, KCl (3M), while a platinum foil served as a counter electrode. Working electrode was rectangular shaped (10 × 3 mm) platinum electrode.

Results and discussion

Three CVs shown in Fig.1 provide representations of the general phenomena considered in this paper. These CVs were recorded during cycling of stationary Pt electrode in 1M CH₃OH + 0.01 M NaOH with UPL set at +460 mV. The working electrode was previously stabilized in 0.01 M NaOH. During the forward sweep one peak appeared at potential of 0.0 V vs. Ag/AgCl. At the reverse scan, two peaks were visible. The relative intensity of these peaks was alternately changing with number of cycle.

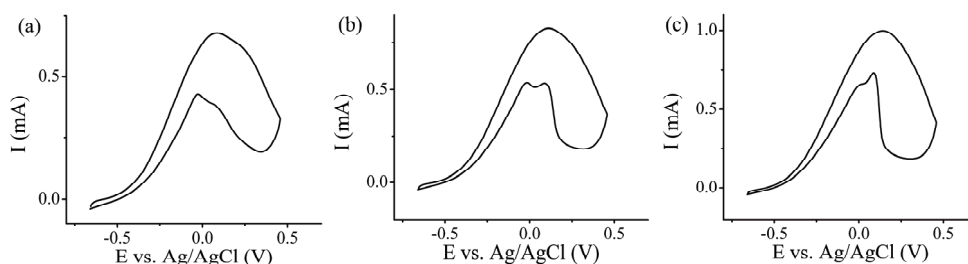


Figure 1 The CVs of stationary Pt electrode in 1M CH₃OH + 0.01 M NaOH, recorded at polarization rate of 100 mV/s with UPL set at +460 mV. Pt electrode was previously stabilized in 0.01 M NaOH. (a) 21th cycle (b) 29th cycle and (c) 37th cycle.

The CVs of electro-oxidation of methanol in different alkaline solutions and pH values of sodium hydroxide solution, obtained at same conditions as in Fig. 1, are presented in Fig. 2a and 2b, respectively. CV obtained in the 1M CH₃OH + 0.01 M NaOH during the experiment performed without previous stabilization of working electrode is shown in Fig. 2c. The phenomenon, shown in Fig. 1, was not observed under all other investigated conditions.

Tripković et al. [4-5] studied methanol oxidation on platinum surface in alkaline media (NaOH, Na₂CO₃ and NaHCO₃) and they found that surface activity was correlated with OH_{ad} coverage on Pt. Investigation has shown that bicarbonate and carbonate anions influence the OH⁻ ion adsorption, as well as the methanol oxidation itself. In fact, these anions decrease the surface activity in the oxidation of methanol by blocking the sites available for OH⁻ ion or methanol adsorption. The surface activity decreases in the sequence sodium hydroxide > carbonate > bicarbonate solution. Therefore, it can be assumed that adsorption of HCO₃⁻ and CO₃²⁻ ions from carbonate and bicarbonate solutions on surface of Pt were responsible for absence of phenomenon shown in Fig. 1. The absence of instable electrochemical behavior in solutions with different pH values, Fig. 2b was

probably influenced by OH adsorption. In order to obtain phenomenon of dynamic instability, of electro-oxidation of methanol the working stationary Pt electrode must be previously stabilized in alkaline solution and also the proper ratio of NaOH and CH₃OH concentrations in solution must be provided.

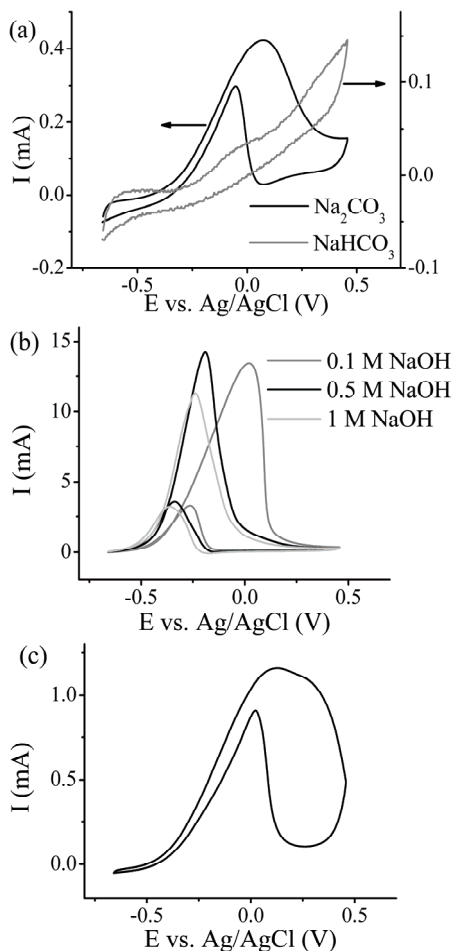


Figure 2 The CVs of stationary Pt electrode in (a) different alkaline solution (b) different pH values of sodium hydroxide solution (c) 1M CH₃OH + 0.01 M NaOH, without previous stabilization of the working electrode in alkaline solution. Other conditions are the same as in Fig. 1.

Conclusions

In this paper the dynamic instability, during electro-oxidation of methanol from alkaline solution using stationary Pt electrode was studied by cyclic voltammetry. Methanol oxidation was carried out in bicarbonate, carbonate and different pH values of sodium hydroxide solution. The phenomenon of alternately changing relative intensity of two peaks obtained at the reverse scan with number of cycle was only found using the ratio of concentration of sodium hydroxide and methanol 1:100. The other important factor for appearance of this phenomenon was stabilization of working electrode in the alkaline solution.

Acknowledgment

This work was supported by the Ministry of Education and Science of the Republic of Serbia (contract No III 45001).

References

- [1] J. Hudson, T. Tsotsis, *Chem. Eng. Sci.*, 1994, 49, 1493-1572.
- [2] Y. Xu, A. Amini, M. Schell, *J. Phys. Chem.*, 1994, 98, 12759-12767.
- [3] M. Schell, Y. Xu, A. Amini, *J. Phys. Chem.*, 1994, 98, 12768-12775.
- [4] A. Tripković, K. Popović, J. Momčilović, D. Dražić, *J. Electroanal. Chem.*, 1996, 418, 9-20.
- [5] A. Tripković, K. Popović, J. Momčilović, D. Dražić, *J. Electroanal. Chem.*, 1998, 448, 173-181.

STUDY OF LITHIUM OSCILLATORY TRANSPORT MECHANISM THROUGH EXCITED CELL MEMBRANE

Č. N. Radenović¹, M. V. Beljanski², G. V. Maksimov³, D. R. Stanisavljev⁴

¹University of Belgrade, Maize Research Institute, Zemun Polje, Serbia

²University of Belgrade, Institute of General and Physical Chemistry, Belgrade, Serbia

³Lomonosov Moscow State university, Faculty of Biology, Moscow, Russia

⁴University of Belgrade, Faculty of Physical Chemistry, Belgrade Serbia

Abstract

Results on variable mechanisms of Lithium transport process, during generating of membrane potential oscillations, across the very excitable *Nitella* cell membrane are presented. Several classes of oscillations were generated using high (10mM) LiCl. Membrane potential oscillations are caused by total oscillatory transport process of Li, K, Na and Cl ions across the excitable cell membrane. Hypothesis on mechanisms of ions oscillatory transport processes is given.

Introduction

Role of Lithium (Li) within biological systems and under physiological conditions, as yet has not been sufficiently clarified. Recent studies suggests that Li could be classified as an essential microelement for some organisms [1]. In medicine, Li is used to treat bipolar disorder [2].

The method of recording biopotentials by the means of microelectrodes is being used to study a variable mechanism of Li action during generating membrane potential oscillations and indirectly during the inducement of the oscillatory Li ions transport across the excitable membrane of the alga *Nitella* cells [3, 4, 5].

Experimental

As a model system cells of freshwater alga *Nitella mucronata* were used. Cells are large (0.6-1.0 x 40-80 mm) and suitable for bio-electrochemical studies. The measurements of rhythmic and membrane bioelectric signals: signal impulses, sequences of impulses and different forms of membrane potential oscillations (ψ_m , mV) was performed after the method with a microelectrode technique, as described previously [4, 6].

Results and Discussion

Equilibrium resting membrane potential, which depends on physiological state of the cells, growing conditions, age season etc, was in ranges from -80 mV to -150 mV [4, 5]. It is possible to observe different classes of membrane potential oscillations, single and local impulses, such as: (a) local impulses can occur in the initial part of the oscillation, but it can be clearly pronounced and easily registered, (b) single impulses can be pronounced more often, and more regularly and can be

D-08-P

simple registered, (c) sequences of single impulses occur often and are simply registered (membrane potential oscillations). Finally (d) it is shown that *Nitella* plasma membrane are capable, under effects of selected stimuli, to generate local and single impulses, as well as, repetitive membrane potential oscillations [4, 5].

Four examples of Li ion oscillations of the membrane potential may be observed;

I Instantaneous generation of Li-oscillations in the direction of membrane potential depolarization,

II Delayed generation of Li-oscillations in the direction of membrane potential depolarization,

III Instantaneous of Li-oscillations in the direction of membrane potential repolarization as presented on Fig. 1. and

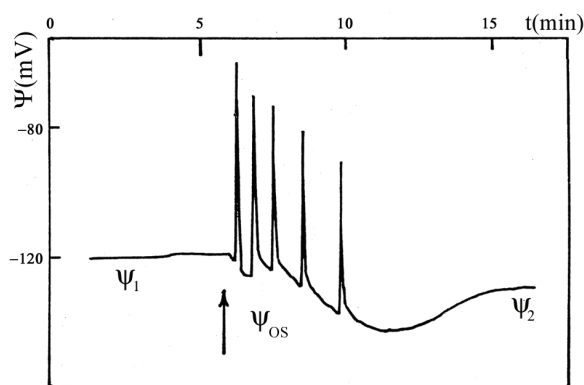


Figure 1. Instantaneous generation of Li-oscillations in the direction of membrane potential repolarisation, triggered by the exchange of standard solution (SR: 0.1 mm KCl, 1.0 mM NaCl), $\psi_1 = -120$ mV, $\psi_2 = -130$ mV, and ψ_{os} corresponding levels of membrane potential, arrow: moment of SR-LiCl replacement, number and duration of oscillations: 5 and 7, respectively, oscillation type: irregular, unsymmetrical and undumped.

IV Instantaneous generation of Li-oscillations with the unaltered level of membrane potential prior to and after oscillation.

On the basis of results obtained, we propose following hypothesis:

(a) Li-oscillations (local and single impulses and other classes of oscillations) of the membrane potential occur when the cell membrane is extremely excited. Such a membrane, as a rule, is accompanied by the changes of ion activities (K, Na, Li, Cl) that are not constant under such conditions in subcellular components (vacuole, cytoplasm, and cell wall).

(b) The usual ion transport process are disturbed under effect of Li: First of all diffusion (concentration gradient is altered), electrodiffusion (electrochemical potential gradient is changed), biocurrents (electric potential gradient is altered) and fluid flow (hydrostatic pressure gradient is modified). The mentioned dynamic

states determine the degree of the of excitability of the extremely excitable cell membrane. Hence, when the cell membrane is extremely excited, than local, single and complete membrane potential oscillations inevitably occur. These oscillations occur in the for of certain classes, but also in the form of different irregularities (chaos). At the same time and under the such conditions, oscillating of active proteins starts in the cell membrane and they rhythmically, regularly, irregularly (state of chaos) induce the transport of ions (Na, K, Li) across the extremely excitable membrane, which takes an oscillatory regime. In such state, ion transport process adopt cooperative character, which induce conformational changes of active ion channels that stretch and contract within the oscillatory regime, and thereby rhythmically modify transport ability of the excitable cell membrane for ions of K, Na and Li.

(c) Under such conditions, oscillatory changes occur in cell supplying, and thereby in supplying of the extremely excitable membrane with energy (electric, osmotic and chemical).

(d) Moreover, the connections between membrane transport process and metabolism are disturbed (weakened). This is particularly related to weakening of the self-regulation of the matter within each cell.

Acknowledgements

This work was support by the Ministry of Education and Science, Republic of Serbia Project No. 172015.

References

- [1] R. Crichton, Some Facts about Lithium. ENC Labs., 2008.
<http://www.enclabs.com/lithium.html>. Retrieved 2010-10-15
- [2] R. J. Baldessarini, L. Tondo, P. Davis, M. Pompili, F. K. Goodwin, Hennen, John Bipolar Disorders, 2006, 8, 625–639.
- [3] L. N. Vorobljev, Č. Radenović, Y. A. Khytrovi L. G. Yaglova, Biofizika, 1967, 12, 10-16.
- [4] Č. Radenović, Ž. Vučinić, Z. Damjanović, in E. Roux(Ed.), Electrical phenomena at the Biological Membrane Level, Elsevier, Amsterdam, 1977, 15-32.
- [5] Č. Radenović Bioelektricne pojave biljnih sistema. Nolit, Beograd, 1974, 7-161.
- [6] Č. Radenović, M. Penčić, Physiologia plantarum, 1970, 23, 697-703.

D-09-P

INCLUSION OF CHOLESTEROL IN HYPOTHALAMIC-PITUITARY-ADRENAL AXIS STOICHIOMETRIC MODEL

V. M. Marković¹, S. Maćešić¹, S. Damjanović², Lj. Kolar-Anić¹

¹*Faculty of Physical Chemistry, University of Belgrade, Studentski trg 12-16, Belgrade, Serbia*

²*Institute of Endocrinology, Diabetes and Diseases of Metabolism, School of Medicine, University of Belgrade, Dr Subotića 13, Belgrade, Serbia*

Abstract

Stoichiometric models constitute a useful theoretical tool to investigate complex oscillatory behavior in highly nonlinear reaction systems, such as a hypothalamic-pituitary adrenal (HPA) axis. To augment the predictive capacity of the model of HPA axis activity, we extended its mechanism by introducing a novel dynamical variable, cholesterol, as a natural precursor of HPA axis steroid hormones, cortisol and aldosterone. Numerical simulations of the proposed model showed that it could emulate well the dynamic behavior of its chemical species in the range of their physiologically relevant concentrations.

Introduction

Predictive modeling based on stoichiometric reaction models and nonlinear dynamics principles constitute powerful and efficient tools to elucidate composite oscillatory dynamics, such as that of the hypothalamic-pituitary-adrenal (HPA) axis, a neuroendocrine system involved in maintaining homeostasis under basal physiology as well as during stress [1].

The four-dimensional stoichiometric model of HPA axis activity proposed by Jelić et al. [2], although containing only four reaction species the most important for regulation of the HPA axis (corticotropin-releasing hormone (CRH), adrenocorticotropin (ACTH), cortisol (CORT) and aldosterone (ALDO)), showed significant predictive capacity to emulate HPA axis dynamics under basal physiological and various acute and chronic stress conditions [2, 3]. The mean concentrations of cortisol and aldosterone were in accordance with experimentally obtained values, whereas the mean concentrations of CRH and ACTH were beyond their physiologically meaningful realm for several orders of magnitude. This discrepancy was a direct consequence of the fact that in this extremely simplified model, there was no cholesterol, a known natural precursor of cortisol and aldosterone. To overcome this shortcoming, we propose a modification of the original model [2], by introducing cholesterol, as an additional dynamic variable, through reaction steps in agreement with the experimental results of the mechanism of adrenal steroidogenesis [1]. We employ numerical simulations to test whether

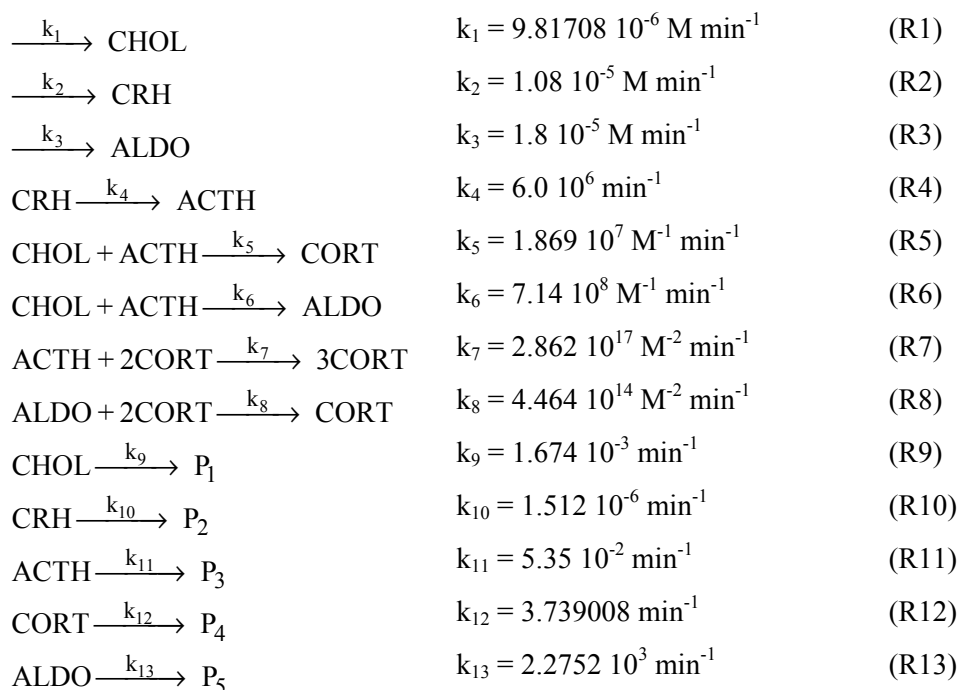
this refinement of the HPA axis model can enhance its biological relevance, both in terms of dynamical behavior and concentration levels of its chemical species.

Results and Discussion

The model of the HPA axis activity with cholesterol as the main precursor of steroid hormones, CORT and ALDO, is presented in Table 1. It is governed by the set of five coupled ordinary differential equations derived from the proposed mechanism in accordance with the mass-action kinetics law, describing ultradian time-evolution of its internal species. The validity of the proposed model was tested by means of numerical simulations performed in Matlab. Time series for cortisol ultradian rhythm is portrayed in Fig. 1.

Like in the original model [2], the circadian rhythmicity is introduced through coupling of the circadian function $D = d_1 - 0.079145093 \cdot d_2 + \{0.064 \cdot \sin(2\pi t / 1440) + 0.12 \cdot \text{abs}[\sin(\pi t / 1440)]\} \cdot d_2$ (d_1 and d_2 are parameters) with the proposed model (Table 1), by multiplying the rate constant of CRH production, k_2 , with D .

Table 1. Modified model of HPA axis activity [2] with cholesterol. P_i ($i = 1, \dots, 5$) are the elimination products of corresponding internal species. $M = \text{mol dm}^{-3}$.



The presented model emulates satisfactorily well the oscillatory dynamics of cortisol and of other key species of the HPA axis, giving rise to ultradian oscillations superimposed on the circadian ones, within the limits of their respective physiological concentrations for all species except ACTH. It should be

noted that one of the future challenges is to try to optimize this model in above-mentioned direction.

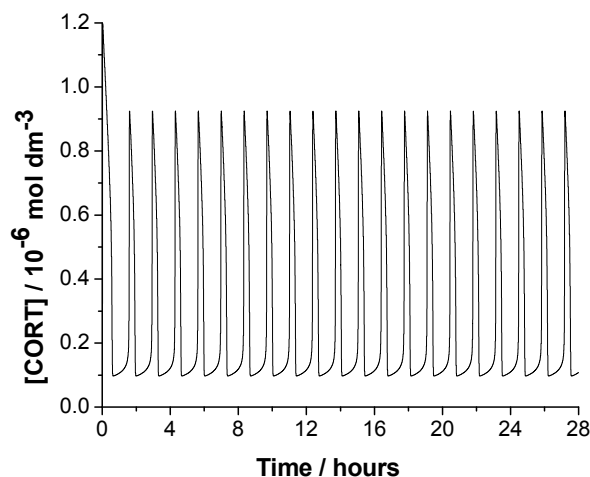


Figure 1. Temporal evolution of cortisol concentration displaying ultradian oscillations (obtained for values of parameters given in Table 1).

Conclusion

The improvement of the stoichiometric HPA axis model through inclusion of cholesterol as an additional dynamic variable, having the role of the natural precursor of adrenal steroids (CORT and ALDO), contributes to enhancement of its biological validity and predictive capability, rendering this refined model a good starting point for future studies of the HPA axis activity in both basal and stress physiology.

Acknowledgement

Presented investigation is performed in collaboration with our colleague Ž. Čupić. This investigation was supported by the Ministry of Education and Science of Republic of Serbia, under the projects No. 172015 and 45001.

References

- [1] G. Chrousos, in L. Frohman (Eds.), *Endocrinology & Metabolism*, P. Felig, McGraw-Hill, New York, 2001, 461-474.
- [2] S. Jelić, Ž. Čupić, Lj Kolar-Anić, *Mathematical Bioscience*, 2005, 197, 173-187.
- [3] V. M. Marković, Ž. Čupić, V. Vukojević, Lj. Kolar-Anić, *Endocrine Journal*, 2011, 58, 889-904.

OPTIMIZATION OF A HYPOTHALAMIC-PITUITARY-ADRENAL MODEL WITH CHOLESTEROL

S. Maćešić¹, V. M. Marković¹, A. Ivanović-Šašić², Ž. Čupić²

¹ Faculty of Physical Chemistry, University of Belgrade, Studentski trg 12-16, 11000 Belgrade, Serbia (wladimirmarkovic@gmail.com)

² Institute of Chemistry Technology and Metallurgy, University of Belgrade, Department of Catalysis and Chemical Engineering, Njegoševa 12, 11000 Belgrade, Serbia

Abstract

Complex oscillatory dynamics of hypothalamic-pituitary-adrenal (HPA) neuroendocrine system cannot be easily predicted, necessitating mathematical modeling and theoretical analysis. To emulate more realistically and to further characterize composite nonlinear behavior of the HPA axis, we analyze stability of an extended HPA axis model with cholesterol, determining under which critical conditions the system changes stability and passes through Andronov-Hopf bifurcation. In that regard, we apply the improved stoichiometric network analysis (SNA) in combination with bifurcation and sensitivity analysis.

Introduction

Hypothalamic-pituitary-adrenal (HPA) axis represents a complex physiological system for maintaining homeostasis in basal physiology as well as in stress conditions [1]. It has become evident that adequate oscillatory dynamics of HPA axis is a necessary prerequisite for its normal functioning and health [2] given that alterations of HPA axis dynamics are associated with many metabolic and psychiatric disorders. Thus, more exhaustive understanding of its dynamic properties is required, accounting not only for experimental data but also for modeling and numerical simulation predictions. Stoichiometric models have shown a strong capacity and contributions to accomplishing these goals [3].

However, to model such oscillatory processes, the values of the model parameters need to be within the oscillatory domain of the instability region in the phase space of the proposed model. This kind of parameter optimization is almost always a non-trivial assignment since the models emulating complex dynamics phenomena demand a larger number of parameters to be included in their description, the values of which are often quite difficult or not even feasible to determine.

A useful assisting to overcome this problem is the application of the improved stoichiometric network analysis (SNA), a powerful mathematical method for stability analysis of complex reaction networks [4-6], when these processes can be represented by adequate stoichiometric models. SNA enables determination of the instability region of an observed system, and thus contributes to determining values

D-10-P

of a control parameter for which main steady state is unstable and where different dynamic states, such as oscillations, can be simulated numerically or attained experimentally.

In order to determine oscillatory region and more comprehensively understand how the stability of an extended HPA axis model with cholesterol [7] is affected by changes of concentrations of internal reactive species and the kinetic rate constants, we employ improved SNA, numerical simulations and bifurcation analysis to discuss the properties of dynamic states arising in the examined model. Furthermore, we ascertain the core of the model's instability, *i.e.* critical reaction steps necessary to give rise to the model's unstable dynamic states.

Results and Discussion

Bifurcation and stability analysis of the five-dimensional HPA model with cholesterol [7] were carried out using routines we wrote in MATLAB.

Table 1. Range of rate constant values yielding oscillatory behavior within the model of HPA axis with included cholesterol.

Rate constants	Range		Fixed values
	Minimal value	Maximal value	
k_1	$1.7 \cdot 10^{-2}$	$3.073 \cdot 10^{-2}$	$3.065 \cdot 10^{-2}$
k_2	$3.148 \cdot 10^{-2}$	$5.804 \cdot 10^{-2}$	$3.156 \cdot 10^{-2}$
k_3	0	$1.2162 \cdot 10^{-2}$	$6.050 \cdot 10^{-3}$
k_4	50	$k_4 \rightarrow \infty$	$2.000 \cdot 10^{10}$
k_5	$3.0 \cdot 10^4$	$6.26 \cdot 10^{11}$	$6.230 \cdot 10^{11}$
k_6	$2.369 \cdot 10^{13}$	$3.9 \cdot 10^{15}$	$2.375 \cdot 10^{13}$
k_7	$3.0 \cdot 10^{20}$	$8.5 \cdot 10^{24}$	$9.540 \cdot 10^{20}$
k_8	0	$1.1710 \cdot 10^{18}$	$9.920 \cdot 10^{17}$
k_9	0	81	$9.184 \cdot 10^{-3}$
k_{10}	0	$1.0 \cdot 10^7$	$5.040 \cdot 10^{-4}$
k_{11}	0	$2.682 \cdot 10^5$	$1.450 \cdot 10^{-7}$
k_{12}	$6.657 \cdot 10^3$	$7.3 \cdot 10^4$	$7.280 \cdot 10^3$
k_{13}	$5.0 \cdot 10^7$	$k_{13} \rightarrow \infty$	$7.890 \cdot 10^7$

Rate constants are given in: ^a $\text{min}^{-1} \text{mol dm}^{-3}$, ^b min^{-1} , ^c $\text{min}^{-1} \text{mol}^{-1} \text{dm}^3$, ^d $\text{min}^{-1} \text{mol}^{-2} \text{dm}^6$.

The model's oscillatory region (Table 1) was determined by varying each of the rate constants describing the model's reaction rates while simultaneously holding all of the remaining rate constants at fixed values (last column, Table 1). This bifurcation analysis showed that the rate constants of reactions R3, R8, R9, R10 and R11 did not affect the oscillatory behavior of the model in their lower limit (minimal values equal zero, Table 1), indicating that removing all of them from the model would have no effect on its stability.

SNA provided the complete instability condition for existence of oscillatory dynamics according to Routh-Hurwitz criterion [8]. Applying the above-mentioned results of the bifurcation analysis, the complete oscillatory condition could be reduced by keeping only the dominant terms to the following expression:

$$2v_7(h_3v_6^3 + 3h_3v_6^2v_7 + h_2v_4v_6^2 + 3h_3v_6v_7^2 + 2h_2v_4v_6v_7 + h_2v_4v_7^2) < \\ v_{12}(4h_3v_6^2v_7 + h_2v_4v_6^2 + 6h_3v_6v_7^2 + 3h_2v_4v_6v_7 + 3h_2v_4v_7^2),$$

where v_i ($i = 1 - 13$) are steady-state reaction rates of corresponding reaction steps and h_j ($j = 1 - 5$) are reciprocal steady-state concentrations of internal species of the model (CHOL, CRH, ACTH, CORT, ALDO, respectively).

Conclusion

By using the improved SNA and bifurcation analysis, the stability of the extended HPA model with cholesterol was examined, determining the oscillatory region of the model's dynamic behavior and dominant reactions crucial for the instability of the investigated model.

Acknowledgement

Presented investigation is performed in collaboration with our colleague Lj. Kolar-Anić. This investigation was supported by the Ministry of Education and Science of Republic of Serbia, under the projects No. 172015 and 45001.

References

- [1] G. Chrousos, in P. Felig, L. Frohman (Eds.), *Endocrinology & Metabolism*, McGraw-Hill, New York, 2001, 461-474.
- [2] S. L. Lightman, B. L. Conway-Campbell, *Nature Reviews Neuroscience*, 2010, 11, 710-718.
- [3] V. M. Marković, Ž. Čupić, V. Vukojević and Lj. Kolar-Anić, *Endocrine Journal*, 2011, 58, 889-904.
- [4] B. Clarke, in *Advances*, in I. Prigogine, S. Rice (Eds.), *Chemical Physics*, Wiley, New York, 1980, 1-216.
- [5] G. Schmitz, Lj. Kolar-Anić, S. Anić, Ž. Čupić, *Journal of Physical Chemistry*, 2008, 112, 13452-13457.
- [6] Lj. Kolar-Anić, Ž. Čupić, G. Schmitz, S. Anić, *Chemical Engineering Science*, 2010, 65, 3718-3728.
- [7] V. M. Marković, S. Maćešić, Ž. Čupić, S. Damjanović, Lj. Kolar-Anić, Inclusion of cholesterol in hypothalamic-pituitary-adrenal axis stoichiometric model, in S. Anić and Ž. Čupić (Eds.), *Physical Chemistry 2012*, Society of Physical Chemists of Serbia, Belgrade, 2012.
- [8] B. L. Clarke and W. Jiang, *Journal of Chemical Physics*, 1993, 99, 4464-4478.

D-11-P

DYNAMICAL SYSTEM ANALYSIS FOR THE BRAY–LIEBHAFSKY REACTION UNDER CSTR CONDITIONS

S. Blagojević¹, Sl. Blagojević², Ž. Čupić³

¹*Institute of General and Physical Chemistry, Studentski trg 12–16*

²*Faculty of Pharmacy, University of Belgrade, Vojvode Stepe 450*

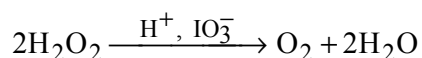
³*IChTM–Department of Catalysis and Chemical Engineering, Njegoševa 12*

Abstract

By numerically simulated Bray–Liebhafsky (BL) reaction in a continuously fed well stirred tank reactor (CSTR) we discussed the attractors and Poincaré 1D maps with respect to flow rate as control parameter. It was shown that there is a difference in 1D maps in a relation with chosen hyperplane where Poincaré section

Introduction

The BL reaction is the decomposition of hydrogen peroxide into the water and oxygen in the presence of iodate and hydrogen ions [1]:



The overall reaction can be understood as the sum of two processes: reduction of iodate to iodine and oxidation of iodine to iodate by hydrogen peroxide. Oscillatory dynamics of the BL reaction under CSTR conditions can be simulated with the model consisting of eight reactions proposed by Lj. Kolar–Anić at all.[2]. Numerical simulations of models have shown that various simple and complex periodic as well as chaotic oscillatory states are obtained for different values of the flow rate j_o as control parameter [3]. To characterize types of dynamical states we employ the following methods for dynamical systems analysis: time–series, attractor analysis and Poincaré maps. Time series method is necessary for determination on the type of dynamics an investigated system exhibits for a given value of a control parameter. Attractor analysis is an advantageous method for distinction between periodic and chaotic dynamic, and particularly for detection of period–doubling. Poincaré or 1D maps made of selected Poincaré section, are another qualitative method capable of providing information regarding period–doubling and/or chaos in the analyzed dynamic state.

Results and discussion

We analyzed time series obtained by numerically simulating the model of BL reaction [2], under isothermal CSTR conditions. Numerical simulations are based on an idealized deterministic model, since they can generate data with high

numerical precision of 10^{-16} . The results in real experimental systems have a precision of 10^{-3} due to some non ideal properties that affect to results. All calculations were performed using MATLAB program package. The differential equations derived from the model were integrated using the ode15s solver. Relative and absolute error tolerance values of 3×10^{-14} and 1×10^{-20} were used in all simulations. Initial values of the concentrations were: $[\text{IO}_3^-]_0 = 0.0474 \text{ mol dm}^{-3}$, $[\text{H}^+]_0 = 0.0958 \text{ mol dm}^{-3}$, and $[\text{H}_2\text{O}_2]_0 = 0.155 \text{ mol dm}^{-3}$. We analyzed time series obtained by numerically simulating the proposed model for different values of the flow rate j_0 as control parameter.

Time series of iodide ions for flow rate $j_0 = 4.831040 \times 10^{-3} \text{ min}^{-1}$ have shown that chaotic dynamics (“mixed-mode structured” chaos dynamics denoting chaotic mixture of predominantly 3^1 and 4^1 sequences) were found (Figure (1)).

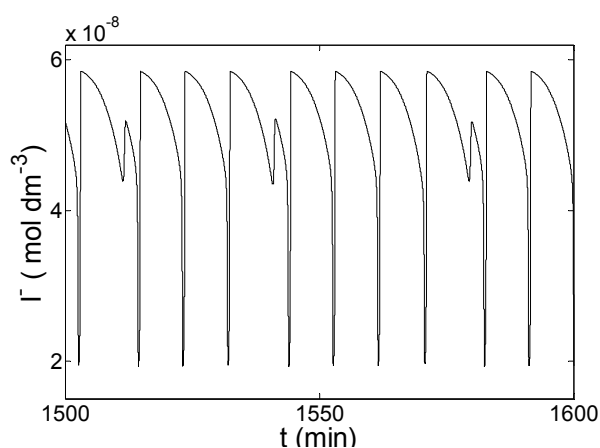


Figure 1. The time series from the simulations, $j_0 = 4.831040 \times 10^{-3} \text{ min}^{-1}$.

In the case of chaotic dynamics, an infinite trajectory (strange attractor) emerging from periodic cycle fills in the part of phase space by spirally cycling in the vicinity of the periodic state 3^1 and 4^1 (Figure 2(a)). The attractor line for the flow rate $j_0 = 4.831040 \times 10^{-3} \text{ min}^{-1}$ is not closed and 1D map have infinitely many points. (Figure 2(b), 2(c) and 2(d)). Dynamics of BL model under CSTR condition and the flow rate as control parameter has been evaluated with 1D maps. It was shown that there is a difference in 1D maps in a relation with chosen hyperplane where Poincaré section was made.

Conclusion

Different shapes of Poincaré 1D maps are found at sections where chosen hyperplane cuts large cycles only (Figure 2(b)), small cycles only (Figure 2(c)) or large and small cycles both (Figure 2(d)).

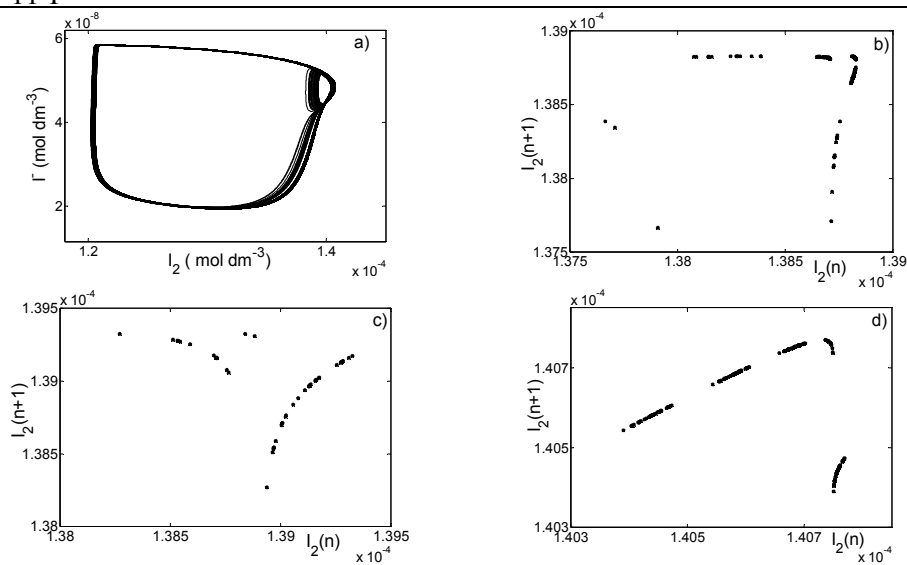


Figure 2. (a) Attractor corresponding to flow rate $j_0 = 4.831040 \times 10^{-3} \text{ min}^{-1}$ and corresponding Poincaré 1D maps made by planes intersecting attractor at: (b) large cycle only ($[I^-] = 3.50 \times 10^{-8} \text{ mol dm}^{-3}$), (c) small cycle only ($[I^-] = 4.80 \times 10^{-8} \text{ mol dm}^{-3}$), (d) both large and small cycle ($[I^-] = 4.80 \times 10^{-8} \text{ mol dm}^{-3}$).

Acknowledgment

The support of this research by the Ministry of Education and Science of Republic of Serbia through projects No.172015 is gratefully acknowledges.

References

- [1] W. C. Bray, H. A. Liebhaufsky, *J. Am. Chem. Soc.*, 1931, 53, 38–44.
- [2] Lj. Kolar–Anić, Đ. Mišljenović, S. Anić, G. Nikolis, *React. Kinet. Catal. Lett.*, 1995, 54, 35–41.
- [3] A. Ivanovic–Šašić, V. Marković, S. Anić, Lj. Kolar–Anić, Ž. Čupić, *Phys. Chem. Chem. Phys.*, 2011, 13, 20162–20171.

NEW RESULTS OF THE NUMERICAL SIMULATIONS OF THE BELOUSOV–ZHABOTINSKY OSCILLATORY REACTION UNDER BATCH CONDITIONS

Sl. Blagojević¹, Sl. Anić²

¹*Faculty of Pharmacy, University of Belgrade, Vojvode Stepe 450, Belgrade*

²*Institute of Chemistry, Technology and Metallurgy, University of Belgrade, Serbia*

Abstract

By numerical calculations based on our previously proposed model we were able to simulate very complex evolution of the Belousov–Zhabotinsky (BZ) reaction under batch conditions. It was shown that bromine evaporation in a closed reactor, significantly influences its oscillatory dynamic state.

Introduction

The Belousov–Zhabotinsky (BZ) reaction is the decomposition of malonic acid, by bromated ions in acid solution containing Ce^{3+} or Ce^{4+} as a catalyst [1]. Numerical results of the complex dynamic behavior of BZ oscillatory reaction under different initial concentrations of the malonic acid under batch condition were carried out by the known model, including the Br_2O species, Table 1. [2]

Results and discussion

We examined a narrow part of the phase space where the concentration of malonic acid varied ($1.00 \times 10^{-3} \leq [\text{MA}]_0 \leq 3.50 \text{ mol dm}^{-3}$) at 30 °C, with constant values of the initial concentrations of other species (in mol dm^{-3}): $[\text{H}_2\text{SO}_4]_0 = 1.05$, $[\text{KBrO}_3]_0 = 6.20 \times 10^{-2}$, $[\text{KBr}]_0 = 1.50 \times 10^{-5}$, $[\text{Ce}_2(\text{SO}_4)_3]_0 = 2.50 \times 10^{-3}$. According to Clegg, Rard and Pitzer [3], $[\text{H}_2\text{SO}_4]_0 = 1.05 \text{ mol dm}^{-3}$ gives $[\text{H}^+]_0 = 1.29 \text{ mol dm}^{-3}$, used in all the simulations.

The simulated results were obtained using the MATLAB program package. The differential equations derived from the model were integrated using the ode15s solver. All numerical simulations were performed with numerical precision of 10^{-16} .

The rate constant of the reaction of bromine evaporation (k_{12}) was varied from 1.00×10^{-4} to $5.50 \times 10^{-1} \text{ s}^{-1}$.

Rich nonlinear temporal phenomena, such as high- and low-amplitude regular oscillations, aperiodic oscillations, mixed-mode oscillations and low-amplitude sinusoidal oscillations are obtained under various initial concentrations of the malonic acid, but without reaction of bromine evaporation (Figure 1(a)).

The numerical calculations based on the model with evaporation of bromine, show that oscillatory evolutions in the whole investigated range of the initial concentrations of malonic acid, is not so complex because aperiodic oscillations and mixed-mode oscillations do not occur (Figure 1(b)).

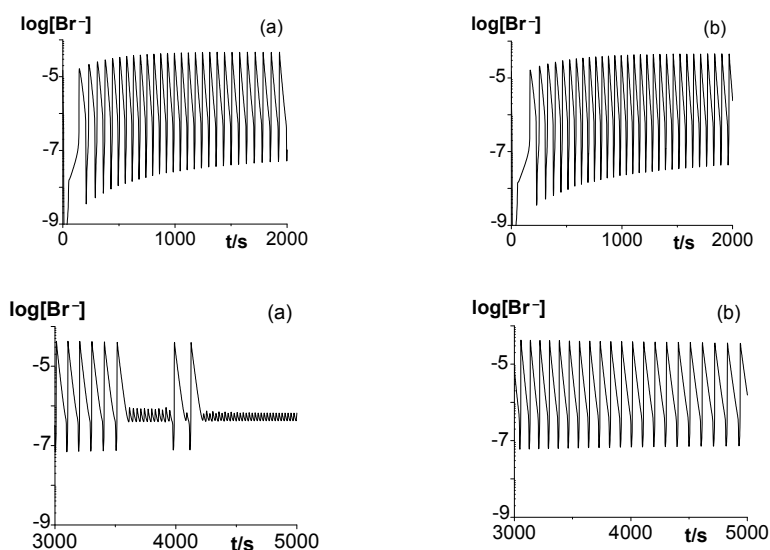
Table 1. The model of the Belousov–Zhabotinsky reaction.[2]

No.	Reaction
R1	$\text{Br}^- + \text{HOBr} + \text{H}^+ \rightarrow \text{Br}_2 + \text{H}_2\text{O}$
R-1	$\text{Br}_2 + \text{H}_2\text{O} \rightarrow \text{Br}^- + \text{HOBr} + \text{H}^+$
R2	$\text{HBrO}_2 + \text{Br}^- + \text{H}^+ \rightarrow 2\text{HOBr}$
R3	$\text{Br}_2\text{O} + \text{H}_2\text{O} \rightarrow 2\text{HOBr}$
R-3	$2\text{HOBr} \rightarrow \text{Br}_2\text{O} + \text{H}_2\text{O}$
R4	$\text{Br}^- + \text{BrO}_3^- + 2\text{H}^+ \rightarrow \text{HOBr} + \text{HBrO}_2$
R5	$2\text{HBrO}_2 \rightarrow \text{BrO}_3^- + \text{HOBr} + \text{H}^+$
R6	$\text{BrO}_3^- + \text{HBrO}_2 + \text{H}^+ \rightarrow 2\text{BrO}_2^\bullet + \text{H}_2\text{O}$
R-6	$2\text{BrO}_2^\bullet + \text{H}_2\text{O} \rightarrow \text{BrO}_3^- + \text{HBrO}_2 + \text{H}^+$
R7	$\text{Ce}^{3+} + \text{BrO}_2^\bullet + \text{H}^+ \rightarrow \text{Ce}^{4+} + \text{HBrO}_2$
R-7	$\text{Ce}^{4+} + \text{HBrO}_2 \rightarrow \text{Ce}^{3+} + \text{BrO}_2^\bullet + \text{H}^+$
R8	$\text{MK} + \text{Br}_2 \rightarrow \text{BrMA} + \text{Br}^- + \text{H}^+$
R9	$\text{MA} + \text{Ce}^{4+} \rightarrow \text{Ce}^{3+} + \text{P}_1 + \text{H}^+$
R10	$\text{BrMA} + \text{Ce}^{4+} \rightarrow \text{Ce}^{3+} + \text{Br}^- + \text{P}_2$
R11	$\text{Br}_2\text{O} + \text{MA} \rightarrow \text{BrMA} + \text{HOBr}$
R12	$\text{Br}_2(\text{sol}) \rightarrow \text{Br}_2(\text{g})$

Abbreviations: MA–malonic acid; BrMA–bromomalonic acid; P₁ and P₂ – products; sol–solution; g–gas. Rate constants are taken from earlier numerical simulations [2].

Conclusion

The numerical calculations based on the presented model indicated that bromine evaporation in a closed reactor, in the investigated domain of initial concentrations of malonic acid, significantly affects the oscillatory evolution of the BZ reaction, particularly the most important oscillatory features (preoscillatory period, the time elapsed between the start of the reaction and the termination of the oscillatory phase, the amplitude and period of oscillations, and the form and number of oscillations).



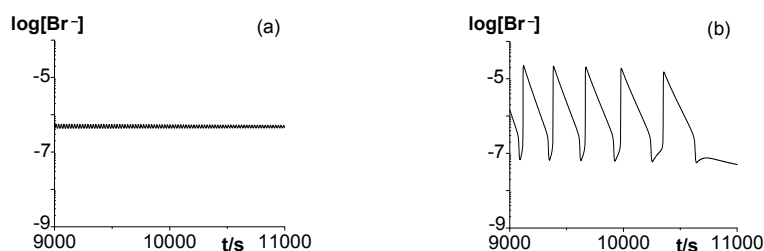


Figure 1. The time dependences of $\log [\text{Br}^-]$ obtained by the numerical simulation of the kinetic scheme [2] without (a) and with (b) the reaction of bromine evaporation (R12). $[\text{MA}]_0 = 8.00 \times 10^{-2} \text{ mol dm}^{-3}$, $k_{12} = 1.10 \times 10^{-2} \text{ s}^{-1}$.

Acknowledgment The present investigations were supported by the Ministry of Education and Sciences of the Republic of Serbia, Grants no. 172015 and no. 45001.

References

- [1] R. J. Field, E. Körös and R. M. Noyes, *J. Am. Chem. Soc.*, 1972, 94, 8649–8664.
- [2] S. Blagojević, S. Anić, Ž. Čupić, N. Pejić, Lj. Kolar–Anić, *Phys. Chem. Chem. Phys.* 2008, 10(44), 6658–6664.
- [3] S. Clegg, J. Rard, K. Pitzer, *J. Chem. Soc., Faraday Trans.*, 1994, 90, 1875–1894.

D-14-P

THE RESPONSE OF IODIDE PEROXIDE REACTION MODEL TO CONSTANT SYSTEM ACIDITY

M. C. Milenković*, D R. Stanisavljev

Faculty of Physical Chemistry, Belgrade University, Studentski Trg 12, Belgrade

**maja.milenkovic@ymail.com*

Abstract

Recently, we have detected the presence of free radicals (HO^\bullet and HOO^\bullet) in the iodide-peroxide system and the appropriate radical model was developed by simulating O_2 pressure, I^- , I_2 , and I_3^- concentrations in the real system. The aim of this work is the theoretical investigation of the response of the model to the constant acidity in the system. According to this, the results of simulations at the constant $[\text{H}^+]$ is compared with the experimental data and simulations in which $[\text{H}^+]$ is treated as variable. Slightly better agreement between experimental and simulated data is obtained when the concentration of H^+ was taken as a variable. In both simulations, fitted rate constants are of the same order of magnitude. It indicates that at the given experimental conditions investigated model is not sensitive to the decrease of $[\text{H}^+]$ accompanying proposed model chemistry.

Introduction

The iodine species are part of the iodate and periodate-based chemical oscillators and the investigation of general iodine chemistry is crucial for better comprehension of oscillatory dynamics. One of the important iodine subsystems is iodide-peroxide reaction. Although seems simple, it takes place through a series of observable intermediates (I_2 , I_3^-) and short lived intermediates such as (HIO). Liebhafsky^{1, 1a} observed complex kinetics of this reaction and determined the rate constant of the rate-limiting step in the formation of a reaction product O_2 . For longer time intervals the reaction can be, more complex, showing, at higher temperatures, even oscillatory evolution and possibly connection with the BL reaction mechanism.²

Recently, we have reported the presence of HOO^\bullet and HO^\bullet radicals in the iodide-peroxide system (at room temperature) in acidic medium³ and appropriate radical model was developed.⁴ The goal of this work is the theoretical investigation of the response of the proposed radical model integrated at the constant $[\text{H}^+]$. Out of 15 rate constants, only two is fitted for the best agreement with previously obtained experimental data.

The same simulation procedure is repeated, with variable $[\text{H}^+]$ during numerical simulations which means that the kinetic differential equation for $[\text{H}^+]$ is added to the set of equations describing time evolution of the model.

Numerical simulations were performed with the E-Z Solve program. The initial concentrations of I^- , H_2O_2 and H^+ in numerical simulations are the same as in real

experiment ($[KI]_0=6.40 \times 10^{-4} \text{ mol/dm}^3$, $[H_2O_2]_0=0.1 \text{ mol/dm}^3$, and $[H^+]=9.38 \times 10^{-4} \text{ M}$). The initial concentrations of intermediate components $[HIO]$, $[I_2]$, $[I_2^-]$, $[I_3^-]$, $[I^\cdot]$, $[O_2]$, $[HOO^\cdot]$, and $[HO^\cdot]$ are approximated by the value of 10^{-9} M .

Results and Discussion

The investigated model of iodide-peroxide reaction, established previously⁴ is represented in Table 1.

Table 1. Radical model reactions with literally known rate constants and optimized parameters X, Y and k_6 .

$H^+ + I^- + H_2O_2 \rightarrow I^\cdot + OH^\cdot + H_2O$	$k_{1a}=Y (0.0115+0.175[H^+]) M^{-1}s^{-1}$	(1a)
$H^+ + I^- + H_2O_2 \rightarrow HIO + H_2O$	$k_{1b}=X (0.0115+0.175[H^+]) M^{-1}s^{-1}$	(1b)
$HIO + H_2O_2 \rightarrow I^- + H^+ + O_2 + H_2O$	$k_2=37 M^{-1}s^{-1}$	(2)
$I^- + HIO + H^+ \leftrightarrow I_2 + H_2O$	$k_3=3.6 \times 10^9$, $k_{-3}=0.0018/H^+ M s^{-1}$	(3)
$I_2 + I^- \leftrightarrow I_3^-$	$k_4=6.2 \times 10^9 M^{-1}s^{-1}$, $k_{-4}=8.5 \times 10^6 s^{-1}$	(4)
$OH^\cdot + H_2O_2 \rightarrow HOO^\cdot + H_2O$	$k_5=4.5 \times 10^7 M^{-1}s^{-1}$	(5)
$I^\cdot + H_2O_2 \rightarrow HIO + OH^\cdot$	$k_6=\text{sim.}$	(6)
$OH^\cdot + I^- + H^+ \rightarrow I^\cdot + H_2O$	$k_7=1 \times 10^{10} M^{-1}s^{-1}$	(7)
$OH^\cdot + I_2 \rightarrow HIO + I^\cdot$	$k_8=1.1 \times 10^{10} M^{-1}s^{-1}$	(8)
$HOO^\cdot + I_2 \rightarrow O_2 + H^+ + I_2^\cdot$	$k_9=1.8 \times 10^7 M^{-1}s^{-1}$	(9)
$I^\cdot + I^- \leftrightarrow I_2^\cdot$	$k_{10}=8.8 \times 10^9$, $k_{-10}=6.88 \times 10^4 M^{-1}s^{-1}$	(10)
$I_2^\cdot + H_2O_2 \rightarrow HOO^\cdot + 2I^- + H^+$	$k_{11}=10^2 M^{-1}s^{-1}$	(11)
$2HOO^\cdot \rightarrow H_2O_2 + O_2$	$k_{12}=7.6 \times 10^5 M^{-1}s^{-1}$	(12)
$OH^\cdot + HOO^\cdot \rightarrow O_2 + H_2O$	$k_{13}=6.6 \times 10^9 M^{-1}s^{-1}$	(13)
$I_2^\cdot + I_2^\cdot \rightarrow I_3^- + I^-$	$k_{14}=2.3 \times 10^9 M^{-1}s^{-1}$	(14)

X and Y represent the fraction of reactants that are converted to HIO and radicals OH^\cdot and I^\cdot (in bulk), respectively ($X+Y=1$). The characteristic time evolutions of oxygen, iodide, iodine and triiodide concentrations during experiment, together with simulated results obtained when $[H^+]$ is kept constant and allowed to vary are represented in Figures 1 a)-d). From these pictures, good agreement between all experimentally monitored parameters (O_2 , I^- , I_2 , I_3^-) and their simulated values is obtained.

The mean values for fitted parameters X, Y, and k_6 for constant and variable $[H^+]$ during integration are:

$$\begin{array}{ll} [H^+]_{\text{const}} & Y=0.05, X=0.95 \text{ and } k_6=2 \times 10^3 M^{-1}s^{-1} \\ [H^+]_{\text{var}} & Y=0.01, X=0.99 \text{ and } k_6=1 \times 10^3 M^{-1}s^{-1} \end{array}$$

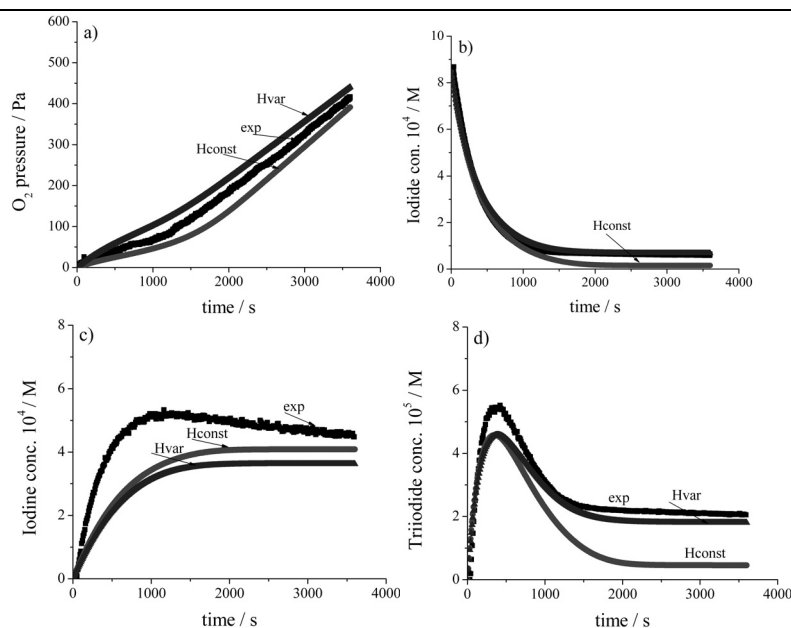


Figure 1. The characteristic time evolutions of oxygen a), iodide b), iodine c) and triiodide d) concentrations during experiment ($[KI]_0=6.40 \times 10^{-4} \text{ mol/dm}^3$, $[H_2O_2]_0=0.1 \text{ mol/dm}^3$, and $[H^+]=9.38 \times 10^{-4} \text{ M}$) black line, together with results obtained by radical model simulations with constant and variable $[H^+]$, gray and light gray line, respectively.

Conclusion

In this work the response of investigated model to constant and variable $[H^+]$ during simulation is compared with existing experimental results. As expected, slightly better agreement with experiments is obtained when $[H^+]$ is considered as a variable. It is interesting that in both cases, fitted rate constants are of the same order of magnitude. It indicates that the proposed radical model under given initial composition is relatively insensitive to the changes of $[H^+]$ during reaction. Whether such response of the model is preserved at different initial acidities will be investigated in future experiments.

Acknowledgment

This work was supported by the Ministry of Education and Science of the Republic of Serbia (project No 172015).

References

- [1] H. A. Liebhafsky, A. Mohammad, J. J. Am. Chem. Soc., 1933, 55, 3977.; a. J. C. Hansen, J. Chem. Educ. 1996, 73, 728.
- [2] A. Olexova, M. Mrakavova, M. Melichercik, L. Treindl, J. Phys. Chem. A, 2010, 114, 7026.
- [3] D. Stanisavljev, M. Milenković, M. Mojović, A. Popović-Bijelić, J. Phys. Chem. A 2011, 115, 7955.
- [4] M. Milenković, D. Stanisavljev, J. Phys. Chem. A, 2012, 116, 5541.

INFLUENCE OF OHMIC POTENTIAL DROP ON THE ONSET OF CURRENT OSCILLATIONS DURING COPPER ELECTRODISSOLUTION

N. I. Potkonjak¹, T. N. Potkonjak², S. N. Blagojević³

¹*Chemical Dynamics Laboratory, Vinča Institute of Nuclear Sciences, University of Belgrade, Mike Petrovića Alasa 12-14, 11001 Belgrade, Serbia*

²*Urban Planning Institute of Belgrade, Palmotićeveva 30, 11000 Belgrade, Serbia*

³*Institut of General and Physical Chemistry, Studentski trg 12-16, 11001 Belgrade, Serbia*

Abstract

The influence of IR drop on current oscillatory behavior during Cu electrodi dissolution in 1 M TFA was studied either by its compensation or by its additional increase. Results are presented to show some new aspects of the role of IR drop on the current oscillations during metal electrodi dissolution.

Introduction

Metal electrodi dissolution-passivation processes can exhibit dynamical instabilities. With an existence of appropriate feedback mechanism, these instabilities can spontaneously induced oscillatory behavior of current [1]. The electric nature of electrochemical oscillators is considered to be decisive for oscillatory phenomena occurrence [2]. Two major features of electrochemical system are considered as important for current oscillatory onset: the negative differential resistance of the current-potential curve and the dynamical variability of ohmic potential (IR) drop, where R represents the total resistance of the electric circuit system [3]. The total resistance of the system is equal to resistance of the electrolyte R_{el} , however it can be modified either by addition of compensated resistance R_{comp} ($R = R_e - R_{comp}$) or external resistance ($R = R_{el} + R_{ext}$) [4]. The effect of the compensation of IR drop by positive feedback method has been shown in our previous study [5]. The aim of this study is to present some further details regarding IR drop correction and its influence on current oscillations.

Experimental

The electrochemical cell consists of copper disc as working electrode, Pt-foil as auxiliary electrode and saturated calomel electrode (SCE) as reference electrode. The electrolyte solution was 1M trifluoroacetic acid (TFA), prepared from TFA (Merck) and deionized water. Electrochemical measurements were carried out using Gamry PC14/750 electrochemical workstation. The working electrode was

polarized by mean of potentiodynamic scan, starting from 0 mV vs. SCE with scan rate 10 mV s^{-1} . Experiments were done with applied positive feedback IR compensation method with compensation resistance ($R_{\text{comp}} = 0, -2, -5, -10, -15 \text{ } \Omega$), and by inserting external resistor ($R_{\text{ext}} = 2, 5, 10, 15, 20, 30$ and $33 \text{ } \Omega$) to the working electrode. All experiments were done under natural convection of the electrolyte.

Results and discussion

Potentiodynamic electrodisolution of copper electrode in 1 M TFA was done with standard connection of the electrochemical cell and the electrochemical instrument or by applying positive feedback IR compensation or inserting external resistor in electric circuit, between instrument and working electrode. In the Fig. 1 are given current–potentia polarization curves obtained under $R_{\text{comp}} = 15 \text{ } \Omega$, $R_{\text{ext}} = 20 \text{ } \Omega$ and under normal conditions (on the same figure E denotes the applied potential). Shift of the oscillatory region (ΔE_{OSC}) was noticed either less anodic (when positive feedback IR compensation was applied) or more anodic (when addition resistor was inserted). Current oscillatory behavior of the electrochemical system was found even when 88 % of IR drop was compensated (estimated $R_{\text{el}} \approx 17 \text{ } \Omega$). Disappearance of oscillatory behavior was noticed when R_{ext} exceeded some critical value ($R_{\text{ext}} \approx 33 \text{ } \Omega$).

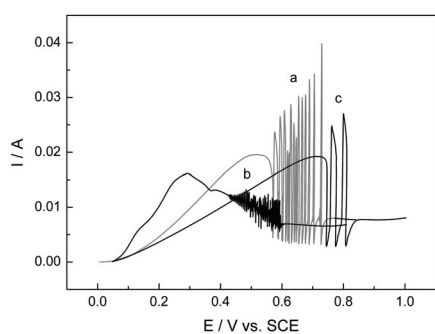


Figure 1. Anodic polarization curves of the Cu electrodisolution in 1M TFA under a) normal conditions, b) IR drop compensation $R_{\text{comp}} = 15 \text{ } \Omega$, and c) increase of IR drop, $R_{\text{ext}} = 20 \text{ } \Omega$.

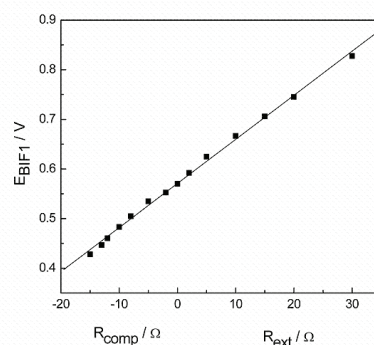


Figure 2. Linear relation between potential of first bifurcation point vs. R_{comp} and R_{ext} .

Shift of the first bifurcation point was found to be linearly dependent on R_{comp} and R_{ext} , Fig. 2. Furthermore, linear correlation was also noticed between width of ΔE_{OSC} and R_{comp} and R_{ext} . Rather complex dependence of the number of current oscillations (N_{OSC}) and the amplitude of first oscillation that appear (A_{11}) on increasing R_u , looking from maximum IR compensation to maximum increase of external resistance, are presented in the Fig. 3 and Fig.4, respectively.

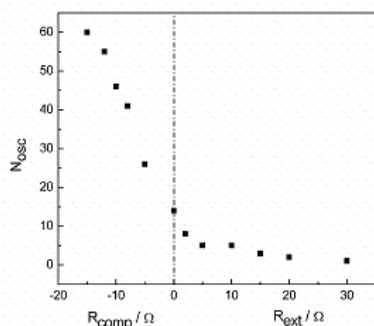


Figure 3. Decrease of the number of current oscillations (N_{OSC}) vs. increase of the uncompensated resistance of the cell.

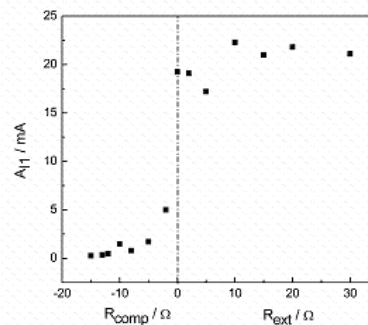


Figure 4. Increase of the amplitude of first current oscillation (A_{11}) vs. increase of the uncompensated resistance of the cell.

Conclusion

Ohmic potential (IR) drop variation was found to be of great influence on several aspects of current oscillatory behavior obtained during anodic dissolution of copper in 1 M TFA. Oscillatory behavior was found even when 88 % of IR drop was compensated. Absence of oscillations was noticed after increase of uncompensated resistance by 33 Ω .

Acknowledgement

This work was financially supported by the Ministry of Education, Science and Technological Development of the Republic of Serbia through Projects No. 172015.

References

- [1] K. Krischer, N. Mazouz, P. Grauel, *Angew. Chem. Int. Ed.*, 2001, 40, 851-869.
- [2] M.T.M. Koper, *Electrochim. Acta*, 1992, 37, 1771-1778.
- [3] R. de Levie, *J. Electroanal. Chem.* 2003, 552, 223-229.
- [4] D. Sazou, M. Pagitsas, *Electrochim Acta*, 2006, 51, 6281-6296.
- [5] N.I. Potkonjak, T.N. Potkonjak, S.N. Blagojević, 10th International Conference on Fundamental and Applied Aspects of Physical Chemistry PHYSICAL CHEMISTRY 2010, 21.-24. September, Belgrade, Serbia, Proceedings, Vol. 1, 248-250.

D-15-P

DEVIL'S STAIRCASE IN MIXED MODE OSCILLATIONS OF THE BRAY LIEBHAFSKY REACTION

B. Stanković¹, Ž. Čupić², Lj. Kolar-Anić¹

¹*Faculty of Physical Chemistry, University of Belgrade, Studentski trg 12-16, Belgrade*

²*IChTM – Department of Catalysis and Chemical Engineering, Njegoševa 12, Belgrade*

Abstract

Devil's staircase, step-by-step evolution of firing numbers, is constructed for two initial hydrogen peroxide concentrations by numerically simulating the model of the Bray-Liebhaafsky oscillatory reaction system in open reactor. A new view on this phenomenon is given as well.

Introduction

Mixed-mode oscillations (MMOs), sequences of large and small-amplitude oscillations, are commonly described using the notation of Maselko and Swinney [1]. The symbol L^S denotes that a sequence of L consecutive large amplitude oscillations is followed by S consecutive small ones. MMOs are the subject of an intense research since they can be found in chemical reaction kinetics [1, 2], biochemical systems [3], plasma physics [4] ...

Hence, each type of oscillations appears in MMOs with characteristic frequency given by L^S notion. Both these frequencies and ratio between them generally depend on the control parameter values. However, these changes are not smooth. MMOs are clarified by phase locking, phenomenon which is generally present in dynamical systems with two competing frequencies. For systems which are phase locked the ratio between their frequencies is a rational number. As one changes the control parameter two frequencies locks onto every single rational value, forming an infinite series of steps. Between any two steps there is infinity of steps, because between any two rational numbers there is infinity of rational numbers. Singular function representing frequency ratio distribution over some control parameter is called the Devil's staircase. In chemical systems, this structure is often obtained by representing the firing number $F = S / (L+S)$ as a function of the control parameter.

Results and Discussion

Previously, we analyzed time series obtained by numerically simulating the model of the Bray-Liebhaafsky oscillatory reaction system in open reactor [5, 6]. With the aim to construct Devil's staircase flow rate as control parameter, was varied in narrow region of values in which MMOs are found for two initial hydrogen peroxide concentrations, 1M (Fig 1 (a)) and 0.155M (Fig 1 (b)). The initial calculations of mentioned phenomenon can be seen in refs [6] and [7].

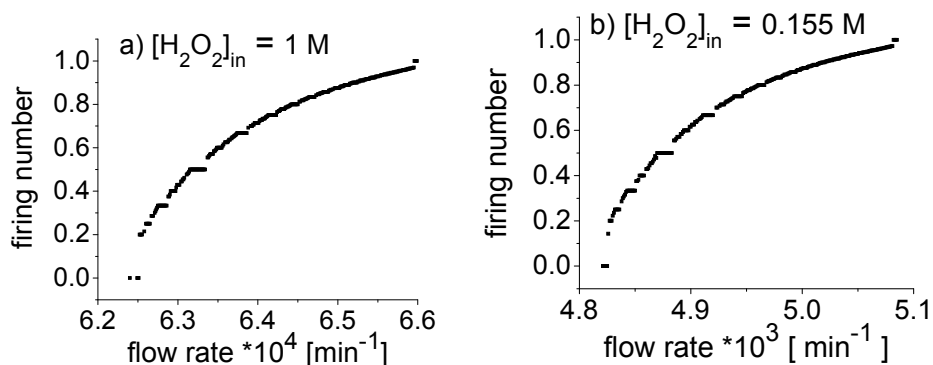


Figure 1. Devil's staircases for two inflow hydrogen peroxide concentrations as a function of flow rate.

We found that MMOs occur in simulations of the BL reaction as a consequence of interactions between two types of singular points in phase space: Folded node singularity and Dynamical Andronov-Hopf bifurcation. In Figs 2 (a) and (b) Devil's staircases are presented as a function of the ratio between their distances to the steady state of the system.

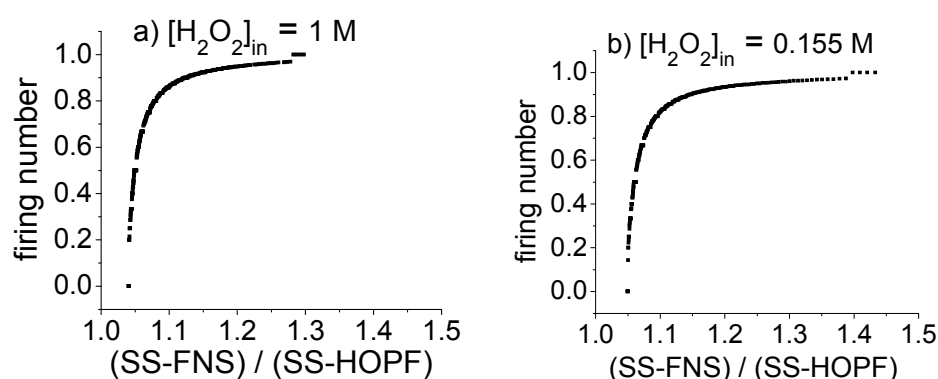


Figure 2. Devil's staircases for two inflow hydrogen peroxide concentrations as a function of ratio between distances of Folded node singularity and Dynamical Hopf bifurcation to the steady state of the system, that is as a function of (SS-FNS)/ (SS-HOPF).

From Fig 2 we can see that in both cases with very different initial hydrogen peroxide concentrations, MMOs and their Devil's staircases occur in the same region of relative distances between singular points. Moreover, with increasing relative distance between folded singularity and steady state, the relative influence of this singularity weakens and portion of large amplitude oscillations decreases.

Conclusion

Devil's staircase is known in science as structure of phase locked oscillations, but to the best of our knowledge, no evidence of their explanation is given. Here is offered one based on interactions between two types of singular points in phase space: Folded node singularity and Dynamical Andronov-Hopf bifurcation.

Acknowledgments

This investigation was supported by the Ministry of Education and Science of Republic of Serbia, under the projects No. 172015 and 45001.

References

- [1] J. Maselko, H. L. Swinney, *J. Chem. Phys.*, 1986, 85, 6430-6441.
- [2] J. Hudson, M. Hart, D. Marinko, *J. Chem. Phys.*, 1979, 71, 1601–1606.
- [3] S. De Brouwer, D. Edwards, T. M. Griffith, *Am. J. Physiol Heart Circ. Physiol.*, 1998, 274, 1315-1326.
- [4] M. Mikikian, M. Cavarroc, L. Couëdel, Y. Tessier, L. Boufendi, *Phys. Rev. Lett.*, 2008, 100, 225005-225008
- [5] Lj. Kolar-Anić, Ž. Čupić, G. Schmitz, S. Anić, *Chem. Eng. Sci.*, 2010, 65, 3718-3728
- [6] G. Schmitz, Lj. Kolar-Anić, S. Anić, T. Grozdić, V. Vukojević, C, *J. Phys. Chem. A*, 2006, 110, 10361-10368
- [7] B. Stanković, Graduate thesis, Faculty of Physical Chemistry, Belgrade , 2012.

INTERMITTENT OSCILLATIONS OBTAINED UNDER CSTR CONDITIONS IN THE BRIGGS-RAUSCHER REACTION MODIFIED BY PHENOL

S. Maćešić¹, J. Maksimović¹, M. Pavlović¹, M. Milenković¹, E. Greco²,
S. Furrow³, R. Cervelatti²

¹*Faculty of Physical Chemistry, University of Belgrade, Studentski trg 12-16,
11000 Belgrade, Serbia*

²*Dipartimento di Chimica "G. Ciamician", Università di Bologna, Via Selmi 2,
Bologna, Italy*

³*Penn State Berks College, Pennsylvania State University, Reading, Pennsylvania,
19610*

Abstract

The intermittent oscillations, the phenomenon where large-amplitude relaxation oscillations are suppressed periodically are obtained under CSTR conditions in the Briggs-Rauscher reaction modified by phenol. The first suppression (induction period for considered phenomenon), the number of oscillations in one cluster of large-amplitude oscillations (or burst), their distance and other visual effects depend on phenol concentration.

Introduction

In 1980 S. Furrow announced [1] that he found intermittent oscillations in a modified Briggs-Rauscher (BR) oscillator [2] under batch conditions. Similar results were obtained later by R. Cervellati and his coworker E. Greco. In last several months, at the Faculty of Physical Chemistry in Belgrade, their results were repeated and new ones obtained under CSTR conditions. In all cases the BR reaction was modified by phenol.

Experimental

All experiments were carried out in CSTR at 25 ± 0.1 °C. The experimental assembly is composed of a 50 mL glass CSTR vessel wrapped in a water recirculation jacket connected to a thermostat. For homogenization of the reaction mixture, a magnetic stirrer was used. Amounts of species in reactor are controlled by peristaltic pumps. Four of the channels were used to deliver the reactants (aqueous solutions of potassium iodate/perchloric acid, malonic acid(MA)/manganese sulfate, hydrogen peroxide and phenol) and one channel of the other pump was used to remove the surplus volume of the reaction mixture through a U-shaped glass tube. In this way, the volume of the reaction mixture keeps constant at 22.2 ± 0.2 mL. The working Pt electrode was connected to a double-junction Ag/AgCl reference electrode. An electrochemical device (PC-Multilab EH4 16-bit ADC) coupled with a personal computer was used to record

the potential-time evolution of the BR oscillator. The start-up procedure was performed in the following way. First, thermostatted and protected from light, the reaction vessel was filled with the reactants, $0.020 \text{ mol L}^{-1} \text{ KIO}_3$, $0.10 \text{ mol L}^{-1} \text{ HClO}_4$, $0.016 \text{ mol L}^{-1} \text{ MA}$, $0.0020 \text{ mol L}^{-1} \text{ MnSO}_4$, $1.20 \text{ mol L}^{-1} \text{ H}_2\text{O}_2$, and deionized water at the flow rate of 5 mL min^{-1} . After 1 min, the stirrer was turned to 900 rpm. After 2.5 min, the flow rate was set to $0.191 \text{ mL min}^{-1}$ and the other pump for removing the surplus volume of the reaction mixture was turned on. After 30 min, deionized water was replaced with phenol. Phenol concentration was varied over the interval $4.6 \times 10^{-5} \text{ mol L}^{-1} < [\text{phenol}] < 9.93 \times 10^{-5} \text{ mol L}^{-1}$.

Results and discussion

By adding various concentrations of phenol, we detected the suppressing effect that phenol has on the oscillatory dynamics of the BR oscillating system. The effect can be seen as appearances of intermittent oscillations. The extent of the oscillations' suppression is highly correlated with the phenol concentrations (Figs. 1 and 2).

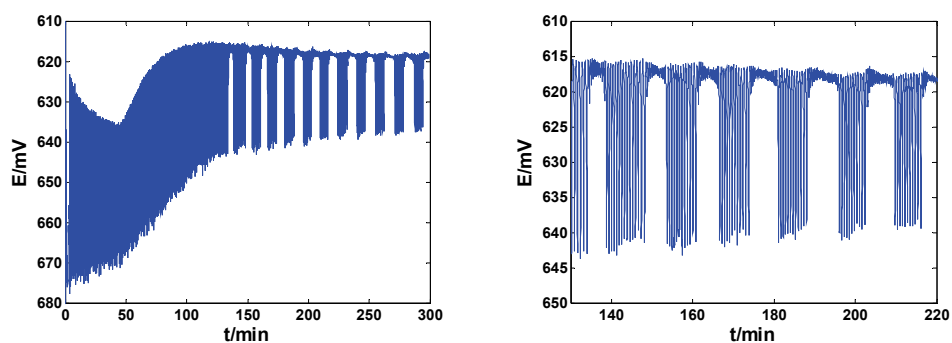


Figure 1. Oscillatory dynamics of the BR reaction modified by phenol having concentration $5.03 \times 10^{-5} \text{ mol L}^{-1}$.

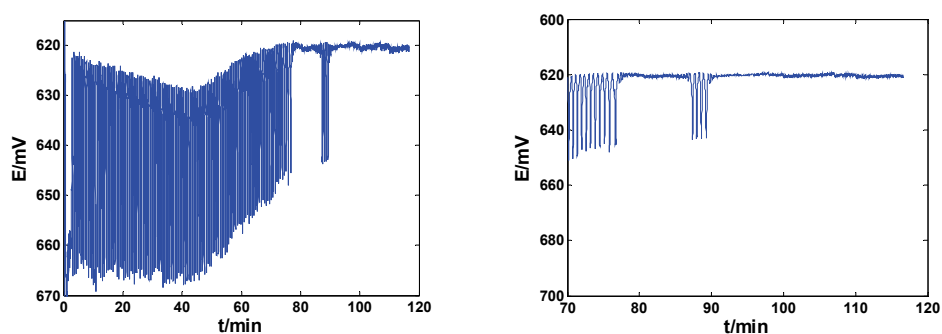


Figure 2. Oscillatory dynamics of the BR reaction modified by phenol having concentration $9.52 \times 10^{-5} \text{ mol L}^{-1}$.

Changing phenol concentrations affects the time necessary for appearances of the intermittent oscillations, the number of the oscillations in one cluster, the amplitude of the small oscillations between two clusters and whether or not intermittent oscillations can be maintained steadily. In the region with lower concentrations of the phenol considered here, time required for system to reach intermittent oscillations increases with decreasing phenol concentration, likewise the number of oscillations in the intermittences. Beside the effects mentioned above, amplitudes of the small oscillations between two clusters increase. On the other hand, higher phenol concentrations have quite the opposite effect on the oscillatory dynamics. Higher phenol concentrations prevent the system from existing permanently in the state of intermittent oscillations. The time required for the system to reach intermittent oscillations decreases as well as the number of the oscillations in the one intermittence. A stable stationary state is eventually reached, as can be seen from Figure 2. For phenol concentrations 9.93×10^{-5} and higher, the system directly reaches a stable stationary state without manifestation of the intermittent oscillations.

Conclusion

In this paper the conditions under which the BR reaction modified by phenol exhibit intermittent oscillations in CSTR are found. The next step is to define a model that would be able to describe the mentioned phenomenon.

Acknowledgement

Presented investigation is performed in collaboration with our colleagues Lj. Kolar-Anić, Ž. Čupić and S. Anić. This work was partially supported by the Ministry for Science of the Republic of Serbia (Grants no. 172015).

References

- [1] S. D. Furrow, Intermittent Oscillations in a Modified Briggs-Rauscher Oscillator, poster presented at a Gordon Conference in the 1980s.
- [2] T. S. Briggs, W.C. Rauscher, *J. Chem. Educ.* 1973, 50, 496.

D-17-P

PERTURBATIONS OF THE BRAY-LIEBHAFSKY OSCILLATING SYSTEM BY ALIZARIN

A. Đerić¹, J. Maksimović¹, N. Manojlović², N. Pejić³

¹*Faculty of Physical Chemistry, University of Belgrade, Studentski trg 12, Serbia*

²*Department of Pharmacy, Medical Faculty, University of Kragujevac, Svetozara
Markovića 69*

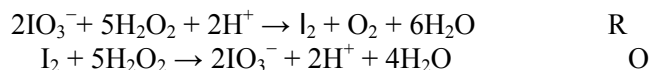
³*Faculty of Pharmacy, University of Belgrade, Vojvode Stepe 450, 11000 Belgrade,
Serbia, e-mail: nata@pharmacy.bg.ac.rs*

Abstract

This paper presents application of Bray-Liebhafsky (BL) reactions to the analysis of alizarin by the analyte pulse perturbation (APP) technique. Alizarin is hydroxyanthraquinone which exhibits a variety of potent biological effects such as antioxidant activity. Applying APP technique on the BL reaction, it is possible to quantitatively determine alizarin.

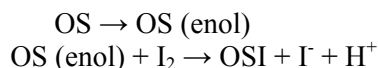
Introduction

The Bray-Liebhafsky reaction is the decomposition of hydrogen peroxide to oxygen and water in the presence of iodate and hydrogen ions by a very complex mechanism that still is not completely explained. Two main pathways of the BL reactions:



The most important intermediates are Γ , I_2 , HIO and HIO_2 . The concentrations of these intermediates function as a trigger for the switching from one pathway to another. The R reaction is well known, whereas the O reaction is still remains the meter of controversy. According to some authors O is radical process [1], while to others is non radical process [2].

Since discovery of oscillating reactions the role of different organic substrate (OS) is almost completely omitted [3], except the following reaction:



Last ten years, the oscillating reactions have been used for quantitative analytical determinations of antioxidants and antioxidant activity by APP technique [4]. Organic species change the amplitude and the period of oscillations or inhibit oscillations for a certain time. The effect depends on the concentration or activity of the antioxidant. In this work, we have perturbed BL system by alizarin to examine possibility for quantitative determinations and antioxidant activity, as well as contribute to elucidation of the oscillating reaction's mechanism.

Experimental

The experiments were carried out in a closed well-stirred (magnetic stirrer of 900rpm) system and thermostated at 60°C. Temporal evolution of the system was monitored potentiometrically using Γ^- ion sensitive electrode and Ag/AgCl as reference electrode. Concentration of the reactant in the system was: $[\text{H}_2\text{O}_2] = 0.007 \text{ M}$, $[\text{KIO}_3] = 0.0735 \text{ M}$, $[\text{H}_2\text{SO}_4] = 0.0479 \text{ M}$. Alizarin was added over the range $4.95 \cdot 10^{-7}$ to $1.0889 \cdot 10^{-5} \text{ M}$.

Results and Discussion

Figure 1a. shows the oscillations of $[\Gamma^-]$ between reduced state R with high $[\Gamma^-]$ and oxidized state O with low $[\Gamma^-]$ in the absence of alizarin.

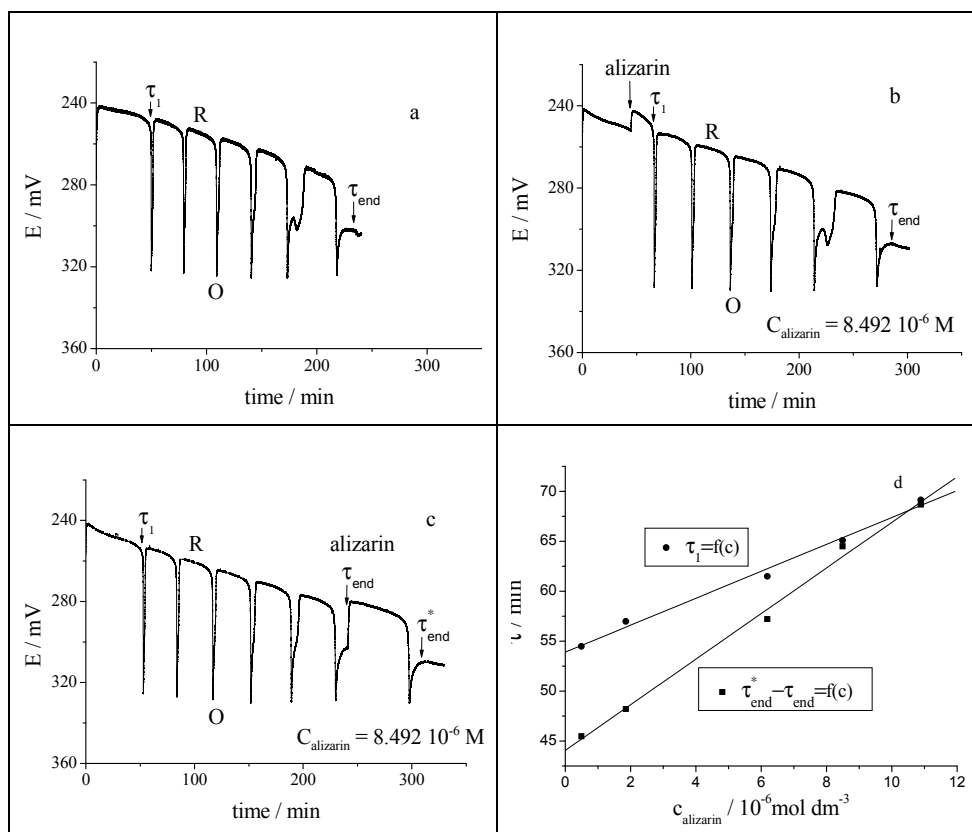
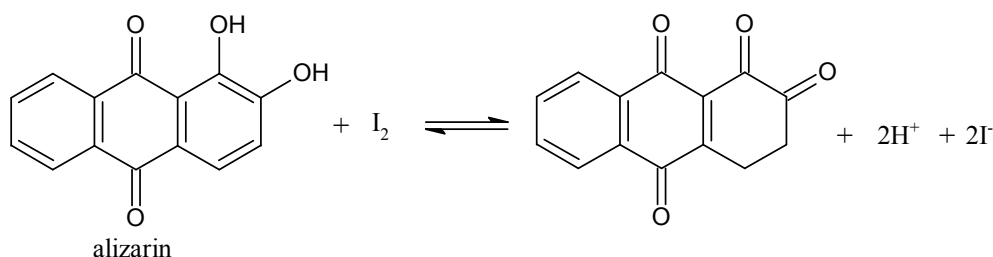


Figure 1. BL oscillograms in the absence (a) and presence of alizarin (b)-(c). Arrows indicate time when alizarin was added. Alizarin was added 45min after the start of reaction (b) and at the end of the oscillations (c). Calibration curves τ_i and $\tau_{end}^* - \tau_{end}$ vs. concentrations (d).

oscillations (τ_{end}). Perturbed system by alizarin promotes reduction state R (increase $[\Gamma^-]$). Adding alizarin in induction period causes increasing the amplitude

D-17-P

of oscillation, the period of oscillation and the induction period τ_1 (Figure 1b). The system resumed to an oscillating regime after exhausting alizarin. When alizarin was added at the end of oscillation τ_{end} system passes through one cycle. The period between the first τ_{end} and the second τ_{end}^* increasing with the concentrations (Figure 1c). The induction period τ_1 and period $\tau_{\text{end}}^* - \tau_{\text{end}}$ are linear function of the concentrations over the range 5×10^{-7} to 2×10^{-5} M (Figure 1c). It would be expected that alizarin inhibits oscillations at higher concentration. According to Hu [5] the direct reaction of alizarin with I_2 causes a rise in Γ^- :



Conclusion

Alizarin perturbs BL oscillating system by changing the amplitude and the period of oscillations and shows antioxidant activity. It is possible to quantitatively determine alizarin by APP technique.

Acknowledgment

The present investigations were supported by the Ministry of Education and Sciences of the Republic of Serbia, Grants no. 172015.

References

- [1] L. Treindl and R. M. Noyes, *J. Phys. Chem.*, 1993, 97, 11354-11362.
- [2] Lj. Kolar-Anić, G. Schmitz, *J. Chem. Soc. Faraday. Trans.* 1992, 88, 2343-2349.
- [3] N. Muntean, G. Szabo, M. Wittmann, T. Lawson, J. Fulop, Z. Noszticzius and L. Onel, *J. Phys. Chem. A*, 2009, 113, 9102-9108.
- [4] R. Cervellati, C. Renzulli, M. C. Guerra and E. Speroni, *J. Agric. Food Chem.*, 2002, 50, 7504-7509.
- [5] G. Hu, L. Chen, J. Zhang, P. Chen, W. Wang, J. Song, L. Qiu, J. Song and L. Hu, *Cent. Eur. J. Chem.*, 2009, 7, 291-297.

PERTURBATION OF THE DUSHMAN REACTION WITH PIROXICAM: EXPERIMENTAL AND MODEL CALCULATIONS

N. Pejić¹, N. Sarap², Sl. Blagojević¹

¹*Faculty of Pharmacy, University of Belgrade, Vojvode Stepe 450, 11000 Belgrade, Serbia*

²*Institute of Nuclear Science Vinča, Radiation and Environmental Protection Department, University of Belgrade, Mihajla Petrovića Alasa 12-14, P.O. Box 522, 11000 Belgrade, Serbia*

Abstract

A novel method for the determination of piroxicam (PX) is proposed and validated. For this purpose, the Bray-Liebhafsky (BL) non-oscillating subsystem (mixture KIO_3 and H_2SO_4), i.e. Dushman reaction (DR) was used. The proposed method relies on the linear relationship between maximal potential shift, ΔE_m , and the logarithm of the injected PX amounts in the concentration range $2.0 \times 10^{-5} \text{ mol L}^{-1}$ – $2.0 \times 10^{-4} \text{ mol L}^{-1}$. The sensitivity of the proposed method is $1.5 \times 10^{-5} \text{ mol L}^{-1}$. Some aspects of the possible mechanism of UA action on the DR matrix system are discussed.

Introduction

For developing of kinetic methods for quantitative determination of various analytes [1], besides BL oscillating system, the BL non-oscillating subsystem, i.e. the reaction of reduction of iodate by iodide in acid solution, known as the Dushman reaction (DR) was used [2]. The DR is a part of the highly sensitive BL oscillating system, but it is also a potential medium for analytical procedures.

Different analytical methods for determination of PX were summarized in [3]. Some of those methods are cumbersome, time-consuming or not enough sensitive. Therefore, some new methods based on relatively simple and inexpensive equipment are desirable. Regarding that, the kinetic method based on employing the analyte pulse perturbation technique to the mentioned non-oscillating DR as well as using the potentiometric monitoring of analyte perturbation, promise alternative to some instrumental methods due to its low cost instrumentation and relatively rapid detection procedure.

Experimental

The instrumental equipment included the 52-mL glass CSTR vessel, thermostat, a magnetic stirrer, a potential measuring system and peristaltic pumps. A PC-multilab EH4 16-bit analog-to-digital converter electrochemistry analyzer was directly connected to the reactor through a Pt working electrode and a double junction Ag/AgCl electrode. The procedure is based upon experiments carried out

D-18-P

in acidic iodate solutions and when the inflow concentration of H_2O_2 is zero. Thermostated at $55.0\text{ }^\circ\text{C}$ and shielded from light, the reaction vessel was filled up by three separate inflows of $5.9 \times 10^{-2}\text{ mol L}^{-1}$ KIO_3 , $7.6 \times 10^{-2}\text{ mol L}^{-1}$ H_2SO_4 and water, at a maximum flow rate of 5 mL min^{-1} . Then, the inflows were stopped, the stirrer was turned on 900 rpm , and the excess of the reaction mixture was sucked out through the U-shaped glass tube to achieve the actual reaction mixture volume, 22.2 mL . After about 30 min , the inflows were turned on at the required specific flow rate $2.95 \times 10^{-2}\text{ min}^{-1}$, and attained steady state perturbed with different concentrations of PX.

The simulated results were performed using the MATLAB program package. The differential equations derived from the model were integrated using the ode15s solver. All numerical simulations were performed with numerical precision of 10^{-16} .

Results and Discussion

Under the CSTR conditions, the effect of concentration of PX was studied; it is found that a variation of its concentration resulted in a variation in ΔE_m ($\Delta E_m = E_p - E_s$, where E_p is the maximal potential value attained after the performed perturbation and E_s is the potential corresponding to a steady state before the performed perturbation (Fig. 1.)). In the PX concentration range between $2.0 \times 10^{-5}\text{ mol dm}^{-3}$ and $2.0 \times 10^{-4}\text{ mol L}^{-1}$, the regression equation of the calibration curve is $\Delta E_m = -214.9 - 43.7 \log (c_{\text{PX}}/\text{mol L}^{-1})$ ($r = 0.997$). The detection limit of the method is $1.5 \times 10^{-5}\text{ mol L}^{-1}$.

In order to propose the nature of the interaction of PX with DR matrix, we have used the proposed DR kinetic scheme [4] and suggest that, the PX oxidation, similarly to its interaction with HOBr [5], performs through interaction with HOI, as a crucial step. Figure 1(b) shows the numerically simulated temporal traces upon PX injections in case when model of DR extended with reaction (1) ($k_1 = 6.0 \times 10^4\text{ mol}^{-1}\text{ L min}^{-1}$):



The numerically simulated forms of signal profiles obtained before and after perturbation of the DR matrix by the PX are in excellent agreement with experimentally obtained results; the obtained linear concentration range is $3.0 \times 10^{-5} - 2.0 \times 10^{-4}\text{ mol L}^{-1}$ and regression equation $\Delta E_m = -235.5 - 50.8 \log (c_{\text{PX}}/\text{mol L}^{-1})$ ($r = 0.991$).

Conclusion

Our results demonstrate the feasibility of the proposed kinetic method for quantitative determination of PX based on perturbing the Dushman reaction in a steady state. An excellent qualitative and quantitative agreement between the experimental and simulated results indicates that the proposed model mechanism,

though extremely simplified, reflects well the dynamics of PX interaction with the DR, and can be used as a very good starting point for further optimization of the method.

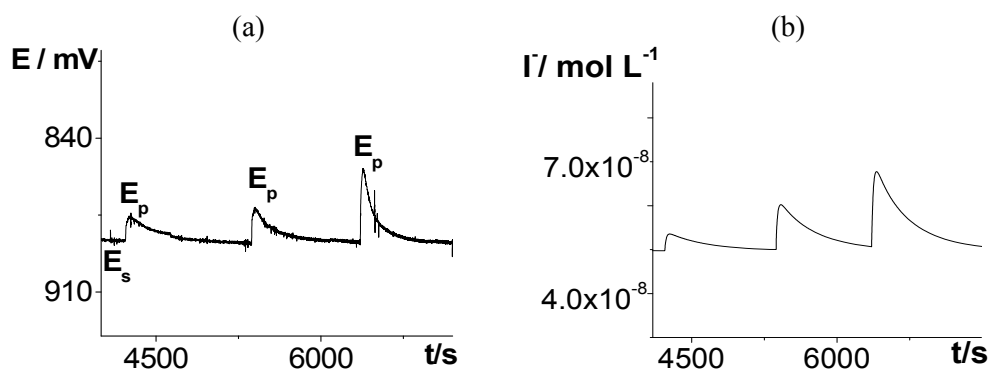


Figure 1. The responses of the DR matrix obtained experimentally (a) and by numerical simulations (b) after its perturbations with different concentrations of PX (from left to right): $1.0 \times 10^{-5} \text{ mol L}^{-1}$, $3.0 \times 10^{-5} \text{ mol L}^{-1}$ and $5.0 \times 10^{-5} \text{ mol L}^{-1}$.

Acknowledgement.

The present investigations were partially supported by The Ministry of Education and Sciences of Serbia, under Projects 172015 and III43009.

References

- [1] V. Vukojević, N. Pejić, D. Stanisavljev, S. Anić, Lj. Kolar-Anić, *Analyst*, 1999, 124, 147–152.
- [2] N. Pejić, J. Maksimović, S. Blagojević, S. Anić^c, Ž. Čupić, Lj. Kolar-Anić, *J. Braz. Chem. Soc.*, in press.
- [3] M. Starek, J. Krzek, *Talanta*, 2009, 77 925–942.
- [4] J.A.B. Agreda, R.J. Field, N.J. Lyons, *J. Phys. Chem.*, 2000, 104 5269–5274.
- [5] P. Van Antwerpen, J. Dubois, M. Gelbcke, J. Neve, *Free Radic. Res.*, 2004, 38, 251.

DETERMINATION OF PIROXICAM IN PHARMACEUTICAL BASED ON AN OSCILLATING CHEMICAL REACTION

N. Sarap¹, N. Pejić², J. Maksimović³

¹*Institute of Nuclear Science Vinča, Radiation and Environmental Protection
Department, University of Belgrade, Mihajla Petrovića Alasa 12-14, P.O. Box 522,
11000 Belgrade, Serbia*

²*Faculty of Pharmacy, University of Belgrade, Vojvode Stepe 450, 11000 Belgrade,
Serbia, e-mail:nata@pharmacy.bg.ac.rs*

Abstract

A novel procedure for kinetic determination of piroxicam (PX) by the concentration perturbations of the Bray-Liebhafsky (BL) oscillatory chemical system was proposed. The response of the BL matrix in a stable non-equilibrium stationary state close to the bifurcation point, to the perturbation by different concentrations of PX, is followed by a Pt-electrode. Under the optimized reaction conditions, the linear relationship between maximal potential shift ΔE_m , and PX concentration was obtained in the concentration range $6.8 \times 10^{-5} \text{ mol L}^{-1} - 1.7 \times 10^{-3} \text{ mol L}^{-1}$ with a detection limit of $3.5 \times 10^{-5} \text{ mol L}^{-1}$. The method had a rather good sample throughput (ST) of 45 samples h^{-1} with the recovery RCV = 103.7 %. Applicability of the proposed method to the direct determination of PX in pharmaceutical formulation (injections) was demonstrated.

Introduction

Piroxicam (PX), is a non-steroidal anti-inflammatory drug from oxicams family with analgesic and anti-pyretic activities. This effective analgesic and anti-inflammatory agent is used in the treatment of rheumatoid arthritis, osteoarthritis, ankylosing spondylitis, and acute pain in musculoskeletal disorder and acute gout. For determination of PX in various real samples, apart from potentiometric, voltametric and fluorimetric techniques, chromatographic and spectrophotometric techniques have been used most extensively [1]. Some of those methods are cumbersome, time-consuming or not enough sensitive. Therefore, some new methods based on relatively simple and inexpensive equipment were desirable. Regarding that, the kinetic method based on employing the analyte pulse perturbation technique (APP) to the Bray-Liebhafsky (BL) oscillatory reaction [2] as very nonlinear system, as well as using the potentiometric monitoring of analyte perturbation, promise alternative to some instrumental methods due to its low cost instrumentation, and relatively rapid detection procedure. The applied method, which has already been described [3], provides simple, effective and convenient method to assay the pharmaceutical samples.

Experimental

The BL matrix was conducted in the CSTR. Peristaltic pumps controlled the flows (inflow and outflow) of reactants (KIO_3 , H_2SO_4 and H_2O_2). The chosen dynamic structure for perturbation analysis is stable non-equilibrium stationary state in vicinity of the bifurcation point that was found under the following experimental conditions: the mixed inflow concentration of reactants $[\text{H}_2\text{SO}_4]_0 = 9.7 \times 10^{-2} \text{ M}$, $[\text{KIO}_3]_0 = 5.9 \times 10^{-2} \text{ M}$, $[\text{H}_2\text{O}_2]_0 = 1.50 \times 10^{-1} \text{ M}$, specific flow rate, $j_0 = 2.95 \times 10^{-2} \text{ min}^{-1}$ and $T = 67.0 \pm 0.2 \text{ }^\circ\text{C}$. Temporal evolution of the BL matrix was recorded by means of a Pt electrode and double junction Ag/AgCl electrode interfaced to a PC-AT 12 MHz compatible computer *via* a PC-Multilab EH4 16-bit ADC. Perturbations of matrix system were performed with 50 μL of the methanol standard solution of PX.

Results and Discussion

From the obtained dynamic structures observed under the above described conditions and the found bifurcation point ($[\text{H}_2\text{SO}_4]_0 = 9.65 \times 10^{-2} \text{ mol L}^{-1}$) [4] we have selected the non-equilibrium stable stationary states of the matrix that will be used for perturbation with PX (the non-equilibrium stationary states that are realized for $[\text{H}_2\text{SO}_4]_0 = 9.7 \times 10^{-2} \text{ mol L}^{-1}$).

The APP used for quantitative determination of PX, is based on potentiometric monitoring of the response of the non-linear matrix to perturbations induced by different concentrations of PX (Fig. 1.). The maximal change in potential (in mV), that is used as indicator of the perturbation strength, is defined as the difference $\Delta E_m = E_p - E_s$, where E_p is the maximal potential value attained after the perturbation is performed and E_s is the potential corresponding to the stable stationary state before the perturbation is performed (Fig. 1.). In the PX concentration range between $6.8 \times 10^{-5} \text{ mol L}^{-1}$ and $1.7 \times 10^{-3} \text{ mol L}^{-1}$, the regression equation of the standard series calibration curve is $\Delta E_m = -5.6 - 1.9 \times 10^4 c_{\text{PX}}$ ($r = 0.995$). The detection limit of the method is $6.5 \times 10^{-5} \text{ mol L}^{-1}$.

In order to study the validity of the proposed method, it was applied to the determination of PX in injections (Pfizer, Greek). The Table 1 shows the obtained results; it can be seen that the RCV is 103.7 % indicating that the developed method is free from interference and it provides accurate results.

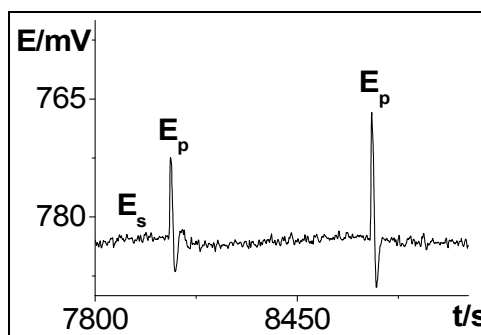


Figure 1. Typical response curves obtained after perturbing the stationary state in the BL reaction by addition of different concentrations of PX (from left to right): $2.9 \times 10^{-4} \text{ mol L}^{-1}$ and $7.7 \times 10^{-4} \text{ mol L}^{-1}$.

Table 1. Precision and recovery of PX in pharmaceutical dosage form.

Sample ^a	Claimed (mg/mL)	Concentration found	RSD (%)	RCV (%)
PX-injection	20	20.62	1.3	103.7

^aSample also containing: benzyl alcohol, ethanol, hydrochloric acid, nicotinamide, propylene glycol, monobasic sodium phosphate, sodium hydroxide and water for injection

Conclusion

The proposed method for the determination of PX is fast (45 samples h⁻¹), accurate (RSD is 1.3 %) and precise (RCV = 103.7 %). It was proved to be very appropriate for routine analysis of pharmaceuticals without any pretreatment of the samples apart from their dissolution; it could be also used for their quality control.

Acknowledgement

The present investigations were partially supported by The Ministry of Sciences and Education of Serbia, under Projects 172015 and III43009.

References

- [1] M. Starek, J. Krzek, *Talanta*, 2009, 77, 925–942.
- [2] W.C. Bray, *J. Am. Chem. Soc.*, 1921, 43, 1262–1267
- [3] N. Pejić, Lj. Kolar-Anić, S. Anić, D. Stanisavljev, *J. Pharm. Biomed. Anal.*, 2006, 41, 610–615.
- [4] N. Pejić, M. Vujković, J. Maksimović, A. Ivanović, S. Anić, Ž. Čupić, Lj. Kolar-Anić, *Russ. J. Phys. Chem. A*, 2011, 85, 66–72.

ONE FREE RADICAL MODEL OF THE BRAY-LIEBHAFSKY OSCILLATORY REACTION

A. Stanojević¹, S. Anić²

¹*Faculty of Physical Chemistry, University of Belgrade, Belgrade, Serbia*

²*Institute of Chemistry, Technology and Metallurgy, University of Belgrade, Serbia*

Abstract

One free radical model of the Bray-Liebhafsky oscillatory reaction is formed that include extended Schmitz model (with 8 reactions, and without free radical species) supplemented by 6 additional reactions. New model can simulate the BL reaction the Bray-Liebhafsky reaction over the wide domain of hydrogen peroxide concentrations ($10^{-3} - 10^{-1}$ M).

Introduction

Earlier extended Schmitz model [1] (Model(R1-R8)) of the Bray-Liebhafsky (BL) oscillatory reaction was capable to effectively describe the evolution of the BL system with high concentration of H_2O_2 . However, applicability of the model to low concentration of H_2O_2 (of the order of magnitude about 10^{-3} M) was not considered then. Hereby, inspired by ref. [2] we intended to include additional reactions to the Model (R1-R8) and examine their influence to simulations of the BL system wide domain of H_2O_2 concentrations. There, we apply previously defined method to calculate concentrations of iodate and hydrogen ion initial concentrations from the stoichiometric concentrations of KIO_3 and H_2SO_4 [3]

Model

Model used in present paper is extended Schmitz model M(R1-R8) supplemented by following 6 reactions [2]:

Table 1. Additional reactions of the new model.

$IO_3^- + H^+$	$\xrightleftharpoons[1.05e9]{1.50e10}$	HIO_3	D1, D-1
$HIO_3 + H^+$	$\xrightleftharpoons[3.60e8]{4.00e7}$	$H_2IO_3^+$	D2, D-2
$H_2IO_3^+ + I^-$	$\xrightleftharpoons[42.20]{2.50e5}$	$H_2I_2O_3$	D3, D-3
$H_2I_2O_3 + I^-$	$\xrightarrow{+H^+, 1.60e5}$	$H_3IO_3 + I_2$	D4
H_3IO_3	$\xrightarrow{1.10e8}$	$HIO_2 + H_2O$	D5
$HIO_2 + H^+$	$\xrightleftharpoons[2.00e4]{7.80e6}$	$H_2IO_2^+$	D6, D-6

Results and Discussion

Simulation based on Model (R1-R8), one based on new Model (R1-R14) and experimentally recorded oscillogram of the BL system, all with the same initial conditions (concentrations of hydrogen and iodate ions: $[H^+] = 8.612 \cdot 10^{-2}$ M, $[IO_3^-] = 5.989 \cdot 10^{-2}$ M), are given in Figs. 1-2.

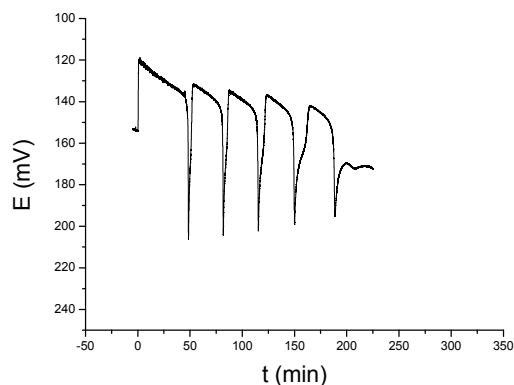


Figure 1. The iodide oscillogram of BL oscillator with constant composition ($[H_2O_2]_0 = 3.00 \cdot 10^{-3}$, $[H_2SO_4]_0 = 5.50 \cdot 10^{-2}$, $[KIO_3]_0 = 6.00 \cdot 10^{-2}$ mol·dm⁻³) and temperature (60 ± 0.2 °C) is generated in the vessel (Methrom EA 876-20). The BL reaction is recorded by digitalized potentiometric method with I⁻-ion sensitive electrode coupled with Ag/AgCl referent electrode. In this aim is used digital equipment (EH4 pH meter) connected with PC computer.

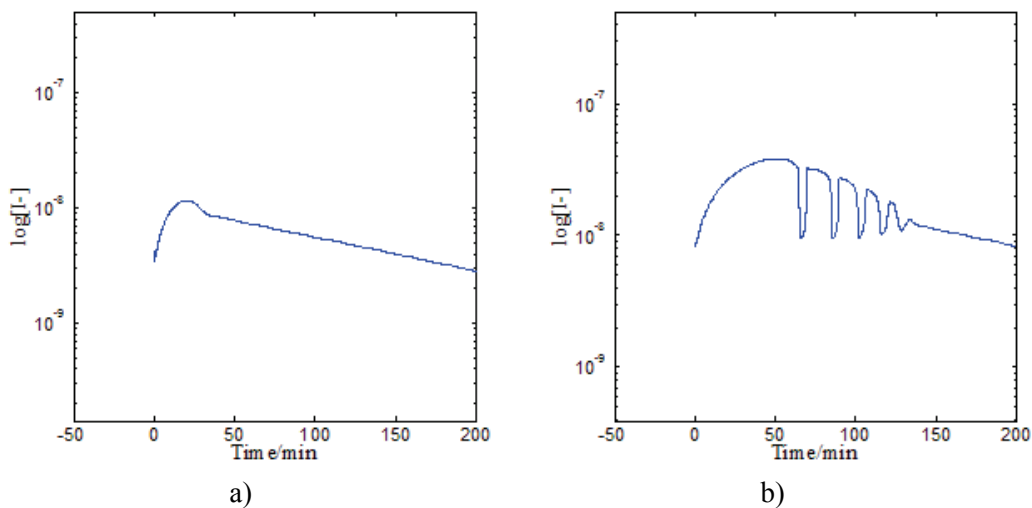


Figure 2. a) Model (R1-R8); b) Model (R1-R14) Numerical simulations for the same initial conditions as in Fig. 1.

It is obvious that Model (R1-R14) enable good simulation of the BL reaction for low H_2O_2 concentrations (see Fig. 2). Nevertheless, it must be said that Model (R1-R8) gives better simulations for high H_2O_2 concentrations.

Conclusion

Model (R1-R14) made advance in simulations of the realistic BL systems with low H₂O₂ concentrations and relatively high acidity. Detailed considerations of its properties and its applicability in wide domain of reaction species concentrations remains our task for the future.

Acknowledgement

Presented investigation is performed in collaboration with Dr Ž. Čupić. This investigation was supported by the Ministry of Education and Science of Republic of Serbia, under the projects No. 172015 and 45001.

REFERENCES:

- [1] Lj. Kolar-Anić, Ž. Čupić, S. Anić, G. Schmitz, J. Chem. Soc. Faraday Trans., 1997, 93, 2147-2152.
- [2] J. A. B. Agreda, R. J. Field, N. J. Lyons, J. Phys. Chem. 2000, 104, 5269-5274.
- [3] Ž. Čupić, S. Anić, Đ. Mišljenović, J. Serb. Chem. Soc., 1996, 61, 893-902

ELECTROCHEMISTRY

COMPUTATIONAL CHEMISTRY APPLIED TO PROBLEMS IN ELECTROCHEMISTRY – SELECTED EXAMPLES AND PERSPECTIVES

I. A. Pašti^{a,*}, D. D. Vasić^b, N. M. Gavrilov^a, S. V. Mentus^{a,c}

^a *University of Belgrade, Faculty of Physical Chemistry, Studentski trg 12-16,
11158 Belgrade, Serbia*

^b *University of Belgrade, Vinča Institute of Nuclear Sciences, Laboratory for
Physical Chemistry, Mike Petrovića Alasa 12, 11000 Vinča, Serbia*

^c *Serbian Academy of Science and Arts, Knez Mihajlova 35, 11000 Belgrade,
Serbia*

* e-mail: igor@ffh.bg.ac.rs

Abstract

Computational approach in electrochemistry, being complementary to the experimental one, provides important information regarding the electrode processes on atomic level. In this contribution, applicability of computational approach to the problems related to electrocatalysis at different levels of complexity is demonstrated. Starting with simple problem of modification of Pd(111) surface with other metal atoms, the data regarding electronic structure and periodic trends upon surface functionalization with p-elements have been offered. Next, Cl adsorption on Pd₃M alloys (M = Fe, Co, Ni, Pd, Rh) and Pd monolayers over (111) surfaces of coinage metals has been analyzed. Besides strong correlation of adsorptive properties and electronic structure, structural changes invoked by Cl adsorption are predicted. Brief overview of mechanistic analysis of ORR on Pt(hkl) surfaces is provided, allowing identification of rate determining steps on different surfaces and reaction paths, finally resulting in simulation of stationary ORR currents. Possibilities and strategies of computational approach in rational design of new electrocatalytic materials are discussed.

Introduction

With the increasing demand for energy on a global level, electrochemistry is expected to play one of the crucial roles in following years. With special interest in energy conversion, research is directed towards i) accumulation of fundamental knowledge and ii) application of this knowledge for development of new highly efficient power sources. Development of new experimental techniques and instrumentations has been followed by significant advance of theoretical methods and computer power. This resulted in application of theoretical methods in surface science and electrochemical studies providing data on atomic level, being complementary to experimental results. Although computational approach is still limited to relatively simple systems and invokes certain degree of approximation, rather important data can be obtained quickly and easily with significant advantage over the experiment: system composition can be controlled to perfection. In

addition, time necessary for *in silico* experiment is usually much shorter compared to conventional experiment.

In this contribution we offer new results obtained using computational approach regarding different problems in electrocatalysis. These problems are listed with regard to their complexity. Starting with relatively simple problem of investigation of electronic structure modification upon functionalization of Pd(111) surface with selected p-elements, we proceed to the investigation of adsorption of Cl on Pd₃M alloys (M = Fe, Co, Ni, Pd, Rh) and Pd monolayers over (111) surfaces of coinage metals and subsequent processes. Then follows a mechanistic analysis of oxygen reduction reaction (ORR) on selected Pt(hkl) surfaces and full simulation of stationary ORR curves. Finally, we discuss the computational approach in rational design of new materials for electrocatalysis.

Methods

Presented results have been obtained using pwscf code of QUANTUM Espresso distribution [1]. Surfaces were modeled in semi-infinite manner using periodic boundary conditions in combination with plane wave basis sets. Convergence was achieved by adjusting kinetic energy and charge density cut-off values. First 2D Brillouin zone has been sampled by appropriate set of k points generated through the general Monkhorst-Pack scheme [2].

Results and Discussion

a) Surface functionalization and periodic trends

Surface functionalization presents an important concept in electrochemistry and electrocatalytic studies. Number of studies has been offered so far demonstrating the effects of surface modification with foreign atoms and molecules on electrocatalytic performance [3]. The most interesting cases here are underpotential deposition (UPD) of metals and formation of surface alloys on single crystal surfaces [4]. This offers the possibilities of investigation of electrocatalytic processes on the level of model systems. UPD of p-metals has been investigated for long time for the case of oxidation of lower alcohols and CO oxidation. Nevertheless, the understanding of all effects is not fully completed. This is due to an altered energetics of adsorption of reactive species and intermediates on modified surfaces invoked by alteration of electronic structure of the surface, changes in adsorbate-adsorbate interactions, changes of work function and so on. Computational approach can provide deep insight into all these quantities, providing data complementary to the ones obtained by electrochemical measurements. In addition, it enables investigation of vast number of systems, some of them being only hypothetical, which allows separation of important factors that govern electrocatalytic activity.

Here we present the results regarding functionalization of Pd(111) surface with selected p-elements. Results obtained indicate there is significant periodicity in these cases. Namely, Ga and In tend to segregate to bulk, while Ge, Sn, Pb, As,

Sb and Te tend to form surface alloys. Remaining atoms, S and Se, favor adsorption on Pd(111). Electronic structure of modified surfaces, described through the position of d-band center and band width, differs greatly (Fig. 1).

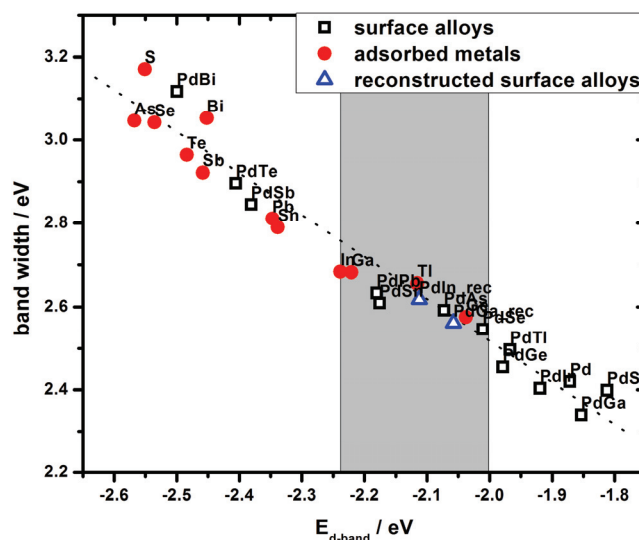


Figure 1. Position of d-band center ($E_{d\text{-band}}$) and band width of Pd(111) modified in different manners with p-elements. Shaded region indicates electronic structure desirable for efficient oxygen reduction.

Besides the data necessary for the understanding of electrocatalytic reactions on selected surfaces, the data regarding surface stability and electronic structure could be used for rational design of new electrocatalysts (see section d).

b) Adsorption of spectator species and stability of alloy surfaces

It has been widely accepted thus far that the adsorption of spectator species on electrocatalyst surfaces affects electrocatalytic activity either through the decrease of the number of available active sites or by invoking electronic effect. The well known example is OH specie in the case of oxygen reduction reaction (ORR). Nevertheless, other species can also affect electrocatalytic performance of given surface, such as chloride ion in the case of ORR investigated in HClO₄ solution [5]. Platinum and palladium alloys have been investigated for ORR performance as due to altered electronic structure with respect to clean host metals which hinders adsorption of OH and enhances ORR performance. However, important question arises regarding other spectator species and whether their presence can induce structural changes in surface layers. We investigated adsorption of Cl on Pd₃M alloys (M = Fe, Co, Ni, Pd, Rh) and Pd monolayers over (111) surfaces of coinage metals [6,7]. Obtained results display both altered electronic structure and adsorption properties, which are mutually dependent (Fig. 2).

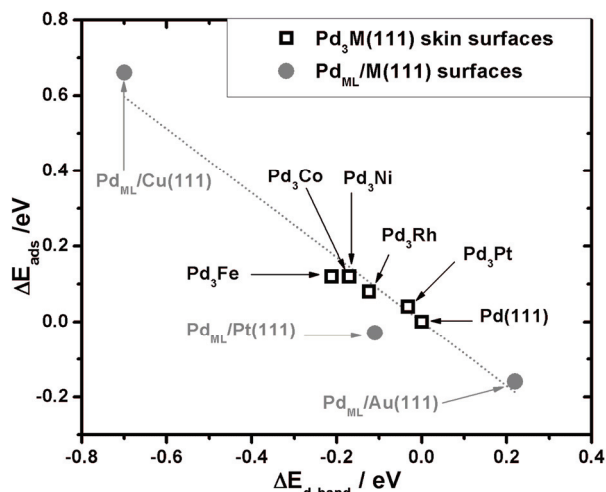


Figure 2. Correlation of Cl adsorption energies, ΔE_{ads} , to the surface electronic structure parameters, $\Delta E_{d\text{-band}}$, of Pd_3M alloys ($M = \text{Fe}, \text{Co}, \text{Ni}, \text{Pd}, \text{Rh}$) and Pd monolayers over (111) surfaces of coinage metals.

More important results arise from the analysis of stability of Pd_3M surfaces with adsorbed Cl. Namely, at elevated temperatures, these surface tend to form Pd skin in the first layer due to thermodynamic tendency of M to segregate to bulk. This provides thermodynamic stability of the surface in ORR media and high electrocatalytic activity. Investigation indicates that the presence of adsorbed Cl can induces structural changes of first two layers, lifting aforementioned reconstruction. This process is to be followed by M dissolution from the first layer, resulting in the loss of activity for ORR. This prediction is yet to be confirmed experimentally.

c) Mechanistic analysis of selected electrocatalytic reactions

Computational studies allow investigation of individual steps of complex electrode reactions. This provides a chance to analyze different mechanisms proposed for the same reaction, analyze single reaction on different metallic surfaces, or to investigate structural sensitivity on the surfaces of the same metal but with different crystallographic orientations. Here we analyzed ORR on low-index Pt surfaces. With complete free energy diagrams (an example is given in Fig. 3) constructed for different mechanisms and different surfaces it was possible to determine preferred reactions paths which differ mutually for the investigated surfaces and to indentify rate determining steps for ORR on different Pt surfaces.

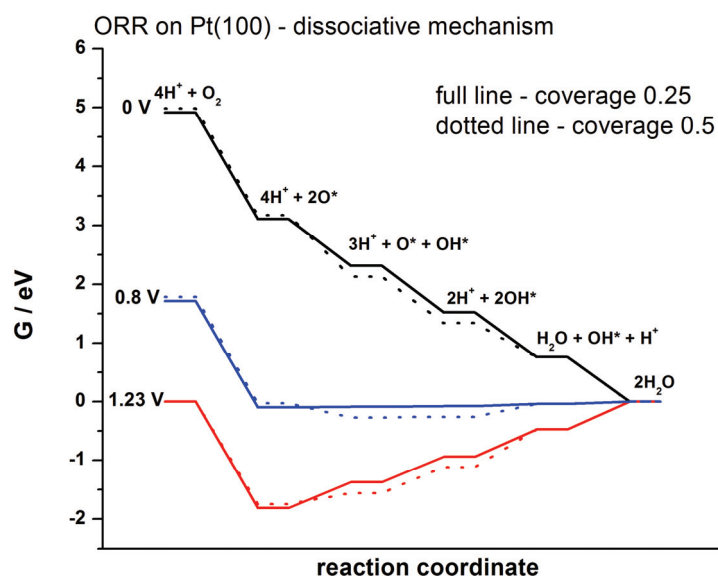


Figure 3. Free energy profiles for ORR on Pt(100) surface under the assumption of dissociative mechanism at three different electrode potentials. Counter electrode is reversible hydrogen electrode in equilibrium, pH = 0.

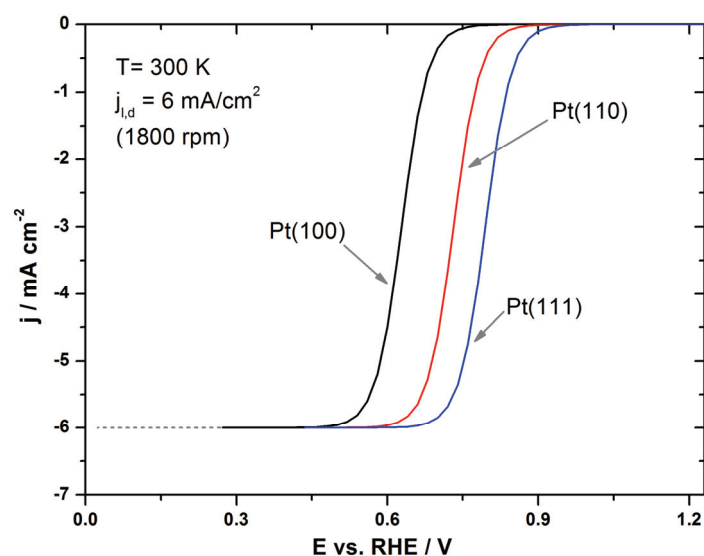


Figure 4. Simulated stationary I-E curves for ORR on rotating single crystal Pt disks with different crystallographic orientation in acidic solution (pH = 0) with the assumption that imposed diffusion limitation correspond to disk rotation rate of 1800 rpm, with electrolyte viscosity, O_2 diffusion coefficient and solubility of 0.1 M HClO_4 solution.

Once the reaction paths have been identified on different single crystal surfaces it was possible to simulate ORR currents on these surfaces (Fig. 4) using the approach described by Nørskov et al. [8], achieving excellent agreement with experiments [9]. Obtained results provide an insight in structural sensitivity of selected surfaces for ORR and shed the light on its origins, but also provide important information when concerned with rational design of new electrocatalysts.

d) Rational design of new materials

Rational design of new catalysts and electrocatalysts present an ultimate goal for computational studies in electrochemistry. Once the set of candidates for new electrocatalysts is defined, two possible directions may follow. The first one is presented in section c. Interactions of all reactive intermediates with selected surfaces is investigated and the most active candidates are further considered. This is often time-consuming and impractical due to high dimensionality of the problem. The second possible direction is to identify electrocatalytic descriptor(s) and investigate limited number of parameters on large number of systems. As an example, hydrogen adsorption energy can be mentioned as a catalytic descriptor for hydrogen evolution reaction. The application of catalytic descriptor significantly reduces dimensionality of the problem and enables true power of computational approach to be realized. The problem can possibly be even more simplified if adsorptive properties of studied surfaces are connected with the electronic structure (Fig. 2). In this way the problem of search for new electrocatalytic materials simplifies to a problem of the search of new materials with predefined electronic structure. Of course, when second approach is applied, strong interdependence between theory and experiment must exist, and these two have to be integrated in a functional entity providing each other mutual feed-back.

Conclusions

In this contribution we have demonstrated applicability of computational approach in problems related to electrocatalysis at different levels of complexity. Starting with simple problem of modification of Pd(111) surface we have provided the data on modification of electronic structure and periodic trends regarding surface functionalization. Then we analyzed Cl adsorption on Pd₃M alloys (M = Fe, Co, Ni, Pd, Rh) and Pd monolayers over (111) surfaces of coinage metals. Besides strong correlation of adsorptive properties and electronic structure we were able to predict structural changes invoked by Cl adsorption. We also provided brief overview of mechanistic analysis of ORR on Pt(hkl) surfaces which allows identification of rate determining steps on different surfaces and reaction paths, finally resulting in simulation of stationary ORR currents. We discussed possibilities and strategies of computational approach in rational design of new electrocatalytic materials, an ultimate goal of computational material science.

One may expect that following years will bring exponential development of computational methods in material science and electrochemistry, resulting in applicability of these methods in progressively more complicated systems.

Nevertheless, this progress must be followed by equivalent evolution of experimental techniques in order to provide mutual feed-back.

Acknowledgement

This work was supported by Serbia Ministry of Education and Science, project no. III45014. S.V.M. acknowledges the support provided by the Serbian Academy of Science and Arts through the project “Electrocatalysis in the contemporary processes of energy conversion”.

References

- [1] P. Giannozzi, S. Baroni, N. Bonini et al., *J. Phys. Condensed Matter*, 2009, 21, 395502.
- [2] H. J. Monkhorst, J. D. Pack, *Phys. Rev. B*, 1976, 13, 5188–5192.
- [3] V. Climent, N. García-Arárez, J.M. Feliu, *Clues for the Molecular-Level Understanding of Electrocatalysis on Single-Crystal Platinum Surfaces Modified by p-Block Adatoms in Fuel Cell Catalysis: A Surface Science Approach* (Ed. M. T. M. Koper), John Wiley & Sons, 2009.
- [4] I. Pašti, S. Mentus, *Mater. Chem. Phys.*, 2009, 116, 94-101.
- [5] M. Arenz, V. Stamenkovic, T. J. Schmidt, K. Wandelt, P. N. Ross, N. M. Markovic, *Surf. Sci.* 2003, 523, 199-209
- [6] I. A. Pašti, S. V. Mentus, *Electrochim. Acta*, 2010, 55, 1995–2003.
- [7] I. Pašti, N. Gavrilov, S. Mentus, *Adv. Phys. Chem.*, 2011, ID 305634, 8 pp.
- [8] J. K. Nørskov, J. Rossmeisl, A. Logadottir, L. Lindqvist, J. R. Kitchin, T. Bligaard, H. Jónsson, *J. Phys. Chem. B*, 2004, 108, 17886–17892
- [9] N.M. Marković, P.N. Ross Jr., *Surf. Sci. Rep.* 2002, 45, 117-229.

OXIDE PROPERTIES FROM FIRST PRINCIPLES

N. V. Skorodumova

Applied Material Physics, Materials Science and Engineering, School of Industrial Engineering and Management, KTH - Royal Institute of Technology, Stockholm, Sweden

Department of physics and astronomy, Division for materials theory, Uppsala university, Uppsala, Sweden

Abstract

Methods of modern computational materials science represent a powerful tool helping us to gain a deeper understanding of fundamental materials properties. We apply state-of-the-art methods to describe technologically important oxide materials exhibiting strong correlations, charge localization and other complex phenomena challenging for theoretical treatment. As examples our recent results on the bulk and surface properties of ceria, titania, tungsten oxide and multi-layered structures of alkaline earth oxides are presented.

Oxide materials are in the heart of many clean energy technologies such as fuel and solar cells, batteries and catalysts. Their adequate theoretical description is important for our understanding of the mechanisms operating in these materials as well as for further rational development of materials with selected properties. Density functional theory (DFT) is one of the most elaborated materials theory tools allowing one to describe the fundamental properties of materials based on the principles of quantum mechanics. Here some examples of the application of DFT to oxides including CeO_2 , MgO , CaO , SrO , WO_3 and TiO_2 are presented. Especial attention is paid to charge localization, or polaron formation, in these oxides and how it influences the oxide properties.

Cerium oxide is a key material for exhaust gas catalysts and solid oxide fuel cells. These applications utilise the ability of ceria to easily form and conduct oxygen vacancies. To improve its oxide-ion conductivity ceria is often doped with rare earth, alkaline earth elements, zirconium or other elements exhibiting a lower, as compared to cerium, valance state. This leads to the formation of oxygen vacancies in ceria matrix and increase of their mobility up to a certain, optimal dopant concentration. Usually doping strategies are based on the considerations of the relative ionic sizes of the constituting cations and mostly done by the trial-and-error method. However, as we demonstrated for ceria doped with rare-earth elements [1] the choice of dopants can be guided by computer simulations. Perhaps the most important lesson one can learn from this study is that the activation energy for oxygen vacancy diffusion has a clear minimum in the lanthanide series, which is determined by the balance between elastic and electronic perturbations of ceria

matrix by dopants. This funding allowed us to suggest an optimal co-doping strategy, which was later confirmed as effective by experiment [2].

It is known that the formation of oxygen vacancies in pure CeO_2 is accompanied by electron localization on cerium 4f-orbitals [3]. An adequate description of this charge localization requires the usage of methods going beyond the approximations of DFT. We have shown that the DFT+U method can give qualitatively correct results for the charge localization and energy of oxygen vacancy formation [4]. The pattern of electronic localization can, however, change depending on vacancy concentration, type of dopants, contamination and the presence of structural defects. In particular, the impurities of some light elements can play a role of electron drain in the oxygen vacancy formation process [5] and dopants, like Pb, for which the initial reduction occurs by $\text{Pb(IV)} \rightarrow \text{Pb(II)}$ instead of the usual localization on cerium or the $\text{Ce(IV)} \rightarrow \text{Ce(III)}$ reaction [6].

The understanding of the charge localization in oxides is highly important for many applications including electrochromic devices and batteries. Here I present our recent results on the electronic localization in WO_3 , the key material for “smart windows” technologies and the hole localization at the MgO/CaO/SrO interfaces, which are perfect model systems to study this complex phenomena. Our results show that an error in the description of charge localization can result in an error in the total energy of the order of eVs. Strain or the presence of an interface with another isostructural oxide has an large influence on the type of polarons forming. To evaluate the mobility of polarons in the studied systems we analyse the transitions between different polaronic states.

Titania films are common elements in many technologies, including solar cells. However, many important properties of titania surfaces as, for example, its interaction with water molecules and the formation of the first water layer are not fully understood. We have recently performed a combined theoretical and experimental study where the detailed atomic mechanism of the formation of the first water layer has been depicted. Our results show that water molecules can dissociate on defect-free (011) TiO_2 and the ratio of dissociated/intact water is determined by specific interactions of water and titania.

References

- [1] D. Andersson, et al. PNAS, 2006, 103,3518.
- [2] Appl. Phys. Lett., 2007, 91, 144106.
- [3] N.V. Skorodumova, et al. Phys. Rev. Lett., 2002, 89, 166601.
- [4] D. Andersson, et al. Phys.Rev.B, 2007, 75, 035109.
- [5] O. Hellman, N. V. Skorodumova, and S. I. Simak, Phys. Rev. Lett., 2012, 108, 135504.
- [6] D. Andersson, et al. Phys. Rev. B, 2007, 76, 174119.

E-03-P

NICKEL – CARBON-PTFE ELECTRODE AS ANODE FOR ALKALINE FUEL CELL

T. D. Grozdić¹, D. Stanisavljev²

¹*Institute of multidisciplinary research, University of Belgrade, Kneza Višeslava 1a, 11000 Belgrade, Serbia, (gtomisi@imsi.bg.ac.rs)*

²*Faculty of Physical Chemistry, University of Belgrade, 11000 Belgrade, Serbia.*

Abstract

The aim of the present work was to make porous nickel-carbon-PTFE electrode for alkaline fuel cell. The electrode is activated by electrochemical reduction without and with the presence of ionic activator in situ in alkaline electrolyte. Electrolyte is 30% KOH. Ionic activator are tris(ethylenediamine)-Co(III)-chloride.

Introduction

A fuel cell is an electrochemical device used to convert the chemical energy of e.g. hydrogen and oxygen directly into electric current with high efficiency. The application of low temperature type (< 100 °C) alkaline fuel cells (AFC) as a primary power sources in electric vehicles and portable equipment has received increasing attention. In AFC system platinum is usually chosen as an electrode electro catalyst. However, Pt is limited for commercial use because of high cost and limited availability. For this reason, inexpensive nickel can be used as catalyst as anode material and silver may be used as catalyst for cathode material. Therefore expensive precious metal catalysts can be avoided. In addition cheap liquid alkaline solution can be used as electrolyte. Considering only the costs of materials the AFC has much higher potential for the commercialization of fuel cells. Low temperature fuel cells represents an important element in pollution-free energy supply for mobile applications [1].

Electrochemical characteristics of porous nickel electrodes as anode can be improved by electrochemical reduction nickel oxide. Addition of the ion activator can also improve anodic oxidation of hydrogen on electrode. Activator, tris(ethylenediamine)Co(III) chloride in KOH solution [2], is added directly in the electrolyte. The electrochemical oxidation of gaseous hydrogen takes places in three-phase border zone between catalyst surface, electrolyte and gas phase. The investigated anodes for AFC applications are a composite of metal catalyst (nickel powder, 100-400 μm), carbon powder (10-50 μm) and polytetrafluorethylene (PTFE) supported by metal web. The PTFE is used as an organic binder to hold the catalyst particles together and yields a hydrophobic pore system that is not flooded by the alkaline electrolyte. The hydrophobic pore system is necessary for the transport fuel gas, supplied from the back side of electrode, through the electrode material. The aim of the present work was to make nickel-carbon-PTFE anode

for alkaline fuel cell. The freshly prepared electrode is activated by electrochemical reduction without and with the presence of ionic activator in alkaline electrolyte. Activation is performed at current density of 5 mA/cm². Electrolyte is 30% KOH. Ionic activator are 1x10⁻³M tris(ethylenediammine)Co(III)-chloride dissolved in KOH.

Experimental

Nickel porous electrode was made of 65% nickel powder, 15% carbon powder (Vulcan XC 72R) and 20% PTFE (Aldrich). Powders were mixed and then pressed on nickel web. The electrodes were activated in an electrochemical cell configuration consisting of the electrode in a holder, which allows the gas supply from the back side of the electrode and Pt counter electrode. The same test set-up was used for the electrochemical characterization of fuel cell electrodes with introducing the Hg/HgO 1M KOH as a reference electrode. The working electrode has geometric area of 6.25 cm². The electrodes were characterized after different activation times at the constant current density of 5 mA/cm².

Electrochemical characterization was done by Gamry Instruments G 750, using linear sweep voltammetry (LSV) and electrochemical impedance spectroscopy (EIS) measurements.

Results and Discussion

Activation time was 24 h and 48 h. Determination of the electrochemical characteristics of electrodes was done by LSV and EIS. The quasi-potentiostatic polarization curves in extended region of potentials is done by LSV, scan rate 1 mV/s, see Figure 1. Intensity of current has similar increase of 30 mA after 24 h and 48 h activation of the electrode relative to the non-activated electrode, curve 4. The increase of anodic oxidation of hydrogen is obvious. This increase of current intensity probably occurs due to the reduction nickeloxide on the nickel powder particles and oxidation absorbed hydrogen. After reduction, nickel powder electrode is probably more active. Improving the anodic oxidation of hydrogen on electrode was attempted by the electrochemical activation and simultaneous addition of ionic activator 1x10⁻³M tris(ethylenediammine)Co(III)-chloride in KOH. In paper [2] has been presented that during the electrolysis (under the similar experimental conditions), a thin film of cobalt is deposited on flat nickel electrode improving electrode characteristics. Therefore, one should expect similar deposition of Co on nickel porous electrode in our experiments. In accordance with this, the concentration of cobalt in the electrolyte, measured by UV-vis spectrophotometer, is not observed in electrolyte after 48h deposition. Potentiostatic polarization of such electrode with electrodeposited Co on the nickel particles in alkaline solution was presented in Fig.1, curve 3. The anodic oxidation of hydrogen in electrode with catalyst, curve 3, is similar as the oxidation in case of electrode activated by electrochemical reduction of nickel porous electrode, curve 2 and 4. [3].

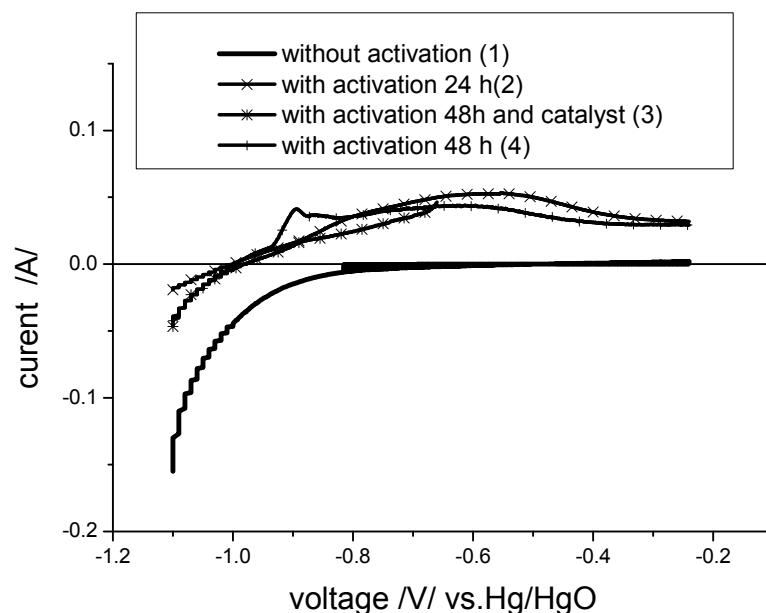


Figure 1. The quasi-potentiostatic polarization curves in extended region of potentials. The LSV scan rate was 1 mV/s. Nickel electrode after electrochemical activation at 5mA/cm² after: 24 h (2), 48h (4) and without activation (1) and with activation of 48 h and the presence of ionic activator (3).

Conclusion

Electrochemical activation for 48 h increased intensity of anodic current in hydrogen potential region for about 30 mA relative to non-activated electrode. The effect can be ascribed to increased surface of metal Ni and adsorbed hydrogen during activation. Ionic activator, 1×10^{-3} M tris(ethylenediammine)Co(III)-chloride in KOH solution., showed similar increase on anodic current without considerable effect on porous Ni electrode. EIS measurements were made of porous electrode. The Niquist curve has the characteristic capacive loop at higher frequencies and diffusion region at lower alternate current frequencies ($R_{ct} = 0,25 \Omega$, $R_{ct} = 1,9 \Omega$, $C_{dl} = 0.0001$ F and $\sigma = 5 \Omega s^{-1/2}$).

References

- [1] M. Shulze, E. Gulzov, G. Shtainhilber, App. surface science, 2001, 179, 251-256.
- [2] D. Stojić, Š. Miljanić, T. Grozdić, D. Globočanin, M. Jakšić, J. Hydrogen energy, 1994, 19, 587-590.
- [3] M. Marceta-Kaninski, S. Miulović, G. Tasić, J. Hydrogen energy, 2011, 36, 5227-5235.

ELECTROCHEMICAL DEGRADATION OF CRYSTAL VIOLET ON Bi_2O_3 ANODES

M. M. Petrović, J. Z. Mitrović, M. D. Radović, D. V. Bojić,
R. B. Ljupković, A.Lj. Bojić

Faculty of Science and Mathematics, Višegradaska 33, 18000 Niš, Serbia

Abstract

Electrochemical degradation of triphenylmethane dye Crystal Violet at Bi_2O_3 anodes, and the influence of the structure of the anodes on their dye removal efficiency have been studied. The anodes were obtained by electrodeposition of Bi_2O_3 films on stainless steel substrate from acidic $\text{Bi}(\text{NO}_3)_3$ solutions using chronoamperometric technique, at different potentials and during different deposition times and were calcined at 500°C . Dye electrolysis was carried out at constant current density and the decolorization times were determined. The anodes obtained under different deposition conditions showed different dye degradation efficiency.

Introduction

Electrochemical oxidation has been widely used for decolorizing and degradation of dyes from aqueous solutions. The oxidation of pollutants can be done with hydroxyl radical, $\cdot\text{OH}$, which is strong, non-selective oxidant, electrogenerated at the anode [1]. Anode material is very important factor for electrochemical degradation of organic pollutants and the electrodes based on metal oxides and their mixtures are often used as the anodes [1-5]. The aim of this work was to investigate the degradation of Crystal Violet on Bi_2O_3 -based anodes obtained by electrodeposition under different conditions and the effect of electrode structure on the dye removal efficiency.

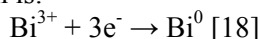
Experimental

All chemicals used were of AR grade. $\text{Bi}(\text{NO}_3)_3 \cdot 5\text{H}_2\text{O}$ was purchased from Carlo Erba, HNO_3 , H_2O_2 and Na_2SO_4 were purchased from Zorka and Crystal Violet was purchased from Sigma. 0.03M Bi^{3+} in 1M HNO_3 water solutions were used for electrodeposition and for the recording of cyclic voltammograms. Crystal Violet solutions of 50 mgL^{-1} of the dye, $10\text{ mM H}_2\text{O}_2$ and $1\text{ mM Na}_2\text{SO}_4$ were used for the dye removal experiments. All electrochemical experiments were carried out using Amel 510 DC potentiostat (Materials Mates, Italy) furnished with VoltaScope software package. The cell was composed of a three electrode system with a stainless steel sheet as a substrate for the Bi_2O_3 film, a Pt sheet as auxiliary electrode and saturated calomel electrode (Amel, Italy) as a reference electrode. The potentials reported in this paper are quoted versus the standard hydrogen electrode (SHE). Electrodeposition was carried out at constant potentials. After the deposition, the electrodes covered with Bi_2O_3 film were washed with distilled water, dried at room temperature and calcined at 500°C for 90 minutes in air. These electrodes served as the anodes for the dye degradation experiments, which were

carried out in two-electrode cell at 10 mAcm^{-2} , with Pt sheet as the cathode. The dye concentrations were determined spectrophotometrically ($\lambda=590 \text{ nm}$).

Results and Discussion

A Bi_2O_3 deposition mechanism is very complex and it takes place through several steps, with the formation of various bismuth species. Several deposition mechanisms have been proposed, depending on the deposition conditions [6-9]. For the H^+ ions concentration $>0.4 \text{ M}$, the aqua Bi^{3+} prevails and the cathodic reaction is:



In our system, this is probably the predominant reaction at the potentials lower than about 0.45 V (Figure 1).

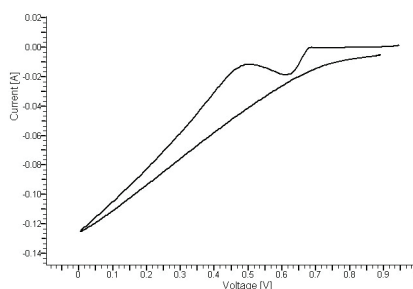


Figure 1. Cyclic voltammogram of stainless steel electrode in 0.03 M Bi^{3+} solution at 20 mV s^{-1} .

The reaction is irreversible (Fig. 1). At higher potentials, the deposited Bi^0 was oxidized to $\text{Bi}(\text{OH})_3$, or some hydrated form of bismuth oxide. The color of the obtained electrodes varied from dark gray to almost white, depending on the deposition conditions and after the calcination in air, their color changed into yellow. Generally, the samples obtained at lower potentials and during the shorter deposition times were darker and after the calcination, their color became bright yellow or even brownish-yellow; the color of those obtained at higher potentials and during longer deposition times was pale gray or white and after the calcination it became pale yellow. Those color differences may have occurred due to a presence of a certain amount of elemental Bi^0 in the structure of the first group; a further characterisation is needed to give an acceptable explanation.

The samples obtained at $0.4, 0.5, 0.6$ and 0.7 V are labeled with: A, B, C and D, respectively, and numbers 5, 10, 30, 60 and 120 are related to a deposition time (for example, sample A30 was obtained at 0.4 V during 30 minutes, etc.). Not all of the samples were of acceptable quality; the decolorization times for the samples that were applied as the anodes are given in Table 1.

Table 1. Decolorization times determined for the different Bi_2O_3 anodes.

Anode	A10	A30	B30	B60	C30	C60	D120
Total decolor. time \pm S	1590 ± 20	1800 ± 30	1350 ± 15	1710 ± 30	1380 ± 15	1200 ± 15	1290 ± 15
D (s)							

The surface structure affects the electrode efficiency (Table 1). Better results are obtained for the pale yellow electrodes, with the smooth, homogenous surface. The cause of lower efficiency of the electrodes with the rough surface may be the adsorption of the dye molecules onto the electrode surface, which may decrease the formation of OH• radicals that oxidize the dye molecules. Bi₂O₃ anodes can also be used as photoanodes [10]. Further study is needed in order to optimize the working conditions.

Conclusion

Color removal efficiency of the Bi₂O₃ anodes, obtained by electrodeposition, depends on the surface structure of the anodes, which depend on the electrodeposition conditions. By optimizing the deposition conditions, it is possible to obtain the most efficient anode. Decolorization rate can be further improved by optimizing the decolorization conditions.

Acknowledgement

The authors would like to thank the Ministry of Education and Science for supporting this work (Grant No TR 34008).

References

- [1] C. A. Martínez-Huitle, E. Brillas, *Appl. Catal. B*, 2009, 87, 105–145.
- [2] J. L. Nava, Ma. A. Quiroz, C. A. Martínez-Huitle, *J. Mex. Chem. Soc.*, 2008, 52, 249-255.
- [3] P. A. Carneiro, C.S. Fugivara, R.F.P. Nogueira, N. Boralle, M.V.B. Zanoni, *Portug. Electrochim. Acta*, 2003, 21, 49-67.
- [4] X. Chen, F. Gao, G. Chen, *J. Appl. Electrochem.*, 2005, 35, 185–191.
- [5] G. B. Raju, M.T. Karuppiah, S. S. Latha, D. L. Priya, S. Parvathy, S. Prabhakar, *Desalination*, 2009, 249, 167-174.
- [6] K. Laurent, G.Y. Wang, S. Tusseau-Nenez, Y. Leprince-Wang, *Solid State Ionics*, 2008, 178, 1735-1739.
- [7] V. Vivier, A. Régis, G. Sagon, J. -Y. Nedelec, L. T. Yu, C. Cachet-Vivier, *Electrochem. Acta*, 2001, 46, 907-914.
- [8] T. P. Gujar, V.R. Shinde, C.D. Lokhande, S.H. Hanb, *J. Power Sources*, 2006, 161, 1479–1485.
- [9] I. Valsiūnas, L.Gudaviėiūtė, A. Steponaviėius, *Chemija*, 2005, 16, 21–28.
- [10] G. Li, H. Y. Yip, C. Hu, P.K.Wong, *Mater. Res. Bull.*, 2011, 46, 153-157.

E-05-P

ELECTROOXIDATION OF *p*-NITROPHENOL ON TMA-BENTONITE MODIFIED ELECTRODES

A. Abu Rabi-Stanković*, Z. Mojović, T. Mudrinić, S. Marinović
Institute of Chemistry, Technology and Metallurgy, University of Belgrade, Center for Catalysis and Chemical Engineering, Njegoševa 12, 11000 Belgrade, Republic of Serbia

*andjela.aburabi@gmail.com

Abstract

A natural bentonite, modified with tetramethylammonium (TMA), was used as an electrode material in a *p*-nitrophenol (*p*-NP) electrooxidation. The influence of TMA loading into the bentonite layers on the electrochemical properties TMA-bentonite (TMA-B) electrodes toward *p*-NP electrooxidation was examined. Electrode sensitivity toward *p*-NP was performed. The detection limit of $1 \cdot 10^{-8}$ mol dm⁻³ was obtained.

Introduction

Nitrophenols are mainly used in the productions of pesticides, herbicides, explosives, dyes and plasticizers [1] causing severe environmental contamination. Due to the carcinogenic risk for humans, methods for phenol detection are highly relevant in environmental sciences. Electrochemical phenol determination may be accomplished by oxidation on modified solid electrodes [2]. The present study was carried out in order to investigate the electrochemical behavior of *p*-NP on bentonite electrode modified by tetramethylammonium (TMA) cation with different TMA/bentonite ratios.

Experimental

The series of organobentonites with different TMA/bentonite ratios (0.127, 0.317, 0.633 and 1.266 mmol/g) was synthesized. The amount of TMA cations was expressed in multiples of CEC with values 0.2, 0.5, 1.0, and 2.0, hence the samples were denoted as 0.2 TMA-B etc.

Nitrogen adsorption-desorption isotherms were determined using a Sorptomatic 1990 Thermo Finning at -196 °C. Specific surface area of the samples (S_{BET}), total pore volume, volume of meso- and micropores were calculated according to different methods [3,4,5,6].

For electrochemical investigations in three-electrode all glass cell the reference electrode was Ag/AgCl in 1M KCl, while a platinum foil served as a counter electrode. Para-nitrophenol behavior was investigated in 10 mM *p*-NP + 0.1 M H₂SO₄ at room temperature. The device used for the electrochemical measurements was 757 VA Computrace Metrohm.

Results and Discussion

X-ray diffractograms showed that the incorporation of TMA led to increase of d_{001} basal spacing, from 1.28 nm for Na-B, up to 1.40 nm for 2.0 TMA-B. The values

of d_{001} basal spacing obtained for all TMA-B samples corresponded to monolayer arrangements of TMA between smectite layers [7].

Textural properties of sintetized TMA-bentonites were calculated from the adsorption isotherms and presented in Table 1.

Sample	Na-B	0.2 TMA-B	0.5 TMA-B	1.0 TMA-B	2.0 TMA-B
S_{BET} (m^2g^{-1})	84	69	96	146	149
$V_{0.98}$	0.088	0.078	0.098	0.102	0.104
V_{μ}^{D} (cm^3g^{-1})	0.033	0.027	0.037	0.060	0.060
V_{meso} (cm^3g^{-1})	0.084	0.080	0.083	0.068	0.070

Table 1. The textural properties of the samples based on the analysis of nitrogen adsorption isotherms (S_{BET} -specific surface area, $V_{0.98}$ -total pore volume according to Gurvitch method for $p/p_0=0.98$, V_{μ}^{D} - micropore volume calculated according to Dubinin-Radushkevich method, V_{meso} - volume of mesopores calculated according to Barrett, Joyner, Halenda method)

With increase of TMA loading the values of textural parameters increased with exception of 0.2 TMA-B. In this sample most probably more significant portion of exchangeable hydrated Na^+ remained in the smectite interlayer and lower outgasing temperature was not sufficient to eliminate water from pores. Textural properties for 1.0 TMA-B and 2.0 TMA-B slightly differed. Specific surface area (S_{BET}) increased from $84 \text{ m}^2\text{g}^{-1}$ for Na-B up to $149 \text{ m}^2\text{g}^{-1}$ for 2.0 TMA-B. Total pore volume ($V_{0.98}$) followed the same trend. Significant increase in pore volume was found in microporous region ($d < 2\text{nm}$), while mesopore volume slightly decreased. Therefore, the intercalation of TMA into smectite interlayer lead to development of microporosity.

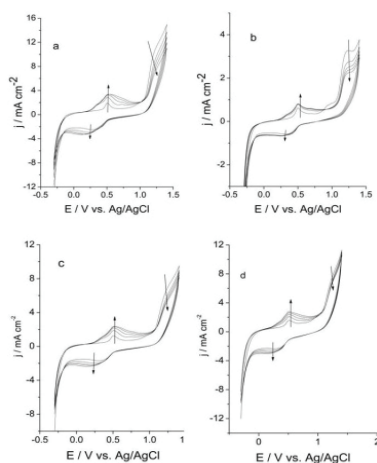


Figure 1. Cyclovoltammograms of organobentonite modified electrodes in 10 mM p -NP + 0.1 M H_2SO_4 , at 10 mV s^{-1} for a) 0.2 TMA-B, b) 0.5 TMA-B, c) 1.0 TMA-B, d) 2.0 TMA-B. Arrows indicate changes during cycling.

Electrochemical behavior of TMA-B based electrodes in p -NP solution is presented in Figure 1. All the investigated electrodes registered a wave at about 1.2 V, which decreased with cycling. The peaks at 0.47 V and 0.54 V, which increased during cycling, were assigned to p -benzoquinone and hydroquinone [8]. The cyclic voltammograms of the investigated electrodes differ only in current density of corresponding peaks. The current density for p -NP oxidation wave at $\sim 1.2 \text{ V}$ increased in following order: 0.5 TMA-B < Na-B < 1.0 TMA-B \approx 2.0 TMA-B < 0.2 TMA-B. With the increase of specific surface area of the investigated TMA-bentonites the electrode activity toward p -NP oxidation increased. Therefore, the

E-05-P

similar electrochemical behavior of 1.0 TMA-B and 2.0 TMA-B electrodes might be ascribed to similar textural properties. The enhanced current density in 0.2 TMA-B based electrodes might be induced by better accessibility to active sites for p-NP oxidation.

The sensitivity of 0.2 TMA-B electrode toward p-NP was investigated using the technique of square wave voltammetry. Anodic peak currents were linearly related to concentration of p-NP over the range from $2 \cdot 10^{-7}$ to $2 \cdot 10^{-4}$ mol dm^{-3} . The detection limit (DL) was estimated by gradually decreasing the concentration of p-NP and it is considered to be $1 \cdot 10^{-8}$ mol dm^{-3} .

Conclusions

A series of tetramethylammonium bentonites (TMA-B) was prepared from domestic bentonite with different TMA/bentonite ratios. X-ray diffraction technique and nitrogen adsorption/desorption isotherms were used for characterization of the samples. X-ray diffractograms confirmed the increase of d_{001} basal spacing upon the incorporation of TMA. The intercalation of TMA into smectite interlayer also lead to development of microporosity. Among all investigated samples, 0.2 TMA-B showed the best activity toward p-NP suggesting that the textural properties did not have dominant role in the electro-oxidation process. Using square wave voltammetry technique calibration plot was determined and detection limit of $1 \cdot 10^{-8}$ mol dm^{-3} was calculated.

Acknowledgements

This work was supported by the Ministry of Education and Science of the Republic of Serbia (Project III 45001).

References

- [1] J. Spain, Annu. Rev. Microbiol., 1995, 49, 523-555.
- [2] T. Spătaru, N. Spătaru, J. Haz. Mat., 2010, 180, 777-780
- [3] F. Bergaya, G. Lagaly, Appl. Clay Sci., 2001, 19, 1-3.
- [4] S. H. Gregg, K. S. Sing, Adsorption, Surface Area and Porosity, Academic Press, New York, NY, 1967.
- [5] F. Rouquerol, J. Rouquerol, K. Sing, Adsorption by powders and porous solids, Academic Press, London, UK, 1999.
- [6] P. A. Webb, C. Orr, Analytical methods in fine particle technology, Norcross, GA, USA: Micrometrics Instrument Corporation, 1997.
- [7] G. Lagaly, M. Ogawa, I. Dekany, Clay mineral organic interactions, in F. Bergaya, B. K. G. Theng, G. Lagaly, (Eds.), Handbook of Clay Science, Developments in Clay Science, Elsevier Ltd., Amsterdam, 2006, 327-330.
- [8] A. Safavi, N. Maleki, F. Tajabadi, The Analyst, 2007, 132, 54-58.

INFLUENCE OF HDTMA/BENTONITE RATIO ON PHENOL ELECTROOXIDATION

Z. Mojović, A. Abu Rabi-Stanković, T. Mudrinić,
A. Ivanović-Šašić, P. Banković

*University of Belgrade, Institute of Chemistry, Technology and Metallurgy,
Department of Catalysis and Chemical Engineering, Njegoševa 12, 11000
Belgrade, Republic of Serbia*

Abstract

Partial and complete substitution of cations in the interlayer region of clay with different amounts of hexadecyl trimethylammonium bromide (HDTMABr) was performed. We investigated the influence of HDTMA/bentonite ratio on phenol electrooxidation. Multisweep cyclic voltammetry was applied to analyze the behavior of clay modified glassy carbon electrode. The influence of phenol concentration was investigated. The reaction order in respect to phenol was determined to be around 2.

Introduction

Electrochemical oxidation of organic molecules can be used to develop sensors for analytical purposes. Detection of phenol in aqueous solution is of great importance due to its high toxicity and solubility in water. Electrooxidation of phenol begins with the formation of phenoxide radical. Further reaction path depends on the nature of the electrode and pH of the solution. In acidic solutions phenoxide radical is usually further oxidized to quinone and hydroquinone, while in alkaline solutions the principal reaction is polymerization [1,2]. Consequentially, the electrooxidation of phenol on many electrodes leads to electrode deactivation due to formation of polymeric coatings. In our previously published paper organomodified bentonite was suggested as electrode material for phenol detection in alkaline solutions. The process of electrode deactivation greatly depends on the content of HDTMA in sample. Therefore, the effect of HDTMA/bentonite ratio on phenol electrooxidation was further investigated. The reaction order in respect to phenol was determined.

Experimental

Na-enriched bentonite (Na-B), used for the preparation of organobentonites, was prepared from the bentonite fraction ($< 74 \mu\text{m}$). HDTMA-Br surfactant was added to Na-B aqueous suspension in different surfactant/clay ratios in order to obtain modified bentonites with different HDTMA loading. The HDTMA-Br to bentonite ratios were 0.127, 0.633, 0.945, 1.266 and 1.899 mol g^{-1} representing 0.2, 1.0, 1.5, 2.0 and 3.0 times of cation exchange capacity (CEC) value. Therefore, the samples were denoted as 0.2 HDTMA-B, 1.0 HDTMA-B, 1.5 HDTMA-B, 2.0 HDTMA-B and 3.0 HDTMA-B, respectively.

The electrochemical investigation was performed in a three-electrode all glass cell. A glassy carbon rotating disc electrode modified by organobentonite was used as a working electrode, in a previously described manner [3]. The supporting electrolyte was 0.1 M NaOH, while phenol concentration was varied in the range 5 – 20 mM. The device used for the electrochemical measurements was 757 VA Computrace Metrohm.

Results and Discussion

After the steady state voltammogram had been obtained in a 0.1 M NaOH solution, phenol was added to the solution. The first cycle obtained for each examined electrode in the phenol containing solution is presented in Fig. 1. For the sake of clarity, only anodic parts of the cycles are presented. Similarly to the behavior of these materials in acidic solution, 0.2HDTMA-B and 1.0HDTMA-B exhibited lower currents for phenol oxidation than the Na-B electrode. The highest current of phenol oxidation was obtained for 1.5HDTMA-B sample.

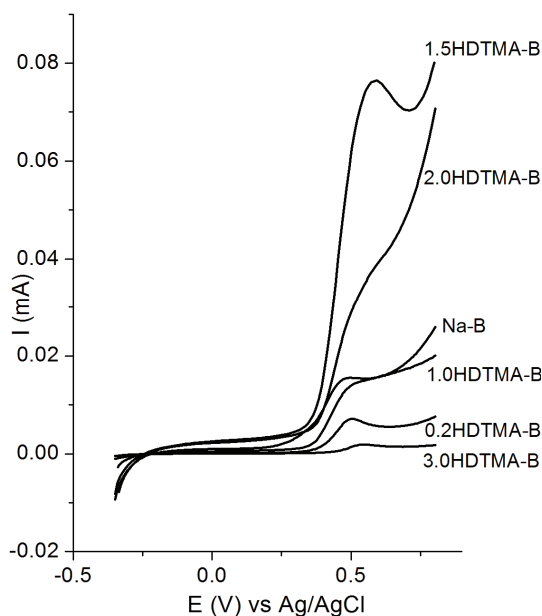


Figure 1. Cyclic voltammograms (the first scan) of investigated electrodes in 10 mM phenol + 0.1 M NaOH, recorded at a polarization rate of 10 mVs^{-1} .

The presence of HDTMA on the electrode surface probably delayed polymerization since the electrode retained its activity for ten consecutive cycles as we previously shown [3]. The role of HDTMA was to „dissolve” the formed products (dimers) and to prevent further polymerization. However, further cycling of organomodified bentonite electrodes in phenol solution led to a gradual deactivation of the electrodes. It took more than 30 cycles to reach electrode deactivation. The concentration of dimers probably increased to the extent that enabled further polymerization.

The current drop occurred for the sample with surfactant loading of 2 CEC and for 3 CEC dropped below the current obtained for 0.2 CEC. This effect can be ascribed to high concentration of phenoxide radicals formed at higher phenol concentration at

the electrode surface [4], which caused faster deactivation of the electrode. The higher phenol concentration was result of higher organophilicity of these samples due to higher surfactant loading.

The effect of the potential scan rate (v) between 10 mVs^{-1} and 700 mVs^{-1} on the peak potential (E_p) and peak current (I_p) was evaluated in a 10 mM phenol solution. A linear relationship between peak height and square root of the scan rate was found ($r=0.99$). The peak potential shifted to more positive potentials as the scan rate increased. Thus, the irreversibility of the process was confirmed, which is in agreement with the absence of signal in the reverse scan.

Tafel slopes obtained for the first cycle were in the range $80 - 75 \text{ mV dec}^{-1}$ and decreased with increased surfactant loading. The electrochemical reaction orders ($d\log I/d\log C$) at various potentials were obtained from the Tafel plots calculated from the first cyclic voltamograms. The reaction order for was 2.5 and 2.2 for 0.2HDTMA and 1.5HDTMA-B, respectively. The reaction order did not vary with potential in the potential range 0.35-0.4V.

Conclusions

HDTMA on clay has two roles: 1) to enable preconcentration of analyte and 2) to „dissolve,, formed dimmers and prevent polymerization that leads to electrode deactivation. HDTMA/clay ratio plays key role in phenol oxidation. If insufficient amount of surfactant is present it only blocks the reactive sites for phenol oxidation on clay. If certain amount of surfactant is exceeded phenol concentration on the electrode surface is great enough for the polymerization to prevail. The reaction order for phenol oxidation in alkaline solution on these electrodes was approximately 2.

Acknowledgment

This work was supported by the Ministry of Education and Science of the Republic of Serbia (contract No III 45001).

References

- [1] G. Avci, B. Yazci, M. Erbil, Russ. J. Electrochem., 2009, 45, 263–270.
- [2] Z. Mojović, A. Milutinović-Nikolić, S. Mentus, D. Jovanović, Chem. Eng. Technol., 2009, 32, 738-744.
- [3] Z. Mojović, N. Jović-Jovičić, A. Milutinović-Nikolić, P. Banković, A. Abu Rabi-Stanković, D. Jovanović, J. Hazard. Mater., 2011, 194, 178–184.
- [4] G. Arslan, B. Yazici, M. Erbil J. Hazard. Mater., 2005, B124, 37–43.

E-07-P

EFFECT OF DEPOSITION OF VANADIUM OXIDE NANOLAYER ON PERFORMANCE OF TiO₂ DYE-SENSITIZED SOLAR CELL ELECTRODE

D. M. Minić¹, L. Vesce², D. G. Minić³, A. Di Carlo², V. A. Blagojević¹

¹*Faculty of Physical Chemistry, University of Belgrade, Studentski trg 16, 11000 Belgrade, Serbia*

²*Department of Electrical Engineering, University of Rome Tor Vergata, Rome, Italy*

³*Kontrola LLC, Austin, TX, USA*

Abstract

Vanadium oxide layer was deposited on TiO₂ in both nanoparticle and film form using self-limiting deposition from precursor solution at room temperature. Efficiency of an electrode modified with vanadium (V) oxide layer revealed a decrease in efficiency, relative to equivalent standard TiO₂ electrode, of around 40%. DFT calculations of vanadium monolayers on anatase and rutile TiO₂ surfaces revealed that the effect of vanadium (V) oxide layer on electronic structure of individual crystal structures is very different, suggesting that while pure anatase TiO₂ film might benefit from deposition of surface vanadium (V) oxide layer, the performance of rutile TiO₂ with the same layer probably decreases significantly.

Introduction

Dye-sensitized nanocrystalline solar cells (DSSC) have emerged as a potential cost-effective alternative to conventional silicon solar cells. The photoanode of DSSC consists of interconnected spherical nanoparticles of TiO₂, which form a mesoporous film, mounted on indium tin oxide or fluorine tin oxide, sensitized by a monolayer of dye molecules [1]. Upon absorption of light, dye molecule injects an electron, into the conduction band of TiO₂, oxidizing in the process. The electron is, subsequently, transported toward and collected by a back-contact electrode. Doping of TiO₂ with vanadium in order to improve its photocatalytic properties has been a focus of particular interest in recent times. V₂O₅ mounted on TiO₂ has been shown to be a good photocatalyst for a number of reactions [2], while nanostructures of vanadium doped TiO₂ have been prepared in both solid phase and solution [3]. Coating of TiO₂ film with isocrystalline vanadium oxide could improve its absorption in the visible spectrum, while, if the vanadium oxide film is thin enough and remains epitaxial [4], the overlap between atomic orbitals of vanadium and titanium could create a continuous band allowing for unimpeded electron transfer from vanadium to titanium, while improving the electron transfer from dye molecules into the modified TiO₂ film.

Results and discussion

Vanadium oxide layer was coated on TiO₂ films using self-limiting deposition reaction from precursor in a solution at room temperature, allowing for deposition of both vanadium (IV) and vanadium (V) oxide layers. The presence of vanadium

(V) oxide in modified TiO₂ films was confirmed using Raman spectroscopy (Fig. 1). TiO₂ films, which were used to fabricate electrodes, contained a mixture of anatase and rutile nanoparticles.

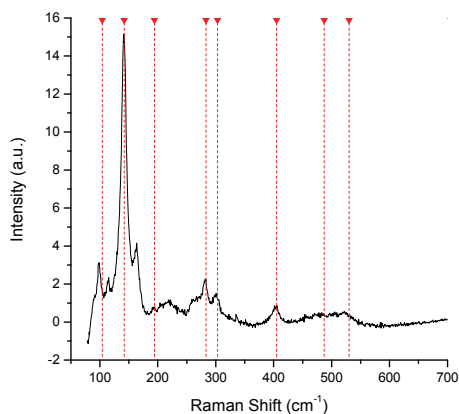


Figure 1. Raman spectrum of vanadium-oxide coated TiO₂ film (vertical lines identify peak positions for V₂O₅).

Measurements of J-V characteristics, to determine the efficiency of DSSC with modified electrode, were conducted by preparing, for each experiment, two equivalent electrodes: one was modified by deposition of vanadium-oxide layer (modified electrode) on to TiO₂ film, while in the other, TiO₂ film was left unmodified (standard electrode). The cell containing modified electrode exhibited 40% lower efficiency than the one containing standard electrode (Fig. 2).

In order to gain further insight into the effect of surface vanadium-oxide layer on the performance of TiO₂ electrode in dye-sensitized solar cell, DFT calculations of vanadium-oxide coated anatase and rutile TiO₂ crystals were conducted. The calculations were performed on periodic vacuum slab surfaces, where the top layer of titanium atoms had been replaced with vanadium atoms. These indicate that the surface vanadium (V) layer interacts differently with anatase and rutile surfaces. Anatase structure exhibits a band gap of 1.014eV, while rutile structure exhibits complete lack of a band gap. Partial density of states indicates that the states in the band gap are mostly d-states, suggesting that these come from vanadium atoms, while the calculated electronic structure of modified rutile structure is similar to behavior of identical VO₂ structure. This indicates that there is insufficient overlap of atomic orbitals of vanadium and titanium causing vanadium orbitals to create a sub-band which closes the band gap, which would mean that an electron injected into surface layer of vanadium (V) oxide would be confined mostly to that layer, effectively trapping the electron and increasing the chance of recombination with the hole on dye molecule.

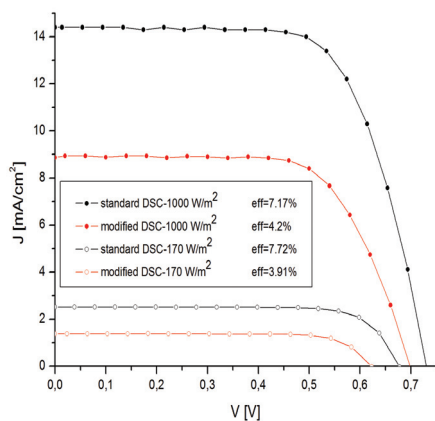


Figure 2. J-V characteristics of modified vs. standard TiO₂ electrode.

Conclusion

Efficiency of a DSSC electrode with vanadium (V) oxide layer revealed a decrease in efficiency, relative to equivalent standard TiO₂ electrode, of around 40%. DFT calculations of vanadium (V) oxide monolayers on anatase and rutile TiO₂ surfaces revealed that its effect on electronic structure of anatase and rutile, respectively, is different, suggesting that while anatase probably creates sufficient orbital overlap of titanium and vanadium orbitals, rutile does not, and would not benefit from deposition of surface vanadium oxide layer.

References

- [1] G. Calogero, G. Di Marco, S. Cazzanti, S. Caramori, R. Argazzi, A. Di Carlo, C. A. Bignozzi, *Int. J. Mol. Sci.* 2010, 11, 254.
- [2] S. Klosek, D. Raftery, *J. Phys. Chem. B* 2001, 105, 2815.
- [3] G. Fu, P. S. Vary, C. T. Lin, *J. Phys. Chem. B* 2005, 109, 8889.
- [4] W. Gao, C. M. Wang, H. Q. Wang, V. E. Henrich, E. I. Altman, *Surface Science* 2004, 559, 201.

ALTERNATIVE, NON-PT ELECTROCATALYSTS FOR O₂ REDUCTION

B Šljukić, J. Milikić^(a), D. M. F. Santos^(b), C. A. C. Sequeira^(b)

(a) *University of Belgrade, Faculty of Physical Chemistry, Studentski trg 12-16, 11158 Belgrade. Serbia*

(b) *ICEMS, Instituto Superior Técnico, TU Lisbon, Av. Rovisco Pais, 1049-001 Lisbon, Portugal*

Abstract

Composites of MnO₂ with activated carbon were prepared *via* two different procedures: high- (htMnO₂/AC) and low-temperature (ltMnO₂/AC) wet impregnation procedure. The electrocatalytic activity of the synthesized materials for O₂ reduction was studied in alkaline solution with htMnO₂/AC exhibiting higher activity for the investigated reaction.

Introduction

O₂ reduction reaction (ORR) keeps attracting attention due to its involvement in numerous electrochemical processes, including energy conversion in fuel cells (FCs). FCs are seen as possible replacement of the existing fossil fuel-based power sources in some application [1]. Efficiency of energy conversion in FCs is determined by anode and cathode materials, as they determine the operational potential. Modification of the electrode surface with a catalyst is a common approach to improve ORR kinetics. Pt is the most commonly used electrocatalyst to date due to its high activity but its high cost limits the commercial production of FCs. In the extensive search for new electrocatalysts for cathodes in FCs, MnO₂ has emerged as a possible alternative electrocatalysts due to its high activity for the ORR comparable to that of Pt-based catalysts as well as lower susceptibility to contamination and lower cost [1]. AC has been chosen as support material for to its high porosity and large [surface area](#).

Experimental

High-temperature synthesis of MnO₂/AC involves stirring AC (1 g) into saturated Mn(NO₃)₂ aqueous solution (25 cm³) for 1 h. The mixture is filtered, dried at room temperature and then heated up to 350°C at 10°C/min rate and left at that temperature for 10 h, leading to transformation of nitrate precursor into MnO₂.

Low-temperature synthesis method involves impregnation of AC (200 mg) in a saturated KMnO₄ aqueous solution (5 cm³) by stirring for 1 h. After filtration, the blend is first dried at room temperature and then left at 120°C overnight, resulting in the conversion of permanganate precursor into MnO₂.

Catalytic ink was made by ultrasonically mixing MnO₂/AC (5 mg) and Nafion (50 µl, 5 wt.%) with ethanol (750 µl). The working electrode was prepared by pipetting 20 µl of the ink onto a glassy carbon electrode (GCE) and leaving it to dry.

All electrochemical studies were done using one-compartment cell with Pt foil as counter and saturated calomel electrode (SCE) as reference electrode. For ORR studies, O_2 was bubbled into 1 M NaOH electrolyte for 10 min prior to measurements.

Results and discussion

Formation of α - MnO_2 by high- and low-temperature procedure has been previously confirmed by electrochemical [2] and XRD analysis [3], respectively.

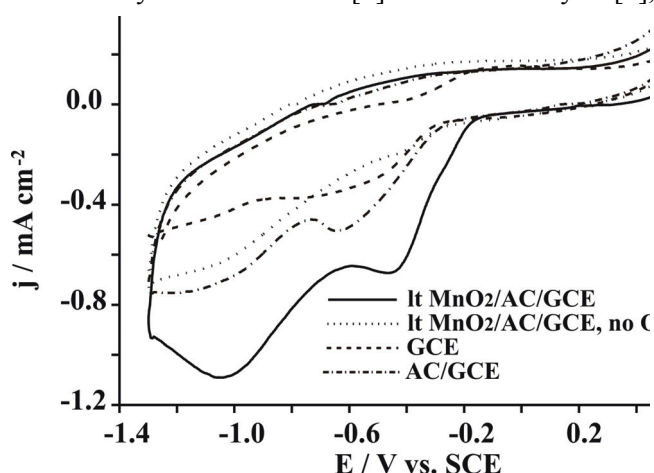


Figure 1. CV of $ltMnO_2/AC/GCE$ in O_2 -saturated 1 M NaOH at 50 mVs^{-1}

Cyclic voltammogram (CV) of $ltMnO_2/AC/GCE$ in O_2 -saturated showed two peaks at -0.40 and -1.00 V due to ORR, that couldn't be observed at the control CV of the same electrode in O_2 -free solution, *Fig 1*. It should be noted that CVs of both bare and AC-modified GCE in the same solution showed a single peak of smaller intensity evidencing electrocatalytic activity of MnO_2 . At the CV of $htMnO_2/AC/GCE$ in O_2 -saturated electrolyte,

only one peak at *ca.* -0.55 V could be seen, *Fig 2*. It could also be observed that current densities obtained on $htMnO_2/AC/GCE$ are considerably higher than those obtained on $ltMnO_2/AC/GCE$. This suggested different mechanisms of ORR at the two electrocatalysts. The appearance of two peaks at the CV of $ltMnO_2/AC/GCE$ indicates that the ORR proceeds *via* two successive two-electron processes with HO_2^- as intermediate, while appearance of a single peak at the CV of $htMnO_2/AC/GCE$ evidences that ORR proceeds as four-electron process.

This was further confirmed by performing linear sweep voltammetry (LSV) studies in O_2 -saturated 1 M NaOH with rotating disc electrode (RDE). Using RDE LSV data, the number of electrons transferred (n) was evaluated using Koutecky-Levich equation [4]. Pure Faradaic currents under O_2 were obtained by subtracting the background current, obtained in an O_2 -free solution under the same conditions. The n value was found to be close to 2 for $ltMnO_2/AC$ corresponding to O_2 reduction to HO_2^- and close to 4 for $htMnO_2/AC$ corresponding to O_2 reduction to OH^- ion. Such feature makes the $htMnO_2/AC$ electrocatalyst more desirable for application in FCs.

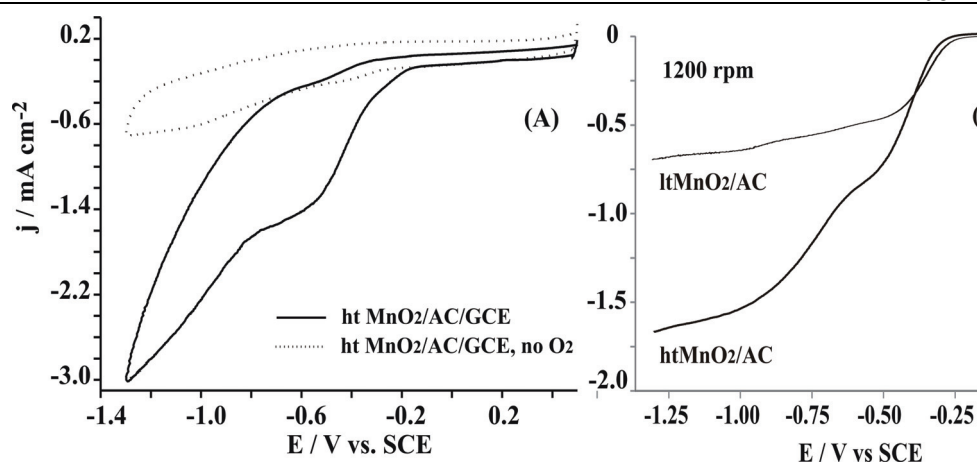


Figure 2. CV of htMnO₂/AC/GCE in O₂-saturated 1 M NaOH at 50 mVs⁻¹ (A) with LSV of both catalysts at 10 mVs⁻¹ and rotation speed of 1200 rpm (B).

Conclusions

MnO₂/AC composites were synthesized *via* high- and low-temperature wet impregnation procedure and their activity for the ORR was investigated in alkaline solution. ORR was found to proceed as 2-electron process at ltMnO₂/AC, and as 4-electron process at htMnO₂/AC electrocatalyst. Also, higher current densities were obtained at htMnO₂/AC suggesting it to be better electrocatalyst for FCs cathodes.

Acknowledgments

The authors would like to thank to Ministry of Edu. and Sci. of Rep. of Serbia for support within the project No III45014 as well to the FCT, Portugal, for postdoctoral research grants SFRH/BPD/77768/2011 (BŠ) and SFRH/BPD/63226/2009 (DMFS).

References

- [1] M. Chatenet, F. Micoud, I. Rouche, E. Chaînet, J. Vondrák, *Electrochim Acta*, 2006 51, 5452–5458.
- [2] C. E. Langley, B. Šljukić, C. E. Banks, R. G. Compton, *Anal. Sci.*, 2007 23 165-170.
- [3] M. Mališić, A. Janošević, B. Šljukić, I. Stojković, G. Ćirić-Marjanović, *Electrochim Acta*, 2012, 74, 158-164.
- [4] M. Chatenet, M. Arousseau, R. Durand, *Electrochim Acta*, 2000, 45, 2823-2827.

E-09-P

ELECTROCHEMICAL BEHAVIOR OF V₂O₅ XEROGEL AND V₂O₅ XEROGEL /GRAPHITE COMPOSITE IN AQUEOUS SOLUTION

M. Medić^b, I. Stojković^a, M. Vujković^a, N. Cvijetićanin^a, S. Mentus^{a,*}

^a*University of Belgrade, Faculty of Physical Chemistry, Studentski Trg 12-16, Belgrade, Serbia*

^b*Vinča Institute of Nuclear Sciences, University of Belgrade, P.O. Box 522, Belgrade, Serbia*

^{*}*The Serbian Academy of Science and Arts, Knez Mihajlova 35, 11158, Belgrade, Serbia*

ivana@ffh.bg.ac.rs

Abstract

The V₂O₅ xerogel and V₂O₅ xerogel /graphite composite were synthesized by sol-gel method. The obtained materials were characterized by X-ray diffractometry and simultaneous thermogravimetry and differential thermal analysis. The electrochemical behaviour was investigated by galvanostatic cycling in aqueous solutions of LiNO₃. Better electrochemical performance was evidenced for composite V₂O₅ xerogel/graphite. Namely, the initial capacity of V₂O₅ xerogel/C was found to be 66 mAh g⁻¹ against 40.4 mA h g⁻¹ for V₂O₅, while capacity fade after 50 cycles was 10 % of initial capacity for V₂O₅ xerogel/ graphite, against 27% for V₂O₅.

Introduction

The rechargeable lithium-ion batteries with organic electrolytes present today the exclusively used power sources of the portable electronic devices. However, the organic electrolytes are toxic, inflammable and expensive, and there is the tendency to replace them by aqueous solutions [1]. The lithium ion batteries with aqueous solution would be more safe and cheaper. The main problem of Li-ion batteries with aqueous electrolyte is the voltage limitation arising due to the low decomposition voltage of water, and relatively poorer electrochemical characteristic of electrode materials.

In the field of lithium-ion batteries with organic and aqueous solutions, different vanadium oxides (VO₂, V₂O₅, Li_{1+x}V₃O₈) were investigated as electrode materials. Vanadium pentoxide (V₂O₅) in both crystalline and amorphous (xerogel) form was often studied. An amorphous (xerogel) form of V₂O₅ displayed higher capacity than the crystalline form in organic and aqueous electrolyte [2-4]. The performances during galvanostatic charging/discharging of xerogel V₂O₅ may be improved by some additives to the electrolyte solution, or by addition of nanodispersed carbon material during synthesis [3,4].

In this work, we synthesized two materials by a simple sol-gel method: xerogel V₂O₅ and composite material V₂O₅ xerogel/C, where C was finely dispersed Carbon. The intercalation/deintercalation of Li ions into both materials was investigated by galvanostatic cycling in a saturated aqueous solution of LiNO₃.

Experimental

Both the xerogel V_2O_5 and the V_2O_5 xerogel/graphite composite (V_2O_5/C) were synthesized in an almost identical way. In both case, the preliminary solution was obtained by dissolving crystalline V_2O_5 powder (p.a. Merck) in 10% solution of hydrogen peroxide H_2O_2 (p.a. Merck) in an amount which provided a 0.06 M solution. To obtain V_2O_5 xerogel /C composite, the natural graphite was added in the V_2O_5 - H_2O_2 solution in an amount to provide mass ratio V_2O_5 : C of 10 in solution V_2O_5 - H_2O_2 . The solution V_2O_5 - H_2O_2 with and without added graphite were mixed by magnetic stirrer 24 h, then poured into a Petri cup and dried in air until the solvent evaporated. The obtained powders were dried at 200 °C for one hour.

The X-ray power diffraction (XRPD) data were collected using Philips PW 1050 with $CuK\alpha_{1,2}$ radiations in 10-70° 2θ range with 0.05° step and 2 seconds exposition time. Simultaneous TGA/DTA measurements were carried out under air flow, at a heating rate of 10 ° min^{-1} using the device TA SDT Model 2960.

The galvanostatic charge/discharge measurements were performed in a two-electrode arrangement, with V_2O_5 xerogel or composite V_2O_5 xerogel/C as active mass of the working electrode and $LiMn_2O_4$ as active component of the counter electrode, using software-controlled device Arbin BT-2042. The active material for working (or counter) electrodes was made by mixing xerogel V_2O_5 or composite V_2O_5 xerogel/C ($LiMn_2O_4$), carbon black and PVDF binder in a weight ratio 85:10:5 in N-methyl 2-pyrrolidone solvent. A drop of the suspension was deposited on stainless steel (Fe-18%Ni) plates (~6.2 cm^2). These electrodes were dried one hour at 80 °C in air and 12 hours at 140 °C under vacuum. The filter paper soaked with saturated aqueous solution $LiNO_3$ separated the electrodes. The coulombic capacity during charging/ discharging process was measured within the voltage window 0.01 to 1.3V, i.e. within the voltage window of water electrochemical decomposition.

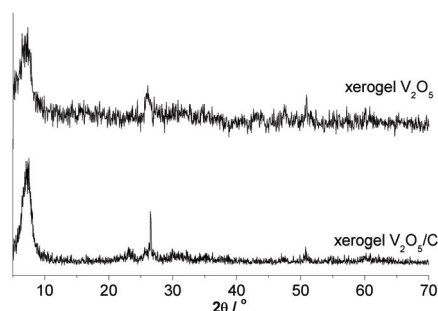


Figure 1. a) The XRD patterns of composite V_2O_5 xerogel and V_2O_5 xerogel /C composite dried at 200°C.

Results and Discussion

XRPD analysis of V_2O_5 xerogel and V_2O_5 xerogel /C composite after drying at 200°C evidenced amorphous structure of V_2O_5 , Figure 1. The broad peak at $2\theta = 25^\circ$ can be observed for composite V_2O_5/C and it belongs to graphite. The both xerogels contained 0.4 mole of H_2O per mole of oxide after heating to 200 °C. The amount of carbon in the synthesized material, calculated from the mass loss caused by combustion, corresponds to the initial amount of carbon in the material.

Figure 2 shows the dependence of discharge capacity (left axis) and efficiency (right axis) on the cycle number of V_2O_5 xerogel and V_2O_5 xerogel/C composite in aqueous solution of $LiNO_3$. The coulombic efficiency of both investigated materials were similar and amounted to about 96%. The V_2O_5 xerogel displayed initial capacity of 40.4 mA h g^{-1} , but its value was only 29.5 mA h g^{-1} after 50 cycles. The V_2O_5 xerogel/C composite displayed much better electro-chemical

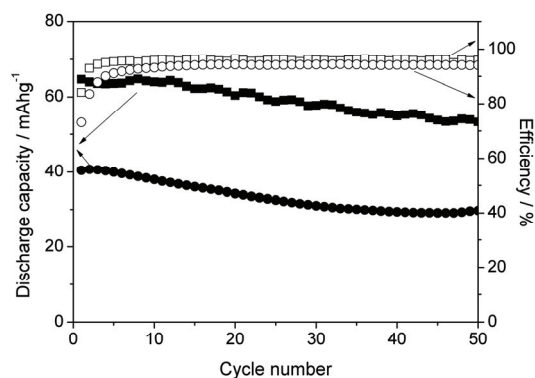


Figure 2. The discharge capacity (full symbols) and coulombic efficiency (empty symbols) of xerogel V_2O_5 (circle) and composite xerogel V_2O_5/C (square) in saturated aqueous $LiNO_3$ solution.

performance both before and during cycling. Its initial discharge charge capacity was 66 mAh g^{-1} and was almost constant during the first 12 cycles. After 12 cycles there appeared slight decrease and 59 mA h g^{-1} was registered after 50 cycles. A similar improvement of cycling performance was perceived for composite xerogel V_2O_5 if carbon black was added in the process of synthesis. Namely, the xerogel V_2O_5 composite /C where C is carbon black displayed initial capacity of 58.8 mAhg^{-1} and after 50 cycles somewhat lower value of 43.1 mAhg^{-1} was measured [4].

Conclusion

The V_2O_5 xerogel /C composite synthesized by dissolving crystalline V_2O_5 in diluted solution of H_2O_2 and adding graphite to the solution presents a promising electrode material for aqueous lithium ion batteries. Initial discharge capacity of this material was found to be 66 mAh g^{-1} , while the capacity after 50 cycles is about 90 % of its initial value.

Acknowledgement

This work was supported by Serbian Ministry of Science and Education, project No. III45014.

References

- [1] N. Cvjeticanin, I. Stojkovic, M. Mitric, S. Mentus, J. Power Sources, 2007, 174, 1117-1120.
- [2] D. Imamura, M. Miyayama, M. Hibino, T. Kudo, J. Electrochem. Soc., 2003, 150, A753.
- [3] I. B. Stojković, N. D. Cvjetićanin, S. V. Mentus, Electrochem. Commun., 2010, 12, 371-373.
- [4] I. Stojkovic, N. Cvjeticanin, S. Mentus, Russ. J. Phys. Chem. A, 2011, 85, 2344-2348.

POLAROGRAPHIC ASSESMENT OF ANTIOXIDANT ACTIVITY OF TEA (*Camellia sinensis*) EXTRACTS

D. Sužnjević^{1*}, F. Pastor², S. Gorjanović¹

¹*Institute of General and Physical Chemistry, P. O. Box 45, 11158 Belgrade 118, Serbia*

²*Faculty of Chemistry, University of Belgrade, P. O. Box 158, 11 001 Belgrade, Serbia*

**desanka.suznjevic@gmail.com*

Abstract

Antioxidant (AO) activity of unfermented (yellow) and fermented (black) tea (*Camellia sinensis*), as well as catechin, has been determined using recently developed direct current (DC) polarographic assay. The assay has been based on sensitivity of anodic current of Hg (II) hydroxo-perhydroxil complex formed in alkaline peroxide solutions, at potential of anodic dissolution of mercury, on antioxidants presence. Upon gradual addition of investigated samples dose-dependant decrease of the current has been followed. The slope of the liner part of curves obtained by plotting percentage of the anodic current decrease versus amount of tested samples has been used to express AO activity. Based on presented results, DC polarographic assay has been recommended for fast, reliable and easy-to-handle measurement of AO activity of both individual and complex samples.

Introduction

Polarographic behavior of anodic current appeared in alkaline buffered solutions of hydrogen peroxide, at potential of mercury dissolution, was studied. Confirmation that the anodic current originates from mixed complex, $[\text{Hg}(\text{O}_2\text{H})(\text{OH})]$, formed at the electrode surface, was provided. Influence of different experimental conditions (pH of medium, H_2O_2 concentration, electrolyte solution temperature) on that current was followed. A rapid, simple and reliable enzyme-free assay for determination of antioxidant (AO) activity based on the anodic current decrease in the presence of AOs was developed and optimized [1]. The assay was applied on a series of benzoic acids along with corresponding cinnamate analogues, as well as on flavonoid myricetine.

The objective of this study was to determine AO activity of unfermented (yellow) and fermented (black) tea infusions as well as individual phenolic compound flavan-3-ol catechin known to be present in tea in high amount.

Materials and methods

The current-potential (*i-E*) curves were recorded using the polarographic analyzer PAR (Princeton Applied Research), model 174A, equipped with X-Y recorder (Houston Omnigraphic 2000). A dropping mercury electrode (DME) with a programmed dropping time of 1 s as working electrode, saturated calomel electrode (SCE) as a reference and a Pt-foil as auxiliary electrode were used. Clark Lubb's

E-10-P

(CL) buffer (pH 9.8) was prepared by mixing 25 mL of 0.4 M H_3BO_3 , 25 mL of 0.4 M KCl and 40.8 mL of 0.2 M NaOH. Starting 5 mM H_2O_2 concentration was obtained by addition of 100 μL of 1.00 M H_2O_2 into 20 mL of buffer in electrolytic cell. Samples (yellow and black tea, and 2 mM catechin) were gradually added into electrolytic cell with buffered H_2O_2 solution. Extraction (10 min) was carried out by pouring 200.0 mL of boiled distilled water in a 250 mL beaker containing 2.0 g of tea. Before each i - E curve recording, a stream of pure nitrogen was passed through the cell solution, during 5 minutes before first recording and during 30 seconds after addition of each aliquot. The inert atmosphere was kept by passing nitrogen above cell solution. The initial potentials were 0.10 or 0.15 V, and potential scan rate was 10 mVs^{-1} . The DME current oscillations were filtered with low pass filter of instrument positioned at 3 s. Decrease of the anodic current of H_2O_2 , i.e. initial i_i value (i_{i0}), obtained by recording 5 mM H_2O_2 solution, upon addition of investigated samples have been recorded.

Results and Discussion

Extracts of yellow (Yin Zhen) and black (Lingia) tea, as well as 2 mM solution of catechin, have been gradually added into initial peroxide solution. Prominent difference between polarograms of 5 mmolL^{-1} solution of H_2O_2 in CL buffer (pH 9.8), recorded before and after the addition of tested samples, has been observed. Effect of addition of yellow tea on the anodic current decrease has been shown in Figure 1.

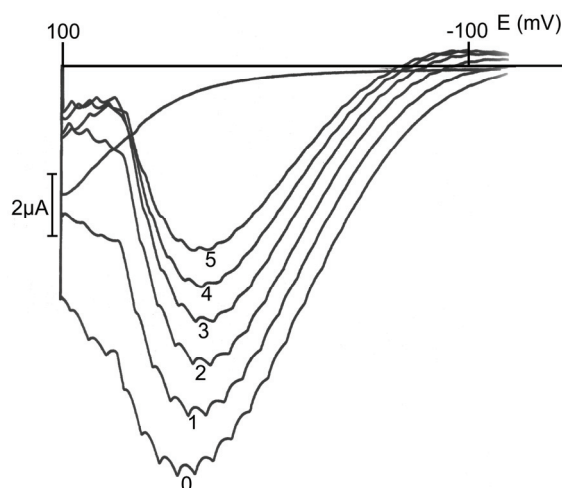


Figure 1. Anodic polarographic curves of 5 mmol L^{-1} solution of H_2O_2 in CL buffer (pH 9.8) before (0) and after addition of five equal aliquots of yellow tea (1-5) 100-500 μL .

Remaining anodic limiting current (i_{lr}) obtained upon gradual addition of tested samples has been compared with height of initial limiting current (i_{i0}). Percentage of i_i decrease has been calculated upon each addition of tested infusion according to eq:

$$\% \text{ scavenged } [\text{H}_2\text{O}_2] = \left(1 - \frac{i_r}{i_{10}} \right) \times 100$$

Plots of percentage of i_l decrease calculated upon yellow and black tea extracts addition vs volume added is shown in **Figure 2**. The slope of the linear part of dose-response curves has been used as criterion of AO activity.

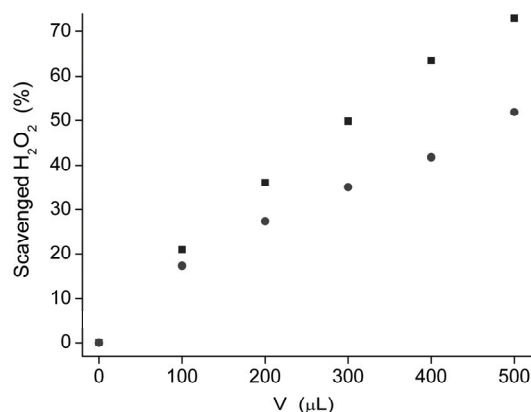


Figure 2. Yellow ■ and black ● tea effects on anodic limiting current of 5 mmol L⁻¹ solution of H₂O₂ in CL buffer (pH 9.8) (% of scavenged H₂O₂ vs volume of added samples).

The observed superiority of unfermented over fermented tea might be explained by prevalent presence of highly active flavan-3-ols found in high amount in unfermented, intermediate in semi fermented, and low in fully fermented teas [2]. High AO activity has been ascribed to catechin (48 ± 3). A significant reduction of catechins noticed in black tea is probably compensated by larger polyphenolic molecules, such as dimmeric theaflavins or polymeric thearubigins.

Acknowledgements

This work has been supported by the Ministry of Education and Science of the Republic of Serbia for support of this research under Project No. 43010 and 31093.

References

- [1] D. Sužnjević et al, *Talanta*, 2011 85 1398-1403.
- [2] C. Cabrera et al, *J. Agric. Food Chem.*, 2003 51(15) 4427-4435.

**BIOPHYSICAL CHEMISTRY,
PHOTOCHEMISTRY,
RADIATION CHEMISTRY**

F-01-SL

ELOA COMPLEXES EXERT TOXICITY BY TARGETING CELL MEMBRANE. COMPARISON WITH HAMLET

Ludmilla Morozova-Roche

*Department of Medical Biochemistry and Biophysics, Umeå University, Umeå,
90781 Sweden*

Abstract

Equine lysozyme with oleic acid (ELOA) and human α -lactalbumin made lethal to tumor cells (HAMLET) belong to the same group of proteinaceous complexes with oleic acid. The major functional feature of both complexes is their newly acquired cytotoxicity absent in original protein molecules, indicating that their self-assembly and interactions with oleic acid can create a new functionality. Modern single molecule – single cell techniques such as fluorescent correlation spectroscopy and confocal microscopy as well as model studies using lipid bilayers and vesicles can provide a powerful insight into the molecular mechanisms of ELOA interactions with cells and specifically how they target and perturb cell membrane. HAMLET-type complexes have significant therapeutic potential in combating various types of cancer and therefore understanding their molecular interactions with cells holds a key how to apply them under variety of *in vivo* conditions for specific elimination of unwanted cells.

Introduction.

The complexes of human α -lactalbumin with OA were discovered by Catharina Svanborg and co-workers two decades ago in mid-1990s [1], and since then the field has drastically expanded, acquiring new members such as ELOA [2]. Recently the OA complexes of bovine β -lactoglobulin and pike parvalbumin, proteins structurally not related either to α -lactalbumins or lysozymes, were also produced and displayed similar cytotoxic activity [3]. This implies that proteins possess intrinsic properties to acquire varying functions depending on their conformational states, associated ligands and environmental conditions. Hence, understanding of the mechanisms of acquired toxicity of ELOA has significance for the whole field and for the practical applications of these complexes for therapeutic purposes.

EL as structural homologous of α -lactalbumin.

EL belongs to an important calcium-binding sub-family within the extended family of lysozymes, i.e. in contrast to common c-type lysozyme EL possesses high

F-01-SL

affinity calcium-binding site, resembling with this regards α -lactalbumins. EL serves as an evolutionary bridge between lysozymes and α -lactalbumins, combining the structural and folding properties of both. EL forms a wide range of partially folded states under equilibrium conditions similar to these of α -lactalbumins. However, EL molten globule is much more structured compared to the “classical” molten globules of α -lactalbumins, possessing an extended native-like hydrophobic core in the α -domain [4]. Like c-type lysozymes, during refolding kinetics EL forms an ensemble of well-defined transient kinetic intermediates, possessing very persistent structures straight after the refolding reaction was initiated. EL forms also linear and ring-shaped amyloid filaments under variety of acidic conditions and calcium binding regulates this process. Thus, EL can be considered as paradigmatic molecule in protein folding and amyloid self-assembly studies as well as in the protein self-assembly regulated by oleic acid, which leads to ELOA formation [4].

Controlled ELOA production using ion-exchange chromatography.

Similar to HAMLET, ELOA was produced at the solid-liquid interface within an ion-exchange chromatography preconditioned with OA [2]. ELOA was eluted as a strong peak by using a 0-1.5 M NaCl gradient. The application of a solid-liquid interface facilitating protein self-assembly and protein-OA interactions proved to be an efficient approach in production of both ELOA and HAMLET complexes. By comparison, the complex of hen egg white lysozyme with oleic acid was also produced under the same conditions, but it was very low populated, unstable and OA can be easily depleted from its structure. Hen egg white lysozyme is much more stable than EL and it is evident that the hydrophobic interface in the column chromatography is not sufficient to cause its partial unfolding and interactions with OA molecules. Indeed, within the ion-exchange matrix bound OA molecules constitute an extended surface, facilitating both charged and hydrophobic interactions with EL molecules, while in solution OA, like many other small aliphatic molecules, would be present as a micelle. In addition, the solid-liquid interface may induce EL partial unfolding and expose its hydrophobic surfaces buried in the native state; this can also be critical for ELOA complex formation.

EL conformation in ELOA.

EL in ELOA acquires a partially folded state similar to human α -lactalbumin in the HAMLET complex, as it is evident from spectroscopic (fluorescence, near and far UV CD) and NMR measurements [2]. ELOA also binds ANS dye indicating that it possesses exposed hydrophobic surfaces. Photochemically induced dynamic nuclear polarization (photo-CIDNP) experiments revealed that there are exposed Tyr, His and Trp residues in ELOA surface, which may contribute to its surface hydrophobicity [5] and facilitate its intersections with lipid membranes. The

F-01-SL

stoichiometry of ELOA was determined by pulsed-field gradient NMR diffusion measurements and also by AFM, evaluating the volume of proteinaceous particles in AFM cross-sections. It may vary and involves typically 4–9 protein molecules present in a molten globule state and from 4 to 40 oleic acid molecules [2].

Mechanisms of ELOA cytotoxicity

Molecular mechanisms of protein complexes interaction with living cells and their primary targets at the cell surface remain highly disputed. Methods with single molecule sensitivity such as Fluorescence Correlation Spectroscopy (FCS) and Confocal Laser Scanning Microscopy (CLSM) imaging by avalanche photodiodes (APD), so called APD imaging, enable quantitative and nondestructive studies of molecular interactions and mobility in living cells. By applying these methods for the studies of ELOA interactions with PC12 cells, we have observed that ELOA inflicts damage and eventually causes plasma membrane rupture and a rapid influx and distribution of ELOA complexes inside already dead cells [5]. Local rearrangements of lipid organization in the plasma membrane of PC12 cells observed using a general lipophilic marker that differently partitions between the ordered and disordered phase of the lipid bilayer (1,1'-dioctadecyl-3,3,3',3'-tetramethylindocarbocyanine perchlorate dye, DiIC18(5)), are consistent with the hypothesis that ELOA may form transient pores in the plasma membrane.

ELOA interaction with lipid membranes

The interactions of ELOA with model phospholipid membranes were studied in detail [6] and compared with the observations on the live cells to clarify the mechanisms of the perturbations within lipid bilayers occurring in the presence of ELOA. Specifically, the binding of ELOA to lipid membranes of giant unilamellar vesicles containing 80:20 DOPC:DOPG ratio was examined by release of Alexa Fluor 633 and calcein dyes to elucidate whether such interactions would lead to membrane collapse. The NBD-labeled ELOA clearly accumulated at the surface of giant unilamellar vesicles in a similar fashion as described for PC12 cells prior to their rupture [5], by contrast, EL alone did not accumulate on membranes, suggesting that ELOA formation is a prerequisite for membrane interaction. However, only small degree of vesicle permeability with leakage levels of 3–6% was detected, indicating that the selected lipid membranes are much more robust compared with cell membranes [6]. Interactions between ELOA and lipid membranes were investigated also by using the quartz crystal microbalance with dissipation [6]. The injection of 3–10 μ M ELOA to lipid bilayers containing 80:20 DOPC:DOPG led to its non-disruptive binding and adsorption into the lipid film, which became increasingly more dissipative and soft until complete desorption from the supportive surface. The membrane rearrangement occurred to a much smaller extent when free OA was added, but not when free OA was removed from

F-01-SL

ELOA by prior incubation with bovine serum albumin, emphasizing the role of OA in this process. All these results indicate that lipid membranes containing 80:20 DOPC:DOPG in vesicular or bilayer forms interact with ELOA, but not to the same extent with EL or OA alone. They are more resistant to the rupture than cell membrane of PC12 cells, suggesting that the lipid content and their packing within the membrane maybe be critical in determining its resistance to ELOA perturbation.

Tryptophan fluorescence emission spectral shift and changes of circular dichroism spectra in far UV region indicate that some restoration of the native-like EL structure occurs upon interaction of ELOA with unilamellar vesicles [6]. Addition of lipids to ELOA led also to a partial recovery of lysozyme activity absent in ELOA, which is 22% of the activity for native EL. This indicates that ELOA pre-incubated with lipids is in a more compact state than ELOA alone. Together, these data support a partial refolding of ELOA towards a native-like conformation upon interactions with lipid membranes, although complete refolding was not observed. The fact that EL displays some native-like characteristics upon interaction of ELOA with lipid membranes can be indicative of ELOA dissociation, leading to EL release from the complex. Indeed, EL and ELOA does not translocate across lipid membranes as described for HAMLET, but instead ELOA may function as a carrier for OA by enhancing its solubility in an aqueous environment while at the same time directing it towards the membrane. Then the release of a large number of OA molecules in a small region may exert a stronger effect than a more diffuse uptake of free OA from solution.

Thus, to date the plasma membrane was identified as a primary target in ELOA interactions with cells and this facts confirmed by model membrane studies. However, the detailed mechanisms of ELOA interactions with different types of cells and the elicited cellular responses remain to be further investigated. The finding that different types of protein can form cytotoxic complexes with oleic acid indicate that oleic acid is an important regulator of the protein self-assembly and this process can occur spontaneously *in vivo*, potentially serving as a natural safeguard against unwanted cells. Their generic ability to eliminate specifically rapidly divided cells, such as cancer cells, has a significant therapeutic potential, which is only at the initial stage of applications in clinical practice.

#

References

- [1] #A.#Håkansson, B. Zhivotovsky, S. Orrenius, H. Sabharwal, C. Svanborg Proc. Natl. Acad. Sci. USA, 1995, 92, 8064-8072.
- [2] K. Wilhelm, A. Darinkas, W. Noppe, E. Duchardt, K.H. Mok, V. Vukojević, J. Schleucher, L.A. Morozova-Roche, FEBS J. 2009, 276, 3975-3989.
- [3] S.E. Permyakov, E.L. Knyazeva, L.M. Khasanova, R.S. Fadeev, A.P. Zhadan, H. Roche-Håkansson, A.P. Håkansson, V.S. Akatov, E.A. Permyakov, Biol Chem., 2012, 393, 85-92.
- [4] L.A. Morozova-Roche, FEBS Lett., 2007, 581, 2587-2592.
- [5] V.Vukojević, A.M. Bowen, K. Wilhelm, Y. Ming, Ce Zhang, J. Schleucher, P.J. Hore, L. Terenius, L.A. Morozova-Roche, Langmuir, 2010, 26, 14782-14787.

F-01-SL

-
- [6] S.B. Nielsen, K. Wilhelm, B. Vad, J. Schleucher, L.A. Morozova-Roche, D. Otzen, *J. Mol. Biol.*, 2010, 398, 351-361.

F-02-SL

QUANTITATIVE ANALYSIS WITH SINGLE- MOLECULE SENSITIVITY USING FLUORESCENCE CORRELATION SPECTROSCOPY

Vladana Vukojević

Department of Clinical Neuroscience, Karolinska Institute, Stockholm, Sweden

E-mail: Vladana.Vukojevic@ki.se

Abstract

Detection of small quantities of biologically important molecules in small sample volumes has important applications in biomedical research, medical diagnostics and forensic analysis. Ultra-sensitive quantitative methods are therefore indispensable tools for any such application. The aim of this work is to present Fluorescence Correlation Spectroscopy (FCS), a quantitative method with the ultimate, single-molecule sensitivity that enables determination of the concentration, transporting and kinetic properties of specific molecules in a few microliters of sample.

Introduction

Fluorescence Correlation Spectroscopy (FCS) is a quantitative method based on statistical analysis of the time course and the amplitudes of fluorescence intensity fluctuations generated in a very small volume element by molecular diffusion and/or chemical reactions, for determining the number of molecules in the observation volume element, their diffusion coefficients and chemical rate constants. Principles of FCS were formulated about forty years ago, when the theoretical background and first experiments were performed [1-3]. The early use of FCS was difficult and thus restricted to a small group of dedicated researchers who during 20 years meticulously revised the mathematical formalism and worked on the instrumentation development. Technological improvements introduced in the 90ties [4] significantly enhanced the sensitivity of FCS, allowing quantitative biochemical studies to be carried out in complex and dynamic environments such as the living cell and made the measurements more amenable to a wider research community.

In modern FCS instruments laser light is sharply focused through the objective of a microscope and collected through a confocal aperture in the image plane (Fig. 1).

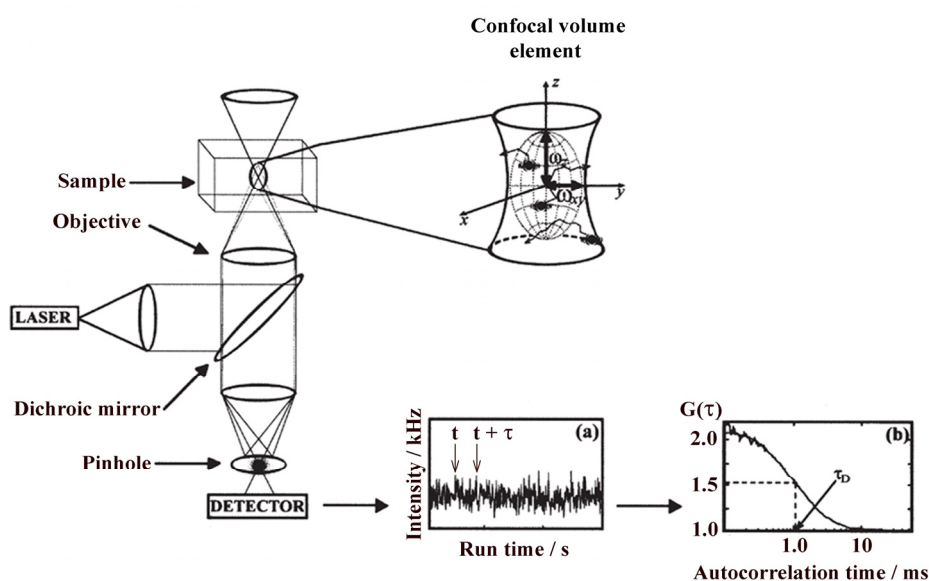


Figure 1. Schematic presentation of the instrumentation for FCS. **A.** To induce fluorescence, the sample is illuminated by incident laser light. The irradiating laser beam is reflected by a dichroic mirror and is sharply focused by the objective to form a diffraction limited volume element. A confocal aperture, set in the image plane to reject the out-of-focus light, further reduces the volume from which fluorescence is detected. This is crucial for collecting light from an elliptical observation volume element that is limited in size by the diffraction of light. After the absorption of energy, fluorescent molecules lose energy through photon emission. Light emitted by fluorescing molecules passing through the confocal volume element is separated from the exciting radiation and the scattered light by a dichroic mirror and barrier filter and transmitted to the detector. The number of pulses originating from the detected photons, recorded during a specific time interval, corresponds to the measured light intensity. **(a)** Fluorescence intensity fluctuations recorded in real time. **(b)** Normalized autocorrelation curve $G(\tau)$ indicating the presence of a single molecular species, characterized with an average diffusion times $\tau_D = 1$ ms. The experimental autocorrelation curve is fitted using the autocorrelation function derived for an underlying model, in this case a free three-dimensional diffusion of a single component with intersystem crossing (transition to the triplet state).

During the course of an FCS experiment, changes in fluorescence intensity are registered in time (Fig. 1 a). Thereafter, statistical methods are applied to detect non-randomness in the data. Typically, this is done by temporal autocorrelation analysis, but other ways of data analysis can also be applied [5,6].

Temporal Autocorrelation Analysis

In temporal autocorrelation analysis, we first derive the intensity autocorrelation function $C(t)$. $C(t)$ gives the correlation between the fluorescence intensity, $I(t)$,

measured at a certain time, t , and its intensity measured at a later time $t + \tau$, $I(t + \tau)$. The intensity autocorrelation function may be defined as an ensemble average:

$$C(\tau) = \langle I(t)I(t + \tau) \rangle \quad (1a)$$

or, alternatively, as a time average of the product $I(t)I(t + \tau)$ measured over a certain accumulation time T :

$$C(\tau) = \lim_{T \rightarrow \infty} \frac{1}{T} \int_0^T I(t)I(t + \tau) dt \quad (1b)$$

Since the unprocessed data in FCS are essentially fluorescence fluctuations over the mean fluorescence intensity $\langle I \rangle$, it is also possible to express the autocorrelation function through fluctuations of light intensities $\delta I(t) = I(t) - \langle I \rangle$ and $\delta I(t + \tau) = I(t + \tau) - \langle I \rangle$, at times t and $t + \tau$, respectively. In this way, the intensity autocorrelation function is defined as:

$$C(\tau) = \langle I \rangle^2 + \langle \delta I(t)\delta I(t + \tau) \rangle \quad (1c)$$

Regardless of the form of expression (1a) – (1c), as they are all equivalent, it is not convenient to use the intensity correlation function in practice because its value depends on properties of the applied experimental setup [5,6]. Therefore, instead of using the intensity autocorrelation function, it is more convenient to use the so-called normalized autocorrelation function, $G(\tau)$, defined as:

$$G(\tau) = \frac{\langle \delta I(t)\delta I(t + \tau) \rangle}{\langle I \rangle^2} \quad (2)$$

$G(\tau)$ is independent of the properties of the experimental setup, such as laser intensity, detection efficiency of the instrumentation and fluorescence quantum yield of the fluorophore.

For further analysis, the normalized autocorrelation function $G(\tau)$ has to be calculated over many autocorrelation times (τ) and plotted for different τ values. This is how an autocorrelation curve, as shown in Fig. 1 (b) is built from the fluorescence intensity fluctuations shown in Fig. 1 (a). In molecular systems undergoing only stochastic fluctuations, we would observe random variations of $G(\tau)$ around the value $G(\tau) = 1$. For processes that are not random, an autocorrelation curve is determined (Fig. 1 b). Typically, one observes a maximal limiting value of $G(\tau)$ as $\tau \rightarrow 0$, decreasing to the value of $G(\tau) = 1$ at long times, indicating that correlation between the initial and the current value has been lost. Very often only the so-called non-uniform part of the normalized autocorrelation function is analyzed. In this case one observes a maximal limiting value of $G(\tau)$ as $\tau \rightarrow 0$ that decreases to the value of $G(\tau) = 0$ at long times. The limiting value of $G(\tau)$, as $\tau \rightarrow 0$, is then inversely proportional to the absolute concentration of the fluorescing molecules, as we shall show later.

Thereafter, the experimentally obtained autocorrelation curve has to be compared to an autocorrelation function that is derived for a corresponding model

system [5,6]. For example, if we are looking at molecules in the medium, we are expecting two processes that may contribute to the fluorescence intensity fluctuations, intersystem crossing (transition to the triplet state) and free three-dimensional diffusion in the medium. We would therefore use an autocorrelation function that takes into account these processes:

$$G(\tau) = 1 + \frac{1}{N} \cdot \frac{1}{\left(1 + \frac{\tau}{\tau_D}\right) \sqrt{1 + \frac{w_{xy}^2}{w_z^2} \frac{\tau}{\tau_D}}} \cdot \left[1 + \frac{T}{1-T} \exp\left(-\frac{\tau}{\tau_T}\right)\right] \quad (3)$$

In equation (3), N is the average number of fluorescent molecules in the observation volume; w_{xy} and w_z are radial and axial radii of the ellipsoidal observation volume element (Fig. 1), respectively, related to spatial properties of the detection volume element, τ_D is the characteristic decay time of the autocorrelation curve, called the average residence time or the average diffusion time of the molecule through the detection volume element. T is the average equilibrium fraction of molecules in triplet state, τ_T is the triplet correlation time, related to rate constants for intersystem crossing and the triplet decay, and τ is the autocorrelation time.

Spatial properties of the detection volume, represented in equations (3) by the square of the ratio of the radial and axial parameters $((w_{xy}/w_z)^2)$, are determined experimentally in calibration measurements [7]. The calibration is performed *in vitro*, by using an aqueous solution of a dye for which the diffusion coefficient (D) is known. The average diffusion time (τ_D) is related to the translation diffusion coefficient D :

$$\tau_D = \frac{w_{xy}^2}{4D} \quad (4)$$

The autocorrelation curve derived in the calibration experiments is fitted by the autocorrelation function (3) using the known diffusion coefficient (D) *i.e.* of the dye as constant in the fitting procedure, and the value of $(w_{xy}/w_z)^2$ is determined from the best fitting curve.

The diffusion time, τ_D , of the investigated molecules is determined from the autocorrelation function that matches best the actual, experimentally determined autocorrelation curve using the value for $(w_{xy}/w_z)^2$ determined from the calibration experiments. As can be seen from equation (3), the limiting value of $G(\tau)$ as $\tau \rightarrow 0$ is related to the average number of molecules in the observation volume (N), *i.e.* it can be used to determine the absolute concentration (c) of the fluorescing molecules. For example, if $G(\tau) = 2.25$ at $\tau = 0$ (Fig. 1 b) and the observation volume element is $V = 2.0 \times 10^{-19} \text{ m}^3$, the concentration of the fluorescent molecules in the sample is $c = 6.6 \times 10^{-9} \text{ mol dm}^{-3}$. In the example

shown in Fig. 1 b, the inflection point at the autocorrelation curve indicates that the average diffusion time is $\tau_D = 1$ ms.

Thus, although the measured fluctuations are utterly stochastic by themselves, their average rate of relaxation to the equilibrium value is not stochastic. Rather, it is constrained by macroscopic properties of the sample. And it is exactly this interrelation that makes it possible to apply fluctuation analysis to obtain information about mobility coefficients, local concentration, apparent hydrodynamic radius, chemical reaction constants and rates, association, dissociation and equilibrium binding constants. In cases other than the example of free diffusion of a single fluorescent species, the autocorrelation function attains forms different from the one given by equation (3) since other processes leading to statistical fluctuations in the fluorescence signal will also show their characteristic decay time in the autocorrelation curve [5,6].

Conclusion

Due to its quantitative character, single-molecule sensitivity and low invasiveness, FCS is steadily providing new information about the molecular mechanism and the kinetics of biochemical reactions in live cells. Recent examples from our research include the study of transcription factor nuclear dynamics and the kinetics of interactions with chromatin [8], lipo-protein complexes interaction with the plasma membrane [9], signal transmission by cell-penetrating neuropeptides [10]. In addition, FCS and its two-colour variant Fluorescence Cross-Correlation Spectroscopy (FCCS) are becoming increasingly interesting for the identification of genetically modified organisms [11]

References

- [1] D. Magde, W.W. Webb, E. Elson, *Phys. Rev. Lett.*, 1972, 29, 705-708.
- [2] E.L. Elson, D. Magde, *Biopolymers*, 1974, 13, 1-27.
- [3] M. Ehrenberg, R. Rigler, *Chem. Phys.*, 1974, 4, 390-401.
- [4] R. Rigler, U. Mets. *SPIE* 1992, 1921, 239-248.
- [5] P. Schwille, E. Hausteiner, *Fluorescence Correlation Spectroscopy: A Tutorial for the Biophysics Textbook Online (BTOL)* <http://www.biophysics.org/education/schwille.pdf>, 2002.
- [6] V. Vukojević, A. Pramanik, T. Yakovleva, R. Rigler, L. Terenius, G. Bakalkin, *Cell. Mol. Life Sci.*, 2005, 62, 535-550.
- [7] K. Weissart, V. Jüngel, S. J. Briddon, *Curr. Pharm. Biotechnol.*, 2004, 5, 135-154.
- [8] V. Vukojević, D.K. Papadopoulos, L. Terenius, W. Gehring, R. Rigler, *Proc. Natl. Acad. Sci. USA*, 2010, 107, 4087-4092.
- [8] V. Vukojević, A.M. Bowen, K. Wilhelm, Y. Ming, Z. Ce, J. Schleucher, P.J. Hore, L. Terenius, L.A. Morozova-Roche, *Langmuir*, 2010, 26, 14782-14787.
- [9] V. Vukojević, A. Gräslund, G. Bakalkin, *Methods Mol Biol.*, 2011, 789, 147-170.
- [10] X. Zhou, D. Xing, Y. Tang, W.R. Chen, *PLoS One*, 2009, 4, e8074.

F-03-O

X-RAY FLUORESCENCE MICROSCOPY AND MULTIVARIATE ANALYSIS OF ELEMENTS DISTRIBUTION IN POPLAR STEM

A. Savić¹, A. Mitrović¹, K. Radotić¹, T. Dučić^{2*}

¹*Institute for Multidisciplinary Research, University of Belgrade, Kneza Višeslava
1, 11030 Belgrade, Serbia.*

²*DESY, Notkestrasse 85, D-22607 Hamburg, Germany*

Abstract

X-ray fluorescence (XRF) microscopy was performed to observe distribution of elements in the two month old *Populus alba* stem sections. We used multivariate image analysis in order to test the spatial relations between the elements, and to find out their possible collocations. The analysis indicates the collocation of K, Cl and P in the regions corresponding to the cambium and xylem on the stem cross section. The microelements Mn and Zn are more accumulated in the cortex and phloem tissues. The analysis clearly indicates grouping of all elements in the three distinctive rings corresponding to the xylem, floem and cortex.

Introduction

Populus alba is a woody species widespread throughout Mediterranean basin, Central Europe and Middle East. It has a good potential for fast growth and biomass production. It also represents a genetic resource to improve tolerance to different environmental stresses.

X-ray fluorescence (XRF) microscopy is a suitable method for element distribution tracing. After excitation, each element has a unique fluorescence spectrum, thus this technique allows multi-element analysis, providing qualitative and quantitative information. Up to now only a few in situ studies of elemental distributions in intact stem plant tissues have been performed [1].

Multivariate technique has been established in chemometrics and recently has been used for the image analysis [2]. Here we used this technique to observe elements spatial relations and collocations on the poplar stem section. When the components and its relative contributions were determined, it was possible to perform the image segmentation based on factor scores, and to reveal if the different elements were accumulated in the same areas of the sample.

Materials and Methods

The experiments were carried out on selected clone of micropropagated *Populus alba* L. plantlets [3] grown *in vitro* on two phase MS/2 medium. Two months old plantlets were 8-9 cm high, with 9-11 internodes developed. Stem sections from the base internode were prepared by free-hand sectioning with razor blade and subsequently freeze dried.

Two dimensional XRF mapping have been accomplished at beamline L at DORIS III (DESY, Hamburg, Germany), at energy 13 keV in order to enable simultaneous detection of trace elements as Fe, Zn, Cu, Ni and Mn as well

as the macro elements: Ca, K, S and Cl. Elements concentration was calculated by using a NIST standard (SRM 612) measured with the same setup. The spectra are subsequently fitted using AXIL software. Sample thickness calculation as well as visible light fluorescence microscopy was performed at Nikon Eclipse Ti microscope (NIKON GMBH).

Multivariate image analysis was performed with the self developed Matlab based software. Images (matrices) were converted into the vectors, and the vectors obtained from the different images (7 images of different elements) were analysed.

Results and Discussion

Light and the XRF elements mapping images of the populus stem are shown in Fig.1. The corresponding true-false matrix with the defined threshold values is presented in Fig 1A.

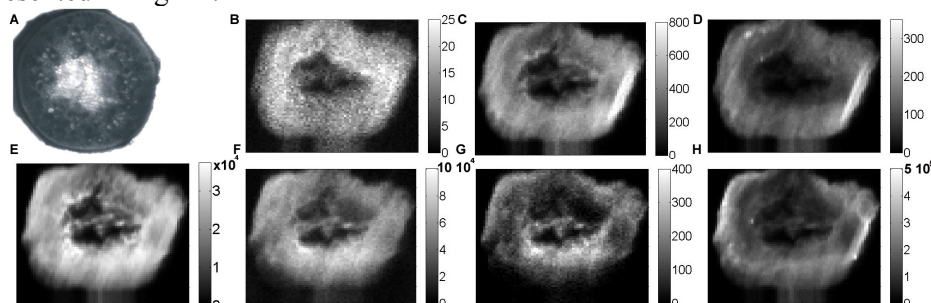


Figure 1. A: Visible light autofluorescence micrograph of the poplar cross-section. B-H: Elements concentration calculated after X-ray fluorescence (XRF) obtained for different elements: Cu (B), Mn (C), Zn (D) K (E), Cl (F), P (G) and Ca (H). The scale bars indicate concentration in ppm. Scanned area: 1070 x 955 μm , pixel size 15 μm and dwell time 1s.

Different spatial distribution patterns among these elements were further analyzed by the multivariate analysis. After the factor scores and their contributions were calculated, 3 distinctive patterns of element distributions (Fig.2.) were revealed. The first principal component (PC) indicates the collocation of K, Cl and P (which corresponds to the position of cambium and xylem on the stem cross section). 2nd PC was dominantly created by combining the microelements Mn and Zn (which were more accumulated in the cortex and phloem tissues). 3rd PC clearly indicates grouping of all elements in the three distinctive rings corresponding to the xylem, floem and cortex.

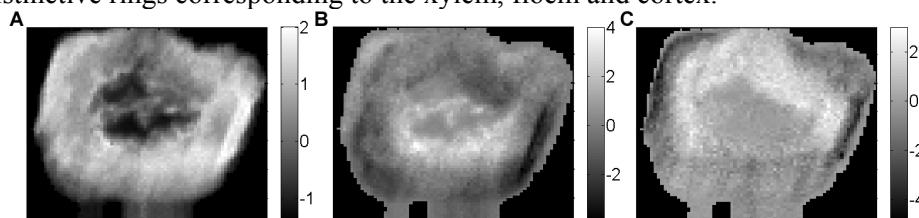


Figure 2. Images rendered from the principal components (PC): A) 1st PC, B) 2nd PC, C) 3rd PC. Components provides a comprehensive view on the anatomical and physiological state of the tissue.

Conclusion

We have presented here a multivariate image analysis of synchrotron X-ray fluorescence study of populus stem cross-section. The multivariate image analysis contributed to enhanced observation of the spatial relations and collocations among the macro- and trace- elements in a plant section. The analysis presented may also be used in future to study other tissues and especially in the plant mutants. Understanding of the physiological processes of plants on the tissue and cellular level requires methods that assess the spatial and chemical alterations, as well as the adequate image analysis.

Acknowledgement

Supported by Serbian Ministry of Education and Science grant No. 173017 and the light source DORIS III, bemailine L at DESY, (HGF): project nr. II-20080239.

References

- [1] E. Lombi, K.G. Scheckel, I.M. Kempson, *Environ. Exp. Bot.* 72 (2011) 3-17.
- [2] M. J. Bruwer,, J. F. McGregor, M. D. Noseworthy, *J. Chemometrics*
DOI: 10.1002/cem.1143.
- [3] A. Mitrović, P. J. Bogdanović, Ž. Marjanović, *International Scientific Conference Forest Ecosystems and Climate Changes, Belgrade, Serbia, Proceedings, 2010, 2,* 67-69.

F-04-P

EFFECTS OF NITRIC OXIDE PRODUCTION ON GLUTATHIONE LEVELS IN AN ANIMAL MODEL OF DEPRESSION

D. Filipović, J. Zlatković, M. Demajo

*Laboratory for Molecular Biology and Endocrinology, VINČA Institute of Nuclear
Sciences, University of Belgrade, P.O.Box 522, Belgrade, Serbia*

Abstract

Stimulation of glutamate receptors induces neuronal nitric oxide (NO) release, which in turn modulates glutamate transmission. The present study evaluated the effects of acute, chronic or combined stress on NO production *via* the accumulation of nitrite, the stable metabolite of NO, in the prefrontal cortex and hippocampus of male Wistar rats. Given that glutathione (GSH) plays a critical role in protecting cells from oxidative stress, as well as maintaining the thiol redox state, GSH levels in cytosolic fractions of both brain structures were examined. A significant increase in nitrite levels was obtained after 3 weeks of chronic isolation stress, followed by combined stresses (chronic + acute stress). Moreover, GSH levels were significantly decreased after chronic and both combined stresses in both brain structures. Our data support the idea that GSH might represent an important buffer of NO toxicity in the brain, indicating that compromised redox buffering controlled by GSH makes neuronal cells susceptible to endogenous physiological flux of NO.

Introduction

Nitric oxide (NO) has been considered as an important neurotransmitter involved in the pathophysiology of depression. A free radical gas molecule, NO is synthesized from L-arginine by the enzyme NO synthase (NOS). In the brain, NO production can occur as a result of activity of either neuronal nNOS, as a dominant constitutive form, and inducible iNOS which has been associated with pathological processes [1]. NO plays a crucial role in synaptic plasticity, neuromodulation and other physiological functions in the brain, while under pathophysiological conditions, it may induce oxidative damage. Overproduction of NO production may lead to alterations of neuronal signaling and to cell damage through the cytotoxicity of NO oxidation derivatives. Chemical inactivation of NO by reaction with oxygen, superoxide, and glutathione (GSH) competes with specific interactions with target proteins. Therefore, our goal was to examine the effects of acute, chronic or combined stresses on NO production in cytosolic fractions of hippocampus and prefrontal cortex of male Wistar rats. Since GSH helps protect brain cells from nitric oxide-peroxynitrite damage, we studied the effects of all stress groups on GSH levels in both brain structures.

Experimental

Adult male Wistar rats, aged three months, were divided at random into four groups: I-controls; II-acute stresses i.e. 2 h of immobilization (IM) or cold (C) stress (4°C); III-3 weeks of chronic social isolation (IS) as an animal model of depression; IV-combined stresses (IS+IM, IS+C) i.e. rats undergo IS stress followed by a single exposure to 2 h of either IM or C stress. Cytosolic NO levels in prefrontal cortex (PFC) and hippocampus (HIPP) were estimated from the amounts of nitrite/nitrate levels (nM/mg of protein) with the colorimetric assay using Griess reagent, whereby nitrates were previously transformed into nitrites by Cd reduction. Briefly, nitrite production was determined by mixing 50 μ L of the assay buffer with 50 μ L of Griess reagent (1.5 % sulfanilamide in 1 M HCl plus 0.15 % N-(1-naphthyl) ethylenediamine dihydrochloride in distilled water, v:v). Nitrite content was calculated from maximum absorbance (550 nm) using the sodium nitrite (μ M) standard curve. GSH levels were quantified from fresh prepared cytosolic fractions of prefrontal cortex and hippocampus and estimated according to the method of Ellman. Data were analyzed by two-way ANOVA followed by the Duncan post-hoc test.

Results and discussion

The effects of acute, chronic or combined stress on NO metabolites (nitrate/nitrite) and GSH levels are presented in Fig.1.

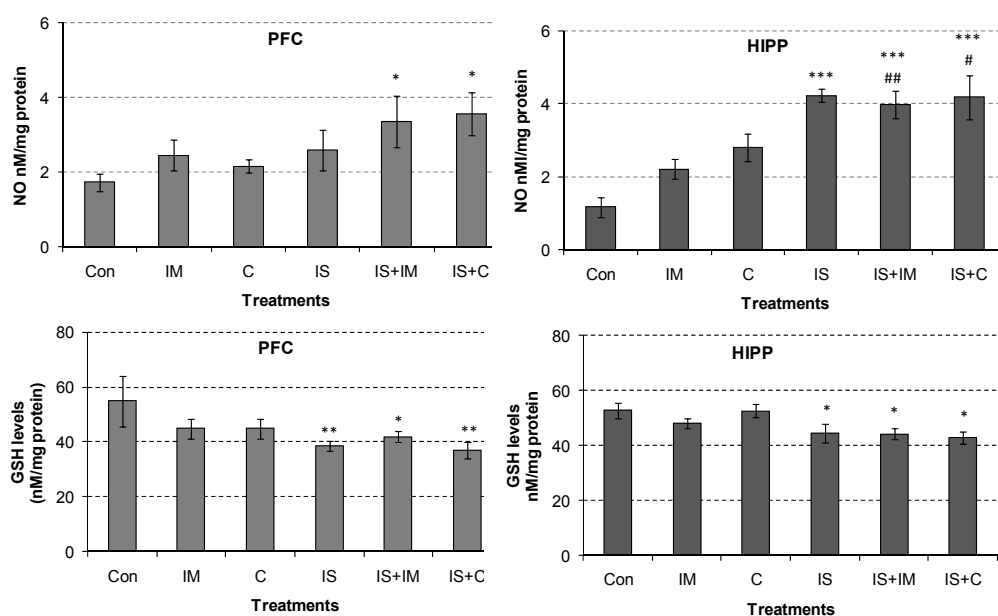


Figure1. Effect of acute (immobilization IM or cold C) stress, chronic isolation (IS) or their combination (IS+IM and IS+C) on nitrite/nitrate levels as well as total GSH in the prefrontal cortex (PFC) and hippocampus (HIPP). Values are mean \pm SEM of 6 animals for each group. ***Compared between stressed animals to the control group ($p < 0.001$); combined stress vs. acute stress ($###p < 0.001$)

F-04-P

Significant increase of nitrite content following acute C and IS stress in HIPP ($p < 0.01$; $p < 0.001$, respectively) was found, while it remained unchanged in the PFC. We previously reported increased nNOS protein expression in all stress groups in PFC and HIPP, while elevated iNOS expression following chronic IS and combined stress was observed only in PFC [2]. Given that elevation of NO due to increased expression of nNOS after acute stress acts predominantly as a neuromodulator by decreasing glutamate release, the observed increase of hippocampal nitrite level under acute C stress could underlie a normal physiological and protective role [3]. No influence was observed in GSH levels following both acute stresses. Moreover, sustained overproduction of nitrite levels observed following chronic IS and both combined stresses ($p < 0.001$ and $p < 0.05$) compared to the control or acute stress alone ($^{##}p < 0.01$; $^{\#}p < 0.05$), indicate prooxidant states in both brain structures. Given that GSH is a major antioxidant capable of scavenging hydrogen peroxide and peroxynitrite, while undergoing oxidation to glutathione disulphide, depletion of GSH, following chronic isolation stress, could be the result of decreased detoxification of peroxynitrite, suggesting that it may be chronically produced by NO overproduction.

Conclusions

Based on the above results, it could be concluded that 3 weeks of chronic social isolation causes NO overproduction in both brain structures causing oxidative/nitrosative stress. Moreover, chronic IS stress may impose a more prominent pro-oxidative condition [4], which may be responsible for GSH consumption, possibly overcoming the capacity of GSH synthesis. Further studies are needed to elucidate the precise mechanisms underlying GSH protection against chronically-induced oxidative stress.

Acknowledgement

This work was supported by the Ministry of Education and Science of the Republic of Serbia, Grant 173044.

References

- [1] G. C. Brown, *Biochem Soc Trans.*, 2007, 35, 1119-1121
- [2] J. Zlatković, D. Filipović, IBRO 2012 Workshop, Szeged, Hungary.
http://ibro2012.shp.hu/hpc/web.php?a=ibro2012&o=detailed_program_5U9d_pp240.
- [3] F. Oosthuizen, G. Wegener, B. H. Harvey, *Neuropsychiatr Dis Treat.*, 2005, 1, 109-123.
- [4] J. L. Madrigal, R. Olivenza, M. A. Moro, I. Lizasoain, P. Lorenzo, J. Rodrigo, J. C. Leza, *Neuropsychopharmacology*, 2001, 24, 420-429.

F-05-P

DIFFERENTIAL EFFECTS OF CHRONIC ISOLATION STRESS ON NNOS AND INOS PROTEIN EXPRESSION IN RAT PREFRONTAL CORTEX AND HIPPOCAMPUS

J. Zlatković, D. Filipović

Laboratory for Molecular Biology and Endocrinology, VINČA Institute of Nuclear Sciences, University of Belgrade, P.O.Box 522, Belgrade, Serbia

Abstract

Stress-related glucocorticoids and glutamate release have been implicated in mood disorders such as depression. Since glutamatergic mechanisms activate nitric oxide synthase (NOS), we examined protein expression of neuronal NOS (nNOS) and inducible NOS (iNOS) in the cytosolic fraction of prefrontal cortex and hippocampus of rats exposed to acute, chronic and combined stresses (chronic stress followed by acute stress). While nNOS protein expression was high in all animal groups in both brain regions, iNOS protein expression was increased only in prefrontal cortex following chronic isolation indicating state of oxidative/nitrosative stress. Moreover, serum corticosterone level, as a marker of neuroendocrine stress response, revealed deregulated HPA axis after chronic isolation stress. Data have shown the ability of hippocampus to maintain homeostasis (redox balance) after exposure of animals to chronic isolation stress, while iNOS may be implicated in the progression of neurotoxicity in the prefrontal cortex.

Introduction

Acute and chronic stress, as well as stress-induced release of glucocorticoids, induces changes in glutamate neurotransmission in the prefrontal cortex and the hippocampus. Numerous studies have indicated the role of glutamate and its receptors in depression. Glutamatergic activation of N-methyl-D-aspartate (NMDA) receptor stimulates nitric oxide synthase (NOS), the enzyme that catalyzes the production of nitric oxide (NO) which possess both neuroprotective and neurodestructive properties. Brain NO is mainly generated either by neuronal (nNOS) which play physiological and protective role or by inducible (iNOS) associated with pathological processes. Therefore, we examined the protein expression of cytosolic nNOS and iNOS in the prefrontal cortex and hippocampus of rats exposed to acute stresses, chronic isolation stress as an animal model for depression or their combination to assess the maladaptive effect of chronic isolation.

Experimental

Adult male Wistar rats were divided into four groups: (I) control group; (II) groups exposed to 2h of acute stress immobilization (IM) or cold (C, 4°C); (III) chronic isolation stress where animals were individual housed for 21 days; IV groups of chronically stressed animals subsequently exposed to 2h IM or C (4°C) stress (IS+IM, IS+C). After series of tissue centrifugations, in obtained cytosolic fractions, iNOS, nNOS protein expression was measured using Western blot technique. Serum

corticosterone (CORT) level was monitored by enzyme-linked immunosorbent assay (ELISA). Analysis of variance (Two-way ANOVA) followed by Duncan post hoc test was used for statistical data analysis.

Results and discussion

Decreased CORT level to a novel IM or C stress of chronically-isolated animals compared to acute stresses alone indicate compromised hypothalamic-pituitary-adrenal (HPA) axis activity by previous experience of chronic IS stress which could not be resumed after subsequent acute stressors (Table 1).

Table 1. Serum CORT level (ng/ml). Symbols depict significant difference between, stress vs. control *** $p < 0.001$; acute vs. combined stress ## $p < 0.01$; chronic vs. combined stress ^^ $p < 0.001$.

	CONTROL	ISOLATION
	142.905±14.16	123.39±10.89
IMMOBILIZATION	648.89±166.78***	477.98±74.03***## ^^
COLD	342.112±112.53**	86.41±37.68##

While nNOS protein expression was high in all animal groups in both brain regions, iNOS protein expression was increased by chronic isolation and remained upregulated after both combined stresses only in the prefrontal cortex (Fig. 1.). Unlike hippocampus, in which activities of MnSOD and CuZnSOD were unchanged, their reduced activities in prefrontal cortex following chronic isolation could be due to oxidative/nitrosative stress caused by increase of iNOS levels [1]. Since cortical iNOS induction is associated with extensive and prolonged release of NO (and further to generation of peroxynitrite) this could be in part responsible for stress-induced neurodegenerative changes [2]. Given that iNOS expression was decreased in hippocampus, increased nNOS expression following chronic isolation suggests its physiological and protective role. Protective role in hippocampus could be also achieved over increased level of inducible heat shock protein that prevents NF- κ B activation and therefore inhibition of iNOS protein expression (manuscript in preparation).

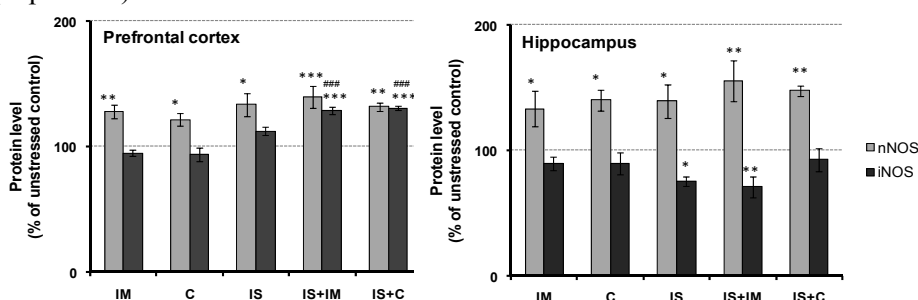


Figure 1. nNOS and iNOS protein level in cytosolic fraction of rat prefrontal cortex and hippocampus, expressed as % of control. Symbols indicate significant difference between stressed groups and control (* $p < 0.05$, ** $p < 0.01$, *** $p < 0.001$); acutely stressed animals and those previously exposed to IS ($p < 0.001$)

Conclusions

Obtained results indicate the ability of hippocampus to maintain homeostasis (redox balance) after exposure of animals to chronic isolation stress, while iNOS expression may be implicated in the progression of neurotoxicity in the prefrontal cortex. In contrast to iNOS, increased nNOS could be involved in synaptic plastic, contributing to learning and memory. Given that antidepressant-like activity can be produced by agents that affect subcellular signaling systems linked to excitatory amino acid receptor of nitric oxide synthase [3], molecular mechanisms involved in the antidepressant-like effect induced by iNOS inhibition will be further investigated.

References

- [1] D. Filipović, J. Zlatković, D. Inta, I. Bjelobaba, M. Stojiljković, P. Gass, *J Neurosci Res.*, 2011, 89, 1461-1470.
- [2] R. Olivenza, M. A. Moro, I. Lizasoain, P. Lorenzo, AP. Fernández, J. Rodrigo, L. Boscá, J. C. Leza, *J. Neurochem.*, 2000, 74, 785-791.
- [3] A. Dhir, S. K. Kulkarni, *Nitric Oxide*, 2011, 24, 125-131.

F-06-P

NITRIC OXIDE AND PROTEIN CARBONYL CONTENT IN THE LIVER OF STRESSED RATS

J. Zlatković, M. Demajo, D. Filipović

Laboratory for Molecular Biology and Endocrinology, VINČA Institute of Nuclear Sciences, University of Belgrade, P.O.Box 522, Belgrade, Serbia

Abstract

Nitric oxide (NO) has been identified as a source of oxidative/nitrosative stress that is known to oxidatively modify DNA, lipids and proteins. One such modification is the addition of carbonyl groups to amino acid residues in proteins. Therefore, the aim of our study was to examine the effects of acute, chronic or combined stress on NO production and protein carbonyl content in the cytosolic fraction of rat liver. Since NO is a highly reactive molecule, the levels of NO metabolites (nitrates and nitrites) as markers of stable end products of NO metabolism were measured. Both acute stresses showed unchanged nitrite levels while only acute IM stress led to an increased level of the carbonyl group. The NO metabolites and protein carbonyl content were increased by chronic isolation and remained upregulated after combined stress. These data indicate that chronic isolation stress with increased NO metabolites led to nitrosative stress, whereby accumulation of oxidized proteins in the liver may induce progressive liver damage.

Introduction

It has been shown that oxidative/nitrosative stress has been implicated as a contributor to liver injury. Moreover, it may derange nitrogen metabolism in hepatocytes where nitric oxide (NO) is involved among the other factors regulating this metabolic pathway. NO is an inorganic reactive nitrogen species synthesized in the liver by inducible nitric oxide synthase found in hepatocytes, Kupffer cells, and endothelial cells, or by endothelial nitric oxide synthase. NO and superoxide react spontaneously to form the potent and versatile oxidant, peroxynitrite. This highly toxic species reacts with lipids, proteins and DNA. Our laboratory has previously demonstrated that chronic isolation stress causes oxidative stress in rat liver, evidenced by compromised CuZnSOD and MnSOD activity [1]. To further elucidate the role of nitrosative stress in the liver, we investigated the effects of acute, chronic or combined stress on NO production. Moreover, the formation of carbonyl derivatives of amino acids was used as an index of protein oxidation associated with oxidative stress.

Experimental

The male Wistar rats (body weight 330–400 g) were divided into four groups: control (Con); acute stress [2 h of immobilization (IM) or cold (C) stress (at 4°C)];

F-06-P

chronic isolation (IS) [individual housing of rats for 3 weeks]; combined stressors (IS+IM, IS+C) i.e. rats undergo IS stress followed by a single exposure to 2 h of either IM or C stress. Nitric oxide production in the cytosolic fraction of liver was quantified by measuring nitrate/nitrite, by the Griess method [2]. Liver protein carbonyl content was determined by the colorimetric method. Briefly, protein samples containing 6 mg/ml of protein were resuspended in 10 mM 2, 4-dinitrophenylhydrazine (DNPH) in 2M HCl and incubated for 60 min. The samples that had been previously precipitated with trichloroacetic acid (20%), centrifuged at $11,000 \times g$ were washed three times with ethanol-ethyl acetate (1:1; v/v) to remove the residual DNPH reagent. The final precipitates were dissolved in 6 N guanidine hydrochlorid and protein carbonyl content was determined by measuring the absorbance at 375 nm, using a molar absorption coefficient of $22,000 \text{ M}^{-1}\text{cm}^{-1}$. Liver cytosolic protein concentration was measured by the Lowry method. Data were analyzed by two-way ANOVA followed by Duncan post hoc test.

Results and discussion

Data presented in [Fig. 1](#) and 2. show NO metabolites (nitrate/nitrite) content and carbonyl content in the cytosolic liver fraction of rat exposed to acute, chronic or combined stress, respectively.

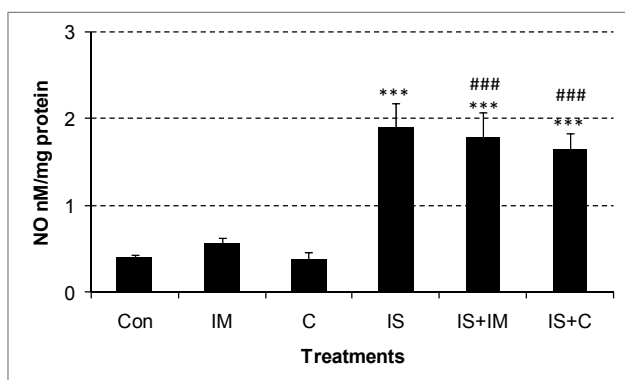


Figure 1. Effect of acute (immobilization IM or cold C) stress, chronic isolation (IS) or their combination (IS+IM and IS+C) on hepatic nitrite/nitrate levels. Values are mean \pm SEM of 6 animals for each group. ***Compared to control group ($p < 0.001$); combined stress vs acute stress ($###p < 0.001$).

Two-way ANOVA analysis revealed a significant effect of chronic stress ($F_{1,30} = 78.72, p < 0.001$) on nitrate content. Both acute IM and C stress did not alter nitrite content when compared to the control ($p > 0.05$). Duncan post hoc test showed a significant increase of nitrite content in chronic IS stress and both combined IS+IM and IS+C stress ($p < 0.001$). Moreover, significant increases of nitrite content of both combined IS+IM and IS+C stress compared to acute stress alone were found ($###p < 0.001$). Increased NO end-product levels in the liver, following chronic IS and combined stress, indicate a state of nitrosative stress which may be responsible for liver damage.

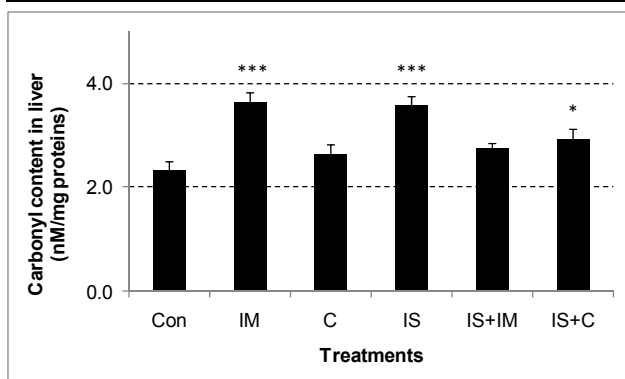


Figure 2. Effect of acute (immobilization IM or cold C) stress, chronic isolation (IS) or their combination (IS+IM and IS+C) on protein carbonyl levels. Values are mean \pm SEM of 6 animals for each group. Asterisk indicates comparison between stressed groups and control group (* $p < 0.05$; *** $p < 0.001$).

The hepatic protein carbonyl content values ranged from 2.14 to 2.50 nM/mg of protein in control rats. Opposite to acute C stress, significant increase in protein carbonyl content was observed following acute IM stress ($p < 0.001$). Moreover, significant increases of carbonyl content following chronic IS and combined IS+C stress were also measured ($p < 0.001$, $p < 0.05$ respectively). The previous reported compromised antioxidant defense mechanisms after chronic IS stress, evidenced by decreased hepatic CuZnSOD and MnSOD activities [1], resulted in increased protein oxidation as indicated by increased protein carbonyl. This suggests that the accumulation of oxidized proteins in the liver may be an early indication of chronic IS stress-induced liver damage.

Conclusions

Chronic IS stress concomitantly increases NO metabolites (nitrate and nitrite) and protein carbonyl levels. Increased levels of NO metabolites, which may be due to an increase in the NO synthase activity, indicate a nitrosative state. Increased protein carbonyl groups suggest that these oxidized species may be useful as diagnostic biomarkers for progressive liver damage.

Acknowledgement

This work was supported by the Ministry of Education and Science of the Republic of Serbia, Grant 173023.

References

- [1] J. Zlatković, D. Filipović, Mol Cell Biochem., 2011, 357, 143-150.
- [2] J. A. Navarro-González, C. García-Benayas, J. Arenas. Clin. Chem., 1998, 44, 679-681.

F-07-P

CHRONIC STRESS IMPAIRMENT OF PREFRONTAL CORTEX ENERGY METABOLISM IS RELATED TO GENDER AND CAN NOT BE AMELIORATED BY ANTIDEPRESSANT FLUOXETINE

M. Adžić, I. Simić, M. Mitić, J. Djordjević, M. Radojčić

Department of Molecular Biology and Endocrinology, VINCA Institute of Nuclear Sciences, University of Belgrade, Belgrade, Serbia

Abstract

The activity of cytochrome c oxidase correlates with neuronal functional activity and is considered as an ideal marker for examining the effects of antidepressant treatment on brain metabolism. We investigated gender specific effects of antidepressant fluoxetine on cytochrome c oxidase activity in the mitochondria of prefrontal cortex (PFC) of chronically isolated female and male Wistar rats. Our results showed that chronic psychosocial isolation (CPSI) increased cytochrome c oxidase activity in female PFC, while in males, this activity was decreased. Fluoxetine treatment did not normalize cytochrome c oxidase activity in either CPSI females or CPSI males. Our data suggest that the pattern of PFC energy metabolism impairment by CPSI is related to gender, but that fluoxetine treatment was unable to ameliorate these defects.

Introduction

Beside well established monoamine theory of depression, an alternative theory has been proposed, called “the mitochondrial dysfunction hypothesis”, suggesting that impaired functions of mitochondria are associated with psychiatric conditions such as bipolar disorder [1], major depression and a spectrum of affective disorders [2].

The complex IV or cytochrome c oxidase (cyt c oxidase) is the terminal respiratory enzyme in the mitochondrial electron transport chain whose activity correlates with ATP synthesis and serves as an endogenous metabolic marker for neuronal functional activity [3]. Moreover, its activity is considered as an ideal marker for examining the effects of antidepressant treatment on brain metabolism [4].

Since a novel therapeutic strategy is to evaluate the effects of antidepressants in regard to their capability to alter/correct energy parameters, in this study we examined the sex dependent effect of antidepressant fluoxetine on cyt c oxidase activity in the mitochondria of prefrontal cortex of chronically isolated female and male Wistar rats.

Experimental

Animals and treatment

The experiments were performed on adult (3 months old) Wistar female and male rats. The animals were divided into four experimental groups: two control groups

F-07-P

(n=12, each) and two stressed groups (n=12, each), respectively. The control groups were intraperitoneally treated with the mass-adjusted volume of vehicle (VEH; water) - *control/vehicle group* or with fluoxetine (5mg/kg per day) - *control/fluoxetine group* between 9:00 a.m. and 9:30 a.m. for 21 days. In the stressed groups, animals were subjected to the chronic psychosocial isolation (CPSI) for 21 days and were intraperitoneally injected with the mass-adjusted volume of vehicle (VEH; water) - *CPSI/vehicle group* or with fluoxetine (5mg/kg per day) - *CPSI/fluoxetine group* between 9:00 a.m. and 9:30 a.m. for another 21 days.

Measurement of cytochrome c oxidase activity

The activity of cyt c oxidase was assayed in the animal's prefrontal cortex according to Rustin et al. [5] and measured by following the decrease in absorbance due to the oxidation of previously reduced cytochrome c at 550 nm. The activities of cyt c oxidase were calculated as nmol/min/mg protein.

Statistical analysis

Data are presented as a mean \pm SEM and in each gender were analyzed with two-way analyses of variance (ANOVA). To determine statistically significant gender differences we used three-way analyses of variance (ANOVA) employing stress, fluoxetine and sex as the factors. All statistically significant differences are given as $p < 0.05$, including $p < 0.01$ and 0.001 .

Results and Discussion

Cytochrome c oxidase activity

It has been described that chronic stress inhibits the cyt c oxidase activity and impairs energy metabolism in rat prefrontal cortex and hippocampus [6]. In our experiments, the CPSI significantly increased the cyt c oxidase activity in the female mitochondria ($F=48.10$, $p<0.05$) (Figure 1), while in the males, the CPSI significantly decreased the cyt c oxidase activity ($F=19.33$, $p<0.05$). Our results indicated gender specific response to CPSI regarding cyt c oxidase activity.

A number of studies reported that antidepressants cause impairment in mitochondrial function [7, 8]. In our study, the FLU treatment of the control females significantly increased the activity of cyt c oxidase ($F=16.46$, $p<0.05$), while, in the control males, it significantly decreased it ($F=18.46$, $p<0.05$). The subsequent FLU treatment of either CPSI females or males did not alter cyt c oxidase activity.

Moreover, the statistical analyses showed the significant gender difference regarding the activity of cyt c oxidase ($F=43.65$, $p<0.05$). Namely, the activity of cyt c oxidase in the male control group was significantly increased in comparison to the female respective control ($p<0.05$), while in response to CPSI, it was significantly decreased in males (sex x stress interaction, $F=54.87$, $p<0.05$). Furthermore, FLU treatment of either control (sex x FLU interaction, $F=33.01$, $p<0.05$) or either CPSI (sex x stress x FLU interactions, $F=20.24$, $p<0.05$) animals showed significant gender difference regarding cyt c oxidase activity.

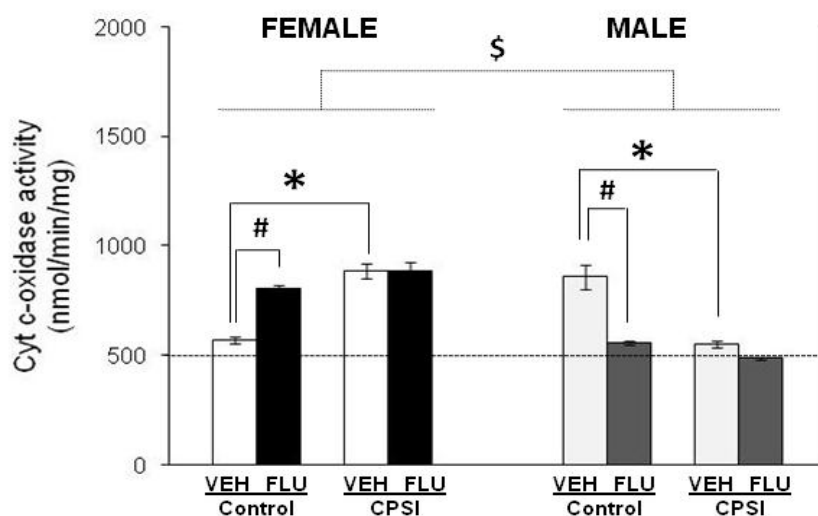


Figure 1. Cytochrom c oxidase activity (nmol/min/mg) in the prefrontal cortex of female and male Wistar rats treated for 21 days with vehicle (VEH) or fluoxetine (FLU) in basal condition (control) or exposed to the chronic psychosocial isolation (CPSI) for 21 days and treated with vehicle or fluoxetine for 21 days. Data are presented as mean \pm SEM. (* vs. CPSI, # vs. fluoxetine treatment, \$ female vs. male).

Conclusion

Impairment of energy metabolism under chronic psychosocial isolation is related to gender and could not be ameliorated by fluoxetine administration. However, it remains to be seen if the effects of fluoxetine on the mitochondrial respiratory chain are specific to changes in animal behavior or the side effects of antidepressant e.g. apoptosis.

References

- [1] C. Konradi et al., Arch. Gen. Psychiatry., 2004, 61, 300–308.
- [2] A. Gardner., Prog. Neuropsychopharmacol Biol. Psychiatry., 2011, 35(3), 730–743.
- [3] M. T. Wong-Riley. Trends. Neurosci., 1989, 12, 94–101.
- [4] H. Gonzalez-Pardo et al., Pharmacol. Biochem. Behav., 2008, 89, 456–462.
- [5] P. Rustin et al., Clin. Chim. Acta., 1994, 228, 35–51.
- [6] B. Tagliari et al., Metab Brain Dis., 2010, 25, 169–176.
- [7] Z. Xia et al., Biochem. Pharmacol., 1999, 57, 1199–1208.
- [8] K. Eto et al., Acta Med. Okayama. 1985, 39, 289–295.

F-08-P

ANTIDEPRESSANT FLUOXETINE NORMALIZES BRAIN JNKs SIGNALING IMPAIRED BY CHRONIC STRESS IN FEMALE BUT NOT IN MALE WISTAR RATS

M. Mitić, I. Simić, M. Radojčić, M. Adžić

*Department of Molecular Biology and Endocrinology, Institute of Nuclear Science
Vinča, University of Belgrade
P.O. Box 522, 11001 Belgrade, Serbia*

Abstract

c-Jun N-terminal kinases (JNKs) are important stress-responsive kinases that act as mediators in synaptic remodeling and neuronal degeneration in response to stress and, thus receiving considerable attention as potential therapeutic targets. In the present study, we investigated how exposure to chronic stress (chronic psychosocial isolation, CPSI) and subsequent therapy with antidepressant fluoxetine (FLU) affects the nuclear JNKs signalling and its phosphorylation status in the hippocampus (HIPPO) of the female and male Wistar rats. Our results showed that CPSI disrupted nuclear JNKs signaling in a gender specific way, while concomitant FLU treatment normalized JNKs only in HIPPO of females.

Introduction

Increasing evidence implicates stress as an important factor in the vulnerability to depressive and other mental illnesses [1]. Pathways mediating the cellular responses to various stressors include activation of c-Jun N-terminal kinases (JNKs), a subgroup of mitogen-activated protein kinases (MAPKs), that are considered as central transducers in the mammalian brain [2]. Indeed, reduced nuclear levels of JNKs were found in depressed patients and connected with different neuropathological events which are considered to be important in pathophysiology of depression [3]. The JNKs are encoded by at least three genes (JNK1, -2, and -3) that encode 46 kDa (JNK1) and two 54 kDa JNK isoforms (JNK2 and 3), respectively which are activated after phosphorylation [4]. Upon activation in the cytosol JNKs are translocated to the nucleus where they phosphorylate different transcription factors, resulting in enhanced or inhibited genes expression [5]. In the present study, we investigated nuclear total JNKs (tJNKs) levels and its phosphorylation status, pJNKs, in hippocampus (HIPPO) of female and male Wistar rats exposed to chronic psychosocial isolation stress (CPSI) and concomitantly treated with the antidepressant fluoxetine (FLU).

Experimental

Adult female and male Wistar rats were divided into four groups (each consisted of n=10): (I) Control, (II) Control+FLU, (III) CPSI (IV) CPSI+FLU. The experiment consisted of two phases and lasted for 6 weeks (42 days). The first phase (CPSI)

lasted 21 days, during which animals of CPSI and CPSI+FLU were exposed to CPSI. The second phase consisted of treatment with vehicle (VEH) or FLU for the next 21 day. The CPSI animals remained isolated during treatment. FLU was dissolved in water and administered intraperitoneally (5mg/kg body mass) at daily base between 9:00 a.m. and 9.30 a.m. 24 hours after receiving the final dose animals were sacrificed, their hippocampi were removed and used for preparation of the nuclear fraction and the molecular analyses.

The proteins of interest, total, and phospho JNKs were detected using Western blot with β -actin as a loading control. Data are presented as a mean \pm SEM and in each gender were analyzed with two-way ANOVA. To determine statistically significant gender differences we used three-way ANOVA employing stress, fluoxetine and gender as the factors. All statistically significant differences are given as $p < 0.05$.

Results and Discussion

Our results showed that in females CPSI significantly decreased all three total JNKs ($F=13.5$, $F=11.8$, $p<0.05$) (Figure 1a and b) and their phospho-isoforms (pJNKs $F=8.7$, $F=7.5$, $p<0.05$) (Figure 1c and 1d), indicating reduced JNKs signaling under chronic stress. The concomitant FLU treatment significantly increased both tJNK and pJNK levels reversing them to the control levels (tJNKs, $F=21.5$, $F=13.1$, $p<0.05$; pJNKs $F=6.6$, $F=12.6$, $p<0.05$) (Figure 1). In males, CPSI exerted the opposite effect and significantly increased all three nuclear pJNKs ($F=16.1$, $F=14.5$, $p<0.05$), not affecting tJNKs levels, suggesting enhanced signaling of the JNK pathway. Concomitant FLU treatment of CPSI males did not exert statistically significant effect on any of analyzed JNKs, although it slightly increased the levels of both tJNKs and pJNKs. Our findings in females were in accordance with literature, showing decreased levels of nuclear JNKs in depressed patients and their concomitant alteration by antidepressant treatment [6]. Moreover, three-way ANOVA revealed significant gender differences upon CPSI and concomitant FLU treatment regarding the nuclear total and phospho JNKs levels (tJNK, gender x CSPI, $F=7.6$, $p<0.05$, gender x CPSI x FLU interaction, $F=16.4$, $p<0.05$; pJNK gender x CSPI $F=15.4$, $p<0.05$; gender x CSPI x FLU interaction $F=10.2$, $p<0.05$). Namely, in females, CPSI decreased nuclear total and phospho JNKs that was reversed with FLU treatment, while in males CPSI exerted the opposite effect and increased JNKs phosphorylation, and in addition, the effect of FLU was not detected.

Conclusion

CPSI disrupted nuclear JNKs signaling in a gender specific way, while concomitant FLU treatment normalized it in females, but not in males. Namely, in females, CPSI reduced JNKs signaling by decreasing both, total and phospho, nuclear JNKs level, while in males CPSI increased JNKs signaling via its phosphorylation. FLU treatment normalized JNKs signaling in females via its influence on the level of JNKs protein, while in males FLU did not target this signaling pathway.

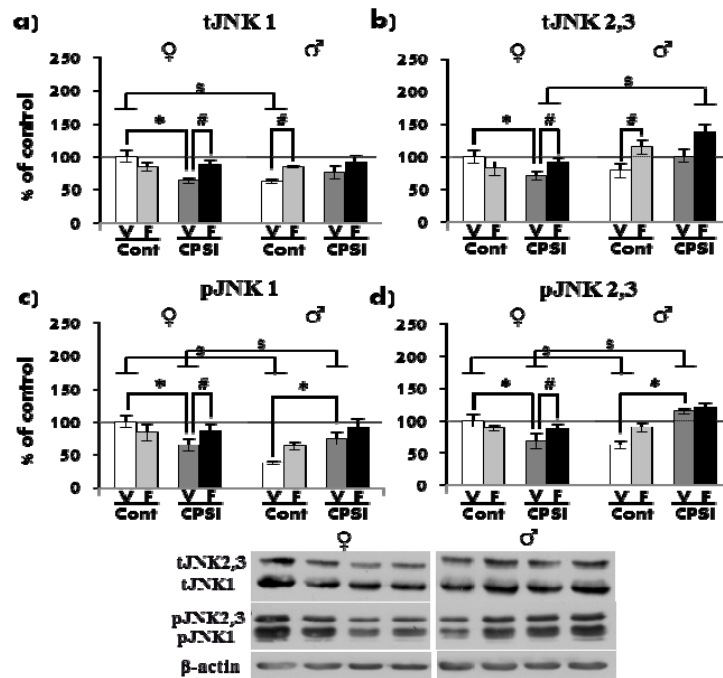


Figure 1. The levels of nuclear total JNKs (tJNK1,2,3) and phospho JNKs (pJNK1,2,3) protein levels (a,b,c,d) in the hippocampus of control (Cont) and stressed (CPSI) female (♀) and male (♂) Wistar rats treated with vehicle (V)/fluoxetine (F). Data are presented as mean \pm SEM (*vs. CPSI, # vs. FLU treatment, \$ female vs. male).

References

- [1] Kendler et al, Am J. Psychiatry. 2001, 158(7), 989-1000.
- [2] Hardegen and Waetzig, Restor. Neurol. Neurosci. 2001, 19, 29-39.
- [3] Spiliotaki et al, Psychoneuroendocrinology 2006, 31, 748-760.
- [4] Gupta et al., Science 1995, 267, 389-393.
- [5] Minden and Karin, Biochim Biophys Acta, 1997, 1333(2) F85-104.
- [6] Chen et al, Psychosom. Med. 2002, 61, 599-617.

F-09-P

CHRONIC STRESS AND CONCOMITANT FLUOXETINE TREATMENT EXERT GENDER-SPECIFIC EFFECTS ON BEHAVIOR AND HIPPOCAMPAL CDK5 SIGNALING IN WISTAR RATS

I. Simic, M. Mitic, M. Radojicic, M. Adzic

Department of Molecular Biology and Endocrinology, Institute of Nuclear Science Vinca, University of Belgrade, P.O. Box 522, 11001 Belgrade, Serbia

Abstract

Depression is one of the most pervasive and debilitating stress-related psychiatric diseases worldwide. Cyclin-dependent kinase 5 (Cdk5) is of particular importance for normal adult brain functioning and has recently been associated with anxiety and depressive disorders. In the present study, we investigated how alterations in depressive-like behavior are accompanied by the changes in hippocampal Cdk5/p35/p25 signaling in female and male Wistar rats exposed to chronic psychosocial isolation (CPSI) and concomitant antidepressant fluoxetine (FLU) treatment. Our results showed that CPSI induced different behavioral responses in female and male rats which were accompanied by dissimilarities in Cdk5/p35/p25 signaling. The effect of concomitant FLU treatment was also gender-specific regarding behavioral responses and Cdk5 levels, but gender-independent regarding p35 levels, which was accompanied with normalization of female and male rat behavior.

Introduction

Stress-related disorders, with depression among the leading ones, are becoming major burden of disease and disability in society worldwide. Animal models of psychosocial isolation are of particular importance, since they appear to be relevant to certain subtypes of human depression [1].

Cyclin-dependent kinase 5 (Cdk5) exerts high activity in the brain and is essential for neuronal synaptogenesis and survival [2]. Cdk5 is activated by neuronal-specific proteins p35 and p25 (C-terminal fragment of p35) through direct binding. The protein p25 has a substantially longer half-life than p35, causes prolonged activation of Cdk5 and is considered to be neurotoxic [2]. Increased activity of Cdk5 in hippocampus has been recently associated with anxiety and depressive-like behavior, suggesting that Cdk5 could be an important target for treatment of emotional disorders [3].

In the present study, we investigated how behavioral changes are accompanied by alterations in hippocampal Cdk5/p35/p25 signaling in female and male Wistar rats exposed to chronic psychosocial isolation (CPSI) and concomitantly treated with the antidepressant fluoxetine (FLU).

Experimental

Adult female and male Wistar rats were divided into four groups: (I) naive rats vehicle treated for 21 days, (II) naive rats FLU treated for 21 days, (III) rats exposed to 21-day CPSI followed by vehicle treatment for 21 days under the same stress conditions and (IV) 21-day CPSI followed by FLU treatment for 21 days under the same stress conditions. FLU dissolved in water was administered intraperitoneally at daily base (at 9 a.m.) with dose of 5 mg/kg of body mass. After the treatments, rats from each group were divided in two sets, one for evaluation of molecular parameters and the other one for testing the behavior. The depressive-like behavior was assessed by the forced swimming test (FST), in which the immobility time during a single 5 min session was used as its relevant measure. The other set of rats was sacrificed, their hippocampi were removed and used for preparation of cytosolic fractions and molecular analyses. The proteins of interest, Cdk5, p35 and p25, were detected using Western blot technique with β -actin as a loading control. Data were analyzed by two-way ANOVA followed by post-hoc Tukey test for examining the effects of CPSI and FLU, or by three-way ANOVA followed by post-hoc Tukey test for examining the effect of gender.

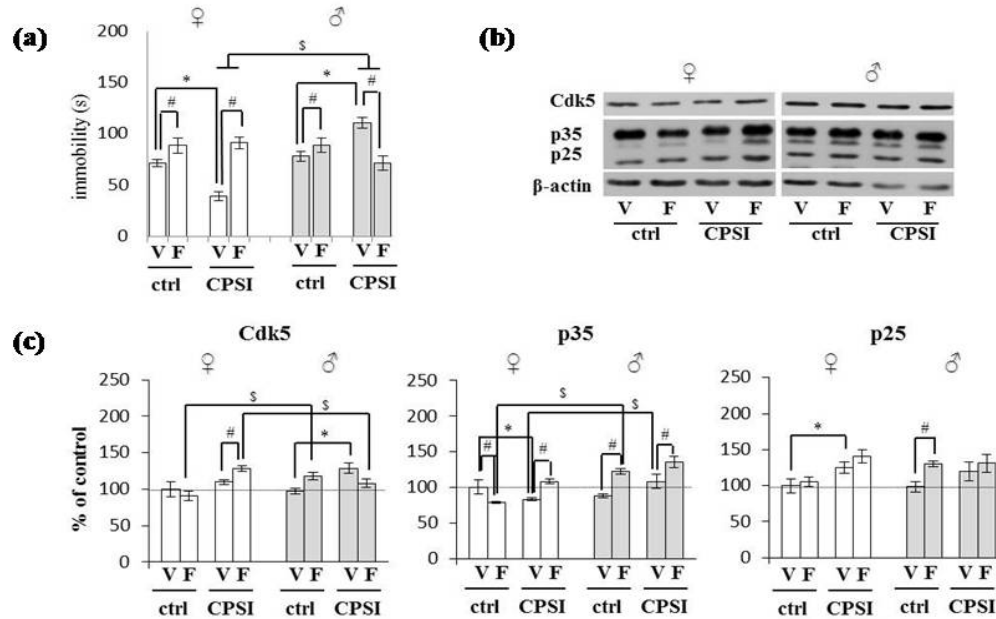


Figure 1. The immobility time in FST (a), representative Western blots (b) and levels of hippocampal cytosolic Cdk5, p35 and p25 (c) in vehicle (V) and FLU (F) treated control (ctrl) and CPSI rats. Data are presented as mean \pm SEM (* ctrl vs. CPSI, $p < 0.05$; # V vs. F, $p < 0.05$, \$ females vs. males, $p < 0.05$).

Results and discussion

Our results showed that FLU treatment normalized depressive-like behavior in rats of both genders, although its effects were opposite in females and males (Figure 1a; gender x CPSI interaction $F = 13.93$, $p < 0.05$; gender x CPSI x FLU interaction

F-09-P

F=28.45, $p<0.05$). Namely, in accordance with our previous studies [4], CPSI increased immobility time in FST in males, (F=4.68; $p<0.05$) and the concomitant FLU treatment reduced it (F=26.54; $p<0.05$). Contrary to that, in females, CPSI decreased their immobility time in FST (F=12.52; $p<0.05$), while concomitant FLU treatment normalized it (F=8.14; $p<0.05$).

CPSI and concomitant FLU treatment also affected hippocampal Cdk5/p35/p25 signaling in a gender-specific manner (Figure 1b, 1c; Cdk5: gender x CPSI x FLU interaction F=25.13, $p<0.05$; p35: gender x CPSI interaction F=5.8, $p<0.05$). Increased depressive-like behavior in CPSI male rats was associated with increased levels of Cdk5 (F=5.75, $p<0.05$) and slight elevation of its activator p35, consistent with previous study [3]. The concomitant FLU treatment, that reduced depressive-like behavior, also slightly decreased Cdk5 levels, but increased the levels of its activator p35 (F=2.13; $p<0.05$). On the other hand, in females, the reduced immobility in FST by CPSI was associated with decrease in p35 (F=3.18; $p<0.05$), but increase in p25 (F=23.72; $p<0.05$), a more potent activator of Cdk5 regarded to be neurotoxic [2]. The normalization of female behavior by concomitant FLU treatment co-occurred with elevation of Cdk5 (F=4.36; $p<0.05$) and p35 levels (F=88.5; $p<0.05$). Our results suggest that although FLU treatment of CPSI rats exerted some gender-unspecific effects (increase in p35), FLU gender-specific effects on Cdk5 levels are at least partly responsible, for normalization of rats behavior in FST in both genders affecting it in opposite ways.

Conclusion

CPSI caused divergent behavioral responses in female *vs.* male rats which was accompanied with dissimilar alterations in hippocampal Cdk5/p35/p25 signaling in both genders. The effect of concomitant FLU treatment on CPSI rats was also gender-specific regarding the behavioral responses and Cdk5 levels, but gender-independent regarding the p35 increase, which was accompanied with normalization of female and male rat behavior.

References

- [1] L. M. Heinrich et al., Clin. Psychol. Rev., 2006, 26(6), 695-718.
- [2] R. Dhavan et al., Nat. Rev. Mol. Cell. Biol., 2001, 2(10), 749-59.
- [3] W. L. Zhu et al., Int. J. Neuropsychop., 2012, 15(6), 795-807.
- [4] A. Djordjevic et al., Prog. Neuropsychopharmacol. Biol. Psychiatry, 2012, 36(1), 92-100.

F-10-P

INTERACTION OF GOLD NANOPARTICLES WITH RAT BRAIN SYNAPTOSOMAL PLASMA MEMBRANE NA⁺/K⁺-ATPASE AND MG²⁺-ATPASE

V. Petrović, V. Vodnik, V. Vasić

*Vinča Institute of Nuclear Sciences, University of Belgrade, PO Box 522, Belgrade,
Serbia*

Abstract

The aim of the work was to investigate the interaction between borate capped gold nanoparticles (AuNPs) and the rat brain synaptosomal plasma membranes (SPM), as well as the effects of these AuNPs on SPM Na⁺/K⁺-ATPase and Mg²⁺-ATPase activity. Influence of AuNPs on Na⁺/K⁺-ATPase and Mg²⁺-ATPase activity was investigated as the function of AuNPs and protein concentration and preincubation time. AuNPs induced the stimulation of Na⁺/K⁺-ATPase activity for more than 100%, while Mg²⁺-ATPase activity remained unaffected. We propose that this stimulation of enzyme activity was a consequence of an increase of the active surface of membranes.

Introduction

Gold nanoparticles (AuNPs) are a very attractive tool in biomedical research, because they have repeatedly shown great potential as substance carriers, active surfaces and even biologically active agents [1]. Since they can be readily taken up by cells [2], they are proposed in the medical sector as new tools in diagnostics [3] and drug delivery systems [4].

The particles themselves are easily modified due to the gold's ability to bond with biologically important molecular groups [5, 6, 7, 8].

Na⁺/K⁺-ATPase and Mg²⁺-ATPase (ecto-ATPase) are membrane enzymes ubiquitous in animal cells that involve 5'-adenosine triphosphate (ATP) as a substrate for their functioning. One of the available model systems for the study of Na⁺/K⁺-ATPase and Mg²⁺-ATPase are the rat brain synaptosomal plasma membrane fragments (SPM) [9]. In this paper we describe the influence of borate capped AuNPs of various sizes on SPM Na⁺/K⁺-ATPase and Mg²⁺-ATPase activity in this model system.

Materials and methods

AuNPs were obtained by the reduction of HAuCl₄ with NaBH₄. Precisely, 100 mL of 0.2 mM HAuCl₄ was reduced by 5.3 mM of NaBH₄ at room temperature, to yield a ruby-red solution. The calculated value of AuNPs concentration was 2.8x10⁻⁹ M, assuming that the reduction from gold (III) to gold atoms was 100% complete. Rat SPM were isolated according to a previously described method and stored at -80° C until use [9].

All spectrophotometric measurements were performed on a Perkin Elmer Lambda 35 UV-vis spectrophotometer with 1 cm path length quartz cuvette.

Results and discussion

The influence of AuNPs within the concentration range from 10^{-10} – 5.25×10^{-10} M on the ATP hydrolysis catalyzed by SPM Na^+/K^+ -ATPase and Mg^{2+} -ATPase was investigated according to a previously described method [9]. Measurements were done in triplicate. In this experiment the medium assay contained 20 μg protein. The catalytic reaction was started by addition of ATP 1 min after the nanoparticles were added into the medium assay and the results are presented in Fig. 1.

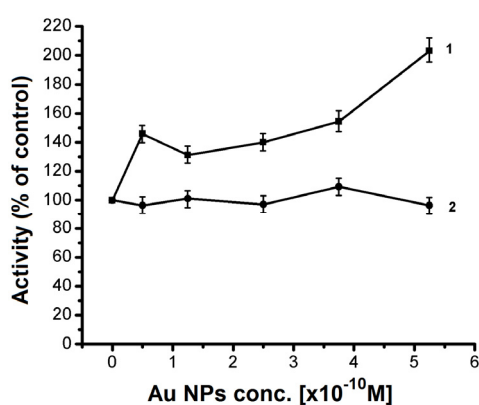


Figure 1. Influence of Au NPs on Na^+/K^+ -ATPase (1) and Mg^{2+} -ATPase (2) activity after 1 min preincubation.

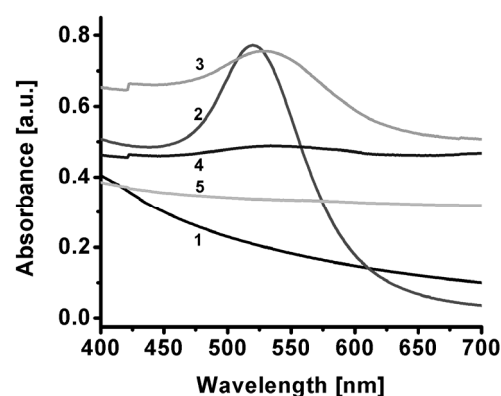


Figure 2. Changes in the UV-vis spectrum of AuNPs (2) upon addition of SPM (1). After 1 min (3), 10 min (4) and 20 min (5)

The results indicated, that the borate capped AuNPs increased the activity of Na^+/K^+ -ATPase in the concentration dependent manner, compared to the control value without nanoparticles, since the activity of Mg^{2+} -ATPase remained constant. Moreover, the increase of the Na^+/K^+ -ATPase activity was more than 100% in the presence of 5.25×10^{-10} M AuNPs.

To see if the deposition of SPM on the surface of AuNPs actually takes place, the surface plasmon resonance peak at 525nm was monitored. The observed changes are shown on Fig. 2. and they indicate that the membrane fragments react with the AuNP surface. The drop in plasmon peak intensity is time dependent and it completely disappears after 20 minutes. Since it is a membrane protein, we propose that the increase of Na^+/K^+ -ATPase activity can be ascribed to the increase of the active surface of SPM. Additional measurements on atomic force microscope and IR spectrophotometer (results shown elsewhere, see [10]) indicate that membranes disperse across the surface of AuNPs, thus increasing the active surface. Since Mg^{2+} -ATPase is not a surface enzyme it is not affected by this phenomenon.

Conclusion

In the presence of AuNPs, the activity of Na⁺/K⁺-ATPase in SPM is greatly increased. The most probable cause of this, according to present data is the increase of the active surface of membranes that is caused by the dispersion on the surface of AuNPs. Other properties of the enzyme, such as sensitivity towards inhibitors, remain unchanged. It is very important to note that in this case it is the physical rearrangement on the molecular level within the investigated material that caused a change in its biochemical properties.

Acknowledgements

This study was supported by the Ministry of Science, Technology and Development of the Republic of Serbia, Project No. 172023.

References

- [1] P. Tiwari, K. Vig, V. Dennis and S. Singh, *Nanomaterials*, 2011, 1, 31-63.
- [2] B. D. Chithrani, A. A. Ghazani and W. C. W. Chan, *Nano Lett.*, 2006, 6, 662-668.
- [3] H. M. E. Azzazy and M. M. H. Mansour, *Clin. Chim. Acta*, 2009, 403, 1-8.
- [4] T. C. Yih and M. Al-Fandi, *J. Cell. Biochem.*, 2006, 97, 1184-1190.
- [5] J. Ralston, J. F. Zhou, D. A. Beattie and R. Sedev, *Langmuir*, 2007, 23, 12096-12103..
- [6] S. Ariyasu, A. Onoda, R. Sakamoto and T. Yamamura, *Dalton Trans*, 2009, 19, 3742-3747.
- [7] D. Li, Q. He, Y. Cui, L. Duan and J. Li, *Biochem. and Biophys. Res. Commun.*, 2007, 355, 488-493.
- [8] R. Kumar, A. N. Maitra, P. K. Patanjali and P. Sharma, *Biomaterials*, 2005, 26, 6743-6753
- [9] V. Vasić, D. Jovanović, D. Krstić, G. Nikezić, A. Horvat, L. Vujisić and N. Nedeljković, *Tox. Lett.*, 1999, 110, 95-104
- [10] V. Petrović, V. Vodnik, I. Stanojević, Z. Rakočević, V. Vasić *Dig. J. Nanomat. Biostr.*, 2012, 7, 423-433.

F-12-P

RADIATION-MEDIATED MODULATIONS OF EXTRACELLULAR NUCLEOTIDE HYDROLYSIS IN ADULT FEMALE RAT BRAIN

D. Drakulić, I. Grković, M. Milošević, S. Petrović, M. Stanojlović,
N. Mitrović, A. Horvat

*Laboratory of Molecular Biology and Endocrinology, VINCA Institute of
Nuclear Sciences, University of Belgrade, P.O.Box 522, 11001, Belgrade,
Serbia*

Abstract

The present study was performed to investigate whether acute whole-body exposure of female adult rats to low dose (0.5 Gy) of ionizing irradiation (IR) is sufficient to alter ectonucleotidase enzyme activities in the brain. All measurements were done at time points 1, 24 and 72h after irradiation. Neuronal synaptic plasma membranes (SPMs) were isolated from whole brains and enzyme activities were determined by monitoring ATP, ADP and AMP hydrolysis *in vitro*. Our results indicate that whole-body IR is able to modulate investigated brain enzyme activities in a time-dependent manner.

Introduction

All over the world each living being is everyday exposed to ionizing irradiation (IR), almost all from natural sources in the environment or for medical reasons. Acute low dose IR is able to cause current and irreversible damages in the brain by forming reactive oxygen species (ROS) that directly or indirectly modulate protein-protein and protein-lipid interactions and thus, inhibit several metabolic processes, disrupt structure of DNA molecule as well structure, permeability and fluidity of plasma membrane [1].

Ectonucleotidases (NTPDase1,2,3 (nucleoside triphosphate diphosphohydrolases 1,2,3) and 5'-NT (ecto-5'-nucleotidase)) are surface-sited synaptic plasma membrane (SPM) enzymes that hydrolyze adenine nucleotides with different affinities [2]. NTPDase1 equally hydrolyzes ATP and ADP; NTPDase2 and NTPDase3 prefer ATP while 5'-NT is essential for AMP degradation to neuroprotective adenosine [2]. The modulation of ectonucleotidase activities caused by different stimuli provokes disruption in synaptic transmission and adenosine formation that leads to cell dysfunction, permanent neuronal injury, apoptosis or necrosis and finally to cognitive and other permanent disorders [2].

Therefore, this study tested the hypothesis that whole-body exposure of adult female rats to low (0.5 Gy) IR dose could alter NTPDase1,2,3 and 5'-NT enzyme activities in the whole brain. The possible enzyme activities modulations were examined through the rate of ATP, ADP and AMP hydrolysis at different time points (1h, 24h and 72h).

Materials and Methods

Animals were kept according to the standards of Ethical Committee for the use of laboratory animals of VINCA Institute of Nuclear Sciences (INN VINCA). Adult (60 days old) female rats of Wistar strain were divided at random into two groups:

F-11-P

I) control non-irradiated animals (C) and II) animals irradiated with 0.5 Gy (IR). The whole-bodies of IR rats were exposed to a single 0.5 Gy dose of γ -rays using 10.7 cGy/min, ^{60}Co source at INN VINCA. During the irradiation procedure animals were confined in plywood boxes while rats from control group were treated as the IR group but not subjected to irradiation. Immobilization for all groups lasted approximately 90 min. Animals were decapitated at different time points (1h, 24h and 72h after treatments) and synaptosomal plasma membranes (SPMs) from whole brains were isolated according to Stanojevic et al. [1]. The rate of ATP, ADP and AMP hydrolysis as indicators of enzyme activities, were measured by colorimetric determination of liberated inorganic phosphate as previously described [1]. The data were obtained from three independent SPMs isolations and all measurements were done in triplicate. Statistical significance was determined by one-way ANOVA followed by Tuckey's posthoc test.

Results and Discussion

The experimental results of synaptosomal ATP, ADP and AMP hydrolysis as indicators of NTPDase1,2,3 and 5'-NT activities in each investigated time-point following acute immobilization are shown in Table 1.

control	1h	24h	72h
ATP	144.5 \pm 5.5	128.2 \pm 6.3	147.8 \pm 9.1
ADP	23.7 \pm 2.2	29.8 \pm 2.7	33.6 \pm 2.0
AMP	18.4 \pm 1.3	16.9 \pm 1.8	27.1 \pm 0.5

Table 1. Specific enzyme activities for control groups presented as a mean nmolPi/min/mg \pm SEM, from 3 independent experiments done in triplicate

In the nerve terminals of 60-days old female Wistar rats, whole-body irradiation with 0.5 Gy was not sufficient to alter ATP hydrolysis in any investigated time point (Fig 1a, left). Although IR provoked decrease of ADP hydrolysis at all time points, the greatest impact appeared after 72h when ADP hydrolysis was reduced by 21% (Fig 1a, right). Thus, in this experimental model system, the ATPase component of investigated enzymes was less sensitive to low dose IR than the ADPase part.

Furthermore, the significant decrease in AMP hydrolysis by 20% was observed 72h after irradiation while after 1h and 24h the investigated hydrolyses were reduced but not considerably (Fig 1b). Knowing that adenosine is an important neuroprotective agent, the observed diminished AMP hydrolysis as an indicator of 5'-NT activity may contribute to lesser extracellular adenosine formation and be harmful for neurons.

Conclusions

In the present study, detected hydrolyzing activities point out that more than one ectonucleotidase is present on the neural cell surface and all of them are differently sensitive to whole-body irradiation. Furthermore, our findings indicate that acute whole-body IR exposure via modulation of the neuronal ectonucleotidases activity in adult female rats might be capable to reduce the formation of adenosine, impair the function of neuronal cells and increase the possibility of cell death occurrence in time-dependended manner.

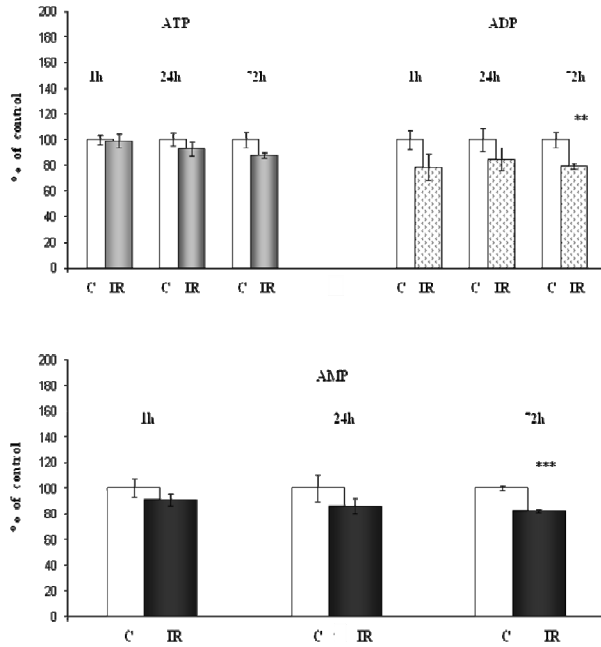


Figure 1. a) ATP and ADP hydrolyses as indicators of NTPDase1,2,3 activities in synaptic plasma membranes 1h, 24h and 72h following acute whole-body irradiation with 0.5 Gy dose. Results are presented as a percentage of control, mean \pm SEM from 3 independent experiments done in triplicate (* $p < 0.05$)

b) AMP hydrolysis as a marker of 5'-NT activity in synaptic plasma membranes 1h, 24h and 72h following acute whole-body irradiation with 0.5 Gy dose. Results are presented as a percentage of control, mean \pm SEM from 3 independent experiments done in triplicate (* $p < 0.05$)

Acknowledgment

This study is supported by Ministry of Education and Science, Project No. 173044.

References

- [1] I. Stanojevic et al, Russ J Phys Chem A, 2009, 83, 9, 1596–1601.
- [2] H. Zimmermann, Naunyn-Schmied, Arch. Pharmacol., 2000, 362, 299-309.
- [3] J. Verheyde, M. A. Benotmane, Brain Res. Rev., 2007, 53, 312-320.

F-12-P

TIME-DEPENDENT EXPRESSION OF BCL-2 AND BAX PROTEINS IN CORTICAL BRAIN AREA OF ADULT WISTAR RATS AFTER PERMANENT BILATERAL OCCLUSIONS

M. Stanojlović, D. Drakulić, I. Grković, N. Mitrović, A. Horvat

VINCA Institute of Nuclear Sciences, Laboratory of Molecular Biology and Endocrinology, University of Belgrade, P.O.Box 522, 11001, Belgrade, Serbia

Abstract

Model of permanent bilateral occlusion of common carotid arteries (2VO) is generally used to investigate mechanisms of chronic cerebral hypoperfusion that occurs in aging and other neurodegenerative processes. The aim of this study was to determine time-dependent modulation of mitochondrial apoptotic signaling in cortical brain area following chronic cerebral hypoperfusion. Using Western blot technique we monitored the changes in the expression of proteins of Bcl-2 family (Bcl-2, Bax) 3, 7 and 90 days following the insult. According to our results the greatest impact of chronic cerebral hypoperfusion occurred on 7th day.

Introduction

Chronic cerebral hypoperfusion may be the cause or at least a partial cause of various neurodegenerative impairments including vascular dementia, stroke, Alzheimer's disease etc. Since these disorders affect large part of population, it is essential to determine mechanisms in which chronic cerebral hypoperfusion modifies function of neuronal cells. Furthermore it is important to understand the time course of these changes.

Bcl-2 protein family governs mitochondrial outer membrane permeabilization. It includes either pro-apoptotic (Bax, BAD, Bak and Bok) or anti-apoptotic (Bcl-xL, and Bcl-w) proteins. It is established that Bcl-2-related anti- and pro-apoptotic proteins are important in the decision step of the intracellular death program initiated by caspase proteasis. Bcl-2 is a prominent anti-apoptotic protein, but its mechanism of action is currently not completely understood [1]. This suppressor of programmed cell death, homodimerizes with itself or forms heterodimers with a homologous protein Bax, a promoter of cell death. Bax can form an oligomeric pore in the outer mitochondrial membrane. Moreover, Bax is believed to interact with the mitochondrial voltage-dependent anion channel and induce its opening. This results in the release of cytochrome C and other pro-apoptotic factors from the mitochondria [2].

The aim of this study was to determine the time course of possible apoptotic changes and peak of neurodegeneration processes in order to define optimal time point for analyzing beneficial effects of certain substances.

Materials and Methods

Animals used in this experiment were kept according to the standards of Ethical Committee for the Use of Laboratory Animals of INN VINCA. Animals were maintained under standard conditions *ad libitum* access to food and water.

Experiments were performed on adult (3 months old) male Wistar albino rats randomly assigned to different experimental groups: I) animals subjected to permanent bilateral occlusions of common carotid artery (2VO), and II) control, sham operated animals. Procedure was performed on chloral hydrate (400mg/kg) anesthetized animals according to [3]. After given time (3, 7 or 90 days) animals were sacrificed. Crude synaptosomal fraction (P2) was isolated from cortex with differential centrifugation as previously described [4]. Western blot was performed using following antibodies: Bcl-2, Bax and β -actin as loading control (Santa Cruz Biotechnology). The data were obtained from three independent P2 isolations and all measurements were done in triplicate. Statistical significance was determined by one-way ANOVA followed by Tuckey's posthoc test.

Results and Discussion

Knowing that the ratio of pro- and anti-apoptotic proteins of Bcl-2 family might define the cell's destiny, we examined the time-dependent protein expression of anti-survival Bax and pro-survival Bcl-2 in cortical brain area of both sham and 2VO rats.

Chronic cerebral hypoperfusion after 3 days caused no relevant alternation in the quantity of Bax. on 7 day after 2VO, in comparison to controls, a significant increase in expression of Bax was detected. The expression of Bax reached control level on 90 day following the 2VO suggesting that neuronal cells begin to recover (Fig 1a). Further, the expression of Bcl-2 was not significantly altered after 3 and 7 days post operation, while 90 days after 2VO insult a significant increase in quantity of Bcl-2 was observed (Fig 1b).

In addition, to correlate the changes in the protein levels of two members of Bcl-2 protein family as indicators of apoptosis, Bax as pro-apoptotic and Bcl-2 as anti-apoptotic molecule, we calculated their relative ratio. The ratio value above one indicates the dominance of Bax and possible pro-apoptotic changes in the cells, whereas value below one points to prevalence of Bcl-2 protein and anti-apoptotic modulations. The calculated protein ratio showed that Bax predominated in cortical brain area after 7 days while Bcl-2 was predominant 90 days following 2VO insult (Fig 1c).

Findings of current study might indicate that 3 days following the 2VO insult might not be sufficient period for pro-apoptotic changes to occur. On the other hand, according to the expression of Bax and Bcl-2, as well their relative protein ratio, the greatest impact of chronic cerebral hypoperfusion might happen after 7 days. 90 days following the insult, anti-apoptotic processes might start as well as the recovery of neuronal cells.

Conclusions

The relevance of this study was to determine at what investigated time point the chronic cerebral hypoperfusion insult was the greatest in order to test neuroprotective effects of certain substances, which is planned for our further experiments.

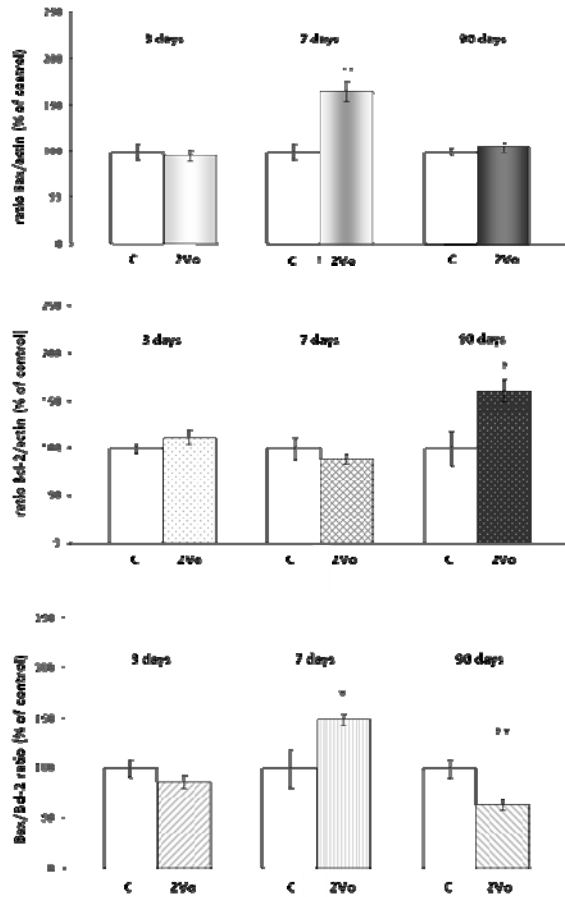


Figure 1. a) Expression of Bax in the cortical P2 fraction on 3, 7, 90 day following permanent 2VO procedure. Results are presented as a percentage of control, mean \pm SEM (* p <0.05).

b) Expression of Bcl-2 in the cortical P2 fraction on 3, 7, 90 day following permanent 2VO procedure. Results are presented as a percentage of control, mean \pm SEM (* p <0.05).

c) Bax/Bcl-2 protein ratio in the cortical P2 fraction on 3, 7, 90 day following permanent 2VO procedure. Results are presented as a percentage of control, mean \pm SEM (* p <0.05).

Acknowledgemnt

This study is supported by the Ministry of Education and Science, Projects No: 173044 and 41014.

References

- [1] J. C. Reed, Blood, 2008, 11, 3322-3330.
- [2] K. G. Wolter et al, Cell Biol., 1997, 139, 1281-1292.
- [3] F. Cechetti et al, J. Med. Biol. Res., 2010, 43, 1178-1183.
- [4] I. Stanojevic et al, Russ. J. Phys. Chem., 2009, 83, 1596-1601.

F-13-P

KINETICS OF DSB INDUCTION AND CHANGES IN CELL CYCLE REGULATION IN MELANOMA CELLS AFTER IONIZING RADIATION

T. Bulat¹, O. Keta¹, L. Korićanac¹, D. Todorović², I. Petrović¹, A. Ristić-Fira¹

¹*Vinča Institute of Nuclear Sciences, University of Belgrade, Belgrade, Serbia*

²*Medical faculty, University of Kragujevac, Kragujevac, Serbia*

Abstract

The effects of γ -rays on the DNA level, i.e. formation of double-strand breaks and expression of p21 were studied *in vitro* on the human HTB 140 melanoma cells. Cells were exposed to the dose range from 2 to 16 Gy. Effects were analyzed 30 min, 2, 6 and 24 h after irradiation. It has been shown that the level of phosphorylated histone H2AX (γ H2AX) is time- and dose-dependent, as well as the expression of p21.

Introduction

Malignant melanoma is a very aggressive type of cancer, generally resistant to different therapeutic approaches. One of the reasons for such behavior is its significant ability to repair DNA breaks [1]. Ionizing radiation (IR) acts on the DNA, either directly by inflicting DNA damages, or indirectly by affecting DNA metabolism and causing damages. As a result, cell cycle checkpoint activation becomes an important determinant of the ultimate response to the treatment. This will benefit existing therapeutic modalities and likely contribute to the development of novel cancer-treatment approaches. Extensive studies uncovered a complex network of genes that cooperate to delay the normal progression through the cell cycle as soon as the damage is registered in the genome [2]. When human cells sustain a DNA double-strand break (DSB), histone H2AX in chromatin surrounding the DNA break becomes phosphorylated at serine 139 (γ H2AX), thus making repair foci [1]. Literature data suggest a correlation between radio-sensitivity and the kinetics of γ H2AX clearance in human tumor cell lines. Radio-sensitive tumor cells retain γ H2AX for a greater duration than radio-resistant ones [3].

The p21 (CIP1/WAF1) protein binds to and inhibits the activity of cyclin-CDK2 or -CDK1 complexes, and therefore functions as a regulator of cell cycle progression at G1. Also, p21 can lead to G2 arrest. H2AX phosphorylation has been shown to be required to maintain p21 level, leading to cell cycle arrest [4].

The aim of this study was to investigate the kinetics of DSB induction in human HTB140 melanoma cells after exposure to γ -rays. This was done through evaluation of the level of γ H2AX and the expression of p21 protein.

Results and Discussion

Irradiations of HTB140 cells with γ -rays were performed using ^{60}Co source, at the Vinča Institute of Nuclear Science in Belgrade. The dose range was from 2 to 16 Gy. The average dose rate was ~ 1 Gy/min. All cell irradiations were carried out in air at $\sim 0^\circ\text{C}$.

After irradiations, cells were incubated for 30 min, 2, 6 and 24 h under standard conditions. The levels of γH2AX and p21 were analyzed by Western blot. Phosphorylation of H2AX has reached the highest value at 2 h after irradiation (Fig. 1). At 6 h, as well as after 24 h post-irradiation (data not shown), there is a tendency of reduction of γH2AX to the pre-irradiation level. This indicates a high level of radio-resistance of the HTB140 cells. Dose dependence is seen in all analyzed time points (Fig. 1A, B, C).

After inhibition of replication H2AX is required for the increase of p21 level, subsequently resulting in checkpoint activation and cell cycle arrest [4]. Consequently, the expression of p21 was analyzed. Obtained results showed that γ -rays induced dose dependent expression of p21 with the highest level attained at 6 h post-irradiation (Fig. 2B).

This implies that the p21 expression increases when the level of γH2AX drops down. Since p21 is involved in the regulation of G1, as well as G2 arrest, these data are in accordance with our previously reported G2 arrest of the HTB140 cells exposed to radiation [5].

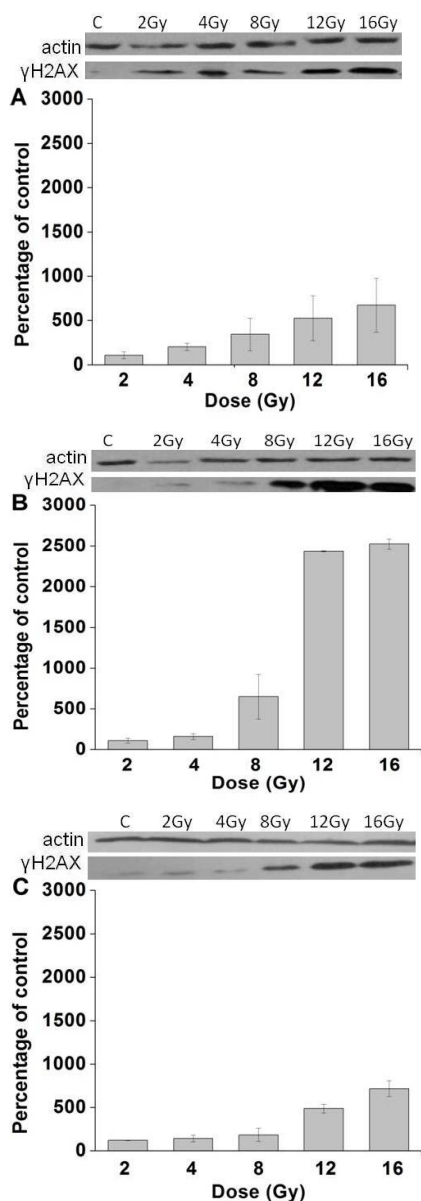


Figure 1. Level of γH2AX in HTB140 cells analyzed by Western blot, 30 min (A), 2 h (B) and 6 h (C) after irradiation. Results are presented as percentage of control (mean \pm S.D.). C-control.

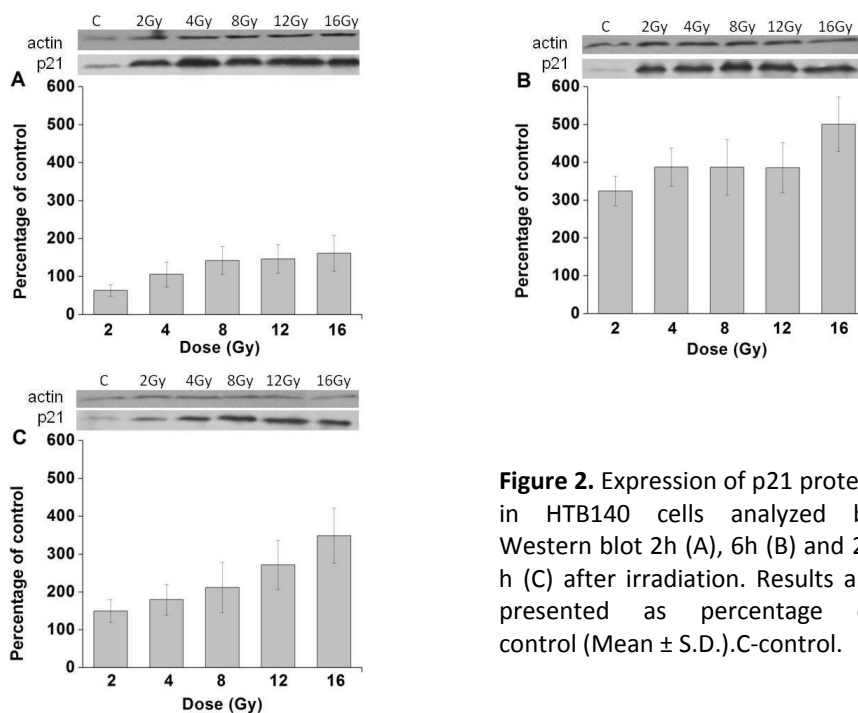


Figure 2. Expression of p21 protein in HTB140 cells analyzed by Western blot 2h (A), 6h (B) and 24 h (C) after irradiation. Results are presented as percentage of control (Mean \pm S.D.). C-control.

Conclusions

Obtained results showed that γ -rays induced time- and dose-dependent phosphorylation of histone H2AX and the expression of p21 protein, indicating that this anti-tumor agent provokes induction of DSBs and changes in the cell cycle regulation in HTB140 cells. Kinetic of γ H2AX loss confirmed radio-resistant nature of the analyzed cells. These findings give useful information about mechanisms of melanoma resistance, since γ H2AX is used as a novel tool for monitoring genotoxic events associated with cancer.

References

- [1] R. Warters et al, *J Invest Dermatol.*, 2005, 124, 807-817.
- [2] G. Iliakis et al, *Oncogene*, 2003, 22, 5834-5847.
- [3] N. Taneja et al, *J Biol Chem.*, 2004, 279(3), 2273-2280.
- [4] M. Fragkos et al, *Mol. Cell. Biol.*, 2009, 29, 2828-2840.
- [5] A. Ristic-Fira et al, *Ann N Y Acad Sci.*, 2007, 1095, 165-74.

SENSITIVITY OF LUNG CARCINOMA CELLS TO γ - RAYS AND ERLOTINIB

O. Keta¹, T. Bulat¹, L. Korićanac¹, D. Todorović², G. Privitera³,
I. Petrović¹, A. Ristić-Fira¹

¹*Vinča Institute of Nuclear Sciences, University of Belgrade, Belgrade, Serbia*

²*Medical Faculty, University of Kragujevac, Kragujevac, Serbia*

³*Institute of Radiology and Radiation Oncology, University of Catania, Italy*

Abstract

In order to increase radio-sensitivity of human lung adenocarcinoma NCI-H1568 cells, targeted therapy drug, erlotinib was used. The impact of radiation and erlotinib on cell behaviour was analyzed using three biological endpoints. Irradiations with γ -rays resulted in reduction of cell survival, viability and proliferation. Erlotinib significantly inhibited cell growth and proliferation capacity. Combined treatments with radiation and erlotinib showed high level of reduction of cell viability and proliferation. Preliminary data encourage further investigations of mechanisms underlying the radiation responses enhanced by erlotinib.

Introduction

Non-small cell lung cancer (NSCLC) represents over 80% of all lung cancers. Radiotherapy and chemotherapy, alone or in combination are standard treatment strategies for this disease. The epidermal growth factor receptor (EGFR) is a member of the human epidermal growth factor (HER) family of receptors that is aberrantly expressed in a broad range of cancers including NSCLC. Ligand binding induces activation of tyrosine kinase (TK) domain of EGFR which leads to the activation of important signaling network involved in tumor cell proliferation and survival [1]. For this reason, blocking this signaling pathway by molecular targeting of EGFR is an attractive therapeutic strategy. Most targeted therapies include anti-EGFR monoclonal antibodies and small-molecule tyrosine kinase inhibitors (TKIs) [2]. Erlotinib (Tarceva) is quinazoline small-molecule inhibitor of HER1/EGFR tyrosine kinase approved by the United States Food and Drug Administration for the treatment of advanced NSCLC and pancreatic cancer [3]. There is evidence that radiation can activate EGFR signaling leading to accelerated proliferation or repopulation of tumour cells [4]. Considering the new insights into the role of EGFR in DNA repair through interaction with DNA-dependent protein kinase (DNA-PK) there is a considerable interest in using EGFR inhibitors for sensitizing tumours to radiotherapy in cancer patients [5].

Trying to improve the anti-tumour activity of γ -rays by erlotinib, combined effects of these agents on the human lung adenocarcinoma cell line NCI-H1568 were analyzed.

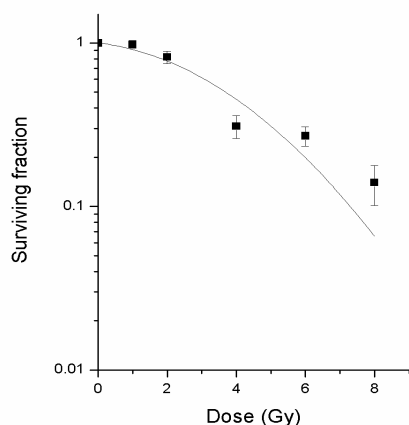


Figure 1. Dose-response curve of NCI-H1568 cells exposed to γ -rays, obtained by clonogenic assay.

Materials and methods

The NCI-H1568 cells were irradiated in air with ^{60}Co γ -rays at the Vinča Institute of Nuclear Sciences, Belgrade, Serbia. Cell survival was assessed 7 days after irradiation in the dose range from 1 to 8 Gy and at the dose rate of ~ 1 Gy/min. Viability and proliferation were measured 7 and 14 days post irradiation using SRB (MP Biomedicals, Inc) and BrdU (Roche Diagnostics GmbH, Mannheim, Germany) assays. The absorbance was measured at 450 and 550 nm for BrdU and SRB assays, respectively (Victor, Wallac, Turku, Finland). In combined treatments, following literature data, 5 μM erlotinib was added immediately after irradiation [6].

Results and Discussion

Dose-dependent inhibitory effects of γ -rays are justified by clonogenic assay. Surviving data were fitted to the linear-quadratic model and the best fit survival curve is given in Figure 1. The surviving fraction at 2 Gy (SF2) is 0.78. Obtained data indicated high level of radio-resistance of analyzed NSCLC cells, especially to lower doses of γ -rays (1 and 2 Gy), while the response of NCI-H1568 cells to higher doses was significant (Fig. 1). Treatment of irradiated NCI-H1568 cells with erlotinib caused very strong inhibition of cell survival and colony formation was not detected.

Based on the fact that analyzed cells are quite resistant to γ -rays, for further experiments dose range was extended with higher doses beyond the therapeutic values (12 and 16 Gy).

Dose-dependent cell viability obtained with SRB assay, 7 days after application of γ -rays, ranged from 31 to 99% (Fig. 2a). NCI-H1568 cells showed strong response to erlotinib alone and in combination with γ -rays, with viability less than 5% (Fig. 2a). Similar data were obtained 14 days after irradiation, where the values were between 16 and 90% while the number of viable cells after single and combined treatment with erlotinib was less than 10% (Fig.2b). For both incubation periods, good dose-dependent response to γ -rays was observed. According to the results obtained by BrdU assay, cell proliferation decreases after exposure to higher doses of γ -rays. Moreover, treatment with erlotinib alone and in combination provokes strong inactivation of proliferation, with values less than 8%, as compared to control (Fig. 2c). Proliferation of treated cells after 14 days of incubation is given in Fig. 2d. Obtained data showed slightly higher proliferation of cells, not exceeding 30%, therefore indicating that the cells recover after applied treatments.

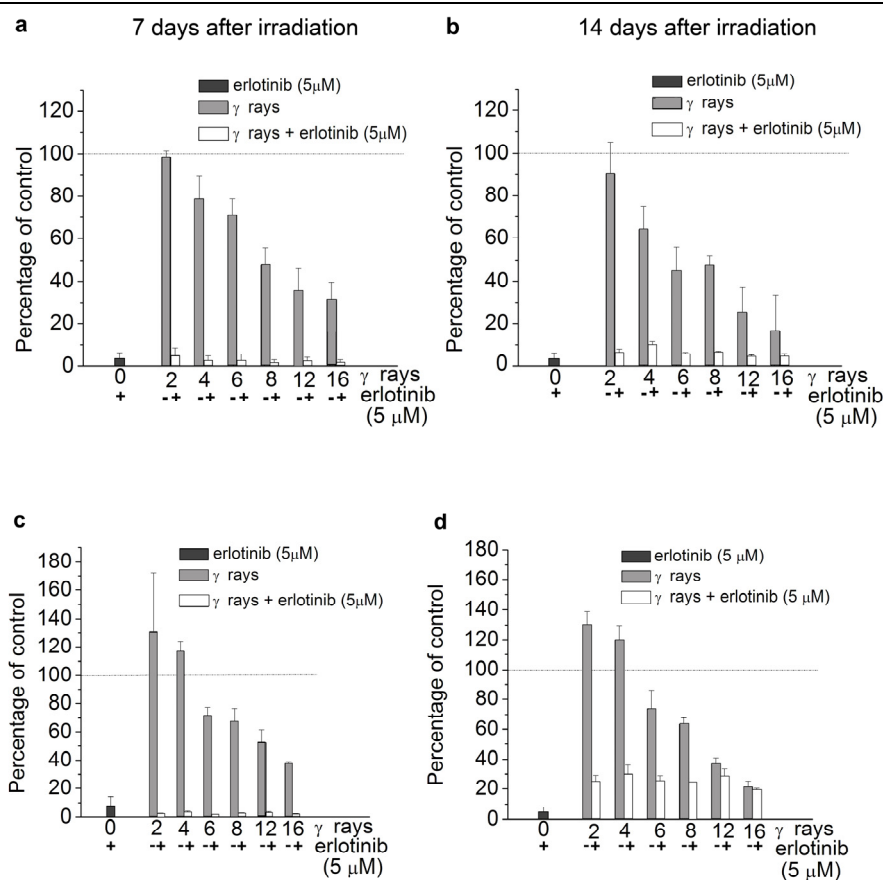


Figure 2. Effects of γ -rays and erlotinib on NCI-H1568 cells, 7 and 14 days after irradiation, estimated by SRB (a, b) and BrdU assays (c, d).

Conclusion

Presented results indicated that γ -rays inactivated NCI-H1568 cells in the dose-dependent way. Treatment with erlotinib highly sensitized the cells to γ -rays, thus making this agent valuable in cancer treatment when used in the synergy with radiation.

References

- [1] D. L. Wheeler et al, *Nat. Rev. Clin. Oncol.*, 2010, 7(9), 493-507.
- [2] O. Dassonville et al, *Crit. Rev. Oncol. Hematol.*, 2007, 62(1), 53-61.
- [3] J. R. Johnson et al, *Clin. Cancer Res.*, 2005, 11(18), 6414-21.
- [4] P. Dent et al, *Mol. Biol. Cell.*, 1999, 10(8), 2493-506.
- [5] D. J. Chen et al, *Clin. Cancer Res.*, 2007, 13(22 Pt 1), 6555-60.
- [6] J. C. Ko et al, *Mol. Cancer Res.*, 2009, 7(8), 1378-89.

F-15-P

T-CELL EPITOPE FREQUENCY IN ORDERED AND DISORDERED PROTEIN REGIONS OF TUMOR-ASSOCIATED ANTIGENS

M. D. Pavlović¹, N. S. Mitić², D. R. Jandrlić³, M. V. Beljanski¹

¹*University of Belgrade, Institute of General and Physical Chemistry, Studentski Trg 12, Belgrade, Serbia*

²*University of Belgrade, Faculty of Mathematics, Studentski trg 16, Belgrade, Serbia*

³*University of Belgrade, Faculty of Mechanical Engineering, Kraljice Marije 16, Belgrade, Serbia*

Abstract

Using epitope predictions it was shown that both Human Leukocyte Antigens class I and class II (HLA-I and HLA-II) epitopes were more frequent in ordered regions of proteins and that epitopes appertaining to ordered protein regions were prevalently hydrophobic. The comparison between predicted and experimentally evaluated epitopes of several tumor-associated antigens, revealed that majority of epitopes, presented by HLA-I and HLA-II molecules, are localized in ordered protein regions.

Introduction

Tumor-associated antigens (TAA) frequently contain long unstructured (disordered) regions [1]. Many of them are immunogenic and are interesting candidates for cancer-vaccine trials. An important question in immunology is whether disorder or order belonging of the peptide T-cell epitopes [2] plays role in immunogenicity. We have compared epitope frequency, affinity and hydrophobicity within predicted ordered and disordered protein regions. The data on predicted and experimentally found epitope localization and dominance, reported for several TAA, were correlated.

Experimental

The database contained 642 proteins, mainly (477) from DisProt database [3]. For epitope prediction NetMHCpan-2.0 [4] and NetMHCIIpan-1.0 [5] methods were used. For predicting disordered regions VSL2 [6], PONDR VL-XT [7] and PONDR- FIT [3] were applied. The Kyte-Doolittle hydrophobicity scale [8] was applied for prediction of hydrophathy profile. We have developed EPDIS (EPitope in DISorder) application, which integrates all of the mentioned methods and offers graphical interface (Fig. 1).

Results and discussion

The number of epitopes (9 AA) in ordered (O) protein regions was 2.84 times higher than in disordered (D) regions for HLA-I alleles and 3.60 times higher for HLA-II alleles. The same trend remains after normalization of the epitope number on 100 AA (epitope frequency), (Table 1.).

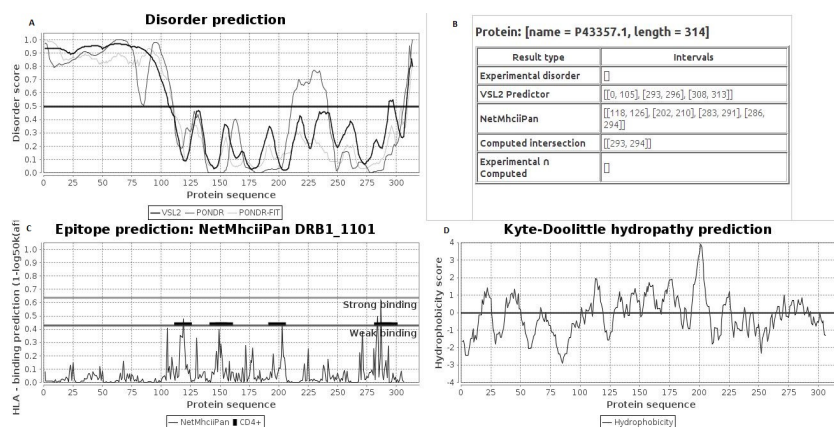


Figure 1. Human MAGE-A3 protein (UniProt Acc No: P43357.1). A: disorder/order prediction, according to VSL-2B, PONDR-VL-XT and PONDR-FIT predictors. B: predicted: disorder regions and epitopes, experimental results and intersections. C: HLA-II epitope prediction, using NetMHCpan method for the HLA-DRB1*1101 allele. Epitopes, designated as , were experimentally found to induce CD4+ T cells. D: Kyte-Doolittle hydropathy plot of a protein sequence, using a window of nine amino acids.

Table 1. Number of weak (WB)- and strong (SB)-binding epitopes/100 AA and Hydropathy of epitopes in regions (HER) in disorder (D), ordered (O) and disordered/ordered-boundary regions (N) for HLA-I and HLA-II class alleles.

HLA	Region type	HLA binding level	Epitopes/ 100 AA	HER*
HLA1	D	SB	88.38	Hydrophilic
		WB	398.19	Hydrophilic
	N	SB	91.05	Hydrophilic
		WB	406.17	Hydrophilic
O	SB	266.1	Hydrophobic	
	WB	1017.83	Hydrophobic	
HLA2	D	SB	11.68	Hydrophobic
		WB	201.81	Hydrophilic
	N	SB	15.11	Hydrophobic
		WB	241.02	Hydrophobic
O	SB	44.04	Hydrophobic	
	WB	668.77	Hydrophobic	

*If the number of hydrophobic epitopes in the region is over 50%, the HER is considered as hydrophobic, otherwise as hydrophilic.

The same conclusion, holds when proteins were grouped according to main taxonomic categories (archaea, bacteria, eukarya, and viridae) (data not shown). From Table 1 it is evident that epitopes, belonging to ordered protein regions are always hydrophobic (for both HLA-I and HLA-II alleles). The results are in

F-15-P

accordance with HLA-I supertype binding motifs [9] and hydrophobic N-terminal positions of the HLA-II class binding peptides [10]. We have chosen several immunogenic TAA, that have been intensively studied in cellular immune response and compared epitopes, predicted to be presented by HLA-I and HLA-II antigens and experimentally found ones [11], and their localization in ordered and disordered protein regions. Majority of predicted and experimentally found epitopes presented by HLA-I and HLA-II alleles are localized in ordered protein regions, as shown for MAGE-A3 CTA, Fig. 1. [12]. In long disordered protein sequences epitopes are frequently flanking the ordered parts of the protein or potential disorder-to-order transition elements.

Conclusion

Using disorder and epitope predictions we have found that both HLA-I and HLA-II epitopes were more frequent in ordered protein regions which may be helpful in mapping potential cancer-vaccine candidate peptides.

Acknowledgements

This work was supported by the Ministry of Education and Science, Republic of Serbia Projects No. 174021, 174002 and TR 31055.

References

- [1] L. M. Jakoucheva, C. J. Brown, J. D. Lawson, Z. Obradovic and K. Dunker, *J. Mol. Biol.*, 2002, 323, 573–584.
- [2] S. Carmicle, N. K. Steede, S. J. Landry, *Molecular Immunology*, 2007, 44, 1159–1168
- [3] Disprot database: <http://www.disprot.org>
- [4] NetMhcPan program: <http://www.cbs.dtu.dk/services/NetMHCpan>
- [5] NetMhcIIpan program: <http://www.cbs.dtu.dk/services/NetMHCIIpan-1.0>
- [6] VSL2 and VL XT predictors: <http://www.ist.temple.edu/disprot/predictorVSL2.php>
- [7] Pondr predictor: <http://www.pondr.com>
- [8] J. Kyte and R. Doolittle, *J. Mol. Biol.*, 1982, 157, 105-132.
- [9] J. Sidney, B. Peters, N. Frahm, C. Brander and A. Sette, *BMC Immunol.*, 2008, 22, 9:1.
- [10] M. Halling-Brown, R. Shaban, D. Framton, C. E. Sansom, M. Davies, D. Flower, M. Duffield, R. W. Titball, V. Brusic, D. S. Moss, *Molecular immunology*, 2009, 46, 2699-2705.
- [11] <http://www.cancerimmunity.org/peptidedatabase/tumorspecific.htm>
- [12] G. Consogno, S. Manicj, V. Facchinetti, A. Bachj, J. Hammer, B-M Conti-Fine, C. Rugarj, C. Traversari and M. P. Protti, *Blood*, 2003, 101, 1038-44.

F-16-P

EPR INVESTIGATIONS OF VANADATE REDUCTION IN MYCELIUM OF *PHYCOMYCES BLAKESLEEANUS*

M. Žižić¹, I. Spasojević¹, M. Stanić¹, M. Živić², J. Zakrzewska³

¹*Institute for Multidisciplinary Research, University of Belgrade, Kneza Višeslava 1, 11030 Belgrade, Serbia.*

²*Faculty of Biology, University of Belgrade, Studentski trg 16, 11000 Belgrade, Serbia.*

³*Institute of General and Physical Chemistry, Studentski trg 12-16, 11000 Belgrade, Serbia.*

Abstract

The interaction of vanadate (+5) and vanadyl (+4) with 24h old mycelium of wild type *P. blakesleeanus* was investigated by EPR spectroscopy. The results show that *P. blakesleeanus* is able to reduce vanadate to V⁺⁴ form, which is then bound to some extent to cell wall components. The reduction takes place in extracellular compartment, although at higher concentrations part of V⁺⁵ enters the cytoplasm.

Introduction

Fungi could be organisms of major interest in biological studies of vanadium, as they are able to take up and accumulate trace metals [1], providing the main way of vanadium entrance into ecosystems [2], and can improve its therapeutic application by forming organic complexes that reduce vanadium toxicity [3,4]. Nevertheless, data about vanadium metabolism in fungi are very scarce, and are obtained almost solely on two ascomycetous yeasts species: *S. cerevisiae* and *H. polymorpha* [5]. In addition, most presented results are far from giving indisputable answers about capability and place of V⁺⁵ reduction, active form of vanadium in cells, and the way of vanadium entrance [6,7].

The aim of this paper is to give the insight into vanadium behavior in *P. blakesleeanus*, filamentous fungus placed near the base of fungal phylogenetic tree.

Experiments

The wild-type strain of the fungus *P. blakesleeanus* (Burgeff) (NRRL 1555(-)) was used. The mycelium was grown in standard minimal medium [8] in Erlenmeyer flasks which were shaken and aerated in the growth cabinet with continuous overhead white fluorescent light of 10 W/m², at temperature of 20°C, and ca. 95% relative humidity.

For the purpose of EPR measurements 30 mg of 24 h old mycelium was placed on an open Teflon holder and treated with sodium orthovanadate or vanadyl sulfate at the final concentration of 7 μmol/g of FW mycelium. For washing experiments 0.3 g of mycelium, was centrifuged twice with the modified minimal medium experimental medium after V⁺⁵ or V⁺⁴ treatments, and then used in EPR experiments.

EPR spectra were recorded using a Varian E104-A EPR spectrometer operating at X-band (9.452 GHz) with the following settings: field center 3610 G; scan range 1000 G; modulation amplitude, 10 G; modulation frequency, 100 kHz; microwave power, 10 mW; time constant, 64 ms; scanning time, 4 min.

Results

The ability of *P. blakesleeanus* to reduce vanadate to vanadyl was tested using EPR spectroscopy, since V^{+5} form is invisible for this technique. The EPR spectrum of *P. blakesleeanus* mycelium 40 min after addition of vanadate is presented in Fig. 1A. The obtained spectrum consists of lines characteristic for EPR spectrum of vanadyl sulfate solution in modified minimal medium (Fig. 1B). The presence of additional lines indicated that there are some other V^{+4} form(s), *i.e.* bounded V^{+4} [9]. The *P. blakesleeanus* mycelium was washed than with modified minimal medium, which resulted in disappearance of free vanadyl lines, making the signal of bound V^{+4} clearly visible (Fig 1C), [9]. In this way, the lines in the EPR spectrum which can be used for investigation of reduction (free V^{+4} , black square) and binding kinetics (bound V^{+4} , white circle) were determined.

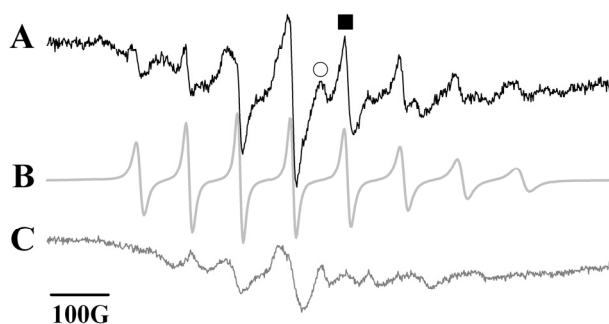


Figure 1. EPR spectra of V^{+4} in the *P. blakesleeanus* mycelium after incubation with vanadate (A), and after washing of mycelium with experimental medium (C). Spectra were compared to that of 'free' V^{+4} obtained in modified minimal medium (B).

The results of kinetic investigations of vanadate reduction and V^{+4} binding are presented in Fig. 2A. It is obvious that changes of intensity of free vanadyl line represent two phase process (Fig. 2A, black square). Namely, up to 25 min, its intensity increases exponentially with time constant of 8.7 min ($r^2= 0.993$), after that linear increase of signal intensity is observed (2.27 a.u./min). On the other hand, intensity of bound V^{+4} line (Fig. 2A, white circle) increases exponentially with time constant of ($\tau=7.81$ min, $r^2= 0.989$), reaching plateau about 30 min after V^{+5} addition, *i.e.*, concomitantly with the observed change in free V^{+4} kinetics. Two processes are responsible for changes of intensity: reduction of V^{+5} and V^{+4} binding. As time constants of reduction and binding are alike in first 30 min, it can be assumed that both processes are parallel and take place in the same cell compartment.

Similar experiment was performed with addition of vanadyl sulfate to *P. blakesleeanus* mycelium (Fig. 2B).

In this case, the intensity of free vanadyl line decreases with time constant of about 6.29 min, whereas binding process consists of two phases: exponential kinetic up

F-16-P

to about 20 min., with time constant of 5.2 min ($r^2 = 0.998$), and further linear increase (0.914 a.u./min). The increase of intensity of V^{+4} complex line in comparison to decrease of intensity of free V^{+4} line is of about 18.6%, meaning that the most of added vanadyl turns into EPR invisible form. Furthermore, intensity of free V^{+4} line at the moment of its addition (Fig 2B, 5 min) is 5.8 times ($\sim 60\%$) larger than V^{4+} line intensity obtained after V^{+5} reduction (Fig 2A, 60 min). It could mean either, that during 60 min. *P. blakesleeanus* can reduce only $\sim 40\%$ of added V^{+5} or that the reduction is more efficient but most of formed V^{+4} is bound in EPR invisible anisotropic complexes.

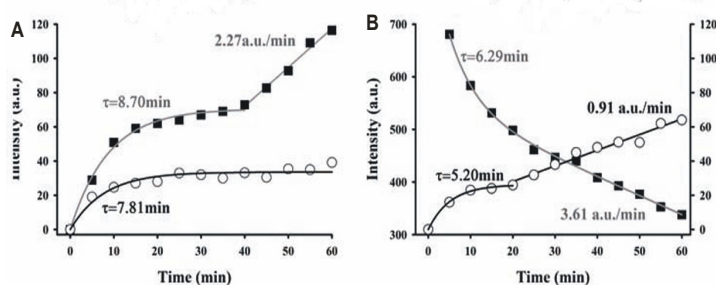


Figure 2. Kinetics of intensity changes of lines of bound (circle) and 'free' (square) V^{+4} in mycelium after vanadate (A), or vanadyl (B) addition.

Conclusions

Although it is mainly accepted that vanadate is reduced to vanadyl once it enters cells, available data presented up to date [6] show that the situation seems to be not so simple in case of fungi. The results presented here show, first of all, that wild type strain of *P. blakesleeanus* has capability of V^{+5} reduction, as confirmed by appearance of EPR spectrum of V^{+4} after addition of vanadate into mycelium, and indicate that the reduction proceeds mostly extracellularly.

Acknowledgement

Supported by Serbian Ministry of Education and Science grant No. 173040.

References

- [1] P. Kalac, L. Svoboda (2000) Food Chem. 69, 273-281.
- [2] N. W. Lepp, S. C. S. Harrison, B. G. Morrell (1987) Environ. Geochem. Health 9, 61-64.
- [3] C. Han, J. Yuan, Y. Wang, L. Li (2006) J. Trace Elem. Med. Biol. 20, 191-196.
- [4] C. Han, B. Cui, J. Qu (2009) Biol. Trace Elem. Res. 127, 278-283.
- [5] I. Mannazzu, (2001) Ann. Microbiol. 51, 1-9.
- [6] L. Bisconti, M. Pepi, S. Mangani, F. Baldi (1997) BioMetals 10, 239-246.
- [7] M. A. Zoroddu, R. P. Bonomo, A. J. Di Bilio, E. Berardi, M. G. Meloni (1991) J. Inorg. Biochem. 43, 731-738.
- [8] R. P. Sutter (1975) Proc. Natl. Acad. Sci. USA 72, 127-130.
- [9] H. P. Bode, C. Friebel, G. F. Fuhrmann (1990) Biochim. Biophys. Acta 1022, 163-170

F-17-P

THE BINDING OF NITROXIDE SPIN LABELS TO HUMAN SERUM ALBUMIN: EPR SPECTRAL DECOMPOSITION AS A TOOL FOR QUANTITATIVE ASSESSMENT

A. Popović-Bijelić, A. Pavićević, A. Ignjatović, M. Mojović, G. Bačić

*University of Belgrade, Faculty of Physical Chemistry, Studentski trg 12-16, 11000
Belgrade, Serbia*

Abstract

Conformational changes of human serum albumin (HSA), induced by certain medical conditions, may be studied by a sensitive spin-labeling technique which involves the use of nitroxide labeled stearic fatty acids that can be detected by the EPR spectroscopy. This study investigates the use of two spin-labels, 5-DS and 16-DS. The results indicate that decomposition of EPR spectra of 5-DS/HSA and 16-DS/HSA complexes may give quantitative information regarding the amounts of strongly and weakly bound spin-labels. This in turn suggest that 5-DS and 16-DS show promising potential to be used as biomarkers for detection and diagnosis of malignancies.

Introduction

Human serum albumin (HSA) is the most abundant blood plasma protein, synthesized in the liver [1]. Under physiological conditions, HSA binds endogenous and exogenous compounds, including a wide range of drugs, bilirubin, hemin, polypeptides, and free metal ions [2,3]. HSA can also bind up to nine equivalents of long chain fatty acids [3]. Metabolic changes associated with certain medical conditions like diabetes, cancer, liver, and kidney failure induce changes in HSA conformation, thus affecting its ligand binding affinity and capacity. Spin-labeled fatty acids are used to detect conformational changes in HSA by electron paramagnetic (EPR) spectroscopy [4,5]. Current literature data suggest the use of 16-doxyl stearic (16-DS) acid spin-label due to its structural congruence with HSA and the position of its nitroxide group at the terminal part of the fatty acid chain [6]. It has been proposed that the EPR spectrum of the bound 16-DS to HSA is composed of three components, strongly bound, weakly bound, and the unbound spin-label [7]. The aim of this work was to compare the binding affinity of two spin-labels, 5-DS and 16-DS, to HSA, in order to investigate their potential use as biomarkers for detection and diagnosis of malignant states. For this purpose, experimental EPR spectra of 5-DS and 16-DS complexes with HSA, recorded in different experimental conditions (varied pH and temperature) were simulated, and spectral decomposition was performed using the spectral analysis package *EPRSIM-C* [8].

Results and discussion

The typical EPR spectra of 5-DS and 16-DS bound to HSA in pH 7.4 phosphate buffer recorded at 22 °C are shown in Figure 1. There are several parameters that can be obtained from these spectra that give information regarding the binding of the spin-label to HSA. These are half-width at half height ($W_{1/2}$) of the low-field EPR line and the distance between the two outer EPR peaks ($2A_{||}$) [5]. It is observed that the spectral widths ($2A_{||}$) of the 5-DS/HSA and 16-DS/HSA complexes are different (69.5 ± 0.5 G for 5-DS, and 65.5 ± 0.5 G for 16-DS), indicating that 5-DS is more immobilized when bound to HSA, as observed in [5,9]. In addition to these parameters, it is possible to quantificate the amount of the bound and unbound spin-labels by EPR spectral decomposition.

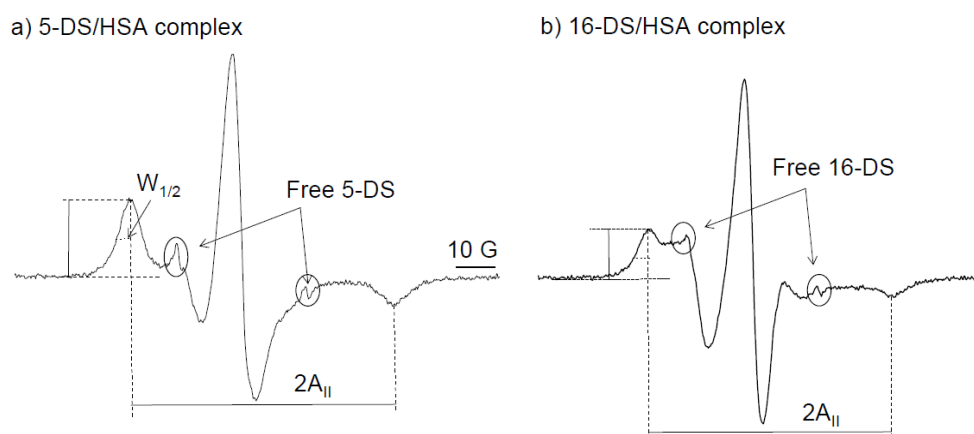


Figure 1. EPR spectra of a) 5-DS/HSA and b) 16-DS/HSA complexes incubated for 30 min at 22 °C. The concentration of HSA (in 0.9 % NaCl, pH 7.4 phosphate buffer) was 0.1 mM, and the ratio of spin-label to protein concentration was 2.

It has been shown that HSA undergoes reversible conformational changes at different pH values [3]. Between 2.7 and 4.3 it is in the fast-migrating form, between pH 4.3 and 8.0 in the neutral form, and at pH > 8.0 in the basic form. Also, the secondary structure of HSA changes with increased temperature (i.e. loss of alpha helix) [10]. Therefore, the shapes of EPR spectra of spin-labels bound to HSA depend on pH and temperature, as previously reported [6]. In this work, we have recorded EPR spectra of 5-DS/HSA and 16-DS/HSA complexes in three different experimental conditions, pH 7.4 and $T = 22$ °C, pH 8.2 and $T = 22$ °C, and pH 7.4 and $T = 37$ °C, in order to investigate how pH and temperature affect the extent of binding. Each experimental spectrum was simulated using a five-component model that takes into account isotropic tumbling (ISO), isotropic spin-exchange label-label (LLE) and label-broadening agent (LBE), anisotropic tumbling with full (MEM) and partial averaging (MES) of all rotations [8]. The contributions from each component for both spin-labels are summarized in Table 1.

Table 1. Five EPR spectral component contributions of the simulated spectra of 5-DS/HSA and 16-DS/HSA complexes at different pH values and temperatures.

EPR spectrum	ISO*	LLE	LBE	MEM	MES	MES/MEM
5-DS/HSA, pH 7.4, 22 °C	0.010	0.048	0.010	0.158	0.774	4.9
5-DS/HSA, pH 8.2, 22 °C	0.010	0.047	0.015	0.108	0.819	7.6
5-DS/HSA, pH 7.4, 37 °C	0.010	0.038	0.009	0.161	0.782	4.9
16-DS/HSA, pH 7.4, 22 °C	0.013	0.007	0.006	0.367	0.607	1.7
16-DS/HSA, pH 8.2, 22 °C	0.013	0.017	0.006	0.417	0.548	1.3
16-DS/HSA, pH 7.4, 37 °C	0.019	0.022	0.006	0.403	0.550	1.4

*The goodness of fits for all simulations was < 5 . Abbreviations are given in the text.

The spectral width of the MES simulation component is greater than that of the MEM component (data not shown), therefore we propose that MES and MEM correspond to the strongly, and weakly HSA bound spin-labels, respectively. The results show that 5-DS binds with higher affinity to HSA than 16-DS since the MES/MEM ratio for 5-DS is three times higher than that for 16-DS.

Conclusion

This study shows that the EPR spin-labeling method which is used for detection of conformational changes in HSA may be improved by utilizing two spin-labels, 5-DS and 16-DS and subsequent decomposition of EPR spectra of 5-DS/HSA and 16-DS/HSA complexes. The quantitative information regarding the amounts of strongly and weakly bound spin-labels is essential for the evaluation of malignancy-induced structural modifications of HSA.

Acknowledgment

The realization of this study was supported by the Ministry of Education and Science of the Republic of Serbia (project #41005).

References

- [1] D. C. Carter et al, *Science*, 1990, 249, 302-303.
- [2] M. Fasano et al, *IUBMB Life*, 2005, 57, 787-796.
- [3] G. Fanali, *Mol. Aspects Med.*, 2012, 22, 209-290.
- [4] R. C. Perkins et al, *Biochemistry*, 1982, 21, 4059-4064.
- [5] T. G. Gantchev et al, *Biochim. Biophys. Acta*, 1990, 1037, 422-434.
- [6] A. Gurachevsky et al., *Biochem. Biophys. Res. Comm.*, 2007, 360, 852-856.
- [7] S. C. Kazmierczak et al, *Clin. Chem.*, 2006, 52, 2129-2134.
- [8] J. Štrancar, http://www.ijs.si/ijs/dept/epr/EPRSIMC_overview.htm
- [9] M. K. Slane et al., *Magn. Res. Med.*, 1986, 3, 699-706.
- [10] A. K. Shaw et al, *J. Photochem. Photobiol. B: Biology*, 2008, 90, 69-77.

F-18-P

ORIENTATION OF CELL WALL POLYMERS IN A CORN STEM (*Zea mays L.*) - POLARISED FTIR STUDY

J Simonović¹, J Stevanic², D Đikanović¹, L Salmén², K. Radotić¹

¹ *Institute for multidisciplinary research, University of Belgrade, Kneza Višeslava 1, 11000 Belgrade, Serbia*

² *Innventia, Box 5604, SE-114 86 Stockholm, Sweden*

Abstract

Mechanical and physical properties of plant fibres are dependent on the orientation of constituent polymers (cellulose, hemicellulose, lignin). Fourier transform infrared (FTIR) microscopy was used to examine the orientation of the main plant polymers in transversal and longitudinal direction of the isolated cell wall of the corn stem. Polarised FTIR measurements indicated an anisotropy, i.e. orientation of the cellulose microfibrils that was more or less parallel to the longitudinal axis of the cell wall. The xylan appeared to have a close link to the orientation of the cellulose and, thus, an orientation more parallel to the axis of the cell wall. Lignin was also found to be organised in a parallel way in relation to the longitudinal cell wall axis, as well as to the cellulose.

Introduction

Cell wall can be considered as a nano-composite in which cellulose, lignin and hemicelluloses are interconnected in a specific manner. It is well recognised that the cell wall development of cell wall expansion and deposition implies an anisotropic arrangement of the cell wall components. Structural organisation of the cell wall and related polymers is important for both mechanical properties of plants and chemical reactions occurring in the wall space, especially in the response to stress. Understanding the arrangement and anisotropy of the polymers in the CW is important for understanding the mechanical properties of plant, which has implications in plant response to stress, but also in possible applications of corn as a source of new biomaterials. By using imaging FT-IR microscopy, run in transmission mode and at different polarisation modes (from 0° to 90°), it is possible to follow the chemical variability and the orientation of cell wall polymers [1]. The orientation of cellulose, glucomannan, xylan and lignin, as essential components of the wood, were analysed by iFTIR with regard to the sample axis.

Materials and methods

The purified isolated cell wall material was obtained from corn (*Zea mays L.*) stem by methanol extraction and subsequent purification using a series of solvents (phosphate buffer, 1% Triton X-100, 1M sodium chloride, distilled water, methanol, acetone) [2]. FTIR microscopy measurements were carried out using a Spectrum Spotlight 400 FTIR Imaging System (Perkin Elmer Inc, Shelton, CT, USA). Spectral resolution: 8 cm⁻¹; spectral range: from 1800 cm⁻¹ to 720 cm⁻¹.

F-18-P

Polarisation: the incident IR radiation was polarised by a gold wire grid polariser from 0° to 90° polarisation in relation to the fibre orientation with intervals of 5° . The sample was mounted on the sample stage as parallel as possible to the orientation of the 0° polarisation. The IR spectra were processed by the software Spotlight 1.5.1, HyperView 3.2 and Spectrum 6.2.0 (Perkin Elmer Inc., Shelton, CT, USA) [1].

Results and discussion

From the in-depth study of polymer orientation, three areas from the sample were selected. The transmission spectra recorded at 0° and 90° polarisation modes were processed using a ratio function to produce an orientation spectrum ($R = A_{0^\circ} - A_{90^\circ}$), where R is the anisotropy spectra, indicating the orientation of components, A_{0° is the absorbance spectra recorded at 0° and A_{90° is the absorbance spectra recorded at 90° . Spectral signals related to absorptions from cellulose, xylan and lignin in the wavenumber range between 1800 cm^{-1} and 720 cm^{-1} can be identified. Figure 1 a) shows the average absorbance spectra at 0° and 90° polarization angle and Figure 1b) shows the average orientation spectra for the corn stem cell wall. In Figure 1b), the positive signals indicate that their corresponding functional groups are arranged in a more parallel orientation to the fibre axis, and the negative signals indicate that their corresponding functional groups are arranged in a perpendicular orientation to the fibre axis.

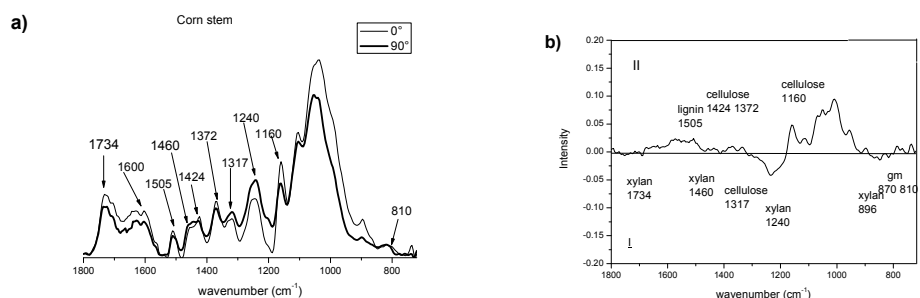


Figure 1. a) Average absorbance spectra of corn stem cell wall at 0° and 90° polarization angle; b) The average orientation spectra of corn stem cell wall.

The relative absorbance spectra are presented (Figure 2) as specific absorption peaks ($RA = (I_p - I_{\min}) / (I_{\max} - I_{\min})$) where RA is relative absorbance, I_p is intensity of the absorbed IR radiation at a given angle of the polarisation, P , I_{\max} is maximal intensity observed for a given vibration and I_{\min} is minimal intensity observed for a given vibration. These relative absorbance values were presented in relation to the angle of the incident IR polarisation (from 0° to 90°).

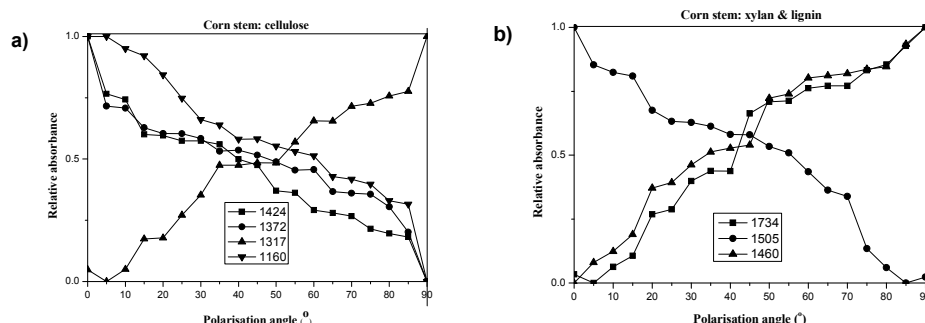


Figure 2. The relative absorbance of IR specific absorption wave numbers plotted against the polarisation angle for the different wood polymers for corn stem.

It is evident (Fig. 2a) that the three cellulose peaks (1160 cm^{-1} , 1370 cm^{-1} and 1424 cm^{-1}) [3-5] had high absorption levels at low polarisation angles, which is a consequence of a more parallel orientation of the corresponding groups to the CW longitudinal axis. The fourth cellulose peak (the perpendicular signal at 1317 cm^{-1}) had the greatest intensity at a high polarisation angle, due to the perpendicular orientation of the corresponding group (Fig. 2a). For the xylan, the characteristic band signals (1460 cm^{-1} , 1734 cm^{-1}) [3-5] increased with an increase in the polarisation angle, in the maple and spruce samples. Due to the parallel orientation of these side groups in xylan, an orientation parallel to the longitudinal CW axis is indicated (Fig. 2b). For the lignin, the characteristic band signals (1505 cm^{-1} and 1600 cm^{-1}) [3-5] decreased with an increase of the polarisation angle (Fig. 2b), indicating that lignin is organised in parallel with the longitudinal CW axis in both wood samples.

Conclusions

It has been demonstrated here that xylan is oriented in parallel to the cellulose and more or less parallel to the axis of a cell wall, in isolated CW fragments from corn stem. There was also a clear indication of lignin being orientated parallel to the longitudinal CW axis.

Acknowledgements

This work was supported by Ministry of Education and Science of Republic Serbia (Project #173017) and COST Action FP0802.

Reference

- [1] J. S. Stevanic, L. Salmén, *Holzforschung*, 2009, 63, 497-503.
- [2] M. Chen et al, *Phytochem. Anal.*, 2000, 11, 153-159.
- [3] R. H. Marchessault, *Pure Appl. Chem.*, 1962, 5, 107-129.
- [4] R. H. Marchessault, C. Y. Liang, *J. Polym. Sci.*, 1962, 59, 357-378.
- [5] M. Åkerholm et al, *Carbohydr. Res.*, 2004, 339, 569-578.

F-19-P

ANALYSIS OF THERMAL DENATURATION OF PEPSIN ON BASIS OF MALDI-TOF MS AND PAGE EXPERIMENTAL DATA

V. Pavelkić¹, K. Antić¹, M. Babić¹, K. Gopčević², M. Petković³

¹*Institute "Kirilo Savić", Vojvode Stepe 51, Belgrade, Serbia;*

²*School of Medicine, University of Belgrade, Višegradska 26, Belgrade, Serbia;*

³*Vinca Institute for Nuclear Sciences, POBox 522, Belgrade, Serbia*

Abstract

To obtain detailed information about properties of pepsin in thermal denaturing conditions, polyacrylamide gel electrophoresis (PAGE) and matrix-assisted laser desorption-ionization time-of-flight mass spectrometry (MALDI-TOF MS) experimental data were analyzed. These methods were used to analyze the changes in the structural properties of pepsin molecule subjected to broad-range temperature variations, from 25 °C to 70 °C, and pH range from 1 to 4.

Introduction

Porcine pepsin A (EC 3.4.23.1) belongs to the aspartic proteases. It is composed of two similar domains and is characterized by having two catalytic acid residues in the binding site [1]. It was shown that thermal modification of pepsin (followed by calorimetric studies) is complex process. It passes through two stages at different temperatures [2]. The aim of this work was to investigate influence of temperature and pH on porcine pepsin stability in a view of MALDI-TOF MS and PAGE methods.

Experimental

MALDI-TOF mass spectra were acquired on a Voyager Biospectrometry DE Pro Workstation (PerSeptive Biosystems, Framingham, MA, USA). The system utilises 20 Hz pulsed nitrogen laser emitting at 337 nm. The spectra were acquired in two mass ranges: from 500 Da to 10 kDa and from 10 kDa to 50kDa in the linear mode and under delayed extraction conditions. Low mass gate was switched on (at 450 Da and at 3500 Da, respectively). All spectra represent the average of 400 single laser shots.

Result and discussion

There are several peaks detectable in the high mass range (10 – 50 kDa) of the positive ion MALDI-TOF mass spectra of pepsin: at m/z about 34 kDa, which corresponds to the single positively charged ion of the protein, and at m/z about 17 000 which arises from the double-charged molecule. On the other hand, a series of peaks are detectable in the low mass range (500 Da to 10 kDa). The intensity and number of these peaks differs in dependence on the experimental conditions, *i.e.* pH and temperature applied. In Figure 1, MALDI-TOF mass spectra of pepsin incubated at pH (1- 4) and at various temperatures (from 25 °C to 70 °C) are shown. Two peaks arising from pepsin are

F-19-P

detectable in the left upside panel: at $m/z=34$ kDa and at $m/z=17$ kDa, which corresponds to the single- and double-positively charged molecule.

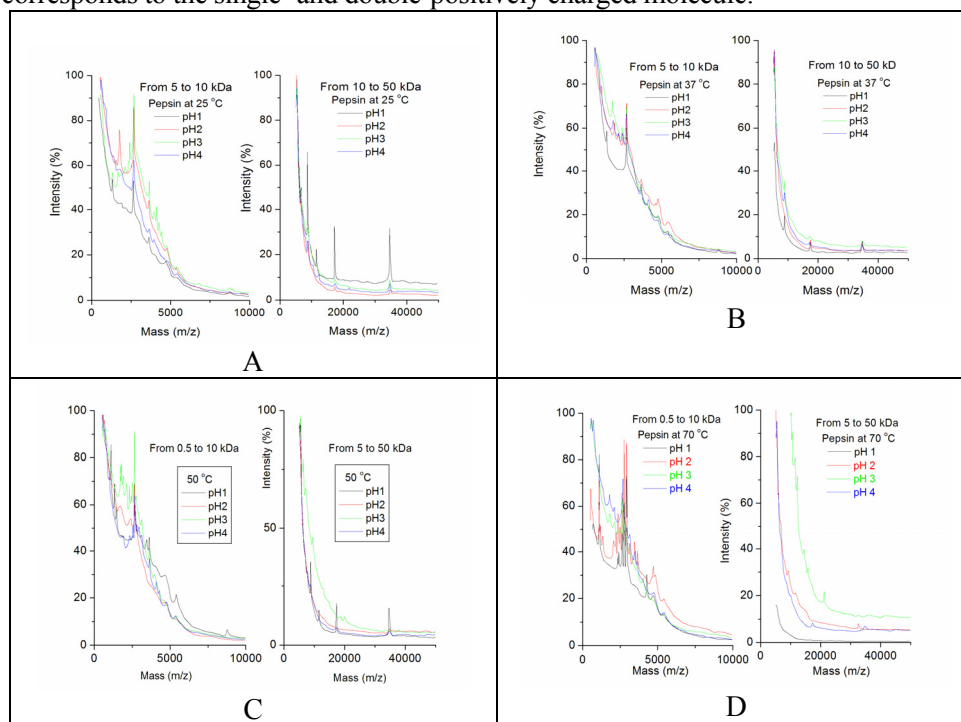


Figure 1. MALDI-TOF mass spectra of pepsin incubated at pH 1, 2, 3, and 4, at 25 °C, 37 °C, 50 °C and 70 °C (A, B, C, D respectively). The mass range from 0.5 to 10 kDa are presented at the left side of each panel A, B, C and D, whereas on the right, are presented the spectra acquired in the mass range from 10 to 50 kDa.

The intensity of these peaks depends on the temperature: at the lowest temperature applied, these peaks are the most intense, whereas at 70 °C they are neglected. Small difference can be observed between the samples incubated at 37 °C and 50 °C (Fig 1B and 1C). In the low mass range, there are a number of peaks that most probably represent the peptide-degradation products of pepsin. The most intense signals arise from the group of peaks with similar masses that appear between $m/z=2500$ and $m/z=3000$. The higher number of peaks is, detectable in the spectra of the sample incubated at 70 °C, that implies the highest number of peptides that arise from pepsin in comparison to samples incubated at lower temperatures. With increase in the temperature the intensity of peaks arising from the native molecule decrease, along with increase in the number of peptides that arise from the molecule. There are, differences observed at pH 3 in comparison to pH1 and 2: the number of peaks arising from peptides in the low mass range is lower and the peaks that correspond to the native molecule disappear already at 50 °C. The lowest number of peaks in the low mass region along with the rather low intensity of these peaks is detected in the spectra of pepsin incubated at pH 4 and at various temperatures. The differences in the intensities of the peaks that arise from the native molecule (higher mass range) are not

F-19-P

so pronounced like when the samples were incubated at lower pH values: the two peaks that correspond to the protein could be clearly observed even at the highest applied temperature.

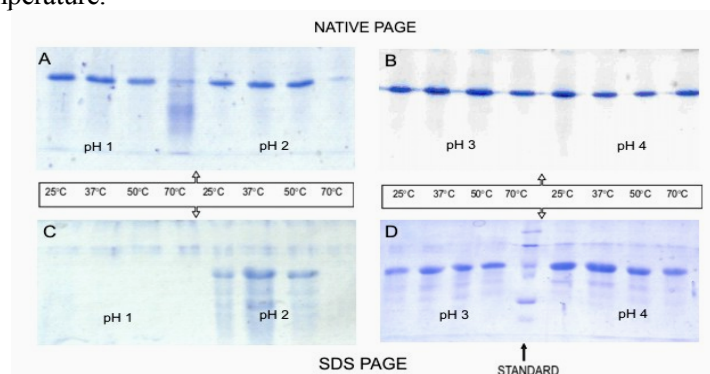


Figure 2. Native (A and B) and PAGE (C and D) electrophoregrams of pepsin on polyacrylamide gel according to the Laemmli procedure [3].

Native PAGE electrophoregrams show pepsin band at R_s value (distance of protein migration vs. distance of tracing dye migration) that corresponds to its native state at all investigated pH and temperature, except at pH 1 and 70°C, which yields 3 additional bands due to denaturation of the protein. On SDS-PAGE electrophoregrams (Figure 2C and 2D), there is an absence of protein band at pH 1, which may be due to the achievements of iso-electric point of pepsin. At pH 2, 3, and 4 (Figure 1D) besides the main pepsin band, there are numbers of bands that represent the fragments with smaller molecular masses – degradation products of denaturated pepsin. Calculated molecular weights of those fragments are in the range from 18 – 28 kDa.

Conclusion

These results imply that the protein is most stable at pH 4. There is an inverse relationship between the presence and intensity of the peaks in the higher mass range and in the lower range obtained from MALDI-TOF MS experiments. The results obtained by two methods are in good agreement.

Acknowledgement

This study was supported by Ministry of Education and Science of Republic of Serbia, Project OI 172015.

References

- [1] T. Tanaka, R. Y. Yada. *Biochem J.*, (1996), 315, 443-446.
- [2] V. M. Pavelkic, M. V Beljanski, K. M. Antic, M. M. Babic, T. P. Brdaric, K. R. Gopcevic, *RJPC* (2011), 85, 2245-2250.
- [3] Laemmli, *Nature*, 1970, 227, 680-685.

F-20-P

HYDROXYL RADICAL GENERATION AND CARBON CENTRE DEPLETION IN THE ROOT CELL WALL ISOLATE ENRICHED WITH COPPER

F. Morina¹, S. Milić¹, M. Mojović², S. Veljović Jovanović^{1*}

¹University of Belgrade, Institute for multidisciplinary Research

²University of Belgrade, Faculty of Physical Chemistry

Abstract

Copper is often accumulated in contaminated soils such as open cast mines, and is toxic to plants. Effect of excess Cu (20 μ M) on free radicals generation in the cell wall was investigated in the root cell wall isolated from *Verbascum thapsus* L. plants. Electron paramagnetic resonance (EPR) spectroscopy of cell wall isolates containing the spin-trapping reagent, 5-diethoxyphosphoryl-5-methyl-1-pyrroline-*N*-oxide (DEPMPO), was used for detection and differentiation between free radicals. EPR analysis showed an increase of DEPMPO/OH adduct concentration induced by Cu accompanied by the decrease of concentration of carbon center (DEPMPO/CH₃) adduct originally determined in the cell wall of control plants. This reaction was suppressed by boiling the cell wall with SDS to denaturate proteins. We show that Cu induced \cdot OH accumulation in the cell wall is enzyme dependent.

Introduction

Excess copper in the soil originating from anthropogenic activities is taken up by the roots leading to perturbation of redox processes at first in the apoplastic space and cell wall matrix, and then to deleterious effects for cell metabolism [1]. As a redox active metal, Cu²⁺ can catalyze formation of reactive oxygen species (ROS) *via* Fenton-type reactions. Apoplastic antioxidants such as ascorbate, phenolic compounds, and enzymes superoxide dismutase and peroxidase, play an important role in maintenance of redox homeostasis [2]. The involvement of ROS in the processes of lignification, suberization, redox signalling and elongation has been well known. This implies a great potential of Cu to interfere with plant development and biomass production, but also a signalling pathway upon pathogen attack. It has been shown that addition of Cu to *Nicotiana tabacum* cell cultures resulted in extracellular accumulation of H₂O₂ (so called, oxidative burst) qualifying Cu as an elicitor of hypersensitive response [3]. Despite the numerous amounts of descriptive data, no explanation has been put forward on the mechanism of copper induced oxidative stress so far.

Material and Methods

Eight weeks old *Verbascum thapsus* L. plants were exposed to 20 μ M Cu in hydroponic solution for three weeks. Roots were washed in 10 mM Na₂EDTA

F-20-P

(pH 7.0) and rinsed with distilled water. Cu was quantified with ICP-OES. Accumulation of free radicals in the root cell wall isolates was determined by EPR, according to [4]. Cell wall proteins were denaturated after addition of 10% SDS and heat treatment of cell wall isolates for 10 min at 95°C, and pellet containing cell wall constituents was used. Simulation parameters used for EPR spectra analysis were: DEPMPO/OH (aP = 46.70; aN = 13.64; aH = 12.78), DEPMPO/CH₃ (aP = 46.95; aN = 14.56; aH = 21.80).

Results and Discussion

Cu is accumulated in a concentration dependant way in the roots but not in the leaves (Table 1). It is known that plants cope with Cu toxicity by retention of excess Cu in the roots and immobilization in the cell wall [1].

Cu (μM)	Cu (mg/kgDW)	
	root	leaf
Control	9.9±7	7±1
6	239±12	12±3
10	497±11	11±5
20	1546±13	12±3

Table 1. Copper concentration in the roots and leaves of *V. thapsus* after 3 weeks of treatment with different Cu concentrations in the hydroponic solution. Values are means ± STDEV from 8 plants.

We have previously shown that the quantity of the redox active metals (Fe and Cu) did not change significantly by the treatment of cell wall isolates with SDS/heat [4], which confirmed that Cu, taken up by the roots, was tightly bound to cell wall components. EPR measurements of root cell wall isolates were performed using spin trap DEPMPO, which can distinguish among various radicals [4]. EPR measurements showed an increased accumulation of both, DEPMPO/OH and DEPMPO/CH₃ adducts, in Cu treated roots compared to the controls (Fig. 1A,B). To test the involvement of enzymes in these reactions, we performed EPR measurements with cell wall fractions after protein denaturation (Fig. 1 C,D). Signals of DEPMPO adducts in the cell wall fractions were completely suppressed in both control and Cu treated plants, indicating the importance of cell wall associated proteins in free radicals generation. Incubation of such denaturated cell wall fraction with 20 μM Cu did not cause any increase of the EPR signal intensity upon addition of DEPMPO (Fig. 1E). Only after addition of 1 mM H₂O₂, the significant increase of DEPMPO/OH was measured which could be explained by the influence of the Fenton reaction (Fig. 1F). Contribution of CH₃ radical increased during incubation of the cell wall with DEPMPO in the roots of control plants (data not shown). However, concentration of DEPMPO/CH₃ adduct decreased in the Cu treated roots, as shown by the spectral simulation, while the concentration of DEPMPO/OH has increased (Fig. 2). The results indicated that consumption of either phenolics or polygalacturonic acid occurred during the production of •OH.

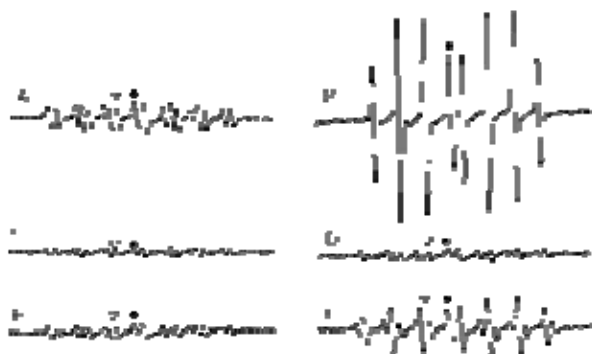


Figure 1. EPR spectra of root cell wall isolates of A) control and B) Cu treated plants; after protein denaturation with SDS/heat treatment; C) control and D) Cu treatment 20 min after addition of DEPMPPO; E) cell wall with denatured proteins incubated with 20 μ M Cu and F) 10 min after addition of 1 mM H_2O_2 . ● and ∇ mark characteristic signal of DEPMPPO/OH and DEPMPPO/ CH_3 respectively.

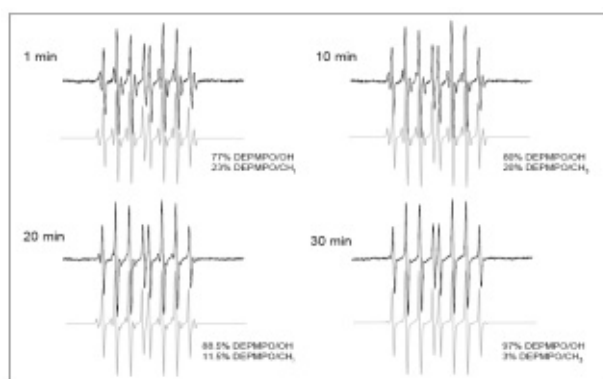


Figure 2. EPR spectra of the root cell wall of Cu treated plants 1, 10, 20 and 30 min upon addition of DEPMPPO. Computer simulations of the contribution of DEPMPPO/OH and DEPMPPO/ CH_3 spin adducts were performed using parameters described in Materials and Methods.

Conclusion

We have shown that the excess of Cu tightly bound to the cell wall in Cu treated plants induced $\bullet OH$ generation through the enzyme dependent consumption of the CH_3 radical.

Acknowledgments

This research was supported by the III43010 project funded by the Ministry of Education and Science of the Republic of Serbia.

References

- [1] S. Sharma, K. J Dietz, Trends Plant Sci., 2009 14, 43–50.
- [2] U. Takahama, T. Oniki, Physiol Plantarum, 1997, 101, 845-852.
- [3] T. Raeymaekers, G. Potters, H. Asard, Y. Guisez, N. Horemans, Protoplasma, 2003, 221, 93–100.
- [4] B. Kukavica, M. Mojović, Z. Vučinić, V. Maksimović, U. Takahama, S. Veljović-Jovanović, Plant Cell Physiol., 2009, 50, 304–317.

F-21-P

STRUCTURE AND MINERAL ELEMENT COMPOSITION OF THE LYOPHILISED FRESHWATER BRYOZOAN *HYALLINELA PUNCTATA*

B. Pejin¹, B. Matović², M. Nikolić¹, A. Hegediš¹, I. Karaman³, D. Mutavdžić¹,
A. Savić¹, M. Horvatović³, K. Radotić¹

¹*Department of Life Sciences, Institute for Multidisciplinary Research, University of
Belgrade, Serbia*

xenia@imsi.rs

²*Department for Material Science, Institute for Nuclear Sciences "Vinča",
University of Belgrade, Serbia*

³*Department of Biology and Ecology, Faculty of Sciences, University of Novi Sad,
Serbia*

Abstract

Structure of the lyophilised colonies of the freshwater bryozoan *Hyalinella punctata* (Hancock, 1850) and their mineral element composition were studied by X ray diffraction, scanning electron microscopy (SEM) and inductively coupled plasma (ICP) spectrometry for the first time ever. The X ray measurements showed amorphous structure of the bryozoan, while SEM indicated porous connected structure without regular structural motifs. Considerable presence of phosphorus (7949.69 µg/ml), sulphur (6204.7 µg/ml) and calcium (6139.58 µg/ml), as well as low heavy metal content was found by ICP. The obtained results jointly indicate the potential of the investigated animal species as a base for bioscaffolds and nanocomposites.

Introduction.

Freshwater bryozoans are sessile invertebrates that grow on submerged substrates. They live in lotic and lentic water and feed on suspended organic particles, which they capture with a whorl of ciliated tentacles. *Hyalinella punctata* (Hancock, 1850) is not a very frequent bryozoan species, but it has been noticed in more European countries including Serbia [1]. Most of previous studies have focused on bryozoans of marine origin, particularly for the reason of their bioactive natural products [2], while freshwater bryozoans have been practically neglected till date. Our structural and elemental study of the lyophilised bryozoan *H. punctata* is aimed to determine its usefulness in term of new natural material for making scaffolds for cell growth and/or the base for construction of the new bionanomaterials. Although there is an increasing number of studies on using invertebrates such are marine sponges, for making bioscaffolds for cell growth and tissue regeneration [3,4], freshwater bryozoans have not been previously studied from this aspect.

Materials and Methods

The colonies of the freshwater bryozoan *Hyalinella punctata* (Hancock, 1850) were collected in Belgrade (the river Danube, Serbia) in November 2011. Voucher specimen has been deposited in the Zoology Collection of the Department of Biology and Ecology of the University of Novi Sad, Serbia (BRY 003). The lyophilised material was used for the experiments.

Crystal structure of powdered bryozoan sample was analysed by X-ray diffraction (XRD) using filtered CuK α radiation (Siemens D5000) preceded by the angular correction with high quality Si standard. The microstructural observation of as-received bryozoan samples was performed by scanning electron microscopy (SEM), on the samples of whole tissue, using a JEOL 6300F microscope at 3 kV accelerating voltage.

Due to mineral element analysis, the lyophilised material (0.2 g) was microwave digested with nitric acid and hydrogen peroxide for 1 h. The elements were determined by an inductively coupled plasma optical emission spectrometer with axial and radial viewing plasma configuration (ICP-OES, SpectroGenesis EOP II, Spectro Analytical Instruments GmbH, Kleve, Germany).

Results and discussion

X-ray diffraction pattern (Fig. 1A) reveals significant broadening of profile diagram indicating the amorphous nature of the bryozoan sample.

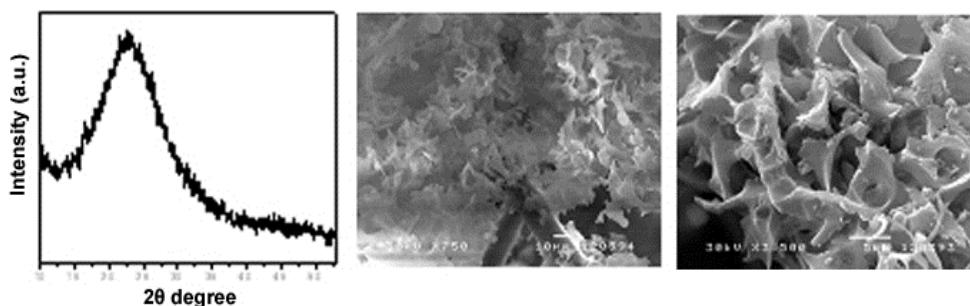


Figure 1. A) X ray diffractogram and B) SEM images of *H. punctata*.

SEM imaging of the bryozoan samples (Fig. 1B) depicts highly porous connected structure with no regular structural motifs, suitable for using as biomimetic materials.

The element composition (in $\mu\text{g/g}$ dry weight) determined by ICP is as follows: P 7949.69, S 6204.7, Ca 6139.58, Fe 3918.96, Al 3128.33, Mg 2036.46, K 1854.69, Na 695.83, Si 335.31, Mn 166.15, Zn 80.89, Ba 24.71, Cu 23.48, B 15.75, Li 14.39, Sr 11.49, Pb 7.12, Cr 5.95, Ni 3.91, Mo 3.42, As 3.28, Se 1.94, Cd 1.61, Co 1.19 and Hg n.d. Considerable presence of phosphorus, sulphur and calcium, as well as non-toxic content of heavy metals [5] is obvious. The bryozoans are calcifying animals, having the structure based on calcium carbonate; indeed,

F-21-P

mineralisation of bryozoan skeleton makes these organisms proven bioindicators [6]. On the other hand, high content of sulphur may originate from its biologically active secondary metabolites containing sulfur, such as alkaloids, which have been found in considerable amounts in some other bryozoans [7]. From mineral element point of view the bryozoan based material seems to be applicative in humans, but it should be seasonally analysed.

In conclusion, the porous connected structure of the *H. punctata* together with its mineral content indicate its potential as a base for bioscaffolds and nanocomposite materials.

Acknowledgement

This work was supported by the Ministry of Education and Science of the Republic of Serbia (grants Nos. 45012, 173040, 173045, 173028 and 43007).

References

- [1] V. M. Martinovic-Vitanovic, V. M. Milankov, V. I. Kalafatic, *Limnologica*, 2010, 4, 73-81.
- [2] J. H. Sharp, M. K. Winson, J.S . Porter, *Nat. Prod. Rep.*, 2007, 24, 659–673.
- [3] D. Green, D. Howard, X. Yang, M. Kelly, R. O. C. Oreffo, *Tissue Eng.*, 2003, 9, 1159-1166.
- [4] Z. Lin, K.L. Solomon, X. Zhang et al, *Int. J. Biol. Sci.*, 2011, 7, 968-977.
- [5] J. Neustadt, S. Pieczenik, *Integr. Med.*, 2007, 6, 26-32.
- [6] C. Lombardi, R. Rodolfo-Metalpa, S. Cocito, M. C. Gambi, P. D. Taylor, *Marine Ecol.*, 2011, 32, 211-221.
- [7] S. Eisenbarth, M. Gehling, A. Harderc, B. Steffana, *Tetrahedron*, 2002, 58, 8461–8464.

F-22-P

THE EFFECT OF GAMMA IRRADIATION ON ETHYLENE PROPYLENE DIENE TERPOLYMER/CHLOROSULPHONATED POLYETHYLENE RUBBER BLEND CURED WITH DIFFERENT SYSTEMS

G.Marković¹, M. Marinović-Cincović², V. Jovanović³, S. Samaržija-Jovanović³,
J. Budinski-Simendić⁴

¹Tigar, Nikole Pašića 213, 18300 Pirot, Serbia; (gordana1markovic@gmail.com)

²University of Belgrade, Institute of Nuclear Science Vinča,

³Faculty of Natural Science and Mathematics, University of Priština,

⁴University of Novi Sad, Faculty of Technology,)

Abstract

This work aimed to study the effects of gamma irradiation on the properties of ethylene propylene diene terpolymer/chlorosulphonated polyethylene rubber blend (EPDM/CSM) 50/50 reinforced with 50 phr (parts per hundred rubber) of carbon black and crosslinked either with sulphur/tetramethyl thiuram disulphide or dicumyl peroxide. Irradiation dose rate were 100, 200 and 400 kGy h⁻¹. It was observed that doses higher than 200 kGy practically destroy the assessed properties for all obtained elastomeric materials, irrespective of used curing system. However samples cured with sulphur showed a pronounced decrease in mechanical properties.

Introduction

Polymer blending was recognized in the last few decades as the most promising way to prepare new material with tailored individual properties. Their chemical and physical properties make them suitable as engineering materials, for chemical industry, electric insulators and many other uses [1]. The use of high energy radiation was already proposed as an advanced technique to allow the industrial reprocessing of scrap rubber [2] and in particular IIR. This work aims to study the effects of gamma irradiation on the properties of vulcanized ethylene propylene diene terpolymer/chlorosulphonated polyethylene rubber blend (EPDM/CSM) (50/50) reinforced with 50 phr of carbon black and cured with sulfur and peroxide.

Experimental

For elastomeric materials preparation two network precursors was used: (a) ethylene propylene diene terpolymer (Vistalon 2504), was supplied by Exxon Mobil, France and (b) Chlorosulfonated polyethylene rubber (Hypalon 40S), was supplied by Du Pont, USA; Stearic acid (2 phr) and zinc oxide (5 phr) were used as activators of vulcanization. Other materials were added: carbon black, type N550 Degussa, Milan, Italy with a high structure (Dibutyl phthalate (DBP) = 121 ml/100

g) and average size of primary particles (40–48 nm) was used as a filler. Tetramethylthiuram disulphide (TMTD; Bayer, Leverkusen, Germany; 2 phr, magnesium oxide (MgO; Bayer, Leverkusen, Germany; 0.8 phr); Sulphur (Zorka, Sabac, Serbia; 1 phr) and Dicumyl peroxide, (Akzo Nobel, Flexsys Holandia 10phr were used as a curing system for blends.

Compounding was done in accordance with ASTM D 3184-89 using a two-roll mill at room temperature. Cure characteristics were studied using a Monsanto Moving Die Rheometer (MDR 2000) according to ASTM D 2240-93. Tensile testing was carried out with a Monsanto Tensometer M500. Irradiations have been performed in air in the Co-60 radiation sterilization unit with the dose rate of 100, 200 and 400 kGy h⁻¹.

Results and Discussion

Mechanical properties were assessed for rubber mixtures, using curing systems with sulfur and peroxide, as a function of irradiation dose. Results for tensile strength at different irradiation doses were presented in Fig. 1.

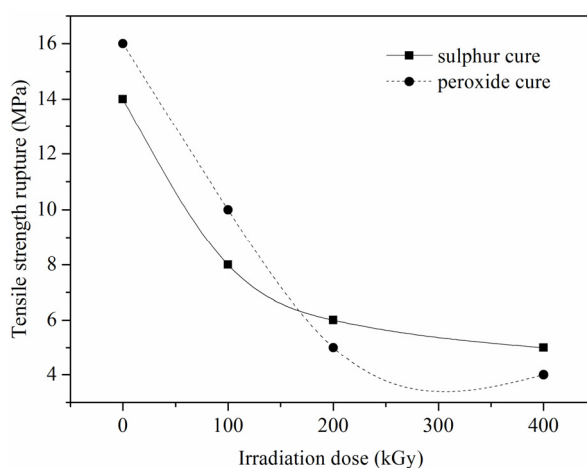


Figure 1. Tensile strength rupture for EPDM/CSM-rubber blend cured with sulfur and peroxide.

The initial stages of degradation of obtained elastomeric materials generally indicate a random breaking of bonds in the polymer chain. In fact, the vulcanized samples with “sulfur” and “peroxide” showed that tensile strength decreases proportionally with the increase in irradiation dose [3]. This decrease was caused by network chain scission. The sample vulcanized with sulfur showed initially a sharp decline in tensile strength even at low doses, probably because of the high flexibility of the tridimensional network structure, due to the presence of polysulfides (C–S–Sn–C), where $n > 1$ [4-5]. At irradiation dose of 200 kGy, the variation of tensile strength for sample cured with peroxide are lower. This is due

to the covalent bonds formed which are shorter and less flexible. When the irradiation dose is increase to 400 kGy, the variation of properties become greather.

Conclusion

The elastomeric materials obtained by different vulcanization systems have quite different sensitivities to irradiation. Sulphur systems influenced no protection of obtained samples against effect of irradiation. The highest degradation occurred in materials prepared by sulfur. It was observed that for low doses the crosslinking was preserved, where for high doses, just degradation process occurred. Samples cured with peroxide were more stable at low doses, as their properties were maintained constant, where—at higher doses they showed severe degradation. At doses higher than 200 kGy there was a major loss observed in the assessed mechanical properties for all elastomers based on EPDM/CSM rubber blends irrespective of the vulcanization system used, except for the samples cured by sulfur.

Acknowledgement

Financial support for this study was granted by the Ministry of Science and Technological Development of the Republic of Serbia (Project Numbers 45022 and 45020).

References

- [1] Z. Mohamad, Characterisation and properties of epoxidised natural rubber (ENR-50) / ethylene vynil acetate (EVA) blends, PhD thesis, 2007.
- [2] J. Manson, L. Sperling, Polymer blends and Composities Plenum Press, New York, 1976.
- [3] D. R. Paul, in D. R. Paul, S. Newman (Eds.), Polymer blends, Vol 1, Chapter 1, Academic Press, New York, 1978.
- [4] G. Mathew, R. Singh, P. Lakshminarayanan, S. Thomas, J. Appl. Polym. Sci., 61 (1996) 2035.
- [5] S. Varghese, Polym. Degrad. Stab., 1994, 44, 55

F-23-P

THE EFFECT OF γ -IRRADIATION ON THERMAL STABILITY UREA-FORMALDEHYDE RESIN WITH TiO_2 AND FURFURYL ALCOHOLE

V. Jovanović¹, S. Samaržija-Jovanović¹, G. Marković², M. Marinović-Cincović³

¹*Faculty of Natural Science and Mathematics, University of Priština: (vojani@sbb.rs)*

²*Tigar, Nikole Pašića 213, 18300 Pirot, Serbia,*

³*University of Belgrade, Institute of Nuclear Science Vinča,*

Abstract

The thermal stability of organic-inorganic nano-composites prepared by a two-stage polymerization of urea-formaldehyde resin (UF) with furfuryl alcohol (FA) and TiO_2 before and after irradiation has been investigated. The two resins of urea-formaldehyde- TiO_2 composites, namely: **Resin 1** (UF+ TiO_2) and **Resin 2** (UF + TiO_2 + FA), were synthesized. The thermal stability of obtained materials was studied by non-isothermal thermo-gravimetric analysis (TG), differential thermal gravimetry (DTG) and differential thermal analysis (DTA). UF hybrid composites have been irradiated (50 kGy) and after that their radiation stability was evaluated on the basis of thermal behavior. The free formaldehyde percentage in all prepared samples was determined. DTG peaks of both UF resin are shifted to a higher temperature after irradiation. The minimum percentage values of free formaldehyde (4% and 3%) for **Resin 1** and **Resin 2**, respectively, after irradiation dose of 50 kGy are detected.

Introduction

UF resins offer unique potential technical advantages in a variety of applications, in abundance unmatched in the competing product. Among those advantages are the above-mentioned low price, the nontoxicity of resin and resin products, and the environmental compatibility of resin bonded products, such as particleboard. As a typical amino resin, UF resin adhesive possesses some advantages, such as fast curing, good performance in the panel, water solubility and lower price [1]. Formaldehyde emissions from pressed-wood products used in home construction was one of the affecting sick building syndromes in an indoor environment. The release of formaldehyde is predominantly determined by the mole ratio of formaldehyde to urea in the adhesive system. The lower mol ratio and the lower post-production formaldehyde emission are out of the produced board. High-energy radiation is a well-known technique for modification of polymers. However, little work concerning the effects of γ -irradiation on the thermal properties of modified UF resins has been done. The goal of this work was to determine the radiation stability of the synthesized TiO_2 -based urea-formaldehyde

(UF) composite materials based on their thermal behavior. The thermal behavior of two types of TiO₂-based UF resin (unirradiated and irradiated) was investigated using non-isothermal TGA, DTG and DTA.

Experimental

The following materials were used in the study reported here: Urea (Alkaloid-Skopje, FYR of Macedonia); 35% formaldehyde (Unis-Goražde, Bosnia and Herzegovina); furfuryl alcohol and TiO₂ (Sigma-Aldrich, Germany). Two types of TiO₂-based UF hybrid composites with formaldehyde-to-urea (F/U) ratio of 0.8 were synthesized using the same procedure. Irradiations were performed in air in the Co-60 radiation sterilization unit with the dose rate of 10 kGy⁻¹ and the total absorbed dose of 50 kGy.

Results and Discussion

The thermal behavior of unirradiated and irradiated UF resins samples occurs in three and two main stages (Figure 1). The mass loss at different temperatures is summarized in Table 1. The rate of the thermal decomposition reaction before and after irradiation, shows more than one maximum rate with temperature is increasing. This behavior indicated that thermal decomposition of these resin passed through multiple stages, depending on the state of decomposition and not on the components [2,3].

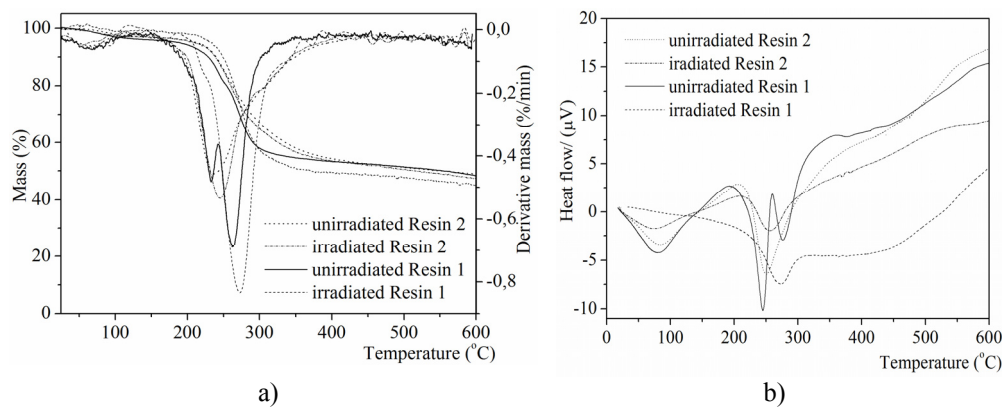


Figure 1 TGA/DTG (a) and DTA (b) curves of unirradiated and irradiated UF resin.

High-energy radiation is a well-known tool for the modification of polymers. In polymer irradiation, two phenomena occur at the same time: cross-linking and chain scission. The balance of cross-linking and scission reactions in polyolefin chains, exposed to high-energy radiation processes that produce free radicals, may result in good properties and new applications.

Table 1. DTG, DTA data of peak values, and total mass loss for unirradiated and irradiated UF resins.

Samples	Dose of γ -irradiation (kGy)	DTG peak values ($^{\circ}\text{C}$)	DTA Endothermic peak values ($^{\circ}\text{C}$)	Total mass loss (%)	Free formaldehyde (%)
Resin 1 UF + TiO ₂	0	75.1 233.1* 263.8*	80.8 245.8 276.6	51.9	15
	50	70.8* 93.8* 161.1 273.3	274.4	54.5	4
Resin 2 UF + TiO ₂ + FA	0	63.9 236.2	85.2 250.6	51.0	10
	50	59.2 245.6	76.1 256.3	52.7	3

*overlapping peaks

Conclusion

1. The free formaldehyde percentage for TiO₂-based UF resin modified with FA is less than for unmodified UF resin. The free formaldehyde percentage is significantly reduced after γ -irradiation.
2. DTG peaks of both UF resins are shifted to a higher temperature after γ -irradiation.
3. The total mass loss for TiO₂-based UF resin modified with FA is less than that of unmodified UF resin.

Acknowledgement

Financial support for this study was granted by the Ministry of Science and Technological Development of the Republic of Serbia (Projects Numbers 45022 and 45020).

References

- [1] B. D. Park, S. M. Lee, J. K. Roh, Eur. J. Wood Prod., 2009,67,121-123.
- [2] K. Siimer, T. Kaljuvee, T. Pehk, I. Lasn, J Therm Anal Calorim., 2010,99,755–762.
- [3] S. Samaržija-Jovanović, V. Jovanović, S. Konstantinović, G. Marković, M. Marinović-Cincović, J. Therm. Anal. Calorim., 201,104,1159–1166.

CHARACTERIZATION OF DOSIMETERS USED IN RADIATION PROCESSING

B. Šećerov, I. Janković, M. Dramićanin

*Vinča Institute of Nuclear Sciences, University of Belgrade, 11001 Belgrade,
P.O.Box 522, Serbia*

Abstract

Aerial L-alanine pellet dosimeter is characterized as the dispersion of dose measurement values in order to determine the level of uncertainty caused by dosimeter itself. The results of repeated measurements indicate that the uncertainty of 1.2% could be attributed to the homogeneity of alanine in dosimeter pellets. It was obtained by analyzing the results of measurements of the different dosimeters from the same batch that the uncertainty due to difference in dosimeter mass is 1%. The total uncertainty due to dosimeter itself is 1.5%.

Introduction

The quality of products treated in radiation processing depends on absorbed dose in product. During irradiation process all parts of product have to receive an absorbed dose within certain prescribed limits. The integral part of absorbed dose measurements in radiation processing is uncertainty (a parameter associated with the result of measurement that characterizes the dispersion of the values that could reasonably be attributed to the measured or derived quantity). In order to establish the accuracy of an absorbed dose measurement it is necessary to first identify and then quantify all possible sources of uncertainty. Hence, the uncertainty associated with an absorbed dose measurement can be estimated by considering the individual components together. There are some international guides for estimating the uncertainty of absorbed dose measurements [1, 2, 3], but there is no recommendation for exact measurement of uncertainty. In this article we have tried to determine the uncertainty due to dosimeter itself experimentally.

Experimental

L-alanine pellet dosimeters (diameter 3 mm, thickness 1.5 mm and mass between 37.5 – 37.6 mg) were purchased from Aerial (Illkirch, France). In the first experiment, the alanine dosimeters were put together with ethanol-chlorobenzene (ECB) dosimeters in the standard cardboard boxes filled with products for irradiation. Boxes were irradiated in common sterilization cycles in Radiation Plant of the Vinča Institute [4]. 40 pairs of alanine - ECB dosimeters were irradiated with nominal dose of 25 kGy and six pairs were irradiated with nominal dose of 12 kGy. In the second experiment, the alanine dosimeters were irradiated by ^{60}Co laboratory source [5] of about 10^{12} Bq activity. The dosimetry at the source was done by Fricke solution. Four alanine pellets were placed in polystyrene vial. Dosimeters in vials were irradiated with doses between 5 - 30 kGy and each dose was repeated three times.

The absorbed doses were measured by the oscillotitrator OK – 302/2 for ECB dosimeters, while the alanine dosimeters were measured by MiniScope MS300 ESR spectrometer using Aer'EDE Version 2.0.4. software for dose calculation. The measurements were repeated each day for five days after irradiation.

Results and Discussion

The results of absorbed doses measured by oscillotitrator and ESR spectrometer are compared for the pairs of alanine and ECB dosimeters. The differences in all examined pairs are less than 2% for 25 kGy nominal dose. For 12 kGy nominal dose the difference is slightly higher. This is expected since the calibration curve residuals for ECB dosimeter have the same trend [6], with the relative error being higher when the measured value decreases.

The results of measurements of alanine dosimeters that were repeated each day for five days after irradiation were analyzed. They can give us the information of homogeneity of alanine in dosimeter pellets. Aer'EDE Version 2.0.4. software calculates absorbed dose taking into account the correction factor of spectrometer variation during measurements using reference dosimeter. The standard deviation of reference value is 1.4% for all measurements. This value can be attributed to standard uncertainty due to instability of instrumentation. 70% of measured dosimeters showed the standard deviation of absorbed doses in this range. 91 % dosimeters have standard deviation of absorbed doses up to 2% and 9 % of measured dosimeters standard deviation between 2 % and 3 %. As the greater part of dosimeters has standard deviation near the midpoint, the standard uncertainty due to difference in homogeneity of alanine in dosimeter pellets is determined as type B [1] and the value is 1.2%.

The results of absorbed dose measurements of alanine dosimeters irradiated by laboratory source are presented in Fig.1. It is obvious that the standard deviation for all measurements is up to 3 % with no dose influence. In this case, the standard deviations of measured absorbed doses were calculated using 4 pellet dosimeters, so beside the homogeneity of alanine in pellets there is the difference in mass of dosimeters. The standard uncertainty is determined as type A [1]. The obtained value of 1.5% is the total uncertainty. As the total uncertainty is the square root of the sum of the squares of the individual components, it is obvious that 0.2% standard uncertainty in mass gives rise of up to 1% standard uncertainty due to the difference in mass of dosimeter pellets. The uncertainty due to the difference in mass of dosimeter pellets is in very close connection with the measurement parameters of ESR signal. When the measurement parameters are adjusted to give us high intensity of ESR signal (in this case modulation amplitude was 6 G and the noise was reduced by 5 passes), i.e. the highest measurement sensitivity, the value of uncertainty due to difference in mass of dosimeter pellets was also the highest. If the sensitivity of measurement is less it is more difficult to detect the difference in mass. However, the total uncertainty of measurement is not getting smaller by reducing the sensitivity of measurements, since the uncertainty due to instability of instrumentation increases.

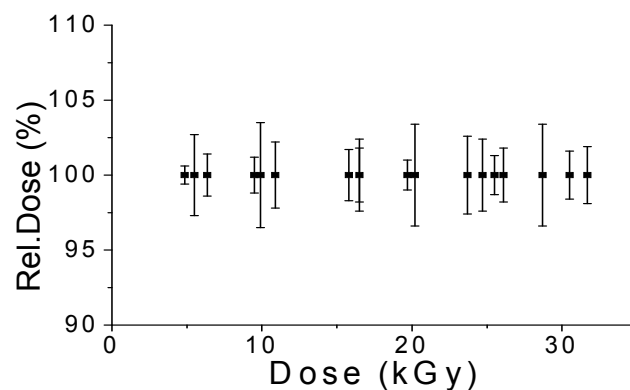


Figure 1. The relative dose response versus the absorbed dose. The error bars represent the standard deviation.

Conclusion

The uncertainty due to dosimeter itself can be determined by observing the absorbed dose measurements during the actual use of dosimeter in radiation processing. The total uncertainty of Aerial L-alanine pellet dosimeter is 1.5%. The components of this uncertainty are the uncertainty due to homogeneity of alanine in dosimeter pellets (1.2%) and uncertainty due to difference in dosimeter mass from the same batch (1%).

References

- [1] ISO/ASTM 51707 – 2002 (E) Standard guide for estimating uncertainties in dosimetry for radiation processing, 2002.
- [2] P. Sharpe and A. Miller, Guidelines for the calibration of dosimeters for use in radiation processing, NPL Report CIRM 29, 1999, available at <http://www.chemdos.npl.co.uk/dosc/NPLReportsCIRM29.pdf>
- [3] IOS, Guide to expression of uncertainty in measurement, International Organization for Standardization, Geneva, Switzerland, 1993.
- [4] V. Marković, R. Eymrey, H. C. Yuanradiat, Phys. Chem., 1977, 9, 625-631
- [5] B. Radak, I. Draganić, Bull. Of the B. Kidrič Institute of Nucl. Sci., 1962, 13, 77-88.
- [6] B. Šećerov and G. Bačić, Nuclear Technology & Radiation Protection, 2011, 26, 271-274.

MATERIAL SCIENCE

FEMTOSECOND LASER ABLATION AND STRUCTURING OF A HARD BI-LAYERED COATING

B. Gaković¹, C. Radu², B. Radak¹, M. Zamfirescu², S. Petrović¹, M. Trtica¹,
I. N. Mihailescu²

¹*Institute of Nuclear Sciences “Vinča”, University of Belgrade, Serbia*

²*National Institute for Lasers, Plasma and Radiation Physics, Magurele, Romania*

Abstract

We studied surface modification of a bi-layered coating (Al₂O₃/TiAlN/steel) induced by fs laser with single and multi-pulse irradiation. The laser pulses ($\lambda=775$ nm, $\tau=200$ fs) were generated by a Ti:sapphire laser. The single pulse threshold fluence for ablation of the top Al₂O₃ layer was $D_{\text{ath}}=0.56$ Jcm⁻². Single pulse actions with fluence increased up to 16.47 Jcm⁻² caused widening of ablated area without significant change of the TiAlN layer underneath. In case of multi-pulse irradiation, periodical surface structures (LIPSS) were induced on the TiAlN layer surface. The average periodicity of created LIPSS was 600 nm.

Experimental

The experimental sample was a hard coating produced by reactive sputtering in a commercial system [1]. The top alumina layer (Al₂O₃) of 1.7 μm and the underlying titanium aluminium nitride (TiAlN) of 1.9 μm were deposited on a polished steel substrate (Fig.1a). From XRD analysis, the alumina layer mainly consisted of the polycrystalline χ -Al₂O₃ phase (Fig.1b).

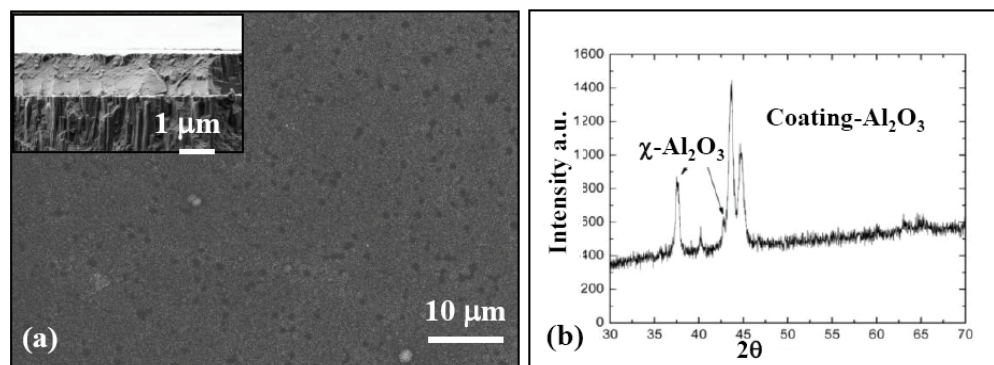


Figure 1. (a) SEM micrograph of the sample surface and cross section (insert) before fs laser pulse action. (b) XRD pattern of Al₂O₃/TiAlN/steel coating.

Laser used in this work was a Ti:sapphire laser source equipped with a chirped pulse amplification system (Clark-MRX 2101). Wavelength of the output beam was 775 nm, with a pulse duration of $\tau_p = 200$ fs [1]. Linearly polarized Gaussian beam was focused perpendicularly to the target surface. Irradiation was done in air with pulse energy E_p and fluence F ranged from 0.5 to 50 μJ and 0.1 to 16.47 Jcm^{-2} , respectively. For better statistics 3x3 spots were made with the same E_p . Surface morphology was examined by optical microscopy and scanning electron microscopy (SEM). SEM was coupled to an energy-dispersive analyzer (EDX) for determining the surface composition. X-Ray diffraction (XRD) was used for inspection of phase composition and crystalline structure of as deposited coating. Non-contact 3D surface profilometry was applied to map-out the geometry of the ablated/damaged area.

Results and Discussion

Interest for laser processing of materials, especially femtosecond laser systems is growing because of numerous possible applications in microelectronics, nanotechnology, tribology, medicine etc. LIPSS have been known since the 1960s. Much work has been done towards explanation of their origin [2,3] but it is still an area of extensive research, especially in the case of femtosecond lasers. Apart from fundamental importance, the damage threshold and the threshold of coating ablation are important parameters for ultra short laser pulse application.

Single-pulse effect. Damage threshold (D_{th}), the lowest fluence that causes irreversible surface modification, was found to be $D_{th}=0.20 \text{ Jcm}^{-2}$. The damage appeared in the form of a doughnut shaped bulge on the surface of the top alumina layer with no composition changes. The ablation threshold (D_{ath}) the lowest fluence that causes removal of the upper alumina layer was determined too, $D_{ath}=0.56 \text{ J cm}^{-2}$. Profilometry for all fluences ($0.56 \text{ Jcm}^{-2} - 16.47 \text{ Jcm}^{-2}$) showed that the depth of ablation region was $1.7 \mu\text{m}$ - the same as the thickness of the alumina layer, with clean, steep walls and flat bottom.

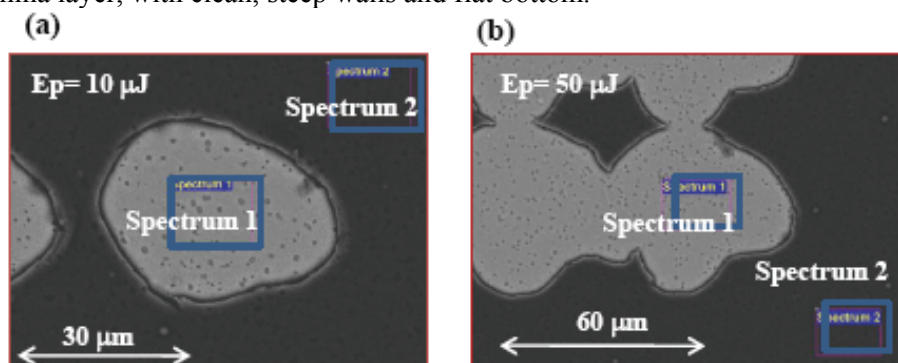


Figure 2. SEM&EDX analyses of $\text{Al}_2\text{O}_3/\text{TiAlN}/\text{steel}$ coating after single fs pulse action: (a) pulse energy/fluence of $10\mu\text{J}/1.86 \text{ Jcm}^{-2}$ and (b) $50\mu\text{J}/16.47 \text{ Jcm}^{-2}$.

Compositions of the ablated regions were checked by EDX (Fig.2). Data taken from blue squares on the Figs.2 a and b showed that the composition of the ablated areas (Spectrum 1) were the same in spite of different fluences (1.86 and 16.47 Jcm^{-2}) applied. Spectrum 1: N~28, O~2.3, Al ~27, Ti ~41 (all in wt%). Spectrum 2 corresponded to the composition of the original coating.

Multi-pulse effect. Irradiation of bi-layered coating ($\text{Al}_2\text{O}_3/\text{TiAlN}/\text{steel}$) by ten fs pulses and constant energy/fluence ($10\mu\text{J}/1.86 \text{ Jcm}^{-2}$) resulted in ablation of alumina layer from the underlying TiAlN and LIPSS formation on TiAlN (Fig.3).

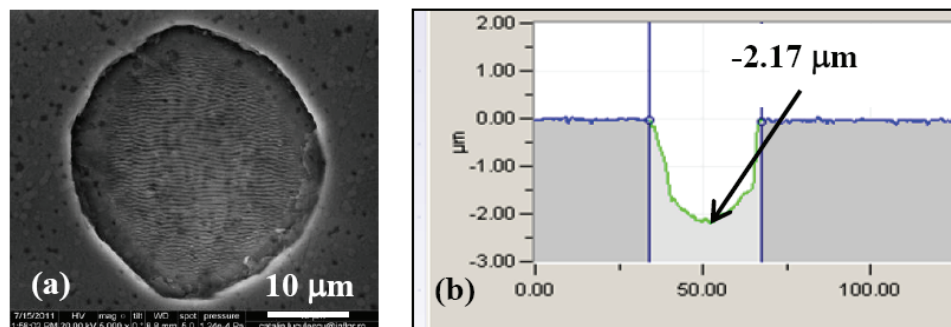


Figure 3. (a) SEM of 10 laser pulses action on $\text{Al}_2\text{O}_3/\text{TiAlN}/\text{steel}$. LIPSS are formed in the spot centre on TiAlN and (b) depth of ablated area obtained by profilometry.

The average periodicity value of the LIPSS formed was 600 nm . Among other explanations, their origin can be explained by interference of the incident laser beam with the so-called surface waves scattered on imperfections at the target surface [3].

Conclusion

Femtosecond laser pulses (200 fs), single and multi-pulse, were used for surface structuring of a bi-layered coating $\text{Al}_2\text{O}_3/\text{TiAlN}$ deposited on steel. The value of single pulse ablation threshold, $D_{\text{ath}}=0.56 \text{ Jcm}^{-2}$, was obtained for ablation of the top Al_2O_3 layer. A significant result is that underlying TiAlN layer remained unchanged after one pulse action (fluence up to 16.47 Jcm^{-2}). Multi-pulse irradiation (10 pulses) with the pulse energy/fluence of $10\mu\text{J}/1.86 \text{ Jcm}^{-2}$ caused Al_2O_3 ablation/exfoliation and appearance of LIPSS on the TiAlN.

References

- [1] B. Gakovic, C. Radu, M. Zamfirescu, B. Radak, M. Trtica, S. Petrovic, P. Panjan, F. Zupanic, C. Ristoscu, I.N. Mihailescu, *Surface & Coatings Technology*, **206** (2011) 411–416.
- [2] I. Ursu, I.N. Mihailescu, A.M. Prokhorov, V.N. Tokarev, V.I. Konov, *J. Appl. Phys.* **61** (1987), pp. 2445-2450.
- [3] D. Bäuerle: *Laser Processing and Chemistry*, Springer, Berlin 2000.

H-02-SL

FROM VIRAL BARRIERS TO PROTON CONDUCTORS – NOVEL APPLICATIONS FOR POLYMERIC MEMBRANES

Filip Radovanović

*IHTM – Centre of Microelectronic Technologies and Single Crystals
Njegoševa 12, University of Belgrade, Serbia*

Abstract

Novel applications for polymeric membranes which address the needs of health care industry and development of alternative energy sources are reviewed in this paper. Polyolefin membranes made by thermally-induced separation process can be used as barriers against biological pathogens and splashes of harmful liquid chemicals, or as separators in lithium ion batteries, which can provide an increased margin of safety by shutting down the electrical current in case of battery overheating. Asymmetric membranes made by a combination of immersion precipitation and photopolymerization can be used as proton exchange membranes in fuel cells. Modifications of this novel process could be used to make membranes for other interesting applications.

Introduction

A polymeric membrane represents a layer of polymeric material which serves as a selective barrier between two phases and shows preferential selectivity to some species in one of these phases when exposed to the action of a driving force. One of the earliest applications of polymeric membranes was blood purification by hemodialysis in the medical field. However, since the original invention of asymmetric membranes by Loeb and Sourirajan [1], the scope of applications for polymeric membranes has significantly expanded to include various treatments for purifying water sources using processes, such as reverse osmosis, ultrafiltration or microfiltration. Medical and water treatment applications represent today the largest business segments where commercial membranes are used, but other applications of polymeric membranes are slowly catching up.

This paper reviews some novel applications for polymeric membranes, which have emerged to address needs of the modern society, including better health care protection and substitution of traditional fossil fuel energy sources with alternative sources of energy. These applications focus either on membranes which serve as barriers against biological pathogens (bacteria, viruses) and harmful liquid chemicals, or on membranes used as separators in rechargeable lithium-ion batteries and proton conductors in fuel cells.

Barrier membranes

Barrier membranes are often produced on an industrial scale using thermally-induced phase separation (TIPS) process [2] schematically presented in Fig. 1. A semi-crystalline polymer and additives are dissolved in a diluent at high

temperature, shaped into a film, cooled down to induce phase separation, followed by optional process steps of diluent extraction and film orientation to produce a microporous membrane. This membrane can be subjected to additional process steps to create the final product (e.g. coating, functionalization, lamination, winding). Fig. 2 illustrates thermodynamics of the phase separation process. At high temperatures polymer and diluent exist as a one phase solution and undergo phase separation by cooling down below the polymer crystallization curve (liquid-solid phase separation) or below the binodal equilibrium curve (liquid-liquid phase separation). After diluent removal and film orientation, a microporous membrane with a structure that is largely dependent on the type of phase separation process forms. Liquid-liquid phase separation creates a cellular microporous structure, while liquid-solid phase separation results in crystalline domains interconnected by polymer fibrils.

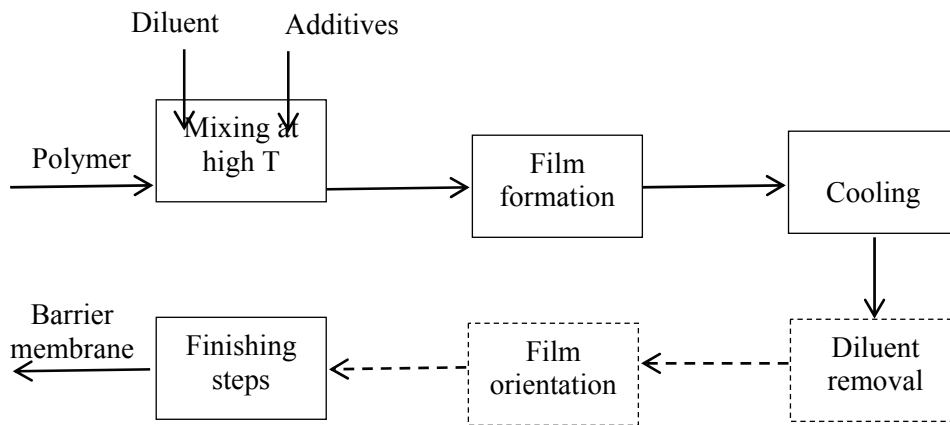


Figure 1. Schematic presentation of TIPS process to make barrier membranes.

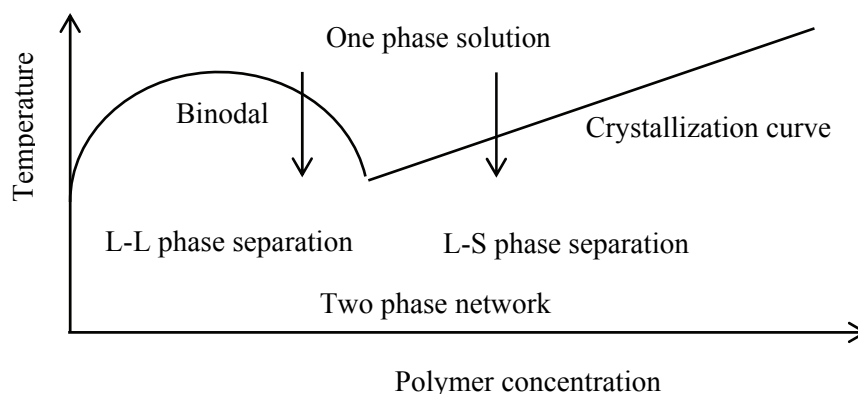


Figure 2. Schematic presentation of thermodynamics of the phase separation process.

If the polymer used in production has a sufficiently low surface energy, the resulting microporous membrane has a hydrophobic character and can serve as a barrier against liquids of higher surface tension (e.g. aqueous solutions). Liquid barrier conditions can be expressed by Laplace (Cantor) equation which determines the liquid breakthrough pressure when the membrane is pressurized with a nonwetting liquid :

$$P = \frac{4\gamma(-\cos\Theta)}{D} \quad (1)$$

where γ is surface tension of liquid, D is the pore diameter of the membrane, and Θ is the contact angle between the membrane and the nonwetting liquid, which must be greater than 90° , as shown in Fig. 3. Equation (1) shows that liquid barrier properties improve if the nonwetting liquid has a higher surface tension, the membrane has a smaller pore size, and the contact angle increases towards 180° (membrane repellency against the liquid increases).

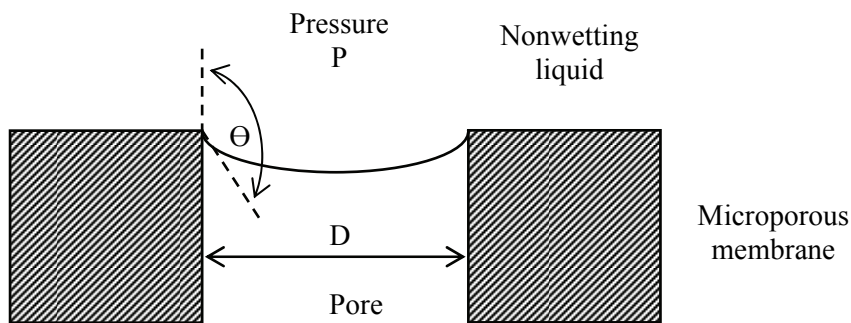


Figure 3. Liquid barrier conditions for a microporous film.

When a hydrophobic semicrystalline polymer, such as polypropylene or polyethylene is converted into a microporous membrane using TIPS process, membrane has a sufficient repellency against water to serve as a liquid barrier. However, liquids of lower surface tension readily penetrate such membranes even in the absence of pressure difference as driving force. A need to develop liquid barrier fabrics against liquids of lower surface tension than water (e.g. blood and body fluids, pesticide and herbicide spray solutions, organic solvents) led to a development of a new class of breathable microporous materials that are comfortable to wear, but still provide better protection against accidental splashes than standard protective garments. An example of such material used to prevent transmission of viruses from a patient to a health care worker is described in US patent literature [3, 4, 5, 6]. Several microporous membranes, in a film or laminate

form, were prepared using TIPS process. The starting raw materials were polypropylene, mineral oil and fluorocarbon oxazolidinone (FCO) which improved barrier properties by increasing repellency (contact angle) against blood and body fluids compared to the control sample without FCO. These membranes were evaluated for viral penetration using an ASTM standard test method [7]. In this test a pressure of 13.8 KPa is applied to the test material through a liquid carrying viral pathogens and viral penetration is observed by swabbing the non-liquid-containing side of the test material, culturing the swabbed exudate for 24 hours, and counting the number of viruses. No viral penetration was typically detected using this test method when liquid repellency was sufficiently high (presence of FCO) and pore size was sufficiently small (TIPS polypropylene membranes). Breathable fabrics that can protect against viral penetration can find their use for surgical and emergency response garments. Liquid barrier properties of polyolefin membranes made by TIPS process can be further improved by coating these membranes with a curable fluorocarbon urethane composition, as described in [8]. Coated membranes were still quite breathable, while exhibiting repellency against liquids having surface tension above 20 dyne/cm (e.g. toluene, octane, ethyl acetate, isopropyl alcohol). Such materials could be useful as breathable industrial garments that can protect against splashes of organic solvents.

Lithium ion batteries exhibit high specific energy and long life power, which made them a source of choice for consumer electronic markets. The separator is a critical component in lithium ion batteries and it serves a dual purpose: physical separation of the battery electrodes and the safety function to shut down electrical current if overheating occurs, thus avoiding thermal runaway reactions that can lead to an explosion [9]. The separator needs to be thin and sufficiently porous to minimize electrical resistance of the electrolyte within its pores, mechanically strong and puncture resistant while having a small pore size to prevent internal shorts due to penetration of dendrites formed during the cycling operations. In addition, the separator needs to shut down the electrical current at a sufficiently low temperature. Commercial separators are usually made as a single or a multilayer structure comprising a polyethylene porous layer which melts in the range from 125 to 130° C to block electrical current and stop battery overheating. Since this temperature range is rather close to the onset of exothermic runaway reactions that can occur in lithium ion batteries, significant efforts have been ongoing to develop a separator with a lower shutdown temperature and ensure an increased margin of safety. As described in patent literature, microporous membranes which meet all aforementioned requirements for the lithium ion battery separator application, while exhibiting a shutdown feature below 120° C, can be made using TIPS process described in Fig. 1 [10, 11, 12]. It was shown that by using a compatible blend of polypropylene and ethylene alpha-olefin copolymer having crystallinity above 20% it was possible to prepare microporous films with a low temperature shutdown feature. Such separators can be used in lithium ion batteries as single layers, or multilayers made by co-extrusion. Fig. 4 shows a top view of a microporous film made by TIPS process, which could be useful as a

H-02-SL

battery separator. Scanning electron microscopy image of the top surface reveals a fine structure with pore sizes well below 100 nm.

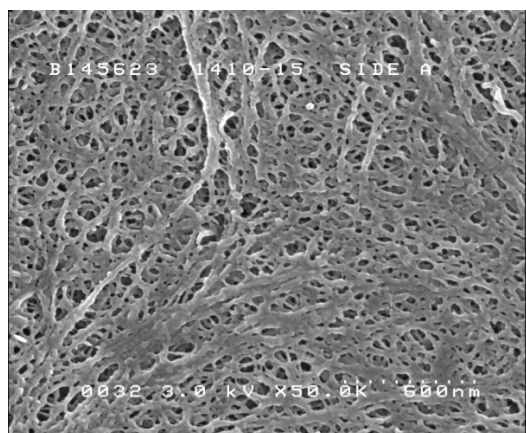


Figure 4. SEM image of a TIPS microporous membrane useful as lithium-ion battery separator [12].

Proton-conducting membranes

Fuel cells using proton exchange membranes have a broad range of applications in the automotive, stationary and portable fields [13]. In these fuel cells, a proton-conducting polymer membrane, such as Nafion available from DuPont de Nemours, serves as an electrolyte. High price of Nafion membranes and their limitations, including high crossover of methanol in Direct Methanol Fuel Cells and performance loss under conditions of low relative humidity, led to investigations of other proton-conducting membranes with interpenetrating networks from less expensive, nonfluorinated materials [14].

A novel method to make asymmetric membranes with interpenetrating proton-conducting morphology has been recently reported in literature [15]. This method, schematically shown in Fig. 5, combines traditional immersion precipitation process for making membranes and photopolymerization. A solution of polymer, monomers and photoinitiator in a common solvent is cast as a film on a glass plate, then immersed in a nonsolvent bath, quickly exposed to UV light to polymerize and crosslink monomers, and dipped in water to solidify the asymmetric structure. Polysulfone was used as polymer, while 2-acrylamido-2-methylpropane sulfonic acid (AMPS) was selected as a proton-conductive monomer. Final membrane had a thin skin layer with fine channels of crosslinked polyAMPS on top of a coarser support of interpenetrating polysulfone and polyAMPS phases.

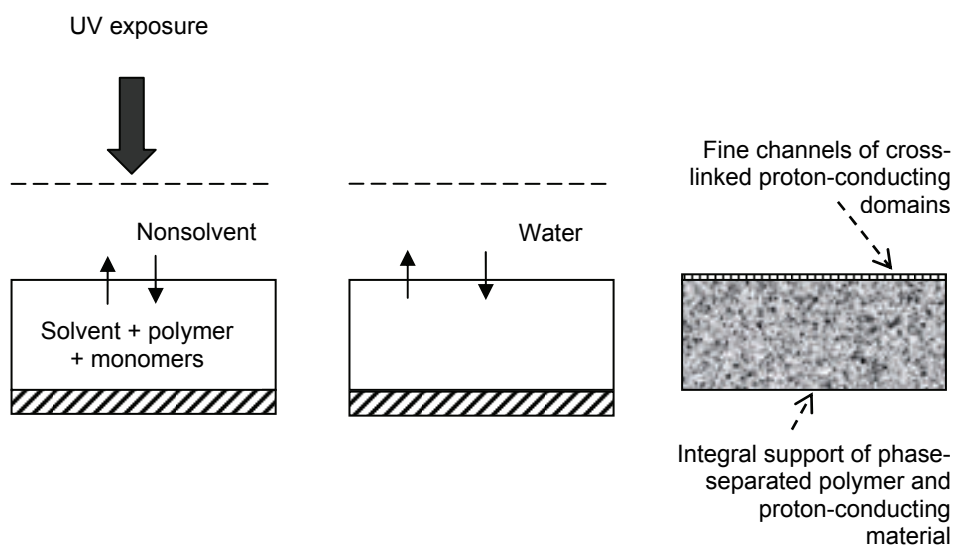


Figure 5. Schematic representation of the process for making an asymmetric membrane with interpenetrating proton-conducting morphology.

Environmental scanning electron microscope (ESEM) image of the top surface of an asymmetric proton-conducting membrane show crosslinked polyAMPS nanodomains of 200-300 nm average size. In-plane conductivity of such membrane, made with 5 mol % of a trifunctional crosslinking agent, was significantly higher than the conductivity of a Nafion 115 membrane, while having improved methanol barrier properties.

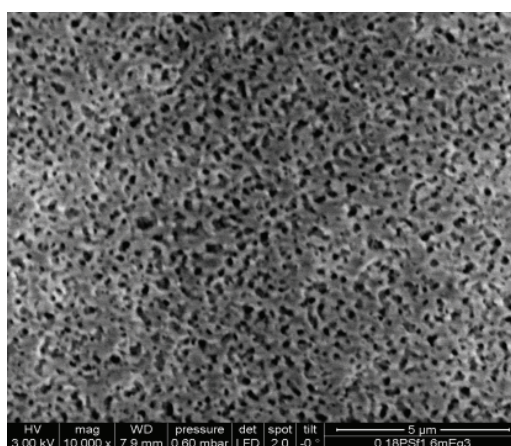


Figure 6. ESEM image of the top surface of an asymmetric membrane made by photopolymerization.

The new method of making asymmetric membranes with interpenetrating morphology is not necessarily restricted to fuel cell applications. Any polymerizable monomer soluble in the same solvent used for membrane casting could be incorporated, which significantly broadens the range of functional features that can be achieved with such materials. Current research in this area is looking into other potential applications, including low-pressure nanofiltration, gas separation and bio-applications using functionalized membranes.

Conclusion

Polypropylene membranes made by thermally-induced separation process can be used in many applications as barrier membranes. Their barrier properties are improved by increasing repellency against contacting liquid and by reducing their pore size. Such properties can lead to their use in garments protecting against biological pathogens and splashes of harmful liquid chemicals. Polyolefin membranes made by thermally-induced phase separation process can also be used as separators in lithium ion batteries, where they can provide an increased margin of safety by their thermal shutdown feature.

Asymmetric membranes made by a combination of immersion precipitation and photopolymerization have exhibited electrical conductivity significantly higher than that of a Nafion 115 membrane, while having improved methanol barrier properties. Such membranes can be useful as proton conductors in fuel cells. Modifications of this novel process for making membranes could also be used to develop membranes for other interesting applications.

References

- [1] S. Loeb, S. Sourirajan, *Adv. Chem. Ser.*, 1962, 38, 117-132.
- [2] D. R. Lloyd, K. E. Kinzer, H. S. Tseng, *J. Membrane Sci.*, 1990, 52, 239-261.
- [3] W. K. Weimer, G. E. Keenan, R. J. Kinney, J. S. Mrozinski, P. D. Radovanovic, US 5690949, 1998.
- [4] W. K. Weimer, G. E. Keenan, R. J. Kinney, J. S. Mrozinski, P. D. Radovanovic, US 5738111, 1997.
- [5] W. K. Weimer, G. E. Keenan, R. J. Kinney, J. S. Mrozinski, P. D. Radovanovic, US 5935370, 1999.
- [6] W. K. Weimer, G. E. Keenan, R. J. Kinney, J. S. Mrozinski, P. D. Radovanovic, US 5981038, 1999.
- [7] American Society for Testing and Materials, ASTM ES22-92, 1993 annual book of ASTM standards, 1993, 11, 806-811.
- [8] J. S. Mrozinski, M. B. Burleigh, P. D. Radovanovic, B. D. Johnson, US 5989698, 1999.
- [9] S. S. Zhang, *J. Power Sources*, 2007, 164, 351-364.
- [10] P. D. Radovanovic, G. P. Krogseng, C. P. Waller, J. S. Mrozinski, D. L. Krueger, US 5993954, 1999.
- [11] P. D. Radovanovic, S. D. Thomas, US 6096213, 2000.
- [12] P. D. Radovanovic, M. A. Perez, S. D. Thomas, US 6461724, 2002.

-
- [13] B. Smiths, S. Sridhar, A. A. Khan, *J. Membrane Sci.*, 2005, 259, 10-26.
[14] N. V. Deluca, Y. A. Elabd, *J. Polymer Sci., Part B: Polym. Phys.*, 2006, 44, 2201-2213.
[15] P. Radovanovic, M. Kellner, J. Matovic, R. Liska, T. Koch, *J. Membrane Sci.*, 2012, 401-402, 254-261.

H-03-SL

CHARACTERIZATION OF Sm³⁺ DOPED TiO₂ AND Ni²⁺ DOPED TiO₂ NANOCRYSTALS

M. Vranješ¹, J. Kuljanin-Jakovljević¹, I. Zeković¹, Z. Konstantinović²,
M. Stoilković¹, J. Nedeljković¹, Z. Šaponjić¹

¹University of Belgrade, Vinča Institute of Nuclear Sciences, Belgrade, Serbia;

²Institut de Ciencia de Materials de Barcelona, CSIC, Campus UAB, 08193
Bellaterra, Spain

Abstract

We report on a new approach toward synthesis of Sm³⁺ doped TiO₂ and Ni²⁺ doped TiO₂ nanocrystals by shape transformation of hydrothermally treated titania nanotubes in the presence of Sm³⁺ or Ni²⁺ ions. The percentage ratio of Sm³⁺ (or Ni²⁺) to Ti⁴⁺ ions in doped nanocrystals was determined using ICP atomic emission spectroscopy. The XRD patterns revealed the homogeneous anatase crystal phase of both 0.4 at% Sm³⁺ doped TiO₂ and 0.12 at% Ni²⁺ doped TiO₂ nanoparticles. An average size of polyhedral Sm³⁺ doped TiO₂ nanocrystals was between 12 and 14 nm. In the orange-red spectral region, room temperature photoluminescence signals associated with ⁴G_{5/2} → ⁶H_J (*J* = 5/2, 7/2 and 9/2) transitions of Sm³⁺ was observed in Sm³⁺ doped TiO₂ nanocrystals. Optically transparent film made of 0.12 at% Ni²⁺ doped TiO₂ nanoparticles showed room temperature ferromagnetic ordering. The coercive field was found to be *H_C* ~ 80 Oe.

Introduction

Doping semiconductors with rare earth ions (Eu³⁺, Sm³⁺) opens the possibility of controlling the optical properties by the band gap structure of the semiconductor host [1]. This type of luminescent material can find applications for visible and infrared light emitting diodes and optical amplifiers. Compared with other host materials, TiO₂ is very effective in light confinement for an optical waveguide amplifier structure because of its high refractive index of about 2.5 and high transparency in visible and infrared wavelength region. On the other hand, wide band metal oxide semiconductors, e.g. TiO₂, after doping with transition metal ions (Co²⁺, Mn²⁺, Ni²⁺), as a diluted magnetic semiconductor which support room temperature ferromagnetism, can be used for the development of the spin-based electronic devices.

Experimental

Scrolled titania nanotubes were synthesized according to Kassuga et al. using TiO₂ powder (Fluka) as a precursor [2]. Sm³⁺ or Ni²⁺ doped TiO₂ nanoparticles were synthesized by hydrothermal treatment (60 min/250 °C) of a suspension containing 25 mg of titania nanotubes (pH 3) as the starting materials in the presence of 5 ×

10^{-3} M $\text{Sm}(\text{NO}_3)_3$ for the synthesis of Sm^{3+} doped TiO_2 or 6.2×10^{-4} M $\text{Ni}(\text{NO}_3)_2$ for the synthesis of Ni^{2+} doped TiO_2 nanoparticles. In order to remove excess dopant ions, the dispersions of Sm^{3+} doped TiO_2 nanoparticles and Ni^{2+} doped TiO_2 nanoparticles were dialyzed against acidified water (pH 3) at 4 °C for three days. Morphology of titania nanotubes and doped TiO_2 nanoparticles was studied by transmission electron microscopy (TEM) technique. Crystallographic properties were studied by X-ray diffraction (XRD) measurements. Photoluminescence measurements were performed at room temperature on Fluorolog-3 Model FL3-221 spectrofluorometer system (Horiba Jobin-Yvon). The magnetization of the films made of Ni^{2+} doped TiO_2 nanoparticles, as a function of magnetic field strength (H), was measured at room temperature with superconducting quantum interference device magnetometer (Quantum Design).

Results and Discussion

Sm³⁺ doped TiO₂ nanoparticles

Hydrothermal treatment of scrolled titania nanotubes in the presence of Sm^{3+} ions results in the formation of polyhedral 0.4 at% Sm^{3+} doped TiO_2 nanoparticles mainly of square/rectangular shape with average dimension between 12 and 14 nm, inset in Figure 1. The powder X-ray diffraction analysis of Sm^{3+} doped TiO_2 nanoparticles showed the existence of a homogeneous anatase (tetragonal, JCPDS 84-1286) crystal phase. The presence of all the characteristic anatase diffraction peaks with preserved intensity ratios implies random orientation of the nanoparticles. Emission spectrum of the 0.4 at% Sm^{3+} doped TiO_2 nanocrystals observed after band-to-band excitations ($\lambda_{\text{exc}} = 365$ nm) is shown in Figure 1. Due to large exciton binding energy in the TiO_2 , indirect excitation of Sm^{3+} by energy transfer from electron-hole pair in the TiO_2 was confirmed by characteristic orange-red emission observed by room temperature photoluminescence measurements. It consists of three emission bands peaking at 582, 612 and 662 nm

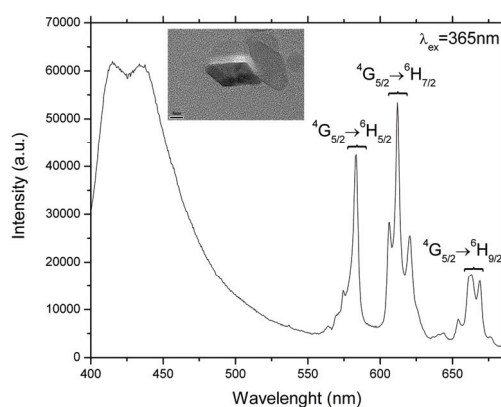


Figure 1. Emission spectrum of Sm^{3+} doped TiO_2 nanocrystals.

originating from of ${}^4G_{5/2} \rightarrow {}^6H_J$ ($J = 5/2, 7/2$ and $9/2$) $f-f$ transitions of the Sm^{3+} in the $4f^5$ configuration. The transitions corresponding to ${}^4G_{5/2} \rightarrow {}^6H_{7/2}$ are most pronounced in accordance to the selection rule $\Delta J = \pm 1$. The line positions of the Sm^{3+} -related emissions are in good agreement with those of Sm^{3+} -doped wide band gap semiconductors and Sm^{3+} -doped glasses. Nonexponential luminescence decay curve of Sm^{3+} (not shown) obtained by monitoring the ${}^4G_{5/2} \rightarrow {}^6H_{7/2}$ transition at $\lambda = 612$ nm under the excitation at $\lambda_{\text{exc}} = 365$ nm, is due to the nonradiative

energy transfer process from Sm^{3+} to their neighboring defects. The luminescence lifetime of ${}^4\text{G}_{5/2}$ was determined to be 970 μs .

Ni^{2+} doped TiO_2 nanoparticles

Ni^{2+} ions were incorporated into TiO_2 nanoparticles through shape transformation of hydrothermally treated scrolled titania nanotubes in the presence of $\text{Ni}(\text{NO}_3)_2$. In the XRD spectrum of 0.12 at% Ni^{2+} doped TiO_2 nanoparticles, there are no peaks that indicate the presence of any other crystal phases except anatase TiO_2 . For the optically transparent film made of 0.12 at% Ni^{2+} doped TiO_2 nanocrystals, the magnetic response was measured at room temperature. The in

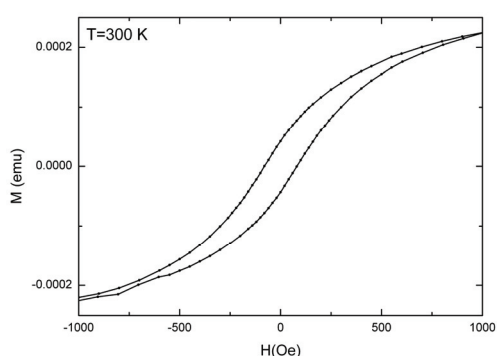


Figure 2. Isothermal magnetization of the film made of 0.12 at% Ni^{2+} doped TiO_2 nanoparticles recorded at 300 K.

plane hysteresis loop, Figure 2, represents distinct evidence, although response is weak, of the ferromagnetic ordering at room temperature. The coercive field was found to be $H_C \sim 80$ Oe. We can conclude that the observed ferromagnetism of the film is an intrinsic property of Ni^{2+} doped TiO_2 nanoparticles taking into account that XRD analysis showed the absence of any peaks that would indicate segregation of Ni in metallic form. The explanation for the observed room temperature ferromagnetic response in

of 0.12 at% Ni^{2+} doped TiO_2 nanocrystals, can be found in the simultaneous existence of Ni^{2+} ions in the nanoparticles core and donor type defects such as oxygen vacancies.

Conclusion

XRD confirmed anatase crystal structure of both types of doped TiO_2 nanocrystals. In the orange-red spectral region, room temperature photoluminescence signals associated with ${}^4\text{G}_{5/2} \rightarrow {}^6\text{H}_J$ ($J = 5/2, 7/2$ and $9/2$) transitions of the Sm^{3+} after band-to-band excitation were observed in Sm^{3+} doped TiO_2 nanocrystals. The Ni^{2+} doped TiO_2 nanocrystals enabled synthesis of optically transparent film that shows room temperature ferromagnetic ordering based probably on the presence of critical amount of oxygen vacancies that mediate interaction between Ni^{2+} spins trapped in the lattice structure of TiO_2 nanoparticles.

References

- [1] Q. Xiao, Y. Liu, L. Liu, R. Li, W. Luo, X. Chen, J. Phys. Chem. C, 2010, 114 9314–9321.
- [2] T. Kasuga, M. Hiramatsu, A. Hoson, T. Sekino, K. Niihara, Adv.Mater., 1999, 11, 1307–1311.

CONTROLLED HYDROTHERMAL PROCESSING OF ZnO POWDERS IN THE PRESENCE OF PVP

A. Stanković, Z. Stojanović, Lj. Veselinović, S. Marković, D. Uskoković

Institute of Technical Sciences of the Serbian Academy of Sciences and Arts, Knez Mihailova 35/IV, Belgrade 11001, Serbia (ana.stankovic@itn.sanu.ac.rs)

Abstract

In this study low-temperature hydrothermal processing was used for synthesis of ZnO powders with controlled morphology, from micro-rods *via* hexagonal prism like to nano-spheres, by the varying of $[\text{Zn}^{2+}]/[\text{OH}^-]$ molar ratio. The synthesized powders were characterized using XRPD, FE-SEM, UV-Vis diffuse reflectance and Raman spectroscopy. It is noticed that the modification of the particle size and morphology from nanospheres to micro-rods resulted in increased visible light absorption. Besides, the band gap energy of the synthesized ZnO powders showed the red shift (~ 0.20 eV) compared to bulk ZnO. The enhanced visible light absorption of the ZnO powders is related to the existence of lattice defects and the particle surface sensitization by PVP.

Introduction

Since the functionality of materials are determined by the phase purity, homogeneity, particle size, morphology, as well as crystallinity, the possibility to control the synthesis process is of utmost importance. Several techniques such as precipitation, sol-gel process, spray pyrolysis, hydrothermal synthesis, and mechanochemical processing are used for the preparation of ZnO materials with controlled properties. Among them, hydrothermal synthesis is the most attractive due to the fact that it allows perfect control of purity, crystallinity, composition, size and morphology by simple tuning of the experimental variables: reaction temperature, time, reactant molar ratio and/or addition of the appropriate polymer surfactants [1,2]. Moreover, hydrothermal synthesis is environmentally safe and economical for large-scale production.

Here, we propose a low-temperature hydrothermal method for the synthesis of phase-pure ZnO powders with a controlled morphology and narrow particle size distribution. This simple and low-cost method allows to tailor the shape and size of ZnO particles, from micro-rods *via* hexagonal prism like to nano-spheres, by the varying of $[\text{Zn}^{2+}]/[\text{OH}^-]$ molar ratio. The synthesized powders were characterized by XRPD, FE-SEM, UV-Vis diffuse reflectance and Raman spectroscopy.

Experimental

ZnO powders were prepared by low-temperature hydrothermal processing. The reaction temperature and time were kept constant, while the $[\text{Zn}^{2+}]/[\text{OH}^-]$ molar ratio in the starting solution was changed in order to tailor the particle size and shape. The $[\text{Zn}^{2+}]/[\text{OH}^-]$ molar ratio was varied from 1:1, 1:3, 1:3.5, to 1:5,

H-04-P

resulting in the pH values of the reaction solution: 8, 10, 11, and 13, respectively. The starting materials were zinc acetate ($\text{Zn}(\text{CH}_3\text{COO})_2 \cdot 2\text{H}_2\text{O}$), sodium hydroxide (NaOH) and polyvinylpyrrolidone (PVP), as a polymer surfactant. After the dissolution of zinc acetate dihydrate and PVP, an adequate amount of the aqueous solution of NaOH was added dropwise, resulting in a white precipitate. The as-prepared suspension was thermally treated in 2 l *Parr* stainless steel reactor up to 120 °C under constant stirring of 400 rpm. The reaction time was 72 h. The synthesized ZnO powders were designated as ZnO8, ZnO10, ZnO11 and ZnO13, where the number signifies the pH value of the reaction solution.

The crystal phases of synthesized powders were identified by XRPD analysis (Philips PW-1050). The morphology of ZnO particles was observed by FE-SEM (SUPRA 35 VP Carl Zeiss). The UV-Vis diffuse reflectance spectra were recorded in the wavelength range 300–800 nm (Evolution 600 UV-Vis spectrophotometer, Thermo Scientific). The μ -Raman spectra were recorded in the frequency interval of 50–3500 cm^{-1} (DXR Raman microscope, Thermo Scientific).

Results and Discussion

The results of XRPD analysis show that the synthesized ZnO powders are pure, highly crystalline, a wurtzite-type hexagonal structure with nanosized crystallites.

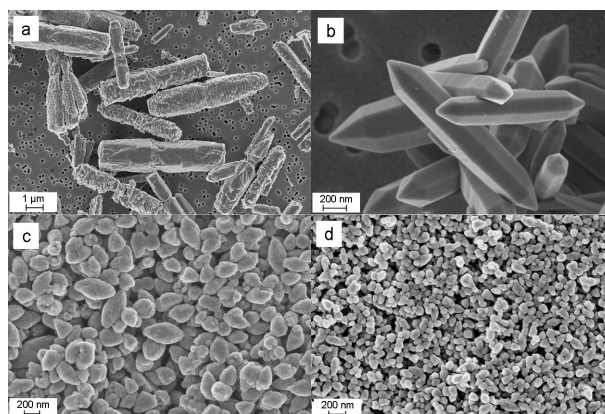


Figure 1. FE-SEM micrographs of: (a) ZnO8; (b) ZnO10; (c) ZnO11, and (d) ZnO13.

The morphologies of the synthesized ZnO powders, examined by FE-SEM, are shown in Fig. 1. The ZnO8 powder is consisted of the micro-rods with a rough particle surface and partially cracked edges with non-uniform particles size distribution; the particle lengths are between 1.4 and 7.1 μm , while the diameters are between 0.3 and 1.7 μm (Fig. 1a). ZnO10 powder, Fig 1b, is composed of the particles with a smooth hexagonal-faceted prismatic morphology with hexagonal pyramidal ends. The most of the rods have rather uniform diameters of about 200 nm and lengths of 1-2 μm . Powder ZnO11, Fig. 1c, is composed of ellipsoidal particles with an average diameter and length of about 200 nm and 500 nm,

respectively. Finally, ZnO13 powder consists of spherical nano-sized particles with uniform size distribution and average diameters of ~ 50 nm, Fig. 1d.

Influence of particles size and morphology on optical properties of ZnO was examined by UV-Vis diffuse reflectance spectroscopy (DRS). Using the recorded UV-Vis DRS and the Kubelka-Munk transformation method, the band gap energies (E_{bg}) were determined, and they are: ZnO8 — 3.16 eV, ZnO10 — 3.18 eV, ZnO11 — 3.19 eV, and ZnO13 — 3.22 eV. It is noticed that all the synthesized ZnO powders show increased absorption in the visible region at room temperature.

Raman spectroscopy was used to explain the improved optical properties of the synthesized ZnO powders (red shift of band gap). The modes that appear in the Raman spectra were assigned to wurtzite crystal structure, to the structural defects (impurities, oxygen vacancies and zinc interstitials) as well as to PVP. According to the Raman spectroscopy study, the red shift of the band gap (~ 0.20 eV) for the synthesized ZnO powders compared to bulk ZnO ($E_{bg} = 3.37$ eV) could be related to two phenomena: the introduction of lattice defects and surface sensitization by PVP, because PVP can improve visible light absorption. Detailed analysis of Raman spectra yields that nano-sized powder ZnO13 and ZnO11 has ordered wurtzite crystal structure with very few defects, while in micro-sized powders, ZnO10 and ZnO8, number of defects and impurities, as well as absorption of PVP at the surface increase.

Conclusion

The effect of the $[\text{Zn}^{2+}]/[\text{OH}^-]$ molar ratio i.e. pH of the reaction solution on the sizes and morphology of ZnO particles synthesized *via* low-temperature hydrothermal processing was examined. Varying the pH from almost neutral, pH=8, to a strong base solution, pH=13, ZnO particles from non-ordered micro-rods, hexagonal-faceted prismatic morphology with hexagonal pyramidal ends, sub-micron ellipsoids to the nano-spheres were prepared. Therefore, it is possible to control morphology and sizes of the ZnO particles by adjusting the pH value of the reaction solution. The synthesized ZnO powders exhibit enhanced visible light absorption in comparison to bulk ZnO. Improved optical properties are related to two phenomena: introduction of lattice defects (impurities, oxygen vacancies and zinc interstitials), also, surface sensitization by PVP.

Proposed synthesis method provides simple, economic and low-temperature approach for a growth of ZnO particles with the different morphology and improved optical properties.

Acknowledgments

This study was supported by the Ministry of Education and Science of the Republic of Serbia under grant no III45004.

References

- [1] Y. Zhang, J. Mu, *Nanotechnology* 2007, 18, 075606 (6 pp).
- [2] H. Zhang, D. Yang, D. Li, X. Ma, S. Li, D. Que, *Crystal Growth & Design* 2005, 5, 547-50.

SYNTHESIS OF NEW TYPE OF CORDIERITE COATINGS

A. Prstić¹, Z. Aćimović-Pavlović², A. Terzić³, L. Pavlović⁴
¹AMI-Beograd, Beograd, Serbia; ²Faculty of Technology and Metallurgy, University of Belgrade, Belgrade, Serbia; ³Institute for Materials Testing, Belgrade, Serbia; ⁴Institute ITNMS, Belgrade, Serbia

Abstract

New refractory coatings based on synthesized cordierite for the casting applications were investigated. The investigation included synthesis of the cordierite and design of the refractory coating as final product. Design and optimization of the coating composition, with controlled rheological properties included, were achieved by application of different coating components, namely different suspension agents and by alteration of the coating production procedure. Cordierite, used as filler, was obtained by means of synthesis in the solid state reaction on the basis of talc, kaolin and alumina. The investigation showed that the application of these particular types of coatings has positive influence on surface quality, structural and mechanical properties of the castings of aluminum alloys.

Introduction

The main role of coating is the creation of an efficient and unbreakable firm refractory barrier separating sandy substrate from the liquid metal flow [1]. Certain coating properties are being required [2]: good refractoriness, suitable gas permeability, simple application, good adhesion to sand mold and polymer model, easy coating layer thickness adjustment, high drying rate. This can be achieved by optimization of the coating composition and production technology [3]. The cordierite was chosen as refractory coating filler due to the following properties: (1) low thermal conductivity: 3 W/(m·K) and low coefficient of linear thermal expansion (α): $1.7 \cdot 10^{-6}/^{\circ}\text{C}$ at 25 °C [4]; (2) high thermal shock resistance (quenching/500) and high maximal use temperature (1371 °C) [5]; (3) extreme resistance on liquid metal absorption [6]; (4) no gas production when in contact with liquid metal. Different additive types and various quantities were tested in order to enable the best possible absorption between additives and the refractory filler particles and, thus, maintenance of the filler in a dispersed state and prevention of the filler building up or segregation.

Experimental

Cordierite used as refractory filler for the coating was synthesized by means of high-temperature reaction in solid state. The raw materials - talc, kaolin and alumina were milled down to the grain size of $1 \cdot 10^{-4}$ m and then mixed in the ratio $2\text{MgO} : 2\text{Al}_2\text{O}_3 : 5\text{SiO}_2$. The samples were sintered at 1300 °C during 8 hours in a laboratory furnace in the oxidation atmosphere. X-ray fluorescence technique was used to conduct chemical element analysis (XRF spectrophotometer ED 2000 –

Oxford). Mineral phase composition was analyzed by means of X-ray powder diffraction (XRD - *Philips PW-1710* diffractometer). DTA was performed with a *Shimadzu DTA-50* apparatus. The microstructure of the samples was characterized by scanning electron microscopy method (SEM) using a *JEOL JSM-6390* Lv microscope. Distribution of refractory filler and bonding agent in a coating suspension was conducted by means of polarized optical microscope with passing light *JENAPOL* type (*Carl Zeiss – Jena*). Analysis of the particle size and shape factor was conducted by means of the PC software *OZARIA 2.5*. Cordierite samples synthetically obtained were applied as refractory filler in three types of coatings. Compositions of refractory coatings included refractory filler, bonding agent, additive and solvent and they were as follows: *Type I* - cordierite (93-95 %) + colophonium ($C_{20}H_{30}O_2$) 2-2.5 % + Bentone 25 0.8-1 % + isopropyl alcohol; *Type II*: cordierite (93-95 %) + colophonium ($C_{20}H_{30}O_2$) 1.2-1.5%, dextrin 0.5-1 % + Bentone SD-3 1.2-1.5%, phenol formaldehyde resins 1.2-1.7 % + isopropyl alcohol; *Type III*: cordierite (92-94 %) + bentonite 1.5-2.5%; bindal H 0.5-1% + suspension maintenance agent: $Na_3P_3O_3$ 1-3%, Carboxymethyl cellulose (CMC) 0.5-1% + water.

Results and Discussion

Synthesized cordierite had following chemical composition (%): MgO 13.2, Al_2O_3 31.9, SiO_2 52.9, Fe_2O_3 1.2, CaO 1.5. The composition of synthesized cordierite is approximately the same as composition of natural cordierite, which approves the soundness of the method applied. Identified crystalline major phases present in the sample were: cordierite, spinel ($MgAl_2O_4$), cristobalite (SiO_2) and quartz (SiO_2). Spinel, cristobalite and quartz were noted in relatively negligible amounts. Their peaks on the diffractogram (Fig 1) are overlapping, thus exact corresponding peaks are hard to detect.

The processes taking place during sample thermal treatment from 20 up to 1200 °C were identified by means of DTA method. The thermal treatment of the cordierite comprises three separate regions that are monitored by three individual peaks. First endothermic effect appearing at relatively low temperatures (up to 200°C) is a consequence of evaporation of physically bonded water. Second endothermic effect was noticed at 507 °C and it corresponds to the α -tridymite \rightarrow α -quartz transformation. The third peak, which is exothermal, corresponds to the reactions between MgO and SiO_2 , where magnesium methasilicate is formed at the temperature of 1121 °C. Microstructure analysis of the coating filler and suspension samples, performed with *OZARIA 2.5*, showed that filler particles are varying in size but mainly maintain more or less uniform morphology – in terms that majority of the filler particles showed coefficients from 0.5 to 0.8. Coefficient values referred to sub-oval shape as mid-solution between needle shape (0) and spherical shape (1). However, further SEM analysis (Fig.2) of the cordierite sample morphology pointed out that its grains are mostly irregularly shaped (hexagonally). Estimated mean size of the filler particles was 35×10^{-6} m. As seen on the microphotograph, morphology of cordierite samples points out that most of the

H-05-P

particles are irregularly shaped. Dimensions of the grains are significantly varying. Small, needle-like shaped particles can be seen on the microphotograph. Such shape of particles is characteristic for quartz. Cordierite grains are commonly large with elongated shapes and are surrounded by smaller quartz particles. Smaller particles are forming clusters by merging together or with bigger grains.

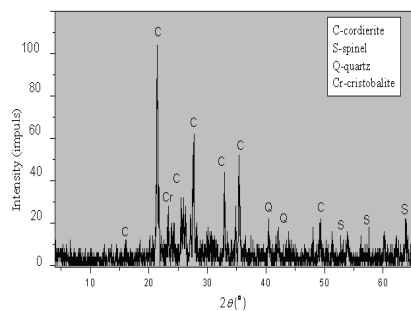


Figure 1. Diffractogram of cordierite.

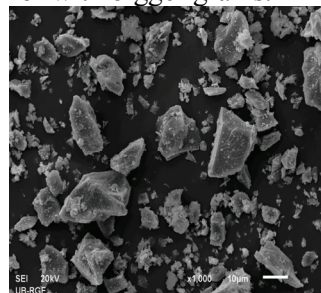


Figure 2. Microphotography of cordierite.

Conclusion

The investigation showed that synthesized cordierite met the casting application requirements. Furthermore, all investigated types of refractory coatings promoted acceptable casting surface finish; they added stiffness to the cluster and allowed the foam decomposition products to escape. The investigated coatings showed possibility of easy application on the sandy molds and polymer models; they evenly flow down during pouring and submerging. After drying, coating surfaces were smooth, coating layers had even thickness all over the surfaces of the molds and models without bubbling, cracks, peeling or taking off.

Acknowledgment

This investigation was supported by Serbian Ministry of Science and Education and it was conducted under following projects: 33007, 172057 and 45008.

References

- [1] R. Monroe, Expandable Pattern Casting, p.71, AFS Inc. USA, 1994.
- [2] Standard: SRPS EN 12890:2000 / CEN/TC 190.
- [3] H. Gökce, D. Agaogulları, M. Lütfi Övecoglu, I. Duman, T. Boyraz,, Journal of the European Ceramic Society, 2011, 31, 2741–2747.
- [4] A. Yamun, S. Honda, K. Sumita, M. Yanagihara, S. Hashimoto, H. Awaji, Microporous and Mesoporous Materials, 2005, 85, 169–175.
- [5] J. Banjuraizah, H. Mohamad, Z. A. Ahmad, Journal of Alloys and Compounds 2011, 509, 1874–1879.
- [6] A. Yamuna, R. Johnson, Y.R. Mahajan, M. Lalithambika, Journal of the European Ceramic Society, 2004, 24 65–73.

SYNTHESIS AND THERMAL PROPERTIES OF CHITOSAN/BENTONITE NANOCOMPOSITES

J. Pavličević¹, A. Aroguz², O. Bera¹, S. Sinadinović-Fišer¹, N. Lazić³,
O. Borota¹, Milovan Janković¹

¹*University of Novi Sad, Faculty of Technology, Republic of Serbia*

²*Istanbul University, Engineering Faculty, Istanbul, Turkey*

³*Institute of General and Physical Chemistry, Belgrade, Republic of Serbia*

Abstract

Biopolymer nanocomposites are often used as superior adsorbents in colored waste water treatment, due to their biodegradable and nontoxic nature. In this study chitosan/bentonite nanocomposites were produced by clay addition into the polymer using solution technique. Bentonite was modified before the composite preparation. The morphology of the composites was studied by scanning electron microscopy (SEM). The glass transition temperature of obtained nanobeads was investigated using differential scanning calorimetry (DSC). It was estimated that finely dispersed clay particles in the polymer matrix affects the adsorption behavior. Taking into consideration the area of application, the chitosan seems to be very promising material as the component in nanocomposites for the adsorption of dye from waste water.

Introduction

Nowadays, the significant attention is paid to resolving the problem of earth-environmental pollution and biopolymer composites are used as excellent adsorbents [1]. Chitosan, a linear polysaccharide formed from randomly distributed β -(1-4)-linked D-glucosamine and N-acetyl-D-glucosamine, is a positively charged polymer that can bind to negatively charged substances [2]. Bentonite is a member of the smectite group minerals and has a layered structure with large adsorption capacities for polymer molecules due to their unique crystal structure [3]. The aim of this applicative investigation was to study the adsorption and thermal properties of chitosan/bentonite composites for their possible application in the industry for colored waste water treatment.

Experimental

In the first step, clay was modified in a following way: bentonite (obtained from MTA, Ankara, Turkey) was dried at 110 °C for 2 h and modified after sieved through 200 μ m sieve. Then, 1g of bentonite was suspended in 100 ml distilled water at room temperature. The surfactant, cetyltrimethyl ammonium bromide (CTAB) was used to form the network structure with chitosan and thus, enhance its adsorption properties. Firstly, CTAB was dissolved in hot water (1 wt. %) and then slowly poured into the bentonite suspension and stirred for 24 h at ambient temperature. Bentonite was filtered, washed three times, dried under vacuum and,

H-06-P

as final product, crushed into powder and sieved again. In order to obtain chitosan solution, biopolymer was suspended in water at 121 °C for 25 minutes and then dissolved by addition of acetic acid, in a sterile medium. The homogeneous solution was obtained after stirring for 48 h. Four different chitosan/bentonite nanobeads (see Table 1) were prepared using the following procedure: modified clay was firstly swelled by 50 ml of distilled water, added to 50 ml chitosan solution and stirred at 60 °C to overnight. The chitosan droplets formed a bead shape in the solution and they were left in the solution for 12 h. The filtered nanocomposite beads were washed by deionized water and stored in distilled water for use. The mean diameter of the beads was 2.5-3.0 mm. The structure of obtained chitosan/bentonite nanocomposites was followed using scanning electron microscope JEOL JSM-6460 at magnifications from 10^3 to 2×10^6 at 25 kV. Thermal properties of obtained nanobeads were investigated by DSC Q20 TA Instruments, from 30 °C to 300 °C, with a heating rate of 10 °C/min.

Table 1. The code and description of obtained chitosan/bentonite nanobeads (sample name, the volume of chitosan/bentonite solution, the weight content of chitosan/bentonite nanocomposites powder, the volume of NaOH solution and the molarity of NaOH solution).

sample code	Chitosan/clay solution, ml	Chitosan/clay powder, wt. %	NaOH, ml	NaOH, mol
Sample 1	3	6	10	1
Sample 2	5	4	10	1
Sample 3	3	6	10	5
Sample 4	2	5	10	5

Results and Discussion

The intercalated structure of different nanobeads is displayed in Fig. 1. On the basis of SEM results, it can be seen that the adsorption properties of chitosan/bentonite nanocomposites final structure is significantly influenced by the concentration of base (NaOH).

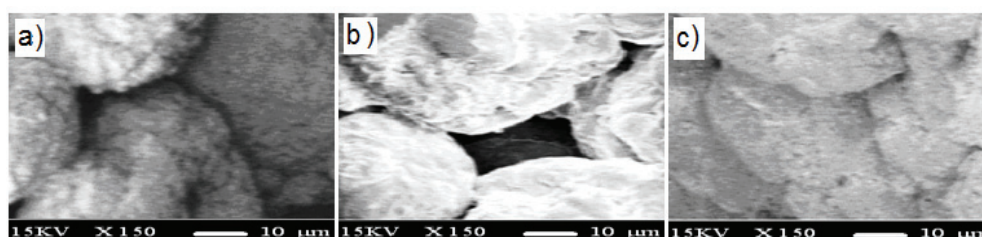


Figure 1. SEM micrographs of a) sample 1, b) sample 2 and c) sample 3.

DSC thermograms of obtained chitosan/bentonite nanocomposites are shown in Fig. 2a. The enthalpy of endothermic peak assigned to adsorbed water evaporation (detected above 100 °C) depends on molarity of NaOH solution. To

erase the effect of moisture, two heating cycles were performed. The first and second runs of chosen sample are shown in Fig. 2b. From the second scan for all investigated samples, the glass transition temperature was found at 144 °C.

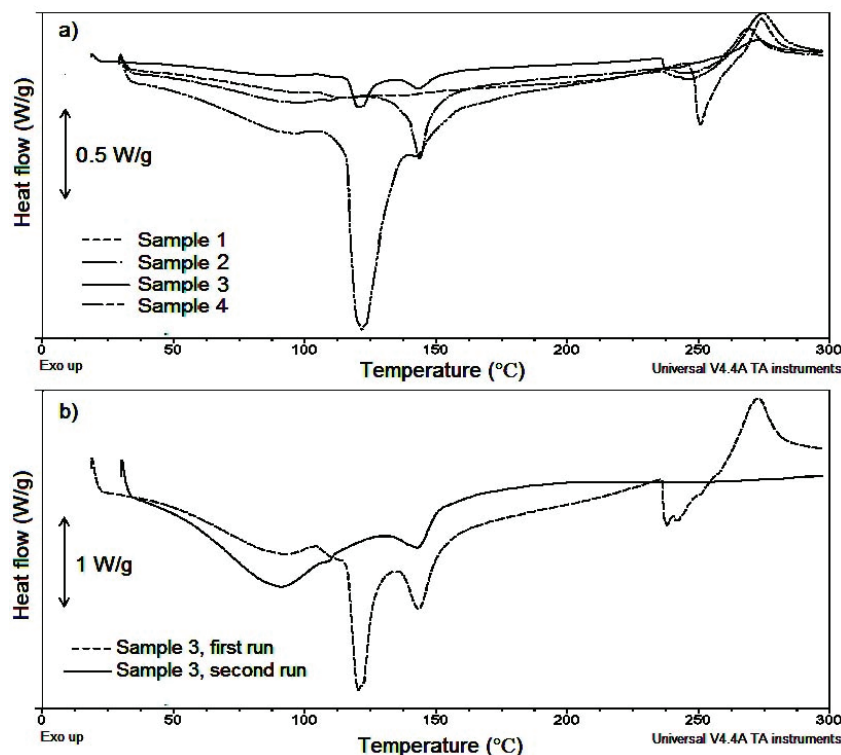


Figure 2. a) DSC curves of prepared chitosan/bentonite nanobeads and b) the first and second DSC run for sample 3.

Conclusions

In this applicative research, with a proper preparation procedure biopolymer nanobeads based on chitosan and bentonite intended for waste water purification were successfully obtained. It was shown that the preparation procedure of nanobeads affects the morphology and thermal behavior of biopolymer nanocomposites. It was found that the concentration of base for composites precipitation is very effective for the final structure of beads. Thermal properties of biopolymer hybrid materials are influenced by bentonite incorporation, thanks to a physical barrier effect of the silicate layers. The addition of bentonite improves adsorption properties of deflocculated chitosan, which is desired for the application of obtained biopolymers in colored waste water treatment.

Acknowledgement

This work is financially supported by Ministry of Education and Science of the Republic of Serbia (Project No. III45022).

References

- [1] K. Sakurai, T. Maegawa, T. Takahashi, *Polym.*, 2000, 41, 7051–7056.
- [2] E. Gunister, D. Pestreli, C.H. Unlu, O. Atıcı, N. Gungo *Carbohyd. Polym.*, 2007, 67, 358–365.
- [3] Q.Y. Yue, Q. Li, B. Y. Gao, Y. Wang, *Sep. Pur. Technol.*, 2007, 54, 279-290.

SYNTHESIS AND STRUCTURAL PROPERTIES OF F-DOPED LiFePO_4/C COMPOSITE

M. Milović¹, D. Jugović¹, M. Mitrić², B. Jokić³, D. Uskoković¹

¹*Institute of Technical Sciences of SASA, Belgrade, Serbia*

²*Vinča Institute of Nuclear Sciences, University of Belgrade, Belgrade, Serbia*

³*Faculty of Technology and Metallurgy, University of Belgrade, Belgrade, Serbia*

Introduction

Olivine type LiFePO_4 is used as a cathode material for Li-ion batteries because of its high energy density (with capacity of 170 mAh/g and plateau voltage of 3.5 V vs. Li^+/Li), stability, safety, environmental friendliness and low cost. However, the low intrinsic electronic and ionic conductivity limits its application.

Effects of cation doping on improving electrochemical performance of LiFePO_4 has been widely studied and debated [1]. On the other hand, anion doping has not been sufficiently investigated. It is generally accepted that doping of LiFePO_4 with fluorine would enhance its electrochemical performance. Several papers are dealing with the influence of small quantities of fluorine dopant on the properties of LiFePO_4 [2, 3]. In this paper, we report on the impact of F doping on the crystal structure of LiFePO_4/C composite obtained through the co-precipitation in molten stearic acid, a new method established by our group [4].

Experimental

F-doped LiFePO_4/C was synthesized by co-precipitation in molten stearic acid [4]. In the molten stearic acid, stoichiometric amounts of aqueous solutions of $(\text{NH}_4)_2\text{HPO}_4$ and $\text{FeSO}_4 \cdot 7\text{H}_2\text{O}$ were added sequentially when precipitation occurred. Dry melt was reground and mixed with solid LiF, which served as both lithium and fluorine source. Thus obtained powder was calcined at temperature of 700°C for 3 hours in a slightly reductive atmosphere ($\text{Ar} + 5\%\text{H}_2$), then washed in distilled water and dried under vacuum. The properties of thus obtained powder were compared with the previously published data of the undoped one obtained under the same synthesis conditions, except for lithium salt [4].

X-ray diffraction data were collected on a Philips PW 1050 diffractometer with $\text{Cu-K}\alpha_{1,2}$ radiation (Ni filter) at the room temperature. Measurements were done in 2θ range of 10-110° with scanning step width of 0.02° and 14 s times per step. Crystal structure refinement was based on the Rietveld full profile method [5] using the Koalariet computing program [6]. Chemical composition of the final compound was $\text{Li:Fe:P} = 0.99:1.00:1.00$ determined by inductively coupled plasma (ICP) analysis. The fluorine in the sample was detected with SA720 ion selective electrode (ISE).

Results and Discussion

X-ray powder diffraction pattern (Fig. 1) was used for phase identification and structural analysis. Olivine type LiFePO_4 was obtained as a major phase with FeS as an impurity phase. There is no evidence of a crystalline carbon, so internal carbon could be treated as a contribution to the background. The structure of F-doped LiFePO_4 has been refined in the space group $Pnma$ (D_{2h}^{16}) in olivine type with following crystallographic positions: Li^+ ions in special crystallographic position $4a$ $[0,0,0]$ with local symmetry $\bar{1}$; Fe^{2+} and P^{5+} ions occupy two different crystallographic $4c$ positions $[x,0.25,z]$ with local symmetry m ; O^{2-} ions occupy three different crystallographic positions: additional two $4c$ positions and one general $8d$ position $[x,y,z]$ with local symmetry 1 .

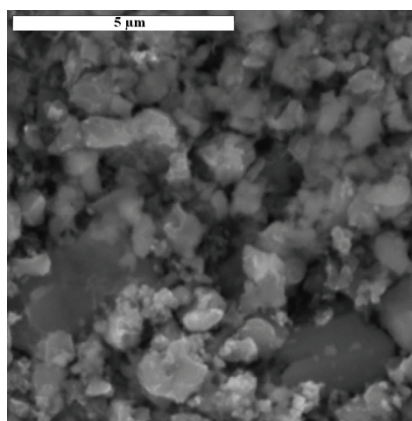
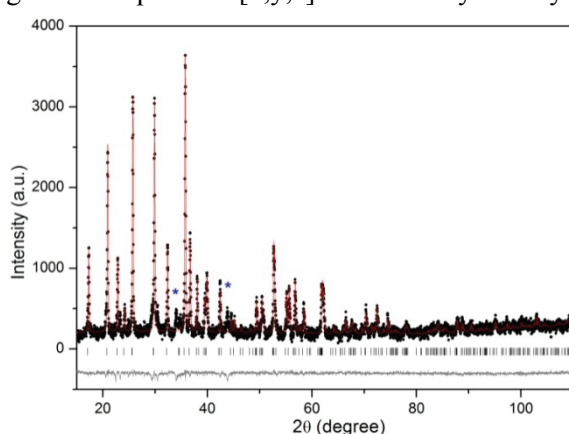


Fig. 1. The observed (\bullet), calculated ($-$), and difference (bottom) X-ray diffraction data of F-doped LiFePO_4/C taken at room temperature; vertical markers below the diffraction pattern indicate positions of possible Bragg reflections; the

Fig. 2. Scanning electron microscopy image of F-doped LiFePO_4/C prepared via co-precipitation method.

The Rietveld refinement results (Table 1 and 2) indicate decreased lattice parameters and primitive cell volume compared with the undoped sample synthesized under the same conditions [4]. This finding is an evidence that F^- ions are successfully incorporated in the lattice, since F^- ions are smaller than O^{2-} ions ($r^{\text{VI}}(\text{F}^-) = 1.33 \text{ \AA}$, $r^{\text{VI}}(\text{O}^{2-}) = 1.40 \text{ \AA}$). There are three kinds of O sites (namely O1, O2, and O3) in the lattice that may be occupied by fluorine separately or randomly. The best refinement was accomplished when O2 site was allowed to be occupied by fluorine ions. The calculated value of dopant concentration matches well with the chemical composition of the powder. Furthermore, doping with fluorine resulted in increased crystallite size. The Rietveld refinement also showed additional electron density on the lithium sites indicating so-called "anti-site" defect in which Li ion (on the M1 site) and Fe ion (on the M2 site) are interchanged.

Table 1. The final results of the structural refinement for undoped [4] and F-doped LiFePO₄.

	Lattice parameters [Å]	Primitive cell volume [Å ³]	Mean crystallite size [nm]	Li site occ. by Fe	O2 site occ. by F	R factor [%]
LiFePO ₄	a = 10.3279(3) b = 6.0096(2) c = 4.6994(1)	V = 291.68(9)	75(10)	0.020(5)	-	Rwp = 4.49
F-doped LiFePO ₄	a = 10.3340(2) b = 6.0086(1) c = 4.6943(3)	V = 291.49(8)	150(9)	0.027(3)	0.04(1)	Rwp = 2.07

Table 2. Fixed and refined atomic coordinates.

Fractional coordinates	LiFePO ₄			F-doped LiFePO ₄		
	x	y	z	x	y	z
Li (4a)	0	0	0	0	0	0
Fe (4c)	0.2820(3)	0.25	0.9749(4)	0.2820(2)	0.25	0.9724(8)
P (4c)	0.0924(4)	0.25	0.4140(6)	0.0939(6)	0.25	0.4155(6)
O(1) (4c)	0.1039(6)	0.25	0.7343(7)	0.1076(9)	0.25	0.7331(2)
O(2) (4c)	0.4563(6)	0.25	0.2100(7)	0.4650(9)	0.25	0.2126(6)
O(3) (8d)	0.1682(1)	0.0426(7)	0.2828(6)	0.1691(9)	0.0365(9)	0.2804(5)

The typical SEM image of as-prepared F-doped LiFePO₄/C composite is presented in Fig. 2. It shows wide particle size distribution, with increased particle size compared to the undoped powder. Apparently, F substitution catalyzes the growth of the primary particles. By comparing mean particle size estimated from SEM image (Fig. 2.) with mean crystallite size (Table 1) it can be concluded that particles are polycrystalline composed of a number of crystallites.

Conclusion

F-doped lithium iron phosphate powder was successfully synthesized by facile co-precipitation in molten stearic acid followed by thermal treatment. Crystal structure refinement showed that doping with fluorine ions preserves olivine structure. According to the Rietveld refinement fluorine ions occupy separately O2 oxygen site. Scanning electron microscopy showed that F substitution catalyzes the growth of the primary particles.

References

- [1] J. W. Fergus, J. Power Sources, 2010, 195, 939-954.
- [2] F. Lu, Y. Zhou, J. Liu, Y. Pan, Electrochim. Acta, 2011, 56, 8833-8838.
- [3] M. Pan, X. Lin, Z. Zhou, J. Solid State Electrochem., 2011, 16, 1615-1621.
- [4] D. Jugović et. al., J. Power Sources, 2011, 196, 4613-4618.
- [5] H. M. Rietveld, J. Appl. Cryst., 1969, 2, 65-71.
- [6] R. W. Cheary, A. Coelho, J. Appl. Cryst., 1992, 25, 109-121.

SYNTHESIS, CHARACTERIZATION AND PHOTOCATALYTIC ACTIVITY OF ANATASE NANOPARTICLES DOPED WITH GADOLINIUM IONS

N. D. Abazović, M. Radoičić, M.I. Čomor

*Vinča Institute of Nuclear Sciences, University of Belgrade, P.O. Box 522, 11001
Belgrade, Serbia*

Abstract

Gd³⁺-doped anatase nanoparticles have been synthesized via acidic hydrolysis of Gd³⁺ and Ti⁴⁺ organic precursors. The resulting products were characterized by X-ray diffraction (XRD) and diffuse reflection spectra (DRS). Experimental results indicated that different Gd³⁺-doping levels make great impact on the optical properties and photocatalytic activity of the obtained TiO₂ nanoparticles. All applied doping concentrations induced enhancement of photoactivity regarding degradation of Rhodamine B (RB), compared to pure TiO₂. The inter-band defect states formed as a result of incorporation of Gd³⁺ ions in the TiO₂ matrix are most probably the cause of observed improved photocatalytic activity and optical properties of the doped TiO₂ nanoparticles.

Introduction

The photocatalytic degradation of pollutants in water and air has attracted much interest in the last several decades. A special attention is focused on the application of anatase titania for photodegradation of various organic pollutants under ultraviolet (UV) or solar light [1]. The band gap of anatase (3.2 eV) is not ideal for solar applications, which limits its wide application in visible range. The development of titania based photocatalysts that can be excited by visible light has received lately great attention. Many methods are attempted, such as dye sensitization, surface modification and transition metals doping [2].

Homogenous hydrolysis of titanium (IV) salts in acidic solution (pH about 1) is very simple preparation method, which can be easy executable in production of titania nanostructures doped with various metal ions [3]. Modification of previously described method [3] was used in preparation of series of titania photocatalysts doped with gadolinium ions. Obtained materials were characterized using XRD, UV/Vis reflectance and absorption, and their photocatalytic activity was checked. Rhodamine B dye (RB) was selected as a model reactant for photodegradation.

Experimental

Chemicals including Ti(O-*i*-C₃H₇)₄ (Sigma-Aldrich), *i*-C₃H₇OH (Baker, HPLC grade), Gd³⁺-acetylacetonate (Aldrich), etc. were commercial products and used as received without further purification. Water was purified by a Milli-Q system (Millipore) and had a resistivity ≥ 18 MV cm.

Routinely, 2 mL of $\text{Ti}(\text{O}-i\text{-C}_3\text{H}_7)_4$, dissolved in 10 mL of $i\text{-C}_3\text{H}_7\text{OH}$, was added into 250 mL of a mixture of water and $i\text{-C}_3\text{H}_7\text{OH}$ (1 : 1, pH~ 1 adjusted by HNO_3) when TiO_2 was synthesized, or solution of appropriate amount of Gd^{3+} - acetylacetonate dissolved into 250 mL of a mixture of water and $i\text{-C}_3\text{H}_7\text{OH}$ (1 : 1, pH~1 adjusted by HNO_3) under vigorous stirring at 0°C . After being continuously stirred at room temperature (20°C) for two days, the reaction solution was dialyzed for purification and adjustment of the pH of the colloidal solution as formed (pH~ 2.3). Finally, the solution was vacuum evaporated at RT to yield powder samples.

The UV/vis diffuse reflectance spectra (DRS) were recorded on an Evolution 600 UV/vis spectrophotometer (Thermo Scientific), equipped with DRA-EV-600 Diffuse Reflectance Accessory.

Photocatalytic activity was obtained using whole spectrum of Xe-lamp, 150 W, as irradiation source used routinely when simulation of solar spectrum is necessary. Experimental solutions were irradiated in cylindrical vessels (20 ml) in the stream of O_2 . In certain time intervals, aliquots were taken from experimental solutions, centrifuged in order to separate powder catalyst and absorption at 552 nm (peak of RB) of the supernatant was measured. Photocatalytic activity was observed as a fraction of RB (C/C_0) still present in the reactor after certain time of irradiation.

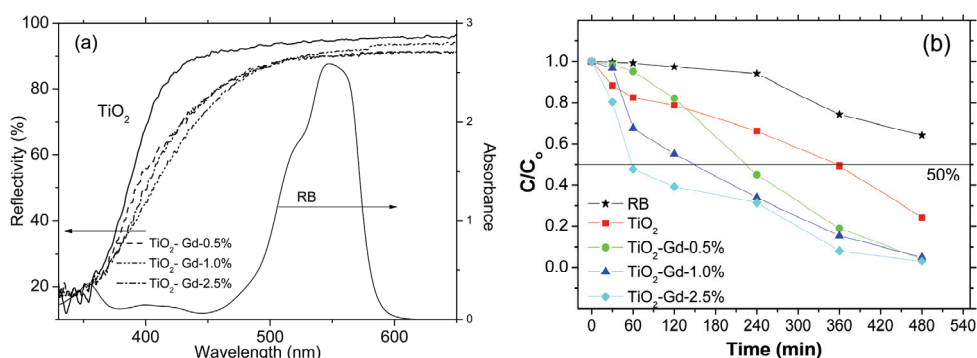


Figure 1 (a) DRS of the obtained powders and absorption spectrum of RB; (b) effect of different photocatalysts on the degradation of RB. Initial concentration of RB was 10^{-5} M; concentration of catalyst was 1 mg/ml. For comparison photolysis of RB is also presented.

Results and Discussion

The DRS spectra of synthesized samples are shown in Fig. 1 (a). The onset of the absorption spectrum of pure TiO_2 appearing at about 400 nm matches well with the intrinsic band-gap of anatase (3.2 eV). Comparing diffuse reflectance spectra of pure TiO_2 and Gd^{3+} -doped samples with Gd nominal amount of 0.5, 1.0 and 2.5 at% it can be seen that there is a significant shift in the onset absorption towards the higher wavelengths for all the Gd^{3+} -doped samples. Firstly, it may be due to appearance of a new electronic state in the TiO_2 band gap. Therefore, the distance of charge transfer between f electrons of the rare earth ions and the conduction or valence band of TiO_2 is narrowed. Accordingly, it leads to visible light absorption

response of obtained samples. Second, Gd^{3+} ions enter into the anatase structure as substitutional defects on the Ti position and act as photo-electron traps, playing an important role in the separation of electron–hole pairs, which could increase the photon efficiency. Consequently, doping with Gd^{3+} might be favorable for the separation of photo-induced electron–hole pairs, which leads to the enhancement of the photo-catalytic activity.

In order to explore this possibility, we used photocatalytic degradation of RB dye. In Fig. 1 (b) comparison of photocatalytic activity of pure, Gd^{3+} -doped TiO_2 and photolysis of RB using Xe-lamp is presented. As shown, there are great differences between photolysis and photocatalytic degradation of RB. After one hour of irradiation, 50% of RB is degraded using TiO_2 doped with 2.5 at.% of Gd^{3+} ions, while photolysis yield almost no degradation and pure TiO_2 degraded ~ 20 % of RB in applied experimental conditions. With longer irradiation times, differences between doped samples decrease, but they are all more active than pure TiO_2 obtained using the same synthetic procedure. So, as already stated the presence of Gd^{3+} ions is beneficial for photocatalytic activity because of separation of photoexcited charges and extended absorption threshold into visible spectral range. Furthermore, substituting Ti^{4+} by Gd^{3+} creates a charge imbalance, which must be satiated [4]. Therefore more hydroxide ions would be adsorbed on the catalyst surface. The hydroxide ions act as hole traps that also inhibit electron/hole recombination and promotes degradation reactions.

Conclusions

Gd^{3+} -doped anatase nanoparticles were synthesized using room-temperature sol-gel process from organic precursors. Obtained powders had absorption thresholds moved to visible spectral range compared to pure TiO_2 . Optical properties were correlated with photocatalytic activity of obtained powders. The best photocatalytic activity regarding degradation of Rhodamine B showed doped TiO_2 nanopowder with 2.5 at% nominal concentration of Gd^{3+} ions. It is shown that doping of TiO_2 with Gd^{3+} is beneficial for improvement of its photocatalytic activity regarding degradation of RB.

Acknowledgment

Financial support for this study was granted by Ministry of Education and Science of the Republic of Serbia, project 172056.

References

- [1] A. Fujishima, T. N. Rao, D. A. Tryk, J. Photochem. Photobiol. C, 2000, 1, 1–21.
- [2] X. Chen, S. S. Mao, Chem. Rev., 2007, 107, 2891-2959.
- [3] D. V. Šojić, V.N. Despotović, N.D. Abazović, M.I. Čomor, B.F. Abramović, J. Hazard. Mater., 2010, 179, 49-56.
- [4] J. Xu, Y. Ao, D. Fu, C. Yuan, Colloids and Surfaces A: Physicochem. Eng. Aspects 2009, 34, 107–111.

GREEN SYNTHESIS OF SILVER NANOPARTICLES USING *BACILLUS LICHENIFORMIS* STRAIN

D. Jakovljević¹, J. Stefanović¹, D. Ilić², G. Gojgić-Cvijović¹, M. Vrvic^{1,2}

¹*ICH_{TM} - Department of Chemistry, University of Belgrade, Njegoševa 12, P.O. Box 473, 11000 Belgrade, Serbia (djakovlj@chem.bg.ac.rs)*

²*Faculty of Chemistry, University of Belgrade, Studentski trg 12-16, P.O. Box 51, 11158 Belgrade, Serbia*

Abstract

The development of eco-friendly technologies in different areas, as well as in nanotechnology, is of great importance to the expansion of the many biological applications of microorganisms. In this work, the synthesis of silver nanoparticles by the reduction of aqueous Ag⁺ ions using the non-pathogenic bacterial strain *B. licheniformis*, under mild conditions, was investigated. The synthesized nanoparticles were characterized by UV-Vis spectroscopy, scanning electron microscopy (SEM), and electron diffraction spectroscopy (EDX).

Introduction

Nanoparticles usually can be synthesized by physical, chemical and biological methods. Nowadays, important segment of nanotechnology is the synthesis of nanoparticles with well-defined chemical composition, size, shape and polydispersity by different microorganisms [1]. In this way the process of obtaining the metal nanoparticles is usually a part of the defense mechanism of microorganisms from highly reactive metal ions. The synthesized nanoparticles are used in many areas, such as catalysis, biosensors or drug delivery systems. Silver nanoparticles have important applications as an antibacterial agent, and also show excellent biocompatibility which makes them suitable for use in nanoimmunology and nanomedicine [1].

The aim of the presented work was the synthesis of silver nanoparticles through a eco-friendly process, by the non-pathogenic *B. licheniformis* strain isolated from petroleum sludge sample taken from Oil Refinery Novi Sad [2].

Experimental

B. licheniformis strain was grown on nutrient broth by incubation at 200 rpm for 24 h at 28 °C. After 24 h, the culture was centrifuged at 15,000 rpm for 15 min. Wet biomass (2 g) was washed with phosphate buffer (pH 7.0), mixed with 1 mM AgNO₃ (3 ml) and incubated for 24 h at 200 rpm followed by sonication (5min, 40 KHz, 20 °C) and centrifugation (10,000 rpm; 30 min) [3]. The culture supernatant was used for the characterization of silver nanoparticles. UV-VIS spectra were obtained using [spectrophotometer GBC Cintra 40](#). Further characterization of particles was performed through analysis of dried sample (obtained by evaporation

of water at 50 °C) by using scanning electron microscope (SEM), Model JEOL JSM-6610LV, that equipped with energy dispersive X-ray spectrometry (EDX).

Results and Discussion

The aqueous silver ions were reduced to metallic silver on exposure to the bacterial biomass. The UV-VIS spectrum of culture supernatant showed a strong, broad absorption maximum at 430 nm (Fig. 1.) characteristic of silver nanoparticles due to its surface plasmon resonance [4].

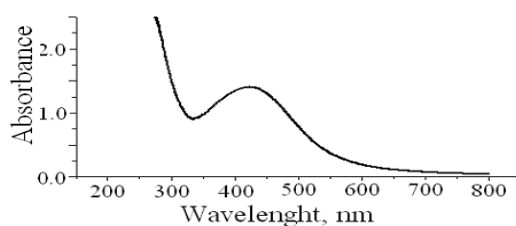
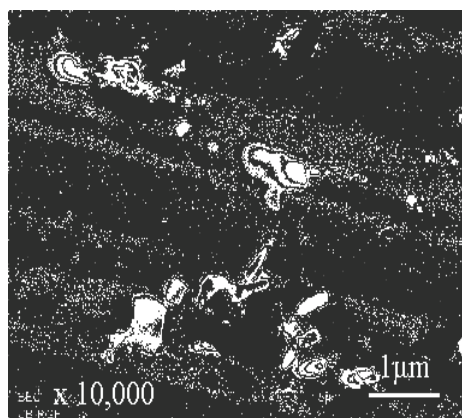


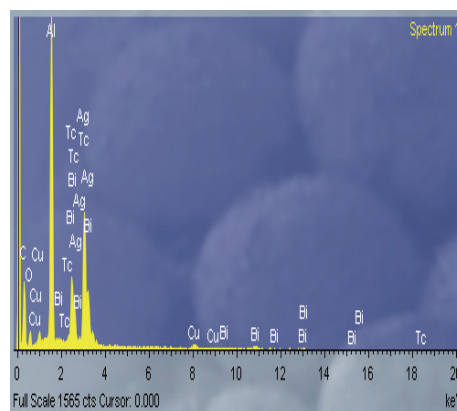
Figure 1. UV-VIS spectrum of silver nanoparticles synthesized by *B. licheniformis* strain.

Their formation was confirmed visually too, by solution color change from colorless to brown. The nano particles formed were

polydisperse and some of them were self-assembled into larger aggregates (Fig 2.a).



(a)



(b)

Figure 2. SEM micrograph (a) and EDX spectrum (b) of the dried sample nanoparticles produced by *B. licheniformis* cells with the treatment of 1×10^{-3} M silver nitrate.

The enzyme involved in this synthesis is likely the nitrate reductase, present in *B. licheniformis*. This nitrate inducible enzyme reduces Ag^+ ions to metallic silver [5].

Presence of silver was confirmed by EDX spectrum (Fig. 2b). Sharp signal in the silver region confirmed the formation of silver nanoparticles (Fig 2). Metallic silver nanocrystals generally show typical absorption peak approximately at 3 keV due to surface plasmon resonance.

Conclusion

The results present in this work showed a route for the production of silver nanoparticles from aqueous solution of AgNO₃ by *B. licheniformis* strain. The synthesis of these particles was confirmed by UV-VIS, SEM and EDX data. The production of nanoparticles by microorganisms is considered to be clean, nontoxic, and environmentally acceptable “green chemistry” procedures.

Acknowledgement

This work was supported by the Ministry of Education and Science of the Republic of Serbia, through Project III 43004.

References

- [1] V. Deepak, K. Kalishwarlal, S. R. K. Pandian, S. Gurunathan, in M. Rai, N. Duran (Eds), *Metal Nanoparticles in Microbiology*, 2011, 17-37.
- [2] G. D. Gojic-Cvijovic, J. S. Milic, T. M. Solevic, V. P. Beskoski, M. V. Ilic, L. S. Djokic, T. M. Narancic, M. M. Vrvic, *Biodegradation*, 2012, 23, 1-14.
- [3] K. Kalimuthu, R.S. Babu, D. Venkataraman, M. Bilal, S. Gurunathan, *Colloids Surf. B: Biointerface*, 2008, 65, 150-153.
- [4] M. Sastry, K.S. Mayya, K. Bandyopadhyay, *Colloids Surf. A*, 1997, 127, 221-228.
- [5] M. Sastry, V. Patil, S.R. Sainkar, *J. Phys. Chem. B*, 1998, 102, 404-1410.

**EFFECTS OF AMBIENT AND ELEVATED DRYING
TEMPERATURE ON MORPHOLOGICAL
CHARACTERISTICS OF POLY(ϵ -CAPROLACTONE)
OBTAINED WITHOUT AND WITH DIFFERENT
STABILIZERS**

*N. Filipović, *M. Stevanović, *D. Uskoković

**Institute of Technical Sciences of the Serbian Academy of Sciences and Arts, Knez
Mihailova 35/IV, Belgrade 11000, Serbia*

Abstract

Biomaterials have drawn a lot of attention in recent years. In this everyday growing field the key is in synthesis procedure. Thus understanding of the effects of different processing parameters allows us to obtain the desired structure and provides insight into the directions of their further development. In this study it has been examined the influence of different drying temperature on morphology of the poly(ϵ -caprolactone) particles prepared without and with addition of two stabilizers. Samples were dried on ambient and elevated temperature and characterized by Fourier transform infrared spectroscopy (FTIR) and scanning electron microscopy (SEM). For some samples the results showed a big difference between obtained structures.

Introduction

Biodegradable polymers represent a class of extremely useful biomaterials that have found a wide range of application in biomedicine and pharmacology [1]. Its expansion and popularity owes mostly to synthetic polymers used for drug delivery and tissue engineering. Among them a special place belongs to the poly(ϵ -caprolactone) (PCL). This aliphatic polyester have been extensively investigated and considered of high interest due to its biocompatibility, non-toxicity, high permeability to many drugs, exceptional ability to form blends with other polymers, very low degradation rate and ability to avoid acidic conditions during degradation (compared to other well-known drug carriers, such as poly(d,l-lactide-co-glycolide)) [2,3].

Experimental

The method we used to obtain PCL micro/nanoparticles was physicochemical method with solvent/non-solvent systems. It consists of dissolving commercial polymer granules in organic solvent (chloroform) followed by abrupt addition of non-solvent (ethanol). Instantaneous formation of a white suspension-precipitation is due to the polymer deposition on the interface between the solvent and non

solvent medium. The obtained suspension was homogenized on magnetic stirrer at 500 rpm, and after that poured into a Petri dish. Three sets of probes were prepared (i) without addition of any stabilizer, (ii) with dropwise addition of polyvinylpyrrolidone (PVP) and (iii) dropwise addition of poly(α , γ , L-glutamic acid) (PGA). Concentration of PVP and PGA in water was 0.05%. All samples were dried at room and elevated temperature (40 °C) during the next 72 h. The morphology of obtained nano/microparticles and porous samples was evaluated by scanning electron microscope (SEM) (JEOL JSM-639OLV).

Results and discussion

The quality analysis of the samples was performed with FTIR spectroscopy. The three characteristic bands are noticeable for all samples. Those are: carbonyl (C=O) stretching band at 1720cm^{-1} , aliphatic carboxyl-hydro band at 2930cm^{-1} , and C-O stretching band at 1190cm^{-1} . Comparing all three spectra there has been no change in appearance or significant shifting of the bands, which was expected bearing in mind that small amounts of stabilizers were used. Only visible changes were observable for the sample prepared with addition of PGA. Bands intensity was significantly increased (probably as the result of overlapping bands from PGA adsorbed on same function groups) and a new band was noted at 1300cm^{-1} , which could be assigned to N-H band from PGA [4]. These results led us to conclusion that PGA managed to adsorb on the surfaces of PCL particles.

For the PCL sample prepared without stabilizer irregularly shaped and strongly agglomerated particles were obtained (Fig. 1.A). When drying was performed at an elevated temperature the resulting morphology was quite different (Fig. 1.B). There were no small, individual units, but one compact structure. Reduce of the coalescence and agglomerations were achieved by the addition of stabilizers. When PVP was used as stabilizer, particles were still agglomerated and irregular in shape, but particles with spherical shape were observed (Fig. 1.C). The same sample only dried at elevated temp. showed slight changes in morphology (Fig. 1.D). Particles were bigger and more agglomerated. It is evident that PVP did not allow the coalescence of the particles and formation of structure similar to the previous sample. Fig. 1.E revealed that spherical particles with a smooth surface and size below one micron were obtained when PGA was used. This can be explained by the formation of thin protective layer of PGA around the suspended PCL particles. In contrast to room temperature condition instead of spherical particles, porous structure was obtained (Fig. 1.F). It is our opinion that increasing of drying temperature has changed the interaction between particles towards increasing tendency for agglomeration. This way the repulsion of stabilized particles was overwhelmed by its coalescence on a surface contact, leaving the pores of different sizes in all directions.

H-10-P

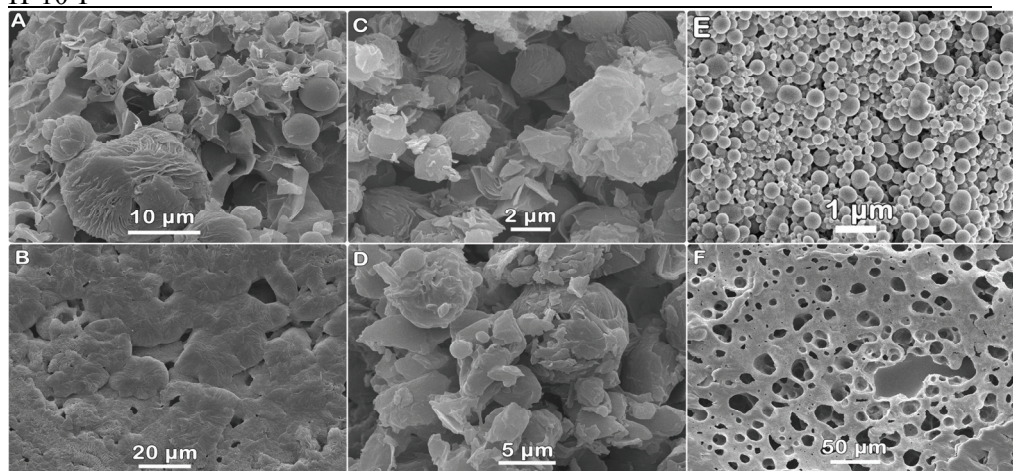


Figure 1. Representative SEM images of different PCL samples. Left column: samples prepared without addition of stabilizer, dried on room (A) and elevated temp. (B); Middle column: samples prepared with PVP, dried on room (C) and elevated temp. (D); Right column samples prepared with addition of PGA, dried on room (E) and elevated temp. (F).

Conclusion

The present study has shown that varying of drying temperature can significantly effect the morphology of obtained particles as well as that this effect is related to the composition of the system. Thus, the changes in morphology was different for all samples after drying at 40 °C: (i) when no stabilizer was used particles were completely coalesced, (ii) for the sample prepared with PVP particles were slightly more agglomerated and bigger, (iii) when PGA was used as stabilizer completely new porous structure was obtained. This highly porous structure could be further investigated as a potential scaffold material.

Acknowledgements

This study was supported by the Ministry of Education and Science of the Republic of Serbia, under Grant No. III45004. Authors would like to thank to Vladimir Pavlović for his help in SEM analysis and Aleksandra Radulović for FTIR measurements.

References

- [1] O. Coulembier et al. *Progr. Polym. Sci.*, 2006, 31, 723–747.
- [2] J. L. Arias, et al. *Colloids Surf. B*, 2010, 75, 204-208.
- [3] T.K. Dash, and V.B. Konkimalla, *J. Control. Release*, 2011, 158, 15-33.
- [4] M. Stevanović, et al. *Int. J. Nanomedicine*, 2011, 6, 2837-2847.

THE INFLUENCE OF CALCINATION TIME ON THE ELECTROCHEMICAL BEHAVIOUR OF $\text{Li}_4\text{Ti}_5\text{O}_{12}$

M. Vujković¹, I. Stojković¹, N. Cvjetičanin¹ and S. Mentus^{1,*}

¹*University of Belgrade, Faculty of Physical Chemistry, Studentski trg 12-16, P.O. Box 137, Belgrade, Serbia, e-mail: milicavuj5@yahoo.com*

* *The Serbian Academy of Sciences and Arts, Knez Mihajlova 35, 11158 Belgrade, Serbia*

Abstract

Nanostructured $\text{Li}_4\text{Ti}_5\text{O}_{12}$ sample was prepared in two steps: hydrothermal reaction at 130°C and post-calcination at 400°C for either 0.5h or 6h. Even half an hour calcination was sufficient to obtain pure spinel $\text{Li}_4\text{Ti}_5\text{O}_{12}$ phase. Its fine crystallite grains enabled favorable electrochemical properties, manifesting themselves by a sharp cyclic voltammograms (CVs) and high charge/discharge capacity. Prolonged calcination made crystallites coarser what corrupted the electrochemical behavior.

Introduction

The safe, cost effective and environmentally acceptable nanostructured electrode materials attract considerable attention in the development of the next generation of Li-ion batteries for automobile industry. Regarding this, $\text{Li}_4\text{Ti}_5\text{O}_{12}$ is one of the most promising candidates. By varying the synthesis condition such as calcination time, Liu et al showed [1] that $\text{Li}_4\text{Ti}_5\text{O}_{12}$ obtained by ball milling method exhibited the best electrochemical performance when calcined for a very long time of 24h. Typical calcination time reported thus far for hydrothermally synthesized $\text{Li}_4\text{Ti}_5\text{O}_{12}$ was 2h [2] and 6h [3]. This study unveiled that much shorter time of annealing suffices for $\text{Li}_4\text{Ti}_5\text{O}_{12}$ to keep favorable electrochemical performance.

Experimental

$\text{Li}_4\text{Ti}_5\text{O}_{12}$ powder was prepared hydrothermally using as starting reactants tetra-n-butyl orthotitanate, LiOH and 30% hydrogen peroxide. After stirred for 1h, the suspension was transferred into a 32 ml Teflon-lined stainless steel autoclave and heated at 130°C for 12 h at the self-established pressure. The solid product was separated by centrifugation, washed with deionized water and dried at 80°C for 4 h. Finally, hydrothermally prepared powder was calcined at 400°C for 0.5h and 6h, in an inert argon atmosphere. For electrochemical investigations, the working electrode was made from the synthesized material (85%), carbon black (10%) and poly(vinylidene fluoride) (PVDF) binder (5%) homogeneously mixed in N-methyl 2-pyrrolidone. The slurry was treated for about 40 min in an ultrasonic bath, homogeneously deposited on a platinum foil ($\sim 2 \text{ cm}^2$), and dried under vacuum at 120-140°C for at least 4h.

The electrolyte was 1M LiClO_4 (Lithium Corporation of America) dissolved in PC (Fluka).

H-11-P

Cyclic voltammetry was performed in a three-electrode electrochemical cell, with the lithium foils as both counter and reference electrodes, using Gamry PCI4/300 Potentiostat/ Galvanostat. The potential was cycled within the limits 2.5 and 1V.

Galvanostatic charging/discharging experiments were performed in a two-electrode arrangement, by means of the software-controlled battery testing device Arbin BT 2042.

Results and discussion

X-ray diffraction (XRD) confirmed that the powders obtained upon annealing of hydrothermally prepared powder precursor for either 0.5h or 6h are pure $\text{Li}_4\text{Ti}_5\text{O}_{12}$ spinel. The morphology of these $\text{Li}_4\text{Ti}_5\text{O}_{12}$ crystalline phases observed by SEM (Fig.1) shows two types of agglomerated spherical particles. The first type of particles, submicron in size, is flower-like spheres composed of numerous homogeneous petals, Fig1 (left). The second type of particles were larger, micron sized particles with a rough surface composed of densely packed rectangular plates, Fig1 (right). With the increase in calcination time, both type of particles became more agglomerated, while the thickness of the plates increased from about 40-60 nm (0.5h annealing) to about 50-80 nm (6h annealing). Thinner and less agglomerated $\text{Li}_4\text{Ti}_5\text{O}_{12}$ nanoparticles obtained at shorter time of annealing are expected to enable shorter diffusion distances of lithium through the solid phase.

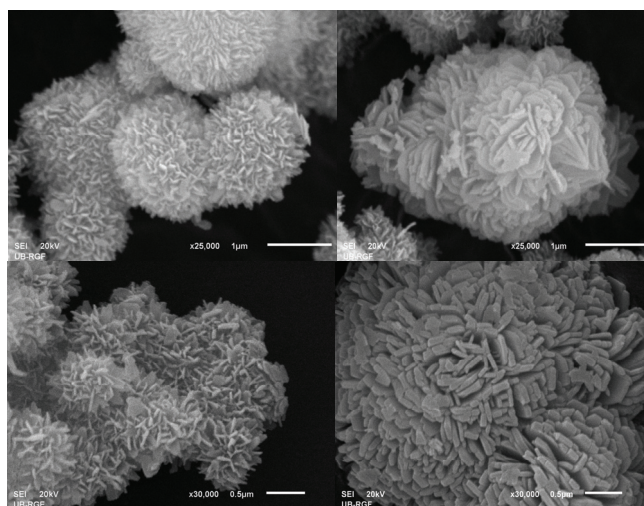


Figure 1. Nanopetals and nanoplates of $\text{Li}_4\text{Ti}_5\text{O}_{12}$ calcined at 400°C for 30min (above) and for 6h (down).

The cyclic voltammograms (CVs) recorded at a common scan rate of 1 mV/s, in 1M LiClO_4/PC electrolyte of $\text{Li}_4\text{Ti}_5\text{O}_{12}$ samples obtained upon different annealing time intervals, are presented in Fig2a. The cathodic and anodic peaks

indicate intercalation/deintercalation of Li ion in/from the spinel lattice, respectively. The shorter peak potential separation and higher peak current density, which is characteristic for faster processes, is observed for the sample treated only half an hour. This may be attributed to the shorter diffusion path for Li ions thanks to the reduced particle size. The initial galvanostatic discharge curves (Fig.2b) displays also higher coulombic capacity utilization for this sample.

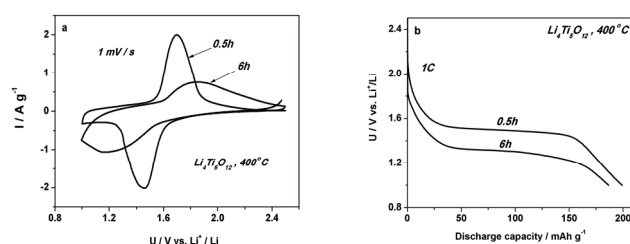


Figure 2. The electrochemical behavior of $\text{Li}_4\text{Ti}_5\text{O}_{12}$ calcined at 400°C for 0.5h and 6h a) CVs, b) Initial discharge curves at a rate of 1C.

Conclusion

The nanostructured $\text{Li}_4\text{Ti}_5\text{O}_{12}$ was successfully synthesized by hydrothermal synthesis at 130°C followed by calcination at 400°C during two time intervals, 0.5 and 6h. Much better electrochemical behavior with respect to lithium intercalation/deintercalation was observed for the sample treated shorter time. Such improvement is attributed to the reduced particle size of this sample. This may help to save time and energy in the process of gross production of $\text{Li}_4\text{Ti}_5\text{O}_{12}$ for Li-ion batteries.

Acknowledgement: The present investigations were supported by the Ministry of Sciences and Environmental Protection of Serbia, Project No III45014.

References:

1. G. Q. Liu, L. Wen, G. Y. Liu, Q. Y. Wu, H. Z. Luo, B. Y. Ma, W. W. Tian, J. Alloys Compd, 2011, 509, 6427-6423.
2. Y. Tang, L. Yang, S. Fang, Z. Qiu, Electrochim. Acta, 2009, 54, 6244-6249.
3. J. Chen, L. Yang, S. Fang, Y. Tang, Electrochim. Acta, 2010, 50, 6596-6600.

H-12-P

**ATR-FTIR MICROSPECTROSCOPIC CHARACTERIZATION OF
NANOMATERIAL CALCIUM PHOSPHATE/POLY-DL-LACTIDE-
co-GLYCOLIDE IN SIMULATED BODY FLUID**

Ž. Mitić¹, M. Vukelić¹, N. Ignjatović², D. Uskoković², P. Vasiljević³,
S. Najman¹, M. Trajanović⁴

¹*Faculty of Medicine, University of Niš, RS-18000 Niš, Serbia
e-mail: zak_chem2001@yahoo.com*

²*Institute of Technical Sciences of the Serbian Academy of Sciences and Arts, RS-
11000 Belgrade, Serbia*

³*Faculty of Sciences and Mathematics, University of Niš, RS-18000 Niš, Serbia*

⁴*Faculty of Mechanical Engineering, University of Niš, RS-18000 Niš, Serbia*

Abstract

The interaction between nanomaterial containing calcium phosphate/poly-DL-lactide-co-glycolide (N-CP/PLGA) and simulated body fluid (SBF) was investigated by Attenuated total reflectance-Fourier transform infrared (ATR-FTIR) microspectroscopy. FTIR results indicate that the basis of morphological changes seen in the material N-CP/PLGA are dissolution of its polymer component and precipitation of the material similar to hydroxyapatite (HA) on its surface. The results obtained in this work indicate that N-CP/PLGA may be a good candidate for application in bone regeneration.

Introduction

Calcium phosphate (CP) crystals, typically a few nanometers in width, incorporated into the polymer matrix are the key components of human bone tissue [1]. Good osteoconductive characteristics of CP, as well as possibility of deriving it from synthetic or natural resources [2], have enabled the development of a wide range of CP based composite biomaterials [3], like hydroxyapatite/bioresorbable polymer composite biomaterials which can be used for the bone tissue reconstruction [4].

Many different types of polymers were used for tissue engineering. Some of the most common polymers include polylactic acid (PLA), polyglycolic acid (PGA), copolymers of PLA and PGA (PLGA), polyanhydrides, polyorthoesters, polycarbonates, etc. [5,6]. Bioresorptive polylactides (PLA) and their copolymers belong to group of nontoxic polymers, because the final products of their degradation (CO₂ and H₂O) enter without difficulty three-carboxylic acid cycle, not disturbing the metabolism of the surrounding tissue. These polymers have been known for their biocompatibility and can be easily seeded with cells and implanted into the recipient [7]. Polymer based nanocomposites will also be briefly introduced as an interesting strategy to improve the biological and mechanical performances of polymer scaffolds, especially for bone tissue engineering [8]. In this paper we compare the interaction between nanomaterial containing calcium

phosphate/poly-DL-lactide-*co*-glycolide (N-CP/PLGA) and SBF by ATR-FTIR microspectroscopy, in order to investigate whether and to what extent ionic composition of human plasma leads to the changes in N-CP/PLGA nanomaterial.

Experimental

The optimization and the entire process of the nanomaterial N-CP/PLGA synthesis, as well as the reaction mechanism of N-CP/PLGA interaction with SBF have been described in detail by Vukelić et al. [9].

FTIR microspectroscopic system, ATR-FTIR spectrometer Bruker Hyperion Tensor-27 in conjunction with a FTIR Bruker Hyperion-1000/2000 microscopy attachment equipped with a 15× objective and a 250-μm liquid nitrogen cooled a narrow-band mercury-cadmium-telluride (MCT) detector (ATR objective GMBH, Germany) with the range of the IR spectrum from 4000 to 400 cm⁻¹, was used in this work. The spectra were measured with 4 cm⁻¹ resolution and 320 scans co-addition.

Results and discussion

The IR spectra of the nanomaterial before and after incubation contain following characteristic bands (Table 1).

Table 1.

$\bar{\nu}$ (cm ⁻¹)	Band assignment	Comment
3570 – 3440	v(O–H)	OH
295 – 3000	v(C–H)	CH
~1760	v(C=O)	carbonyl
1450	δ _{as} (C–H)	CH
1380	δ _{sy} (C–H)	CH
~1420	δ(O–H)	OH
1200 – 1100	v(P=O)	complex band
1100 – 1000	v(P–O)	complex band
950–600	γ(C–H) and γ(O–H)	complex band

The IR spectrum shown in Fig. 1 corresponds to nanomaterial containing calcium phosphate/poly-DL-lactide-*co*-glycolide since it contains groups characteristic of N-CP/PLGA. N-CP is identified within the spectrum by a doublet with maxima at 1050 and 1087 cm⁻¹, which are the most intense and originate from phosphate groups, and by a triplet with maxima at somewhat lower frequencies of 571 and 602 cm⁻¹, arising from the PO₄³⁻ group vibrations, and at 629 cm⁻¹, assigned to OH group vibrations appearing also at 3574 cm⁻¹. PLGA is characterized by an absorption band at 1757 cm⁻¹ corresponding to C=O group vibrations and a lower band at 2940 cm⁻¹ ascribed to C–H group vibrations. Absorption bands at 1454 cm⁻¹ and 1379 cm⁻¹ originates from the CH₃ group bending vibrations. The IR bands changes in the region of OH⁻ and PO₄³⁻ group vibrations, were registered on the nanomaterial after incubation in SBF, correspond to hydroxyapatite similar nanomaterial. The formation of apatite on the surface of

H-12-P

the nanomaterial after immersion in SBF was attributed to the ionic exchange between N-CP/PLGA particles and the SBF solution.

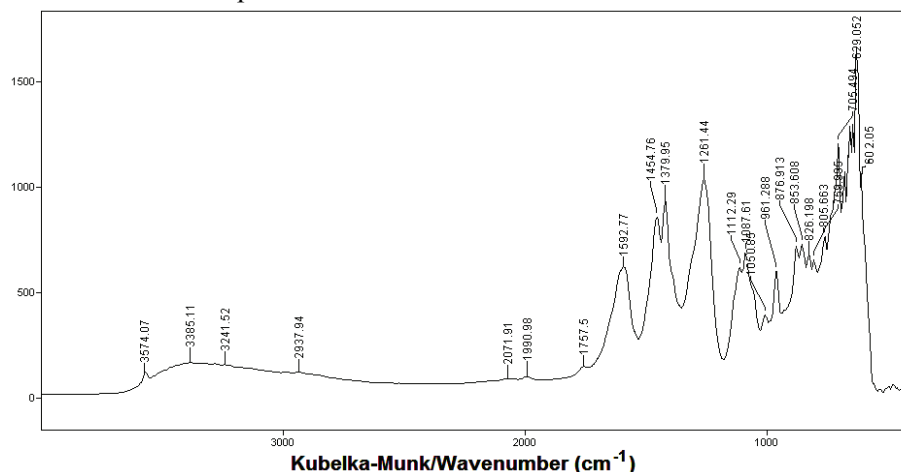


Figure 1. ATR-FTIR spectrum of nanomaterial containing N-CP/PLGA in SBF

Conclusion

The interaction between nanomaterial containing calcium phosphate/poly-DL-lactide-*co*-glycolide (N-CP/PLGA) and simulated body fluid (SBF) was studied by ATR-FTIR microspectroscopy in order to investigate whether and to what extent ionic composition of human blood plasma leads to the changes in the nanomaterial N-CP/PLGA. FTIR results indicate that in SBF nanomaterial N-CP/PLGA undergo precipitation process of the material similar to hydroxyapatite on its surface.

Acknowledgment

This work was realized within **III 41017** project, funded by the Ministry of Education and Science of the Republic of Serbia.

References

- [1] M. Vallet-Regi, J. Gonzales-Calbet, *Prog. Solid State Ch.*, 2004, 32, 1.
- [2] G. Gergely, F. Wéber, I. Lukács, L. Illés, A.L. Tóth, Z.E. Horváth, J. Mihály, C. Balázs, *Cent. Eur. J. Chem.*, 2010, 8, 375.
- [3] R. LeGeros, *Clin. Orthop. Relat. Res.*, 2002, 395, 81.
- [4] N. Ignjatović, V. Savić, S. Najman, M. Plavšić, D. Uskoković, *Biomaterials*, 2001, 22, 571.
- [5] N. Ignjatović, E. Suljovrujić, J. Budinski-Simendić, I. Krakovsky, D. Uskoković, *J. Biomed. Mater. Res. B*, 2004, 71, 284.
- [6] C.M. Agrawal, R.B. Ray, *J. Biomed. Mater. Res.*, 2001, 55, 141.
- [7] R.K. Kulkarni, K.C. Pani, C. Neuman, F. Leonard, *Arch. Surg- Chicago*, 1966, 93, 839.
- [8] A. Gloria, R. De Santis, L. Ambrosio, *J. Appl. Biomater. Biomech.*, 2010, 8, 57.
- [9] M.Đ. Vukelić, Ž.J. Mitić, M.S. Miljković, J.M. Živković, N.L. Ignjatović, D.P. Uskoković, J.Ž. Živanov-Čurlis, P.J. Vasiljević, S.J. Najman, *J. Appl. Biomater. Biomech.*, DOI 10.5301/JABB.2012.9167.

THERMAL PROPERTIES OF POLYCARBONATE-BASED POLYURETHANE/SILICA NANOCOMPOSITES

J. Pavličević¹, S. Petrić², M. Jovičić¹, O. Bera¹, R. Radičević¹,
B. Pilić¹, M. Špírková³

¹*University of Novi Sad, Faculty of Technology, Republic of Serbia*

²*Stock Company for Production of Petrochemicals, Raw Materials and Chemicals
„HIP-Petrohemija“ Pancevo-In Restructuring, Republic of Serbia*

³*Institute of Macromolecular Chemistry, Academy of Sciences of the Czech
Republic, Czech Republic*

Abstract

A series of polyurethane/silica nanocomposites with different nanofiller content were prepared by one-step procedure. All starting components were aliphatic: polycarbonate diol, hexamethylene-diisocyanate (HDI) and 1,4-butanediol (BD) as chain extender. The weight fraction of silica nanoparticles of an average diameter of 150 nm was varied (1, 2, 5 and 10 wt. %). The thermal properties of elastomers were determined using differential scanning calorimetry (DSC). It was found that the melting of hard segments and recrystallization region were influenced by silica addition.

Introduction

The polycarbonate-based polyurethane elastomers are thermoplastic block copolymers consisted of hard (acting as physical crosslinks) and soft (rubbery) segments which form two phase structure on the nanometer level. The properties of polyurethane/silica nanocomposites strongly depend on the type, size and shape of filler, and also on the used preparation method [1, 2]. In our previous research, three phase transitions of polycarbonate-based polyurethanes were detected by differential scanning calorimetry [3]. It was shown that the glass transition temperature of soft segments was not significantly influenced by addition of nanoparticles. This work is aimed at the investigation of the influence of nanosilica content on the endothermic events related to the relaxation of chain segments in the diffused interface between soft and hard segment domains, and melting of hard segments. The effect of silica presence on the recrystallization region of polyurethane hybrid materials was also the subject of interest.

Experimental

The polyurethane nanocomposite films (with the constant layer thickness of 0.4 nm) were obtained by one-step technique. The isocyanate index ($r = [\text{NCO}]/[\text{OH}]$) was 1.05. The number of OH groups belonging to polycarbonate diol and chain extender was equal ($R = [\text{OH}]_{\text{diol}}/[\text{OH}]_{\text{ext}} = 1$). In the first step, the mixture of macrodiol and silica particles was stirred briefly for 24 h. Then, the chain extender and 20 wt. % of catalyst solution were put, and the mixture was degassed. After, as

H-13-P

the last component, diisocyanate was added. The mixture was stirred for 20 min and again degassed. Finally, such prepared multicomponent system was spread on polypropylene sheets using a ruler. All samples were kept in oven at 90 °C for 24 h. The unfilled polyurethane was also analyzed. The investigation of polyurethane phase transition was carried out by means of differential scanning calorimetry (Q20 TA Instruments), from 40 to 180 °C at the heating rate of 10 °C/min. The samples (masses of about 5 mg) were placed in sealed aluminum pans.

Results and Discussion

Figure 1 shows DSC curves of polyurethanes with different silica content in heating and cooling regime. The relaxation of chain segments in diffused interface between soft and hard segment is registered as endothermic event in the temperature range from 40 to 70 °C, while multiple endotherms, assigned to the melting of hard segments (the disruption of physical crosslinks), start above 100 °C (Fig. 1a). From Fig. 1b it can be seen that the recrystallization temperature decreased with the increase of silica content.

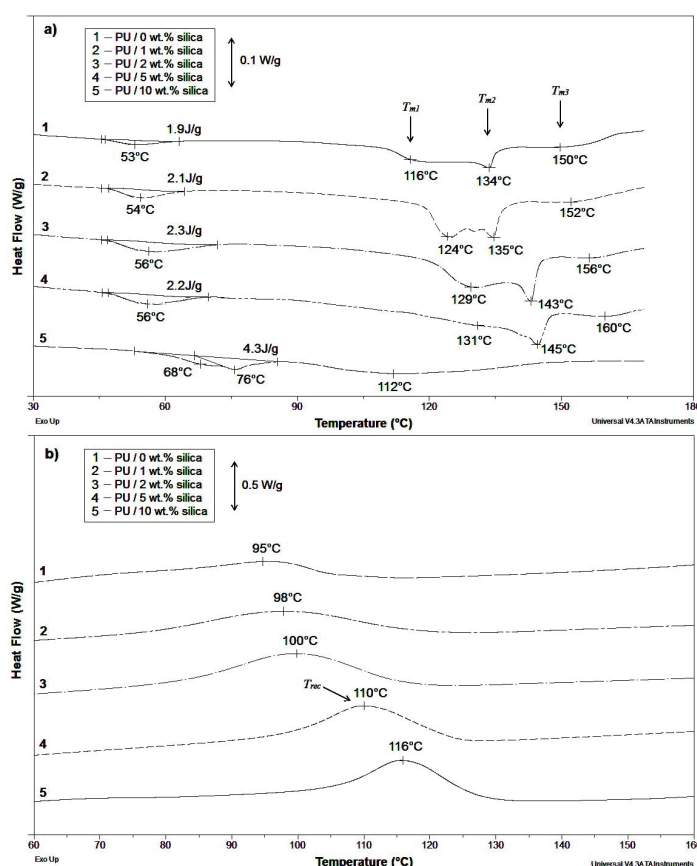


Figure 1. DSC thermograms of polycarbonate-based polyurethanes with different nanosilica content in: a) heating and b) cooling regime.

By the increase of nanofiller content, the melting temperatures (T_{m1} , T_{m2} and T_{m3}) are shifted to higher values, indicating that the silica strongly interacts with hard segments, causing the formation of hydrogen bonding and improving thermal properties of polyurethane. The addition of 1, 2 and 5 wt. % of silica did not cause the significant change of enthalpy of relaxation ΔH_{rel} , enthalpy of fusion ΔH_{fus} and recrystallization enthalpy ΔH_{rec} (Table 1), implying its very good incorporation into the PU matrix. On the other hand, the higher silica concentration (10 wt. %), caused the significant change of enthalpy values and melting mechanism of polyurethane, indicating the heterogeneous structure of obtained nanocomposite.

Table 1. Thermal properties of polycarbonate-based polyurethane with different nanosilica content (relaxation enthalpy ΔH_{rel} , fusion enthalpy ΔH_{fus} and recrystallization enthalpy ΔH_{rec}).

PU code	Silica content (% wt.)	ΔH_{rel} , J/g	ΔH_{fus} , J/g	ΔH_{rec} , J/g
PU / 0	0	1.9	18.9	8.3
PU / 1	1	2.1	18.7	8.1
PU / 2	2	2.3	18.0	7.9
PU / 5	5	2.2	12.3	6.4
PU / 10	10	4.4	11.1	6.1

Conclusions

In this work, a series of polycarbonate-based polyurethane/silica nanocomposites were successfully prepared. By increasing filler content, the melting temperatures of polyurethane nanocomposites are shifted to higher values. The addition of 1, 2 and 5 wt. % of silica negligible changed the enthalpy of relaxation (1.9-2.2 J/g) and the fusion enthalpy (18.0-18.9 J/g), indicating a good silica incorporation into the PU matrix. The higher nanofiller content (10 wt. %) caused significant decrease of ΔH_{fus} , implying the heterogeneous structure of obtained polyurethane/silica nanocomposite.

Acknowledgment

This work is financially supported by Ministry of Education and Science of the Republic of Serbia (Project No. III45022) and Grant Agency of the Czech Republic (Czech Science Foundation, project No. P108/10/0195).

References

- [1] Z. S. Petrovic, I. Javni, A. Waddon, G. Banhegyi, J. App. Polym. Sci., 2000, 76, 133-151.
- [2] X. Chen, L. Wu, S. Zhou, B. You, Polym. Int., 2003, 52, 993-998.
- [3] M. Špírková, J. Pavličević, A. Strachota, R. Poreba, O. Bera, L. Kaprálková, J. Baldrian, M. Šlouf, N. Lazić, J. Budinski-Simendić, Eur. Polym. J., 2011, 47, 959-972.

TEXTURAL PROPERTIES OF MACROPOROUS ACID MODIFIED MONTMORILLONITE NANOCOMPOSITES

M. Žunić¹, Z. Vuković¹, D. Maksin², S. Marinović¹, A. Nastasović³,
A. Milutinović-Nikolić¹

¹*University of Belgrade, Institute of Chemistry, Technology and Metallurgy, Center for Catalysis and Chemical Engineering, Njegoševa 12, 11000 Belgrade, Serbia*

²*University of Belgrade, Vinča Institute of Nuclear Sciences, P.O. Box 522, 11001 Belgrade, Republic of Serbia*

³*University of Belgrade, Institute of Chemistry, Technology and Metallurgy, Center for Chemistry, Njegoševa 12, 11000 Belgrade, Serbia*

Abstract

Macroporous crosslinked copolymer, poly(glycidyl methacrylate-*co*-ethylene glycol dimethacrylate) and its nanocomposites with acid modified montmorillonite (W_A) were synthesized by radical suspension copolymerization. Nanocomposites were obtained by introducing various amounts of W_A into the reaction system. Textural properties of synthesized samples were analyzed by mercury intrusion porosimetry. The synthesized nanocomposites have significantly higher specific surface area in comparison to the copolymer. Total pore volume and the most dominant pore diameter decrease with incorporation of acid modified montmorillonite in copolymer matrix.

Introduction

The study of polymer/clay nanocomposites is currently an expanding field of research because polymer/clay nanocomposites often exhibit a wide range of improved properties over their unmodified starting polymers. The improved properties for these nanocomposites include mechanical, thermal, flammability [1], and textural properties [2,3] and are related to the dispersion and nanostructure of the layered silicate in the polymer.

To our knowledge, we were the first to report the preparation of porous polymer/clay nanocomposites of poly(GMA-*co*-EGDMA) by radical suspension copolymerization [2,3]. Porous materials have numerous applications in such areas as catalysis, chromatography and separation, where control over pore structure and pore size strongly influences the efficiency of the material [4]. Since the application of the obtained nanocomposites strongly depends on its textural properties the goal of the present work was mainly to study the effect of acid modified montmorillonite incorporation on the porous structure of poly(GMA-*co*-EGDMA) based nanocomposites.

The influence of the amount of acid modified montmorillonite introduced into the reaction mixture on the tailoring of textural properties of poly(GMA-*co*-EGDMA) based nanocomposites was investigated.

Experimental

Starting material for acid modification was Wyoming type Na-montmorillonite (Clay Minerals Society Source Clay). Acid modification was performed with 3 M HCl at 90 °C for 2 h. The liquid (acid solution)/ solid (clay) ratio was 4:1. After modification, the clay suspension was filtrated under vacuum. The filtration cake was rinsed with deionized water at 80 °C until the filtrate was Cl^- and/or Fe^{3+} free. After drying to constant mass at 110 °C acid modified clay was reground to pass through a 74 μm sieve and denoted W_A [2,3]. Macroporous crosslinked copolymer, poly(glycidyl methacrylate-*co*-ethylene glycol dimethacrylate) was synthesized by suspension copolymerization in manner that was previously reported [5] and denoted as CP. Nanocomposites were obtained in same manner as CP, only 2.5, 5, 10 mass % of acid modified montmorillonite was introduced into reaction system [2, 3]. The obtained nanocomposites in form of regular spheres (0.15 mm < d < 0.30 mm) were denoted CP-2.5 W_A , CP-5 W_A and CP-10 W_A . The porous structure of samples was determined using Carlo Erba Porosimeter 2000 with Milestone 100 Software System. The specific surface area of samples (S_{Hg}), total pore volume (V_p) and the most dominant diameter in macroporous region (d_{max}) were determined from cumulative pore size distribution curves [6]. Pores have commonly irregular shape and the most similar geometric form is used to represent pore shape [7]. For investigated materials the cylindrical shape is assumed for calculation of textural properties [2, 5].

Results and Discussion

Results obtained by mercury intrusion porosimetry for copolymer and nanocomposites are given in Fig. 1 and Table 1.

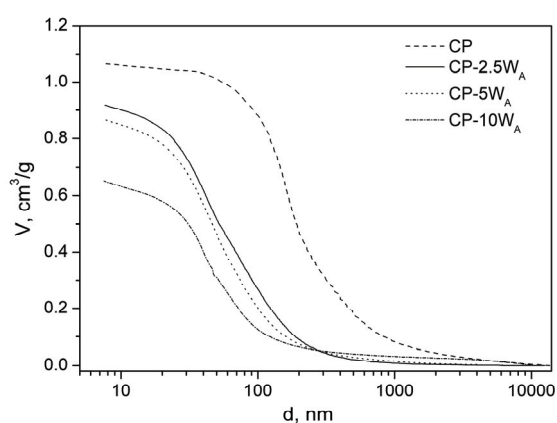


Figure 1. Cumulative pore size distribution curves of the copolymer and nanocomposites with varied amount of acid modified montmorillonite

By comparison of the results obtained for the copolymer and the nanocomposites it can be concluded that all textural properties were affected by the incorporation of the acid modified montmorillonite. The cumulative pore size distribution curve for the copolymer has a plateau in the area of mesopores (<50 nm). On the other hand, the curves for all nanocomposites have a constant increase in the mesoporous area instead of a plateau suggesting the presence of pores <7.5 nm.

H-14-P

Table 1. Porosity parameters of copolymer and nanocomposites.

Sample	S_{Hg} m^2g^{-1}	V_p cm^3g^{-1}	d_{max} nm
CP	33	1.06	170
CP-2.5W _A	88	0.92	58
CP-5W _A	84	0.87	53
CP-10W _A	73	0.66	47

The pore diameter of the nanocomposites shifted toward pores with smaller pore diameters, falling entirely below 200 nm.

Also, a significant increase of specific surface area (almost three times) of the nanocomposites in comparison to the copolymer was obtained. On the other hand, difference in textural properties between nanocomposites with varied amount of incorporated acid modified montmorillonite was less expressed. The values of S_{Hg} , V_p and d_{max} of the nanocomposites slightly decreased with the increase of the amount of introduced W_A.

Conclusion

Macroporous crosslinked copolymer poly(glycidyl methacrylate-*co*-ethylene glycol dimethacrylate) and its nanocomposites with different amounts of acid modified Na-montmorillonite originated from Wyoming (W_A) were synthesized by radical suspension copolymerization. The formation of nanocomposites strongly affected all textural properties. The incorporation of clay filler into copolymer lead to materials with slightly smaller total pore volume but almost three times increased specific surface area in comparison to the copolymer. The difference in textural properties between nanocomposites with varied amount of incorporated acid modified montmorillonite was less expressed.

Acknowledgement

This work was supported by the Ministry of Education and Science of the Republic of Serbia (Projects III 45001 and III 43009).

References

- [1] A. B. Morgan, J. W. Gilman, *J. Appl. Polym. Sci.*, 2003, 87, 1329–1338.
- [2] S. Marinović, Z. Vuković, A. Nastasović, A. Milutinović-Nikolić, D. Jovanović, *Mater. Chem. Phys.*, 2011, [128](#), 291-297.
- [3] S. Marinović, A. Milutinović-Nikolić, M. Žunić, Z. Vuković, D. Maksin, A. Nastasović, D. Jovanović, *Russ. J. Phys. Chem. A*, 2011, 85, 2386-2391.
- [4] J. Normatov, M.S. Silverstein, *Macromolecules*, 2007, 40, 8329-8335.
- [5] S. M. Jovanović, A. Nastasović, N. N. Jovanović, K. Jeremić, Z. Savić, *Angew. Makromol. Chem.*, 1994, 219, 161-168.
- [6] P. A. Webb, C. Orr, *Analytical Methods in Fine Particle Technology*, Micromeritics Instrument Corporation, Norcross, 1997.
- [7] G. Leofanti, M. Padovan, G. Tozzola, B. Venturelli, *Cat. Today*, 1998, 41, 207-219.

OPTICAL PROPERTIES OF ZnO/ZnWO₄ COMPOSITE NANOPARTICLES

T. D. Savić, I. Lj. Validžić, M. I. Čomor

Vinča Institute of Nuclear Sciences, University of Belgrade, P.O. Box 522, 11001 Belgrade, Serbia

Abstract

ZnO/ZnWO₄ composite rod-like nanoparticles were synthesized by low-temperature soft solution method at 95° C with different reaction times (1-120 hours), in the presence of non-ionic copolymer surfactant Pluronic F68. Optical properties such as reflection and room temperature photoluminescence of obtained samples showed strong dependence on their crystallinity and composition.

Introduction

It is well known that ZnO shows good photocatalytic effect and high quantum activity for degradation of environmental pollutants. ZnO has been characterized with its wide bandgap (3.37 eV) and relatively large exciton binding energy (60 meV) at room temperature [1]. ZnWO₄ has been also used for water splitting and mineralization of organic pollutants under UV irradiation [2]. Its commercial application is modest because the photocatalytic activity of ZnWO₄ is not high enough for the requirements of practical application. Literature data regarding band gap energy are different: ranging from 3.8 - 4.6 eV [3].

The subject of this paper is detailed correlation between structure and morphology of ZnO/ZnWO₄ composite nanoparticles and their optical properties. We will show that close junction between ZnO and ZnWO₄ and charge transfer processes define optical properties of nanocomposite

Experimental

All chemicals: Na₂WO₄ x 2H₂O (99% Riedel-de Haën), ZnCl₂ (99% Merck), non-ionic copolymer surfactant Pluronic F68 (Polyoxyethylene-polyoxypropylene block copolymer, M_n~8400 (Aldrich)), NaOH (98% Fluka) and ZnO (≥ 99% Sigma-Aldrich), were of the highest purity available and they were used without further purification. Water employed throughout the work was purified by a Milli-Q system (Millipore) and had a resistivity ≥ 18 MΩ cm⁻¹.

Synthesis of ZnO/ZnWO₄ nanoparticles: 0.1 M ZnCl₂ solution was mixed with 100 ml of copolymer solution (10 g/L). The pH of the solution was adjusted to 8 using 0.1 M NaOH. Under vigorous stirring, 0.1 M Na₂WO₄ x 2H₂O was added drop by drop, and the mixture was refluxed at 95 °C for 1, 5, 48 and 120 hours, assigned as samples A, B, C, D respectively. During the reflux, precipitation of ZnO and ZnWO₄ took place. The obtained ZnO/ZnWO₄ nanoparticles were separated from solvent containing copolymer immediately after synthesis by using ultra-centrifugation. Synthesized ZnO/ZnWO₄ nanoparticles were washed several times with ethanol and distilled water using centrifugation in every washing step

and annealed at 95 °C for 18 hours. XRD measurements of obtained powders were used for characterization: samples were mainly ZnWO₄ with traces of ZnO [3].

Diffuse reflectance spectra (DRS) of the ZnO/ZnWO₄ pellets were recorded using Perkin Elmer Lambda 9 UV-VIS-NIR Spectrophotometer. Photoluminescence (PL) spectra were obtained using Perkin Elmer LS 45 Luminescence spectrometer.

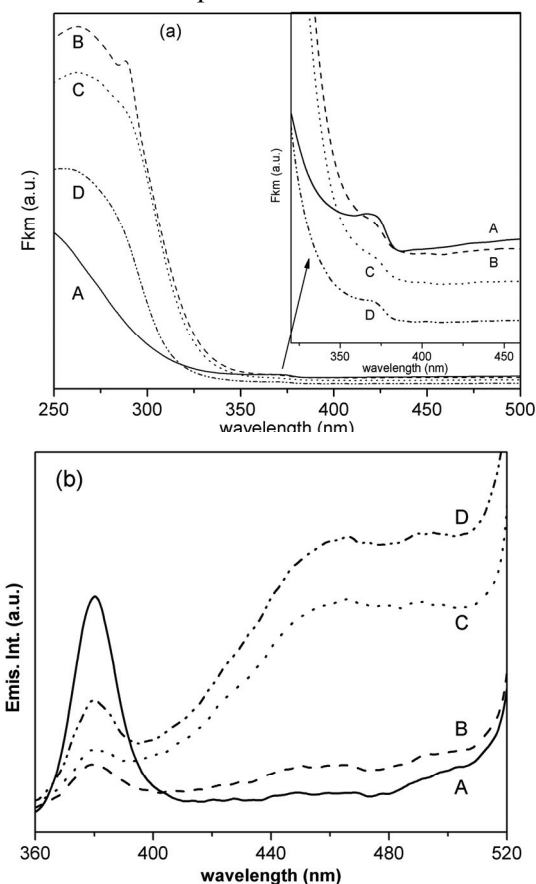


Figure 1. (a) Absorption spectra of obtained powders, calculated from DRS (Kubelka-Munk); (b) PL spectra of obtained powders, $\lambda_{exc} = 270$ nm.

nm can be seen. This broad peak can be assigned to superposition of ZnO and ZnWO₄ absorptions, although its maximum corresponds well with literature data for band gap of ZnWO₄ (≤ 4.6 eV). Sample D showed the lowest intensity of absorption in the region of ZnO absorption, probably because ZnO phase is mostly spent on the ZnWO₄ synthesis. We presumed that sample A is mainly ZnO and sample D is mainly ZnWO₄ with traces of ZnO which can be also detected due to its PL properties.

Results and Discussion

Optical properties of obtained samples were investigated by diffuse reflectance spectroscopy. Obtained data were converted in absorption units (Fkm) using Kubelka-Munk equation and presented in Figure 1 (a). Two regions of the wavelengths can be observed, region which cover ZnO (~ 3.37 eV) absorption, $\lambda \geq 350$ nm, and region that corresponds to band gap of both ZnO and ZnWO₄ (≥ 3.8 eV), $\lambda \leq 350$ nm. The part of the spectra that corresponds to ZnO is enlarged in the inset of Figure 1 (a). As can be seen, sample A shows only one shoulder at about 370 nm, which corresponds well with band gap of ZnO. After that shoulder, absorption increases monotonically with decreasing wavelengths. Most probably in sample A ZnWO₄ phase was not formed yet. According to chemical reactions that lead to precipitation of ZnO/ZnWO₄ [3],

ZnO phase is formed before ZnWO₄. In spectra of samples B, D and C a shoulder at the same position (Figure 1 (a), inset, ~ 370 nm) only less stressed, and broad peak at about 270

In PL spectra of all samples, Fig. 1 (b), peak at about 380 nm can be observed with max intensity for sample A and minimum intensity for sample B. This peak can be assigned to ZnO band edge emission. Prolonging synthesis time from 5 h (B), 48 h (C) to 120 h (D) induced increase of intensity of 380 nm peak as well as green emission intensity ($\lambda \geq 400$ nm). These results indicated that prolonged reaction time gives rise to formation of near-surface oxygen vacancies in ZnO which cannot be blocked by formation of ZnWO₄ layer. Similar PL spectra measured Kim et al [4]

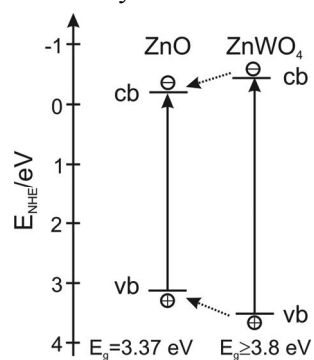


Figure 2. Electronic correlation diagram of the ZnO/ZnWO₄ core-shell nanoparticles.

when nanorod arrays of ZnO were surface covered by different oxides (TiO₂, Y₂O₃, CeO₂, and Er₂O₃). Obviously surface layer of ZnWO₄ favorably induced the formation of oxygen vacancies in ZnO nanoparticles responsible for green emission. Nanostructured ZnO (Fig. 1 (b) curve A) showed only band edge emission that is typical for small ZnO clusters. This effect can be explained by core/shell structure of composite nanoparticles, where ZnO is core and ZnWO₄ exist as a shell which partially cover the surface of ZnO. Figure 2 depicts energetic positions of the conduction and valence bands (cb, vb) of ZnO and ZnWO₄ [5]. So, after excitation, all photogenerated holes and electrons are transferred to ZnO part of the composite due to their band edge positions. All observed PL properties originate from ZnO part of the composite.

Conclusions

A low temperature method which involves non-ionic copolymer surfactant was used for preparation of ZnO/ZnWO₄ composite nanoparticles. The development of ZnO and ZnWO₄ phases was followed by optical absorption measurements. Room-temperature PL was observed for all samples ($\lambda_{exc} = 270$ nm). PL spectra were characterized by band edge emission of ZnO (380 nm) and green emission from oxygen vacancies present in ZnO. Optical properties were correlated and explained by conduction and valence band positions in our composite nanoparticles.

Acknowledgment

Financial support for this study was granted by Ministry of Education and Science of the Republic of Serbia, project 172056.

References

- [1] W. I. Park, G. C. Yi, M. Kin, S. J. Pennycook, *Adv. Mater.* 2003, 15, 526-529.
- [2] X. Zhao, Y. F. Zhu, *Environ. Sci. Technol.*, 2006, 40, 3367-3372.
- [3] I.Lj. Validžić, T. D. Savić, R. M. Krsmanović, D. J. Jovanović, M. M. Novaković, M. Č. Popović, M. I. Čomor, *Mat. Sci. Eng. B*, 2012, 177, 645-651.
- [4] Y. Kim, Y. Kim, S. Kang, *J. Phys. Chem. C*, 2010, 114, 17894–17898.
- [5] M. Bonnani, L. Spanhel, M. Lerch, E. Füglein, G. Müller, *Chem. Mater.*, 1998, 10, 304-310.

H-16-P

MORPHOLOGY AND SURFACE FRACTAL DIMENSION OF TiO₂ FILMS

Lj. Rožić¹, N. Radić¹, B. Grbić¹, J. Dostanić¹, S. Petrović¹, R. Vasilić³, S. Stojadinović²

¹*University of Belgrade, IChTM-Department of Catalysis and Chemical Engineering, Njegoševa 12, Belgrade, Republic of Serbia*

²*Faculty of Physics, University of Belgrade, Studentski trg 12-16, 11000 Belgrade, Serbia*

³*Faculty of Environmental Governance and Corporate Responsibility, Educons University, Vojvode Putnika bb, Sremska Kamenica, Serbia*

Abstract

The effect of calcinations temperature on the morphology and surface fractal dimensions of the TiO₂ films prepared via a spray pyrolysis process was investigated. The morphology and surface fractal dimensions are evaluated by image analysis methods, based on AFM (atomic force microscopy) micrographs. The results indicate that the value surface roughness of TiO₂ films increases with the increase of calcinations temperature. Also, we found that for samples calcined at temperatures in the range of 500 to 700 °C the fractal dimension is nearly constant (2.60 – 2.65). This indicates that the surfaces of TiO₂ films calcined at different temperatures are indeed irregular and may be described by fractal geometry in a certain range of length scale.

Introduction

TiO₂ is one of the most used multifunctional materials. The use of TiO₂ as photocatalyst is an important subject in a few publications [1, 2]. The versatility of preparation procedures has led to a wide variety of structural and morphological characteristics as well as to the variety of potential applications. The morphology structure of the TiO₂ films prepared by physical methods is a crucial factor for photocatalytic processes because of its influence on heat transfer and surface reaction rate. It is known that TiO₂ films have complex surface structure. Therefore, it is hard to characterize the surface morphology objectively and factually by applying standard parameters characterizations such as specific surface area, pore size distribution and pore volume. Atomic force microscopy is considered as one of the most powerful method for surface roughness characterization, because of its accuracy, non-damage to the surface and non-vacuum condition. Fractal dimension can give some useful information about TiO₂ films physical structure [3].

In this study, the feasibility of preparing immobilized Degussa P-25 TiO₂ films on a stainless steel substrate by the spray pyrolysis technique is presented. The prepared samples were annealed at different temperatures and characterized by the AFM techniques and influence of thermal treatment on film morphology was

investigated. Surface roughness obtained by AFM analysis is correlated with surface fractal dimension in order to elucidate surface morphology.

Experimental

Material and methods

TiO₂ thin films supported on stainless steel (SS) foil have been prepared by the spray pyrolysis method. The spray pyrolysis apparatus and procedure for preparing the films immobilized on stainless steel is similar to that reported in a previously published study [4]. As prepared multilayered TiO₂ thin films were treated in a tube furnace in a range of temperature from 500 up to 700 °C. The surface morphology of the samples was investigated by atomic force microscopy (Veeco Instruments, model Dimension V). Micrographs were obtained in tapping mode under ambient conditions, using Tap300 tips (resonance frequency 300 kHz, force constant 40 N/m). Roughness data were obtained using diNanoScope software (version 7.0) and reported values are calculate as mean values for a number of different samples obtained under same conditions. Fractal dimension estimation using ImageJ 1.45s Box Count Method and flooding analysis were done by FracLac 2.5 Release 1e of the images was calculating using box counting method

Results and discussion

The topographies of the TiO₂ thin films supported on stainless steel foil are first presented. Figure 1 shows the typical AFM top view surfaces and 3D images of the four samples obtained with different temperature at the same scan size.

It was found that all the TiO₂ thin films have some roughness. The both, R_a (arithmetic average of absolute value) and R_q (root mean square roughness) gradually increase with the increase of temperature (Table 1).

Table 1. Surface roughness and fractal dimension of TiO₂ thin films as prepared - 460 °C (a) and calcined at 500 °C (b), 600 °C (c) and 700 °C (d)

	<i>Sample</i>			
	<i>a</i>	<i>b</i>	<i>c</i>	<i>d</i>
Temperature (°C)	460	500	600	700
R _q (nm)	333	469	495	555
R _a (nm)	273	367	397	461
Fractal dimension	2.65	2.64	2.62	2.61

According to the fractal analysis, we found that the values of fractal dimension of thin films surface are in the range from 2.60 to 2.65, with the correlation coefficients, R², higher than 0.97.

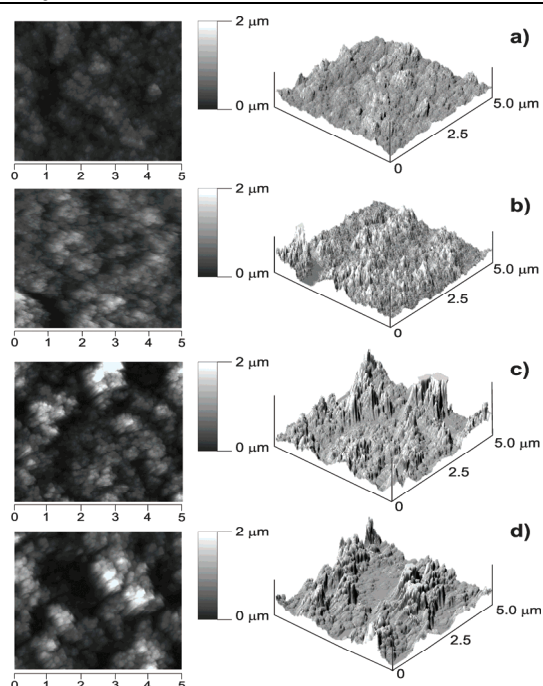


Figure 1. Two and three-dimensional AFM images of TiO₂ thin films, as prepared- 460 °C (a) and calcined at 500 °C (b), 600 °C (c) and 700 °C (d)

As can be observed, all surface exhibit a self-similar behaviour, reflecting the property that a part of the surface is similar to the whole surface. Both films, as prepared and thermally treated at 500 °C show almost identical morphological and structural properties, i.e. anatase phase are dominant. At higher temperatures partial phase transformation anatase to rutile was observed (XRD analysis). This changes lead to the increase of surface roughness value and slight decrease of fractal dimension. The rutile phase formed at these temperatures serves as stabilizer of structure of films.

Conclusion

Based on the obtained results, we can conclude that the Box Count Method is a reliable method for determination of the fractal dimension, and can be used for fractal analysis of AFM images of TiO₂ thin films surface. There is no one to one correspondence between the surface roughness (R_q and R_a) and fractal dimension.

Acknowledgments

This work was supported by the Ministry of Education and Science of the Republic of Serbia (Project number 172015).

References

- [1] H. D. Jang, S. K. Kim, S. J. Kim, *J. Nanopart. Res.*, 2001, 3, 141–147.
- [2] J. Dostanić, B. Grbić, N. Radić, P. Stefanov, Z. Šaponjić, J. Buha, D. Mijin, *Chem. Ing. J.*, 2012, 180, 57-65.
- [3] C. Trapalis, N. Todorova, M. Anastasescu, C. Anastasescu, M. Stoica, M. Gartner, M. Zaharescu, T. Stoica, *Thin Solid Films*, 2009, 517, 6243 – 6247.
- [4] T. Novaković, N. Radić, B. Grbić, T. Marinova, P. Stefanov, D. Stojčev, *Catal. Commun.*, 2008, 9, 1111-1118.

FRACTAL APPROACH TO SURFACE ROUGHNESS OF TiO₂/WO₃ COATINGS

B. Grbić¹, R. Vasić³, N. Radić¹, S. Stojadinović², Lj. Rožić¹, S. Petrović¹

¹*University of Belgrade, IChTM-Department of Catalysis and Chemical Engineering, Njegoševa 12, Belgrade, Republic of Serbia*

²*Faculty of Physics, University of Belgrade, Studentski trg 12-16, 11000 Belgrade, Serbia*

³*Faculty of Environmental Governance and Corporate Responsibility, Educons University, Vojvode Putnika bb, Sremska Kamenica, Serbia*

Abstract

The surface roughness has an effect on many physical properties so that an accurate description of the roughness parameters is of great interest. In this study, we have shown that atomic force microscopy (AFM) is powerful techniques to study the fractal parameters of TiO₂/WO₃ coatings prepared by plasma electrolytic oxidation (PEO) process. The surface roughness, described by root mean squared (R_q) and arithmetic average values (R_a), were analyzed considering the scans of an atomic force microscopy measurement. The results show that the oxide coatings exhibit lower surface roughness in initial stage of PEO process. Also, the surfaces of TiO₂/WO₃ coatings were found to be fractal during the whole process.

Introduction

Titanium dioxide coatings obtained by PEO process of titanium has been widely investigated because of its potential widespread applications, including biocompatible materials, structural ceramics, photocatalysis, sensors, optical coatings, etc. [1]. Plasma-chemical, thermal and anodic oxidation processes are induced at the discharge sites due to increased local temperature and pressure modifying the structure, composition, and morphology of such oxide coatings. Oxide coatings have controllable morphology and composition, excellent bonding strength with the metal, high micro hardness, high-quality wear and corrosion resistance.

It is well known that the optimum performance of coatings requires an exhaustive control of structural characteristics and surface morphology. Hence, the control of structure and the surface roughness are crucial aspects that largely determine the use of these materials [2]. Fractal dimension is a parameter used to quantitatively assess fractal geometry and it represents a measure of the irregularities on the surface of a solid. The value for this parameter may vary from 2 to 3, where the lowest value (2) corresponds to a perfectly smooth surface, while the upper limit (3) corresponds to a totally irregular or rough surface [3]. Within this range of values, subtle variations may be considered significant.

The aim of this work is to obtain further insight into surface morphology by means of fractal geometry of the surface, as a contemporary approach to the surface analysis. Within present study the surface fractal dimension of the

TiO₂/WO₃ coatings was evaluated using high resolution AFM imaging, in order to test its sensitivity with respect to the change of surface morphology as the consequence of PEO process duration.

Experimental

Material and methods

TiO₂/WO₃ oxide coatings were formed by plasma electrolytic oxidation of titanium in 12-tungstosilicic acid (H₄SiW₁₂O₄₀), according to procedure, reported in a previous study [4]. Roughness of the samples was analyzed using an atomic force microscopy (Veeco Instruments, model Dimension V). Micrographs were obtained in tapping mode under ambient conditions, using Tap300 tips (resonance frequency 300 kHz, force constant 40 N/m). Roughness data were obtained using diNanoScope software (version 7.0). The box-counting method is applied and improvement is made to calculate the fractal dimensions of the morphology of coatings using ImageJ software with FracLac 2.5 plugin.

Results and Discussion

AFM images of oxidised TiO₂/WO₃ coatings recorded on (5 μm × 5 μm) are shown on Figure 1. R_q and R_a values of all the AFM images were calculated and listed in

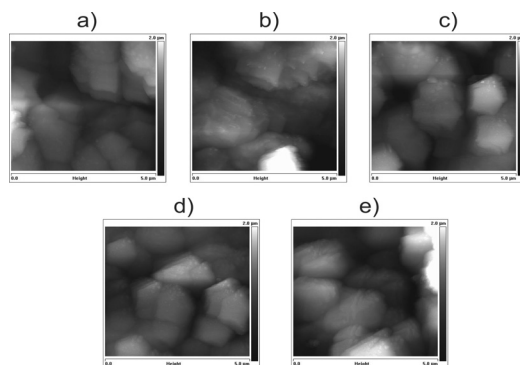


Figure 1. 2D AFM images of oxide coatings formed in various stage of PEO process: a) 30 s; (b) 60 s; (c) 90 s; (d) 180 s; (e) 300 s.

Table 1. The results show that, discharge channels are well distributed and oxide coatings exhibit lower surface roughness (174 nm) in initial stage of PEO process. As the number of discharge channels decreases with time of PEO, non uniformities in the oxide coatings appear causing an increase in surface roughness (307 nm). Also, the influence of flatten order on surface roughness of TiO₂/WO₃ coatings was studied. The AFM images of oxide coatings were flattened with order 1, 2 and 3, successively, and R_q and R_a values of these samples were calculated and presented in Table 1. Obtained results shows that surface roughness decrease for all samples with increase of the flatten order.

The fractal dimensions were calculated from AFM images of oxide coatings formed in various stage of process using only flattened order 2. The fractal dimension values of each samples significantly deviates from 2, consequently, surface morphology of oxide coatings possesses fractal properties. Surface fractal dimension of samples a (30 s), b (60 s) and c (90 s) increases slightly from 2.482, via 2.484, to 2.513 and then decreases to 2.504 for samples d (180 s) and to 2.492 for sample e (300 s). The fractal dimension, as a measure of surface roughness of

coatings, reflects complexity of PEO process, as well as significance of PEO process duration.

Table 1. R_q and R_a calculated from the AFM images of TiO_2/WO_3 coatings with different flatten orders expressed in nm.

<i>Metrology</i>	<i>Flatten order</i>	<i>Sample</i>				
		<i>a</i>	<i>b</i>	<i>c</i>	<i>d</i>	<i>e</i>
R_q	0	322	446	395	287	480
R_q	1	215	349	331	252	439
R_q	2	174	237	294	221	307
R_q	3	138	194	238	201	209
R_a	0	259	335	325	230	400
R_a	1	171	233	278	195	358
R_a	2	144	172	241	164	236
R_a	3	111	131	190	150	164

Conclusion

The AFM images were used to calculate fractal dimensions of TiO_2/WO_3 coatings at various stages of PEO process. Surface roughness and fractal dimension are dependent and sensitive to the time of PEO process, particularly at early stages (30, 60 and 90 s).

Acknowledgments

This work was supported by the Ministry of Education and Science of the Republic of Serbia (Project number 172015).

References

- [1] P. J. Chu, S.Y. Wu, K.C. Chen, J. L. He, A. Yerokhin, A. Matthews, *Thin Solid Films*, 2010, 519, 1723 - 1728.
- [2] J. Dostanić, B. Grbić, N. Radić, P. Stefanov, Z. Šaponjić, J. Buha, D. Mijin, *Chem. Ing. J.*, 2012, 180, 57-65.
- [3] C. Trapalis, N. Todorova, M. Anastasescu, C. Anastasescu, M. Stoica, M. Gartner, M. Zaharescu, T. Stoica, *Thin Solid Films*, 2009, 517, 6243 – 6247.
- [4] M. Petković, S. Stojadinović, R. Vasilić, I. Belča, Z. Nedić, B. Kasalica, U.B. Mioč, *Appl. Surf. Sci.*, 2011, 257, 9555– 9561.

H-18-P

MICROSTRUCTURE AND CRYSTAL GROWTH IN THERMALLY TREATED $\text{Fe}_{73.5}\text{Cu}_1\text{Nb}_3\text{Si}_{15.5}\text{B}_7$ ALLOY

D. M. Minić¹, S. Meseldžija², M. Vasić¹, V. Blagojević¹

¹*Faculty of Physical Chemistry, University of Belgrade, Serbia*

²*Institute for Nuclear Science Vinca, University of Belgrade, Belgrade, Serbia*

Abstract

Thermal treatment of $\text{Fe}_{73.5}\text{Cu}_1\text{Nb}_3\text{Si}_{15.5}\text{B}_7$ amorphous alloy induces structural changes, including crystallization of several different phases and subsequent crystal growth. X-ray diffraction combined with differential scanning calorimetry were used to investigate these, to determine kinetic parameters and mechanism of individual steps, and the dimensionality of crystal growth using Matusita-Sakka method and texture analysis. It was found that after the alloy becomes fully crystalline, crystal growth of individual phases is, in general, impeded, leading to decreased dimensionality of growth. However, this does not impact the texture, due to lack of preferred direction of crystal growth.

Introduction

Metallic glasses (amorphous metallic alloys) are materials characterized by homogenous and isotropic structure with absence of the long-range order, which possess isotropic physical and mechanical properties. Iron based amorphous alloys have attracted much attention in recent times, because of their favorable physical properties. These materials are kinetically and thermodynamically metastable, usually stable at room temperature and can be transformed to polycrystalline materials at higher temperatures. During the crystallization process, microstructure of the alloy changes from amorphous, through hybrid amorphous/crystalline, to purely crystalline structure. Since hybrid amorphous/crystalline materials often have functional properties superior to those of purely amorphous and purely crystalline materials, control of crystallization process of these materials can lead to creation of materials with targeted properties.

The goal of this work was to study influence of thermal treatment on microstructure and crystal growth in $\text{Fe}_{73.5}\text{Cu}_1\text{Nb}_3\text{Si}_{15.5}\text{B}_7$ alloy.

Results and Discussion

Amorphous alloy $\text{Fe}_{73.5}\text{Cu}_1\text{Nb}_3\text{Si}_{15.5}\text{B}_7$ was prepared in form of a ribbon by melt spinning method. The thermal stability and kinetic parameters of the alloy had been investigated in 25-800°C temperature range using DSC. XRD of thermally treated alloy samples was also used, to determine phase composition and perform texture analysis. The alloy was stable up to about 500°C after which two exothermic crystallization peaks are observed in DSC, at around 500°C and 680°C, respectively. Crystallization occurs in a multi-step process. To investigate each

individual step of these processes, complex experimental peaks were deconvoluted using Origin software package. In order to determine kinetic parameters (apparent activation energy, E_a and pre-exponential factor, A) of processes of crystallization, we used Kissinger's [1] and Ozawa's [2] methods. It was observed from Table 1 that the values for E_a and A obtained by these two methods are in good correlation.

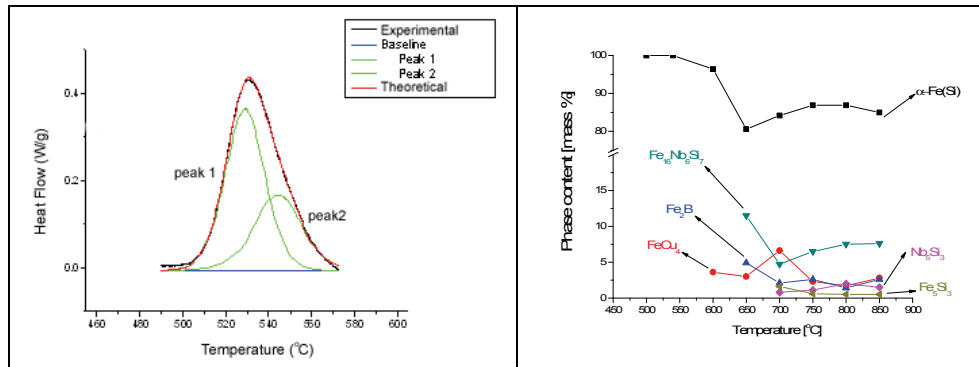


Figure 1. Deconvolution of first experimental DSC peak (left) and phase content of individual crystal phases in thermally treated alloy samples (right).

Table 1. Kinetic parameters of individual steps for the first experimental DSC peak determined by Kissinger's and Ozawa's methods.

		KISSINGER		OZAWA	
		E_a [kJ/mol]	A [min ⁻¹]	E_a [kJ/mol]	A [min ⁻¹]
Experimental peak 1	Peak 1	(316 ± 11)	(1.6 ± 0.1)•10 ²⁰	(313 ± 10)	(1.1 ± 0.1)•10 ²⁰
	Peak 2	(248 ± 13)	(2.5 ± 0.2)•10 ¹⁵	(249 ± 13)	(2.8 ± 0.2)•10 ¹⁵

Crystal growth of α -Fe(Si) phase occurs in two distinct stages: first stage includes nucleation and subsequent growth from amorphous phase, which occurs three-dimensionally ($m=2.7$ in Matusita-Sakka method [3]), while the second stage occurs in fully crystallized alloy, where its crystal growth is impeded by presence of other crystalline phases. This means that, in the second stage, the growth of α -Fe(Si) is prevented on interphase boundaries, which is exhibited as the value of $m=1.7$ in Matusita-Sakka calculation. However, since there is no preferred direction of growth, there is no significant change in texture of α -Fe(Si) phase, even though the growth is nominally not three-dimensional.

The growth of Fe_2B phase also exhibits two distinct stages, due to different sources of crystallization. Initial crystallization of Fe_2B occurs from the amorphous phase, while, later, it also crystallizes from metastable Fe_3B phase [4]. The crystal growth from amorphous phase occurs three-dimensionally, while the growth from metastable Fe_3B phase occurs two-dimensionally, as suggested by change in dimensionality of crystal growth observed using Matusita-Sakka method.

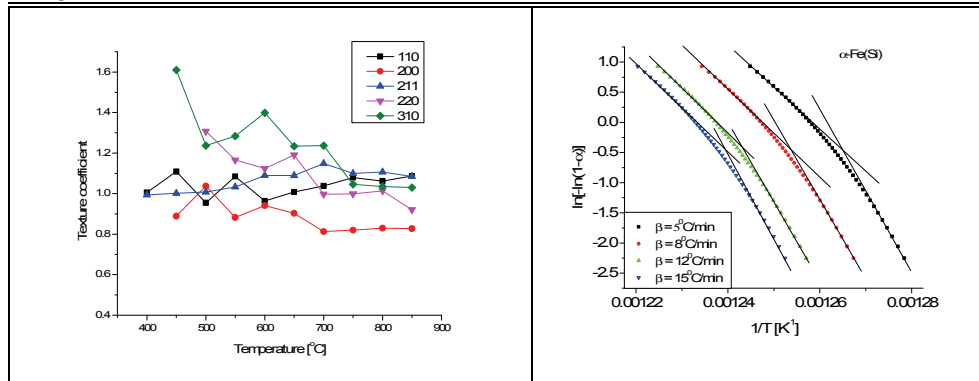


Figure 2. Texture analysis (left) and Matusita curves (right) for α -Fe(Si) phase.

Conclusion

Thermally induced crystallization and crystal growth in $Fe_{73.5}Cu_1Nb_3Si_{15.5}B_7$ amorphous alloy shows that crystallization and growth occurs in two temperature regions: around 500 and 680°C. There are multiple stable and metastable phases observed and it is shown that dimensionality of their crystal growth depends on the degree of crystallization of the alloy, with impeded growth in fully crystallized alloy.

References

- [1] H. E. Kissinger, *Anal. Chem.*, 1957, 29, 1702-1706.
- [2] T. Ozawa, *J. Therm. Anal.*, 1970, 2, 301-324
- [3] K. Matusita, S. Sakka, *J. Non-Cryst. Solids*, 1980, 741, 38-39
- [4] V. A. Blagojević, D. M. Minić, T. Žak, D. M. Minić, *Intermetallics*, 2011, 19, 1780-1785

CRYSTALLIZATION AND SINTERING PHENOMENA OF GLASSES IN THE SYSTEM $\text{La}_2\text{O}_3\text{-SrO-B}_2\text{O}_3$

S. V. Ždrale¹, S. R. Grujić¹, M. B. Tošić², V.D. Živanović²,
A. Z. Bjelajac¹, S. D. Matijašević², J. D. Nikolić²

¹*Faculty of Technology and Metallurgy, University of Belgrade 4 Karnegijeva St,
11000 Belgrade, Serbia,* ²*Institute for Technology of Nuclear and other Mineral
Raw Materials, 86 Franchet d' Esperey St, 11000 Belgrade, Serbia*

Abstract

In this work crystallization and sintering phenomena of glasses in the system $\text{La}_2\text{O}_3\text{-SrO-B}_2\text{O}_3$ (LaSrB) were studied. Hot stage microscope (HSM) technique was used to determine characteristic temperatures for sintering processes and differential temperature analysis (DTA) to determine glass transition temperature, t_g , and onset of crystallization glass temperature, t_x . A combination of these analyses provided information about the quality of glass ceramic by determining differences in glass transition and maximum shrinkage temperatures. It has been shown that with increasing content of La_2O_3 , differences of these temperatures decreased.

Introduction

In the present work sintering and crystallization processes of LaSrB system were studied. Glass ceramics showed improved properties, low thermal expansion, low dielectric constant, high abrasion resistance, chemical resistance. Sintering and crystallization behavior of this system are investigated to obtain high performance material, reduced porosity, for specific application. A combination of HSM and DTA represents a simple approach of determining the sintering and crystallization phenomena [1].

Experimental

The reagent grade mixture of H_3BO_3 , SrCO_3 , $\text{La}_2(\text{CO}_3)_3$ was used to prepare glasses by melting in electrical furnace. Mixture was placed in platinum crucible in electric furnace and melted at 1200 °C for 30 min. The melt was cast and cooled at stainless steel plate in air at room temperature. The obtained glasses were transparent, without visible bubbles in glasses. Obtained glass compositions are given in table 1.

Table 1. Compositions of studied glasses.

Glass, number	x_i (mol%)		
	La_2O_3	SrO	B_2O_3
1	5.7	22.9	71.4
2	9.5	19.1	71.4
3	14.3	14.3	71.4
4	19.1	9.5	71.4

A hot stage microscope, E. LEITZ WETZLAR, that was used, projects the image through a quartz window. The specimens of glass powders were pressed into cylinders and placed on platinum plate, then on alumina support contacted with thermocouple. The temperature was measured by (Pt/Rh/Pt) thermocouple at heating rate $10\text{ }^{\circ}\text{C min}^{-1}$. The obtained temperatures from photomicrographs corresponding to typical viscosity points are: first shrinkage, maximum shrinkage, deformation, sphere, half ball and flow [2-3].

The crystallization properties of the glass samples were determined by differential thermal analysis (DTA) using Netzch STA 409 EP instrument and Al_2O_3 powder as the reference material. Powder glass samples were prepared by crushing and grinding the bulk glass in agate mortar and sieving it up to grain size $< 0.048\text{ mm}$. Glass powder were heated at $10\text{ }^{\circ}\text{C/min}$ rate to determine glass transition temperature, t_g , and onset of crystallization temperature, t_x .

Results and Discussion

Characteristic temperatures of the first shrinkage (t_{FS}), maximum shrinkage (t_{MS}), deformation (t_D), sphere (t_S), half ball (t_{HB}) and flow (t_F) are designated from the results obtained by HSM [3-4]. In Figure 1 are shown characteristic photomicrographs of the shape of glass 1 taken during HSM experiments [2-3].

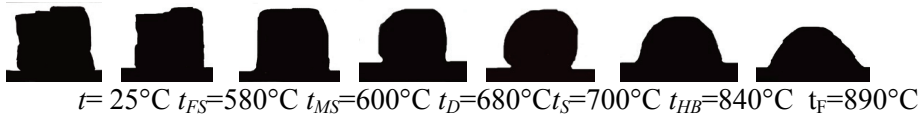


Figure 1. Photomicrographs of the shape sample during the HSM measurements.

The glass transition temperature, t_g , and onset of crystallization temperature are determined from DTA curve in figure 2. Results obtained by DTA and HSM for all samples are shown in table 2. The exothermal temperature peaks at the DTA curves correspond to the crystallization of glass.

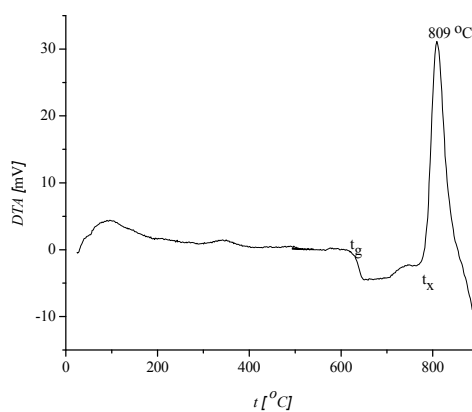


Figure 2. DTA curve obtained for glass sample 1.

It is important to determine temperature differences of onset crystallization and maximum shrinkage in attempt to predict if porous sample will be obtained [2-3]. If t_x is greater than t_{MS} glass powder samples sinter before crystallization. Glass sample number 1 with the lowest content of La_2O_3 shows the greatest difference in these temperatures. With increasing content of La_2O_3 the difference decreased because t_{MS} increased.

Table 2. Temperatures obtained by DTA and HSM.

Glass	$t_g, ^\circ\text{C}$	$t_x, ^\circ\text{C}$	$t_{ms}, ^\circ\text{C}$	$(t_x-t_{ms}), ^\circ\text{C}$
1	622	735	600	135
2	640	763	700	63
3	643	756	720	36
4	644	765	740	25

Conclusion

In this study DTA and HSM techniques provided basic information about crystallization and sintering processes in the system and showed that t_x and t_{MS} differences decreased with increasing content of La_2O_3 which is significant information to determine quality of obtained glassceramics and therefore their application.

Acknowledgment

The authors are grateful to the Ministry of Education and Science, Republic of the Serbia for financial support (Projects 172004 and 34001).

References

- [1] A. R. Bocaccini, B. Hamman, J. Mater. Sci., 1999, 34, 5419–5436.
- [2] C. Lara, M. J. Pascual, M. O. Pradob, A. Duran, Solid State Ionics, 2004, 170, 201- 208.
- [3] M.J. Pascual, A. Duran, Phys. Chem. Glasses, 2004, 46, 512-520.

H-20-P

MESOPHASE BEHAVIOUR OF BINARY MIXTURES OF BENT-CORE AND CALAMITIC COMPOUNDS

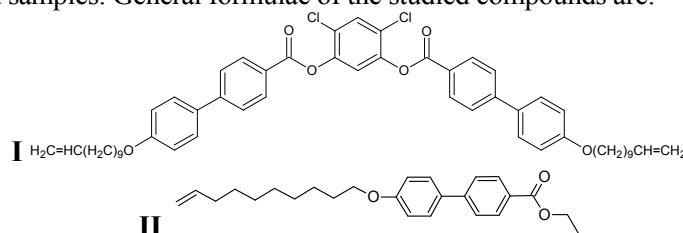
D. Obadović¹, M. Stojanović¹, M. Cvetinović¹, A. Vajda², N. Eber², K. Fodor-Csorba²

¹ Department of Physics, University of Novi Sad, Novi Sad, Serbia

² Institute for Solid State Physics and Optics, Wigner Research Centre for Physics, Hungarian Academy of Sciences, Budapest, Hungary

Abstract

Due to their attractive properties, bent-core liquid crystalline compounds were extensively studied in the last two decades [1]. Here we present the phase diagram for binary mixtures of bent-core and calamitic liquid crystals. One mixing component is the previously prepared 4,6-dichloro-1,3-phenylene bis[4'-(10-undecen-1-yloxy)-1,1'-biphenyl-4-carboxylate] (**I**), which is a nematogenic ester-type banana-shaped compound [2]. The calamitic compound is the well known ethyl 4'-(9-decen-1-yloxy)-1,1'-biphenyl-4-carboxylate (**II**) which exhibits smectic A (SmA) phase in a wide temperature range [3]. A total number of 6 mixtures were prepared and investigated by polarising optical microscopy. Selected mixtures were studied by X-ray diffraction on non-oriented samples. General formulae of the studied compounds are:



In the selected mixtures a nematic phase exists above the SmA phase, with the temperature range of both phases highly dependent on the concentration of the comprising compounds. Lowered melting temperatures were observed for all mixtures with respect to that of the pure compounds.

Introduction

Lowering the transition temperatures of liquid crystals and stabilizing their mesophases over wide temperature range, is always an important aim of the research. In order to respond to these demands, the required liquid crystalline properties can be rather reached by mixing compounds with different molecular structures and properties than by looking for the pure compounds with definite properties. As bent-core compounds exhibit limited miscibility even among themselves, to find mixtures especially with calamitic compounds is always a challenging problem [3].

Results and Discussion

The goal of the present study was to test the miscibility of the bent-core compound **I** with the rod-like material **II**, and to study the mesomorphic behaviour of their binary mixtures. For the detailed study, six mixtures, **Mix1** to **Mix6**, were prepared

with 18, 26, 38, 50, 63 and 80 wt% of the bent-core component **I**, respectively. The phase transition temperatures of pure compounds and their mixtures in heating were detected by polarizing optical microscopy and presented in Table 1.

Table 1. Sequence of Phases, Phase Transition Temperatures [°C]. All these Data were Obtained in Heating. (• the Phase Exists)

Code	Cr	T	Cr2	T	CrE	T	SmA	T	N	T	I
II	•	64.5	•	76.0	•	85.9	•	98.7			•
Mix1	•	53.4	•	61.0	•	79.5	•	81.7	•	99.0	•
Mix2	•	52.2	•	66.0	•	68.0	•	73.3	•	103.0	•
Mix3	•	53.5	•	65.5	•	77.0	•	86.7	•	99.7	•
Mix4	•	54.0	•	61.2	•	69.0	•	79.0	•	99.3	•
Mix5	•	62.3	•	65.9	•	77.4	•	88.0	•	100.9	•
Mix6	•	60.3	•	67.4	•	70.2	•	86.0	•	100.2	•
I	•	71.2	•	78.9					•	102.7	•

The widest temperature range for nematic (N) phase was obtained for **Mix2**. For smectic phase, the widest temperature range of 15.8°C was observed for **Mix6**. The N-I (isotropic) transition temperature reaches its minimum of 99.0°C for concentration of 18 wt% of compound **I** (**Mix1**).

X-ray diffraction studies were carried out in a transmission geometry using a conventional powder diffractometer, Seifert V-14, at CuK α radiation ($\lambda=0.154$ nm), equipped with an automatic high-temperature kit Paar HTK-10. The set-up was calibrated to the two most intense platinum lines: $2\Theta = 39.76^\circ$ (100%) and $2\Theta = 46.23^\circ$ (53%). Molecular parameters, the thickness of the smectic layers d and the average intermolecular distance D between the long axes of neighbouring molecules, could be determined from the positions of the small angle and wide-angle diffraction peaks, respectively, using Bragg's law: $n\lambda=2d \sin\Theta$.

In Figures 1(a) and 1(b) we present typical diffraction spectra for each phase for the pure bent-core compound **I** as well as for the mixture **Mix5**. In all investigated mixtures two crystal modifications (Cr1, Cr2) and a crystalline smectic E (CrE) phase were detected. The CrE phase in **Mix5** is primarily characterized by increased scattering at large angles in proximity of $2\Theta=20.5^\circ$ which is due to the hexatic ordering. Yet in CrE many other peaks appear due to a long range in-plane order. In the SmA phase of **Mix5** one reflection peak appears at the small angle $2\Theta=1.9^\circ$, corresponding to the thickness of the smectic layers of $d=46.64\text{\AA}$. Starting with the minimal concentration of 18 wt% of bent-core compound **I** (**Mix1**) thickness of smectic layers increases, reaching its saturation value of 46.64\AA for 50 wt% of compound **I** (**Mix4**), which might be regarded as the experimental value for the length of compound **I**.

Both the isotropic and the nematic phases are characterized by a broad diffusion peak which appears in the range of $2\Theta=12\text{--}26^\circ$, whose maximum yields D values in the interval $4.22\text{\AA} < D < 4.92\text{\AA}$ for the isotropic phase of **Mix3** and the SmA phase of **Mix5**.

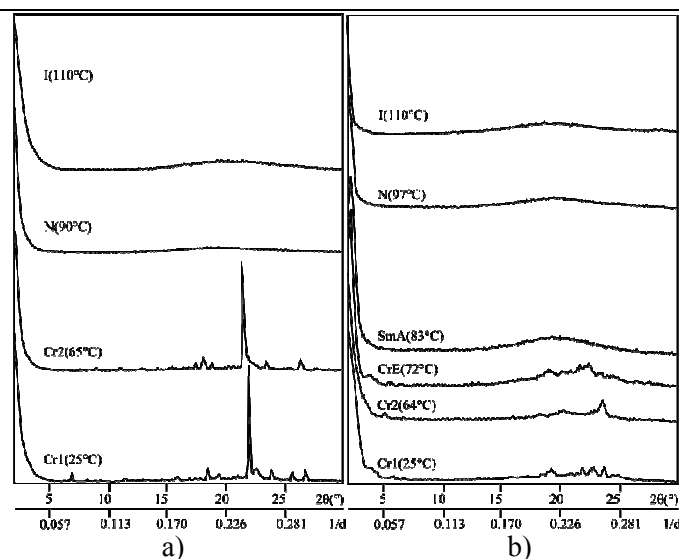


Figure 1. X ray diffractogram of compound **I** (a) and **Mix5** (b).

Conclusion

We found that the polymorphism (I–SmA–Cr phase sequence) of the pure calamitic component **II** is fully preserved in all studied mixtures with addition of nematic phase that follows SmA phase on heating. The layer spacing (d) increases when adding the bent-core compound. The monotropic smectic phase exists in the full concentration range in all studied mixtures. The nematic phase remains detectable even for the highest calamitic content **Mix1**. Therefore, mesophase behaviour existed over a broad composition range in the mixtures and could be extended close to room temperature. The results suggest that mixing conventional calamitics with bent-core mesogens with an appropriate molecular design may be a tool to tune the phase behaviour and properties of different liquid crystal mixtures.

Acknowledgments

This work was partly supported by the research Grant No. OI171015 from the Ministry of Education and Science of the Republic of Serbia, the Hungarian Research Fund OTKA K81250 and the SASA-HAS bilateral scientific exchange project #9.

References

- [1] D. Ž. Obadović, A. Vajda, A. Jákli, A. Menyhárd, M. Kohout, J. Svoboda, M. Stojanović, N. Eber, G. Galli and K. Fodor-Csorba, Mesophase behaviour of binary mixtures of bell-shaped and calamitic compounds, *Liq. Cryst.*, 37, 5, 527 (2010).
- [2] K. Fodor-Csorba, A. Vajda, A. Jákli, C. Slugovc, G. Trimmel, D. Demus, E. Gács-Baitz, S. Holly and G. Galli, Ester type banana-shaped liquid crystalline monomers: synthesis and physical properties, *J. Mater. Chem.*, 14, 2499 (2004).
- [3] Z.-S. Xu, R. P. Lemieux, A. Natansohn, P. Rochon and R. Shashidhar, Synthesis and characterization of novel ferroelectric liquid crystals and copolymers containing biphenyl azobenzene and /or phenyl biphenyl carboxylate mesogenic groups, *Liquid Crystals*, 26 (3), 351 (1999).

A MODEL FOR COMPUTER STUDY OF GRAIN COARSENING IN LIQUID PHASE SINTERING

Z. S. Nikolić¹, K.i Shinagawa²

¹*University of Niš, Faculty of Electronic Engineering, Serbia*

²*Kagawa University, Faculty of Engineering, Japan*

Abstract

Computer study of grain growth by grain boundary migration based on numerical modeling of solution-precipitation during liquid phase sintering will be considered.

Introduction

Grain coarsening is a typical multibody free boundary problem in which the grains alter their morphologies in response to the diffusion field. After solution-precipitation, the grains grow in supersaturated liquid phase, and after the supersaturation becomes small, large grains start to grow at the expense of small grains. This paper describes the computer-based simulation method for simulation of a moving grain boundary on the solid/liquid interface during liquid phase sintering (LPS), where the grain boundary migration means that solid atoms that are dissolved on one side of the boundary transport across the liquid layer and deposit on the other side of the boundary.

Results and Discussion

The main characteristic of the solution-precipitation process is that the smaller solid grains dissolve at solid/liquid interface (thermodynamically unstable), diffuse through the liquid, and precipitate on the larger grains.

If a system consisting of a dispersion of spherical grains with different radii in a liquid in which the solid phase has some solubility is assumed, then the concentration of the dissolved solid, C , around a grain of radius R is given by the Gibbs-Thomson equation

$$\Delta C = C_0 \cdot \frac{2\gamma_{sl}\Omega}{kT} \cdot \frac{1}{R} \quad (\Delta C = C - C_0), \quad (1)$$

where C_0 is the equilibrium concentration of liquid in contact with the flat solid, γ_{sl} is the solid/liquid interfacial energy, Ω is the molecular volume of the solid, and kT has its usual meaning. It can be seen that the concentration at an interface with high curvature will be above that at an interface with low curvature, thus a higher concentration around a smaller grain gives rise to a net flux of matter from the smaller to the larger one. Mass diffusion outside the grains is assumed to be the only mass transfer process defined by the partial differential equation of the parabolic type $\partial C/\partial t = D_L \nabla^2 C$, where D_L is the concentration independent

diffusivity of the solid in the liquid. The effects of the dissolution and precipitation processes can be computed by applying the flux equation $\mathbf{J} = -D_L \nabla C$ at boundary points of solid interface.

Shinagawa *et al.* [1,2] proposed microscopic modeling for viscoplastic finite element analysis of sintering processes. Taking into account the surface tension acting on the pore surface, and assuming that the grains during sintering are viscoplastic and the flow stress is proportional to the viscosity, they calculated deformation behaviors of the grains for slightly compressible materials. This method can be also applied for definition two-dimensional finite element mesh (FEM) within (pendular) liquid bridge as a function of grain size, the contact angle, θ , the normalized liquid volume, ϕ , and the separation distance, d (Fig. 1) and applied for computer simulation of grain coarsening during LPS characterized by small amount of liquid located within liquid bridges only. To the best of our knowledge, there is no theoretical investigation of grain coarsening within liquid bridge only.

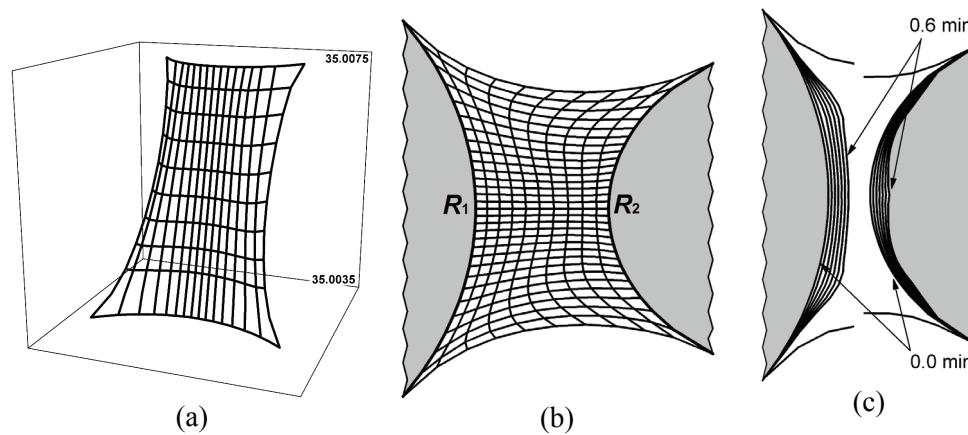


Figure 1. (a) Initial concentration profile. (b) FE mesh within liquid bridge. (c) Time dependent grain coarsening. $R_1 = 10 \mu\text{m}$, $R_2 = 5 \mu\text{m}$, $d = 3 \mu\text{m}$, $\theta = 10^\circ$, $\phi = 0.35$.

Morphological development is governed by diffusion through the liquid between grains. Assuming that solid–liquid system is held isothermally and under interfacial equilibrium condition, coarsening occurs by the exchange of solute between grains.

We will simulate grain coarsening using two unequally sized grains of tungsten connected with liquid nickel as a bridge. For the W–Ni system the next data will be used: $T = 1750 \text{ K}$, $\gamma_{sl} = 0.35 \text{ J/m}^2$, $C_o = 35 \text{ at.\%W}$, $D_L = 10^{-9} \text{ m}^2/\text{s}$, $\Omega = 9.53 \times 10^{-5} \text{ m}^3/\text{mol}$.

As was already mentioned, the concentration on solid–liquid interfaces will be computed by equation (1). The initial concentration of liquid phase within liquid bridge (Fig. 1a) and the flux of materials will be computed on changeable FE mesh

(Fig. 1b), which must be remeshed always when solid–liquid interface on larger grain reaches mesh line.

The time-dependent concentration of liquid phase in contact with the smaller grain is greater than in contact with the larger one. Therefore the smaller one dissolves in the liquid matrix and dissolved atoms flow from the matrix to the larger grain. Pure tungsten dissolved into the liquid, transports through the liquid and precipitates as W(Ni) solid solution on the larger grain (Fig. 1c). It can be seen that due to high concentration gradient in this area, dissolution and reprecipitation processes are very fast. Although the larger grain continues to grow, the separation distance remains essentially constant, but the centers of mass of both grains move to the right. It can be seen that the larger grain undergoing a larger shape distortion than the smaller one.

Conclusion

This paper outlines FE method for the simulation of coarsening of two-grain model during LPS, as a result of matter transport by diffusion from the dissolving smaller grain toward the growing larger one. The time dependent model system geometry is determined by initial topology, by size and shape of precipitates, by growth kinetics and by transport properties of a liquid phase. The numerical model consists of a few basic equations that establish concentration profiles of solid–liquid system at sintering temperature. The accuracy and efficiency of the simulation method depend only on how well the compositions of the solid phase and the diffusion coefficient in the liquid are known. The qualitative and quantitative characteristics of model system should be sound and appear to agree with the expected physical behavior of real system. Theoretical basis of this analysis is general and applicable to any binary system that satisfies three general requirements: there is a liquid phase at the sintering temperature, the solid phase is soluble in the liquid and the liquid wets the solid.

Acknowledgements

The first author was performed present study under the project (No. OI172057) supported by the Ministry of Education and Science of the Republic of Serbia. He would also like to acknowledge partial support for this study by the Japan Society for the Promotion of Science (Invitation Fellowship ID No. S-10175).

References

- [1] K. Shinagawa, K. Osakada and K. Mori, *Computer Aided Innovation of New Materials II*, M. Doyama, J. Kihara, M. Tanaka and R. Yamamoto (Eds), 1993, 1747-1750.
- [2] K. Shinagawa, *JSME International Journal, Series A*, 1996, 39, 565-572.

COMPUTER STUDY OF REARRANGEMENT DRIVEN BY CAPILLARY AND VISCOUS FORCES IN LIQUID PHASE SINTERING

Z. S. Nikolić¹, K. Shinagawa²

¹*University of Niš, Faculty of Electronic Engineering, Serbia*

²*Kagawa University, Faculty of Engineering, Japan*

Abstract

Computer study of rearrangement driven by attractive forces (static and dynamic in nature) during liquid phase sintering will be considered.

Introduction

The rearrangement during liquid phase sintering has been generally accepted that driven by the attractive forces developed between the grains connected by the liquid bridges. Capillary forces usually dominate in cases where the liquid exists as discrete bridges, but viscous forces can become significant when the liquid viscosity is very high or at high inter-grain velocities. This paper outlines computer-based methods for simulation of time-dependent rearrangement induced by both capillary and viscous forces.

Results and Discussion

The capillary force acting normal to the solid-liquid interfaces within a liquid bridge between two grains of radius R_1 and R_2 ($R_1 \geq R_2$) is given by [1]

$$F = 2\pi\gamma x_1 \sin(\varphi_1 + \theta) + \pi\gamma x_1^2 \left(\frac{1}{\rho_2} - \frac{1}{\rho_1} \right), \quad x_1 = R_1 \sin \varphi_1, \quad (1)$$

where γ is the surface tension, ρ_1 and ρ_2 are the radii of the meniscus [1]

$$\rho_1 = R_1 \sin \varphi_1 - \rho_2 [1 - \sin(\varphi_1 + \theta)], \quad \rho_2 = \frac{R_1(1 - \cos \varphi_1) + R_2(1 - \cos \varphi_2) + D}{2 \cos\left(\frac{\varphi_1 + \varphi_2}{2} + \theta\right) \cos\left(\frac{\varphi_1 - \varphi_2}{2}\right)},$$

φ_1 and φ_2 are the angles subtended by the contact at the center of the grains, D is inter-grain distance and θ is the contact angle measured between the solid and the liquid phases.

On the other side, assuming an infinite liquid and the dynamic viscosity of the liquid, η , an expression for the viscous force acting on the spherical grains of radius R can be derived [2]

$$F_{\text{vis}} = \frac{3}{2} \pi \eta R^2 \frac{1}{D} \frac{dD}{dt}. \quad (2)$$

For simulation of time dependent rearrangement we will apply numerical method defined in [1]

$$\Delta \mathbf{D}_{kj}^{n+1} = D_{kj}^n \chi (\mathbf{F}_{kj}^{n+1} - \mathbf{F}_{\text{vis},kj}^{n+1}), \quad (3)$$

where $\Delta \mathbf{D}_{kj}^{n+1}$ is the change of the inter-grain distance between grains k and j after time $t + \Delta t$, D_{kj}^n is the inter-grain distance at previous time step, χ is a constant at a given grain size, \mathbf{F}_{kj}^{n+1} is the capillary force per kj -th contact defined by (1), and

$$\mathbf{F}_{\text{vis},kj}^{n+1} = \frac{3}{2} \pi \eta R_{\text{eff}}^2 \frac{1}{D_{kj}^n} \frac{\Delta \mathbf{D}_{kj}^n}{\Delta t}, \quad R_{\text{eff}} = \frac{2R_1 R_2}{R_1 + R_2}. \quad (4)$$

obtained from equation (2) by assuming $dD/dt \approx \Delta D/\Delta t$.

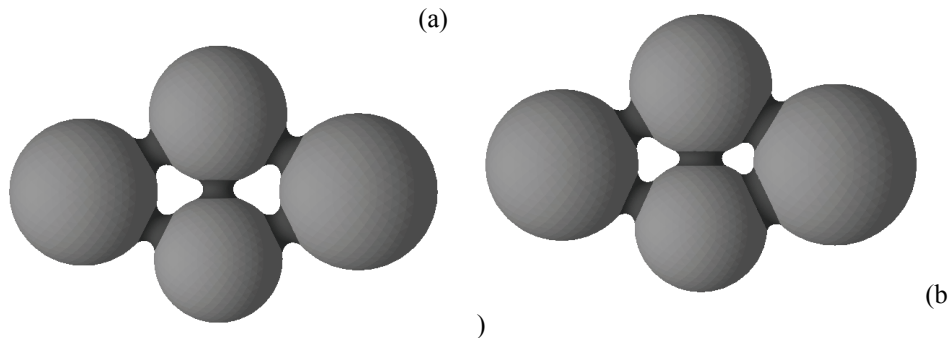


Figure 1. Four-grain model. (a) Initial ($\langle R \rangle = 145 \mu\text{m}$, $\langle D \rangle = 25 \mu\text{m}$). (b) After $t = 4.2 \mu\text{sec}$ ($\langle D \rangle = 12.2 \mu\text{m}$). $\chi = 2 \times 10^{-3} \text{ N}^{-1}$, $\theta = 10^\circ$, $\eta = 5 \text{ mPas}$.

For a proper description of the rearrangement, the existence of the total driving force and the relative-displacement mobile network must both be taken into account. Thus, the model system rearrangement defined by the equation (3) and based on the equations (1) and (4) which relate forces and relative displacements within liquid bridge can be applied for simulation of the relative grain displacement due to both capillary and viscous forces.

Figure 1 shows simple model of four spherical grains connected with liquid bridges, whereas the evolution of the average separation distance for three values of viscosity is plotted in Fig. 2a. As it can be seen, as the time proceeds the inter-grain distances change; the densification is very rapid for low viscosity, while for high viscosity the grain displacements are very small due to almost monotonous decreasing of separation distances, therefore similar densification corresponds to longer rearrangement time. For evaluating the total driving force, the rate-dependent term in the equation (3) defined by the equation (4) has to be taken into account. Figure 2b compares the capillary and the viscous forces during rearrangement and approaching of grains for high viscosity. Interactions correspond to large inter-grain distances are dominated by the capillary forces

(capillary regime), whereas the viscous forces slowly increase due to slow decreasing separation distances but also followed by decreasing of the relative grain displacements. As it can be seen, after $\sim 80 \mu\text{sec}$ both forces become approximately equal (a transitional regime) which corresponds to very small relative displacements. After intermediate separation distances, the total force becomes repulsive (viscous regime). Obtained theoretical predictions pretty well agree with the conclusion given by Pitois *et al.* [2]. They have also presented interesting result that the maximum dynamic attractive force measured was about 3 times higher than the corresponding static one.

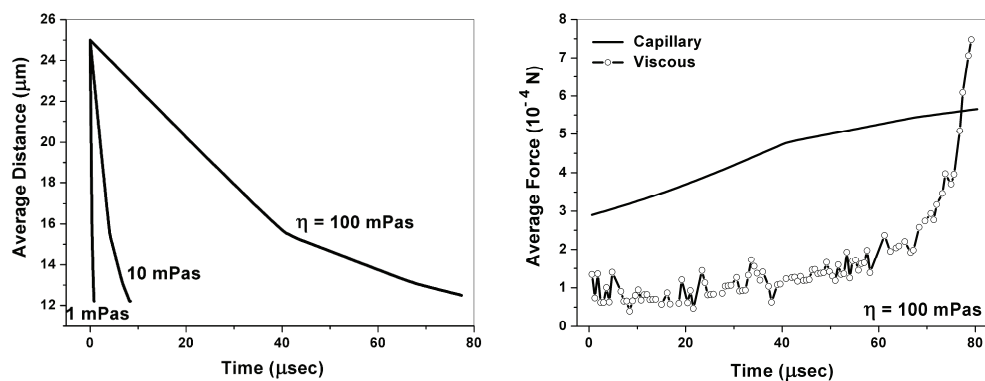


Figure 2. Rearrangement of four-grain model. (a) Time-dependent shrinkage for different values of viscosity. (b) Time dependent driving forces.

Conclusion

In this paper, the theoretical models dealing with the fundamental interaction forces that exist between grains attached by liquid bridges were outlined and the development from these pair-wise interactions to multi-grain model was described. It was shown that the rearrangement is essentially determined by dynamic viscosity and by the ratio of driving forces. However, it was also shown that the rearrangement is governed by geometrical factors (topology of liquid bridges) and nearest neighbor interaction (capillary forces between connected grains).

Acknowledgements

The first author was performed present study under the project (No. OI172057) supported by the Ministry of Education and Science of the Republic of Serbia. He would also like to acknowledge partial support for this study by the Japan Society for the Promotion of Science (Invitation Fellowship ID No. S-10175).

References

- [3] Z. S. Nikolic, F. Wakai, *Math. Comput. Modell.*, 2012, 55, 1251–1262.
- [4] O. Pitois, P. Moucheront, X. Chateau, *J. Colloid Interface Sci.*, 2000, 231, 26–31.

COMPUTER STUDY OF LIQUID BRIDGE RUPTURE IN LIQUID PHASE SINTERING

Z. S. Nikolić¹, K. Shinagawa²

¹*University of Niš, Faculty of Electronic Engineering, Serbia*

²*Kagawa University, Faculty of Engineering, Japan*

Abstract

During rearrangement some liquid bridges become unstable due to elongation and their ruptures occur. In this paper a model for bridge rupture will be considered.

Introduction

The rearrangement process during liquid phase sintering has been generally recognized by remarkable approaching of some grains combined with the filling pores process, but also by the enlargement of some inter-grain distances followed by the growing of some inter-grain pores. The overall effect of separating the grains while keeping constant the liquid volume is therefore an elongation of the bridge, which becomes longer and thinner and less concave. Such liquid bridge elongation combined with rupture of some liquid bridges can reinforce grain rearrangement, but also generate non-uniform distribution of small and large pores. These phenomena will be the subject of our study. The bridge which is not stable any more will be modeled as ruptured bridge replaced by two liquid droplets on the surfaces of grains. Investigation of the model system densification combined with liquid bridge rupture will be analyzed in a simple grain arrangement.

Results and Discussion

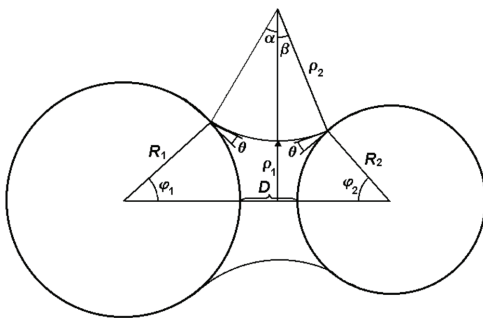


Figure 1. Topology of the liquid bridge.

Let us consider two spherical grains of radius R_1 and R_2 ($R_1 \geq R_2$) joined by a liquid bridge of constant volume (Fig. 1). The liquid meniscus can be carried out using the circle approximation [1] defined by the radii of the meniscus

$$\rho_1 = R_1 \sin \varphi_1 - \rho_2 [1 - \sin(\varphi_1 + \theta)]$$

$$\rho_2 = \frac{R_1(1 - \cos \varphi_1) + R_2(1 - \cos \varphi_2) + D}{2 \cos(\frac{\varphi_1 + \varphi_2}{2} + \theta) \cos(\frac{\varphi_1 - \varphi_2}{2})}$$

where φ_1 and φ_2 are the subtended angles, D is the inter-grain distance and θ is the contact angle measured between the solid and the liquid phases.

When two grains are pulled apart due to rearrangement, the liquid bridge and corresponding capillary force within it evolve from a static state toward a critical configuration in which, at some point, the liquid menisci first touch each other (ρ_1 approaches zero, Fig. 2) and the liquid bridge ruptures. The liquid bridge after rupture can be considered so that it breaks into two smaller liquid droplets adhere to the surface of each grain [2]. We will assume that their volumes are proportional to the grain size ratio, as well as that their shape can be approximated by a perfect sphere because gravity has negligible effects on their small liquid volumes.

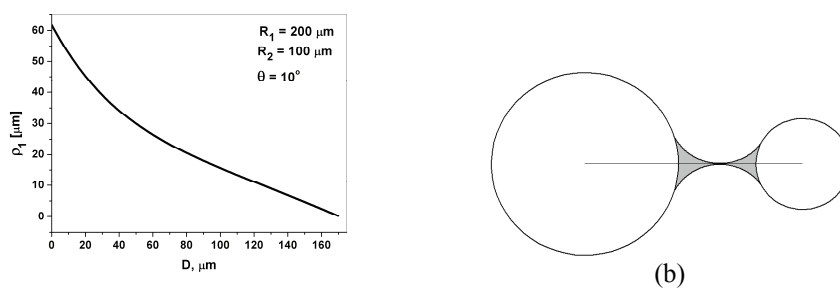


Figure 2. (a) The variation of ρ_1 with D . (b) Critical configuration corresponds to $\rho_1 \approx 0$.

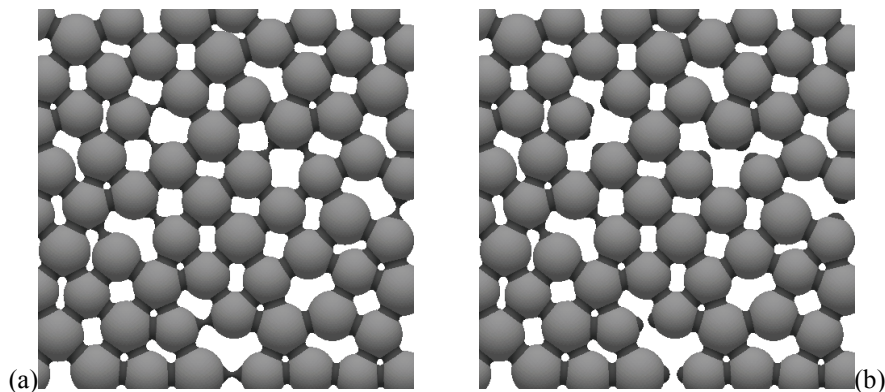


Figure 3. Snapshot of microstructures (a) with no rupture and (b) with rupture.

Time dependent separation distances during rearrangement are determined by the resultant capillary forces [1]. As long as the inter-grain distance is less than the critical separation distance, the rearrangement is governed by the capillary force. Beyond the rupture distance the capillary force will be set to zero.

In order to demonstrate simulation method based on determination the critical rupture distance and the formation of two liquid droplets, the liquid bridge rupture phenomenon will be simulated on planar multi-grain model of spherical grains (W–Cu system, data given in [1]) with the average radius of $\sim 55 \mu\text{m}$ and with the average separation distance of $\sim 9.5 \mu\text{m}$. The result of rearrangement [1] after 2000 rearrangement steps (RS) is shown in Fig. 3a, where the average inter-grain

distance was now $\sim 3.33 \mu\text{m}$ with the average shrinkage of $\sim 65\%$. It can be seen remarkable approaching of most grains combined with the filling pores process, but also much exaggerated enlargement of some separation distances followed by the growing of some inter-grain pores. Due to the overall effect of grain separation liquid bridge elongation occur while keeping constant their liquid volume: they become longer and thinner and less concave. Such bridges are not stable any more and formation of liquid droplets on the surfaces of grains is preferable. Therefore, the rearrangement method [1] will be replaced by new one, which takes into account the fact that at greater separation distance there is a maximum value of the separation distance corresponding to liquid bridge rupture ($\rho_1 \approx 0$). Figure 3b shows obtained simulation result after 2000 RS with the average shrinkage of $\sim 87\%$ and the mean inter-grain distance $\sim 1.3 \mu\text{m}$ that corresponds almost to the equilibrium configuration. It can be seen, however, that during this simulation several new unstable liquid bridges also were generated. It is expected that some of them will be most likely ruptured during next rearrangement. In practice, however, this liquid bridge elongation combined with rupture of some liquid bridges can reinforce grain rearrangement, but also generate non-uniform distribution of small and large pores.

Conclusion

It is well known that during rearrangement some liquid bridges become unstable due to elongation and their ruptures occur. In this paper a model for bridge rupture was considered. For computer study of rearrangement, two different configurations were simulated: the generic configuration characterized by liquid bridge connected grains (inter-grain distance smaller than the critical rupture distance) and the mixed state with connected and separated grains. For this reason it was carried out the calculation of the evolution of multi-grain (planar due to better visualization) system when the constituent grains are pulled apart from each other due to the rearrangement. Such system was characterized from a geometrical (noncontact geometry) and from a quasistatic viewpoint.

Acknowledgements

The first author was performed present study under the project (No. OI172057) supported by the Ministry of Education and Science of the Republic of Serbia. He would also like to acknowledge partial support for this study by the Japan Society for the Promotion of Science (Invitation Fellowship ID No. S-10175).

References

- [5] Z. S. Nikolic, F. Wakai, *Math. Comput. Modell.*, 2012, 55, 1251–1262.
- [6] X. Pepin, D. Rossetti, S.M. Iveson and S.J.R. Simons, *J. Colloid Interface Sci.*, 2000, 232, 289–297.

HIGH PERFORMANCE PROTON CONDUCTING MEMBRANES FOR FUEL CELLS MADE BY PHOTOPOLYMERIZATION OF HYDROLYTICALLY STABLE MONOMERS

M. Kellner¹, F. Radovanovic³, J. Matovic², R. Liska¹

¹*Vienna University of Technology - IAS, Getreidemarkt 9, 1060 Vienna, Austria*

²*Vienna University of Technology - ISAS, Floragasse 7, 1040 Vienna, Austria*

³*IHTM - IMTM, University of Belgrade, Njegoseva 12, 11000 Belgrade, Serbia*

Abstract

Proton conducting membranes were prepared by photopolymerization of 2-acrylamido-2-methylpropane sulfonic acid solutions within the pores of polypropylene membranes. Several commercial and novel multifunctional monomers synthesized in IAS lab were investigated as suitable crosslinking agents for this application. Some membranes made with synthesized crosslinkers at low crosslinker concentrations exceeded 2.5 times the conductivity of Nafion® 115 membrane, while exhibiting a good hydrolytical stability, in contrast to the commercial crosslinkers based on multifunctional (meth)acrylates.

Introduction

Polymer electrolyte fuel cells (PEFC) gained a lot of interest in recent years as a potential solution for an eco-friendly energy production used for automotive transportation [1]. Proton exchange membranes (PEM) for PEFCs require mechanical and chemical stability to ensure high proton conductivity and effective separation of anode and cathode under challenging conditions. Best commercial membranes made from sulfonated fluoropolymers, such as Nafion®, are quite expensive [2]. To improve fuel cell performance at a lower cost, 2-acrylamido-2-methylpropane sulfonic acid (AMPS) was investigated recently [3-4]. In this work, novel formulations based on AMPS have been polymerized by UV-initiated radical polymerization and crosslinked with commercial and multifunctional monomers synthesized in IAS lab. To facilitate conductivity measurements, formulations were constrained within a porous membrane as described by Zhou et al. [5].

Experimental

AMPS and N-methyl-2-pyrrolidone (NMP) were purchased from Sigma Aldrich and used without further purification. Biaxially stretched PP membranes with 115 μ m thickness and 85% porosity were obtained from 3M [6]. N,N-bis(ω -(methacrylamido)polyoxyethylene)methacrylamide (PEA-3MMA), tris[2-(methacryloylamino)ethyl]amine (3(MAAE)A) and polyethyleneimine-co-methacrylamide (PEI-MAA) were synthesized as described in reference [7].

Sheets of PP membrane were hydrophilized by coating with a 5% Triton X-100 solution in acetone. Hydrophilized membranes were dip-coated in a solution

of ionomer, crosslinker and photoinitiator, covered with a Teflon sheet and irradiated with a high intensity Intelliray 600 UVA Lamp (60 sec exposure at 90% intensity and 12 cm distance). After polymerization the membranes were stored in deionized (DI) water for several days with daily exchange of water.

Proton conductivity was measured in the plane of samples using a 4-point DC method: electrical conductivity between two gold-plated inner electrodes placed 1 cm apart at a potential difference between two gold-plated outer electrodes of 100 mV was equal to proton conductivity under these conditions.

Results and discussion

Tetraethylene glycol diacrylate (4EG-DA) and decanediol dimethacrylate (D3MA) were investigated as commercial crosslinking agents with AMPS concentrations from 40 to 83 wt% dissolved in water or NMP (Table 1).

Table 1. Compositions of different proton-conductive formulations.

Formulation no.	AMPS concentration [wt%]	Crosslinker	Solvent
1	40	D3MA	NMP
2	40	4EG-DA	NMP
3	41	4EG-DA	H ₂ O
4	83	4EG-DA	H ₂ O

As Figure 1 shows, membranes made with a hydrophilic crosslinker (4EG-DA) had significantly higher conductivity than membranes with a hydrophobic crosslinker (D3MA) which reduced water uptake. Proton conductivity mainly increased with higher concentrations of monomers. Conductivity of membranes made with commercial (meth)acrylate crosslinkers significantly decreased after heating for 24h in DI water, but remained unchanged when polyAMPS was converted to the sodium salt before heating. This conductivity reduction may have been related to the cleavage of crosslinker ester bonds catalyzed in strongly acidic environments.

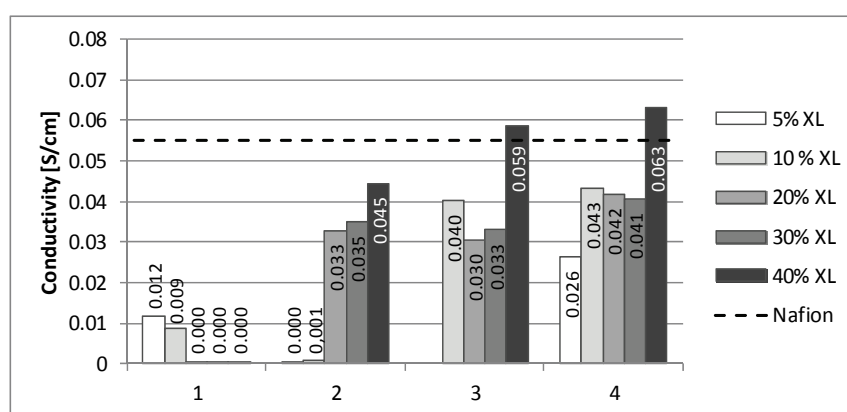


Figure 1. Conductivity as a function of the concentration of meth(acrylate) XL.

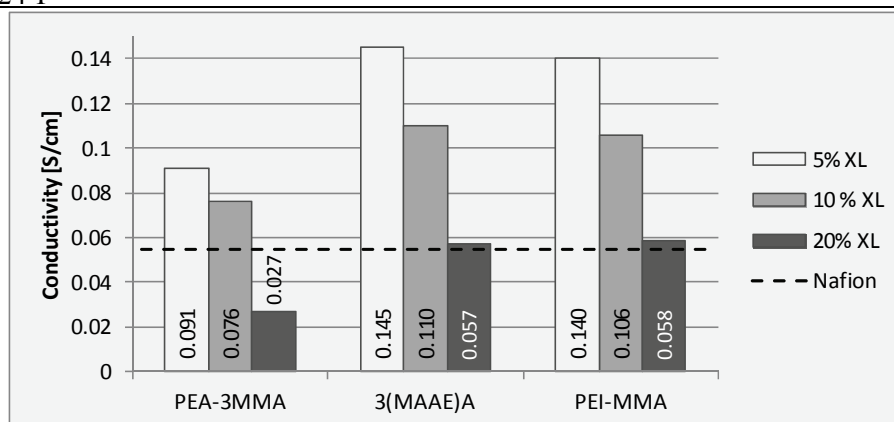


Figure 2. Conductivity as a function of the concentration of methacryamide XL.

Conductivity of membranes made with synthesized multifunctional crosslinkers is shown in Figure 2. Membranes made with 3(MAAE)A and PEI-MMA at a 5% XL level had 2.5 times higher conductivities than Nafion 115 and were significantly more stable than (meth)acrylate crosslinkers when heated in DI water.

Conclusions

The effects of newly synthesized and commercially available crosslinkers on PEM conductivity have been investigated in membrane-constrained polyAMPS gels. Best results in terms of conductivity and hydrolytic stability were obtained with multifunctional acrylamides synthesized in IAS lab.

Acknowledgements

The research leading to these results has received funding from the European Community's FP7- NMP Programme, under the Project Acronym MultiPlat, the Austrian Federal Ministry of Science and Research and the Serbian Ministry of Education and Science within the framework of the project TR 32008. The authors would like to thank 3M and Ciba SC for providing membranes and initiators.

References

- [1] J. Patric, *Current Opinion in Colloids and Interface Science*, 2003, 8, 96-102.
- [2] *Fuel cells I*, 1st ed. *Advances in Polymer Science*, 2008, NY: Springer. 268.
- [3] H. Diao et al., *Macromolecules*, 2010, 43, 6398-6405.
- [4] J. Qiao et al, *J. Mater. Chem.*, 2005,15, 4414-4423.
- [5] J. Zhou et al, *J. Membr. Sci.*, 2005, 254, 89-99.
- [6] D.R. Lloyd et al, *J. Membr. Sci.*, 1990,52, 239-261.
- [7] M. Kellner et al, Novel crosslinkers for high performance Poly-AMPS-based proton exchange membranes for fuel cells, *Designed Monomers and Polymers*, submitted 2012.

FUNCTIONALIZED POLYMER MEMBRANES FOR PLASMONIC SENSING WITH ENHANCED SELECTIVITY

Z. Jakšić¹, F. Radovanović¹, A. Nastasović²

¹ *IHTM – Centre of Microelectronic Technologies and Single Crystals
Njegoševa 12, University of Belgrade, Serbia*

² *IHTM – Centre for Chemistry, Njegoševa 12, University of Belgrade, Serbia*

Abstract

We investigate theoretically and experimentally the concept of enhancing the selectivity of chemical, biochemical and biological (nano)plasmonic sensors utilizing multifunctionalized polymer membranes. Membrane nanocompositing is done by lamination and surface/pore immobilization. A separator/filter and an affinity-based adsorption enhancer are integrated into a single multifunctional membrane structure. Functionalized membrane may be transferred across platforms and even used for different types of sensing devices.

Introduction

Surface plasmon optics is the basis for a novel generation of ultra-sensitive (bio)chemical and biological sensors that are label-free and ultrafast [1]. Typically their active part is a surface composed of metal or metal-dielectric (plasmonic metamaterial) [2] with a negative real part of the relative dielectric permittivity. Two distinct types of surface plasmon resonance are used for such sensing, one of them based on propagating surface waves (surface plasmon polaritons, SPP), the other on nonpropagating (localized) SPP [3]. In both cases analyte particles adsorb on the active surface, modifying the conditions for the existence of SPP. In its basic configuration a plasmonic sensor is thus a refractive index sensor. Its sensitivity may well exceed 10^{-8} refractive index units, i.e. 1 ng/cm^2 (0.003 monolayer) [4].

A problem with plasmonic sensors in their basic form is their relatively low selectivity based solely on refractive index changes, so that different materials with similar refractive indexes cause similar outputs. An approach to overcome this problem is functionalization of the sensor surface by nanocompositing [5]. Here an interaction partner ("ligand") is immobilized to the sensor surface, serving as affinity-based binding material for the target analyte. Another way is to utilize a filter or separator to remove undesired species and allow only the target analyte to reach the sensor surface [5]. Membranes are often used for this, while the separation mechanism may be based on nanopores (e.g. molecular sieves) or nonporous (dense) structures with solution-diffusion mechanism. Built-in electrical charges within the membrane may be also utilized (e.g. ion exchangers).

In this work we investigate the possibility to integrate the separator/filter structure and the affinity-based target-specific adsorption enhancer into a single membrane structure which may further be merged with the sensitive plasmonic

adsorption [6] and enzyme immobilization [7]. Fig. 2a shows a scanning electron micrograph (SEM) of the poly(GMA-*co*-EGDMA) surface.

For the formation of membranes comprising GMA as a precursor for subsequent functionalization we selected a new method recently described in literature [8-9]. It combines a traditional immersion precipitation process for making membranes with photopolymerization and crosslinking of functional monomers included in the casting solution. As the environmental SEM micrograph of the top surface in Fig. 2b shows, the resulting membranes have an integral top skin layer with fine selective channels over a coarser mechanically stable support. The top skin layer has a separation function against undesirable species present in the feed solution. Subsequent functionalization of the epoxy groups entrapped within the membrane provides ligand sites for enhanced plasmonic sensing.

Conclusion

Possibilities to integrate separator and ligand for plasmonic sensor into a single structure are considered. The multifunctionalization ensures a highly tailorable element that is transferable across platforms. This allows for a multiple use of a single sensor type for a larger number of different analytes or massive process parallelization using the identical plasmonic structure as the basic element. At the same one may use built-in (nano)pores to augment the effective surface for adsorption and thus vastly increase the amount of adsorbate, furnishing a further increased sensitivity. Additional reaction enhancements may also be incorporated, including but not limited to catalyst particles. The approach may be extended to other types of chemical and bio sensors.

Acknowledgment

This work has been funded by Serbian Ministry of Education and Science within the framework of the projects TR32008 and III 43009.

References

- [1] W. L. Barnes, A. Dereux, T. W. Ebbesen, *Nature*, 2003, 424, 824-830.
- [2] Z. Jakšić, O. Jakšić, Z. Djurić, C. Kment, *J. Optics A*, 2007, 9, S377-S384.
- [3] M. E. Stewart, C. R. Anderton, L. B. Thompson, J. Maria, S. K. Gray, J. A. Rogers, R. G. Nuzzo, *Chem. Rev.*, 2008, 108, 494-521.
- [4] L. S. Jung, C. T. Campbell, T. M. Chinowsky, M. N. Mar, S. S. Yee, *Langmuir*, 1998, 14, 5636-5648.
- [5] Z. Jakšić, J. Matovic, *Materials*, 2010, 1, 165-200.
- [6] A. Nastasović, Z. Sandić, Lj. Suručić, D. Maksin, D. Jakovljević, A. Onjia, *J. Hazard. Mater.*, 2009, 171, 153-159.
- [7] N. Miletić, Z. Vuković, A. Nastasović, K. Loos, *Macromol. Biosci.*, 2011, 11, 1537-1543.
- [8] P. Radovanovic, M. Kellner, J. Matovic, R. Liska, T. Koch, *J. Membrane Sci.*, 2012, 401-402, 254-261.
- [9] P. Radovanovic, J. Matovic, R. Liska, M. Kellner, Austrian Patent Application, A824/2011.

H-26-P

SENSITIZED GELATIN AS AN EYE PROTECTION FILTER AGAINST DIRECT LASER RADIATION

B. Murić, D. Pantelić, D. Vasiljević, B. Jelenković
Institute of Physics, University of Belgrade, Pregrevica 118, 11080 Zemun, Serbia

Abstract

Tot'hema eosin sensitized gelatin (TESG) layer is used as an eye protection filter against 2nd harmonic Nd:YAG laser light. Compared to classical eye protection filters our material uses microlens formation to protect eye from direct laser radiation. TESG laser safety goggles were manufactured, at the same time satisfying European eye protection standard EN 207. Measurements have shown that the eye is protected from 10W of direct laser beam. Eye protection filters can be manufactured for other wavelengths too, by changing the sensitizer.

Introduction

Due to increasing of lasers use in medicine, science, industry... the laser eye protection become very important. Different parts of the eye can be damaged, depending on the laser wavelength and intensity. UV light (<400 nm) and IR light (>1400 nm) damage the cornea and eye lens. Wavelengths from 400 nm to 1400 nm are focused on the retina, which is the most sensitive part of the eye [1, 2].

Eye protection filters (absorption, reflection...) are mostly plastic materials that protect human eye from diffusely reflected laser light [3, 4]. Direct laser irradiation heats the plastics and laser beam punches a hole in the filter. Different, commercially available, laser safety glasses have a very small transmission for the laser beam, but enough for visible light. They should protect an eye against scattered laser beam, under standardized conditions defined by European laser eye protection standards EN 207 [5] and EN 208 [6]. The same standards require that a laser goggle must be able to protect the user for a minimum of 10 seconds (CW laser) or 100 pulses (pulsed laser), when exposed to direct laser radiation. Maximum permissible exposure (MPE) measured at the cornea of the human eye, is the highest laser power density or energy density that is considered safe for a given wavelength and exposure time [5, 7].

We have shown that TESG can be used as an eye protection filter against the high-power direct laser beam, by utilizing a microlens formation on the protective material.

Experimental

TESG layer is simple to prepare and use. Heated mixture of gelatin, tot'hema and eosin is poured on the polycarbonate (lexan) plate and dried. Crystallization of layer is prevented by adding a small amount of NaCl. After drying, TESG layer is very elastic and sticky, and can be easily peeled and transferred to another substrate. Medical drinkable solution of tot'hema softens gelatin layer, increasing its flexibility. Eosin is a dye used to enhance absorption at 532 nm [8]. Protection

filter was prepared by adhering 1 mm thick TESH layers on both sides of 2 mm thick transparent lexan plate (see Fig.1). Through our experiments 10 W maximum power, 532 nm Nd:YAG laser was used (Fig. 2). Laser power was measured by powermeter placed 2 cm behind 5 mm diameter diaphragm (simulating the human pupil which normally opens about 2 mm in daylight, and 7 mm in the dark [9]).

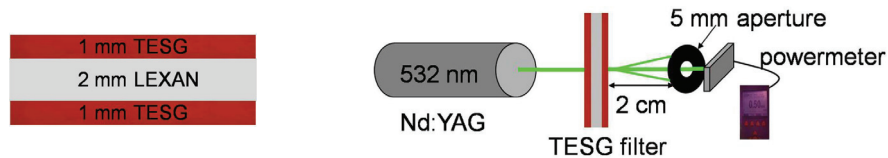


Figure 1. Cross-section of TESH filters. **Figure 2.** Experimental setup.

Results and Discussion

In our previous research transparent, diverging microlenses (focal lengths far below 1 mm) were formed quickly at TESH layer [10, 11]. As shown in Fig. 3 the protection mechanism is influenced by the laser power. Absorption of laser light dominates up to 50 mW, and it doesn't affect the protective layer. Microlenses formation starts above 50 mW. The laser beam diverges and significantly reduces the energy density on the second layer, which effectively absorbs the laser beam. Above 600 mW the protection layer starts to carbonize, producing nontransparent black area, which further blocks the laser beam.

The power density behind the TESH filter, as a function of exposure time, for various laser powers was measured (Fig. 4). Five measurements were made for each laser power and the average values are shown. As can be seen, the protection achieved by TESH filter is below MPE values for all incident laser powers (0.3W – 9.6W).

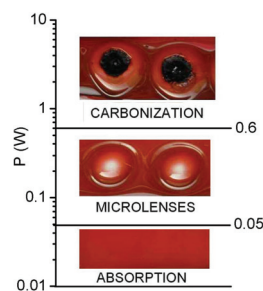


Figure 3. TESH layer appearance as a function of laser power

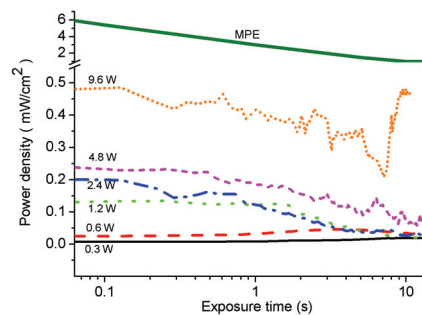


Figure 4. Power density vs. exposure time or different laser powers

We have produced laser protective eyewear by modifying welder's goggles (see Fig. 5). The protection level can be controlled by flipping, up or down, the front set of filters. If a single filter is in use (Fig. 5a), goggles offer lower protection level but allow one to see well and adjust the laser. If both filters are used (Fig. 5b) goggles efficiently protect eyes from direct laser beam.

H-26-P

accidentally damaged TESG layers can be peeled and replaced. Efficiency of TESG goggles is shown in Fig. 5c. We can see that after 30 s of irradiation by 10 W direct laser beam transmitted power is still below 10 μ W.



Figure 5. Photograph of TESG eye-protection goggle: (a) for laser adjustment; (b) for laser protection; (c) irradiated with 10W 532nm Nd:YAG laser for 30 s.

Conclusions

TESG material, used as a protection filter against 2nd harmonic Nd:YAG laser beam, is described. Results have shown that an eye is protected from 10 W of direct laser beam as a result of microlens formation. Effective TESG protection goggles, for laboratory use, were made and tested. Preliminary results have shown that eye protection filter can be manufactured for other wavelengths too, by changing the dye (sensitizer).

Acknowledgments

Paper was written as a part of research on the projects ON 171038 and III 45016 supported by the Ministry of education and science of the Republic of Serbia.

References

- [1] A. Schirmacher, *Medical Laser Application*, 2010, 25, 93-98.
- [2] E. Sutter, A. Schirmacher, *Opt. & Laser Technol.*, 2001, 33, 255-258.
- [3] M. Lenner, C. Spielmann, *Appl. Opt.*, 2005, 44, 3532-3539.
- [4] C. H. Lee, B. Bihari, R. Filler, B. K. Mandal, *Opt. Mater.*, 2009, 32, 147-153.
- [5] EN 207: 2009 Personal eye-protection equipment—Filters and eye-protectors against laser radiation (laser eye-protectors).
- [6] EN 208: 2009 Personal eye-protection—Eye-protectors for adjustment work on lasers and laser systems (laser adjustment eye-protectors).
- [7] Standard Z-136. 1, "Safe use of lasers," ANSI, New York, 1986.
- [8] B. Murić, D. Pantelić, D. Vasiljević, B. Panić, *Opt. Mater.*, 2008, 30, 1217-1220.
- [9] D. A. Atchinson, C. C. Girgenti, G. M. Campbell, J. P. Dodds, T. M. Byrnes, A. J. Zele, *Clin. Exp. Optom.*, 2011, 94, 545-549.
- [10] B. Murić, D. Pantelić, D. Vasiljević, B. Panić, *Appl. Opt.*, 2007, 46, 8527-8532.
- [11] B. Murić, D. Pantelić, D. Vasiljević, B. Panić, B. Jelenković, *Appl. Opt.*, 2009, 48, 3854-3859.

ANALYSIS OF FACTORS INFLUENCING Cu(II) SORPTION BY CLINOPTILOLITE

M. Šljivić-Ivanović, I. Smičiklas, J. Marković

*University of Belgrade, Vin a Institute of Nuclear Sciences, P.O. Box 522,
Belgrade Serbia*

Abstract

The effects of initial metal concentration and pH, as well as the sorbent mass and particle size, on Cu(II) sorption by natural clinoptilolite were evaluated and compared. Full factorial experimental design at two levels was applied. Statistically significant factors were determined considering residual Cu(II) concentrations as a system response.

Introduction

Heavy metals are major pollutants of some ground and surface waters and are often present in industrial or urban wastewaters. Among different methods for water purification, sorption processes are widely investigated using natural and synthetic materials. Clinoptilolite is naturally occurring zeolite, which sorption properties toward heavy metal cations, NH_4^+ , inorganic anions and organic substances were intensively studied [1]. The effectiveness of sorption process can be significantly influenced by variation of operating conditions. The objective of this work was to analyze and compare the effects of initial solution pH, initial metal concentration, sorbent mass and particle size, on Cu(II) removal by natural clinoptilolite, using experimental design methodology [2].

Materials and Methods

The experiments were conducted in batch conditions, at $20 \pm 1^\circ\text{C}$. Variable amounts of solid phase (clinoptilolite, Vranjska Banja, Serbia) were equilibrated for 48 h on a horizontal shaker with 20 mL of Cu(II) solutions. Independent variables and their levels are given in Table 1, while Table 2 presents

coded experimental conditions based on full factorial design and defined by the statistical software. After filtration, residual concentrations of Cu(II) ions were measured by Perkin Elmer Emission Spectrometer Plasma 400, at $\lambda=222.78$ nm.

Table 1. Variables and their levels.

Factor	Level	
	-1	+1
A - initial pH	3	5
B - sorbent mass (g)	0.1	0.4
C - initial Cu(II) conc. (mol/L)	0.0002	0.005
D- particle size (mm)	<100	1-3

Table 2. Experimental design matrix

Results and Discussion

The study of full factorial design consists of exploring all possible combinations of the factors considered in the experiment. Using residual Cu(II) concentrations as system response, Pareto chart (Fig. 1a) and Main effect plot (Fig. 1b) were constructed by statistical software (MINITAB).

In Pareto chart, the absolute values of effects are compared and information about their statistical significance at a confidence interval of 95% is provided. Each bar length in Pareto chart is proportional to the standardized effect, produced by variation of a given factor between lower and higher level [2]. The change of initial metal concentration influenced process the most. The variation of sorbent mass and the interaction between initial Cu(II) concentration and sorbent mass as well produced statistically significant effects.

The Main effect plot (Fig 1b) gives information on whether the change between

two variable levels decreased or increased the selected system response [2]. The horizontal line in the graph represents the overall mean response of the system, for both levels of all factors. From the Fig. 1b, it can be concluded that decrease of concentration and increase of sorbent mass caused reduction of aqueous Cu(II) concentration, while the effects of initial pH and sorbent granulation were negligible.

Finally, for the investigated range of variables, the following mathematical model can be used for process description:

$$Y = 155.3 - 18.26 B + 150.78 C - 16.95 BC$$

where Y is residual Cu(II) concentration, whereas B, C and BC represent effects of sorbent mass, initial metal concentration and their interaction, respectively.

Factor				Response(Y)
A	B	C	D	Cu (mg/L)
1	-1	-1	-1	4.01
1	1	1	1	289.71
1	1	1	-1	233.18
-1	1	1	1	286.39
1	1	-1	1	3.91
-1	1	-1	1	7.21
-1	-1	1	-1	341.47
1	-1	1	-1	328.90
-1	-1	1	1	350.82
-1	-1	-1	-1	10.97
1	-1	-1	1	8.27
-1	1	1	-1	274.16
1	1	-1	-1	1.66
-1	-1	-1	1	0.05
-1	1	-1	-1	0.04
1	-1	1	1	343.94

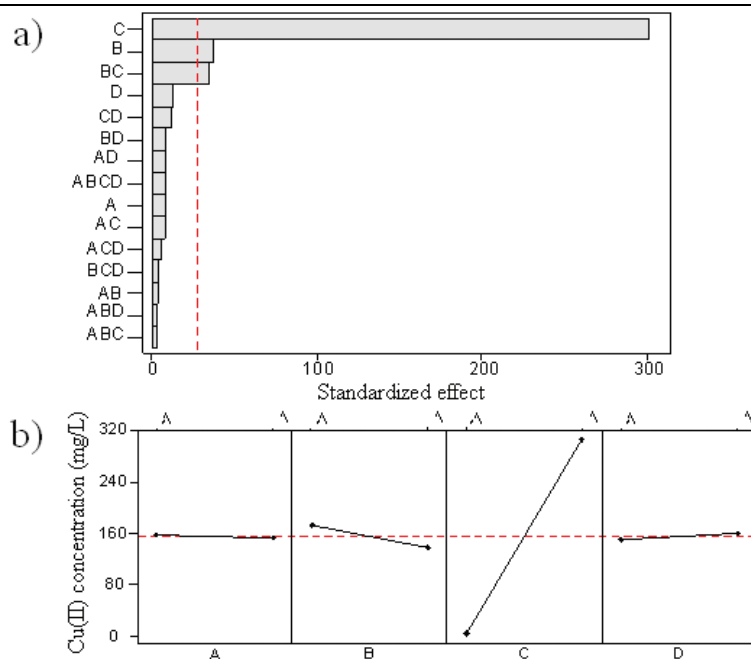


Figure1. a) Pareto chart and b) Main effect plot for residual Cu(II) concentrations

Conclusion

The influence of process variables (initial solution pH, initial metal concentration, sorbent mass and particle size) on Cu(II) removal from aqueous solutions by clinoptilolite was investigated using full factorial design. The effect of initial metal concentration was the most pronounced, followed by the effect of sorbent mass and interaction effect between sorbent mass and sorbate concentration. The empirical equation practical for process description was derived.

Acknowledgments

The work was supported by the Ministry of Education and Science of the Republic of Serbia (Project No. III 43009).

References

- [1] S. Wang, Y. Peng, Chem.Eng. J., 2010, 156, 11–24.
- [2] F. Yates, The Design and Analysis of Factorial Experiments, Imperial Bureau of Soil Science, Harpenden, 1937.

**SOLID STATE
PHYSICAL CHEMISTRY**

PLASMAELASTIC AND THERMOELASTIC EFFECTS IN MICROMECHANICAL STRUCTURES

D. M. Todorović

Institute for Multidisciplinary Research, Beograd, Serbia

Abstract

Plasmaelastic and thermoelastic effects can be important as driven mechanisms for micromechanical structures, based on the plasma, thermal and elastic wave phenomena, generated by absorption of modulated optical power. The plasmaelastic and thermoelastic mechanisms of photoacoustic generation in a micromechanical structure, photogenerated by an intensity-modulated optical beam, were studied. The amplitude and phase of the PA elastic bending in the micromechanical structure were calculated and analysed, including the various plasma and thermal sources. The theoretical results were compared with the experimental data. Experimental data were obtained by the PA elastic bending method, based on the optical excitation of the micromechanical structure and detection of the acoustic response (PA signal) with a very sensitive PA detection system.

Introduction

A new approach for producing compact, lightweight, a highly sensitive detector is provided by micro-(opto)-electro-mechanical systems (MOEMS) technology. The photoacoustic (PA) and photothermal (PT) science and technology extensively developed new methods for study MOEMS. The PA and PT effects can be important as driven mechanisms for micromechanical structures [1].

When a micromechanical structure is exposed to periodic optical excitation, the photogenerated carrier-density (the plasma wave) causes a mechanical stress. The mechanical stress produces periodic elastic deformation in the sample, the so-called electronic deformation [2]. This mechanism of elastic wave generation - plasmaelastic (PE) effect (or the electronic deformation – ED effect) is the property of semiconductors and electronic materials. The PE mechanism is based on the fact that photogenerated plasma in the semiconductor causes a deformation of the crystal lattice, i.e. it causes the change of the potential of the conduction and valence bands in the semiconductor. On the other hand, the photogenerated carrier thermalization and surface and bulk recombination, as thermal sources, cause the thermal wave generation. The thermal waves cause elastic bending in the micromechanical structure - the thermoelastic (TE) effect.

There are three mechanisms of PA generation [3]. The PA signal $S(\omega)$, can be given as a sum of plasmaelastic, $S^{PE}(\omega)$, the thermoelastic, $S^{TE}(\omega)$ and thermodiffusion $S^{TD}(\omega)$, components. The TD component of PA signal $S^{TD}(\omega)$ is a consequence of the heat diffusion processes in the sample, i.e., it depends on the periodic temperature variations at the sample surface and it can be given with well-known Rosencwaig – Gersho theory [4].

I-01-SL

The TE mechanism can have an important influence on the PA signal, especially at higher frequencies. Jackson and Amer [5] developed a theory of piezoelectric photoacoustic detection by treating the sample as an elastic layer. They solved three-dimensional uncoupled quasi-static thermoelastic equations for elastic stress and strain. Rousset et al. [6] analyzed the effect of thermoelastic expansion and bending on PA signal related to measurements of thermal diffusivity of metals. Rosencwaig et al. [7,8] have developed a noncontact PT technique that can be used at high modulation frequencies and detected local thermoelastic deformations of its surface by a focused probe beam. Rosencwaig et al. [9] and Opsal and Rosencwaig [10] used the same method in an investigation of semiconductors. Perondi and Miranda [11] used the so-called open photoacoustic cell technique to study the effect of TE sample bending in the thermal characterization of solid materials.

The PE effect in semiconductors had been studied previously by, among others, Stearns and Kino [2]. They measured the phase of the photoacoustically generated waves and analyzed the contribution of the PE mechanism to the PA signal in silicon samples. The theory of Stearns and Kino included the electronic component of strain in the stress-strain relation in a manner analogous to elastic wave generation by local periodic thermal expansion. Dersh and Amer [12] measured the surface displacement of Si and a-Si:H samples by use of an interferometric technique. Further, Avanesyan et al [13] and Avanesyan and Gusev [14] have shown that the PE mechanism, related to changes in the equilibrium density of photoexcited electron-hole pairs, can contribute more than the TE mechanism to excited acoustic pulses. Sablikov [15] theoretically investigate photothermal surface dilatation of semiconductors including the electronic deformation mechanism. Prak and Lammerink [16] investigated the effect of electronic strain on a photothermally induced mechanical moment in a silicon microstructure.

The theory of Stearns and Kino [2] included the PE mechanism in the photoacoustic effect. Gusev [17] considered the role of free-carriers in the process of photogeneration of longitudinal acoustic waves in semiconductors. The linear theory of longitudinal acoustic wave generation in the case of interband absorption of optical radiation was given by Gusev and Petrosyan [18].

The theoretical analysis of the plasma, thermal and elastic effects in micromechanical structures consists in modeling a complex system by simultaneous analysis of the plasma and thermal wave equations. In this work the plasma, thermal and elastic waves, i.e. the plasmaelastic and thermoelastic effects in a circular plate and square membrane, photogenerated by an intensity-modulated laser beam, are presented. The theoretical PA signal was compared with experimental measured by using the PA elastic bending method [19-21]. The PA elastic bending method implies the optical generation of elastic bending in the sample and detection of this deformation over PA effect (the gas-microphone detection technique with transmission configuration).

The plasma and thermal waves, i.e. the carrier-density and temperature space and frequency distribution in a rectangular plate (3D geometry), photogenerated by a focused and intensity-modulated laser beam, were analyzed in our previously paper [22]. The detailed analysis and relations for TD, TE and ED components of the PA signal for circular thin plate were given in our previously published papers [1,3,23,24].

Plasmaelastic and Thermoelastic Effects

The theoretical treatment enables quantitative accounts of the carrier density field, $n(\mathbf{r},t)$, the temperature field, $T(\mathbf{r},t)$, and the elastic displacement field, $\mathbf{u}(\mathbf{r},t)$. In the case of periodical excitation, with angular modulating frequency of the incident beam $\omega = 2\pi f$, can be assumed as $n(\mathbf{r},t) = \text{Re}[N(\mathbf{r};\omega)\exp(i\omega t)]$, $T(\mathbf{r},t) = \text{Re}[T(\mathbf{r};\omega)\exp(i\omega t)]$ and $\mathbf{u}(\mathbf{r},t) = \text{Re}[\mathbf{U}(\mathbf{r};\omega)\exp(i\omega t)]$ where $N(\mathbf{r};\omega)$, $T(\mathbf{r};\omega)$ and $\mathbf{U}(\mathbf{r};\omega)$ are complex values which define the amplitude and phase of the carrier-density, temperature and displacement fields, respectively.

The electronic elastic displacement $U^{PE}(\mathbf{r};\omega)$, using the strain-stress relations, can be given vs. the $N(\mathbf{r};\omega)$. Also, the thermal elastic displacement $U^{TE}(\mathbf{r};\omega)$, can be given vs. $T(\mathbf{r};\omega)$. Then, the elastic displacement $\mathbf{U}(\mathbf{r};\omega)$ can be given as the vector sum of two components: $U^{PE}(\mathbf{r};\omega)$ and $U^{TE}(\mathbf{r};\omega)$. In accordance with the elastic theory of thin plate, using the elastic Green function method to solve the elastic equation, $U_z^i(x,y,z;\omega) \approx W_d^i(x,y;\omega)$ ($i = TE, ED$; W_d^i is the dynamic elastic bending of the thin plate) are obtained. Then, the PE and TE component of PA signal for square plate can be given vs. integral relations of $W_d^{PE}(x,y;\omega)$ and $W_d^{TE}(x,y;\omega)$, respectively [22,25].

There are three main mechanisms in thermal wave generation, i.e. there are many thermal sources in semiconductors: the thermalization heat source, $Q^T(\mathbf{r},\omega)$, the bulk recombination source, $Q^{BR}(\mathbf{r},\omega)$ and two different heat sources at the plate surface $z=0$, $Q_1^{SR}(\omega)$ and $Q_2^{SR}(\omega)$ at the plate surfaces $z=L_z$. Then, the periodic temperature distribution, $T(x,y,z;\omega)$ in the plate can be given as a sum of four components: the thermalization, $T^{TZ}(x,y,z;\omega)$, surface recombination $T^{SR1}(x,y,z;\omega)$, $T^{SR2}(x,y,z;\omega)$ and bulk $T^{BR}(x,y,z;\omega)$ components of the temperature distribution, respectively [22].

For uniform optical excitation, if the lateral effects are omitted, it is possible to reduce the problem to one-dimensional, i.e. the carrier-density $N(x,y,z;\omega) \approx N(z;\omega)$ and temperature $T(x,y,z,t) \approx T(z,t)$ distribution in the thin Si plate, were calculated and use as a source term in the elastic bending equation. The carrier-density field $N(z;\omega)$ can be find by solving the appropriate plasma differential equation in the Si plate. In order to find the periodic temperature distributions $T(z;\omega)$, the heat-diffusion equations needed to be solved.

The theoretical model, derived in this work, enables to calculate the PA elastic bending signal (PE, TE, and TD components) and compare with experimental data.

Analysis and Discussion

The PE and TE effects in micromechanical structures were measured by using the PA elastic bending method. The PA elastic bending method implies the optical generation of elastic bending in the sample and detection of this deformation over PA effect. The experimental PA elastic bending signals were measured by using specially constructed PA cell [23] (the gas-microphone detection technique with transmission configuration) where the sample is mechanically supported on the edges. In the transmission PA technique, the sample is excited on one side and the PA signal is detected on the other side. The PA cell uses a miniature electrets microphone as an acoustic detector; the sample is mounted directly onto a front surface of microphone, which usually has a circular hole as the sound inlet. It uses the internal microphone air chamber, adjacent to the membrane, as a conventional measuring gas chamber of PA cell. The construction of the PA cell was optimized to get maximum acoustic protection from the surroundings, a good signal/noise ratio and a flat frequency characteristic in the range between 20 and 20000 Hz. These alterations made possible the achievement of high quality PA signals. The sample was mounted in the PA cell between two rigid annular knife-edges, which defined the case of sample mechanical supporting. This is very important for TE and PE components of the PA signal, i.e., for the PA elastic bending signal.

Circular plate The samples were Si circular plate (diameter 10 mm) with different thicknesses ($\sim 380 - 190 \mu\text{m}$). Samples are prepared from 3 inch, $520 \mu\text{m}$ thick, one side polished Si wafers (n-type, $3-5 \Omega\text{cm}$, and $500-1000 \Omega\text{cm}$). The different thicknesses were obtained with mechanical dressing.

Fig. 1 shows typical experimental PA amplitude spectra for the Si circular plate ($378 \mu\text{m}$ thick) and the theoretically calculated components of PA amplitude vs. modulation frequency. It is possible to see that in this case, the TD component is dominant in the frequency range below $\sim 1 \text{ kHz}$; TE component is dominant above $\sim 3 \text{ kHz}$ and PE component; above $\sim 15 \text{ kHz}$.

Contribution of the PE

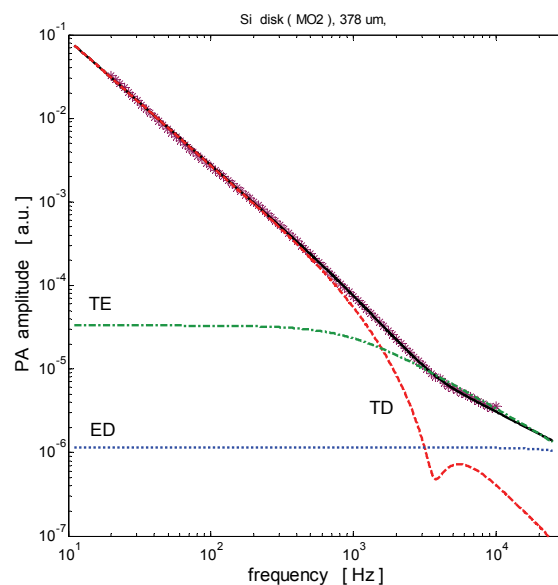


Figure 1. PA amplitude vs modulation frequency for Si circular plate (diameter 10 mm, $378 \mu\text{m}$ thick): (*) experimental; (--) TD component; (-.-) TE; (...) PE; (-) sum (TD + TE + PE).

component (the electronic deformation– ED component) to PA signal can be seen from the previously given results by Todorović et al. [23,24]. The PA signal were measured and theoretically analyzed in the low frequency range ($\sim 60\text{--}4000$ Hz) by using the gas-microphone detection. The analysis showed that, for a typical Si sample, the ED component reaches $\sim 10\%$ of the total PA signal. Then it is possible to see clearly the contribution of the ED component to the normalized PA diagram.

In Fig.2 the PA phase difference of the sum of TD and TE components and the total PA signal (TD+TE+ED) are shown. It can be seen that the ED component significantly changes the slope of the PA phase difference curve for frequencies up to ~ 2 kHz. This shows that the ED component can be detected with a simple detection method at relatively low frequencies as a significant component of the PA signal for semiconductor materials.

Square membrane Si chip with square membranes are prepared from 3 inch, $390\ \mu\text{m}$ thick, double side polished, 3-5 $\Omega\cdot\text{cm}$ n-type Si wafers. Masking material is thermally grown SiO_2 . SiO_2 is grown at $1100\ ^\circ\text{C}$ from oxygen saturated with water vapor. Oxide thickness is about $1\ \mu\text{m}$. Etch square windows ($3200 \times 3200\ \mu\text{m}^2$). Si membranes are fabricated by wet anisotropic bulk micromachining process. Potassium hydroxide (KOH) solution in water is used as etchant of Si. The micromachining is carried out at $80\ ^\circ\text{C}$ using 30 wt% KOH solution. Membrane thickness is function of etching time. After membrane fabrication, and dicing single elements, remaining masking material is completely removed. These PA signals were calculated for Si chip with the square membrane for typical parameters of Si.

Typical experimental amplitude PA elastic bending spectra for different thicknesses of Si square membranes (Si chip, frame 5×5 mm, square membrane 3×3 mm) are given in Fig. 3. Experimental results show that the PA measuring system (PA cell width electrets microphone and lock-in amplifier) has $S/N \sim 20000$ at 100 Hz; ~ 2000 at 1000 Hz; ~ 10 at 10000 Hz and $\sim 1\text{--}2$ at 20000 Hz. It is clear from that analyze that for frequency above 10000 Hz, the PA signal is small and comparable with the noise (coherent electronic noise increase with increasing the

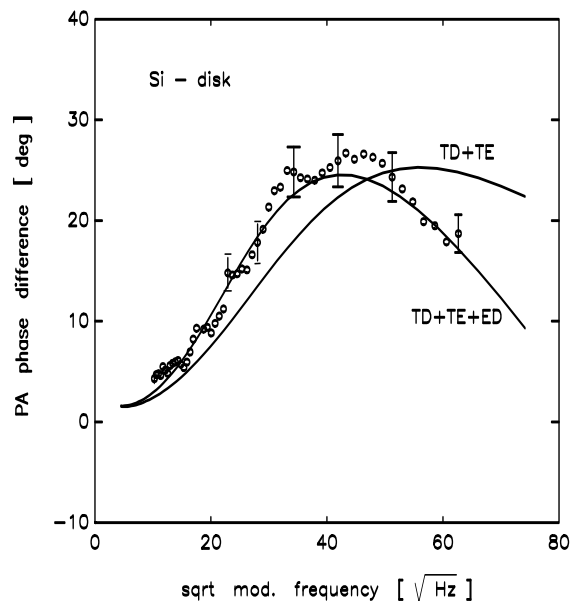


Figure 2. Influence of the ED component to the PA signal of the Si-sample: (o) normalized experimental PA data; (—) TD+TE+ED; (---) TD+TE components.

I-01-SL

frequency; the sensitivity of the acoustic detector, i.e. the electrets microphone decrease in this frequency range).

Then, it is possible to accept the high frequency limit from our PA measuring system at 20000 Hz.

Fig.4 shows a typical example of the PA elastic bending spectra of the square Si membrane with dimensions: $L_x = L_y = L = 2788 \mu\text{m}$ and thickness $L_z = 98.4 \mu\text{m}$. It is possible to see that in the case of square membrane, the TD component is dominant in the frequency range below ~ 10 kHz; TE component is dominant above ~ 20 kHz and PE component; above ~ 40 kHz.

Conclusion

The theoretical model for the frequency distribution of the PA elastic bending signals in a Si chip with square membrane, photogenerated by a uniform and intensity-modulated laser beam was given. The theoretical relations for PA signal, including the plasmaelastic and thermoelastic effects of the elastic bending were derived.

The experimental amplitude and phase were measured vs. frequency by the PA elastic bending method and compare with theoretical ones. These results showed that the PA elastic bending spectra are very

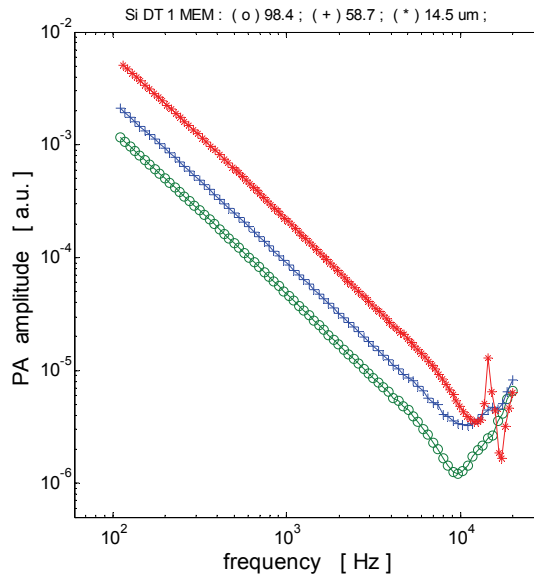


Figure 3. Experimental PA amplitude for different square membranes thicknesses (Si chip, frame 5x5 mm, square membrane 3x3 mm): (o) 98.4 μm ; (+) 58.7 μm ; (*) 14.5 μm ;

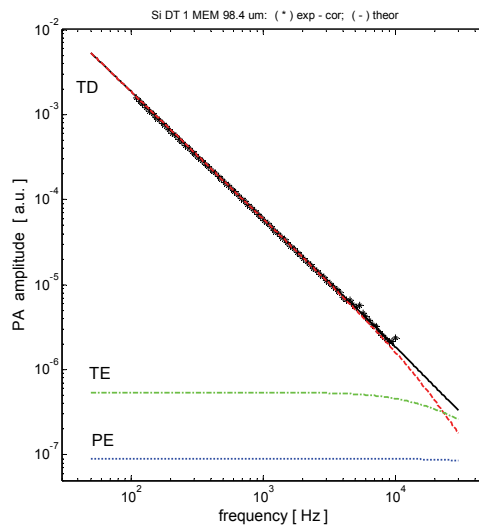


Figure 4. PA amplitude vs. frequency for square membrane (Si chip, frame 5x5 mm, membrane 3x3 mm, 98.4 μm thick): (*) experiment; (- -) TD; (-.-) TE; (...) PE component; (-) TD + TE + PE.

convenient for investigation micro-mechanical structures (the elastic natural modes – spontaneous elastic vibrations). This investigation is in progress. The PA elastic signal is the consequence of PE and TE effects in Si microstructure; these effects may have significant influence at frequencies below ~ 10 kHz.

Acknowledgement

This work was supported by the Serbian Ministry of Education and Science - the projects ON171016 and TR32008.

- [1] D. M. Todorovic, P. M. Nikolic, Ch. 9 in *Semiconductors and Electronic Materials*, A. Mandelis, P. Hess (Eds.), SPIE Opt. Eng. Press, Bellingham, Washington, 2000, 273-318.
- [2] R. G. Stearns, G. S. Kino, *Appl. Phys. Lett.*, 1985, 47, 1048-1050.
- [3] D. M. Todorović, P. M. Nikolić, A. I. Bojčić, K. Radulović, *Phys. Rev. B*, 1997, 55(23), 15631-15642.
- [4] A. Rosencwaig, A. Gersho, *J. Appl. Phys.*, 1976, 47(1), 64
- [5] W. Jackson, N. M. Amer, *J. Appl. Phys.*, 1980, 51(6), 3343.
- [6] G. Rousset, F. Lepoutre, L. Bertrand, *J. Appl. Phys.*, 1983, 54(5), 2383-2391.
- [7] A. Rosencwaig, J. Opsal, D. L. Willenborg, *Appl. Phys. Lett.*, 1983, 43(2), 166-168.
- [8] J. Opsal, A. Rosencwaig, D. L. Willenborg, *Appl. Opt.*, 1983, 22(20), 3169-3176.
- [9] A. Rosencwaig, J. Opsal, W. L. Smith, D. L. Willenborg, *Appl. Phys. Lett.*, 1985, 46(11), 1013-1015.
- [10] J. Opsal, A. Rosencwaig, *Appl. Phys. Lett.*, 1985, 47(5), 498-500.
- [11] L. F. Perondi, L. C. M. Miranda, *J. Appl. Phys.*, 1987, 62(7), 2955-2959.
- [12] H. Dersh, N. M. Amer, *Appl. Phys. Lett.*, 1985, 47(3), 292-294.
- [13] S. M. Avanesyan, V. E. Gusev, N. I. Zheludov, *Appl. Phys. A*, 1986, 40, 163-166.
- [14] S. M. Avanesyan, V. E. Gusev, *Kvant. Elektron. (USSR)*, 1986, 13(6), 1241-1249.
- [15] V. Sablikov, *Soviet. Physics, Semicond.*, 1987, 21(12), 1319-1322.
- [16] A. Prak, T. S. J. Lammerink, *J. Appl. Phys.*, 1992, 71(10), 5242-5245.
- [17] V. E. Gusev, *Akust. Zhurn. (USSR)*, 1986, 32(6), 778-784.
- [18] V. E. Gusev, E. G. Petrosyan, *Akust. Zhurn. (USSR)*, 1987, 33(2), 223-232.
- [19] D. M. Todorović, *Rev. Sci. Instrum.*, vol. 2003, 74 (1), 578-581.
- [20] Y. Song, B. Cretin, D. M. Todorović, P. Vairac, *J. Phys. D: Appl. Phys.*, 2008, 41, 155106.
- [21] D. M. Todorović, B. Cretin, Y. Song, P. Vairac, *J. Appl. Phys.*, 2010, 107, 023516(9p).
- [22] D. M. Todorović, Y. Q. Song, *Journal of Physics: Conference Series*, 2010, 214, 012104.
- [23] D. M. Todorović, P. M. Nikolić, *Opt. Eng.*, 1997, 36(2), 432.
- [24] D. M. Todorović, P. M. Nikolić, A. I. Bojčić, *J. Appl. Phys.*, 1999, 85(11), 7716-7726.
- [25] D. M. Todorović, M. D. Rabasović, D. D. Markushev, V. Jović, K. T. Radulović, *Int J Thermophys*, DOI 10.1007/s10765-012-1242

**MACROMOLECULAR
PHYSICAL CHEMISTRY**

SYNTHESIS OF POLYANILINE-COLLAGEN COMPOSITES BY DOPANT-FREE POLYMERIZATION OF ANILINE IN AQUEOUS SOLUTION

A. A. Rakić^a, V. B. Pavlović^b, G. N. Ćirić-Marjanović^a

^a*Faculty of Physical Chemistry, University of Belgrade, Studentski Trg 12-16, 11158 Belgrade, Serbia*

^b*Institute of Technical Sciences of SASA, Knez Mihailova 35/IV, 11000 Belgrade, Serbia*

Abstract

Polyaniline-collagen (PANI-collagen) composites were synthesized by the oxidation of aniline with ammonium peroxydisulfate (APS) in the presence of collagen in water without added acid. Electrical conductivity of PANI-collagen was in the range $(0.7\text{--}6.8) \times 10^{-3} \text{ S cm}^{-1}$. The increase of initial collagen amount lead to the decrease of aniline polymerization reaction rate. FTIR and Raman spectroscopies are used for resolving molecular structure of composites. The influence of collagen content on the molecular structure, morphology and physico-chemical properties of PANI-collagen composites was investigated.

Introduction

Conducting polymers that inherently conduct electricity, such as polyaniline (PANI), continue to find numerous novel applications in modern technology: rechargeable batteries, fuel and solar cells, antistatic and corrosion protection, sensors, catalysts, actuators, supercapacitors. The preparation of nanostructured conducting polymers and their composites has been the subject of intense research during the recent years owing to their significantly enhanced dispersibility and processibility, and improved performance in many applications in comparison with ordinary granular and colloidal conducting polymers [1]. Biocomposites of conducting polymers and biomacromolecules have received increasing attention during the last decade because of their potential applicability in biosensors, drug delivery, wound dressing, and scaffolds in tissue engineering. Special attention was paid to the biocomposites of PANI because of its tunable conductivity, simple and low-cost synthesis, environmental stability, and unique acid/base doping/dedoping chemistry. Composites of PANI with DNA, RNA, albumin, gelatin, cellulose, starch, chitosan, etc., have been investigated.

Our objective is to synthesize and characterize novel bionanocomposites of PANI and collagen, naturally occurring protein found in animals. The dopant-free template-free falling-pH method of the synthesis of nanostructured PANI [2] has been applied for the preparation of PANI-collagen composites. Characterization of the PANI-collagen samples by conductivity measurements, FTIR spectroscopy and scanning electron microscopy (SEM) has been performed.

Experimental

The aqueous solution (100 ml) of 0.5 M APS was poured into the solution of 0.4 M aniline (100 ml) containing defined amount of collagen, 10 g, 5 g, 1 g, 0.5 g, or 0.1 g. The precipitated product, PANI-collagen composite, was collected on a filter, rinsed, dried in vacuum and characterized by FTIR spectroscopy, SEM and conductivity measurement. As a reference sample, PANI was prepared by the same procedure, without collagen.

Results and Discussion

The temperature profiles for all the PANI-collagen syntheses have similar shape and reveal that the oxidation of aniline with APS in the aqueous solution of aniline and collagen proceeds in two rapid exothermic phases which are well separated by an athermal period (Fig.1, left). The increase of initial collagen mass leads to the significant prolongation of athermal period, i.e. to the delay of subsequent autoacceleration phase of aniline polymerization.

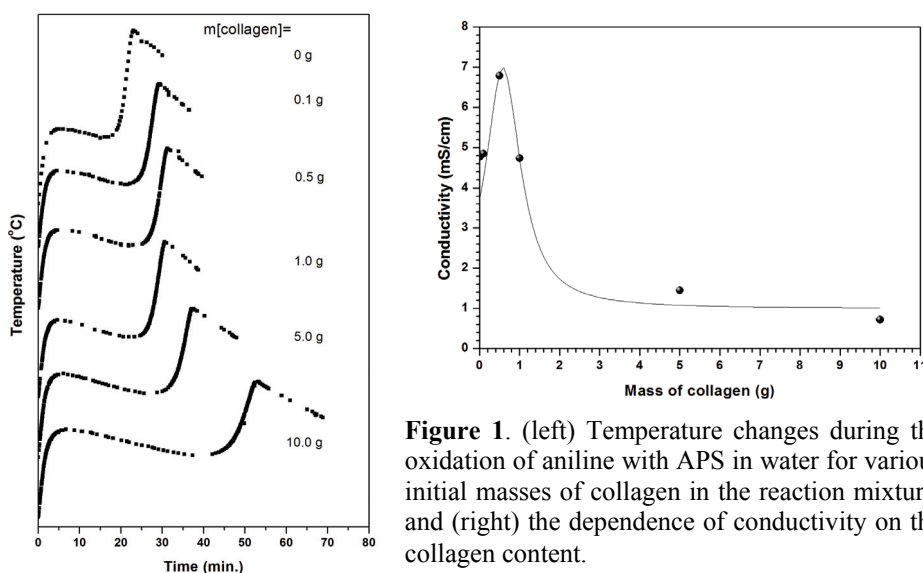


Figure 1. (left) Temperature changes during the oxidation of aniline with APS in water for various initial masses of collagen in the reaction mixture, and (right) the dependence of conductivity on the collagen content.

Electrical conductivity of PANI-collagen composites significantly depends on the content of collagen in the starting reaction mixture (Fig. 1, right). The highest conductivity ($6.8 \times 10^{-3} \text{ S cm}^{-1}$) exhibited the composite which was prepared with 0.5 g of collagen. The significant decrease of conductivity is observed for masses of collagen higher than 0.5 g.

SEM images (Fig. 2.) reveal the heterogeneity in the morphology of PANI-collagen samples. The content of nanorods and nanosheets decreases, while the content of hollow submicrospheres and nanogranules increases, as the initial mass of collagen increases from 0 g to 10 g. FTIR spectra of the PANI-collagen samples are very similar to the spectrum of PANI which was prepared without added collagen (Fig. 3). Characteristic PANI bands are observed at about 1579 cm^{-1} , 518

1497 cm^{-1} , 1300 cm^{-1} , 1242 cm^{-1} , 1146 cm^{-1} and $\sim 824 \text{ cm}^{-1}$ [2]. The band attributable to collagen is observable at $\sim 1660 \text{ cm}^{-1}$ only in the spectra of the composites obtained with 5.0 and 10 g of collagen, and it corresponds to the amide I band (mainly due to the C=O stretching vibration).

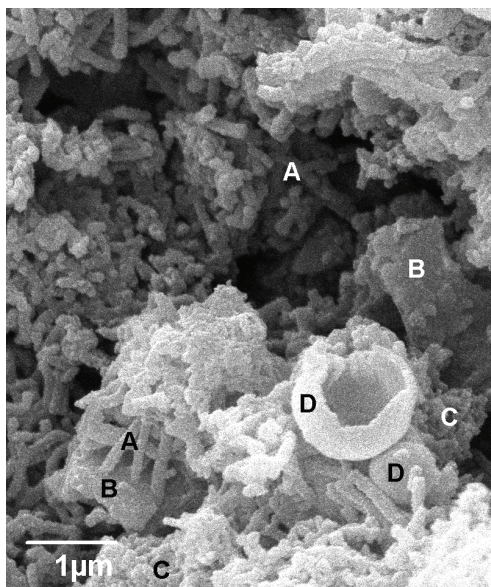


Figure 2. SEM image of the PANI-collagen sample prepared with 1.0 g of collagen: (A) nanorods, (B) nanosheets, (C) nanogranules, (D) hollow submicro- and microspheres.

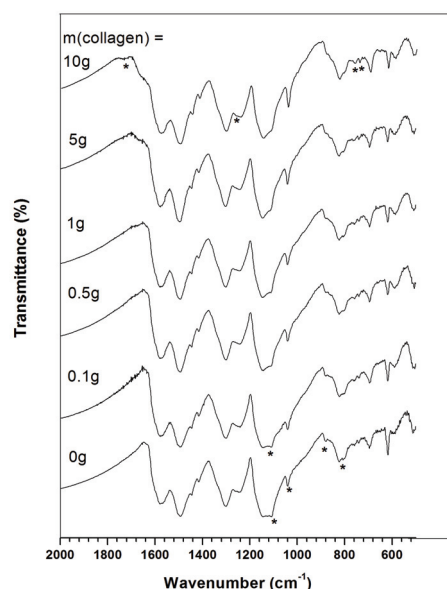


Figure 3. FTIR spectra of PANI-collagen and PANI samples.

Conclusion

Novel semiconducting bionanocomposites of polyaniline and collagen were prepared by the dopant-free template-free falling-pH method. The composites were characterized by various physico-chemical techniques.

Acknowledgement

This work was supported by the Ministry of Education and Science of the Republic of Serbia (projects OI 172043).

References

- [1] G. Ćirić-Marjanović, Polyaniline Nanostructures, Chapter 2, in Nanostructured Conductive Polymers, A. Eftekhari (Ed.), London, John Wiley & Sons, 2010, 19–98.
- [2] A. Rakić, D. Bajuk-Bogdanović, M. Mojović, G. Ćirić-Marjanović, M. Milojević-Rakić, S. Mentus, B. Marjanović, M. Trchová, J. Stejskal, Mater. Chem. Phys., 2011, 127, 501–510.

DOPANT-FREE POLYMERIZATION OF ANILINE IN THE WATER/ISOPROPANOL MIXTURE

A. A. Rakić, G. N. Ćirić-Marjanović
*Faculty of Physical Chemistry, University of Belgrade,
Studentski Trg 12-16, 11158 Belgrade, Serbia*

Abstract

Polyaniline (PANI) was synthesized by the oxidation of aniline with ammonium peroxydisulphate (APS) in the water-isopropanol mixture ($V_{\text{isopropanol}}/V_{\text{water}}=1$). Electrical conductivity of obtained PANI samples ($\sim 2 \times 10^{-6} \text{ S cm}^{-1}$) was more than three magnitude lower compared to PANI ($\sim 5 \times 10^{-3} \text{ S cm}^{-1}$) synthesized in water. FTIR spectroscopy was used for resolving molecular structure, while scanning electron microscopy (SEM) was employed for observing the morphology of synthesised polymerization products. The influence of introduced isopropanol co-solvent and reaction time on molecular structure, morphology and properties of synthesized PANI was studied.

Introduction

The simple and low-cost synthesis, reversible acid/base doping/dedoping chemistry, redox activity, tunable conductivity, and environmental stability ranks PANI high among the most studied conductive polymers. The increased interest has recently been shown for efficient production of PANI nanostructures, such as nanofibers and nanotubes, due to their improved performance in many applications: sensors, catalysis, corrosion protection, data storage, actuators, membranes, solar and fuel cells, rechargeable batteries, and tissue engineering [1]. It has been recognized that the oxidation of aniline with ammonium peroxydisulfate (APS) as an oxidant in aqueous solution, starting at $\text{pH} \geq 3.5$ and finishing at $\text{pH} < 2$ (a falling-pH method), represents an efficient synthetic route to PANI nanostructures, without the use of any external template [2,3].

In order to investigate the impact of the change of solvent polarity on the morphology and physico-chemical characteristics of PANI, we have applied dopant-free template-free falling-pH method for the polymerization of aniline with APS in the mixture of water and isopropanol. Synthesized PANI samples were characterized by FTIR, SEM and conductivity measurements.

Experimental

The oxidation reaction started after pouring an aqueous solution (100 ml) of 0.5 M APS into vigorously stirred 0.4 M aniline solution (100 ml) in isopropanol. After defined time the precipitates were collected on a filter, rinsed, dried in vacuum and characterized by FTIR, SEM and electrical conductivity measurements. The conductivity of the samples pressed into pellets was measured between stainless

pistons, at room temperature, by means of an ac bridge (Wayne Kerr Universal Bridge B 224), at fixed frequency of 1.0 kHz, under pressure of 124 MPA. The samples produced at polymerization times 1.5 h and 24 h are denoted as PANI-IPA-1.5 and PANI-IPA-24, respectively. The referent PANI sample was obtained in water after 0.5 h by the same procedure and under the equivalent experimental conditions as those used for the PANI-IPA syntheses.

Results and Discussion

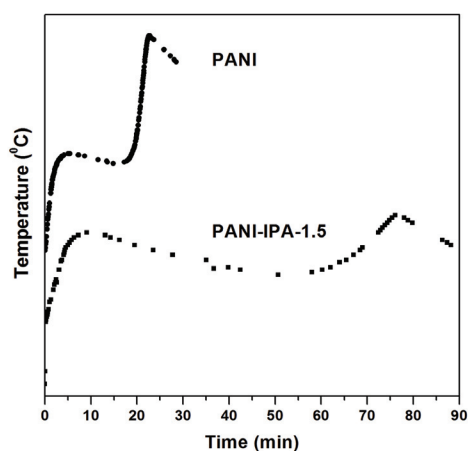


Figure 1. Temperature changes during the oxidation of aniline with APS in water (synthesis of PANI) and in the mixture water-isopropanol (synthesis of PANI-IPA-1.5).

The oxidation of aniline with APS proceeds in two distinct exothermic phases in both syntheses of PANI and PANI-IPA-1.5 (Fig. 1). However, the addition of isopropanol as a co-solvent remarkably slowed the polymerization. In this case the athermal period between two exothermic phases became significantly prolonged (Fig. 1). The introduction of isopropanol into the reaction mixture was accompanied by the decrease of conductivity of polymerization product, from $4.8 \times 10^{-3} \text{ S cm}^{-1}$ for PANI synthesized in water, to $2.1 \times 10^{-6} \text{ S cm}^{-1}$ and $1.5 \times 10^{-6} \text{ S cm}^{-1}$ for PANI-IPA-1.5 and PANI-IPA-24 samples synthesized in water-isopropanol mixture, respectively.

PANI synthesized in water contains nanorods, nanosheets and nanogranules (Fig. 2A). The introduction of isopropanol as a co-solvent into the reaction system leads to the changes in the polymeric product morphology. In the sample PANI-IPA-1.5, nanorods were frequently flattened having the form of nanoribbons, the content of nanosheets was reduced, and some submicrospheres were observed (Fig. 2B). After longer time of synthesis (PANI-IPA-24), majority of nanostructures have been covered with granular PANI (Fig. 2C).

In the FTIR spectra characteristic bands of PANI are observed at about 1579 cm^{-1} , 1493 cm^{-1} , 1300 cm^{-1} , 1242 cm^{-1} , 1146 cm^{-1} and 824 cm^{-1} in all three synthesized samples. Intensity of the band at about 1146 cm^{-1} , which characterizes the conductivity of a sample, decreases in the order: PANI > PANI-IPA-1.5 > PANI-IPA-24. This is in accordance with the results of conductivity measurements. The band at $\sim 756 \text{ cm}^{-1}$, which is indicative for *ortho*-coupling between monomeric units, is relatively much stronger in the spectra of samples synthesized in the presence of isopropanol.

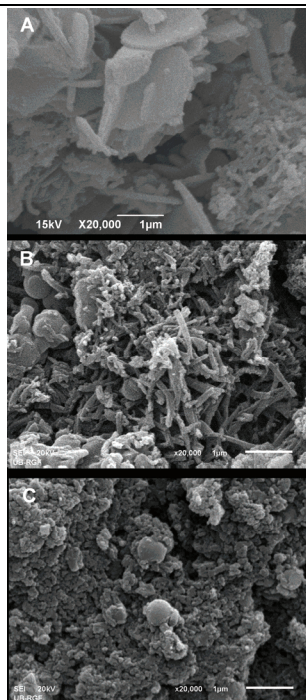


Figure 2. SEM images of: (A) PANI, (B) PANI-IPA-1.5, (C) PANI-IPA-24.

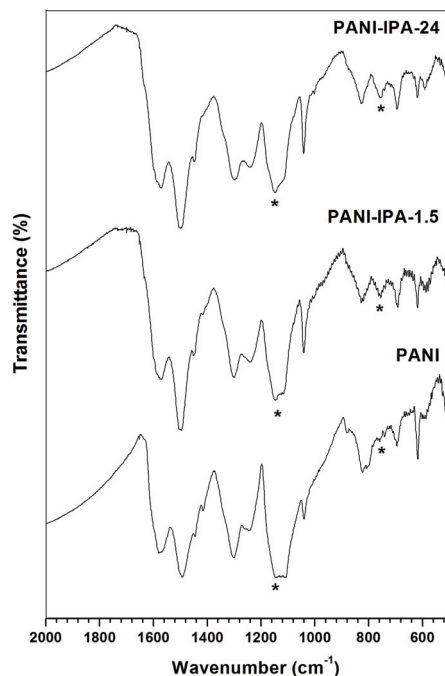


Figure 3. FTIR spectra of PANI and PANI-IPA samples.

Conclusion

Polyaniline synthesized by dopant-free template-free falling-pH method in water/isopropanol mixture had significantly changed physico-chemical properties compared to those of PANI synthesized by the same method in water. Isopropanol slowed down polymerization reaction, remarkably reduced conductivity of PANI and changed its molecular structure and morphology.

Acknowledgement

This work was supported by the Ministry of Education and Science of the Republic of Serbia (project OI 172043).

References

- [1] G. Ćirić-Marjanović, Polyaniline Nanostructures, Chapter 2, in Nanostructured Conductive Polymers, A. Eftekhari (Ed.), London, John Wiley & Sons, 2010, 19–98.
- [2] M. Trchová, E.N. Konyushenko, J. Stejskal, I. Šeděnková, P. Holler and G. Ćirić-Marjanović, *J. Phys. Chem. B.*, 2006, 110, 9461–9468.
- [3] A. Rakić, D. Bajuk-Bogdanović, M. Mojović, G. Ćirić-Marjanović and M. Milojević-Rakić, S. Mentus, B. Marjanović, M. Trchová, J. Stejskal, *Mater. Chem. Phys.*, 2011, 127, 501–510.

POLYANILINE-DECAVANADATE HYBRID NANOMATERIAL: PREPARATION AND CHARACTERIZATION

N. Bošnjaković-Pavlović¹, I. Holclajtner-Antunović¹,
A. Rakić¹, D. Manojlović², G. Ćirić-Marjanović¹

¹*Faculty of Physical Chemistry, University of Belgrade, Studentski Trg 12-16,
11158, Belgrade, Serbia*

²*Faculty of Chemistry, University of Belgrade, Studentski Trg 12-16,
11158, Belgrade, Serbia*

Abstract

Nanostructured polyaniline (PANI) sulfate/hydrogen sulfate was synthesized by the oxidative polymerization of aniline in water, using ammonium peroxydisulfate (APS) as an oxidant. PANI decavanadate (PANI-DV) organic-inorganic hybrid material was then prepared by the treatment of PANI sulfate/hydrogen sulfate with the excess of ammonium decavanadate solution. The incorporation of decavanadate anions into the PANI matrix was confirmed by inductively coupled plasma optical emission (ICP-OES) and FTIR spectroscopies. Scanning electron microscopy (SEM) revealed that the morphology of obtained PANI-DV consisted predominately from nanorods that formed a network. The electrical conductivity of PANI-DV was $4.4 \times 10^{-7} \text{ S cm}^{-1}$.

Introduction

Polyaniline (PANI) is one of the most important conducting polymers, which has extensively been studied because of its simple and cost-effective synthesis by chemical/electrochemical oxidative polymerization of aniline, unique acid/base doping/dedoping chemistry, good electrical conductivity and environmental stability, electroactivity and other properties which enable its versatile applicability. The half-oxidized, protonated, electrically conductive form of PANI (emeraldine salt) contains, depending on synthetic route, various proportions of diamagnetic units $[(-\text{B}-\text{NH}^+=\text{Q}=\text{NH}^+-)_n(-\text{B}-\text{NH}-)_{2n}](\text{A}^-)_{2n}$ and paramagnetic units $[(-\text{B}-\text{NH}^+-\text{B}-\text{NH}-)_n](\text{A}^-)_n$, where B, Q and A^- denote a benzenoid ring, quinonoid ring and dopant anion, respectively. The preparation of PANI nanostructures has been the subject of intense research during the recent years owing to their significantly enhanced dispersibility and processibility, and improved performance in comparison with ordinary granular and colloidal PANI in many applications such as sensors, catalysts, fuel cells, data storage, actuators, membranes, solar cell devices, rechargeable batteries, and electrochemical supercapacitors [1,2].

Polyoxometalates (POMs) are large class of inorganic metal (Mo, V, W)-oxygen macromolecular compounds. The applications of POMs are associated with

their interesting properties: high molecular weight, redox activity, polarity, surface charge distribution, electron and proton transfer/storage ability, and the formation of Brønsted acid centers [3]. They have many potential applications in catalysis, electrochromic devices, energy storage and conversion devices (batteries, supercapacitors, fuel cells), sensors, membranes, and biomedicine [3,4]. The decavanadate anion, $[\text{V}_{10}\text{O}_{28}]^{6-}$, belongs to the group of polyoxovanadates, which are especially interesting because of their biochemical activity. It is known that decavanadate (DV) affects lipid structures, protein function and several biochemical processes. It has been considered as the major protein-binding vanadate species.

To improve the stability, conductivity and catalytic characteristics of POMs, and to make them less dependent on environmental conditions, as well as because many applications of POMs require their use in the form of solid materials or coatings, different procedures for the incorporation of POM into different substrates were developed. Since positive charge of conducting polymer chains may be counterbalanced with negative charge of polyoxoanions, conducting polymers such as PANI provide a suitable network for bulky polyoxoanions incorporation [5]. The purpose of the present work is to prepare and characterize novel nanostructured hybrid material PANI-DV.

Experimental

PANI sulfate/hydrogen sulfate was synthesized by the oxidative polymerization of aniline in water with APS as an oxidant, according to the previously reported procedure [5]. Ammonium decavanadate, $(\text{NH}_4)_6\text{V}_{10}\text{O}_{28}\cdot 5.14 \text{ H}_2\text{O}$ (ADV), was prepared according to the literature method [4]. PANI sulfate/hydrogen sulfate (1.0 g) was treated 40 min with $1.5 \times 10^{-2} \text{ M}$ ADV (80 ml) and then slowly filtered with continuous addition of $1.5 \times 10^{-2} \text{ M}$ ADV (320 ml) as an eluent during 3h. Obtained PANI-DV was dried in vacuum and characterized.

Results and Discussion

Nanorods (possibly nanotubes) predominate in the morphology of PANI-DV, as revealed by SEM (Fig. 1, left). Nanorods have a diameter of 60–90 nm and form a network. The morphology of PANI-DV is not significantly changed in comparison with the morphology of starting PANI sulfate/hydrogen sulfate [5]. The electrical conductivity of PANI-DV was significantly lower ($4.4 \times 10^{-7} \text{ S cm}^{-1}$) than the conductivity of starting PANI sulfate/hydrogen sulfate ($2 \times 10^{-3} \text{ S cm}^{-1}$), indicating that the process of ion exchange (replacement of sulfate/hydrogen sulfate anions with DV anions) was accompanied by partial deprotonation of PANI chains. The elemental composition of PANI-DV shows significantly decreased sulfur content (1.8 wt%) compared with the content of sulfur in PANI precursor (5.86 wt%). This means that sulfate and hydrogen sulfate ions were removed from the polymer matrix during the elution with ADV. ICP-OES analysis revealed that PANI-DV contains 5.2 wt% of vanadium, which corresponds to 9.8 wt% of DV.

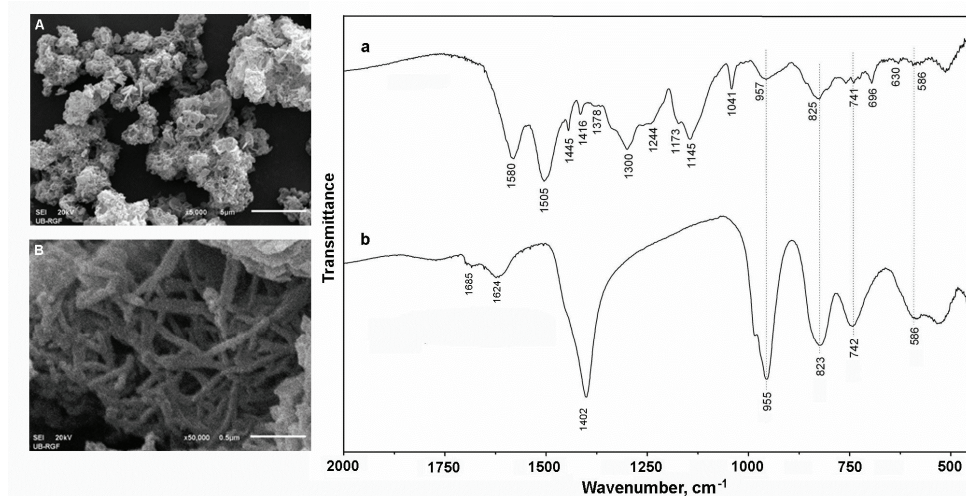


Figure 1. Left: SEM images of PANI-DV at two magnifications: (A) $\times 5000$, (B) $\times 50\,000$. Right: FTIR spectra of PANI-DV (a) and ADV (b).

FTIR spectroscopy confirmed the incorporation of decavanadate ions into the PANI matrix by the characteristic bands of DV ion at 957, 825, 741, and 586 cm^{-1} (Figure 1, right), in the spectrum of PANI-DV. The analysis of bands in the region 2800–3300 cm^{-1} indicates hydrogen bonding interactions between PANI and DV.

Conclusion

Novel nanostructured hybrid material containing DV ions incorporated into the PANI supporting matrix was prepared and characterized by various techniques.

Acknowledgement

This work was supported by the Ministry of Education and Science of the Republic of Serbia (projects OI 172043).

References

- [1] G. Ćirić-Marjanović, Polyaniline Nanostructures, Chapter 2, in Nanostructured Conductive Polymers, A. Eftekhari (Ed.), London, John Wiley & Sons, 2010, 19–98.
- [2] M. Trchová, E.N. Konyushenko, J. Stejskal, I. Šeděnková, P. Holler, G. Ćirić-Marjanović, *J. Phys. Chem. B.*, 2006, 110, 9461–9468.
- [3] U. B. Mioč, M. R. Todorović, M. Davidović, Ph. Colomban, I. Holclajtner-Antunović, *Solid State Ionics*, 2005, 176, 3005–3017.
- [4] M. R. Todorović, U. B. Mioč, I. Holclajtner-Antunović, D. Šegan, *Mater. Sci. Forum*, 2005, 494, 351–356.
- [5] G. Ćirić-Marjanović, I. Holclajtner-Antunović, S. Mentus, D. Bajuk-Bogdanović, D. Ješić, D. Manojlović, S. Trifunović, J. Stejskal, *Synth. Met.*, 2010, 160, 1463–1473.

MICROSTRUCTURAL ORGANIZATION OF POLY(URETHANE-SILOXANE) COPOLYMERS

M. V. Pergal¹, D. Godevac¹, V. V. Antić²,
D. Vasiljević-Radović¹, J. Djonlagić⁴

¹*ICTM-Center of Chemistry, University of Belgrade, Studentski trg 12-16, Belgrade, Serbia,* ²*Faculty of Agriculture, University of Belgrade, Nemanjina 6, Belgrade, Serbia,* ³*Faculty of Technology and Metallurgy, University of Belgrade, Karnegijeva 4, Belgrade, Serbia*

Abstract

The study reports the structure and properties of poly(urethane-siloxane) copolymers, intended to be used as potential biomedical implants. The structural elucidation of poly(urethane-siloxane)s was carried out by ¹H and quantitative ¹³C NMR spectroscopy. The poly(urethane-siloxane) film surface was characterized by AFM and it was found that the surface smoothness increase with increasing soft poly(ϵ -caprolactone)-*b*-poly(dimethylsiloxane)-*b*-poly(ϵ -caprolactone) segment content. The synthesized poly(urethane-siloxane)s were double-crystalline multiblock polymers. Spherulite-like superstructures were observed in copolymers by AFM, which are believed to arise from crystallization of the hard and/or PCL segments, depending on the composition and the length of the hard segments.

Introduction

Thermoplastic polyurethane elastomers (TPUs) are the materials of choice in cardiovascular applications due to their desirable mechanical properties and good blood contacting properties. However, the biostability of TPUs in long-term medical applications remains a concern because many TPU compositions were reported to degrade significantly via hydrolytic and/or oxidative mechanisms. The use of poly(dimethylsiloxane) as the soft segment in biomedical TPUs provide a good alternative to polyester and polyether based TPUs, as these materials exhibit good biocompatibility, biostability, good thermal and oxidative stability, low surface energy, water repellency and physiological inertness. Biocompatibility of TPUs is strongly influenced by the chemical composition, surface hydrophilicity, degree of crystallinity and polymer surface topography [1].

In this work, the influence of the content of soft segments (40-95 wt.%) on the structure, degree of crystallinity and morphology of synthesized TPUs, which are essential for their biocompatibility evaluation, was investigated.

Experimental

Poly(urethane-siloxane) copolymers (TPUs), based on poly(ϵ -caprolactone)-*b*-poly(dimethylsiloxane)-*b*-poly(ϵ -caprolactone) (PCL-PDMS-PCL) as soft segment and 4,4'-methylenediphenyl diisocyanate (MDI) and 1,4-butanediol (BD) as hard segment, was synthesized by two-step solution polyaddition [2].

NMR experiments were performed on Bruker Avance 500 spectrometer. The AFM characterizations were conducted with an AutoProbe CP-Research SPM (TM Microscopes-Veeco) instrument (contact mode). Differential scanning calorimetry (DSC) was done using a DSC Q1000V9.0 Build 275 thermal analyzer.

Results and Discussion

NMR analysis showed that the syntheses of the polyurethanes were successful, resulting in TPUs with different lengths of the hard segments (HS). The synthesized TPUs showed that the average hard segment lengths increased from 1.2 to 14.4 MDI-BD units with increasing hard segment content.

Table 1. The composition of the poly(urethane-siloxane)s, the average length of the hard segments, RMS surface roughness (R_q) and results of DSC (second run).

Polymer	Hard segments, wt. % ^a	L_n (HS) ^b	R_q , nm	T_g , °C	T_{mHS} , °C	T_{mPCL} , °C	X_{cHS} , %	X_{cPCL} , %
TPU-5	4.5	1.2	84	-64	-	49	-	40
TPU-10	11.3	1.7	42	-58	-	47	-	37
TPU-15	13.4	1.9	22	-51	-	46	-	33
TPU-20	16.3	3.8	38	-56	209	45	3	30
TPU-30	26.9	4.0	48	-60	209	45	14	31
TPU-40	36.2	4.7	53	-53	208	44	13	29
TPU-50	47.2	10.2	59	-58	208	44	15	27
TPU-60	62.1	14.4	62	-49	213	36	14	14

^a) Determined by ¹H NMR spectroscopy; ^b) Determined by quantitative ¹³C NMR spectroscopy.

The TPUs were semicrystalline polymers in which both the hard and soft segments participated. Representative DSC curves corresponding to the second heating and cooling of the TPUs are presented in Fig. 1. The results indicated that the glass transition temperature of the PCL segments of the copolymers was in the range from -64 to -49 °C and for the prepolymer was -69 °C.

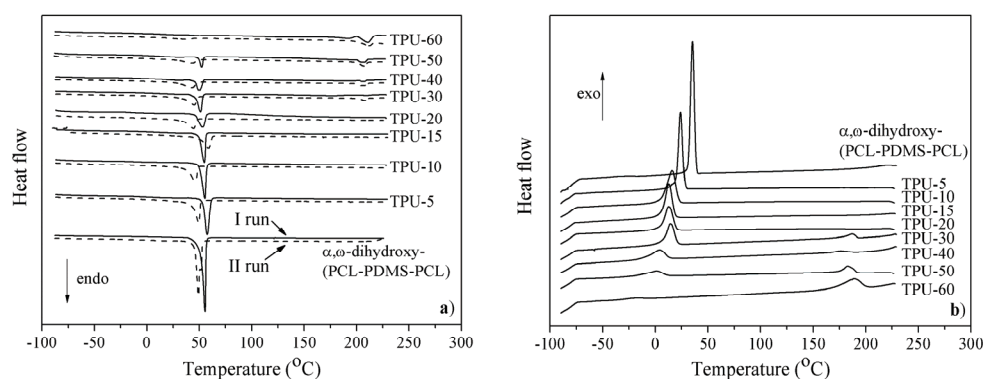


Figure 1. DSC thermograms of TPUs and the α,ω -dihydroxy-(PCL-PDMS-PCL) prepolymer obtained during: (a) heating and (b) cooling run.

The TPUs with HS higher than 20 wt.% showed melting temperature in the range from 208 to 213 °C corresponding to the melting of hard segments. In the thermograms of the TPU samples with a HS content below 20 wt.%, the absence of a melting peak indicates that the HS could not form a crystalline structure, probably because of their short chain length and the lack of their organization. The melting temperatures of PCL-segments in copolymers were decreased from 49 to 36 °C with increasing HS content. The degree of crystallinity of HS, X_{cHS} , tended to increase slightly with increasing content of MDI-BD segments, *i.e.*, HS length. The degree of crystallinity of PCL segments, X_{cPCL} , tended to decrease with increasing HS content, from which it can be concluded that the presence of the hard segments disturbed the crystal growth of the PCL segments.

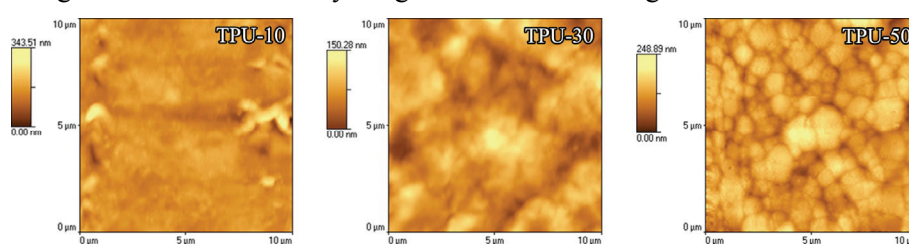


Figure 2. 2D AFM images of selected TPUs (scan area 10 $\mu\text{m} \times 10 \mu\text{m}$).

The surface topography of the TPUs was observed by AFM. The distribution of hard and soft phases of the polymer surface was analyzed by 2D AFM images. It is known that the bright and darker regions represent the crystalline and the amorphous phases. AFM images clearly show that the formation of a spherulitic superstructure was increased on with increasing HS content. The average size of the spherulites was in the range from 1.2 to 1.5 μm . The obtained results showed that the samples with higher R_q values showed rougher copolymer surface.

Conclusions

The TPUs were double-crystalline polymers in which both the hard and soft segments participated. It can be concluded that average lengths from 3.8 to 14.4 MDI-BD units were effective segment lengths for a crystalline HS to be formed. The surface roughness was increased with increasing HS content. AFM images confirmed the presence of a spherulitic morphology, which arises from the crystallization of the PCL segments or/and hard segments depending on HS content.

Acknowledgments

This work was financially supported by the Ministry of Education and Science of the Republic of Serbia (No. 172062).

References

- [1] S. Gogolewski, *Colloid. Polym. Sci.*, 1989, 267, 757-85.
- [2] M. V. Pergal, V. V. Antic, M. N. Govedarica, D. Godjevac, S. Ostojic, J. Djonlagic, *J. Appl. Polym. Sci.*, 2011, 122, 2715-2730.

POLY(URETHANE-SILOXANE) NETWORKS BASED ON HYPERBRANCHED POLYESTER: MECHANICAL AND THERMAL PROPERTIES

M. V. Pergal¹, J. V. Džunuzović¹, R. Poręba², M. Špírková²

¹*ICTM-Center of Chemistry, University of Belgrade, Studentski trg 12-16, 11000 Belgrade, Serbia,* ²*Institute of Macromolecular Chemistry AS CR, v.v.i., Nanostructured Polymers and Composites Department, Heyrovského nam. 2, 16206 Praha 6, Czech Republic*

Abstract

Mechanical and thermal properties, hardness as well as degree of microphase separation of novel poly(urethane-siloxane) networks based on hyperbranched polyester of the fourth pseudo generation were investigated using a variety of experimental methods. According to the combined results obtained from DSC and DMTA experiments, these networks exhibit two glass transition temperatures, of the soft and hard segments, and one secondary relaxation process. The results showed increase of crosslinking density and microphase separation and improvement of mechanical properties with decreasing content of soft ethylene oxide-poly(dimethylsiloxane)-ethylene oxide segment.

Introduction

Polyurethanes (PUs) are considered as one of the most useful class of polymers in coating applications. Contrary to other polymers, PUs have the advantage of using many available reactants as well as superior elastomeric properties. The careful design of PU structure is crucial to obtain good mechanical properties and adhesive strength of the coatings [1]. Macrodiol can play an important role to improve these properties. Poly(dimethylsiloxane) (PDMS) is attractive due to several advantages such as low surface tension, unique flexibility, low glass transition temperature, high thermal stability and good water resistivity. In the last few years, the PDMS has been used in PUs synthesis to improve the properties such as thermal stability, adhesive strength, shape memory properties and water resistance. Recently PU with PDMS has been proposed as a component of marine coating due to its smooth surface, to protect the coating from the fouler attachment. Due to the low surface energy of the PDMS, the PU coating is enriched by Si and makes the surface very smooth. The use of hyperbranched polyester (HBP) as crosslinker for the synthesis of PUs based on PDMS leads to the formation of networks with good chemical resistance and thermal properties [2].

In this work, mechanical and thermal properties, as well as hardness of PU networks based on aliphatic Boltorn[®] hyperbranched polyester of the fourth pseudo generation were investigated using DSC, DMTA, and hardness measurements.

Experimental

The PU networks were synthesized by two-step polymerization in solution (NMP/THF) using α,ω -dihydroxy-(ethylene oxide-poly(dimethylsiloxane)-ethylene oxide) (EO-PDMS-EO, ABCR), 4,4'-methylenediphenyl diisocyanate (MDI, Aldrich) and hyperbranched aliphatic polyester of the fourth pseudo generation with average hydroxyl functionality of 23 (BH-40, Perstorp Specialty Chemicals AB) [2]. The soft EO-PDMS-EO content was varied from 15 to 40 wt.%. In samples with digit numbers, the number shows the EO-PDMS-EO weight content.

Dynamic mechanical thermal analysis (DMTA) of samples was carried out on ARES G2 Rheometer (TA Instruments) in the temperature range from -135 to 180 °C, at strain 0.1 %. Differential scanning calorimetry (DSC) was performed on DSC Q1000V9.0 Build 275 thermal analyzer in the temperature range from -90 to 200 °C, at a heating rate of 10 °C/min. The hardness measurements of the PU films were performed on a Shore A apparatus (Hildebrand, Germany).

Results and Discussion

The influence of soft segment content on the viscoelastic properties of the polyurethane networks was investigated by dynamic mechanical thermal analysis of selected samples. Three peaks can be observed in the temperature dependence of G'' (Fig. 1), indicating existence of microphase separation of PUs.

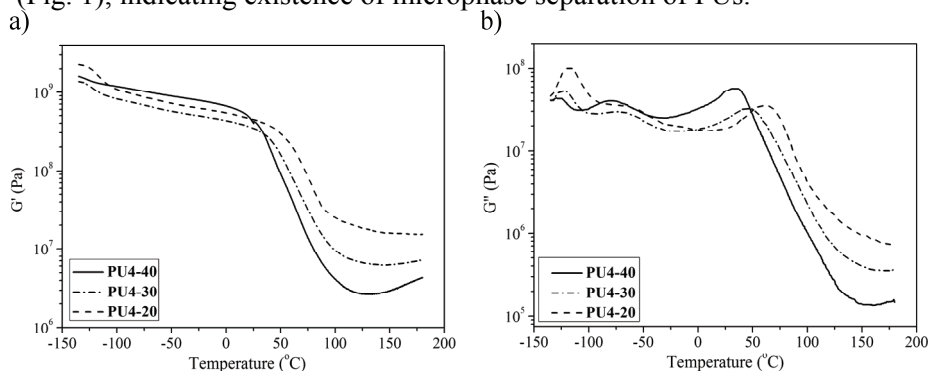


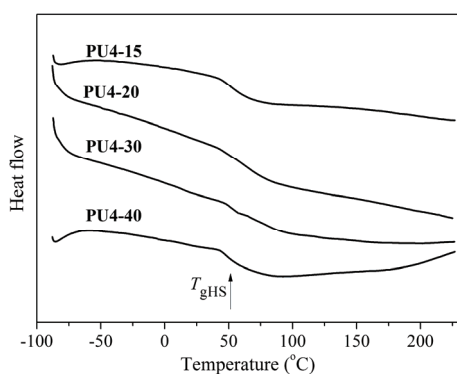
Figure 1. Storage (G') and loss (G'') moduli of the PUs vs. temperature at 1 Hz and a heating rate of 3 °C/min.

From the Fig. 1 it can be observed that all investigated PUs show T_g of the soft EO-PDMS-EO segment, T_{gSS} , in the temperature range between -126 and -118 °C, due to the well phase separation of PDMS. Peak observed in the region between -80 and -67 °C is associated with the subglass relaxation process and is probably a consequence of the movement of the part of the chain which contains urethane groups connected to the Boltorn[®] HBP (BH-40). The third peak detected in the region between 35 and 61 °C is ascribed to the glass transition temperature of the hard segments (MDI-HBP), T_{gHS} , (Table 1). From DMTA results, value of G' for PU samples is higher than values of the loss modulus in the whole investigated temperature region. This observation indicates that cohesion and stability of the PU network is not destroyed under investigated experimental conditions.

Table 1. Results of DSC, DMTA and hardness of PU networks

Sample	G''			$\nu \times 10^4$ (mol/cm ³)	T_{gHS} (DSC) (°C)	Hardness (Shore A)
	T_{gSS} (°C)	T_2 (°C)	T_{gHS} (°C)			
PU4-40	-126	-80	35	9.08	49	94
PU4-30	-124	-72	47	18.48	54	96
PU4-20	-118	-67	61	44.40	56	98

Values of the crosslinking density, ν can be easily calculated from the rubbery plateau moduli and are summarized in Table 1. Crosslinking density of the synthesized PUs decreases with increasing soft EO-PDMS-EO content. The increase of the crosslinking density increased hardness of PUs from 94 to 98 Shore A (Table 1), which is in agreement with DMTA results.

**Figure 2.** DSC thermograms (second run) of the selected synthesized PUs.

Thermal properties of the synthesized PUs were also examined by DSC (Fig. 2). A T_g of synthesized PUs decreases with increasing EO-PDMS-EO content from 56 to 49 °C (Table 1). Higher T_g of PUs is attributed to increased hydrogen bonding and crosslinking density of samples.

Conclusions

DMTA results revealed existence of microphase separation of PUs due to presence of EO-PDMS-EO. Two thermal transitions were detected by DMTA and they depend on the soft segment content. The first one (at -126 to -118 °C), corresponds to the glass transition of soft segments. The second transition, located at 35 to 61 °C, well detectable by DSC and DMTA, corresponds to the glass transition of hard segments. The second relaxation peak is located in the temperature region -80 to -67 °C. The results showed that the decrease of EO-PDMS-EO content enhanced microphase separation, improved mechanical properties and hardness of PUs.

Acknowledgments

This work was financially supported by the Ministry of Education and Science of the Republic of Serbia (No. 172062) and the Grant Agency of the Czech Republic (No. P108/10/0195).

References

- [3] E. Žagar, M. Žigon, Prog. Polym. Sci, 2011, 39, 53-88.
- [4] M. V. Pergal, J. V. Džunuzović, M. Kićanović, V. Vodnik, M. M. Pergal, S. Jovanović, Russ. J. Phys. Chem. A, 2011, 85, 2251-2256.

J-06-P

POLY(URETHANE-ESTER-SILOXANE) NETWORKS

J. V. Džunuzović¹, M. V. Pergal¹, V. V. Vodnik²

¹*ICTM-Center of Chemistry, University of Belgrade, Studentski trg 12-16, 11000
Belgrade, Serbia*

²*Institute of Nuclear Science "Vinča", University of Belgrade, P. O. Box 522,
11001 Belgrade, Serbia*

Abstract

The waterproof performance and formation of hydrogen bonds in polyurethane (PU) networks based on Boltorn[®] hyperbranched polyester of the third pseudo generation (BH-30), α,ω -dihydroxy-(ethylene oxide-poly(dimethylsiloxane)-ethylene oxide) (EO-PDMS-EO) and 4,4'-methylenediphenyl diisocyanate (MDI) were studied in this work. Obtained results revealed that as the content of EO-PDMS-EO decreases, the degree of microphase separation increases, while the water resistance of the prepared PU networks decreases.

Introduction

The application of hyperbranched polyesters (HBP) or PDMS macrodiols for the preparation of polyurethanes has gained great attention over the last years, since these polymers have properties which can be applied to improve and modify performances of PUs for specific applications [1,2]. Besides, it has been shown that the combination of both, PDMS macrodiol and HBP, can also be used for the synthesis of PU networks [3]. Such networks are good candidates for coating applications, because numerous end functional groups in HBP provide fast curing and formation of highly crosslinked system with good mechanical properties, while the presence of PDMS improves thermal and surface properties and brings elasticity in such material, due to its low glass transition temperature. The aim of the present work is the investigation of the influence of EO-PDMS-EO content on the water resistance and the extent of hydrogen bonding in the polyurethane networks synthesized using Boltorn[®] hyperbranched polyester of the third pseudo generation, EO-PDMS-EO and MDI.

Experimental

PUs based on BH-30, EO-PDMS-EO and MDI were synthesized according to the procedure described elsewhere [3]. The last two numbers in the name of PUs represent EO-PDMS-EO content. FTIR spectra of the synthesized PUs were recorded using ATR NICOLET 380 FTIR spectrometer. Water absorption of the synthesized PUs was determined at room temperature by their immersion for 48 h in distilled water. The water contact angles of the synthesized PUs were determined on Krüss DSA100 instrument, using the sessile drop method, at 22 °C.

Results and Discussion

The chemical structure of PUs was examined by FTIR spectroscopy. In the FTIR spectra of PUs (Figure 1a) absorption bands characteristic for the amide II and

amide III vibrations (1258 cm^{-1} and 1537 cm^{-1}), overlapped bands of Si-O-Si and C-O-C groups (1015 and 1080 cm^{-1}), Si-CH₃ linkage (790 cm^{-1}), symmetric and asymmetric -CH₂- and -CH₃ (2961 , 2903 and 2875 cm^{-1}), aromatic C=C (1596 and 1412 cm^{-1}) and H-bonded -NH stretching vibration (3306 cm^{-1}) are visible. The formation of urethane bonds was confirmed from the absence of isocyanate peak at 2260 cm^{-1} .

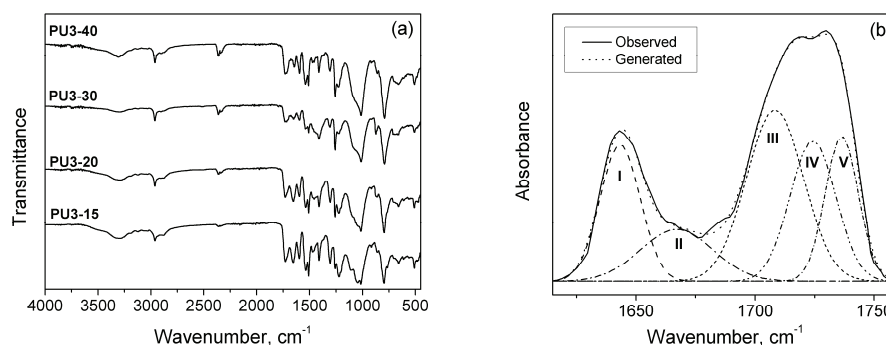


Figure 1. (a) FTIR spectra of PUs and (b) curve-fitting FTIR spectra of PU3-40.

Table 1. Curve fitting results of the C=O stretching regions from the PUs FTIR spectra.

Sample	Area I (CO _{ester-H} bonding) ₂ %	Area II (CO _{order urethane-H} bonding) ₂ %	Area III (CO _{disorder urethane-H} bonding) ₂ %	Area IV (CO _{free} ester) ₂ %	Area V (CO _{free} urethane) ₂ %
PU3-40	16.7	14.2	31.3	22.3	15.5
PU3-30	19.7	17.2	25.9	22.2	15.0
PU3-20	21.5	38.4	10.1	16.8	13.2

To investigate the extent of hydrogen bonding in the synthesized PUs and to obtain individual spectral bands and areas in the overlapping spectra of C=O region, the Gaussian deconvolution method (OriginPro 8) was applied. The absorbance region of the C=O groups of PU3-40 is given in Figure 1b, while curve fitting results for selected PUs are listed in Table 1. Five absorbance peaks were observed in the C=O region corresponding to the: H-bonded C=O groups from ester bonds (1645 cm^{-1}), H-bonded urethane C=O groups in ordered hard domains (1680 cm^{-1}), H-bonded urethane C=O groups in disordered domains (1710 cm^{-1}), free C=O groups from ester bonds (1725 cm^{-1}) and free urethane C=O groups (1735 cm^{-1}) [4]. As the content of EO-PDMS-EO decreases, the possibility for H-bonding between urethane groups and H-bonding between urethane and ester carbonyl groups generally increases, while the fraction of H-bonding between -NH urethane and ether oxygen from EO-PDMS-EO, free ester and free urethane C=O decreases. It can be concluded that ordering of the hard segment domains, i.e. the tendency of H-bonds formation between hard segments is more pronounced in samples with lower EO-PDMS-EO content, resulting in higher degree of microphase separation.

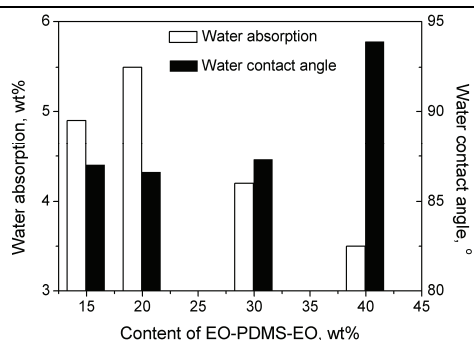


Figure 2. Values of the water absorption and water contact angles of the PU networks.

The waterproof performance of the PU networks was investigated by measuring their water absorption and water contact angle and obtained results are given in Figure 2. The weight percent of the water absorption decreases while the water contact angle increases as the EO-PDMS-EO content increases, due to the hydrophobic character of PDMS and possible migration of the EO-PDMS-EO to the surface of PUs.

Conclusions

The presented results revealed that the tendency of H-bonds formation between hard segments in prepared PU networks decreases with increasing EO-PDMS-EO content. The increase of EO-PDMS-EO content also induced better water resistance of PUs.

Acknowledgments

This work was financially supported by the Ministry of Education and Science of the Republic of Serbia (Project No. 172062).

References

- [1] P. K. Maji, A. K. Bhowmick, *J. Polym. Sci. Part A Polym. Chem.*, 2009, 47, 731-745.
- [2] R. Hernandez, J. Weksler, A. Padsalgikar, J. Runt, *Macromolecules*, 2007, 40, 5441-5449.
- [3] J. V. Džunuzović, M. V. Pergal, S. Jovanović, V. V. Vodnik, *Hem. Ind.*, 2011, 65, 634-644.
- [4] Z. S. Petrović, J. Ferguson, *Prog. Polym. Sci.*, 1991, 16, 695-836.

MICROWAVE SYNTHESIS OF NEW STAR SHAPED POLYESTER POLYOLS BASED ON L-LACTIDE

I. S. Ristić¹, M. Marinović-Cincović², B. Pilić¹, V. Simendić¹, S. Cakić³

¹ *University of Novi Sad, Faculty of Technology, Bulevar cara Lazara 1, Serbia*

² *University of Belgrade, Vinča Institute of Nuclear Sciences, Serbia*

³ *University of Nis, Faculty of Technology, Bulevar oslobođenja 124, Serbia*

Abstract

The molecular architecture of biodegradable polymers can be adjusted by incorporating multifunctional polyols into the polyester backbone to obtain branched polymers. The aim of our work was to prepare biodegradable polyester polyols based on L-lactide and castor oil in presence of tin(II) 2-ethylhexanoate as catalyst in microwave field. The polyester polyol was synthesized by core-first method which involves a polymerization of L-lactide from OH groups on castor oil. FTIR and ¹H NMR spectroscopy measurements were used to confirm the molecular structure of the synthesized products. DSC measurements were used to evaluate the crystallinity of obtained polyols. Thermal stability was investigated by thermogravimetric analysis, and results have shown the dependence of thermal stability on the arm length of the star shaped polyesters.

Introduction

Biodegradable polymers are useful materials for medical and pharmaceutical applications. They have a hydrophobic backbone with hydrolysable anhydride and/or ester bonds that may hydrolyze to monomers in an appropriate medium. Fatty acids are considered as suitable candidates for the preparation of biodegradable polymers, because they are natural body components. Manipulation of mechanical and physical characteristics of these polymers can be achieved by variation of polymer architectures. Star-shaped polymers consist of at least three linear polymeric chains radiating from one single multifunctional branched point [1]. The main feature of star-shaped polymers, make them different from the linear analogues of identical molar masses, is their compact structure and the multiple functionality. Final properties of the resulting star-shaped polymers may be adjusted by choosing the respective chemical structure of an arm and core, depending on the required application [2]. The aim of this work was the synthesis of star-shaped polyester polyol based on L-lactide arms and castor oil as core.

Experimental

Materials

Monomer (3S)-cis-3,6-dimethyl-1,4-dioxane-2,5-dione (L-Lactide), 98% (purity) was purchased from Sigma-Aldrich, Wisconsin. Initiator castor oil (CO) having the hydroxy number (OH_#) 170 mg KOH/g and acid value 1.27 mg KOH/g was

supplied from Merck Chemical Co. Catalyst tin(II) 2-ethylhexanoate (purity of 95%, density 1.251 g cm^{-3} at $25 \text{ }^\circ\text{C}$) was supplied from Sigma-Aldrich.

Microwave synthesis of polyester polyol

Microwave polymerization of L-lactide initiated by castor oil was performed according to our previous work [3]. This involves the addition of the dry monomer and castor oil in the glass ampoule, followed by the addition of tin(II) 2-ethylhexanoate. Very short polymerization times were 10, 20 and 30 minutes and carried out in microwave reactor.

Characterisation of prepared samples

The characterization of molecular structure of obtained materials was carried out by FTIR Bomem Hartmann & Braun MB-series, in the band ranged from 400 to 4000 cm^{-1} . ^1H NMR spectra were recorded on Bruker DPX-300 NMR (300 MHz). Samples were dissolved in deuterated chloroform and chemical shifts are given in δ from Me_4Si as an internal standard. Thermal properties of the samples were investigated by differential scanning calorimetry (DSC) using Setaram 151R instrument (heating rate $10 \text{ }^\circ\text{C min}^{-1}$) and thermogravimetric analysis (TGA) on Setaram Setsys Evolution-1750 instrument in nitrogen atmosphere (heating rate $20 \text{ }^\circ\text{C min}^{-1}$).

Result and Discussion

In the FTIR spectrum of polyester asymmetrical valence vibrations of C-O-C of the aliphatic polylactide chains were shifted at 1187 cm^{-1} , and symmetrical valence vibrations of C-O-C of the aliphatic chain at 1090 cm^{-1} , compared with bands at 1276 and 1099 cm^{-1} , which appeared in monomer L-lactide. Bands at 1455 and 1383 cm^{-1} originated from asymmetric and symmetric bending vibration of C-H from CH_3 , respectively. Band from valence vibration of C=O of aliphatic ester splits at two bands, at 1758 cm^{-1} (in poly(L-lactide) chains), and at 1745 cm^{-1} (in castor oil). In the ^1H NMR spectrum peak H1 originated from proton of terminal methyl group in ricinoleic acid (in castor oil), Figure 1.

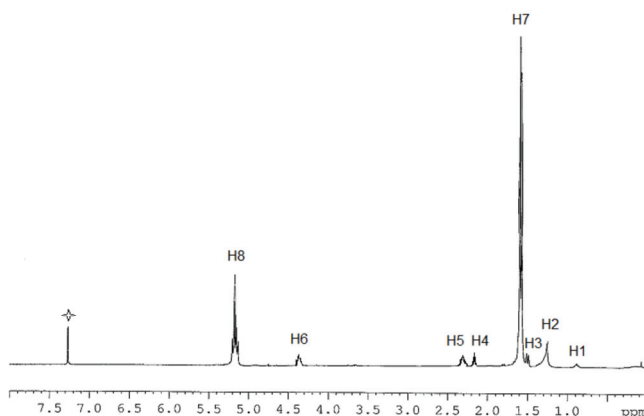


Figure 1. ^1H NMR spectrum of obtained polyester polyol.

Peak H2 ascribed protons in methine groups from C4-C7 and C14-C17 in ricinoleic acid. When lactide polymerisation starts (from castor oil hydroxyl

groups) the peak related methylene proton attached to hydroxyl group ($CH-OH$) at 3.61 ppm [4] nearly disappeared, while a new peak at 4.32 ppm appeared, which represented the methylene protons connected to poly(L-lactide) chains. Peaks H3 and H5, due to chemical bonding between polylactide chains and castor oil, were shifted from 1.4 ppm and 2.21 ppm in crude castor oil [4] to 1.48 ppm and 2.42 ppm in polyester polyol. Peaks at 1.57 and 5.13 ppm (H7 and H8) were assignable to methyl and methine proton originated from lactic acid in main chain. Peak which noted with * originated from solvent.

The results of thermal property investigation were summarized in Table 1. For all synthesized samples was observed crystallization and melting from poly(L-lactide) arms. As expected melting temperature of samples increased as molecular masses of poly(L-lactide) arms increase. For star-shaped polyesters with the different arm length which was denoted by the molar mass of samples, the TGA curves show degradation temperature higher than 295 °C. Longer arms actually mean the higher molar mass of samples which can effectively enhance thermal stability.

Table 1. The DSC and TG data of different polyester polyol samples.

Sample name	T _g (°C)	T _c (°C)	T _m (°C)	T _{dec} (°C)
PE-ol-3000	45.5	86.4	130	295
PE-ol-4000	44.2	82.1	130.8	300
PE-ol-5000	43.8	91	133.2	324
PE-ol-6000	40.6	83.3	134.6	330

Conclusions

Star-shaped polyester polyol was obtained by polymerization of L-lactide, using, as an initiator, castor oil. Used polymerization method can be a fundamental technique for producing a low-melting polyol derived from renewable resources. FTIR and ¹H NMR spectroscopy confirmed presumed structures of obtained star shaped polymers. The polyester polyol has low crystallinity and a low melting point, so that its working properties is good when used in various medical and pharmaceutical applications. The investigation of thermal degradation by TGA method indicated that the novel star-shaped polyesters with higher molar masses have enhanced thermal stability.

Acknowledgment

This paper was supported by Ministry of Education and Science-Republic of Serbia, project number III 45022.

References

- [1] S. Bywater, *Adv. Polym. Sci.*, 1979, 30, 89–116.
- [2] P. F. Rempp, P. J. Lutz, *Polymeric materials encyclopedia*, vol. 10. Boca Raton: CRC Press, 1996, 7880–7885.
- [3] Lj. Nikolic, I. Ristic, B. Adnadjevic, V. Nikolic, J. Jovanovic, M. Stankovic, *Sensors*, 2010, 10, 5063-5073.
- [4] E. Mistri, S. Routh, D. Ray, S. Sahoo, M. Misra, *Ind. Crop. Prod.*, 2011, 34, 900–906.

J-08-P

THE EFFECT OF IONIC CONTENT ON THE THERMAL PROPERTIES OF ANIONIC POLYURETHANE DISPERSIONS

S. Cakić¹, I. S. Ristić², D. T. Stojiljković², J. Budinski-Simendić²

¹ *University of Niš, Faculty of Technology, Bulevar oslobodjenja 124, Serbia*

² *University of Novi Sad, Faculty of Technology, Bulevar cara Lazara 1, Serbia*

Abstract

The thermal stabilities of waterborne polyurethane dispersions have been correlated with content of ionic groups by changing the amount of dimethylol propionic acid (4.5, 7.5 and 10 wt% to the prepolymer weight). Three water-based polyurethane dispersions were synthesized by modified dispersing procedure using polycarbonate diol, isophorone diisocyanate, dimethylol propionic acid, triethylamine and ethylenediamine. The effect of the dimethylol propionic acid content on the thermal properties of polyurethane films was measured by TGA and DSC methods. The physico-mechanical properties, such as hardness, adhesion test and gloss of the dried films were also determined considering the effect of dimethylol propionic acid content on coating properties.

Introduction

Water-based polyurethane dispersion (PUD) show very good mechanical and chemical properties and match the regulatory pressures for low volatile organic compound (VOC) emission. Polycarbonate diols used as the soft segment component in polyurethane synthesis are usually produced from dimethylcarbonate or ethylene carbonate and a linear aliphatic diol [1]. The properties of polyurethane dispersions are related to their chemical structure and they are mainly determined by the interaction between the hard and soft segments and/or between the ionic groups.

In the present study, water-based polyurethane dispersions, with different molar ratio of polycarbonate diol (PCD) to dimethylol propionic acid (DMPA), were prepared by the modified dispersing process. The aim was the investigation of PUDs' structure-thermal properties relationships. The effect of molar ratio of polycarbonate diol to DMPA on the thermal properties of the polyurethane dispersions was investigated.

Experimental

Materials

Polycarbonate diol T5652 with a molecular weight of 2000 (hydroxyl value 56.3 mg KOH/g) was kindly provided by Asahi Kasei Corporation. Isophorone diisocyanate (IPDI) and DMPA were supplied by Aldrich. Ethylenediamine (EDA) was obtained from Zorka, Serbia; 1-methyl-2-pyrrolidone (NMP), dimethyl

formamide (DMF) and triethylamine (TEA) were received from Merk-Schuchardt. The dibutyltin dilaurate used as catalyst was supplied by Bayer AG.

Synthesis of the waterborne polyurethane dispersions

Three waterborne polyurethane dispersions were prepared using NCO/OH = 1.5 by method in which the dispersing procedure was modified. In the modified procedure only the dispersing stage was varied compared to the standard procedure. The prepolymer solution was mixed with a small amount of deionized water for dispersion of polymer in water. Solvent was added to reducing the viscosity, if necessary. The DMPA content was 4.5, 7.5 and 10 wt. % (with respect to the prepolymer weight), in order to change the ionic-group content in the polyurethane ionomers. The formulations used in the preparation of the polyurethane dispersions are summarized in Table 1.

Table 1. The compositions of synthesized polyurethane dispersions.

Sample	IPDI (g)	PCD (g)	DMPA (g)	TEA (g)	EDA (g)	Water (g)	DMPA/PCD (mol/mol)	TRS (%)
PUD 1	20	60	4 (4.5) ^a	3	0.9	204	1.0	30.1
PUD 2	32	60	8 (7.5)	6	1.8	251	2.0	30.0
PUD 3	40	60	12 (10)	9	1.8	280	3.0	30.3

^a Percentage of DMPA content based on prepolymer weight

Characterization of obtained samples

Polyurethane films were prepared by casting the aqueous dispersions on leveled glass surfaces and dried at room temperature for 7 days, and then at 60 °C for 12h. Thermogravimetric analyses (TGA) were performed on the Setaram Setsys Evolution-1750 instrument. Samples were heated from 30 °C to 600 °C at the heating rate of 20 °C min⁻¹ in nitrogen atmosphere with the gas flow rate of 20 cm³ min⁻¹. Differential scanning calorimetry (DSC) was performed on Setaram 151R instrument. The non-isothermal measurement was scanned from -60 to 150 °C with heating rate 5 °C min⁻¹.

Results and discussion

The thermal stability of the polyurethanes was determined by TGA, Figure 1a.

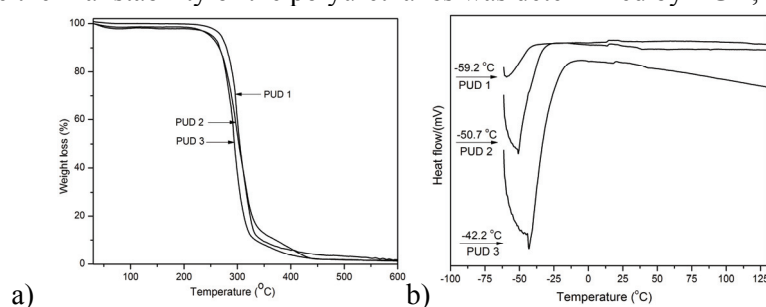


Figure 1. Thermal properties of cured films of PUD 1, PUD 2 and PUD 3
a) TG curves and b) DSC curves.

According to TGA results the decreasing of DMPA content results in slight increase of the decomposition temperature.

The DSC thermograms (Figure 1b) showed only one glass transition temperature. The T_g value of the polyurethane ionomer increases by increasing DMPA content. As expected, increasing DMPA content i.e., hard segment, leads to an increase in the glass transition temperatures of the polyurethane ionomer due to restriction of the soft segment motions by the hard segments [2].

In Table 2 physical and mechanical properties of coating are given. It can be observed from presented results that sample with the highest ionic groups content, PUD 3 exhibits better hardness properties than samples PUD 1 and PUD 2.

Table 2. Physical and mechanical properties of polyurethane films.

Sample	Hardness (s)	Gloss (%)	Adhesion
PUD 1	32.2	147.6	5B
PUD 2	51.0	122.7	5B
PUD 3	67.9	121.7	5B

This is in agreement with previous conclusion that an increase in the ionic groups as hard segment content increased the extent of crosslinking of the polyurethanes. The gloss of the polyurethanes decreases by increasing the DMPA content.

Conclusions

The thermal stability of the polyurethane ionomer was increased by decreasing the DMPA content due to the lower hard segment content. The glass transition temperatures of the polyurethane ionomer was increased by increasing DMPA content, due to restriction of the soft segment motions caused by the hard segments. The increasing of the DMPA content i.e. hard segment caused the increasing of König hardness of the coatings, whereas the gloss of the coatings decreased.

Acknowledgment

This paper was supported by Ministry of Education and Science-Republic of Serbia, project number III 45022 and TR 33034.

References

- [1] E. Foy, J.B. Farrell, C.L. Higginbotham, *J. Appl. Polym. Sci.*, 2009, 111, 217–227.
- [2] V. G-Pacios, V. Costa, M. Colera, J.M. M-Martinez, *Int. J. Adhes. Adhes.*, 2010, 30, 456–465.

CHARACTERISATION OF EXOPOLYSACCHARIDE PRODUCED BY BACILLUS SP. NS032

J. Stefanović¹, D. Ilić², B. Kekez², G. Gojgić-Cvijović¹, D. Jakovljević¹, M. Vrvic^{1,2}

¹*ICH_{TM} - Department of Chemistry, University of Belgrade, Njegoševa 12, P.O. Box 473, 11000 Belgrade, Serbia (jovana_stefanovic@chem.bg.ac.rs)*

²*Faculty of Chemistry, University of Belgrade, Studentski trg 12-16, P.O. Box 51, 11158 Belgrade, Serbia*

Abstract

In this study, the main structural monomer units and configuration of their glycosidic linkages of a exopolysaccharide obtained from a strain of *Bacillus licheniformis* was investigated. The chemical structure of this polymer, after purification of crude material, was analyzed by chemical methods, planar chromatography, elemental analysis and FTIR.

Introduction

Microbial exopolysaccharides are the group of biopolymers whose structural chemistry is very complex. Usually some types of microorganisms can be characterized by the presence of several carbohydrate polymers. The economic significance of these compounds is related to the fact that some of these polymers is nowadays widely accepted products of biotechnology, while others are in various stages of research. The use of microbial polymers varies widely due to good mechanical properties for application as fiber, films, adhesives, rheology modifiers, hydrogels, emulsifiers, and drug delivery agents. Biopolymers with industrial application are often bacterial and fungal products, like levan, dextran, β -glucan, pullulan. In this work we reported a route to produce of purified exopolysaccharide produced by strain of *Bacillus licheniformis*, and determination of main structural characteristics of this polymer.

Experimental

Exopolysaccharide was produced by strain of *Bacillus licheniformis* which was isolated from petroleum sludge sample taken from Oil Refinery Novi Sad. The strain was identified using 16S rRNA gene sequence analysis [1]. The organism was cultivated in sucrose broth for 10 days at 28 oC [2]. After removal of biomass the crude polysaccharide was isolated from fermentation culture by precipitation with two volumes of ethanol.

Polymer was analyzed for its carbon, hydrogen and nitrogen content using the Vario EL III device (GmbH Hanau Instruments, Germany). Nitrogen content usually was indication for the presence of protein as impurities. After treatments with Dnase, Rnase and Pronase and dialysis, purified polysaccharide was precipitated by acetone and lyophilized. In this way was obtained purified polysaccharide, without nitrogen, with content of C and H that corresponded to polysaccharide molecules (Table 1.). Monomer components was determined by planar chromatography of the acid hydrolyzate of the glycan. The ATR-IR spectrum of pure polysaccharide was obtained

using Thermo Nicolet 6700 FT-IR Spectrophotometer with Smart Orbit Diamond ATR (attenuated total reflectance) accessory.

Results and Discussion

Planar chromatography of the hydrolyzed crude polysaccharide, comparing with standards of authentic monosaccharides, showed two main components, fructose and glucose, in about equal proportions. After further treatments, in hydrolysate of purified polymer was detected only one component, D-Fructose, which indicated that investigated polymer is fructan. Additional evidence that purification of polysaccharide was successful was found in the results of elemental analysis of crude and purified polymer (Table 1). The FT-IR spectrum of the purified polysaccharide showed the spectral pattern typical for polysaccharides. As shown in Fig.1, absorption bands between 1128 cm^{-1} and 1014 cm^{-1} corresponded to C-O-C and C-O-H stretching vibrations [3], the bands in the range of $1200\text{-}1500\text{ cm}^{-1}$ ascribed to C-H deformation vibration, the band at 1645 cm^{-1} was due to bound water. Strong, wide band at $3000\text{-}3500\text{ cm}^{-1}$ and band at 2936 cm^{-1} was assigned to the hydroxyl groups stretching vibration of polysaccharide and C-H stretching [4]. Absorption band in the anomeric region ($950\text{-}700\text{ cm}^{-1}$) at 891 cm^{-1} is specific for the β -configuration of the glycosidic linkages. Based on the FT-IR spectra it was concluded that investigated polymer had β -configuration of glycosidic linkages.

Table 1. Elemental chemical composition.

	% N	% C	% H
Crude sample	7.44	30.58	5.13
Purified sample	/	44.42	6.20

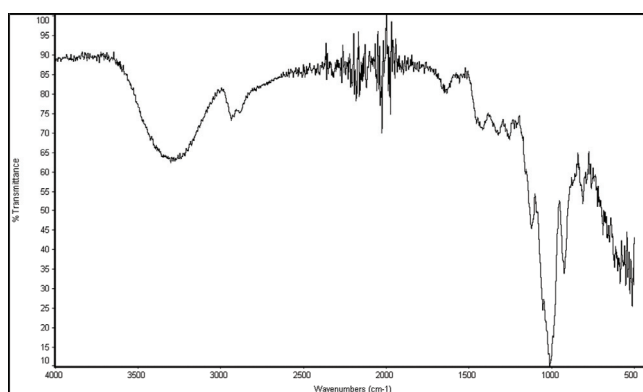


Figure 1. FTIR spectrum of purified exopolysaccharide produced by *B. licheniformis*.

Conclusion

The present study showed, on the basis of chemical methods, planar chromatography, elemental analysis and FTIR, that investigated exopolysaccharide is homopolymer,

composed of a D-fructose, as the O-specific monomer, with β -configuration of the glycosidic linkages.

Acknowledgement. This work was supported by the Ministry of Education and Science of the Republic of Serbia through Project III 43004.

References

- [1] G. D. Gojgic-Cvijovic, J. S. Milic, T. M. Solevic, V. P. Beskoski, M. V. Ilic, L. S. Djokic, T. M. Narancic, M. M. Vrvic, *Biodegradation*, 2012, 23, 1-14.
- [2]. [J. Liu](#), [J. Luo](#), [Y. Sun](#), [H. Ye](#), [Z. Lu](#), [X. Zeng](#), *Biores. Technol.*, 2010, 101, 6077-6083.
- [3] M. Wu, Y. Wu, J. Zhou, Y. Pan, *Food Chemistry*, 2009, 113, 1020–1024.
- [4] M. Mathlouthi, J. L. Koenig, *Adv. Carbohydr. Chem. Biochem.*, 1987, 44, 7–89.

SYNTHESIS OF GUM ARABIC-NATAMYCIN CONJUGATE

J. R. Stefanović¹, D. M. Jakovljević¹, G. Đ. Gojgić-Cvijović¹, M. M. Vrvic²

¹*IchTM - Department of Chemistry, University of Belgrade, Njegoševa 12, P.O. Box 473, 11000 Belgrade, Serbia (jovana_stefanovic@chem.bg.ac.rs)*

²*Faculty of Chemistry, University of Belgrade, Studentski trg 12-16, P.O. Box 51, 11158 Belgrade, Serbia*

Abstract

In this work, natamycin, a polyene antibiotic belonging to the family of macrolides, was coupled to the periodate oxidized polysaccharide gum Arabic. Resulting conjugate was characterized by UV-Vis and FT-IR data.

Introduction

Natamycin (pimaricin) is a polyene macrolide antibiotic produced during fermentation by *Streptomyces natalensis*. This antibiotic (Fig.1.) Has been used for many years in the food industry as well as in veterinary medicine, but insolubility in water limits its wider use. Gum Arabic is a water soluble, highly branched complex polysaccharide, comprised mostly of galactose, arabinose, rhamnose, and glucuronic acid. This polymer is used in many fields due to non-toxicity, water solubility, and biocompatibility. In order to increase solubility of natamycin, coupling of periodate oxidized polysaccharide gum Arabic and antibiotic was performed. Resulting conjugate was characterized by UV-Vis and FT-IR data. Obtained conjugate was soluble in water.

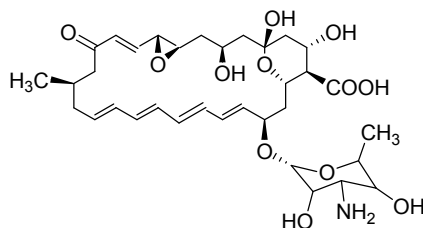


Figure 1. Structure of natamycin.

Experimental

Oxidation of gum Arabic to polyaldehyde derivative was done with sodium periodate in aqueous solution at 20 °C. Excess periodate was removed from reaction mixture by dialysis and oxidized polymer was lyophilized. Aldehyde groups in polysaccharide were determined by titration with standardized iodine solution [1]. In these conditions, sample of 50% oxidized gum Arabic was obtained. Coupling reaction between oxidized gum Arabic and natamycin was done in borate buffer (pH 9,1) in the dark, with continuous stirring, at 40 °C, during 48 h. Resulting conjugate was purified by dialysis and lyophilized.

Results and discussion

Synthesis of gum Arabic-natamycin conjugates was achieved by coupling reaction between aldehyde groups of oxidized polysaccharide and amine groups of antibiotic. Coupling reaction was monitored by UV-Vis (GBC Cintra 40 spectrophotometer) and IR (Nicolet 6700, in ATR mode) spectroscopy, by comparing spectra of oxidized polysaccharide and synthesized conjugate. UV spectra of native and oxidized gum Arabic do not have absorption in UV-Vis range (Fig.2a). After coupling reaction, spectrum of synthesized conjugate was significantly different (Fig.2b), with absorptions (λ_{\max} 294, 309, and 324 nm) slightly shifted in relation to natamycin [2]. Based on this, it can be concluded that aldehyde groups introduced in gum Arabic molecule are successfully coupled with antibiotic.

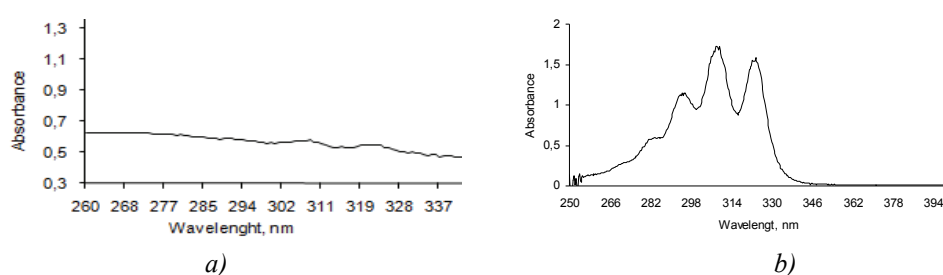


Figure 2. UV spectra of oxidized gum Arabic (a) and gum-arabic-natamycin conjugate (b).

FT-IR data suggest the chemical bonding between oxidized gum Arabic and natamycin, too. FT-IR spectrum of oxidized glycan (Fig. 3a) showed a strong band in the 3000–3500 cm^{-1} region from OH stretching, band at 2800–3000 cm^{-1} correlated to CH_2 stretching, stronger band at 1642 cm^{-1} and the weak band at about 1400 cm^{-1} corresponded to COO-asymmetric and COO-symmetric stretching, respectively. The characteristic bands of dialdehyde glycan at 1730 cm^{-1} and 880 cm^{-1} correlated to the aldehyde symmetric ($\text{C}=\text{O}$), and the hemiacetal, respectively [3]. FT-IR spectrum of the pure natamycin showed bands at 3277 cm^{-1} ($-\text{NH}_2$ deformation), 1715 cm^{-1} ($-\text{C}=\text{O}$ vibration), 1695 cm^{-1} (ester function), 1577 cm^{-1} ($\text{CH}=\text{CH}$ stretch), 1266 cm^{-1} ($\text{C}-\text{O}-\text{C}$ epoxy), 1142 cm^{-1} ($=\text{C}-\text{O}-\text{C}=\text{O}$ vibration). FT-IR spectrum of conjugate (Fig.3b) showed absorption bands characteristic for both, gum Arabic and antibiotic.

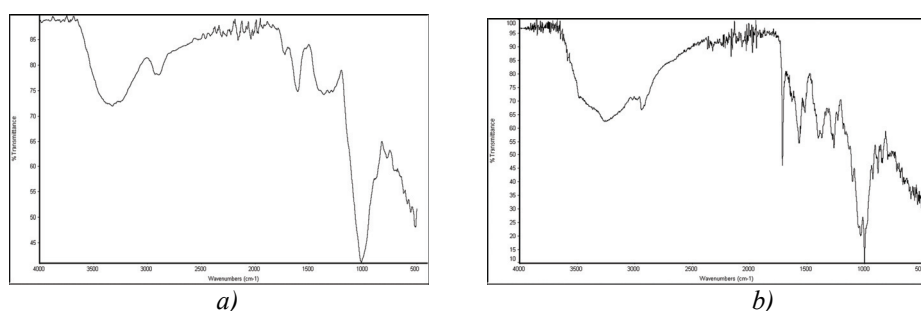


Figure 3. FT-IR spectra of oxidized gum Arabic (a) and gum Arabic-natamycin conjugates (b).

Conclusion

The synthesis of gum Arabic-natamycin conjugate was achieved by covalent coupling between oxidized polysaccharide and antibiotic. Conjugate was characterized by UV-Vis and FT-IR data. Significantly increasing the solubility in water of obtained product can be indication for potential new uses in various pharmacological applications.

Acknowledgement. This work was supported by the Ministry of Education and Science of the Republic of Serbia through Project III 43004.

References

- [1] G. Dryhurst, Periodate Oxidation of Diol and Other Functional Groups, Pergamon Press, London, 1966, 116.
- [2] K.Dornberger, D. Voigt, W. Ihn, J. Vokoun, H. Thrum, Tetrahedron, 1976, 32, 3069-3073.
- [3] U. J. Kim, S. Kuga, M. Wada, T. Okano, T. Kondo, Biomacromolecules 2000, 1, 488-492.

**CELLULOSE ORIENTATION AND PURITY
ASSESSMENT AFTER TWO DIFFERENT PROCEDURES
OF CELL WALL ISOLATION FROM MAIZE STEMS. A
COMBINED MICROSCOPIC FLUORESCENCE
DETECTED LINEAR DICHROISM AND IMAGE
ANALYSIS STUDY**

D. Djikanovic Golubovic¹, A. Savic¹, J. Simonovic¹, G. Steinbach², M. Jeremic³, G. Garab², K. Radotic¹

*1. Institute for Multidisciplinary Research, University of Belgrade, Kneza
Viseslava 1, Belgrade, Serbia*

*2. Institute of Plant Biology, Biological Research Center, Hungarian Academy of
Sciences, H-6701 Szeged, Hungary*

*3. Faculty of Physical Chemistry, University of Belgrade, Studentski Trg 12, 11000
Belgrade, Serbia*

Abstract

The effects on cellulose orientation and purity of two different methods for cell wall isolation from maize stems were investigated by using fluorescence-detected linear dichroism (FDLD) microscopy technique. Image analysis has shown that treatment with sulfuric acid have provided better results than previously applied method for cell wall isolation including enzymatic treatment.

Introduction

One of the most promising new sources for biofuel is "cellulosic ethanol", made from the cellulose contained in fibrous plant material such as cornstalks, grasses and forest trimmings. Maize is nowadays very important plant source for bioethanol. The main problem in obtaining pure cellulose is impossibility to separate it completely from lignin, due to very strong connection between these two polymers in the cell wall.

Linear dichroism (LD) of cell walls carries important information on their molecular organization. We measured LD of of the maize stem cell walls by differential polarization fluorescence imaging [1]. The samples were isolated by two different procedures. The cell wall fragments were stained by Congo Red which predominantly binds to cellulose, a major cell wall component that determines its anisotropy. By monitoring FDLD of the cell walls after various treatments, we could trace the degree of cellulose purity in the intermediate steps during cell wall isolation. FDLD image analysis show different degrees of anisotropy and purity of cellulose contained in the cell

wall. The structural changes were in parallel followed by using FTIR spectroscopy.

Material and methods

Cell walls were isolated from maize stem and purified according to a procedure of Chen *et al.* [2]. Other way of isolation of cell wall is with sulphuric acid [3] and then we treated sample with high pressure and strong mechanical force in FastPrep-24.

The samples were stained with Congo Red, which has been shown to intercalate into the cellulose matrix [4]. Samples were incubated for 2 h in 1 % (w/v) solution of Congo Red (Fluka) at room temperature.

Cell wall samples were measured in the differential polarization laser scanning microscope (DP-LSM) (Carl Zeiss Jena, Jena, Germany).

Results and discussion

During the imaging process, FDL image and fluorescence emission image were stored as two separate channels. Sample was imaged by changing the focal planes with fixed increment. Sets of images were stacked in order to examine 3D structure of samples. As the basis for the surface rendering, fluorescence emission channel was used, while FDL channel was used for object extraction based on threshold level settings.

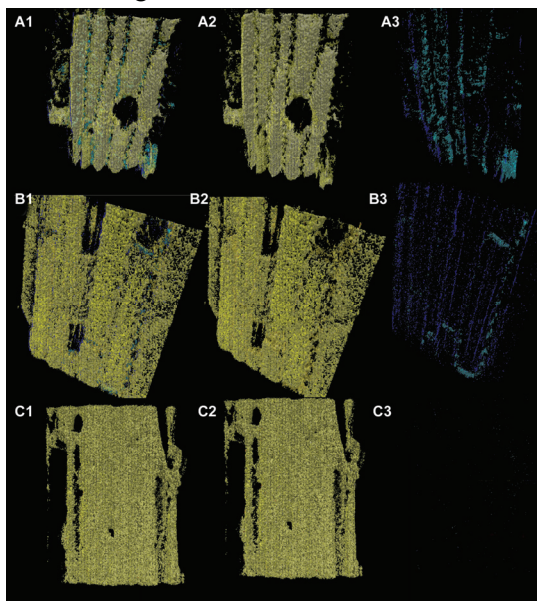


Figure 1. Rendered 3D images from the stacks of fluorescence emission images and FDL images. Color scale: dark blue, 0° polarization, gray, 45° polarization, yellow 90° polarization. 1, all objects presented, 2, extracted objects polarized from 45°-90°, 3, extracted objects polarized from 0°-45° A) untreated cell wall, B) plants treated with cellulase pectinase, C) plants treated with sulphuric acid

The most important aim of the method was to examine if different structures have manifested the same or different FDL values. The color bar scale of FDL intensity was set from dark blue for the 0° orientation, followed by gray for 45° orientation, and finishing as yellow for 90° orientation. For 3D image rendering software 3D Doctor was used.

Conclusion

Comparing the two cell wall isolation procedures, we obtained better results of cellulose purity for the maize stem treatment with acid. With this procedure horizontal elements in fiber structure were absent (Fig 1C3), which indicates that in

this case cellulose is more purified, i.e. more appropriate, for further procedure of ethanol production. In the process where the cell wall was treated with cellulase and pectinase, partially present horizontal structure remained.

These results are consistent with the changes in characteristic bands of cellulose and lignin in FTIR spectra of isolated cell walls in both procedures.

This procedure may be used for application in biofuels industry, in order to facilitate obtaining ethanol from cellulose fibers, which is the subject of our interest.

Acknowledgements

This work was supported by the grants No 45012 and No 173017 of the Ministry of education and science of the Republic of Serbia, as well as by the bilateral Hungary-Serbia project “Structural anisotropy of the plant cell walls of various origin and their constituent polymers, using DP-LSM“, in 2010-2012.

References

- [1] G. Steinbach, I. Pomozi, O. Zsiros, A. Pay, G. V. Horvath, G. Garab, *Cytometry Part A*, 2008, 73A, 202-208.
- [2] M. Chen, A. Sommer, J. W. McClure, *J. Phytochem. Anal.*, 2000, 11, 153–159.
- [3] S. V. Pingali et al, *Biomacromolecules*, 2010, 11, 2329–2335.
- [4] J. P. Verbelen, S. J Kerstens *Microsc* 2000, 198, 101–107.

J-12-P

POLY(NiPAAm-co-IA) HYDROGELS SYNTHESIZED BY γ -IRRADIATION: SWELLING BEHAVIOR IN WATER

J. Spasojević¹, J. Krstić¹, A. Radosavljević¹,
M.a Kalagasidis-Krušić², Z. Kačarević-Popović¹

¹*Vinča Institute of Nuclear Sciences, University of Belgrade, P.O. Box 522, 11001 Belgrade, Serbia (jelenas@vinca.rs), ²Faculty of Technology and Metallurgy, University of Belgrade, P.O. Box 3503, 11120 Belgrade, Serbia*

Abstract

In this study, N-isopropylacrylamide/itaconic acid copolymeric (poly(NiPAAm-co-IA)) hydrogels were synthesized by γ -irradiation induced simultaneous polymerization and crosslinking of monomers. The influence of comonomer concentration (IA) on the swelling behavior in water was investigated. The results showed that values of network parameters increase with an increase of IA, and that the swelling transport mechanism is a non-Fickian transport.

Introduction

Hydrogels are a class of polymeric materials which have been utilized in a wide range of application due to easily adjustable properties. Stimuli-sensitive, also called intelligent polymers, change their structure and physico-chemical properties in response to physical or chemical stimuli. These smart polymers have a vast potential for applications in pharmaceutical technology, biotechnology industry, and in solving environmental problems. Among them, temperature- and pH-sensitive polymers are the most frequently studied [1].

PolyNiPAAm is the best-known temperature-sensitive polymer that attracts huge interest in biomedical applications due to well-defined lower critical solution temperature (LCST) in water around 32 °C, which is close to the body temperature. The temperature-sensitive networks containing ionizable functional groups exhibit pH-sensitivity. With the increase of ionizable groups, the volume change at the transition increases because of increasing electrostatic interaction between the same charged groups and the transition temperature rises. In recent years, a series of papers has been published about hydrogels from the copolymers of acrylamide and diprotic itaconic acid (IA) and maleic acid (MA), and showed that the use of even very small quantities of diprotic acid proved to impart remarkable properties to the hydrogels of starting monomers and/or homopolymers [2].

γ -irradiation induced synthesis has been recognized as highly suitable tool for crosslinking of polymeric hydrogels. This method is relatively simple and do not require addition of any extra materials such as initiator and/or crosslinker. Moreover, the degree of crosslinking, which strongly determines the extent of swelling in hydrogels, can be controlled easily by varying the irradiation dose. Therefore, γ -irradiation is found to be very useful in preparing hydrogels for medical applications, where even a small contamination is undesirable [1-3].

The aim of this work was to synthesized polyNiPAAm and poly(NiPAAm-co-IA) hydrogels by γ -irradiation induced simultaneous polymerization and crosslinking, and to investigate the influence of IA concentration on network parameters and swelling behavior in water, as well as to determine diffusion properties of hydrogels.

Experimental

The NiPAAm monomer was used as a base monomer in the synthesis of hydrogels, while the IA was used as comonomer. Solution of NiPAAm (10 wt.%) was prepared in distilled water. Different amounts of IA were added to 5 ml of NiPAAm solution in order to obtain NiPAAm/IA mass ratios 100/0, 98.5/1.5, 97/3 and 95.5/4.5. Monomer solutions were bubbled with argon for 20 min, to remove oxygen, and exposed to γ -irradiation (^{60}Co source) up to absorbed dose of 50 kGy, at a dose rate of 0.6 kGy/h. The obtained hydrogels were immersed in an excess of deionized water, which is changed every day during one week, to remove uncrosslinked polymer and/or residual monomers, and dried at room temperature. Dynamic swelling measurement was performed in deionized water at 25 ± 1 °C, using dry gels (xerogels). The swelling process was monitored gravimetrically.

Results and Discussion

When a xerogel is brought into contact with a solution, the solution diffuses into the network and volume phase transition occurs, resulting in the expansion of the hydrogel. Diffusion involves the migration of fluid into pre-existing or dynamically formed spaces between the hydrogel chains. The capacity of swelling is one of the most important parameters for evaluation the properties of hydrogels. As can be seen from Table 1, the characteristic parameters obtained from swelling measurement in water of an ionic hydrogel strongly depend on the concentration of ionizable groups in network. The results showed that the equilibrium swelling degree (SD_{eq}) of poly(NiPAAm-co-IA) hydrogels increase as the comonomer concentration increases because of increasing the electrostatic interactions of the neighboring carboxylate groups in IA in the hydrogels [4]. Moreover, the values of network parameters, average molar mass between the network crosslinks (M_c) and distance between the macromolecular chains ie. pore size (ξ), also increase with increasing amount of IA, whereas the xerogel densities decrease.

Table 1. Characteristic parameters obtained from swelling measurement in water at 25 °C. (S0) - (S3) are symbols of the synthesized hydrogels.

<i>poly</i> (NiPAAm/IA)	SD_{eq}	M_c (g/mol)	ξ (nm)	ρ_{xg} (g/cm ³)	k (l/min)	n	$D \times 10^5$ (cm ² /min)
100/0 (S0)	9.2	627	3.7	0.91	0.024	0.52	0.23
98.5/1.5 (S1)	29.1	2905	10.9	0.80	0.014	0.64	1.14
97/3 (S2)	37.1	4041	13.8	0.79	0.013	0.65	1.21
95.5/4.5 (S3)	52.6	7034	20.4	0.78	0.012	0.66	1.28

To obtain a more quantitative understanding of the nature of the sorption kinetic in poly(NiPAAm-co-IA) hydrogels, the initial swelling data were fitted to

equation $M_t/M_{eq} = k t^n$, where M_t is the amount of absorbed water in time t , M_{eq} is the maximum absorbed amount, k is a constant incorporating characteristics of macromolecular network system and the penetrant, n is the diffusion exponent, which is indicative of the transport mechanism. This equation is valid for initial stage of swelling i.e. for the first 60 % of the normalized solvent uptake. The characteristic constants n and k were calculated from the slope and intercept, respectively, of the linear parts of logarithmic form of kinetic equation of swelling. The obtained results are presented in Table 1, and indicated that hydrogel systems show non-Fickian or anomalous diffusion ($0.5 < n < 1$) when the rates of diffusion and polymer chain relaxation are comparable [5].

The study of diffusion phenomena of water in hydrogels is important because that clarifies the polymers behavior. For hydrogel characterization, the diffusion coefficients (D) can be calculated by using the equation $D^n = (k/4) (\pi/r^2)$, where r is the radius of gel disc. The D values are also presented in Table 1. The diffusion coefficients increase with an increase in IA content in the hydrogels. This is due to the hydrophilicity for these copolymeric hydrogels in the order of (S0) < (S1) < (S2) < (S3), and the more hydrophilic groups in the gel, the easier the diffusion for water molecules [1,2].

Conclusion

The poly(NiPAAm-co-IA) hydrogels were successfully synthesized by γ -irradiation. The equilibrium swelling degree (SD_{eq}) of copolymeric hydrogels increase with an increase of IA content, due to incorporation of more specific acid groups into the network and consequent higher swelling capacity of gels. The network parameters M_c and ξ also increase with increasing amount of IA, whereas the xerogel densities decrease. In the diffusion transport mechanism study, the results indicate that the swelling transport mechanism is a non-Fickian transport. The diffusion coefficients (D) of poly(NiPAAm-co-IA) hydrogels increase with an increase of IA content, so the water molecule easily infiltrates into hydrogels for gels containing higher IA content.

Acknowledgements

This work is financed by the Ministry of Education and Science of Republic of Serbia, projects 45005 and 172062, and International Atomic Energy Agency (IAEA), project CRP: F23028, contract No. 15384.

References

- [1] B. Taşdelen, et al, J. Appl. Polym. Sci., 2004, 91, 911-915.
- [2] B. Taşdelen, et al, Rad. Phys. Chem., 2004, 69, 303-310.
- [3] A. Krklješ et al, Polym. Bull., 2007, 58, 271-279.
- [4] B. Taşdelen, et al, Int. J. Pharmaceut., 2004, 278, 343-351.
- [5] J. Krstić, et al., 10th International Conference on Fundamental and Applied Aspects of Physical Chemistry, Proceedings, 2010, Vol. I, 110-112.

CALCULATION OF CROSSLINK DENSITY IN CURED FILMS OF ALKYD/MELAMINE RESINS

M. Jovičić, R. Radičević, J. Pavličević, O. Bera
University of Novi Sad, Faculty of Technology, Novi Sad, Serbia

Abstract

Baking enamels were prepared by mixing the synthesized alkyd resins and a commercial melamine resin (weight ratio of 70:30 based on dried mass). Curing of coating films was performed in an oven at 150 °C for 1 h. The viscoelastic properties of the cured film were evaluated by a dynamic mechanical analysis (DMA). The values of the storage modulus, loss modulus and loss factor $\tan\delta$ were assessed in the temperature range from -30 to 120 °C. DMA were used to determine the crosslink density and the glass transition temperature of cured films.

Introduction

The dynamic mechanical analysis (DMA) is commonly used to characterize a material in response to vibration forces. In principle, DMA techniques detect the viscoelastic behavior of polymeric materials and yield quantitative results for the tensile storage module E' and the corresponding loss module E'' , the loss factor $\tan\delta$ as the quotient of loss and storage, $\tan\delta=E''/E'$ [1]. E' and E'' characterize the elastic and viscous component of a viscoelastic material under deformation, respectively. The interpretations and application of dynamic data provide information on network structure which can be utilized to calculate the crosslink density (ν_e), elastically effective chain length between crosslinks (M_c) and the glass transition temperature of the crosslinked resin [2].

Alkyd resins are widely used in surface coating systems usually in combination with other resins, frequently with melamine resin. The melamine resin is a minor constituent and plays the role of a crosslinking agent. In this work, baking enamels were prepared by mixing the synthesized alkyds with a commercial melamine resin. The viscoelastic properties of the cured film were evaluated by a dynamic mechanical analysis (DMA). According to the height of the storage modulus rubbery plateau, it is possible to obtain the crosslink density of cured resin mixtures. DMA was also used to determine the glass transition temperature of cured films.

Experimental

Three alkyd resins were synthesized differing in values of acid number (AN) and hydroxyl number (HN): alkyd AG based on glycerine ($AN_{AG}=2.1$ mgKOH/g, $HN_{AG}=218.9$ mgKOH/g); alkyd ATMP based on trimethylolpropane ($AN_{ATMP}=9.2$ mgKOH/g, $HN_{ATMP}=241.8$ mgKOH/g) and alkyd AEP based on ethoxylated pentaerythritol ($AN_{AEP}=4.5$ mgKOH/g, $HN_{AEP}=252.7$ mgKOH/g). Detailed information about the synthesis and properties of these alkyd resins can be found in our previous work [3]. Imino type, isobutylated melamine-formaldehyde resin, produced by INEOS Melamines, commercial name Maprenal MF580/55IB, was used as 55 % solution in isobutanol. Baking enamels were prepared by mixing the

synthesized alkyds with a commercial melamine resin in weight ratio of 70:30 based on dried mass. Curing of coating films was performed in an oven at 150 °C for one hour. Dynamic mechanical properties of cured coating films (20×10×1 mm) were determined by DMA 2980 TA Instruments. The DMA spectra of films were recorded in tensile mode in the temperature range of -30 °C to 120 °C at a frequency of 1 Hz and with a heating rate of 5 °C/min.

Results and Discussion

The representative dynamic spectra of E' , E'' and $\tan\delta$ versus temperature of the alkyd AG/melamine coating films are shown in Fig. 1. The breadth and shape of the $\tan\delta$, detected for all samples, indicate the heterogeneity of the ingredients used in the coating formulation [4]. The glass transition temperatures, T_g , which were taken as the maxima of $\tan\delta$ and maxima of E'' in DMA spectra of coating, are reported in Table 1.

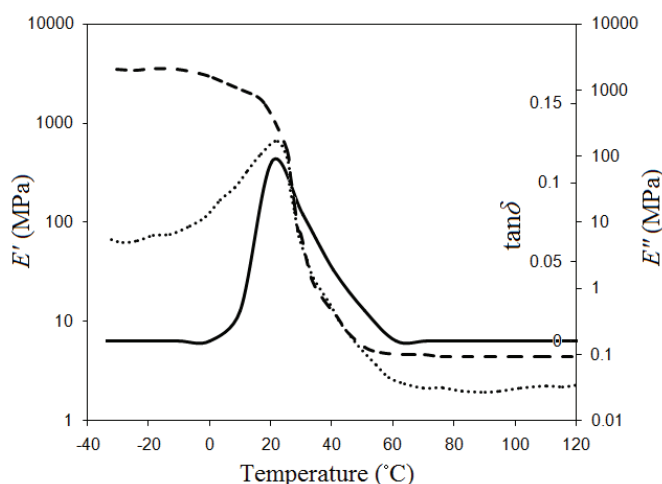


Figure 1. Storage modulus (E'), loss modulus (E'') and $\tan\delta$ versus the temperature for the cured alkyd AG/melamine coating.

The crosslink density (ν_e), the number of moles of elastically effective network chains per cubic centimeter of sample, can be determined from the DMA data using the kinetic theory of rubber elasticity [5]. The E' values in rubbery region at $T > T_g$ (E'_{min}) are taken to calculate ν_e using eq. 1 [4,5]:

$$\nu_e = \frac{E'_{min}}{RT} \quad (1)$$

where R is the gas constant and T is the temperature at E'_{min} .

The weight of sample in grams which contains 1mol of elastically effective network chain (M_c), can be calculated using eq. 2:

$$M_c = \frac{\rho}{\nu_e} \quad (2)$$

where ρ is the density of coating films. The values of ρ were determined experimentally and found to be in the range of 1.01-1.11 g/cm³ for the all coating films. The values of ν_e and M_c of the coatings are reported in Table 1.

Table 1. Values of T_g , E'_{min} , ν_e , and M_c of coatings.

Film	T_g (°C)		E'_{min} (Pa) at 110 °C	ν_e (mol/m ³)	M_c (g/mol)
	E''_{maks}	$\tan\delta_{maks}$			
Alkyd AG/melamine	16	28	$1,90 \cdot 10^6$	631,3	1740
Alkyd ATMP/melamine	17,5	31	$2,48 \cdot 10^6$	835,6	1290
Alkyd AEP/melamine	22	35	$4,36 \cdot 10^6$	1542,4	650

The data obtained for ν_e indicate that the coating alkyd AEP/melamine is having tighter network compared to films alkyd AG/melamine and ATMP/melamine. The above observation is reconfirmed with the observed value of M_c , which is the highest for the alkyd AG/melamine crosslinked film. The mixtures consisting of alkyd resin prepared from ethoxylated pentaerythritol show higher values of the crosslink density than those obtained from alkyd based resins with glycerin or trimethylolpropane due to high hydroxyl number of alkyd AEP.

Conclusions

Dynamic mechanical properties of cured alkyd/melamine coatings were determined by DMA instruments. The DMA data provide information on network structure which were used to calculate crosslink density (ν_e), elastically effective chain length between crosslinks (M_c) and the glass transition temperature (T_g) of the crosslinked alkyd/melamine films. Due to the highest hydroxyl number of alkyd based on ethoxylated pentaerythritol, the alkyd AEP/melamine resins mixture have higher values of the crosslink density than those obtained from alkyd AG/melamine and alkyd ATMP/melamine.

Acknowledgements

The authors wish to express their gratitude to the Ministry of Education and Science of the Republic of Serbia for the financial support (Project III45022).

References

- [1] T. Frey, K.H. Große-Brinkhaus, U. Röckrath, *Progr. Org. Coat.*, 1996, 27, 59-66.
- [2] R. Narayan, K.V.S.N. Raju, *Progr. Org. Coat.*, 2002, 45, 59-67.
- [3] R. Radičević, M. Jovičić, J. Budinski-Simendić, *Progr. Org. Coat.*, 2011, 71, 256-264.
- [4] L.W. Hill, *J. Coat. Technol.*, 1992, 64, 29-41.
- [5] L.W. Hill, *Progr. Org. Coat.*, 1997, 31, 235-243.

**ENVIRONMENTAL PROTECTION
FORENSIC SCIENCES
PHARMACEUTICAL
PHYSICAL CHEMISTRY**

REMOVAL OF URANIUM ANIONIC SPECIES FROM AQUEOUS SOLUTIONS BY POLYETHYLENIMINE – EPICHLOROHYDRIN RESINS

S. Sarri¹, P. Misaelides¹, D. Zamboulis¹, J. Warchol²

¹ Department of Chemistry, Aristotle University, 54124 Thessaloniki, Greece

² Department of Water Purification and Protection, Rzeszow University of
Technology, Rzeszow, Poland

Introduction

The presence of uranium in the biosphere is not only due to natural sources but also to various human activities (e.g. mining, nuclear power production, military activities etc). Uranium is highly soluble in waters and can easily be transferred in the biosphere through aquatic pathways.

The uranyl-ion (UO_2^{2+}) is the most dominant species in low pH aqueous solutions ($\text{pH} < 4.5$), whereas in those of higher pH values ($4.5 < \text{pH} < 7.5$) different uranium hydrolysis products of the general type $(\text{UO}_2)_x(\text{OH})_y^{(2x-y)+}$ are formed. The formation of phases such as $\text{UO}_2(\text{OH})_2$, which can be precipitated, is also possible. In alkaline solutions uranium forms a number of pH-dependent complexes increasing its solubility, availability and mobility in the environment. Uranyl-carbonato-complexes (e.g. $\text{UO}_2(\text{CO}_3)_2^{2-}$ and $\text{UO}_2(\text{CO}_3)_3^{4-}$) can also frequently be found in natural waters in the presence of carbonates [1].

Various natural and synthetic sorbents were investigated and used for the removal of uranium cationic species from aqueous solutions. On the other hand, the number of works on the removal of uranium anionic species is rather limited.

This contribution presents the results of the investigation of the uranium anionic species removal from alkaline aqueous solutions by two recently prepared polyethylenimine – epichlorohydrin resins.

Experimental

Two polyethylenimine - epichlorohydrin resins were prepared using low- and high molecular weight polyethylenimine and characterized at the Chemistry Department of the Aristotle University. A modification of a previously described synthesis method was applied for the preparation of the resins [2].

For the sorption experiments 30 mg of the resins were contacted in polypropylene tubes for 24 hours with 10 mL of uranium solutions (C_{init} : 10 to 2000 mg U/L, pH_{init} 8, 9 and 10 adjusted using NaOH at room temperature). After separation of the solid and liquid phases by centrifugation, the equilibrium pH was measured and the uranium concentration determined spectrophotometrically by means of the Arsenazo III method at 660 nm [3]. The obtained data were used to calculate the uptake capacity in mg/g and construct the corresponding sorption isotherms. The experiments were performed under equilibrium conditions with atmospheric CO_2 .

K-01-SL

The uranium uptake data were modeled using a number of 2-, 3- and 4-parametric isotherm equations (Langmuir, Freundlich, Redlich-Peterson, Langmuir-Freundlich, Toth, Dubinin-Raduszkiewicz) [4].

The sorption kinetics was also investigated for and modeled using the pseudo-first and pseudo-second order equations [4].

The surface and the interior of the resin grains, prior and after the uranium sorption, were examined by SEM/EDS.

Results

The experimental results demonstrated that both resins can very efficiently remove anionic uranium species from aqueous solutions. Fig. 1 presents the isotherms for the sorption of uranium by the low- and high molecular weight (L.M.W. and H.M.W) polyethylenimine – epichlorohydrin resins.

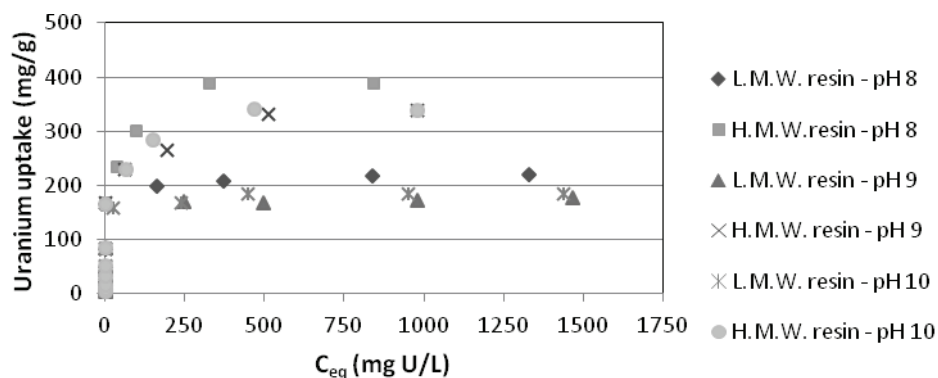


Figure 1. Uranium sorption isotherms for the low- and high molecular weight (L.M.W. and H.M.W) polyethylenimine – epichlorohydrin resins.

The enhanced uranium uptake from solutions of pH_{init} 8 can be explained taking into account its speciation and the ratio charge of the complex to the number of uranium atoms. The increasing competition from the side of the hydroxyl-ions was also one of the reasons for the lower uptake from solutions of pH_{init} 9 and 10.

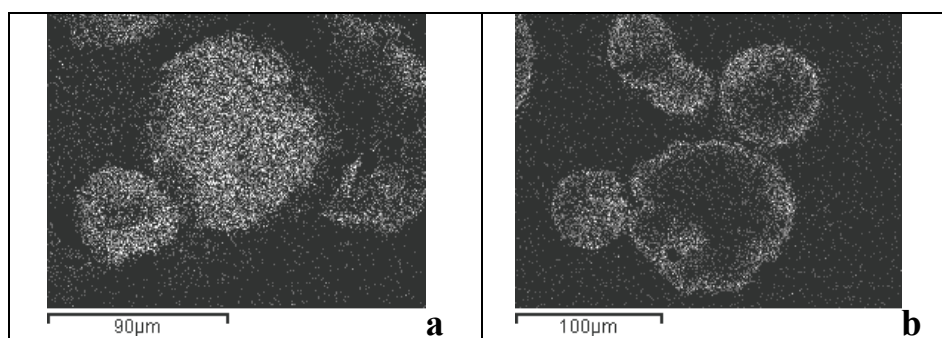
The two resins showed similar behavior. However, the H.M.W. showed higher uptake capacity than the L.M.W. one and was selected for the modeling using the 6 abovementioned isotherm equations (s. example for pH_{init} 8 in Table 1). This Table shows that the uranium uptake data could successfully be reproduced by more than one isotherm equations.

The uranium uptake by the investigated sorbents was very fast. In the first 2 min. ca. 75% of the uranium could be removed from the solutions. The equilibrium was established in less than 15 min. The kinetic data could be very well fitted by the pseudo-second order equation (L.M.W.: $h=125$ mg/(g min), $k=0.008$ g/(mg min), $R^2=1$; H.M.W.: $h=250$ mg/(g min), $k=0.004$ g/(mg min), $R^2=1$).

Table 1. Modeling of the uranium uptake data for solutions of pH_{init} 8.

Isotherm equation	q _{max}	K	n	R ²
Langmuir	338.5	0.4989	-	0.916
Freundlich	-	3.5162	67.58	0.892
Redlich - Peterson	230.2	0.8172	0.9252	0.950
Langmuir – Freundlich	373.3	0.2114	0.7147	0.932
Toth	458.7	1.343	0.3836	0.949
Dubinin–Raduszkiewicz	362.5	0.00252	0.092	0.933

The examination of the resins grains by SEM/EDS revealed that the uranium was concentrated on their surface (s. Fig. 2) indicating that precipitation also contributed to the overall removal. No diffusion in the bulk of the grains was observed as in the case of other anionic species (e.g. chromates, iodides, perhenates).

**Figure 2.** U-mapping ($U M\alpha_1$) of the surface (a) and of a section (b) of resin grains.

References

- [1] C. Moulin et al, *Appl. Spectrosc.*, 52(1998) 528-535.
- [2] D. Ebner et al, *Sep. Sci. Technol.*, 34 (1999) 1277-1300.
- [3] S.B. Savvin, *Talanta*, 11 (1964) 1–6.
- [4] G. Gerente et al, *Environ. Sci. Technol.*, 37 (2007) 41–127.

K-02-SL

APPLICATIONS OF BENTONITE IN THE ENVIRONMENTAL PROTECTION

P. Banković¹, Z. Mojović¹, N. Jović-Jovičić¹, M. Žunić¹, A. Milutinović-Nikolić¹,

¹ *University of Belgrade – Institute of Chemistry, Technology and Metallurgy, Center for Catalysis and Chemical Engineering, Njegoševa 12, Belgrade, Serbia*

Abstract

Smectite rich clay from Bogovina, Serbia, was submitted to pillaring and organomodification. Pillared and organomodified materials were characterized using XRD, ICP-OES and N₂ physisorption methods. The obtained pillared and organoclays were employed as adsorbents, catalysts and electrode materials in the processes of removal and detection of different organic and inorganic water pollutants.

Introduction

Smectites have large surface area, wide pore size distribution, moderate surface acidity, high cation exchange capacity, low anion exchange capacity and ability of water uptake through exchangeable cations hydration, also known as swelling [1, 2]. The ability of cation exchange and swelling make smectites prone to various types of modification enabling their different applications. For instance, pillaring and organomodification of bentonite clays rich in smectite have been widely applied for the obtainment of catalysts and adsorbents for the environmental protection [3, 4].

Pillared clays are hydrothermally stable materials that can be designed for specific catalytic purposes by designing their porosity and the chemical composition of pillars incorporated within their interlamellar region through the control of synthesis conditions and the right choice of pillaring agents and/or impregnation [5–7].

Smectite can be rendered organophilic by organomodification when exchangeable cations are replaced with quaternary alkylammonium ions (QAACs) [8]. Organoclays are attractive materials due to their ability to adsorb both organic pollutants and toxic heavy metals from water [9].

In this work, smectite rich bentonite from local deposits in Bogovina, Serbia, was employed in the synthesis of nanomaterials for prevention and management of water pollution by pillaring and organomodification. Obtained pillared (PILCs) and organoclays (OBs) were also used as electrode materials for the detection of organic pollutants in water.

Materials and Methods

Smectite rich bentonite clay from Bogovina [10] was used in this work. After milling, sieving and hydroseparation, <74 μm and <2 μm fractions were used for

further modifications and denoted as B2 and B74 respectively. Both B2 and B74 were submitted to the Na-exchange procedure (samples Na-B2 and Na-B74).

The procedure according to Baskaralingam [11, 12] was adopted for the organobentonite preparation. Two series of synthesized organobentonites (OBs) were obtained by dropwise addition of surfactant–bromide solutions into a stirred Na-B74 dispersion. In the first series the starting material was modified with different amounts of hexadecyltrimethylammonium (HDTMA) ion with respect to the amount of exchangeable cations (Na^+). The samples were denoted as 0.2HDTMA-B, 0.5HDTMA-B, 1.0HDTMA-B corresponding to 0.2, 0.5, 1.0 and 2.0 times of CEC value, respectively. The second series was obtained using QAACs with different alkyl chain lengths: HDTMA, dodecyltrimethylammonium (DDTMA) and tetramethylammonium (TMA) ions. Here presented samples designated as 0.2HDTMA-B, 0.2DDTMA-B, 0.2TMA-B, 2.0HDTMA-B, 2.0DDTMA-B and 2.0TMA-B.

The process of pillaring was carried out according to a common procedure [13]. Pillaring solutions were adjusted to have the molar ratio $\text{M}^{n+}/(\text{Al}^{3+}+\text{M}^{n+})=0.10$ (where $\text{M}^{n+}=\text{Cu}^{2+}$, Co^{2+} or Fe^{3+}), $\text{OH} /(\text{Al}^{3+}+\text{M}^{n+})=2.0$ and the metal ion/Na-B2 ratio of 20 mmol M^{n+}/g . Obtained samples were denoted AlCu10 PILC, AlCo10 PILC and AlFe 10 PILC. Another series of PILCs with different Fe^{3+} content was also synthesized. In this case the pillaring solutions contained pillaring cations in the following $\text{Fe}^{3+}/(\text{Al}^{3+}+\text{Fe}^{3+})$ molar ratios: 0.00, 0.01, 0.05, 0.10, 0.15 and 0.20. The obtained PILCs were denoted as Al PILC, AlFe1 PILC, AlFe5 PILC, AlFe10 PILC, AlFe15 PILC and AlFe20 PILC, respectively. Pillaring was performed by dropwise addition of pillaring solutions into stirred Na-B2 dispersion. The pillaring procedure was described in details elsewhere [14].

X-ray diffraction (XRD) patterns for powders of investigated samples were obtained using a Philips PW 1710 X-ray powder diffractometer with a Cu anode ($\lambda=0.154178$ nm).

A Spectro Spectroflame M - inductively coupled plasma optical emission spectrometer, was used for the analysis of the chemical composition of all investigated samples.

Nitrogen adsorption-desorption isotherms were determined on a Sorptomatic 1990 Thermo Finnigan at -196 °C. Samples were outgassed at 160 °C, during 20h. Specific surface area of the samples, S_{BET} , was calculated according to Brunauer, Emmett, Teller method [15]. Dubinin-Radushkevich method was used for the calculation of micropore volume, V_{mic} [16].

Catalytic degradation of organic water pollutants (azo-dyes Tartrazine and Acid Yellow 99, phenol and toluene) was tested in Catalytic Wet Peroxide Oxidation (CWPO) process [3] using PILCs as catalysts. Catalytic tests were carried out in a thermostated Pyrex reactor, and equipped with a stirrer. Aqueous solutions (100 ml) of each organic pollutant were stirred with 0.5 g of solid catalyst and 35% hydrogen peroxide in excess. Aliquots were taken at predetermined time intervals. Supernatant solutions were separated from the solid phase by centrifugation and analyzed by UV-Vis spectrophotometry (Electron Nicolet

K-02-SL

Evolution 500 UV-VIS spectrophotometer) or gas chromatography (Shimadzu GC-9A gas chromatograph).

OBs were tested as adsorbents of organic water pollutants (Acid Orange 10 – AO10) and toxic metals (Pb^{2+}). The adsorption experiments were carried out in a thermostated shaker (Memmert WNE 14 and SV 1422). The samples were withdrawn from the shaker at regular time intervals and solid phase was separated from the solutions by centrifugation. Supernatant solution was used for the measurements. AO10 concentration was determined by Thermo Electron Nicolet Evolution 500 UV-VIS spectrophotometer, while Pb^{2+} concentration was measured by ICP-OES (ICAP 6500 Duo ICP, Thermo SCIENTIFIC Spectrometer).

In order to use the PILCs and OBs as electrode materials, the samples were homogeneously dispersed in 5 mass % Nafion solution in mixture of isopropyl alcohol and water. The electronic conductivity of the samples was enhanced by adding 10 mass % of carbon black Vulcan XC72 (Cabot Corp.) into the initial suspension. Each of these suspensions was placed on the surface of a glassy carbon rotating disc electrode and solvent was removed by evaporation. The electrodes served as working electrodes for electrochemical investigations in a three-electrode glass cell. The reference electrode was Ag/AgCl in 1 M KCl, while a platinum foil served as a counter electrode. Phenol degradation was investigated for starting concentration of phenol of 10 mM in 0.1 M H_2SO_4 at room temperature using 757 VA Computrace Metrohm.

Characterization

The influence of applied modification on the smectite (001) basal spacing, d_{001} , and porous structure for selected representative pillared and organobentonite materials is presented in Tables 1 and 2, together with the results of the chemical analysis of the PILCs.

Table 1. Main physical and chemical properties of the starting and PILC materials.

Sample	d_{001} [nm]	S_{BET} [m ² /g]	V_{mic} [cm ³ /g]	mmol/100g sample			
				Al	Fe	Cu	Co
B2	1.53	125	0.051	481,5	107,3	-	-
Na-B2	1.28	123	0.051	474,3	107,3	-	-
Al PILC	1.72	177	0.087	859,3	110,9	-	-
AlFe1 PILC	1.75	203	0.094	740,7	132,4	-	-
AlFe5 PILC	1.74	151	0.070	715,7	178,9	-	-
AlFe10 PILC	1.75	190	0.090	656,4	214,7	-	-
AlFe15 PILC	1.74	187	0.087	637,0	304,1	-	-
AlFe20 PILC	-	197	0.086	629,6	357,8	-	-
AlCu10 PILC	1.58	153	0.063	851,9	107,3	19,7	-
AlCo10 PILC	1.72	142	0.057	851,9	100,2	-	2,9

* S_{BET} – specific surface area, V_{mic} – micropore volume

Table 2. Main physical properties of the starting and OB materials.

Sample	d_{001} [nm]	S_{BET} [m ² /g]	V_{mic} [cm ³ /g]	The Na-exchange process lowered d_{001} smectite basal spacing from 1.53 nm for the starting bentonite to 1.28 nm. Pillaring led to increase in the smectite basal spacing in all obtained PILCs, which is a proof of the successful incorporation of pillaring species in the interlamellar region of smectite. Intercalation of HDTMA ions
Na-B74	1.28	120	0.051	
0.2TMA-B	1.28	148	0.101	
2.0TMA-B	1.40	133	0.062	
0.2DDTMA-B	1.30	35	0.034	
2.0DDTMA-B	1.81	2	-	
0.2HDTMA-B	1.44	20	0.010	
0.5HDTMA-B	1.52	20	0.008	
1.0HDTMA-B	2.00	3	-	
2.0HDTMA-B	2.00	1	-	

increased the basal spacing from 1.28 nm for Na-rich bentonite to 2.00 nm for 1.0HDTMA and 2.0HDTMA-B (Fig. 1). Since the increase of (mol HDTMA)/(mol exchangeable Na⁺) above 1 did not cause the increase of the basal spacing, it can be assumed that additional HDTMA ions, after replacing all Na⁺ cations within interlayer region, were attached to the particle surface. The XRD results of the synthesized organobentonites indicated that monolayers of surfactants were predominantly formed within the interlayer space of 0.2-organobentonites, 0.5 HDTMA and 2.0TMA-B, while pseudo-trilayer were formed in 1.0- and 2.0HDTMA-B [17, 18]. However, the changes obtained in the d_{001} of 0.2-OBs were smaller than those theoretically predicted, which can be expected for lower surfactant loadings [19]. Comparing to Na-B2, S_{BET} values obtained for the PILCs showed increase. The most pronounced increase was in the case of Fe containing PILCs. Among them, the increase was slightly lower in the case of the AlFe5 PILC, possibly due to some inconsistency in the pillaring procedure that might have occurred. However the level of Fe³⁺ incorporation in the AlFe5 PILC was more than satisfying. The incorporation of Cu²⁺ and Co²⁺ was much lower, probably due to incompatibility in the valence and coordination between these ions and Al³⁺. The specific surface area of the OB samples decreased in the order TMA > DDTMA-B > HDTMA-B. The presence of larger organic cations, such as HDTMA and DDTMA, in the interlamellar region resulted in pore blocking that inhibited the passage of nitrogen molecules. On the other hand, the increased S_{BET} value for TMA-B was mainly due to the presence of newly developed micropores in the interlamellar region. Iron to aluminium content in the PILCs corresponded to those in the pillaring solutions.

Adsorption, Catalytic and Electrocatalytic Tests

In figures 1–3 are presented results of adsorption of Acid orange 10 dye (50 ppm) and Pb²⁺ from single-component and their mixed two-component aqueous solutions on the series of HDTMA-B samples with different surfactant loading where curves 1, 2, 3, and 4 correspond to 2.0HDTMA-B, 1.0HDTMA-B, 0.5HDTMA-B and

0.2HDTMA-B, respectively [9]. The influence of alkyl chain length on the adsorption of organic pollutants is here described by the adsorption of AO10 on 2.0TMA-B (1), 2.0DDTMA-B (2) and 2.0HDTMA-B (3) (Fig. 4).

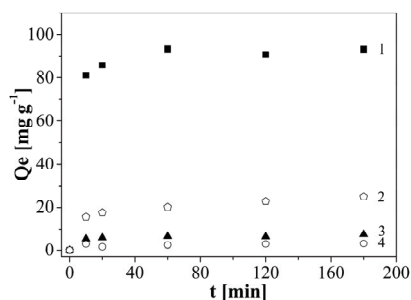


Figure 1. Adsorption of AO 10 from single-component solution.

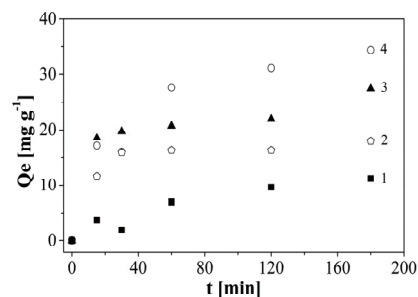


Figure 2. Adsorption of Pb^{2+} ions from single-component solution.

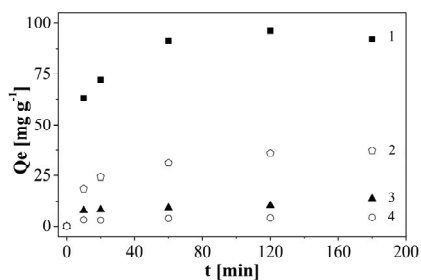


Figure 3. Adsorption of AO 10 from two-component solution.

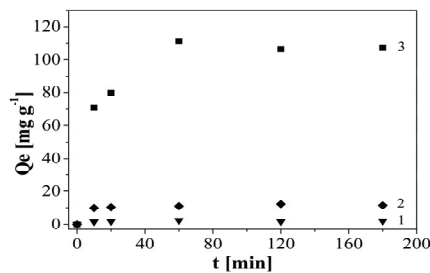


Figure 4. The influence of alkyl chain length on the adsorption of AO10.

Increasing surfactant loading and alkyl chain length led to increased organophilicity which resulted in increased azo dye and decreased Pb^{2+} adsorption. Simultaneous adsorption of AO10 and Pb^{2+} improved the adsorption of the dye by adsorbents with molar ratio QAAC/exchangeable cations up to 1. A possible explanation for this might be the attraction between SO_3^- groups in AO 10 to Pb^{2+} previously adsorbed on surface area free of organic cations.

The influence of Fe content of PILCs and temperature on the CWPO degradation of azo dyes was studied on the example of Tartrazine ($93,6 \times 10^{-6} \text{ mol dm}^{-3}$) as presented in Figs. 5 and 6 [20]. The removal of toluene ($2 \times 10^{-3} \text{ mol dm}^{-3}$) and phenol ($5 \times 10^{-4} \text{ mol dm}^{-3}$) by CWPO were also tested (Figs. 7 and 8, respectively) [21, 22].

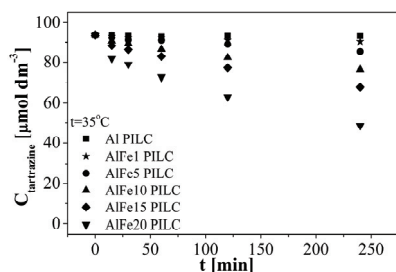


Figure 5. CWPO of tartrazine – the influence of Fe content in the PILCs.

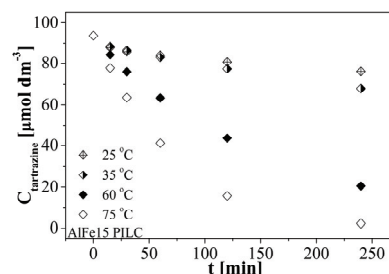


Figure 6. CWPO of tartrazine – the influence of temperature.

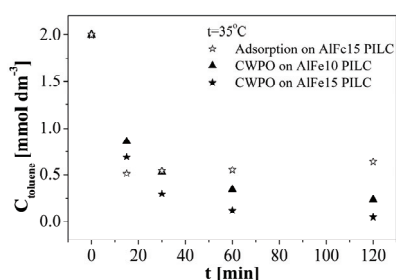


Figure 7. CWPO and adsorption of toluene – the influence of Fe content.

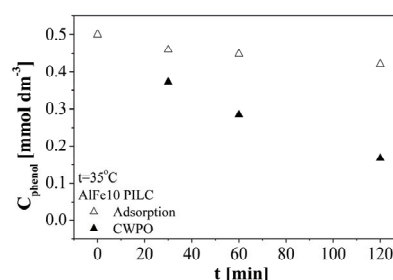


Figure 8. CWPO and adsorption of phenol.

Increasing efficiency of the CWPO removal of tartrazine with increased Fe content in the PILC catalysts confirmed catalytic role of iron. Results of the toluene removal by CWPO corroborated these findings. Higher temperatures promoted the degradation of tartrazine. Phenol removal was the least efficient however still significant with respect to its removal by adsorption.

Increased electrode surface area leads to increased electrochemical activity. Pillaring yields materials with developed micro/mesoporosity. Therefore Al PILC, AlCu10 PILC, AlCo10 PILC and AlFe10 PILC were tested as electrode materials in the electrocatalytic oxidation of phenol in acidic solution [23]. The modification of clay minerals by surfactants is a method to hydrophobize the mineral and therefore to increase the adsorption capacity for organic pollutants. Therefore electrocatalytic oxidation on the series 0.2TMA-B, 0.2DDTMA-B and 0.2HDTMA-B was also investigated [24]. Successive cyclic voltammograms obtained at the polarization rate of 10mVs at AlFe10 PILC and 0.2HDTMA-B electrode (here chosen as the representative ones) are shown in Figs. 9 and 10, respectively. Table 3 summarizes current densities and current density drops after 10 cycles (electrode deactivation) around the potential of 950 mV vs. Ag/AgCl corresponding to phenol oxidation.

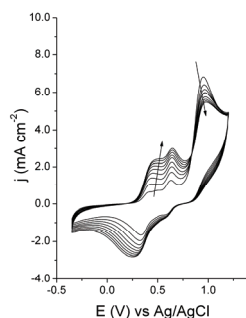


Figure 9. CV for phenol oxidation in H₂SO₄ on AlFe10 PILC electrode.

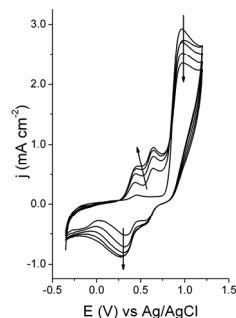


Figure 10. CV for phenol oxidation in H₂SO₄ on 0.2HDTMA-B electrode.

Table 3. Phenol oxidation current densities.

Sample	j_I [mAcm ⁻²]	$(j_I - j_X)/j_I$ [%]
Al PILC	5.42	35.43
AlCo10 PILC	8.71	30.89
AlCu10 PILC	5.95	20.84
AlFe10 PILC	7.45	26.44
0.2TMA-B	7.36	-
0.2DDTMA-B	1.98	-
0.2HDTMA-B	1.08	-

Prolonged cycling resulted in the decrease of current density related to phenol oxidation and simultaneous occurrence and increase in the current densities of cathodic peaks (600 and 300 mV) and anodic peaks (440 and 640 mV) related to phenol oxidation products – hydroquinone and catechol.

Among the PILCs, AlFe10 PILC showed the best performance, i.e. high activity and low deactivation rate, while the best organomodified electrode material was 0.2TMA-B.

Conclusion

Pillared and organomodified clays based on Bogovina bentonite were synthesized and characterized. XRD, chemical and N₂ physisorption analyses confirmed the incorporation of introduced species. Organomodified clays showed good performance as adsorbents for simultaneous removal of organic and inorganic water pollutants. Increasing organophilicity increased dye adsorption. CWPO degradation of organic water pollutants increased with increasing Fe content of the PILCs and temperature. Both PILCs and OBs showed significant activity as electrode materials in electrocatalytic oxidation of phenol.

Acknowledgment

Supported by the Ministry of Education and Science of the Republic of Serbia (Project III-45001).

References

- [1] Vaccari, Catal. Today, 1998, 41, 53–71.
- [2] F. Wypych, K.G. Satyanarayana, Clay Surfaces: Fundamentals and Applications, Elsevier, Amsterdam, 2004.

- [3] M. N. Timofeeva, S. T. Khankhasaeva, Y. A. Chesalov, S. V. Tsybulya, V. N. Panchenko, E. T. Dashinamzhilova, *Appl. Catal. B-Environ.*, 2009, 88, 127–134.
- [4] J.J. Lee, J. Choi, J.W. Park, *Chemosphere*, 2002, 49, 1309–1315.
- [5] P. Cool, E. F. Vansant, *Molecular Sieves Vol. 1*, Springer-Verlag, Berlin-Heidelberg (1998)
- [6] Gil, L. M. Gandia, M. A. Vicente, *Catal. Rev. – Sci. Eng.*, 2000, 42, 145–212.
- [7] J. Klopogge, *J. Porous. Mat.*, 1998, 5, 5–41.
- [8] Y. Chun, G. Sheng, S. Boyd, *Clays Clay Miner.*, 2003, 51, 415–420.
- [9] N. Jović-Jovičić, A. Milutinović-Nikolić, P. Banković, Z. Mojović, M. Žunić, I. Gržetić, D. Jovanović, *Appl. Clay Sci.*, 2010, 47, 452–456.
- [10] Z. Vuković, A. Milutinović-Nikolić, Lj. Rožić, A. Rosić, Z. Nedić, D. Jovanović, *Clays Clay Miner.*, 2006, 54, 699–704.
- [11] P. Baskaralingam, M. Pulikesi, D. Elango, V. Ramamurthi, S. Sivanesan, *J. Hazard. Mater.*, 2006, 128, 138–144.
- [12] N. Jović-Jovičić, A. Milutinović-Nikolić, I. Gržetić, D. Jovanović, *Chem. Eng. Technol.*, 2008, 31, 567–574.
- [13] V. Kaloidas, C. A. Koufopoulos, N. H. Gangas, N. G. Papayannakos, *Microporous Mater.*, 1995, 5, 97–106.
- [14] P. Banković, A. Milutinović-Nikolić, Z. Mojović, N. Jović-Jovičić, M. Žunić, V. Dondur, D. Jovanović, *Appl. Clay Sci.*, 2012, 58, 73–78.
- [15] F. Rouquerol, J. Rouquerol, K. Sing, *Adsorption by Powders and Porous Solids*, Academic Press, London (1999).
- [16] M. M. Dubinin, *J. Colloid Interf. Sci.*, 1974, 46, 351–356.
- [17] G. Lagaly, *Solid State Ionics*, 1986, 22, 43–51.
- [18] G. Lagaly, M. Ogawa, I. Dékány, *Clay mineral organic interactions*. In: Bergaya, F., Theng, B.K.G., Lagaly, G. (Eds.), *Handbook of Clay Science: Developments in Clay Science*, vol. 1. Elsevier, Amsterdam, (2006).
- [19] S. Y. Lee, S. J. Kim, S. Y. Chung, C. H. Jeong, *Chemosphere*, 2004, 55, 781–785.
- [20] P. Banković, A. Milutinović-Nikolić, Z. Mojović, N. Jović-Jovičić, M. Žunić, V. Dondur, D. Jovanović, *Appl. Clay Sci.*, 2012, 58, 73–78.
- [21] P. Banković, A. Milutinović-Nikolić, Z. Mojović, A. Rosić, Ž. Čupić, D. Lončarević, D. Jovanović, *Chinese J. of Catal.*, 2009, 30, 14–18.
- [22] P. Banković, A. Milutinović-Nikolić, N. Jović-Jovičić, J. Dostanić, Ž. Čupić, D. Lončarević, D. Jovanović, *Acta Physica Polonica A*, 2009, 115, 811–815.
- [23] P. Banković, Z. Mojović, A. Milutinović-Nikolić, N. Jović-Jovičić, S. Marinović, D. Jovanović, *Appl. Clay Sci.*, 2010, 49, 84–89.
- [24] Z. Mojović, N. Jović-Jovičić, P. Banković, M. Žunić, A. Abu Rabi-Stanković, A. Milutinović-Nikolić, D. Jovanović, *Appl. Clay Sci.*, 2011, 53, 331–335.

K-03-O

FABRICATION OF MONODISPERSE POLY(DL-LACTIC ACID) MICROPARTICLES USING DROP MICROFLUIDICS

G. T. Vladislavljević,¹ W. J. Duncanson,² H. C. Shum,³ D. A. Weitz²

¹*Department of Chemical Engineering, Loughborough University, Loughborough, LE11 3TU, UK,* ²*Department of Physics, Harvard University, Cambridge, MA 02138, US,* ³*Department of Mechanical Engineering, University of Hong Kong, Hong Kong*

Abstract

Monodisperse poly(dl-lactic acid) particles with a diameter between 11 and 121 μm were fabricated by drop microfluidics/solvent evaporation method using flow focusing glass capillary device. In the dripping regime, the ratio of droplet diameter to orifice diameter was in the range of 0.37–1.34 and was inversely proportional to the 0.39 power of the ratio of the continuous phase flow rate to dispersed phase flow rate.

Introduction

Biodegradable particles have been used for the encapsulation and controlled release of pharmaceutical actives, ultrasound and molecular imaging, fabrication of scaffolds, cell cultivation, etc. The most commonly used biodegradable synthetic polymers are poly(lactic acid) (PLA) and poly(lactic-co-glycolic) acid (PLGA), since they both have good biocompatibility and mechanical strength [1]. Monodisperse particles are favourable in drug delivery and ultrasound imaging because they exhibit predictable biodegradation rate, controlled drug release profile and acoustic response [2]. The conventional methods of droplet generation such as atomization processes, rotor/stator mixing and high-pressure homogenization result in polydisperse particles whose mean size cannot be precisely controlled. As a departure from traditional ‘top-down’ emulsification approach where small droplets are formed by reducing the size of larger droplets, a number of ‘bottom-up’ methods have been recently developed, where small droplets are directly formed by injecting one liquid through a micro -channel or -nozzle into another immiscible liquid. The purpose of this study was to investigate a novel approach to the fabrication of PLA microparticles based on flow focusing microfluidic device [3]. We have chosen borosilicate glass as a construction material for the device fabrication, because glass is more chemically robust than poly(dimethylsiloxane), does not swell, and has more stable surface properties.

Material and Methods

The microfluidic device (Fig. 1 left), set on the stage of an inverted Leica DM-IRBE microscope, was connected to syringes containing the continuous and

dispersed phases via medical tubing. The dispersed phase consisted of a mixture of 5 % (w/w) poly(dl-lactic acid) (PLA) ($15,000 \text{ g}\cdot\text{mol}^{-1}$), 95 % (w/w) dichloromethane (DCM) and 0.1–2 mM Nile red dye. The continuous phase was 5 % (w/w) aqueous solution of polyvinyl alcohol (87–89% hydrolyzed). Each phase was pumped into the device by a separate Harvard Apparatus PHD 22/2000 syringe pump. The droplet formation was recorded using a Phantom V5.1 high-speed camera at the rate of 800–2000 frames per second and frames were analysed using ImageJ v.1.44 software to estimate droplet diameter. The device was fabricated by inserting a round capillary with a tapered tip into the centre of a square capillary. To minimize wetting with DCM, the tip was treated with 2-[methoxy (polyethylenoxy) propyl] trimethoxysilane. Hypodermic needles were glued over both ends of the square tubing to act as tube connectors for the oil and water phase, while the exposed end of the round capillary served for sample collection.

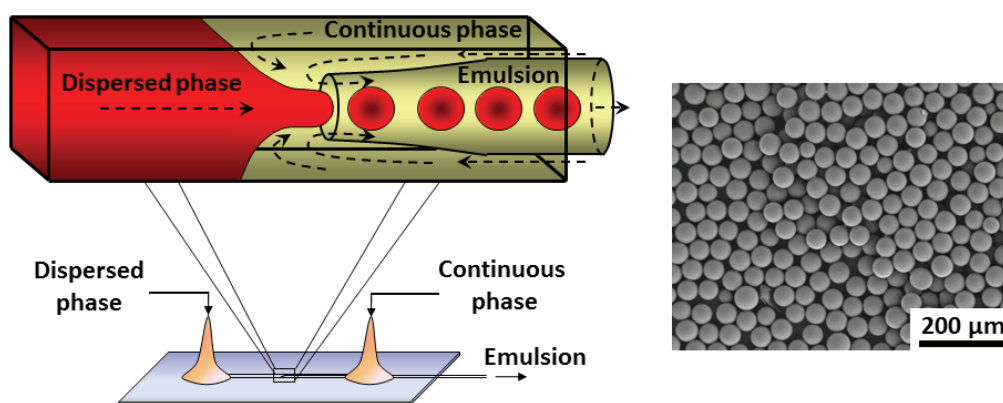


Figure 1. Schematic diagram of flow focusing glass capillary device (left) and Scanning Electron Micrograph of $23 \mu\text{m}$ poly(dl-lactic acid) microparticles (right).

Results and Discussion

Figs. 1 (right) is a Scanning Electron Micrographs of PLA particles showing a smooth surface with negligible porosity and spherical shape. After complete evaporation of DCM, the particle size was 2.7 times smaller than the size of the original droplets.

Fig. 2 is a log-log plot of drop diameters D_d scaled by the orifice diameter D_o versus ratio of volumetric flow rates of dispersed to continuous phase, Q_c/Q_d . Experimental data follows a linear trend with an equation of the best fit line: $D_d/D_o = 0.23(Q_c/Q_d)^{-0.39}$.

Droplets formed in the dripping regime had diameters of $1.34D_o > D_d > 0.37D_o$. In dripping regime, the continuous phase flows through the orifice faster than the dispersed phase and the size of the droplets is determined by the balance between the drag of the continuous phase pulling the droplet downstream and interfacial tension force that resist the flow in the dispersed phase as pinch-off occurs. In jetting regime, the dispersed phase flows faster than the continuous phase and it is

the inertial force of the dispersed phase that must overcome the interfacial tension force. The uniform droplets were obtained only in the dripping regime.

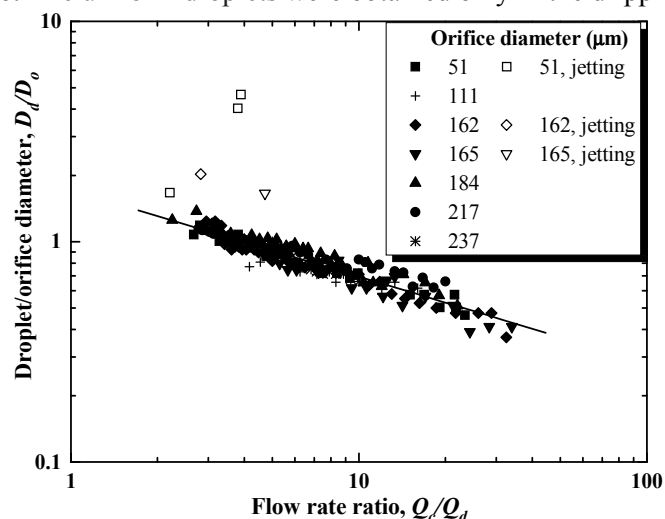


Figure 2. Droplet diameter/orifice diameter versus ratio of volumetric flow rates of dispersed to continuous phase. Open symbols are data points obtained under jetting.

Conclusion

We have developed a novel method for production of poly(lactic acid) particles based on drop microfluidics in glass capillary devices and solvent evaporation. The size of the droplets formed in the microfluidic device has been closely controlled by phase flow rates and orifice size of the collection capillary. Our method is not limited to PLA and can be used to fabricate particles from a wide range of biodegradable material.

Acknowledgment

This work was supported by the Engineering and Physical Sciences Research Council of the UK (grant ref. number EP/HO29923/1) and the Royal Academy of Engineering.

References

- [1] J. M. Anderson, M. S. Shive, *Adv. Drug. Del. Rev.*, 1997, 28, 5–24.
- [2] C. Berklund, M. King, A. Cox, K. Kim, D. W. Packa, *J. Controlled Release*, 2002, 82, 137–147.
- [3] A. S. Utada, L. Y. Chu, A. Fernandez-Nieves, D. R. Link, C. Holtze, D. A. Weitz, *MRS Bull.*, 2007, 32, 702–708.

COMPARISON OF CHROMATOGRAPHICALLY OBTAINED AND COMPUTED HYDROPHOBICITY PARAMETERS OF ACE INHIBITORS

J. V. Odović¹, B. D. Marković², J. B. Trbojević-Stanković³, S. M. Vladimirov², K. D. Karljikovic – Rajić¹

¹ Department of Analytical Chemistry, University of Belgrade-Faculty of Pharmacy, Vojvode Stepe 450, 11221 Belgrade, Serbia

² Department of Pharmaceutical Chemistry, University of Belgrade-Faculty of Pharmacy, Vojvode Stepe 450, 11221 Belgrade, Serbia

³ Clinical Center "Dr Dragiša Mišović", Heroja Milana Tepića 1, 11000 Belgrade, Serbia.

Abstract

The lipophilicity of seven angiotensin – converting enzyme (ACE) inhibitors (enalapril, quinapril, fosinopril, lisinopril, cilazapril, ramipril and benazapril) with significantly different structure was studied. The software packages were used to calculate different ACE inhibitors hydrophobicity parameters, $\log P$ values, while experimentally determined *n*-octanol/water partition coefficients, $\log P_{O/W}$, were obtained from relevant literature. The correlations between all collected $\log P$ values and chromatographically obtained hydrophobicity parameters, R_M^0 and C_0 values were studied. The good correlations ($r > 0.90$) indicate that the $\log P$ calculations can be useful in ACE inhibitors lipophilicity evaluation, as high-throughput screening technique.

Introduction

Lipophilicity is one of the most significant properties of biologically active substances [1]. Lipophilicity is characterized by the *n*-octanol/water partition coefficient ($\log P_{O/W}$) and traditional technique for determination molecules lipophilicity, it's $\log P$ value, is so-called *shake flask* method. The chromatographic techniques are known as well established methods that can yield a significant amount of reproducible retention data for structurally different compounds which can be correlated with their physicochemical and biological properties at the first place lipophilicity [1]. Alternatively, *in silico* hydrophobicity parameters, calculated $\log P$ values, are generally accepted as measure of drug's lipophilicity [2].

In our previous study [3] we reported the lipophilicity of several ACE inhibitors based on RP-TLC research. Continuing this research in the present study correlations between calculated hydrophobicity parameters ($\log P$ values) and chromatographically obtained R_M^0 and C_0 values, as reliable measures of lipophilicity were examined in the aim to establish possible application of *in silico* hydrophobicity parameters in ACE inhibitor's lipophilicity investigations.

Experimental

The seven selected ACE inhibitors were investigated: 1. enalapril maleate, 2. quinapril hydrochloride, 3. fosinopril sodium, 4. lisinopril dihydrate, 5. cilazapril monohydrate, 6. ramipril, and 7. benazepril hydrochloride.

The TLC study of ACE inhibitors lipophilicity, were performed by RP-TLC, as previously reported [3], with additional experiments carried out to include ramipril and benazepril in these correlations.

The Excel 2003 from Microsoft Office and Origin 7.0 PRO (Origin Lab Corporation, USA) were used to perform the statistical analysis of the regression. The software packages Molinspiration Depiction Software (Molinspiration Cheminformatics) [4], Virtual Computational Chemistry Laboratory [5] and CS Chem Office, version 7.0 [6] were used to calculate different ACE inhibitors hydrophobicity parameters, $\log P$ values.

Results and Discussion

The seven ACE inhibitors were studied to evaluate the correlation between their calculated and chromatographically obtained hydrophobicity data. On the base of obtained R_F values the hydrophobicity parameters R_M^0 and C_0 were calculated.

The hydrophobicity parameters, $\log P$ values of the seven investigated ACE inhibitors, were calculated using different software packages (ClogP, AlogP_s, AClogP, AB/logP, MilogP, AlogP, MlogP, KOWWINlogP, XLOGP₂, XLOGP₃) and experimentally determined $\log P_{O/W}$ were obtained from Clarke's Analysis of drugs and Poisons [7]. The differences between calculation methods used led to distinctions between absolute ACE inhibitor's $\log P$ values. The relationships between all collected $\log P$ values were studied. The best agreements were obtained between experimentally determined $\log P_{O/W}$ and three calculated $\log P$ values: KOWWINlogP ($r = 0.9997$), AClogP ($r = 0.9937$) and MilogP values ($r = 0.9742$). In the aim to examine the application and reliability of *in silico* hydrophobicity parameters in lipophilicity evaluation of ACE inhibitors, chromatographically established hydrophobicity parameters R_M^0 and C_0 were correlated with all collected $\log P$ values. The good correlations with $r > 0.90$ were obtained in majority of relationships (Table 1). One of the best relationship was established for KOWWINlogP and R_M^0 ($r = 0.9805$) or C_0 ($r = 0.9768$) parameters obtained by the usage of water-methanol mobile phase. The KOWWINlogP values previously showed the best relationship with experimentally determined $\log P_{O/W}$. The MilogP values showed slightly lower correlation coefficients – corresponding values for water-methanol were 0.9585 for R_M^0 and 0.9575 for C_0 . Although AClogP values showed good correlation with experimentally obtained $\log P_{O/W}$ the lowest r values were obtained – 0.7556 (R_M^0) and 0.7351 (C_0).

Table 1. The correlation coefficients, r , between R_M^0 or C_0 values (for all used modifiers) and different $\log P$ values.

	Water-methanol		Water-acetone		Water-ethanol	
	R_M^0	C_0	R_M^0	C_0	R_M^0	C_0
$\log P_{O/W}$	0,9813	0,9942	0,9929	0,9362	0,8842	0,9174
$C\log P$	0,9373	0,8485	0,8563	0,9606	0,826	0,9607
$A\log P_s$	0,8652	0,7714	0,7907	0,8846	0,7508	0,8959
$AC\log P$	0,5709	0,5404	0,5592	0,5105	0,485	0,5445
$AB/\log P$	0,9499	0,897	0,8911	0,9641	0,8483	0,9454
$Mi\log P$	0,9187	0,9211	0,9232	0,8175	0,8569	0,8606
$A\log P$	0,898	0,8316	0,8494	0,8784	0,8609	0,9251
$M\log P$	0,9423	0,8651	0,8795	0,9423	0,9018	0,9812
KOWWIN	0,9613	0,9541	0,9605	0,9147	0,8468	0,9064
XLOG P_2	0,8639	0,7567	0,7747	0,8889	0,7693	0,9134
XLOG P_3	0,9707	0,902	0,9125	0,9641	0,8625	0,9757

Conclusion

Lipophilicity is one of the most important properties of biologically active substances and lipophilicity calculations have attracted considerable interest in drug research. The correlations between *in silico* hydrophobicity parameters, (calculated $\log P$) and chromatographically obtained hydrophobicity parameters (R_M^0 and C_0) were established. The good correlations indicate that computed $\log P$, with careful selection of method calculation could be used as high-throughput screening technique for ACE inhibitor's lipophilicity evaluation.

Acknowledgment

This work was partly supported by the Ministry of Education and Science, Belgrade, Serbia, as a part of Project TR34031.

References

- [1] R. Kaliszan, Chem. Rev., 2007, 107(7), 3212-3246.
- [2] R. Mannhold, G. I. Poda, I. V. Tetko, J. Pharm. Sci., 2009, 98, 861-893.
- [3] J. Odovic, B. Stojimirovic, M. Aleksic, D. Milojkovic-Opsenica, Z. Tesic, J. Serb. Chem. Soc., 2006, 71(6), 621-628.
- [4] Molinspiration software: www.molinspiration.com
- [5] Virtual Computational Chemistry Laboratory: www.vcclab.org
- [6] CS Chem Office, Version 7.0, Cambridge Soft Corporation, Cambridge, MA, U.S.A., 2001.
- [7] A. C. Moffat, M. D. Osselton, B. Widdop (eds) Clarke's Analysis of Drugs and Poisons. 4th ed., Pharmaceutical Press, London, 2011.

K-05-P

MOLECULAR DOCKING STUDIES, SYNTHESIS AND STRUCTURAL CHARACTERIZATION OF TWO NOVEL SOFT CORTICOSTEROIDS

V. Dobricic,^{1*}, B. Markovic,¹ V. Savic,² N. Milenkovic,¹
S. Vladimirov,¹ O. Cudina,¹

¹*Department of Pharmaceutical Chemistry*

²*Department of Organic Chemistry*

*University of Belgrade-Faculty of Pharmacy, Vojvode Stepe 450, 11221
Belgrade, Serbia*

Abstract

In this study molecular docking calculations were performed on dexamethasone (anti-inflammatory drug) and four derivatives of hydrocortisone and methylprednisolone, simulating the interactions of these structures with the receptor for dexamethasone. Based on these results, methyl ester glycine amides of cortienic acids obtained from hydrocortisone and methylprednisolone were selected as compounds with potential anti-inflammatory activity. These compounds were synthesized in two steps from hydrocortisone and methylprednisolone. The first step is periodic oxydation of hydrocortisone and methylprednisolone to corresponding cortienic acids. The second step is amidation of obtained cortienic acids with glycine methyl ester hydrochloride. These compounds were structurally characterized using spectroscopic methods.

Introduction

Traditional drugs often undergo complex, multiple metabolic conversions to analog metabolites and reactive intermediates. Soft drugs are active as such, and consequently will produce the desired pharmacological activity at the site of application, but a predicted facile enzymatic process will metabolically deactivate the soft drug in a one-step process to an inactive species.[1] Cortienic acid is a metabolite of corticosteroids and it lacks anti-inflammatory activity. Soft corticosteroids are derived from cortienic acid and undergo predictive metabolism that reduces their toxicity. [2] The aim of this study is to select potentially active derivatives of hydrocortisone and methylprednisolone using molecular docking calculations and to synthesize and characterize these compounds.

Results and discussion

Molecular docking experiments

Molecular docking calculations were performed using Autodock v4.2 into the 3D structure of receptor for dexamethasone (pdb code:1m2z). Binding energies of
576

corticoid acids obtained from hydrocortisone and methylprednisolone (compounds 1 and 2, Figure 1) and methyl ester glycine amides of these acids (compounds 3 and 4, Figure 1) were calculated. These values were compared with the binding energy of dexamethasone (Table 1).

Table 1. Binding energies of synthesized compounds and dexamethasone.

Compound	Binding energy (kcal/mol)
Dexamethasone	-12.40
Compound 1	-10.74
Compound 2	-12.59
Compound 3	-11.32
Compound 4	-11.59

Compounds with the highest binding energies (compounds 2 and 4) were selected, synthesized and structurally characterized.

Synthesis of methyl 2-(11 β ,17 α -dihydroxy-3-oxo-androst-4-en-17 β -carboxamido)acetate

Hydrocortisone was oxidized to compound 1 (Figure 1) according to the literature procedure[3]. Compound 1 (50 mg, 0.14 mmol) was dissolved in 1,4-dioxane (10 ml) at room temperature. Subsequently, glycine methyl ester hydrochloride (MGH, 21 mg, 0.17 mmol), dimethylaminopyridine (DMAP, 21 mg, 0.17 mmol) and dicyclohexylcarbodiimide (DCC, 45 mg, 0.22 mmol) were added. After four days, reaction mixture was filtered and evaporated to dryness. Dry residue was dissolved in methanol and purified by preparative thin-layer chromatography, eluting with 95:5:1 (v/v/v) chloroform/methanol/glacial acetic acid, to yield the product (compound 2, Figure 1) as pale-yellow crystalline solid (12 mg, 20%). Melting point: 224-227.8 °C; IR (ATR) ν_{\max} (cm⁻¹): 3423.65, 2921.08, 1742.67, 1653.61, 1515.21, 1238.33; m/z = 418.3 (M⁻¹), 386.23, 368.27, 300.85, 342.27, 350.39, 400.30.

Synthesis of methyl 2-(11 β ,17 α -dihydroxy-6-methyl-3-oxo-androsta-3,4-dien-17 β -carboxamido)acetate

This compound (compound 4, Figure 1) was prepared, starting from methylprednisolone, as described in the preparation of compound 2. White crystalline solid was obtained (yield: 22%). Melting point: 142.5-144.5 °C; IR (ATR) ν_{\max} (cm⁻¹): 3343.26, 2936.29, 1747.05, 1651.57, 1600.25, 1523.47, 1210.84; ¹H NMR (500 MHz, CD₃OD) δ 7.49 (d, 1H, J=10.1 Hz), 6.25 (dd, 1H, J=10.0 and 1.7 Hz), 5.99 (s, 1H), 3.73 (s, 3H), 2.78-2.71 (m, 2H), 1.50 (s, 3H), 1.13 (d, 3H, J=6.3 Hz), 1.00 (s, 3H); ¹³C NMR (500 MHz, CD₃OD) δ 178.07, 177.35, 172.41, 161.02, 127.53, 119.83, 86.59, 71.07, 58.38, 52.73, 52.64, 46.50, 44.86, 41.99, 39.81, 34.67, 34.31, 32.96, 25.12, 22.13, 18.22, 17.88; m/z = 430.1 (M⁻¹), 380.18, 398.22, 354.22, 412.23, 313.13, 362.16.

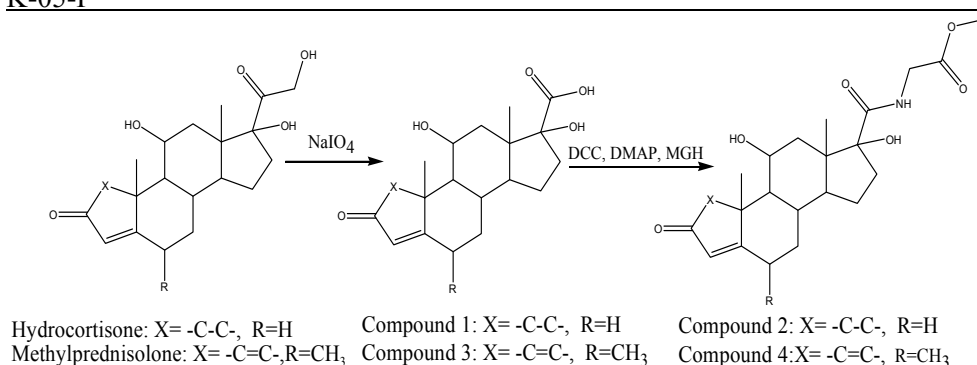


Figure 1. Synthesis of compounds 1-4.

Conclusion

Molecular docking calculations showed that compounds 2 and 4 have higher binding energies than compounds 1 and 3 (corticosteroids). This indicates that compounds 2 and 4 might have anti-inflammatory activity, which will be investigated *in vivo* by using the test of inhibition of croton oil-induced ear edema on rats. As potentially active soft corticosteroids, compounds 2 and 4 were synthesized in two steps and structurally characterized using spectroscopic methods.

Acknowledgement

This work was supported by the Ministry of education and science, Belgrade, Serbia, as part of project No. 172041.

References

- [1] Membranes and Barriers: Targeted Drug Delivery, in S. Rao, Ph. D. Rapaka (Eds), NIDA Research Monograph, 1995, 154.
- [2] N. Bodor, P. Buchwald, Soft drug design: general principles and recent applications, Center for Drug Discovery, University of Florida, Health Science Center, Florida.
- [3] S. Nicholas, N. Bodor, Soft steroids having anti-inflammatory activity, US patent No 4996335, 1991.

COMPARISON OF STATIC AND CONTINUOUS HOLLOW FIBRE LIQUID-PHASE EXTRACTION OF LUTETIUM

K R. Kumrić¹, T M. Trtić-Petrović¹, G T. Vladisavljević²

¹Laboratory of Physics, Vinča Institute of Nuclear Sciences, University of Belgrade, P.O. Box 522, Belgrade, Serbia, ²Loughborough University, Department of Chemical Engineering, Leicestershire LE11 3TU UK

Abstract

This work is a comparative study of the efficiency of the lutetium (III) extraction in membrane-assisted liquid-phase extraction (LPE) carried out under static and continuous operation mode using di(2-ethylhexyl)phosphoric acid (DEHPA) as a carrier. The removal of Lu(III) from the donor solution and its recovery into the acceptor phase were compared for the two operation modes investigated. Additionally, the applicability of both systems for purification of ¹⁷⁷Lu-radiopharmaceutical was discussed.

Introduction

Radionuclide ¹⁷⁷Lu possesses favorable radiophysical characteristics for therapeutic application in nuclear medicine [1]. One of the main steps in the production process of ¹⁷⁷Lu-radiopharmaceutical is the separation of bound from unbound radionuclide. Membrane-assisted LPE offers the possibility of purification of the ¹⁷⁷Lu-radiopharmaceuticals, after the labeling procedure [2, 3].

Membrane-assisted LPE operates in a three-phase system and involves simultaneous extraction and re-extraction. The pores of a microporous hydrophobic membrane are filled with the organic phase (extractant) held by the action of capillary forces, while the feed (donor) and the stripping (acceptor) solutions are placed on each side of the membrane. Membrane-assisted LPE can be performed in a miniaturized system under static or continuous mode of operation.

The aim of the present study was to compare the removal efficiency and re-extraction of Lu(III) achieved in a static and continuous flow membrane-assisted LPE system. The systems were investigated with regard to the potential application in purification of ¹⁷⁷Lu-radiopharmaceutical.

Results and Discussion

Lutetium was extracted using two different membrane-assisted LPE systems: (i) static, hollow fibre LPE system (HF-LPE) in the absence of flow of any phase, and (ii) dynamic, HF-LPE system with recirculation of the aqueous donor and acceptor phases. Microporous polypropylene hollow fibre membrane, ACCUREL 50/280 (Membrana GmbH, Wuppertal, Germany) was used in the experiments. The extraction was performed under predetermined optimum experimental conditions [3]: the donor phase of 2 mg dm⁻³ Lu(III) in 0.2 M sodium acetate buffer at pH 3.5, the organic phase composed of 5% DEHPA in di-hexyl ether and the acceptor

phase of 2 M HCl. The membrane wall was impregnated with the organic phase, the acceptor phase was in the lumen of HF, and the donor phase was outside the HF. The efficiency of mass transfer of Lu(III) through the liquid membrane was evaluated using the following parameters: the removal efficiency (R) that represents the fraction of Lu(III) removed from the donor phase, the extraction efficiency (E) that represents a fraction of Lu(III) initially present in the donor phase that was found in the acceptor after extraction and the memory effect (M) that is the fraction of Lu(III) captured in the organic phase.

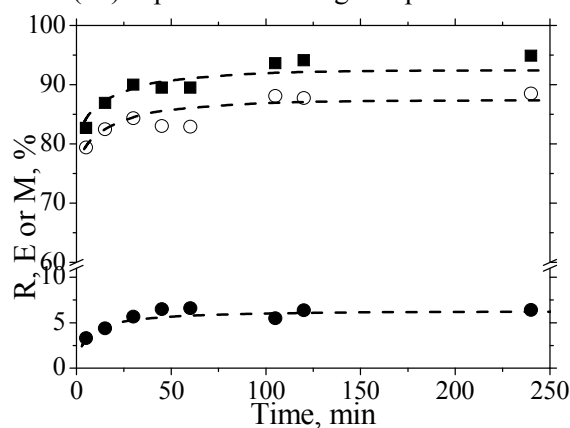


Figure 1. Time dependence of the efficiency parameters R (■), E (●) and M (○) in the static three phase HF-LPE system.

Fig. 1 shows the time-dependent parameters of Lu(III) transfer in HF-LPE under stagnant mode of operation with a volume of acceptor of 0.01 cm^3 . As can be seen, the stagnant system was efficient in terms of the removal of Lu(III) from the donor phase, but poorly efficient in terms of Lu(III) recovery from the organic into the acceptor phase. As the acceptor volume increased from 0.01 to 0.06 cm^3 as a result of increased HF length, the extraction efficiency improved from 5 to 15 % but even at the highest acceptor volume, 85% of the extracted amount of Lu(III) remained in the membrane. A further increase of the acceptor volume beyond 0.06 cm^3 was impractical.

Continuous HF-LPE of Lu(III) was carried out in the self-designed membrane contactor containing a single HF membrane. This configuration enables recirculation of both aqueous phases. Fig. 2 shows the time-dependent efficiency parameters in HF-LPE under recirculation of the acceptor phase (3 cm^3) through the lumen of the fibre and donor phase (20 cm^3) outside the fibre. As can be seen from Fig. 2, continuous HF-LPE system enables not only efficient removal of Lu(III) from the donor to the organic phase, but also its recovery from the organic to the acceptor phase. The accumulation of Lu(III) in the membrane was less than 5%, meaning that re-extraction of Lu(III) was almost complete.

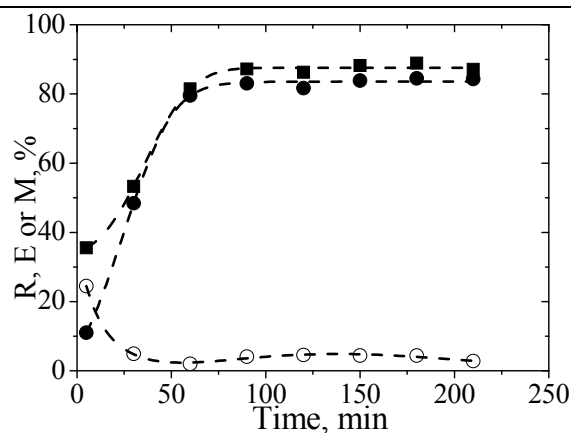


Figure 2. Time dependence of the efficiency parameters R (■), E (●) and M (○) in the HF-LPE system with the recirculation of aqueous phases (donor flow rate: $5.3 \text{ cm}^3 \text{ min}^{-1}$, acceptor flow rate: $0.4 \text{ cm}^3 \text{ min}^{-1}$).

Conclusion

The removal efficiency of Lu(III) from the aqueous donor solution was very high when both static and continuous HF-LPE were applied, which is of prime importance with regard to the potential application in purification of ^{177}Lu -based radiopharmaceuticals. The main advantage of continuous over static system is almost complete re-extraction of Lu(III) into the acceptor phase.

Considering practical aspects, static HF-LPE is easier to operate, which is very important when working with radioactive material, and more suitable for low volume production, as is often the case in radiopharmaceutical production. Continuous HF-LPE requires higher volumes of donor phase for the operation and there are more potential leakage points that can cause accidental release of radioactive material.

Acknowledgment

We acknowledge the support to this work provided by the Ministry of Education and Science of Serbia through project *Physics and Chemistry with Ion Beams*, No. III 45006.

References

- [1] S. Banerjee et al., *Nucl. Med. Biol.*, 2004, 31, 753-759.
- [2] K. Kumrić et al., *Sep. Purif. Techn.*, 2006, 51, 310-317.
- [3] T. Trtić-Petrović et al., *J. Sep. Sci.*, 2010, 33, 2002-2009.

K-07-P

LIQUID-PHASE MICROEXTRACTION IN A SINGLE HOLLOW FIBRE - DETERMINATION OF MASS TRANSFER COEFFICIENT

T. M. Trtić-Petrović¹, K. R. Kumrić¹, T. Vladislavljević²,
J. S. Đorđević¹, J. Åke Jönsson³

¹Laboratory of Physics, Vinča Institute of Nuclear Sciences, University of Belgrade, Belgrade, Serbia, ²Loughborough University, Department of Chemical Engineering, Leicestershire UK, ³Center for Analysis and Synthesis, Department of Chemistry, Lund University, Sweden

Abstract

In this study, the mass transfer coefficient of two local anesthetics in liquid-phase microextraction (LPME), which is performed in a single hollow fibre, was investigated. Previously developed mathematical model has been applied for the determination of the overall mass transfer coefficient based on the acceptor phase, K_A , in an unsteady-state LPME [1].

Introduction

Miniaturized LPME has been developed using flat or hollow fibre membrane and applied to concentrate analytes prior to chromatographic analysis [2]. Recently, an alternative concept of unsteady-state LPME in a single hollow fibre (HF-LPME) has been introduced [3] and focused mainly on sample preparation and equilibrium sampling.

The quantification of mass transport coefficients in LPME is important for a proper design and operation of the process and for the purpose of identification of rate limiting steps during mass transfer of solute(s) through the membrane. The overall mass transfer coefficient based on the acceptor phase, K_A , in HF-LPME has been estimated from time-dependent concentration of extracted analyte in the acceptor phase while maintaining a constant analyte concentration in the donor phase:

$$K_A = -\frac{V_A}{A} \frac{\partial}{\partial t} \left[\ln \left(\frac{C_A^* - C_A}{C_A^*} \right) \right] \quad (1)$$

where V_A is the volume of the acceptor phase, A is the area of the hollow fibre wall, and C_A^* and C_A is the equilibrium and actual concentration of the analyte in the acceptor phase in time t . The proposed conditions can be achieved either using a relatively large volume of the donor phase or tuning the extraction conditions in order to get a very low enrichment factor, so that the analyte concentration in the bulk of the donor phase can be regarded as a constant. The purpose of this work was to determine the overall mass transfer coefficient of the selected drugs in an unsteady-state HF-LPME.

Results and Discussion

The investigated local anesthetics bupivacaine (Bup) and lidocaine (Lid) are amines with the values of the dissociation constants (pK_a) of 8.9 and 8.5, respectively. The equilibrium extraction could be reached by adjusting the pH of

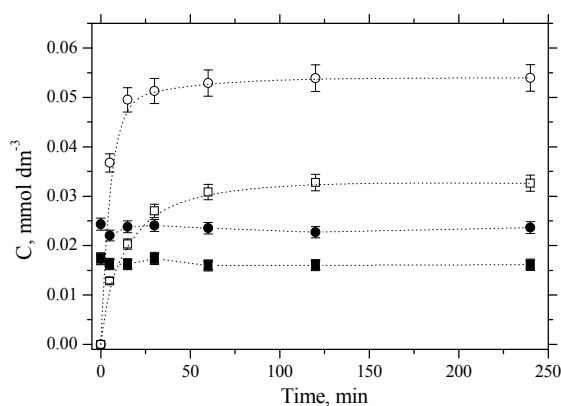


Figure 1. Time dependence of Lid and Bup in the acceptor (C_A) and donor (C_D) phases. Legend: Lid C_D - ●, C_A - ○; Bup C_D - ■, and C_A - □.

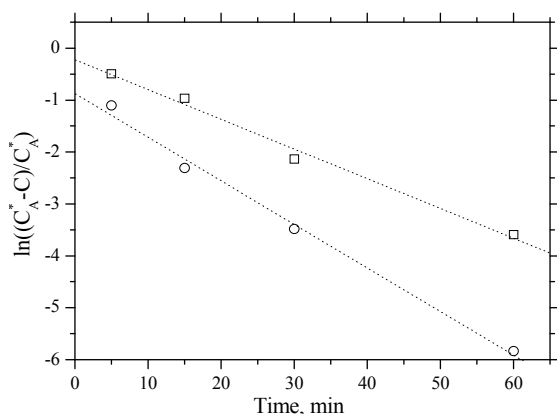


Figure 2. Semi-log plot of the local anesthetics concentration driving force versus time. Legend: ○ - Lid and □ - Bup.

Comparing the initial concentration of the drug in the donor phase (0.025 and 0.018 mmol dm^{-3} for Lid and Bup, respectively) and the concentration at certain extraction time, it can be seen that the depletion of the drug from the donor phase was less than 5%, and Eq. (1) can be applied for determination of K_A .

Fig. 2 is a plot of the ratio of concentration driving force (the difference between the equilibrium and actual concentration of the analyte in the acceptor phase) and equilibrium concentration in the acceptor phase versus time for the studied local anaesthetics. The similar dependence was obtained for the extraction

the acceptor solution. The stripping of the investigated compounds was complete at the acceptor pH at least 3 pH units below the pK_a value of the analyte. With increasing acceptor pH, the amount of nonextractable form of the amines in the acceptor decreased, the back extraction of the amine decreased and the resistance to the mass transfer in the acceptor phase increased.

The investigated drugs were extracted in the three phase extraction system [4], from the donor phase (0.067 mol dm^{-3} phosphate buffer at pH 7.5 or blood plasma), through the organic phase placed in the hydrophobic membrane pores (5% TOPO in di-hexyl ether), and finally reextracted into the acceptor phase. The experimental conditions of the acceptor pH can be found in Ref. [3]. Fig. 1 shows the time dependence of the concentration of the investigated drugs in the donor and acceptor phase.

K-07-P

of the local anesthetics from plasma sample. The slope of $\ln[(C_A^* - C_A)/C_A^*]$ vs. t line is equal to $-K_A A/V_A$ and enables K_A to be determined in a batch system under unsteady-state conditions. The calculated values of K_A of the investigated drugs are given in Table 1. The mass transfer coefficient of the drug with higher protein binding (Bup) was higher for extraction from buffer solution than that from plasma solution i.e. K_A was higher for the higher initial drug concentration.

Table 1. The overall mass transfer coefficient of studied local anesthetics.

Compound	Donor	C_D^{in} , mmol dm ⁻³	pH _A	$K_A \times 10^4$, cm min ⁻¹
Lidocaine	buffer	0.024	7.2	5.0
Lidocaine	plasma	0.024 (^a PB 11%)	7.2	5.1
Bupivacaine	buffer	0.017	7.4	3.4
Bupivacaine	plasma	0.017 (^a PB 69%)	7.4	3.0

^aPB is protein binding defined and estimated in Ref. [4]

Conclusion

The determination of the overall mass transfer coefficient in HF-LPME under non steady-state conditions was demonstrated in this paper. The results show that the developed mathematical model was successfully applied for determination of K_A .

Acknowledgment

We acknowledge the support to this work provided by the Ministry of Education and Science of Serbia through project No. III 45006.

References

- [1] K. Kumrić, et al, J. Sep. Sci., 2012, in press.
- [2] J.Å. Jönsson, et al, J. Sep. Sci., 2001, 24, 495-507.
- [3] S. Pedersen-Bjergaard, et al, J. Chromatogr. A, 2008, 1184, 132-142.
- [4] Trtić-Petrović, et al, J. Chromatogr. B, 2005, 826, 169-176.

^{99m}Tc-COMPLEX OF NOVEL DIAMINE-DIOXIME LIGAND

M. Mirković¹, S. Vranješ-Đurić¹, D. Stanković¹, Đ. Petrović¹, D. Mijin², N. Nikolić¹

¹Laboratory for Radioisotopes, Vinča Institute of Nuclear Sciences, University of Belgrade, P.O.Box 522, 11001 Belgrade, Serbia

²Faculty of Technology and Metallurgy, University of Belgrade, Karnegijeva 4, P.O. Box 3503, 11120 Belgrade, Serbia

Abstract

Novel diamine-dioxime ligand, 4,7-diaza-3,8-diethyldecane-2,9-dione bis oxime (LH₂), derivative of hexamethyl-propylene amine oxime (HMPAO), was synthesized in order to develop new brain perfusion imaging agent, based on ^{99m}Tc(V) complexes. The ^{99m}Tc(V)-d,l-HMPAO complex is well-known radiopharmaceutical for brain imaging. The structures of the synthesized compound were characterized by UV-Vis, IR, ¹H NMR and ¹³C NMR. The procedure for radiolabeling of diamine-dioxime with ^{99m}Tc was developed and radiolabeling yield of the ^{99m}Tc-complex was followed by paper and thin-layer chromatography. The maximum radiolabeling yield was obtained when the reactions were carried out at pH~9 within 10 min at room temperature (RT). Biodistribution studies on rats has shown significant uptake of ^{99m}Tc-complex (2.1% ID), 2 min after injection.

Introduction

The clinical usefulness of ^{99m}Tc-labeled complexes depends on their ability to rapidly cross cell membranes, high stability and rapid clearance from vital organs and tissues [1]. Among radiopharmaceuticals for imaging cerebral blood flow (CBF) by single-photon emission computed tomography (SPECT) in nuclear medicine, ^{99m}Tc-*d,l*-HMPAO (hexamethyl-propylene amine oxime) and ^{99m}Tc-*l,l*-ECD (ethyl cysteinyl dimer), combine the best overall features of high brain uptake, fixed regional distribution within the brain and their distribution in the brain is proportional to CBF in a wide range [2]. Both the ligands form neutral and lipophilic complexes with ^{99m}Tc possessing an oxotechnetium core. The HMPAO belongs to the class of diamine-dioxime compounds, which are good chelating agents due to the presence four nitrogen atoms that coordinate with ^{99m}Tc(V) in aqueous media. The goal of this work was to examine the use of a new ligand, derivative of HMPAO, as a potential candidate for the brain-perfusion imaging in SPECT. Although the ligand shows stereoisomerism, the presented work is based on research of isomeric mixtures of the meso- and *d,l*- diastereoisomers without the diastereo-enantio separation.

Experimental

^{99m}Tc ($T_{1/2}=6$ h, $E_{\gamma}=140$ keV) was eluted from a ^{99}Mo - ^{99m}Tc generator (The Vinča Institute of Nuclear Sciences, Belgrade, Serbia). All reagents obtained from commercial sources were of analytical grade and used without further purification. IR spectra were recorded on a Bomem MB 100 IR spectrophotometer using prepared KBr pellets. The ^1H and ^{13}C NMR spectral measurements were performed on a Varian Gemini 2000 (200 MHz) at RT with deuterated DMSO (d^6 -DMSO) as solvents. The melting points were determined by Mel-Temp melting point apparatus (Laboratory Devices Inc., USA). Radioactivity measurements were done in a NaI(Tl) well-type gamma counter (LKB Wallac Compu Gamma Counter, Finland). Spectrophotometric measurements were carried out using an Uvicon 810/820 spectrophotometer (Kontron Instruments, Austria) with 10 mm quartz cells.

Preparation of ligand. 4,7-diaza-3,8-diethyldecane-2,9-dione bis oxime (LH_2) was prepared using the method described in the literature [3]. Yield: 80%, mp: 133-134 °C. $\lambda_{\text{max}}=205$ nm. Selected IR data (KBr, pellets, cm^{-1}): ν_{OH} 3264, $\nu_{(\text{OH}, \text{NH})}$ 3212. ^1H NMR (200 MHz, DMSO- d_6 , δ ppm): 0.76 ($\text{CH}_3(\text{C}5)$, 3H, t, $J=7.5$ Hz), 1.35-1.50 ($\text{CH}_2(\text{C}4)$, 2H, m), 1.62 ($\text{CH}_3(\text{C}1)$, 3H, s), 2.34 ($\text{CH}_2(\text{C}6)$, 2H, s), 2.90 ($\text{CH}(\text{C}3)$, 1H, t, $J=7.3$ Hz), 10.32 (-OH, 1H, s). ^{13}C NMR (200 MHz, DMSO- d_6 , δ ppm): 10.89 C(1), 157.56 C(2), 63.12 C(3), 25.83 C(4), 8.37 C(5), 46.50 C(6).

Results and Discussion

Radiolabeling procedure. Radiolabeling conditions were optimized to give the maximum yield of ^{99m}Tc -complex. Complexation studies of ligand with $^{99m}\text{Tc}(\text{V})$ were carried out using SnCl_2 as a reducing agent. Dissolution of desire amount of LH_2 in oxygen-free double-distilled H_2O was achieved by acidification with HCl_{conc} to pH 1.5-2. The solution was bubbled with N_2 gas and cooled in an ice bath. Then, appropriate volume of SnCl_2 stock solution (5 mg of anhydrous SnCl_2 in 0.05 ml of HCl_{conc} diluted up to 10 mL of H_2O) was added and the pH adjusted to 9. After the addition of sodium pertechnetate ($^{99m}\text{TcO}_4^-$, 18.5-37 MBq/mL), the solution was gently shaken and allowed to stand 10 min at RT. The total reaction volume in vial was maintained at 4 mL. $\text{Sn}(\text{II})$: LH_2 mole ratio was 1:55.

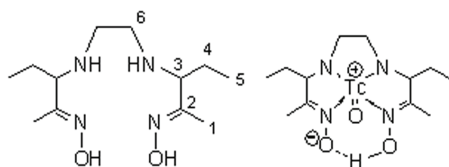


Figure 1. Structure of LH_2 and proposed structure of ^{99m}Tc -complex.

According to the literature data for similar diamino-dioxime ligands and their $^{99m}\text{Tc}(\text{V})$ -labeled complexes [4], proposed structures of LH_2 and ^{99m}Tc -complex are shown in Fig.1. Numbering of C-atoms in Fig.1 was used for ^1H NMR and ^{13}C NMR spectra interpretation.

Radiolabeling yield. The labeling yield as well as the stability of the ^{99m}Tc -complex were determined using a combination of two chromatographic systems: paper chromatography on Whatman No.1 with acetonitrile:water (1:1) as the mobile phase and TLC on silica gel 60 strips with saline as the mobile phase. Stability of the ^{99m}Tc -complex was determined by investigation of radiochemical purity of the complex at different time intervals after labeling (Fig.2A). The content of free $^{99m}\text{TcO}_4^-$ and ^{99m}Tc -reduced-hydrolyzed in the form of $^{99m}\text{TcO}_2$ were considered as radiochemical impurities.

Biodistribution of ^{99m}Tc -complex. Healthy male 8-weeks old Wistar rats, 200-250 g body weight (n=3 per each time point) were intravenously (i.v.) injected through the tail vein with 0.1 mL of ^{99m}Tc -complex (approx. 0.5–1.0 MBq per animal). The animals were sacrificed *via* spinal cord dislocation at 2, 5, 15, 30 and 60 min after injection and the radioactivity in brain was measured. ^{99m}Tc -complex exhibits good uptake in the brain (2.10% of injected dose (%ID)) at 2 min after injection (Fig.2B.)

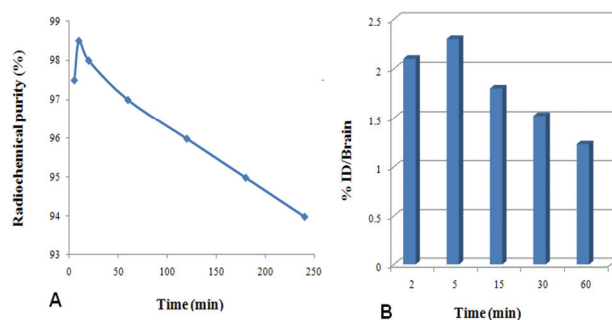


Figure 2. Radiochemical purity(A); Brain uptake(B) of the ^{99m}Tc -complex.

Conclusion

A new diamine-dioxime ligand, 4,7-diaza-3,8-diethyldecane-2,9-dione bis oxime (LH_2) were synthesized in high yields, characterized by UV-Vis, IR, ^1H , and ^{13}C NMR and successfully labeled with $^{99m}\text{Tc}(\text{V})$. From the obtained results, it can be concluded that $^{99m}\text{Tc}(\text{V})$ complex could be made easy with a ligand such as LH_2 . This complex showed good stability, higher than 94% up to 4h during storage at RT. The present study suggests that complex exhibited favorable properties as promising candidates for cerebral perfusion imaging.

References

- [1] M. Mallia, S. Subramanian, et al, Bioorg. Med.Chem. 2006, 14, 7666-7670.
- [2] F. Shishido, K. Uemura, et al, J. Cereb. Blood. Flow Metab. 1994, 14, 66-75.
- [3] S. Banerjee, G. Samuel, et al, Nucl. Med. Biol., 1999, 26, 327-338.
- [4] L. Canning, et al, United States Patent, Patent number 4.789.736, 1988,

K-09-P

^{99m}Tc(I)-TRICARBONYL LABELING OF ETHYLENE DIAMINE-N,N'-DI-3-PROPANOATE DIETHYL ESTER AS POTENTIAL RADIOPHARMACEUTICAL AGENT

M. Lakić¹, D. Janković¹, A. Savić², Lj. Sabo³, T. Sabo²

¹*Vinča Institute of Nuclear Sciences, University of Belgrade, Serbia*

²*Faculty of Chemistry, University of Belgrade, Serbia*

³*Clinical Center of Serbia, Belgrade, Serbia*

Abstract

There is an increasing interest for the ^{99m}Tc labeling of biomolecules by using bifunctional chelating agents like ethylenediamine-N,N'-di-3-propanoate diethyl ester (deeddp). To find new ligand, which can be linked to the small biomolecules and coordinated with [^{99m}Tc(CO)₃(H₂O)₃]⁺ precursor, is a challenging task. Radiolabeling of deeddp with [^{99m}Tc(CO)₃(H₂O)₃]⁺ precursor, stability studies and biodistribution of formed complexes were carried out, including challenge with histidine. Radiochemical yield of ^{99m}Tc(I)-tricarbonyl-deeddp complexes was higher than 95%. These complexes were stable *in vitro* and showed a very good biological behavior. The radiochemical and biological features of the novel ^{99m}Tc(I)-complexes, as well as, the nature of the ligands, make them very promising candidates for labeling of tumor specific biomolecules.

Introduction

Technetium radiopharmaceuticals, as complexes of the ^{99m}Tc radionuclide, are of great importance in diagnostic nuclear medicine. Over the last few years, the chemistry of a novel organometallic species, M(CO)₃⁺ (M=Tc, Re), has been intensively developed and the water soluble technetium tricarbonyl complex [^{99m}Tc(CO)₃(H₂O)₃]⁺ was seen to be very versatile and effective precursor for labeling biomolecules [1]. The three coordinated molecules of water are labile and could be readily exchanged with various mono-, bi- and tridentate ligands. New chelating agents have been synthesized with the aim toward the design and development of site-specific radiopharmaceuticals [2-4]. The aim of this study is to label ligand deeddp with ^{99m}Tc(I)-tricarbonyl precursor. The stability of the formed complexes and their *in vitro* and *in vivo* properties were investigated too.

Experimental

The sample of ligand was prepared by dissolving in water appropriate amount of substance for obtaining 10⁻³ mol/dm³ solutions. pH was adjusted to 9.0. ^{99m}Tc-carbonyl precursor was prepared according to the manufacturer instruction (IsoLinkTM, Mallinckrodt Medical B.V., The Netherlands). ^{99m}Tc(I)-tricarbonyl-ligand complexes were prepared by addition of 0.9 ml of ligand solutions to 0.1 ml of [^{99m}Tc(CO)₃(H₂O)₃]⁺ precursor with appropriate pH values. The vial was heated for 30 min in boiling water bath. The labeling efficiency of ^{99m}Tc(I)-tricarbonyl targeted ligand was determined using gradient HPLC equipped with UV and radioactive γ -detector on Nucleosil 100-5 C-18 column. The 0.1% solution of TFA

(trifluoroacetic acid) in H₂O and 0.1% of TFA in acetonitrile were used as mobile phases. Aliquot of 100 µl of the ^{99m}Tc complexes (final concentration of ligands 10⁻⁶ M) was added to 900 µl of a 10⁻² M histidine solution in PBS (phosphate buffered saline), pH 7.4. The samples were incubated at 37^o C and periodically aliquots were removed and analyzed by HPLC. TCA (trichloroacetic acid) precipitation method for determining the percentage of ^{99m}Tc(I)-tricarbonyl-deeddp bound to proteins (12% human albumin, incubation at 37^oC for different time intervals) was very useful. All lipophilicity measurements were done by solvent extraction method with n-octanol equilibrated with 0.15M phosphate buffers (pH=6.0-7.5). Organ biodistribution studies were carried out on white health Wistar rats (four weeks old). The animals were sacrificed 5, 30, 60 and 120 minutes after application of 0.1ml of ^{99m}Tc(I)-tricarbonyl-deeddp. The radioactivity per organ of interest was measured in a NaI(Tl) detector.

Results and Discussion

The bifunctional chelating agent approach is currently among the cutting edge technologies used in the design of new radiopharmaceuticals. The choice of a chelator agent may be crucial in the biological behavior of a radiopharmaceutical. A novel bifunctional chelating agent deeddp has been synthesized and characterized. Radiolabeling of deeddp with the [^{99m}Tc(CO)₃(H₂O)₃]⁺ precursor with heating at 95^oC and at pH 8-9 led to the formation of ^{99m}Tc(I)-tricarbonyl-coordinated complexes of deeddp with a radiochemical yield higher than 95% as determined by HPLC analysis. The three peaks in the radio-HPLC profile indicated the presence of isomers (Fig.1). Radiochemical stability was monitored during 24 h. ^{99m}Tc(I)-tricarbonyl-deeddp complexes showed a good stability and less than 5% of radiochemical impurities were observed even for the later time point studied. Challenge experiments with up to 1000-fold molar excess of histidine showed no degree of transchelation for radiocomplex during 24 h at 37^oC.

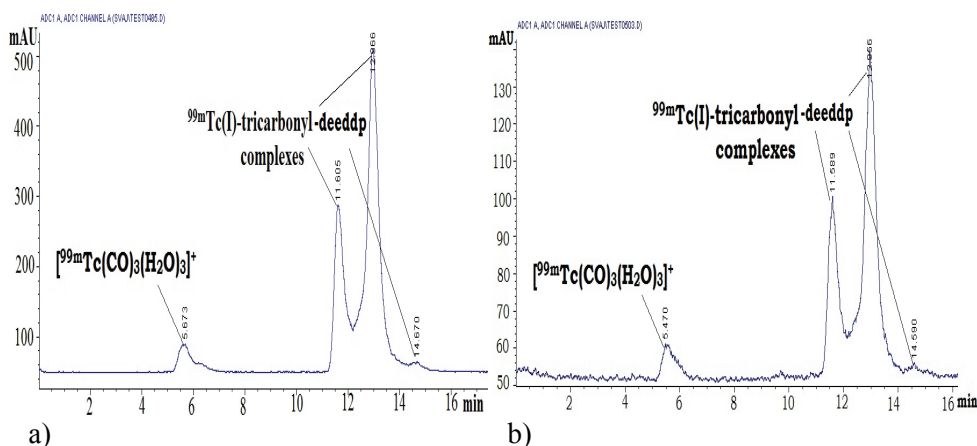


Figure 1. Radiochromatograms of ^{99m}Tc(I)-deeddp complexes a) 30 minutes after labeling b) 24h after labeling.

We assessed the interaction of $^{99m}\text{Tc}(\text{I})$ -tricarbonyl-deeddp complexes with human serum albumin as an important constituent of human blood which could affect on their biological behavior. At 1h, the binding was $10.49 \pm 1.23\%$. The lipo-hydrophilic character of $^{99m}\text{Tc}(\text{I})$ -tricarbonyl-deeddp complexes was evaluated based on the octanol/water partition coefficient (K_d). K_d value was 0.63 ± 0.05 (mean \pm S.D.) arguing for a higher lipophilic character of the complexes.

Figure 2 shows the biodistribution results for $^{99m}\text{Tc}(\text{I})$ -tricarbonyl-deeddp complexes. The first set of biodistribution data, 5 min post injection (pi), showed a very high uptake in liver, kidneys and intestine. The radioactivity was quickly cleared from liver and kidneys, thereby reaching very low levels within 120 min pi. Moreover, a remarkable intestinal uptake was observed for $^{99m}\text{Tc}(\text{I})$ -tricarbonyl-deeddp complexes even at the later time points studied.

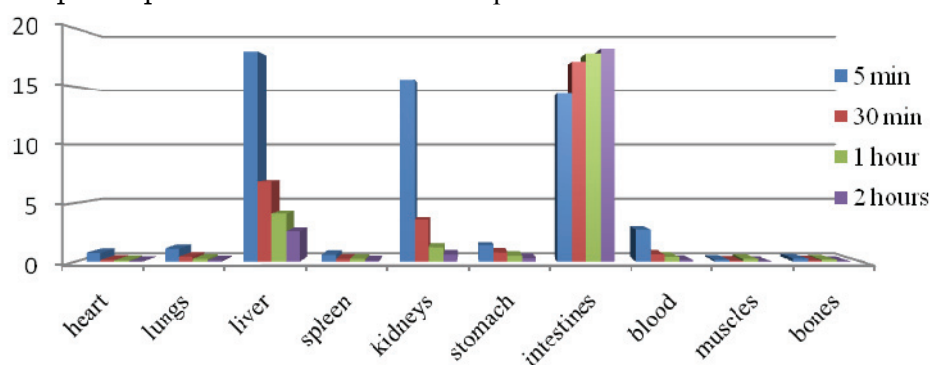


Figure 2. Organ distribution data of $^{99m}\text{Tc}(\text{I})$ - tricarbonyl-deeddp in Health Wistar rats (% ID/g)

Conclusion

The studied ligand, having a bifunctional NN donor atom set, was easily coordinated with $^{99m}\text{Tc}(\text{I})$ -tricarbonyl core in aqueous solution forming neutral complexes. Radiochemical purity and yield of labeling were very high. The complexes were very stable for at least 24 hours. The labeled deeddp ligand has been shown to be very stable against ligand exchange, and due to its relative lipophilicity has a very good biodistribution profile. With these points in mind this chelating agent provides a promising architecture for use in labeling tumor specific biomolecules.

References

- [1] R. Alberto, R. Schibli, A. Egli, P. A. Schubiger, *J. Am. Chem. Soc.*, 1998, 120, 7987-7988.
- [2] R. Schibli, R. La Bella, R. Alberto, et al, *Bioconj. Chem.*, 2000, 11, 345-351.
- [3] M. Santimaria, U. Mazzi, S. Gatto, et al, *J. Chem. Soc. Dalton Trans.*, 1997, 42, 1765-1771.
- [4] G. N. Kaluđerović, T. J. Sabo, *Polyhedron*, 2002, 21, 2277-2282.

PHYSICOCHEMICAL EVALUATION OF TECHNETIUM-99m COMPLEXES WITH BACLOFEN

D. Stanković, D. Janković, M. Mirković, M. Lakić,
S. Vranješ-Djurić, N. Nikolić

*Laboratory for Radioisotopes, Vinča Institute of Nuclear Sciences,
University of Belgrade, P.O.Box 522, 11001 Belgrade, Serbia*

Abstract

The ^{99m}Tc -labeling of baclofen (Bac), a muscle relaxant, as well as physicochemical properties of the labeled compounds are investigated. Two different approaches for the labeling with ^{99m}Tc have been studied: direct reduction with tin(II)chloride and the 'organometallic approach' using $[\text{}^{99m}\text{Tc}(\text{CO})_3(\text{H}_2\text{O})_3]^+$ precursor. The direct labeling approach was not successful and the yield was poor. The use of $[\text{}^{99m}\text{Tc}(\text{CO})_3(\text{H}_2\text{O})_3]^+$ precursor pointed at the formation of $^{99m}\text{Tc}(\text{I})$ coordinated complexes with high yield. In this approach, pH didn't influence the yields. Promising results of *in vitro* experiments suggest that $^{99m}\text{Tc}(\text{I})$ -baclofen may be of potential use for diagnosis of some central nervous system disorders.

Introduction

Baclofen is a structural analogue of gamma-aminobutyric acid (GABA). It is a selective agonist of GABA_B receptors in central nervous system and it's primarily used to treat spasticity. Also, it is in the early stages of use for the treatment of alcoholism. Baclofen is a muscle relaxant medicine commonly used to decrease spasticity related to multiple sclerosis, spinal cord injuries, or other neurological diseases. It could be used in oral use or intrathecal way. Its ways in organism are not well known nowadays [1].

^{99m}Tc has ideal physical properties for many applications in nuclear medicine therefore it is still the radionuclide of choice. A large number of techniques for radiolabeling with ^{99m}Tc have been developed. They are classified as: direct labeling, the preformed chelate approach and the bifunctional chelating or indirect labeling approach. The study of technetium radiopharmaceuticals has been stimulated by the availability of radioactive $^{99m}\text{Tc}(\text{I})$ precursor $[\text{Tc}(\text{CO})_3(\text{H}_2\text{O})_3]^+$ [2]. As the three water ligands are labile, they can be readily exchanged with different mono-, bi- and tridentate donor ligands, like phosphines, thioethers and aromatic amines. Hydrophilic organometallic $[\text{}^{99m}\text{Tc}(\text{H}_2\text{O})_3(\text{CO})_3]^+$ precursor allows the formation of Tc (I) radiopharmaceuticals based on the fac- $[\text{}^{99m}\text{Tc}(\text{CO})_3]^+$ (I) core. This way is known as 'organometallic labeling approach'[3]. In this paper the possibility for the formation of ^{99m}Tc complexes with baclofen was studied.

Experimental

All chemicals used in our experiments were of analytical purity grade (Sigma Aldrich and Merck). The direct labeling method was investigated performing different experiments by varying the reducing agent amount, the labeling mixture pH (3.0-8.0) and the reaction temperature. An aqueous solution of baclofen (10^{-3}M) was prepared.

K-10-P

To a 10 ml vial, 0.3 ml of baclofen solution in H₂O was added and followed by SnCl₂·2H₂O solution (10⁻⁴M) in 0.1 M HCl, thus molar ratios Sn(II):baclofen were 1:1, 1:10, 1:25 and 1:50. The stock solution of SnCl₂·2H₂O was prepared by dissolving of the measure amount of the pure salt in concentrated HCl and then diluting it with doubly distilled water under the define volume. pH of these mixtures was adjusted at 3.0, 5.0 and 8.0, to the total volume of 3.0 ml. 18.5 MBq ^{99m}TcO₄⁻ eluate in 0.9% NaCl, from ^{99m}Tc-generator (Vinča) was added. The reaction mixtures were allowed to stand at room temperature (RT) or heated at boiling temperatures for 30min.

[^{99m}Tc(CO)₃(H₂O)₃]⁺ ion was prepared by addition of 1ml of ^{99m}Tc-pertechnetate (740-1110 MBq ^{99m}TcO₄⁻) to a penicillin vial with lyophilized form of 7.15 mg sodium carbonate, 4.5 mg sodium boranocarbonate, 2.85 mg sodium tetraborate and 8.5 mg sodium tartarate (IsoLink™, Mallinckrodt Medical B.V., The Netherlands). After heating for 30 minutes in a boiling water bath and cooling, pH of solution was adjusted to desired value with 1M HCl. ^{99m}Tc-carbonyl-baclofen was prepared by addition of 0.1 ml of investigated muscle relaxant solutions to 0.9 ml of [^{99m}Tc(CO)₃(H₂O)₃]⁺ precursor. The samples were labeled with ^{99m}Tc (I), without and with heating (30 min in boiling water bath). The complex stability after 24 hour time was investigated, too.

HPLC analysis was performed by isocratic HPLC. All measurements were made on liquid Chromatograph, Hewllet Packard 1050 (C18column (250x4,6mm)) with UV and Raytest gamma flow detector. The different methanol/water mixtures prepared from HPLC grade water, were used as mobile phases.

Results and Discussion

The direct labeling method was not successful and the labeling yield was poor. Varying of the reducing agent amount, the labeling mixture pH (3.0-8.0) and the reaction temperature did not improve the yield substantially. However the use of [^{99m}Tc(CO)₃(H₂O)₃]⁺ precursor, at pH 3.0, 5.0 and 8.0 with and without heating resulted in the formation of ^{99m}Tc(I) coordinated complexes of baclofen in high yields that was shown by radiochromatograms. The best results are obtained at pH 3.0 (Fig.1) and 8.0 at RT. The retention times together with the labeling yield are summarized in Table 1.

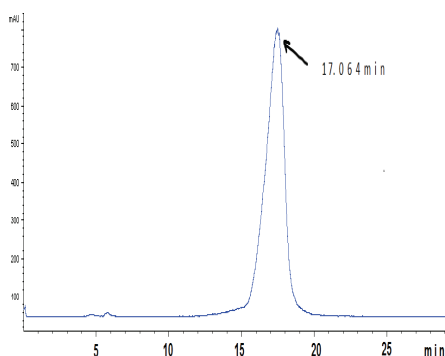


Figure1. HPLC radiochromatogram of ^{99m}Tc(I)-Bac labeled at RT, pH=3.0

Table 1. The influence of pH and heating on retention times (R_t) and labeling yield (Y) of baclofen coordinated to $[^{99m}\text{Tc}(\text{CO})_3(\text{H}_2\text{O})_3]^+$ precursor.

Samples	pH	3.0		5.0		8.0	
	^{99m}Tc -species	R_t (min)	Y (%)	R_t (min)	Y (%)	R_t (min)	Y (%)
$[^{99m}\text{Tc}(\text{CO})_3(\text{H}_2\text{O})_3]^+$ +Bac, at RT	$^{99m}\text{Tc}(\text{CO})_3$	5.238	0.3	5.215	11.2	5.082	1.2
	$^{99m}\text{Tc}(\text{I})\text{-Bac}$	17.064	99.7	16.238	88.8	16.354	98.8
$[^{99m}\text{Tc}(\text{CO})_3(\text{H}_2\text{O})_3]^+$ +Bac, with heating at 95°C	$^{99m}\text{Tc}(\text{CO})_3$	5.296	4.9	5.262	14.9	4.940	6.8
	$^{99m}\text{Tc}(\text{I})\text{-Bac}$	16.770	95.1	14.386	85.1	16.659	93.2
$[^{99m}\text{Tc}(\text{CO})_3(\text{H}_2\text{O})_3]^+$ +Bac, at RT after 24h	$^{99m}\text{Tc}(\text{CO})_3$	5.257	1.6	5.317	14.8	5.267	7.1
	$^{99m}\text{Tc}(\text{I})\text{-Bac}$	17.076	98.4	15.277	85.2	14.417	92.8
$[^{99m}\text{Tc}(\text{CO})_3(\text{H}_2\text{O})_3]^+$ +Bac, with heating at 95°C after 24h	$^{99m}\text{Tc}(\text{CO})_3$	5.325	15.2	5.346	15.9	5.248	8.2
	$^{99m}\text{Tc}(\text{I})\text{-Bac}$	15.327	84.8	15.513	84.1	14.151	91.8

HPLC results revealed that radiolabeling yields were not significantly affected by pH values within the range pH 3.0–8.0 at RT. We assume that the different retention times of formed complexes are a consequence of the influence of pH and temperature on the structure and composition of these complexes. Bac contains both a carboxyl and an amino group and by a change in pH these groups are in their protonated or deprotonated forms. Depending on the forms, Bac can be mono- or bidentate ligand and easily forms different complexes with the *fac*- $[^{99m}\text{Tc}(\text{CO})_3]^+$ (I) core. The following experiments on animals should show the impact of different structures of the complexes on their biological behavior. All complexes showed excellent stability in 24 hour time (>80%).

Conclusion

The results presented in this paper reveal that complexation of the baclofen are highly dependent on the labeling approach and the oxidation state of ^{99m}Tc . Direct ^{99m}Tc -labeling of baclofen, known to be weak-chelating agent, gave high concentrations of $^{99m}\text{TcO}_2^-$ and free $^{99m}\text{TcO}_4^-$. The best labeling yield was obtained with $[^{99m}\text{Tc}(\text{CO})_3(\text{H}_2\text{O})_3]^+$ precursor when labeling was done at RT.

References

- [1] A. C. Miracle, M. A. Fox et al., Am. J. Neuroradiol., 2011, 32, 1158-1164.
- [2] R. Alberto, R. Schibli, A. Egli, P. A. Schubiger, J. Am. Chem. Soc., 1998, 120, 7987-7988.
- [3] A. Egli, R. Alberto, L. Tannatoli, R. Schibli et al, J. Nucl. Med., 1999, 40, 1913-1917.

K-11-P

PREPARATION OF ^{90}Y -LABELED TIN FLUORIDE COLLOID FOR RADIOSYNOVECTOMY

D. Janković, S. Vranješ-Djurić, M. Marković, M. Mirković, D. Stanković, M. Lakić, N. Nikolić

Laboratory for radioisotopes, Vinča Institute of Nuclear Sciences, University of Belgrade, P.O.Box 522, Belgrade 11001, Serbia

Abstract

In this study, tin fluoride colloid (SnF-c) was prepared, labeled with ^{90}Y and characterized with respect to its physicochemical properties.

Particle size of SnF-c, at constant concentration of SnF_2 , was dependent on pH, concentration of NaF, temperature and time. The particle size of SnF-c decreased with an increase in NaF concentration and a decrease in reaction mixture pH. Radiolabeling yield of ^{90}Y -SnF-c at higher temperature increased and it was greater than 98% for the preparation at 95 °C. Due to high labeling yield and stability, ^{90}Y -SnF-c might be a promising agent for radiosynovectomy.

Introduction

Radiosynovectomy (RS) was introduced as a modality for the treatment of rheumatoid arthritis as early as 1950's and the number of studies has been growing each year [1, 2]. Due to its convenience, long-term effects, repeatability and surgery avoidance, RS has been used for the treatment of resistant synovitis of individual joints after failure of long-term systemic pharmacotherapy and intra-articular steroid injections. The method is based on local intra-articular injection of β -emitting radionuclides in colloidal form to counteract and control synovial inflammation. Particle size, shape, charge and stability of a radiocolloid suspension are significant parameters that determine its organ distribution in vivo. The selection of proper radiopharmaceutical for the treatment of large, medium or small joints depends on the penetration range of β -emitting radionuclide and colloid particle size [3]. Yttrium-90 (^{90}Y) is a clinically acceptable β -emitting radionuclide and due to a half-life of 64.4 hours, $E_{\text{max}\beta}$ of 2.27 MeV and a mean/maximum penetration depth of 3.6/11 mm it is ideal for therapy purpose. Our experiments included investigation of the factors influencing preparation of SnF-c and ^{90}Y -labeling, as well as the stability of the prepared radiocolloid.

Experimental

$^{90}\text{YCl}_3$ was purchased from Polatom, Poland, in a no-carrier-added form. All other reagents and solvents purchased from commercial sources were used without further purification.

To prepare ^{90}Y -SnF-c, 1 ml aliquots of nitrogen purged water for injection, containing 0.125 mg SnF_2 and different amounts of NaF with pH maintained at 5.1 and 5.9, were filtered (0.22 μm , Millipore Co.), dispensed into vials under nitrogen atmosphere and lyophilized for 24 h. The level of NaF was varied: 0.2, 0.5, 1, 2.5 and 5 mg/mL designated as SnF-c1, SnF-c2, SnF-c3, SnF-c4 and SnF-c5

formulation, respectively. The final pH of suspensions was kept at 5.1 and 5.9. Freeze-dried formulations (in triplicate) kept in shielded vials were reconstituted with 5 ml of water for injection. Then 5-15 μl of $^{90}\text{YCl}_3$ stock solution (about 185 MBq) was added to each vial. The reaction vials were shaken at room temperature (RT) or at 50 and 95 $^\circ\text{C}$ for 15, 30 or 60 min and cooled to room temperature. Then, the suspensions were additionally shaken at low speed up to 3 h.

The radiolabeling yield (RY) of radiolabeled colloid was determined by instant thin layer chromatography (ITLC). Particle size distribution, polydispersity index and zeta potential (ZP) were measured by Dynamic Light Scattering (DLS) technique using a Zetasizer Nano ZS (Malvern, UK) with 633 nm He-Ne laser and 173 $^\circ$ detection optics (backscatter detection). The radioactive particle size distribution (RPSD) of ^{90}Y -SnF-c was performed by successive membrane filtration steps of a single sample through 1.0, 0.4 and 0.2 μm pore size membrane filters. The stability of ^{90}Y -SnF-c was evaluated for a period up to 7 days by determining its radiochemical purity (RCP) with ITLC at different times after preparation.

Results and Discussion

The main goal of this study, the preparation of ^{90}Y -SnF-c, which can be successfully used for RS was achieved. The SnF-c used in this study as colloid template appears to be very suitable for labeling with beta emitting radionuclides. The SnF-c was prepared in lyophilized form and the particle size of the colloid was adjustable by varying the ratio of SnF_2 to NaF (w/w ratio SnF_2 : NaF up to 1:200).

Radiolabeling of SnF-c with ^{90}Y is a simple procedure, which provides a very high yield of labeled particles. ITLC-SG/saline method enables quantitative determination of ^{90}Y -labeled colloid remained at the origin and unbound ^{90}Y in the form of $^{90}\text{YCl}_3$, which migrates with the solvent front. Although the radiolabeling of SnF-c with $^{99\text{m}}\text{Tc}$ occurs nearly instantaneously, the radiolabeling with ^{90}Y required an extended period of boiling. The RY of ^{90}Y -SnF-c increases as a function of temperature and time, reaching the highest value of >98% at 95 $^\circ\text{C}$, after reaction mixture boiling for 30 min. Obviously, the heating step during SnF-c labeling was essential to get a product with high radiolabeling yield and improved stability. The stability and size-range of all batches of ^{90}Y -SnF-c, prepared by heating and agitation for different times were analyzed. As observed in our set of experiments, temperature, agitation and time affect both the radioactivity tagged to particles and the size of particles. The particles come in contact with each other and the probability of their sticking together depends on repulsive as well as attractive forces, due to increasing temperature and agitation time.

To better understand the formation of ^{90}Y -SnF-c as well as their radiolabeling and to define primary particles (templates), the particle size of lyophilized formulations (for SnF-cT1 to SnF-cT5) reconstituted with water (no YCl_3 added) was measured. Our results of PSD measurement confirmed the existence of primary colloidal particles (templates) with diameter of 123-138 nm in SnF_2 -NaF suspensions at room temperature before radiolabeling. These primary particles in all formulations first aggregate, and finally agglomerate as a function of temperature, agitation and aging (schematic presented in Fig. 1).

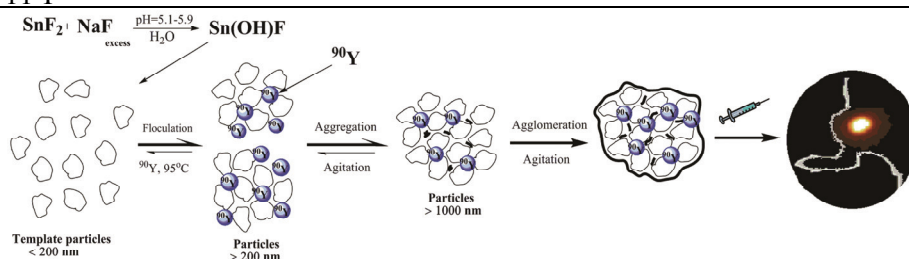


Figure 1. Formation of ^{90}Y -Labeled tin fluoride agglomerates from template particles.

The factors affecting the formation of stable, cemented SnF agglomerates were not well understood. Generally, if an aggregate survives long enough, sufficient cementation will occur to form stable agglomerate that can no longer be ruptured along the lines of contact of the original flocculating particles. To test the formation of stable agglomerate, the sample was withdrawn from the light scattering cell into syringe, re-syringed, put back into the cell and then particle sizes were measured again. The average particle diameter value remained unchanged. According to the results obtained, we conclude that the agglomeration rate increases with increasing temperature during radiolabeling and prolonged time of shaking, and that the large particles are agglomerates of the small ones.

The rate of Sn(II) hydrolysis depends on the concentration of NaF in the reaction mixture. We assumed that SnF_2 in formulations (Y-SnF-c1 - Y-SnF-c3) was partially hydrolyzed because the present NaF concentrations were not sufficient to completely suppress Sn(II) hydrolysis. Higher concentrations of NaF (>1 mg/mL) in the reaction mixture prevented formation of Sn(II) hydroxo complexes in the suspension.

The ^{90}Y -SnF-c demonstrated high *in vitro* stability in either human serum or human synovial fluid at 37 °C up to 7 days.

Conclusion

The present study has shown that ^{90}Y -SnF-c particles can be prepared with high labeling yield and *in vitro* and *in vivo* stability. The particle size of ^{90}Y -SnF-c was controllable by manipulating the conditions under which the colloids form. The optimum size of colloid particles can be easily designed for different therapeutic applications. Promising results suggest that ^{90}Y -SnF-c depending on particle size, may be of potential use for RS.

References

- [1] P. Schneider, J. Farahati, C. Reiners, J. Nucl. Med., 2005, 46, 48-54.
- [2] W. U. Kampen, M. Voth, J. Pinkert, A. Krause, Rheumatology, 2007, 46, 16-24.
- [3] C. Turkmen, J. Coag. Dis., 2009, 1, 29-36.

**THE INFLUENCE OF VARIOUS INORGANIC
CHLORIDE SALTS ON THE SYNERGIC EFFECT IN
THE EXTRACTION OF PARACETAMOL
FROM AQUEOUS SOLUTIONS BY
THE DIETHYL ETHER/1-BUTANOL MIXTURES**

G. M. Nikolić¹, J. V. Živković¹, D. Vlajin¹, D. Atanasković¹, M. G. Nikolić²

¹*University of Niš, Faculty of Medicine, Department of Chemistry, 18000 Niš,
Serbia; e-mail: goranhem@yahoo.com*

²*University of Niš, Faculty of Natural Sciences, Department of Chemistry*

Abstract

We investigated the influence of ammonium-, sodium-, and potassium chloride on the synergic effect in the extraction of paracetamol from aqueous solutions by the diethyl ether/1-butanol solvent mixture. All the salts used in this study improved extraction efficacy of paracetamol and synergic effect was observed in the whole composition range of binary solvent mixtures. Highest distribution rate value was obtained by the use of KCl for the solvent mixture rich in 1-butanol.

Introduction

Determination of paracetamol in various samples is of great importance because its misuse may lead to serious toxic effects (eg. hepatic necrosis) [1]. Diethyl ether alone or in combination with some other organic solvents is often used for liquid-liquid extraction step during the sample preparation for analysis [2]. However, as in the case of some other phenolic compounds [3], paracetamol is poorly extracted with diethyl ether and this problem could be surmounted by the use of salting-out or/and extraction with binary mixtures of organic solvents (synergism) [3, 4]. We already reported the synergic effect in the extraction of paracetamol from aqueous NaCl solution [4] and in this paper we present the results concerning the influence of various inorganic chloride salts on the synergic effect in the extraction of paracetamol from aqueous solutions with the diethyl ether/1-butanol mixtures.

Materials and Methods

All the chemicals used in this study were of analytical grade quality and have been used without further purification. Stock solution of paracetamol (0.01 mol dm^{-3}) was prepared by dissolving exactly weighted mass of pure substance in doubly distilled water and 0.01 mol dm^{-3} solution of HCl was added to adjust the pH value to ~ 2 . For each series of extractions stock solution was diluted 100 times with water or 2 mol dm^{-3} solution of appropriate salt. Extraction was performed by the shake-flask method for each binary solvent mixture composition in triplicate.

The absorbances of aqueous phases were measured by the Evolution 60 UV/Vis scanning spectrophotometer (Thermo Scientific, USA) at 243 nm and the distribution ratio (D) of paracetamol was calculated by using the equation

$$D = \frac{A_0 - A}{A} \times \frac{V_{aq}}{V_{org}}$$

where A_0 and A were absorbances of the aqueous phases before and after extraction, and V_{aq} and V_{org} were the volumes of aqueous and organic phase, respectively.

Synergic effect in the extraction of paracetamol was quantified by calculating the synergic coefficient, K_c , according to the equation

$$K_c = \log (D_{mix}/D_{add})$$

where D_{mix} represented experimental and D_{add} theoretically predicted distribution ratio values, respectively [5].

Theoretically predicted distribution ratio was calculated as

$$D_{add} = D_1 \times x_1 + D_2 \times (1-x_1)$$

where D_1 and D_2 represented distribution ratios of paracetamol for pure solvents, and x_1 was mole fraction of one pure solvent in binary mixture.

Results and Discussion

The dependence of paracetamol distribution ratio on the composition of diethyl ether/1-butanol binary mixture is shown in Fig.1.

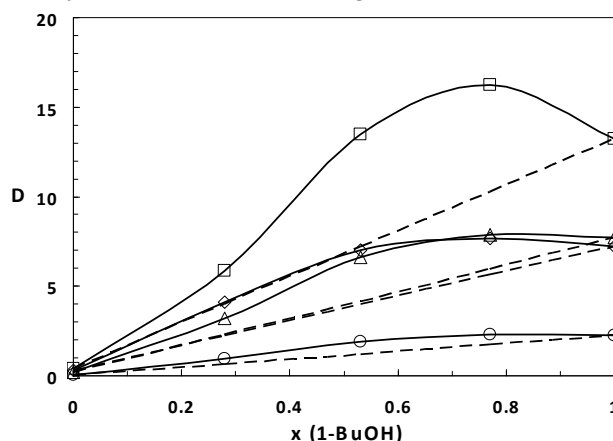


Figure 1. Dependence of paracetamol distribution ratio on the composition of diethyl ether/1-butanol binary mixture from the aqueous solutions with no salt added (circles), NH_4Cl (triangles), NaCl (rhombs), and KCl (squares), respectively. Dashed lines present dependence of respective values for D_{add} on the composition of diethyl ether/1-butanol mixture.

Distribution ratios of paracetamol were higher than theoretically predicted values for all the systems investigated in this work in the whole composition range of the diethyl ether/1-butanol binary mixture. Highest distribution rate value was obtained by the use of KCl for the solvent mixture rich in 1-butanol. It is noteworthy that although D values for pure 1-butanol are much higher than D values for pure diethyl

ether in all cases the highest D values were obtained with the mixtures containing small amounts of diethyl ether. Similar results indicating that solvent mixtures are more efficient than individual solvents have been reported in the literature for the extraction of ascorbic and nicotinic acids by the ethyl acetate/1-butanol and butyl acetate/1-butanol binary solvent mixtures with the explanation that some kind of complexes were formed in the extraction mixture [5].

Values of synergic coefficient, K_c , obtained for systems investigated in this study are shown in Table 1.

Table 1. Values of synergic coefficient, K_c , for the extraction of paracetamol from aqueous solutions by the diethyl ether/1-butanol binary mixtures.

x (1-BuOH)	K_c			
	No salt	NH ₄ Cl	NaCl	KCl
0.28	0.202	0.153	0.264	0.175
0.53	0.219	0.199	0.244	0.270
0.77	0.130	0.117	0.131	0.197

Highest K_c value was obtained again in the system containing KCl but this time at the approximately equimolar composition of solvent mixture. Also it can be noted that presence of NH₄Cl, in contrast to NaCl and KCl, resulted in lower K_c values in comparison to the extraction of paracetamol from pure aqueous solution.

Conclusion

All the salts used in this study improved extraction efficacy of paracetamol and synergic effect was observed in the whole composition range of binary solvent mixtures. Highest distribution rate value was obtained by the use of KCl for the solvent mixture rich in 1-butanol.

Acknowledgements

This work was supported by the Ministry of Education and Science of the Republic of Serbia under the Project TR 31060.

References

- [1.] M. Espinosa Bosch, A. J. Ruiz Sánchez, F. Sánchez Rojas, C. Bosch Ojeda, J. Pharm. Biomed. Anal., 2006, 42, 291-321.
- [2.] H. Li, C. Zhang, J. Wang, Y. Jiang, J. Paul Fawcett, J. Gu, J. Pharm. Biomed. Anal., 2010, 51, 716-722.
- [3.] G. M. Nikolić, J. M. Perović, R. S. Nikolić, M. M. Cakić, Facta Universitatis Ser. Pys. Chem. Techn., 2003, 2, 293-299.
- [4.] G. M. Nikolić, J. V. Živković, M. G. Nikolić, F. Miljković, Eur. J. Pharm. Sci., 2011, 44 (Suppl.1), 183-184.
- [5.] N. Ya. Mokshina, O.V. Erina, O.A. Pakhomova, R.V. Savushkin, Russ. J. Phys. Chem. A, 2007, 81, 1964-1967.

SOME RESULTS OF THE IDENTIFICATION OF CERTAIN PRINTINGS

G. Perović¹, D. Mitrović²

¹*BIA, Kraljice Ane bb, Belgrade, Serbia*

²*Technology and metallurgy faculty, University of Belgrade, Belgrade, Serbia*

Abstract

The results obtained enable determining of specific characteristics of the reproduction proofs, especially those obtained with digital printers. Characteristics of the proofs which can be presented numerically, in the form of diagrams and histograms, as well as photographs of enlarged, characteristic details, make the profile of the given printer. Based on the profile it is possible to determine which of the examination printers made the proof in question.

Introduction

Because of its importance for the functioning of modern society, and their ability to obtain possession of legal or material benefit, of the document (personal documents, notes, banc paper etc) are constantly subject to falsification, or unauthorized reproduction. Although some have elements of protection against forgery, the materials from which they were made (protected paper) and the graphic design and printing techniques which are printed, the documents were produced graphically, that is, using the usual graphics manufacture can be relatively successfully reproduced. The development of computer technology causes rapid and constant increase in performance and quality of personal computers and its peripherals (scanners, digital cameras as input devices and output devices like printers) thus increasing the print quality of reproduced prints, with constantly falling prices of such equipment. Availability of equipment to play, with its high quality, has led to a flood of forgeries done on different types of digital color printer. In this regard, the expert witnesses involved in examination of forged documents, there is a new problem, detection of type and brand (manufacturer) device which was a forgery made, or even detect whether it is done in precise printer.

The aim of this paper was to presents some results obtained by methods for determing certain parameters of the quality of printed impressions, using common PC configuration (computer, scanner, printer) and relatively cheap software, Adobe's Photoshop and Media Cybernets's Image-Pro Plus and the availability of laboratory equipment (microscope and digital cameras).

Results and Discussion

The properties of some fragments of the prints were subject of our investigation, see Figure 1.

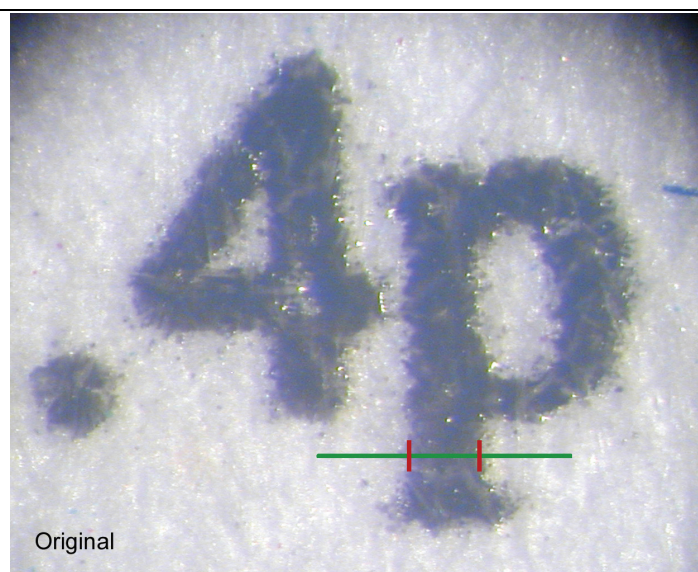


Figure 1. Fragment of the prints.

The sharpness of image was measured by measuring the change in intensity, the angle of inclination of the boundary curve of intensity image (Fig. 1.), and the transition between the printed and not-printed, clean paper. The results of field measurements examined the prints are presented in the Table 1.

Table 3. The angle of inclination of the boundary curve (degrees).

mage	Red ₁	Green ₁	Blue ₁	Red ₂	Green _{n₂}	Blue ₂
Original	17.28	19.09	21.90	31.02	25.86	32.47
HP 2000	29.85	25.68	67.04	63.43	81.64	69.34
Deskjet 990	46.00	56.30	51.91	45.80	31.67	44.14
Tektronix Phaser 780	15.94	34.57	47.65	12.35	23.74	49.61
Tektronix Phaser 860	28.14	26.88	35.35	21.81	35.38	52.03
Ofset B2	13.08	15.60	17.97	31.01	12.93	26.99
Ofset Speedmaster	11.02	17.80	22.34	12.49	17.90	17.10

A small angle means a sharper image, and index 1 and 2 refer to the left and right edge of prints. Due to the fact that all measurements performed on enlarged prints to digital photos, recorded through a microscope, and to sharpenes done manually by observing the desired detail on the camera LCD display, in interpreting the results should be taken, because the sharpnes of the obtained image directly affects the measurement result. As with the measurement accuracy and here is a raster structure hindered the determination of contour images.

Conclusion

Development of computer equipment and software for computer preparation for printing and digital printing processes influenced the increase in production of forged documents. In order to develop methods to recognize fraudulent documents, based on research conducted in this study, it was concluded the following:

- Defined procedure for determining the thickness of protective threads. It was found that neither printed flat offset printing technique and drawn thread with average thicknesses of 156 and 67 micron thickness exceeds several times the original thread of 22 micrometers. Varying the thickness of the original thread is only 5 μm , while the difference of maximum and minimum measured values in print or 69 μm or 67 μm in cartoons.
- Some of the precision and sharpness of reproduction prints, prints measuring segments of known dimensions and measuring the change in intensity at the border between the prints and non-printed paper. Compared to the original, measured 205 micrometers, the most accurate image reproduced with the DeskJet 990 printer with 278 μm . The following Phaser 860 (294 mil), Phaser 780 (305 mil), HP2000 (311 μm), Speedmaster Offset (319 mil) and offset SORMZ B2 (352 mil). The sharpest prints are offset, then prints laser printer and the end of reproduction obtained by using ink-jet printer.

Acknowledgement

This research has been done thanks to the resources of the project 172015 Ministry of Science and Technology, R. Serbia.

References

- [1] H. Andersson, M. Wigilius, 8th European Conference for Police and Government Document Exeperts, Bratislava, Slovak Republic, September 2002.
- [2] G. Perović, Master thesis, Faculty of Technology an Metallurgy, Belgrade, 2004.

PRINTER IDENTIFICATION BASED ON DOT RADIUS

G. Perović¹, T. Grozdić², D. Mitraković³

¹*BIA, Kraljice Ane bb, Belgrade, Serbia*

²*Institute for multidisciplinary research, University of Belgrade Kneza Višeslava 1a, 11000 Belgrade, Serbia, (gtomisi@imsi.bg.ac.rs)*

³*Technology and metallurgy faculty, University of Belgrade, Belgrade, Serbia*

Abstract

Forensic document examiners more and more often have to answer questions related to printing technology, type and model of printer by which the document was produced. In this paper, the microscopically enlarged details of the prints, obtained by different printing technologies (electrophotography, ink-jet, offset lithography), were examined using image analysis software.

Introduction

In today's digital world, the document, as a form of information, have been created on different printers, that are available on the market, and they are increasingly subject to fraud and counterfeiting. Answering the fundamental question – whether the questioned document is original or not? – forensic document examiners more and more often have to respond to requests related to printing technology, type and model of printer by which the document was produced.

These various technologies will make prints of different characteristics, due to differences in the process of reproduction, printer mechanism, image resolution, rasterization method, dot size and shape, type of colorants, bonding to the printing substrate, deformation of print image elements, geometric or dimensional distortion of microscopic details of prints, etc. In recent years many authors have dealt with printer forensics, based on print quality analysis.

Oliver et al. [1] have suggested the application of ImageXpert, machine-vision based, portable device, which is usually used to analyze the print quality, printed circuit board, etc. Mikkilineni et al. [2] have developed strategy for printer identification, that involves a printer characterization based on the unique properties of the printed image called "intrinsic signature", that are characteristic of specific printer or model. As an intrinsic signature these authors reported banding. Another method for banding investigation, in order to identify the printer, has been given by Tchan [3], using digital image analysis system, consisting of a high-resolution CCD camera connected to the computer.

Dasari and Bhagvati [4] have dealt with the identification of a color ink-jet and laser printers and photocopiers using HSV color space (Hue, Saturation, Value or brightness). Gupta et al. [5] have analyzed the reproductions of original documents by microscopic examination of the pattern of the image, using the Video Spectral Comparator and a microscope with a camera. Lampert et al. [6] have proposed a technique that is based on the fact that the texts printed on different printers have a different appearance, especially in the edge area of the prints.

Huber-Mörk et al. [7] have examined relative displacement between prints generated by the different printing processes, which are successively, one after the other applied to the paper, in security documents production.

Kee and Farid [8] have dealt with technique for modeling geometric degradation caused by printer. They determined the deviation in the shape of the selected letters in relation to the ideal geometric shape of this letter. The set of all these deviations makes the printer profile. Otherwise, the methods of Bulan et al. [9] and Wu et al. [10] are not based on analysis of individual print details, but on analysis of whole page document's geometric distortion, that is caused by the imperfection and differences of the paper feeding mechanism of different printers. Akao et al. [11] have dealt with identification of the ink-jet printers by estimation of spur gear teeth number, actually spur marks from these spur teeth, while Ryu et al. [12] have studied identification of the color laser printers, by halftone texture analysis.

Experimental

In our paper two laser printers (Phaser 780 and Phaser 860), two ink-jet printers (HP 2000 and HP DeskJet 990cxi) and two offset lithography printing presses (Heidelberg Offset SORMZ B2 and Heidelberg Speedmaster B1) were examined. Examination of prints, obtained by different printing technologies, based on the Image Pro Plus software. This software analyzes the image detail obtained using a microscope and digital camera.

Results and Discussion

Dot radius was measured from the original crest motif on Serbian (blue) passport data page (offset lithography printing) and scanned reproductions of this motif, obtained by different technologies of printing. The average shape and size of the dots are shown by radial graph (Fig. 1).

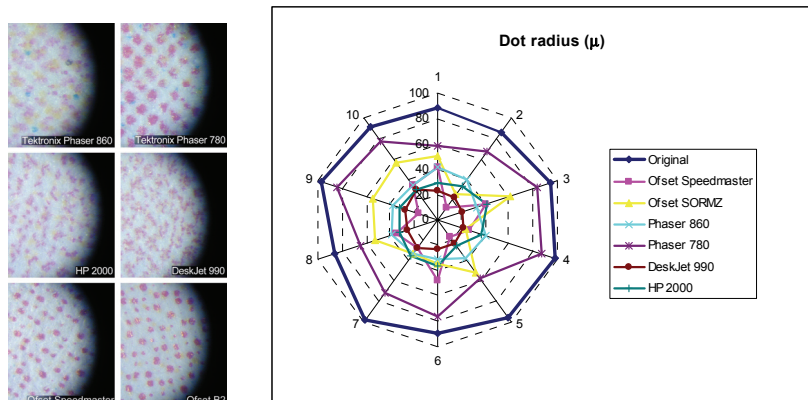


Figure 1. Enlarged print details and results of dot radius measurement.

Compared to the original print, on which the dots are in the range of 85 to 100 μ , all examined reproductions have noticeably smaller dots. Closest to the original print is Phaser 780 printer, whose dot size is between 58 and 86 μ . With this printer we can see the regular halftone texture at an angle of approximately 45°, similar to the original print. Knowing resolution of tested printers, it can be concluded that the size of the dots on the print regularly depends on the resolution and raster frequency. The smallest dot was measured on the print from highest resolution printer (DeskJet 990, 2400x1200 dpi). Same dependence on the resolution occurred when the printers of the same printing technology were compared. Dots printed on offset printing presses vary in size, although the printing plates for both presses were built with the same film. Dots on the print from SORMZ press are larger than those on the print from Speedmaster, because the first one is old, low quality machine, without ink control system, with manually developed plates, resulting in a significant dot gain.

Conclusion

This paper presents the method for determining certain features of prints, by which it is possible to identify corresponding printing devices. The method is based on the fact that different printing technologies and different printer models bring a distinctive noise in the process of reproduction of text and images, which can be identified. The advantage of this method is that they are non-destructive, as opposed to the conventional examinations of documents, which are based on analytical methods of testing the composition of printing ink and paper. Also, these methods do not require complicated and expensive laboratory equipment.

References

- [1] J. Oliver, J. Chen, IS&T's NIP18 Conf., 2002, 218-222.
- [2] A. K. Mikkilineni, P.-J. Chiang, G. N. Ali, G. T.-C. Chiu, J. P. Allebach, E. J. Delp, IS&T's NIP20 Conf., 2004. 20, 306-311.
- [3] J.S. Tchan, Journal of Imaging Science and Technology, 2007, 51(4), 299.
- [4] H. Dasari, C. Bhagvati, Lect. Notes on Comp. Sci., 2006, 3852, 692-701.
- [5] G. Gupta, C. Mazumdar, M.S. Rao, R.B. Bhosale, Digital Investigation, 2006, 3, 43-55.
- [6] C. H. Lampert, L. Mei, T. M. Breuel, CIS, 2006, 1, 639-644.
- [7] R. Huber-Mrök, H. Ramoser, H. Penz, K. Mayer, D. Heiss-Czedik, A. Vrabl, Pattern Recognition Letters, 2007, 28, 2037-2045.
- [8] E. Kee, H. Farid, Proc. ACM MM&SEC'08, 2008, 3-10.
- [9] O. Bulan, J. Mao, G. Sharma, IEEE (ICASSP), 2009, 1401-1404.
- [10] Y. Wu, X. Kong, X. You, Y. Guo, IEEE (ICIP), 2009, 2909-2912.
- [11] Y. Akao, A. Yamamoto, Y. Higashikawa, IWCF, 2009, 25-32.
- [12] S.-J. Ryu, H.-Y. Lee, D.-H. Im, J.-H. Choi, H.-K. Lee, [IEEE \(ICASSP\), 2010](#), 1846-1849.

K-15-P

ABSORPTION CHARACTERISTICS OF CYAN DYES

J. S. Kiurski¹, D. Ž. Obadović², M. Cvetinov², J. Krstić¹, I. Oros¹

¹*Faculty of Technical Sciences, Department of Graphic Engineering and Design,
Trg Dositeja Obradovica 6, Novi Sad, Serbia*

²*Faculty of Sciences, Department of Physics, Trg Dositeja Obradovica 4, Novi Sad,
Serbia*

e-mail: kiurski@uns.ac.rs

Abstract

In this paper, absorption characteristics of cyan dyes with application of UV-VIS spectroscopy, was presented. Samples of printing cyan dyes were taken from the dyes unit on printing machine. The obtained spectral data showed the typical absorption profile of phthalocyanines. All spectra show a strong UV absorption in the 200-300 nm region that can be attributed to the $\pi - \pi^*$ and $n - \pi^*$ of the amino, carboxylic and aromatic moieties. Also, obtained spectra could be a good indicator of dye aging process.

Introduction

The phthalocyanines are widely used in textile, paint, printing ink and plastic industries (Fig.1). Although the shade range of the phthalocyanines is rather limited and covers only the bluegreen regions of the spectrum, their excellent fastness to light, and high absorptivity render them adapt for many applications. The insolubility of phthalocyanines necessitates preparation of soluble derivatives for application as dyes for textile fibbers. Phthalocyanine pigments in the form of aqueous dispersions are used in pad-dyeing with resin emulsions. Because of their excellent stability to acids, alkalis and solvents phthalocyanines are particularly useful in spin dyeing [1].

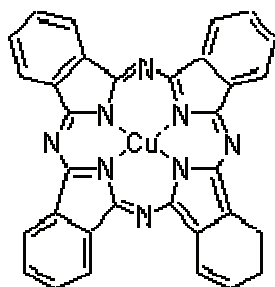


Figure1 Structure of cyan (copper phthalocyanine, CuPc) β -form.

Experimental

The cyan samples were taken from dye unit on offset printing machine before and after 20,000 printed sheets.

Ultraviolet-visible (UV-VIS) absorption spectra were recorded using spectrophotometer UV-VIS SPECORD 205, Analytik Jena. Dye samples were prepared by dilution in appropriate organic solvent (DMSO).

Results and Discussion

The absorption maximum of phthalocyanines is calculated by assuming the Π -electrons to be one dimensional free electron gas, resonating between two equivalent limiting structures of the phthalocyanine ring with constant potential energy along its length. In the normal state, the most stable energy states of the electron gas, each contains two electrons in accordance with Pauli's exclusion principle. The remaining states are empty. The existence of the first absorption band is a consequence of the jump of a Π - electron from the highest energy level. The spectrum of the phthalocyanine in the visible region is composed of at least seven bands, the main absorption occurring between 600 and 700 nm.

The CuPc molecule (copper phthalocyanine) is planar and has fourfold symmetry, and consists of a central copper atom surrounded by four ligands which have pyrrole and benzene rings. It contains an odd number of electrons and the obtained spectrum has two orbitals whose relative position depends rather sensitively on the computational details, as discussed in the literature [2]. One of them is of π symmetry, delocalized over the pyrrole and benzene rings, while the other one is a singly-occupied state of in-plane symmetry, with a large amplitude on the Cu and neighboring N atoms [2]. The current understanding is that the correct ordering of these states has the (doubly-occupied) π orbital as the HOMO, with the (singly-occupied) Cu-related orbital lower in energy. Moreover, it has been shown that errors arising from self-interaction, which are present in standard DFT functionals, artificially shift the position of all molecular orbitals (especially the strongly Cu-localized orbital close to the vacuum level) in some cases giving rise to a spurious crossing with the HOMO level.

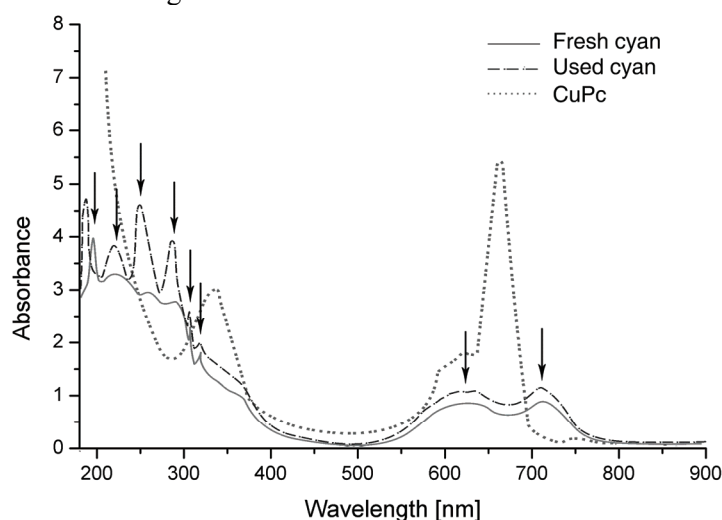


Figure 2 UV-VIS spectra of the cyan dyes before and after printing.

Cu-phthalocyanine shows absorption bands in two regions: the band in the range 600-700 nm is found in the visible region of spectra and it is responsible for the blue color feature of the colorant. Another band between 200 and 400 nm overlaps a wide range of the emission Cu-band. The spectral characteristics for cyan printing dye samples are: 207, 226, 263, 294, 312, 320, 624 and 713 nm, Fig.2. UV-VIS spectrum shows that the bands in region of 624-713 nm split and shift to red, which means successive protonation happened and caused the loss of symmetry. The spectra of the fresh dye were similar to the spectrum of color after 20,000 printed sheets with the difference intensity in the region of 200 - 290 nm. The UV-VIS spectrum obtained showed the typical absorption profile of phthalocyanines. It was detected a strong UV absorption band in the 200-300 nm region in all investigated cyan dyes samples, that can be attributed to the $\pi - \pi^*$ and $n - \pi^*$ of the amino, carboxylic and aromatic moieties [3].

The changes in the absorption intensities are due to the color changes in printing processes during the photochemical aging. The color changes are influenced with products of degradation. In Cu-Pc the blue color is produced by the colorant that has high absorption coefficient, covering the color of polycarbonate matrix which is evaluated with aging process.

Conclusion

Cu-phthalocyanine as cyan dye was investigated using UV-VIS spectroscopy in order to determine the start of aging process. The obtained UV-VIS spectra showed the typical absorption profile of phthalocyanines as a main structure of cyan dye. The spectra of the fresh and used dyes were similar but with different intensity. All spectra showed a strong UV absorption in the region of 200-300 nm which could be attributed to the $\pi - \pi^*$ and $n - \pi^*$ of the amino, carboxylic and aromatic moieties. UV-VIS spectrum shows that the bands in region of 624-713 nm split and shift to red, which means successive protonation happened and caused the loss of symmetry. It was concluded that after 20,000 printed sheets these days can almost used in printed process.

Acknowledgment

The authors acknowledge the financial support of the Ministry of Education and Science of the Republic of Serbia (Projects No. TR 34014 and ON 171015).

References

- [1] P. S. Harikumar, Electrochemical studies on metal phthalocyanines, PhD Thesis, Cochin University of Science and Technology, India, 1990.
- [2] H. Vazquez, P. Jelinek, M. Brandbyge, A. P. Jauho, Corrections to the density-functional theory electronic spectrum: copper phthalocyanine, *App. Phys. A.*, 2009, **95**, 257-263.
- [3] J. Lindon, G. Tranton, J. Holmes. Biomacromolecular application of UV-VIS absorption spectroscopy, Elsevier, 2000, 131-136.

VANADIUM TOXICITY IN *Phycomyces blakesleeanus*

M. Stanić¹, M. Žižić¹, M. Živić², J. Zakrzewska³

¹*Institute for Multidisciplinary Research, University of Belgrade, Kneza Višeslava 1, 11030 Belgrade, Serbia.*

²*Faculty of Biology, University of Belgrade, Studentski trg 16, 11000 Belgrade, Serbia.*

³*Institute of General and Physical Chemistry, Studentski trg 12-16, 11000 Belgrade, Serbia.*

Abstract

We investigated the interactions of vanadium in two physiologically-relevant redox states: vanadate (+5) and vanadyl (+4), with 24h old mycelium of fungus *Phycomyces blakesleeanus*. Vanadate at first caused increased biomass production and synthesis of polyphosphates, and then showed its toxic effects at higher V⁵⁺ concentration. Vanadyl exhibited toxic effects even at low concentrations. Our results suggest that the main pathway of vanadium introduction into the cells of this fungus under natural conditions involves three steps: extracellular V⁵⁺/V⁴⁺ reduction, V⁴⁺ influx and vacuolar storage, and V⁵⁺ import at higher concentrations.

Introduction

The interest in biological investigations for vanadium has increased considerably during the past three decades, in line with its role as an essential ultra-trace element for most, if not all living organisms [1]. Vanadium has been reported to have a therapeutic effect in treatment of diabetes [2] and some types of cancer [3]. The release of vanadium to water and soil occurs primarily as a result of weathering of rocks and soil erosion and involves the conversion of the less-soluble V³⁺ form to the more soluble V⁴⁺ and V⁵⁺ [4]. Taking into account its toxicity, vanadium may pose an environmental threat due to anthropogenic activity-related increase of its level in the environment [5]. Fungi are of major interest regarding both, environmental and medical implications of vanadium, because they take up and accumulate trace metals [6], and represent the main route of vanadium entrance into the ecosystem [7]. Having this in mind, it is perplexing that data on vanadium metabolism in fungi are very scarce, being almost exclusively obtained on two ascomycetous yeast species: *S. cerevisiae* and *H. polymorpha* [8].

Materials and Methods

The wild-type strain of the fungus *P. blakesleeanus* (Burgeff) (NRRL 1555(-)) was used. To determine the influence of both oxidation forms of vanadium on its growth, *P. blakesleeanus* was cultivated on medium [9] without or with sodium orthovanadate (1; 5; 7; 10 and 20mM) or vanadyl sulphate (0.5; 1 and 5mM). For the purpose of NMR measurements, 24 h old mycelium was prepared according to [10]. The ³¹P NMR measurements were performed using Apollo upgrade, Bruker MSL 400

spectrometer operating at 161.978 MHz for ^{31}P . The assignment of NMR spectra and all other experimental details were performed as described previously [10].

Results and Discussion

The growth and development of *P. blakesleeanus* in the presence of vanadate and vanadyl was monitored by ^{31}P NMR spectroscopy, and it was observed that V^{5+} caused increase in PPc (core polyphosphates) and the decrease in Pi (orthophosphates) signal intensity, while V^{4+} had inverse effect on PPc and practically no effect on Pi (Fig. 1).

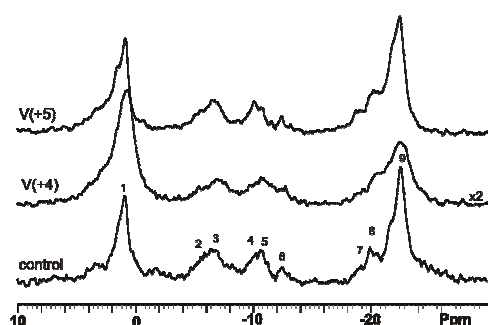


Figure 1. ^{31}P NMR spectra of *P. blakesleeanus* cultivated on V(+4) and V(+5) containing medium.

The signals assignments: (1) Pi -inorganic phosphates, (2) γ ATP, (3) PpT - terminal residues of PolyP and pyrophosphate, (4) α ATP, (5) NAD(H) and UDPG, (6) UDPG - second resonance, (7) β ATP, (8) PPp - penultimate PolyP residues, (9) PPc - central PolyP residues

Also, lower V^{5+} concentrations (1mM, 5mM) had statistically significant stimulating effect ($P < 0.05$, $n=3$) on biomass yield (Fig. 2), while higher V^{5+} concentrations reduced growth. Vanadyl sulfate added into growth medium above concentration of 0.5 mM slows growth. *P. blakesleeanus* could grow and complete its life cycle with used vanadyl (up to 5mM), and vanadate concentrations (up to 20 mM). In case of vanadate, increase in biomass yield is followed by almost unchanged ratio of PPc/Pi signal intensity (Fig. 2), already proposed indicator of fungus growth and development, but only up to concentration of 5mM. At higher concentrations, PPc/Pi signal intensity ratio in ^{31}P NMR spectra decreases. When mycelium was cultivated with V^{4+} it resulted in an immediate decrease of PPc/Pi ratio.

Proposed mechanisms for vanadium detoxification imply reduction of more toxic V^{5+} to V^{4+} , either in the cytoplasm [11] or in the cell wall [12, 13]. Apparently greater toxicity of V^{4+} compared to V^{5+} in *P. blakesleeanus* could suggest different and/or additional mechanism of vanadium detoxification, involving vacuolization. Vacuolar polyphosphates are believed to be the molecules chelating toxic metal ions [14], so vacuolization of V^{5+} leads to increased PolyP synthesis and concomitant reduction in Pi signal intensity. Paramagnetic V^{4+} makes the part of PolyP signal NMR invisible due to broadening, which results in the decrease of PPc signal intensity (Fig. 1). Also, Wilsky et al. have noticed that conversion of V^{5+} to V^{4+} is only possible at low V^{5+} concentrations, while in V^{5+} excess this process cannot keep pace with the rate of V^{5+} influx and it accumulates intracellularly, leading to growth reduction, as shown for V^{5+} concentrations higher than 5mM. Entrance of V^{5+} into the cell only at high concentrations could explain its apparent lesser toxicity compared to V^{4+} .

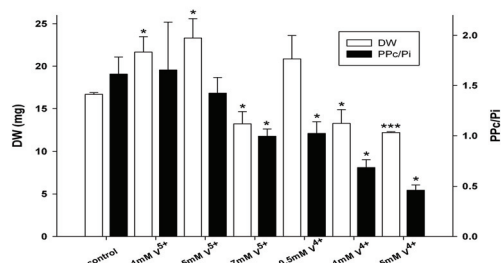


Figure 2. Influence of different concentrations of V⁵⁺ and V⁴⁺ on growth and development of *P. blakesleeanus*. White bars – dry weight (mg), black bars – PPc/Pi. Significance is expressed in relation to control
*** - $p < 0.001$, * - $p < 0.05$

Acknowledgement

Supported by Serbian Ministry of Education and Science grant No. 173040

References

- [1] D. Rehder, Bioinorganic vanadium chemistry, 2008, John Wiley & Sons Ltd.
- [2] K. Thompson, C. Orvig, J. Inorg. Biochem. 2006, 100, 1925–1935.
- [3] A. Bishayee, A. Waghray, M.A. Patel, M. Chatterjee. Cancer Lett., 2010, 294, 1–12.
- [4] T. N. K. Kumar, H.D. Revanasiddappa, J. Iranian Chem. Soc. 2005, 2, 161.
- [5] B. K. Hope, Sci. Total Environ., 1994, 141, 1-10.
- [6] P. Kalac, L. Svoboda, Food Chem. 2000, 69, 273–28.
- [7] N. W. Lepp, S.C.S. Harrison, B.G. Morrell. Environ. Geochem. Health, 1987, 9, 61-64.
- [8] I. Mannazzu, Ann. Microbiol., 2001, 51, 1-9.
- [9] R. P. Sutter, Proc. Natl. Acad. Sci. USA, 1975, 72, 127-130
- [10] M. Živić, J. Zakrzewska, M. Žižić, G. Bačić, Antonie van Leeuwenhoek, 2007, 91, 169-177.
- [11] G. R. Willsky, D. A. White, B.C. McCabe, J. Biol. Chem., 1984, 21, 13273-13281.
- [12] L. Bisconti, M. Pepi, S. Mangani, F. Baldi, BioMetals, 1997, 10, 239-246.
- [13] H.P. Bode, C. Friebel, G.F. Fuhrmann, Biochim. Biophys. Acta, 1990, 1022, 163-170.
- [14] I. Kulaev and T. Kulakovskaya, Annu. Rev. Microbiol., 2000, 54, 709-734.

K-17-P

SEM-EDS ANALYSIS OF THE SYSTEM *BIOMINERAL TISSUE – NATURAL MEDIUMS IN THE FORENSIC EXAMINATION*

N. V. Radosavljević-Stevanović¹, R. S. Nikolić², N. S. Krstić², B. M. Kaličanin³

¹*The National Crime-Technical Centre, Ministry of Interior of the Republic of Serbia, Kneza Miloša Str. 103, 11000 Belgrade*

²*Department of Chemistry, Faculty of Sciences and Mathematics, University of Niš, Višegradska Str. 33, 18000 Niš, Serbia*

³*Department of Pharmacy, Faculty of Medicine, University of Niš, Bulevar dr Zorana Djindjića 81, 18000 Niš, Serbia*

Abstract

In this study the changes of the teeth mineral tissues which were exposed to the influence of the different natural soil and water mediums were analysed by Scanning Electron Microscopy - Energy Dispersive Spectroscopy. Results show alterations of elemental content in mineral tissue and significant changes on the surfaces of teeth samples that were exposed to the soils and waters mediums. Thus, such study can be utilised to direct to the kind of medium in which biomineral teeth tissue was put off.

Introduction

Hard mineral tissues, bones and teeth, are readily available biopsy material which is relatively easily analysed and applied in the forensic examination, especially bones. It is potentially interesting and convenient in the cases when it was exposed to the influence of different outer mediums. The basic structure unit of bones and teeth is hydroxyapatite $\text{Ca}_{10}(\text{PO}_4)_6(\text{OH})_2$ (HAp) [1]. By the influence of the outer mediums agents, the mineral tissue of teeth is altered, what is recognized, among all, according to changes in elemental content of the Hap [2, 3].

According to the qualitative and quantitative alterations that occurred in the mineral teeth tissue after it had been exposed to different types of mediums, the aim of examination was to obtain the information potentially useful for forensic expertises using Scanning Electron Microscopy - Energy Dispersive Spectroscopy (SEM-EDS).

Experimental

The model systems for examination of the interactions natural environment mediums-anthropogenic material were human teeth exposed to the influence of different types of soils: urban city soils from the park (medium I), soils of mostly clay content (medium II) and soils of mostly limestone content (medium III) from the city of Niš and surrounding area, and different types of water: commercial water “aqua viva” (medium IV) and a solution of the “rainwater model system” (medium V). The teeth were exposed to the mention mediums in the mass ratio 100:1 and left for three months at room temperature ($t = 22-25$ °C).

The structural characterization of the mineral teeth matrix, of both – control sample and the group of samples exposed to outer environment mediums influences, was done by the techniques of SEM-EDS analysis. SEM-EDS examination of *in situ* teeth tissue

(covered by the vapour of colloidal gold) was performed by the „FEI QUANTA 200“ in the National Crime-Technical Centre of the Ministry of Interior in Belgrade.

Results and discussion

Results of SEM-EDS analyses of the untreated and the samples of teeth that were exposed to the soils mediums influence are shown in the Figure 1.

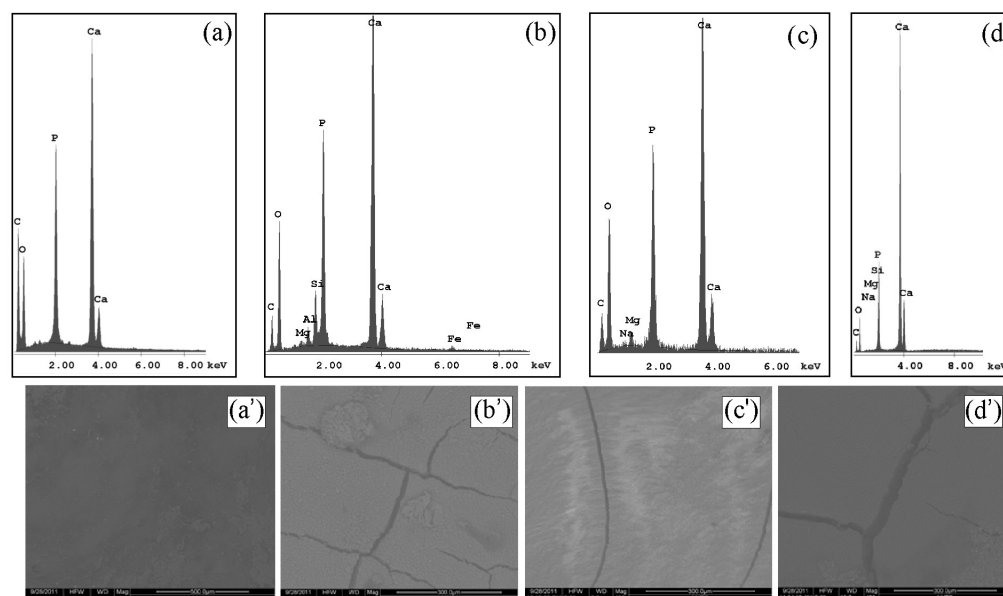


Figure 1. EDS spectra and SEM micrographs for untreated teeth (a), teeth exposed to the medium I (b), medium II (c) and medium III (d)

On the basis of comparison of SEM-EDS analyses results of untreated and treated samples that were exposed to the soils mediums, the alterations in content and the surface appearance of the hard mineral teeth tissue were observed. EDS spectra directs to the local change of metals in the researched mineral tissue that occurs due to the adsorption. Al, Mg, Si and the traces of Fe can be noticed in the teeth tissue that was exposed to the urban city soils (Fig. 1b); the adsorption of Mg and Na is performed from the clay enriched medium (Fig. 1c); the increase of Ca, Si, Mg, Na and significant change of Ca/P ratio are noticed for the teeth samples that were exposed to limestone enriched soils (Fig. 1d). The cracks on the teeth surface were noticed, originated from the teeth interaction with the all surrounding soils environments (Fig. 1b/c/d'). The ratio of Ca/P content is altered probably as the result of adsorption of Ca^{2+} ions from the surrounding environment or adsorption of the excessive content of phosphates on the crystal surface or substitution of Ca^{2+} ions by the ions from the surrounding environment [4, 5]. The small diameters of Na^+ , Mg^{2+} and Al^{3+} ions enable them to migrate easily into the internal teeth tissues [3]. According to comparison of SEM-EDS analyses results of untreated and treated samples that were exposed to the water mediums, slightly alterations in content and no significant change of surface appearance of the hard mineral teeth tissue were observed (Fig. 2). EDS spectra directs to the local change of elements in the researched mineral tissue that occurs due to the

K-17-P

adsorption. Mg can be noticed in the teeth tissue that was exposed to the “aqua viva” water system (Fig. 2b) while the adsorption of Na and Cl is performed from the “rain-water model system”, together with the altered ratio of Ca/P (Fig. 2c) for the reasons already described [4, 5].

Conclusions

SEM-EDS analysis shows alterations of metal content in mineral tissue and changes on the teeth surfaces for the teeth samples exposed to the soils environment. Less intensive changes in mineral content and no significant changes on the teeth surface were noticed for the teeth exposed to water systems. According to the mentioned differences, the directions related to the kind of environment can be performed.

Acknowledgements

This work was supported by the Ministry of Education and Science of the Republic of Serbia under the Projects No. III45017 and TR34008.

References

- [1] J. Andjić, *Osnovi oralne fiziologije i biohemije*, Naučna knjiga, Beograd, 1990.
- [2] B. Nowak, *Analyst*, 1995, 120, 747-750.
- [3] R. Nikolić, B. Kaličanin, N. Krstić, *Connect. Tissue Res.*, 2012, 53(3), 229-235.
- [4] W.H. Arnold, P. Gaengler, *Ann. Anat.*, 2007, 189(2), 183-190.
- [5] S. Kannan, F. Goetz-Neunhoeffler, J. Neubauer, J.M.F. Ferreira, *J. Am. Ceram. Soc.*, 2008, 91(1), 1-12.

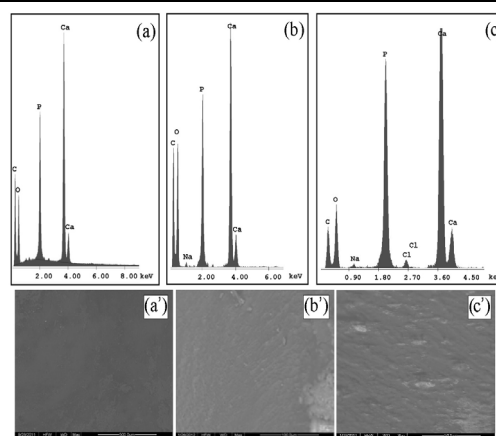


Figure 3. EDS spectra and SEM micrographs for untreated teeth (a), teeth exposed to the medium IV (b), medium V (c).

THE SEDIMENT IN LAKE PALIĆ

T. Grozdić, A. Hegediš, M. Nikčević, G. Mesaroš

Institute or multidisciplinary research, University of Belgrade, Kneza Višeslava 1a, 11000 Belgrade, Serbia, (gtomisi@imsi.bg.ac.rs)

Abstract

The lake serves as the recipient of treated wastewater of the city of Subotica and Palić. Effluent quality is of great importance for lake Palić. Treatment plant inadequately purified waste water and in it have high concentrations of organic matter and phosphorus and nitrogen. To improve the water quality of lakes, it is necessary to reduced nutrients to a minimum. New treatment plant facilities for urban wastewater of Subotica and Palić, ought to ensure that the purified water contains minimal amounts of organic matter and compounds of nitrogen and phosphorus.

Introduction

Palić lake area 576 ha, the width between 360 and 920m, 8250m maximum length, maximum depth 2.0 m, and a total coastline of 20 km [1]. During the first half of the nineteenth century, changes were observed in the lake which indicated that the lake eutrophication progressed. Since 1969th-1971. the concept of rehabilitation is established in the lake Palić. [1] From 1972 to 1975. was partially implemented plan of rehabilitation. Plant for treatment of municipal wastewater, anticipated program of rehabilitation of Palić Lake, was built and put into operation 1975th year. But so purified wastewater continue to be burdened with organic substances, nitrogen and phosphorus compounds. It is not done either aging or processing of bioactive silt.

Construction of new plants for urban waste water treatment began in 2006. year and was completed in 2010. year. The capacity of the cleaner 36 000 m³ for a day without rain and 72 000 m³ for a rainy day. Paper [2] has been analyzed the water quality of Lake Palić. Nutrient concentrations, as indicators of water quality, are also increasing. The concentration of total nitrogen increased at all sites, while high concentrations of orthophosphate and uniform throughout the year. High concentrations of nitrogen and phosphorus as a result of intensive organic production, with negative consequences for eutrophication of the lake. The values of saprobic index, water quality and sectors, corresponding class II-III water quality. The water quality of the lake sector IV belongs to the class IV in the summer. On the basis of results of tests of water quality [2], finds the trend of increasing saprobic lakes and increasing amounts of suspended matter and silt in the lake Palić. Within the phytoplankton community during the year, observed qualitative and quantitative dominance of Bacillariophyta species partition.

The paper discussed the physic-chemical parameters of the chemical analysis of lake sediments sampled in July 2010, a month after the beginning of a new plant for wastewater treatment.

Results and Discussion

Table 1. Results of physic-chemical tests of sediment-mud from Palić Lake in July 2010. year.

Physic-chemical parameters	sector II thickness of sediment 20 cm	sector II thickness of sediment 50 cm	sector III thickness of sediment 20 cm	Sector IV thickness of sediment 20 cm	sector IV thickness of sediment 60 cm
Susp. Solids %	48,39	35,52	52,78	40,12	51,41
Organic sludge %	20,12	22,66	22,82	26,52	20,87
inorganic sludge% on 800° C	79,88	77,34	77,18	73,48	79,13
Total phosphorus mg/L	7010	24300	12900	2880	2890
Total organic carbon TOC mg/L	44000	65900	36590	50000	28000
Total nitrogen mg/L	11000	6800	3000	5000	3600
Carbonates and bicarbonates mg/L	37540	31650	47320	53270	39900
Chlorides mg/L	75	158	85	108	586
Cadmium mg/L	1,4	1,1	0,5	0,4	0,4
Iron mg/L	21100	18100	16000	16100	14500
Manganese mg/L	597,0	711	500	440	411
Chromium mg/L	216	189	52,7	23,1	26,8

In July 2010. year the recorded value of the suspended solids in lakes water is 2 mg/L in the first sector and 46 mg/L in the fourth sector. The recorded value of suspended solids is less than the recorded value for the same sector. Suspended solids for sector I is 37.1 mg/L and for sector IV is 137.4 mg/L in April 2005. year. The thickness of sludge in the lake Palić, especially in the fourth sector, which ranges from 50 - 60 cm and more. Inorganic matter in the sludge has an average of about 79% of these sites, and is dominated by salts of calcium, iron and sodium in the form of carbonates, sulfates and chlorides, see Table 1. The concentrations of sulfates, arsenic, lead, copper, zinc and nickel are within the normal range for lake sediment, and for this reason are not presented in Table 1. By examining the composition and number of inhabitants of lake bottom was confirmed that the living conditions are very unfavorable in the mud. In the third sector of the lake in 2005. The reduced number of registered individuals Chironomidae and Oligochaeta, while in the tourist part of the lake found only a few representatives of Chironomidae [2, 3].

Conclusion

The lake serves as the recipient of treated wastewater and the city of Subotica and Palić. Effluent quality is of great importance for the lake. In order to improve the water quality of lakes, it is essential that the intake of nutrients is reduced to a minimum. New treatment plant for urban wastewater of Subotica and Palić, ought to ensure that the purified water contains minimal amounts of organic matter and compounds of nitrogen and phosphorus. Palić lake water quality could be improved by introducing water from the Tisa River, but large quantities of silt into the lake creating unfavorable conditions for the whole eco system. Eutrophication of the lake is in an advanced stage. Eutrophication of the lake could be decreased by removal of lakes sludge and/or mixing water from lake Palić with water from Tisa river, which is of satisfactory quality.

Acknowledgement

This research has been done thanks to the resources of the project TR 37 009 Ministry of Science and Technology, R. Serbia.

References

- [1] Dj. Seleši, Voda Palićkog jezera od 1781. do 1999. godine, JVP Palić-Ludaš, Subotica, 2000.
- [2] T. Grozdic, *Ecologica*, 2011, 64, 657-663.
- [3] R. Pantle, H. Buck, *Gas und Wasserfach*, 1955, 96(18), 604.

**¹³⁷Cs DESORPTION FROM MOSS
HOMALOTHECIUM SERICEUM (HEDW.) SCHIM.
USING ACID SOLUTIONS**

A. Čučulović¹, D. Veselinović²

¹*INEP-Institute for the Application of Nuclear Energy, University of Belgrade,
Banatska 31b, 11080 Zemun, Serbia, anas@inep.co.rs*

²*Faculty of Physical Chemistry, University of Belgrade, P.O. Box 137,
11000 Belgrade, Serbia*

Abstract

Desorption of ¹³⁷Cs in samples of *Homalothecium sericeum* (Hedw.) Schimp. using: H₂SO₄ (A), HNO₃ (B), H₂SO₄-HNO₃ (C) acid solutions with pH values 4.60, 5.15 and 5.75 and distilled water (D) pH values 6.50 was investigated. After five consecutive desorptions lasting 24 hours it was shown that between 22.8% (solution (C) pH 5.75) and 33.2% (solution (C) pH 4.60) of ¹³⁷Cs was desorbed from the moss. Desorptions performed with solutions (A), (B) and (C) pH 5.75 are the weakest and approximately the same (about 23%).

Introduction

Moss has a slow growth rate and relatively large surface area to biomass ratio; the lack of the waxy cuticles and associated stomata means that many contaminants can be absorbed over the whole external surface; they do not have a rooting system; and they obtain nutrients from dry and wet precipitation by absorption through their leaves which lack cuticles. Mosses may be considered as the most commonly applied organisms for biomonitoring studies of radioactive contamination [1]. Cesium-137 (¹³⁷Cs) is one of the most frequent artificial radionuclides found in the environment because of different anthropogenic discharges such as atmospheric nuclear weapons testing, accidental releases from nuclear power plants, chronic emissions from nuclear power plants, and chronic emissions from nuclear reactors and fuel-reprocessing plants. Cesium-137 is an emitter of gamma and beta radiation, with a long radioactive half-life (30.17 years). The first nuclear weapons were detonated in New Mexico and Japan in 1945. The partial meltdown of the reactor at Chernobyl in April 1986 released high amounts of radionuclides into the environment, especially ¹³⁷Cs. Following the Chernobyl reactor accident, numerous studies involving monitoring of the long-lived fission product ¹³⁷Cs were undertaken using mosses as biological indicators to update the inventory of this long-lived radionuclide [2].

In our previous work we followed ¹³⁷Cs and metal desorption in *Cetraria islandica* lichen, while in this one we follow ¹³⁷Cs desorption in *Homalothecium sericeum* (Hedw.) Schimp. moss [3,4]. In this work we attempted to investigate

whether ^{137}Cs could be isolated with acid solutions as simulated acid rain without destruction of the moss cellular structure, which would imply that the whole amount of ^{137}Cs in the plant is ion-exchangeable.

Material and Methods

Homalothecium sericeum (Hedw.) Schimp. moss, originating from Montenegro was collected in 2002, (10 g dry mass) and covered with 200 mL of distilled water (D) and acid solutions: (A) H_2SO_4 , (B) HNO_3 and (C) $\text{H}_2\text{SO}_4\text{-HNO}_3$. Solutions (A) and (B) were made by adding concentrated H_2SO_4 , HNO_3 , respectively to 200 mL of distilled water (pH 6.50) to the required pH value: 4.60; 5.15 and 5.75. Solution (C) was obtained by mixing 100 mL of solution (A) and 100 mL of solution (B) with identical pH values. Samples were consecutively desorbed with solution five times and desorption series were repeated twice. Desorptions were performed at room temperature and lasted 24 hours. After each desorption, after filtration, moss samples were dried at room temperature to a constant mass. Activity levels of ^{137}Cs were measured in samples before and after each desorption on an ORTEC-AMETEK gamma spectrometer with 8192 channels, resolution of 1.65 keV and efficiency of 34% at 1.33 MeV ^{60}Co , with a measurement error below 5%. Specific activities were calculated based on measurements (Bq/kg). The pH value of a solution was measured on a pH meter (MA 5730 Iskra).

Results and Discussion

Activity levels of ^{137}Cs (Bq/kg) in *H. sericeum* (Hedw.) Schimp. moss before desorption and the percentage of non-adsorbed ^{137}Cs in moss after each of the five consecutive desorptions with solutions (A), (B) and (C), and also distilled water (D), and the total amount (%) of desorbed ^{137}Cs are given in Table 1. Activity levels of ^{137}Cs in samples of moss before desorption were from 476 Bq/kg to 552 Bq/kg. Five successive steps with distilled water desorbed 31.3% of the initial $^{137}\text{Cs}^+$ in *H. sericeum*. With the acid solution (A), (B), (C) the amount of total desorbed $^{137}\text{Cs}^+$ (Table 1) ranged from 22.8% (pH 5.75, solution (C)) of the initial radiocesium in moss to 33.2% (pH 4.60, solution (C)). ^{137}Cs is significantly, but not completely desorbed from moss. Changes of the desorbed amount of ^{137}Cs with the number of consecutive desorptions have an exponential form. The percentage of the total absorbed amount of ^{137}Cs from moss is almost twice times lower than for lichen [2-4].

The final mass of the moss was only slightly decreased after this procedure (approximately 5%), indicating that desorption was achieved without significant destruction of the plant structure.

Moss desorbed using the solutions described above did not undergo any visible structural changes.

K-19-P

Table 1. Activity of ^{137}Cs in moss before desorption (Bq/kg), percentage of remaining ^{137}Cs in moss after each desorption and total desorbed ^{137}Cs from moss (%)

pH	4.60			5.15			5.75			6.50
Solution	A	B	C	A	B	C	A	B	C	D
Activity of ^{137}Cs in moss before desorption (Bq/kg)										
	552	513	498	538	476	493	550	505	490	523
Percentage of remaining ^{137}Cs in moss after each desorption (%)										
I	83.2	85.1	82.3	82.1	84.1	83.2	91.0	87.5	89.1	87.9
II	78.5	81.1	77.2	76.9	80.3	80.0	85.6	81.1	86.4	82.0
III	74.8	78.6	73.5	72.9	77.2	77.1	83.1	78.5	81.8	76.9
IV	71.8	76.7	68.7	70.2	75.1	73.5	77.5	77.1	78.8	71.1
V	68.2	75.2	66.8	69.3	71.1	70.3	76.1	76.6	77.2	68.7
Total desorbed ^{137}Cs from moss (%)										
	31.8	24.8	33.2	30.7	28.9	29.7	23.9	23.4	22.8	31.3

Conclusion

These results indicate that NO_3^- and SO_4^{2-} anions do not have a significant influence on ^{137}Cs desorption. Reduction of the percentage of desorbed ^{137}Cs with increase in the pH value, i.e. reduction of the concentration of H^+ ions, indicated that they have a significant, but not dominant influence on ^{137}Cs desorption from moss.

References

- [1] C. Papastefanou, M. Manolopoulou, T. Sawidis, J. Environ. Radioact. 1989, 9, 199-207.
- [2] A. Čučulović, R. Čučulović, T. Cvetić Antić, D. Veselinović, Arch. Biol. Sci., Belgrade, 2011, 63 (4), 1117-1125.
- [3] A. Čučulović, D. Veselinović, Š. S. Miljanić, J. Serb. Chem. Soc., 2006, 71 (5), 565-571.
- [4] A. Čučulović, D. Veselinović, Š. S. Miljanić, J. Serb. Chem. Soc., 2009, 74(6), 663-668.

SPATIAL VARIABILITY OF ^{137}Cs ACTIVITIES IN THE SOIL OF BELGRADE REGION (SERBIA)

Lj. Janković-Mandić¹, R. Dragović², M. Đorđević², M. Đolić¹,
A. Onjia¹, S. Dragović³

¹*University of Belgrade, Vinča Institute of Nuclear Sciences, P.O. Box 522,
Belgrade*

²*University of Niš, Faculty of Science and Mathematics, Višegradska 33, Niš*

³*University of Belgrade, Institute for the Application of Nuclear Energy, Banatska
31b, Belgrade*

Abstract

In this study, the specific activities of ^{137}Cs in surface soils from the territory of Belgrade in the period 2006-2010 were determined by gamma-ray spectrometry. Mean specific activity of ^{137}Cs was 23 Bq/kg and the corresponding absorbed dose was 1.5 nSv/h. The specific activities of ^{137}Cs in soil were geographically mapped. The significant spatial variability of ^{137}Cs specific activities was observed.

Introduction

As the consequence of the nuclear tests carried out since 1945, large amounts of various radioactive materials were emitted into the atmosphere and subsequently distributed all over the world. Radionuclide ^{137}Cs was introduced into the atmosphere through nuclear weapon tests notably in the northern hemisphere in 1945 and then produced as the result of the accidents especially in Chernobyl in 1986 and routine processes of nuclear reactors. Among radionuclides in the soil deposited after Chernobyl accident, ^{137}Cs poses considerable environmental and radiological problems because of its relatively long half-life (30.17 y), its abundance in the fallout, high mobility and similarity to potassium as the major plant nutrient [1].

The aim of this work was to investigate the spatial variability of the specific activity of ^{137}Cs in soil samples collected across the territory of Belgrade, the capital of Serbia, using gamma-ray spectrometry. The absorbed gamma dose rate in air due to this radionuclide is also assessed.

Materials and Methods

The samples of undisturbed surface soil (n=250) were taken from 70 regions in Belgrade, during 2006-2010. Samples were dried at 105 °C to constant weight, homogenized and passed through a 2 mm mesh sieve. The specific activities of ^{137}Cs were measured by HPGe gamma-ray spectrometer (ORTEC-AMETEK, 34% relative efficiency and 1.65 keV FWHM for ^{60}Co at 1.33 MeV, 8129 channels) for 60 ks. The activity of ^{137}Cs was determined using its 661.66 keV gamma-ray line. The software package Gamma Vision 32 was used to process the spectra obtained [2]. From these results external effective dose rates were calculated according to the internationally accepted activity to dose rate conversion equations [3-6]. The specific activities of ^{137}Cs were geographically mapped using ArcGIS from ESRI [7].

Results and Discussion

Descriptive statistics for the specific activities of ^{137}Cs in soil samples collected from the territory of Belgrade and the corresponding external effective dose rates are presented in Table 1.

Table 1. Descriptive statistics for the specific activity of ^{137}Cs in soil samples collected from the territory of Belgrade during 2006-2010 and the corresponding external effective dose rates.

Parametar	^{137}Cs (Bq/kg)	D_{Cs} (nSv/h)
Mean	23	1.5
St. deviation	20	1.2
Median	15	1.0
Range	84	56
Mode	11	0.6
Minimum	3	0.2
Maximum	87	5.8

The mean of ^{137}Cs specific activity obtained in this study is comparable to those reported for Republic of Srpska (26 Bq/kg), Italy (40 Bq/kg) and FYR Macedonia (71 Bq/kg) [8-10].

The significant variability of the specific activities of ^{137}Cs in analyzed samples of soil was observed (Fig. 1).

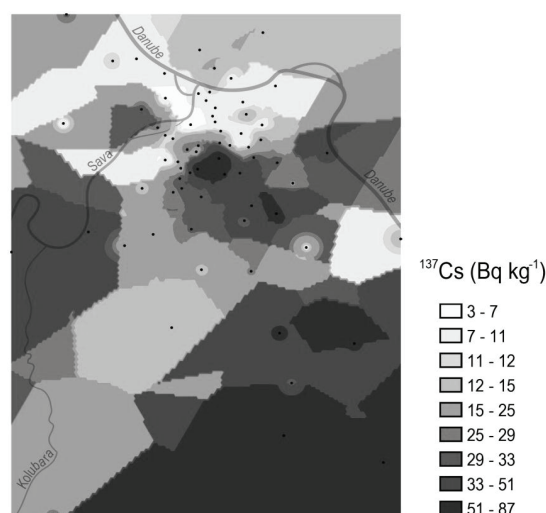


Figure 1. Spatial distribution of the ^{137}Cs specific activity in Belgrade soil.

Conclusion

The presence of ^{137}Cs has been detected in all soil samples, with high variability of its specific activity, ranging from 3 Bq/kg to 87 Bq/kg. The observed range reflects

the inhomogeneity of the deposition process following the Chernobyl accident. The results of the present study will be valuable database for future estimations of the impact of radioactive pollution.

Acknowledgement

This work was supported by the Ministry of Education and Science of the Republic of Serbia (Project No. III 43009).

References

- [1] UNSCEAR, 2000, United Nations, New York.
- [2] ORTEC, Gamma Vision 32, 2001, Oak S.N. Ridge, USA.
- [3] A.Tahir et al., *Radiat. Prot. Dosim.* 2006,118, 345-351.
- [4] K. Jamil, *J. Environ. Radioact.* 1998, 41, 207-216.
- [5] S. Ali et al., *Sci. Total. Environ.* 1996, 187, 247-252.
- [6] J.R. Lamarsh, *Introduction to Nuclear Engineering*, 1983, New York.
- [7] ESRI, 2009. Environmental Systems Research Institute Inc., Redlands, CA.
- [8] M. Janković et al., *Radiat. Meas.* 2008, 43, 1448-1452.
- [9] E. Bellotti et al., *Appl. Radiat. Isot.* 2007, 65, 858-865.
- [10] S. Dimovska et al., *Radiat. Prot. Dosim.* 2010, 138, 144-157.

K-21-P

BIOSORPTION OF Cu(II) ON XANTHATED LAGENARIA VULGARIS SHELL

M. M. Kostić¹, M.D. Radović¹, J. Z. Mitrović¹, D. V. Bojić¹,
D. Milenković², T. D. Anđelković¹, A. Lj. Bojić¹

¹*Department of Chemistry, Faculty of Science and Mathematics, University of Niš,
33 Višegradska Str., 18000 Niš, Serbia*

²*High Chemical Technological School, Department of Chemical Technology,
Kosančićeva 36, 37000 Kruševac, Serbia*

Abstract

This study investigated the feasibility of chemically modified *Lagenaria vulgaris* shell as a novel sorbent for copper removal from water. *Lagenaria vulgaris* has been functionalized by introducing xanthate groups by carbon disulphide treatment in alkaline medium. By investigating effects of contact time and sorption isotherms on the adsorbed amount of Cu(II) ions by xanthated *Lagenaria vulgaris* (xLVB), it was established that sorption equilibrium was reached after 50 minutes of contact time and that there is the best agreement with Langmuir isotherm model.

Introduction

Nowadays, increased presence of heavy metals (cadmium, copper, chromium, lead, mercury, nickel, zinc) in industrial waste waters is major problem for humanity and science. Because of their negative effects to humans, animals and overall environment, it is very important to remove heavy metals from wastewaters [1, 2]. Conventional methods for removing heavy metals from aqueous solutions include chemical precipitation, oxidation/reduction, electrochemical treatment, evaporative recovery, filtration, ion exchange and membrane technologies. These processes may be ineffective or cost-expensive, especially when the metals in solution are in range of 1-100 mg dm⁻³ [3, 4]. In recent years, sorption technology and using biomaterials for wastewaters treatment are developed and used, as high efficient but low-cost method. One of such biomaterials is *Lagenaria vulgaris*.

Lagenaria vulgaris belongs to *Cucurbitaceae* family. It is appropriate adsorbent of heavy metals because of its lignocellulosic composition with a capacity for binding metal cations due to hydroxyl, carboxylic, lactonic and phenolic groups present in their structure. Adsorption capabilities of chemically modified, xanthated *Lagenaria vulgaris* biosorbent (xLVB) were tested for Cu(II) metal ions, through effects of contact time and initial metal concentration.

Experimental

Reagents. All chemicals were of analytical reagent grade and used without further refinement. HNO₃, NaOH, CS₂, CuSO₄ were purchased from Merck (Germany). All solutions were prepared with deionized water.

Preparation of biosorbent. *Lagenaria vulgaris* shell was roughly crushed, washed with deionized water and grounded by laboratory blender. Biomass was soaked in 0.3 M HNO₃ for 24 hours and after that, washed with deionized water and treated with 0.1 M NaOH for 30 min. Excess alkali was removed by thoroughly washing and sorbent was dried in the oven at 55±5°C to constant weight. Dried biomass was fractionized using standard sieves (Endecotts, England).

Xanthation procedure: 5 g of prepared adsorbent (granulation from 0.8 to 1.25 mm) was soaked in 5 M NaOH, stirred for 90 minutes and washed with deionised water; then it was esterified with 0.5 cm³ of CS₂ and 50 ml 2.5 M NaOH for another 90 minutes. After that, biomass was washed with deionized water and dried at 40°C. As a result, xanthated *Lagenaria vulgaris* biosorbent (xLVB) was prepared for removing heavy metals from aqueous solutions.

Batch biosorption experiments. The stock solution of Cu(II) was prepared in 1.00 g dm⁻³ concentration using CuSO₄. Working standard solutions were prepared just before use by the appropriate dilution of the stock solutions. The pH of the solutions was adjusted pH-metrically to the pH 5 with nitric acid or sodium hydroxide (0.01 M) that turned out to be optimal value. Experiment on the adsorption of metal ions by xLVB was carried out in batch conditions, by agitating 125 cm³ of 50.0 mg dm⁻³ metal ion solutions of Cu(II), contacted with 0.5 g biosorbent. At required time intervals: 0, 1, 2, 5, 10, 20, 40, 60, 90, 120 and 180 min, 4.0 cm³ of samples were withdrawn and analyzed using a flame atomic adsorption spectrometer (Analyst A300, Perkin Elmer, USA).

Results and discussion

Contact time effect. In this study the effects of contact time on the sorption of Cu(II) ions on xLVB was studied. As it is shown in Figure 1. sorption process has 2 phases; in the first phase, after 20-30 minutes of sorbent-sorbate contact time it was removed most of Cu(II) ions (10.238 mg g⁻¹). The sorption equilibrium was reached after 50 minutes of contact time (12.364 mg g⁻¹). Initial concentration of investigated ions decreases from 50 mg dm⁻³ to level of 0.54 mg dm⁻³. The effects of contact time on the adsorption of Cu(II) ions by xLVB. are shown in Figure 1.

Sorption isotherms. The sorption data were tested against Langmuir, Freundlich and Temkin adsorption isotherm models. In Table 1 are presented equilibrium model parameters for adsorption Cu(II) onto xLVB and their values, for each model. r^2 (the correlation coefficient) in respect to sorption of Cu(II) ions has values 0.9984, 0.9643 and 0.8310 for Langmuir, Temkin and Freundlich model,

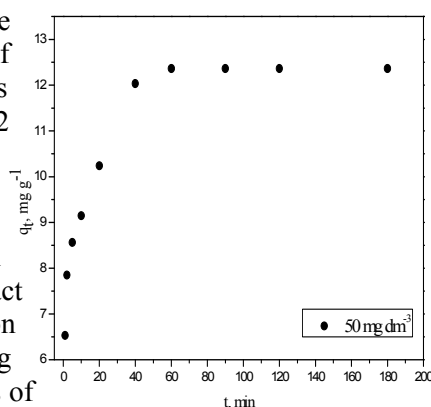


Figure 1. Effect of contact time on adsorption capacity of Cu²⁺.

K-21-P

respectively. Accordingly, the adsorption characteristics of xLVB for Cu(II) ions are the best fitted by Langmuir isotherm model, with regard to the Temkin and Freundlich isotherm model. The enhancement in metal adsorption capacity can be explained using Pearson rule [5]; according to this rule, soft bases will form stable complexes with metals such as copper [6]. Xanthate group can be classified as soft base, thus xLVB will certainly show high adsorption capacity.

Freundlich constant n is a measure of the deviation of the adsorption from linearity. The adsorption is linear if the n has value about 1; if the value of n is higher, adsorption is favorable. Vice versa, if below 1, adsorption is unfavorable. In this study, Freundlich constant n has value 4.06, which implies to favorable adsorption.

Table 1. Equilibrium model parameters for adsorption of Cu(II) onto xLVB.

Langmuir isotherm			Freundlich isotherm			Temkin isotherm		
K_L ($\text{dm}^3 \text{mg}^{-1}$)	q_{max} (mg g^{-1})	r^2	K_F ($\text{dm}^3 \text{g}^{-1}$)	n	r^2	K_t	b_T (kJ/mol)	r^2
0.2886	23.17	0.998	6.839	4.06	0.831	1.003	0.959	0.964

Conclusions

This study show that the xanthated *Lagenaria vulgaris* shell can be used as efficient and inexpensive material for removal Cu(II) from polluted water. Biosorption process is fast and in the first phase (20 min) achieved very high sorption capacity (10.238 mg g^{-1}). Sorption equilibrium was reached after about 50 minutes of contact time with q_e 12.36 mg g^{-1} . Sorption process can be the best fitted by Langmuir isotherm model, which indicates monolayer adsorption at specific energetically homogeneous sites, without interaction between molecules adsorbed on neighboring sites.

Acknowledgement

Authors would like to acknowledge for financial support to the Ministry of Education and Science of the Republic of Serbia (Grant No TR34008).

References

- [1] W. S. Wan Ngah, M.A.K.M. Hanafiah, Bioresour. Technol. 99 (2008) 3935.
- [2] S. Liang, X. Guo, N. Feng, Q. Tian, J. Hazard. Mater. 170 (2009) 425.
- [3] L. Sha, G. Xue-yi, F. Ning-chuan, T. Qing-hua, Trans. Nonferrous Met. Soc. Chna., 2010, 20, 187.
- [4] D. L. Mitić-Stojanović, A. Zarubica, M. Purenovic, D. Bojic, T. Andjelkovic, A. Bojic, Water SA, 37(3) (2011) 303-312.
- [5] R. G. Pearson, Inorg. Chem. 27 (1988) 734
- [6] M. J. Winter, Complexes, d-block Chemistry, Oxford University Press, New York, 1994.

REMOVAL OF Cu(II) FROM WATER USING METHYL-SULFONATED *LAGENARIA VULGARIS* SHELL

M. N. Stanković, N. S. Krstić, R. S. Nikolić, D. V. Bojić,
J. Z. Mitrović, M. D. Radović, A. Lj. Bojić

*Department of Chemistry, Faculty of Science and Mathematics, University of Niš,
Višegradska Str. 33, 18000 Niš, Serbia*

Abstract

Chemical modified *Lagenaria vulgaris* was used as biosorbent for removal Cu(II) from water. The adsorbent removal efficiency was determined as a function of contact time and initial pH. Kinetics models showed that metal adsorption follow a pseudo-second-order kinetic model. Results showed that the Cu²⁺ removal by msLVB increased with increasing pH from 2.0-5.0, and than slightly decrease at pH 6.0.

Introduction

Pollution of natural waters by metal ions is a serious problem nowadays. There are several methods to remove toxic metal ions from waste-waters: chemical precipitation, electrochemical technologies, ion exchange, reverse osmosis and sorption onto activated carbon [1]. But, these methods have high operational costs or leave secondary sludge so are no acceptable in the developing countries.

The shell of *Lagenaria vulgaris* can be used as a low-cost sorbent for heavy metals, largely due to its lignocellulosic composition with a capacity for binding metal cations due to hydroxyl, carboxylic, lactonic and phenolic groups present in their structure. The presented functional groups indicate that the predominant biosorption mechanisms are ion-exchange, complexation and chelation [2]. *Lagenaria vulgaris* is common name in older literature for *Lagenaria siceraria* (Molina) Standley, a species of *Cucurbitaceae* family [3,4].

The effect of contact time and initial pH has been investigated. The sorption process nature has been evaluated with respect to its kinetic aspects.

Experimental

Preparation of biosorbent. Methyl-sulfonated *Lagenaria vulgaris* biomaterial (msLVB) was prepared by adding 200 mL of 1.5% solution of formaldehyde to 10 g of grounded and sieve fractionized raw material. After heating in flask under reflux at 80°C for 2 h, 25 g NaHSO₃ (Merck) was added to and reaction mixture was heated for 3 h at 100 °C again under reflux. After cooling, the material was washed thoroughly with de-ionized water until sulfate reaction was over and oven-dried at 55°C. Obtained material was used for metal sorption studies.

Metal solution. Standard stock solution of Cu²⁺ (1000 mg Cu(II) L⁻¹, CuSO₄·5H₂O, Merck) was used to prepare appropriate concentrations for the sorption studies. The pH of the solutions was adjusted pH-metrically to the required value with nitric

acid or sodium hydroxide (0.01 M), without buffering. pH of solutions was determined pH metrically (SensION3, HACH, USA).

The adsorption equilibrium experiments. The batch adsorption experiments were conducted with constant amount of msLVB (4.0 g L^{-1}) added to 125 mL Cu(II) ion solutions of known concentrations (10, 20, 50, 100, 200, 400 mg L^{-1}) in 250 mL flasks shaken for 240 min at room temperature. Rate of metal sorption by msLVB was determined by analyzing residual Cu(II) ions in the filtered solutions after contact periods of 0, 1, 5, 10, 20, 40, 90, 120, and 240 min.

Cu(II) ions concentrations measurement. The concentrations of unadsorbed Cu(II) ions in the solution before and after adsorption were determined by using an atomic absorption spectrophotometer (AAS Analyst 300, Perkin Elmer, USA) at the wavelength 324.8 nm.

Results and Discussion

Biosorption kinetics. Experiments were performed with model wastewaters containing Cu(II) ions at initial concentrations 50.0 mg dm^{-3} and initial solution pH 5.0, at room temperature. The effect of contact time on the removal efficiency of msLVB for Cu(II) ions is shown at Fig. 1. The adsorption increased sharply with contact time in the first 20 min and reached equilibrium within about 40 min. Further increase in contact time did not show a significant increasing in biosorption.

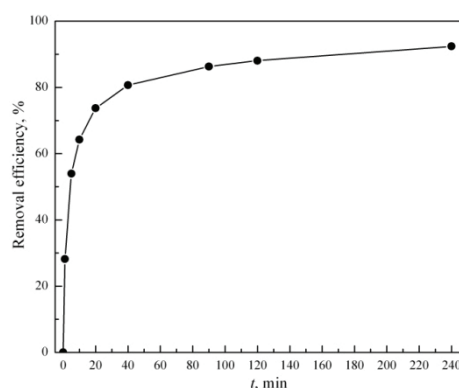


Figure 1. Removal efficiency of Cu(II) ions by msLVB (50.0 mg dm^{-3} Cu(II), pH 5.0, $22 \pm 2^\circ\text{C}$).

In this study, the biosorption kinetic data were analyzed using following theoretical-models: pseudo-first-order, pseudo-second-order and Elovich model. The experimental data fit well to the pseudo-second order kinetic model, where the r^2 values were observed to be close to 1 (Table 1).

Table 1. Constants of pseudo-first order, pseudo-second-order and Elovich model kinetics based on the sorption of Cu(II) from 50 mg L^{-1} solutions, pH 5.0, by 4.0 g L^{-1} msLVB.

(mg g ⁻¹)	Pseudo-first-order			Pseudo-second-order			Elovich model		
	Q (mg g ⁻¹)	K (min ⁻¹)	r ²	Q _{eq} (mg g ⁻¹)	k ₂ (mg ⁻¹ min ⁻¹)	r ²	α	β	r ²
11.40	5.70	0.0221	0.828	11.52	0.018	0.999	27.027	0.698	0.958

Effect of initial pH. The influence of pH in the initial solution of Cu^{2+} was examined at different pH ranging from 2.0 to 6.0. Fig. 2 shows the effect of pH on the removal efficiencies of Cu^{2+} ions by msLVB. The Cu^{2+} removal by msLVB increased with increasing pH and attained values of 93.62 % at an initial pH of 5.0. The Cu^{2+} uptake increased significantly from 29.20% to 92.40% at pH ranging 2.0–5.0, and then slightly decrease on 91.68% at pH 6.0. The pH of the solution is one of the most significant parameters in the adsorption of metal ions from aqueous

solutions. This parameter is straightforward ions with metal ions to active sites on the surface. It shows its minimum values at pH 2.0. At this pH, the active sites became positive and the surface active sites, which results in lower removal efficiency. As the pH increased, the ability of Cu^{2+} ions for complexation increased. Removal efficiency at pH 6.0 is quite lower than at pH 5.0 due to the partial precipitation of Cu(II) ions in form of Cu(OH)_2 through blank experiment (treatment in blank biosorbent).

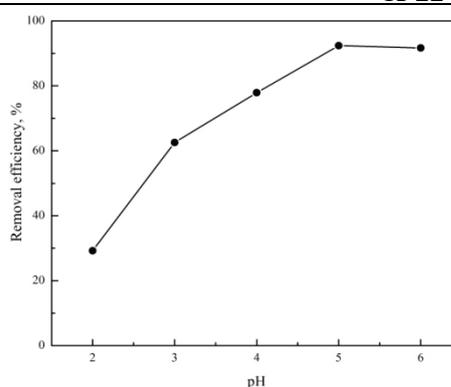


Figure 2. Effect of pH on the sorption of Cu^{2+} from 50 mg dm^{-3} solutions.

Conclusions

This study shows that the methyl-sulfonated *Lagenaria vulgaris* shell can be used for the removal of Cu(II) ions from wastewaters as an efficient low-cost biosorbent. Removal efficiency increased significantly with pH from 2.0 to 5.0, and then slightly decreases at pH 6.0. Biosorption kinetics follows a pseudo-second-order model.

Acknowledgements

This work was supported by the Ministry of Education and Science of the Republic of Serbia, Grant No. TR34008.

References

- [1] R. Han, W. Zou, H. Li, Y. Li, J. Shi, *J. Hazard. Mater.*, 2006, B137, 934–942.
- [2] B. Volesky, Z.R. Holan, *Biotechnol. Prog.*, 1995, 11, 235–250.
- [3] H. M. Burkill, *The useful plants of west tropical Africa*, Royal Botanic Gardens, Kew, 1985, 1,
- [4] B. N. Shah, A. K. Seth, B. S. Nayak, *Der. Pharmacia Lett.*, 2010, 2, 202-205.

K-23-P

DETERMINATION OF PESTICIDE RESIDUES IN WORKING CLOTHES

N. Andrić¹, D. Marković²

¹*Galenika Fitofarmacija AD, Batajnički drum bb, Zemun,* ²*Fakultet za primenjenu ekologiju FUTURA, Lazarevački drum 13, Beograd*

Abstract

The aim of the experiment was to determine possible presence of pesticide residues of active substances in the working clothes which is used in the laboratory for testing of pesticides. For better comparison, the experiment was performed on a sample of clean and work laundry (work clothes from the laboratory). Analysis was done on the gas-mass chromatograph. The results obtained for pure water from washing machine are expected and there is no trace of contamination in them. In the samples of water from washing machine of work clothes one pesticide was found - terbuthylazine, which was the purpose of this experiment. High resistance to hydrolysis of terbuthylazine explains its presence in water samples of work clothes.

Introduction

Pesticides are chemical substances which are used in farming, fruit growing and forestry as well as in communal hygiene. These chemicals are used for plant protection. They are used to control insect pests and plant diseases, for the destruction of weeds and to preserve the quality of agricultural products and increase yields, control of parasites and diseases dangerous to humans and animals.[1]

Because of their stability and durability (particularly organochlorine compounds), they can migrate, redistribute and finally accumulate in plants, animals and other living organisms for years. As a result of this behavior they can act far away from the point of use, which is characterized by global overdue effects. They can move in the form of aerosols, suspensions or solutions by air streaming, by ground and underground water, by migration of birds, animals and people, by transport of raw materials and food. Because of this, pesticides can often cause undesirable secondary effects on the environment. [2,3]

After use, pesticides undergo different physical, chemical and biochemical processes. While in some cases ends up as no hazardous materials, in the majority of cases pesticides occurs as toxic substances in agricultural products, soil and water (in original or modified form). The chemical structure of pesticides is essential. The absence of harmful residues in the environment is best achieved if pesticides are disintegrated to products that are found in abundance in the environment. In other words, pesticide molecules needs to be composed of fragments of biogenic type - amino acids, sugar, lipids, carboxylic acids and

inorganic residues, as in the case of organophosphorus pesticides where in the final stage of decomposition phosphorous acid occurs. [2]

Experimental

This kind of experiment is rare in Serbia because very little attention is given to the contaminated working clothes. Workers who are constantly wearing those clothes can be endangered, because even the small doses of contamination can be harmful considering bioaccumulation effect. Long-term exposition to the pesticides can cause serious health problems. Purpose of this experiment is to draw attention on this type of pollution and to prevent it.

The aim of the experiment was to determine possible pesticide residues of active substances in the working clothes. Working clothes is one that is used in the laboratory for testing of pesticides and involves working coats, shirts, pants, etc. For better comparison, the experiment was performed on a sample of clean and dirty laundry (work clothes from the laboratory). Clean laundry was washed in a washing machine with water only, without addition of detergent. The same was done with work clothes. Samples were stored in PET bottles.

Liter of water from the clean laundry was extracted with dichloromethane in a separating funnel. 400 ml of sample was transferred from PET bottle to the separation funnel and then added 100 ml of dichloromethane. The sample was stirred and extracted in a glass. The same procedure was repeated with next 400 ml. A further 200 ml of water from clean laundry was transferred into the funnel and added 50 ml of dichloromethane. The extract was also transferred into the cup. After these three extractions, in the glass is now 250 ml of dichloromethane and the analytes from the sample. The entire extraction procedure was repeated, only this time three times of 300 ml of sample was extracted with 250 ml of dichloromethane (containing analytes) from the cup. Again, we get 250 ml of dichloromethane containing unknown analytes. This sample was evaporated in the water bath to a volume of 10 ml. In this way the sample was concentrated. Extraction was performed in the same manner with the next liter of water from the clean laundry. The same procedure was applied on water samples of work clothes, ie., contaminated laundry. Analysis of these four samples was performed on the gas-mass chromatograph. [4]

Results and Discussion

The results obtained for pure water are expected and there is no trace of contamination in them. Identified compounds originate from nicotine, alcohol, fat, milk, butter, cosmetics and detergent. The same compounds were found in water samples of work clothes. However, in water samples from the work clothes was found one pesticide - terbuthylazine, which was the purpose of this experiment. Terbuthylazine is herbicide which is used to spray sunflower and maize. It belongs to the triazine group and to the third category of toxins. It is not known whether is carcinogenic, but it has low acute toxicity. Terbuthylazine is irritating to skin, eyes and respiratory tract. If it is found in water, it can affect the growth, physiology and

K-23-P

plant populations. This herbicide accumulates in fish, phytoplanktons and zooplanktons. For a fish is moderately toxic and highly toxic to zooplankton. Terbutylazine is persistent in aquatic systems, because it is poorly hydrolysed and it is resistant to photolysis. If the pH of water is between 5 and 9 this pesticide is stable from 86 to over 200 days. There is no evidence that in small doses terbutylazine is harmful to humans and animals. [6,7]

Conclusion

Although only one pesticide was found, we can consider that the experiment succeeded. High resistance to hydrolysis explains presence of terbutylazine in water samples of work clothes. Work clothes were in contact with other active substances, but their presence was not detected probably due to their instability in aqueous systems. This experiment went only to the qualitative determination of pesticide residues in working clothes, which is a good start for their quantitative determination in the future. The next step is to attempt quantitative determination of pesticides in work clothes.

References

- [1] D. Minić, Hemija pesticida, dobijanje i primena, Panda Graf, Beograd, 1994.
- [2] D. Veselinović, I. Grzetić, Š. Đarmati, D. Marković, Stanja i procesi u životnoj sredini, FFH, Beograd, 1995.
- [3] N. Mitić, Pesticidi u poljoprivredi i šumarstvu u Srbiji i Crnoj Gori, Društvo za zaštitu bilja Srbije, Beograd, 2004.
- [4] V. Jovanović, M. Kopečni, S. Milonjić, A. Ruvarac, A. Spirić, V. Višacki-Hromatografija, teorijski i praktični aspekti, Institut za nuklearne nauke - Vinča, Beograd, 1988.
- [5] http://www.pesticideinfo.org/Detail_Chemical.jsp
- [6] http://www.who.int/water_sanitation_health/dwq/chemicals/terbutylazine.pdf
- [7] <http://www.alanwood.net/pesticides/terbutylazine.html>

REMOVAL OF IODINE FROM AQUEOUS SOLUTIONS BY POLYETHYLENIMINE – EPICHLOROHYDRIN RESINS

S. Sarri¹, P. Misaelides¹, F. Noli¹, L. Papadopoulou², D. Zamboulis¹

¹ *Department of Chemistry, Aristotle University, 54124 Thessaloniki, Greece*

² *Department of Physics, Aristotle University, 54124 Thessaloniki, Greece*

Introduction

The presence of iodine in the biosphere is not only due to natural sources but also to number of human activities (e.g. medical, industrial, nuclear energy production). Iodine isotopes (e.g. ¹³¹I ($t_{1/2} = 8$ days), ¹²⁹I ($t_{1/2} = 1.6 \times 10^7$ yr)) are also among the most abundant fission products and are released to the environment in cases of nuclear reactor accidents and nuclear explosions [1].

In the present study the ability of two recently prepared epichlorhydrin - polyethylenimine resins to remove iodine from aqueous media was investigated under various conditions.

Experimental

Two polyethylenimine - epichlorohydrin resins were prepared using low- (L.M.W.) and high molecular weight polyethylenimine (H.M.W.) and characterized at the Chemistry Department of the Aristotle University. A modification of a previously described synthesis method was applied for the preparation of the resins [2].

For the sorption experiments 30 mg of the resins were contacted in polypropylene tubes for 24 hours with 10 mL of ¹³¹I-labeled NaI solutions (C_{init} : 300 to 5000 mg I /L) at room temperature. After separation of the solid and liquid phases by centrifugation, the iodine concentration in the liquid phase was determined by gamma-ray spectroscopy using HPGe detector (CANBERRA ReGe, resolution 2.1 keV) connected with a computer based gamma-spectroscopy set-up. The obtained data were used to calculate the uptake capacity in mg/g and construct the corresponding sorption isotherms.

Experiments both in absence and presence of background electrolytes (0.1 M NaCl and 0.033 M Na₂SO₄ – constant ionic strength 0.1 M) were performed using iodides solutions of pH_{init} 3 and 7 in the first case and pH_{init} 3 in the second one adjusted by HCl and NaOH.

The surface and the interior of the resin grains, prior and after the sorption, were examined by SEM/EDS (JEOL 840A SEM equipped with an OXFORD ISIS 300 SEM-EDS analyzer).

The experimental results were modeled using the Langmuir and Freundlich isotherm equations [3] and compared with literature data for other sorbents.

Results and Discussion

Both investigated resins could effectively remove iodides from aqueous solutions. The H.M.W. resin showed higher sorption capacity than the L.M.W. one. This effect could be attributed to the structural differences between the two sorbents. The results also indicated that for both sorbents a higher iodine uptake was obtained at $\text{pH}_{\text{init}} 3$. The uptake capacity decreased with increasing pH_{init} . The last can be attributed to the stronger competition from the side of hydroxyl-ions for the same number of sorption sites.

Fig. 1 presents the experimental data obtained for the I^- - sorption by the two resins from solutions of $\text{pH}_{\text{init}} 3$ absence of background electrolyte. In the same figure the curves obtained by fitting the experimental data by the Langmuir isotherm equation and the 95% confidence limits of the fit are also given. All maximum sorption capacity - (Q_{max}), K - and the correlation coefficient (R^2) values are presented in Table 1 along the corresponding parameters obtained from the fitting by the Freundlich equation. The correlation coefficient values showed that the Langmuir isotherm equation could better reproduce the experimental results compared to the Freundlich one.

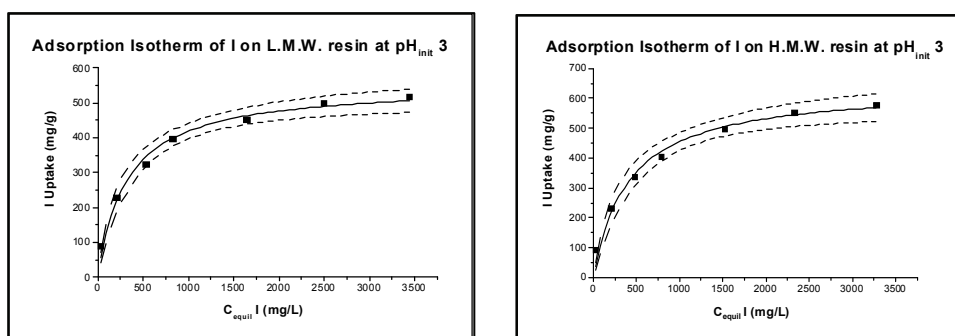


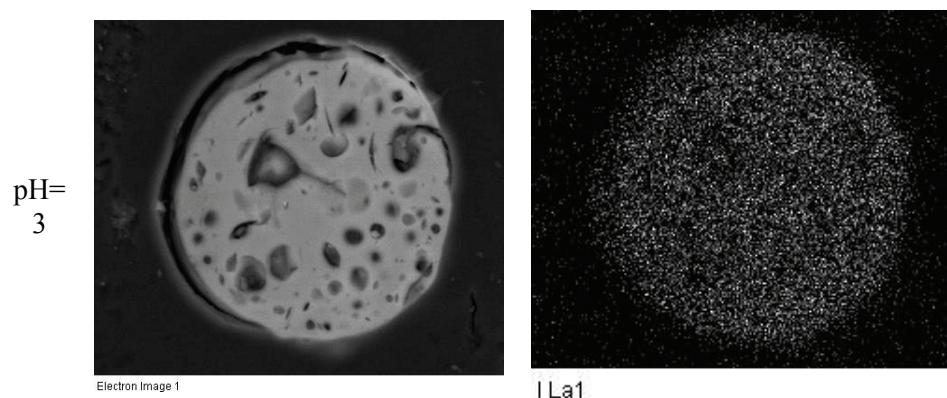
Figure 1. Adsorption isotherms for the I^- - sorption onto the two resins along the corresponding Langmuir isotherm fit. The dashed lines represent the 95% confidence limits of the fit.

Experiments performed in the presence of background electrolyte indicated that the presence of SO_4^{2-} ions in the solutions reduced the I-uptake to a higher extent than the presence of Cl^- ions, probably due to their larger size and charge. The maximum sorption capacity (Q_{max}) was, in the case of presence of Cl^- ions, almost 1/3 of the value determined in absence of background electrolyte whereas the presence of sulfates reduced the I-sorption capacity by ca. 90%.

The examination of intersections of the I-loaded resins grains by SEM/EDS revealed that iodine was evenly distributed throughout the bulk of the resins and not bound only to their surface (Fig. 2).

Table 1. Langmuir- and Freundlich parameter values and corresponding correlation coefficients.

			Q_{\max} (mg/g)	K (L/g)	n	R^2
L.M.W. resin	pH 3	Langmuir	552.4	0.00313	-	0.986
		Freundlich	-	45.91063	3.284	0.965
	pH 7	Langmuir	507.5	0.00377	-	0.986
		Freundlich	-	54.39033	3.652	0.932
H.M.W. resin	pH 3	Langmuir	638.8	0.00247	-	0.982
		Freundlich	-	42.2304	3.030	0.981
	pH 7	Langmuir	603.3	0.0027	-	0.983
		Freundlich	-	43.1532	3.112	0.967

**Figure 2.** SEM image of a cross-section of a H.M.W. resin grain after I uptake (left) and the corresponding I-mapping (right).

The comparison of the experimental results with literature data indicated that the two resins showed higher I-sorption capacity than a number of natural raw and modified sorbents (e.g. Mg–Al (NO₃) layered double hydroxide, Mg–Al hydrotalcite-like compounds) but lower than a series of activated carbons of different origin).

References

- [1] <http://www.atsdr.cdc.gov/toxfags> (last visited 7.5.2012)
- [2] Ebner A.D., Ritter J.A., Pioehn H.J., Kochen R.L., Navratil J.D., Sep. Sci. Technol. 34 (1999) 1277-1300.
- [3] Gerente G. et al., Environ. Sci. Technol. 37 (2007) 41–127.

K-25-P

REMOVAL OF NI(II) IONS BY TEMPERATURE TREATED RED MUD FROM ALUMINUM INDUSTRY

A. Milenković¹, S. Smiljanić², I. Smičiklas¹, M. Šljivić-Ivanović¹

¹*University of Belgrade, Vin a Institute of Nuclear Sciences, P.O. Box 522,*

Belgrade Serbia

²*University of East Sarajevo, Faculty of Technology, Karakaj bb, 75400 Zvornik, Republic of Srpska, Bosnia and Herzegovina*

Abstract

Red mud is a waste produced in excessive amounts by the aluminum industry. Due to heterogenic mineral composition it represents a promising sorbent material. In this study, Ni(II) removal from aqueous solutions was studied. As-received red mud was subjected to temperature treatment, in the range 200-900°C. The influence of annealing temperature and initial solution pH on Ni(II) removal efficiency was analyzed and discussed.

Introduction

Red mud, a waste sludge obtained after alkaline digestion of bauxite ore, is composed mainly of Fe, Al and Si oxides, as well as titania, sodalite, gypsum, calcite, etc [1]. It was intensively studied as an immobilization agent for various toxic substances [1, 2]. The previous experiments on Ni(II) removal from aqueous solutions by thoroughly rinsed red mud from the “Bira” Alumina Factory confirmed the applicability of this industrial waste to remove Ni(II), dominantly by specific sorption and precipitation mechanisms [3]. Ni(II) sorption capacity could be enhanced by annealing rinsed sample at 600°C [3]. The original red mud is highly alkaline, which can benefit the removal of hydrolysable cations such as Ni(II). In this study, the influence of temperature treatment on removal efficiency of as-received red mud was studied, as well as the influence of initial solution pH.

Experimental

As-received red mud (without prior washing or neutralization) was dried at 105°C and milled in the mortar. The 15 g portions of obtained powder were annealed at 200, 400, 600, 800 and 900°C, in the electrical furnace, for 3 h (samples denoted as BRM200-BRM900). Ni(II) ions removal was tested in batch conditions, by agitating 0.1 g of solid phases with 20 mL of $2 \cdot 10^{-3}$ mol/L Ni(NO₃)₂ solution, at room temperature, for 24 h. The initial pH values were adjusted in the range 2-6, by adding minimum volumes of HCl and NaOH solutions. Clear supernatants were separated from the solid phase by centrifugation and filtration. Final pH values were measured. Initial and the residual concentrations of nickel in the supernatants

were determined by flame Atomic Absorption Spectrometer (Philips Pye Unicam SP9, at 232.0 nm).

Results and discussion

Starting material showed the weight losses of 4.13 %, 5.93%, 6.66% 7.93% and 8.13% after annealing at 200°C, 400°C, 600°C, 800°C and 900°C, respectively. The effects of temperature treatment and initial solution pH on Ni(II) removal and final pH values are presented in Fig. 1.

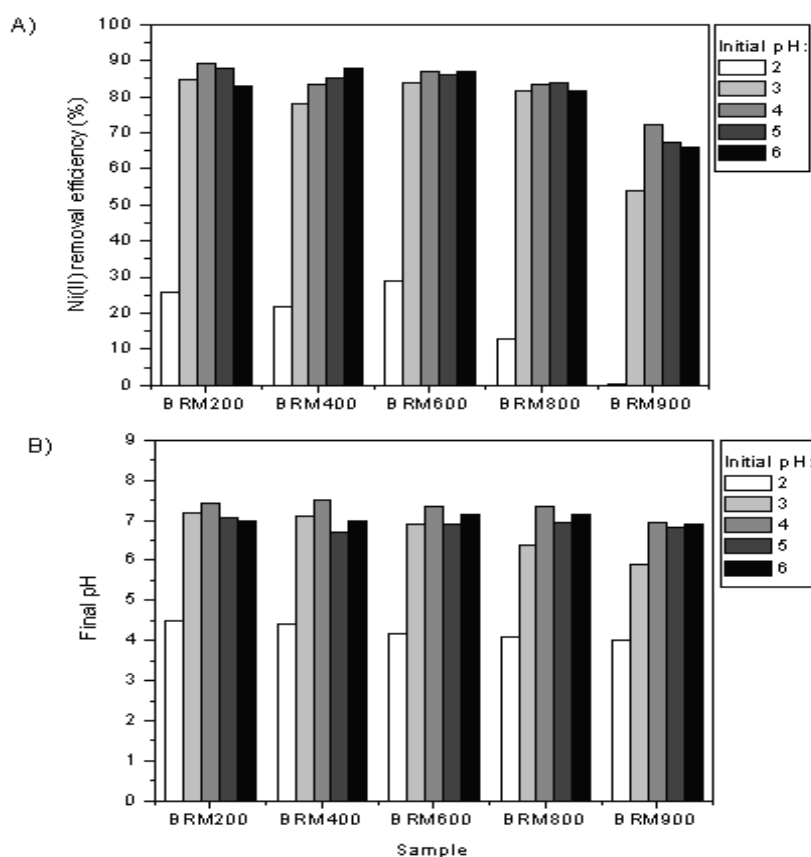


Figure 1. The influence of temperature treatment and initial pH on (A) Ni(II) removal efficiency and (B) final pH values.

Depending on applied sorbent sample, the process efficiency increased rapidly from 0.5%-28.9 % to 53.8%-84.7 % with the increase of initial pH from 2 to 3 (Fig. 1, a), whereas further pH rise up to 6 produced less significant changes. Such behavior can be associated with the buffering capacity of red mud [3]. pH values measured after equilibration (Fig. 1, b) were lowest for initial pH 2, while higher and rather comparable in the initial pH range 3-5.

Heat treatments induce physical and chemical changes in red mud, consequently, thoroughly washed sample showed the maximum sorption after annealing at 600°C [3]. In this study, the excess amounts of NaOH added during ore digestion partially covered the differences between physico-chemical properties of sorbents. The most obvious effect of temperature treatment was decrease of process efficiency using sorbent BRM900 at all investigated initial pH (Fig. 1, a). Furthermore, BRM800 exhibited lower Ni(II) removal at initial pH 2. This can be connected with the increased mineral phase crystallinity of these samples, the effect of particles sintering and somewhat lower final pH values especially in the initial pH range 2-3 (Fig.1, b).

The overall performance of annealed samples was enhanced using as-received red mud than rinsed powder [3]. The additional amounts of Ni(II) removed from the aqueous solutions in this study, can be attributed to the higher equilibrium pH values and the greater contribution of the Ni(OH)₂ precipitation.

Conclusions

Ni(II) removal by annealed red mud increased most rapidly in the initial pH range 2-3. The influence of temperature treatment in the range 200-800°C, on process efficiency was less pronounced using as-received red mud, than in previous experiments with rinsed sample, due to higher and comparable final pH values. Heating at 900°C resulted in lower Ni(II) removal rates in the entire investigated pH range.

Acknowledgments

This work was supported by the Ministry of Education and Science of the Republic of Serbia (Project No. III 43009).

References

- [1] S. Wang, H. M. Ang, M. O. Tad, *Chemosphere*, 2008, 72, 1621–1635.
- [2] Y. Liu, R. Naidu, H. Ming, *Geoderma*, 2011, 163, 1–12.
- [3] S. Smiljanić, I. Smičiklas, A. Perić-Grujić, B. Lončar, M. Mitrić, *Chem. Eng. J.*, 2010, 162, 75-83.

BERYLLIUM-7 CONCENTRATION ANALYSIS IN GROUND LEVEL AIR IN SERBIA

M. M. Janković¹, D. J. Todorović¹, B. Ž. Janković²,
J. D. Nikolić¹, G. K. Pantelić¹, M. M. Rajačić¹

¹University of Belgrade, Institute Vinča, Radiation and Environmental Protection
Department, P.O. Box 522, 11001 Belgrade, Serbia

²Faculty of Physical Chemistry, University of Belgrade, Studentski trg 12–16, P.O. Box
137, 11001 Belgrade, Serbia

Abstract

⁷Be concentration in ground level air at five monitoring stations: Vinča, Zeleno Brdo, Zaječar, Vranje and Zlatibor was determined during the period from May 2011. to March 2012. Concentrations of ⁷Be ranged from 1.5 to 7.9 mBq m⁻³ and exhibit maxima in the spring/summer period. It was found that the value of the symmetrical index n is the highest for Vranje.

Introduction

⁷Be is a radioactive element (half-life 53.3 days) produced by cosmic rays in spallation processes with light elements (N, O, C), in the lower stratosphere (~70%) and the upper troposphere (~30%). Following production, ⁷Be is promptly attached to aerosols with a diameter of 0.3-0.6 μm whose residence time in the atmosphere is around 20 days [1]. In the troposphere, apart from its decay, ⁷Be is removed by wet deposition (the major mechanism for removal) and dry deposition. In ground level air, the residence time of ⁷Be is around 10 days [2]. Ground level ⁷Be has been measured in Belgrade, Serbia, since 1991, as a part of the air radioactivity monitoring programme in the Radiation and Environmental Protection Department Vinča Institute of Nuclear Sciences. The measured values of ⁷Be in Belgrade air are in good agreement with the data for other regions, and showed that the ⁷Be activity reaches its maximum in summer [3]. In this paper, concentrations of ⁷Be measured at different locations in Serbia are presented. Symmetrical index, n , was used as mathematical parameter to describe changes of the concentrations of ⁷Be in ground level air.

Experimental

Aerosol samples were collected on filter papers (Whatman 41, relative efficiency for deposited dust 80 %) by constant flow rate samplers (average air flow 35 m³ h⁻¹). The filter papers were then ashed at temperatures below 400 °C and a monthly composite sample containing 30–31 daily filters was formed (average volume 35×10³ m³). The samples were measured in small metallic containers. The activity of the ⁷Be was determined on an HPGe detector (Canberra relative efficiency 23 %) by standard gamma spectrometry. For calibration of detectors for measuring samples of aerosols, secondary radioactive material in the reference geometry of the plastic container vials was used which received from the primary reference of radioactive material, Czech Metrological Institute, Praha, 9031-OL-116/8, type

ERX, total activity 114.9 kBq on the day 03.03.2008. (^{241}Am , ^{109}Cd , ^{139}Ce , ^{57}Co , ^{60}Co , ^{88}Y , ^{113}Sn , ^{85}Sr , ^{137}Cs , ^{210}Pb). The threshold of detection of the ^7Be in air was 10^{-6} Bq m^{-3} for ^7Be . Counting time intervals were 60000 s.

Results and Discussion

The activities of ^7Be in ground level air at different locations during the period May 2011.- March 2012. are presented in Fig. 1. Concentrations of ^7Be in air were in the range of 1.5–7.9 mBq m^{-3} and exhibited a maximum in summer and a minimum in winter.

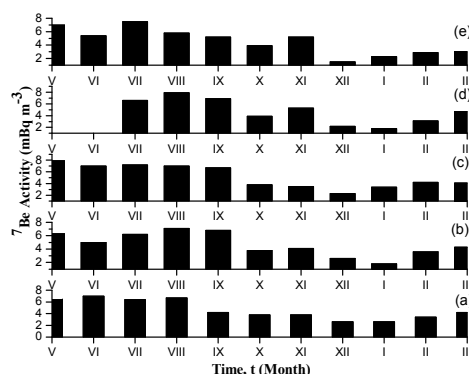


Figure 1. ^7Be activity in the ground level air, at: (a) Vinča, (b) Zeleno Brdo, (c) Zaječar, (d) Vranje and (e) Zlatibor.

The symmetrical index, n , which defines the magnitude of ^7Be content changes with time (in months), can be obtained directly from a derivative of $d^2c(^7\text{Be})/dt^2$ peak curve, based on the following equation:

$$n = 1.88 \frac{\left[\frac{d^2c(^7\text{Be})}{dt^2} \right]_L}{\left[\frac{d^2c(^7\text{Be})}{dt^2} \right]_R} \quad (1)$$

where 1.88 is the constant, indices L and R correspond to the left and right peak $d^2c(^7\text{Be})/dt^2$ values (extrema) on the second derivative $c(^7\text{Be})$ vs. t curves. Equation (1) is similar to the equation, which is present in the second Kissinger technique (Kissinger, 1957). Fig. 2 shows the second ($d^2c(^7\text{Be})/dt^2$) derivative curve of the normalized beryllium-7 concentrations ($c(^7\text{Be})$), in function of time, at different considered locations. The changes of the first and the second derivatives of curves follow the monthly changes of concentrations of ^7Be in time. As can be seen from Fig. 2, course of the second derivate curve for all locations has one expressed minimum which corresponds to the maximum value of ^7Be concentration in summer months. The second minimum occurs for the month November, corresponding to increased concentrations of ^7Be in this month at all locations except Zaječar. Using this graphical method and Eq. (1), the estimation results of the symmetrical index (n) values are as follows: Zlatibor ($n = 1.74$), Vinča ($n = 1.82$), Zeleno Brdo ($n = 2.50$), Vranje ($n =$

2.98) and Zajecar ($n = 1.94$). Values of symmetrical index increase with increasing mean annual concentrations of ^7Be except for Zajecar where the highest mean annual concentration was obtained but symmetrical index was 1.94. It should be emphasized that these are preliminary results for the concentration of ^7Be at locations Zajecar, Vranje and Zlatibor. For better monitoring of changes of symmetrical index, it is necessary to have data for many years.

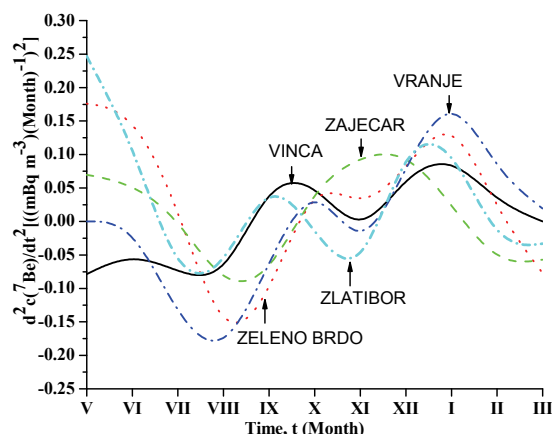


Figure 2. The second ($d^2c(^7\text{Be})/dt^2$) derivative curves of the normalized ^7Be concentrations ($c(^7\text{Be})$) in function of time (in Months), at different locations.

Conclusion

The obtained values of ^7Be concentrations in ground level air at five different locations in Serbia show a fluctuation which has oscillatory characteristics with enhanced activity in summer months. Application of symmetrical index as a mathematical parameter is shown that with increase of the annual mean concentration of ^7Be , values of symmetrical index increases. The results presented in this paper are preliminary, so it is necessary to monitor changes in concentration of ^7Be in ground level air at various locations in Serbia for many years.

Acknowledgment

The investigation was partially supported by the Ministry of Education and Science of the Republic of Serbia under the following Projects III43009.

References

- [1] J. S. Gaffney, N. A. Marley, M. M. Cunningham, Natural radionuclides in fine aerosols in the Pittsburgh Area, *Atmos. Environ.*, 2004, 38, 3191-3200.
- [2] A. Baeza, L. M. Del Río, A. Jiménez, C. Miró, J. M. Paniagua, M. Rufo, Analysis of the temporal evolution of atmospheric ^7Be as a vector of the behavior of other radionuclides in the atmosphere, *J. Radioanal. Nucl. Chem.*, 1996, 207, 331-344.
- [3] D. Todorovic, D. Popovic, G. Djuric, M. Radenkovic, ^7Be to ^{210}Pb concentration ratio in ground level air in Belgrade area, *J. Environ. Radioact.*, 2005, 79, 297-307.
- [4] H. E. Kissinger, Reaction kinetics in differential thermal analysis, *Anal. Chem.*, 1957, 29, 1702-1706.

K-27-P

THE INFLUENCE OF MILLING TIME OF NATURAL CLAY ON ITS HEAVY METAL ADSORPTION BEHAVIOR

K. R. Kumrić¹, T.a M. Trtić-Petrović¹, A. B. Đukić², J. D. Grbović Novaković²,
A. S. Radosavljević Mihajlović², Lj. Matović²

¹Laboratory of Physics, Vinča Institute of Nuclear Sciences, University of Belgrade, P.O. Box 522, 11001 Belgrade, Serbia, ²Laboratory of Materials Sciences, Vinča Institute of Nuclear Sciences, University of Belgrade, P.O. Box 522, 11001 Belgrade, Serbia

Abstract

The influence of different milling times of natural Serbian clay on simultaneous removal of heavy metals (Pb(II), Cd(II), Cu(II), Zn(II)) from an aqueous medium was investigated. Changes in sorption behavior were correlated with changes in microstructure of the clay induced by milling. The highest removal efficiency, more than 95% for all heavy metals, revealed the sample milled for 19h, although the significant improvement was achieved after 2h of milling.

Introduction

Wastewaters with heavy metals originate from a large number of industries. In order to avoid water pollution, the removal of heavy metal ions from the industrial wastewaters is needed before disposal. Adsorption appears to be an attractive process in view of its efficiency and the easiness with which it can be applied [1].

Clay minerals are good adsorbents for metal ions from aqueous solutions due to their high cation exchange capacity and high specific surface area. Also, clay minerals have the advantage of being abundant and inexpensive [2]. To improve sorption properties of clay minerals different techniques of modification were used [3].

The aim of the present study was to investigate the simultaneous adsorption of Pb(II), Cd(II), Cu(II), Zn(II) ions onto the natural clay from Serbian mine Bogovina by measuring the effect of milling time of clay on the adsorption process.

Results and Discussion

A sample of the natural clay was obtained from the mine Bogovina (Serbia). Mechanical milling was performed in Turbula Type 2TC Mixer, in the air, and ball-to-powder ratio 4:1. Samples of natural clay were milled at different times: 1, 2, 10 and 19 h. After the milling, the samples were characterized in terms of microstructure and chemical composition, and the heavy metal sorption from the aqueous solutions was studied using a batch technique.

The XRD pattern of the unmilled clay is presented in Fig. 1. The diffracted X-rays were collected over 2θ range $4-70^\circ$ using a step width of 0.05° and measuring time 1 s per step. The most prominent phase is montmorillonite (M)

with concomitant minerals quartz (Q) and calcite (C). The diffractogram after 19 h of milling is shown in the insert of Fig. 1. The changes of the montmorillonite microstructure after milling are revealed in: increase of basal spacing (derives from the shift of the (100) reflection towards lower 2θ angles), line broadening and the reduction of the diffraction intensities, suggesting the increase of structural disorder, fragmentation and exfoliation of the clay mineral particles.

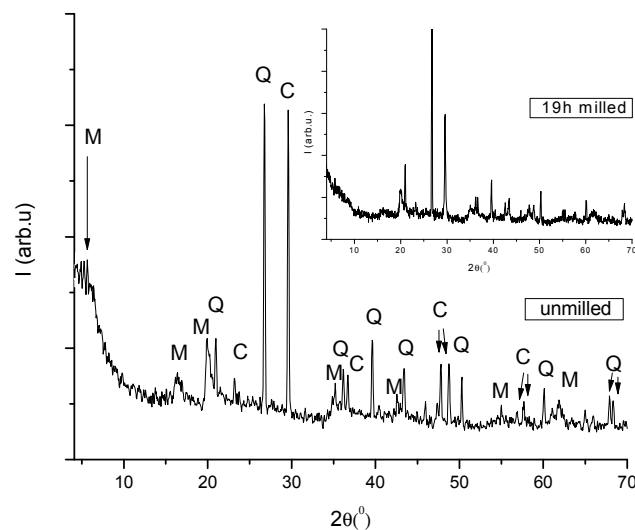


Figure 1. XRD diffractograms of the unmillied clay. In the insert is presented diffractogram of the 19 h milled clay.

Heavy metal sorption experiments were carried out by mixing 0.05 g clay and 25 cm³ aqueous solution of metal ions (total concentration 50 mg dm⁻³, pH 5.5) in closed polypropylene bottles at room temperature. Metal ions solution was prepared in milli-Q water using the analytical reagent grade Pb(NO₃)₂, Cd(NO₃)₂, Cu(NO₃)₂ and ZnCl₂. The samples were shaken for 60 min at stirring speed of 200 rpm. The liquid phases were separated from the solid phases by filtration. The heavy metal ion concentration in each sample was determined with a Metrohm's polarography system 797 VA Computrace analyser by using Metrohm's procedure No. 231/2 e. Adsorption behavior of Pb(II), Cd(II), Cu(II) and Zn(II) on natural clay was determined on non-milled and milled clay samples, in terms of removal efficiency for each metal ion in solution.

The effect of milling time of clay on the removal efficiency of heavy metals is presented in Fig. 2. Removal efficiencies of Pb(II), Cd(II), Cu(II) and Zn(II) using the untreated clay sample are 91.0, 36.5, 79.8 and 34.3%, respectively. On the other hand, heavy metal uptake is significantly improved by milling. It can be seen that removal efficiencies are increased with increasing the milling time of clay. Removal efficiencies of Zn(II) and Cd(II) ions are increased to 95%, while for Pb(II) and Cu(II) ions are greater than 99%. This behavior is related to the increasing of the surface area due to decrease of the mineral particle size, that

causes a larger number of edges sites, as well as exfoliation of the clay mineral particles.

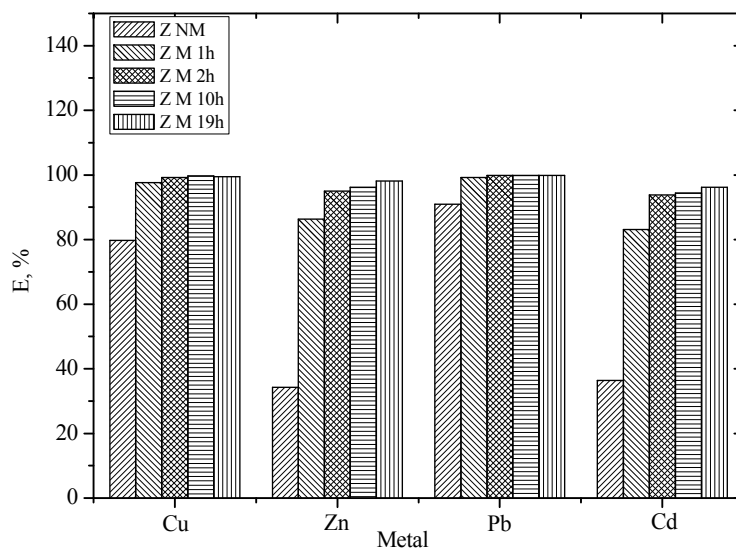


Figure. 2. The effect of milling time on the removal efficiency of heavy metal ions from the aqueous solutions (Z NM - non-milled clay, Z M 1h, Z M 2h, Z M 10h, Z M 19h - 1 h, 2 h, 10 h and 19 h milled clay, respectively)

Conclusion

Highly efficient (>95%) simultaneous removal of heavy metal ions (Pb(II), Cd(II), Cu(II) and Zn(II)) from aqueous solution was achieved by applying different milling times for modification of natural row clay mineral. Thus, one can conclude that the milling represents good alternative to the other techniques of clays modifications for the application in the industrial wastewater treatment.

Acknowledgment

We acknowledge the support to this work provided by the Ministry of Education and Science of Serbia through projects No. III 45006 and 45012.

References

- [1] U. K. Garg et al., *Biores. Technol.*, 2008, 99, 1325-1331.
- [2] M. Malandrino et al., *J. Colloid Interface Sci.*, 2006, 299, 537-546.
- [3] Bhattacharyya, K.G., Gupta, S.S., *Adv. Colloid Interface Sci.*, 2008, 140, 114-131.

COMPARATIVE RADIOLOGICAL IMPACT ASSESSMENT IN AREAS OF ELEVATED NATURAL RADIOACTIVITY IN GREECE AND SERBIA

H. Florou¹, S. Dragović², G. Trabidou¹, M. Čujić², P. Kritidis¹, J. Petrović²,
M. Sotiropoulou¹, J. Kovačević³

¹*National Centre for Scientific Research "Demokritos", Institute of Nuclear and Radiological Sciences and Technology, Energy and Safety, Aghia Paraskevi 15310, POB 60228, Athens, Greece, e-mail: eflorou@ipta.demokritos.gr*

²*University of Belgrade, Institute for the Application of Nuclear Energy, Banatska 31b, Belgrade, Serbia, e-mail: sdragovic@inep.co.rs*

³*Geological Institute of Serbia, Rovinjska 12, Belgrade, Serbia*

Abstract

The activity concentrations of natural radionuclides ²³⁸U, ²³²Th and ⁴⁰K in selected areas of elevated natural background radioactivity in Greece, Milos - an island of volcanic origin in Cyclades Archipelago, Aegean Sea and Serbia - Stara Planina mountain rich in uranium deposits are presented. External dose rates to humans were derived as an indicative parameter for the radiological impact assessment.

Introduction

The island of Milos (36° 42' N, 24° 27' E) in Cyclades Archipelagos is part of the Hellenic volcanic arc, which is located in the southern Aegean Sea, in Greece. This is located parallel to the subduction zone of the lithospheric plates of the Eastern Mediterranean Sea [1]. Besides, the Island is characterized by the presence of geothermal vents, which are used for energy production by the Public Power Corporation. As it has been reported, there is direct and indirect influence on the abiotic materials and organisms inhabited especially the coastal areas of Milos by the underground hydrothermal fluids emitted by the vents [2-3]. The lithospheric environment of the island is characterized by alumino silicate and iron sulfate ores and volcanic ash, whereas soils are mainly texturally calcareous and clay. In terms of Stara Planina (44° 21' N, 19° 14' E), the pre-Tertiary terrigenous sandstones represent the most significant bearers of mineralizations in Serbia. The significant deposit and a number of occurrences are identified in Perm-Triassic sediments of Stara Planina [4-6]. The Stara Planina massif on the western border of the Carpatho-Balkanides is the result of complex tectonic processes that folded and faulted the region during the Baykalian orogeny, Caledonian and Variscan orogenies, and the Alpine orogeny. The activity concentrations of ²³⁸U, ²³²Th and ⁴⁰K in different geological materials, soil and sediment are presented in this paper. In terms of the radiological impact assessment, the outdoor gamma ray exposure at 1 m above ground level was calculated from the soil activity concentrations using

K-28-P

the dose rate conversion factors of 0.462, 0.604 and 0.0417 nGy h⁻¹ per Bq kg⁻¹ for ²³⁸U, ²³²Th and ⁴⁰K, respectively [7].

Results and Conclusions

Table 1. Activity concentrations of the natural radionuclides in abiotic materials from the island of Milos (Greece) and Stara Planina (Serbia) (Bq kg⁻¹) and the total external dose rate range (nGy h⁻¹).

Sample	²³⁸ U	²³² Th	⁴⁰ K	External dose rate (nGy h ⁻¹)
Milos island				
Soil	≤ 1- 1420	26 - 94	458 - 1796	35-848
Caoline	129 ± 66	74 ± 39	298 ± 390	
Perlite	111± 44	84 ± 23	1242 ± 264	
Bentonite	142 ± 78	74 ± 25	456 ± 215	
Alumino silicate	95 ± 45	53 ± 27	838 ± 509	
Volcanic ash	88 ± 7	70 ± 6	758 ± 19	1sample
Iron pyrite	75 ± 5	33 ± 5	991 ± 20	1sample
Baryte	37 ± 6	72 ± 24	246 ± 229	
Volcanic material	295 ± 335	74 ± 35	451 ± 269	
Rock	104 ± 8	63 ± 6	3893 ± 25	1sample
Sediment (coastal-sandy)	85 - 127	26 - 86	429 - 1352	
StaraPlanina				
Soil	19-160	12-130	270-1010	27-195
Greenish to redish sandstones	37 ± 4	53 ± 5	960 ± 10	
Red fine grained sandstones	170 ± 10	65 ± 5	1190 ± 20	
Gray and reddish gray sandstones	760 ± 10	53 ± 5	1190 ± 20	
Gray sandstones and siltstones with organic matter	5560 ± 10	61 ± 3	940 ± 10	
Red sandstones with siltstones	37 ± 5	49 ± 5	880 ± 10	
Arkosic metasandstone	120 ± 10	89 ± 8	690 ± 10	
Schist	45 ± 5	47 ± 5	780 ± 20	
Meta conglomerate	54 ± 5	63 ± 4	560 ± 10	
Metasiltstone	25 ± 5	32 ± 8	530 ± 10	
Albitized microdiorite	150 ± 10	73 ± 5	1940 ± 80	
Diabase	37 ± 5	28 ± 5	410 ± 20	

The range of the calculated total external dose rate from soil in the island of Milos was broad (35-848 nGy h⁻¹). It is noteworthy, that the reported range in the Greek territory varies from 100 to 1000 nGy h⁻¹ (mean value approximately 80 nGy h⁻¹ [8-9]). Therefore, the observed maxima in Milos lay at the upper limit of the reported values for the natural radiation background of Greece. The total external gamma dose rate at the investigated areas on Stara Planina is about 1.5-fold higher of value reported for the whole territory of Serbia [10]. The total external gamma dose rate in the area affected by uranium mining activities was reported to be 91 nGy h⁻¹ [11]. The conclusions can be summarized as:

- The highest value of ²³⁸U (5560 Bqkg⁻¹) in Stara Planina and wider value-range in Milos
- Comparable values of ²³²Th for the various geological settings in between the two national sets
- The highest value of ⁴⁰K in Milos and comparable values in between the two national sets
- Wider range and higher maxima of the dose rates from soil in Milos
- Higher values of the external dose rates in Stara Planina and Milos island if compared to the mean natural background respectively

References

- [1] M. D. Fytikas, *Geophys. Res. I. G. M. R. XVIII*(1), 1975.
- [2] P. Kritidis, H. Florou, *Proc. Nat. Conference Environmental Science and Technology, Aegean University, Mytilini* September, 1989, B, 24-34.
- [3] H. Florou, P. Kritidis, *Rad. Prot. Dos.*, 1992, 45(1/4), 277-279.
- [4] Z. Nikić, J. Kovačević, P. Papić, *Water Air Soil Poll.*, 2008, 192, 47-58.
- [5] J. Kovačević, *Bull. Geoinst.*, 1999, 36, 119-134.
- [6] J. Kovačević, Z. Nikić, P. Papić, *Sed. Geol.*, 2009, 219, 252-261.
- [7] UNSCEAR, *Sources and Effects of Ionizing Radiation, UNSCEAR 2008 Report*. New York: United Nations, 2010.
- [8] H. Florou, G. Trabidou, P. Kritidis, *Proc. Nat. Conference HNPS2012, Athens*, 25-26 May, 2012, 1, 50.
- [9] G. Trabidou, H. Florou, A. Angelopoulos, L. Sakelliou, *Rad. Prot. Dos.*, 1996, 63(1), 63-67.
- [10] S. Dragović, Lj. Janković-Mandić, M. Momčilović, A. Onjia, *Arch. Oncol.* 2007, 15, 78-80.
- [11] M. Momčilović, J. Kovačević, M. Tanić, M. Đorđević, G. Bačić, S. Dragović, *Environ. Monit. Assess.*, 2012, doi 10.1007/s10661-012-2634-9.

K-29-P

RADIOACTIVITY IN DRINKING WATER FROM SMEDEREVSKA PALANKA

M. M. Janković^{a,*}, N. B. Sarap, D. J. Todorović

*University of Belgrade, Institute Vinča, Radiation and Environmental Protection
Department, P.O. Box 522, 11001 Belgrade, Serbia*

Abstract

In this work, a study of the radioactive content of 1 tap and 1 spring water "Kiseljak" from Smederevska Palanka was carried out. The natural activity concentration of alpha emitting radionuclides are within the range recommended by Serbian current regulations. Gross beta activity for Kiseljak water exceeds limit of 1 Bq l⁻¹ given by Serbian current regulations. For this reason gamma spectrometry analysis was performed and it was found that the content of ⁴⁰K in water Kiseljak is 0.9 Bq l⁻¹.

Introduction

The determination of radionuclides in environmental samples is a crucial task in relation to the protection of human health. Natural waters contain both alpha and beta emitters in widely varying concentrations which are responsible for a generally small fraction of the total dose received from natural and artificial radioactivity [1]. The most radiotoxic and of concern to human health among the radionuclides present in ground water is radium, especially ²²⁶Ra. ²²⁸Ra has short half-life and will decay before being transported over long distances. The consumption of water-containing radium can cause its accumulation in bone tissues, leading to accumulation of significant dose, which in turn produces bone and head-sinus cancer. Therefore, the systematic control of water quality has become an important parameter of environmental studies. In Serbia, according to current regulations [2], radioactivity concentrations in drinking water for gross alpha and gross beta should be 0.5 and 1.0 Bq l⁻¹, respectively. If one of the guideline values is exceeded, radionuclides have to be identified by alpha and/or gamma spectroscopy, and their individual activity concentrations need to be measured. These guidelines ensure an exposure lower than 0.1 mSv y⁻¹ assuming a water consumption rate of 2 l d⁻¹. If the estimated dose is higher than 0.1 mSv y⁻¹ the reduction in consumption or radionuclide concentration is necessary. Given the fact that the bottled water Kiseljak was already tested before and the analysis has shown higher gross beta activity, we believe that periodic monitoring of this water is substantially.

Experimental

In order to determine gross alpha and beta activity, volumes of 3 l of water were evaporated to a small volume, under infrared lamp. The remaining was heated to

* Corresponding author. University of Belgrade, Institute Vinča, Radiation and Environmental Protection Department, P.O. Box 522, 11001 Belgrade, Serbia. Tel/Fax: +381 11 806 64 37. E-mail address: marijam@vinca.rs (M. Janković)

dryness at 450 °C [3]. The residues were transferred quantitatively to a stainless-steel planchet. Gross alpha and beta activity in water samples were determined by α / β low level proportional counter Thermo Eberline FHT 770 T. Calibration was performed by using standard source of ^{90}Sr (EM145, Prague) with an activity of 189.4 Bq on the day 1. 8. 2011. for beta activity and standard source of ^{241}Am (EM445, Prague) with an activity of 224 Bq on the day 1. 8. 2011. for alpha activity. The counting gas was a mixture of 90 % argon and 10 % methane. The counting efficiencies for the system are 23 % for alpha and 33 % for beta. The counting time was 3600 s for gross alpha and beta activities. In order to performed gamma spectrometric measurements, water samples were boiled to reduce their volume from approximately 8000 ml to 200 ml and then poured into 250 ml cylindrical polyethylene vials. The samples were stored for 1 month to reach the radioactive equilibrium. Measurements were performed using a HPGe Canberra detector with a counting efficiency of 23 %. Geometric efficiency for water matrices in the plastic bottle of 200 ml was determined by a reference water material (Czech Metrological Institute, Praha, 9031-OL-116/8, type ERX) spiked with a series of radionuclides (^{241}Am , ^{109}Cd , ^{139}Ce , ^{57}Co , ^{60}Co , ^{88}Y , ^{113}Sn , ^{85}Sr , ^{137}Cs , ^{210}Pb) with total activity of 114.9 kBq on the day 03.03.2008. The activity of ^{226}Ra and ^{232}Th was determined by their decay products: ^{214}Bi (609 keV, 1120 keV and also 1764 keV), ^{214}Pb (295 keV and 352 keV) and ^{228}Ac (338 keV and 911 keV), respectively. The activities of ^{40}K were determined from its 1460 keV γ -line. ^{235}U was determined on 185.7 keV corrected for ^{226}Ra (186 keV). ^{238}U was determined by ^{234}Th (63 keV) or by ^{234}Pa (1000 keV) ($T_{1/2}=1.17$ min). The activity of ^{137}Cs was determined from its 661 keV line. Counting time interval was 60000 s.

Results and Discussion

Table 1 shows the results for gross alpha and beta activity concentrations for 1 tap and 1 spring water collected in Smederevska Palanka. Gross alpha activity for both samples is within recommended level of 0.5 Bq l⁻¹. Gross beta activity for tap water is below than recommended level of 1 Bq l⁻¹. For spring water, Kiseljak, gross beta activity was 2.25 ± 0.27 Bq l⁻¹ which exceeds the permitted limit. Because of that, it is necessary to performed gamma spectroscopy. The specific activities of natural radionuclides ^{226}Ra , ^{232}Th , ^{238}U , ^{235}U and produced ^{137}Cs in investigated waters measured by gamma spectrometry were below the detection limits of our measuring system. MDC for ^{226}Ra , ^{232}Th , ^{238}U , ^{235}U and ^{137}Cs was <0.04, <0.03, <0.02, <0.009 and <0.006 Bq l⁻¹, respectively. Serbian law recommends that activity concentration in drinking water should not exceed 490 mBq l⁻¹ for ^{226}Ra , 590 mBq l⁻¹ for ^{232}Th , 2900 mBq l⁻¹ for ^{235}U and 3000 mBq l⁻¹ for ^{238}U [2]. Content of ^{40}K in spring water was (0.9 ± 0.2) Bq l⁻¹. Contribution of ^{40}K in gross beta activity was 0.73 Bq l⁻¹, so we can conclude that in addition to ^{40}K , there are other beta emitters, such as ^{90}Sr , which included in the gross beta activity. Determination of ^{90}Sr in this water is the aim of our next study. Because, gross beta activity in natural water originate from natural long-lived isotopes ^{40}K , ^{210}Pb , ^{228}Ra and artificial isotopes such as ^{90}Sr and ^{137}Cs [4] and the total beta activities should be obviously equal to the sum of activities of beta isotopes. On the other hand, content

K-29-P

of ^{40}K in tap water was below MDC (0.14 Bq l^{-1}). Our results for tap water are comparable with those obtained for tap waters in Vojvodina [5], Turkey [6] as well as Italy [7]. Kiseljak water was analyzed as bottled water by Joksic et al. 2007 [8], and results was showed high beta activity because of presence of ^{40}K in quantity of 2.8 Bq l^{-1} .

Table 1. Gross alpha and beta activity concentrations in tap water and spring water Kiseljak.

Sample	Gross alpha activity concentration / Bq l^{-1}	Gross beta activity concentration / Bq l^{-1}
Tap water	0.046 ± 0.015	0.35 ± 0.05
Spring water Kiseljak	0.078 ± 0.026	2.25 ± 0.27

Conclusion

The data generated in this study provide the radiological characterisation of drinking water from Smederevska Palanka. The results show that although both water can be considered potable from a radiological point of view, it is advisable to regulate their radioactive content periodically and give to the consumer more detailed information about the activity concentration of these waters.

Acknowledgment

The investigation was partially supported by the Ministry of Education and Science of the Republic of Serbia under the following Projects III43009.

References

- [1] UNSCEAR. Ionizing radiation: sources and effects of ionizing radiation, United Nation Scientific Committee on the Effects of Atomic Radiation, Report the General Assembly with Scientific Annexes, United Nations Sales Publication, United Nations, New York, 1993.
- [2] Official Journal, Regulation on limits of radionuclide content in drinking water, foodstuffs, feeding stuffs, drugs, items of general use, building materials and other goods to be placed on the market, 86, 2011.
- [3] EPA, Prescribed Procedures for Measuremen of Radioactivity in Drinking Water. EPA-600/4-80-032. Method 900.0., 1980.
- [3] C. R. Cothorn, W. L. Lappenbusch, J. Michel, Drinking water contribution to natural background radiation, Health Physics, 1986, 50, 33–47.
- [5] N. Todorovic, J. Nikolov, I. Bikit, Gross alpha and beta activity measurements in drinking water using liquid scintillation analysis. The XXVI Symposium of Society for Radiation Protection of Serbia and Montenegro, Proceedings, 12-14. October, Tara, Belgrade, Serbia, 2011, 83-87.
- [6] N. Damla, U. Cevik, G. Karahan, A. I. Kobya, Gross α and β activities in tap waters in Eastern Black Sea region of Turkey, Chemosphere, 2006, 62, 957-960.
- [7] M. Forte, R. Rusconi, M. T. Cazzaniga, G. Sgorbati, The measurement of radioactivity in Italian drinking water, Microchemical Journal, 2007, 85, 98-102.
- [8] J. Joksic, M. Radenkovic, Š. Miljanic, Natural radioactivity of some spring and bottled mineral waters from several central Balkan sites, as a way of their characterization, J. Serb. Chem. Soc., 2007, 72 (6), 621-628.

PLANE (*Platanus acerifolia* Ait.) BARK AND TREE-RINGS AS BIO-INDICATORS

D. M. Marković¹, I. R. Milošević^{2*}, G. Roglić³, D. Manojlović³, Lj. Ignjatović⁴
and D. Vilotić⁴

¹The Faculty of Applied Ecology, Singidunum University, Lazarevački drum 13;

²Institute of Physics, University of Belgrade, Pregrevica 118;

³Faculty of Chemistry, University of Belgrade, Studentski trg 12-16;

⁴Faculty of Physical Chemistry, University of Belgrade, Studentski trg 1;

⁵Faculty of Forestry, University of Belgrade, Kneza Višeslava 1, Serbia,

(* novovic@ipb.ac.rs)

Abstract

By analyzing metal content in bioindicators such as lichen, moss, fern, leaves etc., we can see an integral response to the pollution level in the region. Tree-ring analysis in contrast enables us to return to previous periods accurately and to understand trends of metal accumulation. Tree-rings and bark of plane (*Platanus acerifolia* Ait.) from Belgrade, Serbia was used as an indicator of environmental pollution. The Pb, Cd and Mn content in bark and tree-rings was determined by inductively coupled plasma atomic emission spectrometry (ICP-OES). A slight Pb concentration increasing trend in the plane tree-rings is observed in the entire period of investigation. A similar Cd and Mn concentration trend was noticed for plane tree-rings. Rough barks (linden) accumulate higher contents of the investigated elements than smooth barks (plane).

Introduction

The environment is under great influence from different sources. The use of vegetation provides the cheapest and simplest indicator for monitoring trace metal levels in the environment. Trees of temperate regions usually form visible annual growth rings, which can be dated accurately. It is therefore possible to collect wood samples of different age and analyze their heavy metals content in order to get a chronological record of trace elements pollution in the tree's environment [1, 2, 3].

The plane is a large [deciduous tree](#) growing to 20–35 m (exceptionally over 40 m) tall, with a trunk up to 3 m or more in circumference and it is a popular urban roadside tree. The [bark](#) is usually pale grey-green and smooth.

Experimental

We collected tree-rings and bark of plane (*Platanus acerifolia* Ait.) from the King Aleksandar Boulevard in 2010. In 2010 the reconstruction of the boulevard begins in about 2.5 km and the plane trees were cut. Two trees of similar size were selected (Latitude: 44°47'47" N; longitude: 20°29'47" E and latitude: 44°47'51" N; longitude: 20°29'38" E) for our purposes. Stem disks were taken from felled trees at breast height (1.3 m). For further analysis the disks were cut into segments with a stainless steel knife. Each plane core was divided into 3 year segments starting from 1935 to 2009.

Bark was taken as a separate sample from the stem disk. The content of elements in solution samples was determined by inductively coupled plasma atomic emission spectrometry (ICP-OES). ICP-OES measurement was performed using Thermo Scientific iCAP 6500 Duo ICP (Thermo Fisher Scientific, Cambridge, United Kingdom) spectrometer equipped with CID86 Charge Injector Device (CID) detector, standard glass concentric type nebulizer, quartz torch, and alumina injector. The optical system purged with argon and the Echelle polychromator thermostated at 38 °C. The digestion was performed on an Advanced Microwave Digestion System (ETHOS 1, Milestone, Italy) using HPR-1000/10S high pressure segmented rotor. In the digestion, about 0.5 g of powdered tree-ring sample precisely weighed was mixed in each clean vessel with a mixture of 3 ml H₂SO₄ and 5 ml HNO₃ and then heated with microwave energy for 30 min. The temperature was controlled with a predetermined power program. After cooling and without filtration, the solution was diluted to a fixed volume of 25 ml for tree-rings and 50 ml for soils

Results and Discussion

Figure 1 shows the mean Pb, Cd and Mn concentrations in the plane tree-rings sampled from the King Aleksandar Boulevard.

From Figure 1(a) it can be noticed a slight increasing Pb concentrations trend in the plane tree-rings in almost the entire study period. Also we can observe two periods of low Pb concentrations dating from 1950 to 1964 and from 1989 to 2003. The highest Pb concentration in the plane tree-rings was measured in the period 1980/82.

The Cd concentration in the plane tree-rings (Figure 1(b)) indicates different changes of the concentration trends. From 1938 to 1961 it can be seen decreasing trend of Cd concentrations. The period from 1965 to 1994 can be roughly characterized as a period of small Cd fluctuations in the plane tree-rings. From 1994 to 2009 intense increase in the Cd concentration can be noticed. The maximum Cd concentration was measured in the period 1962/64.

Three characteristic periods, as in the case of Cd, we can observe for Mn (Figure 1(c)). The first period is the period of decreasing Mn concentrations in the

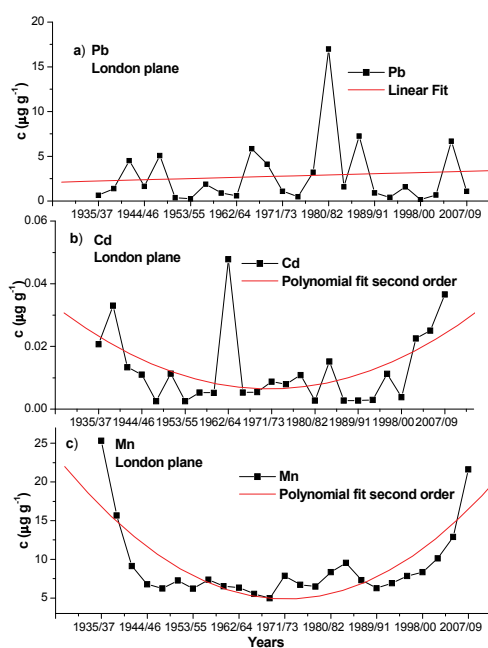


Figure 1. Mean Pb (a), Cd (b) and Mn (c) concentrations ($\mu\text{g g}^{-1}$ dry weight) in plane (*Platanus acerifolia* Ait.) tree-rings at King Aleksandar Boulevard from 1935 to 2009.

plane tree-rings dating from 1935 to 1949. The second period of nearly constant Mn concentrations is observed from 1949 to 1991, while the third dating from 1991 to 2009 is the period of constant Mn increase.

Table 1 shows average Pb, Cd and Mn concentrations in the bark and tree-rings of plane (our study) and Linden [4] as well as bark/wood ratio. Both species are deciduous trees. Bark can be used as an indicator of air pollution for different pollutants [5, 6]. Rough barks are known to accumulate metals more than smooth barks [7]. Linden bark is rough and for the plane it is smooth. From Table 1 it is noticeable that Pb and Mn concentrations in the linden bark were higher than

Table 1. Average Pb, Cd and Mn concentrations ($\mu\text{g g}^{-1}$) in bark and tree-rings (wood) of plane [our study] and Linden [4] as well as bark/wood ratio.

Elements	London plane (Belgrade)		Bark/wood ratio	Linden (Obrenovac)		Bark/wood ratio
	bark	wood		bark	wood	
Pb	2.84	2.77	1.03	23.9	3.0	7.97
Cd	0.013	0.013	1.00	-	-	-
Mn	8.77	9.14	0.96	11.1	2.1	5.29

in the plane bark. By comparing the average concentrations of analyzed elements (Table 1) in the bark and tree-rings of plane and linden it can be seen that in the case of linden considerably higher concentrations were in their bark while in the case of plane approximately the same concentration are in the bark and tree-rings.

Conclusion

Slightly increased Pb concentration trend in the plane tree-rings has been seen in almost the entire period of investigation. The characteristic minimum concentration of Pb was obtained in the period from 1989 to 2003 and can be connected with the crisis of the nineties in our region. There was a similarity in the trend of change in concentration from 1935 to 2009 for Cd and Mn. In the linden bark (rough type bark) were found higher concentrations of analyzed elements than in the plane bark (smooth type bark).

References

- [1] D. M. Marković, I. Novović, D. Vilotić, Lj. Ignjatović, Russ J Phys Chem, 2007, 81, 1493-1496.
- [2] D. M. Marković, I. Novović, D. Vilotić, Lj. Ignjatović, Environ Monit Assess, 2009, 151, 377-382.
- [3] S. A. Watmough, T. C. Hutchinson TC, Environ Pollut, 1996, 93, 93-102.
- [4] D. M. Marković, I. R. Milošević, D. Vilotić, Environ Sci Poll Res, DOI 10.1007/s11356-012-1024-82012, 2012.
- [5] T. El-Hasan, H. Al-Omari, A. Jiries, F. Al-Nasir, Environ Int, 2002, 28, 513-19.
- [6] O. O. Odukoya, T.A. Arowolo, O. Bamgbose, Environ Int, 2000, 26, 11-16.
- [7] D. Barnes, M. A. Hammadah, J. M. Ottaway, Sci Total Environ, 1976, 5, 63-67.

K-31-P

LARCH (*Larix europaea* Lam.) AND DOUGLAS-FIR (*Pseudotsuga menziesii* Mirb.) BARK AND TREE-RINGS AS BIO-INDICATORS

I. R. Milošević^{1*}, D. M. Marković², G. Roglić³, D. Manojlović³, R. Balić³, Lj. Ignjatović⁴ and M. Veselinović⁵

¹*Institute of Physics, University of Belgrade, Pregrevica 118;*

²*The Faculty of Applied Ecology, Singidunum University, Lazarevački drum 13;*

³*Faculty of Chemistry, University of Belgrade, Studentski trg 12-16;*

⁴*Faculty of Physical Chemistry, University of Belgrade, Studentski trg 1,*

⁵*Institute of Forestry, Kneza Višeslava 3, Belgrade, Serbia, (novovic@ipb.ac.rs)*

Abstract

Tree-rings and bark of larch (*Larix europaea* Lam.) and Douglas-fir (*Pseudotsuga menziesii* Mirb.) from two locations in Serbia were used as indicators of environmental pollution. The Cd, Mn and Pb content in bark and tree-rings of larch and Douglas-fir were determined by inductively coupled plasma atomic emission spectrometry (ICP-OES). Average Cd, Mn and Pb concentrations were higher in the tree-rings of larch from the Avala location, while they were higher in Douglas-fir tree-rings for the REIK-Kolubara location. In almost all larch and Douglas-fir bark samples at both sites were measured higher concentrations of examined elements than in tree-rings.

Introduction

Dendrochemistry has emerged in recent years as a valuable tool enabling reconstruction of past pollution episodes. A basic assumption of dendrochemical studies is that the chemical make-up of the annual woody increment at least partly reflects the chemistry of the environment in which it was formed. Increased metal concentrations have been recorded in tree rings formed during periods of high industrial activity, increased urbanization and high traffic loads [1-4]. Douglas-fir is highly recommended species for dendrochemical studies [5].

Experimental

We collected tree-rings and bark of larch (*Larix europaea* Lam.) and Douglas-fir (*Pseudotsuga menziesii* Mirb.) from two locations in Serbia in March 2010. The first one is Avala and it is the mountain located 16 km south-east of Belgrade. Avala is a traditional picnic resort for Belgraders. The second location is REIK Kolubara. Douglas-fir and larch at the Kolubara location have been applied in our country for the rehabilitation by a forestation of the mechanically damaged land. Three larch and Douglas-fir trees of similar size were selected at each location. Stem disks were taken from felled trees at breast height (1.3 m). For further analysis the disks were cut into segments with a stainless steel knife. Each core was divided into 3 year segments starting from 1980 to 2009. Bark was taken as a separate sample from the stem disk. The content of elements in solution samples was determined by inductively coupled

plasma atomic emission spectrometry (ICP-OES). ICP-OES measurement was performed using Thermo Scientific iCAP 6500 Duo ICP (Thermo Fisher Scientific, Cambridge, United Kingdom) spectrometer equipped with CID86 Charge Injector Device (CID) detector, standard glass concentric type nebulizer, quartz torch, and alumina injector. The optical system purged with argon and the Echelle polychromator thermostated at 38 °C. The digestion was performed on an Advanced Microwave Digestion System (ETHOS 1, Milestone, Italy) using HPR-1000/10S high pressure segmented rotor. In the digestion, about 0.5 g of powdered tree-ring sample precisely weighed was mixed in each clean vessel with a mixture of 3 ml H₂SO₄ and 5 ml HNO₃ for tree-ring sample and then heated with microwave energy for 30 min. The temperature was controlled with a predetermined power program. After cooling and without filtration, the solution was diluted to a fixed volume of 25 ml.

Results and Discussion

Figure 1 shows the mean concentrations of Cd (a and b) and Mn (c and d) in larch and Douglas-fir tree-rings from 1980 to 2009 at the Avala and REIK-Kolubara locations. At Avala location (Figure 1(a)) it can be seen a similar Cd concentration trend change for the both examined

tree species (larch and Douglas-fir). In the entire study period, mean Cd concentrations in tree-rings of larch and Douglas-fir have an increasing trend. Higher mean Cd concentrations were measured in the larch tree-rings than in tree-rings of Douglas fir in almost the entire study period at Avala location. Also at Avala location, as well as in the case of Cd, it can be seen similar behavior of Mn concentration trends in tree-rings of larch and Douglas-fir (Figure 1(c)).

Mean Cd concentrations measured in larch and Douglas-fir tree-rings from REIK-Kolubara location are shown on Figure 1(b). In this case also it can be noticed a good correlation between time trend changes of mean Cd tree-rings concentrations in larch and Douglas-fir. However, in this case after the maximum (1983/85) in almost all remain period mean Cd concentrations have a decreasing trend. In contrast to the Avala location at this location were measured higher mean

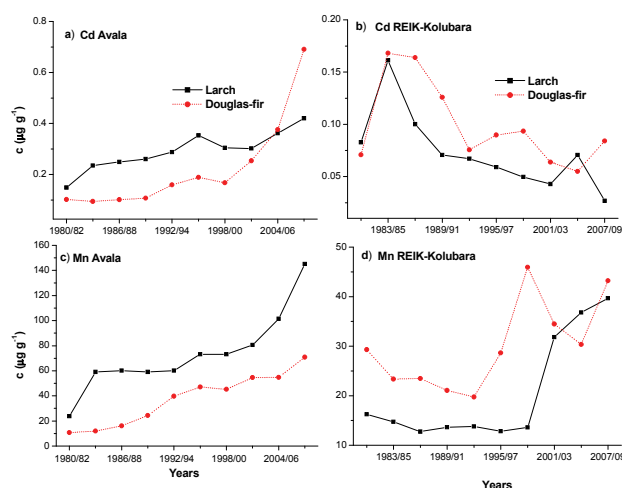


Figure 1. Mean Cd (a and b) and Mn (c and d) concentrations in larch and Douglas-fir tree-rings on Avala and REIK-Kolubara locations from 1980 to 2009.

K-31-P

Cd concentrations in samples of Douglas fir. A similar trend of changes in mean Mn concentrations in larch and Douglas-fir tree-rings can be seen on a REIK-Kolubara location (Figure 1(d)). As in the case of Cd on REIK Kolubara location mean Mn concentrations are higher in Douglas fir tree-rings.

Average Cd, Mn and Pb concentrations in larch and Douglas-fir bark and tree-rings (wood) are shown in Table 1. For both locations in almost all samples higher concentrations of the examined elements are measured in the bark than in tree-

Table 1. Average Cd, Mn and Pb concentrations ($\mu\text{g g}^{-1}$) in bark and tree-rings (wood) of Larch and Douglas-fir from Avala and REIK-Kolubara locations.

Tree Locations Elements	Larch				Douglas-fir			
	Avala		REIK-Kolubara		Avala		REIK-Kolubara	
	bark	wood	bark	wood	bark	wood	bark	wood
Cd	0.75	0.29	0.16	0.07	1.12	0.22	0.60	0.10
Mn	176.2	73.6	154.2	20.6	144.8	37.5	208.9	30.0
Pb	2.46	2.71	1.80	0.37	1.72	1.20	0.91	0.88

rings. Bark accumulates pollutants straight from the atmosphere and they are deposited mainly on the surface. Bark can be roughly divided into living inner bark and dead outer bark [6]. The inner bark reflects the metal ion flow within a tree. Airborne pollutants are mainly accumulated in the outer bark. Element concentrations in the barks reflect concentrations both within the phloem and absorbed to bark predominately via wet and dry atmospheric deposition [7].

Conclusion

Larch and Douglas fir tree-rings showed a similar Mn and Cd concentrations trends in both studied sites. Mean Cd and Mn concentrations in larch tree-rings were higher at the Avala location, while on-site REIK-Kolubara they are higher in Douglas-fir tree-rings. Higher Cd, Mn and Pb average concentrations in larch and Douglas-fir tree-rings were measured at the Avala location for both tree species.

References

- [1] S. A. Watmough, T. C. Hutchinson, *Environ Pollut*, 1996, 93, 93-102.
- [2] D. M. Marković, I. Novović, D. Vilotić, Lj. Ignjatović, *Russ. J. Phys. Chem.*, 2007, 81, 1493-1496.
- [3] D. M. Marković, I. Novović, D. Vilotić, Lj. Ignjatović, *Environ Monit Assess*, 2009, 151, 377-382.
- [4] R. P. Guyette, B. E. Cutter, G. S. Henderson, *J Environ Qual*, 1991, 20, 146-50.
- [5] B. E. Cutter, R. P. Guyette, *J Environ Qual*, 1993, 22, 611-619.
- [6] L. Harju, K. E. Saarela, J. Rajander, J. O. Lill, A. Lindroos, S. J. Heselius, *Nucl Instrum Meth B*, 2002, 189, 163-167.
- [7] N. W. Lepp, *Environ Pollut*, 1975, 9, 49-61.

REMOVAL OF POLLUTANTS BY SURFACTANT MODIFIED ZEOLITES

M. Marković^{1,*}, M. Kragović¹, M. Petrović¹, A. Daković¹, D. Krajišnik², J. Milić²

¹*Institute for Technology of Nuclear and Other Mineral Raw Materials, P.O. Box 390, 11000 Belgrade, Serbia, *e-mail:marija_markovic84@yahoo.com*

²*Department of Pharmaceutical Technology and Cosmetology, Faculty of Pharmacy, University of Belgrade, P.O. Box 146, 11 221 Belgrade, Serbia*

Abstract

In this paper results on adsorption of chromate and lead by the natural zeolite and three organo-zeolites obtained by treatment of zeolite with three different levels (10, 20, 30 mmol/100g) of cetylpyridinium chloride (CPC) are presented. It was determined that adsorption of chromate increased with increasing the amount of CPC at the surface and also with increasing the initial chromate concentration. Presence of surfactant at the zeolite surface had no influence on lead adsorption.

Introduction

Wastewaters from mining operations, electroplanting plants, power-generating plants, etc. contain several toxic heavy metals. These discharges have important levels of cadmium, chromium, copper, lead and mercury. Among the different techniques proposed for heavy metals removal (reduction, precipitation, biosorption, nano and ultrafiltration) adsorption on natural sorbents as low-cost sorbents seems to be quite attractive [1].

Natural zeolites are microporous minerals formed from hydrated crystalline aluminosilicates with three-dimensional structures consisting of the tetrahedral SiO_4 and AlO_4 . The partial substitution of Si^{4+} by Al^{3+} results in a negative charge that is compensated by exchangeable cations (Na^+ , K^+ , Ca^{2+} or Mg^{2+}). The cation exchange properties has been used to modify the surface of the zeolites by adsorbing a cationic surfactants. At a low surfactant concentration (below external cation exchange capacity) the surfactant cations are exchanged with the exchangeable cations of the natural zeolite until a monolayer of surfactant cations is formed at the external surface. At higher concentrations (above external cation exchange capacity) a bilayer and/or admicelle of surfactant molecules are attached to the external surface, where the outer layer of surfactant molecules is bound by hydrophobic interactions. The bilayer formation results in charge reversal on the external surface, providing sites where anions will be retained and cations repelled, while neutral low polar species can partition into the hydrophobic core. Organo-zeolites with amounts of cetylpyridinium chloride (CPC) equal to ECEC of zeolite (10 mmol/100g – sample ZCPC-10) and above ECEC (20 mmol/100g and 30 mmol/100g – samples ZCPC-20 and ZCPC-30) were tested as carriers for drugs (e.g. diclofenac sodium) [2].

Since chromium preferably exist in the nature in anionic form, in this paper preliminary investigations of chromate adsorption on the same organo-modified

zeolites were conducted. Because of known affinity of the natural zeolite for adsorption of heavy metals [3], it was also determined if the presence of CPC at the zeolitic surface has influence on lead adsorption.

Experimental

A sample of natural zeolitic tuff from Zlatokop deposit (Vranjska Banja) was used as starting material. The cation exchange capacity (CEC) was 148 meq/100 g and the external cation exchange capacity (ECEC) was 10 meq/100 g. The zeolite was modified with three levels of cetylpyridinium chloride (CPC). Details on the preparation of organo-zeolites are given elsewhere [2].

Chromate adsorption was performed using 0.5 g of each organo-modified zeolites and 50 ml K_2CrO_4 (concentrations of 6.3 to 27.4 mg/l). For lead adsorption 1.0 g of either the natural zeolite or ZCPC-20 was mixed with 50 ml of aqueous solution of $Pb(NO_3)_2$ (10567 mg/l). In all experiments, after the reaction time (24 h), suspensions were centrifuged at 10000 rpm for 10 min to separate the solution and solid. The initial and non sorbed concentrations of Cr or Pb in supernatants were determined by atomic absorption spectrophotometry using an "Analytic Jena Spekol 300". Percentage of adsorbed chromium or lead was calculated from the difference between the initial and final concentration of each pollutant in the aqueous supernatant.

Results and discussion

Since the natural zeolite, has no affinity for anionic species, in the preliminary experiment it was confirmed that it was ineffective in chromate adsorption. Results on chromate adsorption on the three organo-zeolites are presented at Fig 1. As can be seen from the Fig.1, for the organo-zeolite with the lowest amount of CPC (ZCPC-10), low adsorption of chromate (0.075 mg/g), was observed only for the lowest initial chromate concentration. These results indicated that organo-zeolite with monolayer conformation does not readily adsorb chromate as expected for hydrophobic surface. When the surfactant loading is greater than 100% ECEC (ZCPC-20 and ZCPC-30), the adsorption of anionic chromate species took place progressively with increasing in surfactant loading. At concentration of CPC above ECEC, adsorbed surfactant molecules form bilayer or patchy bilayer and in this condition, anion exchange took place and chromate has a stronger affinity for the positively charged surfactant head group than for the counterions already adsorbed. From Fig. 1 it can be also seen for ZCPC-20 and ZCPC-30 that amount of adsorbed chromate increased with increasing the initial chromate concentration.

For the lowest chromate concentration (6.3 mg/l) amount of adsorbed chromate was 0.56 mg/g for ZCPC-20 and 0.62 mg/g for ZCPC-30. For the highest chromate concentration (27.4 mg/l) adsorption of chromate was 1.28 and 1.96 mg/g for ZCPC-20 and ZCPC-30 respectively. Additionally, results of adsorption of lead by the natural zeolite and ZCPC-20 showed that presence of bilayer of surfactants at the zeolite surface had no influence on adsorption of lead (adsorbed amount of lead 69.9 mg/g for the natural and 72.0 mg/g for ZCPC-20).

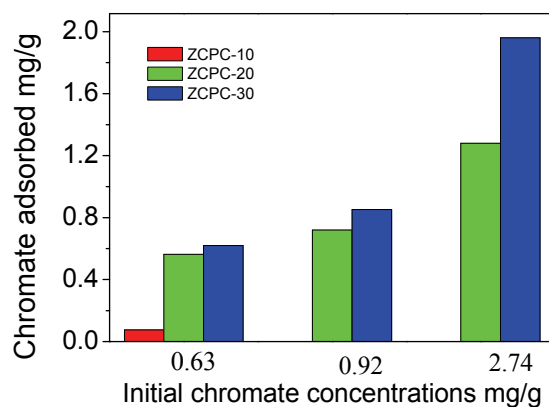


Figure 1. Chromate adsorption by organo-zeolites – ZCPC-10, ZCPC-20 and ZCPC-30.

Conclusion

The results reported in this paper indicated that organo-zeolites were effective in heavy metals removal. The availability of the natural zeolite, its low cost and simple modification with surfactants makes this material suitable for potential practical application for wastewater treatments.

References

- [1] V. M. Boddu, K. Abburi, J. L. Talbott, E. D. Smith, *Environ. Sci. Technol.*, 2003, 37, 4449-4456.
- [2] D. Krajišnik, A. Daković, M. Milojević, A. Malenović, M. Kragović, D. Bogdanovic, V. Dondur, J. Milić, *Colloids Surf. B*, 2011, 83, 165-172.
- [3] M. Kragović, A. Daković, Ž. Sekulić, M. Trgo, M. Ugrina, J. Perić, G. Diego Gatta, *Appl. Surf. Sci.*, 2012, 258, 3667-3673.

K-33-P

XRF ANALYSIS OF HEAVY METAL CONTENT IN SOIL SAMPLES USING MINIPAL 4 SPECTROMETER

M. Kuzmanoski, M. Todorović, M. Aničić Urošević, S. Rajšić, M. Tasić

Institute of Physics, University of Belgrade, Serbia

Abstract

Monitoring of heavy metal content in urban park soil is important, as their elevated concentrations can have detrimental effect on human health. We present preliminary results of test of performance of MiniPal 4 XRF spectrometer for analysis of heavy metal content in soil and the results of analysis of soil from a city park in Belgrade center. The obtained results are generally in agreement with heavy metal content in soil in Belgrade central area, including parks, reported in some other studies.

Introduction

Heavy metals are naturally present in soil. Their elevated concentrations in urban soil can affect human health. Children are at higher risk of exposure to toxic heavy metals in park soil, and more sensitive to their effects. Thus, it is important to monitor level of heavy metals in urban park soil. For this purpose, X-ray fluorescence (XRF) spectrometry is a convenient method, as it is nondestructive, requires little sample preparation and allows multielemental analysis. PANalytical MiniPal 4 is a compact benchtop energy dispersive XRF spectrometer, used primarily in mining and cement industries, but also for research purposes [1]. Here we test the performance of this spectrometer in analysis of heavy metal content in soil samples, and present our preliminary results of the analysis of soil samples collected at different depths from a city park in the center of Belgrade, in Spring of 2011.

Experimental

The soil samples were taken from several locations in the park, from three layers at depths of 0-10 cm, 10-20 cm and 20-30 cm, using steel corer. For each of the layers a composite sample was made. After drying, sieving and milling, 5g of each of the soil samples was pressed into a pellet at the pressure of 30 tons for 60 s. In this study a MiniPal 4 XRF spectrometer was used for elemental analysis. It is equipped with 9W Rh tube and silicon drift detector, with resolution FWHM = 145eV for 5.9keV ⁵⁵Fe. The calibration of the instrument was performed using six reference materials (soil and lake sediment), pressed into pellets. The following elements have been measured: Ba, Ca, Cr, Cu, Fe, K, Mn, Ni, Pb, Rb, Ti, V, Zn and Zr. Optimal measurement parameters (tube voltage, current and filter) were found for different sets of elements. The analysis of the spectral data was performed using MiniPal/MiniMate software.

Results and Discussion

In this study we focus primarily on Cr, Cu, Fe, Mn, Ni and Zn, as common heavy metal pollutants for urban soil. Lead and V are excluded from the analysis because

the calibration results for these elements were not satisfactory. The values of the calibration parameters are shown in Table 1.

Table 1. Calibration results for analyzed elements.

Element	Correlation	Relative RMS (%)	Concentration range (ppm)
Cr	0.9982	6.2	75.0 - 4310.0
Cu	0.9999	1.4	16.9 - 390.0
Fe	0.9832	6.1	32733.0 - 67400.0
Mn	0.9984	3.7	390.0 - 3460.0
Ni	0.9863	12.9	27.8 - 291.0
Zn	0.9981	4.0	44.0 - 345.0

Prior to analysis of soil samples, we analyzed two soil reference materials (SARM42 and GBW07406) as unknown samples, in order to test our calibration method. The average values of element concentrations obtained from three repeated measurements are in agreement with the corresponding certified values, as shown in Table 2.

Our analysis showed very low concentration of Cr, close to the limit of detection, both in the top (0-10 cm) and the deeper layers of soil samples from the park. The concentrations of other elements in the top layer are the following: 27 ppm for Cu, 35431 ppm for Fe, 795 ppm for Mn, 54 ppm for Ni and 100 ppm for Zn. These values are in agreement with those reported in some earlier studies on elemental analysis of soil in the Belgrade central area [2, 3]. Copper and Zn concentrations showed increase with depth, which could indicate washing out of these elements from the top layer of soil. Manganese and Fe concentrations are higher in the top layer than in deeper layers. Variability of Ni concentration with depth was not significant.

More details related to the performance of MiniPal 4 spectrometer in analyzing heavy metals in soil samples from the Belgrade park will be presented.

Table 2. Measured and certified values of concentrations of analyzed elements for SARM 42 and GBW07406 soil reference materials

Element	SARM42		GBW07406	
	Certified (ppm)	Measured (ppm)	Certified (ppm)	Measured (ppm)
Cr	4310	4032	75	62
Cu	17	19	390	390
Fe	32733	33394	56584	57121
Mn	774	785	1450	1489
Ni	125	153	53	51
Zn	44	50	97	95

Conclusion

Test of the applicability of PANalytical MiniPal 4 energy dispersive XRF spectrometer for the analysis of heavy metal content in soil samples showed that it can be successfully used for this purpose. The obtained values for concentrations of

Cr, Cu, Fe, Mn, Ni and Zn are in agreement with those reported for soil in the Belgrade central area in some other studies [2,3].

Acknowledgement

This paper was realized as a part of the project No III43007 financed by the Ministry of Education and Science of the Republic of Serbia within the framework of integrated and interdisciplinary research for the period 2011-2014.

References

- [1] V. Oreščanin, I. Lovrenčić Mikelić, L. Mikelić and S. Lulić, X-Ray Spectrom., 2008, 37, 508-511.
- [2] M. Marjanović, M. Vukčević, D. Antonović, S. Dimitrijević, Đ. Jovanović, M. Matavulj and M. Ristić, J. Serb. Chem. Soc., 2009, 74 (6), 697-706.
- [3] I. Gržetić and R. A. Ghariani, J. Serb. Chem. Soc., 2008, 73 (8-9), 923-934.

EFFECTS OF BIODEPOSIT PRODUCTION IN AMAGASAKI PORT, JAPAN

V. Jovanović¹, Y. Kozuki², R. Yamanaka², M. Miyoshi³

¹*IHTM, University of Belgrade, Belgrade, Serbia;*

²*Department of Ecosystem Engineering, Graduate School of Engineering,
University of Tokushima, Japan*

³*Ecosystem Design, Institute of Technology and Science, University of Tokushima*

Abstract

Effects of biodeposition by mussels *Mytilus galloprovincialis*, was investigated *in situ* during two consecutive summer periods, using sediment traps. Experiment took place in the vicinity of vertical coastal structures, inside of Amagasaki port. The sedimentation rate was found to be doubled due to deposition of faecal material under the quaywall colonized by mussels, comparing to mussel-free referent station. The effect of mussels through the biodeposition was even more significant on the organic carbon and nitrogen fluxes that were three times higher near the wall causing local organic enrichment.

Introduction

Material suspended in the water column precipitates by so called natural sedimentation. On the other hand, mussels filter water column and feed on suspended particles, mainly phytoplankton and detritus. Particles they capture but cannot ingest mussels pack and excrete as faeces and pseudofaeces [1]. Because they are too large and cohesive to be transported further, they rapidly settle to the bottom. Thus, this process, known as biodeposition adds new material to the sediment changing in that way settling rates, composition and quantity of the deposited material. Environmental effects of these processes have yet to be assessed.

In this report we present the results concerning the investigation of natural sedimentation and biodeposition by mussel *Mytilus galloprovincialis*. Their importance arises from the fact that these invasive species have the ability to bind to the vertical concrete surfaces, such as seawalls and quays, which dominate the landscape of Osaka Bay. Here, in the nutrient rich waters, they reach high biomass even when most other species vanish due to the harsh living conditions in mid-summer. Amgasaki port was selected as a case study of Osaka Bay. The experiment was conducted in July 2007 and August 2008 when major deposition events occur due to concentration of phytoplankton and activity of mussels at that time.

Experimental

Particles from natural sedimentation and biodeposition were collected in replicate traps placed at 2.5 m below the water surface and at 7 m below the surface (*i.e.* 2 m from the bottom) on three sampling stations. Two stations were next to quaywall with attached mussels while third, referent station was at 50 m distance from the wall. Traps from this station collected only naturally sedimented material. Construction details of the

traps and their moorings are given schematically elsewhere [2]. Multiple samples of the bottom sediments have been taken on each sampling station.

All pretreatment and analytical procedures were performed in laboratory. The amount of particulate matter (PM) accumulated in sediment traps were determined after freeze drying. Determination of particulate organic carbon (POC) and particulate nitrogen (PN) was performed using *Termo Finnigan CN Soil Analyser* (FLASH EA 1112) after the residue had been treated with HCl solution to remove carbonates. Content of particulate organic matter (POM) in deposited material and sediments was estimated according to Martin and Knauer [3].

Results and Discussion

Figure 1 represents the mass fluxes of particulate matter expressed as dry grams per m² per day, collected in sediment traps in two analyzed periods.

Results show that the quantity of accumulated matter in stations near the wall (stations 1A, 2A, 2B) is significantly higher than control trap values (3A and 3B) for both periods (Mann Whitney U-test; $p < 0.001$).

Amounts of particles that settle in traps at stations 1A and 2B are tripled and doubled respectively, in relation to those in referent traps from the same depth (3A and 3B), mainly as a consequence of mussels activity.

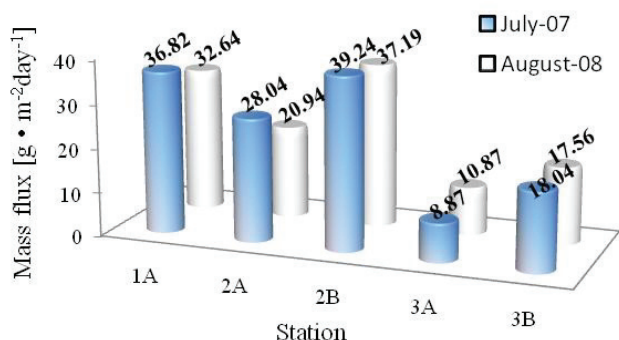


Figure 1. Mass fluxes from different stations at the time of experiments. Letters A and B denote depths of 2.5 m and 7 m below the water surface. Numbers 1 and 2 denote stations near the wall. Referent stations are marked by number 3

Distribution of collected particulate matter among the stations in two years follow the same pattern indicating similarity of the processes affecting downward flux of PM in Amagasaki port.

Composition of settling material and sediments accumulated at different sampling stations is given in Table 1.

On the basis of obtained results, we can say that both POC and PN behave in the same manner: amount of POC and PN are higher in traps and sediments near quaywall (positions 1A, 2A, 2B, 1S and 2S) than those at referent site (3A, 3B and 3S).

The POC/PN ratios, or shorter C/N, varied between 6 and 7 for collected deposits, and between 6 and 10 for the bottom sediments. Such values are characteristic for productive coastal areas indicating phytoplankton, fecal pellets and other easily degraded material [4].

Stations	POC[mg/g]		PN[mg/g]		C/N[ratio]		POM[%]	
	2007	2008	2007	2008	2007	2008	2007	2008
1A	111.1	149.5	16.6	25.8	6.7	5.8	25.6	34.4
2A	118.5	153.3	18.1	26.6	6.6	5.8	27.3	35.3
2B	86.6	114.0	12.9	18.7	6.7	6.1	19.9	26.2
3A	102.5	115.6	15.5	18.7	6.6	6.2	23.6	26.6
3B	59.3	85.9	8.3	13.2	7.2	6.5	13.6	19.7
1S*	129.4	108.6	18.6	17.7	7.0	6.1	29.8	25.0
2S	68.9	64.0	10.1	9.2	6.8	7.0	15.8	14.7
3S	24.6	26.0	2.5	2.8	9.8	9.4	5.7	6.0

Table 1. POC, PN, C/N and POM in sediment traps and sediments at different sampling stations during two analysed periods.

*1S, 2S and 3S are sediments below stations 1-3.

Content of particulate organic matter (POM) ranges between 13.6% (3B) and 35.3 % (2A) implying that both naturally sedimented and biodeposited particles contained mostly inorganic constituents, whose amount tend to increase with depth. Dilution with mineral fractions can explain the drop of organic content in lower traps as well as in sediments.

Sediment samples collected at the referent site (3S) contain lower organic matter comparing to those collected at stations near the wall (1S and 2S), indicating that organic matter, accumulated under the walls, causes local organic enrichment. Due to low current velocities in Amagasaki port, slow tidal flushing (less than 1 m at the time of experiments) and waves directed landwards, organic material couldn't be dispersed. Also, it couldn't be utilized by benthic organisms because most of them escaped or died due to anoxic conditions at the bottom [5]. In collected sediment samples redox potential (Eh) values ranged from -200 to -315 mV^(KCl Ag/AgCl). Because of this, the fate of organic matter depends mainly on microbial degradation, which is tardy in anoxic conditions existing at bottom.

Conclusion

Our results indicate that biodeposit production by mussels *Mytilus galloprovincialis* significantly affect downward flux of particulate matter in the vicinity of coastal structures they inhabit. Sedimentation rates are doubled, and the deposition of POC and PN tripled compared to the control values. In the low oxygen ambient decomposition of organic matter is slow leading to local organic enrichment.

References

- [1] C. B. Jørgensen, Mar. Ecol. Prog. Ser., 1996, 142, 287-302.
- [2] V. Jovanović et al., J.Coastal Zone Studies, 2009, 24, 97-111.
- [3] J. Martin, G. Knauer, Geochimica et Cosmochimica Acta, 1973, 37, 1639-1653.
- [4] T. R. Parsons, Biological oceanographic Processes, Oxford, Pergamon Press, 1977.
- [5] Y. Mishima, A. Hoshika, T. Tanimoto, Journal of Oceanography, 1999, 55, 1-11.

PHASE BOUNDARIES

MULTICOMPONENT MONOLAYER GAS ADSORPTION: THE EFFECT OF MOLECULAR SIZE AND THE NUMBER OF BINDING SITES ON SORPTION RATES

O. Jakšić¹, Z. Jakšić¹, I. Jokić¹, D. Randelović¹, Lj. Kolar-Anić²

¹ *Institute of Chemistry, Technology and Metallurgy, University of Belgrade –
Njegoševa 12, 11000 Belgrade, Serbia, olga@nanosys.ihtm.bg.ac.rs*

² *Faculty of Physical Chemistry, University of Belgrade, Studentski trg 12-16,
11000 Belgrade, Serbia, lkolar@ffh.bg.ac.rs*

Abstract

Multicomponent monolayer gas adsorption on solid surfaces is studied. Master equations for multicomponent gas adsorption are formulated. Sorption rates and the number of free binding sites for each gas species are modeled using physical parameters of the system. The procedure for estimation of surface density of adsorbed molecules is explained and demonstrated on some industrial and semiconductor gases. These results may be used for adsorption based sensor design/technology or related fundamental research.

Introduction

The development in micro and nano technologies leads to the fabrication of new micro and nano structures whose functioning depends highly on adsorption-desorption processes. That dependence can be crucially favorable like for instance in adsorption-based (bio)chemical plasmonic sensors [1], or very undesirable like in microresonators where adsorption-induced mass fluctuations provoke frequency instabilities [2].

In this work we focus on modeling adsorption-desorption process, its constants and parameters, in order to set-up a model suitable for analyzing multicomponent gas adsorption on solids in time span from the beginning till the equilibrium is reached and afterwards. This model could be used in many analytical applications where adsorption-desorption processes play important role in both detection and measurement.

Theory

Starting premises are similar to that of Langmuir's: the surface is homogenous, all molecules of the same gas species are alike. Molecules in gas phase behave as ideal gas, adsorbed molecules do not collide or interact and do not form multilayer islands. Average residential time of adsorbed particles is the same for all particles of the same gas. The flux of arrivals of gas molecules of the species i , $R_{a,i}$, onto the solid surface is proportional to its partial pressure, p_i , and free surface [3]

$$R_{a,i} = \frac{1}{\sqrt{2\pi m_i k_B T}} p_i \left(1 - \sum_{j=1}^r \theta_j \right) \quad (1)$$

Here, θ_j are fractions of occupied surfaces for each of r surrounding gases, m_i is mass of a single molecule of i_{th} gass, k_B is Boltzmann constant, T is temperature.

The rate of desorption of the species i onto the solid surface is proportional to its number of adsorbed molecules, $N_{a,i}$, and inversely proportional to their mean residential time τ_i . According to the ideal gas law, the final expression for rate equation of the number of adsorbed molecules for each gas is then

$$\frac{dN_{a,i}}{dt} = \frac{A\alpha_{s,i}}{\sqrt{2\pi m_i k_B T}} p_i \left(1 - \sum_{j=1}^r \theta_j\right) - \frac{N_{a,i}}{\tau_i} = \frac{A\alpha_{s,i}}{V} \sqrt{\frac{k_B T}{2\pi m_i}} N_{g,i} \left(1 - \sum_{j=1}^r \theta_j\right) - \frac{N_{a,i}}{\tau_i} \quad (2)$$

where $\alpha_{s,i}$ is sticking probability of adsorption for i_{th} gass, $N_{g,i}$ is the number of free gas molecules, A is surface area and V is gas chamber volume. In order to be able to find the solution for the number of adsorbed molecules for each gas or to conduct the stochastic analysis of this process, one must transform equation (2) into a more suitable form.

Results

Adsorption-desorption process is usually studied as a second order reaction, according to the following stoichiometric equation



and the corresponding differential equation:

$$\frac{dN_{a,i}}{dt} = k_{a,i} N_{g,i} N_{f,i} - k_{d,i} N_{a,i} \quad (4)$$

where a free gas molecule A_g and a free adsorption center A_f reversibly transform into an adsorbed molecule A_a , with an adsorption rate k_a and a desorption rate k_d and the number of free adsorption centers for the species i is $N_{f,i}$.

Equations (2) and (4) were analyzed with respect to surface densities of adsorbed molecules for different gases. In case of multi-component environment with r gases, one has r parallel reactions, each of which obeys differential equation

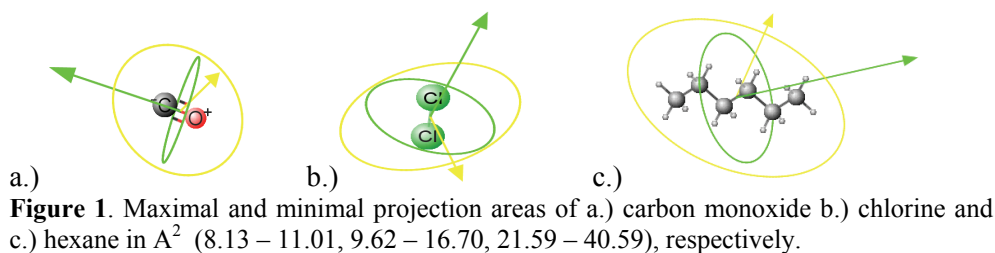
$$\frac{dN_{a,i}}{dt} = \frac{\alpha_{s,i}}{n_{s,i} V} \sqrt{\frac{k_B T}{2\pi m_i}} (N_{0,i} - N_{a,i}) \left(N_{a,i}^{\max} - \sum_{j=1}^r \frac{n_{s,i}}{n_{s,j}} N_{a,j} \right) - \frac{N_{a,i}}{\tau_i} \quad (5)$$

$$k_{a,i} = \frac{\alpha_{s,i}}{n_{s,i} V} \sqrt{\frac{k_B T}{2\pi m_i}} \quad k_{d,i} = \frac{1}{\tau_i} \quad N_{0,i} = \frac{p_i V}{k_B T} \quad N_{a,i}^{\max} = n_{s,i} A$$

$N_{0,i}$ is the overall number of molecules of the species i in the system, $N_{a,i}^{\max}$ is the number of places that molecules of the species i would take to fully populate surface A in monolayer and $n_{s,i}$ is the maximal surface density of adsorbed molecules. As we can see from eq. (4) the adsorption rate constant and the maximum number of binding sites for the species i depend on its molecular size through the surface density.

The constants and parameters in eq. (5) are necessary for further analysis (deriving time evolutions of the number of adsorbed molecules or its mean, determining equilibrium coverages...). In order to provide the surface density of adsorbed molecules the following procedure is used:

The molecule structure is obtained using the chemical structure information available in the [PubChem](#) Substance and Compound database through the unique chemical structure identifier CID. Then, molecular projected surface area was obtained using Marvin 5.9.3, 2012, ChemAxon (<http://www.chemaxon.com>), fig. 1.



Since spheres cannot cover rectangular areas completely, molecular projected surface areas were corrected by a factor of $4/\pi$, before being inversed in order to give the number of adsorption centers per unit area for that species. The obtained data were compared with the experimental results from [4], as shown in table 1.

Table 1. The maximum number of binding sites in 10^{18} molecules/ m^2 .

gas	CH ₄	CO	N ₂	Ar	O ₂	CO ₂
ref [4]	6.3	6.6	6.6	7.7	7.7	6.1
our data	6.52	7.15	7.5	7.08	7.34	6.52

Hence, molecules of different gas species occupy different number of free adsorption centers when adsorbing onto the same surface. Moreover, molecules of the same gas, that have strongly unisotropical geometry, like chain carbohydrates, can also have different estimates of potentially free places for themselves. In that case, we may assume that there are some preferable orientations for adsorption [4].

Conclusion

Procedure has been proposed for the estimation of the number of binding sites, parameter needed for the stochastic and deterministic analysis of multicomponent adsorption. Obtained data were approved by experimental values from literature.

Acknowledgement

This work was funded by Serbian Ministry of Education and Science through the projects TR 32008 and ON 172015.

References

- [1] I. Abdulhalim, M. Zourob and A. Lakhtakia, 2008, *Electromagn.*, 28, 214-242.
- [2] Z. Djurić, I. Jokić, M. Djukić and M. Frantlović, 2010, *Microelec. Eng.*, 87, 1181-1184.
- [3] D. Do, 1998, *Adsorption Analysis: Equilibria and Kinetics*, Imperial College Press, London.
- [4] I. Langmuir, 1918, *J. American Chem. Soc.*, 40, 1361-1403.

L-02-P

ADSORPTION OF CONGO RED ON NATURAL AND ORGANO-ZEOLITES

M. Kragović*, A. Daković, M. Marković and Ž. Sekulić

*Institute for Technology of Nuclear and Other Mineral Raw Materials, Franchet d'Esperey 86, P.O.Box 390, 11000 Belgrade Serbia; * e-mail:*

m.kragovic@itnms.ac.rs

Abstract

Results of Congo Red (CR) adsorption by the natural (NZ) and organo-zeolites obtained by treatment of NZ with three different levels (10, 20, 30 mmol/100g) of cetylpyridinium chloride (NZCP10, NZCP20 and NZCP30) are presented. It was determined that NZCP10 has the best adsorption capacity for CR. Adsorption of CR by NZ and NZCP10 was followed by determination of adsorption isotherms. Much higher adsorption of CR was achieved with NZCP10. The results were fitted to the Langmuir and Freundlich adsorption model. For NZ, adsorption of CR was well described with both models, while for NZCP10 the best fit of experimental data was achieved with the Langmuir model ($r^2=0.98$). From the Langmuir isotherm, calculated maximum adsorbed amount of CR was 21 and 56 mg/g for NZ and NZCP10, respectively.

Introduction

Dyes are important pollutants, causing environmental and health problems to humans and aquatic animals. Several techniques (precipitation, flocculation, adsorption, etc.) are used for removal of dyes from wastewater. It is believed that adsorption is the simplest and the most cost-effective technique [1]. Congo Red (CR) [1-naphthalenesulfonic acid, 3,3'-(4,4'-biphenylenebis(azo)) bis(4-amino-) disodium salt] is a benzidine based anionic diazo dye. It is well known that CR can be metabolized to benzidine, a known human carcinogen. The treatment of CR contaminated wastewater can be complicated due to its complex aromatic structure providing the dye physicochemical, thermal and optical stability, and resistance to biodegradation [2]. Natural zeolite (NZ) is an abundant natural aluminosilicate available all over the world. The most common NZ is clinoptilolite. In the past years, the NZ has been explored as effective adsorbent for removal of CR [3]. In order to improve efficacy of NZ for removal of organic molecules, i.e., dyes, surface of NZ is often modified with long chain organic cations (surfactants). The objective of this research was to investigate adsorption of CR by NZ and organo-zeolites obtained by modification of NZ with surfactant - cetylpyridinium chloride (CP).

Experimental

The starting material was the natural zeolite from the Zlatokop deposit, Vranjska Banja with the particle size <0.043 mm. Cetylpyridinium chloride (CP) was used for the preparation of organo-zeolites. In order to obtain organo-zeolites with

different CP loadings, 10 wt % aqueous suspension of the NZ was treated with CP amounts equivalent to 100%, 200% or 300% of external cation exchange capacity (ECEC) of NZ. The samples were denoted as NZCPC10, NZCP20 and NZCP30.

In the initial dye adsorption study, 25 mL of CR solution ($C=300$ mg/L) was mixed with 0.5 g of either NZ or each organo-zeolite. To study the effect of the initial CR concentrations, 0.5 g of NZ or NZCP10 was mixed with 25 ml of aqueous solutions, containing various initial CR concentrations (100 - 2000 mg/L). In all experiments, after the reaction time (24h), suspensions were centrifuged at 10,000 rpm for 10 min to separate the solution and solid. The initial and non-adsorbed concentrations of the CR in supernatants were determined by using UV/VIS spectrometer Analytic Jena Spekol 1300, at $\lambda=496$ nm.

Results and Discussion

Preliminary results on adsorption of CR by NZ and organo-zeolites NZCP10, NZCP20 and NZCP30 are given at Fig. 1a. As can be seen, adsorption of CR was 11.9 mg/g (78%) for NZ, 15.2 mg/g (100%) for NZCP10, 14.2 mg/g (93.42%) NZCP20 and 13.5 mg/g (88.81%) for NZCP30. Results showed that NZ as well as organo- zeolites were efficient in adsorption of CR. For organo-zeolites, it was observed that adsorption of CR slightly decreased with increasing the amount of CP at the zeolite surface. Thus, the highest adsorption of CR was achieved when the amount of CP was equal to 100% of ECEC.

The isotherms for CR adsorption on NZ and NZCP10 are given at Fig. 1b. From Fig. 1b, it is observed that adsorption of CR by both adsorbents followed a non linear type of isotherm and much higher adsorption of CR was achieved with the NZCP10. For fitting the data, the Langmuir and Freundlich adsorption equations were selected:

$$\text{Langmuir equation: } q_e = (q_m K_L C_e) / (1 + K_L C_e)$$

where, q_e is the amount of dye adsorbed per unit of adsorbent at equilibrium (mg/g), C_e is equilibrium concentration of CR (mg/L), q_m is the maximum amount of CR that can be adsorbed by the solids (mg/g), K_L is the Langmuir constant related to the energy of adsorption (L/mg).

$$\text{Freundlich equation: } q_e = K_F C_e^{1/n},$$

where K_F ($\text{mg}^{-1-1/n} \text{L}^{1/n} \text{g}^{-1}$) and n are the Freundlich adsorption isotherm constants. Table 1 presents the fitted isotherm parameters for the Langmuir and Freundlich isotherms. Both models well described adsorption of CR by NZ (for Langmuir model $r^2=0.94$ and for Freundlich model $r^2=0.96$). For adsorption of CR by NZCP-10, the best fit of the experimental data was achieved with the Langmuir model. From Langmuir isotherm, calculated maximum amount of CR adsorbed by NZCP10 was significantly higher (54.2 mg/g) than for NZ (21 mg/g) . These results indicated that presence of CP at the zeolitic surface increased the adsorption of CR. Also, the value of the Freundlich parameter $n > 1$ for both adsorbents

indicated that CR adsorption is favorable physical process under applied experimental conditions [3].

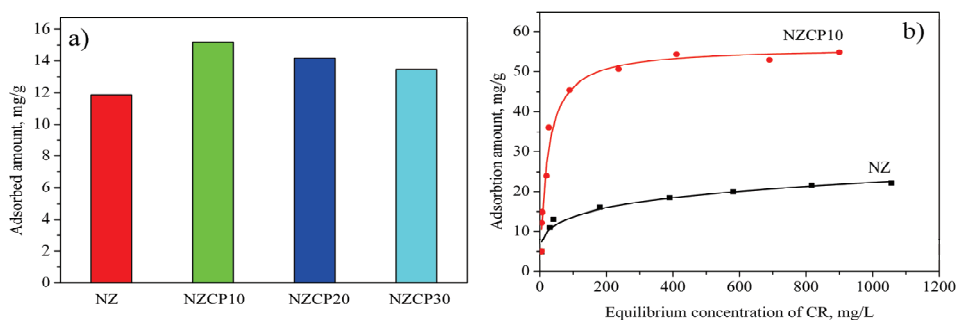


Figure 1. a) Adsorption of the CR by NZ and organo-zeolites; b) Isotherms for adsorption of CR by NZ and NZCP10.

Table 1. Adsorption parameters of isotherms for adsorption CR on NZ and NZCP10.

Materials	Freundlich			Langmuir		
	K_F	n	r^2	K_L	q_m	r^2
NZ	5.11	4.66	0.96	0.0375	21.00	0.94
NZCP10	11.99	4.17	0.84	0.0456	56.24	0.98

Conclusion

Results of adsorption of CR by NZ and its organo-modified form (NZCP10) showed that significantly higher CR adsorption has been achieved on organo-modified zeolite. Both Freundlich and Langmuir isotherms well described adsorption of CR by NZ. Langmuir model best described adsorption of dye by NZCP10. The results suggested that surfactant molecules at the zeolitic surface have positive influence on adsorption of CR.

References

- [1] Sh. Wang, E. Ariyanto J. Colloid Interface Sci., 2007, 314, 25–31.
- [2] M. K. Purkait, A. Maiti, S. DasGupta, S. De, J. Hazard. Mater., 2007, 145, 287-295.
- [3] V. Vimonses, Sh. Lei, B. Jin, Ch. W.K. Chow, Ch. Saint, Chem. Eng. J., 2009, 148, 354-364.

DETERMINATION OF THE POINT OF ZERO CHARGE OF Cu(II), Zn(II) AND Ag(I) DOPED HYDROXYAPATITE

M. Šljivić Ivanović, V. Stanić, A. Milenković, I. Smičiklas

*University of Belgrade, Vin a Institute of Nuclear Sciences, P.O. Box 522,
Belgrade, Serbia*

Abstract

In order to additionally characterize Cu(II), Zn(II) and Ag(I) doped hydroxyapatite (HAP) powders, their points of zero charge (pH_{PZC}) were determined. pH_{PZC} values were similar for all investigated samples (6.51 ± 0.09 for CuHAP, 6.46 ± 0.16 for ZnHAP and 6.65 ± 0.14 for AgHAP). The obtained values were also comparable to pH_{PZC} reported for synthetic calcium hydroxyapatite, indicating that dopant cations were incorporated in crystal lattice during the synthesis.

Introduction

Synthetic hydroxyapatite (HAP, $\text{Ca}_{10}(\text{PO}_4)_6(\text{OH})_2$) exhibit chemical similarity to the mineral component of bones and teeth in mammals, and due to nontoxic and biocompatible properties it has been widely used in the fields of the reconstruction of damaged bone and teeth [1]. Based on the flexibility of HAP structure, Ca^{2+} , PO_4^{3-} , and/or OH^- ions can be substituted by variety of ionic species, which may alter the crystallinity, lattice parameters, morphology, solubility and other characteristics. Cu(II), Zn(II) and Ag(I) doped hydroxyapatite samples (CuHAP, ZnHAP and AgHAP) have shown a promising antimicrobial activity [2, 3]. Surface properties of these materials are important for potential application in purification of microbiologically polluted water and bone tissue engineering. In this study, the points of zero charge (pH_{PZC}) of CuHAP, ZnHAP and AgHAP samples were determined.

Experimental

Doped HAP samples were synthesized by neutralization method, at 95°C , using CaO, as well as CuO, ZnO or Ag_2O dissolved in H_3PO_4 . The details about powders preparation and characterization are reported elsewhere [2, 3]. Samples with $\text{M}/\text{Ca} = 0.4$ mol % (M = Cu, Zn or Ag) were used in this study. All powders were nonstoichiometric, with $(\text{M}+\text{Ca})/\text{P} < 1.67$. The pH_{PZC} values were determined by batch equilibration technique [4]. 20 mL of 0.1, 0.01 and 0.001 mol/L KNO_3 solutions were equilibrated with 0.1g of doped HAP samples for 24 h, on a horizontal shaker, at ambient temperature ($20 \pm 1^\circ\text{C}$). The initial pHs were adjusted

in the range 3-12, by adding minimum amounts of NaOH or HNO₃ solutions. The pH_{PZC} were defined from the plateau parts of the plots pH_{final} vs. pH_{initial}.

Results and Discussion

The dependencies pH_{final} vs. pH_{initial} are given in Fig. 1. Large variations of electrolyte concentration caused small drifts of final pH values, confirming that KNO₃ was an inert electrolyte in respect to all doped HAP surfaces.

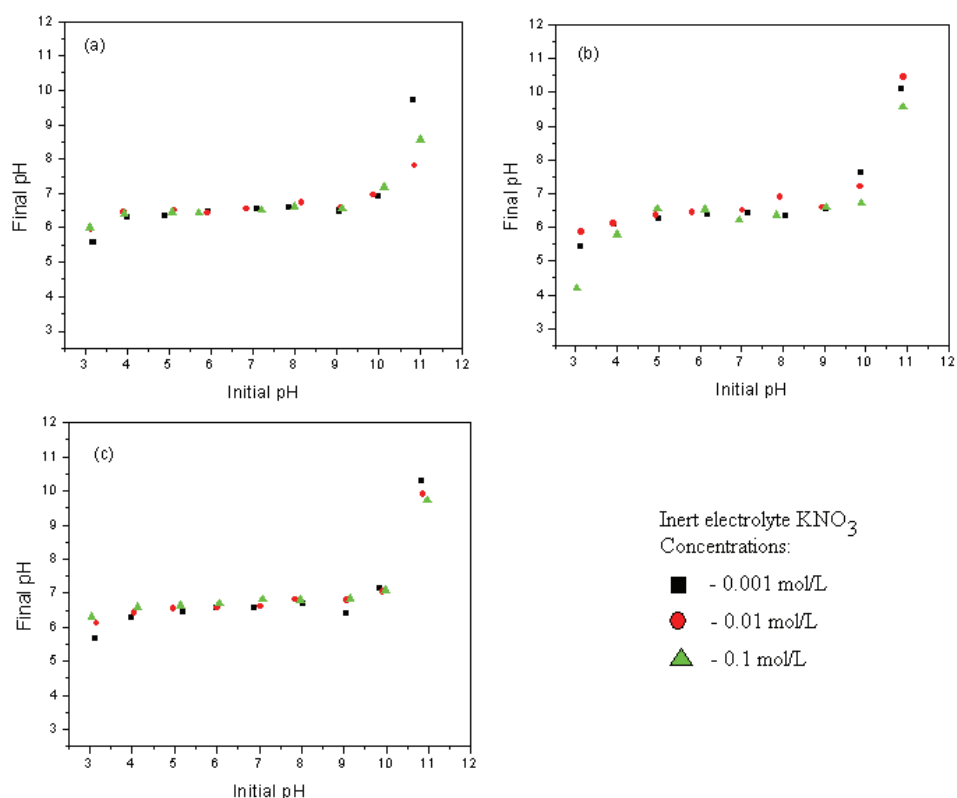


Figure 1. Determination of the point of zero charge (pH_{PZC}) of hydroxyapatite powders doped with (a) Cu(II), (b) Zn(II) and (c) Ag(I) ions.

The obtained curves were of similar shape. Final pH values increased with the increase of initial pH to ~4, where the plateaus began. In the pH range from ~4 to ~10 final pHs were independent of the initial ones, indicating buffering properties of the samples. Further increase of initial pH above 10 caused increase of final pH values.

The calculated pH_{PZC} were: 6.51±0.09 for CuHAP, 6.46±0.16 for ZnHAP and 6.65±0.14 for AgHAP. Dependences between initial and final pH values, as well as the lengths of the buffering pH region, corresponded to the behavior of synthetic HAP [5, 6]. As a consequence of different stoichiometry, crystallinity, degree of CO₃²⁻

incorporation, etc., pH_{PZC} of HAP powders obtained by different synthetic routes may fluctuate as well. The points of zero charge obtained for doped samples were in the range of values determined for synthetic calcium hydroxyapatite samples [5, 6, 7]. These results indicated incorporation of Cu(II), Zn(II) and Ag(I) into the apatite crystal lattice during the precipitation, and thus support the results of previous chemical and instrumental analysis [2, 3].

Conclusion

The points of zero charge of Cu(II), Zn (II) and Ag(I) doped hydroxyapatite were determined by batch equilibration technique. KNO_3 was found to be an inert electrolyte in respect to analyzed powders. The pH_{pzc} for doped HAP samples were comparable with the values obtained for various synthetic calcium hydroxyapatite powders. It can be concluded that dopant cations at applied level were incorporated in HAP crystal lattice by substitution of Ca(II). Electrical charge disbalance which occurred due to incorporation of monovalent Ag, might be compensated by creation of cationic vacancies or simultaneous substitution of PO_4^{3-} by CO_3^{2-} .

Acknowledgments

This work was supported by the Ministry of Education and Science of the Republic of Serbia (Project No.III 43009).

References

- [1] L. L. Hench, J. Wilson, *Science*, 1984, 226, 630-636.
- [2] V. Stanić, Dj. Janačković, S. Dimitrijević, S. B. Tanasković, M. Mitrić, M. S. Pavlović, A. Krstić, D. Jovanović, S. Raičević, *Appl. Surf. Sci.*, 2011, 257, 4510–451.
- [3] V. Stanić, S. Dimitrijević, J. Antić-Stanković, M. Mitrić, B. Jokić, I. Plećaš, S. Raičević, *Appl. Surf. Sci.*, 2010, 256, 6083–6089.
- [4] S. K. Milonjić, A. Lj. Ruvarac, M. V. Šušić, *Thermochim. Acta* 1975, 11, 261–266.
- [5] I. Smičiklas, S. Milonjić, P. Pfindt, S. Raičević, *Sep. Purif. Technol.*, 2000, 18, 185-194.
- [6] Đ. Janačković, I. Janković, R. Petrović, Lj. Kostić Gvozdenović, S. Milonjić, D. Uskoković, *Key Eng. Mater.* 2003, 240-242, 437-440.
- [7] I. Smičiklas, A. Onjia, S. Raičević, *Sep. Puri. Technol.*, 2005, 44, 97–102.

L-04-P

DETERMINATION OF CRITICAL MICELLAR CONCENTRATION OF TENSIDE MIXTURES

S. N. Blagojević¹, N. I. Potkonjak², B. R. Simonović¹

¹*Institute of General and Physical Chemistry, University of Belgrade, Studentski trg 12-16, 11000 Belgrade, Republic of Serbia*

²*Chemical Dynamics Laboratory, Vinča Institute of Nuclear Sciences, University of Belgrade, Mike Petrovića Alasa 12-14, 11001 Belgrade, Serbia*

Abstract

The critical micellar concentration (CMC) of tenside mixtures were determined by conductometric titration method in aqueous solution. It was found that mixtures with nonionic tensides have a much smaller CMC.

Introduction

Surfactants constitute the most important group of detergent components, and they are present in all types of detergents. Increasing surfactant concentration leads to a decrease in both surface tension and interfacial tension until the point is reached at which surfactant clusters begin to form. Above this concentration (the critical micelle concentration CMC) changes in surface and interfacial activity are only minimal. There is a big difference in CMC for anionic and nonionic tensides. Determination of CMC in tenside mixture was done by conductometric method. Washing and cleaning in aqueous wash liquor is a complex process involving the cooperative interaction of numerous physical and chemical influences. In the broadest sense, washing can be defined as both the removal by water or aqueous surfactant solution of poorly soluble matter and the dissolution of water-soluble impurities from textile surfaces.

Surfactants are amphiphilic molecules that possess both hydrophobic and hydrophilic properties. A typical surfactant molecule consists of a long hydrocarbon 'tail' that dissolves in hydrocarbon and other non-polar solvents, and a hydrophilic 'headgroup' that dissolves in polar solvents (typically water)[1]. One example of a dual character molecule having a head-group and a non-polar tail is sodium dodecyl sulphate (SDS), $\text{NaOSO}_3\text{C}_{12}\text{H}_{25}$. When a sufficient amount of SDS is dissolved in water, several bulk solution properties are significantly changed, particularly the surface tension (which decreases) and the ability of the solution to solubilize hydrocarbons, (which increases). These changes do not occur until a minimum bulk SDS concentration is reached. This concentration is called the *critical micelle concentration (CMC)*. Several experiments, including light scattering and NMR[2], show that below the CMC, the surfactant exists mainly as solvated monomeric species, whereas above the CMC these monomers undergo self-assembly to form roughly spherical structures (having an overall diameter of ~5 nm) known as micelles. Micelles are the simplest of all self-assembly structures.[3]

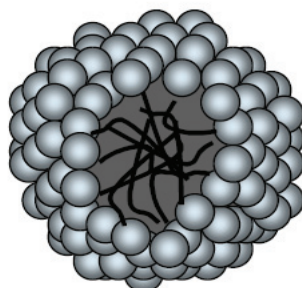


Figure 1. Schematic representation of a spherical micelle.

Modern detergent formulation, always have a mixture of few surfactants and for estimating detergency power and concentration of is it very important to determine critical micelle concentration.

Below the *CMC*, the addition of surfactant to an aqueous solution causes an increase in the number of charge carriers for example $(\text{Na}(\text{aq})^+)$ and $(\text{OSO}_3\text{C}_{12}\text{H}_{25}(\text{aq})^-)$ and consequently, an increase in the conductivity. Above the *CMC*, further addition of surfactant increases the micelle concentration while the monomer concentration remains approximately constant (at the *CMC* level). Since a micelle is much larger than a tenside monomer it diffuses more slowly through solution and so is a less efficient charge carrier. A plot of conductivity against surfactant concentration is, thus expected to show a break at the *CMC* (Fig 2).

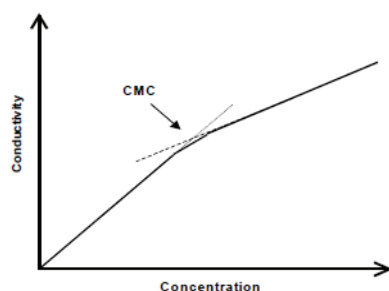


Figure 2. Determination of CMC.

Experimental

All experiments were done in thermostated 50 ml conductometric cell at 25C and in 18MΩ demi water with Hach Sension 5 conductivity meter. The solution of tenside mixture used for conductometric titration was 10g/L, and a titration step from pipette was 0.5ml. The conductivity vs concentration graph was plotted and the CMC was calculated as cross point of two linear parts of graph using ORIGIN software.

Results and discussion

We study CMC for tenside mixture of anionic and nonionic tenside in different ratio. For this study we use SLES and α -olefin sulfonates (anionic) and different amfoteric and nonionic tensides (coco betaine, coco amide, and various etoxylated alcohols) in various ratios.

Table 1. CMC of various tenside mixtures.

	CMC (g/L) /25C
SLES/AOS	0,33
SLES/AOS/coco betaine	0,31
SLES/AOS/coco amide	0,31
SLES/AOS/C12-C15-7EO	0,15
SLES/AOS/C10-7EO	0,12
SLES/AOS/ C9-C11-7EO	0,13

The ratio of SLES/AOS (80/20) and in the other experiment SLES/AOS/tenside (75/15/10)

Conclusion

Nonionic tenside have a great influence for CMC of mixture. Mixture of anionic with nonionic tenside can be used in a lower concentration.

Favorable detergency properties of nonionic surfactants derive largely from the following factors:

- Low critical micelle concentration (CMC)
- Very good detergency performance
- Excellent soil antiredeposition characteristics with synthetic fibers

The low CMC values of nonionic surfactants indicate that they display high detergency performance even at relatively low concentrations.

Acknowledgment

The support of this research by the Ministry of Education and Science of Republic of Serbia through projects No.172015 is gratefully acknowledges.

References

- [1] J. Falbe, Surfactants in consumer product, Springer-Verlag, Berlin, 1987
- [2] G. Zhisheng, et al, J.Colloid and interface science, 1990, 137, issue 1, 137-146.
- [3] P. Latellier, A. Mayaffre, J .Colloid and Interface Science, 2008, 327, 186-190.

COMPLEX COMPOUNDS

**CONDUCTOMETRIC STUDY OF COMPLEX
FORMATION BETWEEN OCTAAZAMACROCYCLIC
LIGAND AND Co^{2+} , Ni^{2+} , Zn^{2+} , Cu^{2+} , Ag^+ AND Cd^{2+}
METAL CATIONS**

B. B. Petković¹, D. Stanković², S. Samaržija Jovanović¹, S. P. Sovilj²

¹*Department of Chemistry, Faculty of Natural Sciences and Mathematics, University of
Priština, 38220 Kosovska Mitrovica, Serbia (bedpet@sezampro.rs)*

²*Faculty of Chemistry, University of Belgrade, P.O. Box 118, 11158 Belgrade, Serbia*

Abstract

The complexation reactions between octaazamacrocyclic ligand $\text{N},\text{N}',\text{N}'',\text{N}'''$ -tetrakis(2-pyridylmethyl)-1,4,8,11-tetraazacyclotetradecane (*tpmc*) and Co^{2+} , Ni^{2+} , Zn^{2+} , Cu^{2+} , Ag^+ and Cd^{2+} metal cations have been studied conductometrically in acetonitrile and aqueous solution. The conductance data show different stoichiometry of the complexes in two studied solutions. Mostly, complexes were formed in molar ratio of 1:1 (ML) in both solutions, but in some cases 2:1 (M_2L) complexes are evident. The stability constants of the resulting 1:1 complexes were determined from computer fitting of the conductance/mole ratio data. The conductometric data and formation constants were compared with sensor behavior and selectivity of recently reported *tpmc* based ISE [1]. The study also should contribute to better explanation of very good selectivity of this ISE.

Introduction

The octaazamacrocyclic ligand *tpmc* with four 2-pyridylmethyl pendant groups ($\text{N},\text{N}',\text{N}'',\text{N}'''$ -tetrakis(2-pyridylmethyl)-1,4,8,11-tetraazacyclotetradecane) as a macrocyclic flexible ring through coordination provides interesting structural and chemical properties [2]. In that respect the ligand should be capable to accommodate a wider variety of cations and form relatively stable complexes. Still, the most of synthesized complexes are dinuclear $\text{Cu(II)}/\text{tpmc}$ complexes, which in addition to *tpmc*, also contain different bridged ligands and small number of some dinuclear cobalt(II) complexes [3a,b].

Therefore, the conductometric study of formation complexes between *tpmc* ligand and different metal ions can contribute to gain new information's concerning the transport phenomena of the ligand–electrolyte complex in the solution, stoichiometry of the reactants and solvent nature impact on complexation process. The selectivity phenomena of binding ligand toward different ions were crucial fact for functioning of ion-selective electrodes. The goal of this work is also to try to find which of copper(II) complexes is responsible for sensor activity of *tpmc* based ion selective membrane and more clarify its sensor properties.

Experimental

The conductometric procedure. acetonitrile or aqueous solution of 1.0×10^{-4} M nitrate salt of examined ions was placed in a titration cell and the conductance of the solution was measured. Then the *tpmc* concentration was increased by adding the ligand solution (5×10^{-3} M) in aliquots of 0.05 cm^3 to the titration cell and the conductance of the resulted solution was measured after each step at the desired temperature. All measurements were done in the solutions adjusted thermostatically to 23°C with constant stirring. A conductometric cell with a cell constant of 0.60 cm^{-1} was used throughout the studies. The complex formation constant and the molar conductance of complex were obtained by computer fitting of the molar conductance-mole ratio data to the appropriate equations [4] using a nonlinear fitting with Matlab.

Results and Discussion

The molar conductances versus ligand/cation mole ratio plots for *tpmc* complexes with examined cations are shown in Figs. 1. and 2. As is seen, addition of *tpmc* to Co^{2+} , Ni^{2+} , Zn^{2+} , Cu^{2+} and Cd^{2+} cations in AN at constant temperature results in an increase in molar conductivity because of more mobility of these *tpmc* cation complexes toward free solvated cations in question, while in aqueous solution opposite situation is observed. When the donor properties of the solvent are low, as in case of acetonitrile, cations are poorly solvated and can easily be complexed by the *tpmc* and formation constants of complexes are higher. The most of cations formed relatively stable mononuclear complexes in both media, while dinuclear complexes are evidenced for Zn^{2+} always, and Cu^{2+} and Ag^+ only in aqueous solution.

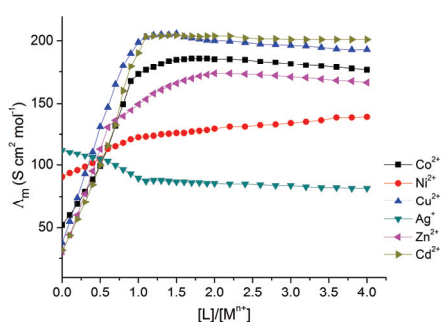


Figure 1. Plot of molar conductance, Λ , vs. V (cm^3 of added ligand) for the binding of Co^{2+} , Ni^{2+} , Zn^{2+} , Cu^{2+} , Ag^+ and Cd^{2+} by *tpmc* in acetonitrile at 23°C .

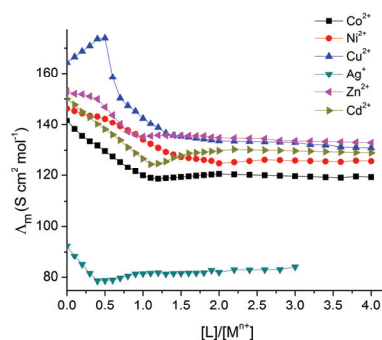


Figure 2. Plot of molar conductance, Λ , vs. V (cm^3 of added ligand) for the binding of Co^{2+} , Ni^{2+} , Zn^{2+} , Cu^{2+} , Ag^+ and Cd^{2+} by *tpmc* in aqueous solution at 23°C .

Recently developed *tpmc* based copper-selective electrode exhibits very good selectivity toward many studied cations. The rate of selectivity coefficients

for these cations was 10^{-3} - 10^{-4} except for silver ion which strong interferes due to its interaction with polymer matrix itself [5]. From conductometric results and formation constants for assumed stoichiometry of 1:1 (Table 1), it is obvious that such selectivity is not based on stability of mononuclear copper/*tpmc* complex. The most likely, the good selectivity of electrode was derived from formation of dinuclear copper/*tpmc* complex, the most conductive of all of examined complexes.

Table 1. Formation constants (K_{ML}) and molar conductance (Λ_{ML}) of different $M^{n+}/tpmc$ complexes in acetonitrile and aqueous solutions.

Cations	Acetonitrile		Aqueous solution	
	$\log K_{ML}^{(SD<0.1)}$	Λ_{ML}	$\log K_{ML}^{(SD<0.1)}$	Λ_{ML}
Co^{2+}	>7	176.4	6.4	119.2
Ni^{2+}	4.1 ^a	188	b	b
Cu^{2+}	>7	193.1	4.9 ^c	130.5
Zn^{2+}	b	b	b	b
Ag^+	5.6 ^c	88.4	b	b
Cd^{2+}	>7	201	>7	125.5

a – value is less certain, assumed stoichiometry taken into calculations did not give a good fit

b – data can not be fitted to equations

c – first data points conditioned by forming dinuclear complexes are not considered in fitting

Conclusion

Solvent properties were considered as the major factors influencing the formation constants of *tpmc*-cation complexes. The nature of the solvent also favoured type of stoichiometry of complexes. Conductometric results suggests that dinuclear complex is main carrier of ISE potentiometric response and provides faster ion exchange at the membrane/aqueous solution interface.

Acknowledgement

Financial support for this study was granted by the Ministry of Science and Technological Development of the Republic of Serbia, Project Number 45022.

References

- [1] B. B. Petković, S. P. Sovilj, M. V. Budimir, R. M. Simonović, V. M. Jovanović, *Electroanalysis*, 2010, 22, 1894.
- [2] J. Costamagna, G. Ferraudi, B. Matsuhira, M. Campos-Vallete, J. Canales, M. Villagran, J. Vargas, M. J. Aguirre, *Coord. Chem. Rev.*, 2000, 196, 125.
- [3] a) E. Asato, H. Toftlund, S. Kida, M. Mikurya, K. Murray, *Inorg. Chim. Acta*, 1989, 165, 207; b) S. P. Sovilj, N. Avramović, N. Katsaros, *Trans. Metal. Chem.*, 2004, 29, 737.
- [4] Gh. H. Rounaghi, A. Soleamani, K. R. Sanavi, *J. Incl. Phenom. Macro*, 2007, 58, 43.
- [5] D. M. Sejmanović, B. B. Petković, M. V. Budimir, S. P. Sovilj, V. M. Jovanović, *Electroanalysis*, 2011, 23, 1849.

M-02-P

CYTOTOXIC ACTIVITY OF AZAMACROCYCLIC Cu(II) DICARBOXYLATE COMPLEXES

M. Antonijević-Nikolić¹, G. Vučković², S. B. Tanasković³,
J. Antić-Stanković³, V. Živković-Radovanović²

¹Higher Technological School of Professional Studies, 15000 Šabac, Serbia

²Faculty of Chemistry, University of Belgrade, P.O.Box 118, 11158, Serbia

³Faculty of Pharmacy, Vojvode Stepe 450, 11000 Belgrade, Serbia

Abstract

Cu(II) complexes with *N,N',N'',N'''*-tetrakis (2-pyridylmethyl) -1,4,8,11-tetraazacyclotetradecane (tpmc) and dianion of one the aliphatic dicarboxylic acids: butanedioic (succinic acid = succH₂), pentanedioic (glutaric acid = glutH₂), hexanedioic acid (adipic acid = adipH₂) and decanedioic acid (sebacic acid = sebH₂) having general formula [Cu₄(L)(tpmc)₂](ClO₄)₆·xH₂O, L=succ (**1**) or glut (**2**), x=2; L=adip, x=7 (**3**); L=seb, x=6 (**4**) were isolated and screened for cytotoxic activity along with free ligands and simple Cu(II) salt as control. They were tested on four human cancer cell lines *in vitro*. In some cases detected activities for the complexes were enhanced compared with the corresponding controls.

Introduction

In literature many reports highlighted the application of transition metal complexes as anticancer agents [1]. Copper is crucial for human life as a component of enzymes and proteins. Furthermore, some of copper(II) complexes were found with anti-inflammatory, antiulcer, anticonvulsant, antiamebic, antidiabetic, antimicrobial and antitumor activities [2]. A number of *in vivo* studies have indicated that biologically active compounds become more bacteriostatic and carcinostatic upon chelation [3]. In addition, Cu(II) complexes with *N,N',N'',N'''*-tetrakis(2-pyridylmethyl)-1,4,8,11-tetraazacyclotetradecane (tpmc) and some of the secondary ligands (aliphatic/aromatic mono- and dicarboxylates or aminocarboxylates) exhibited antibacterial activity *in vitro*.

Previously we described tetranuclear Cu(II)tpmc complex with succinato dianion as bridged ligand which structure is determined by X-ray analysis [4a]. By using somewhat modified procedures, we prepared related complexes containing glutarato, adipato and sebacinato ligands [4b]. In this work, cytotoxic activity of all 4 complexes is tested and considered.

Results and discussion

Based on solved X-ray analysis of succinato complex **1** [4a] and analogy of the analytical and spectral properties of the complexes **2-4** it is proposed the same structure of the complex cation presented in figure 1.

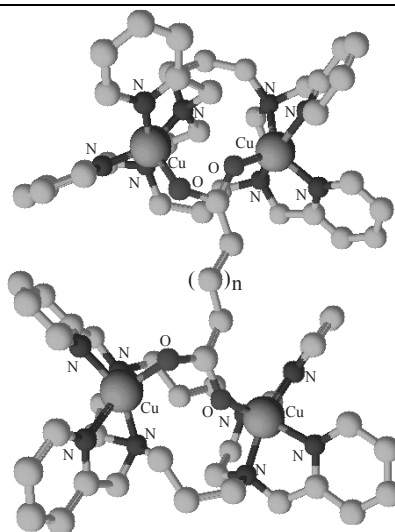


Figure 1. The presentation of the complex cation $[\text{Cu}_4(\text{L})(\text{tpmc})_2]^{6+}$ (L= succ, glut, adip, seb ligands) within complexes **1-4**; n=0-2, or 6.

The cytotoxic effects of the complexes were examined on 4 human tumor cell lines: estrogen-receptor-positive human breast cancer (MCF-7), human cervix adenocarcinoma (HeLa), human malignant melanoma (Fem-x) and human acute monocytic leukemia (THP1) cells. Stock solutions of the test complexes **1-4** and controls were made in DMSO and diluted for use in the nutrient medium (RPMI 1640 without phenol red, supplemented with L-glutamine, streptomycin, penicillin, fetal bovine serum and HEPES, adjusted to pH 7.2) The cells were treated with the appropriate amounts of compounds of interest or corresponding vehicle (control cells), then seeded in duplicate in 96 well plates. MTS test was used to assess the metabolic activity. Significantly different values from control (vehicle-treated cells) are denoted: * $P \leq 0.05$, ** $P \leq 0.01$, *** $P \leq 0.0001$. The obtained cytotoxic properties of the complexes are presented in Figure 2. Ligands and $\text{Cu}(\text{ClO}_4)_2 \cdot 6\text{H}_2\text{O}$ used as controls were inactive under the studied conditions, while all complexes have promoted significant decreases in the viability of the tested cells, which occurred in a dose-dependent fashion. It is obvious that in general going from complex **1** containing μ -succ to complex **4** with μ -seb ligand with increasing the number of $-\text{CH}_2-$ groups in dicarboxylate the cytotoxic activity also increase. This is in accordance with the fact that cell membranes are liposolubile, so the complex with higher degree of hydrophobic properties more easily penetrates inside the cell.

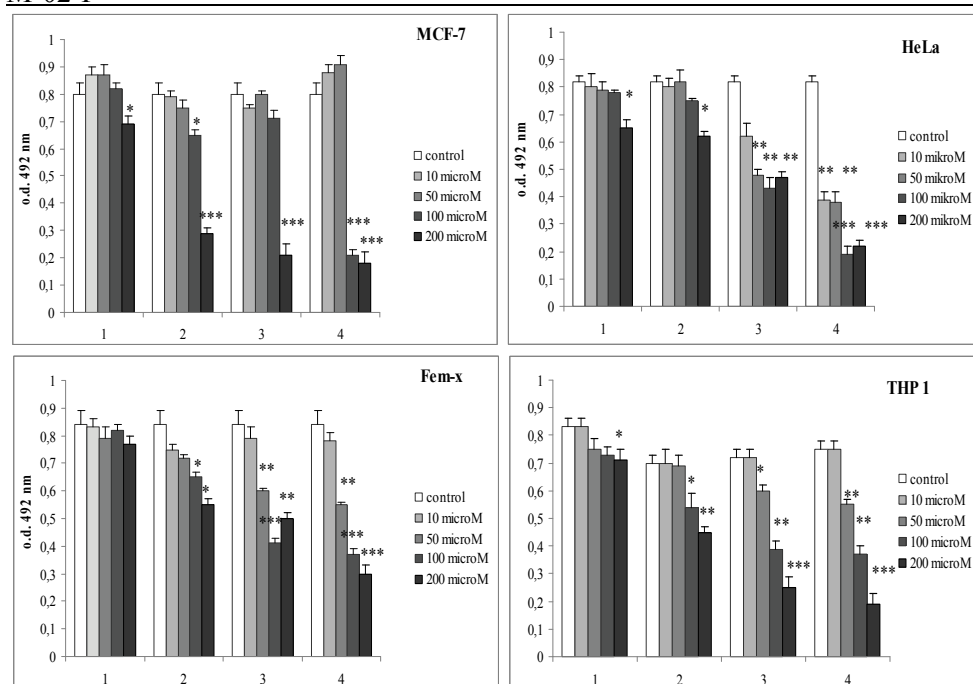


Figure 2. Results of MTS test.

Conclusion

Tetranuclear cationic octaazamacrocyclic Cu(II) complexes with α,ω -dicarboxylates were screened to cytotoxic activity on four human cancer cell lines *in vitro*. The obtained results indicate that the tested complexes have a considerable activity upon the evaluated cell lines in a concentration-dependent manner. These are the first examples of the numerous up to now described metal tpmc complexes which cytotoxicity is considered.

References

- [1] A. C. Barve, S. Ghosh, A. A. Kumbhar, A. S. Kumbhar, V. G. Puranik, *Transition Met. Chem.* 2005, 30, 312–316.
- [2] M. Buczkowska, A. Bodtke, U. Lindequist, M. Gdaniec, P. J. Bednarski, *Arch. Pharm. Chem. Life Sci.* 2011, 344, 605–616.
- [3] Z. H. Chohan, M. Arif, M. A. Akhtar, C. T. Supuran, *Bioinorg. Chem. Appl.*, 2006, 2006, 1-13.
- [4] a) G. Vučković, M. Antonijević-Nikolić, T. Lis, J. Mroziński, M. Korabik, D. D. Radanović, *J. Mol. Struct.*, 2008, 872, 135-144; b) S. B. Tanasković, M. D. Antonijević-Nikolić, G. N. Vučković, 44th Meeting of the Serbian Chemical Society, Belgrade, 2006, Book of Abstracts 55, NH-P03, Proceedings 117-120, in extenso; M. D. Antonijević-Nikolić, S. B. Tanasković G. N. Vučković, 45th Meeting of the Serbian Chemical Society, Novi Sad, 2007, Book of Abstracts 73, NH1, Proceedings 194-197, in extenso; S. B. Tanasković, M. D. Antonijević Nikolić, G. N. Vučković, 46th Meeting of the Serbian Chemical Society, Belgrade 2008, Book of Abstracts 65, NH-01.

COMPLEX OF IRON(II) WITH POTASSIUM 3-DITHIOCARBOXY-3-AZA-5-AMINOPENTANOATE DIHYDRATE

S. R. Trifunović¹, D. Bulatović², M. Kosović², Z. Leka²

¹Department of Chemistry, Faculty of Science, University of Kragujevac, R. Domanovica, P.O. Box 60, Kragujevac, Serbia (e-mail: srecko@kg.ac.rs), ²Faculty of Metallurgy and Technology, University of Montenegro, Cetinjski put bb, 81 000 Podgorica, Montenegro (e-mail: zorica@ac.me)

Abstract

The complex of iron(II) with dithiocarbamate ligand, potassium-3-dithiocarboxy-3-aza-5-aminopentanoate dihydrate, $Kdaap \cdot 2H_2O$, was synthesized and characterized by elemental analysis, infrared and electronic absorption spectroscopy and by measuring the magnetic moment. The spectral data suggest tridentate coordination of $daap^-$ ligand with Fe(II) ion *via* two nitrogen atoms (amino and imino group) and oxygen atom from carboxylic group.

Introduction

A large number of transition metal complexes with dithiocarbamates are known where metal ions are in different oxidation states. The neutral complexes of the type $M(dtc)_x$, where x is the number of dithio related ligands, found wide application in agriculture, medicine and vulcanization [1]. Dithiocarbamates contain sulfur, nitrogen and oxygen donor atoms as ligands forming complex compounds with transition metals. Coordination of transition metal with dithio-ligands is done the most frequently *via* two sulfur atoms the so-called bidentate coordination, forming four-membered chelate ring. Some dithiocarbamate-ligand is possible to bind *via* the nitrogen and oxygen atoms. For heavy metal complexes with dithio-ligands four geometric structures can be assumed: a square-planar, tetrahedral, trigonal or octahedral, depending on the coordination number of the central metal ion.

The previously synthesized and described potassium-3-dithiocarboxy-3-aza-5-amino-pentanoate dihydrate ($Kdaap \cdot 2H_2O$), as uncoordinated ligand contains deprotonated carboxyl group while the dithio group is protonated [2]. The $daap^-$ ligand can coordinate as bidentate *via* two sulfur atoms, forming four-membered chelate ring or as a tridentate *via* nitrogen atoms from amine and imine group and oxygen atoms from carboxylic group, building two five-membered rings. In the previously synthesized and described complexes of Cu(II), Ni(II), Zn(II), Cd(II), Pt(II) and Pd(II), the $daap^-$ ligand was coordinated through the sulfur atoms [3,4].

The aim of this work is the synthesis and physico-chemical characterization of Fe(II)- $daap^-$ complex by elemental analysis, IR and UV spectroscopy and magnetic moment measurements.

Experimental

The ligand, K-daap·2H₂O, was synthesized as it described earlier [2].

Preparation of bis (3-dithiocarboxy-3-aza-5-aminopentnoato)-iron (II), Fe(daap)₂
Iron(II) bis-dithiocarbamate was obtained by direct reaction of Fe(II) and K-daap ligand in 1:2 molar ration.. Aqueous solution of 1 mmol (0.278 g) FeSO₄· 7H₂O was slowly added to aqueous solution of 2 mmol (0.536 g) K-daap with stirring at room temperature for half an hour. During mixing the brown solid was precipitated and separated by filtration, washed with H₂O and acetone and finally dried in air.

Analytical Methods

Elemental analysis C, H, N and S are performed using the standard method, with the Vario III CHNOS Elemental Analyzer, Elemental Analysensysteme GmbH. Fe analysis was performed by atomic absorption spectrometry using the Perkin-Elmer spectrophotometer, Model 1100-B.

IR spectrum in the 4000-400 cm⁻¹ region was recorded on FTIR 8700 (Shimadzu) spectrophotometer using the KBr disc.

UV-VIS spectrum in the 200-440 nm region was recorded using the buck scientific 105 UV-VIS spectrophotometer.

The magnetic moment was determined at room temperature using a MSB-MKI magnetic susceptibility balance, Sherwood Scientific Ltd., Cambridge.

Results and discussion

The complex Fe(II)dtc was synthesized from Fe(II) salt and polydentate dithiocarbamate, K-daap·2H₂O, in the molar ratio 1:2 at room temperature. This complex is air-stable and obtained in high yield. The assumed formula of the obtained complex is [Fe(OOCCH₂N(CSSH)CH₂CH₂NH₂)₂]₂·3H₂O. The results of elemental analysis (Table 1) confirm the composition of the complex in the stoichiometric ratio of metal: ligand = 1:2, while the IR spectrum can confirm the structure of complex. The obtained complex was dark brown, stable at room temperature, slightly soluble in water. In the IR spectrum of Fe(daap)₂·3H₂O dithio complex all major bands characteristic for the dithiocarbamate complexes are observed (Table 2). Pronounced singlet at 948 cm⁻¹ induced by vibration of C-S bond, confirms the equivalence of sulphur atoms in the dithio group (CSS⁻) [5]. The presence of band at 2634 cm⁻¹ represents the characteristic for protonated S-H group, which indicates that the metal is not tied to the ligand *via* sulphur atoms [5]. On this basis it can be assumed that the metal coordinated with ligand *via* oxygen atoms from carboxyl groups and two nitrogen atoms of amino and imino groups. The band in the area of 524 cm⁻¹ can be attributed to vibration of Fe-N bond, and band at 470 cm⁻¹ to vibration of Fe-O bond [6]. The absence of the band in the region 1700-1750 cm⁻¹ indicates the deprotonated carboxyl group of the resulting complex, which also can be confirmed by the bands at 1589 cm⁻¹ and 1411 cm⁻¹ of asymmetric and symmetric vibration of carboxyl groups [5]. The broad band at 1589 cm⁻¹ suggests overlapping COO⁻ and N-C bands. In the IR spectrum of the complex the wider band spears at 3408 cm⁻¹ which can be attributed to vibrations of OH-group [5].

Two absorption bands which lie in the range of 200-400 nm of electronic absorption spectrum can be attributed to d-d transition and the charge transition (with Fe^{2+} in nitrogen) $M \rightarrow L$ [7].

By measuring the magnetic moment at room temperature a diamagnetic d^6 low-spin complex Fe^{2+} was determined and according that the octahedral structure can be assumed.

In the complex with the central metal ion of small electronegativity (as Fe^{2+}) the stability of the complex increases in the series of ligand donor atoms $O < N > S > P$. Thus, Fe^{2+} as the transition acid (between hard and soft) will be coordinated via N rather than via S atoms.

Table 1. Elemental analysis data of the complex.

Empirical formula	Formula weight [g/mol]	Yields [%]	Found (Calcd.) [%]				
			C	H	N	S	Fe
$\text{Fe}(\text{daap})_2 \cdot 3\text{H}_2\text{O}$ $\text{FeC}_{10}\text{H}_{24}\text{N}_4\text{S}_4\text{O}_7$	496	81,59	25,00 (24,20)	4,72 (4,84)	11,15 (11,29)	26,01 (25,80)	10,60 (11,29)

Table 2. Important IR bands (cm^{-1}) for the free ligand and its iron (II) complex.

Compound	COO^-		CSS^-		S-H	$\text{N}=\text{C}$	OH^-	Fe-O	Fe-N
	ν_{as}	ν_{s}	ν_{as}	ν_{s}					
$\text{K-daap} \cdot 2\text{H}_2\text{O}$	1597	1414	963	635	2631	1453			
$\text{Fe}(\text{daap})_2 \cdot 3\text{H}_2\text{O}$	1589	1411	948	644	2634	1589	3408	470	524

Conclusion

In obtained Fe(II) complex, dithiocarbamate ligand, daap^- , acts as tridentate ligand and coordination takes places via O atom of the $-\text{COO}^-$ group, N atom from NH_2 group and imino N atom, resulting in octahedral diamagnetic $\text{Fe}(\text{daap})_2$ complex.

References

- [1] G. Pandey, K. K. Narang, Bioinorganic Chemistry and Applications, 2005, 3, 3-4.
- [2] B. Prelesnik, K. Andjelković, Z. Marković, T. Sabo, S. R. Trifunović, Acta Cryst. 1997, C53, 719.
- [3] S. R. Trifunović, Z. Marković, D. Sladić, K. Andjelković, T. Sabo, D. Minić, J. Serb. Chem. Soc., 2002, 67, 115.
- [4] Z. Leka, S. A. Grujić, S. Lukić, S. Skuban, S. Trifunović, J. Serb. Chem. Soc. 2004, 69(2), 137–143.
- [5] K. Nakamoto, Infrared Spectra of Inorganic and Coordination Compounds, Wiley, New York, 1970.
- [6] S. A. Shaker, Y. Farina, A. A. Salleh, European Journal of Scientific Research 2009, 33(4), 702-709.
- [7] A. B. P. Lever, Inorganic Electronic Spectroscopy, Mir, 1987.

M-04-P

MALDI TOF OF ALUMINIUM FLUOROQUINOLONE COMPLEXES

M. Cvijovic¹, P. Djurdjevic¹, P. Traldi², B. Nastasijevic³, J. Zvezdanovic⁴

¹*University of Kragujevac, Faculty of Science, Chemistry Department, 34000 Kragujevac, Serbia*

²*CNR –ISTM, 35127 Padova, Italy,*

³*Department of Physical Chemistry, Vinca Institute of Nuclear Sciences, University of Belgrade, P.O.Box 522, 11001 Belgrade, Serbia,*

⁴*University of Nis, Faculty of Technology, 16000 Leskovac, Serbia*

Abstract

Mass spectral studies of aluminium fluoroquinolone complexes provided information about species formed in these systems, especially polinuclear species. Metal complexation as means of ionization has been undertaken by ion-molecule reaction involving laser-desorbed metal ions. The formation of FQLs –aluminium ion is effected when the antibiotic loses the acidic proton from carboxylic acid moiety and proceeds to form a covalent bond with metal ion. The most favour binding site is negatively charged oxygen. The administration of drugs which may contain aluminium (III) ion (antacids, phosphate binders, vaccines, etc) may form metal – FQLs complexes. This reaction leads to altered bioactivity of the drug and/or developing aluminum toxic effects.

Introduction

Fluoroquinolones (FQLs) are synthetic antibacterial agents that inhibit the bacterial DNA gyrase and DNA regulation activity [1]. These broad –spectrum antibiotics have been clinically used for several types of infections which include urinary tract infections, skin and soft tissue infections and respiratory tract infections

The complexation has been investigated for fleroxacin, moxifloxacin and ciprofloxacin with aluminium in solutions by equilibrium technique and ESI. Polymerization was not observed by these techniques and owing to importance of such reactions it has been studied by LDI Mass Spectrometry.

FQLs are small molecules and to avoid saturation by matrix ions signals it has been used LDI-MS measurements instead MALDI.

Experimental

LDI-MS measurements were performed using a MALDI-TOF TOF UltrafleXtreme time-of-flight mass spectrometer (Bruker Daltonics, Bremen, Germany), equipped with 1 kHz smart-beam II laser Nd Yag ($\lambda=355$ nm) and operating in the positive reflectron ion modes.

The instrumental conditions employed to analyze molecular species in the m/z range 50-3000 in positive ion mode were: ion source 1 voltage: 25.00 kV; ion source 2 voltage: 22.30kV, lens voltage: 7.70kV, pulsed ion extraction time: 80 ns, reflector voltage: 26.45 kV, and reflector 2 voltage: 13.45 kV. The data aquisitioned by Flex Analysis Bruker Daltonics Software.

Results and Discussion

In the interest of maximizing the abundance of the signal generated by the metal complexes, the effect of the pH of the solution on the formation of the metal complexes was investigated. The most representative spectra are for metal to ligand concentration ratio 2:1 to 1:3 ($C_{Al} = 2.5 \times 10^{-5}$ mol/L) in the pH range 3.0 to 6.0. [2] The MALDI spectra for aluminium and ciprofloxacin system are shown in Fig.1 and Fig. 2. Identified dimer species $[Al_2L_5]$ by MALDI are: for fleroxacin m/z 1894.7, moxifloxacin m/z 2054.3 and for ciprofloxacin m/z 1703.8. These species have not been identified in solutions so probably these species are consequences of cluster formation. From coordination chemistry point of view the coordination of two metal ions with 5 ligands is not probable. The clusters with more deprotonated ligands can form in gas phase, *i.e.* in the plume generated by laser irradiation.

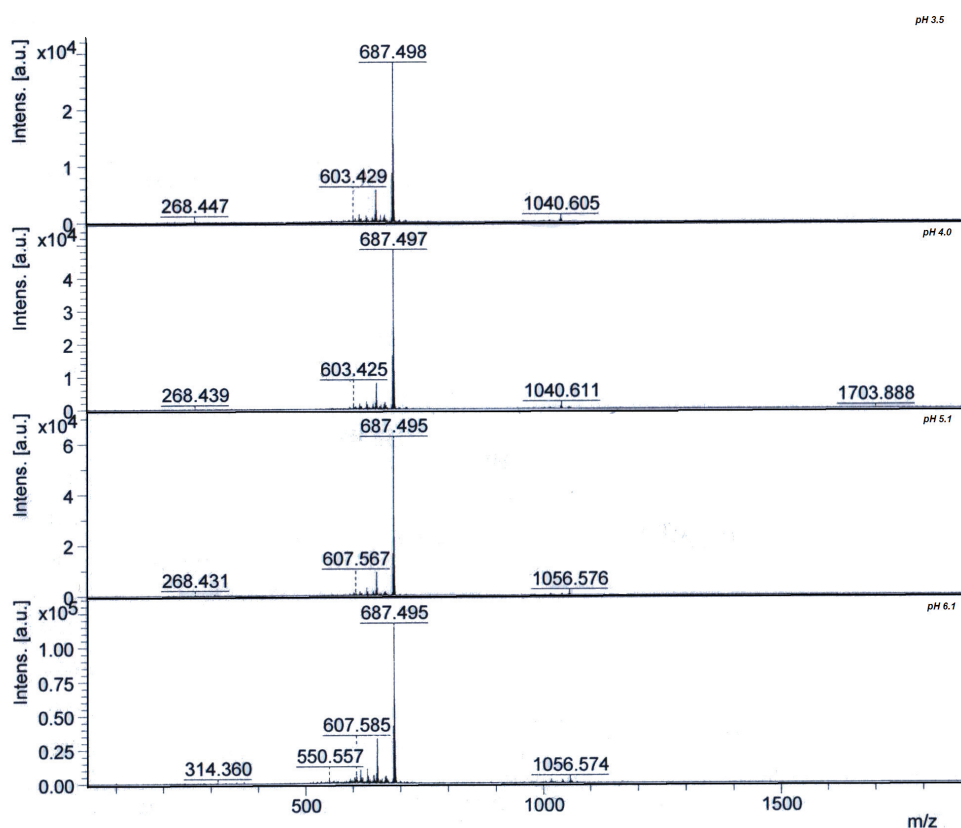


Figure. 1. LDI spectra of aluminium and ciprofloxacin systems for different pH values.

In this figure it is seen complex AlL , AlL_2 and AlL_3 species, but also polymer Al_2L_5 H values.

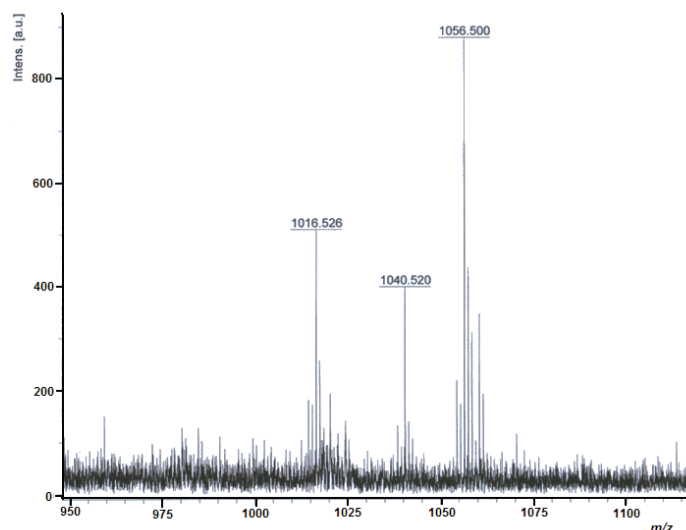


Figure 2. LDI spectrum of aluminium and ciprofloxacin system, zoom area for adduct ions with Na for m/z 1040 and adduct with K for m/z 1056.

Conclusions

The identified dominating species, characteristic for solutions of Al^{3+} and each of the three examined antibiotics (floxacin, moxifloxacin and ciprofloxacin), were the binary complexes AlL , AlL_2 and AlL_3 whose abundance was pH dependent. At pH range pH 4–6, the signal for the $(\text{L} + \text{H})^+$ ions decreases as some percentage of the quinolones deprotonate and the metal complexation begins to dominate. This is in agreement with previous ESI MS investigation of these systems. Polymerization of Aluminium – Fluorquinolone complexes may proceed in the gas phase accompanied by further clustering with deprotonated ligands. LDI indicated the formation Al_2L_2 core. The interaction between FQLs and Al^{3+} in the gastrointestinal tract should be considered with attention by biomedical point of view. Neutral complexes may permeate the membrane [3] and lead to Al toxicity.

References

- [1] P. G. Higgins, A. C. Fluit, F. J. Schmitz, *Curr. Drug Targets*, 2003, 4, 181-191.
- [2] Y. Kawai, K. Matsubayashi, H. Hakusui, *Chem. Pharm. Bull.*, 1996, 44, 1425-1430.
- [3] S. Mazzaferro, I. Perruzza, S. Constantini, M. Pasquali, L. Onorato, D. Sardella, R. Giordano, L. Ciaralli, P. Ballanti, E. Gonucci, A. G. Cinotti, G. Coen, *Nephrol. Dial. Transplant.*, 1997, 12(12), 2679-2682.

COBALT(II)-REDUCED DEXTRAN COMPLEXES CHARACTERIZATION BY ELECTRONIC SPECTROSCOPY

Ž. Mitić¹, M. Cakić², G. M. Nikolić¹, A. Veselinović¹, Lj. Ilić³

¹*Faculty of Medicine, University of Niš, RS-18000 Niš, Serbia*

e-mail: zak_chem2001@yahoo.com

²*Faculty of Technology, University of Niš, RS-16000 Leskovac, Serbia*

³*PCI "Zdravlje", RS-16000 Leskovac, Serbia*

Abstract

The cobalt(II) ion complex formation with reduced low-molecular dextran (RLMD) was investigated by electronic (UV–Vis) spectroscopy, and formation of Co(II)–RLMD complexes was observed at pH 7.0–13.5. With increase in solution pH the light absorbance maxima of complex solutions show red shift compared with $[\text{Co}(\text{H}_2\text{O})_6]^{2+}$ ion. Increase and appearances of the preponderance of absorbance maxima (510, 581 and 628 nm) at pH higher than 13.5 have been connected with the decomposition of Co(II)–RLMD complex next to $[\text{Co}(\text{OH})_6]^{4-}$ ion. Thus, these spectrophotometric criteria can be applied for the confirmation of the success of complex synthesis. The spectrophotometric parameters of the synthesized Co(II)–RLMD complexes are characteristic for Co(II) ion in octahedral (O_h) coordination.

Introduction

Dextran is exopolysaccharide described as a α -(1→6) linked polymer of α -D-glucopyranose units. The numerous investigations have indicated that the polysaccharide dextran and its derivatives have the extraordinary power to forming the water-soluble complexes with various biometals [1–3]. Reduced low-molecular dextran, was chosen as a new material for complexing, and the subsequent interactions with Co(II) ions by electronic spectroscopy were investigated in this study. Electronic spectroscopy can get the relatively reliable information about the ligand arrangement in transitional metal complexes. Co(II) ion builds numerous complex compounds with the different geometric structure, such as tetrahedral (T_d), square-planar (D_{4h}), and octahedral (O_h). The major goal of this work is to use electronic (UV–Vis) spectroscopy to verify the coordination of this type of Co(II) ion complexes.

Experimental

Co(II) ion complex synthesis with RLMD has been described in detail by Mitić et al. [4]. Vis spectra of the water solutions of the complexes were recorded on a VARIAN Cary-300 UV–Vis spectrophotometer, in the wavelength range of 400–900 nm with wavelength accuracy ± 0.2 nm, in quartz cells (1×1 cm) at room temperature with redistilled water as a reference.

Results and Discussion

Depending on pH, Co(II)–RLMD complexes behave differently considering the wavelength at which they show absorbance maxima. This range of wavelengths in the Vis spectra is 583–624 nm (Fig. 1). Bathochromic shifts of the absorbance maxima of the complexes with increasing pH, confirm the presence of different types of complexes. The reddish $[\text{Co}(\text{H}_2\text{O})_6]^{2+}$ ion absorbs at 512 nm, while the synthesized complexes absorb within the range 583–624 nm. With increase in solution pH, the absorbance maxima shift to longer wavelengths compared with the $[\text{Co}(\text{H}_2\text{O})_6]^{2+}$ ion.

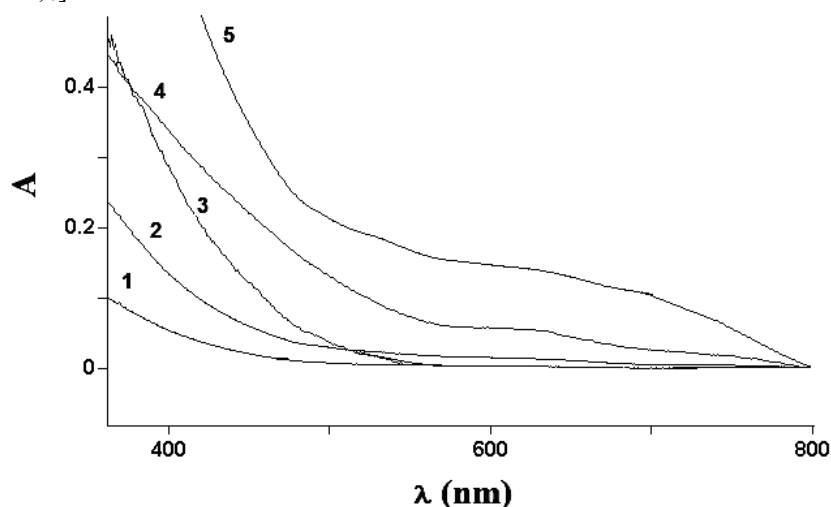


Figure 1. Vis spectra of Co(II)–RLMD complexes were synthesized at pH 7.5(1), pH 11.0 (2), pH 12.0 (3), pH 13.0 (4) and pH 13.5 (5)

In octahedral surroundings of the ligands Co(II) ion builds complex compounds with the coordination number six which can have one from two possible d^7 configurations: high-spin $t_{2g}^5 e_g^2$ with weak-field ligands, or low-spin $t_{2g}^6 e_g^1$ with strong-field ligands. High-spin Co(II) complexes with weak-field ligands; weak Jahn-Teller effect is expected according to the Jahn-Teller theorem [5], complexes are octahedral with tetragonal distortion. Wide absorption bands in the Vis spectra of synthesized Co(II)–RLMD complexes, are the result of preponderance of allowed transitions close by the energy, which manifests like the unique asymmetric absorption band. In the area of wavelength around 500 nm, absorption spectra of the high-spin Co(II) ion complexes in weak-field ligands, with configuration $t_{2g}^5 e_g^2$ and coordination number six were registered. Absorbance maxima, because of the synergistic effect, shift to the red region of Vis spectrum (bathochromic effect). Strengthening of the metal-ligand bond (Co–O) diminishes the splitting energy of d-levels, absorbance maxima shift to larger wavelengths (curve 1–5, Fig. 1). Increase and appearances of the preponderance of absorbance maxima (510, 581 and 628 nm) at pH higher than 13.5 have been connected with the decomposition of Co(II)–RLMD complex next to $[\text{Co}(\text{OH})_6]^{4-}$ ion. Thus, these

spectrophotometric criteria can be applied for the confirmation of the success of complex synthesis.

From the Vis spectra of Co(II)–RLMD complexes, which are synthesized under different reaction conditions, it was possible to see that the wavenumbers interval of the absorbance maxima is found to be from 16,026 to 17,153 cm^{-1} . The ligand crystal field splitting energies (Δ) are from 2.07 to 2.22 eV. According to literature data these energy values, have been found in the area of the energy which is characteristic of the octahedral ligand field (Δ_o) [6]. Co(II) complexes of organic molecules, such as carbohydrates, are known to adopt alternative coordination arrangements, particularly tetragonal and these exhibit distinct spectral properties in the Vis range resulting from Jahn-Teller distortion [5]. This points to the possibility that in the structure of the synthesized Co(II)–RLMD complexes, analogical with copper(II)-dextran complexes [3], Co(II) ions are probably in the octahedral or tetragonally distorted O_h surroundings (square-bipyramidal) with O atoms, which can originate from a ligand or solvent.

Conclusion

$[\text{Co}(\text{H}_2\text{O})_6]^{2+}$ ion absorbs at wavelength 512 nm, while synthesized Co(II)–RLMD complexes absorb within the range 583–624 nm. With increase in solution pH, the absorbance maxima shift to longer wavelengths compared with the $[\text{Co}(\text{H}_2\text{O})_6]^{2+}$ ion. The complex which is decomposed at pH over 13.5 shows the preponderance of absorbance maxima (510, 581 and 628 nm). The spectrophotometric parameters of the investigated complexes are characteristic of a Co(II) ion in the octahedral or tetragonally distorted octahedral coordination with O ligand atoms.

Acknowledgment

This work was realized within OI 172044 project, funded by the Ministry of Education and Science of the Republic of Serbia.

References

- [1] Ž. Mitić, G. Nikolić, M. Cakić, R. Nikolić, Lj. Ilić, Russ. J. Phys. Chem., 2007, 81, 1433–1437.
- [2] M. Cakić, Ž. Mitić, G. S. Nikolić, Lj. Ilić, G. M. Nikolić, Spectrosc. Int. J., 2008, 22, 177–185.
- [3] Ž. Mitić, M. Cakić, G. M. Nikolić, R. Nikolić, G. S. Nikolić, R. Pavlović, E. Santaniello, Carbohydr. Res., 2011, 346, 434–441.
- [4] Ž. Mitić, M. Cakić, G. Nikolić, Spectrosc. Int. J., 2010, 24, 269–275.
- [5] H. Jahn, E. Teller, Proc. R. Soc. London, Ser. A, 1937, 161, 220–225.
- [6] A. B. Lever, Inorganic Electronic Spectroscopy, 3rd Ed., Elsevier, 1986.

M-06-P

ANALYSIS OF COPPER-SALICYLIC ACID COMPLEXES BY ESI-MS

I.Kostić^{1*}, T. Anđelković¹, D. Milojković¹, T. Cvetković², D. Pavlović², D. Anđelković¹

¹*Faculty of Sciences and Mathematics, University of Niš, Višegradska 33, 18000 Niš, Serbia*

²*Faculty of Medicine, University of Niš, Bulevar dr Zorana Đinđića 81, 18000 Niš, Serbia*

Abstract

Interaction of copper(II) with salicylic acid was investigated by electrospray-ionization mass spectrometry (ESI-MS). Quantification was performed by calculating the area of ESI-MS total ion current chromatograms of loop injection obtained by analyzing series of salicylic acid solutions and series of mixed copper-salicylic acid solutions. Compared series of studied systems of salicylic acid and copper(II), showed that with the increase of copper(II) concentration, peak area of salicylate ion in loop chromatogram decreases.

Introduction

Metal complexes play fundamental role in synthetic, biological, and catalytic processes in water and soil, even when they are present at very low concentrations. Determining the coordination structure of complexes at trace levels or in complex mixtures is a very difficult task.

Understanding environmental behavior of some heavy metals, such as Cu(II) in systems containing natural organic matter (NOM) requires knowledge of metal-NOM complexes. Salicylic acid is a commonly used model for NOM and has an aromatic nucleus and phenolic and carboxylic functional groups like humic acid.[1]

All investigated solutions were made in pre-washed polyethylene eppendorf tubes by dilution of concentrated stock solutions with the solvent methanol/water (50/50 v/v). All the obtained solutions were stored at +4°C and in dark place. The presence of 50% deionized water in the solvent is intended to facilitate protonation ESI processes and provide better ion yields.

Solutions of salicylic acid were analyzed by ESI-MS immediately after preparation. Mixed solutions of salicylic acid and copper(II) ion were analyzed after 30 minutes. ICIS[®] modul of *Xcalibur*[™] 1.3 software is used for calculating the areas of each ESI-MS total ion current chromatogram of 20 µL loop injection for the defined mass range of pure solutions of salicylic acid and mixed solutions of salicylic acid and copper(II). The areas are presented in absolute nondimensional units of *Xcalibur*[™] software (*count-second units*) that have no physical meaning. [2, 3]

Results and Discussion

Semiquantification was performed by calculating the area of ESI-MS total ion current chromatograms of loop injection obtained by analyzing series of ligand solution and series of solutions of salicylic acid with copper(II) (Table 1 and Fig. 1).

Table 1. Values of peak area of salicylic acid without and with presence of copper(II) ion.

Concentration of salicylic acid (μM)	Peak area in mass range of salicylate ion (abs. units $\times 10^6$)					
	Cu (μM)	Cu (μM)	Cu (μM)	Cu (μM)	Cu (μM)	Cu (μM)
	0	1	3	5	7	9
3	4.12	3.67	2.86	2.17	1.80	1.53
5	8.51	5.39	4.86	4.41	3.28	3.03
7	9.53	7.57	6.47	6.13	4.83	4.48
9	12.2	9.61	7.64	6.55	5.33	4.88

The quantification is based on the fact that all areas of chromatograms are in direct function of the peak intensities. In systems where there is interaction between salicylic acid and copper (II), the intensity of the observed characteristic ion is reduced. [4]

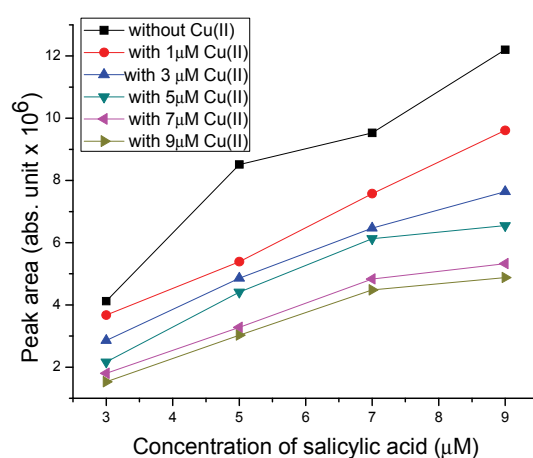


Figure 1. Concentration of salicylic acid *versus* peak area, for different concentrations of Cu(II).

This decrease is caused by coordination bonding or other interactions between copper(II) and salicylic acid and due to change the molecular and ionic composition of the sample. This leads to reduction of number of ions generated in the unit of time. In systems of salicylic acid with copper(II), for identical salicylic acid concentration, proportionally smaller area of chromatographic peak is

obtained, and the relative decrease in area can be related to the strength of the interaction of copper.

Conclusion

ESI-MS technique can be used for semiquantitative analysis of the system Cu(II)-salicylic acid. ESI-MS total ion current chromatograms of 20 μ L loop injections of systems Cu(II)-salicylic acid, indicate a stable peak and signal integrity. Comparing a series of studied systems of copper(II) with salicylic acid, the values of peak area shown that with increase concentration of copper(II) peak area of salicylate ion in loop chromatogram decreases.

Acknowledgements

This study was supported by the Ministry of Science and Technological Development of the Republic Serbia and was performed as a part of Project III 41018.

References

- [1] I. Kostić, T. Anđelković, R. Nikolić, A. Bojić, M. Purenović, S. Blagojević, D. Anđelković, *J. Serb. Chem. Soc.*, 2011, 76, 1325–1336.
- [2] D. Anđelković, PhD Thesis, Faculty of Sciences and Mathematics, University of Niš, Niš, 2012.
- [3] Y. Bai, F. R. Song, M. L. Chen, J. P. Xing, Z. Q. Liu, S. Y. Liu, *Anal. Sci.*, 2004, 20, 1147-1151.
- [4] Z. L. Cheng, K. W. M. Siu, R. Guevremont, S. S. Berman, *J. Am. Soc. Mass Spectrom.*, 1992, 3, 281-288.

ESI-MS AND UV/VIS CHARACTERIZATION OF CHROMIUM(III)-2,2'-BIPYRIDINE INTERACTION

D. Milojkovic^{1*}, T. Andjelkovic¹, R. Nikolic¹, I. Kostic¹,
T. Cvetkovic², D. Pavlović², D. Andjelkovic¹

¹*Faculty of Sciences and Mathematics, University of Niš, Višegradska 33, Niš, Serbia*

²*Faculty of Medicine, University of Niš, Bulevar dr Zorana Đinđića 81, Niš, Serbia*

**Corresponding author: e-mail: dannica.milojkovic@gmail.com*

Abstract

Interaction of chromium(III) and 2,2'-bipyridine was determined by electrospray ionization mass spectrometry (ESI) and UV/VIS spectrophotometry. Obtained data show significant coordination interaction of chromium(III) and 2,2'-bipyridine, which is in accordance with ligand structure complexity. A new approach in semiquantitative determination of ligand in free form is applied, by obtaining Loop-chromatogram of Full Scan mode. ESI-MS characterization provides acquisition of mass spectra directly from solution, analyzing species in their native environment.

Introduction

2,2'-bipyridine (bipy) is characterized as a bidentate chelating ligand, which forms complexes with many transition metals, *i.e.* chromium. Bipy is widely used and has industrial applications and in agriculture as a pesticide in terms.

Complexes of Cr(III) with coordination number 6 and octahedral structure, are the most common and the most stable coordination compounds of chromium, thus their synthesis, crystal structure, stability, electronic spectra and photochemical and other characteristics are extensively studied.

Generally, the coordination properties and reaction pathways of chromium ion and bipy are complex, due to different electrochemical equilibrium states as Cr(II)/Cr(III), the coordination saturation of chromium with anions and molecules of matrix, redox conditions, *etc* [1].

ESI-MS has found application in coordination chemistry, therefore the study of the equilibrium interactions of metals and ligands in solutions. For a complete understanding of species equilibria in solution, it is necessary to know the number, the stereochemistry and stability constants of complex species that occur in a given system, that is usually obtained from spectrophotometry (UV/VIS) measurements.

All reagents used were *pro analysis* or HPLC grade purity. ESI-MS investigation was performed on LCQ Deca Ion Trap Mass Spectrometer (Thermo Finnigan, USA) with auxiliary equipment. UV/VIS characterisation was performed on SHIMADZU UV-1650PC with double beam.

Results and Discussion

Results of UV/VIS spectrophotometric determination of interaction of Cr(III) with bipy are shown in Fig. 1.

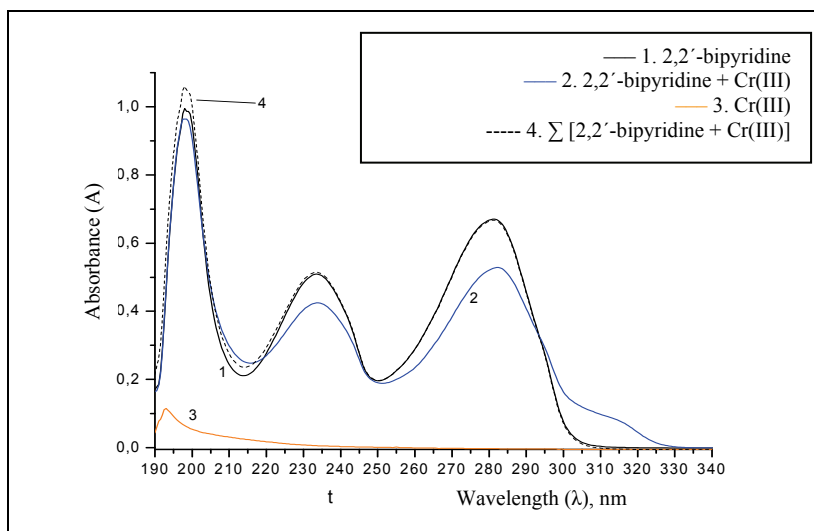


Figure 1. UV/VIS spectra of: (1) bipy, $c = 11.43 \mu\text{mol/L}$, (2) bipy, $c = 11.43 \mu\text{mol/L}$ + Cr(III), $c = 15.00 \mu\text{mol/L}$, (3) Cr(III), $c = 15.00 \mu\text{mol/L}$ and (4) the mathematical representation of the sum of independent spectra of bipy and Cr(III), solvent $\text{CH}_3\text{OH}/\text{H}_2\text{O} = 50/50$.

For the obtained spectral curves corresponding sub-integral area were calculated showing that the interaction exist in the system.

Molecular structure of nucleophilic bipy in the condition of ESI source allows the formation of protonated molecular ion, $[\text{M}+\text{H}]^+$ m/z 157, so the positive polarity mode was chosen (Fig. 2). The main ion m/z 157 (rel. int. 100%) is basic ion, and other ionic species have small signal intensity (rel. int. <13%). Isotopic pattern corresponds roughly to the theoretically calculated. Optimization of operating conditions of the instrument – ESI sources and ion optics – was carried out according to ion m/z 157 of bipy [2]. Quantitative analysis of monocomponent system of bipy was performed by injecting precise volumes of solutions (20 μL) using a Loop device. ESI-MS Loop-chromatograms showed good form and integrity of the signal (Fig. 2), in the total ion current (TIC) for the observed range of m/z 156-158 [3].

Surface of the ESI-MS Loop-chromatograms peaks in the mass range m/z 156-158 for different concentrations of bipy was calculated using the algorithm ICIS (EXCALIBUR[®] program). Analogous experimental procedure and calculation of the surface of ESI-MS Loop-chromatograms peaks for different concentrations of solution of bipy and Cr(III) was done [4]. Difference of areas under peak chromatograms is a result of coordination interaction of bipy and Cr(III). Area obtained from the chromatogram of bipy in the presence of Cr(III) is

67.44% lower than the analogous chromatogram of bipy in the absence of Cr(III), which shows considerable coordination interaction of bipy and Cr(III).

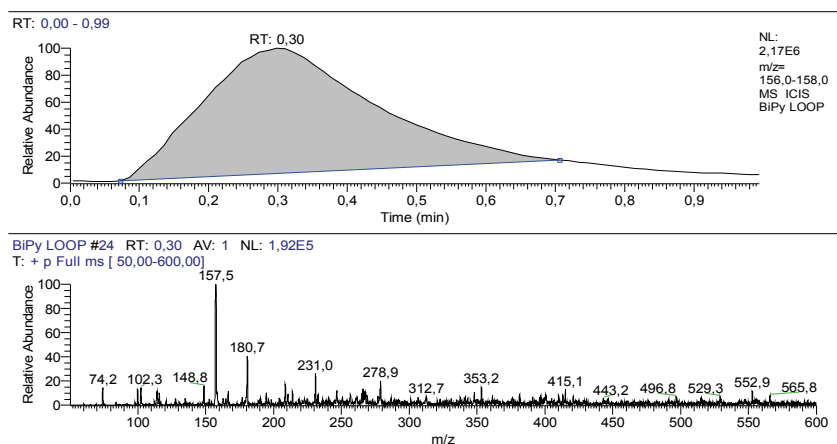


Figure 2. ESI-MS Loop-chromatogram of bipy; $c = 1.057 \mu\text{mol/L}$, solvent $\text{CH}_3\text{OH}/\text{H}_2\text{O} = 50/50$, positive ionisation mode, flow rate = $100 \mu\text{L}/\text{min}$.

Conclusion

Loop-chromatogram technique can be used as a fast technique for obtaining data of type and extent of interaction between chromium(III) and bipy. Analysis of species in their native environment by soft ionization technique - ESI, provides conditions that allow acquisition of mass spectra directly from solution.

Acknowledgements

This work was supported by the Ministry of Science and Technological Development of the Republic Serbia and was performed as a part of Project III 41018.

References:

- [1] J. Wang, K. Ashley, E. R. Kennedy et al., *Analyst*, 1997, 122, 1307-1312.
- [2] F. Sahureka, R. C. Burns, E. I. Von Nagy Felsobuki, *Inorg. Chim. Acta*, 2002, 332, 7-17.
- [3] A. R. S. Ross, M. G. Ikonomou, J. A. J. Thompson., K. J. Orians, *Anal. Chem.*, 1998, 70, 2225-2235.
- [4] D. Andjelković, PhD Thesis, Faculty of Sciences and Mathematics, University of Niš, Niš, 2012.

M-08-P

SPECTROPHOTOMETRIC DETERMINATION OF BORON IN COMPLEX WITH CURCUMIN – EFFECT OF Ca(OH)_2

O. A. Kovačević, S. Zlatanović,
B. T. Kovačević, S. Stanojlović

University of Belgrade, Institute of General and Physical Chemistry, Studentski trg 12/, P.O. Box 551, 11000 Belgrade, Serbia

Abstract

Analytical procedure that includes drying step in the preparation of the sample, after or within some acid treatment, boron has a pronounced tendency to adhere to vessel walls. The consequence is a great decrease of boron concentration in analyzed solution. Accordingly, the absorbance of the boron-curcumin complex formed in the corresponding solution is reduced. The addition of Ca(OH)_2 in the preparation process before the drying step, in an amount less than 0.05 g/mL of test boron solution ($C_B=0.46$ mg/L), allows retention of boron in the solution and/or its recovery to the aqueous solution. In this case, spectrophotometric determination provides real value of the boron content.

Introduction

Two boron-curcumin complexes, rubocurcumin and rosocyanin, were used for spectrophotometric determination of boron in the range from 0.1 to 1 mg/L [1-2]. In our experience, during drying step in the preparation of the sample, after or within some acid treatment, boron has a pronounced tendency to adhere to vessel walls. Then, the recovery of boron in solution is uncertain. In several analytical methods, a similar effect causes interference, known as the “memory effect” [2]. We found that the addition of Ca(OH)_2 in the systems allows the retention of boron in the solution and/or its recovery to the aqueous solution. Surface charge at solid/aqueous interface is pH dependent. At low pH they tend to be positively charged and negatively charged at high pH. Depending on the sign and magnitude of the surface charge an uptake of ionic species from solution occurs. At surface charge equals to zero, which is pH dependent, adsorbed ionic species was released [3]. According to the Pourbaix diagrams [4] boron species in aqueous solution are anionic, mainly B(OH)_4^- , $\text{B}_2\text{O(OH)}_5^-$ and $\text{B}_3\text{O}_3(\text{OH})_4^-$. By addition of Ca(OH)_2 isoelectric point was reached and boron ions was released into solution. The aim of this work was to establish how the addition of Ca(OH)_2 in a boron solution contributes to the determination of boron through boron-curcumin complex.

Experimental

Samples were prepared in accordance with preparation procedure T1 or T2. Procedure T-1: Solution consisting of 2.00 mL of boron solution R_C ($C_B=0.46$

mg/L) and 8.0 mL of curcumin solution (0.04 % curcumin , 3.57 % oxalic acid, and 4 % hydrochloric acid in isopropanol) in PTFE vessel was dried in a water bath at 56 °C. Before the spectrophotometric determination of boron it is necessary to remove turbidity in isopropanol solution. Procedure T-2: Mixture of $\text{Ca}(\text{OH})_2$, up to 0.225 g, and 2 mL of boron solution R_C ($C_B=0.46$ mg/L) was placed in PTFE vessel and dried. At the end of this process, 2.0 mL of deionized water was added, and proceed according to T-1.

The spectra were recorded on a Thermo Electron Corporation, Evolution 600, UV-Visible Spectrophotometer, with bandwidth of 2.0 nm, scan speed of 60 nm/min, data interval of 1.0 nm, using a tungsten lamp. Linear regression analysis shows: $\text{ABS}_{540 \text{ nm}} = -0.00574 + 0.68556C_B$ (mg B/L), $R = 0.99882$.

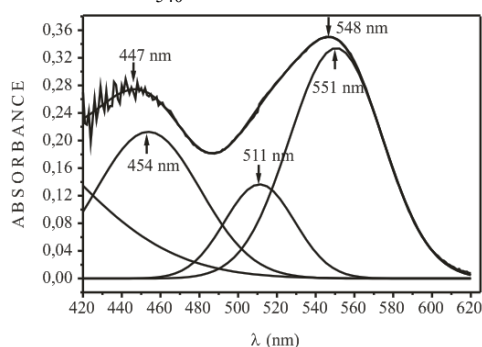


Figure 1. Absorption spectra of boron-curcumine complex; boron solution R_C ($C_B=0.46$ mg/L).

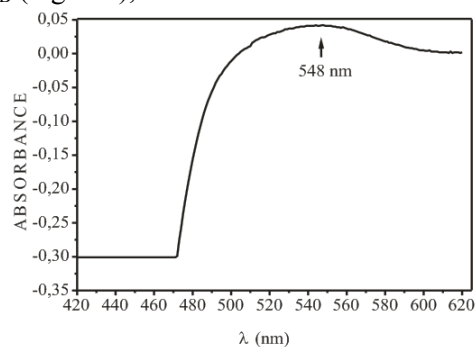


Figure 2. Absorption spectra of boron-curcumine complex; boron solution R_C ; drying treatment without $\text{Ca}(\text{OH})_2$.

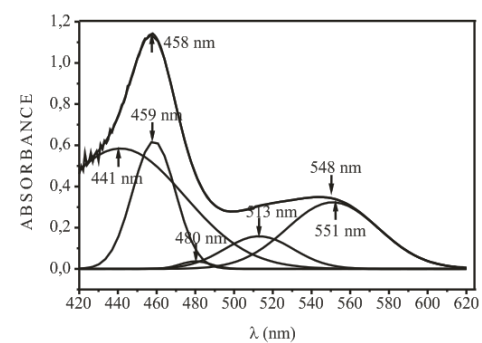


Figure 3. Absorption spectra of boron-curcumine complex; boron solution R_C with 0.0278 g $\text{Ca}(\text{OH})_2$ /mL of R_C .

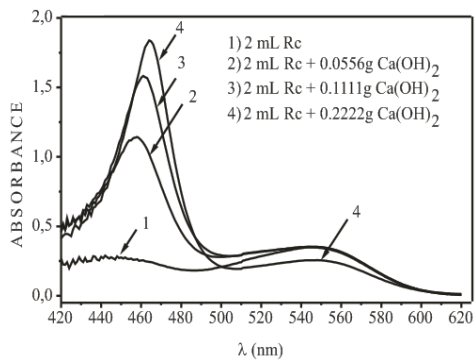


Figure 4. Absorption spectra of boron-curcumine complex; boron solution R_C with $\text{Ca}(\text{OH})_2$ up to 0.11 g/mL of R_C .

Results and Discussion

Recorded spectrum of boron-curcumin complex, and deconvoluted spectrum, corresponding to the control solution R_C , which contains 0.46 mg B/L, were given in Fig. 1. Sample was prepared according to procedure T1. Absorption in the region 500-620 nm is relevant for boron determination. Region below 500 nm usually were not considered, because it is not function of boron content. Figures 1,

M-08-P

2 and 3 give evidence that the peaks in the area below 500 nm are primarily a function of Ca content, present in the system. Fig. 2 shows the resulting spectra of the control solution R_c, prepared by procedure T2, without addition of Ca(OH)₂. The decrease in absorbance in the area from 500 nm to 620 nm, that corresponds to boron content in the system, and particularly a large decrease in absorbance in the region below 500 nm, indicate that the problem with formation of curcumin complex is not only caused by the loss of boron in solution. As it is seen on Fig. 3 and Fig. 4, the addition of Ca(OH)₂ in the system prevents the problem of this kind. On Fig. 3, the spectrum of control solution R_c, and its deconvoluted spectrum, for sample with 0.0278 g Ca(OH)₂/mL of R_c, prepared in accordance with procedure T2, gave evidence that the addition of Ca(OH)₂ does not affect the absorption spectra in the region 500-620 nm. Spectra of control solution R_c, where sample was treated in accordance with procedure T2, and where different amounts of Ca(OH)₂ were added, is shown on Fig. 4. The addition of Ca (OH)₂ in an amount exceeding 0.05 g Ca(OH)₂/mL of R_c, provokes a decrease in the absorption spectrum, and therefore the measured value of the boron content is incorrect.

Conclusions

The addition of Ca(OH)₂ in the preparation process before the drying step, in an amount less than 0.05 g per 1 ml of test boron solution, allows retention of boron in the solution and/or its recovery to the aqueous solution, as can be seen in absorption spectra of boron-curcumin complex.

Acknowledgment

This work was supported by the Ministry of Education and Science of the Republic of Serbia, under the Project No TR-31055 and TR-31093.

References

- [1] W. T. Dible, E. Truog, and K. C. Berger, *Anal. Chem.*, 1954, vol. 26, No. 2, 418-421.
- [2] R. N. Sah and P. H. Brown, *Microchem. J.*, 1997, 56, 285-304.
- [3] M. Kosmulski, *Adv. Coll.Interface Sci.*, 2012, 171-172, 77-86.
- [4] Atlas of Eh-pH diagrams, Geological Survey of Japan Open File Report No. 419, National Institute of Advanced Industrial Science and Technology, May 2005.

**GENERAL
PHYSICAL CHEMISTRY**

SALTING-OUT THIN-LAYER CHROMATOGRAPHY OF AMINO ACIDS ON SILICA GEL USING AMMONIUM SULPHATE SOLUTIONS

V. M. Živković-Radovanović¹, J. Bratić², G. N. Vučković¹,
M. D. Antonijević-Nikolić³, S. B. Tanasković⁴

¹*Faculty of Chemistry, University of Belgrade, P.O.Box 118, 11158 Belgrade;*

²*Faculty of Agriculture, University of East Sarajevo, Vuka Karadžića 30,
71123 Eastern Sarajevo, Bosnia-Herzegovina;*

³*Higher Technological School of Professional Studies, 15000 Šabac; Serbia*

⁴*Faculty of Pharmacy, Vojvode Stepe 450, 11000 Belgrade;*

Abstract

14 amino acids of different structure were separated by salting-out thin-layer chromatography (SOTLC) using ammonium sulphate solutions on silica gel. The obtained results were discussed in aspect of amino acids composition and structure. They were consistent with separation mechanisms of non-polar hydrophobic interactions.

Introduction

Some of the mixed aminocarboxylato Co(III) complexes were successfully separated with ammonium-sulphate or other salts solutions on different sorbents [1]. The proposed mechanism was based on non-specific hydrophobic interactions connected with the coordinated aminocarboxylates. The aim of this work was consideration of the effect of some free amino acids on chromatographing parameters during SOTLC on silica gel using $(\text{NH}_4)_2\text{SO}_4$ solutions.

Experimental

The studied amino acids (Table I) and other chemicals used were of analytical grade. Aqueous solutions of amino acids (50 mg/cm^3) were spotted on Polygram SIL G/UV₂₅₄ sheets for TLC. Aqueous $(\text{NH}_4)_2\text{SO}_4$ solutions of different concentration (1.9-9.2 mol %) were used for ascending chromatographic technique at $20 \pm 2^\circ\text{C}$. Detection as violet spots was achieved by spraying with 0.1 % ethanol solution of ninhydrin and heating at 110°C . Average R_F -values (from at least 3 repeated experiments) were taken for further considerations. Program Origin 61 was used for drawing and calculations.

Results and Discussion Studied amino acids (Table I) could be divided in groups due to their composition and structure: Nos.1-5 are α -amino acids with normal hydrocarbon side chain; Nos. 6-8 are structural isomers of aminoacids 3-5; Nos.1, 9,10. have elongated hydrocarbon chain between $-\text{COOH}$ and $-\text{NH}_2$ group; pairs of α -amino acids: 2 and 11, 12 and 13 and 3 and 14, respectively, instead of -H atom contain $-\text{OH}$ group in hydrocarbon part of the molecule. R_M -values ($\log[(1-R_F)/R_F]$) are given in the same Table 1.

Table 1. R_M -values of investigated amino acids.

No.	Amino acid	Ammonium sulphate mol%				m^*
		1.9	4.0	6.4	9.2	
1	glycine	-0.954	-0.954	-0.954	-0.908	0.006
2	S-alanine	-0.688	-0.659	-0.602	-0.501	0.026
3	S- α -amino- <i>n</i> -butiric acid	-0.477	-0.347	-0.176	-0.052	0.059
4	S- <i>n</i> -valine	-0.308	-0.105	0.052	0.288	0.080
5	S- <i>n</i> -leucine	-0.087	0.140	0.501	0.788	0.123
6	α -amino- <i>i</i> -butiric acid	-0.501	-0.389	-0.213	-0.087	0.058
7	S-valine	-0.347	-0.158	0	0.250	0.080
8	S-leucine	-0.158	0.105	0.432	0.753	0.126
9	β -alanine	-0.659	-0.602	-0.545	-0.477	0.025
10	γ -amino butiric acid	-0.525	-0.410	-0.269	-0.087	0.060
11	S-serine	-1.123	-1.123	-1.061	-0.954	0.024
12	S-phenyl alanine	-0.288	-0.105	0.140	0.432	0.099
13	S-tyrosine	-0.908	-0.720	-0.501	-0.288	0.085
14	S-threonine	-0.826	-0.689	-0.545	-0.432	0.054

* m is the slope of the line: $R_M = R_M^0 + m \cdot \text{mol \% of } (NH_4)_2SO_4$

It is seen that increase of salt concentration causes enhanced retention. The Linear dependence rule [2] was found and the obtained salting-out efficiencies (m -values in Table I) were dependent of hydrocarbon size of the molecule. There is reversed-phase order of the investigated compounds 1-5; 6-8; 1,9,10. However, amino acids with the normal side hydrocarbon chains have slightly stronger retention than their corresponding isomers with branched chain. Differences in chromatographic parameters of amino acids 2 and 3 compared with isomeric one, 9 and 10 are also small. It could be concluded that the size of hydrocarbon part of the molecule is the most important factor of the retention. Significant decrease in retention occurred when one of H-atom is replaced with polar -OH group, which is seen from the Figure 1. All results are consistent with the mechanisms of non-specific hydrophobic interactions.

The size of hydrophobic hydrocarbon part in the studied amino acid molecule was the most important factor affecting their retention and separation during SOTLC on silica gel, whereas the effect of its structure was smaller.

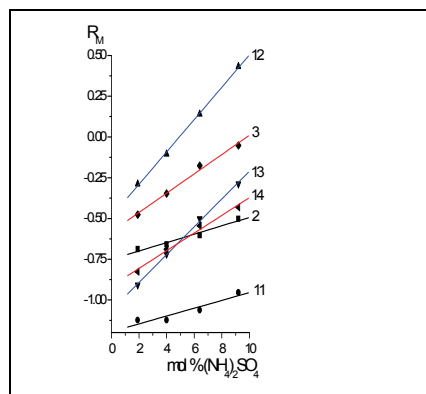


Figure 1. Dependence of R_M -values on mol % of $(NH_4)_2SO_4$. Numbers near lines denote amino acid No. in Table I. Conclusion.

Introduction of the polar –OH group in the hydrocarbon part causes decrease of the retention. All results were consistent with separation mechanisms of non-specific hydrophobic interactions.

References

- [1] a) G. Vučković, D. Miljević, T. J. Janjić, M. B. Čelap, *J.Chromatogr.*, 1992, 609, 427-431; b) T. J. Janjić, V. Živković, G.Vučković, M.B.Čelap, *J.Chromatogr.*, 1992, 626, 305-309; c) J.Janjić, V. Živković, G.Vučković, M.B.Čelap, *Chromatographia*, 1993, 37, 534-538; d) V.Živković-Radovanović, G.Vučković, *Chromatographia*, 2008, 67, 259-267.
- [2] J. Janjić, V. Živković, M. B.Čelap, *Chromatographia*, 1993, 38, 355-358.

N-02-P

Cu(II) EFFECT ON FLOATABILITY AND ZETA POTENTIAL OF SPHALERITE

D. R. Vučinić, S. Đ. Deušić, A. Đ. Tomašević,
Faculty of Mining and Geology, University of Belgrade, Belgrade, Serbia

Abstract

Sphalerite ((Zn, Fe)S; 13% Fe) has very good natural floatability (hydrophobicity) in a acidic medium (86%) and very poor in an alkaline medium (21%). The negative zeta potential in alkaline medium confirms the chemisorption of hydroxyl ions in the electrical double layer of the mineral. The positive zeta potential is at pH below 6.5 due to the surface oxidation and the formation of hydrophobic zinc, iron-deficient sites (Zn_{1-x}, Fe_{1-y})S and H⁺ adsorption. Cu(II) from the solution induces the rise of the flotation recovery up to 95% only in acidic medium. The ion exchange $Zn^{2+} \rightleftharpoons Cu^{2+}$, the Cu²⁺ adsorption on the metal-deficient surface sites and $Cu^{2+} + e \rightarrow Cu^+_{surf}$, $\frac{1}{2} S^{2-}_{surf} \rightarrow \frac{1}{2} S^0 + e$ surface reactions contribute to the negative sphalerite zeta potential, similar to the zeta potential of chalcocite, Cu₂S and elemental sulfur which increases the mineral surface hydrophobicity.

Introduction

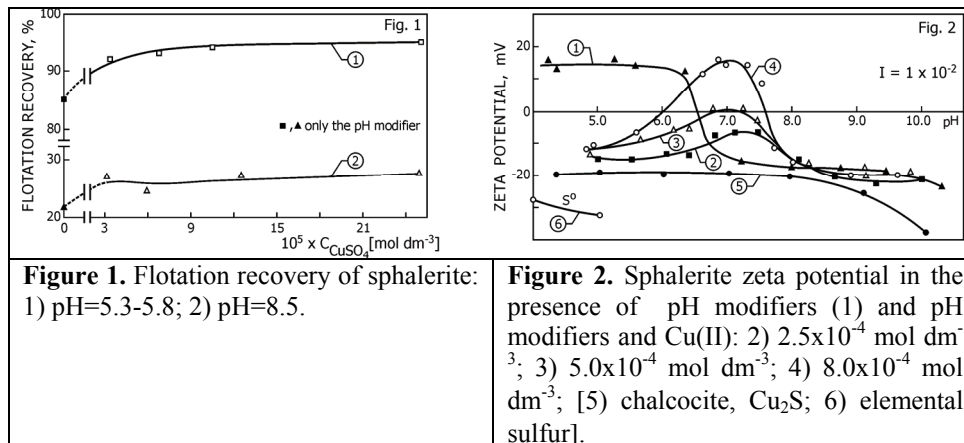
The surface oxidation of sulphide minerals causes the formation of different surface species, promoting or not the natural floatability. The hydrophobic species which made sulphide minerals floatable are metal-deficient sulphide oxidation products and elemental sulfur [1]. The interaction between zinc sulphide and hydrophobic xanthate-type surfactants (RCS₂M) is weak. Successful flotation using xanthates can be accomplished only after activation by heavy-metal ions [2-3]. Adsorption of modifying reagents is controlled by the electrical double layer at the mineral-water interface, because of that zeta potential can be used to delineate the interfacial phenomena [4]. The present paper is an attempt to determine the influence of dissolved copper on the floatability and zeta potential of sphalerite.

Experimental

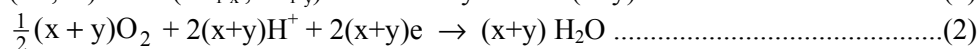
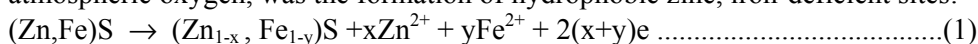
A sphalerite from the Trepča deposit (Zn 53.12 wt%, Fe 13.01%, Pb 250 ppm, Cu 85 ppm, Cd 1520 ppm, Mn 4670 ppm) was used. The pH modifiers were HCl and NaOH. CuSO₄ was added in order to introduce Cu(II) into the mineral suspensions. NaNO₃ was used to adjust ionic strength ($I=1 \times 10^{-2} \text{ mol dm}^{-3}$). All the reagents were of p.a. Flotation tests were conducted in a modified Hallimond tube (the partial size of -208+104 μm). Zeta potential measurements (SSA of sample: 2.25 m² g⁻¹) were taken on a Riddick Zeta-meter using microelectrophoresis. The mineral suspension was stirred for three minutes after each reagent addition.

Results and Discussion

In the presence of pH regulators the tested sphalerite has very good natural floatability (collectorless floatability) in a weakly acidic medium at pH 5.3-5.8 (about 86%) and very poor in an alkaline medium (about 21% at pH 8.5), (Fig.1).



The zeta potential-pH curve of mineral (Fig.2, curve 1) shows a positive zeta potential in acidic media and a negative one in alkaline media, with the IEP at pH 6.5. Many investigators have noted that oxidation at the sphalerite surface is a slow process in air or in alkaline solution, which can be the explanation for a poor floatability of examined sphalerite at pH above 7. Also, the hydrolysis of the surface metal ions from the mineral lattice and adsorption of OH^- may result in the surface sites $\equiv\text{Zn-OH}$, $\equiv\text{Fe-OH}$ or other $\equiv\text{Me-OH}$ (\equiv the surface). The negative values of the sphalerite zeta potential in alkaline medium confirm the chemisorption of hydroxyl ions in the electrical double layer of the mineral. On the other hand, the positive zeta potential is at pH below 6.5 due to the prevalence of positive charged species in the Stern layer of the electrical double layer of sphalerite. As the sphalerite used in this study contained about 13% Fe(II) in the crystal lattice we presumed that the first stage of surface oxidation for our sample $(\text{Zn,Fe})\text{S}$ in the air-saturated acid solution, coupled with cathodic reduction of atmospheric oxygen, was the formation of hydrophobic zinc, iron-deficient sites:



promoting good collectorless floatability and domination of cations in Stern layer. The potential-determining ions are Zn^{2+} and Fe^{2+} passed in the liquid phase by anodic oxidation. Also, the adsorption of H^+ ions at sites $\equiv\text{S}^-$ well as diffusion metal cations from the bulk mineral on the metal-deficient surface sites can effect on positive zeta potential. A small value of zeta potential of about +16 mV confirms a small degree of the electrochemical oxidation, but apparently sufficient for a successful flotation of mineral. Observed weak increase in pH value of suspension for 10 min of acidic conditioning also supports the presumed mechanism. Cu(II) from the solution induces the rise of the flotation recovery up to 95% in acidic medium ((pH=5.3-5.8) (Fig.1, curve 1). However, in alkaline conditions the mineral floats weakly independent of Cu(II) concentration (Fig.1, curve 2). This effect at pH=8.5 can be explained by the formation of surface $\text{Cu}(\text{OH})_2$, which together with the hydrolyzed surface species of

zinc and iron depresses the mineral. The unchanged values of zeta potential in the presence of Cu(II) at pH above 8 favor this explanation (Fig.2, curves 1-4). On the other hand, Cu(II)-modified sphalerite has a negative zeta potential at pH below 6 (curves 2-4). Literature data indicate that the dominant reaction in acidic medium in the system sphalerite-Cu(II) is the ion exchange $Zn^{2+} \rightleftharpoons Cu^{2+}$. The thermodynamic equilibrium constant, $K=6.5 \times 10^9$, calculated as a ratio of the ZnS (2.6×10^{-26}) and CuS (4.0×10^{-36}) solubility products, indicates the high affinity of sphalerite for Cu^{2+} ions from the solution. Also, the Cu^{2+} adsorption on the metal-deficient surface sites of $(Zn_{1-x}, Fe_{1-y})S$ is possible process. Cu^{2+} present on the mineral surface can cause the following reactions: $Cu^{2+} + e \rightarrow Cu^+_{surf} \dots(3)$; $\frac{1}{2} S^{2-}_{surf} \rightarrow \frac{1}{2} S^0 + e \dots(4)$.

Because of that the zeta potential of Cu(II)-modified sphalerite in acidic medium is similar to the zeta potential of chalcocite, Cu_2S (Fig.2, curve 5) and elemental sulfur (Fig.2, curve 6), which increases the hydrophobicity of mineral surface, i.e. collectorless floatability (Fig.1, curve 2). Cu(II) from the solution induces less negative (Fig.2, curves 2-4) or positive (curve 4) zeta potential of sphalerite above pH 5. In the pH range from 6 to 8 the dominant copper species present in the solution are $Cu^{2+}, Cu(OH)^+, Cu_2(OH)_2^{2+}$ [3]. The adsorption of Cu(II)-hydroxy cations in the Stern layer of the electrical double layer of mineral is evidenced by the electrokinetic behavior of sphalerite and by the decrease of the floatability in this pH region. The centers on sphalerite surface for chemical adsorption of copper-cation species are $\equiv S^-$ and metal-deficient $(Zn_{1-x}, Fe_{1-y})S$ sites. The physical adsorption of Cu(II)-hydroxy cations by hydrogen bonds is also possible on some $\equiv M-OH$ and $\equiv SH$ centers.

Conclusion

The examined sphalerite with 13%Fe has a good natural floatability and the positive zeta potential in an acidic medium due to the surface oxidation and the formation of hydrophobic zinc, iron-deficient sites $(Zn_{1-x}, Fe_{1-y})S$ and H^+ adsorption. Cu(II) in acidic solution induces the rise of the flotation recovery up to 95% and a negative zeta potential. The ion exchange $Zn^{2+} \rightleftharpoons Cu^{2+}$, the Cu^{2+} adsorption on the metal-deficient surface sites as well as $Cu^{2+} + e \rightarrow Cu^+_{surf}$, $\frac{1}{2} S^{2-}_{surf} \rightarrow \frac{1}{2} S^0 + e$ surface reactions contribute to the mineral surface hydrophobicity. Also, the adsorbed Cu-hydroxy species on sphalerite at higher pH present the surface sites for interaction with hydrophobic xanthate-type surfactants.

Acknowledgement

The authors are indebted to the Research Fund of the Republic of Serbia for the financial support (projects no. 33007; no.176010).

References

- [1] A. N. Buckley, R. Woods, *Appl. Surf. Sci.*, 1984, 17, 401-414.
- [2] S. Jain, D.W. Fuerstenau, in K. S. E. Forssberg (Ed.), *Flotation of Sulphide Minerals*, Elsevier, Amsterdam, 1985, 159-174.
- [3] J. Ralston, T. W. Healy, *Int. J. Miner. Process.*, 1980, 7, 203-217.
- [4] D. W. Fuerstenau, Pradip, *Adv. Colloid Interface Sci.*, 2005, 114, 9-26.

ZETA POTENTIAL OF MAGNETITE/AQUEOUS SOLUTION INTERFACE AT ELEVATED TEMPERATURES

S. Vidojkovic^{a†}, V. Rodriguez-Santiago^{a, b, †}, M. V. Fedkin^a,
D. J. Wesolowski^d, S. N. Lvov^{a, b, c, *}

^aThe EMS Energy Institute; ^bDepartment of Energy and Mineral Engineering; and
^cDepartment of Materials Science and Engineering, The Pennsylvania State
University, University Park, PA 16802, U.S.A.

^dChemical Sciences Division, Oak Ridge National Laboratory, Oak Ridge, TN
37831-6110, U.S.A.

[†]Present address: Vinca Institute of Nuclear Science, P.O.Box 522, Belgrade, Serbia

Abstract

The effect of temperature on zeta potential at the magnetite/water interface was studied applying high temperature electrophoresis technique. The first reliable experimental data were obtained on the zeta potential of magnetite at the elevated temperature up to 200°C in pressurized aqueous solution. The isoelectric points of magnetite were determined at pH 6.35, 6.00, 5.25, and 5.05 for temperatures 25, 100, 150, and 200 °C, respectively which were found to be consistent with published surface titration and mass titration data. The obtained dependence of the zeta potential of magnetite on pH and temperature can be utilized for development of methods for controlling and reduction oxide deposition in high temperature water cycles.

Introduction

The deposit in industrial systems using high temperature aqueous medium is typically composed of steel oxidation products, uppermost magnetite (Fe₃O₄) [1, 2], which are normally present in the colloidal form and tend to precipitate on the inner surfaces of process lines [1, 2]. The electrokinetic behavior of colloidal particles, involving colloidal stability and potential for aggregation onto a substrate, is determined by zeta potential [3], which influences the extent of the electrostatic interaction between the colloids and other surfaces and strongly depends on pH and ionic strength. In this study, we used an originally developed high temperature microelectrophoresis cell [4] to measure the electrophoretic mobility of magnetite particles and to obtain the zeta potential at the magnetite/aqueous solution interface at temperatures up to 250 °C.

Results and Discussion

Measurements of the electrophoretic mobility of magnetite particles were conducted using the high-temperature zetameter system designed and constructed in our laboratory. The details of the experimental design have been published elsewhere [4, 5]. Electrophoretic experiments were carried out at the following sets of parameters: $t = 25$ °C and $P = 1$ bar; $t = 100$ °C and $P = 20$ bar; $t = 150$ °C and P

N-03-P

= 20 bar; and $t = 200$ °C and $P = 40$ bar, 250°C and $P = 40$ bar. The experimental data obtained from the electrophoresis tests are listed in Table 1.

Table 1. Zeta potential for magnetite at different temperatures and pH.

t (°C)	pH (± 0.05)	ZP, mV
25°C	3.90	32.6
	4.45	26.3
	7.20	-46.5
	8.60	-135.7
100°C	9.50	-140.9
	4.00	68.0
	4.50	105.2
	5.85	50.2
	6.15	-45.9
150°C	7.01	-64.8
	3.70	49.1
	4.90	43.8
	5.70	-61.2
200°C	6.00	-111.8
	7.30	-66.8
	4.00	88.7
	4.85	64.8
	5.60	-115.0
250°C	6.10	-105.1
	7.30	-76.6
	5.53	111.9
	6.31	-155.7
	6.5	-162.4
	6.83	-185.9

Figures 3(a-d) show that at temperatures 25, 100, 150, and 200 °C, the isoelectric points (pH_{IEP} at $ZP=0$) were determined at pH 6.35, 6.00, 5.25, and 5.05, respectively. For the measured temperatures, the zeta potential curves have inverted “s” shape, which is typical of many amphoteric oxides. It was noticed that for all measured temperatures except 25 °C, the zeta potential curves exhibit a very sharp decline at the pH region close to pH_{IEP} . It can be inferred that at elevated temperatures, a small shift in pH causes considerable change in the zeta potential close to the IEP. This may lead to an abrupt overturn of a colloidal system that contains magnetite particles and hence indicates the importance of thorough pH control in high temperature industrial processes. The obtained pH_{IEP} decreases with increasing temperature, which is similar to the trend observed in other surface charge and zeta potential studies at elevated temperatures [5, 6].

Performed experiments provided evidences on sign and magnitude of zeta potential in typical high temperature power plant and pressurized water reactors. Obtained results proved that magnetite surface would maintain a negative charge in neutral and slightly basic environments. It means that high electrostatic repulsion of magnetite particles will ensure its colloidal stability and less probability to deposit under condition of fossil plant water cycles. Aggregation of magnetite particles may be reduced by decrease in solution pH, which would result in more abundant porous deposits that can cause underdeposit corrosion. At the same time, it was demonstrated that probability for precipitation of magnetite in nuclear plants reactors condition will be high. Besides that, it was shown that microelectrophoresis technique can be successfully used for measurements of zeta potential of magnetite at temperatures up to 250°C. On the basis of the acquired zeta potential values it is possible to predict behavior of magnetite particles and their deposition in many other industrial processes and to develop methods for prevention deposition of iron oxides by shifting of sign of charged colloidal particles of iron oxides. Taking in consideration scarcity of zeta potential data of magnetite at high temperatures, results obtained in this study are of great significance for elucidation the nature and extent of interactions between the colloidal particles at the heat exchange surfaces of industrial plants and their further control.

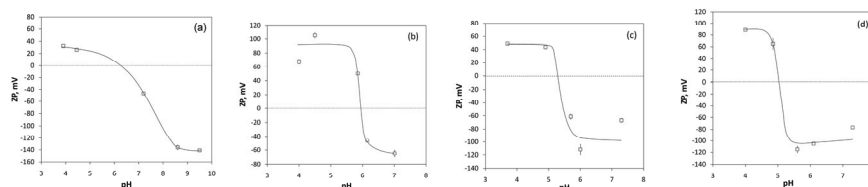


Figure 1. Zeta potential of magnetite versus pH at different temperatures: (a) 25 °C, (b) 100 °C, (c) 150 °C, and (d) 200 °C.

Acknowledgements

We thank Dr. Jorgen Rosenqvist for useful discussions during his visit at Penn State University. This research was supported in part by the National Science Foundation (EAR 07-32559), the Division of Chemical Sciences, Geosciences, and Biosciences, Office of Basic Energy Sciences, U.S. Department (DJW and SNL) through contract with Oak Ridge National Laboratory (DE-AC05-00OR22725), and by the United States Department of State through a Fulbright Grant provided to the first author of the paper (SV).

References

- [1] H. M. Shalaby, *Corrosion*, 2006, 62, 930-941.
- [2] R. L. Tapping, C. W. Turner, R. H. Thompson, *Corrosion*, 1991, 47, 489-495.
- [3] R. J. Hunter, *Foundations of Colloid Science*, Oxford University Press, 2001.
- [4] X. Y. Zhou, X. J. Wei, M. V. Fedkin, K. H. Strass, S. N. Lvov, *Rev. Sci. Instrum.*, 2003, 74, 2501-2506.
- [5] M. V. Fedkin, X. Y. Zhou, J. D. Kubicki, A. V. Bandura, S. N. Lvov, M. L. Machesky, D. J. Wesolowski, *Langmuir*, 2003, 19, 3797-3804.
- [6] D. Wesolowski, M. Machesky, D. Palmer, L. Anovitz, *Chem. Geol.*, 2000, 167, 193-229.

GEOPHYSICAL CHEMISTRY

ASTRONOMICAL RADIATION SOURCES AND ORIGIN OF ATMOSPHERIC OXYGEN OF PRE-OXYGENATED EARTH: SOLAR PHOTON RADIATION

Pavle I. Premović

*Laboratory for Geochemistry, Cosmochemistry and Astrochemistry,
University of Niš, P.O. Box 224, 18000 Niš, Serbia*

Abstract

This preliminary report explores a possibility that the solar photon radiation source is related to the origin of free O₂ derived from oceanic and/or atmospheric water on pre-oxygenated Earth (POE) which has been overlooked in the previous studies. POE was probably subject to intense solar photon radiation (ultraviolet light, X- and γ -rays), greatly increasing during short times of solar flares and superflares. I tentatively suggest that the solar photon radiation and subsequent geochemical processes may have contributed to the origin of O₂ in the atmosphere on POE.

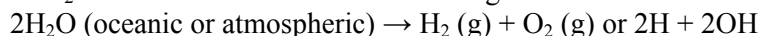
Introduction

Currently, there are two (major) scientific hypotheses about the origin of free O₂ on POE. The first hypothesis, free O₂ was generated through photosynthetic activity of anoxic microorganisms; second hypothesis, free O₂ was produced by the direct solar photodissociation of atmospheric water H₂O. This process is considered to be only capable of yielding small amounts of free O₂. Recently, Premović [1] proposed a third a hypothetical alternative, that a high shock (pressure/temperature) decomposition of H₂O vapor derived mainly from the impacting icy comet in the ocean (or on land) could have been an alternative source of free O₂ in the pre-oxygenated atmosphere. These hypotheses still remain (more or less) speculative and warrant further research.

The purpose of the present review is to explore a possibility that dissociation of oceanic H₂O and/or atmospheric H₂O vapor by the solar photon radiation can generate O₂ in the atmosphere on POE.

Solar ionizing radiation. The Sun has been probably the single greatest source of astronomical radiation to POE on a continuing basis. The ancient Earth was probably subject to intense solar ionizing radiation greatly increasing during short times of solar winds, flares and superflares. There are two types of solar ionizing radiation. The first one is electromagnetic radiation mainly composed of the energetic UV, X- and γ -ray photons; the other main type, so-called solar cosmic rays (SCR), consists predominantly of high energy protons and electrons (95 %). X- and γ -rays and cosmic rays may also originate from non-solar sources often as galactic cosmic radiation coming from outside the solar system.

Overall effect of the above two types of solar ionizing radiation on oceanic or atmospheric H₂O on POE is shown in the following direct dissociation reaction



where g stays for gas phase. This dissociation is followed by escape of H and **H₂** in space. In general, the loss of hydrogen to space should be approximately equal

O-01-P

the total O₂ content in the pre-oxygenated atmosphere. Probably, similar reaction can be written for the atmospheric CO₂ [$2\text{CO}_2 \rightarrow 2\text{CO (g)} + \text{O}_2 \text{ (g)}$]. In this report my attention will be focused only on the decomposition of oceanic and atmospheric H₂O on POE by solar photon radiation.

The amount of H₂O decomposed by the above reaction depends strongly on the timescale of radiation emission and the fraction of the incident radiation that can reach a given level of atmosphere. Under the conditions of the current atmosphere, the photolysis rate of atmospheric H₂O vapor corresponds to about $5 \times 10^5 \text{ g s}^{-1}$. *Some rough calculations.* Before any further discussion, let us do some informative rough calculations. The present atmosphere has mass of $1.2 \times 10^{21} \text{ g}$. A simple calculation shows that $2.5 \times 10^{14} \text{ g}$ of H₂O is necessary to convert by any solar ionizing radiation (or any of their combination) to generate the pre-oxygenated atmosphere with $5 \times 10^{-8} \text{ atm}$ of O₂. Assuming that the mass in the global ocean on POE was about the same as today ($1.4 \times 10^{24} \text{ g}$), it requires to decompose about 3×10^{18} H₂O molecules per cm⁻² of the global ocean.

Solar photon radiation. As stated above, I will consider only dissociation of oceanic H₂O by solar photon radiation, leaving consideration of solar winds, SCR and galactic cosmic radiation for future work. The direct photodissociation of H₂O molecules requires solar photons of wavelengths less than about 200 nm. These are photons of the following radiations: the vacuum ultraviolet light (VUV), X-rays and γ -rays. The present-day (upper) atmosphere absorbs almost all photons of solar VUV, X-rays and γ -rays. The quantity of solar VUV-X radiation received at Earth's surface or at any atmospheric level depends on two main variables: the emission of radiation by the Sun and its extinction through absorption and scattering by the constituents of atmosphere (mainly O₃, N₂ and O₂).

Model atmosphere 1. Models of the pre-oxygenated atmosphere are diverse, and often contradictory, as the evidence on which they are based. In the study of atmospheric composition it is often convenient to use simplified photochemical atmospheric models. Such models have proved very useful in studies of certain aspects of the atmospheric chemistry. I assume for simplicity with a model of the pre-oxygenated atmosphere which is thick enough to prevent complete evaporation of global ocean and with enough ambient heating to prevent complete freezing of this ocean. I will begin with the simplest possible model of this atmosphere which is saturated with H₂O vapor at about 25 °C. I assume that an atmospheric column density is about 30 g cm^{-2} for H₂O vapor or about 10^{24} molecules cm⁻². Of note, the column densities of H₂O vapor in the existing atmosphere are about 2.5 g cm^{-2} . I will name this atmosphere model as MA1 (a short notation for model atmosphere 1). In fact, MA1 is the excellent starting point for my future investigation since it is so thin that the all incident ionizing radiation reach the ocean surface. My model represents a simplification of the real pre-oxygenated atmosphere and, of course, the validity of my conclusions will therefore depend upon the assumptions I made.

VUV-X and γ -ray photons. Astronomical consideration indicates that the overall luminosity of the Sun during the pre-oxygenated period was approximately 70-75 % of the present day luminosity. In contrast, the VUV, X- and γ -ray luminosity

during this time was likely much higher than today. Therefore, much higher fluxes of solar photons of VUV-X radiation and γ -rays were reached POE than at present. However, the present-day solar photon flux of γ -rays compared to that of VUV-X radiation is lesser by at least for five orders of magnitude and thus they were probably far less important in the direct solar photodissociation of pre-oxygenated oceanic and atmospheric H_2O . For this reason, I here limit my discussion to dissociation of oceanic and atmospheric H_2O by solar VUV-X photons.

A mean total photon flux of solar VUV-X reaching this surface is probably about 1.5×10^{11} photons $\text{cm}^{-2} \text{s}^{-1}$ with a mean total energy flux of roughly about 7 ergs $\text{cm}^{-2} \text{s}^{-1}$ (or 4.5 TeV $\text{cm}^{-2} \text{s}^{-1}$). A given photochemical process is generally characterized by the quantum efficiency (QE) which is determined as a ratio between the number of reacted molecules or the molecules of the reaction product and the number of the absorbed photons. The QE (H_2O) for liquid H_2O dissociation under the VUV-X radiation is higher than 1. This gives a minimum photodissociation rate of ca. 1.5×10^7 g s^{-1} of H_2O in the global ocean.

If we make the reasonable assumption that a mean total H_2O photodissociation rate for MA1 is about 2×10^{11} molecules $\text{cm}^{-2} \text{s}^{-1}$, as estimated for the pre-oxygenated atmosphere, then this process would decompose 3×10^7 g s^{-1} of H_2O in MA1.

A major O_2 sink on POE was volcanic gases (primarily H_2). These gases currently consumed ca. 5×10^5 g s^{-1} and suggested that during photosynthetic Earth this consumption was somewhat higher. The photolysis of oceanic and atmospheric H_2O probably generate roughly this amount of O_2 in MA1. If this is correct than QE (O_2) for this photolysis is about 1.7×10^{-2} and it is probably an upper limit.

Solar flares and superflares. Solar flares have energy of 10^{32} erg which is about 10^3 times more than that of the quiet Sun but they only last for about 10^3 s. In the POE's time the Sun would have had on average 5 such flares per day. These flares would photochemically generated at least 3×10^7 g s^{-1} of O_2 (averaged over a year) in MA1. Recently, it is discovered stellar flares with 10^2 to 10^7 times more energy than the largest solar flare. These superflares have durations of hours to days. Let us assume that the superflare did occur with 10^{36} erg once during the pre-oxygenated era and lasted for about a week. This gives 6×10^7 g s^{-1} of O_2 (averaged over a year). However, the superflares appear to take place every few million years so their generation rate of O_2 in MA1 could be much higher. Thus, volcanic gases of pre-oxygenated atmosphere could possibly be overwhelmed (at least for a short time) by the photochemically generated O_2 .

Conclusion

I tentatively conjecture that dissociation of oceanic and/or atmospheric H_2O by solar photon radiation could generate the important levels O_2 (at least for a short time) on POE.

References

- [1] P. I. Premović, Int. J. Impact. Eng., 2003, 29, 575-587.

O-02-P

CRETACEOUS-PALEOGENE BOUNDARY CLAY AT CARAVACA (SPAIN): ARSENIC ANOMALY

Pavle I. Premović

*Laboratory for Geochemistry, Cosmochemistry and Astrochemistry,
University of Niš, P.O. Box 224, 18000 Niš, Serbia*

Abstract

A high As content has been reported in Cretaceous-Paleogene boundary (KPB) clay at Caravaca. One of the interpretations suggests this chalcophile element comes from combustion of fossil fuels such as crude oil, coal or oil shales near the Chicxulub impact KPB site. Combustion was triggered by the KPB asteroid impactor. This report shows that the calculated global As surface density 27 millions times less than the experimental As surface density at Caravaca, contradicting the fossil fuels hypothesis. This calculation is based on proven crude oil reserves (ca. 10^{16} g) of the giant supercharged Pimienta-Tamabra petroleum system close to the Chicxulub impact site.

Introduction

Apart from well-known anomalous Ir, the prominent KPB clays worldwide show the high concentrations of (so-called) non-chondritic trace elements such as chalcophiles As, Sb, Cu, Zn, Mo, Ga, Hg, Re, and Se. According to Hildebrand and Boynton [1], these elements represent a primary geochemical signal of the KPB impact at Chicxulub (Mexico). The source of the chalcophile element anomalies at KPB is still problematic.

Gilmour and Anders [2, 3] examined the distribution of chalcophiles in bulk boundary clays at eight prominent marine sites at Caravaca, Gubbio (Italy), Højerup (Denmark), Woodside Creek, Flaxbourne River (New Zealand), Zumaya (Portugal) and Deep Sea Drilling Project 465A (Central Pacific). These researchers concluded that, in contrast to Ir which is mainly meteoritic, As (like other chalcophiles) is non-meteoritic and non-oceanic in origin. I readily anticipate their conclusion throughout this report. Previously, Gilmour and Anders [2, 3] also proposed that combustion (ignited by the Chicxulub impactor) of fossil fuels (such as crude oil, coal or oil shales) was a possible source of relatively highly volatile As (as well other chalcophiles) in these prominent boundary clays worldwide. This brief report re-examines each of these possibilities mathematically for the case anomalous As in the boundary clays at Caravaca. For this purpose, comprehensive geochemical data for anomalous As in the boundary clay at Caravaca will be used which are published by Schmitz [4].

Results and Discussion

The boundary section Caravaca is among the most continuous and complete marine sections for the KPB transition. The Caravaca section is located in the Betis Cordilleras (southeast Spain). The KPB section at Caravaca consists of a ca. 1

cm-thick Ir-rich dark marl (BC) overlain by a grey-to-brown marl, Fig. 1. A basal 2-3 mm thick red sublayer (RSC) of BC enriched with Ir is marking the KP. B.

Schmitz [4] carried out the analyses of the decarbonated boundary samples from Caravaca using instrumental neutron activation analysis (INAA). Relative error in the precision of the analyses ranges from 5 % to 10 %. Total uncertainties (including accuracy errors) were up to 20 %. Throughout this paper we make a reasonable postulates that As are wholly located in the non-carbonate fraction of the boundary clays studied, i. e. the carbonate fraction of this section is essentially their diluents.

Distribution of As

The abundance distribution of As across the decarbonated BC is given in Fig. 1. This element shows a prominent peak at the RSC (ca. 900 ppm). The duration of the peak in As at Caravaca is similar to that of the Ir anomaly, which is geologically instantaneous. In addition, simultaneous presence of anomalous Ir and As in RSC is rather surprising in view of their separate origins: Ir from the carbonaceous chondrite bolide and As from terrestrial source(s).

According to Fig. 1 the As contents in the decarbonated RSC shows 180-fold increases in its concentration compared with the decarbonated latest Maastrichtian layer. This manifold increase of As strongly argues against a possibility that pulse of calcite dissolution in the shallow water of Caravaca played a major role in the formation of the RSC and its enrichment with As.

As in ejecta fallout may be derived from and the chondrite CI impactor and/or target rocks at Chicxulub. The target rocks probably were mainly derived from the Earth's total (continental + oceanic) crust. Table 1 shows the average concentrations of As in this terrestrial material and CI chondrites. Obviously, none of these sources is adequate for anomalous As in the decarbonated RSC. It is also not possible to explain the As enrichment of the decarbonated RSC by any sedimentary enrichment process (e. g. diagenetic condensation, secondary remobilization and/or redistribution etc.) of As derived from these sources without some dubious argumentation.

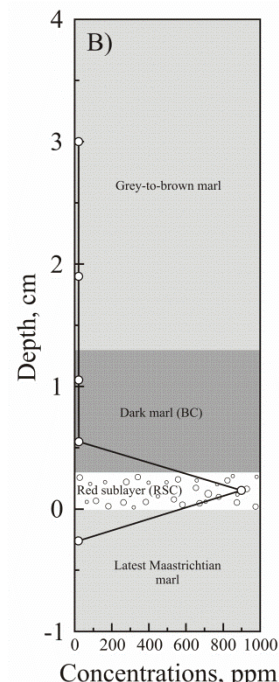


Figure 1. The As profile across BC

Table 1. Average As contents (ppm) of geological materials and CI chondrites

Material	Decarbonated RSC ^a	Continental crust ^b	CI chondrites ^b
Chalcophile			
As	900	1.80	1.90

^a[4]; ^b[5].

As and the mass of crude oil burned

In this note, I will consider a possibility that As in the RSC from combustion of crude oil near the Chicxulub impact site.

The global surface density of As (d_{As}) is given by

$$d_{As} = M_C C_{As} f_B f_S / A_E$$

where M_C is the mass of crude oil burned, C_{As} the average concentration of As in crude oil is about 0.134 ppm [6], f_B is the smoke fraction for crude oil burned, f_S is the fraction of the crude oil As released into into the stratosphere and globally dispersed more or less evenly over the Earth surface area A_E (ca. 5×10^{18} cm²).

The Chicxulub impact crater is located adjacent to the Cantarell very large oil reservoir in the southern Gulf of Mexico, suggesting that abundance of fossil hydrocarbonas in the Chicxulub target rocks was likely to have been above global mean crustal abundance. The formation of the Cantarell oil field is a direct consequence of the KPB impact and it belongs to the giant supercharged Pimienta-Tamabra petroleum system. This system is the most important in the southern Gulf of Mexico and has a cumulative production and remaining reserves of about 10^{16} g of known petroleum.

Let us assume that the amount of crude oil burned during the Chicxulub impact was equal to the crude oil reserves of (ca. 10^{16} g) of the gigantic Pimienta-Tamabra petroleum system.. The average smoke yield for crude oil, determined from laboratory experiments by Ransohoff *et al.* [7], was about 75 g kg⁻¹ of oil burned, i.e., $f_B \sim 0.075$). In general, the smoke emission factor for crude oil is about up to 10 % [8]. Let us then make a peculiar assumption that all As of crude oil burned is emitted into the stratosphere and deposited globally on the Earth surface, i. e. $f_S \sim 1$. Using these values, one can calculate that $d_{As} \sim 20$ pg cm⁻². I estimate from the experimental data of Schmitz (1988) that the surface density of As of the decarbonated RSC is about 540 μg cm⁻² (assuming an average density of 2 g cm⁻³), which are about more than 27 millions times higher than d_{As} .

Proved recoverable coal reserves of the world are about 9×10^{17} g and a mean As concentration in coal is ca. 13 ppm [6]. Assuming that all world coal burns and then its As is uniformly dispersed over the Earth's surface, I estimate this burning would generate a global density of As equals around 2 μg cm⁻², which is about 270 times smaller than d_{As} .

Conclusion

Fossil fuels (crude oil, coal or carbonaceous shales) close to Chicxulub are probably not responsible for As enrichments in worldwide distributed prominent marine KPB clays.

References

- [1] R. Hildebrand, W. V. Boynton, *Meteoritics*, 1989, 24, 277–278.
- [2] I. Gilmour, E. Anders, *Lunar and Planetary Science Conference*, 1988, 19, 389.
- [3] I. Gilmour, E. Anders. *Geochim. Cosmochim. Ac.*, 1989, 53, 503-511.
- [4] B. Schmitz, *Geology*, 1988, 16, 1068-1072.
- [5] *Geochemical Earth Reference Model: Reservoir Data 2012*.
- [6] J. Matschullat, *Sci. Total Environ.*, 2000, 249, 297-312.
- [7] L. M. Ransohoff, K. Knudson, B. W. Bush, R. D. Small, *Pacific-Sierra Research Corporation*, Los Angeles, 1989.
- [8] R. P. Turco, O. B. Toon, T. P. Ackerman, J. B. Pollack, C. Sagan C., *Science*, 1990, 247, 166-176.

O-03-P

**MEGACRYOMETEOR FROM SVRLJIG (SERBIA):
PRELIMINARY PHYSICOCHEMICAL STUDY**

P. I. Premović¹, M. G. Đorđević¹, M. S. Pavlović²,
D. S. Petrović³, M. D. Petrović³, Đ. D. Petrović³

¹*Laboratory for Geochemistry, Cosmochemistry and Astrochemistry, University of Niš, P.O. Box 224, 18000 Niš, Serbia*

²*Institute of Nuclear Sciences Vinča, P.O. Box 522, 11001 Belgrade, Serbia*

³*Mrgudova 13, Svrljig, Serbia*

Abstract

Megacryometeor from Svrljig is probably derived from a tropospheric water at a maximum attitude of about 6 km under anomalous atmospheric conditions.

Introduction

The fall of large ice blocks (weighing about one to hundreds of kilograms) from the clear sky is one of the most interesting and controversial issues in atmospheric sciences. They are recently named megacryometeors by Martinez-Frias and Travis [1] and represent large atmospheric ice chunk conglomerations. In general, the megacryometeors are formed under clear-sky conditions which differ from those of the cumulonimbus cloud conditions of common hailstones. They are neither classical hailstones nor ice products of atmospheric processes at high attitudes; they are often confused even with meteors because they can leave small impact craters. Scientific research shows that the composition of the megacryometeors is similar to the tropospheric rainwater in the areas of their fall [1]. They are not ice junks from aircraft either. Indeed, a detailed historical review of the megacryometeors imply that there many documented cases of their fall which go back to the first half of the 19th century before invention of the airplanes.

At present, no model is able to satisfactory explain how the megacryometeors can be formed and maintained in the atmosphere [1]. It is interesting to mention here that there is a hypothesis that the megacryometeors could be a new type of geoindicators of global climate changes [2].

In our opinion, by use of a detailed physicochemical analysis of megacryometeors it will be possible to learn more about their nature and origin. In this brief paper, we report some observations and preliminary experimental, computer modeling and ballistic estimation results related to megacryometeor from Svrljig.

Observations

On August 9th 2010, at around 1 pm, an ice chunk weighing roughly 6 kg fell from clear sky and crashed through the roof of the old (about 100 years) house of the family Petrović from Svrljig. Mr. Dragan S. Petrović, the owner of the house, was outside in the garden sitting on the grass about six meters from the impact site. He was witness of strong but strange “whistling noise” caused by the ice impactor

followed by a strong bang. Due to the arrangement of the tiles (so-called *ćeramida*) of the roof, an irregular hole $0.75 \text{ m} \times 1 \text{ m}$, were produced.



Figure 1. Megacryometeor from.

Laboratory for Geochemistry, Cosmochemistry and Astrochemistry (University of Niš). This piece of the ice chunk was preserved under frozen conditions for later studies.

A small part of the ice chunk was found situated under the roof in the attic, whereas three relatively large ice fragments (about 2 kg) fell in the garden area. The attic plaster was severely cracked. These pieces were collected and transferred into the freezer.

We picked up one of these megacryometeor fragments (Fig. 1) to perform the physicochemical analyses in

Results and Discussion

The Svrljig megacryometeor has a rather high pH of 9.8 and relatively low conductivity $28 \mu\text{S cm}^{-1}$. For comparison, megamicrometeor water usually has a pH in the range of from 7.0 - 7.9 and conductivity values from $56 - 69 \mu\text{S cm}^{-1}$. Qualitative analysis tests for chloride, carbonate and ammonium ions have not shown traces of these chemical species. Table 1 displays a summary of the concentrations of main trace elements in the ice chunk obtained by the inductively coupled plasma optical emission spectrometry (ICP-OES). These values are comparable with those measured in atmospheric (unequivocally tropospheric) waters.

Table 1. The trace elements concentrations (ppm) of the Svrljig megacryometeor.

Mg	Si	Al	Zn	B	Sr	Mn	Ba	Ag
1.5	1.5	0.1	0.05	0.2	0.05	0.03	<0.005	<0.03
Cu	Cr	Co	Ni	Mn	V	Zn	Fe	
0.03	<0.05	<0.3	0.10	0.05	<0.05	<0.10	<0.20	

Recent computer modelling shows that the mass of the Svrljig megacryometeor was up to 8 kg and its maximum impact speed was 1235 km h^{-1} ; the kinetic energy of this meteor was up to 0.5 MJ. Such an energetic megacryometeor is capable of breaking tiles (*ćeramida*) arrangement with the total

O-03-P

thickness of about 10 cm and to make a roof hole of 40 cm or less. These calculated values roughly correspond to the observed ones. A ballistic trajectory calculation implies that the Svrljig megacryometeor fell from a maximum height about 6 km (troposphere) less than 2 km far from Svrljig. Of note, at this attitude temperature is about -30 °C. It has been suggested that the formation of the megacryometeors occur within a range of temperature from -10 to -20°C [3]. Further study is in progress.

References

- [1] J. Martinez-Frias J and D. Travis D. in S. Leroy, I. S. Stewart(Eds.), Environmental catastrophes and recovery in the Holocene, Abstracts Volume, London, Brunel University, 2002.
- [2] IUGS Geoinicators, <http://www.lgt.lt/geoin/>.
- [3] F. Rull, A. Delgado, J. Martinez-Frias, Philosophical Transactions of the Royal Society A; Mathematical, Physical and Ingeneering Sciences, 2010, 268, 3145-3152.

EDUCATION, HISTORY

METHODOLOGY AND METHODS OF PHYSICO-CHEMICAL ANALYSIS OF KURNAKOV

T. J. Halasi, S. S. Kalamkovic*

Faculty of Sciences, Department of Chemistry, Biochemistry and Environmental Protection, Trg Dositeja Obradovica 3, Novi Sad,

**Primary School "Prva vojvodjanska brigada", Seljackih buna 51a, Novi Sad*

Abstract

Kurnakov was a Russian physicalchemist who was internationally recognized as the originator of [physicochemical](#) analysis and he was one of the principal founders of the [platinum](#) industry in the [USSR](#). During the first decade of the 20th century, Kurnakov was concerned with the solution of industrial problems such as platinum refining, metallic alloys, metallography and salt manufacturing and he played a vital role in the planning and construction of new laboratories.

Kurnakov's biography

Nikolai Semenovich Kurnakov (*Никола́й Семёнович Курнако́в*, December 6, 1860–March 19, 1941) was born in Nolinsk (*Нолинск*, 57° 33' 27" N, 49° 56' 18.96" E) and he died in Barvikha (*Барві́ха*, 55° 44' 30" N, 37° 16' 43" E). He attended a high school at [Nizhny Novgorod](#) (*Ни́жний Новго́род* 56° 20' 0" N, 44° 0' 0" E) and he studied at the Mining Institute, in [Saint Peterburg](#) (*Санкт-Петербу́рг*, 59° 57' 0" N, 30° 19' 0" E) where he graduated at Institute of Mines in 1882. He was a professor of inorganic chemistry (1893), professor of Physical Chemistry and General Chemistry (1902), together with Dmitri Ivanovich Mendeleev (*Дми́трий Ива́нович Менделеев*, 1834-1907) and [Nikolai Aleksandrovich Menshutkin](#) (*Никола́й Алекса́ндрович Меншуткин*, 1842-1907), at the St. Peterburg Polytechnic Institute (1899-1908), director of the General Chemistry Laboratory of the Academy (1922) and upon the death of Chugaev (*Лев Алекса́ндрович Чу́гаев*, 1873-1922), director of the initially-small Institute of Physicochemical Analysis, and the following year he became editor of its Journal *Известия Института физико-химического анализа (Известия Сектора физико-химич. Анализа)*.^{[1][2]} Kurnakov created the Institute of Physical and Chemical Analysis. A mineral was named [kurnakovite](#) in his honor. The Kurnakovs had two children, son Nikolai Nikolaevich Kurnakov (1889-?), a chemist who worked at the Baikov Metallurgical Institute of the Academy of Sciences of the USSR., daughter Vera Nikolaevna Kurnakov (1898-1921). After the death of his wife (1940), Kurnakov's health deteriorated and he died in a sanatorium.^[1]

Kurnakov's work

Kurnakov's first scientific interest was in salts. He completed a series of experiment on the chemistry of coordination complexes that were generalized in

his dissertation *On Complex Metallic Bases* (*Сложных Металлических Основаниях*, 1893), summarized the results of his study of the chemistry of complex compounds, and described the reaction of Pt(II) and Pd(II) isomers with thiourea, now known as Kurnakov's reaction [3][4]. He published his first paper on alum crystallization and sodium thioantimoniate in 1882.[5] His invention of an automatic pyrometer (1903) proved to be a major advance in the technique of thermal analysis, for recording heating and cooling curves-with the aid of which he significantly improved the methodology of thermal analysis.

Physicochemical analysis is based on the phase rule and on the principles of continuity and correspondence, which were introduced by Kurnakov. Kurnakov carried on a systematic study of heterogeneous systems (1898) and he used physicochemical analysis like important method of studying systems made up of two, three, or more components, (alloys, minerals, solutions, carbides, oxides, semiconductors, superconductors, systems formed by organic compounds). Together with Zhemchuzhnyi (*Сергей Фёдорович Жемчужный*, 1873-1929), Kurnakov established the relationships between composition and properties in binary systems, including electric conductivity (measure of how well a material accommodates the transport of electric charge $\sigma = IG/S$) (1906), solidity (1908), escape pressure (1908-1913) and basic composition electroconductivity diagrams for systems of two metals which form continuous solid solutions.[6] Kurnakov and his associates discovered a number of berthollides in metallic systems, as well as the theoretically important case of the formation of daltonides in the transitions of solid solutions of gold and copper. These results permitted Kurnakov to formulate the general conclusion that "a chemical individuum belonging to a specific chemical compound represents a phase, which possess singular or Dalton points on the lines of its characteristics" (1914) [4]. "In equilibrium systems," he said, "discreteness and continuity are intercombined and coexist." Physicochemical analysis involves the measurement of various physical properties of systems, most often phase transition temperatures and other thermal properties (thermal conductivity, heat capacity, thermal expansion), electrical properties (conductivity, dielectric permittivity), and optical properties (refractive index, rotation of the plane of polarization of light), measured the density, viscosity and hardness, as well as the dependence of the rate of the transformations occurring in a system on the system's composition. X-ray diffraction analysis and techniques of microscopic metallography are extensively used in physicochemical analysis. [7] The continuity principle holds that during continuous changes in the parameters of a state the properties of a system also undergo continuous change (provided that the number of phases in the system remains constant), when the number of phases changes, certain properties change abruptly (continuity being broken). According to the correspondence principle, each phase or group of phases of a system corresponds to a certain geometric shape (point, line, surface, volume) on the composition-properties diagram. The onset of phase crystallization corresponds to the liquidus curves (or surfaces), above which is located the region of existence of one liquid phase (solution or melt), the end of crystallization corresponds to the solidus lines

(or surfaces), below which only solid phases exist. During a continuous change in the composition of a system, the components of the system may form a chemical compound. If the compound does not undergo dissociation and has an unvarying composition (daltonide), a singular point is observed on the composition-properties diagrams.

Conclusion

Kurnakov, one of Russia's most distinguished and versatile chemists, was an active force in the development of science and technology both in his homeland and abroad. He is regarded as the founder of a new chemical discipline, physicochemical analysis, probably the largest contemporary school of Soviet chemistry with applications in numerous branches of technology.

References

- [1] G. B. Kauffman, The Life and Work of Nikolai Semenovich Kurnakov, *Platinum Metals Review*, 1982, 26 (3), 129-133.
- [2] G. B. Kauffman, Nikolai Semenovich Kurnakov, the reaction (1893) and the man (1860–1941) a ninety-year retrospective view, *Polyhedron*, 1983, 2 (9), 855-863.
- [3] N. T. Kuznetsov, N. S. Kurnakov's Contribution to Coordination Chemistry, *Russian Journal of Inorganic Chemistry*, 2010, 55 (11), 1777-1783.
- [4] Н. С. Курнаков, Сборник избранных произведений, 1938-1939, томах 2, Ленинград.
- [5] Н. С. Курнаков, Введение в физико-химического анализа, 1940, 4-е изд, Москва.
- [6] Г. Г. Уразов, Академик Н. С. Курнаков - основатель физико - химического анализа. - ИСФХА, 1941, 14, 9-35.
- [7] А. Т. Григорьев, Воспоминания о жизни и деятельности академика Н. С. Курнакова. - В кн.: Николай Семенович Курнаков в воспоминаниях современников и учеников, Москва, 1961, 28-30.

P-02-P

OTTO HAHN'S WORK IN PHYSICAL CHEMISTRY

Tibor Halasi, S. Kalamkovic*, M. Mark**

*Faculty of Science, Department of Chemistry, Biochemistry and Environmental Protection, Trg Dositeja Obradovica 3, 21000 Novi Sad, Serbia, tibor.halasi@dh.uns.ac.rs, *Primary School "Prva vojvodjanska brigada", Novi Sad, Serbia, **Faculty of Sciences, Department of Physics, Novi Sad, Serbia*

Abstract

Otto Hahn was a German physical chemist who discovered the fission of heavy atomic nuclei, and for that work he was awarded with Nobel Prize . He has worked with Meitner, Zincke, Strassman, Born, Flügge and Seelmann-Eggebert. With Meitner he measured the absorption of α -radiation. Hahn was discovered: Radioactinium (RdAc), Thorium C (ThC), Mesothorium I (MsTh1) Mesothorium II (MsTh2), Uranium Z (1921) and nuclear isomers Proactinium.

Hahn's biography

Otto Hahn (March 8th, 1879, Frankfurt-on-Main-July 28, 1968, Göttingen) was a German physical chemist and Nobel-laureate, a pioneer in the fields of radioactivity and radiochemistry. He is regarded as "the father of nuclear chemistry". On November 15th 1945 the Royal Swedish Academy of Sciences announced that Hahn had been awarded the 1944 Nobel Prize in Chemistry "For his discovery of the fission of heavy atomic nuclei". Some historians have documented the history of the discovery of nuclear fission and believe Meitner should have been awarded the Nobel Prize with Hahn. Hahn Otto colleagues considered the "father of the atomic age".

Otto Hahn's father wanted his son to become an architect, but his dream did not realize. Otto did not show enough skills in engineering, is a bad draw and had no sense of space. [1, 2] At the summer of 1901. Otto oral exams and defending a doctoral thesis "On Bromine Derivates of Isoeugenol" in organic chemistry. Professor Theodor Zincke (1843-1928) offers him the position of assistant. Otto Hahn sees its future in the chemical industry.

Hahn's work

September 1904. Otto went to London to investigate radiochemistry, she knew only through newspaper articles. For 100g white barium salt Hahn should have extracted 10 mg of Radium, Marie Curie method (*Marie Sklodowska Curie*, 1867-1934), the method of fractional distillation. Moreover, in addition to radium discovered a substance that releases the active short-lived isotope of thorium, radiotorijum. On one of the classes Plank (*Max Karl Ernst Ludwig Planck*, 1858-

1947), 1907. Otto meets a physicist Lise Meitner (1878-1968), with which he measured the absorption of α -radiation. First they measured the β -radiation Mesothorium I and II by the method used for the Rutherford- α -particles, magnetic removal, (Figure 1). [3]



Figure 1. Otto Hahn and Lise Meitner. [3]

Hahn was discovered: Radioactinium (RdAc), Thorium C (ThC), Mesothorium I (MsTh1) Mesothorium II (MsTh2), Uranium Z (1921) and nuclear isomers Proactinium.[1] Physicists have until 1938. thought that the neutron bombardment of uranium occur such elements whose molecular weights greater than uranium. Physicists haven't presumed that the bombardment of uranium occurring two elements with a lower molecular weight. Born (*Max Born*, 1882-1970), Flüge (*Siegfried Flüge*, 1912-1997), Seelman-Eggebert (*Walter Seelmann-Eggebert*, 1915-1988), Strasman (*Friedrich Wilhelm "Fritz" Strassmann*, 1902-1980), Han and reveal another 25 new elements and 100 new isotopes. Strasman worked with Hahn and he was very helpful when using the method of Fermi (*Enrico Fermi*, 1901-1954) and the discovery of nuclear fission. (Figure 2)^{[4][5]} In Canada, presented the hypothesis that the thorium and radiotorium there must be some other radioactive substance. The substance is a direct product of thorium, which accumulates in the mineral. If you remove thorium from the

P-02-P

mineral remains of its products. So they discovered two immediate thorium products Mesothorium I and Mesothorium II. [1]



Figure 2. Otto Hahn and Fritz Strassman, München, 1938.[5]

Hahn is the January 1915. began to work in groups to produce toxic gases controlled Habera Institute of Chemistry. Max Plank in 1923. Hahn proposed for the Nobel Prize. Kaiser Wilhelm Institute's November 15th 1945. announced that the Nobel Prize "for their discovery of nuclear fission of heavy atomic nuclei" earned Otto Han, and Hahn was then in captivity. "Mainau Declaration", which is supported by 52 scientists, Hahn published in cooperation with Bor 1955. and was open to appeal against the use of nuclear weapons. "In Berlin I learned of all that had happened since Hitler had come to power. Although Geheimrat Haber, Director of the Insitute of Physical Chemistry, was not himself under pressure to resign, he was powerless to prevent 'non-Aryan' members of his staff from being removed from their jobs. He therefore wrote to Minister Rust, offering his ownresignation. Geheimrat Planck, President of the Kaiser Wilhelm Society, and Haber now asked me to take over the director-ship of the Institute of Physical Chemistry, provisionally, alongside my directorship of the Chemical Institute. I agreed to this, but only a few days later I was informed that a new director had been appointed, This was Professor Jander, an active member of the Nazi party. I had refused to join the party."[6]

Conclusion

”The discovery of nuclear fission by Otto Hahn and Fritz Strassmann opened up a new era in human history. It seems to me that what makes the science behind this discovery so remarkable is that it was achieved by purely chemical means.”[7][8]

Acknowledgements

The authors wish to thank the Ministry of Education and Science, Government of Republic of Serbia for supporting the scientific project ”The quality of the education system in Serbia's European perspective” (KOSSEP), Code 179010.

References

- [1] M. Mladenović, Velikani fizike (dvadeseti vek), Faculty of Science, Prirodno-matematički fakultet, Novi Sad, 2008, 377- 400.
- [2] K. Fajans, Otto Hahn, The Journal of Nuclear Medicine, 1966, 397-401.
- [3] P. Rife, "Lise Meitner" Jewish Women: A Comprehensive Historical Encyclopedia, Jewish Women's Archive, March 1st 2009; <http://jwa.org/encyclopedia/article/meitner-lise>, April 30, 2012.
- [4] G. Walton, N., Nuclear fission, Q. Rev. Chem. Soc., 1961, 15, 71-78.
- [5] E. H. Berninger, Otto Hahn, Rowohlt Taschenbuch Verlag GmbH, Hamburg, 1974, 123.
- [6] O. Hahn, My life, (The Autobiography of a Scientist), Herder and Herder, New York, 1970, 144-145.
- [7] http://profpaulcutter.com/PDF/Hi-tech%20Studies/Nazi_Atomic_Bomb.pdf, May 15, 2012.
- [8] L. Meitner, Recollections of Otto Hahn, Stuttgart, 2005.

P-03-P

GERMAIN HENRI HESS AND LAW OF HEAT SUMMATION

Tibor Halasi, S. Kalamkovic*, R. Halasi**

*Faculty of Science, Department of Chemistry, Biochemistry and Environmental Protection, Trg Dositeja Obradovica 3, 21000 Novi Sad, Serbia,
tibor.halasi@dh.uns.ac.rs, *Primary School "Prva vojvodjanska brigada", Novi Sad, Serbia, **DPNNS, Novi Sad, Serbia*

Abstract

This paper presents an overview of the work and creativity of scientists Hess and its significance for the development of physical chemistry. Hess's law made it seem highly likely that the law of conservation of energy applied to chemical changes as well as to physical changes. Indeed, to generalize further, the laws of thermodynamics very likely held in chemistry as in physics. This line of experiment and reasoning made it seem that chemical reactions, like physical processes, had an inherent spontaneous direction in which entropy was increased.

Hess's biography

Germain Henri Hess (*Герман Иванович Гесс, Жермен Анри, Герман Генрих*, August 7, 1802-November 30, 1850) was born in Geneva, Switzerland and he died in [St. Petersburg](#). He was a Swiss-born Russian chemist and [doctor](#), whose studies of heat in chemical reactions formed the foundation of thermochemistry, [Hess's Law](#). He moved with his family to Russia when his father, an artist, became a tutor to a rich family. Hess studied medicine, on the advice of the mother at the University of Tartu, from 1822 to 1826, and became a Doctor of Medicine.[1] Hess turned to chemistry after a meeting with Berzelius (*Jöns Jakob Berzelius*, 1779-1848), the famous Swedish chemist, and went to Stockholm University to study under him and he spent barely a month in Berzelius's laboratories. On his return to Russia, Hess joined an expedition to study the geology of the Urals before setting up a medical practice in Irkutsk. After practicing medicine in Irkutsk for two years, Hess returned to St. Petersburg, where he remained a member of the academic establishment.

Hess's Law of Constant Heat Summation

Hess proposed a law regarding the heats or enthalpies of reaction in 1840 called the Hess's law, the first law of thermodynamics, law on thermochemistry. This law states that "the heat change in a particular reaction is the same whether it takes place in one step or several steps", "in a series of chemical reactions, the total energy gained or lost depends only on the initial and final states, regardless of the

number or path of the steps.” Hess was able to demonstrate that the quantity of heat produced (or absorbed) in going from one substance to another was the same no matter by what chemical route the change occurred, or in how many stages. [2]

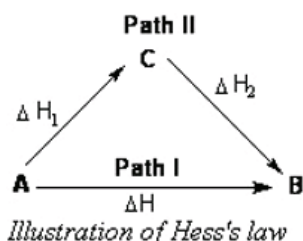


Figure 1. Illustration of Hess's law. [3]

Applications of Hess's law:

- Determination of Heat of Formation
- Determination of Heat of Transition
- Determination of Enthalpy of Transition
- Determination of Heats of Various Reactions
- Determination of Enthalpy of Hydration
- Determination of Standard Enthalpy of Reaction
- Calculation of Bond Energies ($\Delta_{\text{bond}}H^{\ominus}$)
- Bond energy of C – H bond = $(1664) / 4 = 416 \text{ kJ mol}^{-1}$
- Enthalpy of atomization ($\Delta_{\text{a}}H^{\ominus}$)[4]

Hess's work

Hess's other work concerned the investigation of minerals and analysis of [silver-telluride](#) (Ag_2Te , [Hessite](#)). He discovered that the [oxidation](#) of [sugars](#) yielded saccharic acid.

Hess wrote the most successful domestic textbook on chemistry and a truly modern textbook "Foundations of pure chemistry", which went seven editions from 1831 to 1849. and was the standard Russian work for several decades. Hess's textbook has learned a whole generation of local chemists, including Mendeleev (*Дмитрий Иванович Менделеев*, 1834-1907), Butlerov (*Александр Михайлович Бутлеров*, 1828-1886), Zinin (*Николай Николаевич Зинин*, 1812-1880) and Voskresensky (*Александр Абрамович Воскресенский*, 1809-1880).[5][6]

Conclusion

Unfortunately, Hess thermochemical work was truly appreciated until much later, when Ostwald (*Friedrich Wilhelm Ostwald*, 1853-1932) reprinted them in his monograph series "Classics of Science".[7]

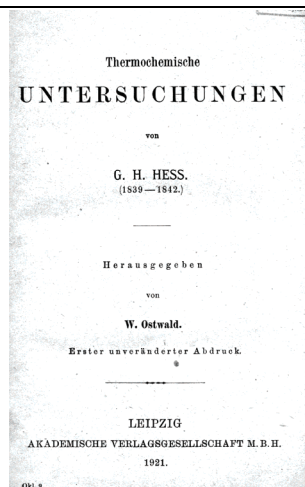


Figure 2. Front Page of The Ostwald's book. [7]

Hess's law is useful in calculating the enthalpies of many reactions whose direct measurement is difficult or impossible ($\Delta H = \Delta H_1 + \Delta H_2$).

Acknowledgements:

The authors wish to thank the Ministry of Education and Science, Government of Republic of Serbia for supporting the scientific project "The quality of the education system in Serbia's European perspective" (KOSSEP), Code 179010.

References

- [1] H. M. Leicester, Germain Henri Hess and the Foundations of Thermochemistry, *The Journal of Chemical Education*, 1951, 28 (11), 581-583.
- [2] E. von. Meyer, *A History of Chemistry from the Earliest Times to the Present Day*, The Macmillan Company, 1898, 507. (cites that Ostwald refers to G. H. Hess, and his 1840 work, *Constanz der Warmesummen*, as being the founder of thermochemistry).
- [3] <http://chemmaster.co.in/showchapter.php?id=7&id2=95&title=Thermodynamics>, May 25th 2012.
- [4] I. Muller, *A History of Thermodynamics - the Doctrine of Energy and Entropy*, New York: Springer, 2007, 154-155.
- [5] В. А. Волков, Е.В. Вонский, Г. И. Кузнецова, *Выдающиеся химики мира*, М. ВШ, 1991, 656.
- [6] А. М. Корзухина, *Русское физико-химическое общество и его роль в русской физике (1870—1917)* ИИЕТ РАН. Годичная научная конференция 2003 г., М. Диполь-Т, 2003, 172-173.
- [7] G. H. Hess, *Thermochemische Untersuchungen*, edited Ostwald, Akademische Verlagsgesellschaft M. B. H., Leipzig, 1921.

FOOD PHYSICAL CHEMISTRY

APPLICATION OF DIFFERENTIAL PULSE POLAROGRAPHY IN ANALYSIS OF PECTIN

S. Milić¹, J. Bogdanović Pristov¹, S. Veljović Jovanović¹,
S. Gorjanović², D. Sužnjević^{2*}

¹*Institute for Multidisciplinary Research, University of Belgrade, Kneza Visislava
1, 11000 Belgrade, Serbia*

²*Institute of General and Physical Chemistry, P. O. Box 45, 11158 Belgrade 118,
Serbia*

Abstract

Differential pulse polarography (DPP) with dropping mercury electrode (DME) was used to determine quantitatively galacturonic acid (GA), methylated polygalacturonic acid (met PGA), pectin (PC) and pectinase (PE) in 0.1 M NaClO₄ as supporting electrolyte. Current peaks of GA, met PGA, PC and PE, at -1.55, -1.50, -1.40 and -1.60 V vs SCE respectively, were found suitable for quantitative determination in the concentration range considered. Enzymatic reaction between PE and PC was followed and possibility to determine simultaneously of PC and PE was proved.

Introduction

Pectin is an acidic polysaccharide consisting of D-galacturonic acid units with very small quantity of neutral sugars. The monomers are linked together by 1-4 glycosidic linkage. Part of the acid is present as methyl ester. The textures of fruits and vegetables are largely influenced by the pectin content. Many food processors and pectin ingredient suppliers need to determine pectin content to control the quality of their products. Various chemical and instrumental methods, including HPLC, GLC, infrared spectroscopy, HPAEC using pulsed-amperometric detection (PAD), were applied for determination of pectin content in food products. Some of the methods, measuring pectin as galacturonic acid content, are quite accurate, and well-correlated to pectin content. In most cases pectin extraction and hydrolysis are required prior to analysis [1-2]. Until now, electrochemical methods have not been often used in pectin determination. The aim of the presented work was to explore possibility to apply differential pulse polarography (DPP), with dropping mercury electrode (DME) in detection and quantification of pectin and polygalacturonic acid.

Materials and methods

Chemicals Pectin (PC) from citrus fruits, methylated polygalacturonic acid (met PGA) from orange, pectinase (PE) from *Aspergillus niger*, sodium perchlorate (Sigma) and D-(+) galacturonic acid (GA) (Fluka) were used. Analytical grade (99.999) gaseous nitrogen was purchased from Messer-Tehnogas (Belgrade). Deionized water was used for preparing all experimental solutions.

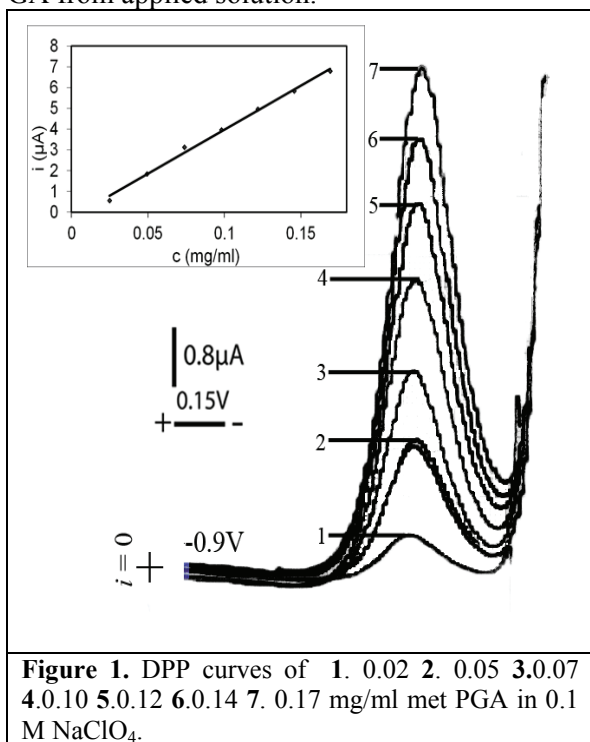
Q-01-P

Instrumentation. The current-potential (i - E) curves were recorded by polarographic analyzer PAR (Princeton Applied Research) model 174A, equipped with X-Y recorder (Houston Omnigraphic 2000). Dropping mercury electrode (DME) with a programmed dropping time of 1 s as working electrode, saturated calomel electrode (SCE) as a reference and a Pt-foil as auxiliary electrode were used. The i - E curves were obtained at different direct current intensity with alternative current modulating pulse of 25mV_{pp} . Scan rate of potential changes was 10 mVs^{-1} .

Procedure. Supporting electrolyte (0.1 M NaClO_4) in the electrolytic cell was deaired by passing nitrogen, than he inert atmosphere was kept constant during i - E curve recording. Dry met PGA, GA, as well as dry PC, or PC solution, with or without PE, dissolved in acetate buffer (pH 5.0), were added in defined amount into the cell solution (20 ml). Then, after bubbling of experimental solution 30 s with nitrogen, the corresponding i - E curves were recorded at room temperature.

Results and discussion

Until now, DPP was not applied for quantitative determination of PC as important ingredient of various natural products. Polarographic behavior of monomer of PGA (GA) at DME, in 0.1 M NaClO_4 as supporting electrolyte, was firstly investigated. A well defined and symmetrical current peak of GA was recorded at potential about -1.55 V vs SCE (not shown). Obtained data gave the opportunity to quantify GA from applied solution.

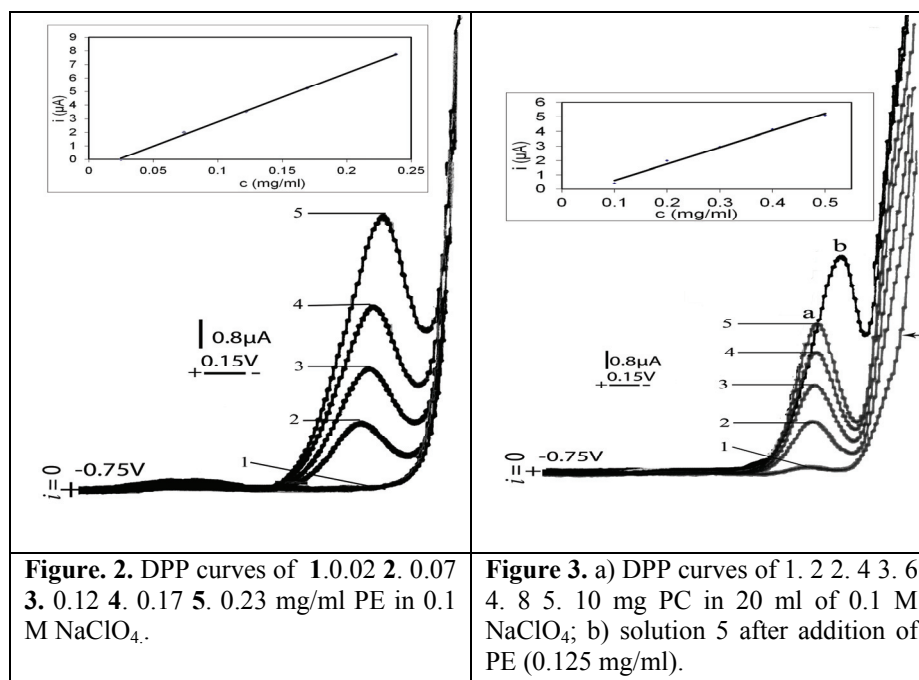


Also, a well defined DPP peak of met PGA was recorded at somewhat less cathodic potential in respect to GA, i.e. at about -1.5 V vs SCE (**Fig. 1**). In concentration range from 0.02 to 0.17 mg/ml , the current linearly depended on PGA concentration (**Fig. 1**, insert).

Possibility for simultaneous determination of PC and PE, an enzyme that breaks PC into simple [sugars](#) and GA, was investigated

A well defined peak of PE at potential about -1.6 V vs SCE , shown in **Fig. 2**, was found suitable for quantitative determination. Peak current showed linear dependence in considered concentration range

(Fig. 2., insert). The measurable current of PE was not detected at concentrations below 0.05 mg/ml , probably due to protein adsorption at the electrode surface.



The solution containing different amount of PC was initially studied (**Fig. 3., curves a, 1-5**). Current peaks recorded at about -1.4 V vs SCE depended linearly on applied PC concentrations (**Fig. 3., insert**). Subsequently, PE was added into solution 5 (**Fig. 3., curve a 5**) and possibility to measure PC and PE simultaneously was proved (**curve b**).

Conclusion

An easy-to-handle, rapid and reproducible method for detection and quantification of galacturonic acid, polygalacturonic acid, pectin and pectinase, based on differential pulse polarography, was developed. Simultaneous determination of pectine and pectinase was shown; it could be widely used to assess contamination of various complex samples after hydrolysis.

Acknowledgements

This research was supported by Ministry of Education and Science of Republic Serbia, grant No. III43010.

References

- [1] M. Monsoor, et al, Food Chem, 2001, 74, 233-2382.
- [2] H. Garna, et al, J. Agric. Food Chem. 2004, 52, 4652-4659

Q-02-P

MASS TRANSFER KINETICS DURING OSMOTIC DEHYDRATION OF SOUR CHERRY IN SUGAR BEET MOLASSES

M. Petrovic¹, T. Brdarić¹, K. Rajkovic² and V. Pavelkić¹

¹Institute "Kirilo Savić", Vojvode Stepe 51, Belgrade, Serbia;

²High Chemical and Technological School for Professional Studies, Kruševac, Serbia

Abstract

The present work aimed to study kinetics of osmotic dehydration (OD) of sour cherry in terms of solid gain and water loss. Sugar beet molasses (solid content 80, 60 and 40%) with NaCl (5%) was used as an osmotic medium. One temperature level of osmotic solution (room temperature) for 300 min was evaluated. Experimental results were fitted in the Peleg's empirical model of osmotic drying kinetics which expresses the influence of analyzed experiment factors on water loss (WL) and solid gains (SG). Mass transfer coefficients of water, Peleg rate constant (k₁) and Peleg capacity constant (k₂), were also estimated.

Introduction

Osmotic dehydration is a process of partial removal of water by submersing fruits in hypertonic solution [1]. This gives rise to two major simultaneously countercurrent mass transfer fluxes, namely water flow from the product to the surrounding solution and solute infusion into the product. Leakage of the product natural solutes quantitatively could be neglected, but may be important for the nutritional value of the product. The kind of osmotic agent used and hence its molecular weight or ionic behaviors strongly affects the kinetics of water removal and the solid gain. The most commonly used osmotic agents are sucrose and sodium chloride [2]. Besides these osmotic agents, sugar beet molasses emerges as a suitable raw-material for the preparation of hypertonic solutions [3]. The purpose of the present work was to study mass transfer parameters during the osmotic dehydration of sour cherry in sugar beet molasses (80%, 60%, 40% with 5% NaCl at room temperature) and examine the predictive capacity of Peleg's equation to the experimental data.

Materials and Methods

Sour chery, used for the experiment, were purchased on the local market in Belgrade, Serbia. Sugar beet molasses was obtained from sugar factory in Pećinci, Serbia. Prior to the treatment, the fruits are thoroughly washed and cut. After cutting, the initial mass of the samples was measured. As osmotic agent pure sugar beet molasses (around 80% solid content) and sugar beet molasses solutions (with 40% and 60% solid content) with the addition of 5% NaCl were used. Solutions were made prior to use. All analytical measurements were carried out in accordance to AOAC methods [4].

The water loss (WL) and the solid gain (SG) of fruit after time "t" of osmotic treatment are defined as [5]:

$$WL(\%) = \frac{(M_0 - m_0) - (M - m)}{M_0} \times 100 \quad SG(\%) = \frac{(m - m_0)}{M_0} \times 100$$

Where M_0 is the initial mass of fresh fruit before the osmotic treatment, M is the mass of sour cherry after time “ t ” of osmotic treatment, m is the dry mass of sour cherry after time “ t ” of osmotic treatment and m_0 is the dry mass of fresh fruit. Peleg’s model [6] is widely used to describe the osmotic dehydration curves and is calculated according to equation:

$$M = M_0 \pm \frac{t}{k_1 + k_2 t}$$

where M is moisture content at time t (g), M_0 is initial moisture content (g), k_1 is the Peleg rate constant (g^{-1}), and k_2 is the Peleg capacity constant (g^{-1}).

Result and discussion

The OD process was studied in a terms of WL and SG as shown in Figure 1 and Figure 2. The increase of WL with the immersion times were observed. The clear trend of higher initial rate of WL, and subsequent slower rate of SG were obtained. The highest value of WL (62.75%) was observed in the samples immersed in the molasses with 80% solid content and with 5% NaCl at room temperature for 300 minutes. Figure 2 presents the degree of penetration of solids from the osmotic solution into the samples (SG value). The increase of concentration of hypertonic solution (molasses) caused a decrease of SG of treated samples at room temperature.

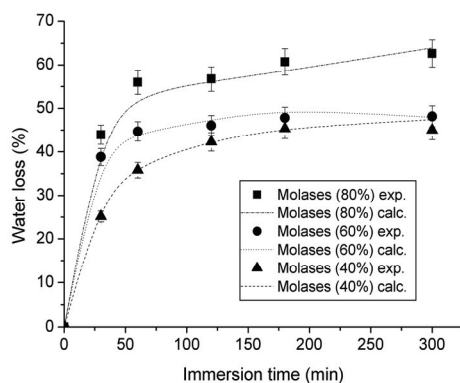


Figure 1. Dependence of water loss on dehydration time of sour cherry treated with beat molasses (solid content of 40, 60 and 80%) - Comparison of experimental and calculated data.

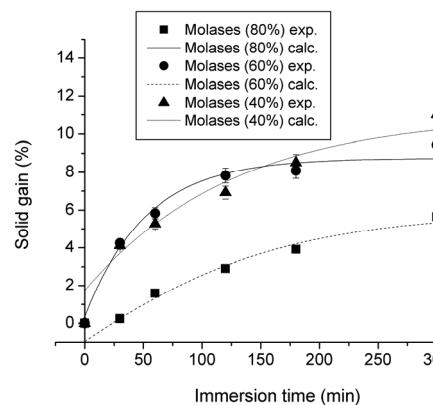


Figure 2. Dependence of solid gain on dehydration time for the different solid content of sugar beet molasses (40, 60 and 80%) - Comparison of experimental and calculated data.

The Peleg’s rate (k_1) and capacity (k_2) constants were evaluated from experimental data (Table 1). High values of R^2 suggest that the Peleg equation in appropriate way describes the mass transfer kinetics during the OD of sour cherry in sugar beet molasses and indicate a good fit to the experimental data.

Table 1. Peleg's equation parameters.

Solid content (%)	Water loss			Solid gains		
	k_1	k_2	R^2	k_1	k_2	R^2
80	0.06±0.01	0.29±0.02	0.997	11.0±0.4	1.80±0.1	0.974
60	0.10±0.02	0.30±0.05	0.979	2.30±0.3	1.50±0.2	0.995
40	0.15±0.05	0.40±0.03	0.989	1.70±0.2	1.30±0.2	0.981

Conclusion

Peleg's equation parameters (k_1 and k_2) for the solid gain and water loss presented a good fitting to the experimental data. The equation parameters exhibit a trend of decreasing with the increase of the solid content in sugar beet molasses for water loss and are inversely proportional for solid gain. The presence of NaCl in osmotic media has some influences on mass transfer kinetics: it increases viscosity of the osmotic media and hence improves solid gain and decreases water loss.

Acknowledgement

This study was supported by Ministry of Education and Science of Republic of Serbia, Project TR 31055.

References

- [1] P. M. Azoubel, F. Elizabeth, X. Murr, , Journal of Food Engineering, 2004, 61,291–295.
- [2] S. Mizrahi, S. Eichler, O. Ramon, Journal of Food Engineering, 2001, 49, 87–96.
- [3] Lj. Lević, V. Filipović, T. Kuljanin, PTEP, 2007, 11, 132-134.
- [4] AOAC, Official method 963. 22, Washington, 2000.
- [5] B. Singh, A. Kumar, A. K. Gupta, Journal of Food Engineering, 2007, 79, 471–480.
- [6] M. Peleg, Journal of Food Science, 1988, 53, 1216–1219.

THERMAL ANALYSIS OF RASPBERRY AND BLACKBERRY SEED FLOUR

D. Micić, S. Ostojić, M. Simonović, M. Dojčinović,
S. Hranisavljević, B. R. Simonović

*University of Belgrade, Institute of General and Physical Chemistry, Studentski trg
12, 11000 Belgrade, Serbia*

Abstract

Thermal characteristic of red raspberry (*Rubus ideaus*) and blackberry (*Rubus fruticosus*) seed flours have been followed by Modulated Differential Calorimetry (MDSC) and Thermogravimetric analysis (TGA). MDSC allows the separation of the (total) heat flow signal into the heat capacity (reversible heat flow) and the kinetics components (non-reversible heat flow). Thermal events in the low temperature region of seed flour have been approximately separated suggesting that there are two independent thermal processes.

Introduction

Fruit seeds are byproducts from fruit processing, and seed flour is the primary byproduct from seed oil production. Recent study showed that red raspberry seed flour obtained from the cold-pressing procedure may contain a significant level of antioxidants [1]. These data suggest the potential of developing novel uses of fruit seed flours as food ingredients rich in beneficial food factors for improving human diets, while enhancing the profitability of fruit production and processing industries. Additional research is required to investigate fruit seed flours for their contents of health beneficial factors to promote their value-added utilization as beneficial food ingredients. MDSC nonreversing signal may contain important information on irreversible processes, such as slow chemical reactions (oxidation, curing, evaporation, etc.) and nonequilibrium phase transitions (crystallization and reorganization); it may even enable to separate the complicated simultaneous fusions, glass transitions and annealings, common in many macromolecules and complex mixtures [2,3].

The present study was conducted to investigate the seed flours of red raspberry (*Rubus ideaus*) and blackberry (*Rubus fruticosus*) for their thermal characteristics by mean of Modulated Differential Calorimetry (MDSC) and Thermogravimetric analysis (TGA).

Experimental

Fruit seed flour preparation. Fruit seed were the solid residues from the cold-pressing fruit pulp. Seeds were drayed at room temperature, to the constant moisture of 6-7% and grinded immediately before thermal analysis.

Thermal analysis. MDSC and TGA of blackberry and raspberry seed flours have been performed on TA Instruments DSC Q 1000, Differential Scanning

Q-03-P

Calorimeter and TGA measurements on TA Instruments TGA Q 500 Thermogravimetric Analyzer under N₂ purge flow of 50ml/min and 60ml/min respectively. MDSC scans were conducted in temperature range from -90 °C to 150 °C, with heating rate Hr = 5 °C/min with modulation of ±0.50 °C amplitude and 40s period of modulation. and TGA scans were performed in temperature range of 25 °C to 700 °C with heating rate Hr = 5 °C/min.

Results and Discussion

In Fig. 1. and 2. are presented MDSC curves of blackberry and raspberry seed flours.

Total DSC curve is characterized with overlapping effect in low-temperature region caused by the freezing and unfreezing of large-amplitude motion [4]. It was shown that thermal transitions, observed in the range of -80 to -10 °C were independent on water content, and they were mainly attributed to lipid melting transitions [5]. Broad endothermic peak with T_m at about 93 °C corresponds to protein denaturation [5].

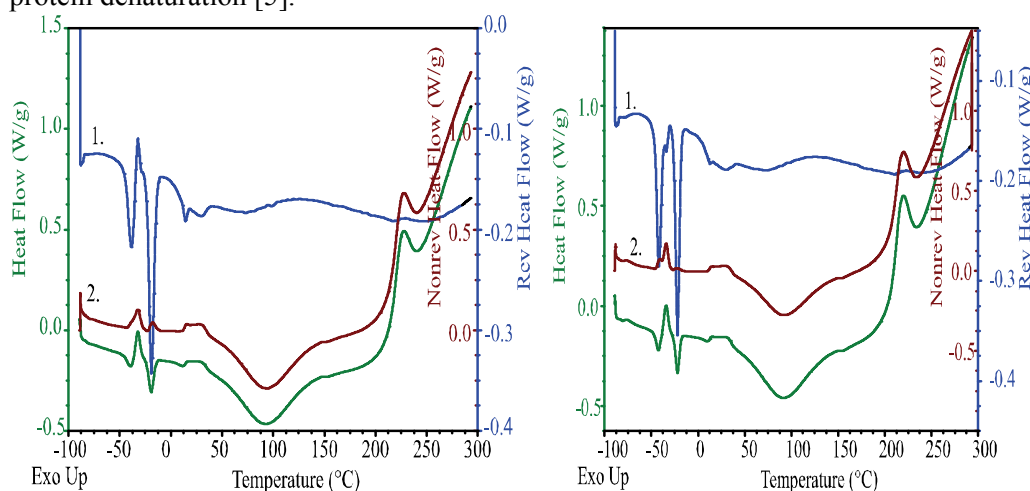


Figure 1. MDSC curves of blackberry seed flour.

Figure 2. MDSC curves of raspberry seed flour.

Using MDSC, the reversing (curve 1.) and nonreversing (curve 2.), thermal events in the low temperature region of seed flour have been approximately separated [4], reversing (curve 1), suggesting that there are two independent thermal processes.

In Fig. 3. TGA curves of blackberry and raspberry seed flour are presented. Results from TGA analysis are shown in Table 1.

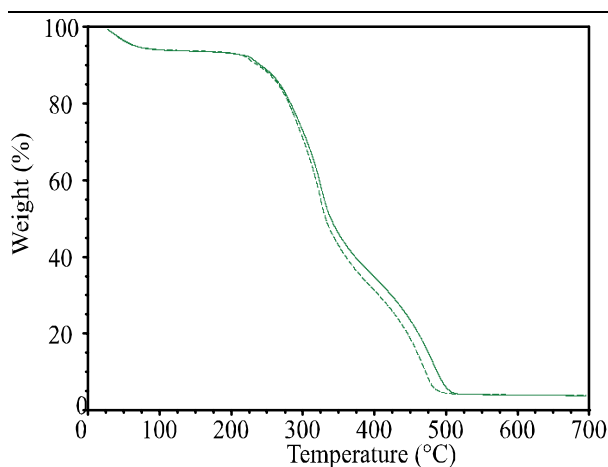


Figure 3. TGA curves of blackberry (dashed curve) and raspberry (solid curve) seed flour.

Table 1. Results obtained from TGA curves of blackberry and raspberry seed flour

seed flour	I weight loss (moisture) (%)	II weight loss (%)	III weight loss (%)	Residue (700 ⁰ C) (ash) (%)
raspberry	6.09	60.92	31.70	1.29
blackberry	6.22	57.33	35.28	1.16

Results obtained from TGA and DSC curves indicated similarity in thermal behavior of raspberry and blackberry seed flour.

Conclusion

Using MDSC, thermal events in low temperature region (MDSC curve) of seed flour have been approximately separated (reversing curve 1), suggesting that there are two independent thermal processes. Similarity of thermal behavior of blackberry and raspberry seed flours suggesting on composition resemblance of these seeds.

Acknowledgements

This work was supported by the Ministry of Education and Science of the Republic of Serbia, under the Projects No TR-31093 and TR-31055.

References

- [1] J. Parry, L. Su, J. Moore, Z. Cheng, M. Luther J.N. Rao, J-Y Wang, L. L. Yu , J. Agric. Food Chem., 2006, . 54, 3773-3778.
- [2] B. Wunderlich, Y. Jin, A. Boller, Thermochemica Acta, 1994, 283, 277-293.
- [3] Lai & Lii, TA Instruments, 1996.
- [4] M. Pyda, B. Wunderlich, Macromolecules, 2005, 38, 10472-10479.
- [5] S. B. Matiacevich, M. L. Castellion, S. B. Maldonado, M. P. Buera Thermochemica Acta, 2006, 448, 117–122.

DRYING KINETICS OF RASPBERRY

L. Pezo, S. Ostojić, S. Zlatanović,
A. Jovanović, S. Stanojlović, O. Kovačević, B. Kovačević
*Institute of General and Physical Chemistry, University of Beograd,
Studentski Trg 12, 11000 Belgrade, Serbia, latopezo@yahoo.co.uk*

Abstract

The drying kinetics of raspberry in a laboratory dryer was studied. The changes of color on raspberry's surface were determined by digital camera. *R* (red) color index frequency was calculated during the experiment. A mathematical model to predict the shrinking of geometrical bodies was proposed, assuming unidirectional drying and two-dimensional shrinkage. Thermal analysis, by means of differential scanning calorimetry (DSC) and thermogravimetry (TGA) of fresh and dried raspberries have been studied.

Introduction

Mathematical modeling is widely used in developing kinetics models to predict the mass transfer of drying process at atmospheric pressure [1]. The main objective of this study was to determine the effects of process parameters: drying air temperature, air velocity and sample surface on the diffusion model coefficients and the values of moisture diffusivity and heat transfer coefficients by using multiple regression analysis, and to test the most appropriate drying model for understanding the drying behavior of raspberry.

Materials and Methods

The raspberries (aver. diameter 11.4 mm, and aver. weight 2.9 g for single fruit), were carefully placed on the trays. The initial and final moisture contents of the products were determined at 105 °C. Raspberries of average initial moisture content 85.7% (wb), were dried, at temperatures of 50°C, relative air humidity 50-55%, at the velocities of drying air of 1.2 m/s. The kinetics models were selected with the correlation coefficient (r^2), the reduced chi-square (χ^2), mean bias error (*MBE*), root mean square error (*RMSE*) and relative standard deviation (*RSD*), to determine the quality of that fitting function [2]. Color images of raspberries during drying process were captured in triplicate, by a common home camera. All the acquired images were 24 bit RGB (16.8 millions of colors). The macro function of the digital camera has been used, to cover a scene area of approximately Ø10 cm. The dimensions of raspberries were measured by a digital micrometer. Differential scanning calorimetry (DSC) and thermogravimetry (TGA) of fresh and dried raspberries have been performed under N₂ purge flow of 50ml/min and 60ml/min respectively. DSC scans were conducted in temperature range from -90°C to 400°C, with heating rate Hr=5C°/min, and TGA scans were performed in temperature range of 25°C to 900°C with heating rate Hr=5C°/min.

Results and Discussion

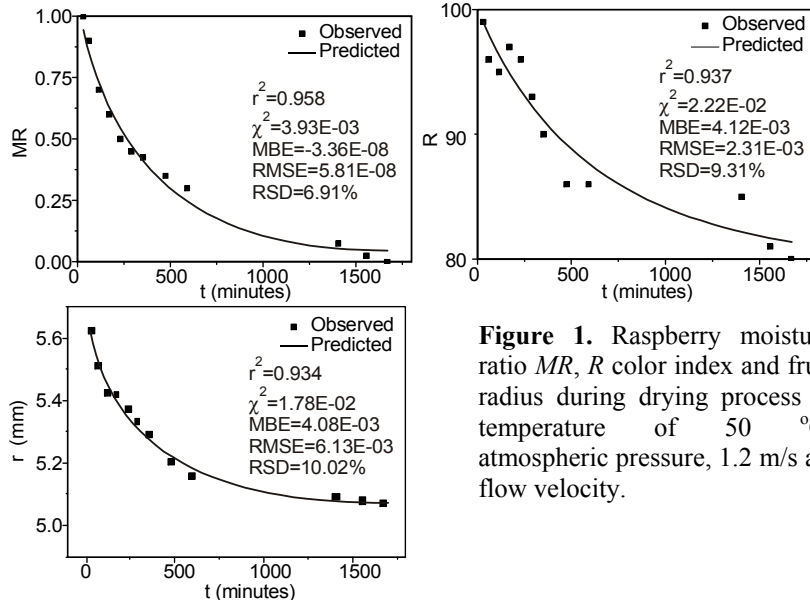


Figure 1. Raspberry moisture ratio MR , R color index and fruit radius during drying process at temperature of $50\text{ }^\circ\text{C}$, atmospheric pressure, 1.2 m/s air flow velocity.

The moisture content data at the given drying conditions fitting computations with the drying time were carried on the several drying models. The moisture ratio (MR), as well as the R color index and overall fruit diameter changes during the drying experiment are presented on Fig. 1. The best model describing the thin layer-drying characteristic was chosen as the one with the highest r^2 and the lowest χ^2 , MBE and $RMSE$. RSD should be below 15%. It was determined that the best fitting results were obtained with logarithmic model, $MR = 0.989 \cdot \exp(-0.003 \cdot t) + 0.034$. Fick's second law was used for effective diffusion calculus, using Arrhenius type relationship, in the temperature range of ($45\text{-}55^\circ\text{C}$, triplicate measurement of MR was performed for each time step). Calculated effective diffusion coefficient was $3.2E-10\text{m}^2/\text{s}$, and activation energy of 20 to 40 kJ/mol , were in accordance to literature values [3]. The best model describing the color changes characteristic was logarithmic model, $R = 19.402 \cdot \exp(-0.002 \cdot t) + 80.494$. The obtained prediction results of fruit radius correspond very well to those achieved by experimental measurement. Obtained DSC and TGA curves of fresh and dried raspberries, (Fig 2.) show differences of thermal stability between fresh and dried fruits caused by water loss during drying process [4]. It can be seen, from DSC curve that phase transition of ice melting and water evaporation are dominant thermal events, as the sample water content is high. High water content (85.7%) is also observed from corresponding TGA curve of fresh raspberries. DSC curve is characterized by three endothermic peaks with maximums at $T_{m1}=-40.7^\circ\text{C}$, $T_{m2}=-20.23\text{ }^\circ\text{C}$ and $T_{m3}=114.0^\circ\text{C}$ respectively and one glass transition $T_g=42.3\text{ }^\circ\text{C}$. Results are in agreement with [4], which showed that glass transition temperatures of raspberries are influenced by water content, [5,6], as it was found that dried food material has similar thermal properties of semi-

crystalline polymers. Water content of dried sample obtained from TGA curve, dashed curve was 19.3%.

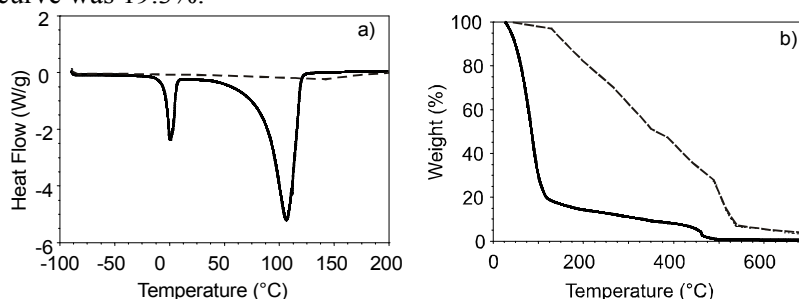


Figure 2. a) DSC curves of dried (dashed curve) and fresh (solid curve) raspberries and b) TGA curves of dried (dashed curve) and fresh (solid curve) raspberries.

Conclusion

The best model adequately describe the drying behavior of raspberry fruit, with gained r^2 of 0.937. Statistical analysis, including comparison tests, showed that the model adequately represent the browning process, showing $r^2=0.958$. Finally, a mathematical model to predict the shrinking of geometrical spherical bodies was proposed, assuming unidirectional drying and two-dimensional shrinkage with accuracy of $r^2=0.934$. Thermal analysis shows differences of thermal stability between fresh and dried fruits caused by water loss during process of drying.

Acknowledgement

The authors acknowledge for the financial support the Ministry of Science of the Republic of Serbia, TR – 31055, TR – 31093, 2011-2014.

References

- [1] A. Kaya, O. Aydın, C. Demirtas, *Biosyst Eng*, 2007, 96 (4), 517–524.
- [2] E. K. Akpınar, *J. Food Eng.*, 2006, 73, 75–84.
- [3] P. P. Lewicki, E. Jakubczyk, *J. Food Eng.*, 2004, 64, 307–314.
- [4] R. M., Syamaladevi, S. S., Sablani, J. Tang, J. Powers, B. G. Swanson, *J. Food Eng.*, 2009, 91, 460–467.
- [5] S. Shyam, S. Roopesh, R. M. Syamaladevi, B. G. Swanson, *Food Eng. Rev.*, 2010, 2, 168–203.
- [6] G. Uretir, M. Ozilgen, S. Katnas, *J. Food Eng.*, 1996, 30, 339–350.

THERMAL ANALYSIS OF OSMOTICALLY DEHYDRATED MEAT

S. Ostojić¹, S. Zlatanović¹, D. Micić¹, D.a Šuput², B. R. Simonović¹, Ljubinko
Lević²

¹ *University of Belgrade, Institute of General and Physical Chemistry, Studentski
trg 12, 11000 Belgrade, Serbia*

² *Faculty of Technology, University of Novi Sad, Bulevar Cara Lazara 1, 21000
Novi Sad, Serbia¹*

Abstract

Besides the water, proteins are the most important component of meat and this approves the relevance of studying their denaturation, particularly that of myofibrillar proteins. Water loss, obtained from thermogravimetric analysis (TGA) and protein stability, obtained from differential scanning calorimetry (DSC), expressed as temperature (T_m) and enthalpy (ΔH) of protein denaturation, during the storage was followed. Results have been compared to fresh pork meat thermal characteristics. Water activity (a_w) of fresh and dehydrated pork meat have been obtained from DSC and TGA results.

Introduction

Knowledge of thermal transitions occurring in foods during processing is essential in evaluating the parameters required for producing the highest quality [1-4]. The advantage of the DSC method is that it can be used in complex mixtures and at high concentrations of proteins, which is the situation occurring in meat. A typical curve from thermal transitions found in a muscle is composed of three major transition zones. The first transition displays its maximum between 54°C and 58°C and has been attributed to myosin [4,5] the second transition, which occurs between 65°C and 67°C, was assigned to collagen [5,6] and to sarcoplasmic proteins [2]. The third transition has been assigned to actin and is found between 80°C and 83°C [6]. For the second transition it has also been shown that both isolated actomyosin and myosin and its sub-units undergo transitions in the same temperature range [2]. The aim of this study was to follow thermal stability and water content in osmotically dehydrated meat samples during two months storage.

Experimental

Osmotic dehydration. Pork meat was osmotically dehydrated (OD) in the solution of sugar beet molasses [7], packed in modified atmosphere (30% CO₂ - 70% N₂) and stored for 2 months under the refrigerator temperature (4°C).

Thermal analysis. DSC and TGA of fresh and osmotically dried pork meat have been performed on TA Instruments DSC Q 1000, and TGA measurements on TA Instruments TGA Q 500, under N₂ purge flow of 50ml/min and 60ml/min respectively. DSC scans were conducted in temperature range 3°C -150 °C, and - 80 °C - 180°C heating rate, Hr=5C°/min, and TGA scans in temperature range 25°C-900°C, Hr=5C°/min.

Results and Discussion

Thermal behavior of pork meat samples is shown in Figures 1, 2, 3, and 4. Fig. 1 is a DSC curve of fresh pork meat with peaks at about -0.3°C , 69°C and 93°C , and total denaturation enthalpy of 970J/g .

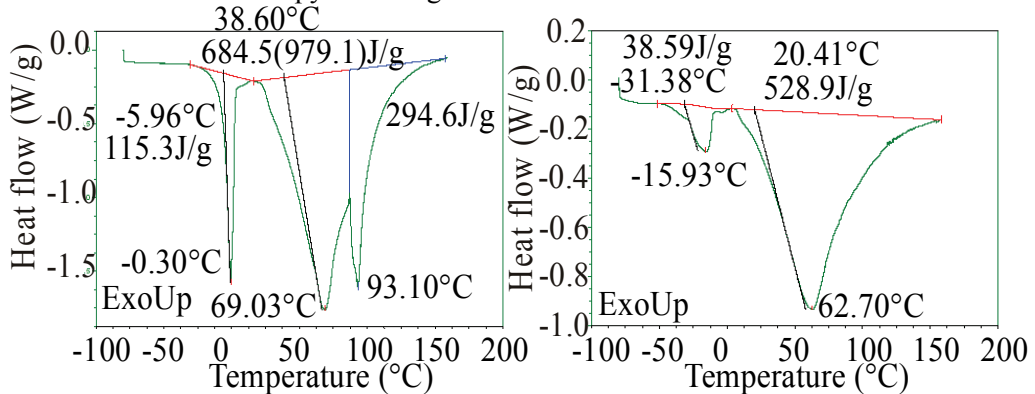


Figure 1. DSC curve fresh pork. meat.

Figure 2. DSC curve of OD pork meat.

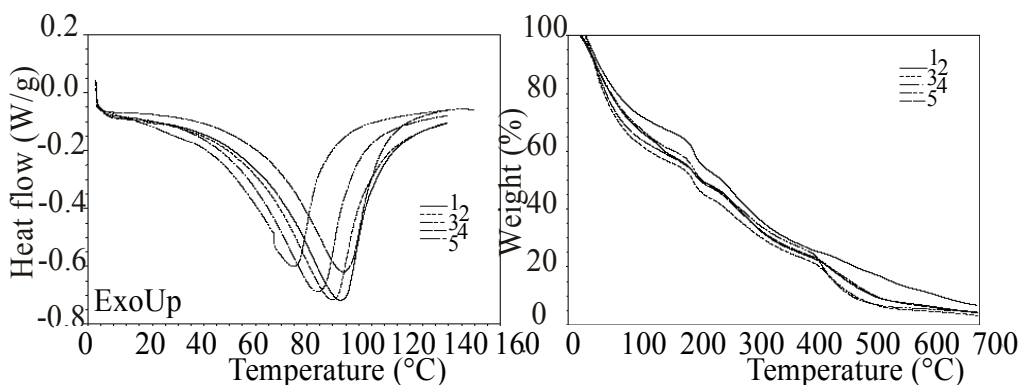


Figure 3. DSC curves of OD pork meat: 1) 7 days, 2) 15 days, 3) 30 days, 4) 45 days 5) 60 days of storage.

Figure 4. TGA curves of OD pork meat: 1) 7 days, 2) 15 days, 3) 30 days, 4) 45 days 5) 60 days of storage.

First transition corresponds to water melting, second transition, which occurs at 69°C , was assigned to collagen [6] and the third transition has been assigned to actin [5]. On Fig. 2. is DSC curve of osmotically dehydrated pork meat, where process of protein denaturation is presented as one broad endothermic peak with temperature maximum $T_m=57^{\circ}\text{C}$ and total denaturation enthalpy (ΔH) of 430J/g . Decreased denaturation enthalpy and temperature maximum of protein denaturation suggesting that destabilization of meat proteins and conformational changes have been induced by process of osmotic dehydration. Thermal stability of osmotically dehydrated pork meat has been followed by DSC and TGA in the storage time period of 60 days. Results are presented on Fig. 3. and 4. and Table 1

Table 1. Thermodynamic parameters of protein transitions for OD and fresh pork meat.

...Time (days)	Onset temp. T_o (°C)	Peak temp. T_m (°C)	Enth ΔH (J/g)	Moisture (%)	Residue at 700 °C (%)	Water activity a_w
0	53.26	89.30	652.3	37.70	5.65	0.745
15	59.65	95.06	668.1	43.78	4.91	0.729
30	35.36	66.81	678.5	41.66	4.76	0.722
45	59.74	79.68	716.7	34.26	4.67	0.735
60	67.16	99.05	694.3	42.27	3.93	0.742
Fresh meat	27.56	81.92	979.1	70.90	1.45	0.938

From results obtained it can be assumed that there were no changes of protein stability during storage period of 60 days, considering enthalpy of (ΔH) and temperature of denaturation (T_m). Slight variations of moisture affected the water activity (a_w) (results obtained by DSC and TGA) of osmotically dehydrated pork meat.

Conclusion

It was shown that sugar beet molasses solution affects thermal stability (DSC results), and water loss (TGA results) of dehydrated pork meat compared to fresh pork meat. No significant changes, during two months storage time have been induced concerning protein thermal stability, but there were slight changes of water content during storage (TGA) what influenced a_w .

Acknowledgements

This work is part of projects No. TR-31055 and TR-31093, supported by the Ministry of Education and Science Republic of Serbia.

References

- [1] F. Jimenez-Colmenero, S. Cofrades, J. Carballo, P. Fernandez, F. J. Fernandez-Martin, *Agric. Food Chem.*, 1998, 46, 4706-4711.
- [2] E. Tornberg, *Meat Science*, 2005, 70, 493–508.
- [3] C. Tortoe, *African Journal of Food Science*, 2010, 4, 303 – 324.
- [4] S. A. Anglea, V. Karathanos, M. Karel, *Biotechnol. Prog.*, 1993, 9, 204-208.
- [5] M. H., Stabursvik, E. M. Martens, *Journal of Texture Studies*, 1982, 13, 291–309.
- [6] E. Stabursvik, H. Martens, *J. Sci. Food Agric.*, 1980, 31, 1034–1042.
- [7] N. M. Misljenovic, G. B. Koprivica, L.L. Pezo, L. B. Levic, B.L. Curcic, V.S. Filipovic, M.R. [Nictin](#), *Thermal Science*, 2012, 16, 43-52 .

Q-06-P

EFFICIENCY OF OSMOTIC DEHYDRATION OF PORK MEAT USING DIFFERENT OSMOTIC SOLUTIONS

L. L. Pezo¹, V. S. Filipović², M. R. Nićetin², B. Lj. Ćurčić²,
N. M. Mišljenović², G. Koprivica², Lj. B. Lević²

¹University of Beograd, Institute of General and Physical Chemistry, Studentski trg 12-16, 11000 Belgrade, Serbia, ²University of Novi Sad, Faculty of Technology, 21000 Novi Sad, Bulevar cara Lazara 1, Serbia

Abstract

In order to analyze the efficiency of mass transfer kinetics during osmotic dehydration (OD), pork meat was dehydrated in three different osmotic solutions (sugar beet molasses, ternary solution and combination of these solutions in a 1:1 ratio) under atmospheric pressure, at room temperature T (20°C), with manual stirring on every 15 minutes. The most significant kinetic parameters of the process: water loss (WL) and solid gain (SG), were determined after 1, 3 or 5 hours of dehydration.

Introduction

OD process as an important method for preserving solid food, which involves partial water removal from food stuff immersed in hypertonic aqueous solutions. Due to low energy consumption and mild temperatures, which is considered minimal processing, OD is suitable as a pretreatment for many processes, to improve nutritional, sensorial and functional properties of food without changing its integrity. The difference in the chemical potential of water between the raw material and the osmotic medium is the driving force for dehydration. Osmotic temperature, concentration of osmotic solution and immersing time are the most important variables in osmotic process. Increasing the osmotic solution concentration induces an increase in the mass transfer [1].

Materials and methods

Initial moisture content of the fresh meat was $74.64 \pm 0.48\%$. Three different solutions were used as hypertonic mediums. Solution 1, ternary osmotic solution, was made from sucrose in the quantity of 1.200g/kg water, NaCl in the quantity of 350g/kg water and distilled water. Solution 2 was combination of the first and third in ratio 1:1. Solution 3, sugar beet molasses, with initial dry matter content of 80.00%, was obtained from the sugar factory Pećinci. The material to solution ratio was 1:5 (w/w). Samples from all three solutions after 1, 3 and 5h were taken out to be lightly washed and gently blotted, to remove excess water. Dry matter content of the fresh and treated samples was determined by drying at 105°C for 24h in a heat chamber until constant weight. Three key process variables were measured: moisture content, change in weight and change in the soluble solids. Using these values, WL and SG were calculated, [2,3].

Results and discussion

The Response surface method was performed to determine the optimum osmotic dehydration conditions for pork meat cubes OD process. Table 1 shows the ANOVA calculation regarding the response models developed when the experimental data fitted (second order polynomial – SOP model), for all the dependent variables.

Table 1. Analysis of variance for the responses, for all solutions.

Term	Source	Sum of squares					
		Solution 1		Solution 2		Solution 3	
		<i>WL</i>	<i>SG</i>	<i>WL</i>	<i>SG</i>	<i>WL</i>	<i>SG</i>
Linear	Time	0.160*	0.011*	0.089*	0.008*	0.037*	0.006*
	Temp	0.056*	0.008*	0.033*	0.001*	0.009*	0.001*
	Conc	0.006*	0.000	0.042*	0.000	0.001*	0.000
Quad.	Time	0.016*	0.001*	0.008*	0.000	0.011*	0.001*
	Temp	0.001*	0.000	0.000	0.000	0.001*	0.000
	Conc	0.000	0.001*	0.000	0.000	0.000	0.000
Cross product	Time Temp	0.001*	0.000	0.000	0.000	0.001*	0.000
	Time Conc	0.003*	0.000	0.002*	0.000	0.002*	0.000
	Temp Conc	0.003*	0.001*	0.001*	0.000	0.003*	0.000
Error	Error	0.002	0.001	0.001	0.001	0.002	0.001
r^2		99.1	95.7	99.2	88.3	98.8	94.4

*Significant at 95% confidence level

ANOVA revealed that the linear terms contributed substantially in most of the cases to generate a significant SOP model. The linear terms of SOP model were found significant, at 95% confidence level, and their influence were found most important in all model calculation. *WL* was significantly affected by all process variables, treatment time, temperature, and concentration, at 95% confidence level, for all osmotic solutions. The main influential variable seems to be the treatment time, while temperature and concentration terms are also very statistically significant at 95% confidence level. *SG* is most affected by treatment time, and temperature terms are also significant at 95% confidence level. All SOP models had insignificant lack of fit tests, and r^2 values for all solutions *WL* (98.8-99.2) and *SG* (88.3-95.7) were found very satisfactory and showed the good fitting of the model to experimental results. The contour plots of *WL* and *SG*, were superimposed to ascertain the optimum osmotic dehydration conditions for pork meat cubes, for all solutions used in the experiment (Fig. 1). An optimum operating area was derived and crosshatched and point A was deduced by approximating the optimum position in obtained area on graph. The optimum OD conditions for solution 1 are as follows: soaking time 4 h, concentration and temperature of 72% and 45°C. The optimum OD conditions for solution 2 should be: treatment time 3 h, concentration 57% w/w, and temperature of 40°C. Coordinates of optimized point for temperature, time concentration graph, for

Q-06-P

solution 3 were: 40°C, 3.7 h and 63% w/w. Contour plots (shown on Fig. 1) of both WL and SG tend to grow with temperature and processing time. The desired responses for the optimum drying conditions in solution 1 were: $WL=0.53$, $SG=0.15$. WL was much lesser for OD process in solution 2 and solution 3: 0.41 and 0.45. SG was very similar to OD in solution 1.

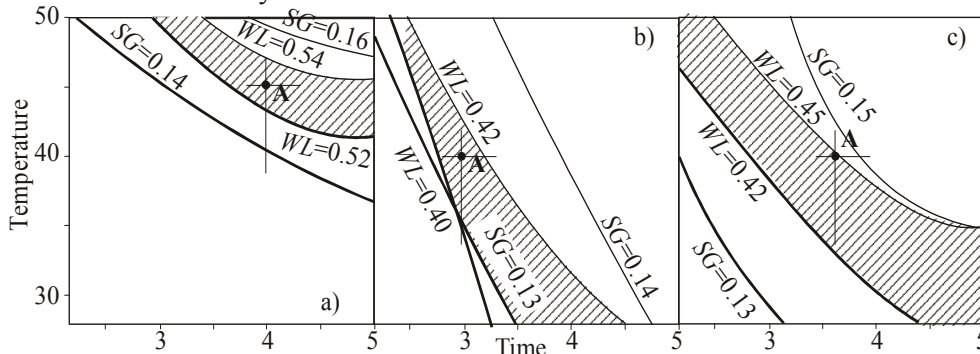


Figure 1. Optimum contour plots of the system responses for a) solution 1, b) solution 2, c) solution 3.

Conclusion

According to presented results it can be concluded that all three solutions are satisfying osmotic mediums. At the end of treatment SG were the lowest in samples immersed in solutions 1 and 2. While, the best results considering WL were achieved using solution 1. During OD of pork meat, in all three osmotic solutions, water removing process was most intensive at the beginning and after 3 hours had tendency of slowing down, and can be limited to 3 hours.

Acknowledgement

These results are part of project supported by the Ministry of Education and Science of the Republic of Serbia, TR-31055, 2011-2014.

References

- [1] M.A.C. Silva, Z.E.Silva, V.C. Mariani, S. Darche, Food Sci. Technol. Int., 2012, 45, 246-252.
- [2] G. Koprivca, N. Mišljenović, Lj. Lević, L. Jevrić, Journal on Processing and Energy in Agriculture, 2010, 14, 27-31.
- [3] N. Mišljenović, G. Koprivca, L. Pezo, T. Kuljanin, M. Bodroža Solarov, B. Filipčev, APTEFF, 2011, 42, 91-100.

APPLICATION OF RESPONSE SURFACE METHOD ON PORK MEAT OSMOTIC DEHYDRATATION

L. L. Pezo¹, B. Lj. Ćurčić², M. R. Nićetin², V. S. Filipović², G. B. Koprivica², N. M. Mišljenović², Lj. B. Lević²

¹University of Beograd, Institute of General and Physical Chemistry, Studentski trg 12-16, 11000 Belgrade, Serbia, ²University of Novi Sad, Faculty of Technology, 21000 Novi Sad, Bulevar cara Lazara 1, Serbia

Abstract

The main objective of here presented article was to examine the influence of different osmotic parameters on the mass transfer kinetics during osmotic treatment of pork meat cubes (*M. triceps brachii*), shaped 1x1x1cm, under atmospheric pressure. The observed parameters included: osmotic solution temperature (20, 35 and 50°C), immersion time (1, 3 and 5 hours) and sugar beet molasses concentration (60, 70 and 80% w/w). The system's response parameters observed were: water loss (WL), solid gain (SG), final dry matter content (DM) and water activity (a_w). The optimization of process parameters was obtained, using response surface methodology (RSM).

Key words: Osmotic dehydration, pork meat, sugar beet molasses, Response surface method

Introduction

Meat represents a cellular system with great biochemical and structural complexity, created by a network of muscular fibers surrounded by connective tissue. One of the most important constituent of meat is water [1, 2]. Physicochemical, sensory and technological properties of fresh meat are related with water content. Water is held in myofibrils, functional proteins of meat, but also it may exist in the intracellular space between myofibrils and sarcoplasm [3]. One of the potential preservation techniques for producing products with low water content and improved nutritional, sensorial and functional properties is osmotic dehydration (OD). In OD process, mass transfer is caused by a difference in osmotic pressure: water outflow from product to solution, solute transfer from solution into the product, and leaching out of the products own solutes [4]. Sugar beet molasses is known as an excellent medium for OD, primarily due to the high dry matter (80%) and specific nutrient content. [4].

Materials and methods

Pork meat was purchased at the butcher shop "Mesara Štrand" in Novi Sad, just before use. Initial moisture content of the fresh meat was 72.83%. Sugar beet molasses solution, with initial dry matter content of 85.04%, was obtained from the sugar factory Pećinci. Distilled water was used for dilution of solutions. The sample to solution ratio was 1:5 (w/w). The process was performed in laboratory jars at solution different temperature with manual agitation on every 15 minutes. After OD, the samples were taken out from

Q-07-P

osmotic solutions to be lightly washed with water and gently blotted to remove excessive water. Dry matter content was determined by drying the material at 105 °C in a heat chamber until constant mass was achieved (Instrumentaria Sutjeska). Water activity (a_w) of the OD samples was measured using TESTO 650, with an accuracy of ± 0.001 at 25°C. Soluble solids content of the molasses solutions was measured using Abbe refractometer, at 20 °C. In order to describe the mass transfer kinetics of the OD, experimental data from three key process variables are usually obtained: moisture content, change in weight and change in the soluble solids. Using these, WL, SG, were calculated for different solutions and processing times [4]. Process variables were coded, according to central composite full factorial design (3 level-3 parameter) with 27 runs (1 block) [5]. RSM was selected to estimate the main effect of the process variables on mass transfer variables, during the OD.

Results and Discussion

The most intensive increase in dry matter content was observed as the increase from initial 27.17 to 71.11 % in sugar beet molasses solution, concentrated to 80% w/w, after 5 hours of experiment. The huge difference in osmotic pressure between hypertonic solution and the meat tissue, causes the vast initial loss of the water at the beginning of the dehydration process, and the WL increased with immersion time. The maximum WL was 0.58, after 5 hours, at maximum concentrations. SG increases with immersion time. The aim of OD is the achievement of as low as possible solid uptake, and the most acceptable results were achieved by using sugar beet molasses concentrated to 80% w/w (0.17 g/g i.s.w.), after 3 hours of osmotic process. During the OD process, total mass of the meat samples was evidently reduced. It was shown that weight reduction ($WR=WL-SG$) is most intensive in the first hour of the process, while at the end of the process, weight reduction value decreased. To determine optimal condition for the WL/SG ratio must be considered. High value of WL/SG ratio is the most important indicator of the effectiveness of OD treatment. The highest value of WL/SG ratio was 3.64, achieved by immersion of meat for 3 hours in sugar beet molasses 70% concentration, at 20°C. The second order polynomials (SOP) were used to predict the system responses. ANOVA calculation regarding the response models developed was used to evaluate the fitting with experimental data. The analysis revealed that the linear terms contributed substantially in all of the cases to generate a significant SOP model, at 95% confidence level, and their influence were found most important in all model calculation. The SOP models for all variables were found to be statistically significant and the response surfaces were fitted to these models. The r^2 values for WL (99.1), SG (95.7), a_w (93.0) and DM (99.3), were found very satisfactory and showed the good fitting of the model to experimental results. Fig. 1 shows the superimposed graph of the dehydration conditions of pork meat in sugar beet molasses solution. An optimum operating area was derived and crosshatched and point A was deduced by approximating the optimum position in obtained area on graph.

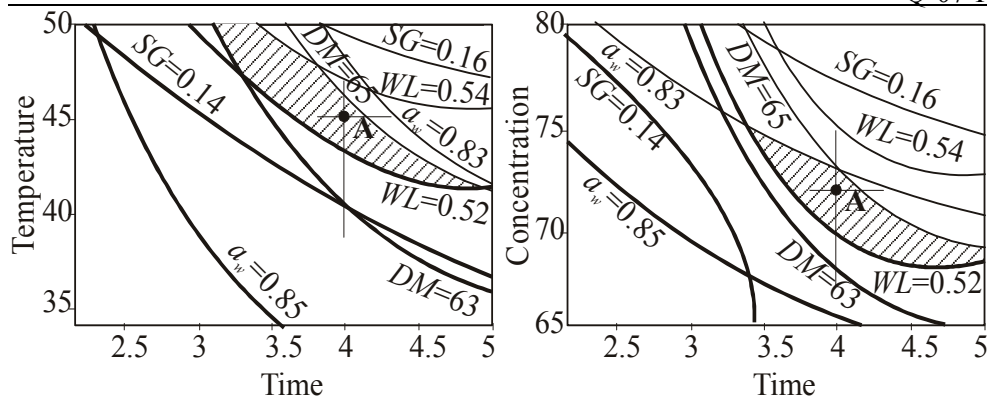


Figure 1. Optimum contour plots of the system responses.

Conclusion

The optimum dehydration process parameters were found by superimposition of the contour plots of all responses. Optimum process parameters, for OD in sugar beet molasses solution were: osmotic time of 4 h, molasses solution concentration of 72% and temperature of 45°C. The predicted responses for the optimum drying conditions in sugar beet molasses solution were: DM of 64.5%, WL in the close vicinity of 0.53, SG about 0.15 and a_w in the range of 0.83 to 0.84. During OD of meat, water removing process was most intensive at the beginning and after 3h had tendency of stabilization. The use of sugar beet molasses as osmotic agent is economy and environmentally reasonable considering that molasses is a side product of sugar industry.

Acknowledgement

These results are part of project supported by the Ministry of Science and Technological Development of the Republic of Serbia, TR-31055, 2011-2014.

References

- [1] M. Castro-Giraldez, P. Fito, J. Food Eng., 2010, 99, 24-30.
- [2] E. Puolanne, M. Halonen, Meat Sci., 2010, 86, 151-165.
- [3] J. Barat, M. Alino, A. Fuentes, R. Grau, J. B. Romero, J. Food Eng., 2009, 93, 108-113.
- [4] G. Koprivca, N. Mišljenović, Lj. Lević, L. Jevrić, Journal on Processing and Energy in Agriculture, 2010, 14, 27-31.
- [5] G.E. P. Box, D. W. Behnken Technometrics, 1960, 2, 455-475.

Q-08-P

MACRO ELEMENTS COMPOSITION OF THE OSMOTICALLY DEHYDRATED PORK MEAT IN SUGAR BEET MOLASSES SOLUTION

S. Zlatanović¹, O. A. Kovačević¹, S. Ostojić¹,
B. P. Dojčinović², M. Pavlović¹ and D. Šuput³

¹ *University of Belgrade, Institute of General and Physical Chemistry, Studentski
Trg 12, 11000 Belgrade, Serbia,*

² *University of Belgrade, Institute of Chemistry, Technology and Metallurgy,
Studentski trg 12-16, 11000 Belgrade, Serbia,*

³ *University of Novi Sad, Faculty of Technology, Bulevar Cara Lazara 1, 21000
Novi Sad, Serbia*

Abstract

An important advantage of sugar beet molasses, which is medium for osmotic dehydration, is enrichment of the food material in minerals and vitamins, which penetrate from molasses into the meat tissue. Macro elements composition of the raw pork meat and osmotic dehydrated pork meat in the solution of sugar beet molasses were investigated. The combination of thermal treatment at 350 °C, and wet acid treatment at 160 °C was used for samples preparation. Detection of elements present in the corresponding solutions was performed by ICP-OES. Results suggests that sugar beet molasses solution affects treated pork meat samples concerning concentration of macro elements. Content of macro elements in the osmotic dehydrated pork meat, compared to the content obtained for the raw pork meat, shows a significant increase of the content of Na, K and Ca cations for 5.5, 4 and 13 times, respectively. Comparing the values of Mg content in the dehydrated and raw pork, significant changes were not found.

Introduction

Sugar beet molasses (SBM) is medium for osmotic dehydration (OD), primarily due to the high dry matter (80%) and specific nutrient content.[1] Minerals and vitamins from sugar beet molasses, as hypertonic solution, penetrate from SBM into the meat tissue and enrichments the food material. Pork meat has a high content of Na, K, Ca and Mg, and variation in macro elements content is mainly determined by food processing. [1-4] In this work, following changes in the content of macro elements, we examined the influence of sugar beet molasses on pork meat in the process of osmotic dehydration.

Experimental

Dry matter content of the samples was determined at 105 °C in a laboratory oven until constant mass was achieved. The combination of thermal treatment at 350 °C, and wet acidic treatment at 160 °C was used for samples preparation. The dry samples were processed for minerals determination by wet digestion, where ca. 5 g

each, were weighed exactly to four decimal places, and transferred to vessels, into which 4.5 ml 65% HNO₃ and 10.5 ml 35% HCl were added. The treatments were repeated to obtain the white sediments that were dissolved in 0.07 M HNO₃. The content of metals present in the corresponding solutions was determined by inductively coupled plasma optic emission spectrometry (ICP-OES). ICP-OES measurement was performed using Thermo Scientific ICAP 6500 Duo ICP (Thermo Fisher Scientific, Cambridge, United Kingdom) spectrometer equipped with RACID86 Charge Injector Device (CID) detector, standard glass concentric nebulizer, quartz torch, and alumina injector. Samples were analyzed in triplicate.

Results

Result of processing the pork meat with the SBM in osmotic dehydration is enriched meat with amended nutritional characteristics. Contents of macro elements, Na, K, Ca and Mg, in SBM before and after osmotic dehydration, raw pork meat, and OD pork meat, were presented in Tab. 1.

Table 1. The content of macro elements in SBM, pork meat and osmotically dehydrated (OD) pork meat, determined by ICP-OES.

Sample	W 105 °C (%)	Na (mg/100 g)	K (mg/100 g)	Ca (mg/100 g)	Mg (mg/100 g)
Sugar beet molasses, before OD	20.73±0.64	749±21	1939±9	289±3	37.9±0.7
Sugar beet molasses, after OD	26.79±0.78	689±7	1731±12	268±6	35.9±0.7
Pork meat.	72.71±0.54	62±1	250±9	6.3±0.3	29.1±0.6
OD pork meat	43.69±0.15	342±10	988±6	89±1	37.8±0.8

From the standpoint of materials analysis, SBM is a very specific material. Selection of appropriate mineral extraction procedure is not an easy task. During the preparation of material, selection and implementation of procedure, and inhomogeneity of the samples, are the main reasons for results dissipation. The results obtained, with relative standard deviations below 5%, enable reliable observation of changes in the macro elements composition in all materials during OD. Comparison of macro elements content between SBM and fresh meat shows significantly higher levels of Na, K and Ca in SBM, which was not the case with Mg content. OD pork meat has a significant increase in the content of Na, K and Ca cations with respect to the content obtained for the raw pork meat for 5.5, 4 and 13 times, respectively. The content of Mg cation in the OD pork meat is slightly raised and reaches a value as in the SBM.

Conclusion

Accurate values for the mineral content of raw and OD meat are thus of special importance as relatively small errors may affect results of dietary surveys and intake estimates to a great extent. Influence of molasses on pork meat in the process of osmotic dehydration was investigated. For this purpose, the contents of macro elements in sugar beet molasses, pork meat and osmotic dehydrated pork meat were determined in the prepared solution by ICP-OES. The results show that sugar beet molasses significantly influence the content of macro elements in pork meat treated in osmotic dehydration process. At the same time, the content of Mg cation is only slightly increased reaching a value of molasses. This work is part of the optimising of the technological process of osmotic dehydration of meat in sugar beat molasses. Findings in this work provide fundamental data for improvement, control and optimising of the technological process (osmotic dehydration) in order to produce nutritionally valuable products.

Acknowledgements

This work was supported by the Ministry of Education and Science of the Republic of Serbia, under the Project No TR-31055 and TR-31093.

References

- [1] B. Filipčev, Lj. Lević, M. Bodroža-Solarov, N. Mišljenović, G.Koprivica, *Int. J. Food Prop.*, 2010,13, 1035-1053.
- [2] M. Della Rosa, F. Giroux, *J. Food Eng.* , 2001, 49, 223-236.
- [3] M A. C. Silva, Z. E. Silva , V. C. Mariani, S. Darche, *Food Sci. Technol. Int.*, 2012, 45, 246-252.
- [4] N. M. Mišljenović, G. B. Koprivica, L. L. Pezo, L. B. Lević, B. L. Ćurčić, V. S. Filipović, M. R. Nićetin, *Thermal Science*, 2012, 16, 43-52.

THE POTENTIAL ANTIMICROBIAL EFFECT OF *Lactobacillus plantarum* IN OSMOTICALLY DEHYDRATED PORK MEAT

M. D. Pavlović¹, M. M. Mandić², D. S. Mitić-Culafić²

¹*Institute of General and Physical Chemistry, University of Belgrade
Studentski Trg 12, Serbia*

²*University of Belgrade – Faculty of Biology, Chair for microbiology,
Studentski Trg 16, Belgrade, Serbia*

Abstract

The potential antimicrobial activity of *Lactobacillus plantarum* against nonpathogenic strain *Listeria innocua*, closely related to foodborne pathogen *Listeria monocytogenes*, as well as its antifungal capacity was investigated. 28-day study of osmotically dehydrated meat inoculated with both strains showed that *L. plantarum* and its products possess antimicrobial and antifungal effects.

Introduction

Listeria monocytogenes is one of the most virulent foodborne pathogens, dangerous and persistent bacteria, considered to be one of the most important agents of foodborne disease [1]. Nonpathogenic strain *Listeria innocua* is often used in microbiological studies as a replacement of *L. monocytogenes*, because of its similarity to pathogenic form. The empirical use of microorganisms and/or their natural products for preservation of foods (biopreservation) has been a common practice in the history of mankind. The lactic acid bacteria produce an array of antimicrobial substances [2] and several *Lactobacillus* strains are used as starter cultures for the manufacture of fermented foods [3]. In meat, osmotically dehydrated in sugar beet molasses, *L. innocua* and *Lactobacillus plantarum* were inoculated with aim to investigate the potential antimicrobial activity of *L. plantarum* and its products on *L. innocua*, used as nonpathogenic surrogate of foodborne pathogen *L. monocytogenes*.

Experimental

The sample of osmotically dehydrated meat was split into four portions: control, portion inoculated with *L. plantarum*, portion inoculated with *L. innocua* overnight culture and portion inoculated with both cultures in 1:1 ratio. The working cultures were prepared from frozen permanents by overnight incubation (37°C) in brain heart infusion (BHI) broth. Portions of inoculated meat were stored at 4°C. The number of bacteria in each portion was determined on the first, 7th, 14th and 28th day of inoculation, for *L. innocua* on BHI agar and de Man, Rogosa and Sharpe (MRS) medium for *L. plantarum*.

Q-09-P

Antimicrobial activity of *L. plantarum* was assessed by the agar-well diffusion method. Briefly, 7 ml of heated top agar was inoculated with 70 µl of an overnight culture of *L. innocua* and poured into a Petri dish. Wells in agar were filled with 50 µl of an overnight culture of *L. plantarum* and its concentrated culture filtrate, respectively. The plates were incubated at 37°C for 24h. After 24h, the diameter of the inhibition zone was observed. For determination of yeasts and moulds, on the 28th day of inoculation, 10-6 dilutions of each sample were plated onto Sabouraud agar plates supplemented with streptomycin (0.5 mg/ml)

Results and discussion

The number of bacteria in samples increased regularly during observed period of 28 days after inoculation. The number of *L. innocua* was increasing until the 14th day. After 14 days the number of *L. innocua* the decreased. In the mixed cultures (*L. plantarum* and *L. innocua*) number of *L. plantarum* colonies increased regularly, but the number of *L. innocua* colonies was significantly lower (Table 1.). Based on the results of the experiment, we presume that *L. plantarum* is better adjusted in competition for nutrients in medium than *L. innocua*.

Table 1. The growth of *L. plantarum* and *L. innocua* on osmotically dehydrated meat.

Day	Control	<i>L. innocua</i>	<i>L. plantarum</i>	<i>L. innocua</i> + <i>L. plantarum</i>	
1	0	2.6x10 ⁴	8.7x10 ³	1.4x10 ⁴	9.3x10 ³
7	yeasts	1.5x10 ⁴	1.5x10 ⁴	5.7x10 ³	2.2x10 ³
14	yeasts	1.1x10 ⁴	5x10 ⁵	1.0x10 ³	1.2x10 ⁵
28	yeasts	n.d.	5.5x10 ⁶	n.d.	n.d.

n.d. not detected

Agar-well diffusion method was used to show that products of *L. plantarum* have certain antimicrobial effect. The largest zone of inhibition was found around well with pure overnight culture of *L. plantarum* (Fig. 1.). Antimicrobial products of *L. plantarum* obtained after filtration of overnight culture (0.45 µm), exhibited lower antimicrobial effect compared to overnight culture. The results of this study showed that *L. plantarum* and its products have antimicrobial effect on nonpathogenic species *L. innocua* and potential antimicrobial effect on closely related foodborne pathogens such as *L. monocytogenes*.

The highest number of yeasts and moulds was identified in control samples. Conversely, the lowest number of yeasts and moulds was found on the plates with mixed cultures of *L. plantarum* and *L. innocua* (data not shown). The decreased growth of yeasts and moulds in the presence of individual and mixed cultures of *L. plantarum* and *L. innocua* pointed the antifungal capacity of these strains.



Fig. 2. Results of agar-well diffusion method (1 – pure overnight culture of *L. plantarum*; 2,3,4 – *L. plantarum* culture filtrates).

Antimicrobial substances certainly do have potential in food applications when used under the proper conditions. Since lactic acid bacteria are commonly found in meat, bacteriocins produced by the tested bacteria have been isolated and explored for the potential use in meat dehydration process.

Conclusion

The potential of using bacteriocins of lactic acid bacteria, primarily used as biopreservatives, represents a perspective, alternative antimicrobial strategy against the continuously increasing problem of antibiotic resistance. The further investigation is needed to isolate and characterize the substances with antimicrobial and antifungal capacity.

Acknowledgement

This work was supported by the Ministry of Education and Science TR 31055.

References

- [1] V. Křepelková, R. Sovják, *Agricultura Tropica et Subtropica*, 2011, 44, 4.
- [2] A. Gálvez, H. Abriouel, R. L. López, N. B. Omar, *International Journal of Food Microbiology*, 2007, 120, 51-70.
- [3] A. Mami, J. E. Henni, M. Kihal, *World Journal of Dairy & Food Sciences*, 2008, 3, 39-49.

Q-10-P

EVALUATION OF TBA METHODS FOR ASSESSING LIPID OXIDATION IN MEAT DEHYDRATED IN MOLASSES

M. D. Pavlović¹, D. Z. Šuput², M. M. Mandić³,
A. P. Jovanović¹, D. S. Mitić-Ćulafić³

¹University of Belgrade, Institute of General and Physical Chemistry, Studentski Trg 12,
Belgrade, Serbia

²University of Novi Sad, Faculty of Technology, Bulevar Cara Lazara 1, Novi Sad, Serbia

³University of Belgrade, Faculty of Biology, Studentski Trg 16, Belgrade, Serbia

Abstract

The effectiveness of different thiobarbituric acid (TBA) methods for measurement of secondary lipid oxidation products was evaluated on pork meat, dehydrated in sugar beet molasses and stored for 105 days at 4°C, under modified atmosphere conditions. Aqueous-acid-extraction TBA method (EM), under different conditions of incubation, and steam distillation TBA method (DM) were tested and low TBA values were obtained in all procedures. Primary lipid oxidation products were also low, except for microbiologically contaminated sample with increased water activity value. TBA-EM may be the inadequate method for the analysis of oxidative stability of meat dehydrated in molasses, due to interferences from molasses which cause erroneously high absorbance at 532 nm.

Introduction

Free fatty acids (FFA), peroxide values (PV) and thiobarbituric acid-reactive substances (TBA-RS) have been most commonly used determinants of the degree of lipid oxidation in meat. Malondialdehyde (MDA), a secondary oxidation product of polyunsaturated fatty acids with three or more double bonds, reacts with TBA to form a stable chromophore with maximal absorbance at 532 nm. High level of sucrose (44-54%), other sugars and their degradation products in molasses [1], used for osmotic dehydration of meat, could generate interfering yellow chromagen overlapping the pink peak of TBA-MDA adduct [2]. The interferences from sucrose can be reduced by incubating TBA and MDA at temperatures lower than 50°C, while the reaction time can be reduced by increasing the concentration of TBA [3]. Modified aqueous-acid-extraction method was used to measure MDA in the presence of sucrose in meat [3]. The effectiveness of different TBA methods [3][4], was evaluated and compared with other lipid oxidation determinants (PV, FFA).

Experimental

Osmotically dehydrated (OD) pork meat (with approximately 10% sucrose), packed under modified atmosphere (MAP) (30% CO₂ : 70% N₂) was stored at 4 ± 0.5 °C for 105 days. Water content of the samples was determined according to [5]. Water activity (a_w) was measured using TESTO 650 (Germany) at 25°C. pH was determined according to [6]. Acid value (FFA) was measured after cold lipid

extraction of samples, according to [7]. Peroxide value (PV) was measured after cold lipid extraction of samples, according to [8]. Secondary lipid oxidation products were determined using EM-TBA [3], and DM-TBA [4] and expressed in TBA-RS. The incubation conditions in EM-TBA were: A) 100°C/25 min with 20 mM TBA, B) 40°C/70 min, with 80 mM TBA and C) 20 °C/20 h with 20 mM TBA. D) DM-TBA. MicroSoft Excel software (MicroSoft Office 2003) was used for statistical analyses. All measurements were performed in triplicate.

Results and Discussion

Dehydration in sugar beet molasses solution caused a significant moisture loss in meat samples, from $75.957 \pm 0.045\%$, before OD, to $40.433 \pm 0.244\%$, after OD, during 105 days of observation. The a_w values decreased with the osmotic treatment from 0.938 ± 0.002 to 0.872 ± 0.002 . During storage a_w values raised to 0.894 ± 0.001 . pH values of OD meat decreased from 6.693 ± 0.11 to 6.387 ± 0.006 and then increased to pH to 6.98 ± 0.004 . The concentration of free fatty acids remained low, in the range of 17.64 ± 0.5 to 22.3 ± 0.54 mg KOH/g of sample (0.049-0.63 % FFA). Peroxide values were also low (PV=0), except for microbiologically contaminated sample with PV=12.98 mg O₂/kg. It is well established that microbial metabolism could influence, both negatively and positively the production of lipid peroxides and carbonyl compounds in infected meat [9].

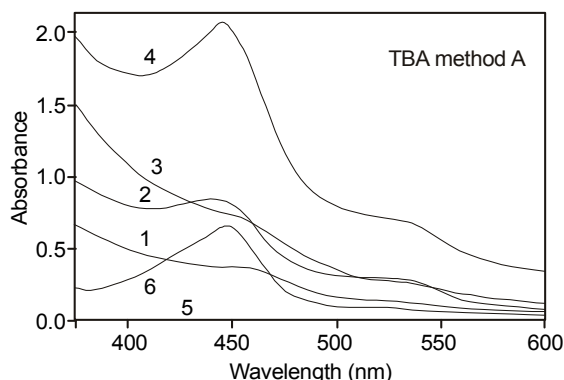


Figure 1. Scans of molasses and sucrose absorbance in TBA method A (TBA-EM, 100°C/25 min, 20 mM TBA). Scans: 1) 10% molasses, before TBA test; 2) 10% molasses, after TBA test; 3) 20% molasses, before TBA test; 4) 20% molasses after TBA test; 5) 10% sucrose before TBA test; 6) 10% sucrose after TBA test.

The effectiveness of different TBA tests in minimizing the interferences of sugar molasses, used as osmotic solution, was measured by EM-TBA under different conditions of incubation (A, B and C). Interferences, which cause erroneously high value of TBA-RS in meat samples dehydrated in molasses, were detected as absorption at 350 nm, 450-460 nm, and 532 nm. The reaction of molasses (Fig. 1, scan 2 and 4) and sucrose (Fig. 1, scan 6) with TBA was dependent on concentration and maximal at 100°C, and diminished when the incubation temperature was decreased to 40°C, (data not shown). The oscillations in TBA-RS, obtained in DM-TBA, (Fig. 2. D.) and EM-TBA-A (Fig. 2. B.) compared to EM-TBA-B (Fig. 2. B.), are also suggestive of interferences from molasses (i.e. difference in molasses content in meat samples). The low TBA values, obtained in

Q-10-P

all TBA procedures may be due to the low level of lipid oxidation. It is also possible that MDA, produced in dehydrated meat, is in volatile chelated form, because of the absence of water, and, therefore, not being held in meat [2].

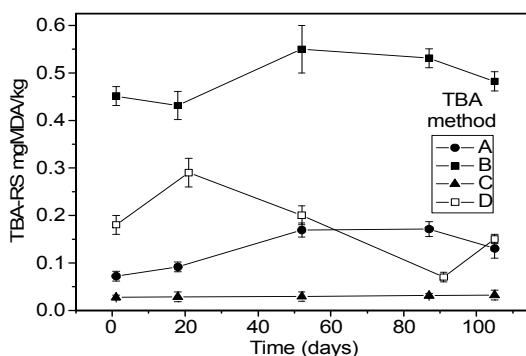


Figure 2. TBA-RS kinetics at 4°C, during storage of pork meat dehydrated in molasses and packed in MAP. TBA method: A) TBA-EM, 100°C/25 min, 20 mM TBA, B) TBA-EM, 40°C/70 min, 80 mM TBA, C) TBA-EM, 20°C/20 h, 20 mM TBA, D) TBA-DM, steam distillation

Conclusion

The effectiveness of different conditions of incubation in minimizing the interferences of molasses ingredients was measured by aqueous acid extraction method and distillation TBA method. Low TBA values were obtained in all TBA procedures. Primary lipid oxidation products were, also, low, except in microbiologically contaminated sample with increased water activity value, where elevated peroxide values was obtained. Low PV and TBA values in all analyzed methods are indicative of low lipid oxidation in OD pork meat under storage in modified atmosphere and 4°C or loss of MDA from dehydrated meat.

Acknowledgement

This work was supported by the Ministry of Education and Science, Republic of Serbia, project No. TR-31055.

References

- [1] M. R. El-Gewely, *Biotechnology Annual Review*, Elsevier, 2007, 13, 315-316.
- [2] J. Fernandez, J. A. Perez-Alvarez & J. A. Fernandez-Lopez, *Food Chemistry*, 1997, 59, 345-353.
- [3] B. Wang, R. D. Pace, A. P. Dessai, A. Bovell-Benjamin, B. Phillips, *Journal of Food Science*, 2002, 67, 2833-2836.
- [4] B. C. Tarladgis, A. M Pearson & L. R. Dugan, *Journal of the Science of Food and Agriculture*, 1964, 15, 602-607.
- [5] ISO 1442:1997: Meat and meat products - Determination of moisture content.
- [6] ISO 11289:1993: Heat-processed foods in hermetically sealed containers - Determination of pH.
- [7] ISO 660:1996: Animal and vegetable fats and oils - Determination of acid value and acidity.
- [8] ISO 3960:1998. Animal and vegetable fats and oils – Determination of peroxide value.
- [9] K. E. Moerckl, H. R. Ball, *J. Agric. Food Chem.*, 1979, 27, 854-859.

COMPARISON STUDY OF HISTAMINE ANALYSIS IN FISH PRODUCTS USING HPLC AND ELISA METHODS

D. Spiric, S. Stefanovic, V. Jankovic, R. Petronijevic,
D. Nikolic, S. Jankovic, B. Borovic

Institute of Meat Hygiene and Technology, Kacanskog 13, Belgrade

Abstract

Histamine is natural neurotransmitter and vital signal molecule in every organism, but it also poses significant issue in food safety, since it is involved in scombroid poisoning and histamine intolerance in humans as well as the disease known as gizzard erosion in chicken consuming fish meal. Regulatory limits are set for histamine in fish and fish products, as well as reference analytical method for its determination. The aim of this study was to compare results of histamine analysis obtained using ELISA and HPLC methods. Twenty three sample units from 71 screen positive samples obtained by ELISA method were confirmed by HPLC method, to contain elevated content of histamine. Results obtained with ELISA method and HPLC method for the same analysed samples generally showed weak linearity in comparison of results obtained ($p < 0.05$; $r = 0.86$), since ELISA results for histamine content higher than 200 mg/kg didn't show linear response.

Introduction

Histamine is a potent biogenic amine with multiple activities in the acute inflammatory and allergic responses [5]. It has many vital functions as neurotransmitter in healthy individuals in control of gastric acid secretion, mediation of vascular permeability, immunomodulation, hematopoiesis and balancing day-night rhythm [9]. Mast cells, basophiles and other cells after synthesis of histidine decarboxylase are major source of histamine in normal tissues [12]. Histamine is also well known as cause of scombroid poisoning and histamine intolerance. Fish with high levels of free histidine (e.g. *Scombroidae*), which is converted to histamine by bacterial histidine decarboxylase, are those most often implicated in scombroid poisoning [2]. Quality loss and histamine accumulation often occur after frozen fish are thawed and kept for long periods of time at room temperature before further processing. Since histamine is heat resistant, it can remain intact in canned products [7]. Action levels have been established for histamine in regulations targeting scombroid poisoning: of the nine samples, two cannot be higher than 100 mg/kg (and 200 mg/kg) levels but none can be higher than 200 mg/kg (or 400 mg/kg for enzyme matured products) [1]. This regulation also prescribes HPLC as reference method for histamine analysis in fish product. The aim of this study was to compare results of histamine analysis using commercial ELISA test kit with results obtained by HPLC method for same samples [4].

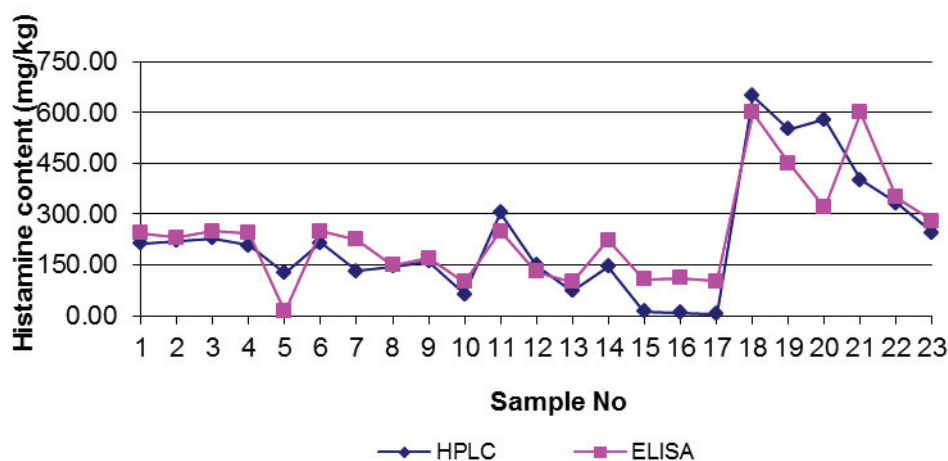
Materials and Methods

Fish samples were prepared according to the test protocol, using 0.1 M HCl and derivatization reaction. A histamine conjugate is bound on the surface of a microtiter plate. Samples and standards containing derivatized histamine and an

Q-11-P

antibody directed against histamine are given into the wells of the microtiter plate. Immobilized and free histamine compete for the antibody binding sites. After 30 minutes incubation period, the wells are washed with diluted washing solution to remove unbound material. A peroxidase conjugate directed against the histamine antibody is given into the wells and after another 30 minutes incubation, the plate is washed again. Then a substrate solution is added and incubated for 20 minutes, resulting in the development of a blue colour. The colour development is inhibited by the addition of a stop solution, and the colour turns yellow. The yellow colour is measured photometrically at 450 nm. The concentration of histamine is indirectly proportional to the colour intensity of the test sample.

Chart 1. Content of histamine in fish products



Confirmatory analysis of screen positive samples obtained by ELISA method, were performed by HPLC method [10]. After extraction with 6% trichloroacetic acid, aliquot portion was treated with 2M NaOH and histamine was derivatized by benzoyl-chloride for 30 minutes at 37°C. Derivatization reaction was terminated with saturated NaCl solution. Histamine was extracted from the aqueous phase using diethyl ether which was evaporated to dryness under nitrogen stream and dry residue was reconstituted in methanol. Extract was filtered through 0.22 µm nylon syringe filters and injected into HPLC system.

Separation was performed on Phenomenex Gemini C18 column on Waters 2695 separation module coupled with Waters 2487 UV detector at 254nm. Data acquisition and processing was performed using Empower software.

Results and Discussion

Seventy one units of fifteen samples (ten tuna cans, two samples of frozen scomber, two samples of frozen tuna and one sample of frozen herrings) were screen positive. All these samples were analysed by confirmatory HPLC method, resulting in 23 units of seven samples with high content of histamine (Chart 1).

Other samples were designed as false positive. Correlation between data was good for histamine content lower than 200 mg/kg but weaker for high histamine contamination ($p < 0.05$; $r = 0.86$).

One of the first studies on good correlation between monoclonal antibody-based immunoassays and HPLC methods for histamine analysis in food revealed good correlations between these two methods [11]. According to other authors [6] among the quantitative kits, "Histamine Food EIA" showed the best correlation with HPLC method for fish products ($R^2 = 0.9132$). Poor correlation was found between Veratox kit and HPLC method, obtained by same authors. Regarding results from wine as matrix analysed, Veratox commercial kit was compared with HPLC method and revealed a good correlation ($r = 0.91$) [8], regarding histamine content. Variations in histamine content obtained by different commercial kits are also studied [3], and it was observed that there was a strong correlation between "Veratox" and "MaxSignal" commercial kit methods, with $R^2 = 0.98$ for the data set overall.

Conclusion

Twenty three units of seven samples were confirmed by HPLC to contain high level of histamine, but seventy one units of fifteen samples (ten tuna cans, two samples of frozen scomber, two samples of frozen tuna and one sample of frozen herrings) were screen positive using ELISA commercial test kit. False positive results are due to the matrix effect, since most of the samles were canned tuna products in brine, oil and vegetable sauce, either because crossreaction with some other biogenic amine with similar antigen structure. Correlation between obtained data set was good for 23 samples, positive by both methods. Since most of the positive samples were canned fish products it is important to prevent use of spoiled fish for conserving, because unlike histamine producing bacteria, histamine is thermoresistant, and also it is very important to use sensitive enough methods for histamine analysis, that can provide results in good correlation with reference method.

Acknowledgment

Study was supported by the Ministry of Education and Science of Serbia within the Project III-46009.

Literature

- [1] COMMISSION REGULATION (EC) No 2073/2005.
- [2] J. M. Hungerford, *Toxicon*, 2010, 56, 231–243.
- [3] J. Hungerford, W.-H. Wu, *Food Control*, 2012, 25, 448-457.
- [4] Immunolab Histamine Senitive GmbH, Germany.
- [5] M. Jutel, T. Watanabe, M. Akdis, K. Blaser, C.A. Akdis, *Current Opinion in Immunology*, 2002, 14:735–740.
- [6] S. Kose et al, 2011, 125, 1490–1497.

Q-11-P

- H.-F. Kung et al, Food Control, 2009, 20, 1013–1017.
- [7] A. Marcobal C Food Research International, 2005, 38, 387–394.
- [8] L. Maintz, N. Novak , American Journal of Clinical Nutrition, 2007, 85, 1185–1196.
- [9] F. Ozogul et al, Ozogul Y., International Journal of Food and Technology, 2002, 37, 515-522.
- [10] D. Serrar et al, Food Chemistry, 1995, 54, 85-91.
- [11] E. Schneider et al, Trends in Immunology, 23, 255-263.

COMPARATIVE ANALYSIS OF THE PRESENCE OF SOYBEAN AND GLUTEN IN MEAT PRODUCTS

V. Janković, V. Matekalo Sverak, S. Lilić, B. Velebit, B. Lakićević, R. Petronijević
Institute for Meat Hygiene and Technology, Kaćanskog 13, Belgrade, Serbia

Abstract

Use of soybean and gluten in production of meat products is topical and attractive both for the producers and consumers. However, soybean and gluten belong to the group of basic allergens and thus they are potentially hazardous for consumers. Therefore, it is necessary to conduct adequate and continuous control of meat products for the presence of the above-mentioned allergens. This work gives an overview of the analysis of meat products from retail shops for the presence of soybean and gluten, using an ELISA method.

Introduction

Use of ingredients of plant origin in production of meat products is topical and attractive both for the producers and consumers. Soybean protein products are widely used in the meat industry because of their high nutritive value, favourable technological and organoleptic characteristics and low price as well [1]. Use of soybean has a favourable effect on the product quality: it increases stability of the filling, enriches the product with proteins and improves its other desirable characteristics. Wheat gluten is used in preparation of various meat and fish products because of its unique adhesive, cohesive and film forming characteristics. Gluten is very effective and it is used for binding meat chunks or trimmings together (to form steaks or chops), and it may be also applied simply by dusting meat pieces with dry gluten. It is also used as an emulsifier in producing sausages and other meat products [1].

The aim of this work was to analyse the presence of soybean and gluten in meat products using reference analytical methods – ELISA, not only because of the product quality and authenticity but also in order to protect the health of consumers.

Materials and Methods

Altogether, 100 samples of meat products from retail shops were tested. Samples were prepared according to the appropriate procedure for the specific kit, and were tested in two repeats.

To analyze meat products for the presence of soybean, the following commercial ELISA kits were used: Tepnel and Romer Lab. To detect the presence of soybean, the Tepnel Biokits Soya protein Assay kit was used, with the limit of detection of 0.5% and the quantification range of 0.7 to 14%, while the Romer Lab assay kit, AgraQuant Soy, was used for detection of allergens, with a quantification range of 40-1000 ppb.

For analysis of gluten, the internationally acknowledged and recommended method ELISA-R5 according to Mendez [2,3,6] was used. For these analyses, the

Q-12-P

Biokits-Tepnel ELISA kit has been recommended by the AOAC (The Association of Analytical Communities). In addition, the Immunolab ELISA kit was also used.

For gluten, the limit of detection by the Tepnel kit is 1 ppm, with the quantification range of 3-50 ppm (with the possibility to extend the range by additional dilution), while the limit of detection for the Immunolab Gliadin/Gluten kit is 0.3 ppm with the limit of quantification is 2 ppm.

Results and Discussion

Table 1. Presence of soybean protein and gluten in samples of retail meat products.

Type of sample	Number of samples	Number of samples with detected presence of soybean proteins	Number of samples with detected presence of gluten	Number of samples without indicated presence of allergens but with detected presence
Boiled sausage (coarse ground boiled sausages)	20	7	2	3 (soybean-2, gluten-1)
Boiled sausage (boiled sausages with meat pieces)	20	4	1	1 (gluten)
Meat tins (chunk meat tins)	20	6	ND	1 (soybean)
Boiled sausages (liver sausages and pâté)	20	11	1	3 (soybean-2, gluten-1)
Fermented sausages	20	1	ND	0

ND – presence not detected

Table 2. Comparative analysis of soybean protein in meat product samples using the Tepnel and Agra Quant test kits.

Type of sample	Tepnel (%)	Agra Quant (ppb)
Boiled sausage (coarse ground boiled sausages)	4.7-5.6	>1000
Boiled sausage (boiled sausages with meat pieces)	8.4-9.6	>1000
Meat tins (chunk meat tins)	1.2-2	>1000
Boiled sausages (liver sausages and pâté)	6-5.9	>1000
Fermented sausages	1.2	>1000

Table 3. Comparative analysis of gluten in meat product samples using the Tepnel and Immunolab test kits.

Type of sample	Tepnel (ppm)	Immunolab (ppm)
Boiled sausage (coarse ground boiled sausages)	8-12	8-12
Boiled sausage (boiled sausages with meat pieces)	7.2	6
Meat tins (chunk meat tins)	ND	ND
Boiled sausages (liver sausages and pâté)	9.1	12
Fermented sausages	ND	ND

Out of the total of 100 samples of meat products, the presence of soybean was detected in 29% of samples, gluten in 4% of samples, while in 67% of samples, the presence of the mentioned allergens was not detected (Table 1). The detected concentration of soybean for the Tepnel kit ranged from 1.2%, to 9.6%, while the values detected by the Agra Quant kit were greater than the quantification range of 1000 ppb (Table 2). As regards gluten, both kits detected almost equal concentrations (Table 3). Out of the total of 27 samples of meat products, the declarations of which did not indicate that they contained soybean or gluten, 8 of them (29.6%) showed the presence of one or both of these allergens. These results were in accordance with previously published research [4,7].

Conclusion

- Both ELISA kits, Tepnel (determination of percentage of soybean protein in the tested samples) and Agra Quant (determination of significantly lower concentrations of soybean allergen), have shown excellent results within their performances, and thus they can be safely used in control of quality and health suitability of foodstuffs,
- Both ELISA kits used, Tepnel and Immunolab, meet all requirements of Codex Alimentarius according to their performances in view of concentration readings (gluten free and very low gluten), and no differences were found by their comparative analysis, and
- Our research has shown that the control of soybean protein and gluten presence in meat products is necessary, because the presence of these allergens was identified in 29.6% of retail meat products, but their presence was not indicated in the meat product declarations, which poses a high risk for consumers.

Acknowledgment

This study was supported by the Ministry of Education and Science of Serbia within Project III-46009.

Literature

- [1] M. Barać, S. Stanojević, S. Jovanović, M. Pešić, Soy Protein Modification - A Review, *Acta periodica technologica*, 2004, 35, 3-16.
- [2] Codex Alimentarius Commission, Report of the 25th session of the Codex Committee on nutrition and foods for special dietary uses, Alinorm 04/27/26, Bonn, Germany, 3-7 November, 2003.
- [3] Codex Alimentarius Commission: Draft revised standard for gluten-free foods, Step 8. <http://www.codexalimentarius.net/web/archives.jsp?year=08> webcite ALINORM 08/31/26 2008.
- [4] V. Janković Vesna, V. Matekalo Sverak, D. Vranić, B. Lakićević Brankica, R. Petronijević, Determination of gluten content in meat products. XIV International Symposium Feed technology-XII International Symposium NODA 2010, Novi Sad, Proceedings, 2010, 53-60.
- [5] K. Kulp, G. Joesph, in *Ponte Handbook of cereal science and technology*, Marcel Dekker, Technology and Engineering, 2000, 118-123.
- [6] J. Pokorná, Comparison of the Results of the ELISA, *Czech J. Food Sci.* 2011, 29(5), 471-479.
- [7] E. Renčová, B. Tremlová, ELISA for Detection of Soya Proteins in Meat Products *ACTA VET. BRNO*, 2009, 78, 667-671.

FREE TOPIC

STABLE ISOTOPE ANALYSIS USING CIRCULAR STATISTICAL METHODS: APPLICATIONS IN TEMPORAL ANALYSIS FOR DOUBLE WEIGHTED DATA

D. Golobočanin¹, N. Miljević²

¹*University of Belgrade, Vinca Institute for Nuclear Sciences, POB 522, 11001,
Belgrade, Serbia*

²*Jaroslav Černi Institute for Development of Water Resources, 80 Jaroslav Černi,
11223 Belgrade, Serbia*

Abstract

Circular data arise in a number of different areas such as geological, meteorological, and hydrological sciences. The new method was developed for analyzing double weighted time series. We have applied the new circular statistical method to 54 years monthly data assembled in Otava meteorological station. The obtained results have been compared with data computed with standard statistical methods. They were statistically significantly different on conventional p-level of 95%.

Introduction

Standard statistical techniques cannot be applied to analyze circular data. This is due to the circular geometry nature of the data space [1]. The sample mean of a data set on the circle is not the usual sample mean. Let $\alpha_1, \alpha_2, \dots, \alpha_n$ be independent observations on the unit circle, such that $0 \leq \alpha_j < 2\pi, j=1, 2, \dots, n$. The mean direction $\bar{\alpha}$ is not given by the simple arithmetic mean. For example if we imagine a circle divided on 360 parts then $(345^\circ + 15^\circ)/2 = 180^\circ$ but the line on 0° represents the true mean obtained by vector addition.

One of the more statistically tractable variable combinations, and one routinely found in the literature, is a case of linear dependent variable and circular independent variable [2]. Circular statistics are appropriate for analysis of data that are circular or directional in nature. For example, January (month 1) follows December (month 12). Arithmetic averaging of a group of numerical months or dates is not appropriate with conventional sample statistics because the counting system is circular not linear. In conducting the analysis of the seasonality of annual maxima or extreme storms, the Julian day of the year was used for describing the date of occurrence. The average day of occurrence is analogous to the arithmetic mean and the seasonality index is analogous to a standardized measure of variation. Specifically, values of the seasonality index range from zero to unity with values near zero indicating wide variation in the dates of occurrence. A seasonality index near unity indicates low variation in the dates of occurrence and strong clustering of dates [3]. Circular statistics for dates of occurrence using Julian day-of-year d_i are computed as follows: Conversion of Julian day-of-year to compass direction (ϕ_i):

$$\phi_i = 360 \cdot \frac{d_i}{d_{tot}} \quad (1)$$

There d_{tot} is a number of days in current year (365 or 366). Compute then vectors for compass direction:

$$S = \sum_{i=1}^n P_i \cdot \sin(\phi_i); \quad C = \sum_{i=1}^n P_i \cdot \cos(\phi_i) \quad \phi_2 = \arctg\left(\frac{S}{C}\right) \quad (2)$$

In our case P_i is amount of precipitation for d_i but can be any other dependent variable.

$$\bar{\phi} = \begin{cases} \phi_2 & \text{if } S > 0 \text{ and } C > 0 \\ \phi_2 + 180 & \text{if } C < 0 \\ \phi_2 + 360 & \text{if } S < 0 \text{ and } C > 0 \end{cases} \quad (3)$$

$$\bar{J} = \frac{d_{tot} \cdot \bar{\phi}}{360} \quad SI = \frac{\sqrt{S^2 + C^2}}{\sum_{i=1}^n P_i} \quad (4)$$

\bar{J} is a seasonal direction for weighted data and SI is a seasonality index. J_i is a day-of-year for given date of interest; d_{tot} is the total number of days in the current year; P_i is the data value for a given date (J_i), and n is the total number of data and date pairs.

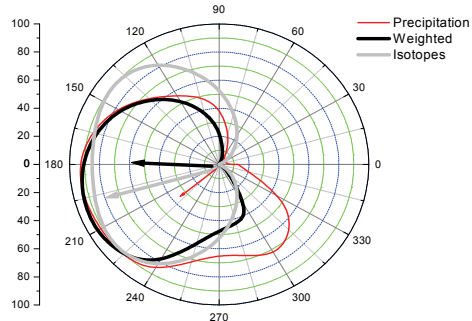
In observed case, we have two more obstacles. First, our P_i input data set is already weighted on oxygen-18 content [4]. Second, experimental isotope oxygen-18 content ($\delta^{18}O$) data set can be often negative. To avoid this we scaled isotopic data to percent scale.

$$P_i = \frac{P_i^{obs} \cdot \delta^{18}O}{\sum_{i=1}^n P_i^{obs}}; \quad \delta^{18}O = \frac{\delta^{18}O_{max}^{obs} - \delta^{18}O_{min}^{obs}}{\delta^{18}O_{max}^{obs} - \delta^{18}O_{min}^{obs}} \cdot 100 \quad (5)$$

Indeed we have weighted our data two times. Equations (5) are our improvement to estimation of \bar{J} and SI of weighted data.

Results and Discussion

We have applied described method to analyze 54 year data assembled from meteorological station Ottawa (1953-2007) [5]. We have calculated simple average for each month for precipitation and for $\delta^{18}O$ values during observed period. Then, we have calculated percent scaled isotopic data and weighted amount of precipitation following equations (5). The values for SI and \bar{J} were obtained following equation (4). These results are showed on Table 1. The angles and intensities were showed as vectors on Figure 1.



	\bar{J}	SI
Precipitation	229	0.14
Isotope content	180	0.21
Weighted	201	0.33

Figure 1. Circular percent diagram for precipitation, average weighted mean isotopic composition of the precipitation and isotopic content.

Conclusion

We have improved a Fisher algorithm for analyzing weighted time series. Circular statistics are appropriate for analysis of hydrological data that have circular nature. We calculate seasonal direction and seasonal index. Standard statistical approach is sensitive to numerate style. In our case results for seasonal direction obtained with both statistics (circular and standard) were statistically significantly different on conventional p-level of 95%. We will apply described method to monthly precipitation data and its $\delta^{18}O$ content for meteorological Station Zeleno Brdo (Belgrade).

References

1. N. I. Fisher, *Statistical Analysis of Circular Data*. Cambridge, University Press, 1995.
2. N. Fisher, A. Lee, *Journal of the Royal Statistical Society, Series B*, 1994, 56, 327-339.
3. S. Rao Jammalamadaka, A. SenGupta., *Topics in circular statistics*, World Scientific Publishing Co. Pte. Ltd., 2001.
4. N. Miljević, D. Golobočanin, N. Ogrinc, A. Bondžić, *Isotopes in Environmental and Health Studies*, 2008, 44, 137–148.
5. GNIP data base, <http://isohis.iaea.org>, Ottawa 1953–2007.

ENZYME-ASSISTED WATER EXTRACTION OF STINGING NETTLE LEAVES

V Rafajlovska^{1*}, S Sinadinović-Fišer², J Simonovska¹, O. Borota², M Janković²

¹*Faculty of Technology and Metallurgy, Ss. Cyril and Methodius University in Skopje, Macedonia*

²*Faculty of Technology, University of Novi Sad, Serbia*

Abstract

Stinging nettle leaves were subjected to an enzyme-assisted water extraction (EAWE) under following conditions: leaves-to-water ratio of 1:18, pH of 8.1, enzyme concentration of 0.9% and an extraction time of 3 hours at 50°C with constant stirring speed of 200 rpm. The yields of obtained pressed residue and extract were determined, as well as the contents of proteins, fats and mineral materials in both fractions. The amount of each measured constituent in extract (around 71% of each) was found to be higher than in the pressed residue. The results were compared with those of conventional extraction with water when, however, higher amounts of proteins (58.29%) and fats (52.87%) related to the total content in leaves remained in the pressed residue.

Introduction

Stinging nettle (*Urtica dioica* L., *Urticaceae*) is a native perennial plant widely used as herb in folk and contemporary medicine, as well as a traditional food. The flavonoids, chlorophylls and carotenoids, vitamins, proteins, mineral materials, organic acids, oil, sitosterols, tannins and other components determined in this plant leaves are the main contributors to the observed medicinal effect.

The limitations of the conventional water extraction regarding yield and stability of extracted components, may be exceeded by the application of an enzyme for the hydrolysis of the cell wall constituents. Therefore, developing of an enzyme assisted extraction is in expansion [1,2].

In order to impose the necessity of using an enzyme in the extraction of stinging nettle leaves with water, in this study the yields of pressed residue and extract, as well as the contents of proteins, fats and mineral materials in both fractions were determined when the enzyme *Alcalase 2.4 L* was used during the extraction with water and the results were compared with those obtained for conventional water extraction (WE).

Experimental

Materials. Leaves of stinging nettle, picked in Jun 2011 from the locality Andon Dukov (350 m altitude), Ohrid region, Macedonia, were dried for 15 days on mats in the shade and at room temperature, spread into thin layers. Before the extraction, leaves were dried in oven at 30°C for 8 h, then milled and sieved to a powder with particle size of 0.2 mm. Enzyme *Alcalase 2.4 L* Food Grade, with specific activity,

optimal pH and temperature values of the activity, of 2.4AU/g, 6.5-8.5 and 50-70°C, respectively, was provided by Novozymes A/S (Bagsvaerd, Denmark).

Chemical analysis. Content of dry matter and content of mineral materials were determined by AOAC methods 925.10 and 923.03, respectively. Content of proteins was calculated from the nitrogen content determined by Kjeldahl method using factor 6.25 (AOAC, 978.04). Content of fats was obtained by extraction using Grossfeld method [3]. Content of proteins in solution was determined using Lowry method [4] with Folin-Ciocalteu reagent by measuring the transmission at $\lambda = 750$ nm by Varian Cary Scan 50 spectrophotometer (Switzerland) in 1 cm quartz cells, at 25°C. The values of the soluble proteins content were estimated using the calibration curve $\log(\%T)=1.9838-0.5694C$ ($r^2=0.9622$) plotted for Bovine serum albumin (22% solution in distilled water) used as standard, where T is the transmission and C is the concentration of proteins expressed in g/L extract.

Extraction of stinging nettle leaves. Extractions were performed with modified procedures given by Dalev *et al.* [5]. The contents of dry matter, proteins, fats and mineral materials were determined in dry leaves and in obtained fractions.

Extraction with water. 50 g of grinded dried leaves was disintegrated in mixer with 300 mL distilled water for 3 min. The homogenous mass was transferred to the flask and 600 mL distilled water was added. After 3 h extraction at 50°C and with a stirring speed of 200 rpm the mixture was filtered through the Buchner funnel using water jet vacuum pump. Pressed residue and extract were separated.

Enzyme-assisted extraction. 50 g of grinded dried leaves was disintegrated in mixer with 300 mL distilled water for 3 min. After addition of 600 mL of distilled water (leaves-to-water ratio 1:18 w/v), the homogenous mass was transferred into the three neck flask and its pH was adjusted from 7.7 to 8.1 using 0.1 mol/L NaOH. Then, 8.4 mL of enzyme *Alcalase* 2.4 L (0.9% v/w) was added and the mixture was incubated at 50°C for 3 h with constant stirring speed of 200 rpm. After 3 h, pressed residue and extract were separated by filtering through the Buchner funnel using water jet vacuum pump.

Results and Discussion

The yields of pressed residue and extract and contents of proteins, fats and mineral materials in dry leaves and in fractions obtained with both water and enzyme-assisted water extraction of stinging nettle leaves are shown in Table 1.

In the stinging nettle leaves the content of dry matter of 91.24% was determined. The contents of proteins, fats and mineral materials related to the dry matter were 27.09%, 7.70% and 18.18%, respectively.

By employing the *Alcalase*, the content of dry matter that remained in the pressed residue was reduced about 1.8 times compared to water extraction, while the rest was transferred to the extract due to the enzymatic hydrolysis of the cell wall constituents. After enzyme-assisted extraction, also 1.9 times smaller amount of proteins, 1.8 times smaller amount of fats and 1.3 times smaller amount of mineral materials remained in the pressed residue than after conventional water

extraction. Hence, by extraction of stinging nettle leaves with enzymatic treatment the extract enriched in proteins, fats and mineral materials was yielded.

Table 1. Content of proteins, fats and mineral materials in dry stinging nettle leaves and in fractions obtained by water extraction of leaves without and with an enzyme treatment^a.

		Dry stinging nettle leaves	WE		EAWE	
			Pressed residue	Extract	Pressed residue	Extract
Yield	(%*1)	100.0	58.78	41.47	32.00	67.58
Proteins	(%*1)	27.09	26.86	94.27	25.27	28.38
	(%*2)	100.0	58.29	40.72	29.85	70.80
Fats	(%*1)	7.70	7.02	23.08	17.00	8.07
	(%*3)	100.0	52.87	47.10	29.15	70.77
Mineral materials	(%*1)	18.18	10.76	66.19	15.47	19.32
	(%*4)	100.0	34.78	66.21	27.23	71.86

^aThe values are expressed as percentage of: *1 - dry matter of fraction; *2 – total proteins; *3 - total fats; *4 - total mineral materials

Conclusions

The extractions of the stinging nettle leaves with both water and water in the presence of an enzyme, investigated in this study, are comparable in respect of the contents of proteins, fats and mineral materials distributed in-between the yielded fractions. Results of the enzyme-assisted extraction showed that the yield of the pressed residue was reduced in regard to those remained after the conventional extraction with water. Moreover, the extract obtained from stinging nettle leaves when the enzyme *Alcalase* 2.4 L was used during the extraction with water was enriched with all measured constituents i.e. with proteins, fats and mineral materials. Thus, the application of the enzyme-assisted extraction is beneficial from the aspect of production the extract with the high content of nutrients.

Acknowledgement

This work is part of the Project #III 45022 supported by the Ministry of Education and Science of the R. Serbia.

References

- [1] M. Pinelo, B. Zornoza, A.S. Meyer, Sep. Purif. Technol., 2008, **63**, 620-627.
- [2] E. Demirhan, D.K. Apar, B. Özbek, Korean J. Chem. Eng., 2011, **28**, 1 195-202.
- [3] J. Trajković, J. Baras, M. Mirić, S. Šiler, Analize Životnih Namirina, Tehnološko-metalurški fakultet, Beograd (1983), 95.
- [4] K. Wilson, J. Walker, Practical Biochemistry: Principles and Techniques Cambridge University Press, Cambridge, 2000, 320-321.
- [5] P. Dalev, A. Ljubomirova, I. Ivanov, Biotechnol. Lett., 1996, **18**, 1 107-110.

INDEX

		INDEX
Abazović N. D.	444	Borovic B. 775
Abu Rabi-Stanković A.	258, 318, 321	Bošnjaković-Pavlović N. 523
Aćimović D.	125	Bratić J. 709
Aćimović-Pavlović Z.	434	Brdarić T. P. 128, 748, 131
Adnađević B.	194, 197, 200	Budinski-Simendić J. 203, 406, 538
Adžić M.	361, 364, 367	Bulat T. 379, 382
Åke Jönsson J.	582	Bulatović D. 689
Aleksić J.	82, 85, 94	Cakić M. 695
Amić D.	128, 131	Cakić S. 535, 538
Anachkov M.	159	Cervelatti R. 285, 239
Andrić N.	630	Chanda S. 55
Anđelković T.	624, 698, 701	Cherkezova-Zheleva Z. 169
Anđelković D.	698, 701	Crisan D. 162
Anđelković K.	191	Cudina O. 576
Aničić-Urošević M.	660	Cvetičanin J. 125
Anić S.	218, 273, 297	Cvetinov M. 480, 606
Antić K.	397	Cvetković T. 698, 701
Antić V. V.	526	Cvijović M. 692
Antić-Jovanović A.	118	Cvjetičanin N. 453, 330
Antić-Stanković J.	686	Čomor M. I. 444, 465
Antonijević-Nikolić M.	686, 709	Čučulović A. 618
Aroguz A.	437	Čupić Ž. 247, 267, 270, 282
Arpacı O. T.	75	Čirić-Marjanović G. N. 520, 523
Atanasković D.	597	Čujić M. 645
Babić M.	397	Čurčić B. Lj. 760, 763
Bačić G.	391	Daković A. 657, 672
Balić R.	654	Damjanović S. 264
Baluja S.	52, 55	Demajo M. 352, 358
Banković P.	49, 321, 562	Deneva M. 159
Banjac N. R.	91	Deušić S. Đ. 712
Baranac-Stojanović M.	82, 85, 94	Di Carlo A. 324
Begović N.	218, 221	Dimić D. 197
Beljanski M. V.	261, 385	Dimitrić Marković J. M. 128, 131
Beljić Durković B.	194	Dimitrijević A. 185
Bera O.	437, 459, 553	Djajić T. 194
Berezin S.	40, 58	Djordjević J. 361
Bezbradica D.	185	Djulinčević B. V. 43
Bhalodia R.	52	Djurdjević P. 692
Bhesaniya K.	55	Dobricić V. 576
Bjelajac A. Z.	477	Dojčinović B. P. 766
Bjelović Z.	203	Dojčinović M. 751
Blagojević S.	270, 279, 678	Dostanić J. 468
Blagojević Sl.	270, 273, 291	Dragović R. 621
Blagojević V.	191, 324	Dragović S. 621, 645
Blagojević V.	474	Drakulić D. 373, 376
Bobin A.	4	Dramićanin M. 121, 412
Bogdanović-Pristov J.	745	Dučić T. 349
Bojić A. Lj.	315, 624, 627	Duncanson W. J. 570
Bojić D. V.	318, 624, 627	Džambaski Z. 82, 85, 94
Borota O.	46, 437, 788	Džunuzović J. V. 529, 532

INDEX

Đerić A.	288	Horvat A.	373, 376
Đikanović-Golubović D.	547	Horvatović M.	403
Đikanović D.	394	Hranisavljević S.	751
Đolić M.	621	Hrdlicka J.	8
Donlagić J.	526	Idakiev V.	162
Đorđević D. S.	100	Ignjatović A.	391
Đorđević J. S.	582	Ignjatović Lj.	651, 654
Đorđević M.	621, 728	Ignjatović N.	456
Đorović J.	128	Ilić D.	447, 541
Đukić A. B.	642	Ilić Lj.	695
Đurđević J.	115	İskeleli N.O.	75
Eber N.	480	Ivanović M. D.	88
Edreva-Kardjjeva R.	162	Ivanović-Šašić A.	49, 267, 321
Ekmešćić B.	206, 209	Ivković M.	134
Eliyas A.	159	Jakovljević D.	447, 541, 544
Etinski M.	109	Jakšić O.	669
Fedkin M. V.	715	Jakšić Z.	495, 669
Filipović D.	352, 355, 358	Jandrić D. R.	385
Filipović N.	450	Janković S.	775
Filipović V. S.	760, 763	Janković B. Ž.	639
Florou H.	645	Janković D.	588, 591, 594
Fodor-Csorba K.	480	Janković I.	412
Furrow S.	227, 285	Janković M.	46, 788, 437
Gabrovska M.	162, 172, 175	Janković M. M.	639, 648
Gaković B. M.	79	Janković V.	775, 779
Gaković B.	417	Janković-Mandić Lj.	621
Garab G.	547	Jelenković B.	498
Gavrilov N. M.	303	Jeremic M.	547
Gavrović-Jankulović M.	185	Jeremić S.	131
Gođevac D.	526	Jokić A. B.	121, 441
Gojgić-Cvijović G.	447, 541, 544	Jokić I.	669
Golobočanin D.	785	Jovanović A. P.	772
Gopčević K.	397	Jovanović D.	49, 159, 1721, 78
Gorjanović S.	333, 745	Jovanović J.	194, 197, 200
Gorodsky S. N.	233	Jovanović V.	406, 409, 663
Grbić B.	468, 471	Jovičić M.	203, 459, 553
Grbović-Novaković J. D.	642	Jović-Jovičić N.	49, 209, 258, 562
Greco E.	285	Jugović D.	441
Grković A.	191	Juranić I. O.	61, 88, 91
Grković I.	373, 376	Kačarević-Popović Z.	212, 550
Grozdić T.	312, 603, 615	Kalagasidis-Krušić M.	550
Grujić S. R.	215, 477	Kalamković S.	733, 736, 740
Gusev V.	3	Kaličanin B. M.	612
Hadač O.	236	Karaman I.	403
Halasi R.	740	Karlijković-Rajić K. D.	573
Halasi T.	736, 740, 733	Kekez B.	541
Hedrih K.	13	Kellner M.	492
Hegediš A.	403, 615	Keta O.	379, 382
Holclajtner-Antunović I.	523	Khakoo M. A.	118

INDEX

Kiurski J. S.	606	Marković D. M.	651
Kohout M.	236	Marković Z. S.	128
Kolar-Anić Lj.	264, 282, 669	Marković B. D.	573
Konstantinović Z.	428	Marković D.	206, 630, 654
Koprivica G. B.	763, 760	Marković G.	406, 409
Korićanac L.	379, 382	Marković J.	206, 501
Kosović M.	689	Marković J.	
Kostić I.	698, 701	Marković M.	594, 657, 672
Kostić M. M.	624	Marković R.	82, 85, 94
Kosyakov A.	40, 58, 704	Marković S.	115, 431
Kovačević J.	645	Marković V. M.	264, 267
Kovačević O. A.	704, 766	Marković Z.	67, 221, 131
Kozuki Y.	663	Matekalo Sverak V.	779
Kragović M.	657, 672	Matijašević S. D.	215, 477
Krajišnik D.	657	Matovic J.	492
Krasnoshchekov S. V.	112	Matović B.	403
Kritidis P.	7, 645	Matović Lj.	642
Krstić J.	169, 172, 175, 212, 606, 550	Medić M.	330
Krstić N. S.	612, 627	Mentus S.	303, 330, 453
Kuljanin-Jakovljević J.	428	Mesaroš G.	615
Kumrić K. R.	579, 582, 642	Meseldžija S.	474
Kuzmanoski M.	660	Mezentseva N.	4
Kuzmanović M.	79, 118	Micić D.	751
Laban B. B.	121	Mihailescu I. N.	417
Laher R. R.	118	Mijin D.	585
Lakić M.	588, 591, 594	Miladinović J. M.	43
Lakićević B.	779	Milanova M.	169
Lazić N.	437	Milenkovic N.	576
Leka Z.	689	Milenković A.	636, 675
Lević Lj.	757, 760, 763	Milenković D.	128, 131, 624
Lilić S.	779	Milenković M.	258, 276, 285
Liska R. T.	492	Milić J.	657
Lončarević D.	49, 172, 175	Milić S.	400, 745
Lučić B.	128, 131	Milikić J.	327
Lvov S. N.	715	Milojkovic D.	698, 701
Ljupković R. B.	315	Milosavić N.	185
Maćešić S.	264, 267, 285	Milošević I. R.	651, 654
Maksimov G. V.	261	Milošević M.	373
Maksimović J.	285, 288, 294	Milovanović M.	106
Maksin D.	206, 209, 462	Milović M.	441
Mandić M. M.	769, 772	Milutinović-Nikolić A.	49, 562, 462
Manojlović D.	523, 651, 654	Miljević N.	785
Manojlović N.	288	Miljković F. S.	188
Marinkovic M.	165	Minić D. G.	324
Marinović S.	258, 318, 462	Minić D. M.	191, 324, 474
Marinović-Cincović M.	406, 409, 535	Mirković M.	585, 591, 594
Mark M.	736	Misaelides P.	559, 633
Markovic B.	576	Mišljenović N. M.	760, 763
			795

INDEX

Mitic M.	367, 361, 364	Pastor F.	333
Mitić N. S.	385	Pašti I. A.	303
Mitić Ž.	456	Pavelkić V.	397, 748
Mitić Ž. J.	188, 695	Pavičević A.	391
Mitić-Culafić D. S.	769, 772	Pavličević J.	437, 459, 553
Mitov I.	169	Pavlovic M. S.	79
Mitraković D.	600, 603	Pavlović D.	698, 701
Mitrić M.	441	Pavlović L.	434
Mitrović A.	349	Pavlović M.	185, 285, 766
Mitrović J. Z.	318, 624, 627	Pavlović M. D.	385, 769, 772
Mitrović N.	373, 376	Pavlović M. S.	728
Miyoshi M.	663	Pejić N.	288, 291, 294
Mojović M.	391, 400	Pejin B.	403
Mojović Z.	258, 318, 321, 562	Pergal M. V.	526, 529, 532
Momcilovic M.	139	Perović G.	600, 603
Morina F.	400	Pervov V.	40
Morozova-Roche L.	339	Petković B. B.	683
Mudrinić T.	258, 318, 321	Petković M.	109, 397
Murić B.	498	Petrić S.	459
Mutavdžić D.	403	Petronijević R.	775, 779
Najman S.	456	Petrovic M.	748
Nastasijevic B.	692	Petrović D. S.	728
Nastasović A.	209, 462, 495	Petrović Đ. D.	585, 728
Naumov A.	40, 58	Petrović I.	379, 382
Nedeljković J.	428	Petrović J.	645
Nešković O.	125	Petrović M.	657, 728
Ničetin M. R.	760, 763	Petrović M. M.	318
Nikčević M.	615	Petrović S.	373, 417, 468, 471
Nikolaychuk P. A.	37	Petrović V.	370
Nikolic D.	775	Petrović Z.	115
Nikolic R.	701	Pezo L.	754, 760, 763
Nikolić J. D.	215, 639, 477	Pilić B.	203, 459, 535
Nikolić G. M.	188, 597, 695	Pokorni S. V.	61
Nikolić M.	403, 597	Polat K.	75
Nikolić N.	585, 591, 594	Poleti D.	191
Nikolić R. S.	612, 627	Popović A.	209
Nikolić Z. S.	486, 489, 483	Popović D. Ž.	43
Nikolova D.	162, 172, 175	Popović-Bijelić A.	391
Noli F.	633	Popović-Đorđević J. B.	88
Obadović D.	480, 606	Poręba R.	529
Odović J. V.	573	Potkonjak N. I.	279, 678
Onjia A.	206, 209, 621	Potkonjak T. N.	279
Oros I.	606	Premović P. I.	721, 724, 728
Ostojić B. D.	100	Privitera G.	382
Ostojić S.	751, 754, 766, 757	Prstić A.	434
Ostrovskii N. M.	151	Putanov P.	139
Pantelić D.	498	Radak B.	417
Pantelić G. K.	639	Radenović Č. N.	261
Papadopoulou L.	633	Radičević R.	203, 459, 553

INDEX

Radić N.	468, 471	Shum H. C.	570
Radojčić M.	361, 364, 367, 444	Sidey V.	58
Radonjić V.	182	Simendić V.	535
Radosavljević A.	212, 550	Simeonov D.	175
Radosavljević-Mihajlović A. S.	642	Simić I.	361, 364, 367
Radosavljević-Stevanović N. V.	612	Simonović B. R.	678, 751, 757
Radotić K.	349, 394, 403, 547	Simonović J.	394, 547
Radovanovic F.	420, 492, 495	Simonović M.	751
Radović M. D.	318, 624, 627	Simonovska J.	788
Radu C.	417	Sinadinović-Fišer S.	46, 437, 788
Radulovic N.	165	Skala D.	178, 182
Rafajlovska V.	46, 788	Skorodumova N. V.	310
Rajačić M. M.	639	Smičiklas I.	501, 636, 675
Rajkovic K.	748	Smiljanić S.	636
Rajšić S.	660	Sotiropoulou M.	645
Rakić A. A.	520, 523	Sovilj P.	121, 683
Rakočević Z.	125	Spasic A. M.	255
Rakovsky S.	159	Spasojević J.	212, 388, 550
Ranđelovic M.	139, 165	Spasov L.	172
Ranđelović D.	669	Spiric D.	775
Rankovic D. P.	79	Stanić M.	388, 609
Ristić I. S.	203, 5355, 38	Stanić V.	675
Ristić M. M.	109	Stanisavljev D.	258, 261, 276, 312
Ristić-Fira A.	382, 379	Stanković A.	431
Rodriguez-Santiago V.	715	Stanković B.	282
Rogić-Miladinović Z.	125	Stanković D.	585, 591, 594, 683
Roglić G.	651, 654	Stanković M.	175, 178, 182, 627
Rožić Lj.	468, 471	Stanojević A.	297
Sabo Lj.	588	Stanojlović M.	373, 376
Sabo T.	588	Stanojlović S.	704
Sadovskaya E.	4	Stefanov Pl.	172
Sadykov V.	4	Stefanovic S.	775
Salmén L.	394	Stefanović J.	541, 544
Samaržija-Jovanović S.	406, 409, 683	Stefanović J.	447
Sandić Z.	209	Steinbach G.	547
Santos D. M. F.	327	Stepanić V.	131
Sarap N.	291, 294, 648	Stepanov N. F.	112
Sarri S.	559, 633	Stevanic J.	394
Savic V.	576	Stevanović M.	450
Savić A.	349, 403, 588, 547	Stoiljkovic M. M.	79, 428
Savić T. D.	465	Stojadinović S.	468, 471
Savovic J. J.	79	Stojanović J. N.	215
Schmitz G.	227	Stojanović Lj.	103
Schreiber I.	236	Stojanović M.	82, 85, 94, 480
Sekulić Ž.	672	Stojanović Z.	431
Sequeira C. A. C.	327	Stojiljković D. T.	538
Shinagawa K. I.	483, 486, 489	Stojkovic N.	165
Shopska M.	178, 182	Stojković I.	330, 453

INDEX

Suručić Lj.	206	Vidojkovic S.	715
Sužnjević D.	333, 745	Vilotić D.	651
Šaponjić Z.	428	Vinić M.	134
Šećerov B.	412	Vitnik V. D.	61, 88, 91
Šljivić-Ivanović M.	501, 636, 675	Vitnik Ž. J.	61, 88, 91
Šljukić B.	327	Vladimirov S. M.	573, 576
Špírková M.	459, 529	Vladislavljević G. T.	570, 579, 582
Šumar Ristović M.	191	Vlajin D.	597
Šuput D.	757, 766, 772	Vodnik V.	121, 370, 532
Tanasković S. B.	709, 686	Vranješ M.	428
Tančić A. R.	97	Vranješ-Djurić S.	591, 594, 585
Tasić M.	660	Vrvić M.	447, 541, 544
Tenchev K.	162	Vučinić D. R.	712
Terzić A.	434	Vučković G.	686, 709
Todorović D.	379, 382	Vujačić A.	121
Todorović D. J.	639, 648	Vujković M.	330
Todorović D. M.	43, 507, 660	Vujković M.	453
Tomašević A. Đ.	712	Vukelić M.	456
Tošić M. B.	215, 477	Vukelić N.	175
Trabidou G.	645	Vukić N.	203
Trajanović M.	456	Vukojević V.	344
Traldi P.	692	Vuković Z.	182, 206
Trbojević J.	185	Vuković Z.	462
Trbojević-Stanković J. B.	573	Warchol J.	559
Trifunović S. R.	689	Weitz D. A.	570
Trpkov Đ.	125	Wesolowski D. J.	715
Trtica M.	417	Yamanaka R.	663
Trtić-Petrović T. M.	579, 582, 642	Zaharieva K.	169
Tsvetkov M.	169	Zakrzewska J.	388, 609
Tyurin A. G.	37	Zamboulis D.	559, 633
Ünver H.	75	Zamfirescu M.	417
Uskoković D.	431, 441, 450, 456	Zarubica A.	139, 165
Vajda A.	480	Zavrazhnov A.	40, 58
Valentić N. V.	91	Zeković I.	428
Validžić I. Lj.	465	Zildžović S. N.	215
Vasić M.	165, 474	Zlatanović S.	704, 754, 757, 766
Vasić D. D.	303	Zlatković J.	352, 355, 358
Vasić V.	121, 370	Zlomanov V.	58
Vasilčić R.	468, 471	Zvezdanovic J.	692
Vasiljević D.	498	Ždrale S. V.	477
Vasiljević P.	456	Živanović V. D.	215, 477
Vasiljević-Radović D.	526	Živić M.	388, 609
Velebit B.	779	Živković J. V.	597
Veličković D.	185	Živković-Radovanović V.	686, 709
Veljović Jovanović S.	400, 745	Žižić M.	388, 609
Vesce L.	324	Žunić M.	49, 462, 562
Veselinović A. M.	188, 654, 695		
Veselinović D.	618		
Veselinović Lj.	431		

CIP Volume I

CIP - Каталогизација у публикацији
Народна библиотека Србије, Београд

544(082)
621.35(082)
66.017/.018(082)

MEĐUNARODNA konferencija iz fundamentalne i
primenjene fizičke hemije (11 ; 2012 ;
Beograd)

Physical Chemistry 2012 : proceedings.
#Vol. #1 / 11th International Conference on
Fundamental and Applied Aspects of Physical
Chemistry, September 24-28, 2012, Belgrade ;
[editors S.[Slobodan] Anić and Ž.[Željko]
Čupić ; organized by Society of Physical
Chemists of Serbia ... et al.]. - Belgrade :
Society of Physical Chemists of Serbia, 2012
(Belgrade : Jovan). - VI, 498 str. : ilustr.
; 24 cm

"The Conference is dedicated to Professor
Ivan Draganić" --> nasl. str. - Tiraž 200. -
Bibliografija uz svaki rad.

ISBN 978-86-82475-27-9
1. Društvo fizikohemičara Srbije (Beograd)
a) Физичка хемија - Зборници b)
Електрохемијско инжењерство - Зборници c)
Наука о материјалима - Зборници
COBISS.SR-ID 193432332

CIP Volime II

CIP - Каталогизacija у публикацији
Народна библиотека Србије, Београд

544(082)
621.35(082)
66.017/.018(082)

MEĐUNARODNA konferencija iz fundamentalne i
primenjene fizičke hemije (11 ; 2012 ;
Beograd)

Physical Chemistry 2012 : proceedings.
#Vol. #2 / 11th International Conference on
Fundamental and Applied Aspects of Physical
Chemistry, September 24-28, 2012, Belgrade ;
[editors S.[Slobodan] Anić and Ž.[Željko]
Čupić ; organized by Society of Physical
Chemists of Serbia ... et al.]. - Belgrade :
Society of Physical Chemists of Serbia, 2012
(Belgrade : Jovan). - VI str., 499-782 str. :
ilustr. ; 24 cm

"The Conference is dedicated to Professor
Ivan Draganić" --> nasl. str. - Tiraž 200. -
Bibliografija uz svaki rad. - Registar.

ISBN 978-86-82475-28-6
1. Društvo fizikohemičara Srbije (Beograd)
a) Физичка хемија - Зборници b)
Електрохемијско инжењерство - Зборници c)
Наука о материјалима - Зборници
COBISS.SR-ID 193433356